D. C. Mosher · R. C. Shipp · L. Moscardelli · J. D. Chaytor ·
C. D. P. Baxter · H. J. Lee · R. Urgeles (Eds.)

Submarine Mass Movements and Their Consequences

with CD-ROM

Springer

Submarine Mass Movements and Their Consequences

Advances in Natural and Technological Hazards Research

Volume 28

David C. Mosher · R. Craig Shipp
Lorena Moscardelli · Jason D. Chaytor
Christopher D.P. Baxter · Homa J. Lee
Roger Urgeles
Editors

Submarine Mass Movements and Their Consequences

4th International Symposium

Springer

David C. Mosher
Natural Resources Canada
Dartmouth, NS, Canada
dmosher@nrcan.gc.ca

Lorena Moscardelli
University of Texas at
Austin, TX, USA
lorena.moscardelli@beg.utexas.edu

Christopher D.P. Baxter
University of Rhode Island,
Narragansett, RI, USA
baxter@egr.uri.edu

Roger Urgeles
Institute of Marine Sciences,
Spanish National Research Council (CSIC)
urgeles@icm.csic.es

R. Craig Shipp
Shell International
Exploration and Production
Inc., Houston, TX, USA
Craig.Shipp@shell.com

Jason D. Chaytor
Woods Hole Oceanographic
Institution, Woods Hole,
MA, USA
jchaytor@usgs.gov

Homa J. Lee
United States Geological
Survey, Menlo Park, CA,
USA
hlee@usgs.gov

Dedication

<div align="center">

William R. Normark   *Bruno Savoye*
1943–2008   *1959–2008*

</div>

This book, "Submarine Mass Movements and Their Consequences IV", is dedicated to the memory of two colleagues whose wide-ranging field studies did so much to advance our understanding of deep-water sedimentation systems: Drs. Bill Normark and Bruno Savoye. I had the good fortune to count them among my closest professional and personal friends. Both were sea-going scientists *par excellence*, both were warm and supportive individuals, who always had time for students, and both were modest about their own accomplishments.

Although many will remember Bill for his work on turbidites and submarine fans, he made important early contributions to our understanding of submarine mass movements. Large slides are a significant component of deep-water terrigenous basins and thus did not escape Bill's curiosity. In 1968, during his Ph.D. work, he acquired seabed imagery and sub-bottom profiles with the Scripps deep-tow system over Ranger slide off Baja California. His 1974 and 1990 papers on this slide are classic Normark: meticulous use of multiple data sets and a clear mind as to what were the important issues. As Chief Scientist of the GLORIA cruise that mapped the seafloor around the Hawaiian islands, he was the first to appreciate the full extent of the flank-collapse debris avalanches, using the terms "prodigious" and "humongous" in the literature (and "giant" when reined in by editors).

Likewise, Bruno is remembered by many for his work on turbidite systems, but he too worked on submarine slides, particularly earlier in his career. The first paper that he and I worked on together described a slide near the wreck of the *Titanic*, where his colleagues at IFREMER had collected a magnificent survey with the next generation of deep-tow technology, the IFREMER SAR, but just missed the wreck. He is well known for his contributions on the 1979 Nice landslide, which triggered both a tsunami and a turbidity current. Bruno brought his enthusiasm and energy, together with his organisational and analytical skills as an engineer, to the science of turbidites and mass movements. He combined the technological expertise OF IFREMER, industry funding and his own instinct of what was necessary to make significant scientific advances at sea.

Mass movements are an important part of the turbidite story. For Bill and Bruno, during much of their careers, mass movements were regarded as the predominant cause of turbidity currents. Both played an important role in challenging that dogma in recent years. Those who study mass movements from the comfort of the seismic work-station or by numerical modelling owe a lot to seagoing scientists like Bruno and Bill who laid the groundwork of where, why and how submarine mass-movements occur in the field.

<div align="right">

David J.W. Piper
Halifax, June 2009

</div>

Contents

SECTION II SUBMARINE MASS MOVEMENTS: CASE STUDIES AND HAZARD ASSESSMENT

SECTION III SUBMARINE MASS MOVEMENTS IN MARGIN CONSTRUCTION AND ECONOMIC SIGNIFICANCE

SECTION IV   SUBMARINE MASS MOVEMENTS AND TSUNAMIS

CD-ROM enclosed

Contributors

V. Abreu
ExxonMobil, Houston, TX, USA

J. Adamy
TOTAL, Paris La Défense, France

N. Albuquerque
Universidade Federal Fluminense, Departamento de Geologia, Av. Gen. Milton Tavares de Souza, s.n., Niterói, RJ, CEP: 24210–346, Brazil

C.R. Alexander
Skidaway Institute of Oceanography, Savannah, GA, USA

M. Angell
Fugro (William Lettis & Associates, Inc.), 1777 Botelho Drive, Suite 262, Walnut Creek, CA 94598, USA

E. Araújo
Universidade Federal Fluminense, Departamento de Geologia, Av. Gen. Milton Tavares de Souza, s.n., Niterói, RJ, CEP: 24210–346, Brazil

L.B. Ashabranner
Shell International E & P Inc. 200 N. Dairy Ashford, Houston, TX 77079, USA

M.V. Avolio
Department of Mathematics, University of Calabria, Arcavacata, 87036 Rende (CS), Italy

N. Babonneau
UBO-IUEM, CNRS UMR6538 Domaines Océaniques, 29280 Plouzané, France

L. Baise
Tufts University, Dept of Civil and Envir Eng, 200 College Ave, Anderson Hall, Rm 113, Medford, MA 02155, USA

J.P. Barry
Monterey Bay Aquarium Research Institute, Moss Landing, CA 95039-9644, USA

C. Basile
Laboratoire de Géodynamique des Chaînes Alpines, UMR-CNRS 5025,
Observatoire des Sciences de l'Univers de Grenoble, Université Joseph Fourier,
Maison des Géosciences, 1381 rue de la Piscine, 38400 St. Martin d'Hères, France

R.T. Beaubouef
Hess Corporation, Houston, TX, USA

A. Bertagnini
Istituto Nazionale di Geofisica e Vulcanologia, Sezione di Pisa, Via della Faggiola,
32 – 56126 Pisa, Italy

J. Benkhelil
IMAGES, University of Perpignan Via Domitia, Perpignan 66860 Cedex, France

N.T.T. Binh
Durham University, Department of Earth Sciences, Science Labs,
Durham DH1 3LE, UK

J. Blees
Alfred Wegener Institute for Polar and Marine Research,
27570 Bremerhaven, Germany
Present address: University of Basel, 4056 Basel, Switzerland

R. Boyd
ConocoPhillips, Houston and University of Newcastle, Australia

F. Bozzano
Dipartimento di Scienze della Terra, Università di Roma "Sapienza",
P.le Aldo Moro 5, 00185 Roma, Italy

A.S. Bradshaw
Merrimack College, North Andover, MA 01845, USA

S. Bull
Cardiff University, 3D Lab, School of Earth, Ocean and Planetary Sciences,
Main Building, Park Place Cardiff CF10 3YE, UK

K.C. Burmeister
University of the Pacific, Department of Geosciences, 3601, Pacific Avenue,
Stockton, California 95211, USA

A. Camerlenghi
ICREA, Istitució Catalana de Recerca i Estudis Avançats, Barcelona, Spain;
Departament d'Estratigrafia, Paleontologia i Geociències Marines, Facultat de
Geologia, Universitat de Barcelona, C/Martí i Franquès, s/n, E-08028 Barcelona,
Spain

D.C. Campbell
Geological Survey of Canada, Natural Resources Canada, Bedford Institute
of Oceanography, 1 Challenger Dr., Dartmouth, NS, Canada, B2Y 4A2;
Department of Earth Sciences, Dalhousie University, Halifax, Nova Scotia,
Canada, B3H 4R2

F. Carol
Laboratoire IMAGES – E.A. 4218, Université de Perpignan Via Domitia,
52 Avenue Paul Alduy, 66860 Perpignan Cedex, France

J. Cartwright
Cardiff University, 3D Lab, School of Earth, Ocean and Planetary Sciences,
Main Building, Park Place Cardiff CF10 3YE, UK

A. Cattaneo
IFREMER, Géosciences Marines, Laboratoire Environnements Sédimentaires,
Plouzané, France

G. Cauchon-Voyer
Laboratoire d'études sur les risques naturels,
Département de géologie et de génie géologique, Université Laval,
Québec, Qc, Canada, G1K 7P4

E. Chapron
Université d'Orléans, CNRS/INSU, Université François Rabelais-Tours,
Institut des Sciences de la Terre d'Orléans (ISTO)-UMR 6113,
1A rue de la Férollerie, F-45071 Orléans cedex 2, France

D.W. Caress
Monterey Bay Aquarium Research Institute, Moss Landing, CA 95039-9644, USA

J.D. Chaytor
United States Geological Survey, Woods Hole Science Center,
384 Woods Hole Rd., Woods Hole, MA 02543, USA

J.Y. Cheon
The University of Texas at Austin, Department of Civil, Architectural
and Environmental Engineering, Geotechnical Engineering Program,
1 University Station, C1792, Austin, Texas 78712-0280, USA

M. Clare
Fugro GeoConsulting Limited, Engineering Geology and Geohazards Team,
Fugro House, Hithercroft Road, Wallingford, Oxfordshire, OX10 9RB, UK

B.T. Cronin
Deep Marine, 9 North Square, Footdee, Aberdeen, AB11 5DX, UK

J.E. Damuth
Department of Earth and Environmental Sciences, University of Texas,
500 Yates St., 107 Geoscience Bldg., Arlington, TX 76019, USA

G. Dan
Université de Brest; CNRS, UMR 6538 Domaines Océaniques; Institut
Universitaire Européen de la Mer, Place Copernic, 29280 Plouzané, France;
FUGRO FRANCE S.A.S, 27 Rue des Peupliers, 92752, Nanterre, France;
IFREMER, Géosciences Marines, Laboratoire Environnements Sédimentaires,
Plouzané, France

S. Day
Aon Benfield UCL Hazard Research Centre, Department of Earth Sciences,
University College London, Gower Street, London WC1E 6BT, UK

F.V. De Blasio
Department of Geosciences, University of Oslo/ P.O. Box 1047 Blindern,
N-0316 Oslo, Norway & International Centre of Geohazards,
P.O. Box 3930 Ulleval Stadion, N-0806 Oslo, Norway

B. Dennielou
IFREMER – French Research Institute for Exploitation of the Sea,
Département des Géosciences Marines, PO box 70, 29280
Plouzané Cédex, France

M.E. Deptuck
Canada-Nova Scotia Offshore Petroleum Board, 1791 Barrington St, Halifax,
NS, B2Y 4A2, B.M. de Lépinay   UMR6526 CNRS Géosciences Azur, Valbonne,
France

J. Déverchère
UBO-IUEM, CNRS UMR6538 Domaines Océaniques, 29280 Plouzané, France

F. Dias
Centre de Mathématiques et de Leurs Applications, Ecole Normale Supérieure
de Cachan and CNRS, France

V. Díaz-del-Río
Instituto Español de Oceanografia, Centro Oceanográfico de Málaga,
Puerto Pesquero, s/n. Apdo. 285, 29640 Fuengirola (Málaga), Spain

S. Di Gregorio
Department of Mathematics, University of Calabria, Arcavacata, 87036 Rende
(CS), Italy

A. Di Roberto
Istituto Nazionale di Geofisica e Vulcanologia, Sezione di Pisa,
Via della Faggiola, 32 – 56126 Pisa, Italy

A. Domzig
Midland Valley Exploration, Glasgow, UK   L.Droz UMR-CNRS 6538, IUEM,
Place Nicolas Copernic, 29280 Plouzané, France

B. Dugan
Rice University, Department of Earth Science, 6100 Main Street, Houston,
Texas 77005, USA

P. Durán-Muñoz
Instituto Español de Oceanografía, Centro Oceanográfi co de Vigo,
Cabo Estay-Canido, Apdo. 1552, 36200 Vigo (Pontevedra), Spain

N. Exon
Department of Earth and Marine Sciences, Australian National University,
ACT 0200, Australia

L. Fantoni
Dipartimento di Scienze della Terra, Università di Modena
e Reggio Emilia, Via S. Eufemia, 19, 41100 Modena, Italy

M.D. Ferentinou
School of Rural and Surveying Engineering, Laboratory of Structural Mechanics,
National Technical University of Athens, 15780 Zografou, Greece

L.-M. Fernández-Salas
Instituto Español de Oceanografia, Centro Oceanográfico de Málaga,
Puerto Pesquero, s/n. Apdo. 285, 29640, Fuengirola (Málaga), Spain

P.B. Flemings
University of Texas at Austin, Jackson School of Geosciences,
1 University Station C1100, Austin, TX 78712-0254, USA

L. Folens
Laboratoire Géosystèmes, UMR 8157, Université des Sciences et Technologies de
Lille 1, Cité Scientifique, Bâtiment SN5, 59655 Villeneuve d'Ascq Cedex, France

A. Förster
MARUM- Center for Marine Environmental Sciences, University of Bremen,
Leobener Straße, PO box 330440, 28334 Bremen, Germany

J. Frey-Martínez
Repsol-YPF, Repsol Oil Operations Libya (Akakus), Airport Road,
Tripoli, Libya

H.M. Fritz
School of Civil and Environmental Engineering, Georgia Institute of Technology,
210 Technology Circle, Savannah, GA 31407, USA

K. Fujino
Kyushu University, 10–1 Hakozaki, Higashi-ku, Fukuoka
812–8581, Japan

F. Gamberi
Istituto di Scienze Marine – CNR, Sede di Geologia Marina di Bologna,
Via Gobetti 101 – 40129 Bologna, Italy

J. Gardner
CCOM, University of New Hampshire, USA

S. Garziglia
IFREMER, BP 70, 29280 Plouzané Cedex, France

V. Gaullier
Laboratoire IMAGES – E.A. 4218, Université de Perpignan Via Domitia,
52 Avenue Paul Alduy, 66860 Perpignan Cedex, France

W.H. Geissler
Alfred Wegener Institute for Polar and Marine Research, Bremerhaven, Germany

Eric L. Geist
U.S. Geological Survey, 345 Middlefield Road, MS 999.
Menlo Park, CA 94025, USA

R.B. Gilbert
The University of Texas at Austin, Department of Civil, Architectural
and Environmental Engineering, Geotechnical Engineering Program,
1 University Station, C1792, Austin, Texas 78712-0280, USA

M.K. Giles
Department of Earth Sciences, Dalhousie University,
Halifax, N.S., Canada, B3H 4J1

G. Gisler
Physics of Geological Processes, University of Oslo, PO Box 1048 Blindern,
0316 Oslo, Norway

M. Gittings
Science Applications International, 3900 North Ocean Dr, #11A,
Lauderdale by the Sea, Florida 33308, USA

R. Givler
Fugro (William Lettis & Associates, Inc.), 1777 Botelho Drive, Suite 262,
Walnut Creek, CA 94598, USA

K. Glenn
Geoscience Australia, Canberra, Australia

C. Gorini
Université Pierre & Marie Curie, Paris VI,.Laboratoire de Tectonique et
Modélisation des Bassins Sédimentaires, UMR 7072, Place Jussieu,
Case 117 tour 46–00, 75252 Paris, Cedex 05, France

Jocelyn L.H. Grozic
Department of Civil Engineering, University of Calgary, ENF 262,
2500 University Dr NW, Calgary, Alberta, Canada, T2N 1N4

P.J. Haeussler
U.S. Geological Survey, Anchorage, AK, USA

T. Hasiotis
Department of Marine Sciences, University of the Aegean, University Hill,
81100 Mytilene, Lesvos, Greece

R. Henrich
University of Bremen, Faculty of Geosciences and MARUM,
PO Box 330 440, 28334 Bremen, Germany

K. Hitchen
British Geological Survey, West Mains Road, Edinburgh, EH9 3LA, UK

C. Hitchcock
Fugro (William Lettis & Associates, Inc.), 1777 Botelho Drive, Suite 262,
Walnut Creek, CA 94598, USA

K. Høeg
Department of Geosciences, University of Oslo, P.O. Box 1047 Blindern,
NO-0316 Oslo, Norway; International Centre for Geohazards (ICG),
Sognsveien 72, 0855, Oslo, Norway

J. Hooper
Fugro GeoConsulting Limited, Engineering Geology and Geohazards Team,
Fugro House, Hithercroft Road, Wallingford, Oxfordshire, OX10 9RB, UK

M. Hornbach
Institute for Geophysics, Jackson School of Geosciences, The University of Texas
at Austin, TX, USA

T. Hubble
University of Sydney, Australia

C. Hübscher
Institut für Geophysik, Universität Hamburg, Bundesstraße 55, 20146 Hamburg,
Germany

K. Huhn
MARUM – Center for Marine Environmental Sciences, University
of Bremen, PO box 330 440, D-28334, Bremen, Germany

T.J. Huppertz
University of Bremen, Faculty of Geosciences, FB 5 Klagenfurter Strasse 28359
Bremen, Germany

K. Jenner
Geological Survey of Canada, Natural Resources Canada,
Bedford Institute of Oceanography, 1 Challenger Drive, Dartmouth,
Nova Scotia, B2Y 4A2, Canada

J.E. Johnson
University of New Hampshire, Durham, NH 03824, USA

T. Kanamatsu
IFREE1, Japan Agency for Marine Science and Technology,
2–15 Natsushima-cho, Yokosuka, Kanagawa 237–0061, Japan

S. Kasten
Alfred Wegener Institute for Polar and Marine Research, 27570 Bremerhaven,
Germany

K. Kawamura
Fukada Geological Institute, 2–13–12 Hon-Komagome, Bunkyo,
Tokyo 113–0021, Japan

R.E. Kayen
U.S. Geological Survey, 345 Middlefield Rd., MS 999,
Menlo Park, CA, USA

J. Keene
University of Sydney, Australia

K.L. Kendell
Canada-Nova Scotia Offshore Petroleum Board, 1791 Barrington St, Halifax,
NS, Canada B2Y 4A2

S. Ker
IFREMER, BP 70, 29280 Plouzané Cedex, France

M. Kinoshita
IFREE1, Japan Agency for Marine Science and Technology,
2–15 Natsushima-cho, Yokosuka, Kanagawa 237–0061, Japan

I. Kock
MARUM – Center for Marine Environmental Sciences, University of Bremen,
PO box 330 440, D-28334, Bremen, Germany

A. Kopf
MARUM – Center for Marine Environmental Sciences
and Faculty of Geosciences, University Bremen, Leobener Str., 28334 Bremen,
Germany

S. Kreiter
MARUM – Center for Marine Environmental Sciences and Faculty
of Geosciences, University Bremen, Leobener Str. 28334 Bremen, Germany

P. Lajeunesse
Université Laval, Centre d'études nordiques & Département de géographie,
Québec, QC, Canada G1V 0A6

M. Lange
MARUM – Center for Marine Environmental Sciences
and Faculty of Geosciences, University Bremen, Leobener Str., MARUM,
28334 Bremen, Germany

T. Langford
NGI, P.O. Box 3930 Ullevål Stadion, NO-0806 Oslo, Norway

P. Lauzière
Iron Ore Company of Canada, Environment Department,
P.O. Box 10000, Labrador City, NL, Canada A2V 2L8

C. Lavoie
Department of Geosciences, Hamilton College, Clinton, New York, 13323 USA

T.P. Le Bas
National Oceanography Centre, Southampton, European Way, Southampton,
SO14 3ZH, UK

I. Lecomte
NORSAR/ICG, P.O. Box 53, N-2027 Kjeller, Norway

G. Ledoux
Université Laval, Centre d'études nordiques & Département
de géographie, Québec, QC, Canada G1V 0A6

H.J. Lee
U.S. Geological Survey, 345 Middlefield Rd., MS 999, Menlo Park, CA, USA

B. Lepillier
Ifremer, GM-LES, BP 70, 29280 Plouzané, France pres. add. TOTAL, Stavanger,
Norway

J. Locat
Université Laval, Dept. of Geology and Geological Engineering, Québec,
 Canada G1K 7P4

L. Loncke
Laboratoire IMAGES – E.A. 4218, Université de Perpignan Via Domitia,
52 Avenue Paul Alduy, 66860 Perpignan Cedex, France

D. Long
British Geological Survey, West Mains Road, Edinburgh, EH9 3LA, UK

O. Longva
NGU/ICG, 7491 Trondheim, Leiv Eirikssons vei 39, Trondheim, Norway

N. López-González
Instituto Español de Oceanografia, Centro Oceanográfico de Málaga,
Puerto Pesquero, s/n. Apdo. 285, 29640 Fuengirola (Málaga), Spain

B. Loubrieu
IFREMER, Géosciences Marines, BP70, 29280 Plouzané, France

E. Lundsten
Monterey Bay Aquarium Research Institute, Moss Landing,
CA 95039-9644, USA

V. Lupiano
Department of Earth Sciences, University of Calabria, Arcavacata,
87036 Rende (CS), Italy

P. Lynett
Texas A&M University, College Station, TX 77843, USA

B. Mackenzie
Fugro GeoConsulting Limited, Fugro House, Hithercroft Road, Wallingford,
Oxfordshire, OX10 9RB, UK

A. Maillard
LMTG, Université UPS (SVT-OMP), 14 Avenue Edouard Belin, 31400 Toulouse,
France

J.D.G. Marr
National Center for Earth-Surface Dynamics, St. Anthony Falls Laboratory,
Minneapolis, MN, USA

M.P. Marani
Istituto di Scienze Marine – CNR, Sede di Geologia Marina di Bologna,
Via Gobetti 101 – 40129 Bologna, Italy

B. Marsset
IFREMER, BP 70, 29280 Plouzané Cedex, France

M. Maslin
Environmental Change Research Centre, Department of Geography,
College London, Gower Street, London WC1E 6BT, UK

D.G. Masson
National Oceanography Centre, Southampton, European Way, Southampton,
SO14 3ZH, UK

P. Mazzanti
Dipartimento di Scienze della Terra, Università di Roma "Sapienza",
P.le Aldo Moro 5, 00185 Roma, Italy

B. McAdoo
Vassar College, Dept of Earth Sci and Geog, Poughkeepsie, NY 12604, USA

M. McGann
U.S. Geological Survey, Menlo Park, CA 94025, USA

F. Mohammed
School of Civil and Environmental Engineering, Georgia Institute of Technology,
210 Technology Circle, Savannah, GA 31407, USA

L. Moscardelli
Bureau of Economic Geology, Jackson School of Geosciences, The University
of Texas at Austin, TX, USA

E.C. Morgan
Tufts University, Dept of Civil and Envir Eng, 200 College Ave, Anderson Hall,
Rm 113, Medford MA 02155, USA

D.C. Mosher
Geological Survey of Canada, Natural Resources Canada
Bedford Institute of Oceanography, 1 Challenger Drive, Dartmouth, Nova Scotia,
B2Y 4A2, Canada

A. Misawa
Tokai University; 3–20–1 Orido, Shimizu, Shizuoka 424–8610, Japan

T. Moerz
MARUM – Center for Marine Environmental Sciences and Faculty
of Geosciences, University Bremen, Leobener Str., 28334 Bremen, Germany

F. Niessen
Alfred Wegener Institute for Polar and Marine Research, Bremerhaven, Germany

M.C. Nodine
GEI Consultants, Inc.,1790 38th St. #103, Boulder, CO 80302, USA

A. Nouguès
Institut Polytechnique LaSalle Beauvais, Département Géosciences, Beauvais,
France; FUGRO FRANCE S.A.S., Nanterre, France

H.C. Olson
Institute for Geophysics, Jackson School of Geosciences, The University of Texas,
10100 Burnet Rd., Bldg. 196 (ROC), Austin, TX 78758, USA

D. Otto
MARUM – Center for Marine Environmental Sciences
and Faculty of Geosciences, University Bremen, Leobener Str., 28334 Bremen,
Germany

M. Owen
Environmental Change Research Centre, Department of Geography,
College London, Gower Street, London WC1E 6BT, UK

G. Parker
Ven Te Chow Hydrosystems Lab, Department of Civil Engineering,
College of Engineering, University of Illinois at Urbana-Champaign,
IL 61802, USA

T. Parsons
U.S. Geological Survey, 345 Middlefield Road, MS 999. Menlo Park,
CA 94025, USA

M. Patriat
IFREMER, Géosciences Marines, BP70, 29280 Plouzané, France

C.K. Paull
Monterey Bay Aquarium Research Institute, Moss Landing,
CA 95039-9644, USA

S. Perkins
Montana State University, 205 Cobleigh Hall, Bozeman
MT 59717, USA

R. Perovano
Universidade Federal Fluminense, Departamento de Geologia, Av. Gen. Milton
Tavares de Souza, s.n., Niterói, RJ, CEP: 24210–346, Brazil

D.J.W. Piper
Geological Survey of Canada, Natural Resources Canada Bedford
Institute of Oceanography, 1 Challenger Drive, Dartmouth,
Nova Scotia, B2Y 4A2, Canada

C. Pirmez
Shell International E and P., Houston, TX, USA

R. Poncet
Centre de Mathématiques et de Leurs Applications, Ecole Normale Supérieure
de Cachan and CNRS, France

A.T. Reis
Universidade do Estado do Rio de Janeiro, Faculdade de Oceanografia,
Rua São Francisco Xavier, 524, 4° Andar, bl E, Rio de Janeiro/RJ.
CEP: 20.550–013, Brazil

V. Riboulot
IFREMER, BP 70, 29280 Plouzané Cedex, France

J.R. Rice
School of Engineering and Applied Sciences (also, for JRR,
Department of Earth and Planetary Sciences), Harvard University,
29 Oxford St., Cambridge, MA 02138, USA

W.R. Roest
IFREMER, Géosciences Marines, BP70, 29280 Plouzané, France

G.A. Romero-Otero
Conoco Phillips School of Geology and Geophysics,
The University of Oklahoma, Norman, OK, USA

M. Rosi
University of Pisa, Dipartimento di Scienze della Terra, Via S. Maria,
53 – 56126 Pisa, Italy

D. Rugg
University of Texas at Austin, Austin, Texas, USA

K. Ruming
NSW Department of Primary Industries, Maitland, Australia

D. Rushton
Fugro GeoConsulting Limited, Fugro House, Hithercroft Road, Wallingford,
Oxfordshire, OX10 9RB, UK

H.F. Ryan
U.S. Geological Survey, 345 Middlefield Rd., MS 999, Menlo Park, CA, USA

S. Saito
IFREE1, Japan Agency for Marine Science and Technology,
2–15 Natsushima-cho, Yokosuka, Kanagawa 237–0061, Japan

M.G. Sakellariou
School of Rural and Surveying Engineering, Laboratory of Structural Mechanics,
National Technical University of Athens, 15780 Zografou, Greece

D.E. Sawyer
University of Texas at Austin, Jackson School of Geosciences,
1 University Station C1100, Austin, TX 78712-0254, USA

M. Sayago-Gil
Instituto Español de Oceanografia, Centro Oceanográfico de Málaga, Puerto Pesquero, s/n. Apdo. 285, 29640 Fuengirola (Málaga), Spain

B. Schlining
Monterey Bay Aquarium Research Institute, Moss Landing, CA 95039-9644, USA

B.F. Schlue
ARCADIS Consult GmbH, Europaplatz, 3, 64293 Darmstadt, Germany

W. Schunn
MARUM – Center for Marine Environmental Sciences and Faculty of Geosciences, University, Bremen, Leobener Str., 28334 Bremen, Germany

T. Shibata
Kochi University, 2–5–1 Akebono-cho, Kochi 780–8520, Japan

J. Shimeld
Geological Survey of Canada, Natural Resources Canada Bedford, Institute of Oceanography, 1 Challenger Dr., Dartmouth, NS, Canada, B2Y 4A2

R.C. Shipp
Shell International E & P Inc. 200 N. Dairy Ashford, Houston, TX 77079, USA

G. Si
Department of Geosciences, University of Oslo, P.O. Box 1047 Blindern, NO-0316 Oslo, Norway

C.G. Silva
Universidade Federal Fluminense, Departamento de Geologia, Av. Gen. Milton Tavares de Souza, s.n., Niterói, RJ, CEP: 24210–346, Brazil

P. Simpkin
IKB Technologies Limited, 1220 Hammonds Plains Road, Bedford, Nova Scotia, Canada B4B 1B4

R.M. Slatt
Conoco Phillips School of Geology and Geophysics, The University of Oklahoma, Norman, OK, USA

B.M. Smith
Canada-Nova Scotia Offshore Petroleum Board, 1791 Barrington St, Halifax, NS, Canada B2Y 4A2

V. Spieß
MARUM- Center for Marine Environmental Sciences, University of Bremen, Leobener Straße, PO box 330440, 28334 Bremen, Germany

R. Stein
Alfred Wegener Institute for Polar and Marine Research, Bremerhaven, Germany

C.J. Stevenson
National Oceanography Centre, Southampton, European Way, Southampton,
SO14 3ZH, UK

J. Stigall
Department of Earth Science, Rice University, 6100 Main Street, MS 126,
Houston, TX 77005, USA

G. St-Onge
Université du Québec à Rimouski, Institut des sciences de la mer de Rimouski
(ISMER), Rimouski, QC, Canada, G5L 3A1

M. Strasser
MARUM – Center for Marine Environmental Sciences and Faculty of Geosciences,
University, Bremen, Leobener Str., 28334 Bremen, Germany

P. Strzerzynski
UBO-IUEM, CNRS UMR6538 Domaines Océaniques, 29280 Plouzané, France

N. Sultan
IFREMER, Géosciences Marines, Laboratoire Environnements Sédimentaires,
Plouzané, France

E. Tahchi
Departament d'Estratigrafi a, Paleontologia i Geociències Marines,
Facultat de Geologia, Universitat de Barcelona, Martí i Franquès, s/n,
08028 Barcelona, Catalonia, Spain

P.J. Talling
National Oceanography Centre, Southampton, European Way, Southampton,
SO14 3ZH, UK

D.R Tappin
British Geological Survey, Nottingham, NG12 5GG, UK

U.S. ten Brink
United States Geological Survey, Woods Hole Science Center,
384 Woods Hole Rd., Woods Hole, MA 02543, USA

S. Thomas
Fugro GeoConsulting Limited, Engineering Geology and Geohazards Team,
Fugro House, Hithercroft Road, Wallingford, Oxfordshire, OX10 9RB, UK

E.K. Tripsanas
Shell International E & P Inc. 200 N. Dairy Ashford, Houston, TX 77079, USA

D. Turmel
Laboratoire d'études sur les risques naturels, Département de géologie
et de génie géologique, Université Laval, Québec, Canada G1K 7P4

D.C. Twichell
U.S. Geological Survey, Woods Hole, MA 02543, USA

S. Unterseh
TOTAL, Paris La Défense, France

R. Urgeles
Departament d'Estratigrafi a, Paleontologia i Geociències Marines,
Facultat de Geologia, Universitat de Barcelona, Martí i Franquès,
s/n, 08028 Barcelona, Catalonia, Spain

W. Ussler III
Monterey Bay Aquarium Research Institute, Moss Landing,
CA 95039-9644, USA

M. Vanneste
NGI/ICG, P.O. Box 3930, Ulleval Stadion, N-0806 Oslo, Norway

B.C. Vendeville
Université de Lille1, 4 UMR 8157 Géosystèmes, Bat. SN5,
USTL, 59655, Villeneuve d'Ascq, Cedex – France

R. C. Viesca
School of Engineering and Applied Sciences (also, for JRR,
Department of Earth and Planetary Sciences), Harvard University,
29 Oxford St., Cambridge, MA 02138, USA

M. Voisset
IFREMER, BP 70, 29280 Plouzané Cedex, France

G.D. Wach
Department of Earth Sciences, Dalhousie University, Halifax,
N.S., Canada B3H 4J1

E.G. Ward
Offshore Technology Research Center, Texas A&M University,
1200 Mariner Drive, College, Station, TX 77845, USA

R.P. Weaver
Los Alamos National Laboratory, MS T086, Los Alamos,
New Mexico 87545, USA

D. Winkelmann
Leibniz Institute for Marine Science (IFM-GEOMAR),
Kiel, Germany

L. Wood
Bureau of Economic Geology, Jackson School of Geosciences,
The University of Texas at Austin, TX, USA

S.G. Wright
The University of Texas at Austin, Department of Civil, Architectural
and Environmental, Engineering, Geotechnical Engineering Program,
1 University Station, C1792, Austin, Texas, 78712-0280, USA

R.B. Wynn
National Oceanography Centre, Southampton, European Way, Southampton, SO14 3ZH, UK

Z. Xu
Canadian Hydrographic Service, Fisheries and Oceans Canada, Maurice-LaMontagne Laboratory PO, Box 1000, Mont-Joli, Quebec, G5H 3Z4 Canada

K. Yelles
CRAAG, Centre de Recherche en Astronomie, Astrophysique et Géophysique, Bouzaréah, Algiers, Algeria

A. Zakeri
Geotechnical Engineering Group, C-CORE, St. John's, Newfoundland, Canada; International Centre for Geohazards (ICG), Sognsveien 72, 0855, Oslo, Norway

Submarine Mass Movements and Their Consequences

D.C. Mosher, L. Moscardelli, R.C. Shipp, J.D. Chaytor, C.D.P. Baxter, H.J. Lee, and R. Urgeles

Introduction

In 1929, an earthquake off the Grand Banks of Newfoundland initiated a submarine mass movement that sheared undersea communication cables and generated a tsunami that resulted in deaths of 27 people along the south coast of Newfoundland. This event initiated the modern realization that the seafloor is a dynamic environment with potential to do harm. More recent catastrophic examples include submarine mass movements off the Nice airport in 1979 that removed part of the runway along with construction equipment and resulted in the loss of several construction workers (Dan et al. 2007; Kopf et al. this volume), and a 1998 event off Papua, New Guinea that caused a tsunami resulting in 2200 deaths (Tappin et al. 2001). On December 26, 2006, a submarine landslide in the Luzon Strait caused failure of undersea cables (Hsu et al. 2009), halting the entire internet network between Taiwan, Hong Kong, and China and affecting communications between Thailand, Malaysia, Vietnam, South Korea and Singapore for 12 h. Given that the combined GDP of Taiwan, Hong Kong and China approximates $7.56 billion per day, the economic impact of this event was severe. As for the offshore hydrocarbon industry, aside from direct risk to exploration and production platforms, the Society for Underwater Technology estimates that the cost of damage to pipelines caused by submarine mass movements is about $400 million annually.

As a result of instances like these and the potential economic and societal impact (an estimated 2.75 billion people worldwide live within 60 km of the coast), an interest in understanding the phenomenon of submarine mass movements has led to concerted efforts on behalf of governmental, non-governmental and international agencies to understand this risk to society, e.g. the United States Nuclear Regulatory Commission, the US National Tsunami Hazard Mitigation Program, the European and Canadian Continental Slope Stability (COSTA) Program, the Integrated Ocean Drilling Program and the joint United Nations Educational Scientific and Cultural Organization's (UNESCO) and International Union of Geosciences (IUGS) International Geosciences Program (IGCP) Project 511. The objective of IGCP project 511 is to bring a world-wide perspective to submarine mass movements and their consequences. This objective is realized by assembling

excellent contributions from active researchers, groups and institutions to provide diverse coverage of the many scientific and engineering aspects of this type of marine and coastal geohazard. To this end, this project has hosted four international symposia, the latest of which is represented by this volume. Previous symposia resulted in two books (Lykousis et al. 2007; Locat and Meinert 2003) and a special issue in the Norwegian Journal of Geology (Solheim 2006).

The Fourth International Symposium on Submarine Mass Movements and their Consequences called for manuscript submissions, addressing the broad issues of submarine mass movements, and meeting the objectives of the project to bring together in a common forum experts from all disciplines pertinent to the topic. This volume is the result: a collection of 62 papers spanning subjects broadly organized under topics of: (1) triggers; mechanics and geotechnical properties; (2) case studies and hazard assessment; (3) margin construction and economic significance; and (4) tsunami genesis from submarine mass movements.

Section I: Submarine Mass Movement Triggers, Mechanics and Geotechnical Properties

A fundamental aspect of submarine mass movement research is understanding trigger mechanisms. This research component, however, is not well developed. In this section, authors explore the role of pore pressure and fluid and gas migration in slope instability. As Masson et al. (this volume) indicate, elevated pore pressures are often essential for mass movement initiation, yet understanding how high pore pressures are generated or how fluid migration affects slope stability is limited. Sediments may be pre-conditioned for failure by the processes that originally deposited them, but the processes and parameters that might control this factor are largely unknown. Continental margin development might also result in focussed fluid flow and elevated pore pressures where sedimentation rates are not particularly high, indicating that margin architecture also plays a significant role in overpressure and the most likely place for occurrence of submarine slope failures (Dugan et al. this volume, Urgeles et al. this volume).

In most historic instances, submarine mass movements were triggered by ground accelerations due to earthquakes. Herein lays a paradox; the majority of submarine mass movements and the largest recognized submarine mass movements occur along passive continental margins, where seismicity is not common. It is a rare instance, therefore, that the actual trigger of a submarine mass movement event has been observed and recorded; the first probably being the 1929 Grand Banks event (Heezen et al. 1952 and 1954). Even during events such as earthquakes, ground accelerations may increase horizontal and vertical loads and cause pore pressure responses in specific geologic horizons. Without instrumented in situ monitoring during such events, the actual physical responses of the geologic column to ground accelerations are not known. The paradox above also illustrates that trigger mechanisms need to be properly balanced against preconditioning factors, especially

sediment characteristics and stress history. For some slopes, the actual trigger mechanism is of little importance; rather, an environment for failure results from a series of preconditioning factors that concur so that the slope may fail under relatively small external loads (triggers).

The second most common trigger mechanism for known historic submarine mass movements has been anthropogenic. For example, coastal construction without due consideration for the local geological and geotechnical conditions, as seen with the Nice airport (Dan et al. 2007) and the port of Skagway, Alaska (Conforth and Lowell 1996). In these instances, increased loads due to construction and ill consideration of pore pressure responses led to down slope sediment movement.

Other submarine mass movement trigger mechanisms have been hypothesised that include elevated pore pressures related to gas accumulation such as might be provided by dissociation of gas hydrate. Gas hydrate dissociation results in loss of solid material, production of free gas, and increased fluid pressures; all which have the effect of reducing sediment strength. Grozic (this volume) explores the relationship between gas hydrate and slope instability in this section through theoretical and laboratory experimentation. A number of other papers explore pore pressure and fluid migration in the roles of mass movement initiation.

A full understanding of slope stability and the kinematics of submarine mass movements requires sediment engineering information. Data need to be at high subsurface resolution in order to identify the presence of geotechnically weak layers upon which a mass movement may initiate. Ideally they would also include large areal coverage to capture lateral variability in sediment properties and changing surface and subsurface morphologies. Detailed digital elevation (bathymetric) maps and correlation with seismic reflection profiles can assist in this requirement. These geotechnical data are technically feasible to obtain, but costly, and if not obtained in situ then questions remain as to their validity. As a result, there are few case studies where sufficient geotechnical data are available; a major shortcoming highlighted in a recent Integrated Ocean Drilling Program offshore geohazard workshop report (Morgan et al. 2009). Section I contains papers using geomechanical testing, physical property measurement and cone penetration testing to assess slope stability and failure kinematics. Typically, we assess failure kinematics based on residual sediment physical properties and failure scar and deposit morphologies. It is rare to know pre-failure conditions and likely impossible to know mechanics of the flow during failure, but numerical modeling (Mazzanti this volume) and flume experiments (Zakeri et al. this volume) for example, can provide insightful information to these important issues.

Section II: Submarine Mass Movement Case Studies and Hazard Assessment

Elevated awareness of the need for better understanding of underwater mass movements is coupled with great advances in underwater mapping technologies over the past two decades. Multibeam sonar, 3D seismic reflection, improved 2D seismic reflection and remote and autonomous underwater vehicle technologies provide

hitherto unparalleled imagery of the geology beneath the oceans. Today, significant portions of continental margins are being mapped with these technologies due to increased offshore exploration and exploitation and government national mapping initiatives (e.g. Pickrill and Kostylev 2007). Increased data coverage has led to an exponential increase in the number of case studies of submarine mass movement deposits; both surficial and buried. Improved resolution has enabled association of mass movement scar and deposit morphologies with kinematics, processes and hazards (e.g. Posamentier 2004; Frey-Martinez et al. 2006). Increased recognition of submarine mass movements also leads to estimation of the relationship between spatial distribution, magnitude and recurrence interval of such events (see for instance Camerlenghi et al. this volume), which is critical for geohazard assessment.

Section 2 consists of case studies of submarine mass movements, demonstrating a variety of failure styles and flow types ranging from slides to debris flows and turbidity currents. These studies also cover a range of tectonic environments, including convergent and passive margins, coastal regions and even lakes and demonstrate risk analysis based on trigger mechanisms (e.g. Nodine et al. this volume).

Section III: Submarine Mass Movements in Margin Construction and Economic Significance

Another outcome of the abundance and resolution of modern marine geoscience data has been identification of mass movement deposits at almost all scales (Camerlenghi et al. this volume). As a result, Section III deals with this realization that mass movements are a natural and geologically common process in slope environments, particularly in coastal regions (e.g. Mosher et al. 2004) and along continental margins (e.g. Mienert et al. 2003). This identification has resulted in cataloging of more and larger submarine mass movement deposits (e.g. Nisbet and Piper 1998; Silva et al. this volume). It is apparent on continental margins, for example, that submarine mass movement deposits form a significant, if not majority proportion of their sedimentary succession (Boyd et al. this volume; Giles et al. this volume). Volumes of single mass movement events can supersede all sources of annual river input to the oceans (e.g. Talling et al. 2007). As a result, they represent a fundamental process in continental margin development, delivering massive amounts of sediment and associated particulate matter (e.g. organics, trace metals) from shallow to deep water. This relatively recent understanding has yet to be adequately accounted for in consideration of sediment and carbon budgets and residence time as well as in sedimentologic and sequence stratigraphic models.

In addition to demonstrating the geologic importance of mass movement deposits in margin construction, Section III demonstrates that these deposits may have an important economic significance. Petroleum geologists are starting to realize that understanding sediment mass movement may be useful in hydrocarbon exploration (Beaubouef and Abreu, this volume; Frey-Martinez this volume e.g. Moscardelli 2006). The capacity of submarine mass movement deposits to modify

the seascape configuration has a profound effect on the distribution of sediments and subsequent stratigraphic relationships. Consequently, submarine mass movements may exert important controls on basin development, reservoir location, geometry, facies distributions, and the possible development of stratigraphic traps. They may also constitute a critical factor in directing fluid flow pathways and in some cases, coarse-grained mass movement deposits may even act as reservoirs (e.g. Beckley et al. 2003; Khafizov and Syngaevsky 2005).

Section IV: Submarine Mass Movements and Tsunamis

Consequences of the 1998 PNG tsunami and the 2004 Sumatran tsunami have been significant improvements in numerical tsunami simulations and recognition that this science requires input from engineering, geoscience, oceanography, geography and mathematics disciplines in order to represent reality. Increased computer processing power and increased sophistication of programming code have led to drastic improvements in numerical simulation of tsunami generation, propagation and inundation in the past few years. Tappin (this volume) emphasises that all forms of submarine mass movements are potentially tsunamigenic, yet there is a paucity of data relating submarine failures to tsunami generation and the physics of the process is still not well understood (Bardet et al. 2003; Lynett this volume).

This final section concerns submarine mass movements and their ability to generate tsunamis, principally through numerical simulation, although analog studies are presented as well (Mohammed and Fritz, this volume). Several papers address the complexities of mass movement materials and processes in tsunami generation. Remaining papers include geologic examples of submarine mass-movements with numerical simulations of tsunamis that may have resulted. In one paper (Poncet et al. this volume), a case is presented for a potential future submarine mass movement and consequent tsunami. In each of these studies, authors address the potential for tsunami generation and assess the hazard to proximal coastlines by estimating wave height, propagation and inundation characteristics. A major limitation to hazard assessment studies is lack of age control and subsequent frequency of occurrence, indicating a need for detailed sedimentological analysis (e.g. Di Roberto et al. this volume).

Looking to the Future

A publication such as this book, stemming from a conference and a call for submission of papers, is somewhat pot-luck. With good fortune, however, a broad cross section of the subject of submarine mass movements and their consequences is represented in this volume. Advancement of the science in this series following the relatively recent inception of the IGCP 511 program has been remarkable. This evolution

is due to the increased area of seafloor mapped at high resolution as well as contributions from industry with quality data sets that are not necessarily accessible to the public or the academic community. In addition, modellers have made great strides in simulating tsunami propagation and inundation.

Despite these great strides, there are yet a number of areas in which advances in the subject area are required. Without a doubt, studies of submarine mass movements drastically lack physical samples, and with samples come geophysical groundtruth, age control and geotechnical information for understanding trigger mechanisms, flow dynamics, recurrence intervals and relationship to Earth's natural climate variations. This shortcoming is because industry generally lacks interest in these deposits and the near-surface section, as it supposedly contains no economic consequence. Despite active academic research interests, scientific drilling is too expensive for individual research institutions to sustain and international scientific drilling programs, such as ODP and IODP have avoided drilling areas with such pronounced geohazards. Even with sample control of mass movement deposits, only so much can be learned; there is a real need to know conditions prior to a submarine mass movement and, if at all possible, conditions during initiation and movement.

The recent increase in exploration and development in deep water has prompted industry interest in sediment mass movement, however. This interest is from both a geohazard perspective and to understand mass movement's role in sediment distribution and its potential for creating hydrocarbon traps and/or reservoirs. Collaboration between industry and academia will be fundamental in the future. In this regard, it is expected that shallow subseafloor and borehole observatories will provide the data to decipher slope conditions at these different stages. For these observatories to succeed, we must be able to identify areas where slope failure is ongoing or might occur in the near feature, and we must put to study the relationship between slope deformation, seismic ground shaking, and pore pressure response, amongst other variables. Presently a number of IODP proposals (www. iodp.org) tackle this aspect.

A second research area in need of advancement is quantitative understanding of mass movement initiation and kinematics and energy coupling between movement of the sediment mass and the overlying water column that generates the tsunami. As real case studies of these factors are rare and likely to remain rare, advances in this field will require numerical simulation. Most submarine mass movement-tsunami models assume a relatively simplistic displacement condition to initiate the tsunami wave. With mathematicians turning their attention to this problem, they will likely advance the science before adequate observational groundtruth will be provided.

We expect over the next 5 years that submarine mass movements and consequent tsunami potential will acquire a much higher public profile, as awareness of their risk is revealed. There have also been recent cases whereby identification of submarine mass movements has permitted extension of the definition of the continental boundary under claims with the United Nations Commission for Law of the Sea. Consequently, it is expected that submarine mass movements will become a higher priority research item for many countries, as has already

occurred in the US (e.g. ten Brink 2009). We also expect their relevance to commercial exploration will become better appreciated, and consequently will be incorporated into stratigraphic and sedimentologic models. These models will help refine estimates of global sediment budgets, residence time and associated geochemical variables to help refine global climate change scenarios and possibly lead to discovery of new reserves.

References

Bardet J-P, Synolakis C, Davis H, Imamura F, Okal E (2003) Landslide tsunamis: Recent findings and research directions. Pure Appl Geophys 160:1793–1809.

Beckly J, Nash T, Pollard R, Bruce C, Freeman P, Page G (2003) The harding field, Block 9/23b. Geol Soc Lond Memoir 20:283–290.

Cornforth DH, Lowell JA (1996) The 1994 Submarine Slope Failure at Skagway, Alaska. In: Senneset K (ed.) Landslides, AA Balkema, Rotterdam, p 527–532.

Dan G, Sultan N, Savoye B (2007) The 1979 Nice harbour catastrophe revisited: Trigger mechanism inferred from geotechnical measurements and numerical modelling. Mar Geol 245:40–64.

Frey-Martínez F, Cartwright J, James D (2006) Frontally confined versus frontally emergent submarine landslides: A 3D seismic characterisation. Mar Petrol Geol 23:585–604.

Heezen BC, Ewing M (1952) Turbidity currents and submarine slumps and the 1929 Grand Banks earthquake. Am J Sci 250:849–873.

Heezen BC, Ericson DB, Ewing M (1954) Further evidence for a turbidity current following the 1929 Grand Banks earthquake. Deep Sea Res 1:193–202.

Hsu SK, Tsai C-H, Ku C-Y et al. (2009) Flow of turbidity currents as evidenced by failure of submarine telecommunication cables. In: Chiocci FL, Ridenti D, Casalbore D, Bosman A (eds.) Intern Conf on Seafloor Mapping for Geohazard Assessment, Extended Abs, Rendiconti online, Società Geologica Italiana 7:167–171.

Khafizov SF, Syngaevsky PE (2005) Turbidite, slump, and debris flow deposits at the Kalchinskoe and Zimnee Oilfields, West Siberian Basin. J Petrol Geol 28:49–66.

Locat J, Meinert J (eds.) (2003) Submarine Mass Movements and Their Consequences: 1st Intern Symp: Advances in Natural and Technological Hazards Research, Kluwer Academic (Springer), The Netherlands, 540 pp.

Lykousis V, Sakellariou D, Locat J (eds.) (2007) Submarine Mass-Movements and their Consequences: Advances in Natural and Technological Hazards Research, v. 27, Springer, The Netherlands, 424 pp.

Mienert J, Berndt C, Laberg JS et al. (2003) Slope Instability of Continental Margins. In: Wefer G, Billet D, Hebbeln D, Jorgensen B, Van Weering TCE, Schlüter M (eds.) Ocean Margin Systems, Springer, New York, 495 pp.

Morgan J, Silver E, Camerlenghi A, et al. (2009) Addressing geologic hazards through ocean drilling, Sci Drilling 7:15–30.

Moscardelli L, Wood L, Mann P (2006) Mass-transport complexes and associated processes in the offshore area of Trinidad and Venezuela. Am Assoc Petrol Geol 90:1059–1088.

Mosher DC, Monahan PA, Barrie JV et al. (2004) Coastal submarine failures in the Strait of Georgia, British Columbia: Landslides of the 1946 Vancouver Island earthquake. J Coast Res 20:277–291.

Nisbet EG, Piper DJWP (1998) Giant submarine landslides. Nature 392:329–330.

Pickrill RA, Kostylev VE (2007) Habitat mapping and national seafloor mapping strategies in Canada. In: Todd BJ, Greene HG (eds.) Mapping the Seafloor for Habitat Characterization: Geol Assoc Canada, Spec Pap 47:449–462.

Posamentier H (2004) Stratigraphy and geomorphology of deep water mass transport complexes based on 3D seismic data. Offshore Technology Conference paper 16740, Offshore Technol Conf., May 3–6, 2004, Houston TX, 7 pp.

Solheim A (ed.) (2006) Submarine mass movements and their consequences. Proc of 2nd Intern Conf., Oslo 2005. Nor J Geol 86:151–372.

Talling PJ, Wynn RB, Masson DG et al. (2007) Onset of submarine debris flow deposition far from original giant landslide. Nature 450:doi:10.1038/nature06313.

Tappin DR, Watts P, McMurtry GM et al. (2001) The Sissano, Papua New Guinea tsunami of July 1998: Offshore evidence on the source mechanism: Mar Geol 175:1–23.

Ten Brink U (ed.) (2009) Tsunami hazard along the U.S. Atlantic coast. Mar Geol doi:10.1016/j.margeo.2009.03.011.

Section I
Submarine Mass Movements: Triggers, Mechanics, and Geotechnical Properties

Interplay Between Gas Hydrates and Submarine Slope Failure

J.L.H. Grozic

Abstract Interest in methane gas production from hydrate deposits has increased dramatically in the last decade. Gas hydrates are solid crystalline compounds that encage gas molecules inside a water molecule lattice. Gas hydrates are linked to large submarine slides, in part because hydrate dissociation results in loss of solid material, production of free gas, and increased fluid pressures; all which have the effect of reducing sediment strength. Laboratory experiments, small scale physical modeling, and theoretical slope stability analyses indicate that dissociation of even a small amount of hydrate can cause significant loss of sediment strength. Hydrate dissociation could be critical in inciting slope failures for low permeability sediments in shallower water depths. This paper presents recent results and advances on the intersection of gas hydrates and submarine slope stability, exploring the role of gas hydrates in triggering and/or propagating submarine mass movements.

Keywords Submarine slope • gas hydrate • geohazard • slope stability • methane gas • dissociation • excess pore pressure

1 Introduction

Methane gas extraction from hydrate reservoirs has received increasing interest in the last few years with this vast supply of natural gas being cited as a globally promising energy resource. Global resource estimates of natural gas contained in hydrate form differ by orders of magnitude ranging from 10^{15} m^3 to 10^{18} m^3 (Milkov et al. 2003). By comparison, estimates of remaining global reserves and undiscovered resources of conventional natural gas total approximately 10^{14} m^3 (Ahlbrandt 2002), which, at even its lowest estimate, puts the hydrate resource an order of

J.L.H. Grozic (✉)
Department of Civil Engineering, University of Calgary, ENF 262, 2500 University Dr NW, Calgary, Alberta, Canada, T2N 1N4
e-mail: jgrozic@ucalgary.ca

magnitude above all other natural gas accumulations. Because of uncertainties associated with characterizing hydrate deposits (such as hydrate saturation, sediment porosity, extent of the hydrate zone) it is even more difficult to estimate volumes of recoverable gas. Still, the sheer quantity of hydrate reserves is indicative of the significance of this resource.

The drive to exploit natural gas from hydrates is a delicate interplay of economics and politics. In Canada, natural gas production is expected to peak in 2010 while our domestic consumption, particularly from power generation, oil upgrading, and petrochemical manufacturing, is expected to increase (CCA 2008). Canada is also the second largest exporter of natural gas with 99% of exports flowing south to the United States. Internationally, countries with few indigenous energy assets, such as Japan, India, and South Korea, pay a high price for imported oil and gas. Potential methane hydrate exploitation in their jurisdictional waters could significantly change the global energy trade picture. From the political perspective, governments of many countries, particularly the United States, have national security concerns over the reliance on imported energy resources. Development of frontier gas hydrate resources ties in with Canada's northern strategy, which aims to increase northern economic development and exercise northern sovereign rights (CCA 2008). There is also increasing pressure on politicians for more environmental sensitivity; natural gas emits significantly less carbon dioxide than oil or coal, making it the cleanest fossil fuel. The recently released Council of Canadian Academies (CCA 2008) report on "Energy from Gas Hydrates" provides an excellent overview of the opportunities and challenges facing gas hydrate production in Canada, encompassing not only the scientific aspects but also political, economical and societal implications.

Despite its promise as a new energy source, there are still technical obstacles to overcome before production from gas hydrates can become a reality. A recent news article was titled "Methane hydrates: Energy's most dangerous game" (Pentland 2008). While over-sensationalized for journalism, hydrates do pose a serious geohazard and all production scenarios need to carefully account for potential risks. Indeed, the hazard posed by gas release from marine hydrates has been known to the offshore oil and gas industry for some time (e.g., Nimblett et al. 2005). Although much evidence is anecdotal and often proprietary, borehole instability, unexplained gas bubbling, and gas blow outs have been reported (Nimblett et al. 2005; Hovland and Gudmestad 2001). These encounters occurred when wells penetrated a hydrate bearing layer while testing or developing a deeper conventional hydrocarbon target. Such experiences have led the offshore industry to improve gas hydrate detection in an effort to design well paths that avoid hydrate zones. Circumstantial evidence also suggests that weakening of hydrate bearing sediments have triggered large underwater landslides along the continental margins (e.g., Booth et al. 1994). Submarine landslides have the potential to destroy offshore equipment, jeopardize safety of personnel, and generate tsunamis which can impact coastal regions located hundreds of kilometers away (e.g., Locat and Lee 2002). Clearly these risks need to be quantified to ensure drilling and production scenarios do not result in seafloor failure and/or sudden release of methane gas.

2 Background

Gas hydrates are solid crystalline compounds comprised of hydrogen-bonded water molecules forming a rigid crystal lattice stabilized by encaged gas molecules, also known scientifically as a clathrate (Max and Dillon 2000; Kvenvolden 2000). The most common natural hydrate former is methane but there are a variety of other gases with the same ability such as light alkanes of higher density like ethane, propane, isobutene and some non-hydrocarbons (Max and Dillon 2000; Kvenvolden 2000). One cubic meter of methane hydrate will decompose at standard temperature and pressure into $0.87\,m^3$ of water and up to $164.6\,m^3$ of methane gas (Makogon 1997; Kvenvolden 2000). The representative density for structure I methane hydrate is around $0.91\,g/cm^3$ but varies according to pressure, temperature, degree of cage occupancy, and methane purity (Helgerud et al. 2009).

Gas hydrate stability is confined to a low-temperature, high-pressure regime where thermodynamic principles govern the kinetics of formation and dissociation. These conditions are found in permafrost regions and under the seafloor on continental slopes around the world as shown in Fig. 1. In-situ natural gas hydrate deposits are generally located in marine sediments at temperatures above freezing, commonly around 5–10 °C. The critical factors influencing hydrate formation and stability are pressure, temperature, gas composition, volume of bulk free water, salinity, gas availability, sediment type, presence of catalysts or inhibitors, etc., (Makogon and Holditch 2001; Kvenvolden 1988). Oceanic gas hydrates are capable of existing at water depths greater than roughly 400 m, while permafrost hydrates are feasible as shallow as 200 m below the ground surface. In both environments, the maximum subsurface extent of gas hydrate is constrained by the geothermal gradient, as illustrated in Fig. 2.
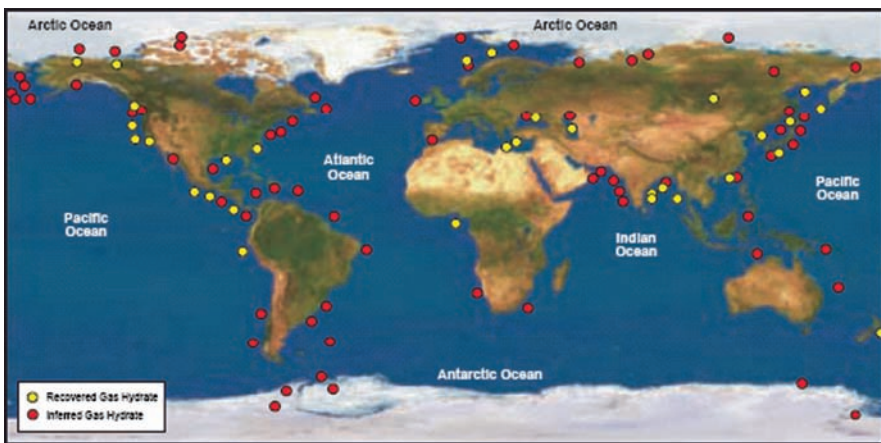
Fig. 1 Worldwide locations of known and inferred gas hydrate occurrences in deep marine and arctic permafrost environments (After Kvenvolden 2002; CCA 2008)
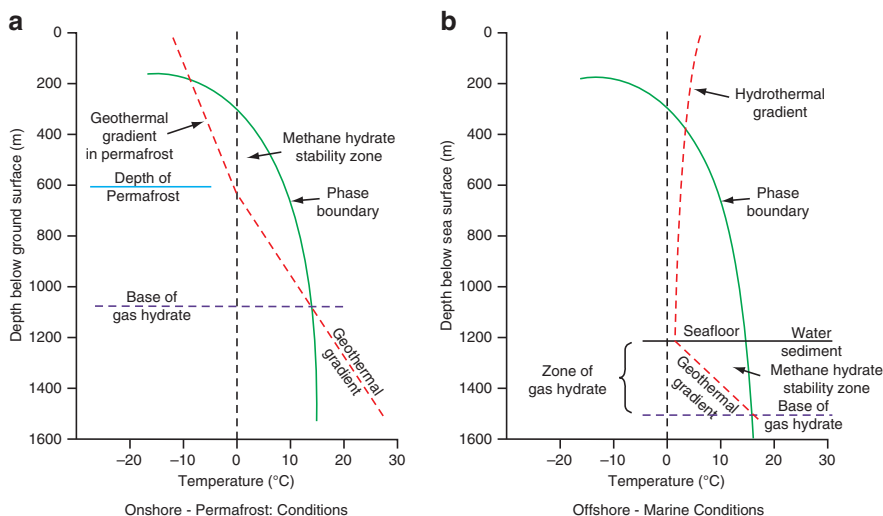
Fig. 2 Hydrate stability zones (After Collett 2002)

The push to develop methane hydrates has resulted in increased activity in recent years, particularly offshore. The success of two ground breaking scientific cruises, ODP Leg 204 to Hydrate Ridge, Oregon in 2002 (Tréhu et al. 2003) and IODP Expedition 311 to the Northern Cascadia Margin in 2005 (Riedel et al. 2006), led to four recent industry led drilling campaigns focused on the commercial exploitation potential of gas hydrates. These projects were in the Gulf of Mexico (Ruppel et al. 2008), offshore India (Collett et al. 2006), in the South China Sea (Zhang et al. 2007) and offshore South Korea in the East Sea (Park et al. 2008). Information obtained from these explorations has increased our understanding of natural hydrate bearing sediments; in particular the influence of pore-scale habit, solubility, and host sediment properties has been highlighted. Waite et al. (2009) present a comprehensive review of the most recent information on hydrate bearing sediment properties.

3   Stress Changes in Hydrate Bearing Layers

The strength of intact pure hydrate can be 20 times that of pure ice (Durham et al. 2003). When contained within sediments, laboratory results show an increase in strength of hydrate bearing sediments over hydrate free sediments (Masui et al. 2005, 2008; Ebinuma et al. 2005), with hydrate and ice bearing sediments having similar strengths (Winters et al. 2004). The strength of hydrate bearing sediments will be a function of the strain rate, temperature, consolidation stress, grain size, density, and cage occupancy (Winters et al. 2004). How the hydrate and sediment

interact also affects bulk sediment strength. As gas hydrate forms within sediment, three main pore habits are possible: pore filling, load bearing, or cementing. Pore filling contributes to an increase in the bulk stiffness and load bearing and cementing increase the sediment shear strength as well as the bulk stiffness (Waite et al. 2009; Dvorkin et al. 1999).

When perturbations to the thermodynamic equilibrium of the gas hydrate system occur, hydrate can be pushed out of the stability zone and dissociation occurs. Dissociation releases water and methane gas, but as an endothermic reaction, requires heat input. If the heat transport fueling dissociation and the pressure increase due to methane gas release occur rapidly compared with pore pressure dissipation processes, excess pore pressure and reduction in effective stress ensues.

3.1   Laboratory Investigations

At a constitutive level, stress changes due to hydrate dissociation have been examined in the laboratory. Grozic and Kvalstad (2007) formed and subsequently dissociated gas hydrates in specimens of Kaolin clay and sandstone. The results indicated some decrease in effective stress for even very small hydrate saturations, S_H (percentage of pore volume occupied by hydrate). Carbon dioxide hydrates have been used to accommodate more rapid laboratory testing as in Wu and Grozic (2008), where hydrates were formed within reconstituted Ottawa sand specimens as illustrated in Fig. 3. Hydrate stability diagrams indicate a theoretical dissociation temperature of 4 °C for test conditions; however, specimen warming induced by confining fluid heating and temperature sensors located outside the specimen contributed to warmer observed dissociation temperatures. Although the boundary condition for dissociation was "undrained" (no flow conditions), a volume expansion of approximately 7% occurred as the gas contained within hydrate form was released. All tests with over 8% pore-space saturation with hydrates exhibited
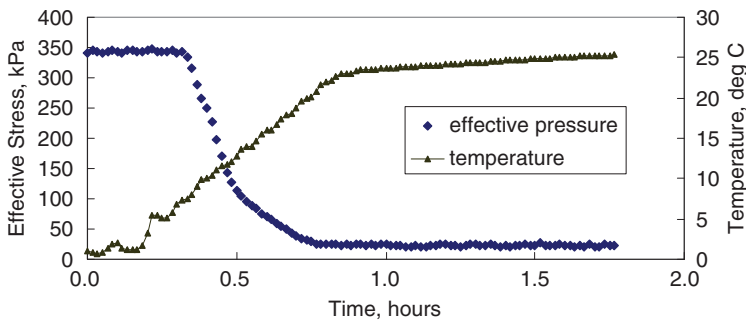
Fig. 3 Effective stress reduction and temperature increase for carbon dioxide bearing hydrates ($S_H = 8.8\%$) (Wu and Grozic 2008)
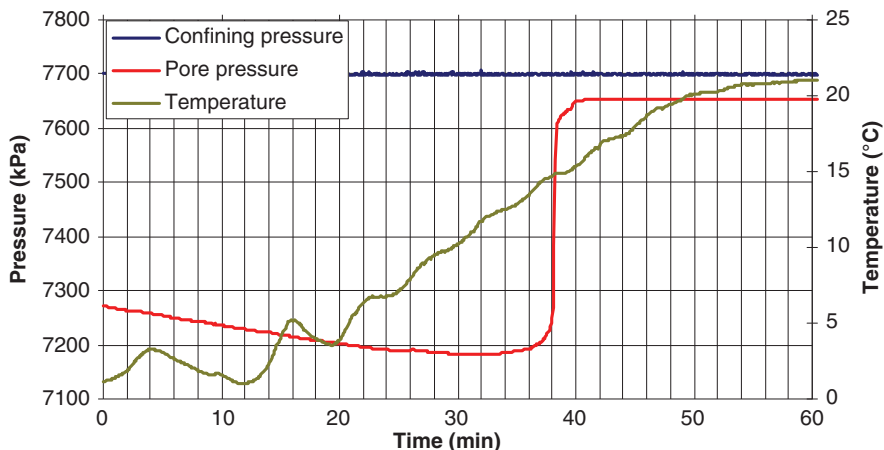
Fig. 4 Confining pressure, pore pressure and temperature response of thermally induced hydrate dissociation in water-saturated methane hydrate bearing sand ($S_H = 0.8\%$) (Jayasinghe and Grozic 2007)

excess pore pressures such that complete reduction of effective stress and loss of soil strength ensued. Similar results have been observed for methane gas hydrates (Jayasinghe and Grozic 2007) formed in water-saturated laboratory sand specimens, where rising temperature caused dissociation producing 450 kPa of excess pressure and an effective stress decrease to less than 50 kPa (Fig. 4). This dramatic stress change was observed for only 0.8% pore-space hydrate saturation, which corroborates well with Waite et al. (2008) who observed a 540 kPa increase in pore pressure for a pore-space hydrate saturation of 0.8% using a novel methane hydrate seeding technique. Again, observed dissociation temperatures are warmer than theoretical (10 °C) for these tests.

3.2 Theoretical Predictions

Theoretical predictions of the stress change induced by hydrate dissociation have also been proposed. Nixon and Grozic (2007) presented a simple model used for preliminary slope stability analyses. This model does not take into account gas solubility or the endothermic nature of hydrate dissociation; both of which would decrease the magnitude of the pore pressure build-up. The model's simplicity makes it attractive to incorporate into slope analyses programs as a conservative initial assessment before complicated modeling is undertaken. Sultan et al. (2004) present a theoretical model to determine the pore pressure response to hydrate dissociation, also based on volumetric conservation, which takes into account the gas solubility dependence on temperature and/or pressure. Xu and Germanovich (2006) put forward a theoretical

model to compute the pore pressure changes upon hydrate dissociation. For a completely confined pore space (when the permeability is low or the dissociation process is rapid), the excess pore pressure generated by small hydrate saturations can be tens of megapascals as illustrated in Fig. 5. Kwon et al. (2008) present an analytical solution to determine the excess pore pressure generated during thermally induced hydrate dissociation in constrained volume conditions (undrained boundary conditions). This model was used to investigate the effects of various parameters including sediment stiffness, variation in gas solubility, and capillary effects. Of note in their findings is the conclusion that "less than 6% volume fraction dissociation may be sufficient to cause the failure of uncemented sediments in the upper 1000 mbsf [meters below seafloor], in the absence of fluid flux" (Kwon et al. 2008). The volume fraction of dissociating hydrate necessary to cause failure is consistent with the laboratory results from Wu and Grozic (2008).

The magnitude of excess pore pressure is significantly reduced if flow is assumed to take place or hydrate re-growth occurs. For example, at an initial pressure of 20 MPa and S_H of 20%, the excess pore pressure without flow is approximately 18 MPa. If flow is assumed with a range of reasonable permeabilities (e.g., Bryant et al. 1975) of $k = 10^{-18}$, 10^{-17}, and 10^{-16} m², the excess pore pressures were reduced to 7, 1, and 0.1 MPa, respectively. Through these results, Xu and Germanovich (2006) highlight the importance of understanding the flow boundaries and host sediment permeability. Gas hydrate re-growth during dissociation may also limit excess pore pressure generation. The endothermic dissociation reaction lowers heat and fluid production raises pressure, both which contribute to re-growth of hydrate crystals.
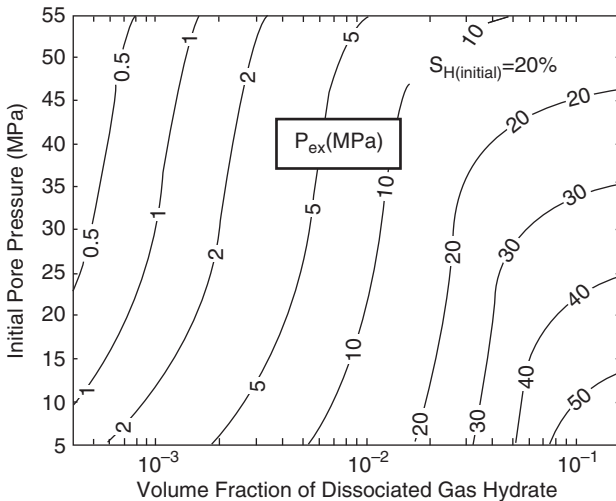
Fig. 5 Excess pore pressure (P_{ex}) caused by dissociation of gas hydrates in confined pore space as a function of the initial pore pressure and amount of dissociated gas hydrate (Modified from Xu and Germanovich 2006)

In addition to hydrate dissociation, hydrate dissolution can also occur. Dissolution occurs as the gas solubility of the surrounding liquid phase increases, which results in the production of water and dissolved gas but generally not free gas (Xu and Germanovich 2006). However, for load bearing hydrates, dissolution can lead to destructuration (loss of particle bonding) and softening, resulting in decreased shear strength and sediment deformation (Sultan 2007). Dissolution is accompanied with only small pore pressures changes; yet these changes can be critical at shallow sediment depths below the seafloor (Sultan et al. 2004; Sultan 2007).

3.3 Small Scale Physical Models

Physical models can facilitate identification of slope stability mechanisms and processes. A small scale physical model was constructed using Laponite, a synthetic smectite clay which forms a translucent gel upon mixing with water, and R-11 (trichlorofluoromethane) synthetic gas hydrates. The chilled materials were placed into a 3,660 cm^3 Plexiglas box mounted on a frame which allowed rotation between 0° and 45°. High speed digital cameras and video were used to capture the processes of hydrate dissociation as the materials warmed to ambient air temperature. Experimental details can be found in Gidley and Grozic (2008) and Gidley (2008). In all test cases, the dissociating hydrate produced sufficient gas to cause large bubble growth around the initial hydrate puck; excess pressures eventually caused expulsion of the gas from the test box and the production of a pockmark type structure on the soil surface (Fig. 6). When the slope angle was sufficiently large (greater than 7°), movement occurred and a slip surface was observed within the Laponite (Fig. 7); however, failure was arrested, most likely because of end influences in the scale model. Although qualitative in nature, the physical model results highlight the role of sediment stiffness in the evolution of pressures and deformations during the dissociation process. In these cases, large pressures (rela-

Fig. 6 Gas bubble generated by hydrate dissociation during the pressure release process. The movement of the gas bubble from the dissociated hydrate cavity to the soil surface took approximately $^1/_{15}$ s (Gidley and Grozic 2008)
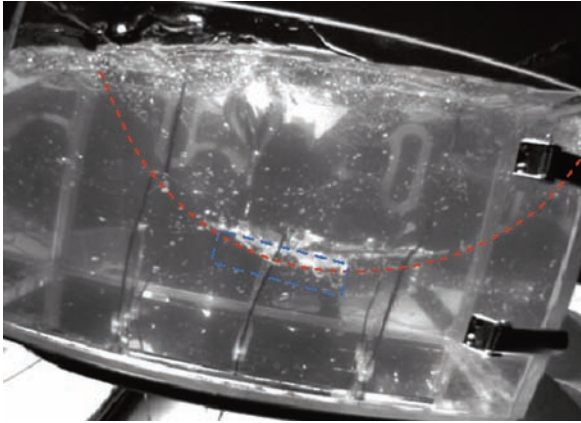
Fig. 7 Circular slip plane formed through the base of the dissociated hydrate puck in a 10° slope (Gidley and Grozic 2008)

tive to the overburden) were generated through dissociation, which due to the low shear strength of the sediment resulted in preconditioning the sediment mass to failure. Upon completion of the testing, the end wall was removed and a slide rapidly developed starting with a rotational failure along the slip plane through the dissociated hydrate.

3.4 Discussion

Both laboratory and theoretical studies have confirmed that gas hydrates dissociation produces excess pore pressures. The magnitude of the pressure generation is highly dependent on the flow boundary conditions, in particular, the host sediment permeability or the presence of a low permeability seal. Gas hydrate is least stable at the base of hydrate stability, where it can be overlain by a low permeability hydrate cap. It is therefore not unreasonable that significant pore pressures could develop with the effect of reducing effective stress and sediment strength.

4 Stability of Hydrate-Bearing Layers

The link between gas hydrate dissociation and submarine slope failures was first postulated in a conceptual model by McIver (1982). Sea level lowering or continuing sedimentation are cited as factors which could induce dissociation at the base of the hydrate layer resulting in loss of cementation, gas production, and overpressurization. The result would be a glide plane along which massive wedges of hydrate cemented sediment would slide (Fig. 8).
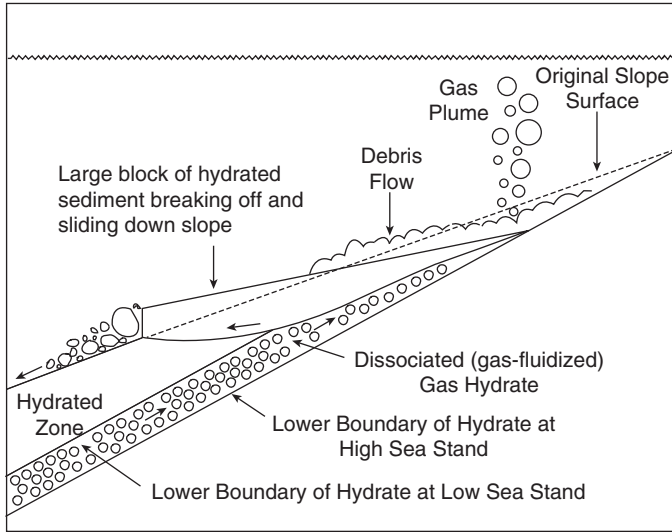
Fig. 8 Conceptual model of mass movement on a slope face by slippage of a solid block along a hydrate-decomposition glide plane (After McIver 1982)

4.1 Environmental Controls on Stability

Since this early work, it has been recognized that numerous environmental factors contribute to the potential for a hydrate bearing sediment to become unstable. As discussed below, host sediment properties, location of the stability zone, water depth and geologic cycles are a few natural parameters that play an important role in stability.

Sediment properties, in particular permeability, are important factors when assessing the potential for hydrate dissociation to initiate slope failure. The low pore fluid dissipation capacity of clayey sediment results in greater excess pore pressures than in sandy sediments during hydrate dissociation (Kayen and Lee 1991). The presence of a low permeability layer, either clay sediments or a cap of hydrated sediment, can suppress fluid dissipation and result in significant excess pore pressure at the base of the stability zone, where most naturally occurring hydrate dissociation takes place (Xu and Germanovich 2006). Even if dissociation is not widespread, localized weak layers can propagate into a shear band parallel to the seafloor (Puzrin and Germanovich 2005). The combination of cementation loss, excess pressure development, and shear propagation could be sufficient to trigger a submarine slide.

As shown in Fig. 2, the gas hydrate stability zone thickness is controlled by the water depth and geothermal gradient in marine settings. As the water shallows, the base of the gas hydrate approaches the seafloor, pinching out the hydrate stability

zone at approximately 400 m water depth. The pinch-out is referred to as the up-dip limit of the gas hydrate stability zone. It is in this feather edge of stability that hydrates experience the greatest impact from water bottom temperature fluctuations. It is also these surficial sediments that have the greatest potential for pressure generation associated with hydrate dissociation simply because ambient pressure controls the relative volume of gas that will be generated from the hydrate. Surficial sediments tend to be only lightly consolidated, thus relatively little change in pressure is required to surpass the lithostatic stress of these weak sediments. Paull et al. (2000) postulate that hydrate-related sediment failures should be most frequent at or just below the up-dip limit as this zone has the greatest potential for instabilities.

Water depth impacts not only the volume expansion during hydrate dissociation as discussed above, but also controls the transition between temperature and pressure dominated hydrate stability. Theoretical modeling indicates that hydrate stability in shallow water (less than about 700 m) is primarily dominated by bottom water temperature and in deeper water by pressure changes under the influence of eustatic sea level rise (Mienert et al. 2005; Leynaud et al. 2009). The transition from temperature dominated stability to pressure dominated stability coincides with the headwall of the Storegga slide, leading researchers to postulate that the slope could have been preconditioned by hydrate dissociation, causing the observed secondary failures along the upper slope in the retrogressive slide development (Mienert et al. 2002, 2005; Vogt and Jung 2002; McIver 1982).

Geologic cycles, specifically glaciation, influence hydrate stability by altering water depth, water bottom temperatures, and sedimentation. The interaction between glaciation and hydrate stability is illustrated conceptually in Fig. 9. At the initiation of glaciation, sea level fall decreases seafloor pressure leading to dissociation (Lee 2009). Paull et al. (1996) showed an association between low sea-level and an increased frequency of sea-floor slumps on continental margins containing gas hydrates. During full glaciation, the stability of hydrates increases on glaciated margins because of cold bottom water masses offsetting pressure drop effects, while the stability of hydrates decreases on non-glaciated margins because warm water masses prevail while the pressure decreases (Maslin et al. 2004). The transition from glacial to interglacial time is accompanied by a rise in sea level (stabilizing hydrates) but also readjustment of major ocean current systems bringing warmer waters to areas, such as northern Europe, potentially destabilizing gas hydrates. During interglacial times, the sea level is high and hydrate stability will be less variable (Lee 2009).

It is difficult to draw precise conclusions about the environmental controls on hydrate stability and its affect on seafloor instability. Sediment properties and hydrate characteristics are highly variable, even on local scales, and the time scales and amplitudes of sea level change and ocean bottom water temperatures can also vary significantly (Leynaud et al. 2009). Pressure changes are assumed to translate through the sediment's interconnected pores affecting hydrate stability immediately, while temperature changes penetrate progressively through the sediments, where it can take thousands of years for oceanic hydrate stability to be affected
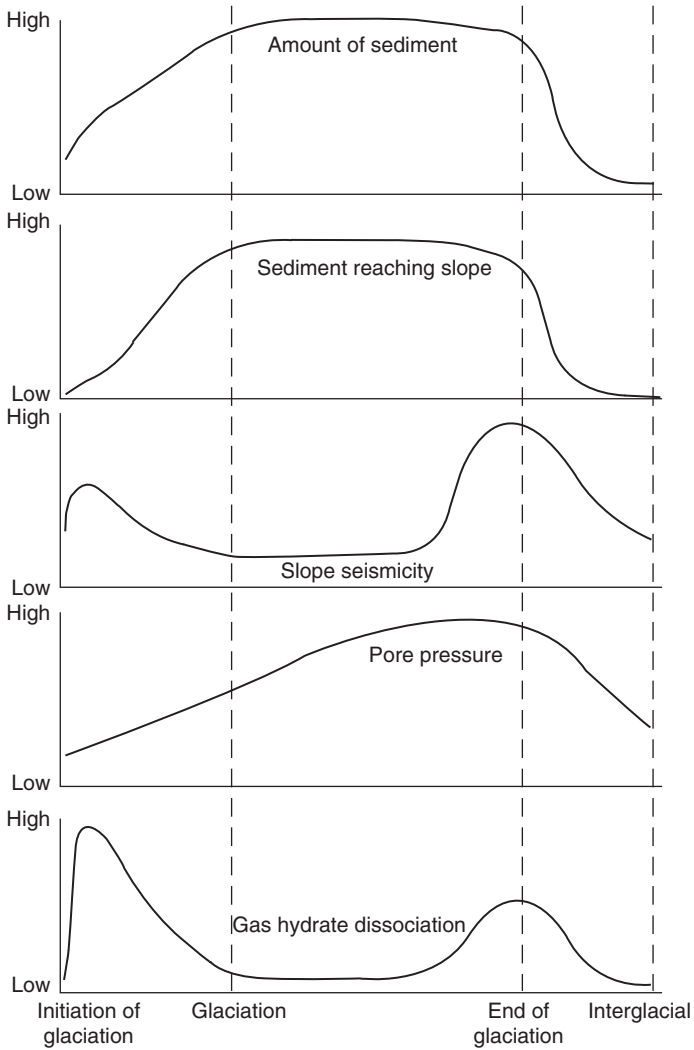
Fig. 9 Approximate impact of time on several factors that influence the stability of submarine slopes (After Lee 2009)

(Fyke and Weaver 2006; Hatzikiriakos and Englezos 1993). Detailed site specific information is required before conclusions can be drawn and landsliding attributed solely to hydrate dissociation.

4.2 Slope Stability Models

Very few quantitative slope stability models have incorporated the effects of gas hydrate cementation and/or dissociation. Sultan et al. (2004) used conservation of energy to predict the excess pore pressure together with limit equilibrium analysis and applied the model to the Storegga slide case history. Model results indicated that changes in gas solubility at the lower portion of the slope could be the origin of a retrogressive failure initiating at the top of the hydrate stability zone. A preliminary quantification of submarine slope failure due to hydrate dissociation was presented by Nixon and Grozic (2007, 2006). The stability model also uses limit equilibrium combined with an excess pore pressure model. A parametric study indicated that water depth, overburden pressures, and hydrate saturation were key in affecting the factor of safety of submarine slopes subject to hydrate dissociation in undrained boundary conditions (Nixon and Grozic 2006; Nixon 2005). Figures 10 and 11 highlight the relevance of water depth and hydrate content, where the factor of safety is shown as a function of hydrate content for four different slope angles, spanning water depths of 150–530 m and 750–1,130 m. For the shallower systems (Fig. 10), failure occurs if there is full dissociation of pore-space hydrate saturations of 5–11%, while for the deeper systems (Fig. 11), failure occurs with dissociation of hydrate saturations of 11–22%; indicating deeper systems require full dissociation of higher pore-space hydrate saturations to reach failure than comparable shallower systems. These results are interesting in their consistency with laboratory and theoretical pore pressure analyses which indicate hydrate
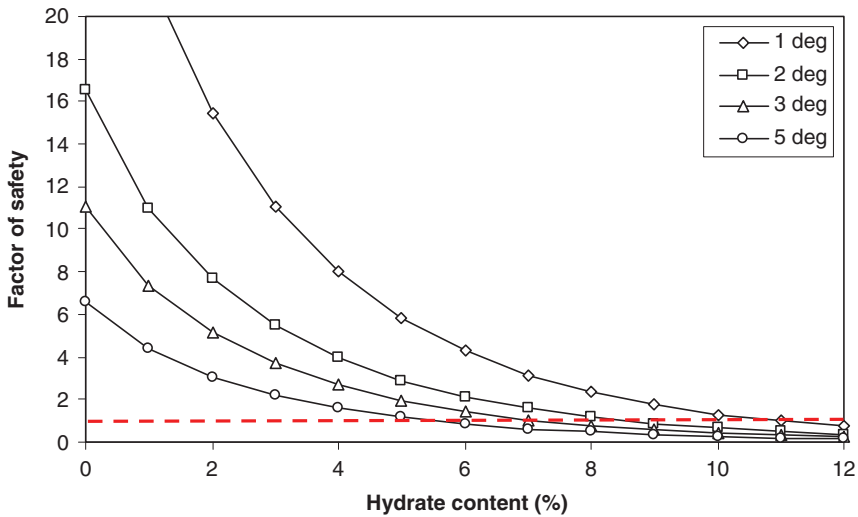
Fig. 10 Factor of safety as a function of hydrate content on four simulated slopes for water depths ranging from 150 to 530 m (Nixon and Grozic 2007)
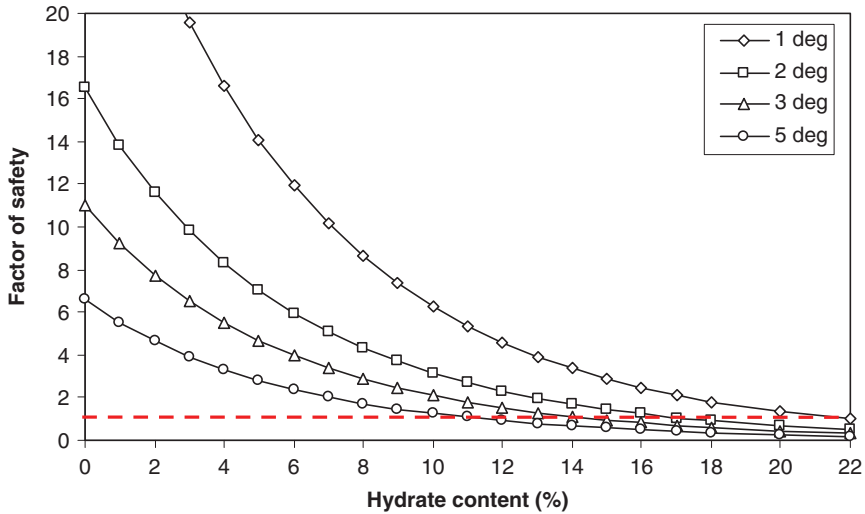
Fig. 11 Factor of safety using summation of discrete points on four simulated slopes for water depths ranging from 750 to 1,130 m (Nixon and Grozic 2007)

dissociation of only 6–8% of the pore-space is sufficient to cause sediment failure. Agreement that hydrate related landslides occur most frequently at shallow water depths is also observed (Xu and Germanovich 2006; Paull et al. 2000; Mienert et al. 2005). Inclusion of shear strength reduction arising from loss of inter-particle bonding would exacerbate sediment failures.

5 Field Observations

In order for gas hydrates to be the cause of a slope failure, three conditions must be met (Booth et al. 1994): (1) gas hydrates must be present and widespread; (2) the slide scar must intersect the boundaries of the hydrate layer; and (3) a low permeability material (sediment or hydrate-bearing sediments) must be common at the base of the hydrate stability zone. There are a number of cases where these conditions have been met and gas hydrates have been suggested, circumstantially, to have played a role in submarine slope failures. Examples of the connection between gas hydrates and submarine slope failures are found throughout the literature and have been summarized by Kvenvolden (1993, 1999) on the continental slope and rise of the west coast of Africa, on the US Atlantic continental slope, in the fjords of British Columbia, and on the Alaskan Beaufort sea continental margin. A few of instances where hydrates could have initiated submarine sliding are described below.

In the US Atlantic margin, the Cape Fear slide shows indications, on seismic profiles, of the presence of gas hydrate and underlying free gas coincident with the slip plane (Popenoe et al. 1993; Schmuck and Paull 1993). The area is also active seismically and with diapirism and the slide occurred during a period of sea-level rise (Lee 2009), thus the triggering mechanism cannot be attributed to hydrate dissociation alone.

Along the continental slope of Alaska, underlying the Beaufort Sea, are a string of almost continuous submarine landslides (Grantz and Dinter 1980). Gas hydrate deposits are coincident with the slide features (Kayen and Lee 1991) and the majority of the hydrate deposits are contained within low permeability sediments. Theoretical calculations of excess pore pressures indicate that hydrate dissociation would be sufficient to initiate seafloor sliding (Nixon and Grozic 2007; Kayen and Lee 1991); however, there is also evidence of seismic activity in the region.

A number of large submarine slides in the Amazon fan are indicated on seismic records (Piper et al. 1997). Although the timing of the slides is not certain, the failures seemed to have occurred during a period of lower sea level, which combined with the presence of gas and gas hydrates, points to a correlation between hydrate dissociation and failure.

The Storegga slide off the western coast of Norway is a well analyzed case history, due in part to its immense size, but perhaps more notable, is that the underlying Ormen Lange gas field is the second largest gas reserve in Norway. Triggering mechanisms considered have included high sedimentation rates, gas charged sediments, gas hydrate dissociation, diapirism and earthquakes (Bryn et al. 2005). Gas hydrates have been inferred from the seismic profile both inside and outside the slide scar (Bouriak et al. 2000) and careful consideration has been given to the possibility that gas hydrate dissociation triggered the Storegga slide (Mienert et al. 2005; Jung and Vogt 2004; Vogt and Jung 2002; Sultan et al. 2004). Bryn et al. (2005) conclude that the failure was earthquake triggered; Mienert et al. (2005) illustrate how gas hydrate dissociation in the shallower waters could have preconditioned the slope for the retrogressive failures that were observed.

Although instances of submarine slope failure potentially involving gas hydrates have been reported, the author is unaware of any slide that can be definitively attributed to gas hydrate dissociation as the singular triggering mechanism. Knowledge of well-scale failures as a result of gas hydrate dissociation is also mostly anecdotal and related to drilling and/or production operations (e.g., Nimblett et al. 2005).

6   Concluding Remarks

Gas hydrates have long been recognized as a geohazard in our exploration for, and production of, conventional offshore hydrocarbon reserves. Small scale theoretical and laboratory investigations have revealed that hydrate dissociation can produce

significant excess pore pressures if the dissociation process is rapid or fluid flow is restricted. Theoretical slope stability models indicate that slope failure due to hydrate dissociation is possible and circumstantial evidence from the field shows coincidence between observed slide scars and the base of the gas hydrate layer. Slopes in shallow water (less than approximately 700 m) are most vulnerable to failure as a result of hydrate dissociation or even hydrate dissolution. On geologic time scales, the sea level fall during the onset of continental glaciation, and the changing of major currents at the beginning and end of glacial cycles, are critical times for gas hydrate destabilization.

Certainly the conclusion that hydrate dissociation can precondition a sediment mass for failure, both by loss of sediment strength and generation of excess pore pressures, can be drawn. Likewise, if failure is triggered through another mechanism, such as earthquake loading, gas hydrate dissociation may play a role in the propagation of the submarine failure. In moving forward with the production of methane gas from hydrate reservoirs, slope failure, particularly the genesis of localized failures, still needs to be carefully considered. This is in part because of our current lack of quantitative data, models, and methodologies for adequately assessing slope stability in hydrate bearing sediments.

To assess the risk of submarine slope failure, particularly in economically viable hydrate reservoirs, we need a better understanding of the geomechanical response of hydrate-bearing sediments to pressure and temperature changes. Characterization of the hydrate deposit will be essential to provide accurate input into constitutive and slope models. The strength, deformation, and permeability properties of both intact, partially dissociated, and fully dissociated hydrate-bearing sediments in a variety of porous media can be modeled at the constitutive level to capture the sediment behavior. Laboratory investigations using both synthetic and natural hydrate-bearing specimens are required to provide the fundamental data required for such an endeavor. Field scale modeling, accounting for geomechanics, kinetics, thermodynamics etc., could then embark on accurately predicting the probability of slope failure and conceivably be used to compare to case histories, should enough quantitative field data be collected.

The complexities of gas hydrates and their interactions with the host sediment, combined with the high cost of laboratory and field investigations, have sufficiently limited our knowledge to the extent that we still cannot obtain a definitive answer to the question "do gas hydrates cause submarine slope failures". However, the increasing interest in gas hydrates as a tantalizing unconventional hydrocarbon resource, along with the growing number of hydrate researchers, imparts every indication that we are indeed moving forward. We are improving our fundamental knowledge and progressing toward being able to quantitatively assess the probability of gas hydrate dissociation triggering submarine mass movements.

References

Ahlbrandt TW (2002) Future petroleum energy resources of the world. Int Geol Rev 44:1092–1104.

Booth JS, Winters WJ, Dillon WP (1994) Circumstantial evidence of gas hydrate and slope failure associations on the United States Atlantic continental margin. Natural Gas Hydrates. Annal New York Acad Sci 715:487–489.

Bouriak S, Vanneste M, Saoutkine A (2000) Inferred gas hydrates and clay diapirs near the Storegga Slide on the southern edge of the Vøring Plateau, offshore Norway. Mar Geol 163:125–148.

Bryant WR, Hottman W, Trabant P (1975) Permeability of unconsolidated and consolidated marine sediments, Gulf of Mexico. Mar Geores Geotech 1:1–14.

Bryn P, Berg K, Forsberg CF, Solheim A, Kvalstad TJ (2005) Explaining the Storegga slide. Mar Pet Geol 22:11–19.

Collett TS (2002) Energy resource potential of natural gas hydrates. Am Assoc Pet Geol Bull 86:1971–1992.

Collett TS, Riedel M, Boswell R, Cochran JR, Kumar P, Sethi AK, Sathe AV, NGHP Expedition-01 Scientific Party (2006) International team completes landmark gas hydrate expedition in the offshore of India. Fire in the Ice, Methane hydrate newsletter, U.S. Department of Energy, Office of Fossil Energy, National Energy Technology Laboratory, Fall, pp. 1–4.

Council of Canadian Academies (CCA) (2008) Energy from gas hydrates: Assessing the opportunities and challenges for Canada. Report of the Expert Panel on Gas Hydrates, J Grace (Chair).

Durham WB, Stern LA, Kirby SH (2003) Ductile flow of methane hydrate. Can J Phys 81:373–380.

Dvorkin J, Prasad M, Sakai A, Lavoie D (1999) Elasticity of marine sediments; Rock physics modeling. Geophys Res Let 26:1781–1784.

Ebinuma T, Kamata Y, Minagawa H, Ohmura R, Nagao J, Narita H (2005) Mechanical properties of sandy sediments containing methane hydrate. 5th International Conference on Gas Hydrates, 12–16 June, Trondheim, Norway.

Fyke JG, Weaver AJ (2006) The effect of potential future climate change on the marine methane hydrate stability zone. J Clim 19:5903–5917.

Gidley ID (2008) Gas hydrate dissociation structures in clay slopes. M.Sc. Thesis, University of Calgary, Calgary, Canada.

Gidley ID, Grozic JLH (2008) Gas hydrate dissociation structures in submarine slopes. 4th Canadian Conference on Geohazards: From Causes to Management, 20–24 May, Laval, Canada, pp. 81–88.

Grantz A, Dinter DA (1980) Constraints of geologic processes on western Beaufort Sea oil developments. Oil Gas J 78:304–319.

Grozic JLH, Kvalstad TJ (2007) Laboratory verification of gas hydrate-sediment response. XIII Pan-American Conference on Soil Mechanics and Geotechnical Engineering, 16–20 July, Margarita, Venezuela.

Hatzikiriakos SG, Englezos P (1993) The relationship between global warming and methane gas hydrates in the earth. Chem Eng Sci 48:3963–3969.

Helgerud M, Waite WF, Kirby SH, Nur A (2009) Elastic wave speeds and moduli in polycrystalline ice Ih, sI methane hydrate, and sII methane-ethane hydrate. J Geophys Res 114:B02212, doi:10.1029/2008JB006132.

Hovland M, Gudmestad OT (2001) Potential influence of gas hydrates on seabed installations. In: Paull CK and Dillon WP (eds.). Natural Gas Hydrates. Washington, DC: American Geophysical Union, Geophysical Monograph Series, 124, pp. 300–309.

Jayasinghe AG, Grozic JLH (2007) An experimental investigation of temperature induced dissociation of methane hydrate in porous media. 60th Canadian Geotechnical Conference, 21–24 October, Ottawa, Canada, pp. 2062–2067.

Jung WY, Vogt PR (2004) Effects of bottom water warming and sea level rise on Holocene hydrate dissociation and mass wasting along the Norwegian-Barents Continental Margin. J Geophys Res 109:B06104, 18 pp.

Kayen RE, Lee HJ (1991) Pleistocene slope instability of gas hydrate-laden sediment on the Beaufort Sea margin. Mar Geotech 10:125–141.

Kvenvolden KA (1988) Methane hydrate - A major reservoir of carbon in the shallow geosphere? Chem Geol 71:41–51.

Kvenvolden KA (1993) Gas hydrates – Geological perspective and global climate change. Rev Geophys 31:173–187.

Kvenvolden KA (1999) Potential effects of gas hydrate on human welfare. Proc Natl Acad Sci USA 96:3420–3426.

Kvenvolden KA (2000) Natural gas hydrate: Introduction and history of discovery. In: Max MD (ed.). Natural Gas Hydrate in Oceanic and Permafrost Environments. The Netherlands: Kluwer Academic, pp. 9–16.

Kvenvolden KA (2002) Methane hydrate in the global organic carbon cycle. Terra Nova 14:302–306.

Kvenvolden KA, Rogers BW (2005) Gaia's breath-global methane exhalations. Mar Pet Geol 22:79–590.

Kwon T H, Cho GC, Santamarina JC (2008) Gas hydrate dissociation in sediments: Pressure-temperature evolution. Geochem Geophys Geosys 9:Q03019, doi:10.1029/2007GC001920, 14 p.

Lee HJ (2009) Timing of occurrence of large submarine landslides on the Atlantic Ocean margin. Mar Geol 264:53–64.

Leynaud D, Mienert J, Vanneste M (2009) Submarine mass movements on glaciated and non-glaciated European continental margins: A review of triggering mechanisms and preconditions to failure. 26:618–632.

Locat J, Lee HJ (2002) Submarine landslides: Advances and challenges. Can Geotech J 39:193–212.

Makogon YF (1997) Hydrates of Hydrocarbons. Tulsa, OK: Penn Well Publishing.

Makogon YF, Holditch SA (2001) Lab work clarifies gas hydrate formation, dissociation. Oil Gas J 99:47–52.

Maslin M, Owen M, Day S, Long D (2004) Linking continental-slope failures and climate change: testing the clathrate gun hypothesis. Geology 32:53–56.

Masui A, Haneda H, Ogata Y, Aoki K (2005) The effect of saturation degree of methane hydrate on the shear strength of synthetic methane hydrate sediments. 5th International Conference on Gas Hydrates, 12–16 June, Trondheim, Norway.

Masui A, Miyazaki K, Haneda H, Ogata Y, Aoki K (2008) Mechanical characteristics of natural and artificial gas hydrate bearing sediments. 6th International Conference on Gas Hydrates, 6–10 July, Vancouver, Canada.

Max M, Dillon W (2000) Natural gas hydrate: A frozen asset? Chem Ind 10:16–18.

McIver RD (1982) Role of naturally occurring gas hydrates in sediment transport. Am Assoc Pet Geol Bull 66:789–792.

Mienert J, Berndt C, Laberg JS, Vorren TO (2002) Slope instability of continental margins. In: Wefer G, Billett D, Hebbeln D, Jørgensen BB., Schluter M, VanWeering T. (eds.). Ocean Margin Systems. Heidelberg: Springer, pp. 179–193.

Mienert J, Vanneste M, Bunz, S, Andreassen K, Haflidason H, Sejrup HP (2005) Ocean warming and gas hydrate stability on the mid-Norwegian margin at the Storegga Slide. Mar Pet Geol 22:233–244.

Milkov AV, Claypool GE, Lee Y-J, Xu W, Dickens GR, Borowski WS, The Ocean Drilling Program Leg 204 Scientific Party (2003) In situ methane concentrations at Hydrate Ridge, offshore Oregon: New constrains on the global gas hydrate inventory from active margins. Geology 31:833–836.

Nimblett JN, Shipp RC, Strijbos F (2005) Gas hydrate as a drilling hazard: Examples from global deepwater settings. Offshore Technology Conference, Houston, Texas, OTC Paper 17476.

Nixon MF (2005) Influence of gas hydrates on submarine slope stability. M.Sc. Thesis, Department of Civil Engineering, University of Calgary, Calgary, AB.

Nixon MF, Grozic JLH (2006) A simple model for submarine slope stability analysis with gas hydrates. Nor J Geol 86:309–316.

Nixon MF, Grozic JLH (2007) Submarine slope failure due to gas hydrate dissociation: A preliminary quantification. Can Geotech J 44:314–325.

Park KP, Bahk JJ, Kwon Y, Kim GY, Riedel M, Hollsand M, Schultheiss P, Rose K, The UBGH-1 Scientific Party (2008) Korean National Program Expedition confirms rich gas hydrate deposit in the Ulleung Basin, East Sea. Fire in the Ice, Methane hydrate newsletter, U.S. Department of Energy, Office of Fossil Energy, National Energy Technology Laboratory, Spring, pp. 6–9.

Paull CK, Buelow WJ, Ussler III W, Borowski WS (1996) Increased continental margin slumping frequency during sea-level lowstands above gas hydrate-bearing sediments. Geology 24:143–146.

Paull CK, Ussler III W, Dillon WP (2000) Potential role of gas hydrate decomposition in generation submarine slope failures. In: Max M (ed.). Natural Gas Hydrate in Marine and Permafrost Environments. Dordrecht: Kluwer Academic, pp. 149–156.

Pentland W (2008) Methane hydrates: Energy's most dangerous game. Forbes Magazine, www.forbes.com, 2 September 2008. Reprinted by www.cbc.ca, 14 October 2008.

Piper DJW, Pirmez C, Manley PL, Long D, Flood RD, Normark WR, Showers W (1997) Mass-transport deposits of the Amazon Fan. In: Flood RD, Piper DJW, Klaus A, Peterson (eds.). Proceedings of the Ocean Drilling Program. Scientific Results, 155, pp. 109–146.

Popenoe P, Schmuck EA, Dillon WP (1993) The Cape Fear landslide: slope failure associated with salt diapirism and gas hydrate decomposition. In: Schwab WC, Lee HJ, Twichell DC (eds.). Submarine Landslides: Selected Studies in the U.S. EEZ: USGS Bulletin 2002, pp. 40–53.

Puzrin AM, Germanovich LN (2005) The growth of shear bands in the catastrophic failure of soils. Proc R Soc Math Phys Eng Sci 461:1199–1228.

Riedel M, Collett TS, Malone MJ and the Expedition 311 Scientists (2006) Proceedings of the Integrated Ocean Drilling Program. Washington, DC: Integrated Ocean Drilling Program.

Ruppel C, Driscoll N, Jones E, Collett T (2008) Initial science results of the March 2005 Gas Hydrate Field Program. U.S. DOE/Chevron Gulf of Mexico Joint Industry Projects. Mar Pet Geol 25:819–829.

Schmuck EA, Paull CK (1993) Evidence for gas accumulation associated with diapirism and gas hydrates at the head of the Cape Fear Slide. Geo-Mar Let 13:145–152.

Sultan N (2007) Comment on "Excess pore pressure resulting from methane hydrate dissociation in marine sediments: A theoretical approach" by Wenyue Xu and Leonid N. Germanovich. J Geophys Res 112:B02103, doi:10.1029/2006JB004527.

Sultan N, Cochonat P, Foucher JP, Mienert J (2004) Effect of gas hydrate melting on seafloor slope stability. Mar Geol 231:379–401.

Tréhu AM, Bohrmann G, Rack FR, Torres ME, et al. (2003) Proceedings of the Ocean Drilling Program Initial Reports, Volume 204.

Vogt PV, Jung WY (2002) Holocene mass wasting on upper non-Polar continental slopes due to post-Glacial ocean warming and hydrate dissociation? Geophys Res Let 29:55-1–55-4.

Waite WF, Osegovic JP, Winters WJ, Max MD, Mason DH (2008) Seeding hydrate formation in water-saturated sand with dissolved-phase methane obtained from hydrate dissolution: A progress report. 6th International Conference on Gas Hydrates, 6–10 July, Vancouver, Canada, 9 p.

Waite WF, Santamarina JC, Cortes DD, Dugan B, Espinoza DN, Germaine J, Jang J, Jung J, Kneafsey T, Shin HS, Soga K, Winters W, Yun TS (2009) Physical properties of hydrate bearing sediments. Rev Geophys, In Review.

Winters WJ, Pecher IA, Waite WF, Mason DH (2004) Physical properties and rock physics models of sediment containing natural and laboratory-formed methane gas hydrate. Am Mineral 89:1221–1227.

Wu L, Grozic JLH (2008) Laboratory analysis of carbon dioxide hydrate-bearing sands. ASCE J Geotech Geoenviron Eng 134:547–550.

Xu W, Germanovich LN (2006) Excess pore pressure resulting from methane hydrate dissociation in marine sediments: A theoretical approach. J Geophys Res 111:B01104, doi:10.1029/2004JB003600.

Zhang H, Yang S, Wu N, Su X, Holland M, Schultheiss P, Rose K, Butler H, Humphrey G, GMGS-1 Science Team (2007) Successful and surprising results for China's first gas hydrate drilling expedition. Fire in the Ice, Methane hydrate newsletter, U.S. Department of Energy, Office of Fossil Energy, National Energy Technology Laboratory, Fall, pp. 6–9.

Advanced Dynamic Soil Testing – Introducing the New Marum Dynamic Triaxial Testing Device

S. Kreiter, T. Moerz, M. Strasser, M. Lange, W. Schunn, B.F. Schlue, D. Otto, and A. Kopf

Abstract Soil mechanical and submarine mass-movement initiation studies often use static and quasi-static approaches to determine the strength of soils against external mechanical stresses. However, many natural processes pose time variant stresses on soils, and hence exert key roles for submarine slope stability and submarine mass-movement initiation. Prominent examples are earthquake-, wind-, wave- and current-forces and alternating man-made loading on offshore constructions. Most soils show a weaker response to periodic loading – making dynamic and cyclic loading experiments mandatory for offshore natural hazard and risk assessment. Dynamic and cyclic triaxial testing are essential in liquefaction studies of granular soils and creep investigations of cohesive and granular sediments. So far, competing setups are used with mechanical spindles, pneumatic actuators or full hydraulic drives.

The new MARUM dynamic triaxial testing device (DTTD) unit is addressing this increasing demand by enabling a wide range of test configurations. At its core it contains an ultra fast, hydraulically-driven ±20 kN cylinder and a 5 kHz real-time controller. This enables up to ±0.5 mm strokes at up to 50 Hz. Advantages to commercial systems are (1) the high flexibility in test setup, (2) the possibility to feed arbitrary signals derived from in situ measurements, and (3) full system access to all controls to expand and adjust the system abilities on the hard and software level. Applications so far include cyclic creep studies for offshore wind farms, liquefaction experiments on artificial sand–clay mixtures and studies on the behavior of submerged soils under dynamic stress conditions to evaluate slope stability and submarine landslide initiation.

S. Kreiter, T. Moerz (✉), M. Strasser, M. Lange, W. Schunn, D. Otto, and A. Kopf
MARUM – Center for Marine Environmental Sciences and Faculty of Geosciences,
University Bremen, Leobener Str. 28334 Bremen, Germany
e-mail: tmoerz@uni-bremen.de

B.F. Schlue
ARCADIS Consult GmbH, Europaplatz, 3, 64293 Darmstadt, Germany

1 Introduction

The response of continental margins to time variant stresses has become an important element in offshore risk assessment. Dynamic and cyclic loading exerts a key role in submarine slope stability and tsunamigenic submarine landslide initiation (Sultan et al. 2004; Biscontin et al. 2004). Cyclic loading is important for long-term securing of offshore installation such as wind energy plants (Lesny and Hinz 2006; Lesny and Wiemann 2005). The time variant stresses from seismic or storm loading may either affect the natural system directly or be transmitted through manmade constructions. In the last few years, large research efforts have been undertaken to understand the influence of rapid and transient stress changes on slope stability in the marine realm (Sultan et al. 2004, 2008; Biscontin et al. 2004, Biscontin and Pestana 2006; Azizian and Popescu 2006, Stegmann et al. 2007; and many others). Under cyclic loading, the sediment behavior is influenced by the intensity and duration of the cyclic stress. The soil properties relevant for the cyclic and dynamic behavior are the stress history, density or consistency respectively, sensitivity (for cohesive soils), degree of saturation, grain size distribution, and fine content (Kramer 1996). Cyclic stresses may lead to plastic deformation and to degradation in the stress–strain and strength properties of the sediment, which may result in the initiation of sediment mobilization. Additionally sands may show total liquefaction (Ishihara 1985; Pestana et al. 2000).

To simulate and study the wide variety of cyclic and episodic natural processes in the laboratory a testing system with maximum flexibility is required. Various dynamic shear systems have been developed over the previous decades. The majority of them are limited in their performance with regard to the frequency of the load applied. During recent years, results of undrained monotonic and cyclic ring shear tests on saturated cohesionless soils have been reported in the literature by Trandafir and Sassa (2004, 2005a, b), which are limited to 5 Hz. Research cyclic triaxial test systems at e.g. the Kyoto University or at the University of Duisburg-Essen work with pneumatic actuators or a combination of servo motor and pneumatic actuaors to apply the time variant loads up to approximately 1 Hz. The latest generation of commercially available dynamic triaxial systems are driven by electro-hydraulic servo actuators at 0.5 kHz, limiting their maximum frequency to 10 Hz or less (see www.geocomp.com and www.oce.uri.edu). In order to overcome these limitations, to avoid the disadvantage of restricted modification access using commercial systems, and to address sediment deformation with earthquake loads, which frequency spectra contain relevant energies up to 20 Hz, the MARUM dynamic triaxial testing device (DTTD) project was initiated.

2 MARUM Dynamic Triaxial Testing Device

The MARUM DTTD project was started in 2005 when the German Science foundation granted the second phase of the DFG Research Center MARUM (http://www.marum.de). The system was developed in house from components with the

initial guidance of the industry partner Hansa-Flex Hydraulik GmbH – a company specialized in hydraulic system design and setup (http://www.hansa-flex.com).

The test equipment compasses a servo-driven hydraulic cylinder with a free configurable real time controller, a hydraulic power unit, displacement-, load- and pore pressure transducers, a load frame, a pneumatically controlled confining and backpressure unit, and a control station with a user interface to initiate the testing scenarios (Fig. 1). At the heart of the system is a servofloat® quality hydraulic testing cylinder built by Herbert–Hähnchen GmbH & Co. KG. This cylinder contains a patented annular gap seal and is characterized by stick-slip-free cylinder movements and ultra low-friction at all piston speeds. The test cylinder operates at up to 32 MPa (25 kN) and the maximum piston speed is 4 m/s. The test cylinder is physically controlled by a 10 l/min D765 series servo MOOG valve directly mounted on to the cylinder via a voltage interface. The system performance is enhanced by two 1 l accumulator tanks (orange bulbs on the photo of Fig. 1) that prevent insufficient flux at the feed and the return side of the MOOG valve.

The oil cooling unit of the (11 kW) hydraulic power unit proved to be valuable in providing a constant oil viscosity and cylinder response. The unit delivers 28 MPa with a maximum flux of 15 l/min, allowing maximum oil flux at full servo valve opening which leads to frequencies up to 50 Hz and distance amplitude in access of ±0.5 mm.

The confining- and backpressures are provided via three independent servo-controlled valves (AirCom GmbH) of the PQ type with a pressure range from 0 to 2 MPa.
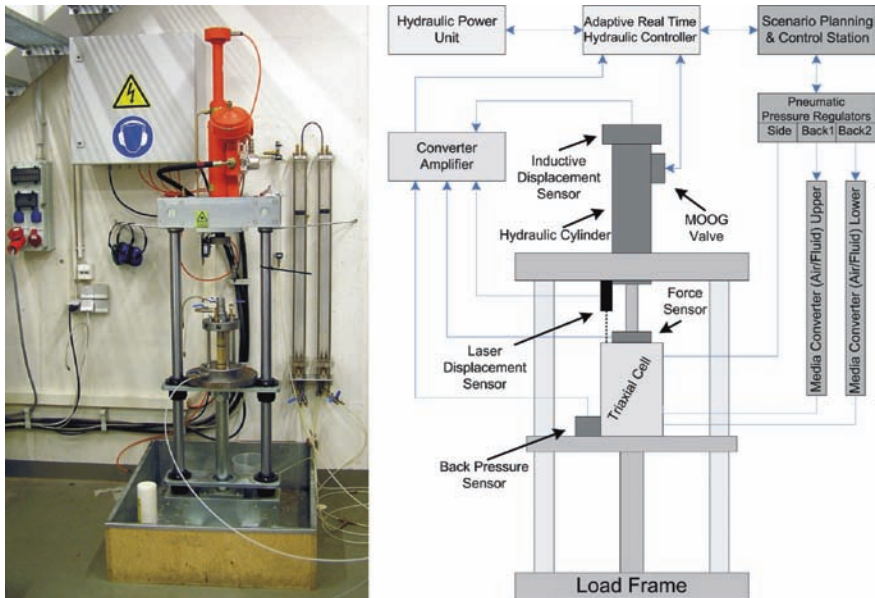
Fig. 1 Photograph and schematic drawing of the MARUM dynamic triaxial testing device

The valves are equipped with separate pressure transducers that report the pressure back via a 0–10 V interface. The heavy load frame is built around two parallel guiding rods that allow height adjustment for different experimental cells of up to 40 cm width. The load frame is mounted to massive concrete walls at the basement of the MARUM building, internal vibrations are suppressed via rubber shock-absorbers.

The real time data acquisition, processing and control unit (ADwin-light-16) comprises a SHARC™ digital signal processor from Analog Devices with a 40 MHz 32-bit FPU. Load and distance information is analog to digital converted and digitally processed by low phase digital filtering send to the control PC and to the PID (proportional, integral and differential) servo algorithm (Fig. 2). The resulting control signal is connected to the MOOG valve via an analog output of the ADwin system. All calculations are repeated every 0.2 ms resulting in a 5 kHz feedback loop and two orders of magnitude oversampling at maximum frequency of 50 Hz.

The distance information is currently provided via (1) an internal inductive displacement sensor (WLH 250-K-0.5%, MESSOTRON) within the hydraulic cylinder and (2) an external laser optical triangulation system from MICRO-EPSILON.
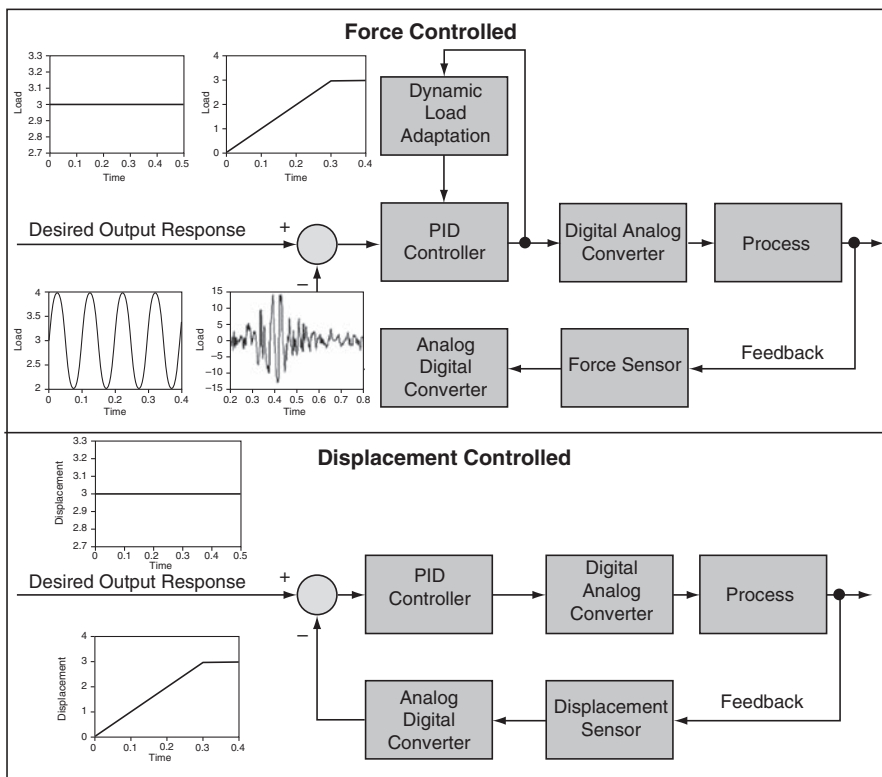
Fig. 2 Flowcharts of the force and displacement control processes in the real-time 5 kHz circuit

The internal inductive displacement control proved to be too temperature-sensitive and its resolution did not allow us to quantify sample deformations with the desired precision. However, the inductive sensor output is still used for safety reasons where distance control over the full stroke length is required. The external class II laser sensor ILD 1700 (Fig. 1) with a measuring range of 100 mm has a dynamic resolution of 0.003 mm (Fig. 3) at 2.5 kHz sampling frequency – accurate and fast enough to track the strain of stiff materials under dynamic loads of up to 50 Hz.

Load information is acquired via high-precision force transducers from GTM (Gassmann Testing and Metrology GmbH) with a range of 20 kN and 0.002% full scale accuracy. The GTM load transducers are directly mounted to the hydraulic cylinder rod (Fig. 1). Two ultra-low noise carrier frequency HBM amplifiers are used to collect the data of the force- and differential pore pressure transducers (Validyne) prior to analog/digital conversion. The input signal is logged and processed at 5 kHz by the ADwin unit.

Process control and data storage is accomplished with the scenario planning & control station, a PC-based system running a Labview (National Instruments™) routine developed in-house. The control station coordinates the real-time ADwin unit with the back- and side pressure unit. This main user interface allows for the performance of user-defined scenarios in force-controlled and displacement-controlled modes (Fig. 2).

3 Performance Examples

To evaluate the actual status (capability, compliance, etc.) of the MARUM DTTD, various performance tests have been conducted on materials of variable stiffness. In Figs. 3 and 4, experimental results on the stiffest end member, an aluminum cylinder placed inside a standard triaxial testing cell, are presented. It can be seen that at 1 Hz and 60 kPa cyclic loading, the input function and system response are in excellent agreement. At 10 Hz and 60 kPa dynamic loading, a phase offset and slight waveform distortion can be observed.
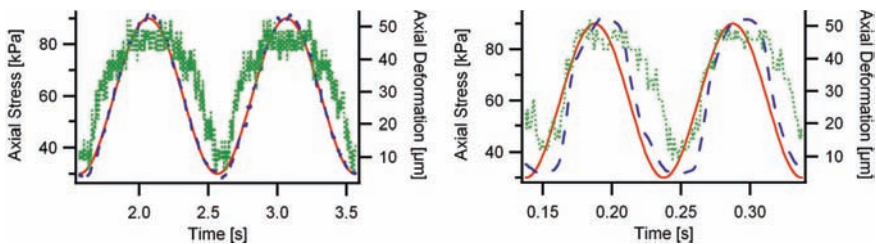
Fig. 3 System response using an aluminum test cylinder at 1 Hz left and at 10 Hz right. Red solid lines: predefined stress; blue dashed lines: measured stress, green dotted lines: sample deformation
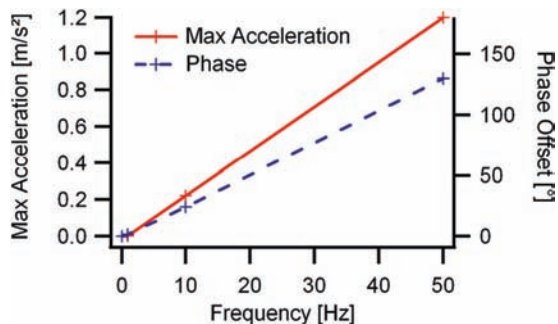
Fig. 4 Summary of the MARUM dynamic triaxial device response on an aluminum test cylinder at different frequencies

Frequencies of up to 10 Hz are well reproduced on stiff material (Fig. 4). However, the phase offset increases linearly for higher frequencies. Phase and amplitude offsets of the system response at higher frequencies or softer materials are tackled in an ongoing development effort to automatically modify the PID settings using a dynamic load adaptation (Fig. 2) This procedure will be especially valuable in experiments where soil properties are subject to change during complex runs.

The arbitrary signal function offers the possibility for testing soils with self-generated or recorded time – load signals to analyze the soil response to complex, but realistic multi-frequency dynamic loading scenarios under laboratory conditions. The performance example given here simulates a ground-motion record of the 1989 Loma Prieta earthquake (Mw 7.1) of a stratum 2 m subbottom. The time versus stress input function was derived using a procedure proposed by Seed and Idriss (1971) based on the empirical stress reduction factor from Iwasaki et al. (1978):

The shear stress function $\tau(t)$ on a potential horizontal failure plane at depth z of a soil column moving horizontally as a rigid body according to a horizontal acceleration function $a(t)$ (i.e. the signal recorded by strong-motion seismometers) can be calculated using Newton's laws of motion. In reality the soil column is internally deformable and the actual shear stress is less than that estimated from the above described rigid body model. This discrepancy is empirically corrected by the stress reduction coefficient r_d. The shear stress evolution $\tau(t)$ is therefore defined by

$$\tau(t) = \frac{a(t) \cdot \gamma}{g \cdot z} r_d \tag{1}$$

where γ is the unit weight and g is the gravitational acceleration. On the basis of a variety of soil-response data sets, Iwasaki et al. (1978), proposed $r_d = 1 - 0.015$ z/m. This allows for the assessment of shear stress history of a soil at a given depth from seismometer acceleration recordings.

Figure 5 shows the input arbitrary signal function and the measured system response measured on a soft foam test specimen (Young's modulus 235 kPa).
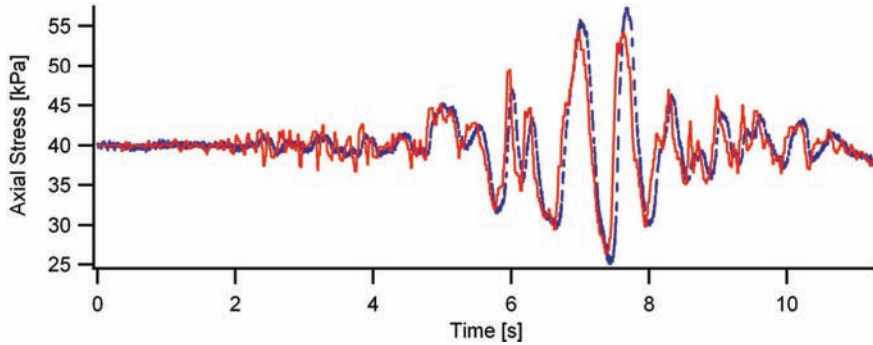
Fig. 5 Load time history: red solid line: arbitrary signal input function derived from acceleration time history of strong motion record from the Gilroy station #1, Channel 1 – at 090° for the 1989 Loma Prieta earthquake (Mw 7.1; 11 km from the rupture area) at Gilroy (CA), data from the Centre for Engineering Strong Motion Data (CESMD) http://strongmotioncenter.org. Blue dashed line actual load measured on the load sensor

The satisfactory reproduction of the input signal confirms that the DTTD system is able to adequately reproduce the ground acceleration of a given earthquake. Hence, any other arbitrary load signal derived from storm wave and tidal loading, traffic load (railways and motorways), foundations (bridges, dams, offshore platforms, etc.), or data from in situ measurements can be simulated.

4 Data Examples

4.1 Liquefaction of Sand

When initially loose, saturated granular sediment is exposed to strong dynamic or cyclic stresses (e.g. during an earthquake), the grains may reorganize to take up less space viz. the sediment may contract. Under undrained conditions the tendency toward pore water release reduces the effective stress by increasing the excess pore-water pressure. High cyclic stress amplitudes on loose granular soils may cause a drop in the effective stress to zero, which implies that the stress is taken up by the fluid rather than the particles: the soil is then liquefied (e.g. Ishihara 1985; Ishihara and Tsukamoto 2004).

Two variables are often used in cyclic failure assessment: the cyclic stress ratio (CSR) and the cyclic resistance ratio (CRR) (Kramer 1996). The cyclic stress ratio CSR is defined as $\sigma_{d,cyc}/2\sigma'_{3,i}$, where $\sigma_{d,cyc}$ is the cyclic deviator stress and $\sigma'_{3,i}$ is the initial effective minor principal stress at the start of the cyclic loading. Hence, the CSR is a measure of the cyclic load. The CRR is the CSR for a given number of cycles at failure. Hence, the CRR is a measure for the capacity of a sediment

layer to resist liquefaction and stress softening (Sultan et al. 2004). The ratio between both values is the factor of cyclic safety.

The CRR of natural quartz-rich dune sand has been determined with the new MARUM DTTD for various configurations. The sand was initially cleaned of organic material and sieved to a grain size ranging from 0.1 to 0.45 mm. The void ratio was $e_{max} = 0.59$ in its densest state and $e_{min} = 0.96$ in its loosest state. The sand was prepared dry in the cell and subsequently saturated by 500 ml flow of deaired water through the sample. Multiple samples were then back-pressured up to 500 kPa until full saturation (B-values > 95%) was reached and consolidated to the desired initial effective minor principal stress $\sigma'_{3,i}$. Then the samples were subjected to cyclic loading by applying load cycles with different CSR values and frequencies.

Figure 6 presents an example result of such a cyclic triaxial test with dense sand at a density index $I_D = 0.87$, corresponding to an initial void ratio of $e_0 = 0.64$, a B-value = 0.96 at 500 kPa backpressure, consolidated σ' 30 kPa, equivalent to an in-situ depth of ~5 m. The CSR was set to 0.3 at 1 Hz, which is typical for strong earthquakes (see Seed and Idriss 1971, and Eq. 1). The normalized pore pressure (pore pressure/total stress) increases continuously with increasing numbers of cycles, reaching 1 after ~17½ cycles (dashed line Fig. 6). Deformation starts after 15¾ cycles, when normalized pore pressure values are around 0.8 (solid line in Fig. 6). The negative strain reveals a dilatational behavior of the sand during liquefaction. As proposed by Kramer (1996) liquefaction of a soil element is considered to occur at excess pore pressures equal to 90% of the mean total stress (dotted vertical line in Fig. 6). Hence, the cyclic resistance of this sand under the given circumstances is equivalent to 16½ cycles, resulting in a CRR of 0.3 at 16½ cycles.
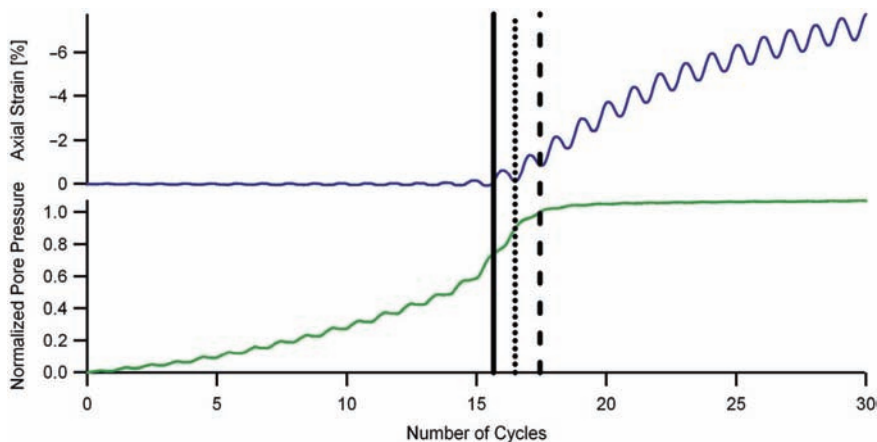
Fig. 6 Cyclic triaxial test of an artificial sand sample. *Top* graph: axial strain; *bottom* graph: pore pressure evolution. Vertical lines mark different liquefaction definitions: Solid line is onset of axial deformation; dotted line is pore pressure reaches 90% of total stress; dashed line is pore pressure reaches 100% of total stress
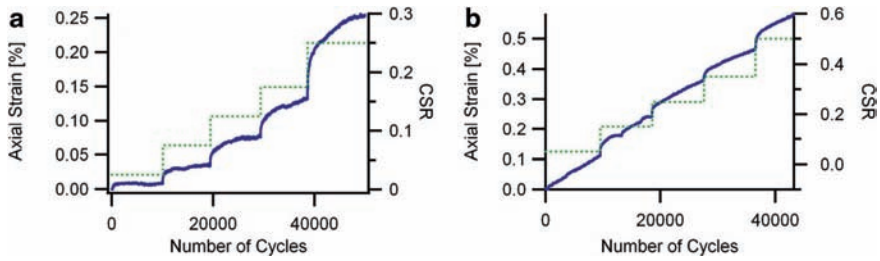
Fig. 7 Cyclic triaxial test results of samples from a North Sea wind farm area. Cyclic frequency is 5 Hz, cyclic σ_1 is stepwise increased every ~10,000 cycles. Blue solid line: axial strain; green dotted line: CSR. (**a**) Slightly overconsolidated silty clay, $\sigma_{3,i}$ is 200 kPa. (**b**) Highly overconsolidated clay, $\sigma_{3,i}$ is 100 kPa

4.2   Cyclic Creep in Clays

The behavior of cohesive sediments under cyclic load is fundamentally different to the usual cyclic response of granular media. Commonly stiffness and shear strength of clayey sediments degrade under cyclic loads. Figure 7a illustrates cyclic stress-induced deformation behavior of slightly overconsolidated silty clay, tested with every 10,000 cycles increased cycles cyclic stress ratios. At low CSRs the clay deforms incrementally during the first 1,000 cycles, followed by a *shake down* in deformation. At higher cyclic stress levels the deformation does not cease completely, and the clay deforms at lower and lower rates not likely leading to failure (*stabilization*). Under even higher CSRs the plastic deformations of clays may accumulate with ongoing cyclic loading and lead to *progressive failure*; however such a behavior has not been observed here for the CSR tested (Fig. 7a). *Shake down, stabilization* and *progressive failure* are the three most common behavior types of cohesive sediments (Mallikarjuna 1992; Lesny and Richwien 2004).

But cohesive soils show a variety of creep deformation responses. Figure 7b illustrates a CSR independent creep of strongly overconsolidated plastic clay. Here the number of stress cycles seems to be more important for the deformation behavior than the incrementally increased CSR. So far it is unclear whether (1) a critical consolidation ratio exists, (2) if a certain type of mineralogy is required for CSR independent creep behavior, and (3) if such a behavior could be described by a cyclic deformation rate, describing the material deformation by a rate to be multiplied by the number of stress cycles, not regarding the CSR. These are open questions currently addressed in an ongoing study.

5   Summary and Conclusion

The increasing awareness of the importance of cyclic and dynamic loading in hazard initiation stimulated worldwide efforts to build adequate testing devices. In this paper, the setup of the MARUM DTTD is presented and the crucial components

and control functions are discussed in the context of commercial systems. The full dynamic capabilities of servo-valve controlled hydraulic systems, however, can only be exploited if the force and displacement transducers have excellent accuracy and dynamics. The programmable digital signal processor of the DTTD allows flexible system operation modes. A series of performance tests have been performed to benchmark the system's capabilities. Frequencies up to 10 Hz can be used with confidence for soil testing. Higher frequencies up to 50 Hz are easily reached by the DTTD system, but lead to large phase offsets. The linear trend in acceleration suggests that the hydraulic system is capable of even higher dynamics. An earthquake equivalent stress signal is reproduced confirming that the MARUM DTTD is capable of accurately simulating multi-frequent arbitrary signals. Test carried out using standardized sand samples resulted in high quality strain and pore pressure data that allow a reliable CRR determination. Tests on highly overconsolidated clays revealed critical cyclic behavior of CSR-independent creep, stimulating further in depth studies. Cyclic creep, cyclic softening and liquefaction tests are now routinely conducted at the MARUM in the context of various ongoing projects, such as (1) the design of offshore wind power plants, and (2) slope stability analysis and submarine landslides studies (e.g. 1979 Nice Airport Slide, Cretan Sea, Nankai Trough). However, future work is required to implement the dynamic load adaptation routine that modifies the PID settings according to the changing stiffness of the samples.

References

Azizian A, Popescu R (2006) Three-dimensional seismic analysis of submarine slopes. Soil Dyn Earthq Eng 26:870–887

Biscontin G, Pestana JM (2006) Factors affecting seismic response of submarine slopes. Nat Haz Earth Syst Sci 6:97–107

Biscontin G, Pestana JM, Nadim F (2004) Seismic triggering of submarine slides in soft cohesive soil deposits. Mar Geol 203:341–354

Ishihara K (1985) Stability of natural deposits during earthquakes. In: Balkema AA (ed.) 11th International Conference on Soil Mechanics 1:321–376

Ishihara K, Tsukamoto Y (2004) Cyclic strength of imperfectly saturated sands and analysis of liquefaction. Proc Japan Acad Ser B 80:372–391

Iwasaki T, Tatsuoka F, Tokida K, Ysauda S (1978) A practical method for assessing soil liquefaction potential bas on case studies at various site in Japan. In: Proc. 2nd International Conference on Microzonation for Safer Construction: Research and Application

Kramer SL (1996) Geotechnical Earthquake Engineering. Prentice-Hall, Upper Saddle River, NJ

Lesny K, Hinz P (2006) A Concept for a Safe and Economic Design of Foundations for Offshore Windenergy Converters. In: Forkiewicz M (ed.) New Approach to Harbour, Coastal Risk Management and Education – Littoral, Gdansk

Lesny K, Richwien W (2004) Mindestanforderungen an die Baugrunderkundung. 3. Tagung Offshore-Windenergie, Germanischer Lloyd, Hamburg

Lesny K, Wiemann J (2005) Design Aspects of Monopiles in German Offshore Wind Farms. In: Gouvernec S, Cassidy M (eds.) Proceedings of the International Symposium on Frontiers in Offshore Geotechnics, Perth

Mallikarjuna RK (1992): Behavior of Vertical Piles Subjected to Static and Cyclic Lateral Loading. Ocean Engineering Centre, Indian Institute of Technology, Madras

Pestana JM, Biscontin G, Nadim F, Andersen K (2000) Modeling cyclic behavior of lightly over-consolidated clays in simple shear. Soil Dyn Earthq Eng 19:501–519

Seed HB, Idriss IM (1971) Simplified procedure for evaluation soil liquefaction potential. Soil Mech Found Eng SM 9:1249–1273

Stegmann S, Strasser M, Kopf A, Anselmetti FS (2007) Geotechnical in situ characterisation of subaquatic slopes: The role of pore pressure transients versus frictional strength in landslide initiation. Geophys Res Lett 34:L07607 1–5

Sultan N, Cochonat P, Canals M, Cattaneo A, Dennielou B, Haflidason H, Laberg JS, Long D, Mienert J, Trincardi F (2004) Triggering mechanisms of slope instability processes and sediment failures on continental margins: A geotechnical approach. Mar Geol 213:291–321

Sultan N, Cattaneo A, Urgeles R, Lee H, Locat J, Trincardi F, Berne S, Canals M, Lafuerza S (2008) A geomechanical approach for the genesis of sediment undulations on the Adriatic shelf. Geochem Geophys Geosyst 9:Q04R03 1–25

Trandafir AC, Sassa K (2004) Undrained cyclic shear response evaluation of sand based on undrained monotonic ring shear tests. Soil Dyn Earthqu Eng 24:781–787

Trandafir AC, Sassa K (2005a) Seismic triggering of catastrophic failures on shear surfaces in saturated cohesionless soils. Can Geotech J 42:229–251

Trandafir AC, Sassa K (2005b) Evaluation of catastrophic landslide hazard on gentle slopes in liquefiable soils during earthquakes. In: Proceedings of the International Conference on Landslide Risk Management, Vancouver (Canada) A.A. Balkema

Clustering of Geotechnical Properties of Marine Sediments Through Self–Organizing Maps: An Example from the Zakynthos Canyon–Valley System, Greece

M.D. Ferentinou, T. Hasiotis, and M.G. Sakellariou

Abstract A methodology is proposed in order to investigate clustering tendency of data referring to geotechnical properties that describe the recent sedimentary cover at the head of Zakynthos canyon/valley system in western Greece. Furthermore, the technology of unsupervised artificial neural networks (ANNs) is applied to the particular data sets coming from a submarine environment. Self-organizing maps (SOMs) are used due to visualization and clustering capabilities for analyzing high dimensional data. SOMs implement an orderly mapping of a high-dimensional distribution onto a regular low-dimensional grid. The detected clusters correspond to different sediment types (thus, they have a clear "physical meaning") recognized from sedimentological analysis in each of the examined data sets. The algorithm is also designed for classification in terms of supervised learning and was applied in order to predict the appropriate sediment type in new data incorporating geologists' knowledge. A coupled model of SOMs using interaction matrix theory was finally applied in order to rate the examined geotechnical properties in an objective and quantified approach. The results were reasonable and illustrate that the most dominant parameters in the studied area are undrained shear strength, water content and silt percentage.

M.D. Ferentinou (✉) and M.G. Sakellariou
School of Rural and Surveying Engineering, Laboratory of Structural Mechanics, National Technical University of Athens, 15780 Zografou, Greece
e-mail: mferen@mail.ntua.gr

T. Hasiotis (✉)
Department of Marine Sciences, University of the Aegean, University Hill, 81100 Mytilene, Lesvos, Greece
e-mail: hasiotis@marine.aegean.gr

1 Introduction and Scope

Submarine instabilities of slope deposits are an important mechanism of sediment transport and redeposition as well as a hazard to offshore development. Although marine geophysical surveys may report the occurrence of recent and old failures, it is the geotechnical character of collected sediment cores that is used (together with other parameters) for the computation of slope stability under various environmental forces (i.e. Lee and Baraza 1999; Lykousis and Chronis 1989; Lykousis et al. 2002, 2008, references therein). Relationships between geotechnical properties give evidence of the physical conditions of sediments and a crude evaluation of their potential for instability (i.e. very low shear strengths, water content higher than the liquid limit etc.).

In this paper the application of new mathematical tools is proposed in order to provide an integrated interpretation of geotechnical properties and discover tendencies of property variations, which may explain the geotechnical behaviour of the submarine slope sediments. The technology of unsupervised ANN is applied to the evaluation of the visualization and clustering capabilities of SOM for analyzing high dimensional data, coming from marine environments. This methodology is suggested in order to investigate clustering tendency of data collected from sediment cores, in clusters which have a clear physical meaning (i.e. sediment types) evident by the sedimentological analysis. An important characteristic of SOM is that they implement an orderly mapping of a high-dimensional distribution onto a regular low-dimensional grid. Moreover, the analysis is focused on the rating of the importance of the related parameters, their dominance and interaction intensity using generic interaction matrix theory (Hudson 1992). Coupling SOM with generic interaction matrix theory was successfully applied in order to rate slope stability controlling variables in sub aerial slopes (Ferentinou and Sakellariou 2007).

The input training data in this study are geotechnical properties of marine sediments (sand silt and clay percentage, $CaCO_3$, water content, Atterberg limits, wet bulk density and undrained shear strength), which were collected from the head of the Zakynthos valley/canyon system (Fig. 1).

2 Kohonen – Self Organising Maps

Kohonen (1994) has established techniques for unsupervised learning based on associative properties. These techniques involve nets that learn to respond in different parts to differences in input signals and they are called ordered maps. This method was first applied to speech recognition, and subsequently has been used for data analysis in system recognition, image analysis, environmental analysis, and geotechnical engineering. Basically, SOM is a visualization, clustering and projection tool, which illustrates structures in the data in a different manner than, for example, multivariate data analysis. SOM networks combine competitive learning with dimensionality reduction by smoothing the clusters with respect to an "a priori"
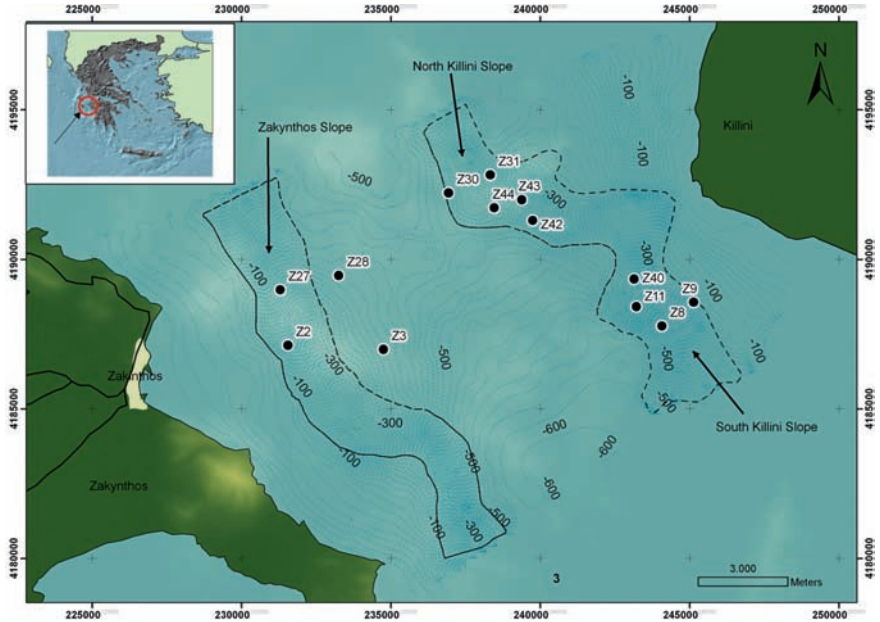
Fig. 1 Location of the study area and sediment core stations. Isobaths in meters

grid and provide a powerful tool for data visualization. Due to all the above mentioned characteristics, this specific training algorithm was applied to marine geotechnical data in order to investigate the non-linear relations and tendency of cluster creation among the sediment geotechnical properties.

The second version of the SOM Toolbox for Matlab (Vesanto et al. 1999) was used to perform the training of the ANNs. In SOM, each neuron is presented by a weight or prototype vector, which has as many components as the dimension of the input space (i.e. as the number of input variables). In this study, during batch training the sample vectors of the input data are presented to SOM as a whole. The interactive process involves calculating and comparing the Euclidian distances between each sample vector and all the weight vectors of the SOM. For each particular input vector, the neuron whose weight vector is the best match (minimum distance) is chosen and called the Best Matching Unit (BMU). During each training step, the weight vectors are updated in such a way that the new vectors are weighted averages of the input data vectors. The neurons are connected to adjacent neurons with a neighbourhood function which dictates the structure and the topology of the map. Each neuron of the SOM has an associated dimensional prototype vector, equal to the dimension of the input space of the prototype vector and another in the output (lower dimension) space, on the map grid. This ordered grid (Fig. 2) can be used as a convenient visualization surface for showing different features of the SOM.
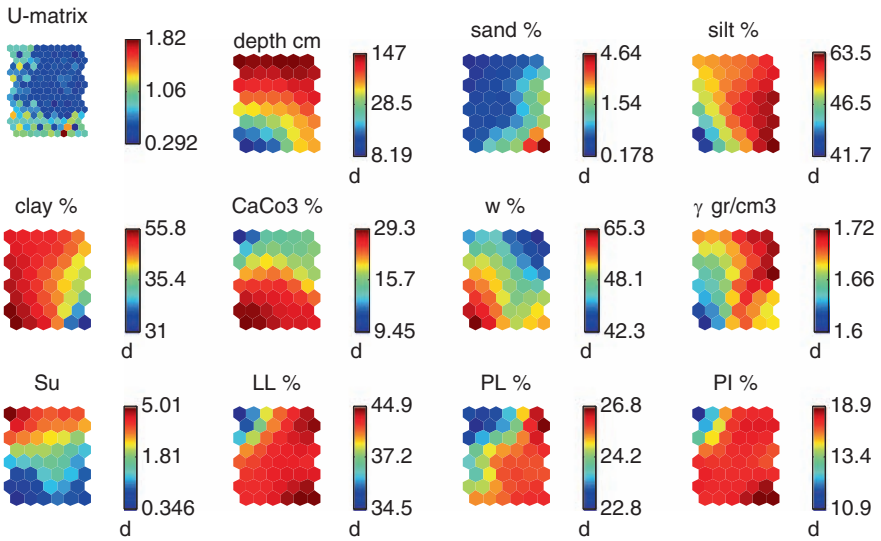
Fig. 2 Clustering visualizations using similarity coloring for south Killini slope. U-matrix on *top left*, component planes (as many as variables). Each map corresponding to one variable should be compared to the label map representing the distribution in Fig. 3

3   Source Data

The Zakynthos Valley/Canyon system is located within the narrow inner shelf – slope of the western Hellenic Trench and is characterized as a structural basin trending parallel to the local tectonic zones (Brooks and Ferentinos 1984) (Fig. 1). The recent sedimentation processes at the head of Zakynthos canyon were studied by Hasiotis et al. (2005) using a suite of high resolution seismic profiles and 47 sediment cores. Zakynthos canyon is not directly connected to any fluvial drainage system and it does not have a high energy wave regime, nor are there available data for internal wave resuspension and transportation of sediments to deeper waters. The head of the canyon is bounded by Killini and Zakynthos slopes, which are fault-controlled and are covered by a recent sediment drape.

Extensive and complex mass movements affect both the recent sedimentary sequences and the fault-escarpment face. Along the Killini slopes the main type of failure is repeated retrogressive sliding, which was caused by the absence of downs-lope support of the leading blocks. The south Killini slope is also sculptured by large buried extensive slide scarps. Along the Zakynthos slope, layered sediments overlie buried slumped and mass flow deposits. Extensive and complex failures affect the central part of the slope. Oversteeping of the slope due to the salt diapirism has produced slide scarps up to 30 m in height. The Zakynthos valley is filled

Table 1 Summarized description and interpretation of the observed sediment types

Sediment type, color, thickness	General description	Interpretation
ST1: Pale yellowish – brown mud (1.5–26 cm)	Surficial deposit; homogeneous high carbonate content	Calcareous mud. Accumulation from suspension
ST2: Grey mud (mm up to 100 cm)	Almost homogeneous; locally displaying color banding	Hemipelagic mud. Accumulation from suspension
ST3: Light brown to grey mud (3–9.5 cm)	Relative sharp contacts with the surrounding sediments; low shear strength and high water content.	Mud of high depositional rate Accumulation from suspension
ST4: Sand to sandy mud (0.5–26 cm)	Sandy horizons	Turbiditic sand to sandy mud. Gravity flow deposit
ST5: Plant debris (0.5–6 cm)	Well preserved debris of *Posidonia oceanica*; at the top of ST4 or intercalated with it	Turbiditic origin

Table 2 Sediment core data studied (S: sand, Z: silt, C: clay, w: water content, γ: wet bulk density, Su: undrained vane shear strength, LL: liquid limit, PL: plastic limit, PI: plasticity index)

Morphological unit	Core number	Sediment types	Studied parameters
North Killini slope	Z30, Z31, Z42, Z44	ST1, ST2, ST4,	Depth (cm), $CaCO_3$ (%), w (%), γ (gr/cm^3), Su (kPa)
South Killini slope	Z8, Z9, Z11, Z40	ST1, ST2, ST3, ST4	Depth (cm), S (%), Z (%), C (%), $CaCO_3$ (%), w (%), γ (gr/cm^3), Su (kPa), LL, PL, PI
Zakynthos slope	Z2, Z3, Z27, Z28, Z34	ST1, ST2, ST3, ST4	Depth (cm), S (%), Z (%), C (%), $CaCO_3$ (%), w (%), γ (g/cm^3), Su (kPa), LL, PL, PI

by extensive intercalated turbidtic/hemipelagic sediments and mass flow deposits. The extensive seafloor instabilities are attributed mainly to local tectonic activity, intense seismic activity and salt diapirism in relation to deep-seated gas ascension (Hasiotis et al. 2005).

The sedimentological analysis of the collected cores revealed the existence of five main sediment types (Table 1). In the current work attention is focused on the geotechnical properties (coming from laboratory measurements) of the sediments, which were retrieved from the north and south Killini slopes and the Zakynthos slope and were analysed in the laboratory (Fig. 1 and Tables 2, 3).

Table 3 Range of sediment core geotechnical values, (N. Kil: north Killini slope, S. Kil: south Killini slope, Zak: Zakynthos slope, d: core depth, S: sand, Z: silt, C: clay, w: water content, γ: wet bulk density, LL: liquid limit, PL: plastic limit, PI: plasticity index, Su: undrained vane shear strength)

		d (cm)	S (%)	Z (%)	C (%)	CaCO$_3$ (%)	w (%)	γ (gr/ cm^3)	LL	PL	PI	Su (kPa)
N. Kil	min	0	–	–	–	4.90	20.66	1.50	–	–	–	0.10
	max	107				29.90	87.77	1.91				33.60
S. Kil	min	0	0.12	40.80	30.82	5.00	40.23	1.52	34	22	10	0.10
	max	220	5.08	64.10	58.70	31.50	80.00	1.76	47	28	20	8.00
Zak	min	0	0.30	37.00	24.98	2.00	25.49	1.45	47	27	16	0.10
	max	190	15.20	70.32	62.00	33.50	94.39	1.91	52	32	22	11.20

4 Results of Clustering

The data were organized in a matrix [*dlen* x *dim*], where *dlen* is the number of samples, and *dim* is the number of input parameters. The proper data preparation is the most important step during the analysis procedure. It aims to (i) select variables and data sets to be used, (ii) clean erroneous or uninteresting values from the data, (iii) transform the data into a format which the modelling tool can best utilize and (iv) normalize the values in order to accomplish a unique scale and avoid parameter prevalence according to high values.

In order to perform the following analysis using SOM Toolbox, scripts originally written by J. Vesanto (1999) in Matlab were rewritten in order to satisfy the needs of the specific data set. A batch training algorithm was used. Three grids were created one for each examined geographical subunit. The initialization of the initial weights was random. Training took place in two phases. The initial phase is a robust one, whereas the second one is fine-tuning with a smaller neighbourhood radius and smaller learning rate. The neighbourhood function that was used was Gaussian. The methodology aims to cluster detection (projection in a lower dimension space) and to discover non linear relations between data base items. The small multiples technique was used, between others (scattered diagrams, hit histograms, trajectory analysis), for data visualization. Objects in small multiples can be linked together using similar position or place.

In Fig. 2 a map display is constructed using SOM algorithm for the south Killini data set. A multiple visualization consisting of 12 hexagonal grids is demonstrated. The first map on the upper left is a SOM, with values indicated using similar coloring. This map visualizes the training results and gives information about the general structure of the data and the clustering tendency (see color code map in Fig. 3). The multiple visualization is completed with the 11 maps which are called component planes. Each component plane refers to an input parameter. In these SOMs high values (hot colors) indicate the borders of the clusters, though low values (cold
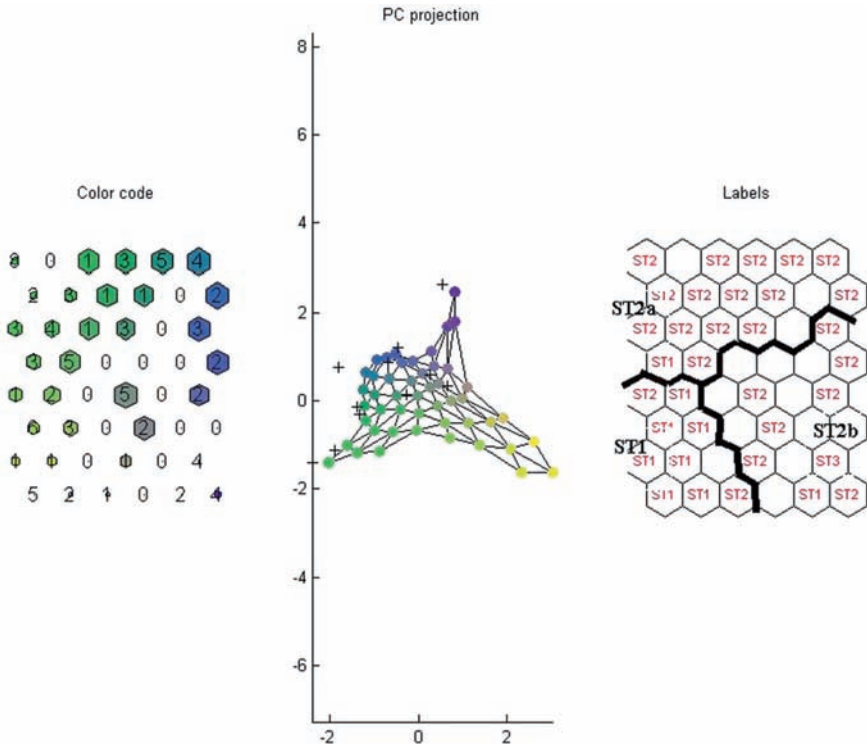
Fig. 3 Projection of South Killini data set (color code, PC projection and label map). The BMUs (35) are illustrated in color code map with score numbers. The black line defines the borders of the three clusters. Starting from *upper left* the clusters correspond to ST2a, ST2b, ST1

colors) characterize the clusters themselves. These visualizations can only be used to obtain qualitative information. The default number of colors in the colormaps and colorbars is 64. However, it is often advantageous to use less colors in the colormap. This way the components planes visualization becomes easier to interpret. Here the eleven component planes are visualized using 64 colors, but we also applied 'hot' colormap visualization using only three colors. This is how we classified the parameters in Table 4 to low, medium and high. It should be mentioned that there is shrinkage of parameters range values presented on the columns adjacent to each component compared to range values presented in Table 3.

The first step in the analysis of the map is visual inspection (see enlarged label map in Fig. 3) that shows the existence of three main clusters. Two clusters clearly correspond to ST2. They are almost homogeneous and exhibit low carbonate content, low water content, and high wet bulk density. These subgroups differ in clay percentage, Atterberg limits, undrained shear strength and core depth. The third cluster corresponds to ST1, which is an almost homogeneous surficial unit and

Table 4 Clustering results according to SOM (S: sand, Z: silt, C: clay, w: water content, γ: wet bulk density, Su: undrained vane shear strength, LL: liquid limit, PL: plastic limit, PI: plasticity index)

	North Killini slope			South Killini slope			Zakynthos slope		
	1st cluster	2nd cluster	3rd cluster	1st cluster	2nd cluster	3rd cluster	1st cluster	2nd cluster	3rd cluster
depth	Low	High	Medium	High	Medium	Low	Low	High	Low
S	–	–	–	Low	Low	Low	Low	Low	High
Z	–	–	–	High	High	Low	Low	Low	High
C	–	–	–	High	Medium	High	High	High	Low
CaCO$_3$	High	Low	Low	Low	Low	High	High	Low	High
w	High	High	Low	Low	Low	High	High	Medium	Low
γ	Low	Medium	High	High	High	Low	Low	Low	High
LL	–	–	–	Medium	High	Low	–	–	–
PL	–	–	–	Low	High	High	–	–	–
PI	–	–	–	Low	High	Medium	–	–	–
Su	Low	Low	High	High	Low	High	Low	Medium	High
ST	ST 1	ST 2a	ST2b	ST 1	ST 2a	ST2b	ST 2a	ST 2b	ST1

exhibits low values of silt, wet bulk density and shear strength and high values of carbonate content, water content and Atterberg limits. In general, undrained shear strength seems to increase with core depth, whereas wet bulk density is inversely correlated with water content. General trends arising from the current analysis reveal an association between grain size, water content and Atterberg limits. The general trends are also in accordance with Lykousis et al. 2008.

A principal component projection is made for the data and is applied to the map (Fig. 3). Three visualizations are illustrated: the color code, with clustering information and the number of hits in each unit, the projection and the labels. The projection confirms the existence of three different clusters and interpolative units seem to divide ST2 group into two subclasses, the difference being mainly clay percentage, shear strength, Atterberg limits and core depth.

The most informative visualizations of all offered by SOM are simple scatter plots and histograms of all variables (Fig. 4). The sediment type information is coded as an 11th parameter. Original data points, N = 96 are in the upper triangle, map prototype values on the lower triangle and histograms on the diagonal. The color coding of the data samples has been copied from the color code map (from the BMU of each sample). This visualization reveals quite a lot of information, distributions of single and pairs of variables both in the data and in the map.
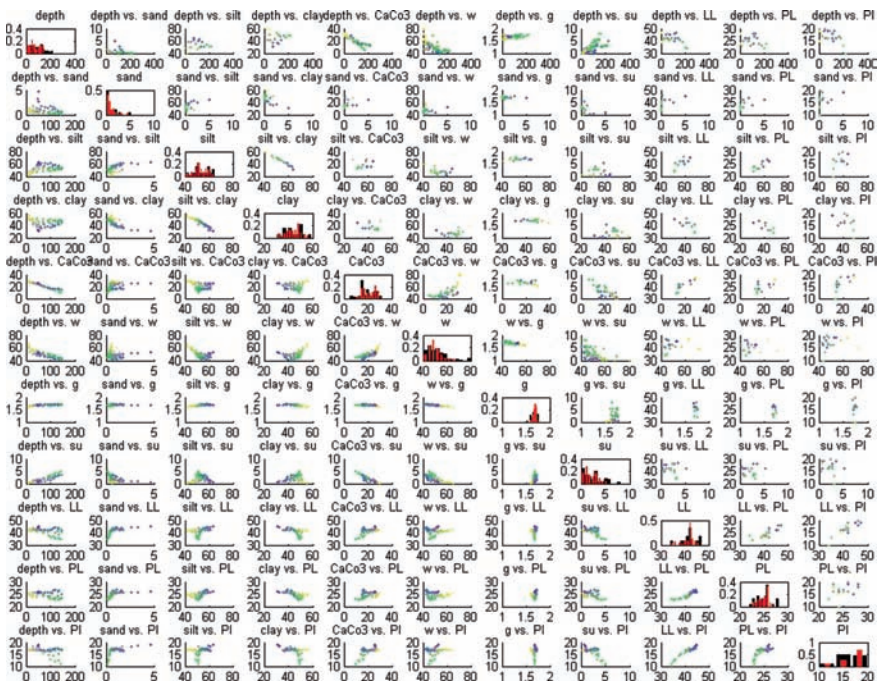
Fig. 4   11 × 11 scatter diagram for the South Killini data set, for 96 samples, N = 96

From this visualization many of the earlier conclusions are confirmed. For example, there appear to be three clusters, ST2a (dark green, blue), ST2b (green) and ST1 (yellow). Shear strength has a high linear correlation to core depth, and carbonate content is highly correlated to LL and PI.

The training of north Killini and Zakynthos slopes data sets (Table 4) also revealed three clusters, from which two correspond to subgroups of ST2 and one to ST1. The geotechnical properties trends are also similar to the south Killini slope. Shear strength is linearly correlated with core depth and water content is inversely correlated with wet bulk density. The algorithm was also applied for classification, in order to predict the appropriate sediment type incorporating geologists' knowledge, in case of new data, and the calculated accuracy was 79.2%, 65% and 89.1% for the south Killini, the north Killini and the Zakynthos data sets, respectively. Chang et al. (2002) used SOM in well log data and predicted lithofacies identity with 78.8% accuracy.

5 Parameters Rating: Interaction Matrix Theory and Cause/Effect Plot

Hudson (1992) suggested an analytical approach for representing rock engineering systems, as opposed to a synthetic approach, with the development of the interaction matrix device in order to represent the relevant parameters, their interaction, and the rock mass/construction behaviour. The principal factors considered relevant to the problem are listed along the leading diagonal of a square matrix (top left to bottom right) and the interactions between pairs of principal factors form the off-diagonal terms.

Ferentinou and Sakellariou (2007) applied the method in landslide hazard estimation and extended the interaction matrix to soil mechanics. The method proposes coding of the interaction matrix and studying the interaction intensity and dominance of each parameter. For each principal factor, its "Cause – Effect" (C, E) coordinates can be developed. These are the sums of the values in the row and column through each principal factor. The coordinates are plotted in a 'Cause – Effect' space (Fig. 5). Cause (C) is the way that the parameter affects the system, though effect (E) is the effect of the system to the parameter. Parameter interaction intensity increases from zero to a maximum value which is actually equal to the dimension of the matrix. The associated maximum possible parameter dominance values rise from zero to a maximum of 50% parameter interaction intensity and then reduce back to zero. This idea of interaction matrix was applied in the three studied data sets. The scatter diagrams (Fig. 4) produced for each data set were coded using a binary system. The elements not belonging to the main diagonal were attributed a value of 1 in case they had severe correlation, otherwise they were attributed the value of 0. The elements of the leading diagonal yield a value of 0. The produced cause effect plots for each data set are presented in Fig. 5.
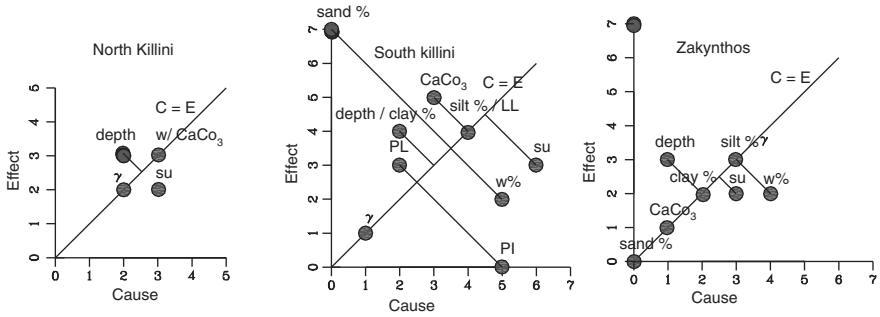
Fig. 5 Cause effect plots for the three data sets

According to the three data sets the most dominant parameter is undrained shear strength and water content. The most interactive parameter is carbonate content for North Killini slope, and silt percentage for south Killini and Zakynthos slopes. Sand percentage is the least dominant and least interactive.

6 Discussion – Conclusions

Although marine geotechnical properties are thoroughly studied, mainly for the evaluation of slope stability, this is the first time that marine sediment properties are manipulated with the above mentioned methodology. This study reveals that SOM can be an effective tool in order to successfully classify different sediment core samples according to their similar litho-geomorphological type. More specifically, the three data sets from the slopes bounding the upper part of the Zakynthos canyon/valley system revealed three clusters, taking into account the integration of multiple variables. These clusters correspond to different sediment types (thus, they have a clear "physical meaning") recognised from sedimentological analysis in each of the three data sets. One cluster corresponds to surficial deposit of pale yellowish brown mud (ST1) and the other two correspond to subgroups of grey mud (ST2a, ST2b).

Another advantage given by SOM is that it offers real insight to the data set, especially through the simple scatter plots. For example, although wet bulk density does not show any clear trend with core depth in the three data sets, map training of Zakynthos and north Killini data sets lead to the conclusion that there is a linear correlation, but within each subcluster. SOM component planes reveal useful information to interpret more easily the results that sometimes remain hidden with traditional approaches.

On the other hand, one of the drawbacks of SOM is that it eliminates outlier data. This is probably why ST3 was not considered as an important sediment type by the

ANN and was not recognised as a clear cluster. The core data representing this thin layer were generally few (one thin layer in each core) and sometimes incomplete; consequently there were not enough input data to represent this sediment type within the data set. ST4 unit has a high score in the map corresponding to Zakynthos data set, though it was also recognised in south Killini, where it appears to have a low score. Again this particular lithological unit is not adequately represented in the data set. Generally, ANN in order to converge and predict successfully, have to be trained with representative data of the system they have to simulate.

A coupled model of SOM networks using interaction matrix theory was finally applied in order to rate the examined geotechnical properties in an objective and quantified approach. The results are again reasonable and illustrate that the most dominant parameters in the studied area are undrained shear strength, water content and silt percentage.

References

Brooks, M. Ferentinos, G., 1984. Tectonics and sedimentation in the Gulf of Corinth and Kephalonia – Zante Straits, Ionian Sea, Greece. Tectonophysics, 101, 25–54.

Chang, H-C., Kopaska-Merkel D.C., Chen H-C., 2002. Identification of lithofacies using Kohonen self-organising maps. Computers and Geosciences, 28, 223–229.

Ferentinou, M., Sakellariou, M., 2007. Computational intelligence tools for the prediction of slope performance. Computers and Geotechnics, 34, 362–384.

Hasiotis, T., Papatheodorou, G., Ferentinos G., 2005. A high resolution approach in the recent sedimentation processes at the head of Zakynthos Canyon, Western Greece. Marine Geology, 214, 49–73.

Hudson J.A., 1992. Rock Engineering Systems: Theory and Practice, Horwood, Chisesteractice.

Kohonen T. 1994. Self-Organising Maps. Springer, New York.

Lee, H., Baraza, J., 1999. Geotechnical characteristics and slope stability in the gulf of Cadiz. Marine Geology, 155, 173–190.

Lykousis, V., Chronis, G., 1989. Mass movements, geotechnical properties and slope stability in the outer shelf-upper slope, NW Aegean Sea. Marine Geotechnology, 8, 231–247.

Lykousis, V., Roussakis, G., Alexandri, M., Pavlakis, P., Papoulia, I, 2002. Sliding and regional slope stability in active margins: North Aegean Trough (Mediterranean). Marine Geology, 186, 281–298.

Lykousis, V., Roussakis, G.,Sakellariou D., 2008. Slope failures and stability analysis of shallow water prodeltas in the active margins of Western Greece, northeastern Mediterranean Sea. International Journal of Earth Sciences, 98, 807–822.

Vesanto J., 1999. SOM-based data visualisation methods. Intelligent Data Analysis, 3, 2, 11–126.

Identification of Shear Zones and Their Causal Mechanisms Using a Combination of Cone Penetration Tests and Seismic Data in the Eastern Niger Delta

S. Garziglia, N. Sultan, A. Cattaneo, S. Ker, B. Marsset, V. Riboulot, M. Voisset, J. Adamy, and S. Unterseh

Abstract In a site investigation of the eastern part of the offshore Niger delta, cone penetration tests (CPTU) showed significant drops in tip resistance, associated with decreases in sleeve friction and induced excess pore pressures at the interface between superficial sediments and the underlying deposits of a mass-transport complex (MTC) called NG1. Such signature characteristics of weakened zones are clearly expressed at three sites where the drop in tip resistance reaches more than 40% over 2–3 m-thick intervals. Correlations between CPTU profiles and both 3D and ultrahigh-resolution 2D seismic data suggest that the weakened zones surround syndepositional the within the frontal part of NG1. Hence, weakening appears associated with the remobilization of thrust faults, inducing localized plastic shear. Relatively recent, deep-seated structural movements affecting NG1 are suspected to have remobilized these thrusts faults. When considering the sole influence of gravity, the fact that shear strength is mobilized within scattered, limited zones along steeply dipping syndepositional faults is not favorable for the further development of a continuous slope-parallel failure surface above NG1.

Keywords Cone penetration tests • shear zone • 3D seismic data • ultrahigh-resolution 2D seismic • mass-transport complex • slope stability

1 Introduction

The Niger delta has prograded since the early Tertiary onto the oceanic crust of the Gulf of Guinea to form one of the world's largest modern delta systems. It has a distinctive structural zonation resulting from large-scale gliding and spreading

S. Garziglia, N. Sultan, A. Cattaneo, S. Ker, B. Marsset, V. Riboulot, and M. Voisset,
IFREMER, BP 70, 29280 Plouzané Cedex, France

J. Adamy and S. Unterseh
TOTAL, Paris La Défense, France

(Hooper et al. 2002). Early to middle Tertiary overpressured shales provide regional detachment levels that link updip extension, downdip contraction and compensating translation of the intervening overburden. Superimposed on the primary accommodation created by these structural movements, compensation is provided by depositional processes (Hooper et al. 2002). Submarine slope failures and related products can induce both destructive and constructive compensation (Hooper et al. 2002).

In the frame of a collaboration project between IFREMER and TOTAL, the ERIG3D cruise was conducted in 2008 to study slope failure processes in the eastern part of the Niger delta. A large-scale buried mass-transport complex (MTC), initially identified on 3D seismic data and called NG1 (Fig. 1), was targeted for a thorough investigation using multidisciplinary methods. In this paper, special attention is paid to weakened zones that were identified in the upper part of NG1 using in situ geotechnical measurements. While slope failure often develops within weakened zones (Leroueil 2001; Urciuoli et al. 2007), geophysical, sedimentological, and geotechnical data were combined to unravel the origin and the geometry of the weakened zones as a key to assess the present-day slope stability in the area.

2 Materials and Methods

The 3D seismic volume used in this study was short-offset processed and pre-stack time migrated to enhance the resolution in the shallow part (Fig. 1b). The inline spacing is 6.25 m, and the crossline spacing is 12.5 m. The vertical and horizontal resolutions are approximately 7 and 15 m, respectively. Seismic interpretation and attribute analyses were done using the Sismage software developed by TOTAL.

Ultrahigh-resolution (UHR) seismic lines were acquired during the ERIG3D cruise using a new deep-sea sub-bottom profiler developed by IXSEA and IFREMER (Le Gall et al. 2008). It consists of a single light transducer working in the 1.8–6.2 kHz frequency band and a three hydrophones array as a receiver. This system was mounted on an autonomous underwater vehicle (AUV) to acquire 16 seismic lines (43 km) at constant altitude (80 m) with a shot spacing of 1.8 m (Fig. 1c). The vertical resolution is close to 20 cm.

The 21.4 m long Calypso piston-core ER-CS09 was recovered to reach the upper part of NG1 (Fig. 1c). Before splitting, the bulk density was measured using a GEOTEK multi-sensor core logger (MSCL, www.geotek.co.uk). Analyses on split sections included lithological descriptions, water content determination, undrained shear-strength measurements (vane shear test) and P-wave velocity measurements (celerimeter, see Sultan et al. 2008). The Atterberg consistency limits were determined using the fall cone method described by Koumoto and Houlsby (2001). Compressibility tests using an oedometer with incremental loading were carried out on four samples (see later figure).

In situ measurements were carried out using the Penfeld piezocone with both a standard CPTU cone and a sonic cone (for more details see Sultan et al. 2007). With the standard CPTU cone, continuous measurements of the tip resistance (q_c), sleeve
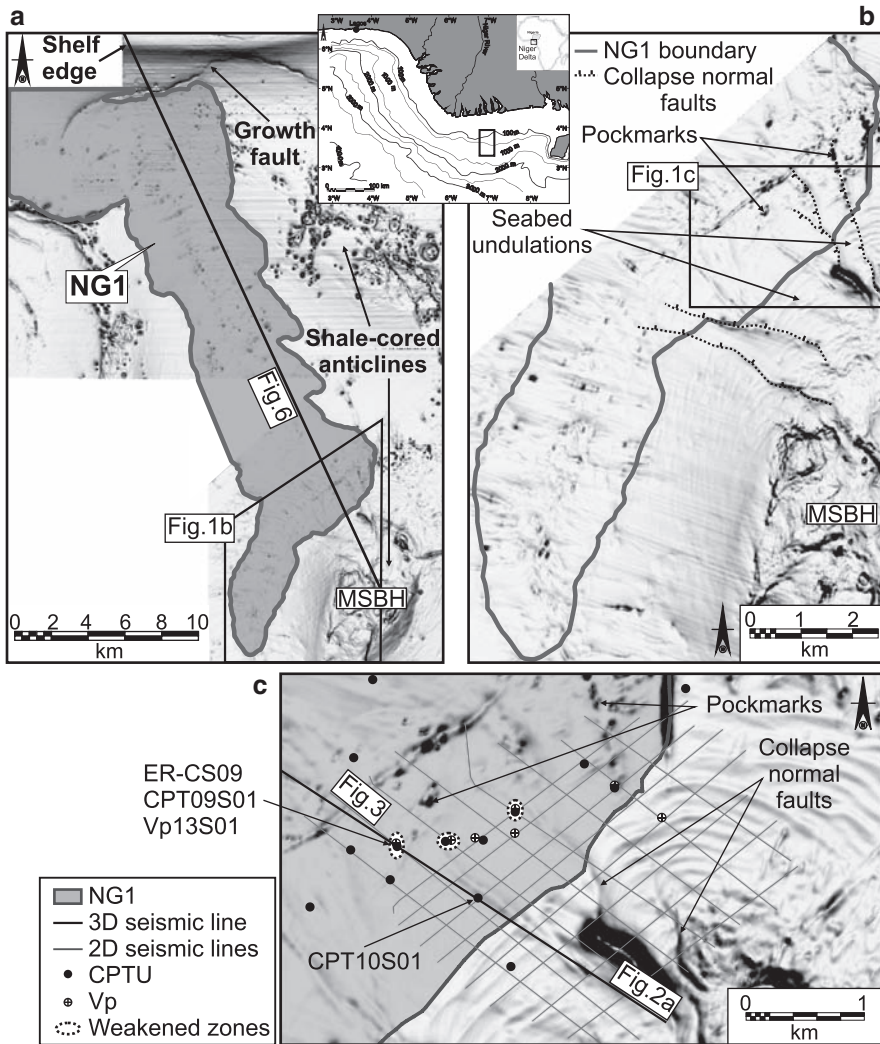
Fig. 1 (**a**) Seabed dip map from three 3D seismic volumes showing the main deformational structures surrounding the MTC NG1 whose areal extension is indicated in grey. (MSBH: mid-slope bathymetric high). (**b**) Dip map showing the main seabed features above the distal part of NG1 bounded by the dark grey line. (**c**) Seabed dip map showing the location of the data acquired during the ERIG3D cruise. Location of the seismic lines, core and CPTU profiles presented in Figs. 2–4 (core location ER-CS09), and Fig. 5 (sample site CPT10S01)

friction (f_s) and induced excess pore pressure (Δu_2) were performed at 14 sites down to 30 m below seabed (mbsb) (Fig. 1c). The measured excess pore pressure (Δu_2) was used to calculate the corrected tip resistance (q_t).

At five sites, in-situ P-wave velocity (V_p) measurements were performed down to 30 mbsb using the sonic cone (Fig. 1c). These were used to relate time to depth in order to accurately correlate sedimentological, geotechnical, and geophysical data.

3 Results

3.1 Morphostructure of the Study Area

Extending from the shelf edge at ~200 m below sea level (mbsl) to the mid-slope at ~900 mbsl, the study area shows a morphology controlled by structural movements (Fig. 1). Normal growth faults occur on the upper slope, where an arcuate escarpment suggests relatively recent activity (Fig. 1). Downslope, two shale-cored anticlines form dome-shaped bathymetric highs. The most prominent one, referred to here as the mid-slope bathymetric high (MSBH), culminates at ~50 m above the surrounding seabed. On its NW flank, seabed undulations show crests orientated perpendicular to the maximum slope (Fig. 1). Whether these features result from sediment deformations, deposition or a combination of both is as yet unclear. In the same sector, the seabed topography is also affected by collapse normal faults related to the growth of the underlying shale-cored anticline (Fig. 1b, c). Oval depressions interpreted as pockmarks affect a large portion of the seabed (Fig. 1). Some of them are clearly aligned along collapse normal faults surrounding the shale-cored anticlines. Other pockmarks seem related to buried sedimentary bodies (Fig. 1).

3.2 Seismic Analysis

The MTC NG1 was identified on 3D seismic data, using criteria established from previous studies (Frey-Martinez et al. 2006 and references therein). Mapping of its upper and lower bounding surfaces reveals that it covers, at least, an area of ~200 km² for an estimated volume of ~12 km³ (Fig. 1a). These values are underestimates since the continuation of NG1 beyond the NW border of the 3D seismic dataset could not be mapped. The areal extent of NG1 roughly presents a boot shape, with the heel resting at the base of the MSBH (Fig. 1). The most proximal deposits of NG1 identified, lie on the upper slope at ~300 mbsl. (Fig. 1a). The upslope part of NG1 is affected by arcuate growth faults (Fig. 1a). Its toe rests at mid-slope at ~900 mbsl. The thickness of the sediment overlying NG1 is up to 120 m on the upper slope and decreases progressively to ~15–30 m at mid-slope. Based on the combined analyses of its architectural geometry and deformational structures, NG1 is a composite feature preserving multiple genetically related mass-wasting events.

The present study focuses on the distal part of NG1, between 700 and 900 mbsl, where the thickness of its overburden does not exceed the maximum penetration
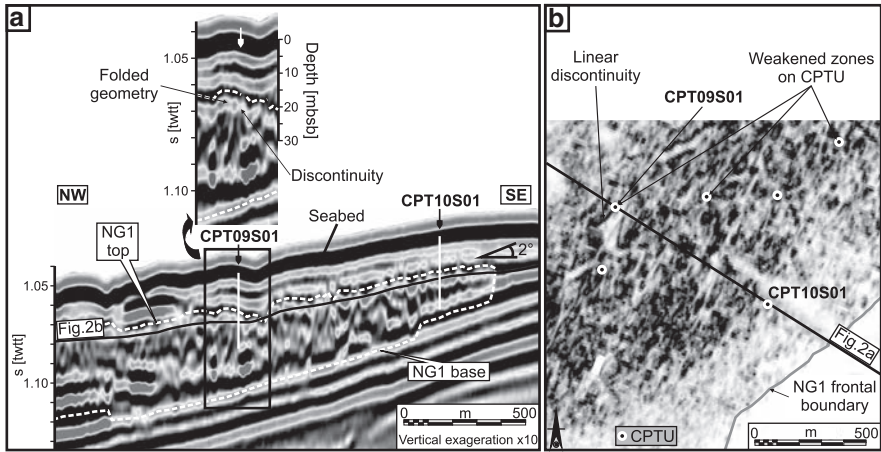
Fig. 2 (**a**) *Below*: 3D seismic line across the frontal part of the MTC NG1 on the flank of the MSBH (location shown in Figs. 1c and 2b). The location of the coherency slice presented in Fig. 2b is indicated by a black line cross-cutting the upper part of NG1. *Above*: Close-up of a folded geometry on the top of NG1 discussed in the text. The white arrow indicates the location of the CPT09S01. (**b**) Coherency slice cross cutting the upper part of NG1 (position of slice shown in Fig. 2a). Zones of lower coherency appear in darker tones. The circles show location of the CPTU measurements. Note that the location of the CPT09S01, where a weakened zone is clearly expressed, ties to a linear discontinuity

depth of the corer and the piezocone (i.e. 30 mbsb) (Fig. 1b). In this area, the pathway of NG1 appears to have been deflected toward the SW by the MSBH (Fig. 1). While the eastern edge of NG1 rests on the flank of the MSBH dipping at 1–3° to the NW (Fig. 2a), the bulk of its deposits spread along a gentle (≤1°) south-westward dipping slope.

On 3D seismic data, NG1 is generally characterized by internal chaotic reflections of low amplitude overlaid by reflections of higher amplitude and continuity which form a hummocky top with gentle topographic relief (Fig. 2a). The higher relief on the top of NG1 correlate to folded geometries generally adjacent to steeply dipping discontinuities (~35°) (Fig. 2a). In planform, such as observed on a coherency slice cross-cutting the upper part of NG1, the most prominent of these discontinuities appear as lineations oriented perpendicular to the slope direction (Fig. 2b). The base of NG1 shows a highly irregular surface cross-cutting stratigraphy (Fig. 2a).

On 2D seismic data, NG1 appears as a transparent body underlain by a continuous, high amplitude reflector (Fig. 3). It is generally bounded above by hyperbolic reflections and high amplitude patches ascribed to the blocky nature of its top surface. However, in some places, the top of NG1 is only faintly discernible or even invisible (Fig. 3). On the flank of the MSBH, the frontal part of NG1 is buttressed against continuous reflections of undeformed strata (Fig. 3).
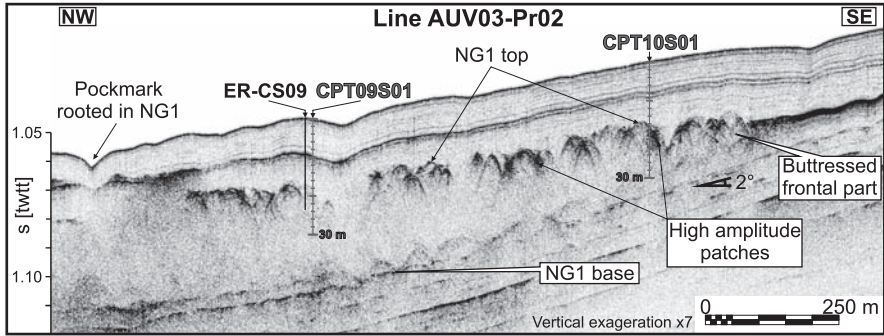
Fig. 3 Ultrahigh-resolution seismic line acquired with the AUV across the frontal part of the MTC NG1 on the flank of the MSBH (location shown in Fig. 1c). Location of core ER-CS09, CPT09S01, and CPT10S01 shown in Figs. 4 and 5 are identified
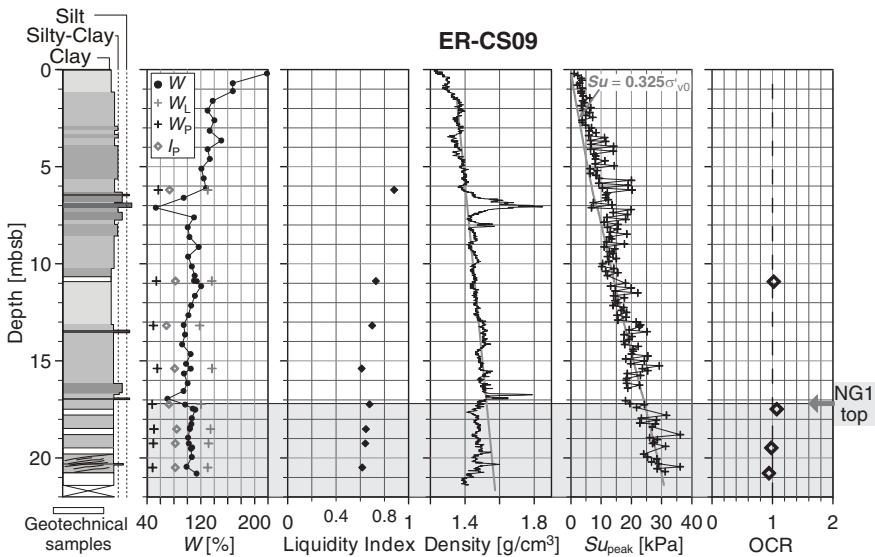
Fig. 4 Lithological and geotechnical logs of core ER-CS09 (location shown on Fig. 1) (*W*: water content, W_L: liquid limit, W_P: plastic limit, I_P: Plasticity Index, Density from MSCL, Su_{peak}: Undrained vane shear strength, OCR: overconsolidation ratio from oedometer tests on four samples)

3.3   Sediment Core Analyses

The core ER-CS09 was collected at a site where only faint hyperbolic reflections enable to identify the top of NG1 on 2D seismic data (Fig. 3). The ER-CS09 lithology is dominated by dark silty clay (Fig. 4). At 7 and 17 m, two silt layers are clearly marked by a decrease in water content and an increase in bulk density (Fig. 4).

Deformational structures are only observed at the base of core ER-CS09 (19.76–20.76 m) in an interval containing tilted bedding and small-offset faults (Fig. 4). The top of NG1 deposits is not visually discernable. Based on the correlation between laboratory and in situ V_p measurements, which were tied to 2D seismic data, the top of NG1 should be located at 17.2 m in the core, just below a silt layer (Fig. 4). Below this depth, the water content is between 6% to 14% higher than the decreasing trend of the overlying sediment represented by the grey curve in Fig. 4. This observation coincides with a density profile with values between 1.48 and 1.39 g/m³, which are between 6% and 12% lower than the grey line representing the trend of the overlying sediments (Fig. 4). These changes in water content and bulk density trends are interpreted to reflect the transition from undeformed sediments above to NG1 deposits below.

The plastic limit (W_p) is quasi-constant within the core, in the range 52% +/– 5%, while the liquid limit (W_L) is slightly more variable, ranging from 118% to 136% (Fig. 4). The plasticity index (I_p) varies between 69% and 84%. The liquidity index (L_L) decreases with depth from 0.88 at 6.2 m to 0.61 at 20.5 m (Fig. 4). None of the index properties show any significant change between undeformed sediments and NG1 deposits.

The transition at 17.2 m is also not clearly marked on the shear strength (Su) profile, which is quasi-linear from the top to the base of core ER-CS09 (Fig. 4). Consolidation tests indicate that the four tested samples are normally consolidated (i.e. 0.94 < OCR < 1.07) (Fig. 4). The ratio of undrained shear strength to vertical effective stress (Su/σ'_{v0}) is estimated to 0.325 for normally consolidated sediments. From the grey line representing this theoretical ratio on the strength profile in Fig. 4, the upper part of NG1 is normally consolidated.

3.4 In-situ Analyses

Two distinct units are identified on the 12 CPTU profiles performed in the area of NG1. The upper unit is characterized by a quasi-linear increase of the corrected tip resistance (q_t), the sleeve friction (f_s) and the induced excess pore pressure (Δu_2) from the seabed down to ~18–20 mbsb (Fig. 5). By analogy with core analyses, the upper unit consists primarily of clay-rich sediments. In the lower unit, q_t, f_s and Δu_2 show irregular profiles, with higher values than those of the upper unit (Fig. 5). These characteristics, reflecting the chaotic internal nature of NG1, suggest that during its emplacement, stress and strain were partitioned in a complicated fashion, varying both vertically and horizontally.

Based on the method recommended by Demers and Leroueil (2002), continuous profiles of preconsolidation pressure (σ'_p) were derived from CPTU data using the following equation: $\sigma'_p = (q_t - \sigma_{v0})/N_{\sigma t}$ (σ_{v0}: in situ total vertical stress, $N_{\sigma t}$: cone factor). Two σ'_p profiles were calculated by using a $N_{\sigma t}$ factor of 3.4, as suggested by Demers and Leroueil (2002), and a site specific $N_{\sigma t}$ factor. A site specific $N_{\sigma t}$ factor of 4.85 was deduced by relating the σ'_p obtained from the oedometer test on the sample taken at 10.90 m in core ER-CS09 to the corresponding value of ($q_t - \sigma_{v0}$)
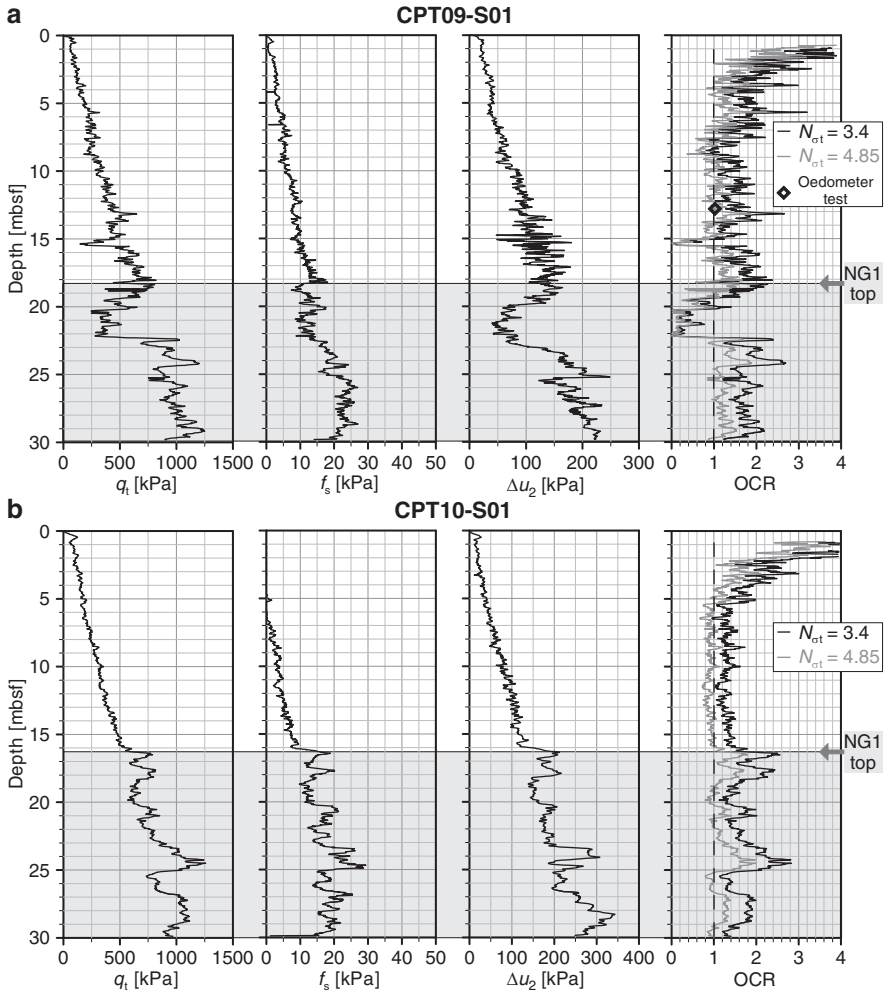
Fig. 5 CPTU profiles inside the frontal part of NG1 (q_t: corrected tip resistance, f_s: sleeve friction, Δu_2: induced excess pore pressure, OCR: overconsolidation ratio, $N_{\sigma t}$: cone factor) The grey area indicates the location of NG1 body from correlations with seismic data, constrained by detailed time to depth relationship derived from in-situ V_p measurements using the sonic cone

from the CPT09S01 performed 15 m apart. To correctly relate these two measurements, the in-situ depth of the oedometer sample was previously estimated from correlation between V_p measurements on core and in-situ at the nearby site Vp13S01 (see Fig. 1). Because no significant change in lithology was identified on core ER-CS09, the use of a single $N_{\sigma t}$ factor is considered reliable for estimating the σ'_p profiles for the superficial sediments, as well as for the underlying deposits of NG1. Vertical effective stress profiles (σ'_{v0}) were used to deduce profiles of overconsolidation ratio (OCR) as OCR = σ'_p/σ'_{v0}.

From the OCR profile calculated for CPT09S01 with $N_{\sigma t}$ = 3.4, the sediments overlying NG1 show magnitude of overconsolidation (Fig. 5a) that is not noticeable within core ER-CS09, according to the shear-strength profile and its relation to the Su/σ'_{v0} = 0.325 (Fig. 4). Therefore, estimates of OCR using the site specific $N_{\sigma t}$ are considered as more reliable in the study area. According to the OCR profiles thus calculated, the bulk of NG1 deposits are slightly underconsolidated to overconsolidated (0.8 < OCR < 2) (Fig. 5). The upper part of NG1 is most commonly overconsolidated (Fig. 5b). However, at three sites, simultaneous decreases of more than 40% of q_t and Δu_2 are observed within the upper 2–3 m of NG1 (Fig. 5a). These losses of resistance indicate local degree of weakening of the sediments. The most severe weakening is identified on the CPT09S01 profile, where the decrease in tip resistance reaches 80% over a 3 m interval (Fig. 5a). It is noteworthy that on the CPTU profiles obtained outside NG1, at a reference site and within the adjacent seabed undulations (Fig. 1c), no weakened zones are identified.

4 Discussion and Conclusion

Based on the combined analyses of the seismic, sedimentological and geotechnical data, the internal chaotic structure of the distal part of NG1 reflects complex stress and strain partitioning during its emplacement. The high amplitude patches observed in the upper part of NG1 on 2D seismic lines coincide with overconsolidated zones inferred from CPTU data (Figs. 3 and 5b). Besides, the simultaneous decreases of q_t, f_s and Δu_2 observed at three sites within the upper 2–3 m of NG1 are, according to Demers et al. (1999) and Delisle and Leroueil (2000), the characteristic signature of weakened zones related to the presence of fissures in clay.

These weakened zones show a scattered areal distribution suggesting that they result from local processes rather than being related to a spatially continuous weak layer (Fig. 1). On 2D seismic lines, the weakened zones are located in areas where the top of NG1 is of reduced reflectivity (Fig. 3). On 3D seismic lines, these areas appear as steeply dipping discontinuities along which the top of NG1 is offset (Fig. 2a). Only few of these discontinuities have enough lateral continuity to be detected on the coherency slice as relatively linear features, running parallel to the frontal boundary of NG1 (Fig. 2b). Following Frey-Martinez et al. (2006), these discontinuities are interpreted as highly deformed zones surrounding thrust faults which are consistent with the development of a compressional stress regime through buttressing of the frontal part of NG1 against the MSBH (see Fig. 3). By tying CPTU profiles with both 2D and 3D seismic observations, it is interpreted that weakening is associated with local shearing surrounding syndepositional thrusts faults.

The shear strength along thrust faults likely decreased to the ultimate strength during the emplacement of NG1, but it should have been recovered to some extent following post-depositional consolidation and burial, as suggested by Gibo et al. (2002). Hence, recent changes in boundary conditions, emphasizing local differences in the stress field in NG1, are required to account for the weakened zones identified. NG1
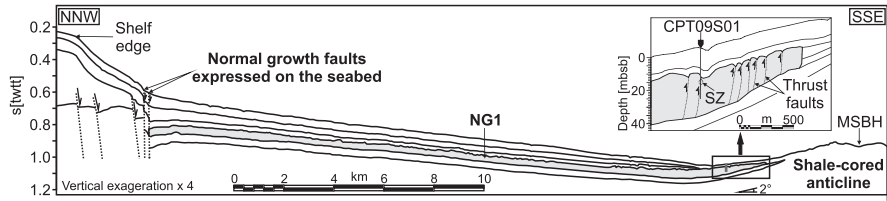
Fig. 6 Line drawing depicting the main structural elements bounding NG1 on the upper and mid-slope regions (MSBH: mid-slope bathymetric high). Inset shows a close-up of the frontal part of NG1, highlighting the correlation between the shear zone identified on CPT09S01 and the occurrence of a thrust fault (SZ = shear zone)

lies in a complex thin-skinned tectonic setting which points toward structural movements as an obvious candidate for inducing changes in boundary conditions. On the upper slope, NG1 is affected by normal growth faults, which, according to the escarpment observed on the seabed, appear to have been active relatively recently (Figs. 1 and 6). Moreover, the distal part of NG1 lies above a shale-cored anticline whose relatively recent uplift is manifested by collapse normal faults discernible on the seabed (Figs. 1 and 6). Movements along the growth faults (on the upper slope) and the uplift of the shale-cored anticline (at mid slope) are likely to induce redistribution of the state of stress within NG1. Such a mechanism is suspected to have mobilized syndepositional thrust faults within the frontal part of NG1, resulting in localized plastic shear responsible for the identified weakened zones. These last are consequently referred to as shear zones in the following discussion.

Considering the occurrence of shear zones raises the concern about their further propagation, leading potentially to general slope failure (Urciuoli et al. 2007; Puzrin et al. 2004). Without an estimation of the stresses imposed by structural movements, the propagation of the shear zones might be considered under the sole influence of gravity, as in the mechanism of catastrophic failure described by Puzrin et al. (2004). These authors showed that the key parameters controlling the catastrophic shear band propagation and bringing the slope to failure are: (1) the depth and length of the discontinuity surface; (2) the residual shear strength along the discontinuity surface; (3) the gravitational shear stress; and (4) the average values of the active and passive lateral pressure. The relatively low residual shear strength within the shear zones in NG1 may favor such catastrophic process (Fig. 5b). However, the low slope angle (<3°) implies low gravitational shear stress. Thereupon, considering that the shear zones are scattered and suspected to result from the remobilization of steeply dipping syndepositional thrust faults within NG1, these conditions are likely not favorable for the propagation of a continuous slope-parallel failure surface.

In an attempt to evaluate the impact of structural movements on the potential mobilization of NG1 and on the subsequent activation of the shear zones identified, further studies will use numerical models and integrate the data monitored, over a 1 year period, by two piezometers and inclinometers deployed in the frontal part of NG1.

References

Delisle M-C, Leroueil S (2000) Détection, à l'aide du piézocône, de zones ramollies dans des pentes argileuses et évaluation de leur comportement mécanique, Report GCT-98–23 prepared for the Ministère des Transports du Québec, Québec: Université Laval

Demers D, Leroueil S, d'Astous J (1999) Investigation of a landslide in Maskinongé, Québec. Can Geotech J 36:1001–1014

Demers D, Leroueil S (2002) Evaluation of preconsolidation pressure and the overconsolidation ratio from piezocone tests of clay deposits in Quebec. Can Geotech J 39:174–192

Frey Martinez J, Cartwright J, James D (2006) Frontally confined versus frontally emergent submarine landslides: a 3D seismic characterisation. Mar Pet Geol 23:585–604

Gibo S, Egashira K, Ohtsubo M, Nakamura S (2002) Strength recovery from residual state in reactivated landslides. Géotechnique 52:683–686

Hooper RJ, Fitzsimmons RJ, Grant N, Vendeville BC (2002) The role of deformation in controlling depositional patterns in the south-central Niger Delta, West Africa. J Struct Geol 24:847–859

Koumoto T, Houlsby GT (2001) Theory and practice of the fall cone test. Géotechnique 51:701–712

Le Gall Y, Pacault A, Mosca A, Greninguey G, Vial M, Aissa JC (2008) Ultra-deep low-frequency sub-bottom profiler for AUV and ROV, Acoustics'08, Paris, France

Leroueil S (2001) Natural slopes and cuts movement and failure mechanisms. Géotechnique 51:195–243

Puzrin AM, Germanovich LN, Kim S (2004) Catastrophic failure of submerged slopes in normally consolidated sediments. Géotechnique 54:631–643

Sultan N, Voisset M, Marsset B, Marsset T, Cauquil E, Colliat JL (2007) Potential role of compressional structures in generating submarine slope failures in the Niger Delta. Mar Geol 237:169–190

Sultan N, Cattaneo A, Urgeles R, Lee H, Locat J, Trincardi F, Berne S, Canals M, Lafuerza S (2008) A geomechanical approach for the genesis of sediment undulations on the Adriatic shelf. Geochem Geophys Geosyst 9:1–15

Urciuoli G, Picarelli L, Leroueil S (2007) Local failure before general slope failure. Geotech Geol Eng 25:103–122

Mass Wasting Dynamics at the Deeper Slope of the Ligurian Margin (Southern France)

A. Förster, V. Spieß, A.J. Kopf, and B. Dennielou

Abstract Submarine landslides are very common on the tectonically and seismically active Ligurian margin, NW-Mediterranean Sea. We present geophysical, sedimentological and geotechnical results from two extensive landslide complexes in water depth exceeding 1,500 m on the steep continental slope (>11°) near the Var Canyon.

At the Western Landslide Complex, facing the Var Canyon, we observe multiple headwalls and tilted layering. Undisturbed and failed sediments are characterised by a downward increase in bulk density and shear strength, the failed portion of which shows low intrinsic friction coefficients of 0.27. Otherwise, at the Eastern Landslide Complex, which shows smooth headwall features containing debrites and hemipelagic silty clays with pebbles, we observed constant bulk density of the failed sediments; however the shear strength in the remobilized sediment is lower than in the hemipelagites. This indicates that the failed material may have incorporated seawater and has retained its underconsolidated state until the present. The material is hence prone to future landsliding in case of seismic loading and/or the occurrence of other factors destabilizing the sediment.

Keywords Ligurian Basin • landslide • geotechnical characterization

A. Förster (✉), V. Spieß, and A.J. Kopf
MARUM- Center for Marine Environmental Sciences,
University of Bremen, Leobener Straße,
PO box 330440, 28334 Bremen, Germany
e-mail: annika.foerster@uni-bremen.de

B. Dennielou
IFREMER – French Research Institute for Exploitation of the Sea,
Département des Géosciences Marines, PO box 70,
29280 Plouzané Cédex, France

1 Introduction

Submarine landslides are an important process in transporting sediment to deeper water and are attracting increasing interest due to their tsunamigenic potential or their role as potential hazards for offshore platforms, cables, pipelines, and other installations. The trigger mechanisms of submarine landslides are still incompletely understood (Locat and Lee 2002), so that the study of submarine landslides and mass wasting processes in general at continental margins is a priority in the study of ocean margins (e.g. Hampton et al. 1996; McAdoo et al. 2000; Bryn et al. 2005).

In the Ligurian Basin, a tectonically complex and seismically active area at the NW-Mediterranean Sea, the Var Canyon and its adjacent slopes are particularly susceptible to sediment failure and landslide processes. While previous studies focused largely on the 1979 Nice Airport Slide or Var Canyon processes (e.g. Cochonat et al. 1993; Piper and Savoye 1993; Mulder et al. 1994; Klaucke and Cochonat 1999; Klaucke et al. 2000; Dan et al. 2007), our study uses geophysical data and core material from two landslides located on the deeper (>1,500 m water depth), steep Ligurian slope. Data acquisition took place during expedition M73/1 of R/V *Meteor* in July 2007 (Fig. 1). This paper focuses on the geometry of the landslide complexes from bathymetric and seismic data, the sedimentary record of the failed sediments relative to adjacent hemipelagic sediments, the physical properties and the geotechnical character of the sediments. Dating of the events has not been performed yet, but is required to comprehend timing of mass wasting.
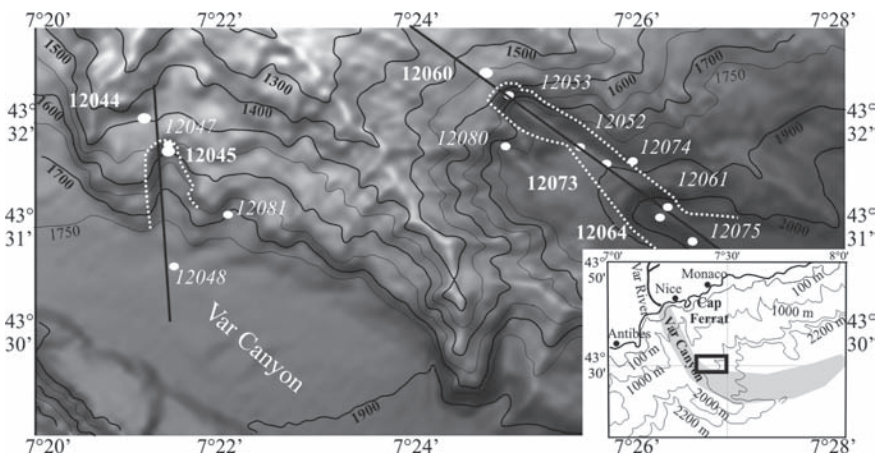
Fig. 1 Shaded relief bathymetric display with contour lines of the study area with core locations of cruise M73/1 in water depths ranging from 1,170 to 2,100 m. Cores used in this study are outlined by bold numbers. Profile lines see Fig. 2. Small map: map of the Ligurian continental margin (Modified after Piper and Savoye 1993) with the study area indicated by the black box

1.1   Geological Background in the Study Area

The Ligurian Basin is a marginal back-arc basin that formed by rapid continental extension during the Upper Oligocene-Miocene (Burrus et al. 1987; Pasquale et al. 1996). Drift of the Corsica-Sardinian block and formation of the Apennines range until the early Miocene are major consequences. During the Messinian (late Miocene), Mediterranean sea level drawdown subaereal erosion affected the margin to a depth of about 1,500 m below the pre-Messinian sea level (e.g. Ryan 2009). In the present-day basin active deformation occurs offshore at a small rate of about 1.1 m/ka (Bethoux et al. 1998). Furthermore, seismic activity is well known in this area with earthquakes of magnitudes up to M 6.3 (July 1963), although more common are smaller magnitude earthquakes of M 2.2–M 4.5 (Rehault and Bethoux 1984).

The Quaternary uplift of the Alps and associated erosion supply large volumes of sediment to the Ligurian Basin. The system is fed from small mountain-supplied rivers (Var, Paillon and Roya rivers). During floods, suspended sediment concentration can reach tens of kilogram per cubic meters, resulting in hyperpycnal flows and, later, underconsolidated deposits (Mulder et al. 1998). The submarine Var Canyon system represents the offshore extension of the Var River, one of the major rivers entering the Ligurian Basin west of Nice (Fig. 1). The area is characterised by a very narrow continental shelf (2–3 km) and a steep continental slope with an average angle in excess of 11° (Cochonat et al. 1993). While sediment supply in the Var system is high, Sultan et al. (2004) have quantified sedimentation rates as 8 m/ka between ~12 ka and ~7 ka BP, and 3.5 m/ka from 7 ka BP until now.

2   Methods

During R/V Meteor cruise M73/1 the entire Var Canyon area and adjacent slopes were mapped using a bathymetry system (SIMRAD EM120 and EM710) and a high-resolution, 16-channel seismic reflection system. For more comprehensive descriptions of the instruments and measurement techniques used, refer to Kopf et al. (2008). Based on the multibeam swathmapping and seismic reflection data, 16 gravity cores (length 2–10 m, 0.1 m diameter; further details in Kopf et al. 2008) were taken in two large-scale landslide complexes (Fig. 1). To illuminate the mass wasting dynamics and timing of the events, coring took place at various locations outside the landslide complexes and within the slide complex in various locations from the headwalls down to the run-out zones. All cores were studied sedimentologically and sediment physical properties were recorded by using a Multi-Sensor Core Logger (MSCL), whose results can be found in Kopf et al. (2008). For this post-cruise study, we selected two cores from each landslide complex for dedicated geotechnical measurements. Reference sites (GeoB12044 and -12060) and cores of the slide body

(GeoB12045 and -12064) should give information about the textural change and evolution of the sediments during failure.

In addition to the physical properties, the sediment samples were tested for their stiffness to detect "weak layers". For this, the undrained shear strength C_u was determined using a Vane shear apparatus (Blum 1997). To compare the strength of small clasts to that of the matrix in the landslide sediment, we used a falling cone penetrometer (Wood 1985) to calculate C_u-values at discrete sampling points that were too small for the use of the Vane shear apparatus.

Furthermore, information about the frictional response of the sediments was collected by means of direct shear tests on remolded samples (drained shear strength values). The core sampling strategy was based on the results from the MSCL runs as well as from core descriptions. The drained shear strength values were normalised against the normal stress, where the coefficient of friction, μ, is the ratio between shear stress and normal stress. The compressibility of the specimens was measured using a fix-ring oedometer apparatus. In direct shear and oedometer tests, the experimental setup corresponds with the current stress state of the sediment; therefore, the load was increased incrementally up to 300 kPa. For the direct shear tests, a sliding velocity of 0.01 mm/min was chosen. The maximum stress the sediment experienced (i.e. the preconsolidation pressure σ_{pc}) was determined after Casagrande (1936). The consolidation status of the sediment was estimated from the overconsolidation ratio (OCR) of preconsolidation stress, σ_{pc} to vertical effective stress, σ_{eff}:

$$OCR = \sigma_{pc}/\sigma_{eff} \tag{1}$$

3 Results

3.1 Geophysical Characterization

Bathymetric, seismic reflection and parasound data reveal two different extensive slide complexes between 7°20' E to 7°30' E and 43°30' N to 43°33' N in about 1,500–2,000 m water depth (Figs. 1 and 2). The Western Landslide Complex lies within the Var Canyon and shows many steep (32°) elongated head scarps with heights of ~40 m and talus at their base. Above the headwall area rough seafloor reflectors are visible. Failed sediments could not be unambiguously observed in the seismic profile (Fig. 2a). At the transition to the Var Canyon valley the slope angle decreases to ~11°. A similar, Eastern Landslide Complex is found farther away from the Var Canyon, striking to the Southeast in an area with slope angle of about 20° (Figs. 1 and 2b). It is characterized by a single, rather smooth headwall (Fig. 2b). In contrast to the Western landslide complex, we observe several indications for mass wasting processes, such as the failed deposits along a SSE-trending pathway, including hummocky topography and transparent units in the seismic reflection lines (Fig. 2b).
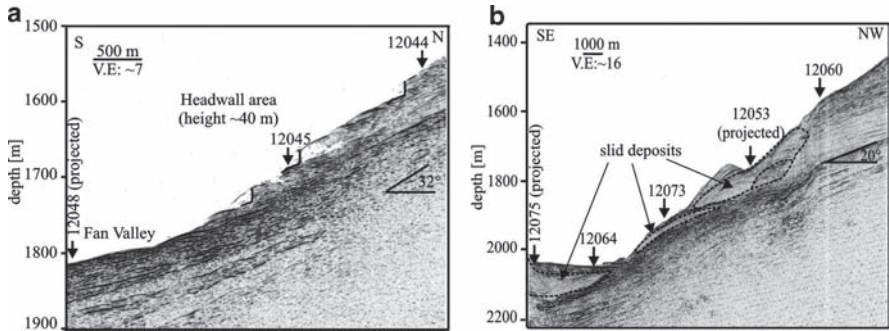
Fig. 2 Headwall striking profiles with core locations of the (**a**) Western (with incisions in the headwall area) and (**b**) Eastern Slide Complex (with failed deposits). For locations of the profiles see Fig. 1

3.2   Western Landslide Complex

On top of the majority of the five cores taken at the Western Slide Complex (Ch. 2) a similar lithostratigraphic succession (back-ground sediment) characterized by homogeneous, but in places also bioturbated, fine-grained hemipelagic silty clay with some coarser-grained intervals. Minor lithology is pelagic ooze with shell fragments (mostly pteropods shell debris, Kopf et al. 2008). Sediments interpreted as reworked along the assumed pathway of the landslide consist of dark grey silty-clay with some sandy intervals and inclusions of organic material or pelagic ooze (Fig. 3a, b; Kopf et al. 2008).

In the reference core GeoB12044 sharp oblique contacts (20–45°) are present both within the hemipelagic sediment drape and into the underlying dark-grey, stiff silty clay. Bulk density increases slightly downward from ~1.75 g/cm^3 in the hemipelagic sediments to 1.90 g/cm^3 while C_u remains more or less constant. Following Cochonat et al. (1993), we calculated the C_u/σ_{pre}-values to eliminate the effect of apparent overconsolidation on normally consolidated sediments (C_u/σ_{pre} = 0.2–0.4). As can be seen in Fig. 4a, the undisturbed sediments are more or less normally consolidated (station GeoB12044). In the reworked silty clays of core GeoB12045 collected near the headwall bulk density and C_u increase downward from 1.95 to ~2.08 g/cm^3 and from 25 to ~75 kPa with a sharp gradient at the transition between the hemipelagics above and the silty clays below at 3.2 m core depth (from 1.82 to ~1.95 g/cm^3 and from 3 to ~25 kPa (Figs. 3b and 4a).

The residual coefficient of friction (μ_{res}) of the hemipelagic sediments is between 0.36 and 0.42, which is typical for normally consolidated clay-rich silt sediments (Kopf and Brown 2003). However, μ_{res} of silty clays in core GeoB12045 located in the deeper portion of the headwall is 0.27–0.29, significantly lower than in the hemipelagics, and argues for a different sediment compositions (see above). The overconsolidation ratio (OCR) of the hemipelagic sediment slightly exceeds 1, thus
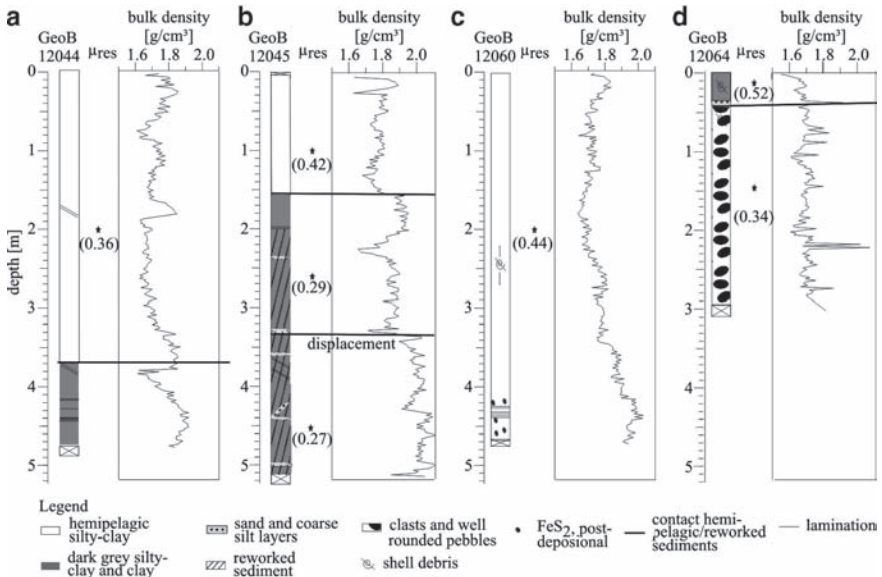
Fig. 3 Core description, bulk density (MSCL) and residual coefficient of friction (μ_{res}) from direct shear tests: Western Slide Complex core taken above (**a**) and below the headwall (**b**). Eastern Slide Complex cores taken above the headwall (**c**) and further downslope (**d**). Positions of the cores: Fig. 1
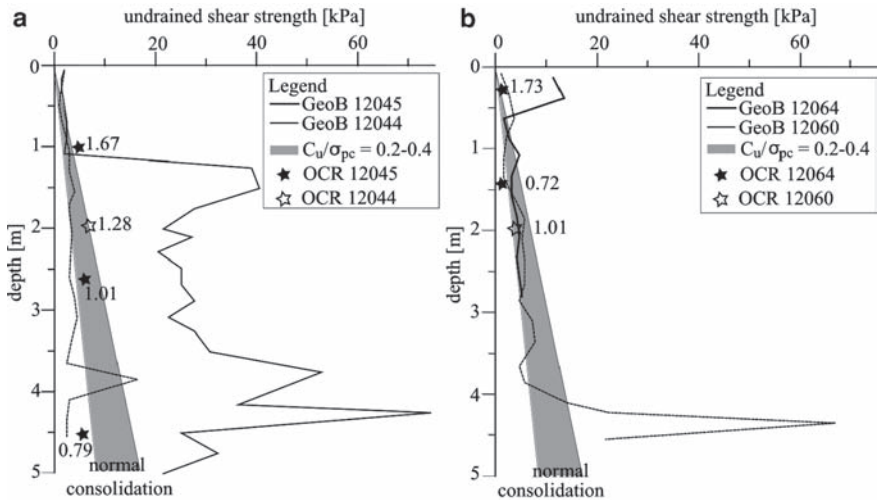
Fig. 4 Undrained shear strength from Vane shear apparatus, OCR, and C_u/σ_{pre} used as an indicator for normal consolidation state (From Cochonat et al. 1993) from Western (**a**) and the Eastern (**b**) landslide complexes. For calculation of OCR, see text and Eq. (1)

indicating a slight overconsolidation, whereas the reworked silty clays results show either normally consolidated (OCR = 1) or slightly underconsolidated (OCR = 0.79) (Fig. 3a).

3.3 Eastern Landslide Complex

On the Eastern Slide Complex, the hemipelagic drape comprises a mixture of bioturbated silty mud and mud with varying contents of sand and clay (Fig. 3c). In these sediments there are diagenetic fronts determined by colour banding and pyritization of shell fragments (Fig. 3c; Kopf et al. 2008). In contrast to the Western Slide Complex, the debrites resulting from mass wasting contain poorly rounded, indurated clasts and pebbles in a dark silty-clay matrix (Fig. 3d; Kopf et al. 2008). Hemipelagic drape in core GeoB12060 shows a linear increase in bulk density and undrained C_u downward, reaching $1.90 \, g/cm^3$ and ~20 kPa respectively. Peaks between 4.2 and 4.8 m correlate with pyrite layers (Fig. 3c). The reworked sediments are characterized by lower bulk density $1.70 \, g/cm^3$, and variable C_u from 5 to 15 kPa (Figs. 3d and 4b). While hemipelagic sediment above the headwall (core GeoB12060) are normally consolidated, those sampled farther downslope in Core GeoB12064 are slightly overconsolidated (OCR = 1.73). Reworked sediments are slightly underconsolidated (OCR = 0.72; Fig. 4b). Surprisingly, there is no significant difference in shear resistance between the hemipelagic and the reworked sediments (μ_{res} ranging between 0.34 and 0.52; Fig. 3c, d).

4 Discussion

4.1 Mechanical Behaviour of the Sediment

In both landslide complexes the OCR-values obtained for the hemipelagic sediments indicate slight overconsolidation (Fig. 4). This may result from "apparent" overcon-solidation (e.g. Sultan et al. 2000) that is typical for superficial sediments and is often associated with colour banding (syn- as well as post-depositional), pyritization, burrows and other evidence for physico-chemical and biogeochemical processes (Ch. 3.2 and 3.3; Kopf et al. 2008). To eliminate the effect of the "apparent" overconsolidation on the interpretation of the data, C_u/σ_{pre}-values were consulted. Based on this correction, hemipelagic sediments in both landslide complexes are normally consolidated (Fig. 4).

The recovered failed deposits at the Eastern Slide Complex (downslope location GeoB12064) are slightly underconsolidated (OCR = 0.72, C_u = ~3 kPa in 1.5 mbsf), most likely because of incorporation and amalgamation of surface sediments. Such rapid redeposition inhibits fluid expulsion to the overlying sediment column.

As a consequence excess pore pressure may be preserved during burial (Dugan et al. 2000; Sultan et al. 2004) and result in underconsolidation of the sediments.

Further upslope of station GeoB12064 (Fig. 1), in the seismic profile across the landslide, some deposits along the slope appear as if they have failed (Fig. 2b), however, in the core no evidence for debrites has been found (e.g. at station GeoB12073 at the middle part of the landslide body). Instead we recovered very stiff silty-clay sediments, covered by hemipelagic sediment, characterised by high C_u-values of 12 kPa at 1mbsf and bulk density values up to 1.85 g/cm^3 (Kopf et al. 2008). This mismatch may be explained by low core penetration (core length: 1.7 m), lack of vertical resolution of the multichannel seismic system (see review Kopf et al. 2008), or the fact that the stiff silty-clay material recovered at GeoB12073 represents older sediment that has been unroofed when the slide complex formed.

In the downslope location GeoB12064, we observe clasts in the normally consolidated debrite deposits with the same composition, color and similar C_u-values of 10–15 kPa when compared to the stiff sediments of core GeoB12073. Also the clasts are poorly rounded and hence suggest a short transport distance downslope. These observations support two hypotheses of the slide development. Our first contention is that the Eastern Slide may originate in at least two stages: One initial phase that caused the upper portion of the landslide scar removed some of the overlying sediment. In order to readjust the slope angle, some of the unroofed material (of GeoB12073-type) may have then been amalgamated in a silty clay mass flow in the deeper portion of the slide (as evidenced by GeoB12064). A second alternative hypothesis is that the slide developed as split debris flow with high density at the base and a lower density at the top. The high density debris flow is characterised by stiff sediments (high C_u-values) and arrives only at the midslope part of the landslide body (GeoB12073). Due to higher flow velocity, the low density flow, characterized by low C_u-values, arrives further downslope (GeoB12064) and would partly rework sediments from the underpassing debris unit so that some clasts of the high density/stiff unit may then be deposited further downslope within the low density unit (Postma et al. 1988). However, in the absence of the exact dating or deeper coring/drilling, no final conclusion of timing of the landslide can be drawn.

At the Western Slide Complex, the mechanical behaviour of the sediments (GeoB 12045) during failure seems to have been different (Figs. 3a, band 4a). Two distinct excursions could be observed in the bulk density values, each accompanied by a strong initial increase. Interestingly, one lies between the hemipelagite and the reworked silty-clay, but the other within itself (Fig. 3b). These steps may be related to different failure events. In addition, several layers containing coarser-grained material interrupt the dark silty-clay sediment column. Furthermore, in the deeper part of core GeoB12045, the failed sediments are characterized by overconsolidation with C_u up to 30 kPa at 2.8 mbsf and 52 kPa in 3.8 mbsf. These high C_u-values may result from removal of overlying sediments by mass wasting prior to the deposition of the hemipelagic drape (Fig. 4a). We could estimate a removal of a ~20 m thick sediment column for the upper part and a missing sediment sequence of ~13 m between the lower and the upper part of the failed material. The generally low

intrinsic friction values of 0.27–0.29 provide sufficient weakness for repeated failure events, which may be mirrored by tilted layers with angles of 25–40° observed in the hemipelagic sediments as well as in the assumed reworked sediment column (Fig. 3a, b). Also, seismic reflection data show a rough seafloor above and several incisions in the headwall area (see Fig. 2a), which might be a result of older sliding activity or multiple small failure events. However, the glide plane and other sliding induced features are not clearly visible owing to a lack of resolution in the profiles (e.g. Fig. 2; see also Kopf et al. 2008). Given the above-mentioned observations, we suggest that the sedimentological features as well as the different thickness of sediment removal could be explained by different time shifted slide events with contortion of strata along curved slide surfaces at a spacing of meters.

4.2   The Role of the Slope Angle to Determining Failure Type and Variability of Failure Events

Slope angle as a governing factor for slope instability in both granular and cohesive materials, has been shown by stability analysis (Cochonat et al. 1993). Assuming that C_u-values increase linearly downward in the sediment column (see review by Bartetzko and Kopf 2007), normally consolidated sediments with a strength of 8 kPa in 2.5 mbsf may fail at a slope angle of 20° (Cochonat et al. 1993). With a lower slope angle of 10° these sediments may fail at a sediment thickness of 6 mbsf with C_u-values of 12 kPa (Cochonat et al. 1993; Mulder et al. 1994). In our study, we observed high slope angles of ~32° at the Western Slide Complex adjacent to the Var Canyon flanks (Figs. 1 and 2a). In the Var Canyon upper Fan valley, in which hyperpycnal flows that transfer sediment from the shelf to the deeper basin have been described, the accumulation rate is high (Migeon et al. 2006). We suggest that these conditions together with the mechanical behaviour of the sediments (Ch. 4.1) and a high slope gradient greatly enhance the frequency of failure events at the Western Slide Complex, because it does not favor the development of thick stable deposits (Klaucke and Cochonat 1999).

To produce voluminous landslides, thick deposits of fine-grained material are necessary. Such units may evolve by low sediment accumulation rates in areas with moderate slope angles if sufficient time is allowed (Klaucke and Cochonat 1999; Migeon et al. 2006). The Eastern Slide Complex, with moderate slope angles of ~20° (Fig. 2b), is located further away from the Var Canyon and therewith east of the Cap Ferrat Ridge (Fig. 1). Klaucke and Cochonat (1999) show that this area is not connected to sediment sources from rivers or canyons, but covered by hemipelagic sediments with low sedimentation rates. Given such conditions and the above mentioned geotechnical data (Ch. 4.1), we follow the interpretation of those workers that less frequent but more voluminous landslide activity may be prevalent here in contrast to the Western Complex.

Among the trigger mechanisms of failure events in the area are sedimentary loading or seismic loading (Mulder et al. 1994; Klaucke and Cochonat 1999), and

undercutting (see review by Densmore et al. 1997) of the slope sediments adjacent to Var Canyon. At this stage of the investigations, the discussion of the trigger mechanisms for both the Eastern and Western Slide Complex is very speculative; however, we can rule out undercutting for the Eastern Slide complex. To identify the trigger mechanisms for each slide complex, sedimentological analysis, dating of the events, and measurements of geotechnical parameters across the failure plane seem mandatory.

References

Bartetzko A, Kopf A (2007) The relationship of undrained shear strength and porosity with depth in shallow (< 50 m) marine sediments. Sediment Geol 196: 235–249.

Bethoux N, Ouillon G, Nicolas M (1998) The instrumental seismicity of the western Alps: spatio-temporal patterns analysed with the wavelet transform. Geophys J Int 135: 177–194.

Blum P (1997) Physical properties handbook: a guide to the shipboard measurement of physical properties of deep-sea cores. Technical Note 26, ODP, doi:10.2973/odp.tn.26.1997.

Bryn P, Berg K, Forsberg CF, Solheim A, Kvalstad TJ (2005) Explaining the Storegga Slide. Mar Petrol Geol 22: 11–19.

Burrus J, Bessis F, Doligez B (1987) Heat flow, subsidence and crustal structure of the Gulf of Lion (NW Mediterranean): A quantitative discussion of the classical passive margin model. In: Beaumont C, Tankard AJ (Eds.) Sedimentary Basins and Basin-Forming Mechanisms. AGS Spec Publ 5, Mem Can Soc Pet Geol 12: 1–15, Halifax.

Casagrande A (1936) The Determination of the Pre-consolidation Load and its Practical Significance. Proc Int Conf SMFE 3: 60–64.

Cochonat P, Bourillet JF, Savoye B, Dodd L (1993) Geotechnical characteristics and instability of submarine slope sediments, the Nice slope (N-W Mediterranean Sea). Mar Georesourc Geotech 11: 131–151.

Dan G, Sultan N, Savoye B (2007) The 1979 Nice harbour catastrophe revisited: Trigger mechanism inferred from geotechnical measurements and numerical modelling. Mar Geol 245: 40–64.

Densmore AL, Anderson RS, McAdoo BG, Ellis MA (1997) Hillslope evolution by Bedrock landslides. Sciences 275: 369–372.

Dugan B, Flemings PB (2000) Overpressure and fluid flow in the New Jersey continental slope: implications of slope failure and cold seeps. Sciences 289: 288–291.

Hampton MA, Lee HJ, Locat J (1996) Submarine landslides. Rev Geophys 3: 33–59.

Klaucke I, Cochonat P (1999) Analysis of past seafloor failures on the continental slope off Nice (SE France). Geo-Mar Lett 19: 245–253.

Klaucke I, Savoye B, Cochonat P (2000) Patterns and processes of sediment dispersal on the continental slope off Nice, SE France. Mar Geol 162: 405–422.

Kopf A, Brown KM (2003) Friction experiments on saturated sediments and their implications for the stress state of the Nankai and Barbados subduction thrusts. Mar Geol 202: 193–210.

Kopf A, Cruise Participants (2008) Report and Preliminary Results of Meteor Cruise M 73/1: LIMA-LAMO (Ligurian Margin Landslide Measurements & Observatory), Cadiz, 22.07.2007 – Genoa, 11.08.2007. Berichte Fachbereich Geowissenschaften, Universität Bremen, 264.

Locat J, Lee HJ (2002) Submarine landslides: advances and challenges. Can Geotech J 39: 193–212.

McAdoo BG, Pratson LF, Orange DL (2000) Submarine landslide geomorphology, US continental slope. Mar Geol 169: 103–136.

Migeon S, Mulder T, Savoye B, Sage F (2006) The Var turbidite system (Ligurian Sea, northwestern Mediterranean) – morphology, sediment supply, construction of turbidite levee and sediment waves: implications for hydrocarbon reservoirs. Geo-Mar Lett 26: 361–371.

Mulder T, Tisot JP, Cochonat P, Bourillet JF (1994) Regional assessment of mass failure events in the baie des Anges, Mediterranean Sea. Mar Geol 122: 29–45.

Mulder T, Savoye B, Syvitski JPM, Piper DJW (1998) The Var Submarine System: understanding Holocene sediment delivery processes and their importance to the geological record. In: Stoker MS, Evans D, Cramp A (Eds.) Geological Processes on Continental Margins: Sedimentation, Mass Wasting and Stability. Spec Publ Geol Soc Lond 129, Ocean Drilling Program, College Station, TX, pp. 145–166.

Pasquale V, Verdoya M, Chiozzi P (1996) Heat flux and timing of the drifting stage in the Ligurian-Provencal basin (Northwestern Mediterranean). J Geodyn 21: 205–222.

Piper DJW, Savoye B (1993) Processes of late Quaternary turbidity current flow and deposition on the Var deep-sea.fan, northwest Mediterranean Sea. Sedimentol 40: 557–582.

Postma G, Nemec W, Kleinspehn KL (1988) Large floating clasts in turbidites: a mechanism for their emplacement. Sed Geol 58: 47–61.

Rehault JP, Bethoux N (1984) Earthquake relocation in the Ligurian Sea (Western Mediterranean): geological interpretation. Mar Geol 55: 429–445.

Ryan, WBF (2009) Decoding the Mediterranean salinity crisis. Sedimentol 56: 95–136.

Sultan N, Cochonat P, Dennielou B, Bourillet JF, Savoye B, Colliat JL (2000) Surconsolidation apparente et pression osmotique dans un sédiment marin. C R Acad Sci Paris – Ear Planet Sci 331: 379–386.

Sultan N, Cochonat P, Canals M, Cattaneo A, Dennielou B, Haflidason H, Laberg, JS, Long D, Mienert J, Trincardi F, Urgeles R (2004) Triggering mechanisms of slope instability processes and sediment failures on continental margins: a geotechnical approach. Mar Geol 213: 291–321.

Wood DM (1982) Cone penetrometer and liquid limit. Géotechnique 32: 152–157.

Characterization of Micaceous Sand for Investigation of a Subsea Mass Movement

T. Langford and S. Perkins

Abstract A recent project involved a shallow slope failure of a deposit of loose sand and a site investigation and laboratory test program was initiated to investigate the cause of the slide and evaluate the likelihood of any further movement. The sand was found to have an elevated mica content, which affected the density, compressibility and shearing behavior. Existing correlations between relative density and cone resistance were evaluated to better understand the *in-situ* density of the soil. Undrained triaxial tests were used to investigate the static strength and material anisotropy, while static and cyclic direct simple shear tests helped study behavior during undrained cyclic loading. The test results are summarised and key conclusions are presented which are of relevance for sites worldwide where micaceous sands are prevalent.

1 Offshore Investigation

A recent project offshore Norway involved a shallow slope failure of a deposit of loose sand. An initial geophysical survey of the slope revealed a classic 'fan' shape failure. A detailed site investigation and laboratory test program was initiated to investigate the cause of the slide and evaluate the likelihood of further movement. The investigation included geophysical techniques to investigate the bathymetry and shallow stratigraphy, eight geotechnical vibrocore (VC) samples to obtain

T. Langford (✉)
NGI, P.O. Box 3930 Ullevål Stadion, NO-0806 Oslo, Norway
e-mail: thomas.langford@ngi.no

S. Perkins (✉)
Montana State University, 205 Cobleigh Hall, Bozeman MT 59717, USA
e-mail: stevep@ce.montana.edu
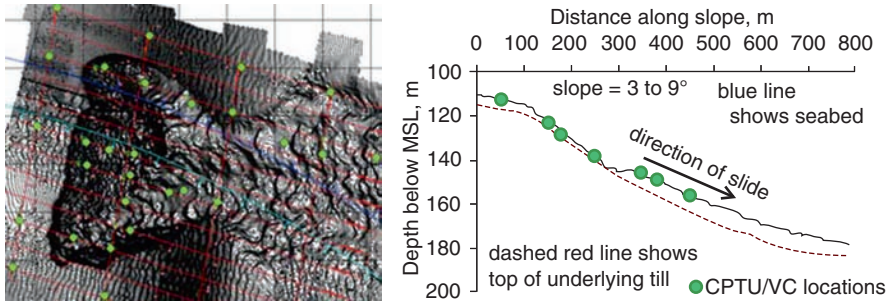
Fig. 1 Seabed bathymetry and cross section through slope showing approximate thickness of overlying sand

material for laboratory testing and 28 Cone Penetration Tests with measurement of pore pressure (CPTU) to investigate the *in-situ* properties of the soils. The geophysical investigation clearly revealed a debris fan, as shown in Fig. 1.

A corresponding cross-section after the slide shows how the sand has accumulated at the lower end of the slope. The following describes the general stratigraphy (descriptions of sand density are qualitative):

Unit Ia very loose to medium dense sand, micaceous, shells and shell fragments
Unit Ib loose to medium dense sand inter-layered with soft to firm clay
Unit II till, consisting of firm to stiff sandy clay with inclusions of sand and gravel

The geophysical and geotechnical data confirmed the slide had occurred within the upper loose sand deposit on a shallow gradient of around 5° to 10°. The project's main focus was therefore to characterise this loose sand deposit, and investigate its cyclic behavior for potential seismic loading.

2 General Characteristics of Upper Sand

The fact that the slide occurred in micaceous sand was reminiscent of the well-documented 'Jamuna Bridge' project in Bangladesh (Hight et al. 1998), where a series of failures occurred due to dredging of shallow slopes formed of loose sand. Subsequent testing of material from the bridge site revealed how the sand's behavior was affected by the mica content. Mica particles are flat and platy, resulting in loose packing and a significant increase in voids ratio when compared with other 'additives', as illustrated in Fig. 2.

The upper sand was found to be well graded, with few fines (see Fig. 3). Examination of the sand from the current project in the onshore laboratory revealed that it was indeed micaceous. The minimum and maximum void ratios were also
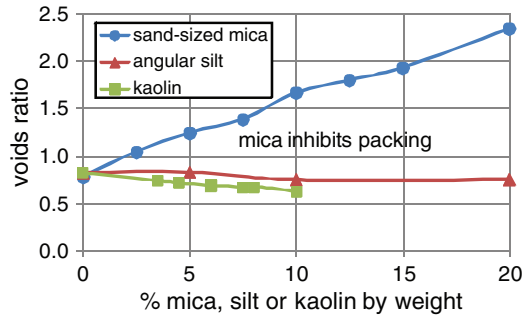
Fig. 2 Effects of mica content on voids ratio (adapted from Hight et al. 1998)
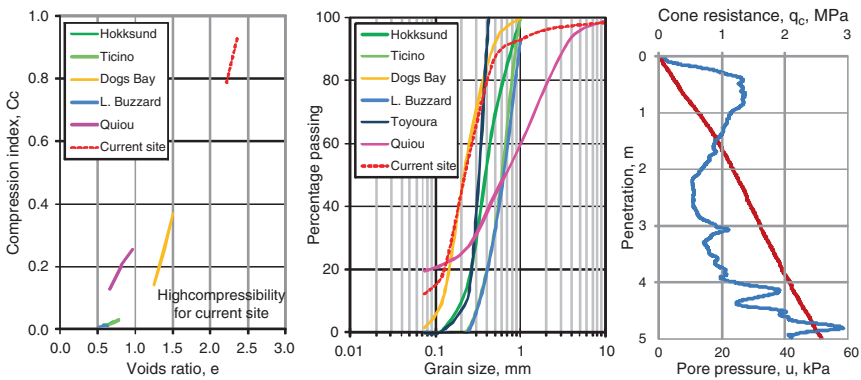
Fig. 3 Grain size distribution and compression index for different sands; typical CPTU data for the site

investigated and these are presented in Table 1 together with data for other 'well-tested' sands, based on information from Lunne et al. (1997).

The voids ratios measured for the current site are high compared with other sands in the literature, and much higher than those for Hokksund and Ticino sands which were used to develop the widely-used correlations between CPT cone resistance and relative density based on calibration chamber testing. Note that measurement of minimum and maximum voids ratio involves a degree of uncertainty, depending on the method used. The values in Table 1 are mainly based on the ASTM approach.

Calibration chamber testing has been performed by several institutions, including ENEL CRIS (Bellotti et al. 1988), ISMES (Baldi et al. 1986), NGI (Parkin and Lunne 1982), and Oxford University (Houlsby and Hitchman 1988)

Table 1 Properties of sand for current sites and sands from calibration chamber tests

Sand name	G_s	e_{min}, e_{max}	Mineralogy (for guidance)	Compressibility
Current site	2.70	0.9–2.1	10% mica, 40% quartz, 50% shells	High
Hokksund	2.70	0.5–0.9	35% quartz, 10% mica	Medium
Ticino	2.67	0.6–0.9	30% quartz, 5% mica	Medium
Toyoura	2.64	0.6–1.0	90% quartz	Low
L. Buzzard	2.65	0.5–0.7	Quartz	Low
Dogs Bay	2.75	1.1–1.8	90% carbonate	High
Quiou	2.71	0.5–1.3	74% shell fragments, 12% quartz	High
Sand A	2.70	0.8–1.6	Carbonate	High
H. Mines	3.02	0.6–1.1	Feldspar, quartz, mica	High
Monterey	2.65	0.6–0.8	Quartz with feldspar	Low
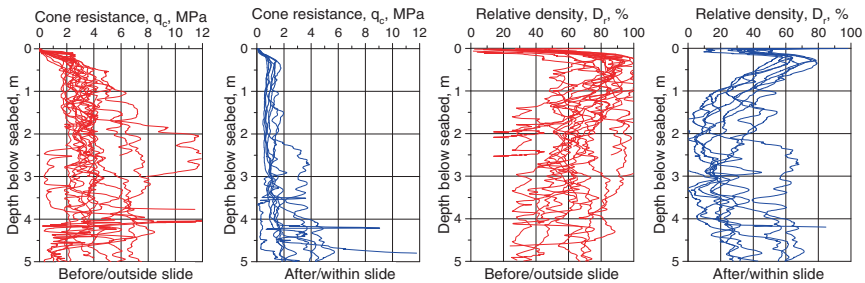
Fig. 4 Profiles of CPTU cone resistance and relative density before (or outside) the slide and after (within) the slide

and Southampton University (Last et al. 1987). Although many of the tests were performed on low to medium compressibility sands, some highly compressible sands were also tested, such as Dogs Bay and Quiou Sand. Research into highly compressible sands has generally focused on materials with a large proportion of 'carbonate' or 'calcareous' particles, whereas the engineering properties of the current sand appear to be governed by both the mica and carbonate particles.

Many calibration chamber test results are presented in Lunne et al. (1997) together with descriptions of the equipment. Grain size curves for some of the sands are shown together with the compressibility measured in oedometer tests on Fig. 3. A typical profile of cone resistance and pore pressure from the slide material is also shown.

Figure 4 shows the range in CPTU cone resistance measured at locations before (or outside) the slide and after (within) the slide. Very low values were measured within the slide and the average profile is much lower than that measured before the slide.

3   Interpretation of Relative Density

The cone penetration test is an excellent tool for evaluating the variability in soil strength or density across a site. For sands, relative density is typically used as a reference parameter, where this is the relationship between the current *in-situ* voids ratio and the maximum and minimum voids ratios, e_{max} and e_{min}, referring to the loosest and densest possible states. The use of relative density as a design parameter itself is questionable. However, the parameter is used in the geotechnical laboratory during preparation of reconstituted sand specimens to the *in-situ* density since it is extremely challenging to obtain an 'undisturbed' sand sample during a site investigation.

Cyclic testing was planned for the current site to investigate liquefaction susceptibility of the sand and a reasonable estimate of the relative density was required to reconstitute the specimens, since the vibrocore method caused significant densification of the original material. The low cone resistance measurements were initially correlated with the relative density using the general correlation presented by Baldi et al. (1986) for normally consolidated deposits of clean sand:

$$D_r = \frac{1}{2.41} \cdot \ln\left[\frac{q_c}{157 \cdot \sigma'_{v0}{}^{0.55}}\right] \tag{1}$$

Where D_r is relative density, q_c is cone resistance and σ'_{v0} is the *in-situ* vertical effective stress. The corresponding profiles of relative density as calculated above are shown in Fig. 4. The *Baldi* correlation is probably the most widely used within current engineering practice and therefore serves as a reference for other correlations between cone resistance and relative density.

The relative density profiles inside the slide are greatly reduced, as are the cone resistance profiles shown in Fig. 4. The lowest interpreted relative densities for some locations are below 10% for some locations between 1 and 4 m penetration. These values are extremely low when compared with previous experience in both hydraulic fills and natural soils. Several studies suggest a minimum relative density around 25% in sand deposits (e.g. Lee et al. 1999). The same general figure applies in the laboratory where it is difficult to prepare a stable specimen in a looser state. These low calculated densities were therefore treated with caution.

The *Baldi* correlation is accepted to give reasonable results for deep deposits of uniform soils that match well with 'standardised' and less compressible materials in the literature (i.e. Ticino and Hokksund sands). Unfortunately, the correlation is less reliable for other types of soil. Differences in grain size distribution, angularity and especially mineralogy will affect the measured cone resistance for a given relative density. Furthermore, the existing correlations generally provide a less reliable indication of actual soil density for shallow soils (the upper 5 m) since the lowest confining stress used in the calibration chamber tests was 50 kPa.

Compressibility has previously been used as a qualitative factor to explain some of the scatter in the data from calibration chamber testing. Jamiolkowski et al. (1985)

show how correlations between relative density and cone resistance are seen to change with varying compressibility. The results confirm the intuitive trend that more compressible sand will give a lower cone resistance for a given relative density when compared with less compressible sand. Kulhawy and Mayne (1990) suggest an empirical correlation accounting for compressibility:

$$D_r^2 = \frac{q_{c1}}{305 \cdot Q_C \cdot Q_{OCR} \cdot Q_A} \tag{2}$$

Where q_{c1} is the normalised cone resistance = $(q_c/p_a)/(\sigma'_v/p_a)^{0.5}$, Q_C is a compressibility factor, Q_{OCR} is an overconsolidation factor = $OCR^{0.18}$ and Q_A is an ageing factor. The compressibility factor is based on qualitative evaluation as opposed to any specific measurement with suggested values of 0.91 for high compressibility, 1.0 for medium compressibility and 1.09 for low compressibility, corresponding to the trend mentioned above.

Wehr (2005) presents another correlation based on a series of recent calibration chamber tests from Karlsruhe University (unpublished), including compressible calcareous sands. The correlation modifies the cone resistance using a 'shell correction factor', f_{shell}. The updated cone resistance is then given by $q_{c,shell} = q_c \cdot f_{shell}$ and the relative density may be recalculated.

$$f_{shell} = 0.0046 \cdot D_r + 1.3629 \tag{3}$$

These relationships are compared on Fig. 5 with data for different sands from calibration chamber testing. The *Baldi* correlation tends to the lower bound of relative density for low values of normalised cone resistance ($q_{c1} < 50$).
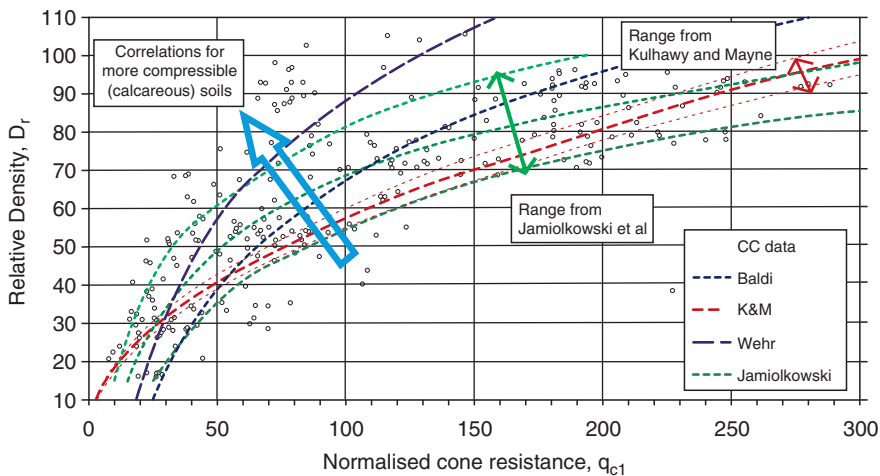
Fig. 5 Relative density versus normalised cone resistance, comparing empirical relationships with calibration chamber test data

Figure 5 shows clear scatter in test data which may be predominantly attributed to sand type. The high compressibility of the sand for the current site is demonstrated in Fig. 3. Uncertainty on how to reliably interpret the relative density for laboratory testing meant that the project chose to re-evaluate calibration chamber test data, including more recent experience with calcareous sands (see Table 1). The data points from Figure 5 are divided into sand type on Fig. 6 using a logarithmic plot to provide more detail at low values of normalised cone resistance.

Figure 6 suggests that the data for more compressible sands (Dogs Bay, Quiou and Sand A) indeed plot 'above' the *Baldi* line, agreeing with the trend indicated by the various published correlations. Furthermore, a fitted line through all data for low, medium and high compressibility sands also plots above the *Baldi* correlation, which is based predominantly on Ticino and Hokksund sands. Since no calibration chamber testing was performed for the current site, this 'best-fit' correlation is compared with the *Baldi* correlation in Fig. 7 for the range of CPTU data shown previously in Fig. 4.

Figure 7 shows the mean for all locations together with the mean ±1 standard deviation for the *Baldi* and 'best-fit' correlations. There is relatively little difference in the relative density for CPTUs performed before or outside the slide zone where the average is around 70% (medium dense). However, there is a marked increase for the CPTUs performed within the slide zone where the relative density is significantly lower. This fits with the trend shown on Fig. 6, where the intersection between the *Baldi* correlation and the logarithmic fit to calibration chamber test data is for a relative density of around 70% (or a normalised cone resistance just over 100).

Based upon the profiles shown in Fig. 7, the project agreed that the likely *in-situ* relative density of the sand was higher than predicted by the *Baldi* correlation.
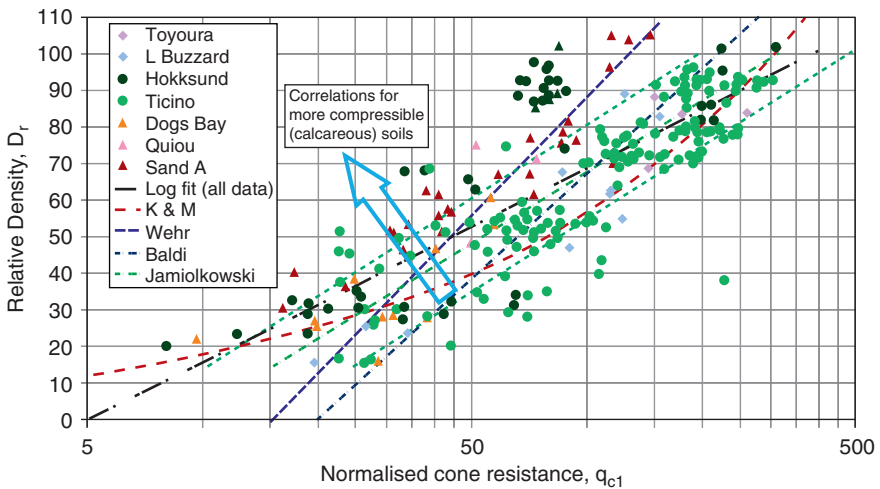
Fig. 6 Relative density versus normalised cone resistance, showing data for different sand types
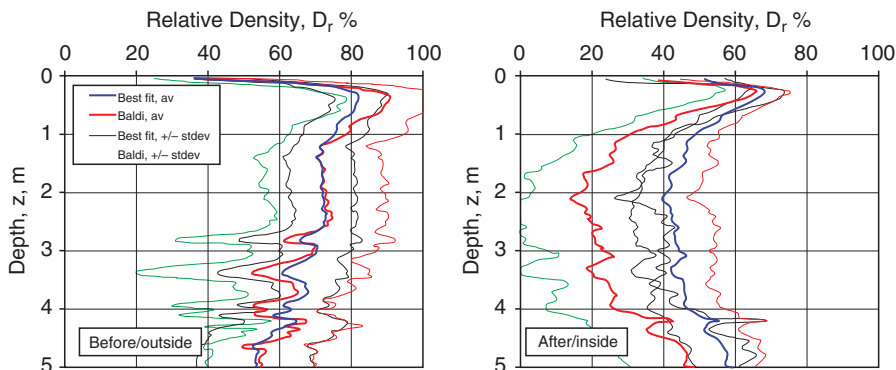
Fig. 7 Profiles of relative density before (or outside) the slide and after (within) the slide, based on *Baldi* and 'best fit' correlations for all calibration chamber test data

Nonetheless, a range of 20% to 25% was conservatively applied for much of the advanced laboratory testing due to remaining uncertainties.

4 Laboratory Testing of Sand

An extensive laboratory test program at NGI and Montana State University was undertaken to investigate the behavior of the sand. A series of Anisotropically Consolidated Undrained triaxial (CAU) tests sheared in compression and extension were used to evaluate anisotropy. Cyclic constant volume Direct Simple Shear (DSS) tests were used to investigate the liquefaction potential.

The CAU triaxial tests were performed at the lowest achievable relative density, ranging between 25% and 45%, with a consolidation stress coefficient K_0 around 0.5. Figure 8 shows normalised stress paths for a total of ten tests, with six sheared in compression and four in extension. The mean and shear stresses have been normalised by the mean consolidation stress, p'_0.

The results are compared with the range given by Hight et al. (1998) for Jamuna Bridge sand with a mica content of 0% to 40%. The results agree well with these previous findings, showing clear anisotropy with a much weaker response during initial shearing in extension than compression. According to the Jamuna Bridge results, the addition of a relative small proportion of mica (less than 2.5% by weight) resulted in a more unstable response, whereas larger proportions actually increased the stability of the sand. No detailed quantitative evaluation of the mica content was performed for the current site, but an estimate was made of 10% content by volume which is equivalent to a much lower proportion of the weight. Hight et al. (1998) discuss the importance of sample preparation and grain orientation on results. Moist tamping was used exclusively for preparing samples for the current site, although care was taken to keep the relative density as uniform as possible,
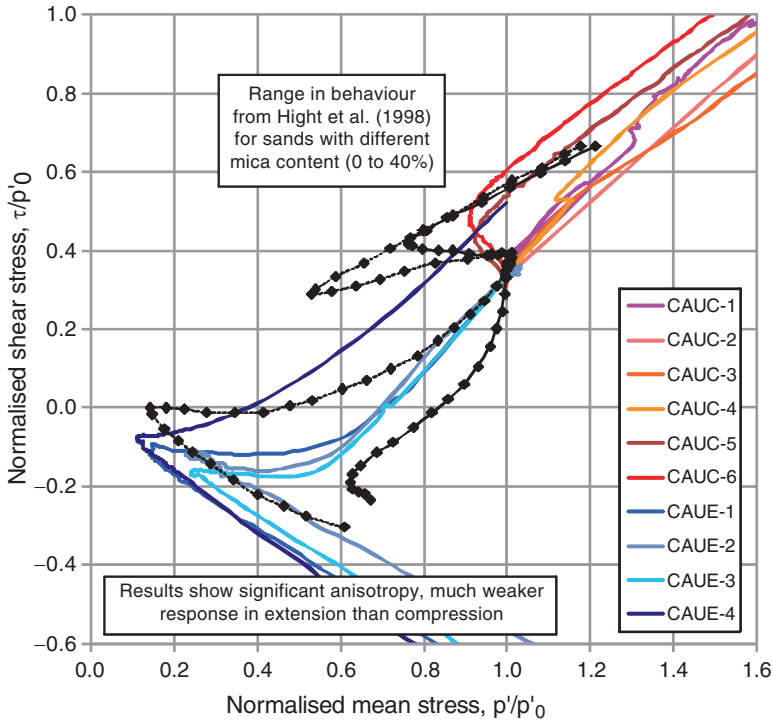
Fig. 8 Normalised stress paths from anisotropically consolidated undrained triaxial tests

with the lowest practical achievable relative density around 25% for the triaxial specimens and 20% for the DSS tests.

The results for the current site suggest static stability would be low for a trigger mechanism involving unloading at the base of the slope, similar to the Jamuna Bridge case. However, in the absence of the trigger mechanism, the slope stability was found to be adequate.

Cyclic DSS tests were performed for two levels of relative density, namely around 20% and 50%. The samples were sheared with different levels of normalised cyclic shear stress, τ_{cy}/σ'_{vc}, and an average shear stress $\tau_{cy}/\sigma'_{vc} = 0$. Results are summarised on Fig. 9 in terms of normalised cyclic shear stress versus number of cycles to failure. The scatter in data around $\tau_{cy}/\sigma'_{vc} = 0.25$ is thought to be due to natural variability in the material.

The resulting 'strength' of the material with the relative density of 50% is much greater than that with the lower relative density. The DSS testing was used to evaluate the liquefaction potential of the soils during seismic loading, where this can be evaluated by comparing the Cyclic Stress Ratio (CSR) and Cyclic Resistance Ratio (CRR) so that the resulting factor of safety is given by CRR/CSR.

The CSR represents the relative shear stress caused by the seismic event, whereas the CRR represents the relative shear resistance of the soil to a given event.

Seed and Idriss (1971) suggest a procedure for evaluating the CSR (here excluding the depth reduction coefficient):
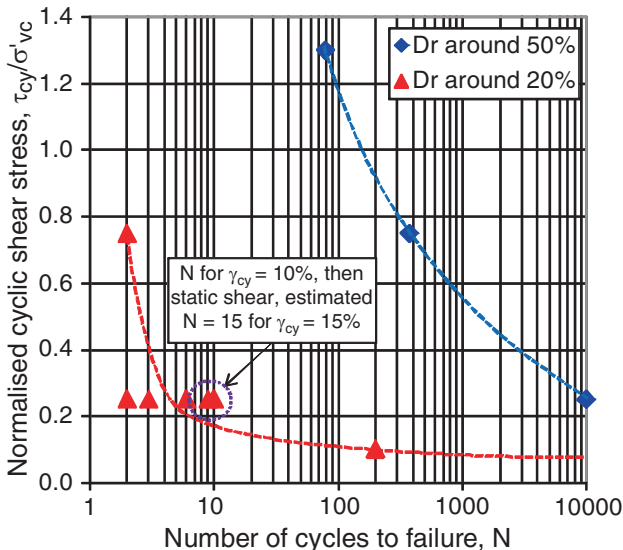
Fig. 9 Summary of results from cyclic DSS tests at two levels of relative density

$$CSR = \frac{\tau_h}{\sigma'_v} = 0.65 \cdot \frac{a_{max}}{g} \cdot \frac{\sigma_v}{\sigma'_v} \tag{4}$$

Where τ_h is the horizontal shear stress caused by the seismic event, σ'_v is the vertical effective stress, σ_v is the vertical total stress and a_{max} is the seabed acceleration.

Two seismic events were evaluated for the site: a 100 year event and more extreme 10,000 year event. This allowed the CRR to be evaluated from the cyclic DSS tests. The 100 year event assumed an equivalent number of cycles (N_{equiv}) of 3, giving the CRR as 0.4. The Peak Ground Acceleration (PGA) at bedrock was given as 0.02 g. The 10,000 years assumed N_{equiv} as 5, giving the CRR as 0.2. The PGA in this case was given as 0.1 g. A site response analysis suggested the accelerations in the sand layer could be amplified by a factor of around 1.0 to 1.5. The total unit weight of the soil is taken around 16 kN/m³, which is equivalent to a relative density around 20%.

The CSR for the 100 year event is found to be between 0.04 and 0.06 for the 100 year event, which is far lower than the CRR of 0.4. The corresponding CSR for the 10,000 year event is found to be between 0.18 and 0.28 compared with the CRR of 0.2. The resulting safety factor suggests a possibility of failure for the extreme 10,000 year seismic event. However, additional analyses showed the predicted maximum displacements resulting from the extreme seismic event to be minimal, which suggest that a catastrophic failure would be unlikely. Furthermore, the DSS results presented here are based upon a conservatively low relative density.

The prior evaluation of calibration chamber CPTU data suggests that these low values are likely to underestimate the *in-situ* field density.

The very shallow (<5°) slope at the base of the slide area where the loose sand is currently deposited gives an additional normalised average shear stress $\tau_{av} / \sigma'_v =$ $\sin 5° = 0.07$. This shear stress acts permanently on the slope and can therefore be taken to act drained. Although no specific tests were performed in this case, experience with other sands indicates that a small degree of drained average shear stress does not reduce the resistance to undrained cyclic stress.

Additional tests were performed to investigate the post-cyclic static strength of the sand, in order to evaluate the sand's behavior after the unlikely event of seismic failure. Figure 10 shows the normalised cyclic shear stress versus shear strain and normalized effective vertical stress. The tests were run as before up to a limit of 10% cyclic shear strain at which point the cyclic stress was set to the zero point. Without allowing any intermediate drainage, the specimens were then sheared statically to failure in either the 'forwards' or 'reverse' directions.

The cyclic tests show the typical trend of increasing shear strains with number of cycles, which would usually lead to failure for a cyclic test. The post-cyclic static test appears to follow a similar path as the final cycle of the cyclic tests. The average effective vertical stress for the cyclic tests gradually reduces towards zero, although the response of the static test for larger strains forms an envelope due to dilation of the sand. This suggests that the sand would develop additional capacity at larger strains. This means that even if a slide were to occur due to a seismic trigger, the slope would likely stabilize after limited displacements.

The results from the *in-situ* and laboratory testing were then implemented in analyses to evaluate the static and cyclic stability of the slope as part of an ongoing investigation. Initial results suggest that the current stability is within acceptable levels.

5 Conclusions

A detailed site investigation and laboratory testing program was used to study the properties of a loose micaceous sand involved with a shallow slope failure offshore Norway. The soil exhibited elevated voids ratios and higher compressibility than many other documented sands. A subsequent re-evaluation of existing correlations between cone resistance and relative density suggested that the common *Baldi* correlation would not be valid, and a higher range of relative densities was used for reconstitution of samples in the laboratory.

Anisotropically consolidated undrained triaxial test results showed that the sand responded in a similar fashion to the well-documented Jamuna Bridge sand. The elevated voids ratio and platy mica particles promote a significantly anisotropic response during static undrained shearing. Direct simple shear testing revealed that the current sand would develop additional capacity at larger strains during post-cyclic static shear.
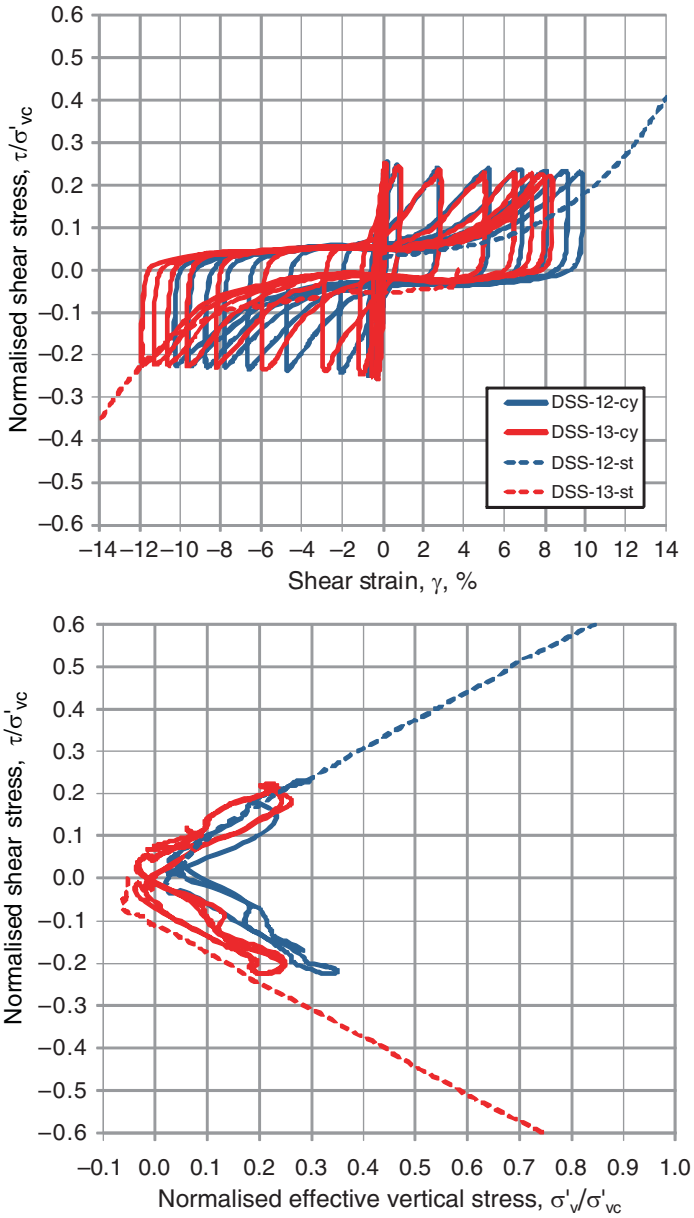
Fig. 10 Results from cyclic and post-cyclic static DSS tests in forward and reverse directions

For the Jamuna Bridge project, the failure was found to be initiated by a trigger mechanism with excavation at the base of the slope. A similar mechanism is anticipated to be responsible for the failure at the current site; an investigation is ongoing and the laboratory testing results have been implemented in analyses to evaluate the static and cyclic stability of the slope. The results for this material may also be relevant for other sites worldwide where micaceous sands are encountered.

References

Baldi G, Bellotti R, Ghionna N, Jamiolkowski M and Pasqualini E (1986) Interpretation of CPTs and CPTUs. 2nd Part: Drained Penetration of Sands. 4th International Geotechnical Seminar, Field Instrumentation and In-Situ Measurements, Singapore

Bellotti R, Crippa V, Pedroni S and Ghionna VN (1988) Saturation of Sand Specimen for Calibration Chamber Tests. Proceedings of the 1st International Symposium on Penetration Testing, Orlando, FL

Hight DW, Georgiannou VN, Martin PL and Mundegar AK (1998) Flow Slides in Micaceous Sand. Problematic Soils, Sendai, Japan

Houlsby GT and Hitchman RC (1988) Calibration Tests of a Cone Penetrometer in Sand. Géotechnique, 38:39–44

Jamiolkowski M, Ladd CC, Germaine JT and Lancellotta R (1985) New Developments in Field and Laboratory Testing of soils. Theme Lecture. Proceedings of the 11th International Conference on Soil Mechanics and Foundation Engineering, San Francisco, CA

Kulhawy FH and Mayne PH (1990) Manual on estimating soil properties for foundation design. Electric Power Research Institute, EPRI, August 1990

Last NC, Butterfield R and Harkness RM (1987) An Investigation of Full-Scale Penetrometers in a Large Triaxial Calibration Chamber – March 1983 to February 1986, Civil Engineering Department, University of Southampton, Final Report to SERC

Lee KM, Shen CK, Leung DHK and Mitchell JK (1999) Effects of Placement Method on Geotechnical Behavior of Hydraulic Fill Sands. ASCE J Geotech Geoenviron Eng 132: 832–846

Lunne T, Robertson PK and Powell JJM (1997) Cone Penetration Testing in Geotechnical Practice, Spon Press, London

Parkin AK and Lunne T (1982) Boundary Effects in the Laboratory Calibration of a Cone Penetrometer in Sand. Proceedings of the 2nd International Symposium on Penetration Testing, Amsterdam

Seed HB and Idriss IM (1971) Simplified Procedure for Evaluating Soil Liquefaction Potential. J Soil Mech Foundations Div, ASCE, 97(9):1249–1273

Wehr W (2005) Influence of the Carbonate Content of Sand on Vibro-compaction, 6th International Conference on Ground Improvement Techniques, Coimbra, Portugal

Estimating Drag Forces on Suspended and Laid-on-Seafloor Pipelines Caused by Clay-Rich Submarine Debris Flow Impact

A. Zakeri

Abstract Estimating the impact drag forces exerted by a submarine debris flow on a pipeline is a challenge. The conventional geotechnical based methods available to estimate drag forces on buried pipelines in unstable slopes are not applicable to a debris flow impact situation as they ignore or significantly underestimate the shear rate effects in the soil-structure interaction. The results of recent investigations indicate that a fluid dynamics approach in conjunction with rheological principles of non-Newtonian fluids provides a more appropriate way in the study of soil-pipe interaction for submarine debris flow impact situations. To that extent, this paper summarizes the results of a recent investigation on the impact of clay-rich submarine debris flows on suspended (free-span) and laid-on-seafloor pipelines. It presents a method to estimate the drag forces, longitudinal and normal to the pipe axis, for various angles of impact. The investigation comprised experimental flume tests and Computational Fluid Dynamics (CFD) numerical analyses.

1 Introduction

Submarine landslides and debris flows are amongst the most destructive geohazards, economically and environmentally, for installations on the seafloor. Estimating the drag forces caused by these geohazards is an important design consideration in offshore engineering. Failure of a hydrocarbon pipeline may be economically and environmentally devastating. With offshore oil and gas activities pushing into deeper water, there is a need to better assess and quantify the risk associated with geohazards. Research in the area was inspired in the wake of the 1969 Hurricane

A. Zakeri (✉)
Geotechnical Engineering Group, C-CORE, St. John's, Newfoundland, Canada
e-mail: arash.zakeri@c-core.ca

Camille in the Gulf of Mexico, during which three offshore platforms and the associated network of pipelines suffered significant damage. Subsequent studies concluded that the damage was mainly due to wave induced mass movement at the seafloor and not the wind and surface wave action alone (Coleman and Prior 1978 Schapery and Dunlap 1978). As a result, a number of techniques were developed between the mid 1970s and late 1980s to assess the drag forces arising from soil-structure interaction. The problem was investigated from two perspectives: a geotechnical approach and a fluid dynamics approach. In the former, the drag forces are directly linked to the soil shear strength either linearly or through a power-law relationship including the rate of shear. The latter approach considers the soil fully fluidized and applies fluid mechanics principles. These methods are limited and provide a wide range of estimates for the drag forces. Further, the methods seem often to be misinterpreted and incorrectly applied to situations outside the methods' validity (Zakeri 2009a).

A moving failed mass from a submarine landslide undergoes a series of complex processes from initial disintegration to glide blocks to fast moving fluid-like debris flows and turbidity currents. It is this complex process that has led to considerable confusion of nomenclature in the literature and inappropriate use of the methods in assessing soil-structure interaction forces. For example, geotechnical-based methods that were developed for the case of fully or partially buried pipeline in an unstable slope are sometimes applied to the problem of debris flow impact. Mulder and Alexander (2001) provide a clear and simple classification system for sedimentary density flows based on their physical flow properties and grain support mechanisms encompassing both cohesive and cohesionless soils. Clay-rich submarine debris flows are often fully remoulded and in a fluid state of pseudoplastic type.

The method presented here to estimate the drag forces deals with the impact of clay-rich submarine debris flow on suspended and laid-on-seafloor pipelines. It is based on an experimental program consisting of physical flume experiments (Zakeri et al. 2008) complemented by numerical analyses using the Computational Fluid Dynamics (CFD) method (Zakeri 2009b; Zakeri et al. 2009). For the case of suspended pipelines, the method covers various angles of incidence making it possible to estimate the impact drag forces parallel and normal to pipe axis. The paper begins with a brief discussion on the experimental program.

2 Experimental Program

2.1 Flume Experiments

The physical flume experiments involved subaqueous gravity flow of various clay-rich slurries impacting a model pipe in a direction normal to its axis. The slurries were a mixture of kaolin clay, sand and water. A total of 50 experiments were carried out in a 0.20 m wide and 9.5 m long flume suspended inside a 0.6 m wide tank (Fig. 1). The flume slope was adjustable (3° and 6°) and the bed was rough. The instrumentation consisted of:
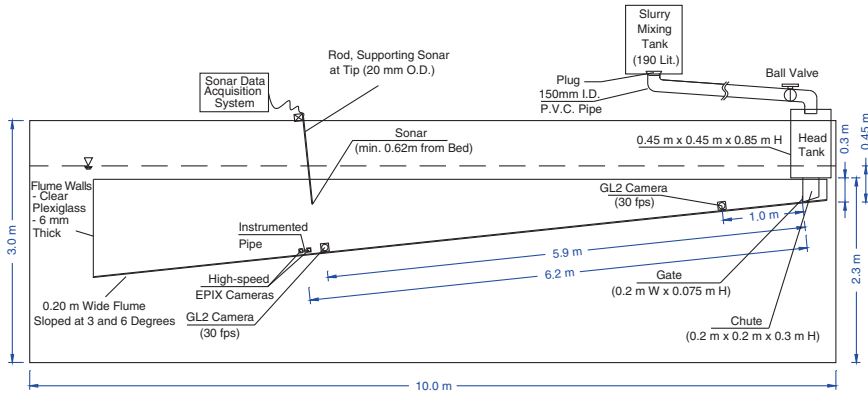
Fig. 1 Experimental setup for flume experiments

- Two Canon GL2 cameras for measuring the slurry head velocities near the gate and 5.9 m downstream – 720 W × 480 H pixels frame size at 30 frames/s (fps)
- Two high-speed EPIX cameras covering the area immediately upstream and downstream of the pipe to investigate the impact and flow characteristics in the wake – 1,280 W × 1,024 H pixels frame size at 30 fps and 550 W × 600 H pixels at 96 fps
- Four load cells to measure the drag and vertical forces – sampling rate of 1,000 Hz
- One submersible sonar to measure slurry flow and overriding turbidity heights. Transducer: A301S-SU, Olympus NDT and pulser/receiver: DPR300, JSR Ultrasonics

Each time, 190 l of slurry was prepared in the mixing tank located some 6 m above the flume and conveyed into the head tank. Two copper model pipe sizes, 22.2 and 28.6 mm O.D., were used. The high frequency sonar system consisted of a stationary 500 kHz submersible transceiver just below the mean water surface oriented normal to the sloping bed surface, approximately 0.62 m above the bed surface. The data collection protocol involved two sampling periods: the first period at 50 Hz for 60 s and the second period at 6 Hz for the next 30 min. For each ping, the system sampled backscatter at a rate of 8 MHz for 10,000 samples (1.25 ms). The plexiglass flume walls are smooth and the shear stress induced on the slurries was assumed to be negligible (Crowe et al. 2001). The experiments attempt to model about 2 s of continuous flow, ideally under constant head condition. Prior to the flume experiments, an extensive rheological study using laboratory rheometers was carried out to determine the slurry properties and suitable mix design. Table 1 presents the different slurry compositions and material properties.

The Brookfield DV-III Ultra vane-in-cup rheometer was used to determine the rheological properties of the slurries. The slurry preparation and rheology experiments were carried out in accordance with the ASTM (D2196-05) procedures. The results of the rheological experiments and mathematical models are presented on Fig. 2.

Table 1 Slurry composition and material properties

| | Percentage material by mass | | | | Sand gradation | |
Slurry	Clay	Water	Sand	Density (kg/m³)	Mesh Size (mm)	% Passing
					0.425	100
10% Clay	10	35	55	1,681.0	0.300	99.5
15% Clay	15	35	50	1,685.7	0.212	95.5
20% Clay	20	35	45	1,687.7	0.150	77.5
25% Clay	25	35	40	1,689.6	0.106	33.5
30% Clay	30	35	35	1,691.6	0.075	8.5
35% Clay	35	35	30	1,694.0	0.053	0.5

Notes:

Sand properties: Specific Gravity = 2.65, Uniformity coefficient (Cu) = 1.7 defined as the ratio of the maximum particle size of the smallest 60% (d_{60}) over that of the smallest 10% (d_{10}) of the granular sample. Cu = 1 for a single-sized soil, Cu < 3 a fairly uniform grading and Cu > 5 a well-graded (Whitlow 2001).

About 5% of the mass of sand was replaced by black diamond coal slag for visual purposes. The black diamond slag had the same specific gravity and grain size distribution as the sand.

Slurry	Herschel-Bulkley	Power-Law
10%Clay	$\tau = 7.3 + 3\dot{\gamma}^{0.35}$	$\tau = 10.3\dot{\gamma}^{0.14}$
15%Clay	$\tau = 20.5 + 5.5\dot{\gamma}^{0.35}$	$\tau = 25\dot{\gamma}^{0.125}$
20%Clay	$\tau = 43 + 10\dot{\gamma}^{0.35}$	$\tau = 50\dot{\gamma}^{0.12}$
25%Clay	$\tau = 85 + 12\dot{\gamma}^{0.4}$	$\tau = 91.5\dot{\gamma}^{0.11}$
30%Clay	$\tau = 110 + 15\dot{\gamma}^{0.45}$	$\tau = 118\dot{\gamma}^{0.125}$
35%Clay	$\tau = 161 + 25\dot{\gamma}^{0.4}$	$\tau = 165\dot{\gamma}^{0.13}$
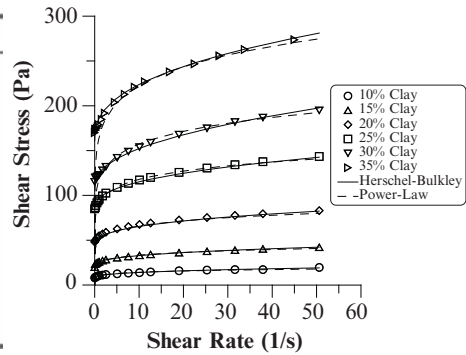
Fig. 2 Results of the rheological experiments and Herschel-Bulkley and Power-Law mathematical model fits. Shear stresses are in Pascal

All the results of the rheological experiments were repeatable within ± 5%. Both the Herschel-Bulkley and Power-Law models had a confidence of fit of 98% or greater.

2.2 Numerical Analyses

The situations tested in the experiments were numerically analyzed using Computational Fluid Dynamics (CFD) method. The analyses were carried out using the CFD software, ANSYS CFX 11.0, which is based on the Finite Volume (FV) method for unstructured grids. The FV method uses the integral form of the conservation equations.

With tetrahedra or hexahedra Control Volumes (CVs), unstructured girds are best adapted to the FV approach for complex 3D geometries (Ferziger and Perić 2002). The flume experiments constitute an incompressible two-phase, water and slurry, flow regime. The inhomogeneous two-phase separated Eulerian–Eulerian multiphase flow model of the CFX program was used to simulate the experiments. A general description of the theory and the associated differential form formulations used to analyze the flume experiments are included in Appendix A.

The computational procedures consisted of first setting up and calibrating a numerical model to simulate the flume experiments using the rheological models given in Fig. 2. The numerical analyses were quite successful in closely simulating the subaqueous slurry flow characteristics (e.g. slurry head velocities, hydroplaning, slurry flow and overriding turbidity heights) as well as calculating the impact forces (normal drag and vertical) on the pipe models. Further, the flow parameters such as slurry velocity and shear rate profiles (upstream and around the pipe) computed in the CFD numerical analyses together with the high-speed camera images indicated that the experimental setup for suspended pipeline appropriately modelled the prototype situation. The model was then used to complement the flume data by running additional simulations with different slurry velocities and pipe diameters for both the suspended and laid-on-seafloor cases. Later, the numerical model was extended to cover all angles of incidence for the suspended pipeline case. As a result, both the normal and longitudinal (with respect to the pipe axis) impact drag forces on a suspended pipeline were investigated (Zakeri 2009b).

3 Method Developed to Estimate the Impact Drag Forces

The drag forces measured in the physical experiments and calculated in the simulations were correlated to the slurry head velocities measured upstream of the model pipe within a distance between 5 to 10 times the pipe diameter. It was observed in the experiments that in this range, the slurry flow is not affected by the presence of the pipe and therefore, the slurry head velocities could be considered as the free upstream flow velocity, U_∞. The fluid flow characteristics around an object of a given shape strongly depend on parameters such as the object size and orientation, relative velocity between object and fluid, and fluid properties. For the drag force, it is customary to use the inertia type of definition (White 2006), and define it by using a drag coefficient, C_D, through dimensional analysis by Eq. 1:

$$C_D = \frac{F_D}{\frac{1}{2}\rho \cdot U_\infty^2 \cdot A} \tag{1}$$

where, F_D and A are the total drag force and the projected slurry-pipe contact area (i.e. pipe diameter times the contact length), respectively, and ρ is fluid density. For the normal drag force, F_{D-90}, A is the pipe cross-sectional area projected onto

the plane normal to the flow direction and for the longitudinal drag force, F_{D-0}, onto the plane parallel to the flow direction. C_D is a function of both the Froude number (Fr) and the Reynolds number (Re), which are the most important dimensionless parameters for studying incompressible fluid flow around an object. For many flows the gravitational effects are unimportant such as for the flow around a body or an airfoil where gravity waves are not generated. In that case, the Froude number is irrelevant and the drag coefficient becomes only a function of the Reynolds number (Kundu and Kohen 2004). The classical definition of the Reynolds number for a Newtonian fluid is:

$$\text{Re}_{Newtonian} = \frac{\rho U_\infty D}{\mu} \tag{2}$$

where, μ is the absolute (dynamic) viscosity, and D is the length characteristic – here, the pipe diameter. This definition is not directly applicable to the problem of non-Newtonian fluid flow past a circular cylinder. Hence, an ad hoc Reynolds number was proposed for shear-thinning, non-Newtonian fluids described by the Power-law or Herschel-Bulkley rheological models. It was based on the apparent viscosity as opposed to the absolute viscosity. The apparent viscosity is defined as the ratio of shear stress to the rate of shear of a non-Newtonian fluid. The apparent viscosity changes with changing rates of shear and must, therefore, be reported as the value at a given shear rate. Here, for the impact situations the shear strain rate immediately outside the boundary layer is defined as:

$$\dot{\gamma} = \frac{U_\infty}{D} \tag{3}$$

where, U_∞ is the approaching debris head velocity. The pipe diameter is taken as the length scale. In shear-thinning fluids of the Power-law or Herschel-Bulkley models, the apparent viscosity, μ_{app}, is defined as:
Power-law fluid:

$$\tau = a \cdot \dot{\gamma}^n \text{ thus}: \mu_{app} = a \cdot \dot{\gamma}^{n-1} \tag{4}$$

Herschel-Bulkley fluid:

$$\tau = \tau_C + K \cdot \dot{\gamma}^n \text{ thus}: \mu_{app} = \frac{\tau_C}{\dot{\gamma}} + K \cdot \dot{\gamma}^{n-1} \tag{5}$$

In the above equations, τ and τ_C are the fluid shear stress and fluid yield stress, respectively, and the parameters a, n and K are model parameters which are determined from rheology testing. The Bingham model is a special case of the Herschel-Bulkley model where the fluid parameter, n, is equal to unity and the consistency, K, is the same as the Bingham viscosity, μ_B. The behaviour of most clay-rich debris flows can be described by the Herschel-Bulkley model (Locat 1997). The results of the numerical analyses indicated that Eq. 3 provides a reasonable approximation for the rate of shear induced on the slurry upon impact with the pipe as the magnitude

of the shear rate induced on the slurry drops significantly away from the pipe surface – an order of magnitude within about a millimeter away from the pipe surface and two orders of magnitude within about 3 mm. This relatively small distance from the pipe surface basically constitutes the boundary layer thickness. Hence, the use of Eq. 3 is also appropriate for the field situation of submarine debris flow impact on pipelines. Using the shear rate defined by Eq. 3 and the apparent viscosity, defined by Eq. 4 or 5, the following form of the Reynolds number is proposed for the problem of debris flow impact on pipelines:

$$\text{Re}_{Newtonian} = \frac{\rho . U_\infty^2}{\mu . \dot{\gamma}} \text{ thus : Re}_{non-Newtonian} = \frac{\rho . U_\infty^2}{\mu_{app} \cdot \dot{\gamma}} = \frac{\rho . U_\infty^2}{\tau} \tag{6}$$

The drag coefficient, C_D, was obtained using the total drag force (i.e. the sum of the viscous and inertia forces) measured from the experiments and calculated in the simulations using Eq. 1, and its dependency on the Reynolds number defined by Eq. 6 was then investigated. Ultimately, the following relationships were proposed for estimating the normal drag force on a pipeline for design purposes:
Suspended Pipeline:

$$C_{D-90} = 1.4 + \frac{17.5}{\text{Re}_{non-Newtonian}^{1.25}} \tag{7}$$

Laid-on-seafloor Pipeline:

$$C_{D-90} = 1.25 + \frac{11.0}{\text{Re}_{non-Newtonian}^{1.15}} \tag{8}$$

The above proposed relationships (dashed line for Eq. 7 and bold solid line for Eq. 8) are shown on Fig. 3 along with the results of the physical and numerical experiments.
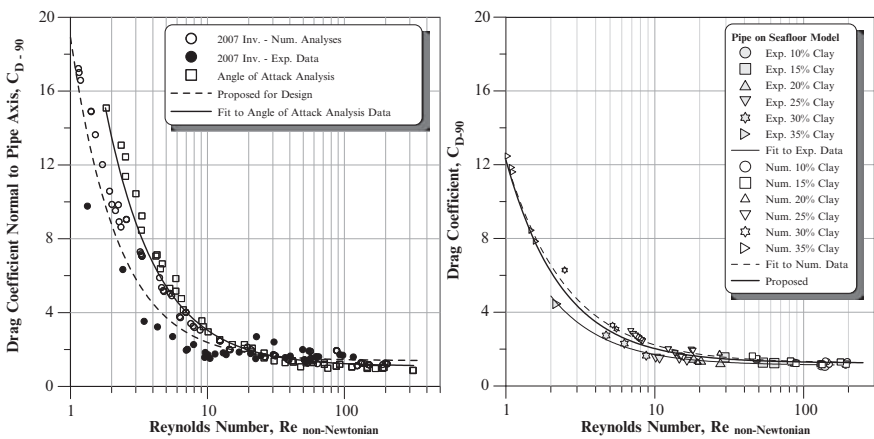
Fig. 3 Drag coefficient versus Reynolds number curves: (*left*) suspended pipe model and (*right*) pipe on seafloor model. The angle of attack is normal to the pipe axis

Fig. 4 Drag coefficient versus
Reynolds number: suspended
pipeline, longitudinal impact
drag force
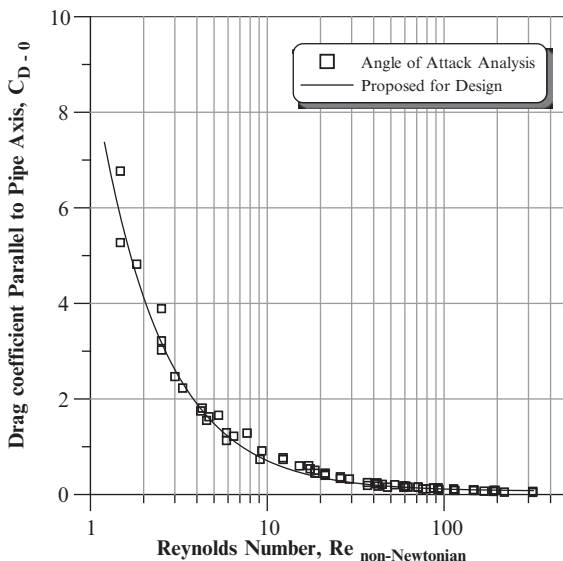
For the longitudinal drag force, the following C_{D-0}-Re relationship was proposed:

$$C_{D-0} = 0.08 + \frac{9.2}{\mathrm{Re}_{non-Newtonian}^{1.1}} \tag{9}$$

The above relationship which is based on CFD numerical analysis is shown on
Fig. 4. The drag force normal to pipe axis is developed as a result of both dynamic
pressures and viscous forces around the pipe whereas, the longitudinal drag force
is due to the shear stress on the pipe surface. As such, the drag coefficients
(i.e. C_{D-0}) computed from the CFD model are believed to be representative of the
prototype.

4 Discussion

The experiments together with the simulations covered Reynolds numbers between
about 2 and 320 (i.e. more than two log cycles), and therefore, the results are con-
sidered appropriate for practical applications. From the results, it was noted that the
numerical analysis predicts a slightly higher drag forces than those measured in the
flume experiments when the Reynolds number is less than about 10 – see Fig. 3.
This difference was explained as follows. In the prototype the fluid-pipe interaction
in an impact with a submarine debris flow takes place in a relatively short duration
after which, the debris has either passed the pipeline or slowed down in the
upstream velocity. This was also the case for the flume experiments. In the CFD

simulations of the flume experiments however, the slurry was given a slightly longer time to develop its flow around the pipe which in turn, also results in a larger contact area between the pipe surface and the slurry flow and therefore, larger drag forces. Further, small pockets of water may have become trapped between the slurry flow and copper pipe surface in the flume test (i.e. causing partial slippage), which in turn, results in lower drag force measurements for the low velocity and highly viscous slurry experiments. This, together with the no-slip boundary condition, explains why the drag coefficients computed by the CFD simulations are higher than those estimated from the flume experiments for the Reynolds numbers of about 10 and less. As such, slightly lower curves than the ones predicted by the CFD analyses were proposed for the design in the region of low Reynolds numbers.

It should be noted that the method assumes that the pipeline is moored to the seafloor and does not deform when hit by the debris flow. Two conceptual measures to control and mitigate the impact drag forces have been discussed by Zakeri et al. (2009). These measures consist of an upstream berm to protect a laid-on-seafloor pipeline in shallow waters or fjords crossings and a cable-controlled system for pipelines installed in deep waters.

5 Conclusions

A combined experimental and numerical approach was used to develop a simple method for estimating the drag forces on suspended and laid-on-seafloor pipelines caused by a clay-rich debris flow impact. The method was based on fluid dynamics principles where the drag force is presented in the non-dimensional form – drag coefficient. An ad-hoc Reynolds number was defined to describe flow characteristics of clay-rich debris flows of shear-thinning non-Newtonian fluid behaviour described by Bingham or Herschel-Buckley rheological models. Drag coefficients were calculated for situation where the impact causes drag forces both normal and longitudinal to the pipe axes.

The experimental setup, instrumentation and testing procedures in the flume as well as the CFD simulations worked very satisfactorily. In practice, submarine pipe diameters range between 0.1 to 1.0 m. Assuming a debris flow velocity between 1 to 10 m/s, density of 1,600 kg/m^3 and shear stress between 0.5 and 2.0 kPa, the shear rate upon the impact with a pipe would be in the range of $1 s^{-1}$ and $100 s^{-1}$, and one would find the corresponding Reynolds number to be between 0.8 and 320. The experiments covered the Reynolds numbers between about 2 and 320 (i.e. more than two log cycles), and therefore, are considered appropriate for practical purposes.

References

ASTM (D2196-05) Standard Test Methods for Rheological Properties of Non-Newtonian Materials by Rotational (Brookfield type) Viscometer. In Materials AS fT (ed) D2196–05: ASTM Int

CFX (2007) CFX Solver Theory, CFX-Program (Version 11.0) Theory Documentation. Canonsburg, USA: ANSYS Inc

Coleman JM, Prior DB (1978) Submarine Landslides in the Mississippi River Delta 2: 1067–1074. Proc 10th Ann Offshore Tech Conf Houston, Texas

Crowe CT, Elger DF, Roberson JA (2001) Engineering fluid mechanics. New York: Wiley

Ferziger JH, Perić M (2002) Computational Methods for Fluid Dynamics. Berlin: Springer

Kundu PK, Cohen IM (2004) Fluid mechanics. Amsterdam: Elsevier Academic

Locat J (1997) Normalized Rheological Behaviour of Fine Muds and Their Flow Properties in a Pseudoplastic Regime. In Debris-Flow Hazards Mitigation: Mechanics, Predication and Assessment, Water Resources Engineering Division (pp. 260–269): Am Soc Civil Eng (ASCE)

Mulder T, Alexander J (2001) The physical character of subaqueous sedimentary density flows and their deposits. Sedimentology 48: 269–299

Schapery RA, Dunlap WA (1978) Prediction of Storm Induced Sea Bottom Movement and Platform Forces. Proc 10th Ann Offshore Tech Conf, Houston, Texas, p. 1789–1796

White FM (2006) Viscous fluid flow. Boston: McGraw-Hill Higher Education

Whitlow R (2001) Basic soil mechanics (3rd ed.). Harlow, England: Prentice Hall

Zakeri A (2009a) Review of the State-of-the-Art: Drag Forces on Submarine Pipelines and Piles Caused by Landslide or Debris Flow Impact. J Offshore Mech Arctic Eng, Am Soc Mech Eng 131: DOI: 10.1115/1111.2957922

Zakeri A (2009b) Submarine Debris Flow Impact on Suspended (Free-Span) Pipelines: Normal and Longitudinal Drag Forces. Ocean Eng 36: 489–499.

Zakeri A, Høeg K, Nadim F (2008) Submarine debris flow impact on pipelines – Part I: Experimental investigation. Coast Eng 55: 1209–1218

Zakeri A, Hoeg K, Nadim F (2009a) Submarine Debris Flow Impact on Pipelines: Numerical Modeling of Drag Forces for Mitigation and Control Measures. SPE Projects, Facilities and Construction, 4(1): 1–11

Zakeri A, Høeg K, Nadim F (2009b) Submarine debris flow impact on pipelines – Part II: Numerical analysis. Coast Eng 56: 1–10

Appendix A – Theory for CFD Numerical Analysis

A general description of the theory and the constitutive equations used in the CFD analyses are briefly presented here. In the formulation, the different phases are denoted by lowercase Greek letters, α and β, and the total number of phases is NP. In the inhomogeneous model, each phase has its own velocity and other relevant flow fields while the pressure field is shared between the incompressible fluid phases (CFX 2007). In this model, the fluids interact via the inter-phase mass and momentum transfer terms. The phase continuity equation is expressed by:

$$\frac{\partial}{\partial t}\left(r_\alpha \rho_\alpha\right) + \nabla \bullet \left(r_\alpha \rho_\alpha U_\alpha\right) = S_{MS_\alpha} + \sum_{\beta=1}^{N_P} \Gamma_{\alpha\beta} \qquad (A.1)$$

where, r_α, ρ_α, and U_α are the phase volume fraction, density and velocity, respectively, and SMSα is the user specified mass sources. $\Gamma_{\alpha\beta}$ is the mass flow rate per unit

volume from phase β to phase α, which must obey the rule: $\Gamma_{\beta\alpha} = -\Gamma_{\beta\alpha} \Rightarrow \sum\limits_{\alpha=1}^{N_P} \Gamma_\alpha = 0$.

It is important to define the direction of the mass transfer in the conservative equations. A convenient method is to express $\Gamma_{\alpha\beta}$ by: $\Gamma_{\alpha\beta} = \Gamma_{\alpha\beta}^+ - \Gamma_{\beta\alpha}^+$. The term $\Gamma_{\alpha\beta} > 0$ represents a positive mass flow rate per unit volume from phase β into phase α. The volume fraction is bound by: $\sum\limits_{\alpha=1}^{N_P} r_\alpha = 1$. The momentum equation for a continuous fluid phase is:

$$
\frac{\partial}{\partial t}\left(r_\alpha \rho_\alpha U_\alpha\right) + \nabla \bullet \left(r_\alpha \left(\rho_\alpha U_\alpha \otimes U_\alpha\right)\right)
$$
$$
= -r_\alpha \nabla P_\alpha + \nabla \bullet \left(r_\alpha \mu_\alpha \left(\nabla U_\alpha + \left(\nabla U_\alpha\right)^T\right)\right) \tag{A.2}
$$
$$
+ \sum\limits_{\beta=1}^{N_P} \left(\Gamma_{\alpha\beta}^+ U_\beta - \Gamma_{\beta\alpha}^+ U_\alpha\right) + S_{M\alpha} + M_\alpha
$$

where, P_α and μ_α are the pressure and viscosity, respectively, and $S_{M\alpha}$ is the user defined momentum sources due to external body forces. T is the matrix transpose operation. M_α is the sum of interfacial forces acting on phase α due to the presence of other phases and is obtained from:

$$
M_\alpha = \sum\limits_{\beta \neq \alpha} M_{\alpha\beta} = M_{\alpha\beta}^D + M_{\alpha\beta}^{LUB} + M_{\alpha\beta}^{VM} + M_{\alpha\beta}^{TD} + ... \tag{A.3}
$$

where, the terms indicated above, in order, represent the inter-phase drag force, lift force, wall lubrication force, virtual mass force and turbulence dispersion force. Finally, the term $\left(\Gamma_{\alpha\beta}^+ U_\beta - \Gamma_{\beta\alpha}^+ U_\alpha\right)$ represents the momentum transfer induced by the inter-phase mass transfer. The governing transport equations result in $4 \times N_P + 1$ equations with $5 \times N_P$ unknowns that correspond to (u, v, w, r, P)$_\alpha$ for $\alpha = 1$ to N_P, where u, v, and w and the velocity components in the x, y and z directions, respectively. Given that the fluids in the inhomogeneous multiphase flow share the same pressure field, the transport equations are solved by imposing the constraint of $P_\alpha = P$ for all $\alpha = 1$ to N_P.

Experimental Investigation of Subaqueous Clay-Rich Debris Flows, Turbidity Generation and Sediment Deposition

A. Zakeri, G. Si, J.D.G. Marr, and K. Høeg

Abstract The characteristics of submarine debris flows and the generated turbidity as well as their relationship with the deposit thickness are discussed herein. There is a gap in our understanding of the processes in which a submarine debris flow and the overriding turbidity form seabed deposits and how the deposits relate to the parent landslide. The experimental program reported here studied subaqueous gravity flows of different clay-rich slurries in a flume. The flume results provide insight into the thickness of the slurry flows with the overriding turbidity clouds and the deposited sediments and lays groundwork for future studies. The thickness of the slurry head tends to decrease with increasing slurry clay content whereas the thickness of the turbidity overriding the slurry head tends to decrease with increasing clay content. Further, the thickness of the deposited layer measured a few seconds after termination of the slurry flow increases with clay content. Geometrically, the flume experiments represented flowing debris of a landslide from 50 m to 120 m water depths with a 600 m travelling distance and downstream velocities between 5 and 13.5 m/s.

Keywords Rheology • model scaling • subaqueous clay-rich debris flow • overriding turbidity thickness • deposited sediment thickness

---

A. Zakeri (✉)
Geotechnical Engineering Group, C-CORE, St. John's, Newfoundland, Canada
International Centre for Geohazards (ICG), Sognsveien 72, 0855, Oslo, Norway
e-mail: arash.zakeri@c-core.ca

G. Si
Department of Geosciences, University of Oslo, P.O. Box 1047 Blindern,
NO-0316 Oslo, Norway

J.D.G. Marr
National Center for Earth-Surface Dynamics, St. Anthony Falls Laboratory, Minneapolis, MN, USA

K. Høeg
Department of Geosciences, University of Oslo, P.O. Box 1047 Blindern,
NO-0316 Oslo, Norway; International Centre for Geohazards (ICG),
Sognsveien 72, 0855, Oslo, Norway

1 Introduction

The dynamics of submarine debris flows and the resultant turbidity currents are not fully understood. These processes are important as their occurrence can have severe consequences for infrastructure (e.g. pipelines). Subaqueous debris flows undergo various flow transformations, involving dilution and stripping of surface materials into the ambient water in the form of an overriding, suspended sediment cloud (turbidity), penetration of ambient water into the flow interior, and detachment or disintegration of hydroplaning flow fronts (Sohn 2000b). Unlike subaerial debris flows, the head of a submarine debris flow devoid of permeable girth of gravel and coarser particles, tends to hydroplane over a wedge of ambient water sandwiched between the substrate and the overriding debris. The phenomenon has been observed and studied in a number of recently conducted laboratory experiments (e.g. Harbitz et al. 2003; Ilstad et al. 2004a, b; Mohrig et al. 1998; Zakeri et al. 2008) and numerically simulated (e.g. Gauer et al. 2006; Marr et al. 2002; Zakeri et al. 2009).

   The development of acoustic techniques for mapping the seafloor and imaging the subsurface has led to a significant increase in understanding geomorphology and geology. In particular, it has led to the identification of numerous deposits of submarine landslides and debris flows on continental slopes. Interpretation of submarine debris flow deposits resulting from slope failures is hampered by the paucity of information concerning their dynamics. This lack of information hinders the development and evaluation of numerical models necessary to understand deposition from submarine debris flow (Mohrig et al. 1999). Estimating debris flow thickness from a deposit thickness is difficult given that debris flows typically have several surges. A deposit forms as result of the main debris flow event as well as the progressive aggregation of individual surges. In many cases, deposition from surges has laterally variable thickness, which complicates back-analysis of a debris flow. As a result, some authors have resorted to the assumption that deposit thickness reflects flow thickness in their studies (e.g. Sohn 2000a).

   There is a gap in understanding the process in which a submarine debris flow and the overriding turbidity form the seabed deposits and how the deposits relate to the parent landslide. The results of the experimental program reported herein partly fill this gap. They lay the groundwork for future studies on clay-rich submarine debris flow dynamics, generated turbidity and sediment deposition. The experimental program was part of a research study aimed at investigating drag forces on submarine pipelines exerted by clay-rich debris flows. The slurries were a mixture of kaolin clay, sand and water. Prior to the flume experiments, an extensive rheological study using laboratory rheometers was carried out to determine the slurry properties and suitable mix design. The situations tested in the experiments have also been numerically analyzed using Computational Fluid Dynamics (CFD) methods (Zakeri et al. 2009). Sonar data in particular proved important to assess deposition from the debris flows during and shortly after termination of the flow process.

2 Experimental Program

2.1 Rheology Experiments

Table 1 presents slurry compositions and material properties for the different experiments. Sand grain size plays an important factor in flow dynamics as slurries made with coarse sand particles are prone to gradual particle settlement during the flow causing change in rheology. As such, the slurries were prepared using two different gradations of sand, Sand A (coarse) and Sand B (fine), to investigate the effects of sand particle coarseness and to select a suitable sand for the experiments.

Two different rheometers were used: the Brookfield DV-III Ultra vane-in-cup and the Physica Modular Compact Rheometer (MCR) 300 Ball Measuring System (BMS). The vane-in-cup rheometer has a number of advantages over others: minimal disruption to the sample during vane spindle immersion; low possibility of wall slip effect; and more flexibility with the use of coarse grain size than the coaxial-cylinder geometry (Barnes and Carnali 1990). The BMS rheometer was initially developed in 1999 with the purpose of determining rheological behavior of construction materials (e.g. plaster and mortar) with maximum particle size of 10 mm, and later adapted to conventional rotation rheometers (Schatzmann et al. 2003). This exercise was carried out to determine which rheometer more appropriately determines the rheological properties of the slurries when compared with the results of the CFD back-analysis of the flume experiments.

Table 1 Slurry composition and material properties

| | | | | | Sand gradation | | |
| | Percentage material by mass | | | | Mesh Size (mm) | % Passing | |
Slurry	**Clay**	**Water**	**Sand**	Density (kg/m³)		Sand A	Sand B
					2.0	100	–
					1.0	96.5	–
					0.425	76.8	100
10% Clay	10	35	55	1,681.0	0.300	–	99.5
15% Clay	15	35	50	1,685.7	0.212	12.0	95.5
20% Clay	20	35	45	1,687.7	0.150	–	77.5
25% Clay	25	35	40	1,689.6	0.106	0.6	33.5
30% Clay	30	35	35	1,691.6	0.075	–	8.5
35% Clay	35	35	30	1,694.0	0.053	–	0.5

Specific Gravity, Gs: Sand A = 2.7 and Sand B = 2.65

Uniformity coefficient (Cu) = 1.7 for both sands defined as the ratio of the maximum particle size of the smallest 60% (d_{60}) over that of the smallest 10% (d_{10}) of the granular sample. Cu = 1 for a single-sized soil, Cu < 3 a fairly uniform grading and Cu > 5 a well-graded (Whitlow 2001)

About 5% of the mass of sand was replaced by black diamond coal slag for visual purposes. The black diamond slag had the same specific gravity and grain size distribution as the sand

The slurry preparation and vane-in-cup rheology experiments were carried out in accordance with the ASTM (D2196-05) procedures. Given the relatively recent development of the BMS as a rheometer, there are no standards available to which non-Newtonian fluids such as the slurries presented here could be tested. As such, the ASTM (D2196-05) guidelines were followed as closely as possible in the BMS tests. The slurries exhibited significant rheopectic behavior, as the fluid shear strength increased with time. Therefore, time-dependency tests were also performed on each slurry sample by studying the hysteresis loop. The Brookfield vane rheometer also has the capability of directly measuring the static yield stress (undrained shear strength) of a sample. For this purpose, a separate batch of slurry samples was prepared and the tests were carried out in accordance with the ASTM (D 4648-94) procedures.

2.2 Flume Experiments

The flume experimental program was designed at the International Centre for Geohazards (ICG) at the Norwegian Geotechnical Institute (NGI) and conducted in the St. Anthony Falls Laboratory (SAFL), Minneapolis, USA, in the spring of 2007. A total of 50 experiments were carried out in a 0.20 m wide and 9.5 m long flume suspended inside a 0.6 m wide tank (Fig. 1). The bed was rough with adjustable slope (3° and 6°). For each experiment, 190 L of slurry was prepared in the mixing tank located some 6 m above the flume and conveyed into the head tank. The instrumentation to image the flow consisted of:

- Two Canon GL2 cameras for measuring the slurry head velocities near the gate and 5.9 m downstream − 720 W × 480 H pixels frame size at 30 frames per second
- One submersible sonar to measure slurry flow and overriding turbidity heights. Transducer: A301S-SU, Olympus NDT and pulser/receiver: DPR300, JSR Ultrasonics
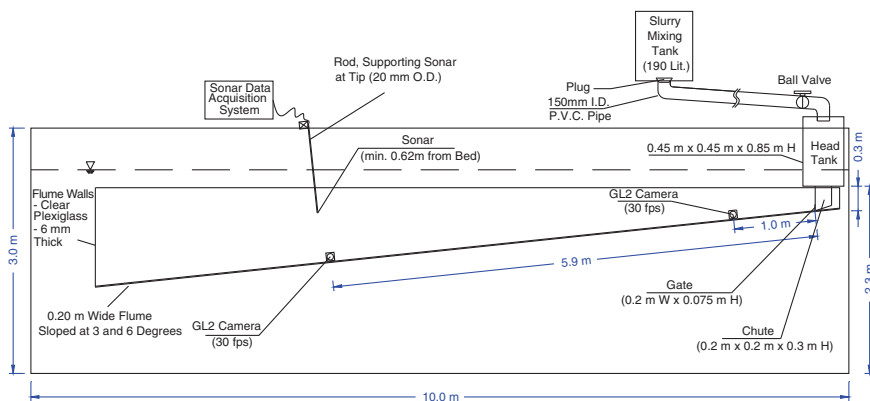

Fig. 1 Experimental setup for flume experiments

The high frequency sonar system is a stationary 500 kHz transceiver oriented normal to the sloping bed, approximately 0.62 m above the bed surface (just below the mean water surface). The data collection protocol involved two sampling periods: the first period at 50 Hz for 60 s and the second period at 6 Hz for the next 30 min. For each ping, the system sampled backscatter at a rate of 8 MHz for 10,000 samples (1.25 ms). Zakeri et al. (2008) give the details of the experimental procedures.

3   Model Scaling to Prototype Situations

Geometrically, the length scale in the flume experiments corresponds to 0.01. It should be noted that the flume experiments only model a mass gravity flow of a landslide that has turned into debris subsequent to failure (i.e. not the full scale slope failure from triggering and initial disintegration). Thus, prototype water depths at the gate and the sonar are 50 and 120 m, respectively, with a travel distance of about 600 m. The water flow is turbulent both in the flume and prototype hence, the Re similitude for the water is met on fixed boundaries. Slurry head velocities in the experiments ranged between about 0.5 and 1.35 m/s that correspond to Froude numbers $(Fr = (U/\sqrt{\Delta \rho g l / \rho}))$ in the range of 0.45 to 1.25. The Froude number formulation, l is some characteristic length of the prototype, g is gravitational acceleration, U is fluid velocity, and ρ and $\Delta \rho$ are fluid density and differential density with respect to the ambient fluid, respectively. Given that the ratio of the model to prototype velocities is equal to the square root of the geometric length scale, the flume velocities correspond to a range of about 5 to 13.5 m/s in the prototype. The slurries are non-Newtonian fluids, therefore the Reynolds numbers depend on the apparent viscosity which is a function of the shear rate. The shear rate at the base is quite high – in the order of 10^3 s^{-1} or higher – dropping to 10 s^{-1} at about 2 mm from the base (Zakeri et al. 2009). Given the high shear rates at the base, the Re similitude is also met for the slurry. The ratio of the model to prototype viscosities is equal to the geometric length scale to the power 1.5. As such, the viscosity of the slurries corresponds to debris flow viscosities that are about three orders of magnitude higher (i.e. slurry stresses of between about 7 and 250 Pa versus 7 to 250 kPa in a prototype situation). This is at least an order of magnitude higher than what is expected in the prototype. Therefore, the similitude of the slurries is distorted. However, this distortion mainly affects the study of the flow dynamics within the slurry itself and not the system as a whole. The shear rates at the slurry-water interface are high and therefore, the Re similitude at this free-surface holds. A criterion in the flume experiments was that the slurry properties should remain constant (i.e. no sand particle settling). A given grain size can be regarded as part of a fluid if the time scale of settling exceeds the duration of the debris flow, particularly when the grains have diameter of about 0.05 mm or less (Iverson 1997). Hence, only the Bagnold number (N_{Bag}), was considered. The Bagnold number is defined as:

$$N_{Bag} = \frac{\rho_s \delta^2 \gamma}{\mu_{app}} \lambda^{1/2} \tag{1}$$

where, ρ_s is grain density, δ is grain diameter, γ is shear strain rate, and μ_{app} is slurry/debris flow apparent viscosity. λ is the linear concentration defined by Bagnold (1954) and is obtained from the following expression:

$$\lambda = \frac{V_s^{1/3}}{V_{max}^{1/3} - V_s^{1/3}} \tag{2}$$

where, V_s is the grain volume fraction and V_{max} is the maximum volume fraction equal to 0.74 for spheres of equal diameter (Bagnold 1954) and 0.64 for well-graded natural sands (Bagnold 1966). Assuming the maximum volume fraction for Sand B to be 0.70, the linear concentration of Bagnold would be equal to 8.42. For Sand B 10% clay slurry, the N_{Bag} at or very close to the base is about 8 and 17 for the d_{60} and d_{90} grain sizes, respectively. These values are far below the 40 limit, and therefore viscous effects are dominant must be considered for the flume experiments. For Sand A slurries, these N_{Bag} values are close to or greater than 40.

4   Experimental Results, Analysis and Discussion

4.1   Results of Rheology Tests

Figure 2 presents the rheology test results. Slurries made with Sand B experience a larger range of shear stresses than those made with Sand A. Particle size affects the rheological behavior of suspension fluids through the specific surface defined as the grain surface area per gram of mass (m^2/g) – the smaller the particle, the higher the specific surface. The behavior of fine-grained slurries is mainly controlled by the clayey matrix. Decrease in sand size largely increases total surface area of particles per unit volume, which in turn, increases the amount of bound water, and decreases the amount of free water in the slurry system (Major and Pierson 1992). Sand A particles are about 2.6 times larger in diameter than Sand B which gives significantly higher specific surface for Sand B. This influences rheological characteristics of the 10% clay slurry made with Sand A having shear stresses roughly twice than that of the 15% clay (Fig. 2).

Sand A particles in the 10% clay slurry settle at high shear rates in the rheology tests, and at high rates of shear the fluid's apparent viscosity decreased. Sand A 35% clay slurry exhibited a flow curve with decreasing shear stress (see the dip in curve in Fig. 2 left) for shear rates less than about $5 \, s^{-1}$. As such, Sand B was used for the slurries in the flume experiments. Results of the rheological experiments were repeatable within ± 5%. The four mathematical models had a confidence of fit of greater than 95% through the data (Table 2). All slurries exhibited strong rheopectic characteristics (i.e. the shear strength increased with time). Therefore,
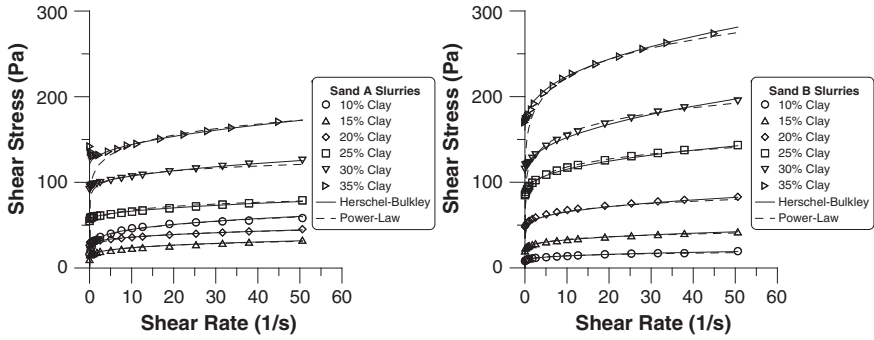
Fig. 2 Rheological experiments results and Herschel-Bulkley and Power-Law mathematical model fits: (*left*) Sand A (*coarse*) slurries and (*right*) Sand B (*fine*) slurries

Table 2 Slurry rheological models for slurries made with Sand B (fine). Shear stresses are in Pascals

Slurry	Herschel-Bulkley	Power-Law	Casson	Bingham
10% Clay	$\tau = 7.5 + 3\dot{\gamma}^{0.35}$	$\tau = 10.3\dot{\gamma}^{0.125}$	$\sqrt{\tau} = \sqrt{9.0} + \sqrt{0.04\,\dot{\gamma}}$	$\tau = 10.6 + 0.20\dot{\gamma}$
15% Clay	$\tau = 20.5 + 5.5\dot{\gamma}^{0.35}$	$\tau = 25\dot{\gamma}^{0.125}$	$\sqrt{\tau} = \sqrt{23.6} + \sqrt{0.06\,\dot{\gamma}}$	$\tau = 26.7 + 0.37\dot{\gamma}$
20% Clay	$\tau = 43 + 10\dot{\gamma}^{0.35}$	$\tau = 50\dot{\gamma}^{0.12}$	$\sqrt{\tau} = \sqrt{50.4} + \sqrt{0.10\,\dot{\gamma}}$	$\tau = 55.9 + 0.66\dot{\gamma}$
25% Clay	$\tau = 85 + 12\dot{\gamma}^{0.4}$	$\tau = 91.5\dot{\gamma}^{0.11}$	$\sqrt{\tau} = \sqrt{88.3} + \sqrt{0.16\,\dot{\gamma}}$	$\tau = 97.6 + 1.11\dot{\gamma}$
30% Clay	$\tau = 110 + 15\dot{\gamma}^{0.45}$	$\tau = 118\dot{\gamma}^{0.125}$	$\sqrt{\tau} = \sqrt{115.2} + \sqrt{0.27\,\dot{\gamma}}$	$\tau = 127.7 + 1.80\dot{\gamma}$
35% Clay	$\tau = 161 + 25\dot{\gamma}^{0.4}$	$\tau = 165\dot{\gamma}^{0.13}$	$\sqrt{\tau} = \sqrt{168.0} + \sqrt{0.31\,\dot{\gamma}}$	$\tau = 12. + 5.5\,\dot{\gamma}$

slurry preparation and release in the flume experiments were designed to strictly comply with that of the standard rheology tests. The flow curves measured from the BMS rheology tests were generally 10% to 30% less than those obtained from the vane-in-cup rheometer. The results of the CFD simulations of the flume experiments suggest that the vane-in-cup rheometer provides a better estimate of the rheological characteristics of the slurries (Zakeri et al. 2009).

The undrained shear strength (static yield stress) test results obtained by using the vane rheometer in accordance with the ASTM (D 4648–94) procedures. In magnitude, the yield stress values were close to the shear stresses measured at very low shear rates ($<< 1\,\mathrm{s} - 1$) in the vane-in-cup rheology tests.

4.2   Results of the Sonar Observations

Sonar data provide information on the internal structure of the gravity flow. The outgoing initial ping moves toward the bed, and as it density and/or velocity contrasts, it is partially reflected back to the transducer and recorded as backscatter. It
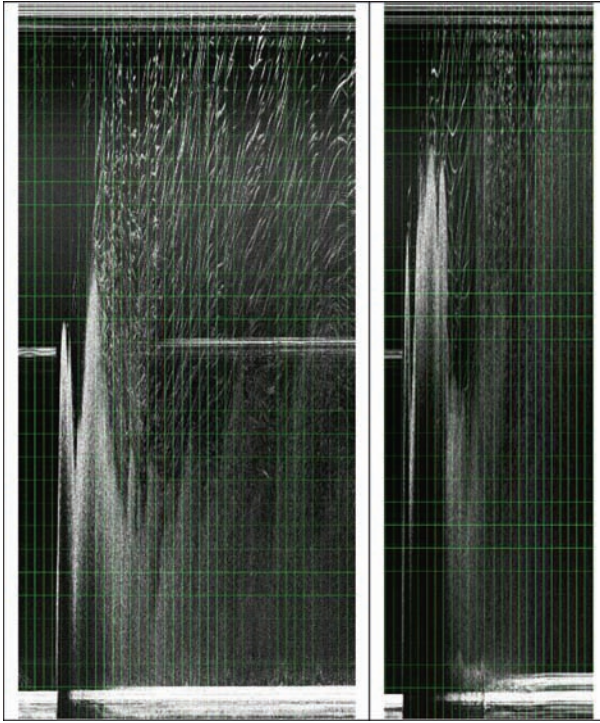
Fig. 3 Greyscale rendering of the backscatter data (*left*) 38 s of recording: 15% clay slurry, head velocity: 0.74 m/s and (*right*) 25 s of recording: 20% clay slurry, head velocity: 1.33 m/s. Vertical grid spacing: 20 mm, horizontal grid spacing: 1 s

allows for accurate measurements of the flow geometries including thickness of the initial slurry head, overriding turbidity but also the deposited layer after the termination of the flow. Examples of the greyscale rendering of the backscatter data from the runs are shown on Fig. 3. Figure 4 presents the summary results from the rendered images. Table 3 summarizes the results for all 50 runs based on sonar data and camera recordings. A major portion of the turbidity is generated from the slurry head. As the head flows downstream, thin sheets of materials are peeled off and diffuse into the ambient water forming the turbidity. The water entrainment into the slurry flow is restricted to a thin zone located at the surface of the slurry. The ambient water does not penetrate deep enough into the slurry to affect its rheology. The generated turbidity can be divided into two categories: the one overriding the slurry head and the trailing turbidity over the deposited sediments. In general, the thickness of the slurry head decreases with increasing clay content, whereas the thickness of the overriding turbidity decreases with the increasing clay content. However, the trailing turbidity thickness appears to be approximately the same for all slurries reaching the water surface shortly after termination of the flow. The thickness of the deposited layer measured a few seconds after termination of the slurry flow increases with the
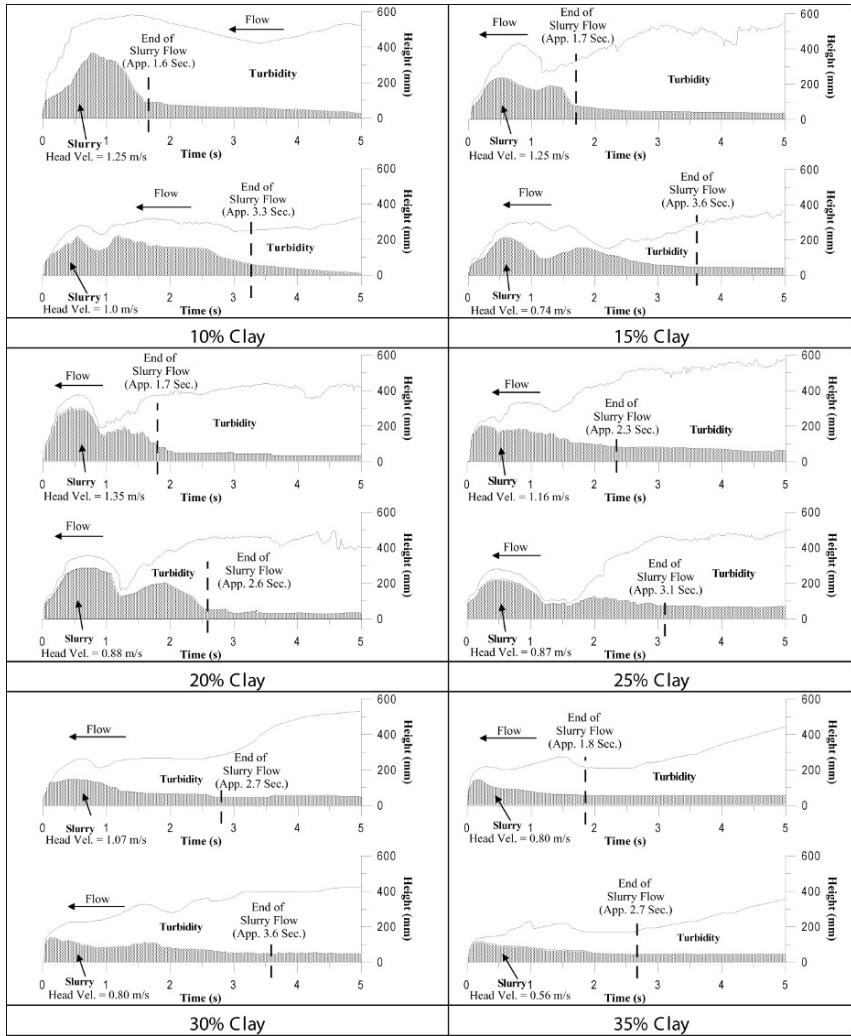
Fig. 4 Analysis results of the grayscale rendered images produced from the experiments with the maximum and minimum slurry head velocities

clay content, after which gravity-controlled compaction or consolidation will start. The distinct shape of the slurry head (single or double-hump) is a result of the velocity field developed in the water due to the momentum transfer between the water and slurry (Zakeri 2007; Zakeri et al. 2009). The flow in the water is in the form of large circulating eddy vertices slightly lagging behind the slurry head, which in turn affects the its shape. The extent of which the shape of the slurry head is affected by this momentum transfer depends on the strength of the slurry (e.g. a more pronounced double hump shape in slurries of 25% clay and less).

Table 3 Analysis results based on the rendered grayscale sonar data and camera recordings

Slurry (% Clay)	Flowing slurry head characteristics				Turbidity thickness overriding slurry head (mm)[a]		Thickness of deposited layer (mm)[b]		Deposit thickness as percentage of slurry flow	
	Velocity (m/s)		Height (mm)[a]							
	Min.	Max.	Min.	Max	Min.	Max	Min.	Max	Min. (%)	Max (%)
10%	1.0	1.25	225	365	95	215	5	10	2.2	2.7
15%	0.74	1.25	210	270	140	165	27	35	12.9	13.0
20%	0.88	1.35	300	310	60	70	32	35	10.7	11.3
25%	0.87	1.16	210	225	70	155	52	62	24.8	27.6
30%	0.80	1.07	150	185	90	95	52	64	34.7	35.1
35%	0.56	0.80	120	145	90	75	53	65	44.2	44.8

[a] The measured values were rounded off to the nearest fifth millimeter dividend
[b] The readings were rounded off to nearest millimeter

5   Conclusions

The effects of particle size and time-dependency characteristics have to be considered when studying sediment deposition from debris flows. The vane-in-cup rheometer better captures the rheological behavior of the kaolin-sand-water slurries than the BMS rheometer. The slurry head velocities in the flume experiments ranged between about 0.5 and 1.35 m/s, which correspond to prototype velocities ranging from 5 to 13.5 m/s for a clay-rich submarine debris flow. Flume experiments modelled transition between subcritical and supercritical flow regimes.

Using sonar data, it is possible measure flow geometries accurately, including the thickness of initial slurry head, overriding turbidity, and the layer deposited after termination of the flow. The results showed that the thickness of the slurry head tends to decrease with increase in clay content whereas the thickness of the overriding turbidity decreases with clay content. However, the trailing turbidity thickness is approximately the same for all slurries reaching the water surface shortly after termination of the flow. The thickness of the deposited layer measured a few seconds after termination of the slurry flow increased with the clay content. With further investigation, it may be possible to relate the measured deposit thicknesses to those of similar prototype conditions (e.g. with the help of the conventional consolidation theory, etc.). The work presented here outlines the procedures for similar type experiments and lays the groundwork for future studies.

References

ASTM (D2196–05) Standard Test Methods for Rheological Properties of Non-Newtonian Materials by Rotational (Brookfield type) Viscometer. In: Materials ASfT (ed) D2196–05: ASTM Internat

ASTM (D 4648–94) Standard Test Method for Laboratory Miniature Vane Shear Test for Saturated Fine-grained Clayey Soils. In: Materials ASfT (ed) D 4648 – 94: ASTM Int

Bagnold RA (1954) Experiments on a gravity-free dispersion of large solid spheres in a. Newtonian fluid under shear. R Soc Lond Proc A225: 49–63

Bagnold RA (1966) An approach to the sediment transport problem from general physics. Geol Surv Prof Pap 422-I: 37

Barnes HA, Carnali JO (1990) The vane-in-cup as a novel rheometer goemetry for shear thinning and thixotropic materials. J Rheol 34: 841–866

Gauer P, Elverhoi A, Issler D et al. (2006) On numerical simulations of subaqueous slides: back-calculations of laboratory experiments of clay-rich slides. Nor J Geol 86: 295–300

Harbitz CB, Parker G, Elverhoi A et al. (2003) Hydroplaning of subaqueous debris flows and glide blocks: analytical solutions and discussion. J Geophys Res-Solid Earth 108(B7)

Ilstad T, De Blasio FV, Elverhoi A et al. (2004a) On the frontal dynamics and morphology of submarine debris flows. Mar Geol 213: 481–497

Ilstad T, Elverhoi A, Issler D et al. (2004b) Subaqueous debris flow behaviour and its dependence on the sand/clay ratio: a laboratory study using particle tracking. Mar Geol 213: 415–438

Iverson RM (1997) The physics of debris flows. Rev Geophys 35: 245–296

Major JJ, Pierson TC (1992) Debris flow rheology – experimental-analysis of fine-grained slurries. Water Resource Res 28: 841–857

Marr JG, Elverhoi A, Harbitz C et al. (2002) Numerical simulation of mud-rich subaqueous debris flows on the glacially active margins of the Svalbard-Barents Sea. Mar Geol 188: 351–364.

Mohrig D, Elverhoi A, Parker G (1999) Experiments on the relative mobility of muddy subaqueous and subaerial debris flows, and their capacity to remobilize antecedent deposits. Mar Geol 154: 117–129

Mohrig D, Whipple KX, Hondzo M et al. (1998) Hydroplaning of subaqueous debris flows. Geol Soc Am Bull 110: 387–394

Schatzmann M, Fischer P, Bezzola GR (2003) Rheological behavior of fine and large particle suspensions. Am Soc Civil Eng J Hydraul Eng 129: 796–803

Sohn YK (2000a) Coarse-grained debris-flow deposits in the Miocene fan deltas, SE Korea: a scaling analysis. Sed Geol 130: 45–64

Sohn YK (2000b) Depositional processes of submarine debris flows in the Miocene fan deltas, Pohang Basin, SE Korea with special reference to flow transformation. J Sed Res 70: 491–503

Whitlow R (2001) Basic soil mechanics (3rd ed.). Harlow, England: Prentice Hall.

Zakeri A (2007) Report on Experimental Program, Submarine Debris Flow Impact on Pipelines. Oslo: Int Centre Geohaz (ICG)

Zakeri A, Høeg K, Nadim F (2008) Submarine debris flow impact on pipelines – Part I: Experimental investigation. Coast Eng 55 1209–1218

Zakeri A, Høeg K, Nadim F (2009) Submarine debris flow impact on pipelines – Part II: Numerical analysis. Coast Eng 56: 1–10

The Kinematics of a Debris Avalanche on the Sumatra Margin

A.S. Bradshaw, D.R. Tappin, and D. Rugg

Abstract The kinematics of submarine landslides is important both for evaluating tsunami hazard potential as well as for evaluating hazards to seabed structures. This paper presents a kinematics analysis of a debris avalanche that was identified in deep water off the northwest coast of Sumatra. A numerical model is derived and used to investigate the relative influence of slide density, hydrodynamic drag, basal resistance, and hydroplaning. The model predicts a maximum slide velocity of 40–47 m/s. The slide density and shear strength of the sediments beneath the slide play a key role in the kinematics behavior.

Keywords Submarine landslide • Sumatra • debris • avalanche • kinematics • tsunami

1 Introduction

Submarine landslides have been known to generate tsunamis and have the potential for adversely affecting seabed installations. The three most important factors influencing gravity-driven slide motion are the mass of the slide, the hydrodynamic drag on the slide body, and the frictional resistance between the slide and the underlying sediments. Research in this area has also focused on hydroplaning, where water becomes entrained under the frontal portion of the slide body, as this seems to

A.S. Bradshaw (✉)
Merrimack College, North Andover, Massachusetts, MA 01845, USA
e-mail: aaron.bradshaw@merrimack.edu

D.R. Tappin
British Geological Survey, Nottingham, NG12 5GG, UK
e-mail: drta@bgs.ac.uk

D. Rugg
University of Texas at Austin, Austin, Texas, USA
e-mail: rugg.dennis@gmail.com

explain the large run out distances observed in many submarine slides (e.g., Locat and Lee 2002; Harbitz et al. 2003; De Blasio et al. 2004a). Numerical analysis of the kinematics of documented landslide events (e.g., Locat et al. 2003; De Blasio et al. 2004b) can provide insight on the various factors involved.

This paper presents a numerical analysis of a submarine landslide event identified in deep water off the northwest coast of Sumatra. The failure was documented by a team of scientists and engineers as part of a research cruise aimed at identifying the cause of the 2004 Indian Ocean tsunami (Moran and Tappin 2006). In order to investigate the kinematics of the observed mass failure, a very simple model is derived which attempts to represent the major slide features observed in bathymetric and seismic records. A series of model runs are performed to investigate the sensitivity of the various factors including the slide mass, hydrodynamic drag, basal shear resistance, and hydroplaning.

2 Description of the Mass Failure

A large submarine mass failure was identified offshore off the northwest coast of Sumatra as shown in Fig. 1. Using a combination of multibeam and seismic data Tappin et al. (2007) interpreted this slide as a *debris avalanche,* which is characterized by cohesive blocks that travel very rapidly a top a fine-grained sediment flow. A complete interpretation of the submarine mass failure is given in Tappin et al. (2007). However, the relevant features of the slide are described in this section to understand qualitatively the motion of the slide such that a representative kinematics model can be developed.

The mass failure, shown in the multibeam bathymetry in Fig. 2, originated from the flanks of a thrust fold in water depths of about 3,400–4,000 m. The failure is characterized by a group of blocks arranged in a triangular pattern on the abyssal plane with the largest "outrunner" block forming the apex of the triangle. The landslide scarp is clearly identifiable on the upper slope of the thrust fold.

Fig. 1 Map showing the location of the landslide site The Sumatra margin is shown by the *red/dashed lines* and the landslide location is indicated with a *star* (adapted from Tappin et al. 2007)
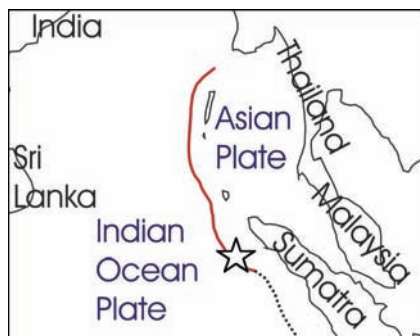
The outrunner block is trapezoidal in shape with a thickness of about 80 m and a length (parallel to slope) of about 1,400 m along its base. The block is located approximately 9 km from the base of the thrust fold. The failure scarp is about 3,400 m in length and extends up from about mid-slope to the slope crest. The slope ranges from 7 degrees on the lower slope to 15 degrees on average within the scarp.

A seismic cross section taken through the blocks and lower slope (line SCS 4 in Fig. 2) indicates the presence of a blocky debris flow located between the thrust fold and the outrunner block. As shown in the cross section in Fig. 3, the bottom of the debris flow unit is horizontally planar and there is no evidence that the slide eroded the underlying sediments. The debris flow has a thickness of about 10–50 m and extends from the base of the thrust fold to beneath the outrunner block where
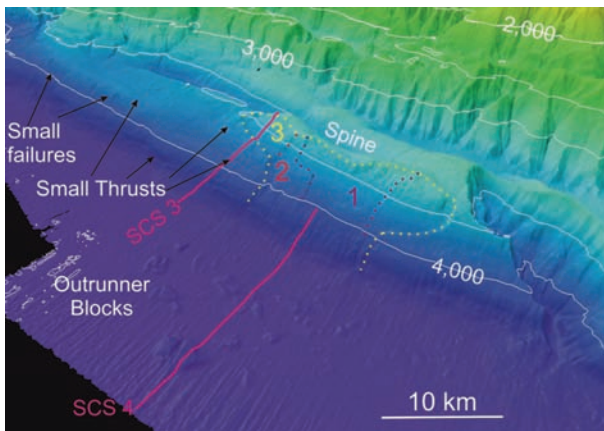

Fig. 2 Multibeam bathymetry looking northward showing the debris avalanche slide (Tappin et al. 2007)
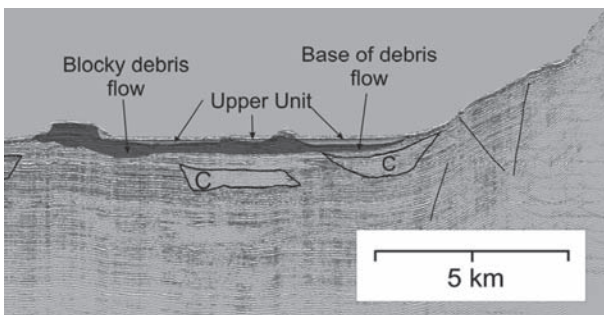

Fig. 3 Seismic transect through the slide and lower slope (Tappin et al. 2007)

it pinches off in the seaward direction. This suggests that the block, or at least a significant portion of the block, traveled on top of the debris flow.

The failure scarp also runs parallel to the inclined bedding on the thrust ridge suggesting that the debris flow failed along a continuous weak sediment layer or bedding plane. The thickness of the largest outrunner block that is furthest from the base of the thrust fold is similar to the depth of the excavated failure on the thrust fold. Therefore, it is interpreted that the failed sediment formed a debris flow in the manner of Hampton (1972), disintegrating as it moved down slope and out onto the abyssal plain.

3 Kinematics Model

The purpose of the modeling was to investigate the sensitivity of the various factors influencing the kinematics behavior of the outrunner block. A simple two-dimensional kinematics model was developed as shown in the schematic in Fig. 4. The model consists of a rigid block sliding on top of a shear layer and thus is similar in concept to the model described in Imran and Parker (2001). An entrained water layer was also incorporated into the model to account for hydroplaning, which causes a reduction in the frictional resistance at the bottom of the slide. A trapezoidal block shape was assumed which resembled the shape of both the failure scarp and the outrunner block (Fig. 3). The equation of motion was derived using and approach that was consistent with Grilli and Watts (2005), Bradshaw et al. (2007), and Taylor et al. (2008):

$$
\left(\frac{\rho}{\rho_w}+C_m\right)\frac{d^2s}{dt^2}=\left(\frac{\rho}{\rho_w}-1\right)g\sin\theta-\frac{\tau(B-B_w)+\tau_wB_w}{\rho_wA_l}-C_d\frac{T}{2A_l}\left(\frac{ds}{dt}\right)^2 \quad (1)
$$

Where; ρ = bulk density of the slide block, ρ_w = density of water, C_m = hydrodynamic added mass coefficient, s = position of the slide block, g = acceleration due to gravity, θ = slope angle, τ = shear stress at the top of the shear layer, τ_w = shear stress at the top of the water layer, B = slide length, B_w = length of entrained water layer, A_l = longitudinal sectional area of slide, T = slide thickness, C_d = hydrodynamic drag coefficient, and t = time. For a trapezoidal block, $A_l = TB − T^2/\tan \alpha$ where α = angle of the trapezoid. A Bingham model (Locat and Lee 2002) was used to model the shear behavior of the sediment in the shear layer. Assuming a linearly
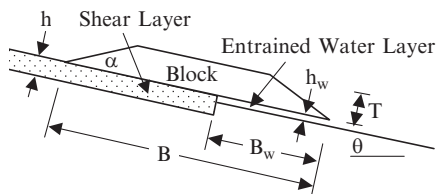

Fig. 4 Kinematics model used in this study

decreasing velocity profile with depth (i.e. simple Couette flow) the shear stress at the top of the layer is given by the following equation:

$$\tau = \tau_y + \eta \frac{u}{h} \tag{2}$$

Where; τ_y = plastic yield strength, η = Bingham viscosity, u = velocity of the slide block, and h = thickness of the shear layer. Similarly, assuming a linearly velocity profile in the entrained water layer, the shear stress at the top of the layer given by the following equation:

$$\tau_w = \mu \frac{u}{h_w} \tag{3}$$

Where; μ = viscosity of water, h_w = thickness of the entrained water layer.

Interpretation of the bathymetric and seismic data indicates that the block degenerated into a flow as it travelled down slope. Since the height of the failure scarp and the thickness of the outrunner block are consistent, it was assumed that only the slide length changed during its motion. Experiments by Watts and Grilli (2003) show that slide deformation scales with slide motion. Assuming that the rate of change of the slide length was directly proportional to velocity (i.e. no motion, no deformation) the following empirical equation was derived:

$$B = B_0 - C_B s \tag{4}$$

Where; B_0 = initial slide length, and C_B = slide length reduction coefficient. C_B was iteratively adjusted during the modeling such that the final slide length was equal to that observed in the field.

4 Model Parameter Estimates

Upper and lower bound estimates were made of all model parameters based on typical values from the literature and available geotechnical data from Moran and Tappin (2006). Intermediate values of model parameters were then selected to serve as a baseline for investigating the sensitivity of each parameter individually. The parameters used in the analysis are summarized in Table 1 and the basis for their selection is discussed below.

The initial length of the slide (B_0) was taken as the average length of the failure scarp of 3,400 m. The final length was approximated to be 1,400 m based on the cross-sectional length of the outrunner block. An average angle of 10 degrees was used for the trapezoid angle (α). A slide bulk density (ρ) of about 1.7 Mg/m^3 was measured in box core samples taken of the near surface sediments (Moran and Tappin 2006). It is anticipated that the bulk density would be higher at depth within the slide body due to overburden stress and therefore an upper bound of 1.9 Mg/m^3 was assumed.

Table 1 Summary of model parameters

Parameter	Lower	Upper	Intermediate
ρ (Mg/m³)	1.7	1.9	1.8
C_m	0.8	1.2	1.0
C_d	0.8	1.2	1.0
τ_{y1} (kPa)	30	45	38
h_1 (m)	0.01	0.1	0.05
τ_{y2} (kPa)	1	20	10
h_2 (m)	10	50	30

Wave tank studies by Watts (2000) indicate a slight dependence of the hydrodynamic added mass coefficient (C_m) on the ratio of water depth to slide length (*D/B*). At the debris avalanche site the *D/B* is about one and therefore a range of 0.8 to 1.2 was assumed. The hydrodynamic drag coefficient (C_d) was also assumed to range from 0.8 to 1.2 consistent with ellipsoidal shapes (Grilli and Watts 2005).

Since clay sediments are sheared undrained during slide triggering and subsequent motion, the peak undrained strength (S_u) is mobilized initially but rapidly reaches steady state conditions after only about 2 cm of movement (Stark and Contreras 1996). The steady state strength or residual undrained strength (S_{ur}) remains constant at large displacements and therefore can be used as an estimate of the yield strength (τ_y). The yield strength of the sediments below the slide was divided into two distinct portions along its path: the strength on the failure scarp sediments (τ_{y1}) and the strength of the debris flow (τ_{y2}) that was assumed to have developed down slope of the failure scarp.

A static limit equilibrium slope stability analysis was used to estimate the lower bound strength of the failure scarp sediments. If a seismic pseudo-static stability analysis were used, it would result in a higher estimated strength. The average S_u at failure was about 120 kPa, which corresponds to a S_u / σ_{v0}' ratio of about 0.2 where σ_{vo} is the initial effective vertical stress. Undisturbed and remolded miniature vane shear measurements taken in box core sediments at the site indicate a sensitivity (S_u/S_{ur}) value of about 4. Therefore, the lower bound S_{ur} on the failure scarp was estimated at about 120 kPa/4 = 30 kPa. An upper bound S_{ur} value of 45 kPa was estimated by multiplying the effective vertical stress by a S_u / σ_{v0}' ratio 1.5 times larger and dividing by the sensitivity of 4.

The lower bound estimate of the yield strength of the debris flow (τ_{y2}) was obtained from remolded vane shear measurements of the box core samples. An average S_{ur} value of about 1 kPa was measured in the upper 15 cm of sediments (Moran and Tappin 2006). The upper bound S_{ur} estimate assumes that the 80 m of sediment composing the slide mixes uniformly. Therefore, it was obtained by calculating the average S_u within a depth of 80 m assuming a S_u / σ_{v0}' of 0.3 and dividing by a sensitivity of 4.

Studies by Locat (e.g., Locat and Lee 2002) suggest that the Bingham viscosity (η) is well correlated to the yield strength. Therefore, the following empirical correlation was used:

$$\eta = 0.0052\tau_y^{1.12} \tag{5}$$

Where; η = Bingham viscosity (in kPa), and τ_y = plastic yield strength (in kPa). On the failure scarp, it is anticipated that the shear layer is thin because the failure was initiated within a continuous weak sediment layer. Therefore, a range of 1–10 cm was assumed for the shear layer thickness on the failure scarp (h_1). However, interpretation of the seismic records indicates that the thickness of the debris flow ranged from 10 to 50 m and therefore this range was used for the thickness of the shear layer downslope of the failure scarp (h_2). Field observations by De Blasio et al. (2004a) suggest the thickness of the entrained water layer (h_w) is on the order of 0.1 m which was assumed in this study.

5 Modeling Results and Discussion

The equation of motion was solved numerically using an explicit finite difference scheme. A sensitivity analysis was performed by first performing the analysis using the intermediate values of all input parameters, and then varying each parameter individually using the upper and lower bound values.

A typical time history of acceleration, velocity, position and slide length is shown in Fig. 5. The results suggest that the slide event lasted about 11 min. The maximum acceleration occurred at the start of landslide motion (Fig. 5a), which is an important aspect for tsunami generation (e.g., Watts and Grilli 2003; Grilli and Watts 2005; Harbitz et al. 2006). For block slides on planar slopes, theoretically the initial acceleration scales with slide bulk density, slope angle, basal resistance, and added mass coefficient (Watts and Grilli 2003). The modeled results are consistent
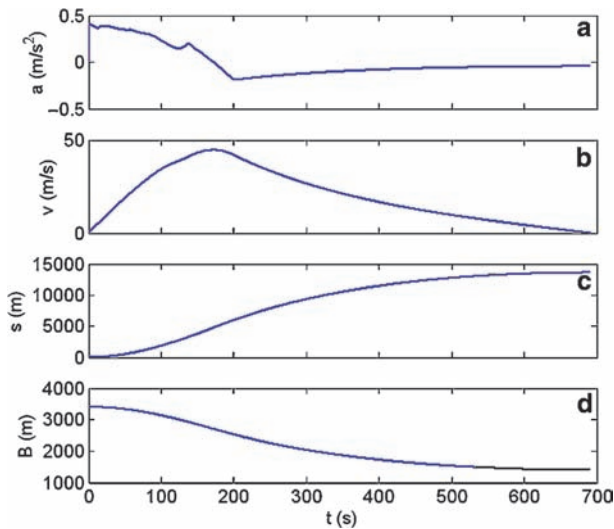

Fig. 5 Typical time histories of (**a**) acceleration, (**b**) velocity, (**c**) position, and (**d**) slide length

with the theory indicating that the initial acceleration is most influenced by the slide density, followed by the shear strength of the failure scarp sediments, followed by the added mass coefficient. Given the range of properties, the maximum accelerations varied from 0.35 to 0.47 m/s^2.

For planar slopes, the maximum velocity occurs when the slide reaches its terminal velocity which scales with bulk density, slope angle, and basal resistance (Watts and Grilli 2003). However, the geometry or length of the slope may prevent a slide from reaching its theoretical terminal velocity. This was the case for this slide where maximum velocities of 40–47 m/s were reached as the slide began to move onto the abyssal plain at $t \sim 170$ s (Fig. 5b). The velocity was most affected by the slide bulk density and the shear strength of the debris flow. The velocities from this study are consistent with those obtained in other numerical case studies; up to 45 m/s for the Palos Verdes debris avalanche (Locat et al. 2003) and up to 60 m/s for the Storegga slide (De Blasio et al. 2004b).

Basal resistance has a significant influence on the run out distance of a submarine slide (e.g., Locat et al. 2003, De Blasio et al. 2004b). Assuming that the origin is located at the middle of the failure scarp, the observed position of the outrunner block mass center is at about 13,620 m. Using the assumed range of properties, the model predicted the observed position of the outrunner block in most cases to within about 2,000 m (~15%). However, the final slide position was significantly affected by the strength properties of debris flow. When the lower bound yield strength of 1 kPa was used, the model predicted that the block would overshoot the observed position by 9,250 m (~70%). Whereas the upper bound value predicted that the block would undershoot the observed position by 4,550 m (~33%).

Assuming intermediate values of all parameters, additional model runs were performed to back analyze the yield strength of the debris flow required to match the observed position. The time history for this condition was shown previously in Fig. 5. If hydroplaning does not happen, the yield strength of the debris flow must be approximately 7 kPa to match the observed position. If hydroplaning occurs than the yield strength must be higher (e.g., 8.5 kPa for $B_w = 300$ m). Both values of yield strength are reasonable but they are higher than some of the published data for marine sediment flows, which have values typically less than about 1 kPa (Locat and Lee 2002).

6   Conclusions

This paper analyzed the kinematics of a submarine debris avalanche observed off the northwest coast of Sumatra. Based on existing bathymetric and seismic records, a kinematics model was derived which incorporates forces due to gravity, hydrodynamic drag, and basal resistance. A sensitivity analysis was performed using a range of input parameters estimated from the literature and from measured sediment properties. The model predicted maximum slide accelerations ranging from 0.35 to 0.47 m/s^2 and maximum velocities ranging from 40 to 47 m/s. The modeled slide position was matched to the observed position using reasonable values of input

parameters. The parameters that had the most influence on the motion of the debris avalanche were the slide bulk density and undrained shear strength of the sediments beneath the slide block. Therefore, accurate prediction of the kinematics of future slides relies, at least in part, on accurate characterization of the bulk density and shear strength properties of the slope sediments. The prediction of the strength properties of the sediments after they transition into a debris flow remains a challenge.

References

Bradshaw AS, Baxter CDP, Taylor O-DS, Grilli S (2007) Role of soil behavior on the initial kinematics of tsunamigenic slides. In: Lykousis V, Sakellariou D, Locat J (eds) Submarine mass movements and their consequences III: 387–394 Springer, The Netherlands.

De Blasio FV, Engvik L, Harbitz CB, Elverhøi A (2004a) Hydroplaning and submarine debris flows, J Geophys Res 109, doi:10.1029/2002JC001714.

De Blasio FV, Issler D, Elverhøi1 A, Harbitz CB, Ilstad T, Bryn P, Lien R, Løvholt F (2004b) Dynamics, velocity and run-out of the giant Storegga slide. In: Locat, J, Mienert J, Boisvert J (eds) Submarine mass movements and their consequences I: 223–230, Kluwer, The Netherlands.

Grilli ST, Watts P (2005) Tsunami generation by submarine mass failure: modeling, experimental validation, and sensitivity analyses, J Waterw P C 131(6): 283–297.

Hampton M (1972) The role of subaqueous debris flow in generating turbidity currents, J Sediment Petrol 42: 775–993.

Harbitz CB, Løvholt F, Pedersen G, Masson DG (2006) Mechanisms of tsunami generation by submarine landslides: a short review, Nor J Geol 86: 255–264.

Harbitz CB, Parker G, Elverhøi A, Marr JG, Mohrig D, Harff PA (2003) Hydroplaning of subaqueous debris flows and glide blocks: analytical solutions and discussion, J Geophys Res 108 (B7), doi:10.1029/2001JB001454.

Imran J, Parker G (2001) A numerical model of muddy subaqueous and subaerial debris flows, J Hydrodyn Eng 127(11): 959–968.

Locat J, Lee HJ (2002) Submarine landslides: advances and challenges, Can Geotech J 39: 193–212.

Locat J, Lee HJ, Locat P, Imran J (2003) Numerical analysis of the mobility of the Palos Verdes debris avalanche, California, and its implication for the generation of tsunamis, Mar Geol 203(3–4): 269–280.

Moran K, Tappin D (2006) SEATOS 2005 Cruise Report: Sumatra Earthquake and Tsunami Off shore Survey (SEATOS). http://ocean. oce.uri.edu/seatos. Accessed 16 October 2007.

Stark TD, Contreras IA (1996) Constant volume ring shear apparatus, Geotech Test J, 19(1): 3–11.

Tappin DR, McNeil LC, Henstock T, Mosher, D (2007) Mass wasting processes- offshore Sumtra. In: Lykousis V, Sakellariou D and Locat J (eds) Submarine mass movements and their consequences III: 327–336, Springer, The Netherlands.

Taylor O-DS, Bradshaw AS, Baxter CDP, Grilli S (2008) The effects of basal resistance and hydroplaning on the initial kinematics of seismically induced tsunamigenic landslides. In: Reddy KR, Khire MV, Alshawabkeh AN (eds) proc GeoCongress, Am Soc Civil Eng: 522–529.

Watts P (2000) Tsunami features of solid block underwater landslides, J Waterw P C 126(3): 144–152.

Watts P, Grilli S (2003) Underwater landslide shape, motion, deformation, and tsunami generation. Proc 13th Int Offshore and Polar Eng Conf, ISOPE03 3: 364–371.

3D Numerical Modelling of Submerged and Coastal Landslide Propagation

P. Mazzanti, F. Bozzano, M.V. Avolio, V. Lupiano, and S. Di Gregorio

Abstract The analysis of the propagation phase plays a fundamental role in the assessment and forecasting of risks related to the occurrence of submerged and coastal landslides. At present there are few numerical models able to simulate the propagation of such a type of events. This paper presents fully 3D models and approaches developed by the authors and suitable for the simulation of both completely subaqueous landslides and combined subaerial–submerged ones (i.e. coastal landslides with a subaerial source which propagate underwater). A Cellular Automata model is described which has been specifically designed for combined subaerial–submerged landslides. Moreover, a new approach able to simulate submerged mass movements using commercial 3D software, originally developed for subaerial landslides, is presented. Calibration and validation of these models upon a real and well constrained coastal debris flow at Lake Albano (Rome, Italy) is also presented.

Keywords Landslides • propagation • numerical modelling • coastal and submerged landslides

1 Introduction

The analysis of the post-failure stage is a fundamental part in the assessment of landslide risk. Events like debris flows, rock and debris avalanches usually affect very large areas during their propagation, whereas they induce limited damage before or during

───────────────

P. Mazzanti and F. Bozzano (✉)
Dipartimento di Scienze della Terra, Università di Roma "Sapienza", P.le Aldo Moro 5, 00185 Roma, Italy
e-mail: paolo.mazzanti@uniroma1.it

M.V. Avolio and S. Di Gregorio
Department of Mathematics, University of Calabria, Arcavacata, 87036 Rende (CS), Italy

V. Lupiano
Department of Earth Sciences, University of Calabria, Arcavacata, 87036 Rende (CS), Italy

the failure close to the source area. This is even more valid for coastal and submerged landslides whose secondary hazard (i.e. tsunami) is closely related to the landslide behaviour during propagation (velocity, thickness, runout etc.).

The propagation over an irregular morphology of a heterogeneous mixture of soil and water, which changes frequently its properties (such as volume, shape, percentage of water etc.) is difficult to be defined and solved in terms of differential equations and its modelling needs several simplifications. The analytical difficulties are amplified for phenomena occurring underwater or, still more, for phenomena which change environment (from air to water) during the propagation.

Laboratory experiments and studies of real events are the basis to improve the knowledge in this very complex field. As regards the analysis of real landslides in the last few years, several efforts have been focused on two main directions: empirical approaches based on historical data and approximated numerical methods. The former, the most common method to predict the runout distances, deals with an apparent inverse relationship between the volume and the *Fahrböschung* (Heim 1932) of landslides. Several linear regression equations have been proposed (e.g., Scheidegger 1973; Corominas 1996), which are able to predict the landslide runout and velocity, given the landslide volume. De Blasio et al. (2006) also obtained a similar plot by comparing different types of subaerial and submerged landslides. Such an approach, even if extensively used for predictive purposes, has several limitations mainly related to the large variability of landslide features such as topography, rheology and other peculiarities which a simplified approach is not able to account for. On the other hand, the analytical and numerical approach is based on the mechanics of the flow and involves the solution of a system of governing equations of motion, either in a closed-form or numerically (Hungr et al. 2005).

2 Numerical Modelling of Landslide Propagation: State of the Art

Due to the high complexity of mechanisms involved in the post-failure stage of an extremely rapid subaerial landslide (Cruden and Varnes 1996), few models have been built that try to capture the "real" physics of the flow or part of it (Campbell et al. 1995; Denlinger and Iverson 2004). The most appropriate and commonly used models adopt a semi-empirical approach based on the principle of the equivalent fluid, formalized by Hungr (1995). This approach assumes that the flowing mass behaves like a fluid, whose rheological features cannot be measured through laboratory or in situ testing, but can only be obtained by the back-analysis of real past events. The approach is defined as semi-empirical since it uses a numerical model which accounts for the main physical features of the phenomenon but, at the same time, needs a large historical record of real events in order to calibrate the parameters.

In recent years, these models have been becoming fully 3D, i.e. are able to simulate the distribution of the mass in a real topography, and reliable enough to be used in the assessment of risks related to catastrophic, fast subaerial landslides. Their effectiveness

is the result of several back-analyses of past phenomena, which allowed us to constrain the parameters. However, even if these models are calibrated upon real events and can thus be considered more "practical" than "theoretical", they are often based, or at least validated, through laboratory experiments (Bagnold 1954; Savage and Hutter 1989; Iverson and LaHusen 1993).

With regard to landslides occurring underwater, less experimental results are available (Marr et al. 2001; Ilstad et al. 2004; Breien et al. 2007) and the direct observation of real phenomena is almost impossible. Furthermore, analysis of landslide deposits is more difficult in the submerged environment, therefore indirect information is also limited. As a consequence, few rheological and phenomenological constraints are available and, thus, few numerical models have been developed. Imran et al. (2001) built the bi-dimensional BING model suitable for analyzing muddy and viscous flow-like mudflows or cohesive debris flows. Fernández-Nieto et al. (2008) developed a bi-dimensional model which is able to simulate underwater granular flows like rock and debris avalanches, using a Savage–Hutter type approach. However, few 3D numerical models are available for submerged flow-like mass movements although recently a 3D Cellular Automata model for turbidity currents has been developed and applied to real cases by Salles et al. (2007).

A further degree of complexity is related to the simulation of combined subaerial–submerged events since they are characterized by a complicated air–water transition.

In spite of the larger difficulties in the investigation and modelling of submerged and coastal landslides, an increasing number of case studies will be available in the near future, thus allowing the constraining and calibration of models or numerical approaches for such a type of phenomena. Hence, an effort has to be made to build new and powerful 3D models able to simulate the real distribution of a landslide over an irregular terrain.

3 Equivalent Fluid Equivalent Medium Approach by DAN3D: Theory and Example

The first approach here proposed, suitable for the numerical modelling of completely submerged or subaerial–submerged landslides is named EFEM (Equivalent Fluid Equivalent Medium) (Mazzanti 2008a). This approach allows for using codes specifically designed for subaerial landslides to simulate mass movements propagating underwater. In fact, it can account for the interaction between the moving mass and the surrounding fluid (in the case of submerged movements), through some expedients. Furthermore, the air to water transition in coastal landslides can be also simulated by this approach. In greater detail, the following aspects are considered: (1) a sudden change of properties during the air–water transition; (2) the drag forces; (3) buoyancy forces and (4) peculiar mechanisms like hydroplaning. For example, the drag force is simulated by using the Voellmy rheology proposed by Hungr (1995) and increasing the turbulence basal coefficient of friction, which is proportional to the square of the landslide velocity.

In addition, a reduction of the landslide unit weight allows one to account for the Archimedean forces. In this way, the main physical mechanisms which differentiate subaerial and subaqueous landslides can be reasonably accounted for, thus obtaining reliable results in terms of mass distribution and velocity along the path. Application of this approach to a real combined subaerial–submerged debris flow that occurred in 1997 at Lake Albano (Rome, Italy) has been made by DAN3D model (McDougall and Hungr 2004). This model is an extension of the DAN-W code (Hungr 1995) since it retains the key features of the original quasi-3D model, though satisfying the need to consider a complex topography.

The 1997 Lake Albano debris flow has been simulated by using a 1 m quare DTLM (Digital Terrain and Lacustrine Model), obtained by combining a subaerial DTM (Digital Terrain Model) collected by means of an aerial LiDAR survey (Pietrantonio et al. 2008) and a high resolution bathymetry (Fig. 1). The pre-landslide morphology
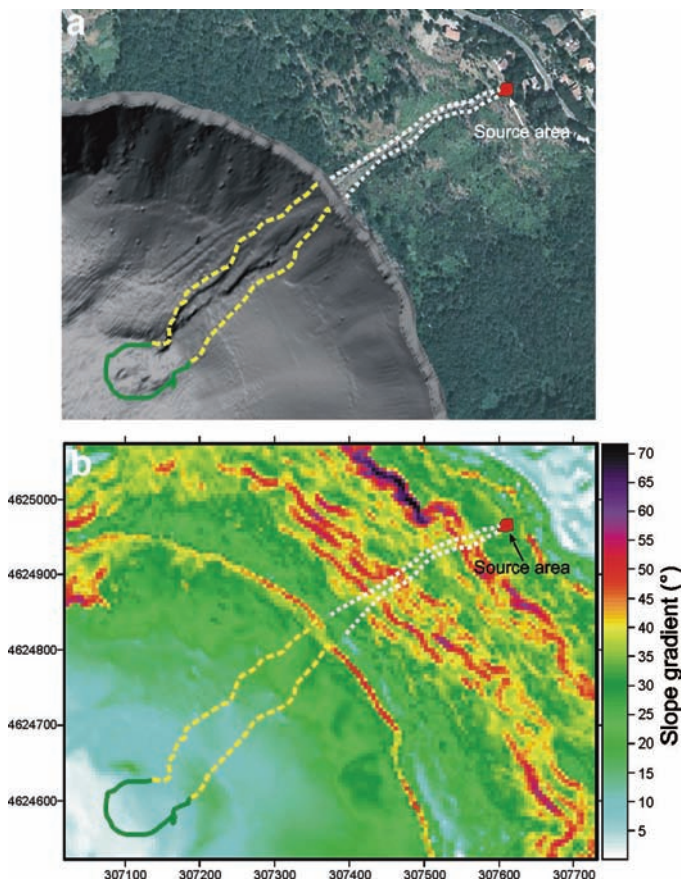

Fig. 1 (**a**) Aerial photo merged with the actual bathymetry; (**b**) slope gradient map. White dotted lines bound the subaerial landslide erosive chute; yellow dashed lines bound a submerged erosive channel; green full line bounds the subaqueous landslide deposit

has been reconstructed by using high resolution aerial photos for the subaerial part of the slope and reshaping the submerged one. The new submerged morphology was obtained by creating a regular and homogeneous morphology and by considering that both the submerged channel and deposit were shaped by the 1997 event (Mazzanti et al. 2007). The initial value of the failed mass used in the simulation was $600 \, m^3$, in order to account for both the initial source (about $300 \, m^3$) and a second landslide triggered along the path (about $300 \, m^3$). Different values of entrainment were set in the subaerial and the submerged part of the slope during the simulations. Specifically, erosion rates (see McDougall and Hungr 2004 for further details) between 0.007 and 0.004 have been assumed in the subaerial part while submerged erosion was used only in a few runs. Several back-analyses have been performed and the best results in terms of areal and thickness convergence between real and simulated event have been achieved by using the Voellmy rheology and setting the following parameters:

– Subaerial slope: Unit Weight = $15 \, kN/m^3$; Friction Coefficient (μ) = 0.1; Turbulence Coefficient (ξ) = $500 \, m/s^2$; Erosion Rate = 0.007
– Submerged slope: Unit Weight = $15 \, kN/m^3$; Friction Coefficient (μ) = 0.1; Turbulence Coefficient (ξ) = $350 \, m/s^2$; Erosion Rate = variable

The achieved final maximum runout and areal landslide distribution are comparable with the real landslide. Moreover the landslide volume at water impact is similar to that obtained by comparing pre- and post aerial photos of the subaerial part of the flow. Best results in terms of final landslide distribution have been achieved by neglecting submerged erosion and mass entrainment despite evidence of a deep incised (2–3 m) submerged channel in the continuation of the subaerial one. As a matter of fact, estimated volume of the submerged deposit is not in accordance with subaerial and submerged erosion (Mazzanti et al. 2007) so it can be assumed that the submerged channel is not related to the 1997 event.

The mass reaches the water surface after 25 s after the failure with a volume of about $10,000 \, m^3$. The main flow stops after 80 s when the final deposition area is reached, while only minor movements are still occurring in the submerged slope. The width of the flow is quite limited (less than 10 m) in the suberial flow, since it occurs inside a pre-existing channel, but it spreads more when the submerged slope is reached. The spreading in the submerged slope occurs even if a pre-existing channel is present and erosion in the submerged slope is neglected. The computed landslide thickness during the propagation is between 1 and 1.5 m in the subaerial and in the first part of the submerged pathway, whereas a value up to 2 m is reached in the final part of the movement before its deposition. Velocity during the overall propagation is shown in Fig. 2. A rapid initial acceleration of the flow is recorded, thus reaching values close to 15 m/s after only 12 s; then, such a value is maintained until plunging into water (at ~25 s). A maximum velocity close to 17–18 m/s is obtained just at the shoreline in the frontal part of the flow. In the submerged part, the velocity of the mass decreases rapidly below 12 m/s until it stops. The reliability of the achieved results is confirmed by the similarity between simulated velocities and velocity of similar recorded debris flows events (Berti et al. 1999; Hürlimann et al. 2003).
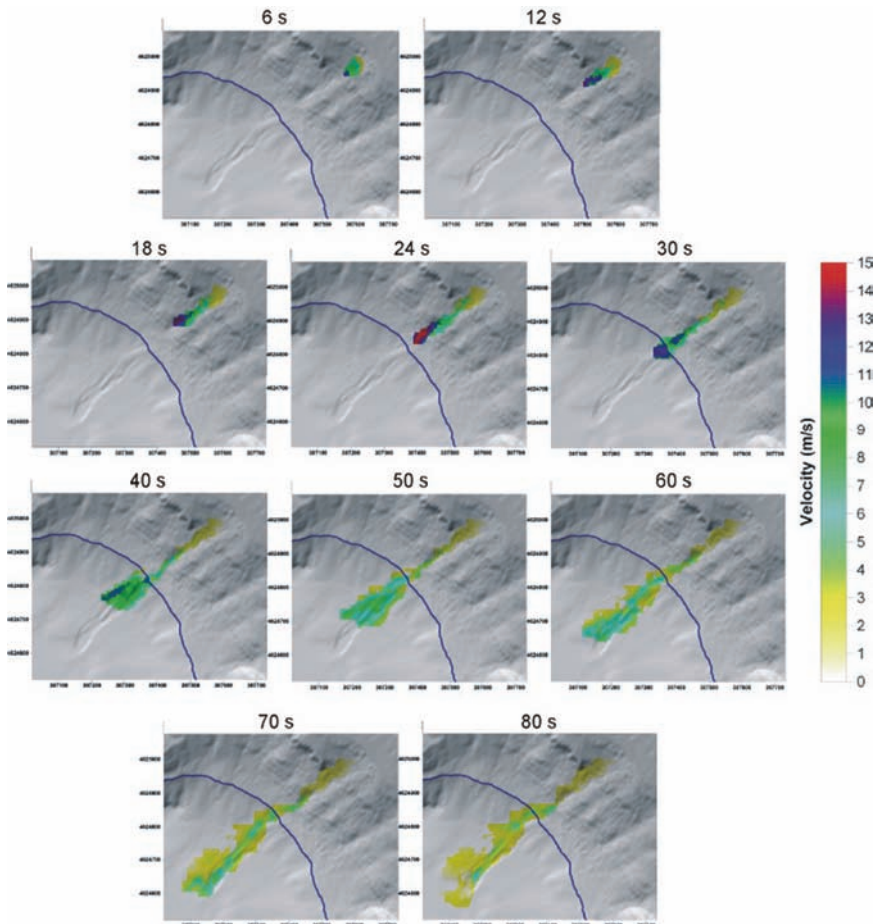
Fig. 2 Time sequence of the landslide velocity distribution during the flow

4 The Cellular Automata Code SCIDDICA SS2: Theory and Example

SCIDDICA-SS2 model is a Macroscopic Cellular Automaton for simulating subaerial–subaqueous flow-type landslides specifically developed by some of the authors (Avolio et al. 2008) as an extension of the model proposed by D'Ambrosio et al. (2003). It consists of a finite matrix of identical hexagonal cells. Each cell corresponds to a portion of that real surface, involved in the landslide. A list of values (of substates) is assigned to each cell, accounting for the local features relevant to the development of the phenomenon: elevation, depth of erodible soil cover, attributes of superficial material (average thickness, co-ordinates of its mass center, kinetic head), attributes of outflows crossing hexagon's edges (co-ordinates of their

mass center, kinetic energy, velocity). A computation unit (a finite automaton) is embodied in each cell; it computes (computation step) the variation of the cell substates that occurred in a fixed time interval, on the basis of the substates' values of the current cell and its adjacent cells. The time interval depends on the cell dimension and the maximum possible flow speed (an outflow may not overcome the adjacent cell); it ranges between hundredths of seconds and minutes. The computation step is performed simultaneously for all the cells and considers the following physical processes in sequence. Debris outflows are computed from determination of mass quantities, to be distributed from a cell to adjacent cells in order to minimise differences in height (kinetic energy is also considered); their shift is deduced by simple motion equations accounting for slope, friction, turbulence effects, eventually water resistance and buoyancy effect. Detrital cover erosion is computed proportionally to the kinetic energy of the mass overtaking a threshold value (empirically defined) with corresponding variation of cell elevation, flow thickness and kinetic energy. Air–water transition involves computation of mass loss (finer components), energy dissipation by water resistance at the impact and buoyancy effect. Composition of matter inside the cell (remaining matter plus inflows) and determination of new thickness mass center, co-ordinates and kinetic energy are all computed at the end. The complexity of the phenomenon emerges from the simple computations of the interacting cells step by step updating of the substates. The same DTLM with a 1 m cell used for DAN3D simulations has been set as input topography. Two source areas have been considered which correspond respectively to the scar located in the upper part of the channel and to a further scar, located along the slope, which is activated when it is reached by the flow. Figure 3 shows the best simulation in terms of areal fit between real and simulated event. The most effective parameters used in the simulation are listed below:

– Subaerial slope: Density = 15 g/cm³; Friction Coefficient = 0.08; Energy dissipation by turbulence = 0.005; Energy dissipation by erosion = 0.3
– Submerged slope: Density = 15 g/cm³; Friction Coefficient = 0.1; Energy dissipation by turbulence = 0.006; Energy dissipation by erosion = 0.1

The best fit value, that considers a normalised value between 0 (simulation completely failed) and 1 (perfect simulation), is computed by the function $\sqrt{((R \cap S)/(R \cup S))}$, where R is the set of cells affected by the landslide in the real

Fig. 3 Intersection between the real event and the simulated event

event and S the set of cells affected by the landslide in the simulation. In this case, the achieved result is 0.83 which is considered a quite good value for the simulation of such a complex phenomenon.

Figure 4 shows the time history of the first 2 min of simulation in terms of velocity distribution of the flow. As it can be seen, the mass reaches the water surface about 24 s after the failure with a volume of few thousands of cubic meters. The main flow stops after 2–3 min when the final deposition area is reached and only minor flows are still occurring in the submerged slope. The area affected by the landslide is quite narrow (less than 10 m) on the subaerial slope since it occurs inside a pre-existing channel, while it experiences a larger spreading when the submerged slope is reached.

In Fig. 5 the final results in terms of landslide thickness, velocity and erosion, are reported, respectively. The maximum values of thickness during the whole simulation are computed in the subaerial part of the flow where a value up to 10 m
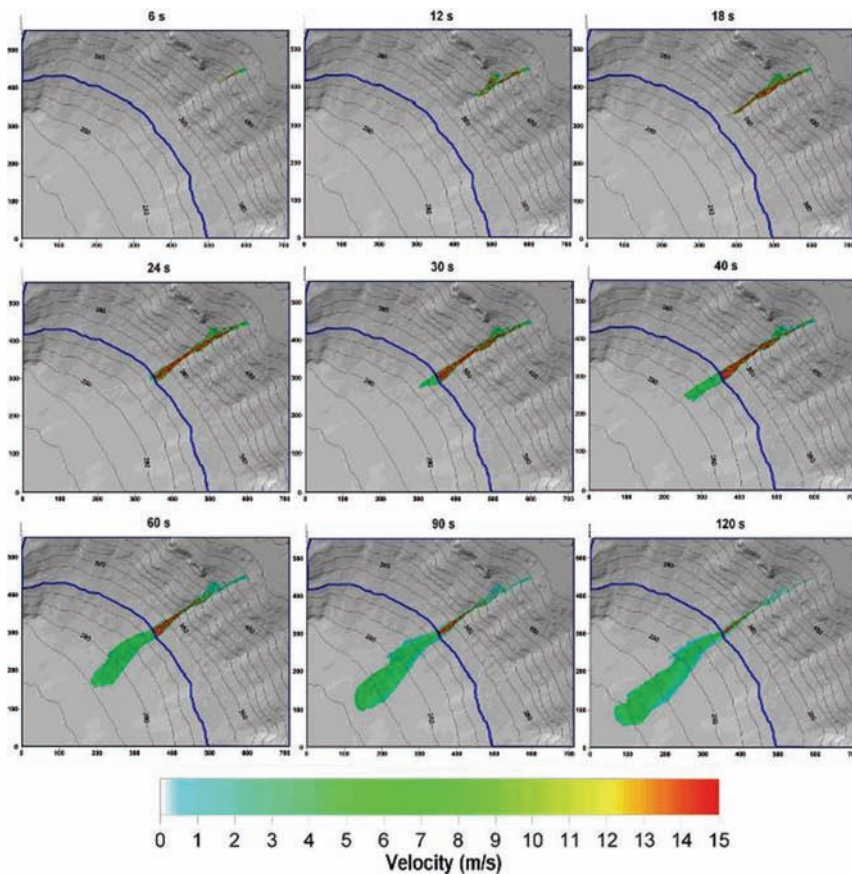

Fig. 4 Time sequence of the landslide velocity distribution during the flow
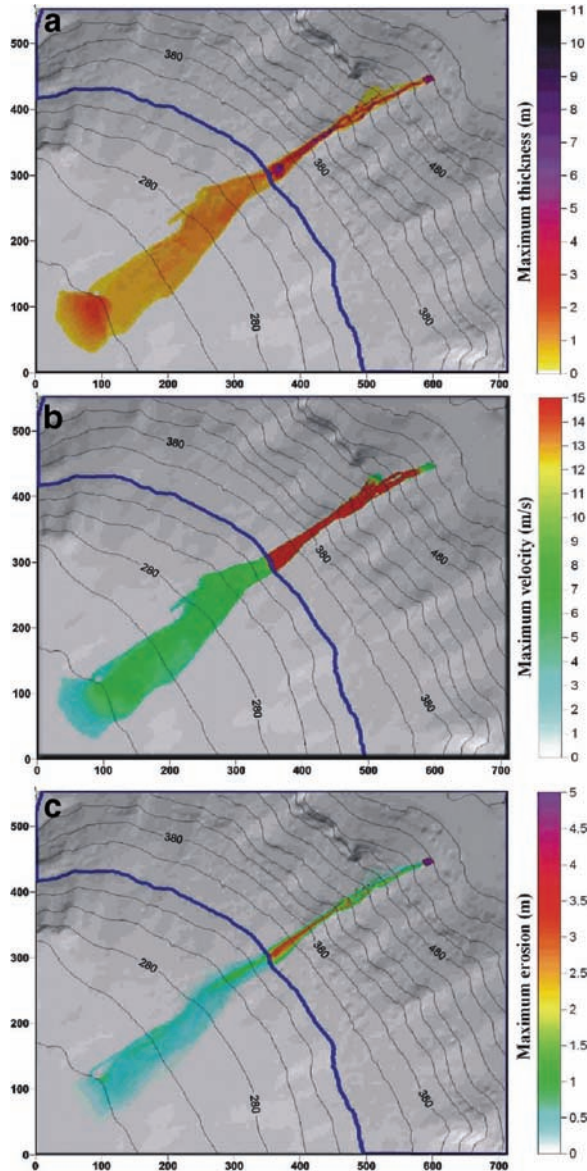
Fig. 5 Maximum values of (**a**) thickness, (**b**) velocity and (**c**) erosion during the overall simulation

is reached. Such a high value corresponds to the shoreline and this is probably due to the slope break and the sudden reduction of velocity during the first stages of the underwater flow.

Figure 5b points out that the value of 15 m/s is reached in the subaerial part whereas underwater the velocity decreases below 10 m/s immediately after submergence. Concerning

the erosion (Fig. 5c), values up to 3–4 m are computed in the subaerial slope whereas underwater only a very limited erosion (less than 1 m) is obtained.

5   A Comparative Analysis of Codes

Both SCIDDICA SS2 and DAN3D can be considered fully 3D models based on the equivalent fluid approach but, apart from these common characteristic, they are characterized by different features. First of all, they use a dissimilar numerical approach: (a) the SPH method (Monaghan 1992) based on the solution of differential equations of motion is used in DAN3D; (b) a Cellular Automata method, discrete in time and space, with transition functions based on proper equations of motion is used in SCIDDICA SS2.

Furthermore, other important aspects which differentiate the two models, are briefly listed below:

– SCIDDICA SS2 is a model specifically developed for combined subaerial–subaqueous landslides whereas DAN3D is a model developed for subaerial landslides and its application to coastal landslides is carried out through the EFEM approach.
– DAN3D accounts for the inner earth pressures (Pirulli et al. 2007) of the moving mass using active and passive stresses differently from SCIDDICA SS2 which considers, at present, only adjusted hydrostatic and isotropic earth pressures.
– SCIDDICA SS2 is able to simulate the erosion accounting for both the consequent loss of energy and increase of the mass due to entrainment; DAN3D computes the entrainment only by a pre-defined value of erosion rate.
– SCIDDICA SS2 updates the morphology step by step when erosion and deposition occur; on the contrary, DAN3D uses the original topography during the whole simulation.
– In SCIDDICA SS2, different sources can be set occurring at pre-defined time, whereas only one source can be set in DAN3D.

With regard to the 1997 Lake Albano debris flow, results achieved by using the two codes are quite similar in several respects. First of all, the similar deposit distribution suggests that the use of adjusted hydrostatic pressure (in SCIDDICA SS2) is suitable for debris flows and hyper-concentrated flows. Concerning erosion, the simulation performed by SCIDDICA SS2 shows that it is quite difficult to produce a deeply incised channel in the subaqueous slope (comparable with the real one discussed in Mazzanti et al. 2007) due to the low energy available in the 1997 event. Following both SCIDDICA simulation results and the geomorphological evidence of a limited submerged deposit, DAN3D simulations have been performed with and without setting underwater erosion; the best back-analysis has been obtained neglecting the entrainment. These combined results suggest that the subaqueous channel should be not related to the 1997 event. This is also consistent with the small volume of final deposit detected by the high resolution bathymetry (5,000–7,000 cubic meters).

Moreover, the small submerged deposit (whose volume is lower than the material reaching the shoreline) suggests that part of the material was transformed into a turbidity current after the impact, moving separately from the main debris flow. This effect cannot be simulated using DAN3D but has been considered, in a straightforward way, in SCIDDICA SS2, by setting an instantaneous loss of mass at the water level.

However, some differences in the results obtained with the two models have been observed; for example, the maximum thickness of the flow is up to 3 m with DAN3D and up to 10 m in SCIDDICA SS2. The peak value in SCIDDICA SS2 has been computed at the shoreline and could result from the sudden reduction of velocity at the impact with water.

Apart from the different value at the shoreline, the mass thickness during the flow is quite comparable between the simulation performed by DAN3D and SCIDDICA SS2 and this is particularly true in the submerged part of the slope. Even the simulation time sequences are quite similar; the mass plunges into water after 24 and 25 s from the beginning of the flow using SCIDDICA SS2 and DAN3D, respectively. Slightly different velocities are computed in the submerged path between the two models (a bit lower with SCIDDICA SS2); nevertheless, both values seem reasonable for this type of event.

6 Conclusions and Outlook

In spite of the increasing evidence of submerged landslide instabilities and of their large mobility, few numerical models are available which can be considered suitable for the simulation of underwater or coastal mass movements' propagation over a real 3D topography. In this paper a new approach for the simulation of coastal and submerged landslides has been proposed which allows us to use 3D models originally developed for subaerial landslides. Furthermore, a new 3D Cellular Automata model (SCIDDICA SS2), specifically developed for combined subaerial–submerged flow-like landslides has been presented. The two approaches have been tested by simulating in back-analysis a coastal debris-flow at Lake Albano. Both models have been able to reproduce the real event in terms of runout distance and areal distribution of the mass. Reasonable values of landslide velocity have been also computed, which represent input needed for the analysis of induced tsunamis. Further back-analyses of real submerged landslides by the proposed methods will allow to better constrain the parameters of the codes. The future development of this research aims to obtain useful numerical tools for forecasting analyses related to the propagation of both combined subaerial/submerged landslides and completely subaqueous ones.

References

Avolio M V, Lupiano V, Mazzanti P, Di Gregorio S (2008) Modelling combined subaerial-subaqueous flow-like landslides by Macroscopic Cellular Automata. In: Umeo H et al. (ed) ACRI 2008, LNCS 5191: 329–336.

Bagnold R A (1954) Experiments on a gravity-free dispersion of large solid spheres in a Newtonian fluid under shear. Roy Soc Lond Proc ser A 225: 49–63.

Berti M, Genevois R, Simoni A, Tecca P R (1999) Field observations of a debris flow event in the Dolomites. Geomorphol 29: 265–274.

Breien H, Pagliardi M, De Blasio F V, Issler D, Elverhøi A (2007) Experimental studies of subaqueous vs. subaerial debris flows – velocity characteristics as a function of the ambient fluid. In: Lykousis V, Sakellariou D, Locat J (ed) Submarine Mass Movement and Their Consequence: 101–110.

Campbell C S, Cleary P W, Hopkins M (1995) Large-scale landslide simulations: Global deformations, velocities and basal-friction. J Geophys Res 100: 8267–8283.

Corominas J (1996) The angle of reach as a mobility index for small and large landslides. Can Geotech J 33: 260–271.

Cruden D M, Varnes D J (1996) Landslide types and processes. In: Turner A K and Shuster R L (ed) Landslides Investigation and Mitigation; Transportation Research Board. Nat Res Council Spec Rep 247. Washington, DC: 36–75.

D'Ambrosio D, Di Gregorio S, Iovine G (2003) Simulating debris flows through a hexagonal cellular automata model: SCIDDICA S3-hex. Nat Haz Earth Sys Sci 3: 545–559.

De Blasio F V, Elverhøi A, Engvik L E, Issler D, Gauer P, Harbitz C (2006) Understanding the high mobility of subaqueous debris flows. Nor J Geol 86: 275–284.

Denlinger R P, Iverson R M (2004) Granular avalanches across irregular three-dimensional terrain: 1. Theory and computation. J Geophys Res 109: F01014.

Fernández-Nieto E D, Bouchut F, Bresch D M, Castro Díaz J, Mangeney A (2008) A new Savage–Hutter type model for submarine avalanches and generated tsunami. J Comput Phys 227: 7720–7754.

Heim A (1932) Bergsturz und Menschenleben, Zürich, pp. 218.

Hungr O, Corominas J, Eberhardt E (2005) Estimating landslide motion mechanism, travel distance and velocity. In: Hungr O, Fell R, Couture R, Eberhardt E, In Landslide Risk Management. A.A. Balkema, Leiden: 99–128.

Hungr O (1995) A model for the runout analysis of rapid flow slides, debris flows, and avalanches, Can Geotech J 32: 610–623.

Hürlimann M, Rickenmann D, Graf C (2003) Field and monitoring data of debris flow events in the Swiss Alps. Can Geotech J 40: 161–175.

Ilstad T, Elverhøi A, Issler D, Marr J (2004) Subaqueous debris flow behaviour and its dependence on the sand/clay ratio: a laboratory study using particle tracking. Mar Geol 213: 415–438.

Imran J, Harff P, Parker G (2001) A numerical model of submarine debris flow with graphical user interface. Comput Geosci 27: 717–729.

Iverson R M, LaHusen R G (1993) Friction in debris flows: Inferences from large-scale flume experiments. In: Shen H W, Su S T, Wen F (ed) ASCE Natural Conference on Hydraulic Engineering. Am Soc Civil Eng, San Francisco, CA, pp. 1604–1609.

Marr J G, Harff P A, Shanmugam G, Parker G (2001) Experiments on subaqueous sandy gravity flows: the role of clay and water content in flow dynamics and depositional structures. Geol Soc Am Bull 113 (11): 1377–1386.

Mazzanti P, Bozzano F, Esposito C (2007) Submerged landslide morphologies in the Albano Lake (Rome, Italy). In: Lykousis V, Sakellariou D, Locat J (eds) Submarine Mass Movement and Their Consequence: 243–250.

Mazzanti P (2008a) Analysis and modelling of coastal landslides and induced tsunamis, PhD Thesis "Sapienza" University of Rome, Department of Earth Sciences.

Mazzanti P (2008b) Studio integrato subaereo-subacqueo di frane in ambiente costiero: i casi di Scilla (RC) e del lago di (RM) Albano, Giornale di Geologia Applicata 8 (2): 245–261 – doi: 10.1474/GGA.2008-08.2-21.0211 (In Italian).

McDougall S and Hungr O (2004) A model for the analysis of rapid landslide motion across three-dimensional terrain. Can Geotech J 41: 1084–1097.

Monaghan J J (1992) Smoothed particle hydrodynamics. Ann Rev Astron Astrophys 30: 543–574.

Pietrantonio G, Baiocchi V, Fabiani U, Mazzoni A, Riguzzi F (2008) Morphological updating on the basis of integrated DTMs: study on the Albano and Nemi craters. J Appl Geodesy 2 (4): 239–250.

Pirulli M, Bristeau M O, Mangeney A, Scavia C (2007) The effect of the earth pressure coefficients on the runout of granular material. Environ Model Software 22: 1437–1454.

Salles T, Lopez S, Cacas M C, Mulder T (2007) Cellular automata model of density currents. Geomorphol 88: 1–20.

Savage S B, Hutter K (1989) The motion of a finite mass of granular material down a rough incline. J Fluid Mech 199: 177–215.

Scheidegger A E (1973) On the prediction of the reach and velocity of catastrophic landslides. Rock Mech 5: 231–236.

Peculiar Morphologies of Subaqueous Landslide Deposits and Their Relationship to Flow Dynamics

P. Mazzanti and F.V. De Blasio

Abstract The morphology of subaqueous landslide deposits is seldom analyzed quantitatively or at least semi-quantitatively with regard to the dynamics of the flow. However, the peculiar morphology of the deposits can reveal information on the mechanics of propagation of the mass movement and on the mechanism of emplacement. Horseshoe-shaped deposits and oriented blocks are two peculiar morphologies of subaqueous landslide which have been identified in this paper. Both morphologies have been described in a qualitative way by considering the shape of the deposit and the geomorphological features of the areas of emplacement. Furthermore, these morphologies have been analyzed in a quantitative way by means of mathematical and numerical approaches. The close relationship between these morphologies and the landslide mechanism of propagation and emplacement has been thus preliminary demonstrated by accounting for the interaction between moving mass and the ambient fluid.

Keywords Subaqueous landslides • landslide dynamics • landslide deposits • horseshoe-shaped deposits • oriented blocks

1 Introduction

The dynamics of subaqueous landslides is still poorly understood. One of the most remarkable features is the low frictional resistance met by subaqueous landslides, which implies that water has the effect of enhancing the flow (De Blasio et al. 2006b).

P. Mazzanti (✉)
Dipartimento di Scienze della Terra, Università di Roma "Sapienza",
P.le Aldo Moro 5, 00185, Roma, Italy
e-mail: paolo.mazzanti@uniroma1.it

F.V. De Blasio (✉)
Department of Geosciences, University of Oslo/ P.O. Box 1047 Blindern, N-0316 Oslo,
Norway & International Centre of Geohazards, P.O. Box 3930 Ulleval Stadion,
N-0806 Oslo, Norway
e-mail: f.v.d.blasio@geo.uio.no

Mechanisms like hydroplaning (Mohrig et al. 1998), pore pressure augmentation (Gee et al. 1999) or sediment dilution at the base (De Blasio et al. 2005) have been suggested as mechanisms for the increase in the mobility, but a deep understanding of the fluid dynamics of subaqueous landslides is still lacking. Laboratory experiments may assist in the development of ideas (Mohrig et al. 1998; Ilstad et al. 2004a, b; Breien et al. 2007), but they bring to conclusions not readily applicable to real events because of scaling problems.

An alternative approach in the understanding of subaqueous landslides dynamics is the analysis of the morphology of the final deposits to extract information about the mechanism of propagation and emplacement (see Mazzanti 2008; De Blasio and Elverhøi 2009). In this paper we examine some peculiar landslide deposits which can be recognized in open, closed or semi-closed basins, like lakes or fjords. In particular, we consider: (1) horseshoe-shaped deposits, and (2) oriented blocks. After a brief geomorphological description, we attempt a correlation of these peculiar morphologies to the landslide dynamics of emplacement.

2   Horseshoe-Shaped deposits

Horseshoe-shaped deposits are a typical morphology observed in certain types of subaqueous and coastal landslides. These morphologies appear like fairly regular semi-circular rims higher than the rear part. Deposits characterized by such a morphology have been recognized in several subaqueous landslides in open, closed or semi-closed basins. In Fig. 1 we show some examples of horseshoe-shaped deposits at Lake Tahoe (Gardner et al. 2000), Norwegian Fjords (Blikra et al. 2006) and Lake Albano (Mazzanti et al. 2007).

Even if some frontal and lateral ridges have also been recognized in subaerial rock-avalanches, it is only in subaqueous landslide deposits that they appear to be very regular and perfectly semi-circular. This evidence suggests a direct and strong relationship between morphology of landslide deposits, landslide propagation and the ambient fluid. In addition to surrounding water, a primary role seems to be played by the landslide path; these morphologies, in fact, are typical of mass movements in areas characterized by a sudden change in the slope gradient (i.e. from a relatively steep slope to an extremely flat area).

Furthermore, these deposits are characterized by a very short runout (distance between the source area and the final part of the deposit) if compared to usual subaerial (Legros 2002) and subaqueous landslides (Gardner et al. 2000; Blikra et al. 2006; Mazzanti et al. 2007). Such morphologies are possibly the result of the landslide mechanism of emplacement which is strongly affected by the landslide dynamics.
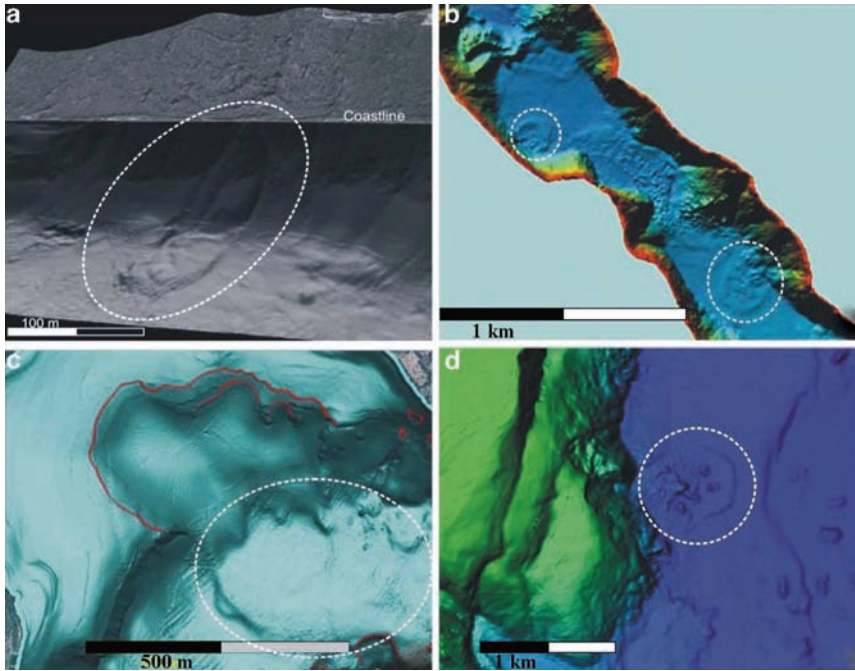
Fig. 1 Horseshoe-shaped deposits at: (**a–c**) Albano Lake (Italy) (Mazzanti et al. 2007); (**b**) Tafjord (Norway) (Blikra et al. 2006); (**d**) Lake Tahoe (USA) (Gardner et al. 2000). Horseshoe-shaped deposits are enclosed in dotted white ellipses

2.1 Possible Emplacement Mechanisms of Horseshoe-Shaped Deposits

The main differences in the dynamics of subaerial and subaqueous landslides are related to some physical processes like: the buoyancy effect, the drag and lift forces exerted on the moving body and peculiar mechanisms like hydroplaning (Mohrig et al. 1998; De Blasio et al. 2004). A body moving in a fluid, like a landslide in water or an airplane in air, is affected by both drag and lift forces. The drag force works parallel and in opposition to the direction of movement and can be divided into two components: the front drag (also called form drag, which acts on the frontal area of the body, and, thus, is strongly dependent on the object form) and the skin drag (which mainly depends on the viscous friction between the fluid and the upper and lower surface of the moving mass). Instead, the lift force is perpendicular to the direction of travel or, in other words, normal to the drag force and to the flow direction.

The importance of the lift force in subaqueous landslides is demonstrated by the phenomenon of hydroplaning (Mohrig et al. 1998; De Blasio et al. 2004). The lift force D (as well as the drag force) is dependent on the square of the mass velocity U (De Blasio et al. 2006a)

$$D = \frac{1}{2} \rho_W C_L U^2 A \tag{1}$$

where ρ_w is the density of water, U is the velocity of the mass, A is the reference area of the moving mass (corresponding to the projection area of the object on a plane perpendicular to the direction of motion) and C_L is the dimensionless lift coefficient. At high values of velocity, the lift force could become greater than the pressure load exerted by the mass (De Blasio et al. 2006a) and thus the frontal part of the mass is lifted up.

Laboratory experiments performed by Ilstad et al. (2004a) show that the lifting up of the frontal part of the gravity flow under particular conditions can be drastic enough to result in a "flip-back". This phenomenon consists of a significant rising of the frontal part of the flow which is then flipped back by the front drag force (significantly increased at that point due to the thickening of the mass head). Such an increase of the front drag force also results in a sudden reduction of velocity. The mechanisms discussed above occur mainly in the case of cohesive flows (low sand/clay ratios) in the experiments by Ilstad et al. (2004b). We suggest here that the flip-back phenomenon could explain the horseshoe-shaped deposits discussed above. Assuming that all the frontal part of the landslide is affected by the flip-back mechanism, the result would be a frontal ridge with a semi-circular shape (the mass in a non confined and flat area moves radially from the source with a maximum velocity in the flow direction and decreasing velocities in the direction of spreading; see Fig. 2). The occurrence of the flip-back could also explain the limited runout of these deposits as a consequence of a drastic increase of the front drag force which is able to quickly stop the mass and therefore freeze the subaqueous landslide.

To estimate whether the front flipping may occur with the flow velocities expected for small subaqueous landslides, we adopt a model for the front as a straight parallelepiped of width W, length L and thickness T. The condition for flipping to occur is that the torque exerted by the drag force be greater than the one due to gravity. This condition leads to a minimum velocity for flipping which is independent of L and W

$$U_{FL} \approx \sqrt{2 \frac{\Delta\rho}{\rho_W} \frac{g\ T\ \cos\vartheta}{C_D\ \sin^2\vartheta}} \tag{2}$$

where C_D, ϑ are the front drag coefficient and the angle of inclination of the front with respect to the horizontal. Evidently, an angle ϑ different from zero is necessary to initiate flipping, a condition that must occur frequently considering that the flow of the subaqueous landslide is irregular and the landslide is never perfectly horizontal. With values

$$\frac{\Delta\rho}{\rho_W} = 1;\ L = 50\,m;\ \vartheta = 45^0;\ C_D = 0.5;\ T = 3\,m \tag{3}$$

Fig. 2 Sketch showing the emplacement of the frontal ridge
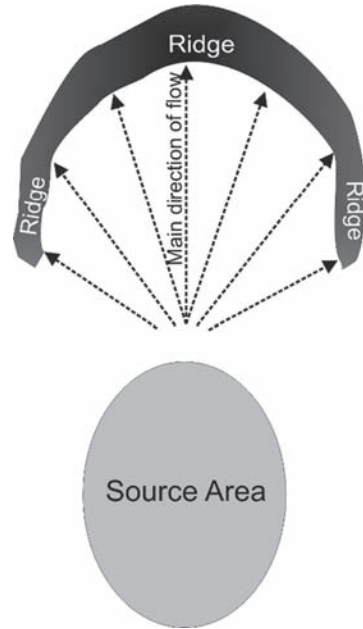
we find a flipping velocity of the order 13 m/s, a value that looks reachable also according to numerical simulations of similar events (Mazzanti 2008). The uncertainties in these estimates are probably not crucial for the final conclusions. Values of the drag coefficient might be greater than that used here, but probably not >1. It is also interesting to estimate the deceleration to which the landslide is subjected when the front is raised from an angle $\vartheta = 0$ to the maximum level $\vartheta = 90°$. If the flipping front is detached from the rest of the body, the deceleration is of the order of

$$\Delta a \approx \frac{1}{2} \frac{\rho}{\rho_{solid}} \frac{1}{\alpha} C_D U^2 \left(L^{-1} - T^{-1} \right) \tag{4}$$

where α accounts for the added mass (in this rough calculation we take this constant equal to one) and with U = 13 m/s it is found that $|\Delta a| \approx 6.7\, m\, s^{-2}$, nearly as high as the gravity acceleration. Such a high value also implies a prompt stoppage of the landslide front. If the front is coupled to the rest of the landslide body, the mass that enters the calculation is higher because it contains a part of the landslide mass. The resulting deceleration is consequently smaller. Nevertheless, these estimates show that the raising of the front likely leads to a substantial braking of the landslide. The body will continue to move inertially, underriding the front that topples backwards. Because the front of the landslide is semi-circular, the toppling material will have a horseshoe-shaped morphology (Fig. 2).

An alternative explanation for the horseshoe-shaped morphology is suggested by Hampton et al. (1996) and confirmed by Schnellmann et al. (2005). Several seismic profiles collected in Lake Lucerne (Switzerland) allowed them to recognize several

fold-and-thrust belt structures in soft sediments, induced by the superimposition of subaqueous landslides resulting in a bulge in the frontal part of the deposit. We suggest here that such mechanisms should produce, if observed in plain view, a horseshoe-shaped morphology around the main landslide deposit. In this case, in contrast to the flip-back hypothesis, the frontal semi-circular ridge results from the deformation of lacustrine sediments. Therefore, it is a consequence of the emplacement of the landslide mass, and not of the intrinsic dynamics of the landslide. However, in both explanations, the rate and mode of emplacement of the landslide can be considered the main reason for the development of frontal ridges. Further seismic reflection investigations in ridge zones will probably shed light, by looking at the sub-bottom geometry of the deposit, on the most probable model.

3   Oriented Blocks

Isolated blocks are not uncommon in subaqueous landslide areas. Whereas some outrunner blocks may travel alone far away from the main accumulation of underwater landslides (Longva et al. 2003; Prior et al. 1982a, b, 1984; Kuijpers et al. 2001; Nielsen and Kuijpers 2004), others may be transported as rafted blocks by the flowing landslide, probably transformed into a debris flow (Lastras et al. 2005; De Blasio and Elverhøi 2009). Rafted blocks are typically much smaller than the original landslide, with maximum recorded volumes of 10^6 m^3 (Vanneste et al. 2009) and exhibit an extraordinary mobility, travelling for kilometres along gradients as low as 1° or even less. Blocks show in some cases a very low aspect ratio (De Blasio et al. 2006a).

An interesting characteristic of some subaqueous blocks is the orientation of the main axis with respect to the flow direction. Most outrunner blocks usually have the main axis perpendicular to the flow direction (De Blasio et al. 2006a), which is consistent with the fluid mechanics of isolated bodies moving in a fluid (Batchelor 1967). The same conclusion holds for blocks rafted by mass flows, the main difference being that for rafted blocks the interaction force with the mass flow is more important than that with water. Thus, rafted blocks are oriented by the action of the viscous mass flow rather than by water. Axial orientation parallel to the flow is expected only for the Stokes regime of very low Reynolds numbers (Rhodes 1998), a condition hardly met for large-scale blocks. However, as shown in Fig. 3, the outrunner blocks at Lake Albano (Mazzanti et al. 2007) show a higher value of the height/length ratio and, in contrast to the cases described by De Blasio et al. (2006a) the maximum axis is sub-parallel to the direction of flow. As an example, at Lake Albano we can recognize blocks oriented with the main axis in the direction of flow having a planar dimension of nearly 30 × 10 m, a maximum height of about 3–4 m and which have covered distances up to 280 m in a very flat area (Fig. 3; Mazzanti et al. 2007).

In the following, a possible mechanism for block orientation is investigated. This mechanism can also shed light on the dynamics of subaqueous mass flows. We suggest that a velocity gradient within the mass flow may turn the blocks with
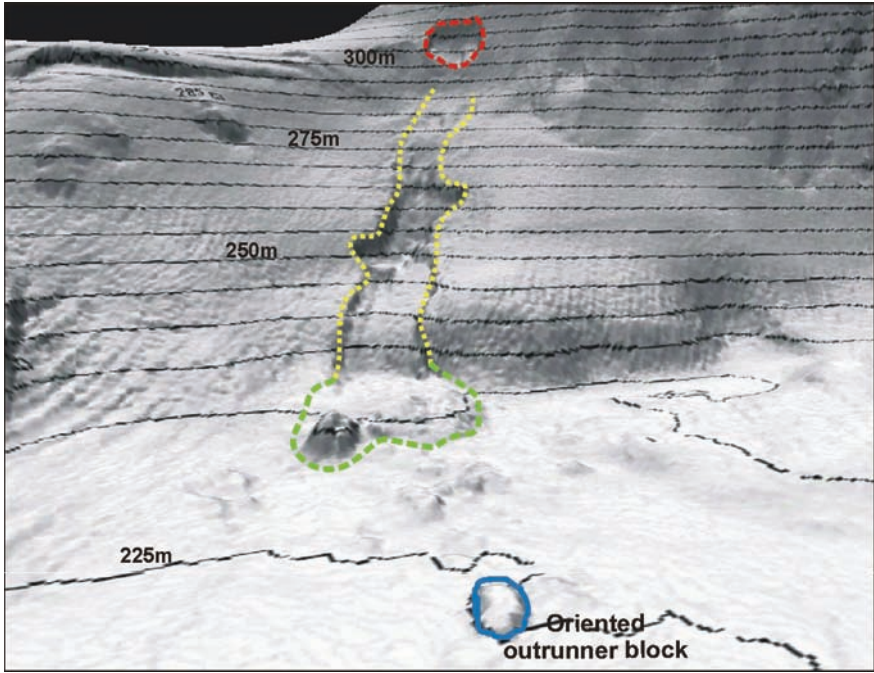
Fig. 3 Prospective view with 5 m contour lines of a completely subaqueous debris flow at Lake Albano (Mazzanti et al. 2007). Red dashed line bounds the landslide scar; yellow dashed lines identify the landslide erosive channel; green dashed line bounds the main landslide deposit; blue full ellipse encloses an oriented block. Distance between the front and the background is nearly 650 m
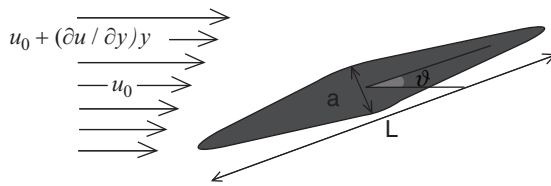

Fig. 4 Scheme for the calculation of the torque acting on the block

axis nearly parallel to the flow direction. Let us assume a very simple model of a block as a cylindrical ellipsoid of semi-axes a, L, and thickness W. The block is immersed in a fluid with a velocity gradient as shown in Fig. 4. Because of the velocity gradient, the block is subjected to a torque that we approximate as:

$$M \approx \frac{1}{2} \rho W \int_{-L/2}^{L/2} \left[u(y') \cos \vartheta \right]^2 y' \, dy' \tag{5}$$

where ϑ is the angle between the block axis and the velocity current and W is the block thickness (perpendicular to the plane of Fig. 4). Assuming a constant velocity gradient $u(y) = u_0 + (\partial u/\partial y)y$, it is readily found that:

$$M \approx -\frac{1}{12} W\, u_0\, \rho\, (\partial u/\partial y) L^3 \sin^3 \vartheta \tag{6}$$

In the absence of a velocity gradient, a torque tends to line up the block with axis perpendicular to flow (Batchelor 1967):

$$T \approx \frac{1}{4} W \rho\, u_0^2\, L^2 \left(1 - \frac{a^2}{L^2}\right) \sin \vartheta \cos \vartheta \tag{7}$$

We assume that the two contributions can be linearly summed:

$$N = M + T = -\frac{1}{12} W\, u_0\, \rho\, (\partial u/\partial y) L^3 \sin^3 \vartheta + \frac{1}{4} W \rho\, u_0^2\, L^2 \left(1 - \frac{a^2}{L^2}\right) \sin \vartheta \cos \vartheta \tag{8}$$

Thus, in this approximation the block has a tendency to line up with the axis parallel to the flow if:

$$\frac{L}{u_0} \frac{\partial u}{\partial y} > \frac{3K \cos \vartheta}{\sin^2 \vartheta} \left(1 - \frac{a^2}{L^2}\right) \tag{9}$$

where $K \approx 1$ in the present approximations. As a result, parallel orientation is possible if the velocity gradient is sufficiently large in relation to the block length and the average landslide velocity. Note also that the factor $\sin^2 \vartheta$ in the denominator of Eq. 9 implies that the block must have a minimum obliquity with respect to the velocity vector to start rotation. Assuming a length of 20 m, a velocity of 20 m/s, ϑ = 45°, and a = 5 m, we find that a gradient of about 4 s^{-1} is necessary for the block to line parallel to the flow, but with ϑ = 80° only 0.5 s^{-1} is necessary. The highest gradients are obtained at the sides of the mass flow, where the velocity abruptly goes to zero. We thus predict that parallel blocks could be more common at the sides of the mass flow, whereas in the central part they will mostly flow with the main axis perpendicular to the flow. To illustrate this phenomenon, we performed some simple preliminary experiments with a viscous fluid simulating an incoming mass flow and some pieces of rubber standing for blocks (Fig. 5). We observed that irrespective of the original orientation of the rubber blocks, they tend to become parallel to flow at the sides of the fluid, and maintain a perpendicular orientation in the middle of the flow (characterized by small velocity gradient). We noticed however that as predicted by Eq. 9, blocks acquired a rotation with difficulty when they are perfectly parallel to the mass flow velocity.

Figure 6 reports some calculations of a theoretical subaqueous landslide performed by DAN3D model (Mc Dougall and Hungr 2004). The lines of constant velocity illustrate the presence of a strong gradient at the sides of the flow. According to our model, a block at the sides of the mass flow will rotate as shown in the figure. Note that in this preliminary work the movement of the block is not calculated, but only superimposed on the calculated curves for illustrative purposes. It would be interesting to include the presence of blocks in a three-dimensional model.
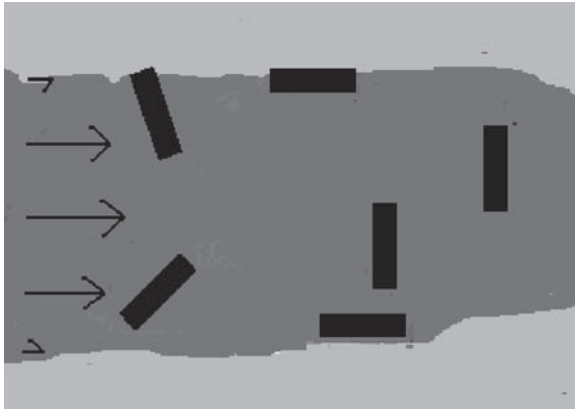
Fig. 5 Sketch obtained from a series of preliminary experiments where a viscous fluid flowing down a flat inclined plane (from *left* to *right* in the figure) strikes against some pieces of rubber and plastic material of different aspect ratios. The initial configuration is chosen with blocks perpendicular, parallel to the fluid velocity, or with random orientation. Irrespective of the initial orientation, after the passage of the fluid the blocks tend to lineate with flow only at the sides. The length of the experimental board is approximately 1 m
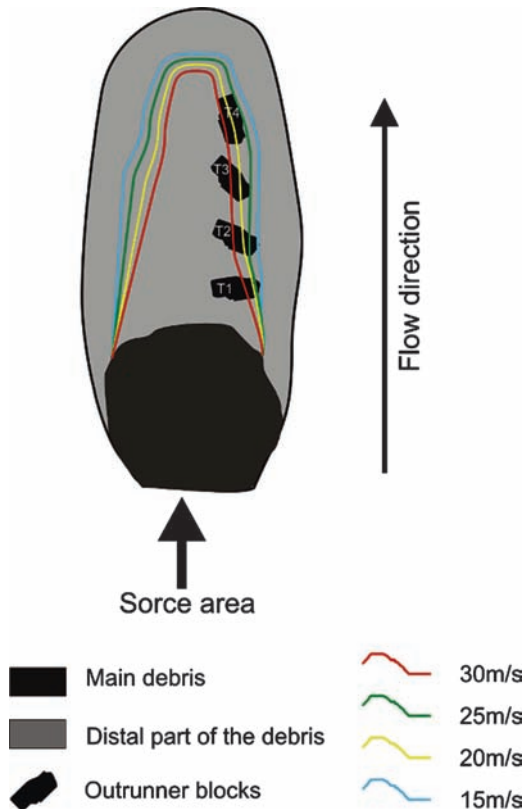

Fig. 6 Sketch showing the orientation mechanism of a block parallel to the landslide flow direction

4   Discussion and Conclusion

To gain insights into landslide flow dynamics in the subaqueous environment, we have analysed some peculiar morphologies of subaqueous landslide deposits. We focused on two morphologies which can be recognized in open, closed or semi-closed basins: (1) horseshoe-shaped deposits and (2) oriented blocks. These features are typical of certain types of subaqueous landslides. Hence, we suggest that their origin is closely related to the interaction between the water and the moving mass during the landslide propagation and emplacement. It has been shown that horseshoe-shaped deposits may be the results of a generalized flipping back of the landslide front during propagation and that the rising of the frontal part of the landslide can explain also the short runout of such landslides. Once validated and calibrated, the proposed model may allow us to infer the landslide velocity based on the morphology of its deposit. This is a relevant issue, because it represents a key requirement in the assessment of tsunami potential of coastal landslides. Furthermore, we suggest that the occurrence of the flip-back could significantly increase the tsunami potential since the sensitivity of tsunami-wave generation to the landslide front thickness has been widely demonstrated (Harbitz et al. 2006). We have also considered the problem of the enigmatic orientation of rafted blocks parallel to the axis of a subaqueous landslide. We show that the orientation parallel to flow may occur in zones of high velocity gradient, namely at the sides of the mass flow deposit. This paper represents a preliminary step in the understanding of subaqueous landslides dynamics based on peculiar morphological features of their deposits. However, further investigations must be carried out in order to better understand and constrain such phenomena. Once constrained, these hypotheses could allow for an estimation of past landslides' velocity of emplacement. Then, statistically based methods (based on the analysis of past events) could be designed that would allow us to perform forecasting analysis of future landslide velocity of propagation and emplacement.

References

Batchelor G K (1967) An Introduction to Fluid Dynamics. Cambridge University Press, New York.

Blikra L H, Longva O, Braathen A, Anda E, Dehls K, Stalsberg K (2006) Rock slope failures in Norwegian fjord areas: examples, spatial distribution and temporal pattern. In: Evans S G, Scarascia Mugnozza G, Strom A, Hermanns R (eds) Massive Rock Slope Failure, NATO Science Series, Kluwer Academic, Springer Netherlands, pp. 475–496.

Breien H, Pagliardi M, De Blasio F V, Issler D, Elverhøi A (2007) Experimental studies of subaqueous vs. subaerial debris flows – velocity characteristics as a function of the ambient fluid. In: Lykousis V, Sakellariou D, Locat J (eds) Submarine Mass Movement and Their Consequence, Springer Heidelberg, pp. 101–110.

De Blasio F V, Elverhøi A (2009) Properties of mass-transport deposits as inferred from dynamical modelling of sub-aqueous mass wasting: a short review. In Shipp C, Weimer P, Posamentier H (eds) The Importance of Mass-Transport Deposits in Deepwater Settings. Soc Sediment Geol Spec Pub (In press).

De Blasio F V, Elverhøi A, Engvik L E, Issler D, Gauer P, Harbitz C (2006b) Understanding the high mobility of subaqueous debris flows. Nor J Geol 86: 275–284.

De Blasio F V, Engvik L, Harbitz C B, Elverhøi A (2004) Hydroplaning and submarine debris flows. J Geophys Res 109: C01002, doi:10.1029/2002JC001714.

De Blasio F V, Engvik L, Elverhøi A (2006a) Sliding of outrunner blocks from submarine landslides. Geophys Res Lett 33: L06614, doi:10.1029/2005GL025165.

De Blasio F V, Elverhøi A, Issler D, Harbitz C B, Bryn P, Lien R (2005) On the dynamics of subaqueous clay rich gravity mass flow – the giant Storegga slide, Norway. Mar Pet Geol 22: 179–186.

Gardner J V, Mayer L A, Hughs Clarke J E (2000) Morphology and processes in Lake Tahoe (California-Nevada). Geol Soc Am Bull 112 (5): 736–746.

Gee M J R, Masson D G, Watts A B, Allen P A (1999) The Saharan flow: an insight into the mechanics of long runout submarine debris flows. Sedimentol 46: 317–335.

Hampton M A, Lee H J, Locat J (1996) Submarine landslides. Rev Geophys 34: 33–59.

Harbitz C B, Løvholt F, Pedersen G, Masson D G (2006) Mechanisms of tsunami generation by submarine landslides: a short review. Nor J Geol 86: 255–264.

Ilstad T, De Blasio F V, Elverhoi A, Harbitz C B, Engvik L, Longva O, Marr J G (2004a) On the frontal dynamics and morphology of submarine debris flows. Mar Geol 213: 481–497.

Ilstad T, Elverhøi A, Issler D, Marr J (2004b) Subaqueous debris flow behaviour and its dependence on the sand/clay ratio: a laboratory study using particle tracking. Mar Geol 213: 415–438.

Kuijpers A, Nielsen T, Akhmetzhanov A, De Haas H, Kenyon N H, van Weering T C E. (2001) Late Quaternary slope instability on the Faeroe margin: mass flow features and timing of events. Geo-Mar Lett 20: 149–159.

Lastras G, De Blasio F V, Canals M, Elverhøi A (2005) Conceptual and numerical modeling of the Big'95 debris flow, western Mediterranean Sea. J Sed Res 75: 784–797.

Legros F (2002) The mobility of long-runout landslides. Eng Geol 63: 301–331.

Longva O, Janbu N, Blikra L H, Bøe R (2003) The 1996 Finneidfjord slide; seafloor failure and slide dynamics. In: Locat J, Mienert J, Boisvert L (eds) Submarine Mass Movements and Their Consequences, 1st International Symposium, Kluwer Academic Publishers, Dordrecht, pp. 531–538.

Mazzanti P (2008) Analysis and modelling of coastal landslides and induced tsunamis. PhD Thesis Università di Roma "Sapienza", Dipartimento di Scienze della Terra.

Mazzanti P, Bozzano F, Esposito C (2007) Submerged Landslides Morphologies in the Albano Lake (Rome, Italy). In: Proceedings of 3rd International Symposium "Submarine Mass Movements and Their Consequences", Series: Advances in Natural and Technological Hazards Research, 27, Springer, Heidelberg, pp. 243–250.

McDougall S and Hungr O (2004) A model for the analysis of rapid landslide motion across three-dimensional terrain. Can Geotech J 41: 1084–1097.

Mohrig D K, Whipple C E, Parker G (1998) Hydroplaning of subaqueous debris flows. Geol Soc Am Bull. 110: 387–394.

Nielsen T, Kuijpers A (2004) Geohazard studies offshore the Faroe Islands: Slope instability, bottom currents and sub-seabed sediment mobilisation. Geol Soc Den Greenland Bull 4: 57–60.

Prior D B, Borhold B D, Coleman J M, Bryant W R (1982b) Morphology of a submarine slide, Kitimat Arm, British Columbia. Geology 10: 588–592.

Prior D B, Borhold B D, Johns M W (1984) Depositional characteristics of a submarine debris flow. J Geol 92: 707–727.

Prior D B, Coleman J M, Borhold B D (1982a) Results of a known sea floor instability event. Geo Mar Lett 2: 117–122.

Rhodes M (19989 Introduction to Particle Technology. Wiley, Chichester, 320 pp.

Schnellmann M, Anselmetti F S, Giardini D, McKenzie J A (2005) Mass movement-induced fold-and-thrust belt structures in unconsolidated sediments in Lake Lucerne (Switzerland). Sedimentol 52: 271–289.

Vanneste M, Harbitz C B, De Blasio F V, Glimsdal S, Mienert J, Elverhøi A (2009) The Hinlopen-Yermak landslide, Arctic Ocean. Geomorphology, landslide dynamics and tsunami simulations. In Shipp C, Weimer P, Posamentier H (eds) The Importance of Mass-Transport Deposits in Deepwater Settings. Soc Sediment Geol Spec Pub (In press).

Large Landslides on Passive Continental Margins: Processes, Hypotheses and Outstanding Questions

D.G. Masson, R.B. Wynn, and P.J. Talling

Abstract The volume, area affected, and runout of submarine landslides can exceed those of terrestrial events by two orders of magnitude. The Storegga Slide off Norway affected an area the size of Scotland and moved enough sediment to bury the entire country to a depth of 80 m. Modern geophysics provides a clear picture of large landslides and what their source and depositional areas look like. From this, we can deduce the processes that operated during downslope transport. However, our understanding of many aspects of landslide processes is based on hypotheses that are difficult to test. Elevated pore pressures are essential for landslide initiation on low continental margin slopes, yet understanding of how high pressures are generated or how fluid migration affects slope stability is limited. Sediments may be pre-conditioned for failure by the processes that originally deposited them, e.g., through creation of weak layers, but the processes and parameters that might control this are largely unknown.

Keywords Submarine landslide • slope instability • pore pressure • fluid migration • continental slope • bedding plane failure • trigger • preconditioning • methane hydrate • flow transformation

1 Introduction

Sedimentary deposits resulting from submarine mass movements (hereafter [submarine] landslides) occur on every passive continental margin, and are the dominant facies on many (e.g., NW African or US East Coast margins; Weaver et al. 2000; Hühnerbach et al. 2004; Twichell et al. in press). The scale of submarine landslides can exceed terrestrial events by two orders of magnitude and is almost impossible to comprehend. For example, the Storegga Slide off Norway (Fig. 1)

D.G. Masson (✉), R.B. Wynn, and P.J. Talling
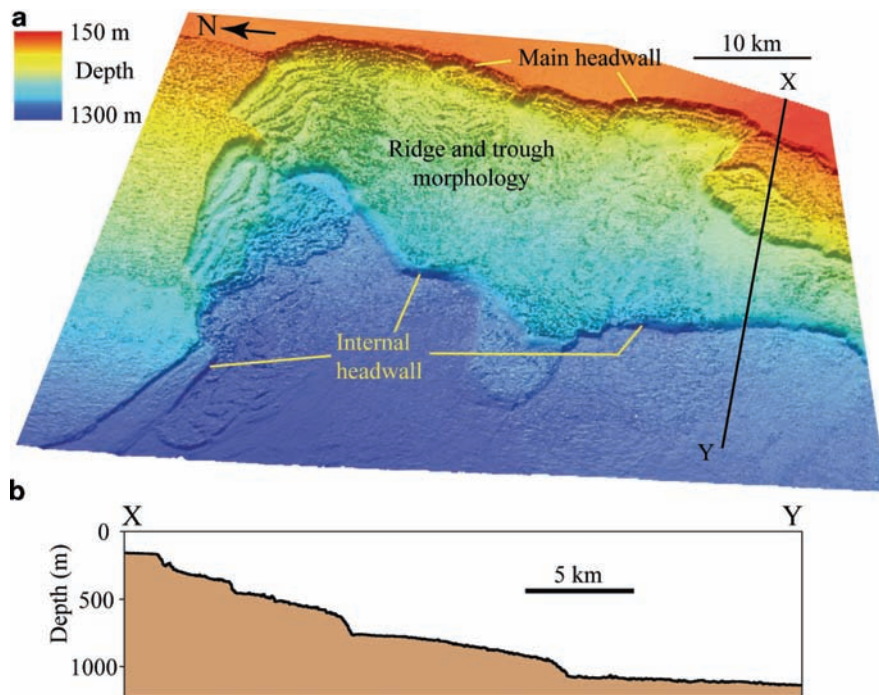National Oceanography Centre, Southampton SO14 3ZH, UK
e-mail: dgm@noc.soton.ac.uk

Fig. 1 (**a**) Shaded relief bathymetry image of the central part of the upper Storegga Slide, illuminated from the northeast, illustrating typical retrogressive landslide morphology. The ridge and trough topography is generated by lateral spreading, a landslide process in which a slab of sediment undergoes extension on a deforming softer layer (Micallef et al. 2007). The weak layers controlling failure progressively step up to shallower stratigraphic layers upslope. Areas controlled by different weak layers are separated by internal landslide headwalls, giving a characteristic step-like profile through the landslide scar (**b**)

affected an area similar to that of Scotland or the state of Kentucky (95,000 km²) and moved sufficient sediment (~3,000 km³) to bury either area to a depth of 80 m. The landslide occurred on a slope of about 1° (Haflidason et al. 2004).

Modern geophysical techniques provide a clear picture of where landslides have occurred and what their source and depositional areas look like. From this, the processes that operated during downslope transport (predominantly sediment slides, debris flows and turbidity currents) can often be deduced. For historical landslides, the trigger may also be known, with earthquakes, storms and anthropogenic effects among the most important. However, for many aspects of landslides our 'understanding' is based on hypotheses that are currently difficult to test in the real world. For example, it is generally agreed that elevated pore pressures are required to initiate landslides on typical low continental margin slopes, yet understanding of how these elevated pressures are generated or how fluid migration might affect slope stability is limited. To what extent are sediments pre-conditioned for failure by the processes that originally deposited them, for example through the creation of weak layers or by diagenesis? Is slope stability and landslide frequency

affected by climate or sea-level change? Can changes in methane hydrate stability generate slope failure? Why do some landslides form slides or debris flows and others turbidity currents (while only a few are known to have formed both) and what controls transformations between flow types? How is several hundred cubic kilometers of sediment dispersed in an even larger volume of water during the formation of large turbidity currents? This paper presents the authors' view of current understanding of large landslides on passive continental margins, based mainly on observations of known landslide events.

2 Interpretation of Landslide Morphology

High-resolution bathymetry and sidescan sonar data show that many large landslides have similar morphology (Figs. 1, 2). This suggests a common failure process. In particular, landslides typically occur on a failure surface (or surfaces) conformable with the sediment bedding (O'Leary 1991).

2.1 Characteristics of Bedding Plane Parallel Landslides

Examples of large bedding plane parallel landslides on passive margins worldwide include the Storegga and Traenadjupet Slides offshore Norway (Bugge et al. 1988; Laberg and Vorren 2000; Haflidason et al. 2004; Micallef et al. 2007, 2009), the
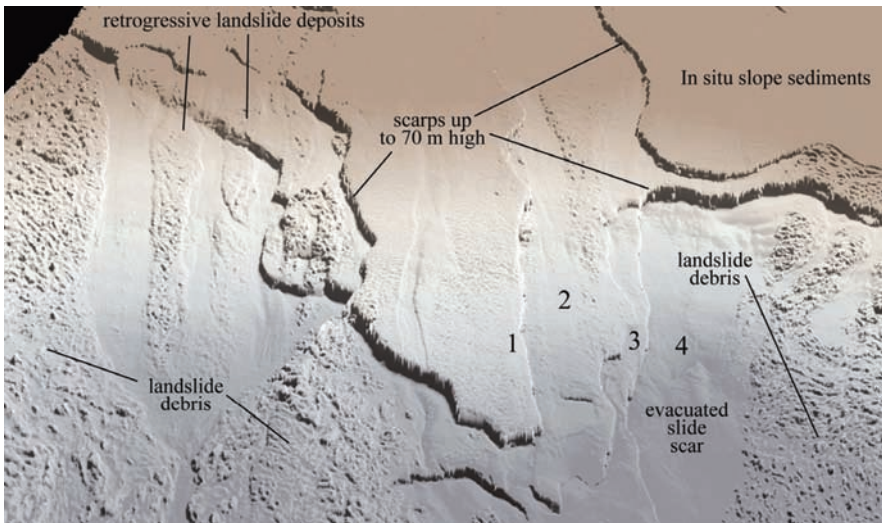

Fig. 2 Shaded relief image of part of a large landslide on the West African continental margin. Water depth varies from about 600 m (*top*) to 2,000 m (*bottom*). Image is approximately 25 km from *left* to *right*. Numbers indicate four distinct bedding plane parallel levels on which various sections of the landslide failed

Saharan and Mauritania Slides off West Africa (Georgiopoulou et al. in press; Krastel et al. 2006) and the Grand Banks and other slides on the eastern margin of North America (Piper et al. 1999; O'Leary 1991; Mosher et al. 2004). On the eastern flank of the Eivissa Channel in the Mediterranean Sea, four separate small landslides, all sharing the same failure surface, occur in parallel-bedded sediments (Lastras et al. 2004). These show continuity of a failure-prone layer over a distance >100 km.

The upper parts of bedding plane parallel landslides exhibit complex morphology that distinguishes landslide areas from adjacent areas of undisturbed smooth slope (Figs. 1, 2). Headwalls consist of multiple scarps ranging from a few meters to 100 m or more in height; internal headwalls separate different levels of failure surface (e.g., Bryn et al. 2003). This gives the landslide scar a staircase appearance, with the shallowest failure surfaces and thinnest failed section occurring farthest up slope (Figs. 1, 2). In some cases, tongues of debris that originated upslope in the landslide drape scarps downslope, indicating retrogressive landslide behavior (Fig. 2; Haflidason et al. 2004; Micallef et al. 2007). For most retrogressive landslides, the timescales over which retrogression occurs are not known. However, modeling of the tsunami associated with the Storegga Slide indicates that retrogression must have been rapid, with the entire slide mobilized in less than a few hours (Bondevik et al. 2005). *In situ* sediments adjacent to such landslides are characterized by parallel-bedded sequences (Fig. 3). Landslide failure surfaces are parallel to bedding and correspond to a limited number of key reflectors across the landslide (Figs. 1–3).
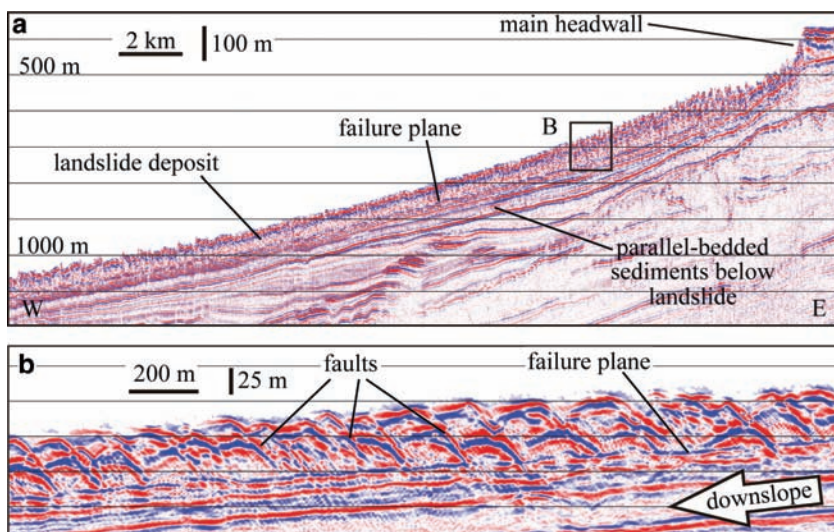

Fig. 3 Seismic profile from the Storegga Slide showing: (**a**) the steep headwall and apparently chaotic landslide deposit overlying the parallel-bedded *in situ* slope sequence. (**b**) Detail showing that the landslide deposit actually consists of coherent sediment blocks that preserve the pre-landslide stratigraphy, separated by distinct faults. Modified from Micallef et al. (2007)

Two distinctive end-member seafloor textures, one smooth and one rough, are typically seen within landslide scars (Figs. 1, 2). The smooth seafloor corresponds to evacuated landslide scar devoid of residual debris deposits. In contrast, the rough seafloor is covered by landslide debris up to a few tens of meters thick (Fig. 3). The structure of the debris, best illustrated by the bathymetry data, consists of closely packed blocks of only slightly deformed sediment separated by narrow depressions with a preferred alongslope orientation, interpreted as zones of more intense deformation (Figs. 1–3). The degree of fragmentation is highly variable, with the largest coherent blocks up to several kilometers across.

Because of the lower spatial resolution of seismic profiles relative to bathymetry, most landslide debris appears chaotic in profile, with individual blocks only poorly resolved (Fig. 3a). However, high-resolution profiles confirm the interpretation suggested by the bathymetry, imaging the coherent stratigraphy of the blocks interrupted by extensional normal faults (Fig. 3b). At the seabed, the faults correlate with seafloor depressions, confirming that the pattern of depressions seen in the bathymetry represents the plan view fault pattern (Micallef et al. 2007). The limited resolution of the seismic data restricts resolution of the thickness of any 'weak layer', suggesting only that it is less than a few meters thick. Cores that penetrate the failure surface typically show landslide debris overlying undisturbed older sediment; a distinctive layer may be seen at the level of the failure surface (Gee et al. 1999), but is not always recognized.

3 Failure Processes

3.1 Triggers and Preconditioning Factors

Many publications list the factors that contribute to initiation of submarine landslides (e.g., Hampton et al. 1996; Canals et al. 2004). Typically, such lists consist of two types of parameter that can be categorized either as 'triggers' or 'preconditioning factors'. Triggers are relatively short-period events that act to destabilize submarine slopes. Earthquakes, the trigger for most large historical submarine landslides (e.g., Hampton et al. 1996; Masson et al. 2006), are by far the best known, but low tides, storm wave loading, tectonic movements (e.g., tilting due to margin subsidence or salt movement), changes in methane hydrate stability and sealevel change also fall into this category. For the most part, the way in which these operate to trigger landslides, usually through rapid changes in sediment pore pressure, is understood, at least in principle. Preconditioning factors are related to properties of the sediments and are acquired during, or evolve from, the depositional process. Preconditioning includes aspects of the gross structure and stratigraphy of the sediments (e.g., presence or absence of sediment layers that might evolve into failure planes), water content, and pore pressure related to deposition (Canals et al. 2004). Slope might also be considered to be a preconditioning factor, but although a slope is clearly required, slope

steepness does not seem to be important (Hühnerbach et al. 2004), although changes in steepness, e.g., due to tectonic movement, are important (e.g., Faroe Islands margin; van Weering et al. 1998). The importance of the overall fluid flow regime beneath the slope may also be important, as will be discussed later. Much less is understood about the role of preconditioning factors (in comparison to triggers) in the initiation, size and frequency of giant landslides.

3.2 Pore Pressure

Elevated sediment pore pressures, which act to reduce vertical effective stress in sediments (and thus the frictional resistance to landsliding), are among the key factors facilitating submarine slope failure (Canals et al. 2004; Kvalstad et al. 2005; Strout and Tjelta 2005). For example, it has been shown that the effective stress at the depth of the failure plane of the Storegga Slide needed to be reduced to only 10% of lithostatic stress (predicted on the basis of overlying sediment thickness) before failure could occur (Kvalstad et al. 2005). The required excess pore pressures were modeled by lateral migration of pore fluid from adjacent areas with much higher sedimentation rates and sediment thickness. This causes instability because fluid pressure can approach lithostatic stress where the overburden is thin. A similar process of lateral fluid migration has also been observed on the eastern continental margin of the United States (Dugan and Flemings 2000, 2002) and in the Gulf of Mexico (Flemings et al. 2008). At both these locations, pore pressure migration has been proposed as a cause of landslides.

4 Models for Large Bedding Parallel Landslides

The accepted view of continental slope sedimentation is that sediments derived from terrestrial erosion are transported over the continental shelf edge and deposited on the slope, building a seaward-thinning wedge-shaped deposit (Fig. 4a). Short-term sedimentation rates are highest on the upper slope, creating high pore pressures that lead to slope failure. The resulting landslides then propagate downslope through a combination of slope loading and erosion of the superficial slope sediments (Gee et al. 1999). Landslides that conform to this model are common on submarine deltas (e.g., those of the Nile and Mississippi rivers), where rapid deposition of muddy sediments on the upper slope predominates (Prior and Coleman 1982; Loncke et al. 2002). However, analysis of landslide morphology and water depth of landslide headwalls on continental slopes around the North Atlantic does not support the wide applicability of this model. Firstly, landslide headwalls are most abundant in mid-slope at 500–1,500 m water depth (some deeper than 3,000 m), rather than immediately seaward of the shelf edge (e.g., Saharan Slide and several landslides on the US East Coast margin (Hühnerbach et al. 2004;
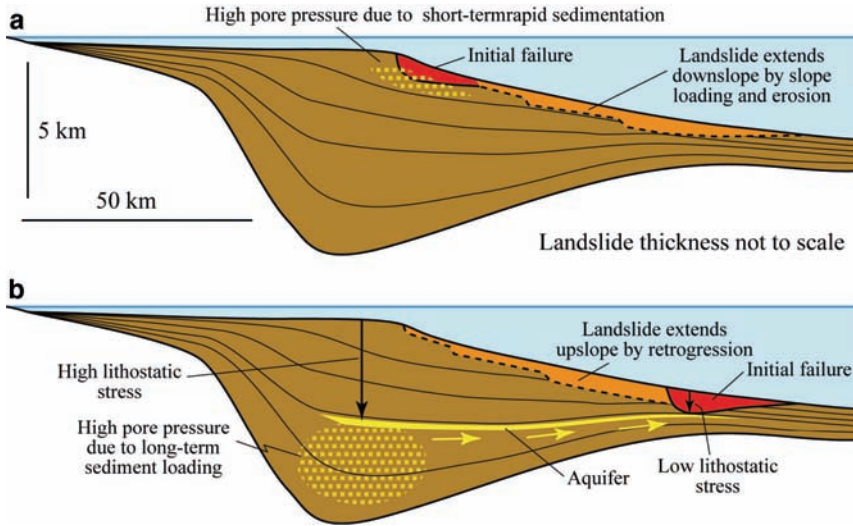
Fig. 4 Schematic illustration of a continental margin illustrating contrasting 'end member' initiation mechanisms for giant landslides. Landslide thickness is exaggerated to improve presentation. (**a**) Landslide initiated on the upper slope due to rapid sedimentation. (**b**) Landslide initiated on the lower slope due to lateral advection of high pore pressure from thicker sediment accumulation beneath the upper slope. In both (**a**) and (**b**), development of the landslide beyond the initial failure is controlled by weak layers within the parallel bedded slope sediment sequence

Georgiopoulou et al. in press; Twichell in press). Secondly, many large continental slope landslides are located on slopes characterized by moderate (when compared to submarine deltas) sedimentation rates (e.g., off NW Africa or the east coast of the USA; Weaver et al. 2000; McHugh and Olsen 2002). Thirdly, many landslides are retrogressive (Figs. 1, 2; Canals et al. 2004; Micallef et al. 2007). Observations of seafloor affected by retrogressive landsliding show that headwall retreat of tens of kilometers by this mechanism is common, indicating that the water depth at which the landslide initiated must have been considerably deeper than the final observed headwall water depth.

Our observations of headwall water depths and the retrogressive style of giant landslides are best explained by giant continental margin landslides that are initiated on the middle or lower continental slope. In particular, our proposed model (Fig. 4b) explains the depth distribution of landslide headwalls, the retrogressive nature of most giant landslides, and the progressively shallower depth of failure planes upslope. The lateral transfer of high pore pressure through the continental slope sediment sequence is key to landslide initiation on the lower slope. This requires (i) deposition of thick sediments on the upper slope, often on medium to long-term timescales, to generate initial high pore pressure, (ii) layering of relatively permeable and impermeable sedimentary horizons, to generate conditions where it is easier for pore fluid to migrate laterally over long distances along permeable horizons than to migrate vertically across the stratification, and (iii) good

lateral continuity of the stratigraphy to ensure containment of the fluid flow system. For example, submarine canyons dissecting margin sediments may cut the stratigraphy and create a lateral escape route for high pore pressure, defusing the potential for large-scale landsliding. Thus areas of continental slope cut by canyons, and those affected by large-scale landsliding, are largely mutually exclusive (Weaver et al. 2000; Twichell et al. in press). In addition, the landslide initiation mechanism described above requires thick sediments rather than high sedimentation rates. This can explain landsliding in areas such as off NW Africa or on the eastern US continental margin, where sedimentation rates are moderate but have been continuous over long periods of time.

Once initiated, landslides can retrogress upslope because of loss of support for the sediment above the evolving headwall. This is most effective where specific sediment layers (weak layers) focus strain-softening behavior (strain concentration and loss of strength). Where such layers exist, the retrogressive failure mechanism can be modeled in accordance with conventional engineering principles (Kvalstad et al. 2005; Micallef et al. 2007). The sedimentology of weak layers is not well understood, mainly because they are destroyed in areas where landslides have occurred and it is not known how to identify them before they fail. High-resolution profiles from landslide scars show that failure planes almost always follow individual bedding planes, so it seems likely that weak layers correspond to specific sediment beds (Haflidason et al. 2003; Krastel et al. 2006) although "mechanical discontinuities" between beds of differing engineering properties have also been suggested (Haflidason et al. 2003; Canals et al. 2004).

Lateral propagation of high sediment pore pressure and the occurrence of laterally continuous, parallel-bedded sediments are two of the most important factors controlling occurrence of giant submarine landslides. Thus understanding the giant landslide potential of any continental margin requires a comprehensive understanding of the whole margin system. Geotechnical studies of the upper sediment sequence, as typically carried out by offshore industry, address only local slope stability issues, and on their own give little information on regional slope stability. Modeling of the pore pressure regime beneath the slope can be effective (Kvalstad et al. 2005), but full assessment of the fluid flow regime requires knowledge of the geology and physical properties of the sediment sequence beneath the continental slope, and is only possible where deep drilling information is available.

5   Outstanding Questions

Understanding of many aspects of landslide processes is based on hypotheses that are difficult to test. In many instances, we can infer how a landslide has behaved (e.g., in terms of flow processes or flow transformations) without understanding why it has behaved in this way. Some key questions to which, at best, we have only partial answers, are discussed below.

1. Why do some areas fail when adjacent areas don't? While it is recognized that bedding plane parallel landslides seem to occur where there is stratigraphic continuity over large areas of margin, it is also true that often only part of such an area fails, and a landslide area may change gradually into *in situ* slope through a zone of partial failure (e.g., northern margin of Storegga Slide; Haflidason et al. 2003). This is presumably due to subtle variations in pore pressure distribution, the spatially varying effects of the triggering event (e.g., an earthquake) or the mechanical properties of the basal 'weak' layer, but we have very little understanding as to the nature of these variations.

2. Climate and sea-level change appear to influence the distribution and frequency of continental margin landslides by changing the sediment delivery to margins, or more indirectly through changes in the gas hydrate stability zone or the frequency of earthquakes related to ice loading or unloading (e.g., Owen et al. 2007). Understanding of climatic influence on landslide frequency is particularly important for hazard analysis, since past frequency of landslides that may have occurred under a different climatic regime is often used as an indicator of future hazard. However, few submarine landslides have been dated with accuracy, limiting the effectiveness of slide frequency analyses. Most landslide ages are based on the age of sediments overlying the landslide deposit and should only be regarded as minimum ages; rough, elevated landslide topography may inhibit post-landslide sedimentation leading to erroneously young dates. Dating multiple cores from a landslide can overcome this problem, as in the case of the Storegga Slide (Haflidason et al. 2005). Alternative approaches include dating cores that penetrate the edge of a landslide deposit into the underlying sediments, thus giving a minimum and maximum age (e.g., Saharan Slide, Gee et al. 1999) or dating landslide-related turbidites (Weaver and Kuipers 1983) although establishing definitive landslide-turbidite correlation may be difficult.

3. Can changes in the methane hydrate stability zone on continental margins triggering submarine landslides? Such changes, leading to pore pressure increases or mechanical weakening of hydrate-bearing sediments have been suggested as a triggering mechanism for landslides on several continental margins including the Norwegian Sea and parts of the US East Coast margin (Maslin et al. 2004; Sultan et al. 2004; Hornbach et al. 2007 and references therein; Owen et al. 2007; Berndt et al. 2009). However, evidence supporting this theory is largely circumstantial and it remains controversial. Many landslides have occurred in areas where there is no evidence for the development of gas hydrates, although the difficulties in identifying hydrate bearing sediments in areas where bottom simulating reflectors (BSR) are not recognized on seismic profiles is acknowledged. Recent recognition that many large margin landslides were initiated in deep water (Hühnerbach et al. 2004; Twichell et al. in press) also mitigates against the involvement of hydrates in their triggering, since hydrates are most susceptible to dissociation at depths <1,000 m (Sultan et al. 2004; Hornbach et al. 2007). In the case of the Storegga Slide, the recognition that the slide probably initiated at water depths between 1,500 and 2,000 m appears to rule out hydrate dissociation as a triggering mechanism, since post-glacial warming of

the Norwegian Sea was limited to water depths <700 m, with deeper waters remaining below 0°C to the present day (Bryn et al. 2005).

4. Long runout, sometimes for many hundred kilometers on very low slopes (<1°), characterizes many continental margin landslides. This requires either a low viscosity flow (not generally supported by the cohesive nature and often only moderate deformation of the debris flow material) or a mechanism that lowers friction at the base of the flow. High pore pressure in a basal layer (Gee et al. 2001) and hydroplaning (Mohrig et al. 1998) have been suggested in this context. Are both these mechanisms possible, do they operate in similar or different settings, and how might the resulting deposits be distinguished?

5. Why do some landslides form slides or debris flows and others 'ignite' to form turbidity currents, and what controls transformations between flow types? On the West African margin, the Saharan Debris Flow, one of the largest landslides in the area (around 600 km^3; Gee et al. 2001), did not produce a significant turbidite (Georgiopoulou et al. in press), and is not recorded in the Madeira Abyssal Plain downslope (Rothwell et al. 1992). Yet other landslides on the same margin are the sources for the large turbidites (some >100 km^3) that form the fill of the same abyssal plain (Rothwell et al. 1992). All the landslides have essentially the same composition, yet behavior clearly differs significantly. Could the presence of thin sandy turbidite bases in some areas be important in the formation of turbidity currents? What is the influence of the topography over which the flow is moving?

6. How is several hundred cubic kilometers of sediment dispersed in an even larger volume of water during the formation of large turbidity currents? What causes the large-scale mixing that is required and how is the cohesion of the sediment overcome? Is it possible that hydroplaning facilitates injection of water into the base of the landslide, triggering flow instability and mixing?

6 Conclusions

Features that are common to many large landslides include:

(i) They occur in parallel-bedded sediment sequences that have stratigraphic continuity over large areas. Sediments are dominantly fine-grained.

(ii) Landslide headwalls typically occur at 500–1,500 m on the upper slope, although retrogression may extend the failure upslope to the shelf edge.

(iii) Failure occurs on one or more surfaces parallel to the sediment bedding, giving the landslide scar a staircase-like appearance. The failed section is typically 10–100 m thick.

(iv) The same layers fail over wide areas.

(v) Evacuated slide scars give areas of smooth seafloor. Residual debris within landslide scars consists of blocky, fragmented sediment.

(vi) Initial breakup of the landslide slab is by brittle deformation.

Taken together, these features suggest that bedding-plane parallel landslides result from failure of distinct 'weak layers' within sequences of otherwise stable sediments. True failure conditions only occur at the weak layer level.

Elevated pore pressure at the base of the landslide is clearly the key to failure. Such elevated pressure can be generated by rapid sedimentation, e.g., on submarine river deltas, and typically leads to landslides that initiate on the upper slope and propagate downslope. However, observations of many continental margin landslides suggest that they originate in areas with only moderate sedimentation rates and that they initiate in mid to lower slope and retrogress upslope. These are best explained by a model where high pore pressure generated deep beneath the upper slope migrates laterally into thinner sediment sequences beneath the lower slope, triggering failure of these sediments.

For many aspects of landsliding, the landslide deposits record how the landslide behaved, although we often don't fully understand the underlying mechanisms. Why specific areas fail, how far the resultant landslide flows downslope, and how and why flows transform as they evolve during downslope transport, are among the more important outstanding questions.

References

Berndt C, Brune S, Nisbet E, Zschau J, Sobolev SV (2009) Tsunami modeling of a submarine landslide in the Fram Strait. Geochem Geophys Geosystems 10. doi:10,1029/2008GC002292

Bondevik S, Løvholtb F, Harbitzb C, Mangerudc J, Dawsond A, Svendsenc JI (2005) The Storegga Slide tsunami – comparing field observations with numerical simulations. Mar Pet Geol 22: 195–208.

Bryn P, Solheim A, Berg K, Lien R, Forsberg CF, Haflidason, H, Ottesen D, Rise L (2003) The Storegga Slide complex: repeated large scale landsliding in response to climatic cyclicity. In: Locat J, Mienert J (eds), Submarine Mass Movements and their Consequences. Kluwer Academic, Dordrecht, pp 215–222.

Bryn P, Berg K, Solheim K, Kvalstad TJ, Forsberg CF (2005) Explaining the Storegga Slide. Mar Pet Geol 22: 11–19.

Bugge T, Belderson RH, Kenyon NH (1988) The Storegga Slide. Phil Trans Roy Soc Lond A 325: 357–388.

Canals, M et al. (2004) Slope failure dynamics and impacts from seafloor and shallow sub-seafloor geophysical data: case studies from the COSTA project. Mar Geol 213: 9–72.

Dugan B, Flemings PB (2000) Overpressure and fluid flow in the New Jersey continental slope: implications for slope failure and cold seeps. Science 289: 288–291.

Dugan B, Flemings PB (2002) Fluid flow and stability of the US continental slope offshore New Jersey from the Pleistocene to the present. Geofluids 2: 137–146.

Flemings PB, Long H, Dugan B, Germaine J, John CM, Behrmann JH, Sawyer D, IODP Expedition 308 Scientists (2008) Pore pressure penetrometers document high overpressure near the seafloor where multiple submarine landslides have occurred on the continental slope, offshore Louisiana, Gulf of Mexico. Earth Planet Sci Lett 274: 269–283.

Gee MJR, Masson DG, Watts AB, Allen PA (1999) The Saharan Debris Flow: an insight into the mechanics of long runout debris flows. Sedimentol 46: 317–335.

Georgiopoulou A, Wynn RB, Masson DG, Frenz M (in press) Linked turbidite-debrite resulting from recent Sahara Slide headwall reactivation. Mar Pet Geol.

Haflidason H, Sejrup HP, Berstad IM, Nygård A, Richter T, Bryn P, Lien R, Berg K (2003) A weak layer feature on the northern Storegga Slide Escarpment. In: Mienert J, Weaver PPE (eds), European Margin Sediment Dynamics. Springer, Berlin, pp. 55–62.

Haflidason, H, Sejrup HP, Nygård A, Mienert J, Bryn P, Lien R, Forsberg CF, Berg K, Masson, D (2004) The Storegga Slide: architecture, geometry and slide development. Mar Geol 213: 201–234.

Haflidason H, Lien R, Sejrup HP, Forsberg CG, Bryn P (2005) The dating and morphometry of the Storegga Slide. Mar Pet Geol 22: 123–136.

Hampton MA, Lee HJ, Locat J (1996) Submarine landslides. Rev Geophys 34: 33–59.

Hühnerbach V, Masson DG, COSTA Porject partners (2004) Landslides in the north Atlantic and its adjacent seas: an analysis of their morphology, setting and behaviour. Mar Geol 213: 343–362.

Hornbach MJ, Lavier LL, Ruppel CD (2007) Triggering mechanism and tsunamogenic potential of the Cape Fear Slide complex, U.S. Atlantic margin. Geochem Geophys Geosyst 8. doi:10,1029/2007GC00001722.

Krastel S, Wynn RB, Hanebuth TJJ, Henrich R, Holz C, Meggers H, Kuhlmann H, Georgiopoulou A, Schulz HD (2006) Mapping of seabed morphology and shallow sediment structure of the Mauritania continental margin, Northwest Africa: some implications for geohazard potential. Nor J Geol 86: 163–176.

Kvalstad TJ, Andresen L, Forsberg CF, Berg K, Bryn P, Wangen M (2005) The Storegga Slide: evaluation of triggering sources and slide mechanics. Mar Pet Geol 22: 245–256.

Laberg JS, Vorren TO (2000) The Traenadjupet Slide, offshore Norway – morphology, evacuation and triggering mechanisms. Mar Geol 171: 95–114.

Lastras G, Canals M, Urgeles R, Hughes-Clarke JE, Acosta J (2004) Shallow slides and pockmark swarms in the Eivissa Channel, western Mediterranean Sea. Sedimentol 51: 1–14.

Loncke L, Gaullier V, Bellaiche G, Mascle J (2002) Recent depositional patterns of the Nile deep-sea fan from echo-character mapping. Am Assoc Pet Geol Bull 86: 1165–1186.

Maslin M, Owen M, Day S, Long D (2004) Linking continental-slope failures and climate change: testing the clathrate gun hypothesis. Geology 32: 53–56.

Masson DG, Harbitz CB, Wynn RB, Pedersen G, Løvholt F (2006) Submarine Landslides – processes, triggers and hazard prediction. Phil Trans Roy Soc Lond, A 364: 2009–2039.

McHugh CMG, Olson HC (2002) Pleistocene chronology of continental margin sedimentation: new insights into traditional models, New Jersey. Mar Geol 186: 389–411.

Micallef A, Masson DG, Berndt C, Stow DAV (2007) Morphology and mechanics of lateral spreading: A case study from the Storegga Slide. J Geophys Res 112: doi:10.1029/2006JF0007.

Micallef A, Masson DG, Berndt C, Stow DAV (2009) (in press) Development and mass movement processes of the north-eastern Storegga Slide. Quat Sci Rev.

Mohrig D, Whipple KX, Hondzo M, Ellis C, Parker G (1998) Hydroplaning of subaqueous debris flows. Geol Soc Am Bull 110: 387–394.

Mosher DC, Piper DJW, Campbell DC, Jenner KA (2004) Near-surface geology and sediment-failure geohazards of the central Scotian Slope. Am Assoc Pet Geol Bull 88: 703–723.

O'Leary DW (1991) Structure and morphology of submarine slab slides: clues to origin and behaviour. Mar Geotech 10: 53–69.

Owen M, Day S, Maslin M (2007) Late Pleistocene submarine mass movements: occurrence and causes. Quat Sci Rev 26: 958–978.

Piper, DJW, Cochonat P, Morrison ML (1999) The sequence of events around the epicentre of the 1929 Grand Banks earthquake: initiation of debris flows and turbidity current inferred from sidescan sonar. Sedimentol 46: 79–97.

Prior DB, Coleman JM (1982) Active slides and flows in underconsolidated marine sediments on the slope of the Mississippi delta. In: Saxov S, Nieuwenhuis JK (eds), Marine Slides and Other Mass Movements. Plenum Press, New York, pp. 21–49.

Rothwell RG, Pearce TJ, Weaver PPE (1992) Late Quaternary evolution of the Madeira Abyssal Plain, NE Atlantic. Basin Res 4: 103–131.

Strout JM, Tjelta TI (2005) In situ pore pressures: what is their significance and how can they be reliably measured. Mar Pet Geol 22: 275–285.

Sultan N, Cochonat P, Foucher JP, Mienert J (2004) Effect of gas hydrates melting on seafloor slope instability. Mar Geol 213: 379–401.

Twichell DC, Chaytor JD, ten Brink US, Buczkowski B (2009) Morphology of late Quaternary submarine landslides along the U.S. Atlantic continental margin. Mar Geol 264: 4–15.

Weaver PPE, Kuijpers A (1983) Climatic control of turbidite deposition on the Madeira Abyssal Plain. Nature 306: 360–363.

Weaver PPE, Wynn RB, Kenyon, NH, Evans J (2000) Continental margin sedimentation with special reference to the Northeast Atlantic margin. Sedimentol 47: 239–256.

Van Weering TCE, Nielsen T, Kenyon NH, Akentieva K, Kuijpers A (1998) Sediments and sedimentation at the NE Faeroe continental margin; contourites and large-scale sliding. Mar Geol 152: 159–176.

Origin of Overpressure and Slope Failure in the Ursa Region, Northern Gulf of Mexico

B. Dugan and J. Stigall

Abstract Sedimentation-fluid flow-stability models predict the evolution of overpressure (pressure above hydrostatic) and stability of sediments in the Ursa region, northern Gulf of Mexico (IODP Expedition 308). Two-dimensional models across the Ursa region from 65–0 ka simulate overpressure up to 2 MPa in the shallow subsurface at Site U1324 and near 1 MPa at Site U1322, which is consistent with measurements. Overpressure history is controlled by sedimentation rate and distribution. Today overpressure is decreasing, but past high sedimentation periods were important overpressure sources. Infinite slope stability analyses indicate the slope is stable. Overpressure increase and stability decrease is most prevalent along the boundary between mud-rich mass transport deposits and silt-rich channel-levee deposits between Sites U1323 and U1322. This is controlled by high overpressure driving fluids laterally along permeable sediments to where overburden is thin. Even with high sedimentation rates at Ursa and lateral flow, unstable conditions are not simulated. Seismic and core observations, however, document recurring slope failures in the mud-rich deposits. We conclude that sedimentation-driven overpressure and lateral transfer of pressure created a marginally stable slope, but additional driving forces, such as extremely high sediment inputs or seismic accelerations created by salt tectonic-related earthquakes were required to initiate failure.

Keywords Mass transport deposit • overpressure • slope stability • Gulf of Mexico • basin modeling • IODP 308

B. Dugan (✉) and J. Stigall
Department of Earth Science, Rice University, 6100 Main Street,
MS 126, Houston, TX 77005 USA
e-mail: dugan@rice.edu

1   Introduction

Mass transport deposits (MTDs) are the sedimentary record of marine sediments that have been remobilized, transported downslope, and redeposited. These records occur worldwide, can be created by a variety of mechanisms including turbidity currents, debris flows, submarine landslides, or creep (Hampton et al. 1996), and occur in a range of sizes and a variety of slopes (McAdoo et al. 2000). The type and size of slope failure and resulting MTD are partly dependent on the initial sedimentary conditions (e.g., slope, porosity, lithology) and external forces (e.g., overpressure, earthquake shaking).

The Ursa region is an area of active hydrocarbon exploration and is known to have MTDs and shallow overpressure (pressure above hydrostatic) (Ostermeier et al. 2000). Integrated Ocean Drilling Program (IODP) Expedition 308 used the region as a hydrogeology study area to investigate the origin of shallow overpressure and its influence on slope failure. The region served as a direct test of the flow focusing hypothesis that lateral fluid flow in permeable layers is controlled by rapid, asymmetric loading by low permeability sediments and this could create low effective stress and slope instability where overburden is thin (Dugan and Flemings 2000).

We present two-dimensional, forward models of the Ursa region that couple sedimentation, overpressure generation, fluid flow, and slope stability. The models use documented lithologic, hydrologic, and strength properties. We use models to study sedimentation histories and explore how they affect overpressure generation and stability at Ursa. We conclude that flow focusing affects overpressure, but additional pressure sources or seismic accelerations are required to initiate failures in the Ursa region.

2   Ursa Region

The Ursa region is located 210 km offshore New Orleans, LA (USA) on the continental slope in the northern Gulf of Mexico (Fig. 1). This region is on the eastern flank of Mississippi canyon, has shallow overpressures, slope failures, and low tectonic activity (e.g., Winker and Booth 2000; Ostermeier et al. 2000). This region has extensive seismic, log, and core data from industry-related drilling, shallow hazard studies, and IODP Expedition 308. Based on continuous, seafloor-parallel seismic reflections from 0–30 m below seafloor (mbsf) and age control at Sites U1322 and U1324 (Flemings et al. 2006), we interpret the seafloor has been relatively stable over the last 10 ka.

Core, log, and seismic data have been used to characterize in situ overpressure (Flemings et al. 2008), bulk physical properties (Long et al. 2008; Flemings et al. 2006), and distribution and lithology of channel-levee deposits and MTDs (Sawyer et al. 2007). Direct pressure measurements and laboratory experiments show that overpressure starts near the seafloor and generally increases to the top of the Blue
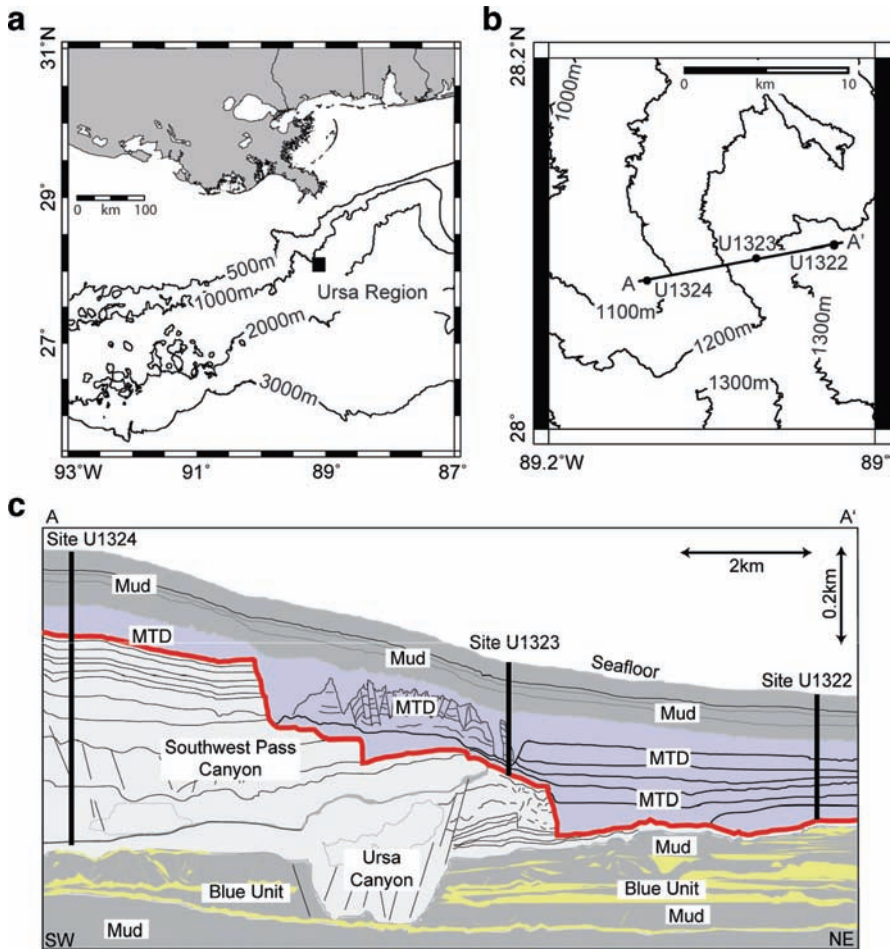
Fig. 1 (**a**) Bathymetric map locating Ursa in the northern Gulf of Mexico. (**b**) Bathymetric map of the Ursa region. (**c**) Interpreted cross-section based on seismic data from the Ursa region (Flemings et al. 2006). Mud indicates hemipelagic mud and MTD indicates mass transport deposits that are mud-rich. Blue unit is interbedded sand (yellow) and hemipelagic mud. Ursa Canyon and Southwest Pass Canyon are channel-levee deposits associated with silt. Surface between base of MTDs and channel-levee deposits (red line) is surface along which factor of safety is characterized (Section 4.2; Fig. 4).

unit (Flemings et al. 2008; Dugan and Germaine 2008). These overpressures range from 50–70% of the hydrostatic effective stress. For slope failure to occur due to overpressure alone, overpressure must exceed 93% of the hydrostatic effective stress (Flemings et al. 2008).

High sedimentation rates are the primary source of overpressure in the Ursa region. When deposition of high porosity, low permeability mud occurs at rates greater than ~1 mm/y, overpressure generation is common (e.g., Gibson 1959). In the Ursa region, sedimentation rates were consistently above 1 mm/y and exceeded

10 mm/y during some periods (Fig. 2). At Site U1324, the average sedimentation rate over the last 65 ka is 9.3 mm/y; at Site U1322 the average sedimentation rate is 3.6 mm/y (Flemings et al. 2006). This difference in sedimentation rate has created an asymmetric, mud-dominated sediment wedge overlying the sand of the Blue unit (Fig. 1c).

MTDs within the Ursa region have recurred through the burial history of the Blue unit (e.g., Urgeles et al. 2007). MTDs appear to be confined to the mud-rich sediments that overlie the silt-rich channel-levee deposits (Fig. 1c). The mud between Sites U1323 and U1322 are dominated by MTDs from the top of the channel-levee deposits to 85 mbsf (meters below sea floor). This includes one large MTD that extends across the entire Ursa region from 100–160 mbsf (Site U1324) to 100–195 mbsf (Site U1323) to 85–125 mbsf (Site U1322) (Fig. 1c). This MTD is underlain by channel-levee sediments at Sites U1324 and U1323 and stacked MTDs at Site U1322 (Fig. 1c).

3   Basin Modeling

We use a two-dimensional, sedimentation-fluid flow model to simulate pressure, consolidation, stability, and temperature evolution of the Ursa basin. The system is modeled using Basin2 (Bethke et al. 1993, 1988) (Eq. 1).

$$\phi \beta_f \frac{\partial P}{\partial t} = \frac{\partial}{\partial x}\left[\frac{k_x}{\mu}\frac{\partial P}{\partial x}\right] + \frac{\partial}{\partial z}\left[\frac{k_z}{\mu}\left(\frac{\partial P}{\partial z} - \rho_w g\right)\right] - \frac{1}{1-\phi}\frac{\partial \phi}{\partial t} + \phi \alpha \frac{\partial T}{\partial t} \qquad (1)$$

ϕ is porosity [m^3/m^3], β_f is fluid compressibility [1/Pa], P is fluid pressure [Pa], t is time [s], x is horizontal distance [m], z is vertical distance [m], k_x is horizontal permeability [m^2], k_z is vertical permeability [m^2], ρ_w is fluid density [kg/m^3], μ is water dynamic viscosity [Pa·s], g is acceleration due to gravity [m/s^2], α is water thermal expansion coefficient [1/^{o}C], and T is temperature [^{o}C]. Equation (1) describes changes in fluid pressure due to horizontal/vertical Darcy flow, pore volume changes, and thermal expansion of water. All simulations have no fluid flow lateral/basal boundaries and a hydrostatic seafloor. The east and west boundaries are located >5 km from Sites U1324 and U1322 to minimize boundary effects. Each simulation begins with a 750-m-thick, hydrostatic mud layer. The Blue unit is deposited on this unit. This is followed by erosion of Ursa canyon and deposition of the Ursa channel-levee complex. Next we erode the Southwest Pass Canyon and subsequently deposit its channel-levee complex (Fig. 1c). The last stage is deposition of MTDs and hemipelagic mud (Fig. 1c).

We model the Ursa region (Fig. 1c) with three lithologies: mud; silt; and sand. Sand interbedded with mud is used to create the permeable Blue unit. Silt is deposited to create the Ursa Canyon and Southwest Pass Canyon channel-levee systems. These systems are capped with mud for the MTDs and hemipelagic mud. Sediments are deposited following the age constraints to recreate the observed basin geometry. We independently define the physical properties of each lithology.

Consolidation of sediments is modeled as an exponential relation between porosity (ϕ) and vertical effective stress (σ_v' [Pa]) (e.g., Rubey and Hubbert 1959).

$$\phi = \phi_o e^{-\beta\sigma_v'} + \phi_{irr} \qquad (2)$$

ϕ_o is a reference porosity [m^3/m^3] and ϕ_{irr} is the irreducible porosity [m^3/m^3], such that ϕ_o plus ϕ_{irr} is the depositional porosity. β is the bulk sediment compressibility [1/Pa]. Only a portion of primary consolidation is elastic, so we assume unloading compressibility (β_{ul}) is 10% of bulk compressibility ($\beta_{ul} = 0.1\beta$). We use data from consolidation experiments (Long 2007; Long et al. 2008) to constrain ϕ_o, ϕ_{irr}, and β (Equation 2) for mud and silt (Table 1). For sand, we assume a low bulk compressibility to maintain a near-constant porosity reflecting the fine-to-medium sand at Ursa (Table 1).

Intrinsic permeability for mud and silt is based on data from constant-rate-of-strain consolidation experiments. We follow the approach of Mello et al. (1994),

$$\log(k_x) = A\phi + B \qquad (3)$$

Schneider et al. (2008) characterized the empirical coefficients A [$\log(m^2)$] and B [$\log(m^2)$] for mud and silt from the Ursa region (Table 1). We assume mud and silt have permeability anisotropy (horizontal/vertical, k_x/k_z [m^2/m^2]) of 100 based on the permeability-layering model of Schneider et al. (2008). No permeability data exist for sand from Ursa, therefore we assign a constant, isotropic permeability of 1×10^{-12} m^2 for the sand (Table 1). This is representative of a fine-to-medium-grained sand (e.g., Freeze and Cherry 1979), which is consistent with the sand in the Blue unit.

For a simple assessment of slope stability evolution in the Ursa basin, we calculate the factor of safety (FS) using an infinite slope approximation (e.g., Lambe and Whitman 1969; Dugan and Flemings 2002).

$$FS = \frac{c' + [(\sigma_v - \rho_w gz)\cos^2\theta - P^*]\tan\phi_f'}{(\sigma_v - \rho_w gz)\sin\theta\cos\theta} \qquad (4)$$

Factor of safety (FS) > 1 represents a stable slope and FS $\leq$ 1 represents an unstable slope. Sediment cohesion for effective stress (c' [Pa]), total vertical stress (σ_v [Pa]), hydrostatic pore pressure ($\rho_w gz$ [Pa]), seafloor slope angle (θ[°]), angle of internal friction for effective stress (ϕ_f' [°]), and overpressure (P^* [Pa]) are required to

Table 1 Sediment properties used in Ursa region models. ϕ_o, ϕ_{irr}, and β define the consolidation parameters (Eq. 2). A and B define the horizontal permeability (k_x) function (Eq. 3) and k_x/k_z defines the horizontal-vertical permeability ratio (anisotropy).

Lithology	ϕ_o[m^3/m^3]	ϕ_{irr}[m^3/m^3]	β[1/Pa]	A [$\log(m^2)$]	B [$\log(m^2)$]	k_x/k_z
Mud	0.4	0.2	3.5×10^{-7}	9.00	−20.16	100
Silt	0.4	0.2	3.5×10^{-7}	9.19	−17.77	100
Sand	0.3	0.1	5×10^{-8}	0.00	−12.00	1

assess stability. Total vertical stress, hydrostatic pore pressure, and overpressure are calculated in the sedimentation-consolidation model (Equation 1). We assume cohesion is 0 and angle of internal friction is 26° for effective stress conditions based on shear strength experiments on sediments from the Ursa region (Dugan and Germaine 2009). We use a constant seafloor slope angle of 2° based on the regional seafloor gradient.

The infinite slope analysis is appropriate for addressing stability of slopes where failure can be considered in one dimension, such that the failure is thin, parallel to the seafloor and edge effects can be neglected wide. This approximation provides a reliable stability calculation for regional, thin slope failures similar to some failures in the Ursa region. This simple assessment can identify potentially unstable regions that may require more advanced failure analysis, such as deep-seated rotational failures (e.g., Bishop 1955). Thus our analysis provides an initial stability calculation and identifies regions that warrant detailed stability calculations.

4   Results and Discussion

We completed a suite of models for the Ursa region with various sedimentation histories that recreate the time-averaged sedimentation rates for Sites U1324 and U1322 and produce the basin architecture documented by seismic and log data. We present details of two sedimentation histories (Fig. 2) that capture the general behavior of the system as well as the important details of sedimentation history.
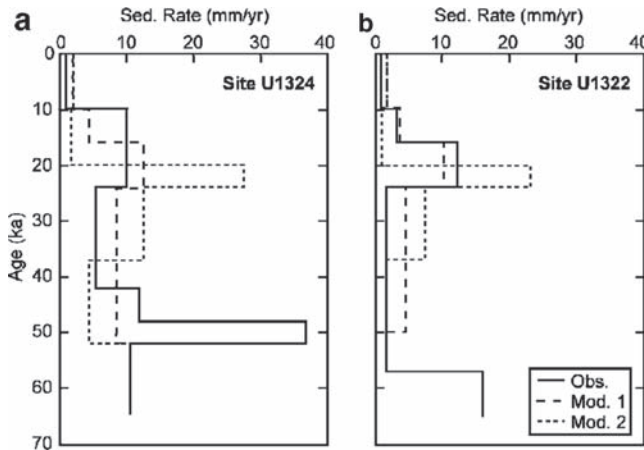
Fig. 2 Sedimentation rates for Sites U1324 (**a**) and U1322 (**b**). Solid lines (Observations = Obs.) are from biostratigraphic markers (Flemings et al. 2006). Dashed (Model 1 = Mod. 1) and dotted (Model 2 = Mod. 2) lines are two modeled sedimentation histories at Sites U1324 and U1322 used to recreate the observed basin architecture (Fig. 1) while maintaining the time-averaged rates. Model rates match observations before 55 ka.

We focus on high sedimentation from 37–16 ka because this period has the best age constraints and corresponds with MTDs in the Ursa region. Sedimentation rate variations during this period likely changed due to changes in sediment discharge from rivers and channel switching/migration. For this study, we have not evaluated the high sedimentation period near 50 ka at Site U1324, which is poorly constrained and is difficult to correlate across the basin. The transient basin models provide estimates of fluid pressure, effective stress, and stability throughout the evolution of the basin. We present two aspects of the basin model results: (1) modern-day overpressure and (2) evolution of basin stability.

The Ursa region has overpressure that begins near the seafloor and extends to the Blue unit (Fig. 3) (Flemings et al. 2008; Dugan and Germaine 2008). Site U1324 has overpressure that increases to 1 MPa by 200 mbsf; below this overpressure is approximately constant to the top of the Blue unit (Fig. 3a). For our basin models, we predict the modern-day overpressure increases to 1 MPa by 200 mbsf, but continues to increase to a maximum <2 MPa at 400 mbsf, and then is constant to the top of the Blue unit (Fig. 3a).

At Site U1322, overpressure increases to ~1MPa by 200 mbsf, however the deepest pressure measurement shows an abrupt pressure decrease (Fig. 3b). This pressure decrease may reflect pressure loss due to hydrocarbon exploration in the region over the last 15 years (Flemings et al. 2008). Sedimentation Model 1 and Model 2 (Fig. 2) both match the observed pressures at Site U1322 well with overpressure reaching 1–1.25 MPa at 250 mbsf, just above the Blue unit. We are unable to recreate the pressure decrease just above the Blue unit.

Overall our basin model pressure predictions are consistent with the measured pressures at Ursa (Fig. 3). Even though Model 2 has higher sedimentation rates than
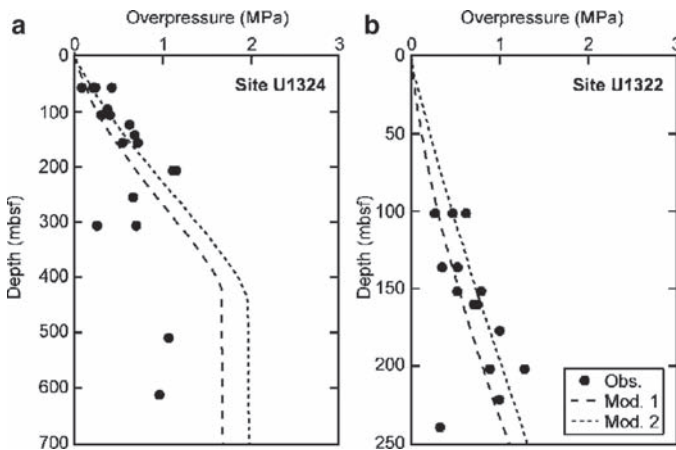
Fig. 3 Measured and simulated overpressure at IODP Sites U1324 (**a**) and U1322 (**b**). Observations (Obs., solid circles) are based on penetrometer data (Flemings et al. 2008). Model 1 (Mod. 1) and Model 2 (Mod. 2) are the simulated overpressure profiles based on two separate sedimentation histories shown in Fig. 2.

Model 1 until 20 ka, both models are good matches to the shallow data at Sites U1322 and U1324 (Fig. 3). While the modeled pressure histories are different, the lower sedimentation rates from 20 ka to present (Model 2) or from 16 ka to present (Model 1) and the relatively high porosity and high permeability of the shallow sediments facilitate dissipation of fluid pressure to the observed conditions. Therefore low sedimentation rates have helped increase effective stress along the slope and modern, low sedimentation rates will allow this process to continue.

At Site U1324, we overpredict pressures below 200 mbsf (Fig. 3a). This may be attributed to drainage by higher permeability sand layers interbedded in the silt of the channel/levee systems below 200 mbsf. Thin sand layers were documented on IODP Expedition 308 (Flemings et al. 2006) however we neglected these layers in our model because they are at a scale finer than our model layers. If these layers are interconnected, they could explain the observations. Future models could test the importance of thin sand layers. We also overpredict the deepest pressure observation at Site U1322 (Fig. 3b). This pressure low may be related to pressure dissipation in mud due to pressure depletion in sands of the Blue unit from industry wells. We did not simulate drilling-related pressure depletion so were not able to recreate this decrease.

We track the stability of the Ursa region (Equation 4) to understand the relation between sediment loading, fluid flow, and slope failure. We present general stability results along the boundary between the MTDs and the channel-levee deposits (red surface, Fig. 1c). We focus on this surface because it is the surface upon which MTDs started to form in the Ursa region. For all Ursa simulations we observe three key stability results: (1) decreased slope stability during periods of high sedimentation with minimum stability near the end of a rapid sedimentation period; (2) decreased stability east of Site U1323 and west of Site U1322; and (3) FS > 1 for a range of sediment properties and sedimentation rates constrained by Ursa data.

The simulated decrease in FS associated with sediment loading is controlled by increases in overpressure generation and lateral flow along the Blue unit. While the sand in the Blue unit allows rapid pressure equilibration, the silt that comprises the channel-levee deposits is also important to the pressure distribution and stability. The top of the silt-rich channel-levee deposits is important to basin stability because the mud-prone sediments above it are deposited rapidly; overpressure generation is rapid, but overburden is thin so the total stress is low. These features combine to lower FS (Equation 4). This suggests that lithologic contrasts and pressure transients are key features to controlling slope failure in the Ursa region. Similar decreased stability due to pressure transients has been interpreted for subaquatic slopes of Lake Lucerne based on observations and measurements (Stegmann et al. 2007). Hubbert and Rubey (1959) also suggested pressure transients were critical for decreasing stability and initiating slip on faults.

Based on our models, we predict the lowest FS exists east of Site U1323 and extends toward Site U1322. This is controlled by lateral flow along permeable sand and silt from areas of thick sediment loading to regions of thin overburden. Qualitatively this is consistent with more MTDs between Sites U1323 and U1322
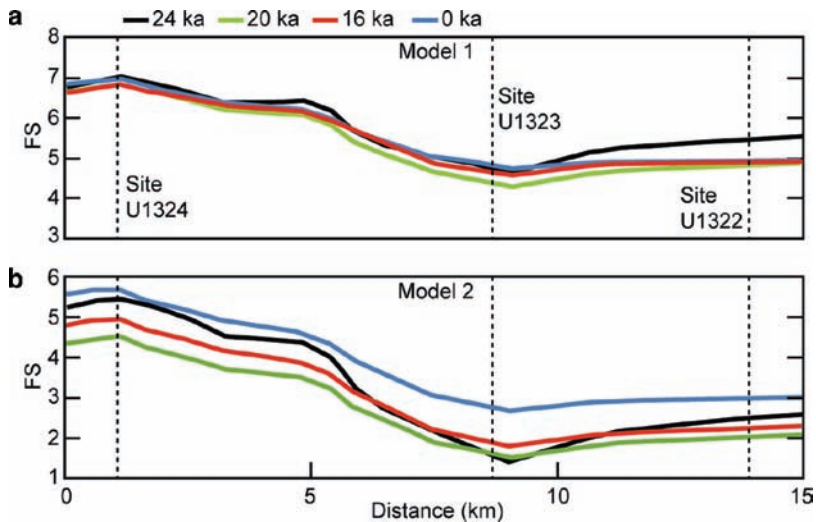
Fig. 4 Factor of safety (FS) along the MTD basal boundary (red surface Fig. 1c) at 24, 20, 16, and 0 ka. Dashed lines locate Sites U1324, U1323, and U1322 (Fig. 1). (**a**) Predicted FS for Model 1 (Fig. 2) shows stable conditions (FS > 4) with minor temporal variation. (**b**) Predicted FS for Model 2 (Fig. 2) shows FS decrease toward 1.5; stability increases from 20 to 0 ka. FS scales differ between (**a**) and (**b**).

in the Ursa region (Fig. 1c). Quantitatively, our models did not simulate unstable conditions (FS < 1); we only predicted marginally stable conditions with FS ~1.5 during rapid overpressure generation (Fig. 4b). Additional decreases in FS could be induced by additional pressure sources. Potential pressure sources could be short periods of higher sedimentation that we have not simulated based on limited age data or increased pore pressure from seismic loading (Biscontin et al. 2004). Seismic acceleration due to local earthquakes can also contribute to destabilization of low angle, overpressured slopes (Strasser et al. 2007; ten Brink et al. 2009).

Earthquakes in the Gulf of Mexico are neither frequent nor large, however, M_w 4.6–5.8 earthquakes were observed in 2006 (Gangopadhyay and Sen 2008). These small earthquakes, potentially driven by stress differences due to mechanical properties of salt and basin sediments (Gangopadhyay and Sen 2008), could create seismic accelerations that decrease the marginally stable (FS < 1.5) Ursa sediments during periods of rapid sedimentation and rapid overpressure generation. The seismic accelerations necessary to decrease stability can be defined as a function of the magnitude of the earthquake and the proximity of the earthquake to the slope failure region (ten Brink et al. 2009). Preliminary models suggest that M_w ~5 earthquakes located less than 100 km from the Ursa region are necessary to initiate failure. Further research on the magnitude and distribution of Gulf of Mexico earthquakes is required to quantify the exact distance–magnitude relationships for earthquake-induced failure in the Ursa region.

5 Conclusions

Sedimentation-fluid flow models of the Ursa region predict that overpressure begins near the seafloor and increases to the top of the Blue unit. The magnitude of overpressure has varied through time, increasing rapidly when sedimentation increases and decreasing when sedimentation decreases. Lateral flow in the permeable sand and silt has also controlled the magnitude and distribution of overpressure. In the modern environment overpressure is decreasing because sedimentation rates are low. Over the past 65 ka high sedimentation rates at Site U1324 (average 9.3 mm/y) created overpressures that approach 2 MPa whereas the lower sedimentation rates (average 3.6 mm/y) at Site U1322 created overpressures reaching approximately 1 MPa. This overpressure gradient from Site U1324 to U1322 drives lateral fluid flow through permeable sand and silt in the Blue unit and the channel-levee deposits. Without the flow focusing effect, Site U1322 would have lower pressures than are observed and predicted.

The evolution of overpressure and flow focusing is a dominant control on stability of the Ursa region. From our infinite slope analysis, we predict stable conditions (FS > 1) from 65–0 ka. The minimum FS predicted (1.5) is controlled by the sedimentation history and lateral flow in permeable sand and silt. Without overpressure FS would exceed 12 at Ursa, thus overpressure provides a significant FS decrease. FS minima occur during periods with the highest sedimentation rates, which result in the greatest overpressure generation rate. FS is lowest on the east side of the Ursa region between Sites U1323 and U1322. These low FS values occur in a region of low sedimentation rates for the Ursa region, but they are influenced by higher sedimentation rates on the west side of the region and lateral transfer of fluids from the west (Site U1324) to the east through permeable layers. The silts in the channel-levee deposits play a key role in flow focusing and we predict that the boundary between the channel-levee silt and the overlying mud is consistently a low stability surface. This is consistent with the regionally extensive MTDs in the Ursa region occurring immediately above this boundary. The results of our simulations indicate that additional driving forces are required to initiate slope failure. These additional driving forces could be pressure generation or seismic accelerations. Pressure sources could be from extremely high sediment inputs beyond our age resolution. Seismic accelerations, created by salt tectonic earthquakes, could destabilize the slope through horizontal accelerations and overpressure generation.

References

Bethke, CM, Harrison, WJ, Upson, C, Altaner, SP (1988) Supercomputer analysis of sedimentary basins. Science 239:261–267, doi:10.1126/science.239.4837
Bethke, CM, Lee, M-K, Quinodoz, H, Kreiling, WN (1993) Basin Modeling with Basin2, A Guide to Using Basin2, B2plot, B2video, and B2view. University of Illinois, Urbana

Biscontin, B, Pestana, JM, Nadim, F (2004) Seismic triggering of submarine slides in soft cohesive, soil deposits, Mar Geol 203:341–354, doi:10.1016/S0025-3227(03)00314-1

Bishop AW (1955) The use of the slip circle in the stability analysis of earth slopes. Geotechnology 5:7–17

Dugan, B, Flemings, PB (2000) Overpressure and fluid flow in the New Jersey continental slope: Implications for slope failure and cold seeps. Sciences 289:288–291

Dugan, B, Flemings, PB (2002) Fluid flow and stability of the US continental slope offshore New Jersey from the Pleistocene to the present. Geofluids 2(2):137–146

Dugan, B, Germaine, JT (2008) Near-seafloor overpressure in the deepwater Mississippi Canyon, Northern Gulf of Mexico. Geophys Res Lett doi:10.1029/2007GL032275

Dugan, B, Germaine, JT (2009) Data Report: Strength Characteristics of Sediments from IODP Expedition 308, Sites U1322 and U1324, Proc. IODP 308. doi:10.2204/iodp.proc.308.210.2009

Flemings, PB, Behrmann, JH, John, CM, et al. (2006) Proceedings of the Integrated Ocean Drilling Program. Vol. 308, Ocean Drilling Program Management International, Inc., College Station, TX. doi:10.2204/iodp.proc.308.2006

Flemings, PB, Long, H., Dugan, B, et al. (2008) Pore pressure penetrometers document high overpressure near the seafloor where multiple submarine landslides have occurred on the continental slope, offshore Louisiana, Gulf of Mexico, Earth Planet Sci Lett 269:309–324, doi:10.1016/j.epsl.2007.12.005

Freeze, RA, Cherry, JA (1979) Groundwater. Prentice-Hall, Englewood Cliffs, NJ

Gangopadhyay, A, Sen, MK (2008) A possible mechanism for the spatial distribution of seismicity in northern Gulf of Mexico. Geophys J Int 175(3):1141–1153, doi:10.1111/j.1365-246X.2008.03952.x

Gibson RE (1958) The progress of consolidation in a clay layer increasing in thickness with time. Geotechnique 8:171–182

Hampton, MA, Lee, HJ, Locat, J (1996) Submarine landslides. Rev Geophys 34(1):33–59

Hubbert, MK, Rubey, WW (1959) Role of fluid pressure in the mechanics of overthrust faulting: Part I. Geol Soc Am Bull 70:115–166

Lambe, TW, Whitman, RV (1969) Soil Mechanics. Wiley, New York

Long, H (2007) Interpreting pore pressure in marine mudstones with pore pressure penetrometers, in situ data, and laboratory measurements. Ph.D. Thesis, Pennsylvania State University

Long, H, Flemings, PB, Germaine, JT, et al. (2008) Data report: Consolidation characteristics of sediments from IODP Expedition 308, Ursa Basin, Gulf of Mexico. Proc IODP 308. doi:10.2204/iodp.proc.308.204.2008

McAdoo, BG, Pratson, LF, Orange, DL (2000) Submarine landslide geomorphology, US continental slope. Mar Geol 169:103–136

Mello, UT, Karner, G, Anderson, RN (1994) A physical explanation for the positioning of the depth to the top of overpressure in shale-dominated sequences in the Gulf Coast basin, United States. J Geophys Res 99:2775–2789

Ostermeier, RM, Pelletier, JH, Winker, CD, et al. (2000) Dealing with shallow-water flow in the deepwater Gulf of Mexico. Proc Offshore Tech Conf 32:75–86

Rubey, WW, Hubbert, MK (1959) Overthrust belt in geosynclinal area of western Wyoming in light of fluid-pressure hypothesis: Part 2. Geol Soc Am Bull 70(2):167–205

Sawyer, DE, Flemings, PB, Shipp, C, Winker, C (2007) Seismic Geomorphology, Lithology, and Evolution of the Late Pleistocene Mars-Ursa Turbidite Region, Mississippi Canyon Area, Northern Gulf of Mexico. Am Assoc Petrol Geol Bull. 91(2):215–234, doi:10.1306/08290605190

Schneider, J, Flemings, PB, Dugan, B, et al. (2008) Porosity vs permeability behavior of shallow mudstones in the Ursa basin, deepwater Gulf of Mexico. Eos Trans Am Geophys Union 89(53):OS11A–1105

Stegmann, S, Strasser, M., Anselmetti, F, Kopf, A (2007) Geotechnical in situ characterization of subaquatic slopes: The role of pore pressure transients versus frictional strength in landslide initiation. Geophys Res Lett. 240:77–97 doi:10.1029/2006GL029122

Strasser, M, Stegmann, S, Bussmann, F, et al. (2007) Quantifying subaqueous slope stability during seismic shaking: Lake Lucerne as model for ocean margins. Mar Geol 240:77–97

ten Brink, US, Lee, HJ, Geist, EL, Twichell, DL (2009) Assessment of tsunami hazard to the U.S. East Coast using relationships between submarine landslides and earthquakes. Mar Geol. 264:65–73, doi:10.1016/j.margeo.2008.05.011

Urgeles, R, Locat, J, Dugan, B (2007) Recursive failure of the Gulf of Mexico continental slope: Timing and causes. In Lykousis, V, Sakellariou, D, Locat, J (eds) Adv in Natural and Technological Hazards Res 27: Submarine Mass Movements and Their Consequences: 207–219, Springer, Heidelberg

Winker, CD and Booth, JR (2000) Sedimentary dynamics of the salt-dominated continental slope, Gulf of Mexico: Integration of observations from the seafloor, near-surface, and deep subsurface. Deep-Water Reservoirs of the World: Proc. GCS SEPM 20:1059–1086

History of Pore Pressure Build Up and Slope Instability in Mud-Dominated Sediments of Ursa Basin, Gulf of Mexico Continental Slope

R. Urgeles, J. Locat, D.E. Sawyer, P.B. Flemings, B. Dugan, and N.T.T. Binh

Abstract The Ursa Basin, at ~1,000 m depth on the Gulf of Mexico continental slope, contains numerous Mass Transport Deposits (MTDs) of Pleistocene to Holocene age. IODP Expedition 308 drilled three sites through several of these MTDs and encompassing sediments. Logs, sedimentological and geotechnical data were collected at these sites and are used in this study for input to basin numerical models. The objective of this investigation was to understand how sedimentation history, margin architecture and sediment properties couple to control pore pressure build-up and slope instability at Ursa. Measurements of porosity and stress state indicate that fluid overpressure is similar at the different sites (in the range of 0.5–0.7) despite elevated differences in sedimentation rates. Modeling results indicate that this results from pore pressure being transferred from regions of higher to lower overburden along an underlying more permeable unit: the Blue Unit. Overpressure started to develop at ~53 ka, which induced a significant decrease in FoS from 45 ka, especially where overburden is lower.

R. Urgeles (✉)
Institute of Marine Sciences, Spanish National Research Council (CSIC)
e-mail: urgeles@icm.csic.es

J. Locat
Université Laval, Dept. of Geology and Geological Engineering, Québec G1K 7P4, QC, Canada

D.E. Sawyer and P.B. Flemings
University of Texas at Austin, Jackson School of Geosciences, 1 University Station C1100, Austin, TX 78712-0254, USA

B. Dugan
Rice University, Department of Earth Science, 6100 Main Street, Houston, Texas 77005, USA

N.T.T. Binh
Durham University, Department of Earth Sciences, Science Labs, Durham DH1 3LE, UK

1 Introduction

Pleistocene sedimentation in the Gulf of Mexico from the Mississippi River is characterized by rapid sedimentation upon a mobile salt substrate (Worrall and Snelson 1989). Offshore Texas and Western Louisiana, individual slope minibasins are surrounded by elevated salt highs (Pratson and Ryan 1994) producing a remarkable hummocky topography. This morphology is obscured in front of the Mississippi delta, where sedimentation has been very rapid, exceeding 25 m ky^{-1} (Expedition 308 Scientists 2005).

Ursa Basin (~150 km due south of New Orleans, Louisiana, USA) lies in ~1,000 m of water (Fig. 1). From bottom to top, the Pleistocene to Holocene sedimentary sequence in Ursa Basin consists of: (1) the lower Mississippi Canyon Blue Unit, a late Pleistocene, sand-dominated, "ponded fan" (Winker and Booth 2000; Sawyer et al., 2007), (2) a mud dominated channel-levee assemblage with dramatic along-strike variations in thickness and (3) a mud drape deposited during the last ~20 ky (Fig. 2; Flemings et al. 2006). The mudstone package, belonging to the eastern
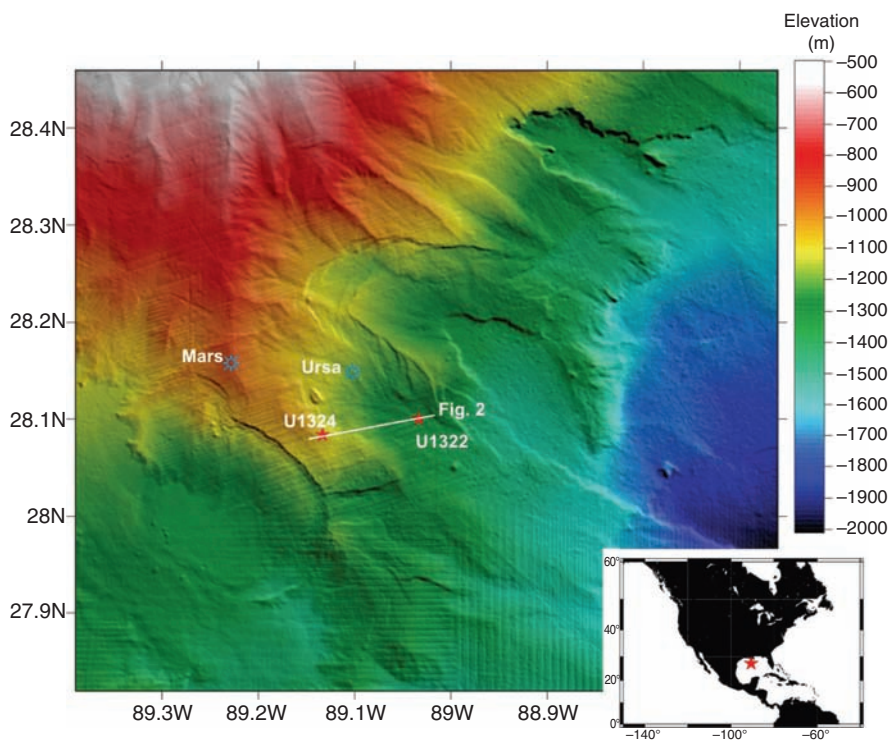
Fig. 1 Detailed swath bathymetry (US national archive for multibeam bathymetric data) shaded relief of the Mars Ridge (eastern levee of the Mississippi Canyon) showing location of Ursa drill sites U1322, U1324 and seismic line shown in Fig. 2. Profuse evidence of mass-wasting processes is evident. Inset shows location
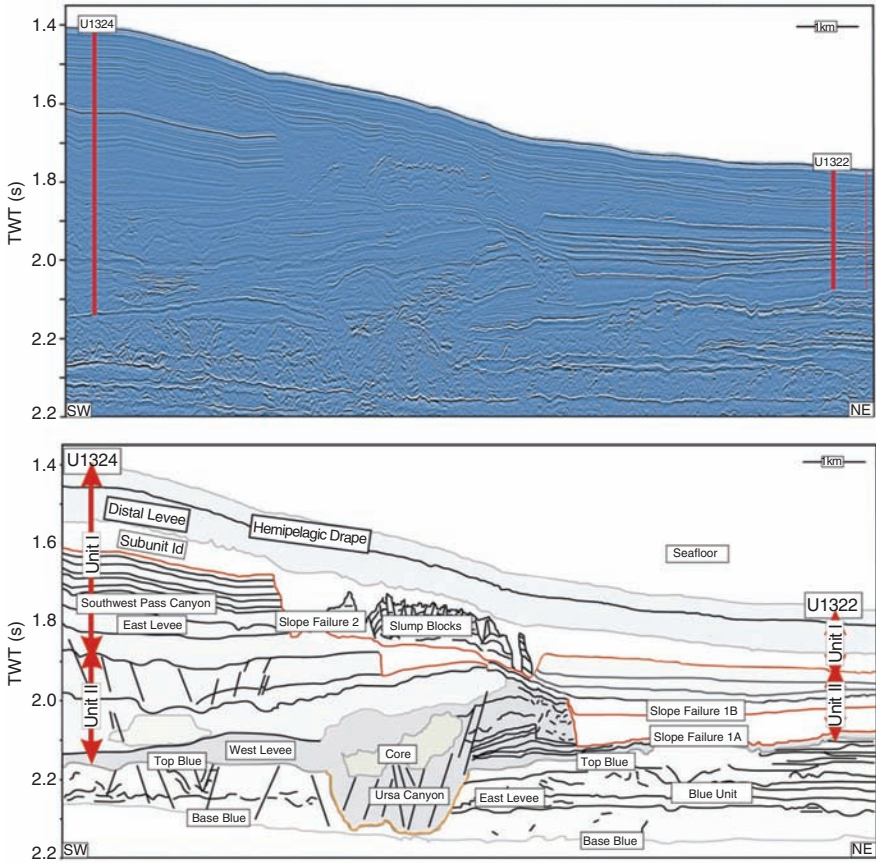
Fig. 2 Top. Seismic cross-section (for location see Fig. 1). Bottom. Interpreted cross-section. The sand-prone Blue Unit has been incised by a channel-levee complex and then overlain by a thick and heavily slumped hemipelagic mudstone wedge that thickens to the west (*left*). The Blue Unit sands are correlated to a distinct seismic facies. The thickness of the hemipelagic mudstone above the Blue Unit does not change significantly in the north-south direction. Major lithostratigraphic units identified during IODP Exp. 308 are labeled for correlation with Figs. 3–5. Seismic section reproduced with permission of Shell Exploration and Production Company (After Flemings et al. 2006)

margin of the larger channel-levee system of the Mississippi Canyon, has Mass Transport Deposits (MTDs) that record failure of the margin during the Pleistocene (Figs. 1 and 2; Flemings et al., 2006; Sawyer et al., 2007). Holocene failures have also been mapped all along the Gulf of Mexico, with the largest ones originating from Ursa Basin (Fig. 1; see also McAdoo et al. 2000). Ursa Basin is of economic interest because of its prolific oilfields, which are currently being exploited in the nearby tension leg platforms of Mars and Ursa. Geohazard characterization is therefore essential for safe offshore activities. For the purpose of this paper, we use data from two boreholes (Figs. 1–3) acquired during IODP expedition 308
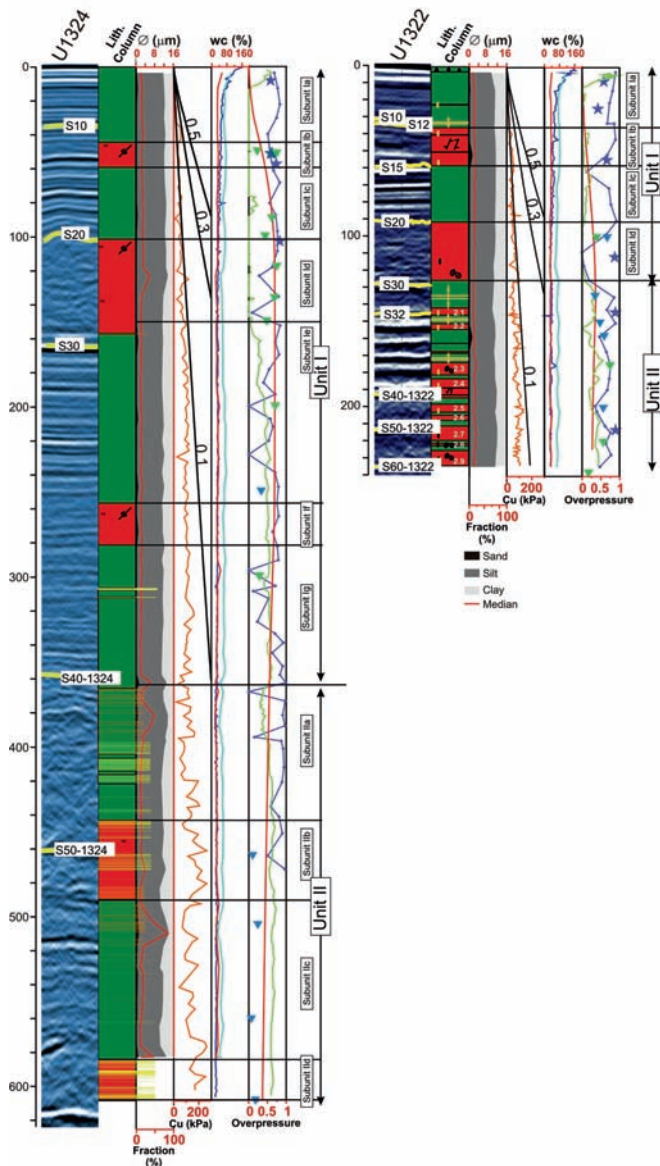
Fig. 3 Stripe of seismic profile with major reflectors labeled and lithologic log (MTDs in red, non-failed sediments in green) for drill sites U1324 and U1322 (see also Expedition 308 Scientists 2005). Logs of physical properties correspond from *left* to *right* to: (1) Median grain size (red line) and grain size fraction abundance; (2) Undrained shear strength as determined from shipboard motorized vane tests and trends for $Cu\cdot(\gamma'z)^{-1}$ ratios of 0.1, 0.3 and 0.5; (3) Plastic limit (red), liquid limit (cyan) and shipboard measured water content (blue) and (4) Overpressure determined from Skempton's (1957) eq. (blue line), porosity vs. stress relationships (green line with dots), preconsolidation pressures measured in oedometer tests, DVTPP (blue inverted triangles and T2P (green inverted triangles) piezometers and 1-D modeling results (red line)

(Expedition 308 Scientists 2005, Flemings et al. 2006), including Logging While Drilling (LWD), measurements of physical properties and geotechnical analysis performed on whole round samples.

The aim of this paper is to document how pressure, stress, and geology couple to control fluid migration on Ursa Basin, illuminate the controls on slope stability and understand the timing of sedimentation and slumping.

1.1 Methods

To accomplish the objectives stated above a laboratory testing program was established, which included grain size analysis using a Coulter LS100 laser diffractometer and Atterberg Limits determined using a British Fall cone device (Feng et al. 2001), isotropically consolidated undrained (CIU) triaxial tests, and uniaxial incremental loading tests (see also Urgeles et al. 2007). The data resulting from these tests are here discussed together with IODP Expedition 308 Shipboard data (Expedition 308 Scientists 2005; Flemings et al. 2006), including visual core descriptions, moisture and density data, vane shear and pocket penetrometer strength determinations and in-situ pore pressure measurements using the DVTPP and T2P piezoprobes (see Flemings et al. 2008; Long et al. 2008 for further details on these measurements). In this paper, pore pressure is most often described in terms of overpressure (λ), defined as:

$$\lambda = (P - P_h)/(\sigma_v - P_h) \tag{1}$$

where P is pore pressure P_h is hydrostatic pressure and σ_v is lithostatic or total stress. A value of 0 implies hydrostatic conditions, a value of 1 means pore pressure equals the lithostatic stress.

2-D margin simulations along the transect of Fig. 2 were carried using the Finite Element Software "BASIN" (Bitzer et al. 1996, 1999), which allows for stratigraphic, tectonic, hydrodynamic and thermal evolution to be modeled. In "BASIN" compaction and fluid flow are coupled through the consolidation equation and the nonlinear form of the equation of state for porosity, allowing non-equilibrium compaction and overpressuring to be calculated.

2 Results

In Ursa basin, Site U1324 (on the upslope part) was drilled to more than 600 mbsf and site U1322 (downslope) to about 250 mbsf (Fig. 2). The sediments drilled at these sites included several MTDs (5 at Site U1324 and 9 at U1322). On seismic reflection profiles the thicker MTDs are characterized by discontinuous and/or transparent to low amplitude reflections. MTDs show increased resistivity and density in logs, presumably due to transport-induced compaction, while folds, some with half-wavelengths of a meter or more, are apparent both in cores and logs.

Despite differences in visual aspect and physical properties the sediment composition shows no major differences between MTDs and non-failed deposits. Sediment grain size analyses indicate that at both sites the sediments are made of ~30% clay and ~70% silt, the mean grain size is about 4 microns, and these values remain fairly constant with depth (Fig. 3). The sediment plastic limit is at about 35%, while the liquid limit decreases from 70% to 55% in the upper 10 m of sediment column and then becomes relatively constant around the latter value (Fig. 3). The sediment water content moves from values at or higher than the liquid limit for the upper 20 mbsf and then gradually decreases to values close to the plastic limit at 100–125 mbsf. From that depth downhole the water content sticks to the plastic limit (IL =0%). On the Casagrande plot, samples from both sites plot on a line parallel and above the A-line identifying the sediment as clays of high plasticity.

The vane shear and pocket penetrometer data show similar values of undrained shear strength at equivalent depth for both drill sites, ranging from a few kPa near the seafloor to about 250 kPa at about 600 mbsf (Fig. 3). CIU triaxial tests (see Urgeles et al. 2007) were carried out on samples obtained from MTDs and non-failed deposits at Sites U1324 and U1322. Prior to shearing the samples were isotropically consolidated. Some of the samples were brought into the normally consolidated state others remained in the overconsolidated state prior to shearing. However, on the stress path plot the whole set of tests show relatively consistent results with a friction angle of 28° and little cohesion of around 7 kPa.

Using consolidation theory, overpressure was estimated from pre-consolidation pressures determined from incremental loading consolidation tests, and measurements of pore pressure using the DVTPP and T2P pressure probes (Fig. 3; see also Flemings et al. 2006, 2008; Long et al. 2008). Despite significant scatter, results appear to show overpressures in the range of 0.6 to 0.8, suggesting that non-equilibrium consolidation occurs in Ursa Basin (Fig. 3).

The consolidation tests results also provide parameters that can be used in basin and interstitial fluid flow modeling. These parameters include the initial porosity, hydraulic conductivity and specific storage (see Table 1 and Fig. 4). Consolidation tests were performed in sediments of the Southwest Pass Canyon Formation and hemipelagic sediments above (corresponding to Lithostratigraphic Units I and II in the cores; see Fig. 2 for equivalence). Unfortunately, no samples could be retrieved

Table 1 Parameters for basin and fluid flow modeling

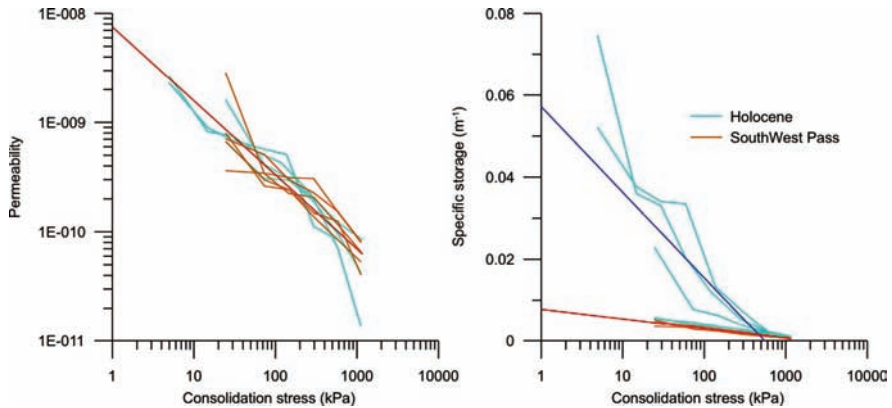|	Recent (%)	Upper SW Pass Canyon Fm. (%)	Lower SW Pass Canyon Fm. (%)	Ursa Canyon Fm. (%)	Blue unit (%)	Initial porosity (%)	Initial specific storage (m^{-1})	Grain density (kg/m^3)	Hydraulic conductivity (m/s)
Sand	0	0	0	10 (Core 40)	70	60	0.001	2,650	1×10^{-8}
Silt	0	0	20	30 (Core 30)	20	70	0.004	2,650	5×10^{-8}
Hemipelagic drape	100	0	0	0 (Core 40)	0	80	0.09	2,650	3×10^{-9}
SW Pass Canyon Fm.	0	100	80	60 (Core 30)	10	75	0.07	2,650	3×10^{-9}

Fig. 4 Permeability and specific storage vs. effective stress derived from incremental loading consolidation experiments used to derive the set of initial parameters for 2-D basin modeling within "BASIN". For location of experiments see Fig. 3

from the Blue Unit and central sandier part of the Ursa Canyon, as drilling within these formations implied a high risk for shallow water flow sands. Parameters for Sand and Silt which, according to industry well-log data (Sawyer et al. 2007) are a significant constituent of the Blue Unit and core of the Ursa Canyon are taken from the literature (Table 1; Reed et al. 2002).

3 Discussion

As shown above, overpressure estimates and measurements performed in various ways, indicate that an overpressure of 0.6–0.8 is present in Ursa Basin (Fig. 3; see Flemings et al. 2006; Long et al. 2008). Despite the significant scatter observed in these estimates and measurements, all data suggest that similar overpressure exists at Sites U1324 and U1322. 1-D modeling results however indicate that given the sedimentation rates at both sites, which are much higher at Site U1324 than at U1322, there should be a significantly higher overpressure at Site U1324 (Fig. 3). Mean sedimentation rates at Site U1324 are 9.6 m/ky with peaks exceeding 25 m/ky, while at site U1322 mean sedimentation rates are 3.5 m/ky with peaks at 16 m/ky (Expedition 308 Scientists 2005). According to 1-D modeling results, these sedimentation rates imply that overpressure should be around 0.8 at Site U1324 and only around 0.2 at U1322 (Fig. 3). Using the 2-D modeling software "BASIN" the margin stratigraphic evolution and the resulting interstitial fluid flow pattern and overpressure generation can be better understood (Fig. 5). For this experiment initial and boundary conditions are: (1) no flow occurs at the basement and model sides, (2) initial conditions are hydrostatic, (3) no subsidence occurs and (4) the initial (decompacted) thickness of the various formations can be estimated from van Hinte's (1978) equation:
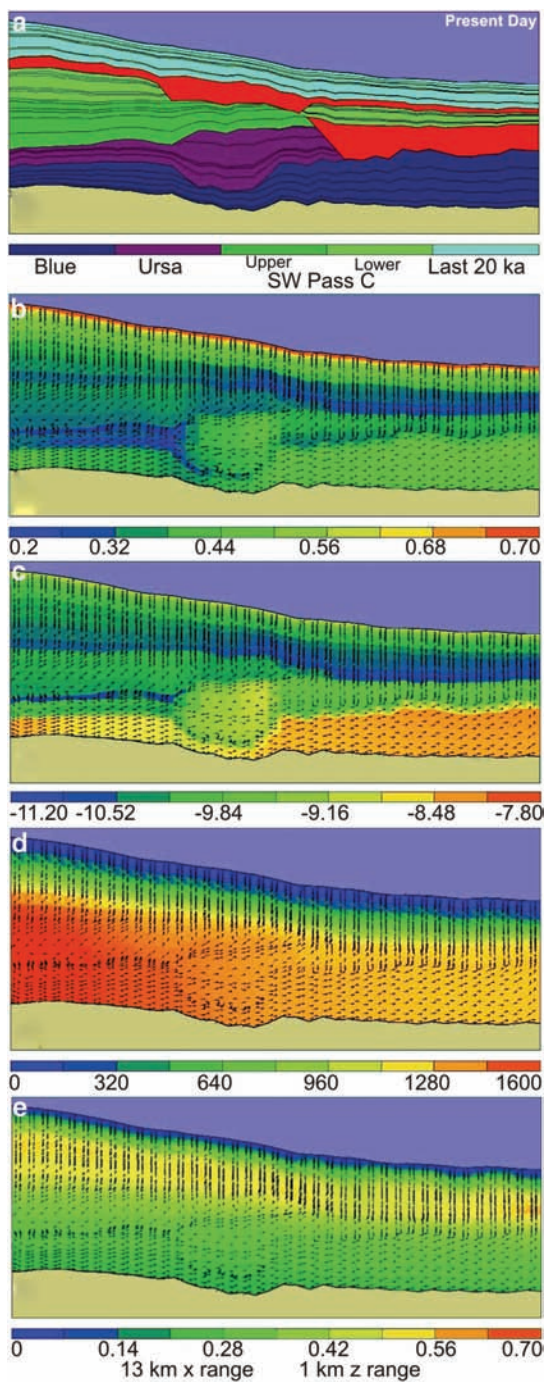
Fig. 5 Margin stratigraphic and hydrodynamic modeling with "BASIN" at final simulated present-day conditions. (a) Margin stratigraphy (red MTDs) according to seismic profile depicted in Fig. 2. (b) Fractional porosity. (c) Log hydraulic conductivity (m/s). (d) Excess pore pressure (kPa). (e) Overpressure (λ)

$$T_0 = \frac{(1-\Phi_N)T_N}{(1-\Phi_0)} \qquad (2)$$

where φ_N, T_N are the present-day porosity and thickness (assuming v_p: 1,600 m/s; Flemings et al. 2005) and φ_0, T_0 are the original porosity and thickness. MTDs removed/added little overburden because the failed masses did not evacuate the failing zone and therefore have little to no effect in both 1-D and 2-D simulations.

The margin stratigraphic evolution is modeled since deposition of the Blue Unit, roughly 100 ka ago, along the seismic line shown in Fig. 2. Margin modeling is performed using a set of initial sediment types and their corresponding hydraulic conductivity and specific storage shown in Table 1. Each stratigraphic unit is made of a mixture of the different sediment types (Table 1), which result in averaged initial physical properties (see Bitzer et al. 1999 for further details). The "BASIN" simulations show that, as it should be expected, porosity and hydraulic conductivity decrease with time and depth along the section (Fig. 5b, c). However, high hydraulic conductivities ~$10^{-8.5}$ m/s remain in the sandier Blue Unit and in the core of the Ursa Canyon after the whole sedimentary package has been deposited. The hydraulic conductivities on the muddy sediment wedge above the Blue Unit are between 1 to almost 3 orders of magnitude lower (Fig. 5c). The modeled porosity and hydraulic conductivities result in fluid flow from West to East along the Blue Unit and Ursa Canyon and a vertically upward migration on the overlying muddy formations. The model also shows that pore pressures above hydrostatic started to develop at ~53 ka with onset of the Southwest Pass Canyon sedimentation, which deposited more clayey material (Fig. 5d). Due to the higher sedimentation rates excess pore pressure develops further near Site U1324, where the overburden is thicker. The more permeable nature of the lower Blue Unit allows fluid to flow laterally from Site U1324 to U1322 inducing higher excess pore pressures at this Site than should be expected given the sedimentation rate at this location (Fig. 5). This effect is better seen in terms of overpressure (λ). Figure 5e clearly shows similar, or sometimes higher, overpressure at Site U1322 compared to Site U1324. The 2-D simulation results agree better with the estimated and observed overpressures at both Sites. It also shows that the higher overpressures concentrate within the depth range of 100 to 200–350 mbsf.

Overpressure build up in Ursa Basin has probably played an important role in slope failure generation. Major additional controls in slope stability in Ursa Basin include variations in slope angle due to depositional processes and salt tectonics. Presently the regional slope in Ursa Basin does not exceeds 2°, and local slopes rarely exceed 4°. The Gulf of Mexico is an area where large seismic ground motions are not probable (Petersen et al. 2008). No large earthquakes have been reported recently with the exception of two $5 < M_w < 6$ earthquakes (Preliminary Determination of Earthquakes (PDE) Catalog 1973–present). Recent studies, suggest however that these are a result of shallow slippage (most probably large-scale gravitational sliding) rather than deep-seated tectonic processes (Nettles 2007, Dewey and Dellinger 2008), and therefore we will not consider seismic ground motions as potential triggering mechanism.

The main characteristics of MTDs in Ursa Basin are: (a) they occur on a more or less uniform slope, (b) the failure planes are subparallel to the seafloor and (c) the

length of the failure surfaces is large compared to the failure thickness (Figs. 1 and 2). Therefore, it is considered that an "infinite slope" approach provides a first approximation to the margin stability. Urgeles et al. (2007) show the results of a drained slope stability evaluation in Ursa Basin using the parameters identified from the CIU triaxial tests (c = 7 kPa, $\Phi = 28°$). Urgeles et al. (2007) show that for the range of overpressures observed in Ursa Basin and the present regional slope gradient, the slope can be considered safe. For failure to occur overpressure values close to 0.9 are needed, or slope gradients need to approach angles between 7.5 an 11° depending on the overpressure. Using undrained shear strengths the slope appears in the stable to metastable conditions (Urgeles et al. 2007).

Using the output from the overpressure simulations it is also possible to investigate the margin stability conditions during the last 100 ky. Figure 6a shows that the margin remained relatively stable with a Factor of Safety (FoS) ~6 until ~45 ka, and then an overall decrease in margin stability occurred. Despite several oscillations, the
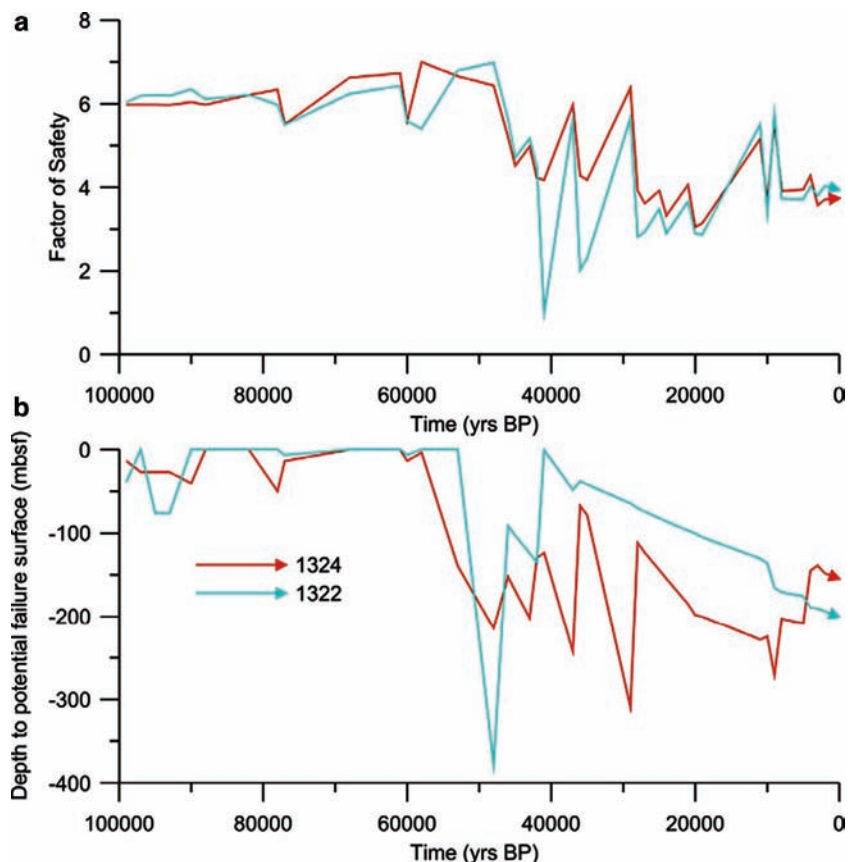
Fig. 6 (**a**) Ursa Basin FoS at Sites U1324 and U1322 using the output from overpressure (λ) simulations performed with "BASIN". (**b**) Depth to the potential failure surface (depth of lowest FoS) at Sites U1324 and U1322

margin's FoS (Fig. 6a) has remained lower at the site of lower overburden (Site U1322) until about 20 ka, in agreement with core evidence showing that most failures are found at this Site. From 20 ka onwards the FoS became similar for both sites. Using the output from the overpressure simulations it is also possible to investigate the depth at which failure could most likely have occurred. Figure 6b indicates that the reduction in the margin's FoS was accompanied by an increase in thickness of the potentially unstable sedimentary package. It is also found that the potentially unstable sediment package is thinner at Site U1322 than at Site U1324 in agreement with the thicker MTD found at the latter site (Fig. 6b).

4 Conclusions

Physical property data and geotechnical measurements indicate that sediments from Ursa Basin are largely overpressured, inducing effective stresses that are only 25% of those that would exist under hydrostatic conditions. At Sites U1324 and U1322 similar overpressures are found despite large differences in sedimentation rates. Modeling simulations show that this most probably results from excess pore pressure being laterally transferred through the Blue Unit from places of high to low overburden. The highest overpressures concentrate in the depth range between ~50 and 250–350 mbsf. 2-D modeling results indicate that pore pressure started to build up with onset of deposition of the South West Pass Canyon Formation ~53 ka ago.

Basic regional slope stability analysis suggests that the slope is stable under current conditions. For the slope to fail it is necessary that the overpressure exceeds a value of ~0.9 or the regional slope steepens above 7°. Using the output from the margin stratigraphic and hydrodynamic evolution it is found that the margin's fluid flow pattern induced lower stability at the foot of the slope where sedimentation rates are lower. The margin stability reduced significantly from ~45 ka onwards. The decrease in margin's stability was accompanied by increased thickness of the potential failure package.

References

Bitzer K (1996) Modeling consolidation and fluid flow in sedimentary basins. Comput Geosci 22: 467–478

Bitzer K (1999) Two-dimensional simulation of clastic and carbonatesedimentation, consolidation, subsidence, fluid flow, heat flow and solute transport during the formation of sedimentary basins. Comput Geosci 25: 431–447

Dewey JW, Dellinger JA (2008) Location of the Green Canyon Event (Offshore Southern Louisiana) of February 10, 2006. U. S. Geol Surv Open-File Rep 2008–1184

Expedition 308 Scientists (2005) Gulf of Mexico hydrogeology—overpressure and fluid flow processes in the deepwater Gulf of Mexico: slope stability, seeps, and shallow-water flow. Integrat Ocean Drill Prog Prel Rept 308. doi:10.2204/iodp.pr.308.2005

Feng T-W (2001) A linear log d–log w model for the determination of consistency limits of soils. Can Geotech J 38: 1335–1342

Flemings PB, Behrmann JH, John CM, Expedition 308 Scientists (2006) Proc Integr Ocean Drill Prog 308. IODP Management International, Inc., College Station TX, doi:10.2204/iodp.proc.308.2006

Flemings PB, Long H, Dugan B, et al. (2008) Pore pressure penetrometers document high over-pressure near the seafloor where multiple submarine landslides have occurred on the continental slope, offshore Louisiana, Gulf of Mexico. Earth Planet Sci Lett 269: 309–325

Long H, Flemings PB, Dugan B, et al. (2008) Data report: penetrometer measurements of in situ temperature and pressure, IODP Expedition 308. In: Flemings, P.B., Behrmann, J.H., John, C.M., and the Expedition 308 Scientists (eds.), Proceedings of Integration Ocean Drilling Program 308: College Station, TX doi:10.2204/iodp.proc.308. 203.2008

McAdoo BG, Pratson LF, Orange DL (2000) Submarine landslide geomorphology, US continental slope. Mar Geol 169: 103–136

National Oceanic and Atmospheric Administration (2009) US national archive for multibeam bathymetric data. http://www.ngdc.noaa.gov/mgg/bathymetry. Accessed 15 April 2009

Nettles M (2007) Analysis of the 10 February 2006 Gulf of Mexico Earthquake from Global and Regional Seismic Data: 2007 Offshore Tech Conf abs 19099

Petersen MD, Frankel AD, Harmsen SC, et al. (2008) Documentation for the 2008 Update of the United States National Seismic Hazard Maps: U.S. Geol Surv Open-File Rep 2008–1128

Pratson LF, Ryan WBF (1994) Pliocene to Recent infilling and subsidence of intraslope basins offshore Louisiana. Am Assoc Pet Geol Bull 78: 1483–1506

Reed AH, Briggs KB, Lavoie DL (2002) Porometric properties of Siliciclastic Marine Sand: a comparison of traditional Laboratory Measurements with image analysis and effective medium modeling. IEEE J Ocean Eng 27: 581–592

Sawyer DE, Flemings PB, Shipp C, et al. (2007) Seismic geomorphology, lithology, and evolution of the late Pleistocene Mars-Ursa Turbidite region, Mississippi Canyon Area, Northern Gulf of Mexico. Am Assoc Pet Geol Bull 91: 215–234

Skempton AW (1957) Discussion: the planning and design of the new Hong Kong airport. Proc Inst of Civil Eng 7: 305–307

Urgeles R, Locat J, Dugan B (2007) Recursive failure of the Gulf of Mexico continental slope: Timing and causes. In: Lykoussis V, Sakellariou D, Locat J (eds.), Submarine Mass Movements and Their Consequences. Springer, Dordrecht

U.S. Geological Survey (2009) Preliminary Determination of Earthquakes (PDE) Catalog (1973–present). http://www.neic.cr.usgs.gov. Accessed 15 April 2009

van Hinte JE (1978) Geohistory analysis—application of micropaleontology in exploration geology. Am Assoc Pet Geol Bull 62: 201–222

Winker CD, Booth JR (2000) Sedimentary dynamics of the salt-dominated continental slope, Gulf of Mexico: integration of observations from the seafloor, near-surface, and deep subsurface. Deep-Water Reservoirs of the World: Proc GCSSEPM 20th An Res Conf, pp. 1059–1086

Worrall DM, Snelson S (1989) Evolution of the northern Gulf of Mexico, with emphasis on Cenozoic growth faulting and the role of salt. In: Bally AW, Paler AR (eds.), The Geology of North America—An Overview (Vol A). Geological Society America, Boulder, CO

How Does Fluid Inflow Geometry Control Slope Destabilization?

I. Kock and K. Huhn

Abstract Destabilization of submarine slopes and initiation of submarine mass wasting events depend on numerous factors e.g. transient rapid pore pressure changes due to earthquake shaking, fast sediment accumulation, ground water pumping or mineral dehydration to name a few. The major goal of our work is the quantitative analysis of how local pore pressure changes affect the destabilization of stable slope sediments. Here, we report on how the location and extent of fluid inflow within undisturbed slope sediments affect the onset of destabilization. We developed a 2D numerical slope model utilizing a new model approach. We combine a granular model which simulates a sediment package with a gridded fluid flow model. Our results indicate that the entry point of fluid flow greatly changes the location of destabilization. Failure zones of mass movements develop at different places, both vertically and laterally as a function of fluid flow input. Even with a simplified model setup we were able to identify three different destabilization scenarios.

Keywords Submarine landslide • discrete element model • fluid flow

1 Introduction

Large scale sediment mass-transport processes occur in very different geological settings, for example passive continental margins and volcanic slopes, whereas diffuse and smaller scale mass movements are more commonly found at accretionary wedges (McAdoo and Watts 2004). Initiation of submarine mass wasting events

I. Kock (✉) and K. Huhn
MARUM – Center for Marine Environmental Sciences, University of Bremen,
PO box 330 440, D-28334, Bremen, Germany
e-mail: ikock@uni-bremen.de

depend on numerous short and long term factors, for example oversteepening, seismic loading and fast sediment accumulation to name a few (Sultan et al. 2004). These factors can lead to fluid flow and transient pore pressure changes. Thus, effective stress is reduced and instabilities on the slope can occur (Behrmann et al. 2006; Dugan and Flemmings 2000; Flemmings et al. 2008).

In-situ pore pressure measurements (Flemmings et al. 2008; Stegmann et al. 2007) confirm this theoretical model. Furthermore, many laboratory and associated numerical studies (Biscontin et al. 2004; Sultan et al. 2004) have investigated this effect. Large scale numerical slope models link slope failure and slide dynamics to pore pressure changes and are able to reproduce specific slides quite well, such as the Storrega slide (Kvalstad et al. 2005). Additionally, infinite slope stability simulations implementing pore pressure changes can be used to assess past and present slope stability (Dugan and Flemmings 2002). However, in finite element models a failure plane has to be predefined by incorporating a mechanically weak layer, which limits the model interpretation significantly.

Our approach is an effort to resolve this problem. We combine two modeling approaches: (i) a simple eulerian fluid flow model to calculate fluid pathways and pressure distribution and (ii) a granular slope model based on the Discrete Element Method to simulate sediment mechanical behavior and mass wasting processes. Our goal is to analyze the onset of the slope's destabilization in relation to fluid flow geometry and position. In addition, we will test the potential of such models to investigate fluid/sediment interaction on a large scale level.

2   Method and Model

2.1   Discrete Element Method

The Discrete Element Method was developed by Cundall and Strack (1978, 1979) and has been used for the investigation of microscopic (Abe and Mair 2005; Cheng et al. 2004; Kock and Huhn 2007a) as well as macroscopic (Campbell et al. 1995) geologic processes. The method is based upon a granular modeling approach. Hence, materials are built up by an assembly of spherical shaped particles. These particles interact according to simple physical contact laws at their respective contacts. Forces and moments between them are calculated. Resulting particle motions are applied and their respective positions are updated which leads to a new particle configuration where the calculation cycle begins again. For more details see Cundall (1987, 1989), Cundall and Strack (1978, 1979, 1983) and Cundall and Hart (1989).

We use a commercial implementation of the code, PFC2D by Itasca, Inc. (Itasca 2004). In our model the deformation at the particle scale obeys a Coulomb-like friction law in accordance to crustal material behavior in nature. Particle fracture is not allowed.

2.2 Fluid Coupling

PFC2D provides a fluid coupling scheme (Itasca 2004), which solves the continuity and Navier–Stokes equations in Eulerian Cartesian coordinates. This scheme is based upon an approach by Tsujii et al. (1993) and has for example been successfully used to model liquefaction of granular soils (Zeghal and El Shamy 2008). Pressure and velocity are calculated for each grid cell. Hence, grid size has to be defined in respect to the smallest particle diameter, because the presence of DEM particles is considered in each cell. Thus, porosity is calculated for each cell separately.

Forces caused by fluid flow are applied to each particle, whose motions are accordingly modified. In turn, resulting body forces from the particles' motion (e.g. from settling) are added to the fluid equations.

2.3 Model Setup

The model is a simplified slope with an extension of 10 km and a height of approx. 1,730 m which corresponds to a slope angle of 10° (Fig. 1, Table 1). This value
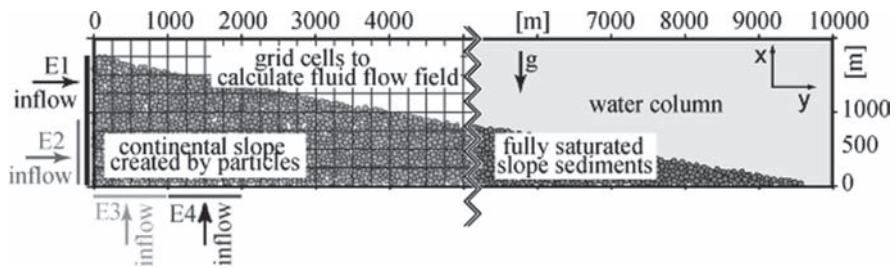
Fig. 1 Sketch of model setup. *Left side*: Fluid grid, particles and inflow locations. *Right side*: Water column and saturated slope sediments

Table 1 Properties used in discrete element model

Slope model	Property
Width (m)	10,000
Height (m)	1,736
Resolution	19,350 particles
Particle radii (m)	25, 37.5, 50, 62.5, 75
Friction micro/macro (peak)	0.5/0.34
Particle density (kg/m³)	2,500
Fluid model	Property
Width (m)	10,000
Height (m)	2,000
Resolution	50 × 10 cells
Cell size (m)	200 × 200
Fluid density (kg/m³)	1,000
Fluid viscosity (Pas)	1 e^{-3}

represents an end member of continental slope angles (O'Grady et al. 2000). However, the major aim of this study is to test the feasibility of this model approach.

The complete slope consists of 19,350 particles with varying radii where 3,870 particles exist for each radius (see Table 1). These particles are created randomly in the defined slope area. Gravity is set to 9.81 m/s² and particles are allowed to settle after generation creating the wedge shaped geometry with a nearly plane surface. Since all particles' properties are identical, no stratification exists after settling.

The properties of the particle assemblage are defined in accordance to generate natural slope sediments (Huhn et al. 2006) by assigning microproperties for all particles, e.g. particle friction and density (Table 1). Due to a 2D effect (Hazzard and Mair 2003), macroscopic peak friction for the whole particle assembly is ~0.34 and thus smaller than single particle friction, but well in the range of observed friction data for submarine landslides (Kopf et al. 2007)

The grid simulating the fluid extends over 10 km laterally and 2 km vertically to cover the whole slope and the water column (Fig. 1). Hence, in the slope region fully saturated sediments are simulated whereas the other part represents the pure water column. The upper boundary is on sea level height where pressure is set to zero. Due to gravity, pressure within the fluid increases with depth. The fluid is modeled on a rectangular 50×10 grid with 200×200 m cell size. On average, approximately 50 particles fit into one cell. Density and viscosity of the fluid are set to 1,000 kg/m³ and 1 e⁻³Pas, respectively, for this first test series.

2.4 Modeling Scheme and Measurements

We conducted a suite of four numerical experiments, subsequently called E1 to E4, where we varied only the geometry of the incoming fluid flow (Fig. 1). All other parameters were kept constant between model runs. In addition, benchmark tests were conducted where the effect of different initial particle packing was examined (e.g. with model E4, see Results section).

In the initial state, fluid flow in and out of the model as well as all particle velocities are close to zero. The left, right and lower boundaries are initially impermeable. Initial fluid velocities entering on the left boundary and right boundaries are set to zero.

In E1, fluid flow enters from the complete left boundary, where in E2 the fluid inflow occurs only from the bottom half of the left boundary (Fig. 2a, c). Fluid input is set to 0–1,000 m and to 1,000–2,000 m at the lower boundary in experiments E3 and E4, respectively.

The calculation timestep throughout the simulations is governed by the DEM and is very low (3.66 * 10⁻⁴ s). Thus, to achieve results in a reasonable amount of computing time, fluid velocity is scaled up to 1 m/s and simulations show results after only 1 h of inflow. However, fluid pathways and therewith location of slope destabilization are unaffected and fluid velocities are not taken into account in our
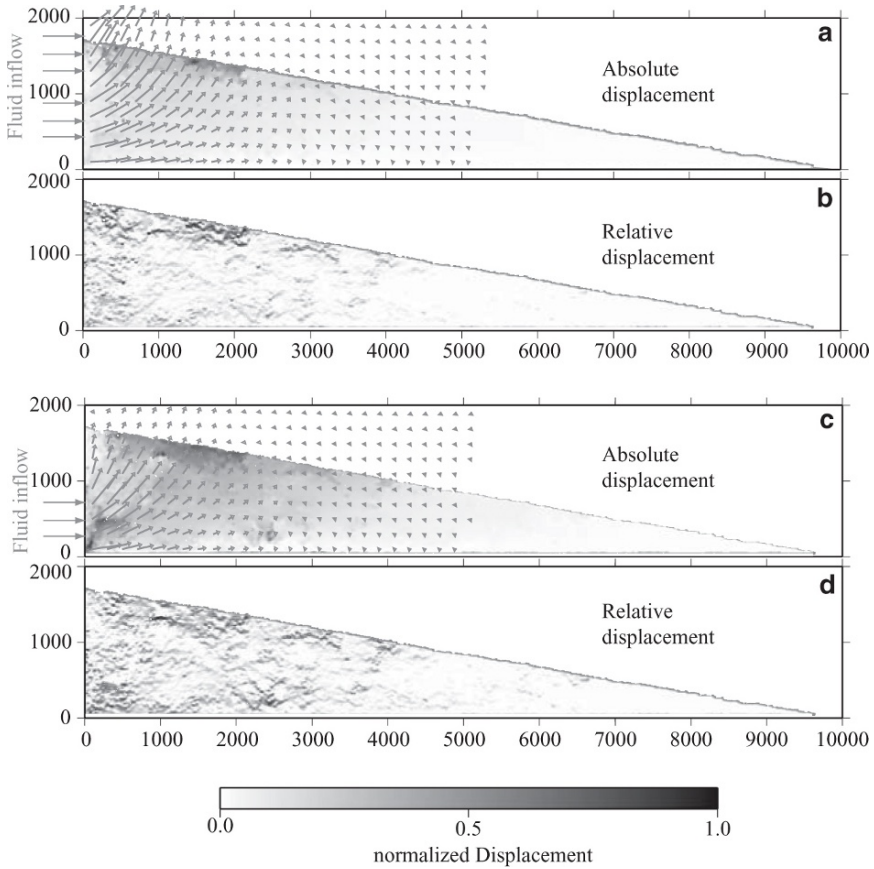
Fig. 2 **(a)** Fluid flow and particle movement for model E1. All values normalized. Black color indicates high displacement, white no displacement. Due to scaling, fluid flow vectors < 1*10-6 m/s are not displayed. **(b)** Relative displacement for model E1. Black colors indicate high relative displacement (shear planes) and white colors not relative displacement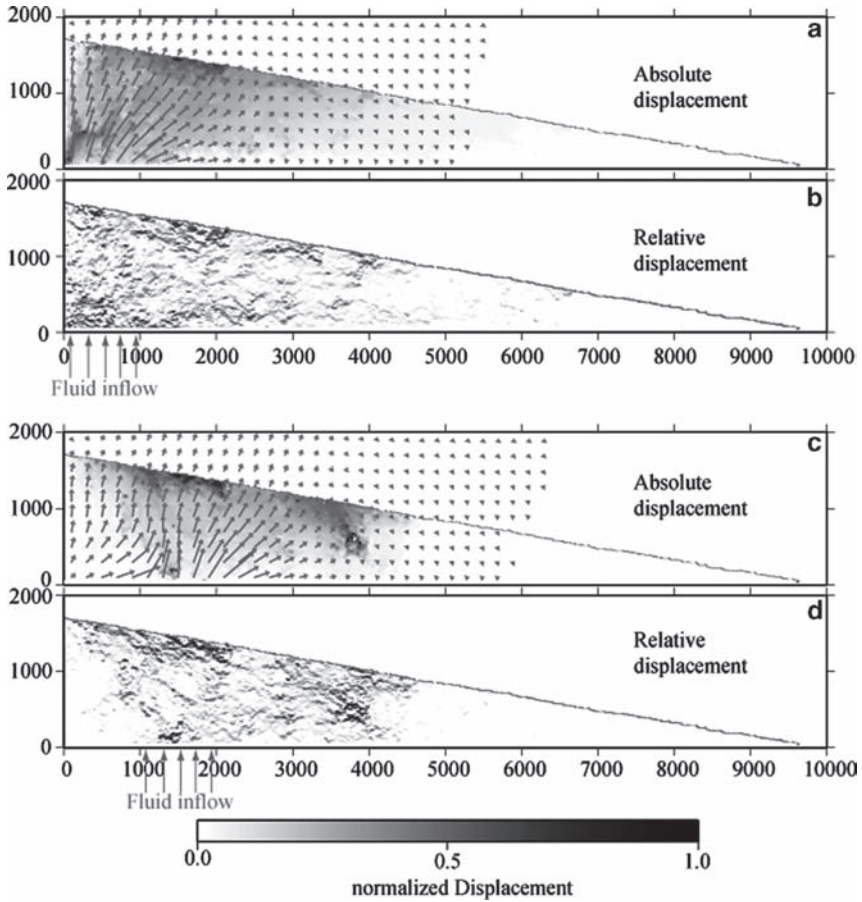. **(c)** Fluid flow and particle movement for model E2. Coloring same as in a). **(d)** Relative displacement for model E2, coloring same as in b)

interpretations. For each model run, fluid flow vectors and displacement vectors $\vec{v}$ were normalized with:

$$\vec{v}_{normalized} = \frac{\vec{v}_{measured} - \vec{v}_{min}}{\vec{v}_{max} - \vec{v}_{min}}$$

(1)

Hence, although many parameters are recorded during simulation we concentrate mainly on fluid flow vectors indicating fluid pathways and on particle displacement particularly along the slope surface. Both are monitored continuously.

These data are then gridded and displayed with the software Generic Mapping Tools (Wessel and Smith 1991). Furthermore, the gradient of displacement is computed with GMT. Thus, relative displacement can be made visible. High relative displacement indicates shear zones and failure planes (Kock and Huhn 2007b; Morgan and Boettcher 1999).

3   Results

The fluid flow vectors in model E1 which enter from the left side are directed towards the slope surface within the first 2,000 m (Fig. 2a). At a lateral distance greater than 5,000 m fluid flow is extremely small compared to input (<10⁻⁶ m/s), so that no normalized values could displayed. Particle movement is strongest at the upper part of the slope, approximately at a distance of 1,700–2,000 m from the left boundary. With increasing sediment depth, particle displacement decreases, most of the movement is concentrated on the top 50–100 m. Greatest relative displacement in terms of shear zones and shear planes mainly exist at these locations (Fig. 2b). Some more shear planes are also found at the fluid entry and approximately at 3,000 m lateral distance on the surface of the slope.

In model E2, fluid flow vectors also are turned towards the surface after entering the sediment (Fig. 2c). However, at the sediment/water boundary fluid vectors are almost vertically inclined with respect to the sediment surface. Interestingly, the location of greatest particle movement is comparable to model E1. Greatest movement occurs between 500 and 2,000 m lateral distance on the slope surface (Fig. 2c). In this case though, displacements reach further into the sediment and the lateral extent is also greater (Fig. 2d). Locations of large particle movement coincide with maximum fluid flow to a high degree. Shear planes can be observed up to 4,000 m laterally and from top to bottom on the left boundary.

Results obtained for model E3 are very similar to model E2. Fluid vectors point almost straight to the sediment/water boundary, and are also close to orthogonal to the sediment surface (Fig. 3a). Thus, greatest particle movements occur between 500 to 2,000 m at the slope surface. Comparable with experiment E2, particle movement reaches far into the sediment. Shear planes exist mainly at the top slope, between 1,000 and 2,000 m lateral distance and reach into the sediment for ~200 m (Fig. 3b). Furthermore, shear planes can also be found deep into the sediment at the bottom boundary where the fluid enters the slope sediments.

Model E4 differs strongly from the previous settings. Fluid pathways at approximately 1,500 m lateral distance point almost vertically from the bottom boundary up to the sediment/water interface (Fig. 3c). At a greater distance of ~2,000 m, however, fluid flow vectors are directed further downslope. Consequently, greatest particle movement occurs at two locations. The first location is comparable to the previous models is located between 1,000–2,000 m laterally on the slope surface. The second location is situated downslope, between 3,000 and 4,000 m lateral distance on the slope surface. In between these two locations there is considerably less sediment movement. On both locations, movement reaches far into the sediment, in case of the second location movement increases with increasing depth. These results are mirrored by values for relative displacement (Fig. 3d). Two foci of shear plane development exist. The first is located upslope and close to the sediment surface whereas the second on is located downslope and well inside the slope. Additionally, shear planes also occur at the fluid entry location, in particular at 1,500 m lateral distance. To verify these observa-

Fig. 3 (**a**) Fluid flow and particle movement for model E3, coloring same as in Fig 2a). (**b**) Relative displacement for model E3, coloring same as in Fig 2b). (**c**) Fluid flow and particle movement for model E4. Coloring same as in (**a**). (**d**) Relative displacement for model E4, coloring same as in (**b**)

tions and to exclude the effect that initial particle positions govern displacement patterns, a control run of model E4 was conducted which in essence yielded the same results.

4 Discussion

The results presented above indicate that the position of fluid inflow affects the location of particle movement on a sediment slope. We interpret large particle movements as the onset of destabilization of the slope. Failure planes are indicated by high relative movement (e.g. Fig. 3d).

One controlling factor leading to focused particle movement is the redirection of fluid pathways after the fluid enters the system. The redirection of fluid flow is both a function of inflow position and overburden pressure. Due to the high pressure induced by the sediments upslope, fluid flow paths tend to be focused downslope. Although fluid flow is strongest directly at the junction left boundary/slope surface in model E1, most of the particle movement does not take place at this location, but further down the slope. Possibly the angle between fluid vectors out of the sediment and sediment surface plays a role, but clarification requires further experiments.

Remarkably, models E2 and E3 exhibit similar displacement patterns, although the origin of fluid flow is conceptually very different between these cases. However, near the sediment/water boundary fluid flow patterns are essentially the same, both in magnitude and direction, which explains the similarities in absolute and relative displacement.

The most interesting setting is E4, where two foci of displacement can be observed. These foci are largely the result of two fluid flow directions which control this setting: one vertical and one diagonal flow path. The fluid does not flow in the upslope direction, simply because overburden pressure is lower downslope. Consequently there exists a sharp boundary on the left side of the model where no sediment movement occurs.

Since we did not implement any fluid conduits or boundaries in terms of low or high permeability layers, the development of distinct locations of sediment movement in models E1 and E4 is quite unexpected. As stated above, this may be related to a favorable combination of fluid flow magnitude and angle at the sediment surface. This is also supported by the fact that the shear planes associated with these foci are relative shallow, with the notable exception of the rightmost focus in model E4, which lies deep into the sediment.

Conceptually, our models may be linked to different geological conditions. In principle, model E1 resembles a rapid sediment accumulation model (Dugan and Flemmings 2000), except that in our models an aquifer is not implemented. In model E2, inflow conditions are more similar to this location, since the inflow at the bottom left boundary could be attributed to a change in the sedimentation environment (e.g. glacial/interglacial). On the other hand, fluid inflow from the bottom may be linked to structural or sedimentological features further down at the basement. For example, different fluid input locations in models E3 and E4 could be the result of a fault ending just below the model boundary and which could serve as a conduit for fluids. Clearly, our model setup opens the possibility for specific case studies to investigate the above mentioned geologic settings and conditions. However, with our current simplified model setup, we are not simulating natural environments. Nevertheless, our results are transferable in principle to natural settings, but have to be further extended to fully capture a specific location.

5   Conclusion

In this paper, we combined two numerical model approaches successfully to study the onset of destabilization in relation to fluid inflow. We show that this model approach enables us to investigate this interplay. Despite many simplifications, this

study reveals mechanisms which are in accordance to theory and field observations. Hence, our results indicate that sediment movement focuses in different locations when fluid inflow location is changed (Fig. 4). We could identify three general scenarios: (i) Fluid inflow from the upslope boundary leads to concentrated movement on the upper slope (Fig. 4a). (ii) Fluid inflow from the bottom part of this boundary and from the bottom, but upslope side of the model leads to distributed movement throughout the upper slope reaching deep into the sediment (Fig. 4b). (iii) When fluid inflow is set to a region slightly further downslope two distinct foci of displacement can be observed (Fig. 4c).

Distributed or focused sediment movement occurs both in the absence of a high or low permeability layer which could have served as a mechanism to concentrate fluid flow into a specific direction. Despite using a simple model, different models may be linked to different geological processes, such as upslope rapid sediment accumulation for model E1 and for example fluid escape conditions for model E4.

With this study we could show that our combined model approach is in principle applicable to such a setting. Further work is in progress, especially to enhance the model with respect to more natural conditions, such as different permeabilities within the slope and realistic fluid flow velocities. Major goals are the investigation of complex ocean margins settings and the detailed kinematics of mass movements (Huhn and Kock 2008).
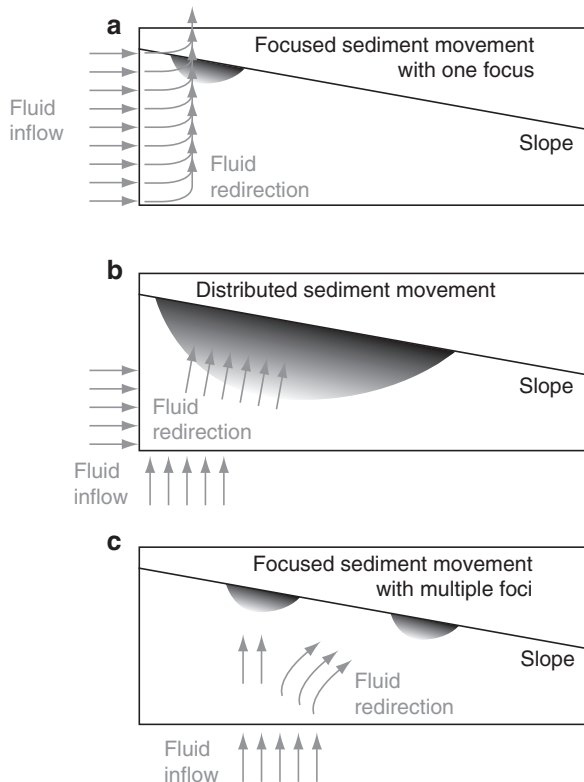
Fig. 4 Conceptual sketches. (**a**) Focused sediment movement with one focus. (**b**) Distributed sediment movement. (**c**) Focused sediment movement with multiple foci

References

Abe S and Mair K (2005) Grain fracture in 3D numerical simulations of granular shear. Geophys Res Lett 32 doi:10.1029/2004GL022123

Behrmann JH, Flemmings PB, John CM and scientists Ie (2006) Rapid Sedimentation, Overpressure, and Focused Fluid Flow, Gulf of Mexico Continental Margin. Sci Drill 3 doi:10.2204/iodp.sd.3.03.2006

Biscontin G, Pestana JM and Nadim F (2004) Seismic triggering of submarine slides in soft cohesive soil deposits. Mar Geol 203 doi:10.1016/S0025–3227(03)00314–1

Campbell CS, Cleary PW and Hopkins M (1995) Large-scale landslide simulations: Global deformation, velocities and basal friction. J Geophys Res 100 (B5): 8267–8283

Cheng YP, Bolton MD and Nakata Y (2004) Crushing and plastic deformation of soils simulated using DEM. Geotech 54:131–141

Cundall PA (1987) Distinct Element Models of Rock and Soil Structure. In: *Analytical and Computational Methods in engineering Rock Mechanics* (edited by E. T. Brown). Allen & Unwin, London

Cundall PA (1989) Numerical experiments on localization in frictional materials. Ingenieur-Archiv 59:148–159

Cundall PA and Strack ODL (1978) BALL - A program to model granular media using the distinct element method. In: *Technical Note, Advanced Technology Group*. Dames and Moore, London

Cundall PA and Strack ODL (1979) A discrete numerical model for granular assemblies. Géotechnology 29:47–65

Cundall PA and Strack ODL (1983) Modeling of microscopic mechanisms in granular material. In: *Mechanics of Granular Materials: New Models and Constitutive Relations* (edited by Jenkins JT, Satake M). Elsevier Science Amsterdam

Cundall PA and Hart RD (1989) Numerical Modeling of Discontinua. In: *Proceedings, 1st U.S. Conference on Discrete Element Method* (edited by Mustoe GGW, Henriksen M, and Huttelmaier H-P), CSM Press, Golden, CO

Dugan B and Flemmings PB (2000) Overpressure and fluid flow in the New Jersey continental slope: Implications for slope failure and cold seeps. Sciences 289 doi:10.1126/science.289.5477.288

Dugan B and Flemmings PB (2002) Fluid flow and stability on the US continental slope offshore New Jersey from the Pleistocene to the present. Geofluids 2:137–146

Flemmings PB, Long H, Dugan B, Germaine J, John CM, Behrmann JH, Sawyer D and Scientists I (2008) Pore pressure penetrometers document high overpressure near the seafloor where multiple submarine landslides have occurred on the continental slope, offshore Louisiana, Gulf of Mexico. Earth Planet Sci Lett 269 doi:10.1016/j.epsl.2007.12.005

Hazzard JF and Mair K (2003) The importance of the third dimension in granular shear. Geophys Res Lett 30:1708, doi:10.1029/2003GL017534

Huhn K and Kock I (2008) How does lateral variation in basal friction control the evolution of accretionary wedge as well as interactions between fault kinematics and surface processes? In: *Eos Trans. Am Geophs Union* 89 Fall Meet. Suppl., Abstract T23B-2018

Huhn K, Kock I and Kopf A (2006) Comparitive numerical and analogue shear box experiments and their implications for the mechanics along the failure plane of landslides. Nor J Geol 86:209–220

Itasca (2004) PFC 2D 3.1 Manual. Itasca Consulting Group, Minneapolis, MN

Kock I and Huhn K (2007a) Influence of particle shape on the frictional strength of sediments - a numerical case study. Sediment Geol 196:217–233 doi:10.1016/j.sedgeo.2006.07.011

Kock I and Huhn K (2007b) Numerical investigation of localization and micromechanics in a stratified soil specimen. J Struct Geol 29:1679–1694; doi:10.1016/j.jsg.2007.07.013

Kopf A, Stegmann S, Krastel S and Förster A (2007) Marine deep-water free-fall CPT measurements for landslide characterisation off Crete, Greece (Eastern Mediterranean Sea) Part 2: Initial data from the Western Cretan Sea. In: *Submarine Mass Movements and Their Consequences 3rd International Symposium* (edited by V. Lykousis, D. Sakellariou and J. Locat) **3**. Springer, Dordrecht, The Netherlands, 424

Kvalstad T-J, Andresen L, Forsberg CF, Berg K, Bryn P and Wangen M (2005) The Storegga slide: Evaluation of triggering sources and slide mechanics. Mar Petrol Geol 22:245–256

McAdoo BG and Watts P (2004) Tsunami hazard from submarine landslides on the Oregon continental slope. Mar Geol 203:235–245

Morgan JK and Boettcher MS (1999) Numerical simulations of granular shear zones using the distinct element method 1. Shear zone kinematics and the micromechanics of localization. J Geophys Res 104:2703–2719

O'Grady DB, Syvitski JPM, Pratson LF and Sarg JF (2000) Categorizing the morphologic variability of siliciclastic passive continental margins. Geol 28:207–210

Stegmann S, Strasser M, Anselmetti F and Kopf A (2007) Geotechnical in situ characterisation of subaquatic slopes: The role of pore pressure transients versus frictional strength in landslide initiation. Geophys. Res. Lett. 34 doi:10.1029/2006GL029122

Sultan N, Cochonat P, Canals M, Cattaneo A, Dennielou B, Haflidason H, Laberg JS, Long D, Mienert J, Trincardi F, Urgeles R, Vorren TO and Wilson C (2004) Triggering mechanisms of slope instability processes and sediment failures on continental margins: a geotechnical approach. Mar Geol 213 doi:10.1016/j.margeo.2004.10.011

Tsuji Y, Kawaguchi T and Tanaka T (1993) Discrete particle simulation of two-dimensional fluidized bed. Powd Technol 77:79–87 doi:10.1016/0032–5910(93)85010-7

Wessel P and Smith WHF (1991) Free software helps map and display data. EOS Trans. AGU 72 441

Zeghal M and El Shamy U (2008) Liquefaction of saturated loose and cemented granular soils. Powd Technol 184:254–265 doi:10.1016/j.powtec.2007.11.032

Geochemical Evidence for Groundwater-Charging of Slope Sediments: The Nice Airport 1979 Landslide and Tsunami Revisited

A.J. Kopf, S. Kasten, and J. Blees*

Abstract In October 1979, a period of heavy rainfall along the French Riviera was followed by the collapse of the Ligurian continental slope adjacent to the airport of Nice, France. A body of slope sediments, which was shortly beforehand affected by construction work south of the airport, was mobilized and traveled hundreds of kilometers downslope into the Var submarine canyon and, eventually, into the deep Ligurian basin. As a direct consequence, the construction was destroyed, seafloor cables were torn, and a small tsunami hit Antibes shortly after the failure. Hypotheses regarding the trigger mechanism include (i) vertical loading by construction of an embankment south of the airport, (ii) failure of a layer of sensitive clay within the slope sequence, and (iii) excess pore fluid pressures from charged aquifers in the underground. Over the previous decades, both the sensitive clay layers and the permeable sand and gravel layers were sampled to detect freshened waters. In 2007, the landslide scar and adjacent slopes were revisited for high-resolution seafloor mapping and systematic sampling. Results from half a dozen gravity and push cores in the shallow slope area reveal a limited zone of freshening (i.e. groundwater influence). A 100–250 m wide zone of the margin shows pore water salinities of 5–50% SW concentration and depletion in Cl, SO_4, but Cr enrichment, while cores east or west of the landslide scar show regular SW profiles. Most interestingly, the three cores inside the landslide scar hint towards a complex hydrological system with at least two sources for groundwater. The aquifer system also showed strong freshening after a period of several months without significant precipitation. This freshening implies that charged coarse-grained layers represent a permanent threat to the slope's stability, not just after periods of major rainfall such as in October 1979.

A.J. Kopf (✉)
University of Bremen, MARUM Research Centre, 28359 Bremen, Germany
e-mail: akopf@uni-bremen.de

S. Kasten and J. Blees
Alfred Wegener Institute for Polar and Marine Research,
27570 Bremerhaven, Germany

*Present address: University of Basel, 4056 Basel, Switzerland

1 Introduction

The sedimentary instability of submarine slopes represents a major geohazard and threatens coastal infrastructure both on- and offshore (Locat and Lee 2002). The Ligurian Margin, Southern France, represents an area of fluid-charged, metastable slope deposits, which today pose a geohazard to the French Riviera. This portion of the Mediterranean coastline receives millions of tourists each year and comprises valuable infrastructure all along. Understanding the preconditioning factors and governing trigger mechanisms for near-shore submarine slope instability is one of the key objectives to be addressed. The Nice airport area represents such a potentially unstable continental slope where factors favoring instability include seismicity, groundwater charging, presence of weak minerals, high sediment accumulation rates, anthropogenic impact by construction, and slope oversteepening. The hydrological system in the Var Valley, adjacent to the city of Nice, represents an alluvial aquifer recharged by seepage from the river Var and by subsurface infiltration from its foreland (Guglielmi and Mudry 1996). Water sources are the Alps as well as Provencal foreland series, comprising Mesozoic sedimentary rocks, Pliocene pudding stones (representing an old delta), overlain by Pleistocene gravel and Holocene clastic series of variable grain size in the Var Valley and river mouth (Dubar and Anthony 1995). Groundwater from those domains is geochemically distinctly different, and is migrating oceanwards (along permeable, coarse-grained, gently southward- dipping beds (Guglielmi 1993). Recent work by Guglielmi and Prieur (1997) has attested that subsurface pathways are rather complex and result in three areas of submarine fresh water seepage in the Nice airport area east of the Var river mouth.

In general, the anthropogenic impact on the Var River system in the twentieth century had a profound effect on its stability and increased the vulnerability to hazards such as floods, spill overs, and delta-front slope instability. Land reclamation for developments such as the Nice international air-port as well as industrial and administrative estate resulted in bed extraction of gravel and other deposits in the 1960s and 1970s (Anthony 2007). As a consequence of the narrowing and deepening of the Var channel, the average bed was lowered by approximately 10 m, so that the aquifer was lowered too (Guglielmi 1993). Most importantly, this did not only change the hydrological pathways, but resulted in saltwater intrusion in the Nice area and increasing risks of flood damage of the lower channel during periods of higher river discharge (e.g. during spring floods or the high-precipitation period in fall).

After such a period of heavy rain, a major submarine landslide ($\sim 8.7 \times 10^6$ m^2) affected the coastal system offshore Nice on the 16th of October 1979 and resulted in destruction of an embankment at the Nice airport (Fig. 1a, dashed line), a debris flow cutting two submarine cables tens of kilometers away from the sliding area

Fig. 1 (**a**) Combined satellite image and bathymetric data of the Nice airport area and submarine slope (courtesy of IFREMER), illustrating the failure scar immediately south of the international airport. Dashed line shows former embankment south of the runways, which collapsed in 1979. (**b**) Bathymetric map shows the locations of the *Seamonice* long-term piezometer, CPTU deployments, gravity cores used in this study, and water column sampling by Guglielmi and Prieur (1997). See text

and a tsunami wave of 2–3 m height at the nearby coast (Dan et al. 2007). It was proposed several years ago that overpressuring linked to the hydrogeological condition could be the trigger mechanism of the Nice Airport failure, and slight freshening

of the seawater in parts of this area further suggested fresh groundwater is released offshore by coastal aquifers (e.g. Guglielmi 1993; Guglielmi and Prieur 1997). The hydrogeological triggering model is also supported by sedimentary and seismic reflection data indicating permeable layers of sediments may provide aquifer pathways in the shallow subsurface (e.g. Guglielmi and Mudry 1996), and possibly down to a maximum depth of 150 m.

The major objective of this study was to decipher whether the slope sediments off the airport of Nice show evidence for groundwater charging, and if so, in which horizons these occur. The result is used to assess whether such influx may have served as a trigger for the Nice airport landslide.

2   Previous Marine Expeditions

An investigation of the superficial marine sediments (max. 30 m subbottom depth) was recently performed in close collaboration between France (e.g. PRISME cruise with RV *L'Atalant*e, 2007) and Germany (e.g. M73/1 cruise with RV *Meteor*, 2007). The study included geophysical acquisition, *in situ* pore pressure and shear strength measurements (CPTU devices, Penfeld penetrometer) as well as gravity coring (Fig. 1). For long- and mid-term measurements, a long-term piezometer, which acquires the pore pressure at five different depth levels within the sediment, was installed by IFREMER in 2006. Short-term measurements were carried out using a marine shallow-water CPTU (cone penetration testing with pore pressure measurement) probe by MARUM Bremen (Stegmann et al. 2006) and piezometer instruments by IFREMER, while data down to 30 m depth were acquired using the Penfeld penetrometer (Sultan et al. 2004, 2008).

The main results at this stage include: (1) The main failure surface of the Nice airport slide localised in ~30–50 mbsf and is located in sensitive clays interbedded with coarse-grained sediment (Sultan et al. 2004). (2) Long-term pore pressure measurements (Nov. 2006–Nov. 2007 at Seamonice station) in the scar of the 1979 landslide with a piezometer indicate a direct relationship to precipitation events, as the variability of the measured pore pressure follows the rate of rainfall (N. Sultan, personal communications, 2008). (3) Mid-term pore pressure records (34 h) acquired in the landslide scar at different depth levels show contrasting pore pressure evolutions. At 4.25 m below seafloor an increase of pore pressure (~2 kPa) over time could be observed, whereas the pressure in the other levels steadily decreases over time (Sultan et al. 2008). (4) CPTU short-term deployments (25–310 min.) in the area of the Nice Airport indicate higher than hydrostatic pore pressures in sediments in the upper part of the slope, close to the scar of the 1979 landslide (Kopf et al. 2008). (5) ROV surveys as well as high-resolution geophysical data indicate that in some portions of the slope, the surface sediment is currently creeping. (6) Klaucke and Cochonat (1999) further identify slumping as one of the most fundamental processes in the Var valley and adjacent slopes. (7) Initial shipboard geochemical pore water analyses hint towards groundwater flux in the scar of the 1979 landslide (Kopf et al. 2008) and were the starting point for our study.

3 Methods

After a multibeam bathymetric survey (Simrad EM710) across the southern margin of the Nice airport, a total of six gravity cores were taken during cruise M73/1 (Kopf et al. 2008). Five of those cores are used for this predominantly geochemical study (Fig. 1b). The pH was measured directly in the sediment using a punch-in electrode before the pore water was extracted. The pore water was then retrieved by means of rhizons (pore size 0.1 μm) according to the procedure described by Seeberg-Elverfeldt et al. (2005). The gravity cores were each processed in this way within a few hours after recovery. Depending on the porosity of the sediments, the amount of pore water recovered ranged between 4 and 20 ml. Solid phase samples of the majority of cores were taken for total digestions, sequential extractions and mineralogical analyses at 25 cm intervals, kept in gas-tight glass- and heavy plastic bottles under an argon atmosphere and stored at 4°C. Pore water analyses of ammonium, alkalinity and salinity were carried out onboard. Ammonium was measured using a conductivity method. Alkalinity was calculated from a volumetric analysis by titration of either 0.5 or 1 ml of the pore water samples with 0.01 M HCl. Salinity was measured using a conductivity probe placed directly into the pore water samples.

In addition, aliquots of the remaining pore water samples were diluted 1:10 and acidified with $HNO_{3\ (suprapure)}$ for determination of cations with an inductively coupled plasma optical emission spectrometer (ICP-OES; Iris Intrepid [Type Duo], Thermo Nicolet GmbH). Subsamples for sulfate and chloride analysis were diluted 1:50 and measured at the AWI in Bremerhaven using ion chromatography (Metrohm IC Net 2.3). For solid-phase analyses, sediment samples were taken at 5 cm intervals, freeze-dried and pulverized with an agate mortar and pestle. A subsample of ca. 50 mg was digested in a CEM Mars microwave system using a concentrated acid mixture of HNO_3 (3 ml), HCl (2 ml) and HF (0.5 ml). Element concentrations were analyzed by ICP-OES.

For all additional data presented in the context of this paper, in particular Cone Penetration Testing and pore pressure measurements, refer to cruise reports (Sultan et al. 2008; Kopf et al. 2008).

4 Results

All six gravity cores taken in the Nice airport area underwent sedimentological description and basic geotechnical characterization, while geochemical analysis was done on the pore water for five and on the solid sediment for two of them.

Core GeoB12019 represents a reference core of undisturbed slope deposits west of the Var river mouth, and comprises silty clay interbedded with layers of silt and red clayey layers (Fig. 2). Cores GeoB12088, -43 and –42 in the upper northern portion of the headwall, only a few 10s of meters south of the airport, show silty clay to clay with dm-thick gravel deposits close to the seafloor. Core GeoB12003
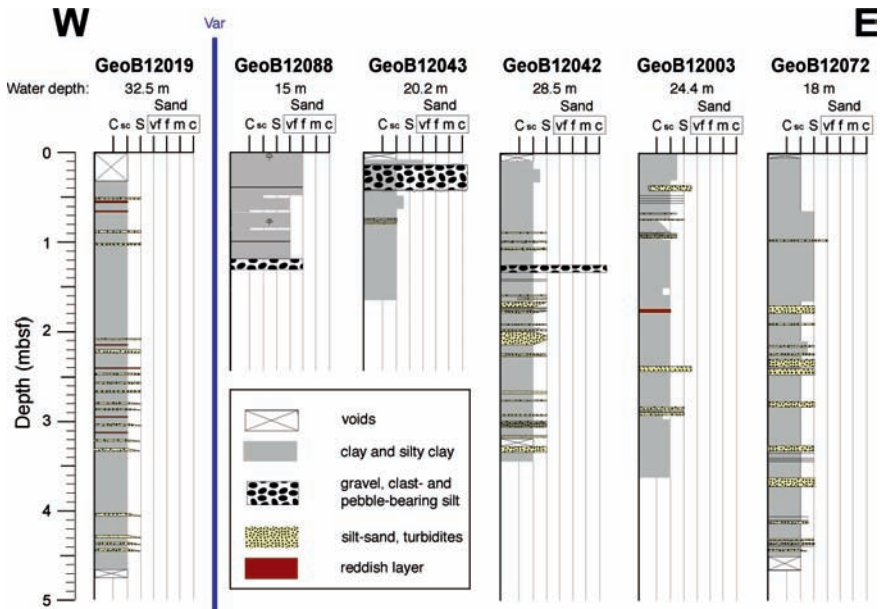
Fig. 2 Visual core description for cores GeoB12003, -42, –43, -72 and –88 taken in the Nice airport area. Numbers beneath Site labels indicate water depth at each site. See Fig. 1b for location. For details refer to Kopf et al. (2008)

is located at the eastern rim of the headwall and consists of silty clay without gravel, but fine sand layers at various depths (Fig. 2). A sixth gravity core east of the 1979 landslide scar is located in the stable slope, where silty clay and silt dominate the sedimentary succession. Frequent sand layers and turbidites are found in the interval between 1.5–4.5 m sediment depth (see Fig. 2, right). For a detailed description of the cores, as well as sediment physical property measurement using a Multi-Sensor Core Logger, refer to Kopf et al. (2008). Undrained shear strength using a miniature Vane shear apparatus was determined immediately after core splitting, and ranged between 2 and 8 kPa for the uppermost silty clays, and rarely exceeded 20 kPa further down and in the sandy intervals. The only exceptions were remoulded (so called "marble cake") intervals and gravel-bearing portions of the core (see Kopf et al. 2008).

Onboard conductivity measurement of pore waters revealed that the three sampling sites situated inside the landside scar (GeoB12003, -42, -43) are significantly freshened below 70–90 cm sediment depth. Core GeoB12042 displayed the most pronounced reduction in salinity, whereas core -43 slightly farther west and -03 at the eastern margin of the headwall scar show weaker freshening (Fig. 3). This is best explained by the lower water depth of Core GeoB12042 (Fig. 2) owing to which material from 10 m lower in the sedimentary section – and thus closer to the main failure surface – was sampled (see also Ch. 2, and Sultan et al. 2004). Core GeoB12072 east of the 1979 landslide scar showed regular salinity.
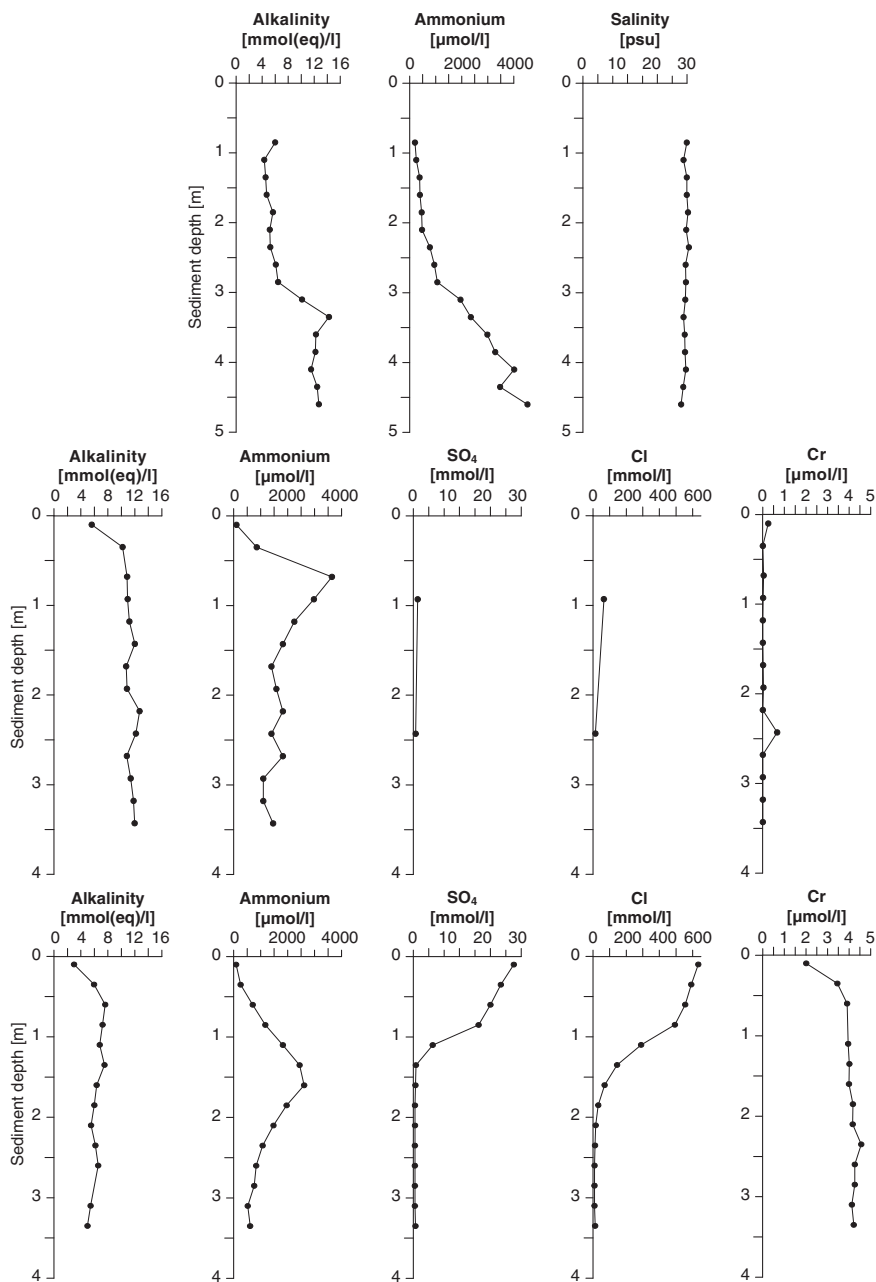
Fig. 3 Pore water concentration profiles for core GeoB12019 (Background core; *uppermost* graph) as well as cores GeoB12003 (*center*) and –42 (*lowermost* graph) retrieved in the headwall area. See Fig. 1b for location. While site GeoB12019 shows typical marine depth/concentration profiles, sites GeoB12003 and -42 display very low chloride (Cl) contents in the lower parts of the cores. Note the distinctly different Cr contents at these two sites

Sulfate and chloride measurements of the pore waters confirmed the initial shipboard results obtained by means of a conductivity probe. Although only two samples were available for sulfate and chloride analyses for core GeoB12003 low concentrations of these pore water constituents clearly indicate a groundwater charging of sediments below about 70–90 cm sediment depth at sites GeoB12003, -42 and –43 (Fig. 3).

While these three sites display very similar pore water depth profiles of chloride and sulfate they substantially differ with respect to dissolved chromium contents. At station GeoB12003 Cr concentrations are mostly below the detection limit of the ICP-OES. In contrast, dissolved Cr contents in pore waters of sites GeoB12042 and -43 increase downcore to reach maximum values of 4.5 μmol/l (Fig. 3). The inverse correlation of Cr with Cl and SO_4 suggests an association with inflowing groundwater; moreover, the variation in Cr implies that this groundwater originates from more than one source. We will address this point in conjunction with geochemical data on the solid phase and mineralogical data in the discussion (Ch. 5).

5   Discussion

Submarine discharge of groundwater in the coastal zone of Nice has previously been reported by Guglielmi and Prieur (1997). Those authors used chemical variations in samples taken in the water column along two arcuate profiles around the Nice airport "peninsula" (see Guglielmi and Prieur 1997, their Fig. 2). A subtle decrease in salinity and Ca^{2+}, Mg^{2+} and K^+ ions, associated with a notable increase in temperature and silica (the latter related to Pliocene pudding stones) has been observed in three areas along the profiles. The central of these three areas, station 9 in Guglielmi and Prieur (1997), corresponds to the 1979 Nice airport slide where we observe the profound freshening.

Guglielmi and Mudry (1996) characterized the chemical composition and estimated the spatial and temporal variability in the flux of surface and subsurface waters into the alluvial aquifer of the river Var. They could show that the water of the river Var contains relatively high levels of sulfate (100–300 mg/l; corresponding to about 1–3 mmol/l) while groundwater in the area typically has lower SO_4 contents. In the two cores from the headwall area presented here sulfate decreases downcore in accordance with chloride, supporting the presence of groundwater in these sediment levels. Sulfate contents in the deeper parts of the cores fluctuate around 0.5 mmol/l and thus are lower than in the upstream area as given by Guglielmi and Mudry (1996). This implies that either (i) groundwater with even lower sulfate contents infiltrates into the coastal (submarine) deposits, that (ii) seawater is infiltrating an otherwise groundwater-saturated aquifer in the reclaimed land mass and/or lower Var valley units (i.e. Pliocene pudding stones and Pleistocene gravel; as discussed in Guglielmi and Mudry 1996), or that (iii) a portion of sulfate has been consumed in the the the degradation of organic matter by dissimilatory sulfate reduction.

Dissolved Cr contents found in the pore waters of GeoB12042 (Fig. 3) and -43 (not shown here) are unusually high (up to 4.5 μmol/l) and exceed the natural

concentrations of Cr in western Mediterranean seawater (max. ~4.5 nmol/l, Achterberg and Van den Berg 1997) by a factor of 1,000. The inverse down-core correlation between Cr and Cl (and sulfate) further suggests a supply of Cr with the infiltrating groundwater. Strikingly, Cr contents were not found elevated at the third groundwater-influenced site GeoB12003 nearby (see Fig. 1b). These findings raise the question whether the extremely high Cr contents at GeoB12042/-43 are supplied by (1) involving groundwater (maybe owing to pollution), (2) desorption of Cr from clay minerals, or (3) result from a significant difference in mineralogy in the source area. Either scenario would hint towards a hydrological system with locally different groundwater sources, with the sources either close to Nice airport (scenarios 1 & 2) or with a distant source of meteoric water with Cr leached from weathering rocks farther north (scenario 3). In order to decide which scenario is most likely, we carried out chemical and mineralogical analyses on the solid phase (Fig. 4). The total element concentrations of the sediments recovered at sites GeoB12003 and -42 demonstrate
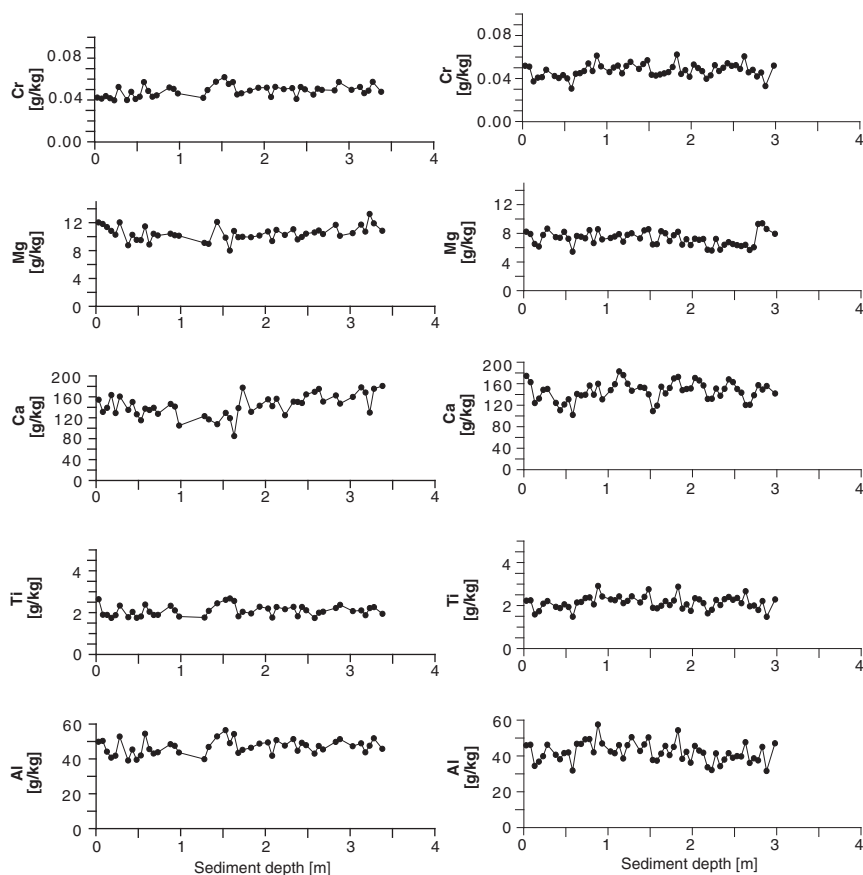
Fig. 4 Total element concentrations of the solid phase recovered in cores GeoB12003 (*upper* graph) and –42 (*lower* graph) near the headwall area of the 1979 landslide. See Fig. 1b for location

that Cr closely covaries with Al and Ti representing the typical elements of the terrigenous sediment fraction. A comparison between the two sites also shows that no significant difference in total Cr is observed. XRD analyses on two samples from cores GeoB12003 (220 cm depth) and -42 (260 cm depth) did not reveal any Cr-bearing minerals (i.e. being present in concentrations above 1 wt%) and did not reveal any significant differences between the two sites with respect to mineralogical composition. However, there are significant amounts of phyllosilicates in the sediment, mirroring source rocks farther upstream of the river Var. Main constituents include quartz, calcite, chlorite (largely clinochlore), muscovite, corundum, albite and attapulgite. No garnet-bearing Alpine rocks are found anywhere adjacent to the study area, so that we exclude direct Cr-sources to the Var river system. However, it should be noted that in order to obtain the Cr concentrations measured at sites GeoB12042 and -43, relatively low amounts of Cr-bearing minerals would suffice. Also, Cr may have got adsorbed to clay minerals, muscovite or clinochlore, offering the potential for desorption and liberation into the pore water. Given that we used rhizons (rather than a hydraulic press) to extract the water, only *in situ* desorption needs consideration. Given the overall low effective stresses in the sediment and the equally low flux rates from ROV CTD surveys (see Ch. 2), we consider this rather unlikely.

These rather preliminary geochemical and mineralogical investigations therefore favor the first hypothesis, i.e. that the high dissolved Cr contents at sites GeoB12042/-43 are most likely supplied by seaward groundwater flow. We exclude infiltration of seawater into the groundwater-charged horizons, because this would cause elevated concentrations of sulfate and other ions enriched in seawater in the interstitial water of the sediments. On the other hand, the removal of sedimentary layers during the landslide event puts seawater in contact with fresh-water saturated sediments, which were originally buried at some depth below the seafloor. The sharp gradients at sites GeoB12003 and -42 (Fig. 4) could be advection-diffusion transients associated with the 1979 event rather than steady-state profiles. Cores -19 and -72 were taken outside of the landslide scar, which leaves the possibility that the fresh water simply cannot be reached because the cores are only 5 m long (but the failure plane is at 30 m; Sultan et al. 2004).

Long-term piezometer measurements (Fig. 1b; *Seamonice* station) in the 1979 landslide scar attest a more or less direct correlation between precipitation in the Nice area and transient pore pressure increase in the more permeable, coarse-grained series where we detected fluid freshening (N. Sultan, personal communications, 2008). Those results indicate a southward-directed submarine groundwater outflow, which lowers the effective strength of the underground and may contribute to slope failure, in particular during or shortly after periods of heavy precipitation. The long-term seasonal variability with spring floods in the Var River system (caused by snow melting, but also a lot of rain usually during the month of May) may have significantly affected the fluid chemistry during the period of pore water sampling, in particular since a permeability of 10^{-8} m/s for the slope sediments south of the airport (Dan 2007) implies that some of the May 2007 rainfall (>70 mm) still remained in the system when we sampled in July 2007. This perception is indirectly supported by elevated pore pressure values at the Seamonice station (Fig. 1b), which

rose approximately simultaneously with higher precipitation around May 22nd, 2007, but then remained at an elevated level until mid-August, although average rainfall dropped drastically from May (71 mm) via June (21 mm) and July (1 mm) to August (4 mm) (N. Sultan, personal communications, 2008).

In conclusion, we tentatively propose that the hydrological system at the Var river mouth and adjacent coastal region near the Nice airport varies on a small scale. Guglielmi and Prieur (1997) already attested that there are at least three areas of groundwater flux into the Ligurian submarine slope. In our study area (their station 9), we attest additional complexity and evidence for two different groundwater sources, one of which shows Cr contents that are three orders of magnitude above seawater (Fig. 3) and may be explained by anthropogenic impact (e.g. dumping of scrap metal during 1960s landfill operations, present-day pollution, etc.), either being released now or originating from *in situ* desorption from clay. To substantiate our assumptions, more detailed geochemical studies are needed in an "amphibic" approach where fountains on land near Nice as well as groundwater seeps south of the Nice airport are regularly sampled and analyzed to identify seasonal variations and the regional hydrological variability.

References

Achterberg EP, Van den Berg CMG (1997) Chemical speciation of chromium and nickel in the western Mediterranean. Deep-Sea Res Pt II 44: 693–720

Anthony EJ (2007) Problems of hazard perception on the steep, urbanised Var coastal floodplain and delta, French Riviera. Mediteranee 108: 91–97

Dan G (2007) Processus gravitaires et évaluation de la stabilité des pentes: approches géologiques et géotechnique. Application à la marge algérienne et à l'effondrement de l'aéroport de Nice en 1979. Unpublished Ph.D. thesis (Thèse de doctorat), Ifremer/UBO

Dan G, Sultan N, Savoye B (2007) The 1979 Nice harbour catastrophe revisited: Trigger mechanism inferred from geotechnical measurements and numerical modelling. Mar Geol 245: 40–64

Guglielmi Y (1993) Hydrogéologie des aquifères Plio-Quaternaires de la Basse Vallée du Var. Thèse d'Etat, Académie d'Aix-Marseille

Guglielmi Y, Mudry J (1996) Estimation of spatial and temporal variability of recharge fluxes to an alluvial aquifer in a fore land area by water chemistry and isotopes. Ground Water 34: 1017–1023

Guglielmi Y, Prieur L (1997) Essai de localisation et de quantification des résurgences sous-marines d'un aquifère captif à porosité d'interstices: exemple de la nappe alluviale de la basse vallée du Var (Méditerranée, France). J Hydrol 190: 111–122

Klaucke I, Cochonat P (1999) Analysis of past seafloor failures on the continental slope off Nice (SE France). Geo-Mar Lett 19: 245–253

Kopf A, shipboard science party (2008) Report and preliminary results of Meteor cruise M73/1: LIMA-LAMO. Berichte aus dem Fachbereich Geowissenschaften der Univ. Bremen, No. 264

Locat J, Lee HJ (2002) Submarine landslides: advances and challenges. Can Geotech J 39: 193–212

Seeberg-Elverfeldt J, Schlüter M, Feseker T, et al. (2005) Rhizon sampling of porewaters near the sediment-water interface of aquatic systems. Limnol Oceanogr-Meth 3: 361–371

Stegmann S, Moerz T, Kopf A (2006) Initial Results of a new Free Fall-Cone Penetrometer (FF-CPT) for geotechnical *in situ* characterisation of soft marine sediments. Norway J Geol 86: 199–208

Sultan N, Cochonat P, Canals M, et al. (2004) Triggering mechanisms of slope instability processes and sediment failures on continental margins: a geotechnical approach. Mar Geol 213: 291–321

Sultan N, Shipboard party (2008) Prisme Cruise (R/V Atalante Toulon - Toulon; 2007): Reports and Preliminary Results. IFREMER Internal Report, Ref: IFR CB/GM/LES/08–11

Modeling Slope Instability as Shear Rupture Propagation in a Saturated Porous Medium

R.C. Viesca and J.R. Rice

Abstract When a region of intense shear in a slope is much thinner than other relevant geometric lengths, this shear failure may be approximated as localized slip, as in faulting, with strength determined by frictional properties of the sediment and effective stress normal to the failure surface. Peak and residual frictional strengths of submarine sediments indicate critical slope angles well above those of most submarine slopes—in contradiction to abundant failures. Because deformation of sediments is governed by effective stress, processes affecting pore pressures are a means of strength reduction. However, common methods of examining slope stability neglect dynamically variable pore pressure during failure. We examine elastic-plastic models of the capped Drucker-Prager type and derive approximate equations governing pore pressure about a slip surface when the adjacent material may deform plastically. In the process we identify an elastic-plastic hydraulic diffusivity with an evolving permeability and plastic storage term analogous to the elastic term of traditional poroelasticity. We also examine their application to a dynamically propagating subsurface rupture and find indications of downslope directivity.

Keywords Landslide • slope stability • slip surface • friction • pore pressure • storage • diffusivity • poroelasticity • plasticity • dynamic rupture • finite element

1   Introduction

How sediments deform and pore fluid flows during the shearing process has not been precisely determined for the variety of styles of landslides. While some failures may occur at a stratigraphic discontinuity, others may occur within the sediment column.

R.C. Viesca and J.R. Rice (✉)
School of Engineering and Applied Sciences (also, for JRR,
Department of Earth and Planetary Sciences), Harvard University, 29 Oxford St.,
Cambridge, MA 02138, USA

When failure is within the sediment, to what extent that failure is localized is uncertain. Not knowing when and where failure may start hampers field observations of failure initiation and progression. However, a failure location and time can be constrained by artificially creating failure conditions. For example, Cooper et al. (1998) induced slump failure in a naturally deposited clay slope by artificially elevating pore pressures. Excavation revealed an O(mm) thick intense shear zone within an O(cm) thick disturbed region.

Observations of local deformation and apparent progressive failure (Bjerrum 1967; Bishop 1971) inspired treating the shear zone as a slipping fracture and examining criteria for unstable rupture propagation – i.e., criteria for rupture to continue propagation without further loading, presumably the inception of complete slope failure. Palmer and Rice (1973) examined the propagation of rupture from the base of a cut within an overconsolidated clay slope and estimated the rupture length required to initiate unstable growth by gravitational loading. Puzrin and Germanovich (2004, 2005) similarly examined the case of a rupture paralleling the slope surface with the intention of extending the analysis of Palmer and Rice to the failure of slopes composed of normally consolidated clay or incohesive soil. With experimental observations of shear bands in such soils in mind, they postulate that slope failure in these soils would ultimately occur in local deformation-weakening shear zones similar to the failure of overconsolidated clays. Such an analysis lends itself towards examining effective stress controls on slope stability. This is an appealing approach for studying failure in the submarine environment, where slopes are often too shallow for failure to be explained by infinite slope or limit equilibrium analyses. In this environment, processes affecting pore pressure such as local fluid flux (Dugan and Flemings 2000) or methane hydrate dissociation (Xu and Germanovich 2006) have been proposed as mechanisms for initiating failure. The works of Palmer and Rice, and Puzrin and Germanovich, considered the shear strength on the surface to degrade with the amount of slip, assumed that the length of the rupture was much greater than its depth and that the stress-strain relationship of the overlying sediments was linearly elastic until passive or active failure.

The role of fluid in rupture initiation, propagation, and runout is often central in landslide processes. In the experiment of Cooper et al. (1998), decreases in measured pore pressure during early-stage slope movement indicate a stabilizing dilative suction preceding total slope failure. Subaerial flume studies of densely or loosely packed sandy sediment also show a tendency for dilatant stabilization in the case of dense sediments and transition to debris flow when loosely packed (Iverson et al. 2000). Monitoring shearing rates and pore pressures in a ring shear apparatus, Moore and Iverson (2002) observe the diffusive nature of such stabilization in relatively coarse- and fine-grained sediments.

The question remains how to appropriately determine the pore pressure within a finite thickness shear zone approximated by a sliding surface. Specifically, contributions from processes within the shear zone may be lumped into the surface behavior in addition to contributions from material deformation beyond the shear zone. When concerned with slip-surface pore pressures, current modeling of dynamic rupture propagation has included inelastic porosity changes as either a

slip-proportional porosity change (Rice 1980; Suzuki and Yamashita 2008) or a transition to a rate-dependent steady-state porosity (Segall and Rice 1995, Bizzarri and Cocco 2006). Other work has examined slip propagating quasi-statically or dynamically in a saturated poroelastic or poro-elastic-plastic media, but neglected the effect of pore pressure changes on the fault on shear strength (de Borst et al. 2006; Réthore et al. 2007; Viesca et al. 2008).

In addition to the inelastic processes occurring within the surface-approximated shear zone are those about the rupture tip. The rupture criterion set by the surface weakening behavior eliminates stress singularities, however there remain significant stress concentrations. It is well known in dynamic shear rupture that in such cases regions of inelastic deformation grow, with propagation, to dimensions significant in comparison to rupture length (e.g., Templeton and Rice 2008) and one can expect such regions of failure around the rupture tip in the quasi-static limit. In the following we propose a model in which pore pressure on the slip-surface is determined by the poro-elastic–plastic deformation and consequent fluid flux surrounding the slip surface. This parallels efforts to discretize the poro-mechanical deformation of a finite-thickness shear zone (e.g., White and Borja 2008).

2 Determining Pore Pressures at a Sliding Interface with Plastically Deforming Surroundings

The saturated porous material deforms elastically until a yield condition is met. The condition is given by a function F of the effective stress (positive in tension) $\bar{\boldsymbol{\sigma}} = \boldsymbol{\sigma} + p\mathbf{I}$, where $\boldsymbol{\sigma}$ is the total stress tensor and p is the pore fluid pressure, and potentially a function of other state variables, such as the void ratio or a magnitude of plastic strain. $F(\bar{\boldsymbol{\sigma}}) = 0$; is the yield condition. Here the yield function is expressed in terms of the stress invariants $\operatorname{tr}\bar{\boldsymbol{\sigma}}/3$ and $\bar{\tau} = \sqrt{\mathbf{s}:\mathbf{s}/2}$; where $\mathbf{s} = \boldsymbol{\sigma} - \operatorname{tr}\boldsymbol{\sigma}\mathbf{I}/3$ is the deviatoric part of the stress tensor. Figure 1 is an illustration of such a function where $\mu = \partial F/\partial\,(\operatorname{tr}\,\bar{\boldsymbol{\sigma}}/3)$; is the local measure of the pressure-dependence of the criterion and b is the cohesive strength. During continued plastic deformation, the stress state must satisfy either $\partial F/\partial\bar{\boldsymbol{\sigma}}{:}d\bar{\boldsymbol{\sigma}} = 0$; to move along the yield surface or $\partial F/\partial\bar{\boldsymbol{\sigma}}{:}d\bar{\boldsymbol{\sigma}} > 0$; to follow the outward evolution of the yield surface. Here, we

$$F(\bar{\boldsymbol{\sigma}}) = \bar{\tau} - f\left(tr\bar{\boldsymbol{\sigma}}/3\right) \text{ where } f(0) = b,$$
$$f'(tr\bar{\boldsymbol{\sigma}}/3) = -\mu$$
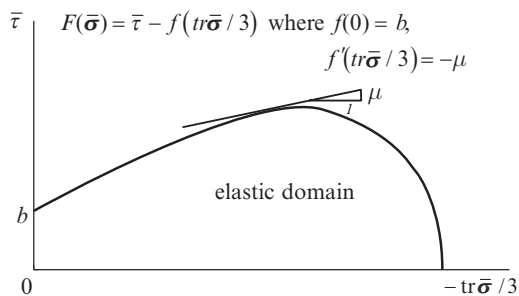
Fig. 1 Illustration of pressure-dependent yield criterion F

allow the yield surface to evolve with plastic strain and define the hardening modulus, $\partial F/\partial\overline{\sigma}:d\overline{\sigma} = hd\gamma^{pl}$; where $d\gamma^{pl} = \sqrt{2d\mathbf{e}^{pl}:d\mathbf{e}^{pl}}$, and $d\mathbf{e}^{pl} = d\boldsymbol{\varepsilon}^{pl} - (\mathrm{tr}\ d\boldsymbol{\varepsilon}^{pl})\mathbf{I}/3$. A second potential $H(\overline{\sigma})$; (here, of similar form to F) indicates the direction of plastic strain increments: $d\boldsymbol{\varepsilon}^{pl} = d\gamma^{pl}\partial H/\partial\overline{\sigma}$. From the potentials F and H, we define the second order tensors

$$\mathbf{Q} = \frac{\partial F}{\partial\overline{\sigma}} = \frac{\mathbf{s}}{2\tau} + \frac{\mu}{3}\mathbf{I} \qquad \mathbf{P} = \frac{\partial H}{\partial\overline{\sigma}} = \frac{\mathbf{s}}{2\tau} + \frac{\beta}{3}\mathbf{I} \qquad (1)$$

where $\beta = \partial H/\partial(\mathrm{tr}\overline{\sigma}/3)$ is the ratio $\mathrm{tr}\ d\boldsymbol{\varepsilon}^{pl}/d\gamma^{pl}$. More explicitly, we decompose the total strain increment into elastic and plastic components $d\boldsymbol{\varepsilon} = d\boldsymbol{\varepsilon}^{el} + d\boldsymbol{\varepsilon}^{pl}$, and the plastic strain increments may be written as $d\boldsymbol{\varepsilon}^{pl} = \mathbf{P}(\mathbf{Q}:d\overline{\sigma})/h$. Increments in the Biot effective stress $d\sigma + \alpha dp\mathbf{I}$ are determined by increments in elastic strain, $d(\sigma + \alpha p\mathbf{I}) = \mathbf{L}:(d\boldsymbol{\varepsilon} - d\boldsymbol{\varepsilon}^{pl})$, where $\mathbf{L}$ is the elastic stiffness tensor described below.

The increments of elastic–plastic total stress and pore fluid mass m (with fluid density ρ) may be written in terms of those of strain and pore pressure (e.g., Rudnicki 2001)

$$d\sigma = \left(\mathbf{L} - \frac{(\mathbf{L}:\mathbf{P})(\mathbf{Q}:\mathbf{L})}{h + \mathbf{Q}:\mathbf{L}:\mathbf{P}}\right):d\boldsymbol{\varepsilon} - \left(\alpha\,\mathbf{I} + \frac{(1-\alpha)\,\mathrm{tr}\,\mathbf{Q}\,(\mathbf{P}:\mathbf{L})}{h + \mathbf{Q}:\mathbf{L}:\mathbf{P}}\right)dp \qquad (2)$$

$$\frac{dm}{\rho} = \left(\frac{\alpha(1-\alpha B)}{KB} + \frac{(1-\alpha)^2\,\mathrm{tr}\,\mathbf{P}\,\mathrm{tr}\,\mathbf{Q}}{h + \mathbf{Q}:\mathbf{L}:\mathbf{P}}\right)dp + \left(\alpha\,\mathbf{I} + \frac{(1-\alpha)\,\mathrm{tr}\,\mathbf{P}\,(\mathbf{P}:\mathbf{L})}{h + \mathbf{Q}:\mathbf{L}:\mathbf{P}}\right):d\boldsymbol{\varepsilon} \qquad (3)$$

In all bracketed terms preceding dp and $d\boldsymbol{\varepsilon}$, the first term corresponds to the elastic response and the second to the contribution of plastic deformation. The elastic coefficients are $\mathbf{L}$, the fourth-order linear-elastic stiffness tensor (i.e., for isotropic elasticity and a second-order symmetric tensor $\mathbf{A}$, $\mathbf{L}:\mathbf{A} = \mathbf{A}:\mathbf{L} = K\mathbf{I}\,\mathrm{tr}\,\mathbf{A} + 2G\,\mathrm{dev}\,\mathbf{A}$, where K and G are the bulk and shear moduli), and B, the poroelastic Skempton coefficient.

Taking the boundary-layer approximation and considering gradients parallel to the slip surface to be much smaller than the normal gradients, the conservation of fluid mass near the surface requires $\partial q/\partial y = -\partial m/\partial t$, where q is the pore fluid mass flux given by Darcy's law $q = -(\rho k/\eta)\partial p/\partial y$, k being the permeability and η the permeating fluid viscosity. Combining fluid conservation and Darcy's law

$$\frac{\rho k}{\eta}\frac{\partial^2 p}{\partial y^2} = \frac{\partial m}{\partial t} \qquad (4)$$

In calculating the rate of the fluid mass, we consider the region around the slip surface as consisting of material that may differ in mechanical behavior (e.g., elastic stiffness, dilation, and internal friction) from the typical response of the sediment further away from the slip surface (i.e., a disturbed region about the slip surface). The adjoining materials are coupled by the continuity of certain components of stress σ_c (σ_{yx}, σ_{yy}, σ_{yz}) and strain ε_c (ε_{xx}, ε_{zz}, ε_{xz}), the remaining free components of stress

and strain are designated as σ_f (σ_{xx}, σ_{zz}, σ_{xz}) and ε_f (ε_{xy}, ε_{yy}, ε_{yz}). With this in mind, we rearrange (2) and (3) into vector and matrix notation where

$$\{d\sigma\} = d\left\{\begin{matrix} \{\sigma_c\} \\ \{\sigma_f\} \end{matrix}\right\} \text{ and } \{d\varepsilon\} = d\left\{\begin{matrix} \{\varepsilon_c\} \\ \{\varepsilon_f\} \end{matrix}\right\} \tag{5}$$

such that

$$\{d\sigma_c\} = [N_{11}]\{d\varepsilon_c\} + [N_{12}]\{d\varepsilon_f\} + \{U_1\}dp$$

$$\{d\sigma_f\} = [N_{21}]\{d\varepsilon_c\} + [N_{22}]\{d\varepsilon_f\} + \{U_2\}dp$$

$$\frac{dm}{\rho} = Cdp + \{M_1\}^T\{d\varepsilon_c\} + \{M_2\}^T\{d\varepsilon_f\} \tag{6–8}$$

[N], {M}, {U}, C are the matrix, vector, and scalar coefficients whose components are determined by the constitutive relationships (2) and (3). For example, in xy plane strain

$$\{U_1\}^T = \left\{-\left(\alpha + \frac{(1-\alpha)\mu\left(Gs_{xy}/\overline{\tau}\right)}{h+G+\mu\beta K}\right) \quad -\frac{(1-\alpha)\mu\left(\beta K + Gs_{yy}/\overline{\tau}\right)}{h+G+\mu\beta K}\right\} \tag{9}$$

Expressing $\{d\varepsilon_f\}$ in terms of $\{d\varepsilon_c\}$, $\{d\sigma_c\}$, and dp, (10) reduces to

$$\frac{dm}{\rho} = \beta_{stor}dp + \{R\}^T\{d\varepsilon_c\} + \{S\}^T\{d\sigma_c\} \tag{10}$$

where $\beta_{stor} = C - \{M_2\}^T[N_{12}]^{-1}\{U_1\}$, $\{R\}^T = \{M_1\}^T - \{M_2\}^T[N_{12}]^{-1}[N_{11}]$, and $\{S\}^T = \{M_2\}^T[N_{12}]^{-1}$.

During elastic response, β_{stor} is the poroelastic storage coefficient under one-dimensional consolidation ($d\varepsilon_{xx} = d\varepsilon_{zz} = 0$), $\beta_{stor} = \beta_{stor}^{el} = \left[(K_u + 4G/3)/(K+4G/3)\right]\alpha/BK_u$, where $K_u = K/(1 - \alpha B)$ is the undrained bulk modulus. During plastic deformation, $\beta_{stor} = \beta_{stor}^{pl}$ is a plastic storage coefficient for one-dimensional straining that reflects a compressibility increase with yielding. We see from (2–3) that during plastic loading the components depend not only on the elastic–plastic material parameters, but also on the scaled deviatoric stress components. For plane conditions ($s_{xz} = s_{yz} = 0$) and $s_{zz} = 0$ ($s_{xx} = -s_{yy}$), $\overline{\tau} = s_{xx}^2 + s_{xy}^2$. Deviatoric stress states can then be characterized by an angle ϕ ($s_{xx} = -s_{yy} = \overline{\tau}\cos\phi$, $s_{xy} = \overline{\tau}\sin\phi$), and the expression for β_{stor}^{pl}; is reduced to a dependence on ϕ and material parameters. Considering poro-elastic–plastic parameters representative of a low-porosity rock (e.g., Rudnicki and Rice 1975; Rice and Cleary 1976), for which yielding will occur on the dilative side of the yield surface ($\mu > \beta > 0$) for some stress states, the storage may increase threefold (Fig. 2). For sediment with pore fluid and component particles much stiffer than the matrix as a whole (i.e., $\alpha = B = 1$) yielding on the compacting side of the yield surface (right side of Fig. 1), we find the plastic storage may increase sixfold.
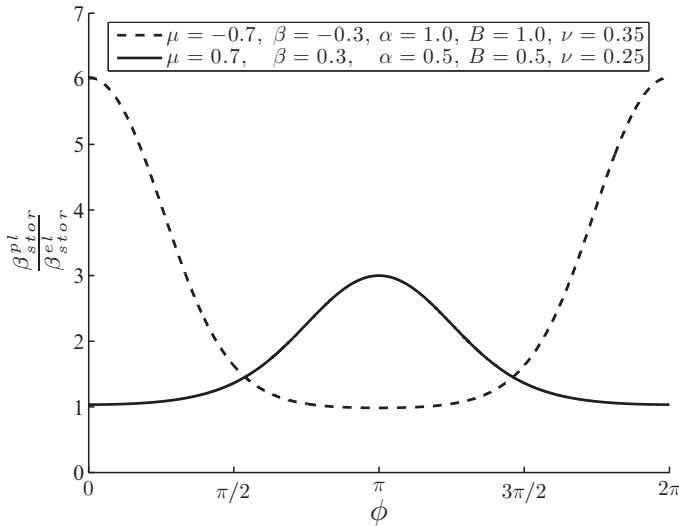
Fig. 2 Plot of factor of increase in storage coefficients (compressibilities) with onset of ideally plastic ($h = 0$) yielding for compacting sediment (*dashed*) and dilating rock (*solid*) over a range of stress states for which $s_{zz} = 0$, $s_{xy}/\bar{\tau} = \sin\phi$, and $s_{xx}/\bar{\tau} = -s_{yy}/\bar{\tau} = \cos\phi$

Setting $dm = 0$ in (10) defines the undrained pore pressure increment dp_u adjacent to the slip surface. (10) can be rewritten $dm/\rho = \beta_{stor}\, d(p - p_u)$ and (6) reduces to

$$\frac{k}{\beta_{stor}\eta}\frac{\partial^2 p}{\partial y^2} = \frac{\partial}{\partial t}(p - p_u) \tag{11}$$

In the poroelastic case, $dp_u = -[2G(d\varepsilon_{xx} + d\varepsilon_{zz}) + d\sigma_{yy}]B(1 + \nu_u)/3(1 - \nu_u)$ where the increments in these stresses and strains can be considered explicitly as functions of time (i.e., within the boundary layer of the disturbed region there is no y-dependence of these increments, which are determined by the coupling to the bulk). Consequently, (11) can be rewritten such that the pressure difference from the undrained value satisfies

$$\alpha_{hy}\frac{\partial^2}{\partial y^2}(p - p_u) = \frac{\partial}{\partial t}(p - p_u) \tag{12}$$

where $k/\beta_{stor}^{el}\eta$ is the hydraulic diffusivity α_{hy}. Keeping fluid flux and pore pressures continuous across the slip surface, the pore pressure across the surface can be determined. Rudnicki and Rice (2006) found an analytical solution for the surface pressure based on the undrained pressures and hydraulic properties above (+) and below (−) the surface

$$dp_s = \zeta^+ dp_u^+ + \zeta^- dp_u^- \qquad \zeta^\pm = \frac{\left(\sqrt{k\beta_{stor}^{el}}\right)^\pm}{\left(\sqrt{k\beta_{stor}^{el}}\right)^- + \left(\sqrt{k\beta_{stor}^{el}}\right)^+} \tag{13}$$

In mode-II shear rupture, one side of the ruptured surface undergoes compression (pressurization) and the other extension (suction). The influence of each side on the surface pressure is determined by the hydraulic property contrast in the weighting (13). Dunham and Rice (2008) modeled plane-strain bilateral dynamic ruptures with the above solution and found preferences in rupture direction for hydraulic property contrasts thought to be typical of faults.

However, this solution breaks down once the material begins to yield. Most notable is the expected change in permeability with plastic deformation. For some fine-grained sediment, moderate changes in void ratio (0.1–0.2) can produce 1–2 order of magnitude changes in permeability (Lambe and Whitman 1969). For low-porosity rock, monitoring of permeability and inelastic deformation during triaxial tests of intact granodiorite and granite shows 1–2 orders of magnitude increases in permeability for axial inelastic strains of the order 0.1% (e.g., Mitchell and Faulkner 2008). This effect on its own introduces a time-dependence to the hydraulic diffusivity not accounted for in (13). More subtle effects may result when considering changes in pore pressure across the slip surface. One such effect may be that these changes result in some slip surface adjacent material moving away from yield (i.e., some material within each boundary layer deforms plastically, and some elastically). An even more subtle effect with plastic deformation is the effect that the changes in pressure have in determining deviatoric stress components. The poroelastic expression for dp_u could explicitly be written as a function of time (i.e., no y-dependence) and as a result the diffusion equation could be reached. This is generally not the case during plastic deformation. In the expression for dp_u there is a dependence on the components of $\mathbf{s}/\overline{\tau}$, which will vary with the changes in pressure across the slip surface introducing a y-dependence of dp_u.

Solving for the pore pressure at the slip surface requires addressing these deviations from the poroelastic diffusion equation. However, such a solution is nontrivial and we seek to make it more tractable. One such simplification is to assume that permeability changes are uniform within each boundary layer. Consistent with this is to neglect switching between elastic or plastic deformation within each boundary layer (i.e., the boundary layer undergoes either elastic or plastic deformation). Lastly, we neglect surface-normal variations in $\mathbf{s}/\overline{\tau}$ such that dp_u and β_{stor}^{pl} are determined by the coupled stress components (i.e., depend explicitly on time alone). With these assumptions, (11) becomes

$$\alpha_{hy}^{pl}(t)\frac{\partial^2}{\partial y^2}\left(p - p_u\right) = \frac{\partial}{\partial t}\left(p - p_u\right) \tag{14}$$

where $\alpha_{hy}^{pl}(t) = k(t)/\beta_{stor}^{pl}(t)\eta$ is an elastic–plastic diffusivity.

3 Finite Element Model of a Dynamic Subsurface Rupture

We use the finite element method (with ABAQUS/Explicit) to examine the dynamic propagation of a subsurface shear rupture. Dynamic rupture propagation (i.e., where inertial effects are in the equation of motion and shear rupture speeds are of the order

of the shear wave speed c_s), while not typically considered for slope stability, is actively investigated in the earthquake rupture community. We use such an approach here to gain insights into influential processes at the rupture front. The treatment of the model domain is similar to that described in Templeton and Rice (2008) and Viesca et al. (2008), who examined rupture in an unbounded medium. Four-noded plane-strain, reduced-integration elements compose the bulk and a predefined split-node interface represents a likely failure plane. The surface corresponds to the slope surface, and absorbing elements ("infinite elements" in ABAQUS) are applied downslope and upslope, and at a slope-perpendicular depth to simulate infinite slope conditions and minimize reflections other than from the free surface.

The shear strength τ at the slip surface is effective-stress dependent, $\tau = f\bar{\sigma} = f(\sigma - p_s)$ where the scalar total and effective surface-normal stresses (σ and $\bar{\sigma}$) are positive in compression. The friction at the slip surface follows a slip-weakening description and drops from static f_s to dynamic f_d linearly over a characteristic slip D_c: $f_{sw} = f_s - (f_s - f_d)min\{\delta, D_c\}/D_c$. In addition to the depth of the slip surface H, the friction law sets a second model length scale proportional to $GD_c / \bar{\sigma}_o(f_s - f_d) \equiv \tilde{R}$. Rupture is nucleated by the Andrews (1985) forced expansion of slip as described by Dunham and Rice (2008), $f_e(x,t) = max\{f_d + A(|x| - v_e t), f_d\}$ where $A = (f_s - f_d)/\tilde{R}$ and $\tilde{R}v_e = 0.144c_s$. The imposed friction coefficient is $f = min\{f_{sw}, f_e\}$ such that the friction coefficient is determined by f_{sw} beyond nucleation. Furthermore, the slip-surface strength is time-regularized to follow $d\tau/dt = -[\tau - f(\sigma - p)]/t^*$ where t^* is the associated timescale, here small in comparison to a physical slip-surface timescale $\tilde{R}/c_s$.

The initial state of stress is uniform, consistent with the components of stress of a material element in a submerged infinite slope at a depth H (consistent shear and normal tractions are applied at the surface to maintain the initial state). A nonuniform stress state of depth-dependent stresses would not affect slope-parallel rupture if the surroundings deform elastically. The material away from the slip surface may deform elastically or elastic–plastically. The material yield strength model is based on a heavily overconsolidated clay assuming changes of stress occur in the dilative region of the yield surface where strength is approximated by a linear dependence on effective pressure (i.e., constant μ) and neglecting drained cohesion (i.e., $b = 0$). Under dynamic rupture the rapid deformation leaves little time for fluid flux and undrained conditions are assumed away from the surface. To calculate the pore pressure change on the surface, in the elastic regime we use (13), and during elastic–plastic deformation (localized at the rupture tip), we approximate the surface pressure with a similar weighting, replacing β_{stor}^{el} with β_{stor}^{pl} given at the onset of yielding and neglect changes in permeability. We calculate the undrained pore pressure increment used in that expression as that resulting from (11) with $dm = 0$. Near surface (disturbed region) material parameters are consistent with far-field parameters, except for a twofold reduction of the shear modulus near the slip surface. Model poroelastic parameters and stress state are summarized in the caption of Fig. 3.

The effects of the slope surface on the slip surface become significant when the lengths become comparable. For $H/\tilde{R} \to \infty$ the solution approaches that of a crack in an unbounded medium under uniform initial loading, the case typically considered in earthquake source physics. In that limit, there is no effective normal
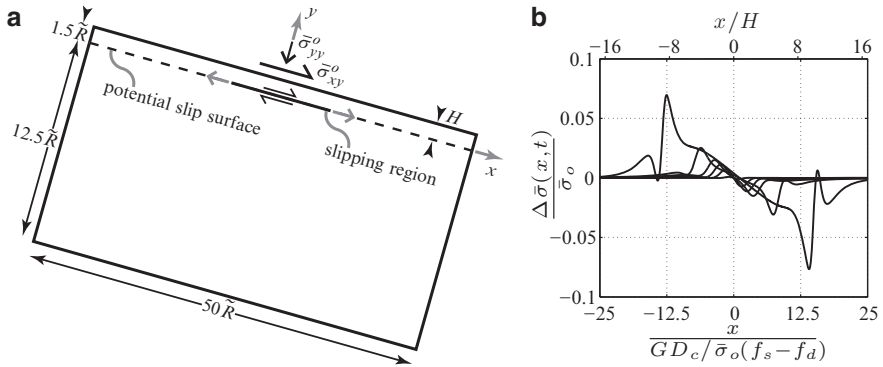
Fig. 3 (**a**) Schematic of portion of model domain (actual downdip length $\widetilde{R}$), initial stresses, and subsequent behavior. (**b**) Snapshots of effective normal stress along the slip surface at intervals of $3.75\,\widetilde{R}/c_s$ for a subsurface rupture at a depth $H = 1.5\,\widetilde{R}/c_s$ in a saturated poroelastic body. Rupture shows preferred downslope propagation and significant normal stress changes. Model initial stress state is defined as $\overline{\sigma}^o_{yy} = (\gamma_b - \gamma_w)H\cos\theta$, $\overline{\sigma}^o_{xy} = (\gamma_b - \gamma_w)H\sin\theta$, $\overline{\sigma}^o_{xx} = K_o\overline{\sigma}^o_{yy}$, and $\overline{\sigma}^o_{zz} = (\overline{\sigma}^o_{xx} + \overline{\sigma}^o_{yy})/2$, where $\gamma_b = 1.75\gamma_w$, $\theta = 15.75°$, and $K_o = 1$. Surface frictional parameters are $f_p = 0.45$, $f_r = 0.2$, and $t^* = 0.015\,\widetilde{R}/c_s$. Bulk poroelastic parameters are $G = 600\overline{\sigma}^o_{yy}$, $\nu = 0.35$, $\nu_c = 0.483$, and $B = 0.94$

stress change on the slip surface and no preferred rupture direction for a poroelastic medium when there is no contrast in material properties across the surface. For the poroelastic case when H and $\widetilde{R}$ are comparable, total normal stress changes on the fault induce corresponding pore pressure changes and the net effective stress change induces a downslope preference for rupture (Fig. 3b). Here, rupture propagation is below the Rayleigh wave speed c_r (for $\nu_u = 0.483$, $c_r \approx 0.95c_s$) until about the last time step plotted in Fig. 3b where the rupture begins a transition to rupture propagation beyond the shear wave speed (so-called supershear rupture), first in the downslope direction and shortly followed by a transition in the upslope direction (not shown). These transitions are remarkable since in an unbounded elastic medium this would normally occur for initial slip-surface shear stress states satisfying $r = (\overline{\sigma}^o_{xy}/\overline{\sigma}^o_{yy} - f_r)/(f_p - f_r) \gtrsim 0.36$ (Andrews 1976) and here $r = 0.32$ (note $r = 1/(1 + S)$ where S is a similar measure commonly used in earthquake rupture studies).

With the introduction of plasticity, we find the preference for downslope rupture propagation is enhanced when pressure changes at the slip surface are included compared to when they are not. For initial simplicity, we maintain the conditions as in Fig. 3 and take $\mu = 0.42$, $\beta = 0.3$, and $b = 0$. Neglecting surface pore pressure changes (Fig. 4a) results in a preference to upslope rupture, which reaches supershear propagation speeds first, while the downslope rupture continues at subshear speeds. In the case considering surface pore pressure change (Fig. 4b) there is longer delay to the supershear transition and a slight downslope preference with an initial transition to supershear occurring in the downslope direction, followed shortly by an upslope transition.
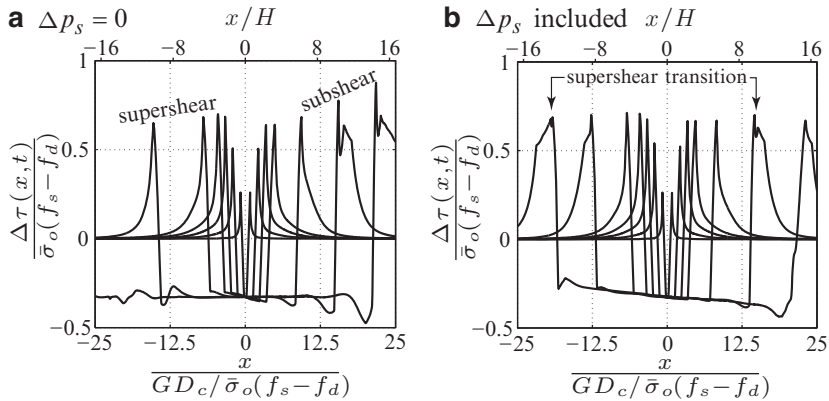
Fig. 4 Snapshots of slip surface shear stress changes in elastic–plastic saturated medium (**a**) neglecting slip surface pore pressure changes and (**b**) including elastic–plastic effects on pore pressure changes

4 Conclusions

We considered a slip surface within a saturated, porous elastic–plastic medium and derived an approximate equation governing the pore pressure around that surface. That equation takes the form of a diffusion equation with a plastic hydraulic diffusivity, which, in addition to an evolving permeability, also includes a plastic storage coefficient. The storage coefficient may be several times larger than the original elastic storage, which decreases the diffusivity for fixed permeability. We applied this consideration to the dynamic propagation of a slope-parallel subsurface shear rupture. We found that considerable surface effects, most notably normal stress changes, provide a downslope directionality.

References

Andrews DJ (1976) Rupture velocity of plane strain shear cracks. J Geophys Res 81: 5679–5687

Andrews DJ (1985) Dynamic plane-strain shear rupture with a slip-weakening friction law calculated by a boundary integral method. Bull Seismol Soc Am 75: 1–21

Bishop AW (1971) The influence of progressive failure on the choice of the method of stability analysis. Géotechnique 21: 168–172

Bizzarri A, Cocco M (2006) A thermal pressurization model for the spontaneous dynamic rupture propagation on a three-dimensional fault: 1. Methodological approach. J Geophys Res 111(B05303), doi:10.1029/2005JB003862

de Borst R, Réthoré J, Abellan M-A (2006) A numerical approach for arbitrary cracks in a fluid-saturated medium. Arch Appl Mech 75: 595–606, doi: 10.1007/s00419–006–0023-y

Bjerrum L (1967) Progressive failure in slopes of overconsolidated plastic clay and clay shales. Trans Am Soc Civil Eng SM 93: 3–49

Cooper MR, Bromhead EN, Petley DJ, Grant DI (1998) The Selbourne cutting stability experiment. Géotechnique 48(1): 83–101

Dugan B, Flemings PB (2000) Overpressure and fluid flow in the New Jersey continental slope: implications for slope failure and cold seeps. Sci 289: 288–291, doi:10.1126/science.289.5477.288

Dunham EM, Rice JR (2008) Earthquake slip between dissimilar poroelastic materials. J Geophys Res 113(B09304), doi:10.1029/2007JB005405

Iverson RM, Reid ME, Iverson NR, LaHusen RG, Logan M, Mann JE, Brien DL (2000) Acute sensitivity of landslide rates to initial soil porosity. Sciences 290: 513–516

Lambe TW, Whitman RV (1969) Soil mechanics. Wiley, New York

Mitchell TM, Faulkner DR (2008) Experimental measurements of permeability evolution during triaxial compression of initially intact crystalline rocks and implications for fluid flow in fault zones. J Geophys Res 113(B11412), doi:10.1029/2008JB005588, p. 16

Moore PL, Iverson NR (2002) Slow episodic shear of granular materials regulated by dilatant strengthening. Geology 30(9): 843–846, doi:10.1130/0091–7613(2002)030<0843:SESOGM>2.0.CO;2

Palmer AC, Rice JR (1973) The growth of slip surfaces in the progressive failure of over-consolidated clay. Proc R Soc Lond A 332: 527–548

Puzrin AM, Germanovich LN (2005) The growth of shear bands in the catastrophic failure of soils. Proc R Soc A 481: 1199–1228 doi:10.1098/rspa.2004.1378

Puzrin AM, Germanovich LN, Kim S (2004) Catastrophic failure of submerged slopes in normally consolidated sediments. Géotechnique 54: 631–643

Réthoré J, de Borst R, Abellan M-A (2007) A discrete model for the dynamic propagation of shear bands in a fluid-saturated medium. Inter J Numer Anal Meth Geomech 31: 347–370, doi: 10.1002/nag.575

Rice JR (1980) The mechanics of earthquake rupture. In: Dziewonski AM, Boschi E (eds) Physics of the Earth's interior (Proc International School of Physics 'Enrico Fermi', Course 78, 1979), Italian Phys Soc and North-Holland Publications, Amsterdam, pp. 555–639

Rice JR, Cleary MP (1976) Some basic stress diffusion solutions for fluid-saturated elastic porous media with compressible constituents. Rev Geophys Space Phys 14: 227–241

Rudnicki JW (2001) Diffusive instabilities in dilating and compacting geomaterials. In: Chuang TJ, Rudnicki JW (eds) Multiscale deformation and fracture in materials and structures, Kluwer Academics, New York

Rudnicki JW, Rice JR (1975) Conditions for the localization of deformation in pressure-sensitive dilatant materials. J Mech Phys Solid 23: 371–394

Rudnicki JW, Rice JR (2006) Effective normal stress alteration due to pore pressure changes induced by dynamic slip propagation on a plane between dissimilar materials. J Geophys Res 111(B09314), doi:10.1029/2006JB004314, p. 18

Segall P, Rice JR (1995) Dilatancy, compaction, and slip instability of a fluid-infiltrated fault. J Geophys Res 100(B11): 22155–22171

Suzuki T and Yamashita T (2008) Nonlinear effects of temperature, fluid pressure, and inelastic porosity on dynamic fault slip and fault tip propagation: emergence of slip strengthening and pulse-like fault slip. J Geophys Res 113(B07304), doi:101.1029/2008JB005581, p. 13

Templeton EL, Rice JR (2008) Off-fault plasticity and earthquake rupture dynamics: 1. Dry materials or neglect of fluid pressure changes. J Geophys Res 113(B09306) doi:10.1029/2007JB005529

Xu W, Germanovich LN (2006) Excess pore pressure resulting from methane hydrate dissociation in marine sediments: a theoretical approach. J Geophys Res 111(B01104), doi:10.1029/2004JB003600, p. 12

Viesca RC, Templeton EL, Rice JR (2008) Off-fault plasticity and earthquake rupture dynamics: 2. Effects of fluid saturation. J Geophys Res 113(B09307), doi:10.1029/2007JB005530, p. 13

White JA, Borja RI (2008) Stabilized low-order finite elements for coupled solid-deformation/fluid-diffusion and their application to fault zone transients. Comput Method Appl Mech Eng 197, 4353–4366, doi: doi:10.1016/j.cma.2008.05.015

Section II
Submarine Mass Movements: Case Studies and Hazard Assessment

Submarine Mass Transport Within Monterey Canyon: Benthic Disturbance Controls on the Distribution of Chemosynthetic Biological Communities

C.K. Paull, B. Schlining, W. Ussler III, E. Lundsten, J.P. Barry, D.W. Caress, J.E. Johnson, and M. McGann

Abstract Documenting mass transport within Monterey Canyon and Fan has been a focus of remotely operated vehicle (ROV) observations, sampling, monitoring, and multibeam mapping studies. These efforts indicate that major mass transport events occur within upper Monterey Canyon (<2 km water depths) with a sub-annual recurrence frequency. However, ^{14}C-stratigraphies indicate that a sand carrying event has not penetrated through lower Monterey Canyon (>2 km water depths) and onto Monterey Fan for ~100 years. Simultaneous efforts to document the distribution of benthic taxa observed in the video records from 668 ROV dives conducted by the Monterey Bay Aquarium Research Institute (MBARI) provide a uniquely detailed record of the occurrence of chemosynthetic biological communities (CBC). The combined results of these studies provide an understanding of the relationship between disturbance caused by episodic mass wasting events and the distribution of CBC. CBC are common within the canyon's axis below ~2.5 km water depth, but have not been found within the canyon's axis at depths shallower than 2 km. Moreover, CBC occur on the canyon walls at essentially any depth, primarily within young (~hundreds of years old) slump scars. The distribution of CBC provides evidence about the disturbance history of the seafloor. Major mass transport events will destroy communities that lie in their path. Erosion associated with major mass transport events can create environments to support CBC by exposing methane-bearing strata. This can happen as a result of slumping events on the sidewalls of the canyon or where major gravity flow events have excavated the base of canyon walls. Once fresh strata are exposed, geochemical conditions to support CBC will persist for a few centuries. Because CBC are composed of

C.K. Paull, B. Schlining, W. Ussler III, E. Lundsten, J.P. Barry, and D.W. Caress
Monterey Bay Aquarium Research Institute, Moss Landing, CA 95039-9644, USA

J.E. Johnson
University of New Hampshire, Durham, NH 03824, USA

M. McGann
U.S. Geological Survey, Menlo Park, CA 94025, USA

slow-growing and long-lived organisms, it will take decades for these communities to be established. Their existence indicates that environmental stability has occurred over a similar time scale.

Keywords Canyons, turbidites • chemosynthetic biological communities • disturbance fauna

1   Introduction

The impact of mass transport events on chemosynthetic biological communities (CBC) within Monterey Canyon (Fig. 1) is considered here. Mass wasting events clearly exert a significant influence on seafloor ecology. Disturbance to seafloor biological communities will include the destruction, burial, and death of many,
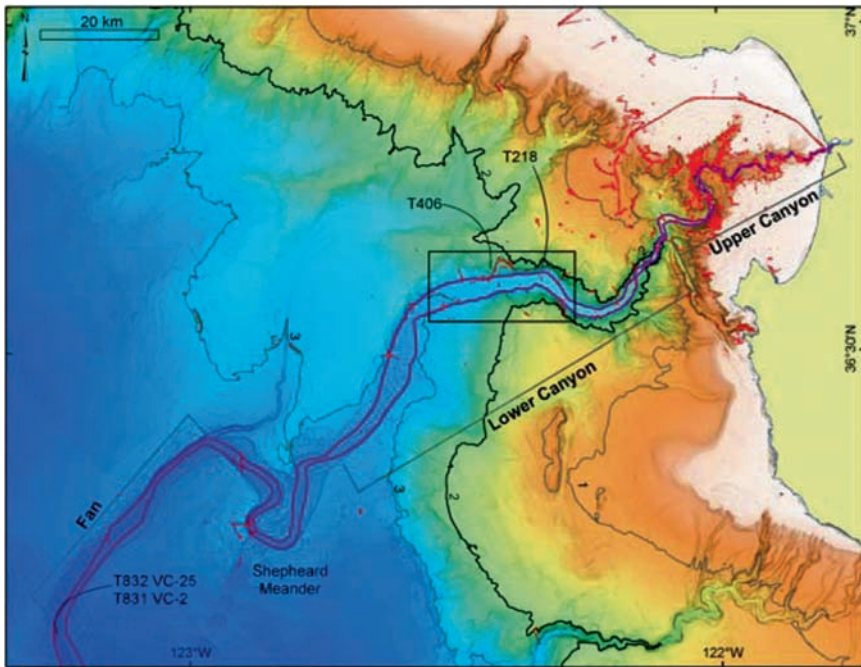
Fig. 1 Map showing bathymetry of Monterey Canyon and Fan. Location of annotations within the VARS (Video Annotation and Reference System) database associated with seafloor observations are indicated with small red dots. Purple lines show boundaries that outline the area of canyon floor analyzed here. Contour interval is 1 km. The boundary between upper and lower canyon groupings shown in Table 2 is at 2 km (bold contour). Location of area shown in Fig. 4, which shows numerous slide scars on the canyon walls, is indicated by the black box

if not most benthic megafauna during the turbulent phase of mass wasting events. Recovery of the communities will occur through recolonization and ecological succession following each event. The successional status of deep-sea communities along the canyon axis should thus reflect the time since the occurrence of the most recent mass transport event. Conversely, the presence of slow-growing taxa indicates prolonged stability of the environment over the time periods associated with development of the organisms.

The impact of mass wasting events on seafloor ecology has been difficult to investigate in part because knowledge of when the last event occurred is rarely possible (e.g., Mayer et al. 1988). The re-colonization of the seafloor with benthic foraminifera following large bottom disturbances produced by historic volcanic events (Hess and Kuhnt 1996; Hess et al. 2001), and turbidity currents in a Norwegian fjord (Alve 1999) and Cape Breton Canyon (Anschutz et al. 2002; Hess et al. 2005) has been examined. These studies tracked changes in the living benthic foraminifera populations by repetitively coring the same sites. Significant re-colonization by benthic foraminifera occurs within a decade. The recovered benthic foraminifer populations include both survivors of the event and re-colonization from outside the disturbed area. Foraminifera commonly have been utilized for these studies because they leave carbonate tests in the sediment, their small size allows statistically meaningful populations to be recovered in individual cores, and they have relatively short life spans.

The ability to understand the recovery and succession of benthic megafaunal communities is usually hampered by a lack of information on when the disturbance associated with the last mass transport event occurred and of methods to document the subsequent changes in the communities. The combination of data from the extensive video archives collected with MBARI remotely operated vehicles (ROVs) to characterize megafaunal communities, stratigraphic data obtained from ROV-collected sediment cores throughout the canyon system, and monitoring activities has allowed the impact of mass transport events on the benthic megafauna to be assessed within the axial channel of Monterey Canyon.

1.1 Mass Transport Events in Monterey Canyon

The axial channel within Monterey Canyon and Fan has been the focus of high-resolution multibeam surveys, ROV observations and sampling, and current meter deployments. Multibeam bathymetry shows that numerous slide scars occur on the flanks of Monterey Canyon (Greene et al. 2002). These features indicate periodic failures of the canyon walls occur. Presumably these failures result in gravity flows that first move down the steep canyon walls (commonly with >20° slope) and subsequently merge into the main axial channel (<2° slope).

Smith et al. (2005, 2007) and Xu et al. (2008) have shown that the floor of uppermost Monterey Canyon changes shape between repeated multibeam surveys. Cores show that gravel and coarse sand, with a composition similar to

sand found on local beaches, accumulate near the canyon head and regularly move down into the canyon as episodic gravity flow events (Paull et al. 2003; 2005a; Xu et al. 2004). These observations demonstrate that upper Monterey Canyon is active out to 2 km water depth and the recurrence interval for gravity flow events is subannual (Barry et al. 2006). Current meter deployments within the axial channel in 3,450 m water depth at Shepard Meander (Fig. 1) indicate that the recently observed gravity flow events within the upper canyon have not flushed through the axial channel of the lower canyon (>2 km water depths) and out onto Monterey Fan (Barry et al. 2006). However, stratigraphic data obtained from sediment cores in lower Monterey Canyon and Fan provide some constraints on the timing of the last major sediment transport event within the axial channel.

1.2   Chemosynthetic Biological Communities

Chemosynthesis is a biological process similar to photosynthesis whereby carbon is fixed using chemically-reduced inorganic compounds or simple hydrocarbons rather than sunlight as the energy source. Large populations of organisms (i.e., CBC) dependent on chemosynthetic production occur at sites where the appropriate biogeochemical conditions occur. Monterey Bay, California is known to contain many CBC (Barry et al. 1996; Paull et al. 2005b, c). The CBC include bacterial mats (i.e., *Thioploca* spp. and *Beggiatoa* spp.), several species of vesicomyid clams that contain endosymbiotic chemolithoautotrophic bacteria (e.g., *Calyptogena* spp.), and tubeworms (previously called Vestimentifera; Barry et al. 1996). The taxonomy of segmented worms (commonly referred to as tubeworms) is now being placed within the Family Siboglinidae (Rouse 2001). Siboglinidae include several genera that are associated with hydrothermal vents, methane seeps, reducing sediments, plant debris and whale falls. The existence of these organisms requires that hydrogen sulfide or methane be available in the immediate subsurface at these sites.

Because continental-margin sediments are frequently organic-rich, a series of biogeochemical reactions occur with increasing depth below the seafloor that involve the progressive chemical reduction in the pore waters and the accumulation of methane below the depth of sulfate depletion (Claypool and Kaplan 1974). Conversely, when methane-rich, sulfate-free sediments are exposed on the seafloor, methane will be oxidized aerobically where it is in contact with oxygenated seawater and anaerobically where it is exposed to oxygen-depleted sulfate-bearing seawater (Reeburgh 1976). Anaerobic oxidation of methane (AOM) produces hydrogen sulfide, the most common chemical substrate to support CBC (Barry et al. 1996). Thus, CBC may occur wherever a sustained source of hydrogen sulfide is available; whether from local production, upward flow of subsurface fluids or exposure of fresh sediment containing methane, hydrogen sulfide, or oil-bearing fluids exposed by geologically rapid seafloor erosion.

1.3 Life Cycles of Organisms Within CBC

The life cycles of the dominant and visually identifiable organisms within CBC vary considerably. Bacterial mats may form and die off on time scales of weeks. Vesicomyid clams live for years to perhaps a century (Lutz et al. 1985; Barry and Kochevar 1998; Barry et al. 2007). Some Siboglinidae may live over 250 years and are known to survive on very low supplies of hydrogen sulfide (Fisher et al. 1997; Freytag et al. 2001; Barry et al. 2007).

Chemosynthetic metazoans require for their survival access to both oxygen and chemically-reduced compounds: resources that in marine sediments are typically separated in space above and below the redox boundary. Various chemosynthetic taxa are capable of exploiting chemically-reduced compounds at different depths below the seafloor. Bacterial mats (e.g., *Thioploca* spp.) occur where both oxygen and hydrogen sulfide are in close proximity (~1 cm) to the seafloor (McHatton et al. 1996). Vesicomyid clams and siboglinid tubeworms morphologically straddle the redox boundary between oxygen and hydrogen sulfide. The occurrence of vesicomyid clams indicates that hydrogen sulfide-bearing-sediments occur within ~20 cm of oxygenated seafloor (Sibuet and Olu 1998). Siboglinid tubeworms are known to have "roots" which grow as a posterior extension and may extend over 2 m into the seafloor to obtain hydrogen sulfide, whereas their anterior end is exposed to oxygenated seawater (Jullian et al. 1999; Freytag et al. 2001). Thus, old, established Siboglinidae have the capacity to mine hydrogen sulfide dissolved in sediment pore waters at substantially greater depths below the seafloor than either vesicomyid clams or chemosynthetic bacterial mats.

1.4 Distribution of CBC in Monterey Bay

Extensive ROV operations conducted by MBARI have made the seafloor of Monterey Bay, California among the most observed continental margins in the world. This data provides a uniquely detailed understanding of the distribution of CBC and authigenic carbonates within this area (Paull et al. 2005b).

A systematic analysis of dive videos and navigation from the 1,192 benthic ROV dives conducted by MBARI provided the first quantitative evaluation of the distribution of CBC along a continental margin (Paull et al. 2005c). Living CBC are common, occurring within 2% of the 25 × 25 m grid cells within which there have been bottom observations within 45 km of the head of Monterey Bay, and within 9% of the visited cells that are below 550 m water depth.

In this paper we expand the area of analysis to consider where CBC occur and where they have not been observed in Monterey Bay, especially within the channel that extends through Monterey Canyon and onto Monterey Fan. These observations are then compared with the existing knowledge of where and when mass transport events have occurred to establish patterns of disturbance and areas of seafloor stability.

2 Methods

2.1 Sediment Cores: Axial Channel of Monterey Canyon and Fan

The adaptation of vibracoring systems onto MBARI's ROVs has allowed precisely located and closely spaced sampling within Monterey Canyon and Fan (Paull et al. 2001; Conway et al. 2003). As part of a larger study of the canyon facies and the recurrence interval of turbidity currents (Johnson et al. 2006), 245 ROV-collected vibracores have been obtained from the axial channel of Monterey Canyon and Fan ranging from 86 to 3,886 m water depths. These cores typically are over a meter long and have been split and described. The cores are now archived at the USGS in Menlo Park, California. Short ROV-collected push cores were also frequently collected adjacent to the vibracore sites to characterize the uppermost sediment cover.

Some of the vibracores collected within the axial channel contain organic-rich layers composed of twigs, bark, and other woody material embedded in fining-upward sand layers associated with the last mass transport event deposit (Fig. 2). To place time constraints on mass transport events, sub-samples of organic debris from these layers were taken for ^{14}C measurement. Radiocarbon measurements were made at the Center for Accelerator Mass Spectrometery (CAMS) facility at Lawrence Livermore National Laboratory (Roberts et al. 1997) and the National Ocean Sciences Accelerator Mass Spectrometry Facility (NOSAMS).

The presence or absence of the pesticide DDT and its residues (DDTr) within the sediments that overlie the last mass transport deposit provides additional chrono-stratigraphic constraints on the timing of the last major mass transport event. The presence of DDTr in marine sediments has both chronologic and tracer significance as DDTr did not occur in the environment prior to 1945. Thus, fine-grained sediments with detectable DDTr came from the land and were deposited since 1945 (Paull et al. 2002). Profiles of DDTr concentrations within the fine-grained sediments in ROV-collected push cores that cap the last sandy deposits from the axis of Monterey Fan channel is the topic of another study looking at recent sediment transport to the Fan (Paull et al. submitted). However, some observations are summarized here to help constrain the timing of the most recent turbidity current to sweep the channel of Monterey Fan.

2.2 Seafloor Observations on the Distribution of CBC

The *R/V Point Lobos* has operated as the support ship for the ROV *Ventana* for day operations in Monterey Bay in up to 1.8 km water depths since 1989. The *R/V Western Flyer* has supported the ROV *Tiburon* in up to 4.0 km water depths since 1998. Both ROVs are equipped with multiple high-resolution video cameras. Continuous videotapes of one camera are routinely recorded during each dive,
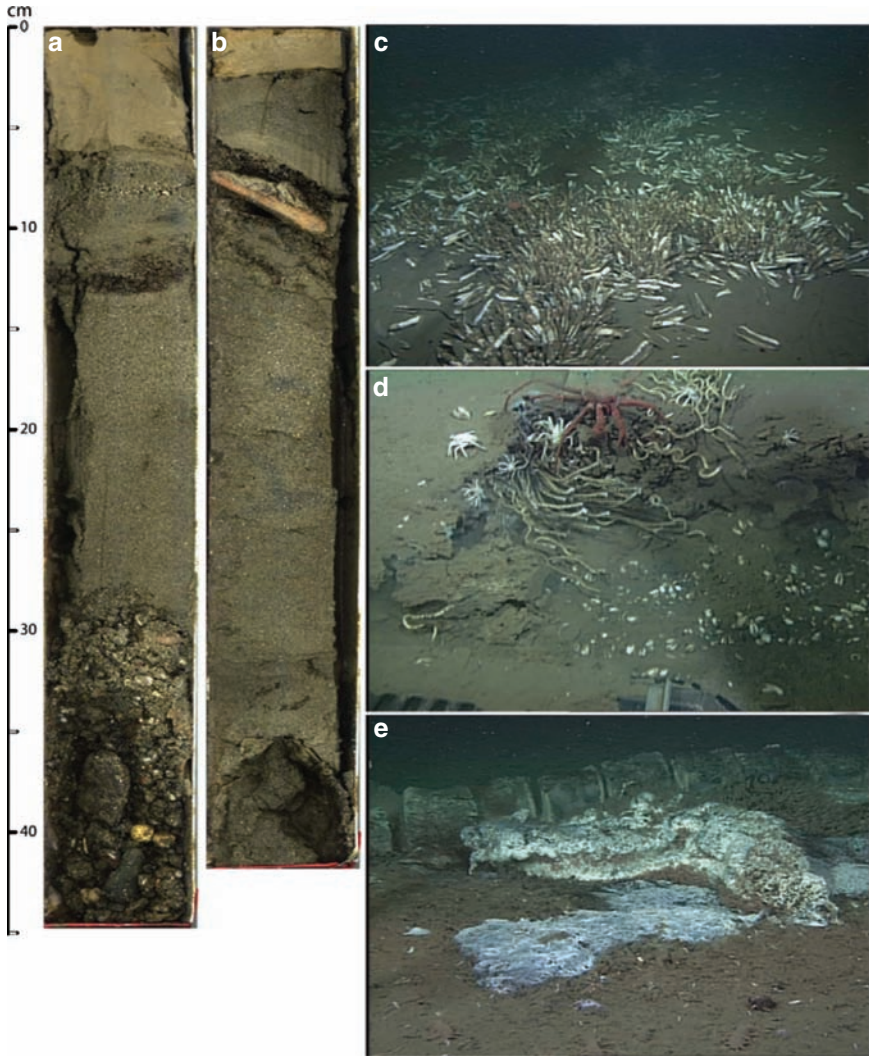
Fig. 2 Photographic mosaic showing two characteristic cores (**a** & **b**) and images of CBC collected during ROV dives within the axis of Monterey Fan (**c– e**). Cores (A- T832 VC-25; B- T831 VC-2, both from 3,674 mbsl) illustrate the fining-upward sequence event deposits that fill the axial channel on the Fan. Organic layer at 13 cm in A and wood branch at 8 cm in B provided material for ^{14}C dating. Part C illustrates a dense bed of vesicomyid clams within the axis of lower Monterey Canyon (2,882 mbsl, dive T406). Part D illustrates a CBC on the flanks of lower Monterey Canyon (note siboglinid tubeworms and vesicomyid clams; 2,208 mbsl, dive T218). Part E illustrates a chemosynthetic bacterial mat adjacent to a whale skeleton within the axis of lower Monterey Canyon (2,896 mbsl, dive T406). The locations of cores and photos are labeled in Fig. 1

and >15,000 h of video footage are archived in MBARI's video library. These data provide both qualitative and quantitative data on the occurrence and distribution of CBC.

All videotapes collected during MBARI ROV dives are systematically viewed by professional, science-trained video archivists (Schlining and Stout 2006). Major features identified on the tapes are entered into the VARS (Video Annotation and Reference System) database, which was designed to systematically record and quantify scientific observations made on all ROV dives. Keyword entries allow archivists to quickly annotate important observations (e.g., objects and organisms). As of December 2008, more than 15,000 h of videotapes have been annotated.

Annotations in the VARS database for the terms Vesicomyidae, Siboglinidae, bacterial mat, seep, shell fragment, and carbonate have been analyzed here. Vesicomyidae and Siboglinidae are direct indicators for CBC as they are the most conspicuous taxa within these communities. The other annotation categories (bacterial mat, seep, shell fragment, and carbonate) are proxies for methane and/or hydrogen-sulfide-rich seafloor environments.

Bacterial mats are commonly associated with CBC, but are not restricted to them. The category "seep" is defined in the video archivist instructions as an area where "gray or black sediments, bacterial mats, and/or living chemosynthetic fauna are observed." Although shell fragments may come from many sources, they commonly occur in broad areas surrounding CBC whether or not living communities are encountered. Many of the carbonate annotations are associated with methane-derived authigenic carbonates, which form near the seafloor in methane-rich environments (Paull and Ussler, 2008).

A previous systematic review of MBARI's ROV dive observations was made with respect to CBC distribution based on all the existing data at that time out to 45 km from shore (Paull et al. 2005b). Here a similar analysis of the ROV observations has been done with a focus on dives exploring the seafloor within the 320-km long channel that extends from the head of Monterey Canyon (~100 m water depth) down slope to 3,886 m water depths on Monterey Fan. The area of the entire canyon and fan channel floor is 349 km² with just 19 km² in less than 2 km water depth (Fig. 1). A total of 668 ROV dives have occurred within this area that produced entries in the VARS database.

MBARI ROV navigation data are derived from acoustic ultrashort-baseline (USBL) tracking systems, which measure range and bearing from the ship to the ROV. These data, combined with ROV depths derived from pressure sensors, allow the vehicle's position to be calculated with respect to the ship. *R/V Point Lobos* was navigated with a Mini-Ranger system and backed up with Loran-C from 1992 to 1995, prior to the availability of differential-GPS (Global Positioning System) systems. Since then, the navigation data of the *R/V Point Lobos* and all *R/V Western Flyer* data have been based on differential-GPS. The real-time estimates of ROV latitude, longitude, and depth were logged at least every 5 s.

Raw USBL-based ROV navigation data often contain spurious fixes. This noise is dominated by errors in the USBL bearing. Jumps between individual fixes are often implausible because large speeds and accelerations for the ROV are implied. Data processing involved first interactively removing large spikes in the navigation and then solving for a plausibly smooth navigation track that minimizes acceleration and speed while fitting the original navigation data in a least-squares sense.

To determine where and how much of the Monterey Bay seafloor has been investigated using ROVs, processed ROV navigation from on-bottom parts of benthic dives from April 1989 through December 2008 were converted to UTM coordinates and binned by 25-m-square grid cells. Simrad EM-300 30 kHz multibeam bathymetry data are available for water depths greater than 90 m throughout Monterey Bay from surveys conducted for MBARI during 1998 (Greene et al. 2002). Comparing water depths for the gridded ROV navigation with an equivalent 25-m-square multibeam bathymetry grid cell identified on-bottom grid cells. ROV navigation grid cells were excluded wherever the ROV navigation depth differed by >20 m from the depth in the corresponding bathymetry grid cell as done in Paull et al. (2005c). In this analysis we further reduced the data to include only the grid cells that contain one or more annotations within the VARS database.

3 Results

3.1 Event Deposits in Monterey Canyon and Fan Channel

Vibracores from Monterey Canyon show that the near seafloor deposits from the axial channel typically contain a surface layer up to 20-cm-thick of soft, poorly-consolidated fine-grained hemipelagic sediments (Figs. 2a and b, 3). Underneath this surface layer are fining-upward sequences that contain gravel, pebbles, coarse sand, and rip-up clasts. These high-energy event deposits fine upward into variable thicknesses of undifferentiated fine to medium sand. Such deposits are classic
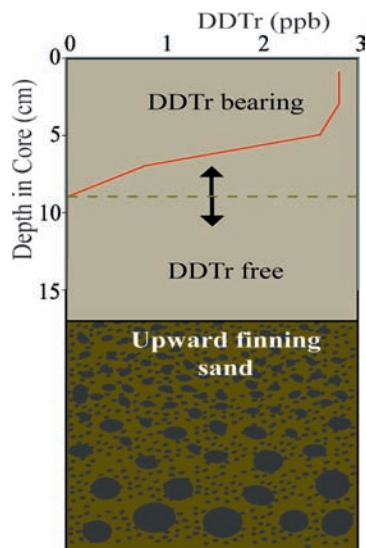
Fig. 3 Cartoon based on data from T401 PsC-53 illustrates an idealized stratigraphy for cores from the axial channel of Monterey Fan. Characteristically, there is a cap of fine-grained clay-rich sediment that ranges in thickness from 0–20 cm over thick gravity flow deposits that consist of fining upward sequences ending in fine sand. The upper half of the fine-grained cap is DDTr-bearing whereas DDTr-free fine-grained sediments overlie the uppermost sand horizon

gravity flow deposits laid down in mass transport events. These lithologies were documented previously in the upper canyon (<1.8 km; Paull et al. 2005a). Since then, transects of ROV-collected vibracores have been collected across the channel out to 3.9 km water depth. Sediments in the cores from the lower Monterey Canyon channel (Fig. 2a and b) are indistinguishable from those collected in upper Monterey Canyon (Paull et al. 2005a).

Measurements of the ^{14}C content of woody material deposited within event deposits and DDTr stratigraphies within the overlying clay caps provide constraints on the timing of the last event within the channel on Monterey Fan. Radiocarbon measurements of eight woody debris samples from the uppermost event deposit within the Fan channel yielded ages as young of 125 ± 30 RC years B.P. (Table 1). Wood samples found in this environment constrain a maximum age for the event, because the wood grew on land and was transported to this environment. However, two wood samples from the upper Monterey Canyon contain modern carbon and confirm that major mass transport events in this area occur regularly today (e.g., Paull et al. 2003; Xu et al. 2004; Barry et al. 2006).

The timing of the last sand-depositing event within the channel of Monterey Fan is constrained also with DDTr (Paull et al. 2002). Although DDTr consistently occurs in the uppermost clay-rich sediments, it is commonly absent in the clays that overlie the uppermost sand deposit. This indicates that the youngest sediment mass transport event in these cores occurred more than 60 years ago (Fig. 3). The combination of DDTr and ^{14}C data suggests that the last major sediment transport event to deposit sand within the channel of Monterey Fan occurred more than 60 years ago and less than RC 125 years ago.

3.2 ROV Observations of CBC Occurrence in Monterey Canyon and Fan

MBARI's VARS database contains observations made from the videotapes collected on ROV dives conducted in Monterey Bay and Fan by both *Ventana* and *Tiburon*. These dives were collected for a variety of purposes and the distribution of ROV dive effort is not uniform. Many more benthic dives have occurred at shallower depths within upper Monterey Canyon (<2 km water depth) than in lower Monterey Canyon or Fan.

For this analysis, we have differentiated the area associated with the bottom of the canyon from the seafloor on the canyon's flanks and the areas outside of the canyon (Fig. 1; Table 2). These areas have been further subdivided to show occurrences of the CBC indicators both shallower and deeper than 2 km water depths. This distinction was selected as it is associated with a natural break in the channel width, dividing the narrow upper Monterey Canyon from the broader channel associated with lower Monterey Canyon and Fan.

Because the area within the axial channel in upper Monterey Canyon (19 km^2) is much less than lower Monterey Canyon and Fan (330 km^2), the percentage of

Table 1 AMS ¹⁴C measurements on wood or twigs found within the uppermost sand layer within the axis of Monterey Fan Channel and in Upper Monterey Canyon

Lab #	Sample	Depth in core (cm)	Lat. (°N)	Long. (°W)	Water Depth (m)	δ¹³C	% Modern ±1 σ	Age RC Year B.P. ±1 σ
91,332§	T401 PsC-56‡	18	35.5441	123.0064	3,866	−28.3	98.1 ± 0.38	155 ± 35
91,329§	T400 VC-A20‡	62–63	36.2190	123.1584	3,612	−28.2	91.7 ± 0.40	700 ± 35
91,376§	T405 VC-38‡	19–20	36.2266	122.8779	3,431	−25.0	92.6 ± 0.46	620 ± 45
91,378§	T405 VC-46‡	40–42	36.2244	122.8851	3,446	−26.8	97.8 ± 0.03	180 ± 25
118,789§	T831 VC-2*	18	36.0796	123.2498	3,674	−24.4	97.7 ± 0.33	190 ± 30
118,876§	T832 VC-25^	22	36.0769	123.2535	3,674	−29.3	94.4 ± 0.35	465 ± 35
120,514§	T401 VC-33*	40	35.5435	123.0051	3,870	−26.4	98.5 ± 0.36	125 ± 30
118,877§	T400 PsC-56^	18	36.2164	123.1560	3,581	−26.0	98.0 ± 0.37	160 ± 30
OS-69023ᴮ	V3119 VC-143	107–108	36.8026	121.8025	117.39	−16.0	1.03 ± 0.003	>Mod
OS-69024ᴮ	V3120 VC-144	115–116	36.8026	121.8030	119.48	−24.6	1.08 ± 0.004	>Mod

§CAMS lab number; ᴮNOSAMS lab number; *wood; ‡organic mat; ^twig; RC = radiocarbon age, not reservoir corrected. Core locations shown in Fig. 1 except for dive T401.

Table 2 Number of 25-m-square grid cells associated with entries in the VARS database for concepts that are either direct indicators of CBC or proxies for CBC occurrence. Data are divided into four groups, depending on whether the observations are associated with the canyon floor or not and at greater or less than 2 km water depths

	Less than 2 km canyon # – %	Less than 2 km other # – %	Greater than 2 km canyon # – %	Greater than 2 km other # – %
Vesicomyidae	0 – 0%	676 – 1.6%	81 – 3.5%	80 – 2.0%
Siboglinidae	0 – 0%	95 – 0.2%	1 – 0.04%	80 – 2.0%
Bacterial mat	0 – 0%	424 – 1.0%	34 – 1.5%	49 – 1.2%
Seeps	0 – 0%	338 – 0.8%	7 – 0.3%	19 – 0.5%
Carbonate	1 – 0.05%	378 – 0.9%	6 – 0.3%	9 – 0.2%
Shell fragments	8 – 0.4%	569 – 1.4%	36 – 1.5%	50 – 1.3%
Total # grid cells with data entries	2,128	41,579	2,337	3,979

seafloor within the axial channel that has been inspected during ROV dives is much higher (Fig. 1, Table 2). Although there are a similar total number of grid cells with entries in the VARS database from the canyon floor in greater than 2 km water depths (2,337 entries) and shallower than 2 km water depth (2,128 entries), a larger proportion of upper Monterey Canyon has been explored. The seafloor of Monterey Canyon, especially in the upper canyon, is relatively barren. Thus, the number of entries within the VARS database for this area may underestimate the amount of bottom coverage as some grid cells may have been explored, yet are not associated with any annotations in the VARS database.

Indicators of seepage or CBC on the floor of upper Monterey Canyon are rare or absent. The 2,128 grid cells with VARS annotations for the floor of upper Monterey Canyon shallower than 2 km water depth contain no observations of living CBC (i.e., no annotations for Vesicomyidae, Siboglinidae, bacterial mat, or seep). Furthermore, there is for this area only one VARS annotation for carbonate and just eight entries for shell fragment. In contrast, CBC were relatively common within lower Monterey Canyon (Fig. 4). Of 2,337 grid cells with VARS annotations within the floor of lower Monterey Canyon (>2 km water depths), there were 81 annotations for Vesicomyidae, 34 for bacterial mats and 7 for seeps. However, only 1 annotation for Siboglinidae in the lower canyon exists in the database. This siboglinid occurrence is associated with the bone-eating siboglinid Osedax, found on a whale carcass on the canyon floor (Rouse et al. 2004; Goffredi et al. 2004; Fig. 2e). Thus, the indicators of CBC that can become established in less than a century are evident in the lower canyon, but absent from the more frequently disturbed upper canyon.

The total number of grid cells within each of the four analysis groupings (Table 2) differs enormously, especially with respect to the number of observations away from the canyon floor. Table 2 also contains a percentage occurrence number for each area. This was obtained by dividing the number of grid cells containing one or more annotations in the VARS database associated with a particular observation by the total number of grid cells for which there is at least one annotation of any phenomenon
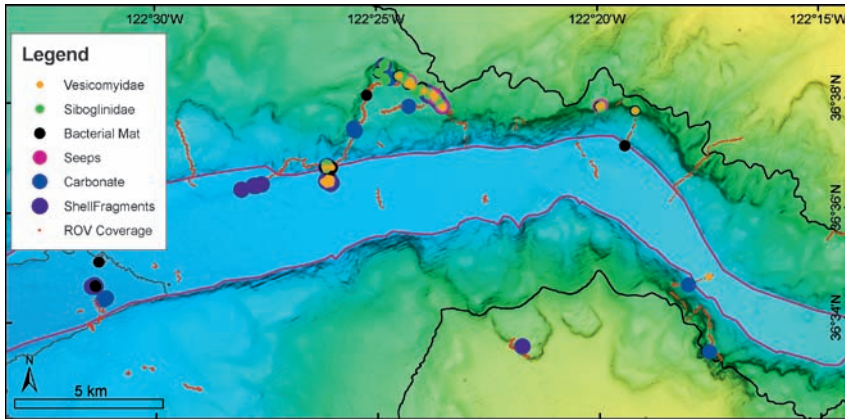
Fig. 4 Map showing a section of lower Monterey Canyon's flank and floor. Location of annotations in the VARS database associated with seafloor observations are indicated with small red dots. Sites where video annotations indicate occurrence of Vesicomyidae, Siboglinidae, bacterial mat, seeps, carbonate, and shell fragments are indicated with filled colored circles. Note that the occurrences of these CBC indicators are common both within the canyon axis and on the obvious slide scars on the canyon flanks. The greatest concentration of dives is associated with Tubeworm Slump on the north side of the canyon (Naehr et al. 2000). The 2 km water depth contour is highlighted in black.

within the VARS database. This provides an indication of how common the particular phenomenon is (e.g., Siboglinidae) with respect to the total ROV dive effort within any prescribed region and makes comparisons among regions easier.

The percent occurrence numbers suggest that Vesicomyidae are most common (3.5%) on the canyon floor in water depths greater than 2 km, and occur less frequently on the canyon flanks both in the upper (1.6%) and lower canyon (1.6%). Vesicomyidae have not been found within the channel of the upper canyon. In fact the shallowest occurrence within the canyon floor is at 2,657 m whereas they occur as shallow as 399 m on its flanks. The percent occurrence numbers associated with entries for seeps, carbonates, and shell fragments follow a similar pattern, being either absent or in very low abundance within the floor of the upper canyon, but occurring more frequently within the other areas. However, the percent occurrence numbers of Siboglinidae show a different pattern. These taxa are most common on the canyon flanks below 2 km, but have only one entry within the canyon floor and it is associated with a whale fall at 2,890 m water depth. Although the repeated ROV visits to this whale fall between its discovery on February 2, 2002 and October 24, 2006 show the progressive decay of its skeleton (Rouse et al. 2004), its persistence provides further evidence that no sediment gravity flows penetrated to this depth during the same period that major events occurred within upper Monterey Canyon (Paull et al. 2003; Xu et al. 2004).

Isolated patches of vesicomyid clams form the most common CBC type encountered on the canyon floor below 2 km water depth (Fig. 2c; Table 2). In addition, observations made during ROV dives show that CBC also occur on lowermost sections of the canyon walls of lower Monterey Canyon and Fan channel where nearby

surfaces are relatively smooth, lack a sediment drape, and are noticeably under-colonized with epifauna. The CBC are especially common on lower walls of outside bends of lower canyon and fan channel meanders where the erosive forces of sediment transport events within the channel would be focused.

4 Discussion

The occurrence of CBC (as indicated by the direct and proxy indicators cataloged within the VARS database) shows two patterns: (1) They are common on the steep flanks of the canyon walls, especially in areas associated with geologically fresh slide scars as previously argued and documented (Paull et al. 2005b, c). (2) They are common within the floor of the axial channel of lower Monterey Canyon (2 to 3.2 km water depth) and Fan channel (>3.2 km water depth).

This dataset not only establishes where visually identified phenomena occur, but is large enough to assess where CBC do not occur. CBC are noticeably absent within the axis of Monterey Canyon out to 2 km water depths. These observations are discussed with respect to our independent information on both the timing and locations of gravity flow events within the axis of Monterey Canyon and Fan channel.

4.1 Mechanisms to Supply CBC with Dissolved Hydrogen Sulfide

While the occurrence of CBC on the seafloor along the continental margin off Monterey, California indicates that dissolved hydrogen sulfide is available locally to support these communities, several different mechanisms can provide hydrogen sulfide. CBC were initially discovered on the floor of the Monterey Fan channel off central California between 3,000 and 3,600 m water depths (Embly et al. 1990). These CBC were attributed at the time to either (1) local hydrogen sulfide production associated with microbial decomposition of organic material buried within the seafloor or (2) hydrologic flow through the exposed, eroded flanks of the channel. Clumps of kelp are commonly seen on the seafloor within the axial channel of Monterey Canyon and Fan. Layers of woody material are also common within sediment cores from the axial channel on Monterey Canyon and Fan (Fig. 2). Decomposition of this organic debris could generate hydrogen sulfide to support CBC. Local additions of organic matter associated with marine mammal falls (Goffredi et al. 2004) also result in hydrogen sulfide production that can support CBC.

CBC distribution within Monterey Bay has been attributed to fluid-flow stimulated by compressional tectonics (Orange et al. 1999; Stakes et al. 1999) that drives fluids out along fault conduits, bringing methane or hydrogen sulfide to the seafloor. There are places in Monterey Bay where active flow is unequivocally demonstrated (e.g., LaBonte et al. 2007). Such CBC sites support dense apparently

healthy CBC. In contrast, many of the known CBC sites consist of sparser communities. Although fluid flow along fault conduits may support some CBC, the overall distribution of CBC in Monterey Bay does not mimic the independently mapped fault distribution and thus, does not strongly support the hypothesis that they are primarily associated with tectonically-driven flow through regional faults (Paull et al. 2005b).

Diffusion from methane-bearing pore water within the sediment sequences exposed on geologically young slide scars has been proposed as an alternative mechanism for supporting many of the CBC on the flanks of Monterey Canyon (Paull et al. 2005b). Slides that remove enough of the sediment overburden to expose methane-bearing sediments on the seafloor would stimulate production of hydrogen sulfide by AOM. The retreat of the zone of AOM into exposed sediments will control a succession of CBC organisms beginning with bacterial mats, then vesicomyid clams, and eventually siboglinid tubeworms (Paull et al. 2005c). Community succession will depend on the rate at which sulfate diffuses into the sediment and how quickly the zone of AOM retreats. The occurrence of numerous slide scars on the sidewalls of Monterey Canyon, the exposure of apparently fresh, recently-eroded strata on the canyon walls, the active tectonics and regional compression of the area, and the bold topography which might expose aquifers, provide multiple mechanisms to support CBC within Monterey Canyon and Fan. While disturbances associated with mass wasting events may be one mechanism to stimulate conditions to support CBC, for CBC to develop the right balance between stability and disturbance needs to be achieved.

4.2 Frequency of Submarine Mass Wasting Disturbance and CBC Distribution

No CBC have been encountered within the channel that runs through upper Monterey Canyon shallower than 2 km water depth. This area also corresponds with the region where the most ROV dives have occurred, adding credence to the implication that they do not occur within the channel shallower than 2 km water depth. Conversely, CBC are common in the axial channel extending in water depths deeper than 2.5 km from lower Monterey Canyon across the Fan. Water depth itself is not the controlling factor, as CBC are common in Monterey Bay between 550 and 2,000 m water depth especially on steep sections of the canyon walls associated with geologically young slide scars (Paull et al. 2005b, c). Slides will expose methane-bearing sediments that are then subject to colonization with CBC fauna. CBC undergo a succession of organism types that takes decades to perhaps centuries to complete. The existence of mature CBC requires a high degree of seafloor stability after slope failure.

The pattern of CBC distribution observed within the axial channel of Monterey Canyon and Fan also appears to be controlled predominantly by the stability of the seafloor. Relatively slow-growing vesicomyid clams do not occur within the axial channel of upper Monterey Canyon because the frequency of high-energy events

has not allowed slow growing communities to become established and develop to maturity. Conversely, the existence of CBC within the axial channel of lower Monterey Canyon and Fan implies that this area has been stable long enough for diverse populations of vesicomyid clams to be established and developed. Stratigraphic data independently shows that the last sand-carrying event within this channel occurred more than 60 years ago but less than 125 years ago, which is consistent with the life-spans of vesicomyid clams and siboginid tubeworms.

5 Conclusions

The occurrence of CBC in Monterey Bay is controlled by the pattern of disturbance and stability introduced by mass wasting events. Mass transport events in upper Monterey Canyon occur at sufficient frequency to disturb the seafloor, preventing establishment of CBC. The disturbed areas on the canyon walls that support CBC appear to be related to periodic slope failures that expose methane-bearing sediments that support CBC through AOM near the seafloor. The seafloor in lower Monterey Canyon and Fan channel where CBC occur indicates stability for approximately century-long periods of time.

References

Alve E (1999) Colonization of new habitats by benthic foraminifera: A review. Earth Sci Rev 46:167–185.

Anschutz P, Jorissen FJ, Challiou G, Abu-Zeid R, Fontanier C (2002) Recent turbidite deposition in the eastern Atlantic: Early diagenesis and biotic recovery. J Mar Res 60:835–854.

Barry JP, Kochevar RE (1998) A tale of two clams: Differing chemosynthetic life styles among vesicomyids in Monterey Bay cold seeps. Cah Biol Mar 39:329–332.

Barry JP, Greene HG, Orange DL, Baxter CH, Robinson, BH, Kochevar RE, Nybakken JW, Reed DL, McHugh CM (1996) Biologic and geologic characteristics of cold seeps in Monterey Bay, California. Deep-Sea Res I 43:1739–1762.

Barry JP, Paull CK, Xu JP, Buck KR, Whaling PL, Ussler W, Caress D (2006) The tempo and intensity of turbidity flows in Monterey Canyon. AGU Ocean Sciences Meeting, Feb. 20–24, 2006 Honolulu, Hawaii.

Barry JP, Whaling PJ, Kochevar RK (2007) Growth, production and mortality of the chemosynthetic vesicomyid bivalve, *Calyptogena kilmeri* from cold seeps off central California. Mar Ecol 28:169–182.

Claypool GE, Kaplan IR (1974) Methane in marine sediments. In: Kaplan IR (ed.), Natural Gases in Marine Sediments, Plenum Press, New York, pp. 99–139.

Conway M, Prickett R, Erickson J, Paul C, Graves D, Ussler W III, Mitts P, Greene HG (2003) Vibracore sediment sampling using ROV's. Underwater Intervention Conference, New Orleans, LA, February 11, 2003, 5 p.

Embley RW, Eittreim SL, McHugh CH, Normark WR, Rau GH, Hecker B, DeBevoise AE, Greene HG, Ryan, WBF (1990), Geological setting of chemosynthetic communities in the Monterey Fan Valley system. Deep-Sea Res Part A 37:1651–1667.

Fisher CR, Urcuyo IA, Simpkins MA, Nix E (1997) Life in the slow lane: Growth and longevity of cold-seep vestimentiferans. Mar Ecol 18:83–94.

Freytag JK, Girgus PR, Bergquisht DC, Andras JP, Childress JJ, Fisher CR (2001) A paradox resolved: Sulfide acquisition by roots of seep tubeworms sustains net chemoautrophy. PNAS 98:13,408–13,413.

Goffredi SK, Paull CK, Fulton-Bennett K, Hurtado LA, Vrijenhoek RC (2004) Unusual benthic fauna associated with a whale fall in Monterey Canyon. California, Deep-Sea Res 51:1295–1306.

Greene HG, Maher N, Paull CK (2002) Physiography of the Monterey Bay Marine National Marine Sanctuary and implications about continental margin development. Mar Geol 181:55–62.

Hess S, Kuhnt W (1996) Deep-sea benthic foraminifera recolonization of the 1991 Mt. Pinatubo ash layer in the South China Sea. Mar Micropaleo 28:171–197.

Hess S, Kundt W, Hill S, Kaminski MA, Holbourn A, deLeon M (2001) Monitoring the recolonization of the Mt. Pinatubo 1991 ash layer by benthic foraminifera. Mar Micropaleo 43:119–142.

Hess S, Jorissen FJ, Venet V, Abu-Seid R (2005) Benthic foraminiferal recovery after a recent turbidite deposition in the Cap Brenton Canyon, Bay of Biscay. J Foram Res 35:114–129.

Johnson JE, Paull CK, Normark W, Ussler W (2005) Late Holocene turbidity currents in Monterey Canyon and fan channel; implications for interpreting active margin turbidite records. EOS Trans Am Geophys Union Suppl Abs 86(52)OS21A–1521.

Jullian D, Gaill F, Wood E, Arp AJ, Fisher CR (1999) Roots as a site of hydrogen sulfide uptake in the hydrocarbon seep vestimentiferan *Lamellibrachia* sp. J Exp Biol 202:2245–2257.

LaBonte AL, Brown KM, Tyron MD (2007) Monitoring periodic and episoide flow events at Monterey Bay seeps using a new optical flow meter. JGR 112:B02105.1–B02105.14.

Lutz RA, Fritz LW, Rhoads DC (1985) Molluscan growth at deep-sea hydrothermal vents. Bull Biol Soc Washington 6:199–210.

Mayer LA, Shor AN, Hughes Clarke J, Piper DJW (1988) Dense biological communities at 3850 m on the Laurentian Fan and their relationship to the deposits of the 1929 Grand Bank earthquake. Deep-Sea Res Part A 35:1235–1246.

McHatton SC, Barry JP, Jannasch HW, Nelson DC (1996) High nitrate concentrations in vacuolate, autotrophic marine *Beggiatoa* spp. Appl Environ Microbiol 62:54–958.

Naehr TH, Stakes DS, Moore WS (2000) Mass wasting, ephemeral fluid flow, and barite deposition on the California continental margin. Geology 28:315–318.

Orange DL, Greene HG, Reed D, McHugh CM, Ryan WBF, Maher N, Stakes DS, Barry J (1999) Widespread fluid expulsion on a translational continental margin; mud volcanoes, fault zones, headless canyons, and organic-rich substrate in Monterey Bay, California. GSA Bull 111:992–1009.

Paull CK, Ussler W III (2008) Re-evaluation of the significance of seafloor accumulations of methane-derived carbonates: Seepage or erosion indicators? Proceedings of the 6th International Conference on Gas Hydrates (ICGH 2008), Vancouver, British Columbia, Canada, July 6–10, paper #5581, 12 pp.

Paull CK, Stratton S, Conway M, Brekke K, Dawe TC, Maher N, Ussler W III (2001) Deep sea vibracoring system improves ROV Sampling Capabilities. EOS 82:325–326.

Paull CK, Greene HG, Ussler W III, Mitts, PJ (2002) Pesticides as tracers of sediment transport through Monterey Canyon. Geo-Mar Lett 22:121–126.

Paull, CK, Ussler W III, Greene HG, Keaten R (2003) Caught in the act: The December 21 gravity flow event in Monterey Canyon. Geo-Mar Lett 22:227–232.

Paull CK, Mitts P, Ussler W III, Keaten R, Greene HG (2005a) Trail of sand in upper Monterey Canyon. Geol Soc Am Bull 117:1134–1145.

Paull CK, Schlining B, Ussler W III, Paduan JB, Caress D, Greene HG (2005b) Distribution of chemosynthetic biological communities in Monterey Bay, California. Geology 33:85–88.

Paull CK, Ussler W III, Greene HG, Barry J, Keaten R (2005c) Bioerosion by chemosynthetic biologic communities on Holocene submarine slide scars. Geo-Mar Lett 25:11–19.

Paull CK, Ussler W III, Caress D, Lundsten E, Barry J, Covault J, Maier K, Xu J, Augenstein S (201_) Origins of large crescent-shaped bedforms within the axial channel of Monterey Canyon. Geospheres (submitted) 40 ms p.

Reeburgh WS (1976) Methane consumption in the Cariaco Trench waters and sediments. Earth Planet Sci Lett 28:337–344.

Roberts ML, Bench GS, Brown TA, Caffee MW, Finkel RC, Freeman SPHT, Hainsworth LJ, Kashgarian M, McAninch, Proctor ID, Sothon JR, Vogel JS (1997) The LLNL AMS Facility. Nucl Instrum Meth Phys Res B123:57–61.

Rouse GW (2001) A cladisstic analysis of Sibloginidae Caullery, 1914 (Ploychaeta, Annelida): Formerly the phyla Pogonopora and Vestmentifera. Zoo J Linnean Soc. 132:55–80.

Rouse GW, Goffredi SK, Vrijenhoek RC (2004) Osedax: Bone-eating marine worms with dwarf males. Science 305:668–671.

Schlining BM, Stout NJ (2006) MBARI's video annotation and reference system, OCEANS 2006, 10.1109/OCEANS.2006.306879.

Sibuet M, Olu K (1998) Biogeography, biodiversity and fluid dependence of deep-sea cold-seep communities at active and passive margins. Deep Sea Res II 45:517–567.

Smith DP, Ruiz G, Kvitek R, Iampietro PJ (2005) Semi-annual patterns of erosion and deposition in Upper Monterey Canyon from serial multibeam bathymetry. GSA Bull 117:1123–1133.

Smith DP, Kvitek R, Ruiz G, Iampietro PJ, Wong K (2007) Twenty-nine months of geomorphic change in upper Monterey Canyon (2002–2005). Mar Geol 236:79–94.

Stakes DS, Orange D, Paduan JB, Salamy KA, Maher N (1999) Cold-seeps and authigenic carbonate formation in Monterey Bay, California. Mar Geol 159:93–109.

Xu JP, Noble MA, Rosenfeld LK (2004) In situ measurement of currents structures with turbidity currents. Geophys Res Lett 31. L0911, doi:10.1029/2004GL019718.

Xu JP, Wong FL, Kvitek R, Smith D, Paull CK (2008) Sandwave migration in Monterey Submarine Canyon, Central California. Mar Geol doi:10.1016/j.margeo. 2007.11.005.

Multi-direction Flow in a Mass-Transport Deposit, Santos Basin, Offshore Brazil

L.B. Ashabranner, E.K. Tripsanas, and R.C. Shipp

Abstract The complex Quaternary Rebelde Slide is located on the northeastern corner of the Sao Paulo Plateau at the base of the upper continental slope in water depths of 1,600–1,700 m. This mass-transport deposit (MTD) is up to 300 m thick, 10 km wide where confined, 36 km long, and is buried beneath 50–65 m of hemipelagic drape. The Rebelde Slide is unusual because it appears to have flowed parallel to the slope. The majority of the failure is confined to a contouritic moat that runs along the base of the upper continental slope. The sliding surface of the failure is undulating, and coincides with the top of an underlying sediment wave. The Rebelde Slide consists of three components. Each one is characterized by different structural characteristics and direction of movement, as if the entire interval collapsed under its own weight on a multi-directional sliding surface. The coincidence of the sliding surface of the Rebelde Slide with the source area of fluid-expulsion features observed near the moat suggests failure along a zone of overpressured, geotechnically weak layers.

Keywords Mass-transport deposit • contourite • sediment drifts

1 Introduction

Most sediment failures tend to occur on specific layers of low shear-strength commonly referred to as "weak" layers. These weak layers can be sand intervals with high water content (e.g., Tripsanas et al. 2008), or relatively overpressured mud-prone intervals (J. Newlin, personal communications, 2009). Most examples of sediment failures in literature are from unidirectional slopes that result in the formation of simple (e.g., Gulf of Corinth failures in Hasiotis et al. 2004) or complex mass movements (e.g., Storegga slide in Bryn et al. 2005). Very few studies exist on the

L.B. Ashabranner (✉), E.K. Tripsanas, and R.C. Shipp
Shell International E & P Inc. 200 N. Dairy Ashford, Houston, TX 77079, USA
e-mail: Lisa.Ashabranner@shell.com

development of failures in areas with complex multi-directional slopes (e.g., Moscardelli et al. 2006)]. Such failures are comprised of several, multi-directional flow components.

This study investigates an unusual MTD that exists at the intersection of the upper continental slope and the Sao Paulo Plateau, approximately 200 km southeast of Rio de Janeiro (Fig. 1). The Rebelde Slide is an example of a complex failure that has evolved on the multi-directional slope environment of a contouritic (sediment-drift) deposit. The purpose of this study is to describe the morphology, internal character, and depositional processes of this unusual MTD. Additionally, this study explores the relationship to an underlying sediment-drift complex, establishes a model for progression of the failure, and speculates on possible triggering mechanisms.

The study area is covered by high quality 3D post-stack time migrated seismic data. Geco-Prakla Exploration Services conducted the non-proprietary 3D survey in 2000. Dissemblance volumes (also known as coherency volumes) based on correlation coefficients between traces in a user-defined matrix around each trace were used to facilitate interpretation.
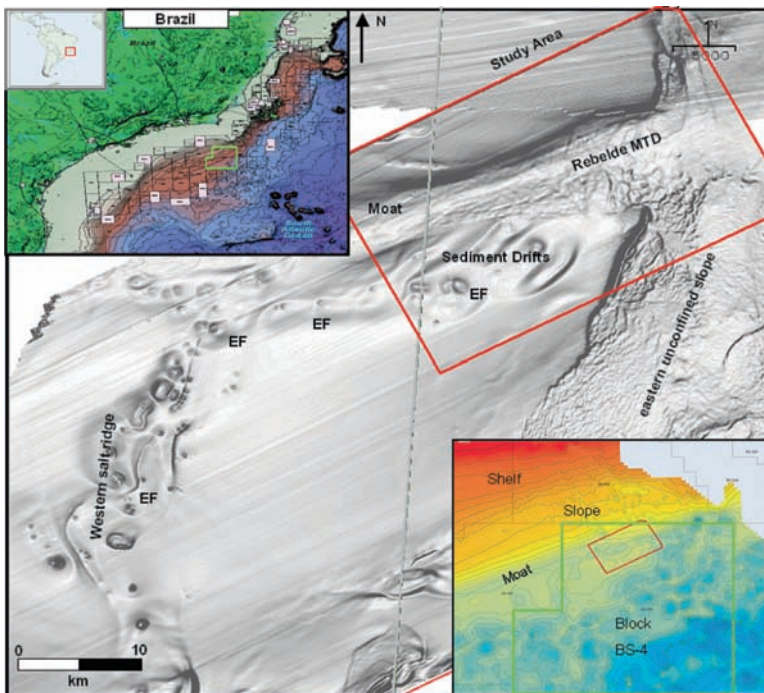
Fig. 1 Seafloor dip map of the Santos Basin, offshore Brazil. Study area is approximately 200 km south of Rio de Janeiro and is positioned at base of the upper continental slope. Upper left inset is a location map, the BS-4 concession block is outlined in green. Lower right inset: a seafloor relative bathymetry map (*red is shallow, blue is deep*). Study area is outlined in red. EF: expulsion features.

2 Geological Setting

The dominant source of clastic sediment input into the Santos Basin was an ancestral river system that focused sediment into the northern and central parts of the basin during the Late Cretaceous and Paleogene (Modica and Bush 2004). This depositional pattern was altered as the river system was tectonically redirected to the north into the Campos basin during the Oligocene. This resulted in a starved and eventually drowned Santos continental shelf. The diversion of the dominant clastic source away from the Santos Basin resulted in a Late Tertiary to Holocene section consisting predominately of marine muds.

The study area is located at the base of the upper continental slope (Fig. 1), and is characterized by complex seafloor morphology. The western and central parts exhibit predominantly smooth morphology, punctuated by the occurrence of fluid-expulsion features (pockmarks). In the west, a north-south trend of pockmarks and undulating topography is related to an underlying salt ridge. At the base of a slope, sediment waves, pockmarks and an east-west trending depression or "moat" characterize the seafloor. This base of slope depression and sediment wave complex is interpreted as a large sediment drift (H. Lu, personal communications, 2005), with the prominent east-west depression interpreted to be a contouritic moat. The eastern part of the study area consists of a southeasterly inclined slope that is characterized by a rugose topography, attributed to near surface MTDs. This rugose topography is also found to extend westward into the contouritic moat along strike to the continental shelf and represents the seafloor expression of the Rebelde Slide.

3 Results

3.1 Structural Characteristics

The Rebelde Slide occupies a contouritic moat, is up to 300 m thick, is at water depths of 1,600–1,700 m, and is buried under 50–65 m of hemipelagic sediment (Figs. 2 and 3). Underlying the MTD is a thick sequence of undulating sediment-drift deposits. A northeast-southwest salt-rooted fault zone is truncated at the base of the MTD (Fig. 3b). The base of the Rebelde Slide consists of three elongated depressions. The eastern-most depression is open at its eastern boundary and connects with the unconfined inclined eastern slope (Fig. 2a).

The Rebelde Slide can be subdivided into three major components (A, B, and C) characterized by different types of movement and sediment remobilization (Fig. 2b). The A component is 20 km long, 1.9–3.3 km wide, occupies two elongated depressions in the moat, the western depression (WD) and the eastern depression (ED) (Fig. 2a). It has a wedge-like shape, which thins from 250 m in the east to less than 150 m to the west. Analysis of seismic traverses indicates that the A component is
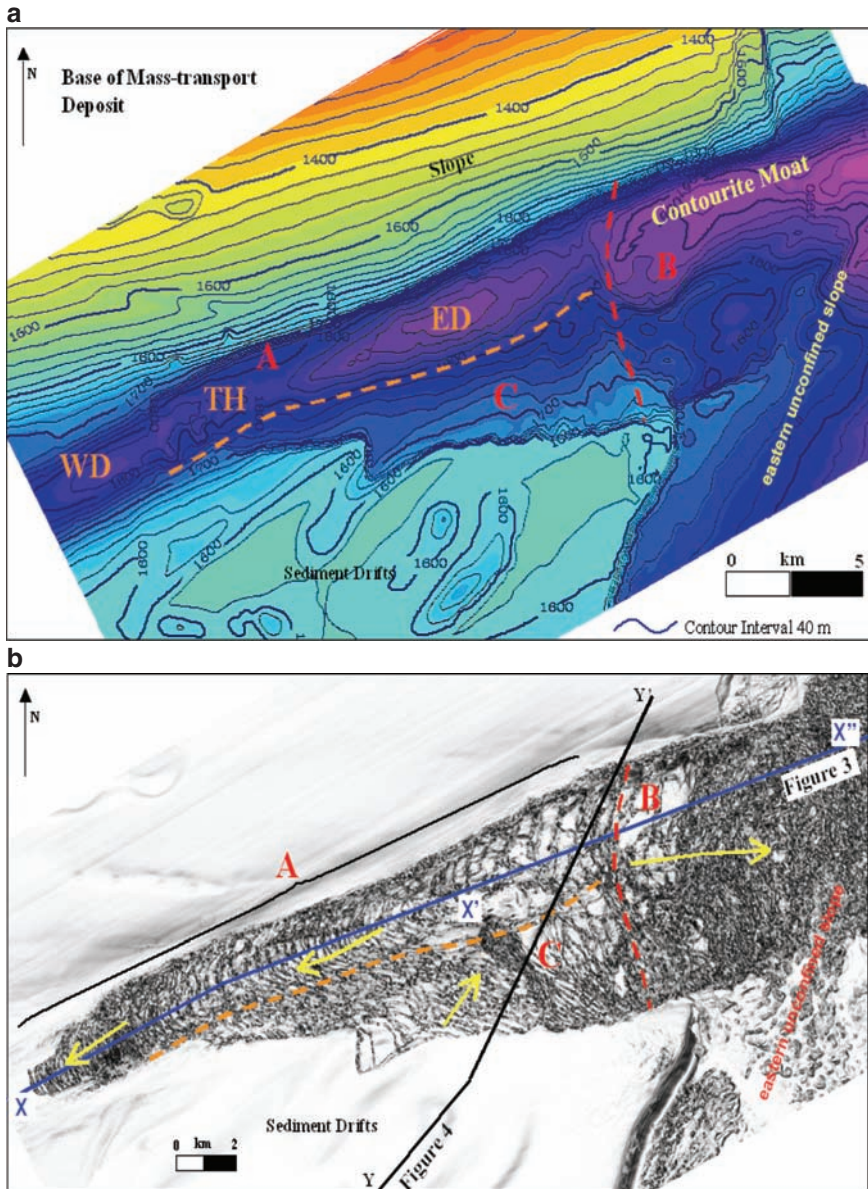
Fig. 2 Map view of the Rebelde Slide. (**a**) A structure map of the basal surface of the failure (*green line in Figs. 3 and 4*). The main components (A, B, C) are identified. The basal surface of component A is defined by underlying sediment drifts with a western depression (WD), a central area of topographic high relief (TH) and an eastern depression (ED). (**b**): A flattened dissemblance slice 100 ms above the base of the failure. Yellow arrows indicate flow direction. Dashed lines represent the boundaries between the components in both images.
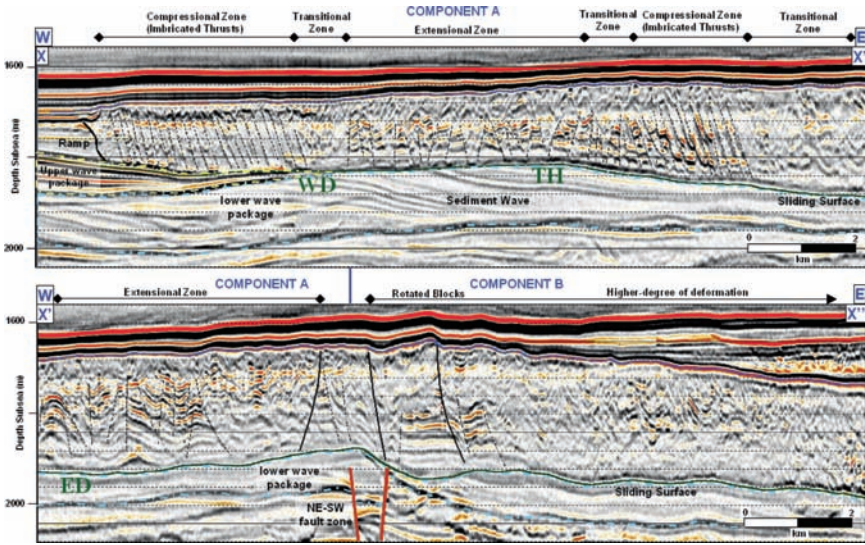
Fig. 3 A seismic traverse down the length of the moat, see Fig. 2 for line of section: X–X′ upper image and X′–X″ lower image. The compressional western terminus of the A component is shown in upper image. The upper wave package is outlined in yellow dashed lines (*western edge of upper image*) and the lower wave is outlined in dashed blue lines. Transition to the B component is shown in lower image. WD: western depression, TH: topographic high, ED: eastern depression. Underlying northeast-southwest faults in brown.

composed of a complex of alternating compressional and extensional zones (Fig. 3). Internal reflections, correlated to the stratigraphy of the pre-failed sediments, are preserved in this component, and provide a very useful tool for the assessment of the fragmentation of the failed sediment mass. The compressional zones are characterized by imbricated thrusts, which in map view form crescent-shaped compressional ridges. Two compressional zones (2 and 3.5 km long) are observed in the A component, one at the western terminus and another (2 km long) on the western flank of the eastern depression (ED on Fig. 2a). Two extensional zones (4.5 and 6 km long) are observed, one along the western flank of the central area topographic high relief (TH on Fig. 2a) and the other along the eastern flank of the eastern depression (ED). Fragmentation of the strata in both of the extensional zones resulted in the formation of alternated horst and graben-like structures. The downward bending of the reflections in the down-dropped blocks indicates collapse of the strata at these locations, which is in agreement with the stretching of the sediment prism. The dissemblance slice in Fig. 2b shows that sliding blocks in the extensional zones form arcuate bands, indicating that the movement along the axis of the A component was larger (up to 1 km) than at its edges. Transitional zones (1–2 km long) exist between the compressional and extensional zones, across which the change in sediment-remobilization style occurs. Two transitional zones occur at the center of the elongated basal depressions,

and are characterized by a more incoherent seismic signature, implying a much higher degree of fragmentation and/or plastic deformation of the sediment at these locations. The transitional zone at the topographic area of high relief (TH on Fig. 2a) is characterized by a complex fragmentation, having extensional and compressional features that are antithetic to those of the extensional and compression zones to the west and east, respectively.

The B component occupies the eastern unconfined part of the Rebelde Slide, and is up to 300 m thick. The junction between the A and B components is coincident with the underlying salt-rooted fault zone. Four large coherent blocks are present above and on the eastern flank of the fault zone (Figs. 2b and 3). In some areas these blocks display stratified continuity with the underlying strata that suggest minimal movement. East of these blocks, the seismic character becomes incoherent, indicating a larger degree of sediment fragmentation and/or plastic deformation. This component is unconfined to the east and becomes indistinguishable from the confluence of larger, regional failure complexes on the eastern unconfined slope.

The C component of the Rebelde Slide is 16 km long, 3.5 km wide and up to 250 m thick, and occupies the southern part of the failure (Fig. 2). Near the walls of the moat along the southern margin, this component consists of back-tilted rotated blocks (Fig. 4). Clusters or individual stratified blocks, similar to those from the extensional zones of the A component, lie along the northern part of this component and alternate with incoherent seismic zones. It is separated from the A component at its northern boundary through a 100–500 m thick, transitional or shear zone, in which several lineations are observed in the dissemblance data (Fig. 2b). This zone has a semitransparent seismic character and an undulating surface, resembling lateral ridges (Fig. 4). Thrust fault-like features are also observed in this transitional zone.
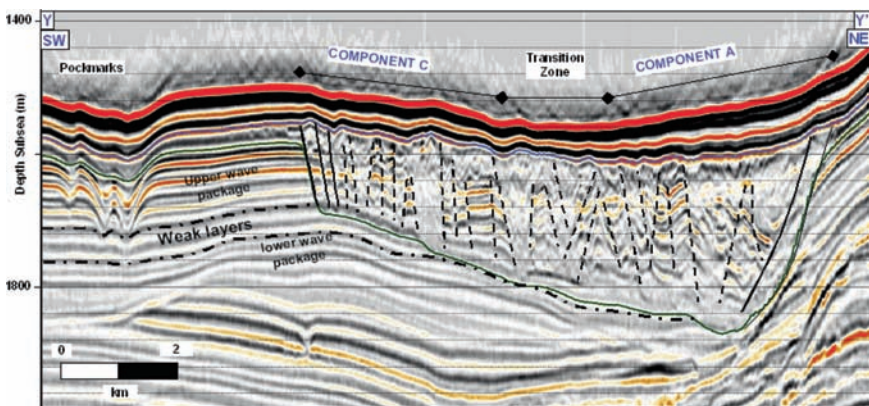
Fig. 4 Seismic traverse Y–Y′ (see Fig. 2b for line of section) through the C component, the transition zone and the A component. Green surface is sliding surface (*map view of surface in Fig. 2a*). Black-dashed lines represent the boundaries of the 'weak' zone.

3.2   Stratigraphic Characterization

The Rebelde Slide has been developed on a large sediment-drift deposit, and is confined to the strike-oriented moat (Fig. 2). Two packages of sediment waves are observed that correlate to the basal sliding surface of the Rebelde Slide (Figs. 3 and 4). The upper sediment-wave package is present only at the western edge of the failure, and is expressed by high-amplitude reflections that onlap the lower package. Large parts of this sediment package have been remobilized and incorporated into the Rebelde Slide (Fig. 4). The lower package is up to 200 m thick and consists of eastward migrating sediment waves, in which the upper boundary is characterized by an undulating surface (Figs. 2 and 3).

The sliding surface of all components that form the complex Rebelde Slide immediately overlies this lower sediment wave. Many pockmarks observed around the moat (Figs. 1, 2, and 4) appear to originate from a 20–25 m thick zone of parallel seismic reflections (dashed lines, Fig. 4). This zone can be traced to the Rebelde Slide, where it coincides with the sliding surface and the top of the lower sediment wave.

4   Discussion

The Rebelde Slide consists of three major components, each one of which is characterized by different geometric characteristics. The A component is confined to the contouritic moat and consists of multiple extensional and compressional zones (Fig. 3). Failures with similar characteristics have been classified by Frey-Martinez et al. (2006) as confined failures. The eastward dipping thrusts (Fig. 3) in combination with the westward pointing arcuate ridges (Fig. 2b) indicate a westward movement for this component. The only exception occurs in the transitional zone along the western flank of the topographic area of high relief (TH on Figs. 2a and 3) that separates the eastern and western depressions (Figs. 2a and 3). This transitional zone is characterized by extension to the west and compression from the east, which is expressed by thrusts that are antithetic to the thrust of the eastern compressional zone (Fig. 3). These characteristics suggest that there was a local eastward motion in the A component. However, it is not certain whether this motion took place during or after the development of the Rebelde Slide.

The B component comprises the eastern part of the Rebelde Slide, and is separated from the A and C components by a basal scarp coincident with the underlying fault zone. Moderately deformed, coherent blocks, which grade vertically and laterally to higher-deformed sediment with floating blocks to the east, indicate an easterly flow direction for the movement of this component (Fig. 3). Based on this observation, the B component is interpreted to have an eastward, unconfined, and emergent flow. Beyond the confines of the contouritic moat, the B component becomes indistinguishable from the larger regional MTDs.

The C component evolves from the collapse of the southern wall of the moat and consists of rotated blocks near the head-scarp, which evolved into coherent sliding

blocks separated from each other by zones of higher sediment deformation (Fig. 4). Through the orientation of the blocks, a northeasterly to easterly motion is indicated for the C component (Fig. 2b). The C component is separated from the A component by a 100–500 m thick zone that is characterized by presence west-northwest to east-southeast lineations in dissemblance time slices (Fig. 2b). In seismic traverse, this zone is expressed by an incoherent and semi-transparent acoustic character and thrust-like features (Fig. 4). This transitional zone is interpreted as a zone of collision and shear between these two components, which led to the easterly diversion of the northeasterly flowing C component.

All components of the Rebelde Slide occur over the same sliding surface, which corresponds to the top of an underlying sediment wave package (Figs. 3 and 4). This condition in combination with the colliding and shearing boundaries of the Rebelde A and C components suggests that each component of this complex failure occurred simultaneously. The coincidence of this sliding surface with the layer from which the expulsion features are sourced suggests that the Rebelde Slide was caused by simultaneous failure along an underlying geotechnically "weak" zone, a zone that was likely comprised of relatively overpressured, under-compacted formations. A similar mechanism has also been proposed for other failures occurring in sediment-drift deposits (e.g., Afen Slide in Wilson et al. 2004). Such a mechanism can explain the different types and directions of motion taking place in a single failure, where the entire section collapsed under its own weight after loosing its basal support. The pre-failed slope inclination and that of the underlying weak layers probably determined the direction of motion.

Two triggering mechanisms are proposed for the loss of basal support in Rebelde. The first possible triggering mechanism is through the cyclic loading of weak layers through an earthquake. In the Gulf of Corinth, Greece, an earthquake resulted in the liquefaction of a sand layer that resulted in the formation of multiple sediment failures and sand volcanoes (Papatheodorou and Ferentinos 1997). Earthquakes in passive margins are rare events but not absent. A good example is the 1929 "Grand Banks" earthquake that resulted in the development of multiple failures in the passive eastern Canadian continental margin (Piper et al. 1999). A second possible triggering mechanism is the migration of gas through faults and its accumulation in a zone of higher permeability (e.g., Frey-Martinez et al. 2009).

5 Conclusions

The composite Rebelde Slide has developed in a contouritic moat, and consists of three major components, each one of which is characterized by different type of sediment deformation and direction of motion.

The sliding surface of the Rebelde Slide coincides with the top surface of an underlying sediment wave.

Pockmarks around the moat are interpreted as fluid-expulsion features, which are sourced by a thin (up to 25 m thick) stratigraphic interval. This interval coincides with the sliding surface of the Rebelde Slide.

The development of the Rebelde Slide is attributed to loss of basal support of a "weak" underlying zone.

References

Bryn P, Berg K, Foreberg CF, Solheim A, and Kualstad TJ (2005) Explaining the Storegga Slide. Mar Petrol Geol 22:11–19.

Frey-Martinez J, Cartwright J, and James D (2006) Frontally confined versus frontally emergent submarine landslides: A 3D seismic characterization. Mar Petrol Geol 23:585–604.

Frey-Martinez J, Bertoni C, Gerard J, and Matias H (2010) Submarine slope failure and fluid migration processes on the Ebro continental margin: Implications for offshore facility planning, *in* Shipp RC, Weimer P, and Posamentier HW, eds., Mass-transport Deposits in Deepwater Settings: Society of Economic Paleontologists and Mineralogists Special Publication 95, in press.

Hasiotis T, Papatheodorou G, Bouckovalas G, Corbau C, and Ferentinos G (2002) Earthquake-induced coastal sediment instabilities in the western Gulf of Corinth, Greece. Mar Geol 186:319–335.

Modica CJ and Brush ER (2004) Postrift sequence stratigraphy, paleogeography, and fill history of the deep-water Santos Basin, offshore southeast Brazil. Am Assoc Petrol Geol Bull 88(7):923–945.

Moscardelli L, Wood L, and Mann P (2006) Mass-transport complexes and associated processes in the offshore area of Trinidad and Venezuela. Am Assoc Petrol Geol Bull 90:1059–1088.

Papatheodorou G and Ferentinos G (1997) Submarine and coastal sediment failure triggered by the 1995, $M_s = 6.1$ R Aegion earthquake, Gulf of Corinth, Greece. Mar Geol 137:287–304.

Piper DJW, Cochonat P, and Morrison ML (1999) The sequence of events around the epicenter of the 1929 Grand Banks earthquake: initiation of debris flow and turbidity current inferred from sidescan sonar. Sediment 46:79–97.

Tripsanas EK, Piper DJ, Jenner KA, and Bryant WR (2008) Submarine mass-transport facies: New perspectives on flow processes from cores on the eastern North American margin. Sediment 55:97–136.

Wilson CK, and Long D, and Bulat J (2004) The morphology, setting and processes of the Afen Slide. Mar Geol 213:149–167.

Small-Scale Insights into Seismic-Scale Slumps: A Comparison of Slump Features from the Waitemata Basin, New Zealand, and the Møre Basin, Off-Shore Norway

S. Bull and J. Cartwright

Abstract The results of a comparison between two different submarine mass wasting events, using differing methods of investigation are presented in this study. Remotely sensed geophysical data types, such as 3D seismic, can be used to image and analyze large-scale examples. The strengths of such techniques lie in the ability to image large areas (i.e. 10's of square kilometers), allowing consideration of the broad-scale architecture of the units. In contrast, field-outcrop studies allow more detailed analysis of geological features, down to a millimeter scale. Two slumps have been compared; one exposed in outcrop, the other imaged using 3D seismic data. The outcrop example comes from the Miocene of the Waitemata Basin, northern New Zealand, and the seismic example comes from the Pliocene of the Møre Basin, off-shore Norway, and occurs on a scale some 100 times greater that the field outcrop example. Despite this, the two examples exhibit similarities in their gross architecture, with each showing a bi-partite anatomy, well developed slump folds and geometrically similar basal shear surfaces. The results of the comparison emphasize the complexity of large-scale events, and illustrate the potential value of combining field outcrop data with geophysical data types.

1 Introduction

Historically, much insight into the dynamic evolution and emplacement mechanisms of submarine mass wasting events has come from field-based studies of ancient outcrops, which typically allow fine-scale, two-dimensional analysis (e.g. Farrell 1984).

S. Bull (✉) and J. Cartwright
Cardiff University, 3D Lab, School of Earth, Ocean and Planetary Sciences, Main Building,
Park Place Cardiff CF10 3YE, UK
e-mail: SBULL@talisman-energy.com
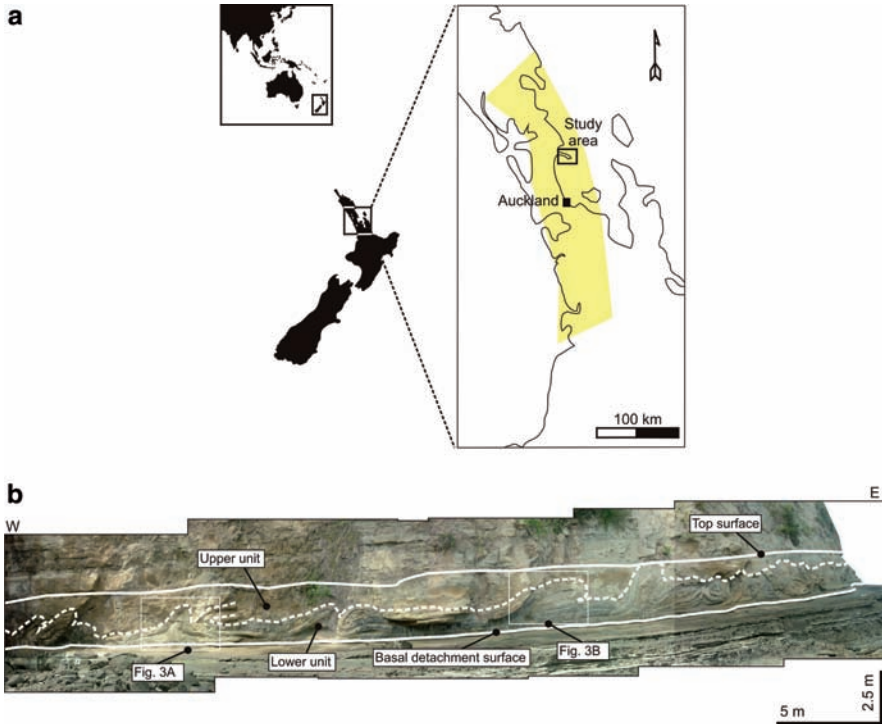
Fig. 1 (**a**): Location of the field outcrop area. Shaded area indicates extent of the Waitemata Basin (after Strachan 2002). (**b**): Photomontage of part of the outcrop. Note the sequence of folds defined by coherently-deformed coarse sandstone beds, and the segregation of the slump into two structurally and sedimentologically distinct units, termed the upper and lower units

An increasingly common technique is the analysis of remotely sensed, geophysical data such as three-dimensional (3D) reflection seismic (e.g. Frey Martinez et al. 2005). The advantages of using such data lie in the ability to perform complete volumetric and geometrical analysis of both external and internal elements of sedimentary units over large areas. A drawback is the limitation imposed by seismic resolution, typically in the region of c. 10 m vertically. In order to address this scale problem, observations from an outcrop study of the Miocene-age Little Manly Slump from New Zealand (Fig. 1a), chosen because of the excellent 2D exposure and its compact scale, have been compared with a much larger slump from the Pliocene of the Møre Basin, offshore Norway (Fig. 2a). This slump, referred to as 'Slump W' (after Lawrence and Cartwright 2009) has been chosen because it is well imaged by high quality seismic data, and occurs on a scale some 100 times greater than the field outcrop example.

The aim of this paper is to compare observations made in the field to the seismic example in order to gain insight into processes involved in the dynamic development and emplacement of large-scale mass wasting events, beyond that which is evident from comparatively low-resolution geophysical data types.
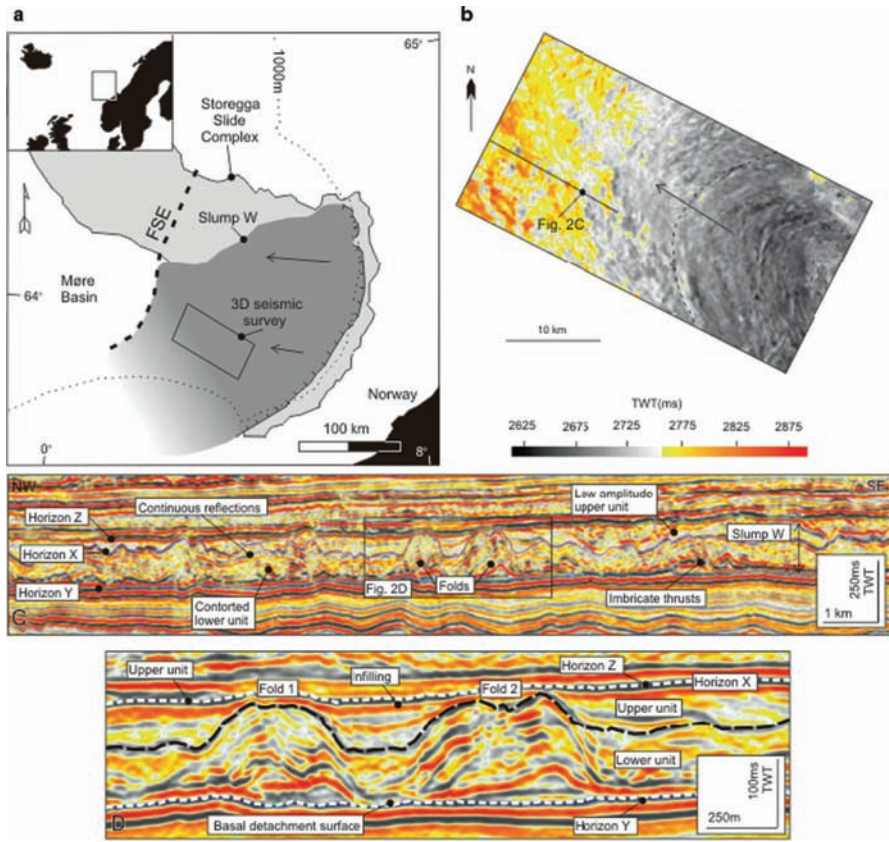
Fig. 2 (**a**): Map showing the location of the seismically imaged Slump W. The extent to which Slump W has currently been mapped is indicated by the dark grey shading (after Lawrence and Cartwright 2009). Arrows indicate transport direction. FSE: Faeroe-Shetland Escarpment. Outline of Storegga Slide Complex shown. (**b**): Outline of 3D seismic survey with time structure map of Horizon X, which divides Slump W into two distinct seismic facies packages. The arcuate lineations (*dashed line*) are interpreted to be the result of compression. Arrow indicates transport direction. (**c**): Representative seismic dip-profile through Slump W. Note upper and lower packages. Location shown in (b). (**d**): Zoom in of seismic profile showing two slump folds. Note disharmonic, stacked nature of the reflections within the folds and brittle discontinuities. Location shown in (c)

2 Dataset and Methodology

The data used in this study consists of a set of field observations and photographs from the Little Manly Slump, taken during fieldwork conducted in 2007, and a modern, industrially acquired 3D reflection seismic survey which images Slump W. An integrated 3D seismic interpretation approach has been applied (Cartwright 2007), and the resolution of the seismic data has been calculated as c. 9 m vertically (maximum vertical resolution = $\lambda/4$; Sheriff and Geldart 1983) using an assumed average seismic velocity of 2,000–2,100 m s^{-1} for the interval of interest. Horizontal resolution is estimated at 45 m (taken to approximate the dominant seismic wavelength).

3   Geological Settings

Little Manly Slump: the field study area is located c. 40 km north of Auckland on the Whangaparaoa Peninsula, where the slump is exposed for c. 600 m at Little Manly Beach, in 8–15 m high cliffs made accessible by wavecut platforms. The Little Manly Slump occurs in the Miocene infill of the Waitemata Basin (Fig. 1a), whose initiation is thought to be linked to the development of a new convergent plate-tectonic regime represented in the present day by the Alpine Fault/Hakurangi Trough plate boundary (Ballance et al. 1982). The basin fill reflects initial shallow marine conditions followed by rapid deepening, with the basin receiving mostly turbiditic clastic sediments (Ricketts et al. 1989). The Little Manly Slump is inter- preted to have developed in an outer fan-setting, translating downslope to the SW (Strachan 2002). The slump incorporates three main lithologies: medium- and coarse-grained turbidite sandstones, and a fine-grained mudstone interpreted as background hemipelagic sedimentation (Strachan 2002).

   Slump W is found in the Møre basin on the passive Norwegian continental mar- gin. Initiating in the Cretaceous, the basin underwent continuous, thermally driven subsidence (Brekke 2000), and was filled by fine-grained hemipelagic oozes of the Palaeogene age Brygge Formation and Miocene – earliest Pliocene age Kai Formations (Evans et al. 2002). The Plio-Pleistocene Naust Formation, within which Slump W occurs, comprises of contourites, hemipelagites and glacigenic sediments (Evans et al. 2002). Slump W is believed to have developed between 1.8 and 4 Ma and is confined against the volcanic palaeo-high of the Faroe-Shetland Escarpment (Lawrence and Cartwright 2009). Lawrence and Cartwright (2009) concluded that limited translation of the slump mass has occurred (estimated at 2–3 km), with a transport direction from east to west.

4   Little Manly Slump Description

The Little Manly slump has recently been the subject of previous studies (e.g. Strachan 2002, 2008) and as such the dynamic evolution and emplacement mecha- nisms are well constrained. The Little Manly Slump comprises a c. 2.5 m thick unit which is divisible into distinct upper and lower packages, the lower featuring many contorted beds and a high degree of lateral variation in the style and intensity of deformation, and the upper consisting of a massive sand (Fig. 1b). The lower unit exhibits a variety of ductile, brittle, compressional and extensional structures, including folds of various styles and sizes and intra-slump to slump-scale normal and thrust faults. The upper unit varies in thickness between 0.01–2 m and exhibits occasional large-scale cross bedding, broad undulations and clasts in the lower part. The top surface of the upper unit is sharp and overlain conformably by further sand- rich units. Segregation of the slump into two depositional units is interpreted to be the result of progressive deformation of the lower unit during slump translation

with co-eval development and deposition of the upper unit, thought to be a turbidite sourced from the deforming mass below (Strachan 2008).

The structural style of the **lower unit** is dominated by ductile folding, exhibiting a variety of fold styles and scales (Fig. 2b). A large part of the outcrop is dominated by a spectacular sequence of folds defined by c. 0.2 m thick, coarse sandstone beds which appear to have been deformed in a relatively competent manner, with significant continuity and uniform bed thickness exhibited (Fig 1b), and faults which affect the thickness of the beds present at the fold hinges (Strachan 2002).

An interesting observation is the apparently 'less competent' behavior of other lithologies also present within the folds. Figure 3a shows an example of a coarse sandstone fold which has been truncated by the upper unit. In the 'core' of the fold, above the basal shear surface, a 'plug' of coarse-grained material is present (indicated in Fig. 3a), along with an intensely deformed mudstone bed which appears to have partially mixed with the coarse-grained material. The mudstone bed exhibits intense folding and a lenticular 'pinch and swell' morphology with occasional complete bed rupture resulting in isolated inclusions of the mudstone within the coarse-grained material (Fig. 3a).

A separate fold also features similar competency contrasts and variation of deformation. Figure 3b shows the fold which is defined by two competent sandstone beds. Again within the 'core' of the fold, the medium-coarse grained lithology and the mudstone have deformed in a relatively less-competent manner (Fig. 3b).
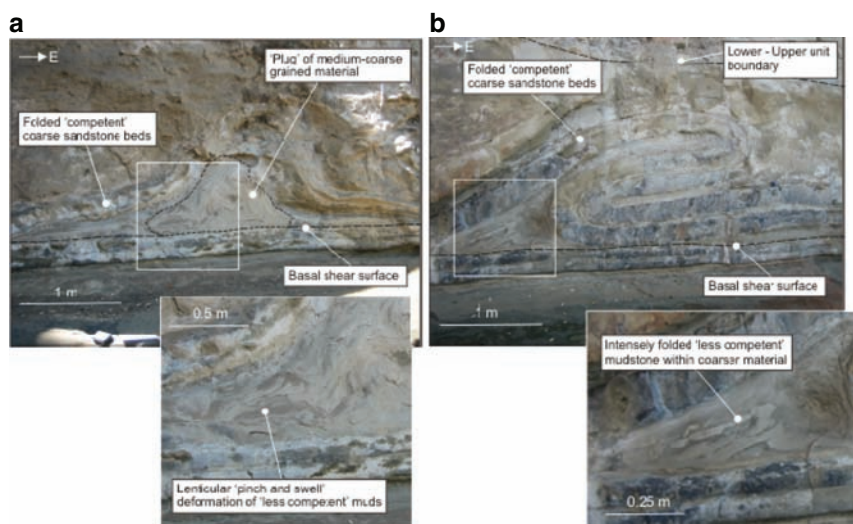
Fig. 3 Example of folds from lower unit of Little Manly Slump. (**a**): Fold formed by coarse sandstone bed. The 'core' of the fold is occupied by a plug of medium-coarse grained material around which a thin, fine-grained mudstone has deformed in an intense, highly ductile manner. (**b**): Example of a recumbent fold defined by coarse sandstone beds. Between fold limbs, the medium-coarse grained lithology and fine-grained mud exhibit competency contrasts and intense ductile deformation. Locations shown in Fig. 1b. 'E' indicates east

Here too the mudstone bed is intensely folded and exhibits variations in thickness expressed as an overall 'pinch and swell' morphology, within the more homogenous matrix of the medium-coarse grained material. Where the fold limbs are very tightly folded both the medium-coarse grained lithology and mudstone are present with the mud once again having deformed in a ductile sense within the coarser material (Fig. 3b).

These features were attributed by Strachan (2008) to shearing resulting from deformation of surrounding material and competency contrasts between the varying lithologies. Gregory (1969) remarked that some of the deformational fabrics exhibited by the lower unit of the Little Manly Slump attested to the '…plasticity, verging on fluidity of sediments during deformation…' and considered that 'thixotrophic mixtures of mud, silt and sand have flowed or been squeezed into their present positions.'

The **basal shear surface** occupies a single discrete horizon (Figs. 1b and 3), and occurs for the most part above a coarse sandstone bed but ramps up and down locally, by up to 0.5 m. Occasionally, beds below the basal shear surface are disrupted, fragmented or rotated, interpreted to be the result of shear from the overlying slump, and as such could be considered to be part of the slump (Strachan 2002). Ptygmatically folded dykes are present beneath the sandstone bed which predominantly underlies the basal shear surface of the slump, where they cross-cut a fine-grained, laminated mudstone unit and are aligned parallel to the slumping direction (Strachan 2008). The dykes are interpreted to be the result of contemporaneous mobilization of underlying sandstones related to slump-induced loading and lateral shearing (Strachan 2008). The basal shear surface is thought to originally have been a low stress, clay rich horizon, possibly of volcaniclastic origin (Strachan 2002).

5 Slump W Description

Slump W covers an area of over 21,000 km^2 (Fig. 2a) and averages 200–250 m in thickness. Two distinct seismic facies packages can be identified, separated by a continuous seismic reflection (labeled Horizon X on Fig. 2c) which can be traced throughout the 3D survey area (Fig. 2b, c). The lower unit is characterized by discontinuous, contorted reflections bound at the base by a relatively flat-lying, bed parallel reflection (labeled Horizon Y in Fig. 2c). The interval between Horizon X–Horizon Y varies from a maximum thickness of 100 m to a minimum of <5 m and comprises a number of partially continuous, high amplitude reflections (Fig. 2c). The amplitude, continuity and deformation of the various reflections varies considerably across the survey area. Some zones appear highly disaggregated while in other places reflections continuous over a distance of up to 1 km define recognizable deformational features such as folds and thrust faults (labeled on Fig. 2c). Horizon X is interpreted as representing the upper geological boundary of the lower unit of Slump W, and is highly-undulatory in character (Fig. 2b). A time structure map of Horizon X shows that the undulations in seismic profile correspond to a

series of parallel to sub-parallel, linear to arcuate ridges continuous across the survey area (Fig. 2b). The most likely origin of these structures is compression, resulting from close proximity to the confining distal margin of the slump (Lawrence and Cartwright in press).

The upper unit, whose lower boundary is Horizon X, also shows internal variation in the amplitude, continuity and deformation of internal reflections (Fig. 2c). The upper unit is of generally lower seismic amplitude than the lower unit and contains much fewer and less well defined reflections (Fig. 2c). This characteristic is interpreted to represent a package comprising of fewer lithologically contrasting beds which have experienced a lesser degree of deformation than the lower unit. The top surface of the upper unit (labeled 'Horizon Z' on Fig. 2c) is mildly undulatory in character, exhibiting up to 10 m in vertical relief (Fig. 2c).

The internal deformational character of the **lower unit** varies across the survey area, and features evidence of a variety of ductile and brittle deformational styles (Fig. 2c). The predominant deformational style is reminiscent of a series of ductile, predominantly upright folds with varying internal character (Fig. 2c). Two of the structures in the lower unit have a similar gross morphology to some of the folds observed at Little Manly (Fig. 2d). The structures have been interpreted as slump folds and are labelled 'Fold 1' and 'Fold 2' in Fig. 2d. Horizon X forms the top of the folds, which exhibit some 100 m of vertical relief and have outward dipping flanks which slope at 7° (Fig. 2d). Inside the folds, continuous, stacked reflections have been deformed into packages of convex-upward, disharmonic folds which also appear to be affected by internal brittle discontinuities (Fig. 2d). The folds are elongate in planform, measuring up to 1.75 km in length, 1 km across and are c. 250 m high. Above Horizon X, the folds are infilled by the upper unit (Fig. 2d).

Horizon Y is interpreted as being a close approximation to the **basal detachment surface** of Slump W (Fig. 2c), as it is the first relatively continuous, un-distorted reflection occurring below the deformed slump interval. Below Horizon Y, small, localized deformational zones are observed (Note that reflections here are not completely flat-lying due to the influence of an underlying faulted unit; Fig. 2d). The package of reflections directly underlying the lower unit of Slump W, including Horizon Y, exhibit localized, mild disruption, small offsets and lateral changes in amplitude (Fig. 2c, d), which are here attributed to deformation caused by the emplacement of the overlying slump.

6 Discussion

The most striking observation made from the Little Manly Slump is the complexity and intensity of deformation which is evident beyond the larger-scale gross geometry of the unit as a whole. Considering Slump W, which provides an example of a slump on a scale some 100 times larger than the Little Manly example, the question is raised of what features or evidence for similar processes may be present in Slump W, but simply not captured by the seismic image? To help address this question,
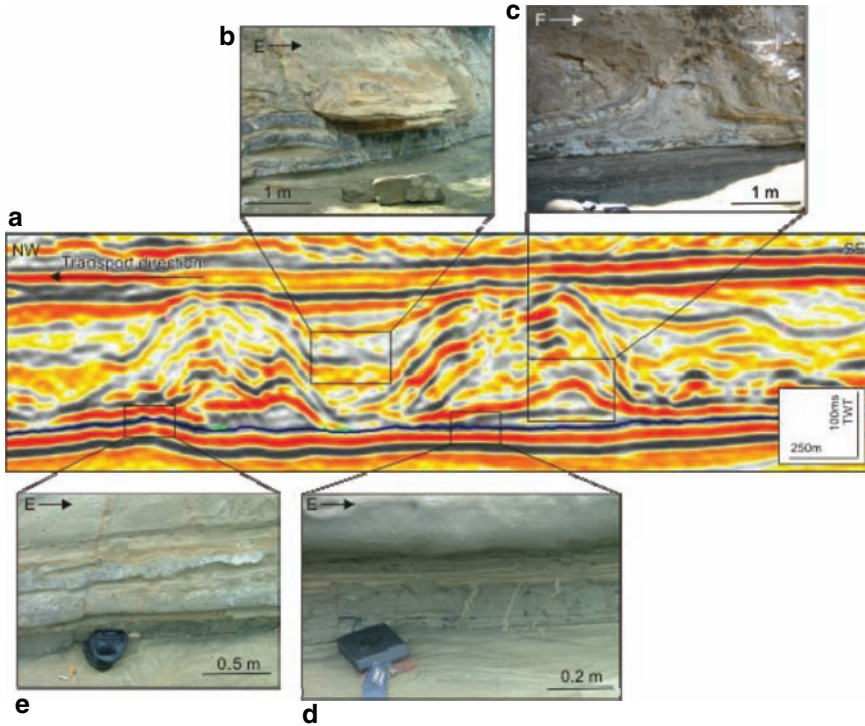
Fig. 4 (**a**): Seismic profile (originally shown in Fig. 2d) from Slump W populated with field photographs from Little Manly to illustrate potential complexity of such a large-scale depositional unit. (**b**): Infilling of lower unit by upper unit; (**c**): Slump folds with complex competency contrasts and highly ductile deformation; (**d**): Clastic dykes below the basal shear surface; and (**e**): disruption of beds below the basal shear surface. 'E' indicates east

Fig. 4 shows a zoomed in cross-sectional view of some of the key structural elements described from Slump W, populated with field photographs of comparable elements from Little Manly. Despite large differences in the sizes of the slumps, both examples show remarkably similar gross-scale architecture and internal elements including: (1) a bi-partite upper and lower unit division,; (2) internal folding comprised by various lithological units of differing competencies and (3) basal shear surfaces which are generally flat-lying and in places show localized disruption of units immediately below. These characteristics introduce the possibility that the Little Manly Slump may represent a useful analogue to Slump W and could be used to restore information relating to deformational elements and emplacement processes which are not resolved by the seismic data.

A common characteristic of both slump examples is the clear division into upper and lower units. In both cases, an intensely deformed lower unit, dominated by ductile deformation, is overlain by a less complex unit which infills the topography of the lower unit (Figs. 1b and 2c). For Little Manly, a co-eval scenario is invoked whereby a bi-partite 'couplet' comprising a lower unit deforming ductily and a more

fluid-like upper unit, moved downslope and were deposited together (Strachan 2008). In the case of Slump W, it is possible that a similar model could be accountable, although evidence is difficult to pinpoint given the current dataset. However, by drawing upon the field example, some inferences can be made.

That Slump W features a lower unit dominated by the predominantly ductile deformation of coherent lithological units such that they were able to form upright slump folds, suggests that like Little Manly, the lower unit of Slump W was emplaced by way of a typical, progressively deforming slump mechanism (Martinsen 1994). The upper unit of Slump W is interpreted to consist of a less deformed, more uniform lithology than the lower unit. While evidence which supports the interpreted co-eval scenario for Little Manly, such as sedimentary structures and inclusions from the lower unit cannot be identified from the seismic data, the upper units from both slumps can be likened on a broad scale. While there is scope to invoke further scenarios for the development of Slump W, the co-eval model borrowed from Little Manly illustrates how slumps studied in the field can be used as a basis for comparison to seismically imaged examples, and to direct further analysis.

Evidence for intense shearing and possible mobilization of less competent lithologies was intimately linked to the well developed folds in the competent coarse sandstone beds at Little Manly, occurring within and around the folds and between beds of differing competency. The folds from Slump W shown in Fig. 4 are clearly comprised of many layers of deformed material, but from the seismic record, it is not clear which lithologies are behaving relatively competently and which are behaving relatively incompetently – only the gross configuration is apparent. Although the gross geometry of the folds suggests a ductile but 'competent' nature of deformation, it is clear from Little Manly that some lithologies could be behaving in a potentially fluid manner, and that small scale liquefaction could be involved in the development and final geometry.

Sheared dykes and slump-scale faults were observed to affect the basal shear surface at Little Manly, with dykes of c. 0.1 m in height and 0.02 m across (Fig. 4d). The basal shear surface of Slump W was approximated to a single moderate-amplitude trough in the seismic record (Horizon Y), with no evidence of shear or further deformation observed other than local undulation and mild disruption (Fig. 2c). Given the required conditions, i.e. presence of an over-pressured sand unit beneath Slump W, it is possible that the basal shear surface of Slump W may also be associated with clastic dykes, which due to their scale and vertical geometry would not be imaged by the seismic data. The flat lying, concordant nature of the Little Manly Slump basal detachment indicates that the slump moved over flat lying bedding (Strachan 2008), and the same is taken to be true for Slump W. At Little Manly, disruption and rotation of beds in close underlying proximity to the basal shear surface was interpreted to result from lateral shear and loading by the overlying slump, and possibly representative of down-cutting and entrainment of underlying beds by the slump mass (Strachan 2002, 2008). This can also be applicable to Slump W as evidenced by amplitude variations and localized disruption of Horizon Y and of reflections immediately underlying it (Fig. 4e).

7   Conclusions

Comparison of several key characteristics of two slumps, one studied in outcrop and one imaged by modern 3D seismic data, has served to illustrate the level of complexity that may be present in large-scale examples, but is beyond the resolution limitations of modern geophysical data. The present study has shown how the application of field-scale observations to increasingly common geophysical studies can help to restore sub-resolution information and provide a basis for the development of depositional models, ultimately leading to an improved understanding of the depositional units resulting from submarine mass wasting events.

References

Ballance PF, Pettinga JR, Webb C (1982) A model of the Cenozoic evolution of northern New Zealand and adjacent areas of the southwest Pacific. Tectonophys 87: 37–48

Brekke H (2000) The tectonic evolution of the Norwegian Sea and continental margin with emphasis on the Vøring and Møre basins. In: Nøttveddt A et al. (eds.), Dynamics of the Norwegian Margin. Geological Society, London, Special Publications 167, pp. 327–378

Cartwright J (2007) The impact of 3D seismic data on the understanding of compaction, fluid flow and diagenesis in sedimentary basins. J Geol Soc Lond 164: 881–893

Evans D, McGiveron S, Harrison Z, Bryn P, Berg K (2002) Along-slope variation in the late Neogene evolution of the mid-Norwegian margin in response to uplift and tectonism. In: Doré AG, Cartwright JA, Stoker S, et al. (eds.), Exhumation of the North Atlantic Margin: Timing, Mechanisms and Implications for Petroleum Exploration. Geological Society, London, Special Publications 196, pp. 139–151

Farrell SG (1984) A dislocation model applied to slump structures, Ainsa Basin, South Central Pyrenees. J Struct Geol 6: 727–736

Frey-Martinez J, Cartwright J, Hall B (2005) 3D seismic interpretation of slump complexes: examples from the continental margin of Israel. Basin Res 17: 83–108

Gregory MR (1969) Sedimentary features and penecontemporaneous slumping in the Waitemata Group, Whangaparaoa Peninsula, North Auckland, New Zealand. New Zeal. J Geol Geophys 12: 248–282

Lawrence GMW, Cartwright JA (2009) Initiation of sliding on the mid Norway margin in the Møre Basin. Mar Geol 259: 21–35

Martinsen OJ (1994) Mass movements. In: Maltman A (ed.) The Geological Deformation of Sediments. Chapman & Hall, London

Ricketts BD, Balance PF, Hayward BW, Mayer W (1989) Basal Waitemata Group lithofacies: rapid subsidence in an early Miocene interarc basin, New Zealand. Sedimentol 36: 559–580

Sheriff RE, Geldart LP (1983) Exploration Seismology, volume 2: Data-processing and Interpretation. Cambridge University Press, Cambridge

Strachan LJ (2002) From geometry to genesis: a comparative field study of slump deposits and their modes of formation. Unpublished Ph.D. Thesis, Cardiff University

Strachan LJ (2008) Flow transformations in slumps: a case study from the Waitemata Basin, New Zealand. Sedimentol 55: 1311–1332

The Block Composite Submarine Landslide, Southern New England Slope, U.S.A.: A Morphological Analysis

J. Locat, U.S. ten Brink, and J.D. Chaytor

Abstract Recent multibeam surveys along the continental slope and rise off southeast New England has enabled a detailed morphological analysis of the Block composite landslide. This landslide consists of at least three large debris lobes resting on a gradient less than 0.5°. The slide took place on gradients of between 1° and 5° in Quaternary sediments likely deposited at the time of low sea level and high sedimentation rates associated with glaciations. The slide debris lobes are very close to each other and cover an area of about 1.125 km² of the sea floor. With an average thickness of 50 m, the total volume of the deposit is estimated at 36 km³. In some cases, the departure zone appears to be near the crest of the continental slope, at a water depth between 500 and 2,000 m with debris spreading over about 20 km at a depth ranging from 2,500 to 2,600 m. From preliminary analysis, at least one lobe of the Block Composite slide (lobe 2) would require further study to evaluate its tsunamigenic potential.

Keywords Geomorphology • slopes • instability • shear strength • tsunami • canyons

1 Introduction

Submarine mass movement along the U.S. and Canadian Atlantic coasts have been the subject of recent and ongoing investigations. (e.g. Twichell et al. 2009; see ten Brink [2009] for a summary along the U.S. coast and Piper and McCall [2003] for the Canadian coast). As more multibeam data become available, these regions are

J. Locat (✉)
Department of Geology and Geological Engineering, Laval University, Québec, Canada, G1Y 2P1
e-mail: Jacques.locat@ggl.ulaval.ca

U.S. ten Brink and J.D. Chaytor
United States Geological Survey, Woods Hole Science Center, 384 Woods Hole Rd.,
Woods Hole, MA 02543, U.S.A.

found to exhibit extensive mass failure features showing prominent escarpments but little sediment on the failure plane. In many cases, the failed mass is seen as a significant source for turdidites for which deposition extends over very large areas of the continental rise and the abyssal plain. The southern New England (SNE) continental margin is a classic passive continental margin, characterized by an almost flat continental shelf (average gradient <0.5°), relatively steep (2–10°) and narrow continental slope incised by canyons, and a wide and shallowly sloping (average slope of ~1°) continental rise.

The geology of the margin comprises three major phases: (1) Early Jurassic-age rifting and salt deposition, (2) Middle Jurassic to Middle Cretaceous carbonate platform development (Poag 1991), and (3) Cenozoic deposition of marine and non-marine clastic sediment in marginal basins and on the rise (Poag and Sevon 1989; Ryan 1978). The most important period in regard to active submarine landslide processes along the SNE-margin is the Cenozoic, particularly the Quaternary, when large volumes of river and glacially-derived sand and gravel were deposited onto 3 km thick sequence of stratified Tertiary sediment, composed largely of chalk (Tucholke and Mountain 1986; Robb et al. 1981; Poag and Sevon 1989). In the southern NE region, the Quaternary sedimentary section is approximately 200–300 m thick near the top of the continental slope (Austin et al. 1998), thinning seaward and becoming absent in places along the lower slope. The majority of landslides along the southern NE continental margin have occurred entirely within the Quaternary section along the slope, but truncated beds of Eocene chalk crop out in places, suggesting involvement of deeper margin strata (Twichell et al. 2009).

The Block Composite (BC) slide area off the coast of New England is located east of the Hudson Canyon, where the continental margin changes its orientation from northeast to east (Twichell et al. 2009).The Block Composite (BC) landslide (Fig. 1) is investigated here in more detail with the goal of understanding the nature of the mass movements that comprise it and their potential for generating tsunamis.
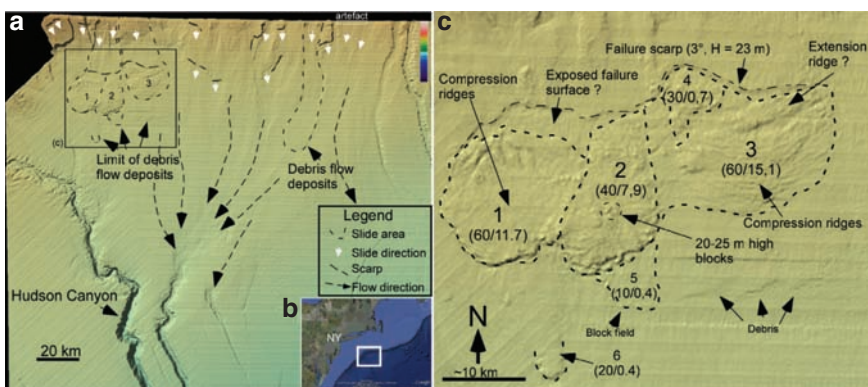
Fig. 1 General view of the sea floor around the Block composite submarine landslides shown here with the three major lobes (labeled 1, 2, and 3). Turbidity current or debris flow transport routes are shown feeding into active or inactive canyons. Major failure surfaces are also indicated by white arrows. (c): location map. (c) Details of the morphology in the BC slide area. In parenthesis are given the thickness in meters and volume in cubic kilometers. Inset location map from Google.com

At this stage, the study presented here addresses the description of the morphology of the BC slide area and points towards elements that are to be explored further as part of an ongoing stability and mobility analysis. At this point, particular attention will be paid to the morphology of the various sloping surfaces in the area which may provide clues about the intact strength of the sediments mobilized by the various mass movements. In addition, possible failure scenarios and overall displacement of the failed masses involved in the BC slide are considered. Some of the interpretation presented here may change significantly as we complete the multibeam coverage of the area and acquire cores for geotechnical testing and for dating various failure surfaces. At his time, when necessary, geotechnical properties will be inferred from a detailed studied of the Hudson Apron slide area carried out by Locat et al. (2003) and on cores of the ODP site 1073 on the Hudson Apron (Austin et al. 1998).

2 Methods

A Digital Elevation Model (DEM; Fig 1) with a cell resolution of 100 m was constructed from bathymetric data set (Fig. 1) acquired by the National Oceanic and Atmospheric Administration and the University of New Hampshire Joint Hydrographic Center in support of the U.S. Law of the Sea Study (Gardner et al. 2006) and extracted from the NOAA National Geophysical Data Center bathymetry database to partly fill data gaps along the continental slope (see Fig. 1).

Using the hull-mounted Knudsen 320B/R deepwater echosounder on the R/V Oceanus, approximately 1,065 km of 3.5 kHz sub-bottom data were collected during a 6 day cruise between April 18–23, 2008. Power and gain settings were modified as appropriate to maximize penetration, although they were predominantly fixed throughout the cruise at the following parameters: 12 kHz channel turned off, pulse length of 6 ms, manual gain between 145–205, AGC/TVG/processing gain/sensitivity turned off, and range set at 100 m (autophased). Sub-bottom penetration varied based on the composition of sediments and reached a maximum of 50 m.

3 Results

3.1 Geomorphology of the Block Composite Slide Area

The BC slide region extends from the continental shelf, at a depth of about 300 m, down to the upper continental rise at about 3,000 m (Figs. 1 and 2). Mass movement activity along the continental slope off New England has been intense as shown by various failure surfaces that are demonstrated in Fig. 1a. Most of these failure surfaces are devoid of displaced sediments (failure deposits), although there is some evidence on the continental rise that some of these slides may have generated debris flow deposits which can be traced down to a water depth of about 2,700 m (Figs. 1a and 2).
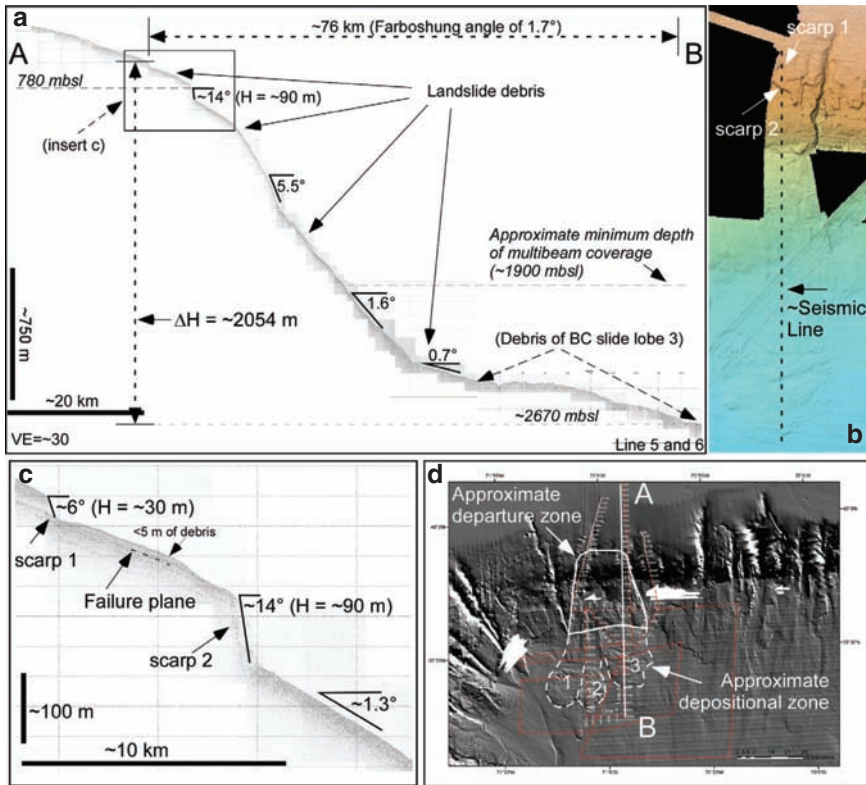
Fig. 2 (**a**) 3.5 kHz echosounder line across one of the lobes of the slide and morphological details of (**b**) position of seismic line in (**a**), (**c**) morphology of the BC slide on the upper continental rise, (**d**) an enlargement of the upper escarpment seen in (**a**), and (**e**) the morphological settings showing the potential extent of the BC slide and the location of the seismic lines (shown in white for the cross section in (**a**) and in red for the other ones)

3.2   The Block Composite Slide

Debris lobes of the BC slide are shown in Fig. 1. A detailed analysis of these lobes (Fig. 1c) reveals the presence of a failure escarpment 20–30 m high and inclined at about 2–3° which stretches sinuously for about 45 km in an east–west direction. The lobes are segmented into three primary lobes (1–3) of similar size (Fig. 1c) and three smaller secondary lobes (4–6). Lobes 1 and 3 are characterized by a series of compression ridges located downstream from the failure escarpment. For lobe 1, the compression ridges are spaced about 400–500 m apart with amplitudes less than 5 m. For lobe 3, compressions ridges are spaced about 700–800 m apart with amplitudes between 5 and 10 m. If the depression identified in Fig. 1c as a failure surface is valid, lobe 1 would have moved about 3 km on a surface inclined at less than 0.5°, which is close to the general gradient for the upper continental rise. Lobe 3 would have move less than 1 km over a gradient less than 0.2°. Interestingly, lobe 2 has no

compression ridges but consist of a blocky deposit that cut across the compression ridges of both lobe 1 and 3, indicating a later event. From its morphological characteristics, lobe 2 likely is a debris flow deposit which may have come from higher elevation than lobe 1 and 3. These latter lobes may have been only displaced locally. In addition, lobe 2, much like lobe 4, contains large blocks up to 25 m high and about 500 m in diameter. Lobe 4 has morphology similar to lobe 2 and appears to cover parts of lobe 3. Lobe 5 consists largely of a field of blocks that appears smoothed by sediment accumulation. Lobe 6 is an out-runner block possibly from a previous slide. Like lobe 2, debris from lobe 6 must have come from higher elevation, (i.e., high enough to have gained the necessary momentum to reach its final position). The total volume of sediments included in all lobes is estimated at 36 km^3.

With the limited data available, an attempt has been made to reconstruct a morphological cross section of the BC slide by coupling the multibeam and seismic data, as shown in Fig. 2. The first observation is the lack of penetration of the seismic signal in the sediments due to the near absence of high-frequency coherent layering in the sediments.

Some landslide debris is visible in Fig. 2c in the shallower parts of the continental slope suggesting that some failed mass did remain on the failure plane. As shown in Fig. 2c, the failure plane appears to follow a stratigraphic layer which may represent sandy sediments as seen in core 1073 (Austin et al. 1998; Locat et al. 2003). Figure 2c shows that the upper headwall scarp is 30 m high and has an angle of 6° while the lower scarp has an angle of 14° and a height of 90 m. If this had been a single event, it would suggest that the total section of sediments involved in the slide was about 120 m thick.

As indicated by O'Leary (1993), many of the submarine mass movements in this area have a failure plane controlled by a stratigraphic layer and therefore, failures at various locations often tend to follow the same stratigraphic horizon. The locations of two escarpments are shown in Fig. 2b, c. Below the lower scarp (Fig. 2b, c) the gradient of the slope increases sharply to a value of 5.5° and that surface appears to be largely free of any debris. This area is likely acting as a bypass zone where any sliding mass would gain significant mobility and energy allowing it to disintegrate and flow down slope and eventually be deposited on the lower slope, or travel as a debris flow or a turbidity current to reach the continental rise. The BC slide deposit lies on a gradient of about 0.7° on the upper continental rise (Fig. 2a) and if the departure zone for the event was along the upper continental slope (i.e. at depths less than 700 m), then the *farboschung* of this event would be about 1.7° (Fig. 2a).

3.3   *Morphology of Slopes and Strength*

The BC slide area provides an opportunity to illustrate some of the processes by which a given slope can be generated. There are few classes of slopes: (1) sedimentation or accumulation slopes that are somewhat analogous to clinoforms (1a) and mass transport deposition (1b), (2) eroded slopes by processes like canyon formation

(2a) and open slope instabilities related to scarp slopes (2b) and failure surface slopes (2c). A third group could correspond to a slope formed by tectonic processes such as plate tectonics (3a), diapirism (3b), or collapse (3c) and a forth type (4) associated with volcanism. It was shown by Locat and Lee (2002) and by Locat et al. (2009) that eroded slopes (type 2) reflect the intact strength of the material involved in a slide while accumulated slopes (type 1b) composed of debris flow deposits relate partly to the remolded strength of the material.

An analysis of height and surface slope data at specific points on the continental slope and rise in the BC slide area (located on Fig. 3a, c, d) is shown in Table 1 and Fig. 3f. For this analysis, geometric information was obtained for open slopes (white number in Table 1), landslide scarp slopes and heights (green numbers in Table 1), failure plane slopes (yellow number in Table 1), and canyon slopes and heights (red in Table 1). The data for eroded slopes are bound by an assumed friction angle of 30° (taken here from the work on the Hudson Apron Locat et al. [2003]) and by slope angle of the continental slope (i.e. typically <5°). If geotechnical properties of samples from the Hudson Apron area (Locat et al. 2003) are applied to the Quaternary sediments in the BC slide area, the drained shear strength parameters obtained from triaxial testing indicate that the cohesion is less than 5 kPa. This value suggests that cohesion is not significant for slopes higher than 20–50 m (Locat et al. 2009). On the other end, if the sediments become indurated by various cementation processes, than the actual cohesion will increase sharply and the maximum slope angle could be greater than the friction angle,
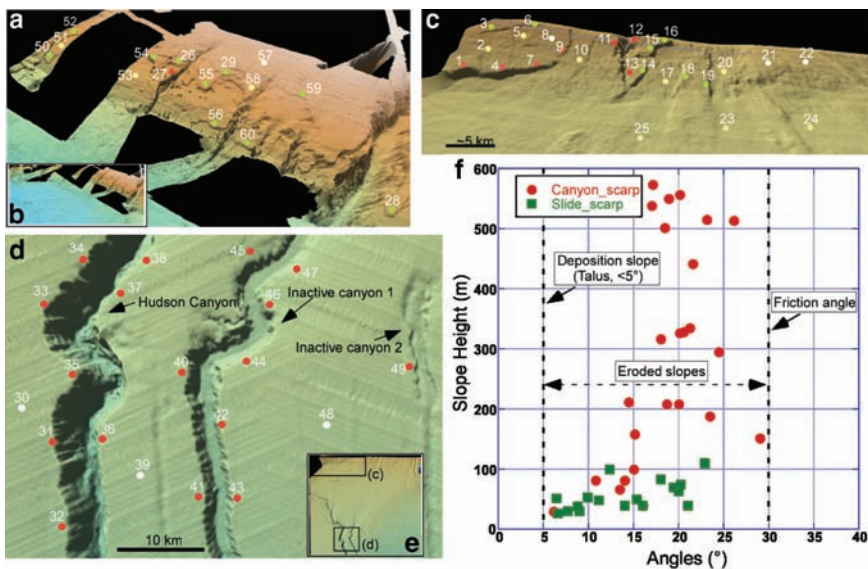
Fig. 3 (**a, c, and d**): Position of the various points where height and slope angle of escarpments and angle of planes listed in Table 1 were measured. (**f**): comparing eroded slopes with deposition slopes (Data is from Table 1)

Table 1 Values of slope heights (H) and angle of slopes and planes (S) at various sites around the BC landslides shown in. Red boxes are for canyon slopes, green for scarp slopes, yellow for failure surfaces, and white for open slopes (apparently unfailed)

No	H(m)	S	No	H(m)	S(°)	No.	H(m)	S(°)	No	H(m)	S(°)
1	40	16	16	49	11.1	31	556	20.1	46	211	14.5
2	–	2	17	–	1.9	32	550	18.9	47	159	15.1
3	40	6	18	35	8.8	33	573	17.1	48	–	0.6
4	100	15	19	26	6.6	34	501	18.4	49	81	10.8
5	–	2.9	20	–	1.6	35	515	23.1	50	64	20.0
6	51	6.4	21	–	1.5	36	538	17.0	51	–	5.0
7	66	13.4	22	–	1.2	37	513	26.1	52	50	15.3
8	–	3.1	23	–	0.6	38	441	21.6	53	–	4.9
9	30	6.1	24	–	0.2	39	–	0.7	54	110	22.9
10	–	1.9	25	–	0.4	40	335	21.2	55	70	19.5
11	189	23.5	26	84	18	41	317	18.0	56	75	20.2
12	209	20.0	27	152	29	42	329	20.6	57	–	1.5
13	81	14.0	28	40	14	43	327	20.1	58	100	12.3
14	39	8.8	29	30	9	44	295	24.4	59	30	7.7
15	54	9.9	30	–	0.33	45	208	18.7	60	40	21

even for a high slope. It is seen from Fig. 1c that debris accumulates on slopes of about 5° and also on slopes less than 1° (Fig. 2a), indicating that the strength of the material does vary as a function of the degree of remolding achieved during a given failure process.

4 Discussion on Slopes, Strength, Triggering and Tsunamis

There may be situations where actual strength of sediments involved in a given slide are not readily known although a preliminary slope stability assessment may be necessary, as is the case here. Understanding slope formation in a given region, therefore, may help provide an estimate of strength properties.

In the case of the BC slide area, scarp slopes (class 2b) were considered separately for open slopes and for canyons. As indicated above, open slope failures seen along the southern NE sector of the US Atlantic margin have their failure plane largely controlled by bedding planes that can become weaker following various triggering mechanisms (e.g., earthquakes). In most cases, the height of scarp slopes are much less than those of canyon slopes and their gradients are also generally lower. For scarp slopes, it is also interesting to note that the scarp slope angle is higher for older stratigraphic units, i.e. scarp slopes located deeper on the continental slope are cut into older (and stronger) sediments. This is particularly the case for points 59, 58 and 56 in Figure 3a that are respectively at 7.7°, 12.3° and 20.2°, for which the slope angle is much higher than the dip of the bedding plane or the 'unfailed' nearby slope angles. The open slope failures are only covered with a thin layer of debris (Fig. 2c) indicating

that most of the failed mass disintegrated and flowed down onto the lower part of the continental slope or onto the upper continental rise.

For canyon walls, there may be a continuous process between erosion and instability development. For this reason, the failure plane angle would correspond more or less to the actual canyon wall gradient. By inspection of Fig. 1a, canyons that cut the continental slope generate a longitudinal profile more or less perpendicular to the general gradient of the continental slope. Therefore, the bedding plane, a pseudo-structural component of the sediment, was apparently unable to control the angle of the failure plane, since the direction of movement had to be towards the canyon, i.e. in a direction at about 90° from the dip of the bedding plane. On the upper rise, the canyons meander (Fig. 1a) but most of the canyon walls are steep and close to the friction angle. The potential bedding plane in that area is very close to the actual slope angle (i.e. <1°) which is typical for very steep slopes if cohesion becomes a significant strength parameter. It is interesting here to note that as the canyon becomes inactive, it is filled with sediments so that the slope height decreases while the slope angle remains more or less the same (these canyons are filled by debris flows which force them to become inactive). The crescent like shape seen along the edges of the canyons may be used to indicate that the sliding mechanism is closer to that of a circular failure (e.g. Haflidason et al. 2004). The increase in the scarp slope angle with depth may also indicate that the shear strength is also increasing with depth. Dugan and Flemming (2002) discuss the role of pore pressure on slope stability and concluded that significant excess pore pressures were present under the continental slope around the Hudson Apron. Some excess pore pressures may still exist on the slope as indicated by Robb (1984) who has observed spring sapping on the slope. That being said, the very low strength values obtained in ODP 1,073 cores (Austin et al. 1998; Locat et al. 2003) may result from a low degree of consolidation. However, the steep slopes of the canyons and the relatively high slopes in the area would support the argument that the strength values obtained in the ODP 1,073 cores were largely disturbed, possibly by the presence of gas (Kayen and Lee 1993), although these geotechnical test results may not be applicable in the BC slide region.

Regarding triggering mechanism, preliminary analysis of the BC slide area suggests that for most of the open-slope failures to take place, either significant excess pore pressures (or its equivalent, i.e., generated by gas hydrates Sultan et al. 2004), seismic acceleration, or both were required. When considering a slope angle of 8°, a scarp slope of 12°, a failure surface of 2°, a failure thickness of 45 m, and a slope height of about 700 m, an excess pore pressure equivalent to about 40% of the overburden weight for a seismic acceleration coefficient of about 0.3 is required for instability to be generated (i.e., F = 1.0). With no seismic acceleration coefficient, the required excess pore pressure would need to be on the order of 90%. This is similar to what has been modeled for the Hudson Apron slide by Locat et al. (2003).

The tsunamigenic potential of a slide is mainly a function of the following parameters: slide volume, sliding mechanism, slide acceleration, and water depth (Geist et al. 2009). The slide volume calculated for the major lobes of the BC slide varies between 7.9 and 15.3 km^3. As an example, for the Storegga (Nadim and Locat 2005),

third party risks (i.e. those not related to the 'owner', e.g. coastal infrastructures) in the Storegga slide area, were considered to become significant for a slide volume greater than $5\,km^3$, in a situation where the sliding mechanism was a circular failure and at a water depth of about 200 m. Similarly, for the Currituck area, Geist et al. (2009) have shown that a landslide volume of about $150\,km^3$ could generate a coastal run up of 5 m. An important issue here with regards to the tsunamigenic potential of these slides, which is still to be resolved by dating and coring, relates to the sequence of events leading to the formation of these failure surfaces and of their initial volume. It is likely that some amphitheaters may be part of a single event, as concluded for the Currituck slide (Locat et al. 2009) and the Storegga slide (Haflidason et al. 2004), but others may not. It is still not clear yet as to where the slide was initiated.

The detailed morphology of the BC slide lobes (Figs. 1c and 2) indicates that at least lobe 2 could have originated from the slope (scenario 1) while for lobe 1 and 3, adjacent scarps may actually indicate a local source on the upper continental rise (scenario 2). As for lobe 1, it remains to be demonstrated how a mass of that size would acquire the necessary mobility to slide over a distance of about 3 km on a slope less than 1°, as it would require excess pore pressure greater than 0.9 or a very strong earthquake with seismic acceleration much greater than 0.3. Another scenario (scenario 3) may also consider a slide initiated on the continental slope that accumulated on the upper reaches of the continental rise, like lobe 2, but that quickly overloads (dynamic loading) the underlying sediments to trigger a secondary slide that carries the debris over some distance. Scenario 2 would not generate a significant tsunami because of the depth (more than 2,000 m) and the limited acceleration which could be expected for a slide initiated on such a low slope angle. On the other hand, an analysis of the mobility of the slide responsible for lobe 2 may indicate a much greater potential than for a scenario 3 slide. The mobility analysis is still underway and the forthcoming results will also help evaluate the failure dynamics in the BC slide area.

Conclusions

The analysis of the seafloor geomorphology in the vicinity of the Block Composite (BC) slide has provided some insight on failure processes in this area that lead to the following conclusions:

1. Slopes in canyons are much steeper than on failure scarps. It is speculated that the generation of weak layers along bedding planes is more effective for cases where the dip of the slope is in the same direction as the dip of the bedding plane.
2. Eroded slopes in the area indicate that the in situ sediment strength increases significantly with burial depth to a point where values reach close to their friction angle (i.e. about 30°).
3. The BC slide is composed of three major lobes for a total of $36\,km^3$, one of which may have originated from the continental slope with a potential for

generating a tsunami. The other major lobes do not appear to have traveled over long distances and are not considered tsunamigenic.

4. A preliminary analysis of the slope stability of lobe 2 indicates that for that failure to occur, significant excess pore pressures needed to have been generated and that the main potential agent would likely have had to have been an earthquake.

5. More multibeam and seismic data along with coring and geotechnical testing is required to better understand slide initiation and timing of the many failure surfaces observed in this area.

References

Austin JA Jr, Christie-Blick N, Malone MJ, et al. (1998) Proceedings of the Ocean Drilling Program, Initial Reports, Vol. 174A (CD-ROM)

Dugan B, Fleming PB (2002) Fluid flow and stability of the US continental slope offshore New Jersey from Pleistocene to the present. Geofluids 2: 137–146

Gardner JV, Mayer LA, Armstrong AA (2006) Mapping supports potential submission to U.N. Law of the Sea. EOS transactions. Am Geophys Union 87: 157–159

Geist EL, Lynett PJ, Chaytor JD (2009). Hydrodynamic modeling of tsunamis from the Currituck Landslide. Mar Geol 264: 41–52

Haflidason H, Sejrupa HP, Nygårda A, Mienert J, Bryn P, Lien R, Forsberg CF, Berg K, Masson D (2004) The Storegga Slide: architecture, geometry and slide development. Mar Geol 213: 201–234

Kayen RE, Lee HJ (1993) Slope stability in regions of sea-floor gas hydrate: Beaufort Sea Continental Slope. In: Submarine landslides: Selected studies in the U.S. xexclusive economic zone. US Geol Surv Bull 2002: 97–103

Locat J, Lee HJ (2002) Submarine landslides: Advances and challenges. Can Geotech J 39: 193–212

Locat J, Desgagnés P, Leroueil S, Lee HJ (2003) Stability of the Hudson Apron slope off New Jersey. In: Submarine mass Movements and Their Consequences, Locat and Mienert, Eds., Kluwer series on Natural and Technological Hazards, Dordrecht, 19, pp. 257–270

Locat J, Lee H, ten Brink U, Twichell D, Geist E, Sansoucy, M (2009) (in press) Geomorphology, stability and mobility of the Currituck Slide. Mar Geol 264: 28–40

Nadim F, Locat J (2005) Risk assessment for submarine landslides. In: Landslides and Risk Management, Hungr, Fell, Couture, Eberhardt, ed., Taylor & Francis Group, London, pp. 321–334

O'Leary DW (1993) Submarine mass movement, a formative process of passive continental margins: The Munson-Nygren Landslide Complex and the Southeast New England Landslide Complex. In: Schwab WC, Lee HJ, Twichell DC (Eds.), Submarine Landslides: Selected Studies in the U.S. Exclusive Economic Zone. U.S. Geological Survey Bulletin 2002, USA, pp. 23–39

Piper DJW, McCall C (2003) A synthesis of the distribution of submarine mass movements on the eastern Canadian margin. In: Submarine Mass Movements and Their Consequences, Locat and Mienert, ed., Kluwer series on Natural and Technological Hazards, Dordrecht, 19, pp. 291–298

Poag CW (1991) Rise and demise of the Bahama-Grand Banks gigaplatform, northern margin of the Jurassic proto-Atlantic seaway. Mar Geol 102: 63–130

Poag CW, Sevon WD (1989) A record of Appalachian denudation in postrift Mesozoic and Cenozoic sedimentary deposits of the U.S. middle Atlantic continental margin. Geomorphology 2: 119–157

Robb JM (1984) Spring sapping on the lower continental slope, offshore New Jersey. Geology 12: 278–282

Robb JM, Hampson JC, Twichell DC (1981) Geomorphology and sediment stability of a segment of the U.S. Continental Slope off New Jersey. Sciences 211: 935–937

Ryan WBF, Cita MB, Miller EL, Hanselman D, Nesterhoff WD, Hecker B, Nibbelink M (1978) Bedrock geology in New England submarine canyons. Oceanol Acta 1: 233–254

Sultan N, Cochonat P, Foucher JP, Mienert J (2004) Effect of gas hydrates melting on seafloor slope instability. Mar Geol 211: 379–401

ten Brink, U.S., Tsunami Hazard Along the U.S. Atlantic Coast, 2009. Mar Geol 10, doi: 1016/j.margeo.2009.03.011

Tucholke BE, Mountain GS (1986) Tertiary paleoceanography of the western North Atlantic Ocean. In Voigt PR, Tucholke BE (Eds.), The Geology of North America, Volume M, The Western North Atlantic Region. Geol. Soc. Am., pp. 631–650

Twichell DC, Chaytor JD, ten Brink US, Buczkowski B (2009) Morphology of late Quaternary submarine landslides along the U.S. Atlantic continental margin. Mar Geol 264: 4–15

Post-Megaslide Slope Stability North of Svalbard, Arctic Ocean

D. Winkelmann, W.H. Geissler, R. Stein, and F. Niessen

Abstract In the light of a warming globe, increasing coastal population and human offshore activities, slope stability issues steadily gain significance. The Arctic Ocean is predicted to exhibit most drastic changes. Following the enormous Hinlopen/Yermak Megaslide north of Svalbard 30,000 years ago, the adjacent slopes developed several failure types as a consequence of the partial removal of the Hinlopen trough mouth fan. The local slope to the east is structured by several detachment surfaces that facilitate large scale creeping. This soft sediment deformation includes turbulent structures like folds on a meter-scale. The creeping sediments partly cover the eastern main slide debris of the megaslide within Sophia Basin. The timing of this gravity-driven mass transport can roughly be assessed by the time interval that occurred between the megaslide and today. These features mark the slope as unstable.

Keywords Submarine landslide • mass-failure • tsunami • geohazard • seafloor morphology • submarine slope stability • submarine debris flow • post-slide slope stability

1 Introduction

1.1 Indication for Slope Failure?

Large-scale gravity-driven slope failures (e.g. submarine landslides) represent a natural hazard to any sea-floor infrastructure as well as to coastal communities due to their ability to generate large-scale tsunamis. The predictability of these events

D. Winkelmann (✉)
Leibniz Institute for Marine Science (IFM-GEOMAR), Kiel, Germany
e-mail: dwinkelmann@ifm-geomar.de

W.H. Geissler, R. Stein, and F. Niessen
Alfred Wegener Institute for Polar and Marine Research, Bremerhaven, Germany

may be inferred from recurrence rates or from numerical modelling. Both approaches are based on the assumption that the cause of the slides and their trigger-mechanisms are fully described. The intrinsic problem with investigations of slope failures is that the remaining slope (sedimentary properties, structures etc.) actually characterises a stable environment (it has not failed). Thus, the identification of indications for future failure remains a key target. Among the variety of proposed trigger-mechanisms, one refers to the acceleration of slow failures along detachment horizons (e.g. creeping sediment) leading to sliding.

In the light of a warming globe, increasing coastal population and human offshore activities, slope stability issues gain steadily significance. The Arctic Ocean is predicted to exhibit most drastic changes.

1.2 Research Area

The Arctic Svalbard archipelago comprises the main islands of Spitsbergen and Nordaustland and further islands reaching from rather large to numerous small-scale islands. It is neighboured by the semi-enclosed submarine Sophia Basin to the north (Fig. 1). The archipelago was repeatedly glaciated by the Svalbard-Barents Sea-Ice-Sheet (SBIS) which shaped the modern landscape with mountain ridges, fjords and cross-shelf troughs by glacial erosion. The shelf north of Nordaustland
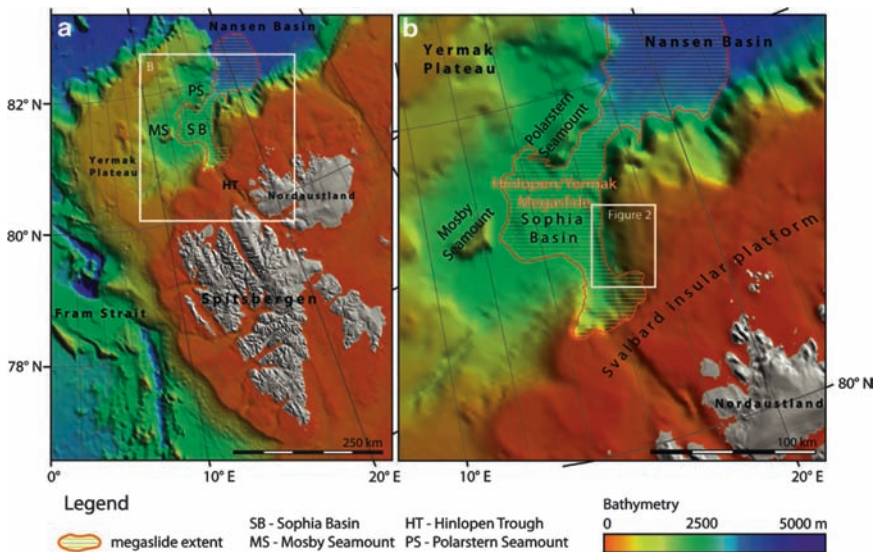
Fig. 1 (*left*) Overview map of Svalbard archipelago and the eastern Fram Strait region; (*right*) close up of the Sophia Basin with the outline of the Hinlopen/Yermak Megaslide and location of Fig. 2. Bathymetry: IBCAO2 (Jackobson et al. 2008)

has, in comparison to the Barents Sea, hardly been investigated due to its natural sea ice cover. The first systematic seismic surveys were carried out in 1990, 1993 (NPD-MOF-90/93) and 1999 (Geissler and Jokat 2004). The research area is the western slope of this shelf facing the Sophia Basin. This area is situated directly adjacent to the headwall area and deposits of a giant submarine slide.

This giant slope failure was first described by Cherkis et al. (1999) but was discussed controversially due to its enormous dimensions. Later studies (incl. two cruises of the ESF EUROMARGINS project SPACOMA in 2004) confirmed the existence of a submarine slide complex with thick debris deposits which occurred 30,000 years ago (Vanneste et al. 2006; Winkelmann et al. 2006, 2008a; Winkelmann and Stein 2007).

This slide complex consists of one major failure event, the Hinlopen/Yermak Megaslide. It removed partly the Hinlopen Trough Mouth Fan (TMF) and drastically affected the post-slide stability of the adjacent slopes leading to a variety of slope failures (Winkelmann et al. 2008a). The potential for repeated failures, thus, is significant. While Winkelmann et al. (2008a) focused on the megaslide's dynamics, we concentrate in this paper on the post-slide instability issue.

1.3 Material and Methods

Parametric echo-sounding (Atlas PARASOUND, 4 kHz parametric frequency of 18 and 22 kHz primary frequencies; footprint: $4° \times 4.5°$), high-resolution swath bathymetry (Atlas HYDROSWEEP DS-2, 15.5 kHz; 118 beams, 90° insonification angle) data were acquired aboard RV "Polarstern" during ARK-XX/3 in 2004 (Stein et al. 2005). Additional high-resolution swath bathymetry data (Simrad EM 300, 30 kHz; 135 beams; 150° insonification angle; Vanneste et al. 2006) were integrated. The data were gridded at 20 m resolution and adjusted for system-related offsets. Slope angles are based on these grids. Further, we interpreted multi-channel reflection seismic data of profile MF-908100 acquired during the regional survey NPD-MOFF-90 and owned by the Norwegian Petroleum Directorate. Gravity coring was accomplished with a giant gravity corer (35×35 cm; kastenlot). Core description and x-ray radiography were performed aboard the vessel directly after recovery.

2 Results

High-resolution bathymetry reveals several bulges of sediment (frontal slope angles >6°) on the continental slope north of the Hinlopen/Yermak Megaslide's headwalls (Fig. 2). The parametric echo-sounding data from a profile running down-slope across several bulges displays staircase structures and an upper transparent unit that drapes acoustically stratified sediments below. The acoustic profile crossing one of these bulges more or less slope-parallel displays that the upper transparent unit is characterised by a lateral transition into acoustical stratification (Fig. 3). This indicates a lateral shift of the internal acoustic character of the bulge.
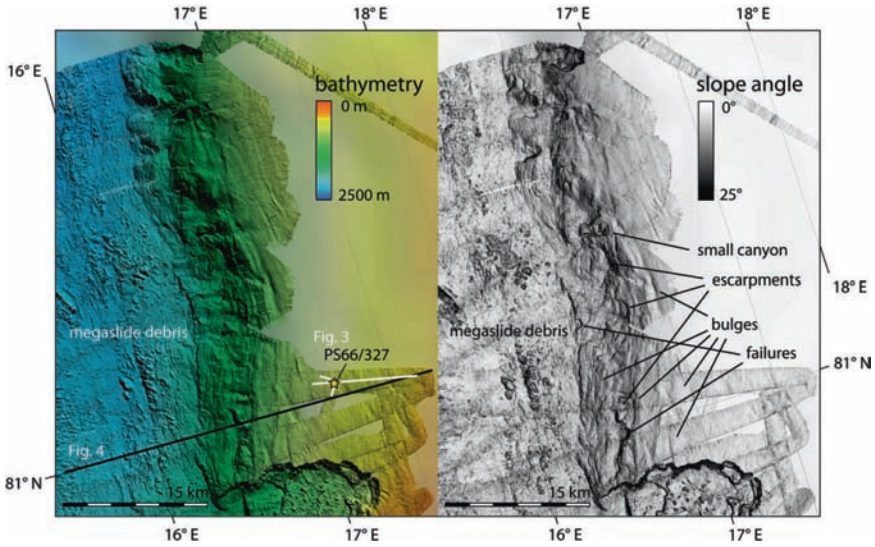
Fig. 2 Maps of the eastern Sophia Basin (see Fig. 1 for location): (*left*) shaded bathymetry and (*right*) associated slope angles displaying creeping sediments with numerous escarpments, small-scale failures and canyons on the continental slope adjacent to the removed Hinlopen Trough Mouth Fan. Slide deposits of the Hinlopen/Yermak Megaslide are visible in the western part of the maps. Position of core PS66/327–3, location of seismic profile (Fig. 4) and acoustic profiles (Fig. 3) are indicated

The kastenlot PS66/327–3 (see Fig. 2 for location) was placed into this upper acoustically transparent unit (Fig. 3) and recovered 5.5 m of sediment. The examination of the core revealed tilted sedimentary layers involved in deformational structures like folds at different scales. These structures are clearly visible throughout the core, identifying a heavily disturbed sediment. The uppermost 40 cm of this core contains a fairly sorted silt unit (containing sand and gravel) with sharp contact at its base. We interpret this uppermost 40 cm to be a turbidite in its early stage (being less sorted). The sedimentological classification of the rest of the core would be close to a debris flow. But since the initial structures are not completely disintegrated, it does not reflect the flow of debris in a strict sense. We interpret the deformational structures of the core to reflect creeping of soft sediment.

3 Discussion

Textural structures in PS66/327–3 indicate soft sediment deformation. The same range of glaciomarine sediments that were recovered within the Sophia Basin (c.f. Winkelmann et al. 2006, 2008a, b) are obviously involved in this slope failure type. No indication for any special failure-related sedimentary component (e.g. gaseous sediment, high porosity sands/oozes or hydrates etc.) was found. There are several
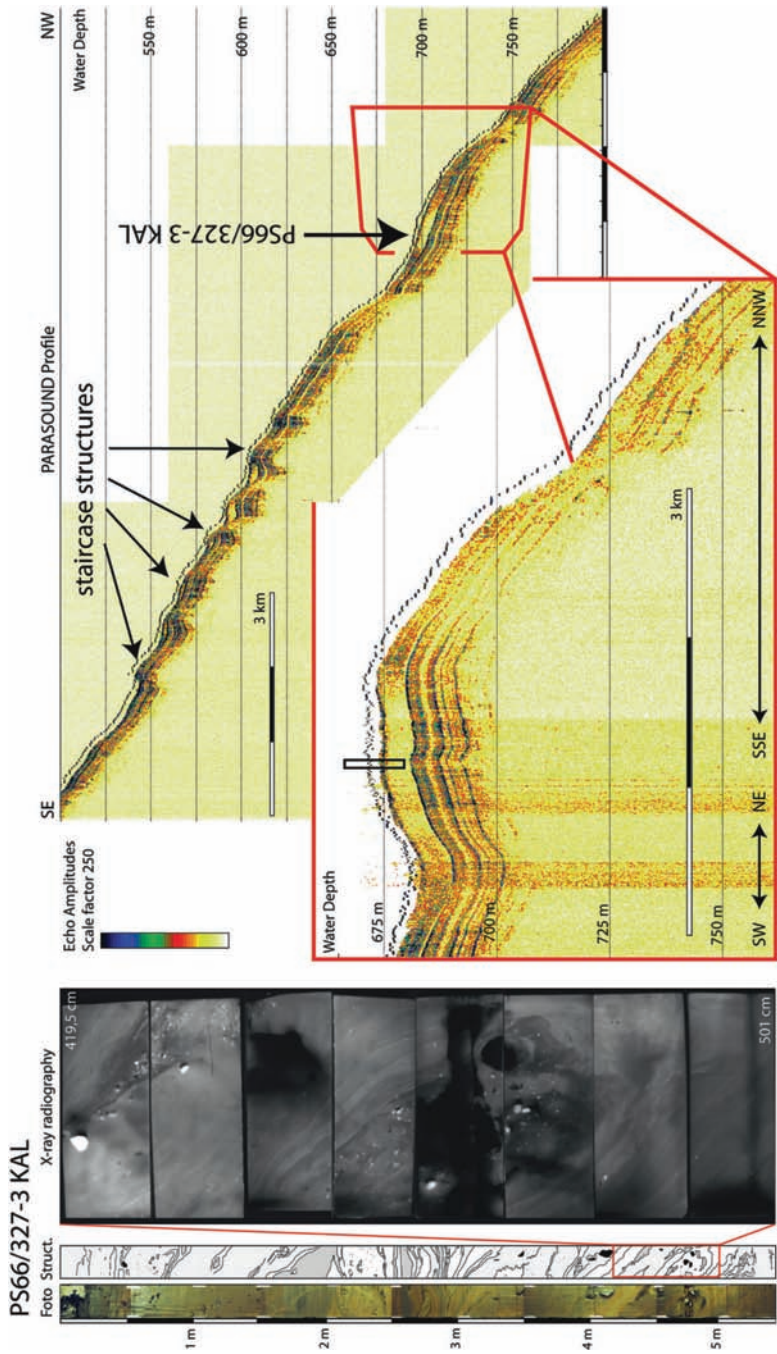
Fig. 3 PARASOUND profiles and gravity core PS66/327–3 (5.5 × 0.35 × 0.35 m). The core recovered strongly deformed siliciclastic glaciomarine sediments (silty clays with IRD-layers) from the upper acoustically transparent unit. For location of profiles and core see Fig. 2. Note that the lower profile changes direction on core position (*up* and *down* the slope)

conditions to produce the folding in core PS66/327–3: (a) undisturbed glaciomarine sedimentation (with changing sedimentary input during interglacial and glacial cycles) to produce the well developed layers; (b) deformation of these layers. Since the cored sediments (and deformed sediments between 675 and 750 m) are below any reasonably reconstructed grounding line of the SBIS, the remaining force should be gravity.

Gravity-driven movement requires a sufficient inclination of the slope. Since the sediments have been deposited quietly before their deformation, we interpret the cause for the gravity-driven deformation to be over-steepening. The initiation of movement may be attributed to seismic activity (repeated excitation by frequent earthquakes) but may have another cause.

Intended to obtain a highly resolved Holocene record, the cored material was ordered to be disposed back to sea. However, the core was photographed and sampled for x-ray analysis before. Synoptic investigation as well as x-ray radiography identified no significant difference in sedimentary properties of undisturbed sediments from the Sophia Basin (c.f. Winkelmann et al. 2006, 2008a, b).

The cause for the over-steepening of the slope can be seen in the structural adjustment of this continental slope following the removal of the Hinlopen TMF. This western continental slope north of Nordaustland is characterised by a set of detachments. These detachments have been speculated to be the cause for the megaslide (Cherkis et al. 1999) and re-interpreted to simply represent boundaries between sedimentary layers (Vanneste et al. 2006). The wavy sediments would reflect sediment waves of contourites according to Vanneste et al. (2006). We examined the seismic reflection profile MF-908100 (Cherkis et al. 1999) and identified several detachment surfaces that obviously facilitate large-scale deformation within the slope. These detachments can also be seen in seismic reflection profile 04JM059 (Vanneste et al. 2006). Three main detachment surfaces are sub-horizontally aligned and often combined with low-angle listric faults that route in these detachments. The listric faults steepen upwards and often transform into another detachment or low-angle fault (Fig. 4). The deepest detachment outlined by Cherkis et al. (1999) could not be confirmed. The sediments bound between these structures and which appear like large-scale waves are deformed packages of sediments bound and slowly displaced between the detachments.

The upper part of the slope exhibits indications for further deformation into the shallow sediments. The staircase structures (Fig. 3) imaged in the parametric echo-sounding data require another, shallower detachment horizon which is not imaged in the PARASOUND data nor resolved in seismic reflection data. We speculate that its sub-bottom depth may be between 30 and 50 m. The creeping sediments on top obviously require another, even shallower detachment surface. This is the boundary towards the stratified sediments below (between 2 and 7 m bsf.).

The chaotic and partly acoustically transparent signature of shallower sediments displayed in profile 04JM059 may resemble debris flows. This may have led Vanneste et al. (2006) to interpret these shallower slope sediments bound between
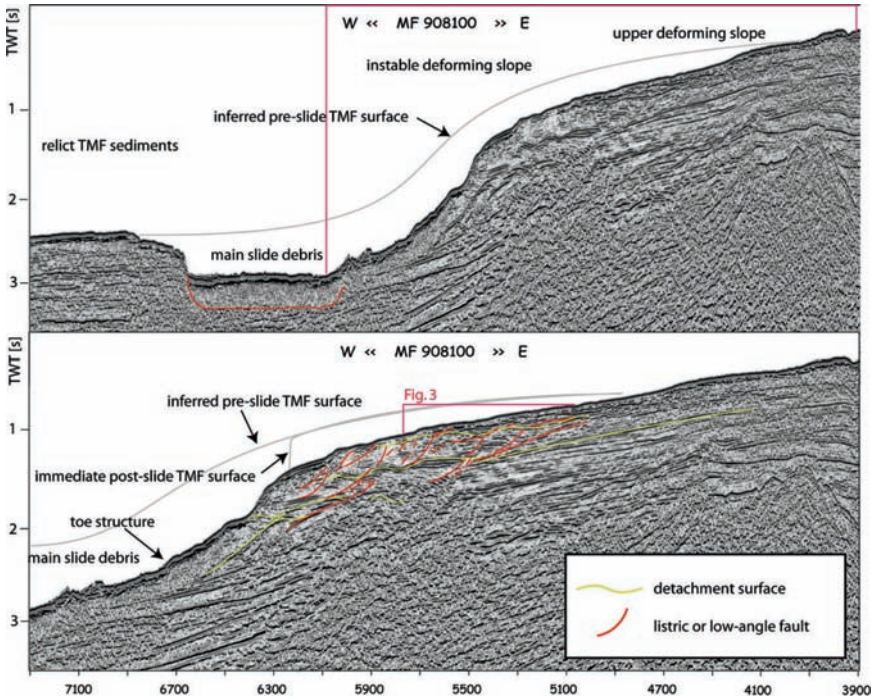
Fig. 4 Multi-channel seismic reflection profile across the eastern continental slope adjacent to the megaslide scar; yellow solid lines indicate position of main detachments, red solid lines indicate low-angle or listric faults, grey solid lines inferred pre-slide and immediate post-slide sea-floor morphology; approximated location of acoustic profiles (Fig. 3) indicated as red box in lower image

the detachments as glacigenic debris flows. However, some of those supposed debris flows show clear stratification, some of them deformed. In fact, the cored upper transparent unit has no clear lateral boundaries, but rather develops gently into acoustically stratified sediments. We interpret this to be related to the system-immanent acoustic footprint of the PARASOUND system (4 × 4.5°). The absence of a sufficiently large and consistent (with regard to the footprint) intra-sedimentary surfaces prevents the record of consistent internal reflectors. Thus, these sediments appear transparent in the acoustic imagery of sedimentary structures (Fig. 4). This indicates one problematic aspect of the acoustic identification of gravity-driven mass movements.

The timing of this deformation is difficult to constrain since we did not recover undisturbed sediments below and the lack of younger non-deformed sediments on top. However, Winkelmann et al. (2008b) have shown that terrigenous input events (TIEs) of the Sophia Basin formed discrete sedimentary layers which develop acoustically recordable sub-buttom reflectors in the parametric echo-sounding data. These can be used for acoustic stratigraphy or sedimentologically as stratigraphic marker horizons (Winkelmann et al. 2008b). Judging from the

PARASOUND imagery (Fig. 3), the well developed strata below the upper trans-
parent unit resemble the sequence of TIEs of MIS 3–7 (and older below). Since
the Hinlopen/Yermak Megaslide occurred in MIS 3 (30 ky ago), this would cor-
roborate a post-megaslide age of the deformation. If correct, this would also
confirm the gravity-driven mechanism as a result of slope over-steepening.
However, the reflectors below the deformed sediments of the upper transparent
unit may be older.

In summary, there are at least five detachments structuring the slope. The
nature of these detachments may be explained by sediment layers with low shear
strength but remains to be investigated. Their cause is probably the partial TMF
collapse that led into the Hinlopen/Yermak megaslide (Hinlopen/Yermak
Megaslide; c.f. Winkelmann et al. 2006, 2008a). The continental slope lost its
stabilisation by the adjacent TMF sediments. This led to instability, down-slope
movement along weak horizons that acted as detachment (c.f. Cherkis et al.
1999) and to creeping due to over-steepening of the upper slope. This scenario
is corroborated by toe structures. They indicate that the western part of the
megaslide's deposits has partly been covered by slope sediments creeping
onto them. The bulges of sediment along the slide's debris (Fig. 2) support this
interpretation.

The investigated slope appears unstable. The sediments may persistently or
repeatedly move. Whether the areas of deforming sediments are about to fail within
fast failure events (e.g. slides) remains debatable. The present detachments already
act as slip plane. Seismic excitation may stimulate creeping into faster slope failures
(slides). Younger failures in the eastern headwall area (evident as detachment
ridges; c.f. Vanneste et al. 2006; Winkelmann et al. 2008a) document the acute
failure potential.

4 Conclusion

The western shelf north of Nordaustland is structured by at least five detachments. They
have probably formed as a consequence of the partial collapse of the Hinlopen
TMF during the Hinlopen/Yermak Megaslide. The slope sediment moves down-
slope along these detachments and covers partly the eastern main slide debris of the
Hinlopen/Yermak Megaslide. Staircase structures and creeping sediment are identi-
fied in the upper sediments and point to over-steepening. The eastern headwalls
may likely be related to this slope instability that post-dates the megaslide. Further
high-resolution acoustic, seismic and geotechnical data are needed to understand
this soft sediment deformation.

References

Cherkis, N.Z., Max, M.D., Vogt, P.R., Crane, K., Midthassel, A., Sundvor, E., 1999, Large-scale mass wasting on the north Spitsbergen continental margin, Arctic Ocean. Geo-Mar Lett 19: 131–142.

Jakobsson, M., Macnab, R., Mayer, L., Anderson, R., Edwards, M., Hatzky, J., Schenke, H.W., Johnson, P., 2008, An improved bathymetric portrayal of the Arctic Ocean: Implications for ocean modeling and geological, geophysical and oceanographic analyses. Geophys Res Lett 35: L07602, doi:10.1029/2008GL033520.

Geissler, W.H., Jokat, W., 2004, A geophysical study of the northern Svalbard continental margin. Geophys J Int 158: 50–66, doi: 10.1111/j.1365–246X.2004.02315.x.

Stein, R. (Ed.), 2005, Scientific Cruise Report of the Arctic Expedition ARK-XX/3 of RV "Polarstern" in 2004: Fram Strait, Yermak Plateau and East Greenland Continental Margin, Rep Polar Mar Res 517.

Vanneste, M., Mienert, J., Bünz, S., 2006, The Hinlopen Slide: A giant, submarine slope failure on the northern Svalbard Margin, Arctic Ocean. Earth Planet Sci Lett 245: 373–388.

Winkelmann, D., Jokat, W., Stein, R., Winkler, A., 2006, Age and extent of the Yermak Slide north of Spitsbergen, Arctic Ocean. Geochem Geophys Geosyst 7, Q06007, doi:10.1029/2005GC001130.

Winkelmann, D., Stein, R., 2007, Triggering of the Hinlopen/Yermak Megaslide in relation to paleoceanography and climate history of the continental margin north of Spitsbergen. Geochem Geophys Geosyst 8: Q06018, doi:10.1029/2006GC001485.

Winkelmann, D., Geissler, W., Schneider, J., Stein, R., 2008a, Dynamic and timing of the Hinlopen/Yermak Megaslide north of Spitsbergen, Arctic Ocean. Mar Geol 250: 34–50.

Winkelmann, D., Schäfer, C., Stein, R., Mackensen, A., 2008b, Terrigenous events and climate history of the Sophia Basin, Arctic Ocean. Geochem Geophys Geosyst 9: Q07023, doi:10.1029/2008GC002038.

Geomorphology of the Talismán Slide (Western slope of Hatton Bank, NE Atlantic Ocean)

M. Sayago-Gil, D. Long, L.-M. Fernández-Salas, K. Hitchen, N. López-González, V. Díaz-del-Río, and P. Durán-Muñoz

Abstract The Spanish interdisciplinary research project ECOVUL/ARPA focuses on the western slope of Hatton Bank (NE Atlantic Ocean). As part of this project, interpretation of multibeam bathymetry data, very high resolution seismic profiles and sediment samples collected by the Instituto Español de Oceanografía, permitted to identify the Talismán Slide, an underwater landslide developed within the deepwater sediments of the Hatton Drift. Within the slipped mass, present day sea-bed morphology is rough, comprising blocks, ridges, steps and secondary slides. Seismic profiles show the slide mass to be supported by a sequence of contouritic deposits. Trigger mechanism for the Talismán Slide is likely a combination of several causative factors such as erosion (caused by bottom currents) and an earthquake event which accelerated the slide process.

1   Introduction

The Spanish interdisciplinary research project ECOVUL/ARPA (Instituto Español de Oceanografía) focuses on the western slope of Hatton Bank (Rockall Plateau, NE Atlantic Ocean). During this project, the Talismán Slide has been identified as an underwater landslide located at 57°35'N, 20°18'W and developed

M. Sayago-Gil(✉), L.-M. Fernández-Salas, N. López-González, and V. Díaz-del-Río
Instituto Español de Oceanografia, Centro Oceanográfico de Málaga, Puerto Pesquero,
s/n. Apdo. 285, 29640 Fuengirola (Málaga), Spain
e-mail: miriam.sayago@ma.ieo.es

D. Long and K. Hitchen
British Geological Survey, West Mains Road, Edinburgh, EH9 3LA, UK

P. Durán-Muñoz
Instituto Español de Oceanografía, Centro Oceanográfico de Vigo, Cabo Estay-Canido,
Apdo. 1552, 36200 Vigo (Pontevedra), Spain

within the deep-water sediments of the Hatton Drift at about 1,358 to 1,900 m water depth.

Many factors (such as size, location, sedimentology of migrating depocenters, changes in seafloor pressures and temperatures, variations in seismicity and volcanic activity, changes in groundwater flow conditions, presence of gas hydrates, internal sea waves, etc.) are relevant to submarine slope instability (Holmes et al. 1998; Konrad and Dubeau 2003; Maslin et al. 2004; Lawrence and Cartwright 2009). Lee (2009) proposes that the dominant factor influencing the timing of submarine landslides occurrence in NE Atlantic Ocean margin is glaciation. An association likely exists because of the formation of thick deposits of sediment on the upper continental slope during glacial periods making it more prone to fail and increased seismicity caused by isostatic readjustment during and following deglaciation.

In this paper we present a study of the morphologic, seismic and sedimentary aspects of the Talismán Slide, in order to establish a hypothesis about its origin and the trigger mechanism for its initiation. Slides on remote margins, as Talismán Slide, are rarely reported. The Talismán Slide is a slope failure on deep water, sediment starved, contourite dominated margin with no direct glacial sediment input which is in contrast to failure on other NW European margins. Data obtained in this study cover only the proximal and mid portions of the slide. Consequently, all interpretations given in this work correspond solely to these specific parts of the slide.

1.1 Setting

Hatton Bank comprises the western part of the Rockall Plateau which is a broad topographically-elevated region with respect to the adjacent Iceland ocean basin (Fig. 1). The Rockall Plateau is underlain by continental crust which, before the opening of the North Atlantic Ocean in the Mesozoic to early Cenozoic (Stoker et al. 1998; Roberts et al. 1999; Doré et al. 1999; Coward et al. 2003), was juxtaposed between SE Greenland and NW Europe. The present configuration of the Rockall Plateau is the result of a complex geological evolution involving tectonism, massive volcanism and differential subsidence and inversion. The western margin of Hatton Bank is a slope remote from any major terrigenous sediment supply at present and it is over 360 km from the closest onshore sediment source (MacLachlan et al. 2008).

The study area is located on a plastered contourite-drift (the Hatton Drift) (McCave and Tucholke 1986) developed on the western flank of Hatton Bank. Contourite drifts are deep-sea sediment deposits that accumulate under the influence of strong thermohaline bottom currents (Stow and Lovell 1979) that have been active since the Miocene at least based upon DSDP holes in the study area (Bianchi and McCave 2000; Huizhong and McCave 1990). Bottom currents can erode, mould, transport and redistribute sediments supplied to the slope and rise by downslope flows and vertical settling (Weaver et al. 2000) as well as by alongslope transport which is the main responsible of the contourite deposits (Stow and Holbrook 1984). The western slope of Hatton Bank is influenced by a branch of *Labrador Sea Water* which meets with the *Iceland-Scotland Outflow Water* (Fig. 1)
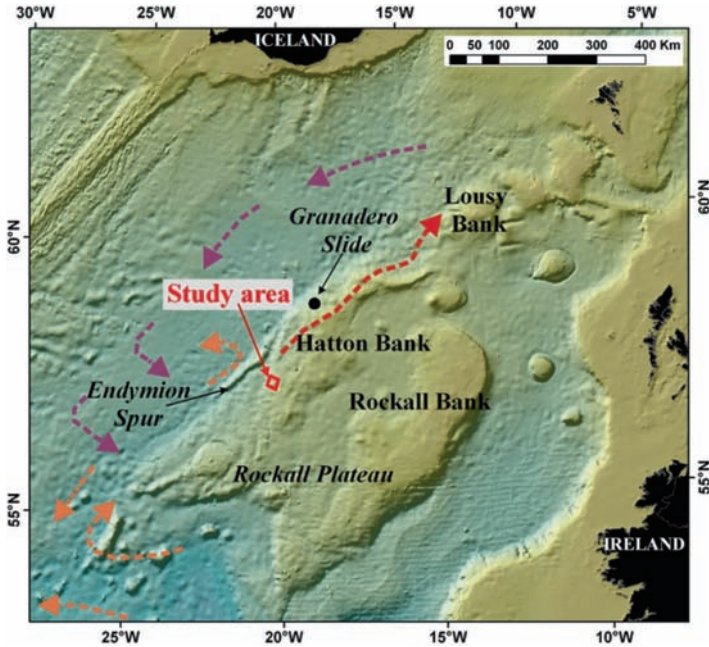
Fig. 1 Study area location on general bathymetry. Dashed arrows: bottom currents; Purple: Iceland-Scotland Outflow Water, Orange: Lower Deep Water, Red: Deep Northern Boundary Current (Modified from Bianchi and McCave 2000; MacLachlan et al. 2008)

forming the *Deep Northern Boundary Current* (DNBC) (McCartney 1992) and possibly the *Lower Deep Water* (Bianchi and McCave 2000) which travels to the Iceland Basin where they circulate anticlockwise (Van Aken 1995).

Despite difficulties in detecting seismic activity in the Hatton Bank area because of distant land-based seismometers, two recent earthquakes have been recorded in 1998 on Hatton Bank (Richter Local Magnitude (RLM) = 3.5) and in 1999 on Lousy Bank (RLM = 3), 550 km to the north-east. This shows that although Hatton Bank is located on a 'passive' margin, it is not aseismic (Simpson and Ford 1999; Simpson et al. 2000) and the intra-plate earthquake events are not unusual.

1.2   Methodology

This work has been carried out using three kinds of data sets: multibeam bathymetry, seismic data and sediment samples.

Kongsberg-Simrad-EM300 multibeam echosounder data were collected over the western slope of Hatton Bank between 2005 and 2007, providing 100% coverage (50 m resolution grid) from 1,300 to 1,900 m water depth with a total covered surface of 390 km^2. All data have been integrated into ArcGIS Desktop for visualization.

A network of 80 km (approx.) of very high-vertical resolution seismic profiles was collected with the parametric echosounder Topas from 2005 to 2007. Seismic data have been interpreted using Kingdom Suite software to investigate the sequence stratigraphy.

Two samples of surficial sediment (Box-Corer, 0.25 m^2) have been obtained to a distance of ~40 km from the Talismán Slide. The percent of the main components and foraminifera content of the sediments have been determined by means of wet sieve, Sedigraph 5120 and trinocular microscope.

2 Results

The western slope of Hatton Bank shows a range of water depth between 600 and 2,900 m and the slope break is located at 1,000 m (approx.) (MacLachlan et al. 2008). The study area is located on the western middle slope of Hatton Bank. The overall gradient of the western slope of the bank is approximately 2° although locally up to 40° (in determined morphologies). The bank has a SW–NE orientation in the southernmost part (where the Talismán Slide is located) and W–E in the north. Talismán Slide is located within the Hatton Drift (a contourite deposit). Based on the seismic data, this deposit is characterized by a variable sediment thickness (up to 250 ms), generally increasing basinward, onlapping upslope as a wedge with well stratified layers.

The maximum upslope extent of the headwall of the Talismán Slide scar is located at 1,358 m water depth and the main trend of the slide scar is ESE-WNW. The slide scar area covers a minimum of 194 km^2 and extends at least 15 km downslope, reaching at least 1,900 m water depth.

2.1 *Morphometrical Features*

The *Headwall Scarp* is 7.7 km long and is located between 1,358 and 1,386 m of water depth. It shows a NNE-SSW trend with an irregular form, slightly curved basinward. The headwall scarp varies in height between 50 and 76 m and it has a slope angle about 30°. The Northern Sidewall has an ESE-WNW trend and a linear form. The scarp height is between 76 and 100 m with a slope of 34°. The Southern Sidewall shows a NE–SW trend with a zigzag pattern. It has a scarp height of 50 m decreasing downslope to 30 m and shows the gentler slope of the scarp (25°) (Fig. 2).

The minimum volume of geological material removed by the slide is ~15 km^3 based on the average thickness of the slipped mass (approximately 75 m) and the slide scar area (194 km^2). The present day relict basal surface has a mean slope of 1°–2° and displays various discontinuous morphologies, some of which have positive relief up to 20 m (blocks) whereas others occur as negative relief (depressions)
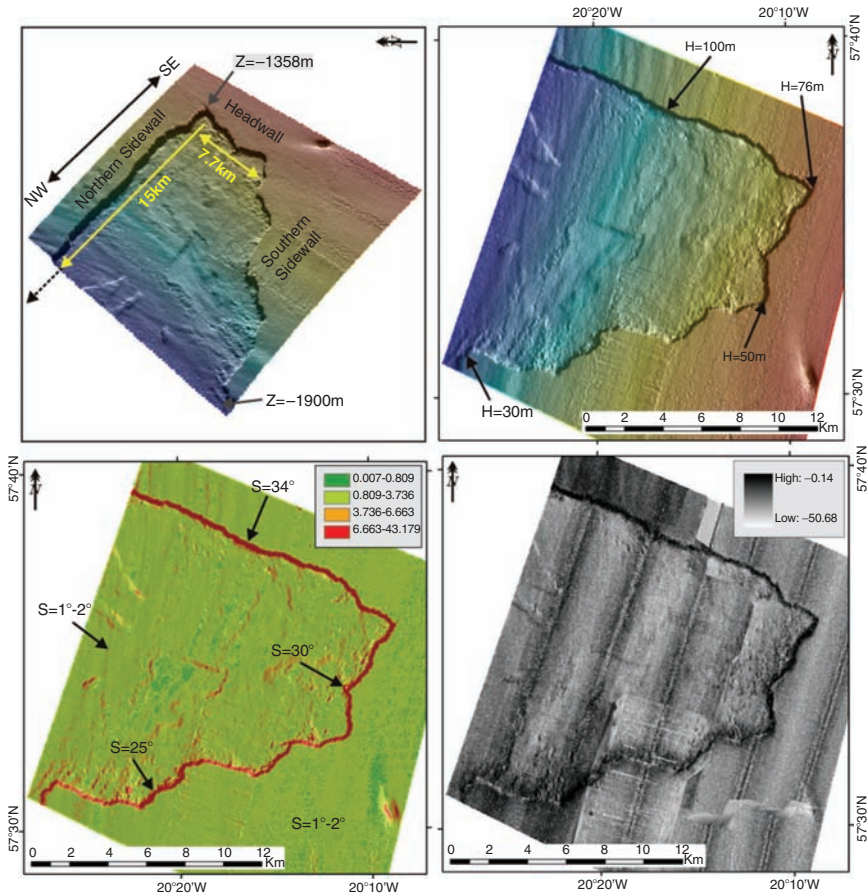
Fig. 2 Main features of the Talismán Slide. (**a**) 3D visualization and general description of the slide. Z = water depth. (**b**) Scarp heights of different points on the sidewalls and headwall. H = scarp height. (**c**) Slope angle of different points on the sidewalls and headwall. S = gradient of the slope. (**d**) Backscatter image obtained by means of multibeam echosounder

both of which have a step-like appearance. Many of these forms are perpendicular to the scar. Within the slide scar, secondary scarps occur both perpendicular and at various angles to the sidewall scarps. Secondary ridges are mainly transverse to the scar at right angles to the direction of movement (Fig. 3). Moreover, some deposits are seen attached to the southern sidewall (i.e. sidewall collapse deposit). Based on the backscatter data it is possible to observe the highest values (−0.14 dB) in the steepest zones and the lowest values (−50.68 dB) into the mass slide (Fig. 2d) that have contributed additional information about roughness, slope and sediment type in order to obtain a morphological sketch of the slide.
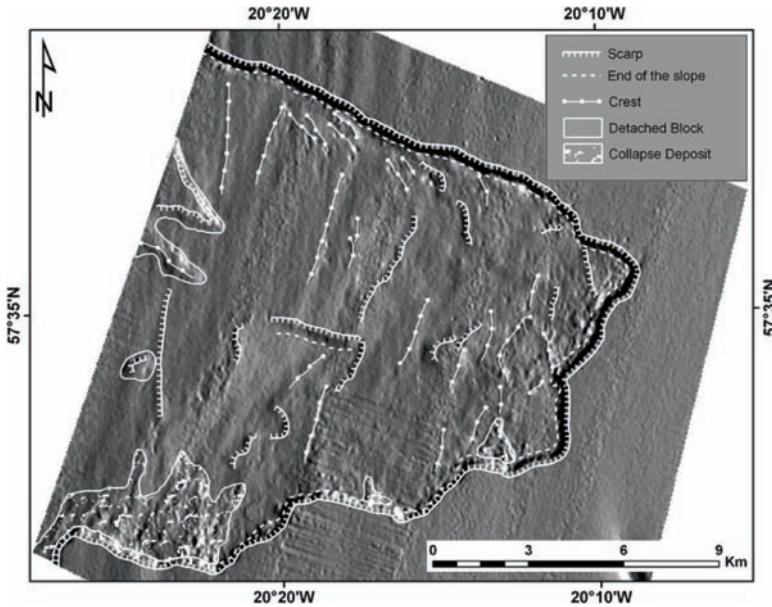
Fig. 3 Morphological sketch of the part studied of the Talismán Slide

2.2 Seismic Features

Seismic profiles show that the slid mass is bounded by very steep sidewalls (Fig. 4a) and a steep headwall scarp (Fig. 4b). Under the seabed three seismic facies can be differentiated: the deepest is shown as a well stratified unit preserving the internal structure which has been interpreted as a contourite sequence (Hatton Drift); above a chaotic unit has been interpreted as the remnant debris deposit; finally on top, a thinner unit can be observed that is composed by recent post-slide sediments. The average thickness of the slipped mass is approximately 75 m and the resulting chaotic deposit (debris unit) has a maximum thickness of 20 m. The slide plane cuts into the sequence of contouritic deposits that are overlain by the chaotic unit of the slide mass. The contourite sequence and the uppermost unit thicken towards the northern sidewall of the slide. The chaotic unit does not show a clear trend of thickness increase.

2.3 Sedimentary Features

Analyses of two samples from the contourite drift at a similar water depth to the headwall of the slide show that the present day sea-bed sediments in the area of the Talismán Slide are muddy sands and sandy muds (Fig. 5). In both samples, the sand fraction is composed of carbonate rests of planktonic foraminifera, mainly from genus Orbulina and Globigerina (Fig. 5).
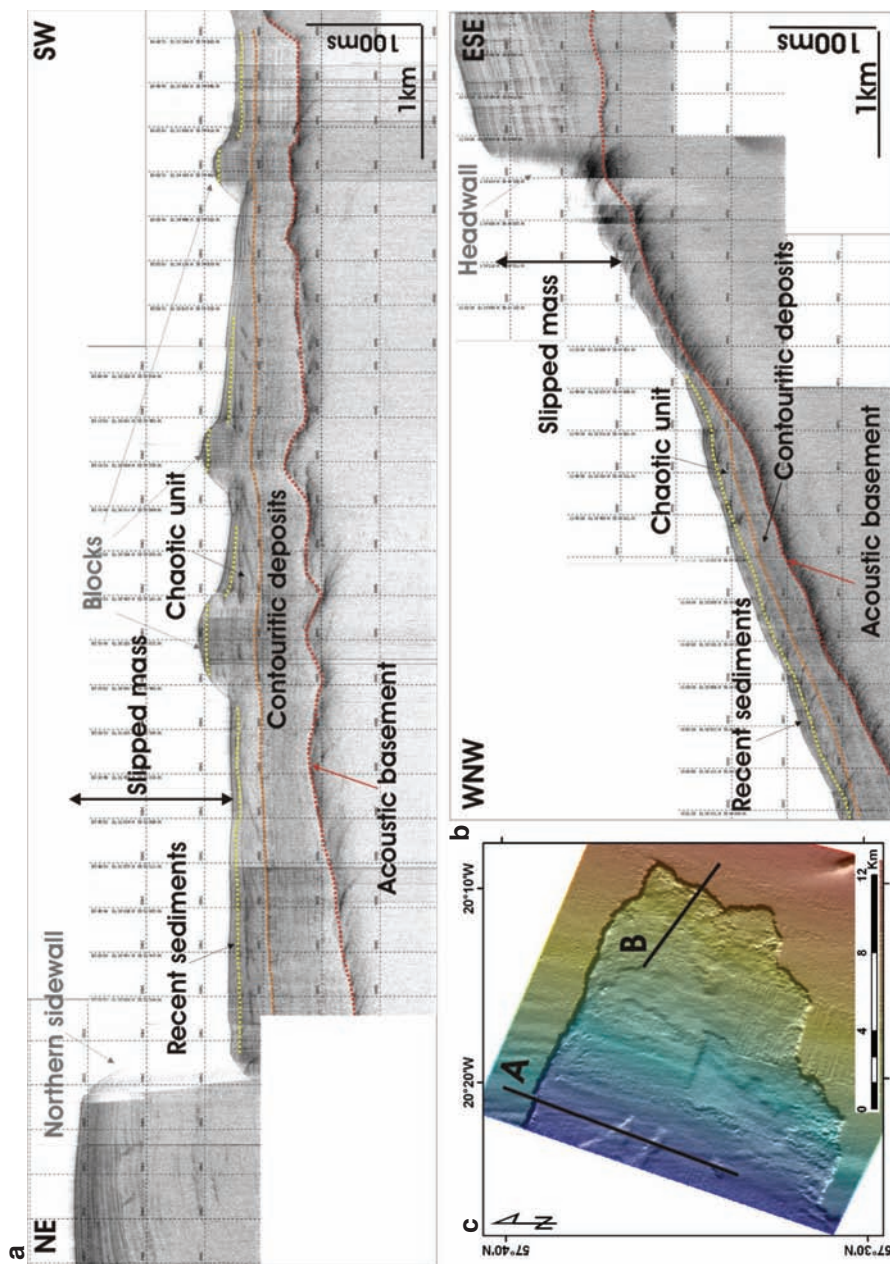
Fig. 4 Topas seismic profiles obtained on Talismán Slide. (**a**) Cross seismic section showing the northern sidewall and the sediment deposit. (**b**) Longitudinal seismic section showing the steep headwall of the Talismán Slide. (**c**) Location of seismic sections A and B on multibeam bathymetry
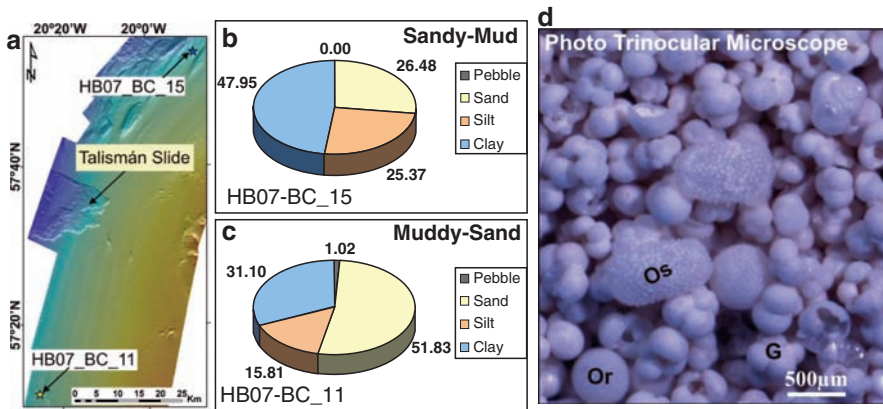
Fig. 5 (**a**) Location of the sediment samples of Box-Corer. (**b**) Percent of main components of the sample HB_BC_15. (**c**) Percent of main components of the sample HB_BC_11. (**d**) Photograph of the trinocular microscope. Or: Orbulina. G: Globigerina. Os: Ostracod

Table 1 Principal dimensions submarine landslides in the NE Atlantic Ocean including the part studied of the Talismán Slide in this work

Name	Location	Water depth (m)	Area (km²)	Volume (km³)	Run-out (km)	Width (km)
Storegga Slide (Bryn et al. 2003; Issler et al. 2003; Bryn et al. 2005)	Norwegian margin	200	90,000	3,300	450	180
Miller Slide (Long et al. 2003)	West Shetland slope	600	6,100	360	50	35
Afen Slide (Bulat 2003; Wilson et al. 2004)	Faroe-Shetland Channel	830	40	0.4	12	4
Walker Slide (Long et al. 2003)	Faroe-Shetland Channel	850	2	0.002	1.5	1
Part of Talismán Slide	Slope of Hatton Bank	1,358	>194	>20	>15	17

2.4 Other Slides

A partially-buried slide, here informally named the *Granadero Slide*, has been reported by MacLachlan et al. (2008) about 160 km north of the Talismán Slide and with a E–W orientation. Volumetrically the depression requires almost 26 km³ of sediment to anneal it to the surrounding slope. Its headwall scarp is at 1,400 m water depth and the slide extends to 2,500 m water depth. It has been described as a funnel-shaped depression of 17 km long downslope. At its upslope termination is more than 13 km wide but narrows downslope. MacLachlan et al. (2008) proposed that this slide may have been triggered by undercutting from turbidity currents.

Four other slides in the NE Atlantic Ocean have been taken into account in order to develop a hypothesis about a possible trigger mechanism for the Talismán Slide. Table 1 shows the principal dimensions of the other slides compared with the part of the Talismán Slide covered in this study.

3 Discussion and Conclusions

The Talismán Slide, which is located on Hatton Drift (middle western slope of Hatton Bank), can be considered as translational slide, based on the classification of Varnes (1978) which defines this type of slide as 'a landslide mass moves along a roughly planar landslide surface with little rotation or backward tilting'.

Different morphologies have been described on Talismán Slide (Fig. 3). Secondary scarps and localised crests, within the area of the slide scar, occur both perpendicular and at various angles to the direction of slide movement. Crests parallel to the scar are interpreted as extensional ridges of the proximal part of the slide mass. Some gravitational deposits (southern sidewall collapse deposits), which occurred after the main slide, have been identified adjacent to the southern sidewall and may explain its lower scarp heights and angles compared with the northern sidewall scarp (Fig. 2). This process may also have caused retrogression and the irregular shape of the southern sidewall. Therefore the shape of the southern sidewall, after the first phase of the slide event, could be different (e.g. linear) and the slide scar could be narrower. Some scarps, on the remnant surface, define depressions which could represent several phases of a single slide event.

The chaotic unit of the slide mass defined on the seismic profiles, is interpreted as the remnant debris flow of the main slide although it could be composed of units derived from several phases of movement. The debris flow unit is draped by more recent sediments which possess well-defined layers and a maximum thickness of 10 m. In some locations, this uppermost layer wedges out against blocks of the debris flow. The contourite sequence and the uppermost unit thicken towards the northern sidewall of the slide which indicates an accumulation of sediments in the north part of the slide, probably due to the action of the bottom currents flowing toward North in this area.

The Talismán and Granadero slides occur at similar water depths on the continental margin slope of Hatton Bank, deeper than comparable slides in NE Atlantic Ocean (Table 1). Granadero Slide was defined as a failure complex with a polyphase failure history. It shows a 17 km long funnel-shaped depression downslope and there is no evidence for the displaced mass, which could be buried or eroded by the turbidity currents associated with the Maury Channel system (MacLachlan et al. 2008). A similar slide morphology was reported for the Afen Slide (Wilson et al. 2004). The slide scar of the Talismán Slide extends, at least, 15 km downslope but scour and the debris lobe combined might extend for several tens of kilometres Iceland-basinward. The Talismán slide is poorly imaged on the wide-range side-scan sonar data (GLORIA) gathered in 1987 covering the deepwater west of Hatton Bank (Elliott and Parson 2008) andrefore is not well constrained downslope from the ECOVUL/ARPA multibeam coverage. Elliott and Parson (2008) and MacLachlan et al. (2008) examined a multibeam data set (CD118) down slope of the Talisman Slide and make no mention of disturbed material. This may imply that the slide is of limited extent down-slope or that displaced material has subsequently been buried or eroded by the strong bottom currents active in the area (DNBC).

The Talismán Slide occurs within an acoustically well-layered drift sequence. Changes in current regime may have eroded the toe of the drift thereby removing
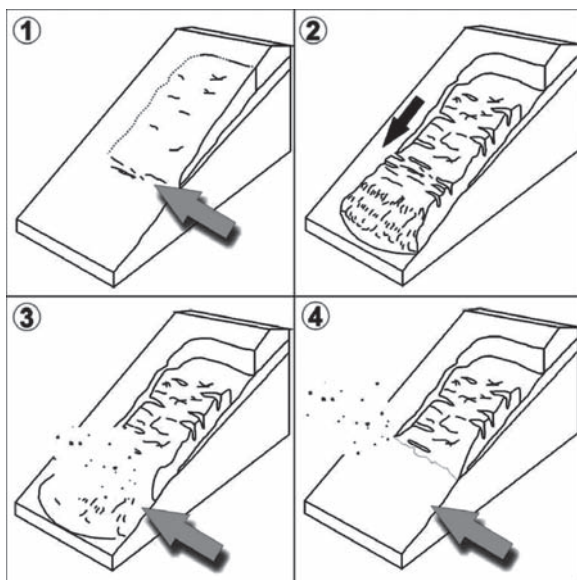
Fig. 6 Sketch illustrating the evolution proposed in this work for the Talismán Slide in order to establish a hypothesis about its origin and the trigger mechanism for its initiation (Grey arrow: bottom current; Black arrow: movement of the slide mass)

support at the base of slope and initiating failure (Fig. 6). Alternatively increases in sedimentation at the top of the slope could have overloaded the upper part of the drift causing instability. Along-slope currents further down-slope, east of Endymion Spur, have created an erosional channel (MacLachlan et al. 2008) and may have eroded supporting sediments causing failure of the slope.

In addition, two recent earthquakes recorded on Hatton Bank and Lousy Bank (Simpson and Ford 1999; Simpson et al. 2000) evidence that local minor earthquakes are not unusual in the area. In this sense, the trigger mechanism for the Talismán Slide is likely a combination of several causative factors such as erosion (caused by the bottom currents) and an earthquake event which accelerated the slide. Other contolling factors such as steep topography or lithology could be involved.

Other slides that occurred in the NE Atlantic Ocean (e.g. Storegga, Miller, Afen and Walker slides) occur relatively close to the emerged continent (Table 1). Most of these slides are also associated with contourite deposits and several of them occurred, at least their last phase, during the Holocene. However the Talismán Slide has up to 10 m of sediments draped over the debris flow unit and occurs in an area of low sedimentation rates compared to other parts of the margin. It is thus suggested that the Talismán Slide is older than, at least, the last phase of the slides in Table 1, but younger than the Granadero Slide which has a thicker sediment cover.

References

Bianchi GG, McCave IN (2000) Hydrography and sedimentation under the deep western boundary current on Björn and Gardar Drifts, Iceland Basin. Mar Geol 165:137–169

Bryn P, Solheim A, Berg K, et al. (2003) The Storegga Slide complex: repeated large scale sliding in response to climatic cyclicity. In: Locat J, Miennert J (eds.) Submarine Mass Movements and Their Consequences, Kluwer Academic, The Netherlands

Bryn P, Berg K, Forsberg CF, et al. (2005) Explaining the Storegga Slide. Mar Petrol Geol 22: 11–19

Bulat J (2003) Imaging the Afen Slide from commercial 3D seismic-methodology and comparisons with high-resolution data. In: Locat J and Miennert J (eds.) Submarine Mass Movements and Their Consequences, Kluwer Academic, The Netherlands

Coward MP, Dewey J, Hempton M, et al. (2003) Tectonic evolution. In: Evans D, Graham C, Armour A, et al. (eds.) The Millennium Atlas: Petroleum Geology of the Central and Northern North Sea. Geological Society, London

Doré AG, Lundin ER, Jensen LN, et al. (1999) Principal tectonic events in the evolution of the northwest European Atlantic margin. In: Fleet AJ, Boldy SAR (eds.) Petroleum Geology of Northwest Europe: Proc 5th Conf, Geological Society, London

Elliott GM, Parson LM (2008) Influence of sediment drift accumulation on the passage of gravity-driven sediment flows in the Iceland Basin, NE Atlantic. Mar Pet Geol 25: 219–233

Garrison LE, Sangrey DA (1977) Submarine Landslide. USGS Yearbook, Fiscal Year 1977

Holmes R, Long D, Dodd LR (1998) Large-scale debrites and submarine landslides on the Barra Fan, west of Britain. Geol Soc Lond Spec Pub 129: 67–79

Huizhong W, McCave IN (1990) Distinguishing climatic and current effects in mid-Pleistocene sediments of Hatton and Gardar Drifts, NE Atlantic. J Geol Soc Lond 147: 373–383

Issler D, De Balsio FV, Elverhoi A, et al. (2003) Issues in the assessment of gravity mass flow hazard in the Storegga area off the western Norwegian coast. In: Locat J, Miennert J (eds.) Submarine Mass Movements and Their Consequences. Kluwer Academic, The Netherlands

Konrad JM, Dubeau S (2003) Cyclic strength of stratified soil samples. In: Locat J, Miennert J (eds.) Submarine Mass Movements and Their Consequences. Kluwer Academic, The Netherlands

Lawrence GVM, Cartwright JA (2009) The initiation of sliding on the mid Norway margin in the More Basin. Mar Geol 259: 21–35

Lee HJ (2009) Timing of occurrence of large submarine landslides on the Atlantic Ocean margin. Mar Geol 264:53–64.

Long D, Stevenson AG, Wilson CK, et al. (2003) Slope failures in the Faroe-Shetland channel. In: Locat J, Miennert J (eds.) Submarine Mass Movements and Their Consequences. Kluwer Academic, The Netherlands

MacLachlan SE, Elliott GM, Parson LM (2008) Investigations of the bottom current sculpted margin of Hatton bank, NE Atlantic. Mar Geol 253: 170–184

Maslin M, Owen M, Day S, et al. (2004) Linking continental-slope failures and climate change: testing the clathrate gun hypothesis. Geol 32: 53–56

McCartney MS (1992) Recirculating components to the deep boundary current of the northern North Atlantic. Prog Oceanogr 29: 283–383

McCave IN, Lonsdale PF, Hollister CD, et al. (1980) Sediment transport over the Hatton and Gardar contourite drifts. J Sed Pet 50: 1049–1062

McCave IN, Tucholke BE (1986) Deep-current controlled sedimentation in the Western North Atlantic. In: Vogt PR, Tucholke BE (eds.) The Geology of North America M, the Western North Atlantic Region. Geological Society, America

Roberts DG, Thompson M, Mitchener B, et al. (1999) Palaeozoic to Tertiary rift and basin dynamics: mid-Norway to the Bay of Biscay-a new context for the hydrocarbon prospectivity in the deep water frontier. In: Fleet AJ, Boldy SAR (eds.) Petroleum Geology of Northwest Europe: Proc 5th Conf, Geological Society, London

Simpson BA, Ford GD (1999) NW Scotland Offshore Seismicity: Third Annual Report to 31 March. British Geol Surv Tech Rep No. WL/99/24C

Simpson BA, Ford GD, Walker AB (2000) NW Scotland Offshore Seismicity: Fourth Annual Report to 31 March. British Geol Surv Tech Rep CR/00/24.

Stoker MS, Akhurst MC, Howe JA, et al. (1998) Sediment drifts and contourites on the continental margin off northwest Britain. Sed Geol 115: 33–51

Stow DAV, Holbrook JA (1984) Hatton Drift contourites, northeast atlantic, Deep Sea Drilling Project LEG 81. University of Edinburgh. Report number: 25

Stow DAV, Lovell JPB (1979) Contourites: Their recognition in modern and ancient sediments. Earth Sci Rev 14: 251–291

Van Aken HM (1995) Mean currents and current variability in the Iceland Basin. J Sea Res 33:135–145

Varnes DJ (1978) Slope movements types and processes. In: Schuster RL, Krizek RJ (eds.) Landslides-Analysis and control: National Research Council, Washington, DC, Transportation Research Board. Spec Rep 176

Weaver PPE, Wynn RB, Kenyon NH, et al. (2000) Continental margin sedimentation, with special reference to the north-east Atlantic margin. Sedimentol 47: 239–256

Wilson CK, Long D, Bulat J (2004) The morphology, setting and processes of the Afen Slide. Mar Geol 213: 149–167

Investigations on the Peach 4 Debrite, a Late Pleistocene Mass Movement on the Northwest British Continental Margin

M. Owen, S. Day, D. Long, and M. Maslin

Abstract The Peach 4 debrite is the most recent in a series of large scale Pleistocene MTDs within the Barra fan on the northwest British continental margin. Geophysical data indicate that Peach 4 was formed through a combination of blocky and muddy debris flows and affects an area of ~700 km². BGS core sample 56 -10 36, located directly over the Peach 4 debrite, provides a minimum age of 14.68 ka cal BP for the last major failure. An upwards fining turbidite sequence in BGS core sample 56 -10 239 is associated with increased As and S concentrations, indicators of diagenetic pyrite which forms under anoxic conditions. It is proposed that As and S concentrations may provide a method of distinguishing between contourite and turbidite sedimentation, although further research is required.

Keywords Submarine mass movement • submarine landslide • mass transport deposit • debrite • debris flow • turbidite • Barra fan • British ice sheet • arsenic • sulphur • pyrite

1 Regional Setting and Sedimentation on the Barra Fan

The Peach 4 debrite is located on the northwest British continental margin within the Barra fan. Sedimentation on the fan is governed by a combination of down-slope and across-slope mechanisms. The primary across slope process is driven by contouritic

M. Owen (✉) and M. Maslin
Environmental Change Research Centre, Department of Geography, College London, Gower Street, London WC1E 6BT, UK
e-mail: m.owen@ucl.ac.uk

S. Day
Aon Benfield UCL Hazard Research Centre, Department of Earth Sciences, University College London, Gower Street, London WC1E 6BT, UK

D. Long
British Geological Survey, Murchison House, West Mains Road, Edinburgh EH9 3LA, UK

current circulation, resulting in contourite deposits such as the Barra Fan Drift. This deposit consists of sediment waves with a length of ~3 km and height of 15–30 m, smaller local contourite deposits are also located on the Barra Fan (Knutz et al. 2002).

The largest down-slope sedimentation feature on the Barra Fan is the Peach debris flow complex, the location of which is shown on Fig. 1a. Holmes et al. (1998)
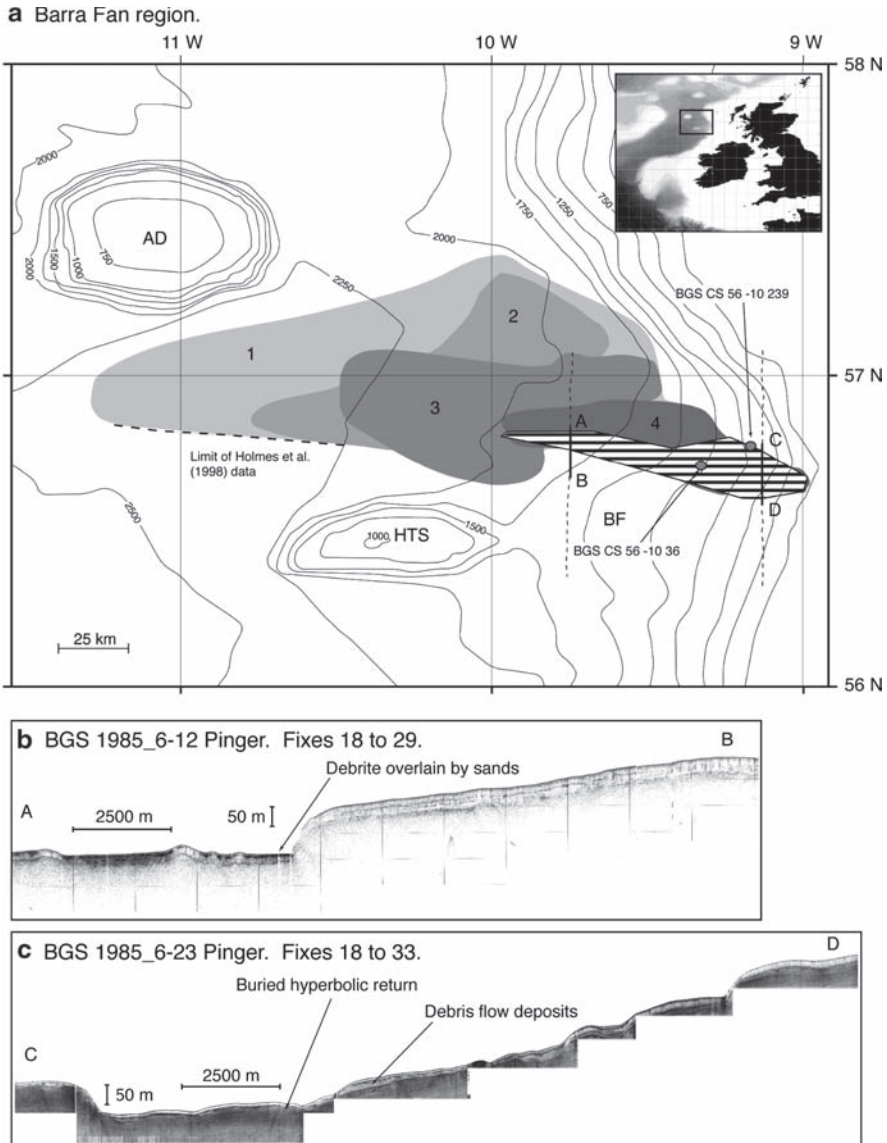
Fig. 1 Regional setting of the Peach debris flow complex. (**a**) The Barra fan region with the approximate extents of Peach debrites 1–4 (from Holmes et al. 1998) hatched area indicates zone of major failure, BGS seismic lines 1985_6–12 and 6–23, Barra fan (BF), Anton Dohrn seamount (AD) and Hebrides Terrace sea-mount (HTS) shown; (**b**) and (**c**) 3.5 kHz lines 1985_6–12 and 6–23 plotted with ×10 vertical exaggeration

mapped the complex, which covers an area of ~1600 km^2, identified four major units of Pleistocene age: debrite 1 (823 km^3), debrite 2 (673 km^3), debrite 3 (199 km^3) and debrite 4 (135 km^3). Using the age/depth profile of Knutz et al. (2001), Maslin et al. (2004) estimated the age of the three most recent debrites: 2, 3 and 4 as 36.5, 21 and 10.5 ka cal BP respectively; this most recent date we revise below.

This paper first investigates the morphology and timing of the Peach 4 debrite and then analyzes the sedimentology and geochemistry of a sediment core from the boundary of the major failure in order to understand recent sedimentation processes.

2   Methods

2.1   *Geophysical Data and Model Construction*

This project utilises British Geological Survey 3.5 kHz Pinger and Deep Towed Boomer data, and LOIS Shelf Edge Survey Multibeam Echo sounder (MBE) data. The 3″ resolution of the MBE data at this latitude represents 50 m resolution in Easting and 90 m in Northing. All positional data was converted to WGS 84 UTM and then plotted, with sediment core sample positions, in AutoCad: producing a model covering the area between 56.5° N -9.0° W and 57.0° N -10.0° W. Rendering of the DTM was performed with an artificial light source from the north-northeast to allow clearer 2D presentation.

2.2   *Sediment Samples*

BGS CS 56 -10 36 was collected at 1290 mbsl, 56.7095° N -9.3275° W and has been described previously (see Kroon et al. 1997; Kroon et al. 2000). Kroon et al. (2000) date planktonic foraminifera from 4.3 m depth in the core at 12.62 reservoir corrected ^{14}C ka BP, corresponding to 14.68 ka cal BP (Fairbanks et al. 2005).

The sediment analysis presented here focuses on BGS CS 56 -10 239 which was collected at 1030 mbsl, 56.7822° N -9.1698° W. It was sub-sampled at 2 cm intervals for the first 2 m of its length with continuous 2 cm samples taken between 0.92–0.98, 1.92–1.98 and 2.07–2.13 m; between 2.00–2.07 and 2.15 and 2.50 m the core was sampled at 1 cm intervals.

2.2.1   Particle Size Analysis

Sub-samples were freeze-dried and then wet-sieved between 250 and 63 μm (2–4 Φ), analysis of <63 μm diameter fraction was performed by SediGraph 5120 and >250 μm by dry sieving. SediGraph analysis was performed on a solution concentration of <3%

(see Coakley and Syvitski 1991). Up to eight analyses were performed on each sub-sample and standard deviations were low compared to inter-sample variability.

2.2.2 XRF Geochemical Analysis

Prior to wet sieving ~4 g of freeze-dried bulk sediment from each sub-sample was finely ground, weighed and placed in containers with a tightly stretched polypropylene film base. Analysis was performed under Helium gas flush (for further detail regarding XRF methodology under Helium gas flush see Wien et al. 2007). Samples were analysed up to four times and standard deviations were low relative to inter-sample variability.

3 Peach 4 Debrite Transport Processes and Age of Emplacement

3.1 *Extent and Morphology of the Peach 4 Debite*

The primary failure zone of debrite 4 has an area of approximately 700 km^2, failure scarps with heights of up to 90 m are observed and runout distance is at least 60 km. The greatest slope angles were observed on the northern and northeastern debrite boundary (up to 11.8°), associated with a scarp slope of up to 90 m height. The southern boundary of the debrite is associated with gentler angles of around 6.4° and a maximum scarp slope height of 50–60 m. The majority of the debrite deposits are overlain by a sedimentary unit between 5 and 11 ms TWT thick. Assuming sound velocity of 1650 m/s^{-1} through these sediments the thickness may be estimated at 4 to 9 m.

Outside of this major failure zone a secondary zone of less deep-seated failures is observed. Immediately south from the major scar a smaller slump scar and deposit are visible (Fig. 2c). North from the major failure seismic data reveal surficial sediment failures, which may be associated with the Peach 4 debrite (Fig. 2b).

Several distinct MTD seismic facies are clearly visible (Figs. 1b, c, and 2b). Highly acoustically transparent, mounded facies, with sharp basal contacts, are potentially deposited from muddy debris flows (see Embley 1980; Piper et al. 1999). Buried, or surficial, hummocky, blocky facies with hyperbolae are indicative of larger debris (Jacobi 1976; Normark and Gutmacher 1988). Also visible in Fig. 1b are stratified and high amplitude facies which overlie blocky, chaotic facies: these are interpreted as sands (contourite or turbidite) overlying debris flow deposits. Armishaw et al. (1998) state that the Peach debrite is a composite feature. In a similar manner, Peach 4 has been formed through the action of several mass movement mechanisms within one event. The different seismic facies observed, supports a combination of blocky debris flows, muddy debris flows and possibly sandy turbidites contributing to the overall structure of the Peach 4 debrite.
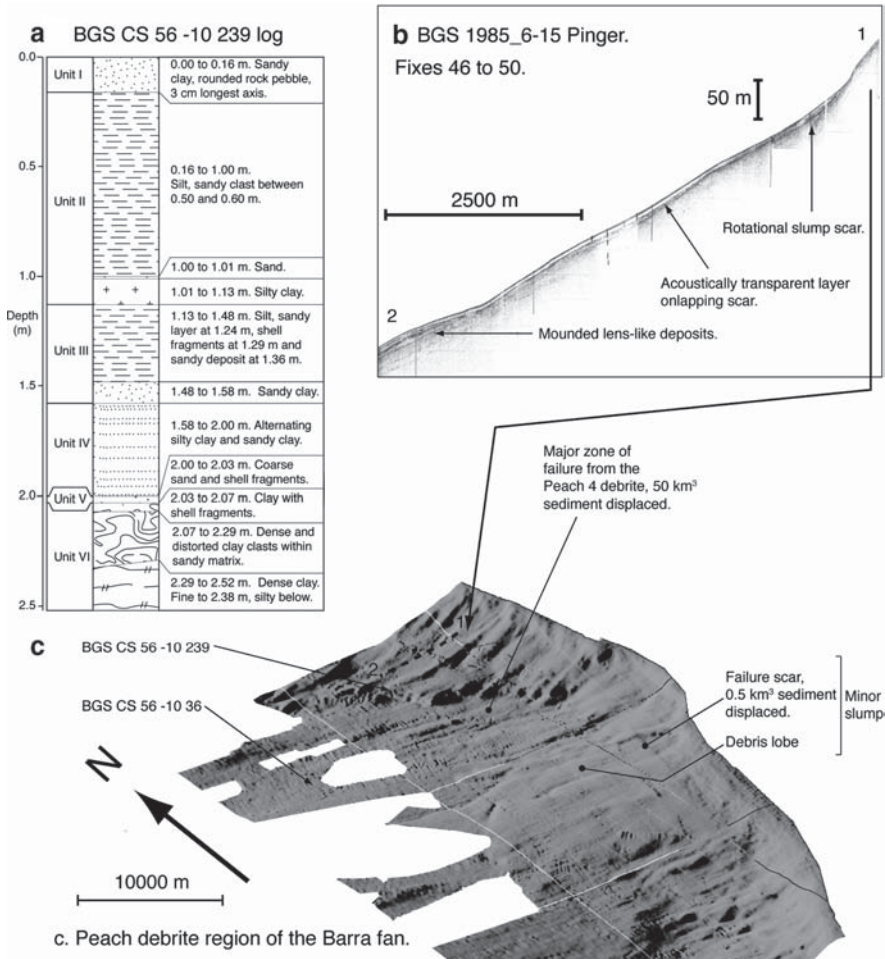
Fig. 2 Location and description of gravity core BGS CS 56 -10 239: (**a**) BGS CS 56 -10 239 log; (**b**) BGS 3.5 kHz profile, 1985_6-15, shown with a ×10 vertical exaggeration; and (**c**) shaded relief shown with a 4× vertical exaggeration and light from the NNW, locations of BGS CS 56 -10 36 and 56 -10 239 shown

3.2   Emplacement Age of the Peach 4 Debrite

The model constructed for this project locates BGS CS 56 -10 36 in hemipelagic sediments overlying deposits from the Peach 4 debrite (see Fig. 2c). This means that this core constrains the minimum age of Peach 4. Combined with the Holmes et al. (1998) argument that the Peach 4 debrite truncates ice-berg scour marks, this suggests that the timing can be constrained to between 14.68 (the oldest material within BGS CS 56 -10 36 dated by Kroon et al. 2000) and 19 ka cal BP (the oldest estimate for the disintegration of the BIS in the Barra fan region; Knutz et al. 2007).

Kroon et al. (2000) date the Bölling period, using planktonic foraminiferal assemblages, at slightly after 14.6 ka cal BP in the Barra fan region (Kroon et al. 2000 ^{14}C dates, Fairbanks et al. 2005 radiocarbon calibration). Coupled with the marine data from Knutz et al. (2007) it seems plausible that factors associated with the deglaciation may have played a role in increasing the susceptibility of the continental slope to failure and increasing the likelihood of triggers to slope failure occurring (see Owen et al. 2007).

4 Sediment Analysis Results and Interpretation: BGS CS 56 -10 239

4.1 Location of BGS CS 56 -10 239 in Relation to MTDs

BGS CS 56 -10 239 is located on the northeastern boundary of the Peach 4 failure, though within the zone of minor sedimentary failure (see Fig. 2c). Upslope from the core BGS 3.5 kHz Pinger profile 1985_6–15 (Fig. 2b) reveals a rotational, scoop-like, slump scar containing lensed slump deposits. Onlapping and downslope of these, is a unit with a strong seabed return over an acoustically transparent layer (3 ms TWT thick) which in turn overlies chaotic and distorted facies which are likely the disaggregated blocky deposits of the rotational failure. Downslope mounded lens-like deposits are visible as acoustically transparent units with a high amplitude upper boundary.

4.2 Particle Size Variations

Particle size analysis results are summarised in Fig. 3. Mean grain size decreases from 4 to 7Φ from seabed to 0.16 m depth, this is due to the shift from foraminiferal sand to terrigenous silt and clay dominated sediments. Φ and sand/silt/clay percentages are relatively constant until 1.13 m when there is a peak in clay composition of 54%.

Between 1.13 and 1.55 m depth there is a stepped increase in mean grain size, which is coincident with a minor peak in silt composition at 1.25 m and a major sand peak of 48% at 1.55 m. σ also displays a stepped trend during this interval, with a succession of poorly sorted to very poorly sorted sediments between 1.13 and 1.25 m and between 1.33 and 1.41 m. Between 1.55 and 2.00 m Φ values increase to 7 reflecting the decrease in the proportion of sand particles and the increase in silts and clays; sediments remain very poorly sorted though silt is the dominant size class. At 2.00 m a large increase in particle size occurs associated with a 3 cm thick erosive sand layer. Below 2.03 m there are two pronounced oscillations in Φ values between 7 and 8, which are reflected in inversely related sand and clay percentages, σ values shifting from poorly sorted to very poorly sorted.
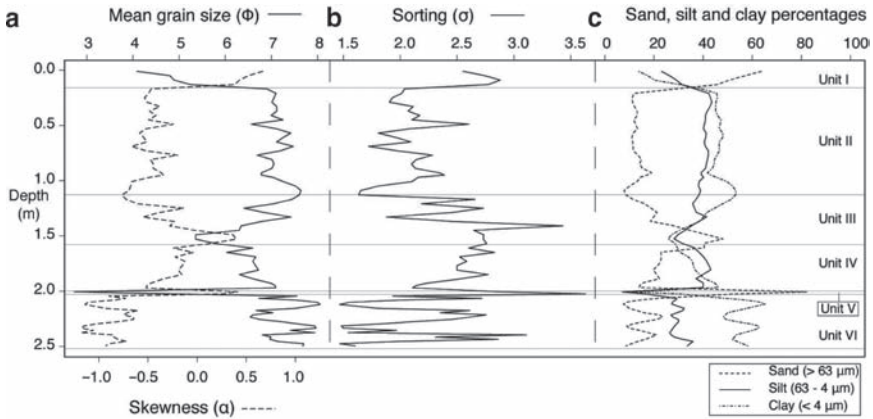
Fig. 3 Particle size analysis for BGS CS 56 - 10 239. **a.** Mean grain size and skewness; **b.** Sorting; and **c.** Sand, silt and clay percentage composition
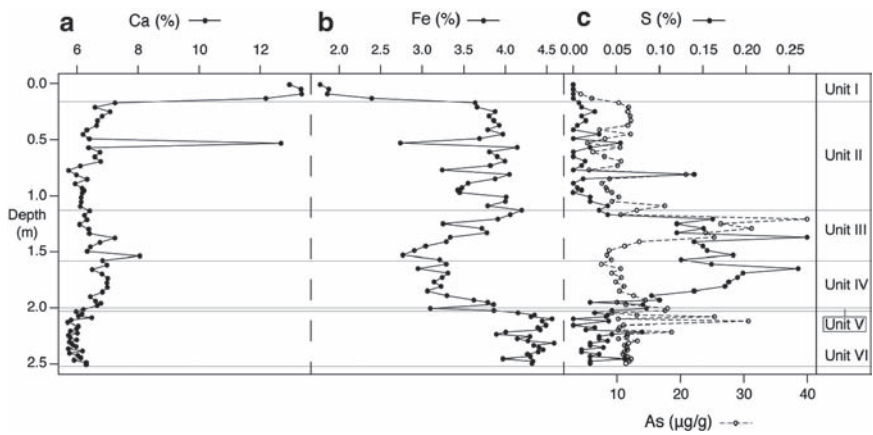
Fig. 4 Selected XRF analysis result for BGS CS 56 -10 239. (**a**) Calcium; (**b**) Iron; and (**c**) Sulphur (all plotted as percentage bulk sediment) and Arsenic (µg/g bulk sediment)

4.3 XRF Geochemical Analysis

The results for bulk sediment sample data for Ca, Fe, S and As contents are presented in Fig. 4. Ca declines sharply, from >12.0% to levels ~6.0% below 0.16 m. An increase to 8.0% at 1.53 m is coincident with the 48% sand peak at 1.55 m (see Fig. 3). Other than the initial increase in concentrations (1.8–3.9%) the primary feature of note in the Fe record is a marked reduction in concentrations (4.0–2.8%) between 1.13 and 2.03 m, coincident with the increase in sand (and decrease in clay) content, as

shown in Fig. 3. With the exception of an isolated peak at 0.81 m, S concentrations are close to 0.0% between 0.0 and 1.00 m. However, a dramatic increase occurs from 1.13 m as values peak at 0.27% concentration at 1.37 m depth. S concentrations then decline to ~ 0.15% before peaking again at 0.26% at 1.65 m, prior to declining to background levels below 2.00 m. Elevated S levels are bracketed by a primary As peak of 40 μg/g at 1.21 m and a secondary As peak of 31 μg/g at 2.12 m.

4.4 Unit Lithology of BGS 56 -10 239

BGS CS 56 -10 239 is subdivided into six lithological units on the basis of the visual inspection and particle size analysis:

1. Unit I: sandy sediments with high Ca and low Fe content indicating a dominant marine sediment source (0.0 to 0.16 m), likely to be Holocene drape or contourites.
2. Unit II: mainly silts and clays with low Ca and high Fe content indicating a dominant terrestrial sediment source (0.16 to 1.13 m). The unit displays a sharp upper boundary, whereas the lower boundary is less distinct, probably due to bioturbation. Likely to be hemipelagite.
3. Unit III: clays, silts and sand layers with frequent shell fragments (1.13 to 1.58 m), interpreted as a succession of turbidites. Particle size data (Fig. 3) support this interpretation with a stepped upwards fining and alternation between less sorted (associated with coarser grains) and more sorted (associated with finer grains) sediments. This unit has a distinct geochemical signature, with Fe concentrations reducing down core, a pronounced As peak and elevated S concentrations (see Fig. 4).
4. Unit IV: alternating sandy clay and silty clay, in which silts are the dominant fraction (1.58 to 2.00 m), possibly hemipelagic or contouritic sediments. Fe concentrations remain low, S concentrations relatively high and, distinct from unit III, As concentrations return to background levels (see Fig. 4).
5. Unit V: a coarse grained, poorly sorted, sand layer with large shell fragments (2.00 to 2.03 m), which erodes into the unit below and is interpreted as a turbidite.
6. Unit VI: dense and distorted clay intraclasts with sandy matrices (2.03 to 2.52 m). From 2.03 to 2.29 m the unit is characterised by highly distorted clay clasts, at times within a sandy matrix. Below 2.29 m the appearance is more homogeneous. Oscillating mean grain size and sorting values (see Fig. 3), support a debris flow hypothesis for the formation of this unit; potentially through a succession of slurries or as a low-viscosity cohesive debris flow (see Tripsanas et al. 2008).

We can therefore be certain that units V and VI are associated with mass transport, and units I and II with background sedimentation (pelagic, hemipelagic or contouritic) which postdates mass transport. Difficulty occurs when attempting to assign units

III and IV to either mass transport or background sedimentation. This ambiguity has important implications when attempting to date mass transported material through use of overlying sediments. We now consider whether geochemical data can help resolve this issue.

5 Sedimentation Processes in BGS CS 56 -10 239 – Can Sulphur and Arsenic Concentrations Be Used as Indicators of Turbidite Deposition?

The difficulty of distinguishing between sandy turbidites and sandy contourites in marine sediments is well known (Stow 1979) and it is well established that these are important components of the Barra fan sedimentary system (see Armishaw et al. 2000; Knutz et al. 2002). We consider whether S and As concentrations can be used to distinguish between turbidites and contourites.

A striking feature of unit III is a marked increase in As and S concentrations, inversely related to Fe (see Fig. 4). We hypothesise that this is due to the rapid deposition of sediments which create anoxic conditions, favourable to pyrite (FeS_2) formation through organic matter decomposition via the actions of sulphate reducing bacteria (see Berner and Raiswell 1983). The As peak at 1.21 m (potentially a signal from arsenian pyrite) provides further support for this hypothesis, as As in marine sediments is generally an indicator of FeS_2 (Rothwell et al. 2006), which has been shown to be enriched in As by as much as 10% wt (Blanchard et al. 2007). The peak in clay particle composition, directly above the As peak, at 1.13 m further supports this hypothesis as formation of As enriched FeS_2 generally occurs in colloidal sized particles (Cook and Chryssoulis 1990).

The organic matter required for FeS_2 formation in the the anoxic environment created by the rapid deposition of unit III is possibly provided by unit IV. This unit is characterised by an upwards coarsening of sediments and high concentrations of silt particles (Fig. 3a), possibly indicating a strengthening of contouritic currents. High concentrations of S are maintained, though As concentrations return to background levels.

It is possible that the As and S record is displaying two separate signatures: increased S concentrations related to increased organic matter concentrations (Berner and Raiswell 1983), primarily in unit IV; and increased As and S concentrations due to production of diagenetic pyrite (Blanchard et al. 2007) under anoxic conditions in the interstital waters of unit III. Increased As and S concentrations may then be a potential indicator of anoxic conditions caused through rapid sedimenation; and combined elevated concentrations of both elements may be indicate turbidite rather than contourite sedimentation.

Alternatively, anoxia and FeS_2 formation may have occurred via through flow of geologically derived CH_4 through the more permeable sandy layers. Further research is required: sedimentation in the region is extremely complex with both contourite and turbidite sediments potentially being reworked. As such a unit may

display the sedimentological characteristics of a contourite and the geochemical signature of a turbidite. Investigations into benthic foraminiferal assemblages and TOC content would provide insights into whether sediments have been subject to mass transport and whether S concentrations are reflecting a diagenetic or primary signal.

6   Conclusions

1. The most recent MTD in the Peach slide complex was deposited through a combination of blocky debris flows and low viscosity cohesive debris flows. The primary zone of failure has an area of approximately $700\,km^2$.
2. The positioning of BGS CS 56 -10 36 helps constrain the timing of the Peach 4 debrite's major failure to between 14.68 and 19 ka cal BP.
3. A turbidite succession in BGS CS 56 -10 239 is associated with a substantial increase in As and S concentrations. It is proposed that rapid deposition of sands, capped with silts and clays, creates anoxic conditions favourable to the formation of diagenetic pyrite. We suggest that elevated As and S concentrations within sediments may provide a means of distinguishing turbidite from contourite sediments.
4. Further work is required: analysis of benthic foraminiferal assemblages and TOC content will provide greater insight into whether sediments have been subject to mass transport and what processes are controlling S and As concentrations.

References

Armishaw JE, Holmes RW, Stow DAV (1998) Morphology and sedimentation on the Hebrides Slope and Barra Fan, NW UK continental margin. In Stoker MS, Evans D, Cramp A (eds) Geological Processes on Continental margins: sedimentation, mass-wasting and stability. Geol Soc Lond.

Armishaw JE, Holmes RW, Stow DAV (2000) The Barra Fan: a bottom-current reworked, glacially-fed submarine fan system. Mar Pet Geol 17:219–238.

Berner RA, Raiswell R (1983) Burial of organic carbon and pyrite sulfur in sediments over Phanerozoic time: a new theory. Geochim Cosmochim Ac 47:855–862.

Blanchard M, Alfredsson M, Brodholt J et al. (2007) Arsenic incorporation into FeS_2 pyrite and its influence on dissolution: a DFT study. Geochim Cosmochim Ac 71:624–630.

Coakley JP, Syvitski JPM (1991) SediGraph technique. In Syvitski JPM (ed), Principles, methods and applications of particle size analysis. Cambridge Univ Press, New York.

Cook NJ, Chryssoulis SL (1990) Concentrations of invisible gold in the common sulfides. Can Mineral 28:1–16.

Embley RW (1980) The role of mass transport in the distribution of deep-ocean sediments with special reference to the north atlantic. Mar Geol 38:23–50.

Fairbanks R, Mortlock R, Chiu T et al. (2005) Radiocarbon calibration curve spanning 0 to 50,000 years BP based on paired Th/U/U and C dates on pristine corals. Quat Sci Rev 24:1781–1796.

Holmes R, Long D, Dodd LR (1998) Large-scale debrites and submarine landslides on the Barra Fan west of Britain. In Stoker MS, Evans D, Cramp A (eds) Geological Processes on the continental margins: sedimentation, mass-wasting and stability. Geol Soc Lond.

Jacobi RD (1976) Sediment slides on the northwestern continental margin of Africa. Mar Geol 22:157–173.

Knutz PC, Austin WEN, Jones EJW (2001) Millenial-scale depositional cycles related to the British ice sheet variability and North Atlantic paleocirculation since 45 kyr B.P., Barra Fan, U.K. margin. Paleoceanogr 16:53–64.

Knutz PC, Jones EJW, Austin WEN, et al. (2002) Glacimarine slope sedimentation, contourite drifts and bottom current pathways on the Barra Fan, UK North Atlantic Margin. Mar Geol 188:129–146.

Knutz PC, Zahn R, Hall I (2007) Centennial-scale variability of the British Ice Sheet: implications for climate forcing and Atlantic meridional overturning circulation during the last deglaciation. Paleoceanogr doi:10.1029/2006PA001298.

Kroon D, Austin WEN, Chapman MR et al. (1997) Deglacial surface circulation changes in the northeastern Atlantic: temperature and salinity records of NW Scotland on a century scale. Paleoceanogr 12:755–763.

Kroon D, Shimmield G, Austin WEN et al. (2000) Century-to-millennial-scale sedimentological-geochemical records of glacial-Holocene sediment variations from the Barra Fan (NE Atlantic). J Geol Soc Lond 157:643–653.

Maslin M, Owen M, Day S et al. (2004). Linking continental-slope failures and climate change: testing the clathrate gun hypothesis. Geol 32:53–56.

Normark WR, Gutmacher CE (1988) Sur submarine slide, Monterey Fan, central California. Sedimentol 35:629–647.

Owen M, Day S, Maslin M (2007) Late Pleistocene mass movements: occurrence and cause. Quat Sci Rev 26:958–978.

Piper DJW, Hiscott RN, Normark WR (1999) Outcrop-scale acoustic facies analysis and latest Quaternary development of Hueneme and Dume submarine fans, offshore California. Sedimentol 46:47–78.

Rothwell GR, Hoogakker B, Thomson J et al. (2006) Turbidite emplacement on the southern Balearic Abyssal Plain (western Mediterranean Sea) during Marine Isotope Stages 1–3: an application of ITRAX XRF scanning of sediment cores to lithostratigraphic analysis. In Rothwell GR (ed) New techniques in sediment core analysis. Geol Soc Lond.

Stow DAV (1979) Distinguishing between fine-grained turbidites and contourites on the Nova Scotian deep water margin. Sedimentol 26:371–387.

Tripsanas E, Piper D, Jenner K et al. (2008) Submarine mass-transport facies: new perspectives on flow processes from cores on the eastern North American margin. Sedimentol 55:97–136.

Wien K, Kölling M, Schulz HD (2007) Age models for the Cape Blanc Debris Flow and the Mauritania Slide Complex in the Atlantic Ocean off NW Africa. Quat Sci Rev 26:2558–2573.

Redistribution of Sediments by Submarine Landslides on the Eastern Nankai Accretionary Prism

K. Kawamura, T. Kanamatsu, M. Kinoshita, S. Saito, T. Shibata, K. Fujino, A. Misawa, and K.C. Burmeister

Abstract During a recent survey of the Nankai Trough region by JAMSTEC R/V *KAIYO*, ten piston cores were collected along a NW-SE transect through the Shikoku Basin, Kashinozaki Knoll, and Nankai Trough areas. The purpose was to demonstrate the influence of landslide processes on sediment distribution patterns on an accretionary prism. The Shikoku Basin is a flat abyssal plane covered by ca. 1 m thick hemipelagic mud, and underlain by a ca. 10 cm thick tuffaceous sand corresponding to the Aira-Tn tephra layer (25120 ± 270 yr. B.P.). The sedimentation rates in the Shikoku Basin are 3–4 cm/ky. At least three submarine landslide scars are observable on Kashinozaki Knoll. The abyssal plane surrounding the Kashinozaki Knoll is covered by a characteristic yellowish pumiceous mud intercalated with the hemipelagic mud. Immediately below thelandslide scars, these pumiceous mud layers thicken. Pumiceous mud was likely derived from the flanks of the volcanic Kashinozaki Knoll. These scars and deposits suggest that submarine landslides redistributed material from the knoll to the basin by mass-wasting. More than six trench turbidite beds were observed in a sequence that overlies a submarine landslide deposit at the foot of the accretionary prism within the

---

K. Kawamura (✉)
Fukada Geological Institute, 2–13–12 Hon-Komagome, Bunkyo, Tokyo 113–0021, Japan
e-mail: kichiro@fgi.or.jp

T. Kanamatsu, M. Kinoshita, and S. Saito
IFREE1, Japan Agency for Marine Science and Technology, 2–15 Natsushima-cho, Yokosuka, Kanagawa 237–0061, Japan

T. Shibata
Kochi University, 2–5–1 Akebono-cho, Kochi 780–8520, Japan

K. Fujino
Kyushu University, 10–1 Hakozaki, Higashi-ku, Fukuoka 812–8581, Japan

A. Misawa
Tokai University; 3–20–1 Orido, Shimizu, Shizuoka 424–8610, Japan

K.C. Burmeister
University of the Pacific, Department of Geosciences, 3601, Pacific Avenue, Stockton, California 95211, USA

Nankai Trough. The geomorphology of the axial channel suggests that the flow of turbidite deposits along the axial channel was blocked by this submarine landslide deposit, forcing the flow path and gradient of the channel to re-establish itself. In this event, sediment ponding would occur upstream of the blockage, while the downstream portion of the axial channel would be starved of sediment.

Keywords NanTro SEIZE • Submarine landslide • Kashinozaki Knoll • Nankai Trough • Frontal thrust

1 Introduction

Seamount subduction/collision at convergent margins is thought to induce gravitational collapse at accretionary prisms (Dominguez et al. 2000; von Huene et al. 2004; Kobayashi et al. 1987; Yamazaki and Okamura 1989). Those gravitational collapses (e.g. slope failures and submarine landslides) are a key to understanding lateral variation of sedimentation in subduction trenches. When the axial channel of the trough is dammed by structural blockage due to uplift of the trough floor, seamount collision, or submarine landslide deposition at the toe of the prism, downstream of the dam becomes a sediment starved trench as shown by Underwood and Backman (1982). In contrast to the downstream portion, thick rapidly deposited turbidite sequences accumulate in the upstream portion. This lateral variation in processes leads to potential lateral variations in grain size distribution, sediment physical-mechanical properties and pore fluid pressure that can affect accretionary processes and characteristics of the decollement zone (Saffer and Bekins 2002; Spinelli and Underwood 2004; Ike et al. 2008).To address this sedimentation pattern, this present paper studies in detail the depositional systems related to submarine landslides around the eastern Nankai Trough, off Kii Peninsula. Results from multibeam bathymetric data and 10 piston cores are presented.

The Kashinozaki Knoll is located on the Nankai Trough, SW Japan. The Nankai margin hosts one of the largest subduction zones and accretionary prisms in the world and has been studied for more than 20 years (Kobayashi 2002). The Nankai Trough is located between the southwest Japan arc on the Amur plate and the Philippine Sea Plate. The convergence rate between these plates is approximately 4–7 cm/yr (Seno et al. 1993; Miyazaki and Heki 2001). The Kashinozaki Knoll is an isolated basement high of volcanic origin within the Nankai Trough that will presumably collide with the Nankai prism (Ike et al. 2008).

The survey encompasses the area from 32°N, 137°E to 33°N, 136°30'E, ranging from the Shikoku Basin to the Nankai Trough (Fig. 1a, b). We obtained bathymetric data using the SeaBeam 2112.004 system (SeaBeam Co. Ltd., Germany) during the cruise by KY07–01 of the Japan Agency for Marine Science and Technology (JAMSTEC) R/V *KAIYO* in the period from Jan. 4–19, 2007 (Fig. 1b).
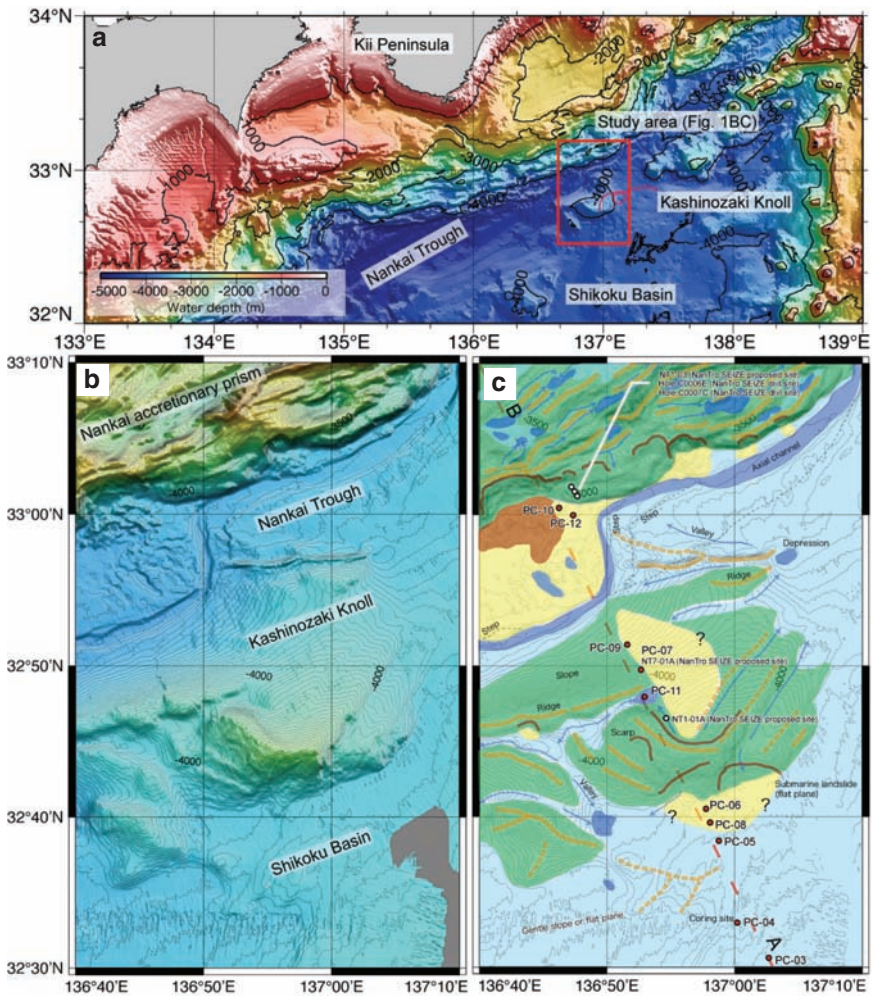
Fig. 1 (**a**) Location of study area within the Nankai Trough off the southeastern coast of Japan. (**b**) Detailed SeaBeam bathymetric map of study area. (**c**) Geomorphic regions within the study area: (1) flat plane or gentle slope (*light blue*), (2) slope (*green*), (3) depression (*blue*), (4) channel (*blue*), (5) valley (*blue arrows*), (6) ridge (*orange lines*), (7) scar (*brown lines*) and (8) step (*broken lines*). Contour intervals are 2,000 m in (**a**), and 50 m in (**b**) and (**c**). NanTro SEIZE (Nankai Trough seismogenic zone experiment) is one of the international projects in Integrated of Ocean Drilling Program (IODP) (see Tobin and Kinoshita 2006)

The margin's geomorphology is divisible into eight areas based on the bathymetric features as shown in Fig. 1c. Submarine landslides are distinct mounds located just below the scar, as indicated by the yellow- and brown- colored areas in Fig. 1c. Based on these geomorphic features, the region can be subdivided into three areas: the Shikoku Basin, Kashinozaki Knoll and Nankai Trough (Fig. 1b). The Shikoku basin area is an abyssal plane.

1.1 Topographic Features of the Study Area

The Kashinozaki Knoll is a wide slope area, whereas the landward slope at the toe of the prism is composed of small slopes with many depressions and ridges. The Nankai Trough area in this study area is characterized by an axial channel and deposition of submarine landslides from the toe of the prism. Three steps are located on the east side of the large submarine landslide on the Nankai Trough floor. These steps occur over two ridges, suggesting that the formation of the steps predates ridge development.

To confirm the above geomorphic interpretations, ten piston cores numbered from PC-03 to PC-12 were obtained along a NW to SE transect between the Shikoku Basin and the axis of the Nankai Trough (Fig. 1c; Table 1). PC-03, 04 and 05 were recovered from the Shikoku Basin area, PC-06, -07, -08, -09 and -11 were from the Kashinozaki Knoll area, and PC-10 and -12 were from the Nankai Trough area (Fig. 2).
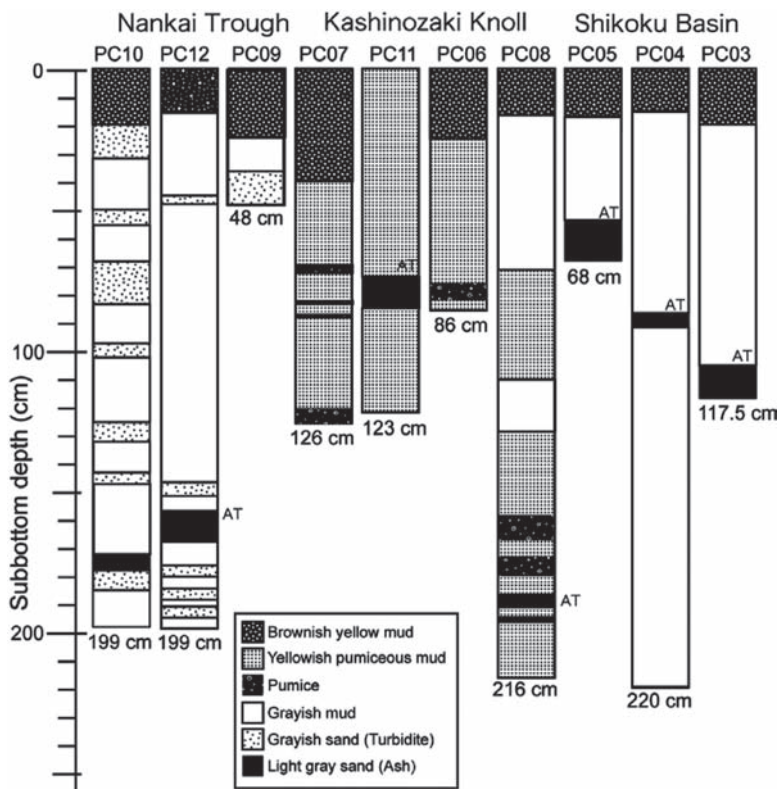
Fig. 2 Lithofacies of sediment cores collected along a transect from Shikoku Basin to Nankai Trough

Table 1. Location of core sampling sites

PC	Longitude		Latitude		Depth	
PC-03	137°02.6995	′E	32°30.8178	′N	4084	m
PC-04	137°01.5006	′E	32°33.0296	′N	4127	m
PC-05	136°58.7877	′E	32°38.4092	′N	4167	m
PC-06	136°57.8005	′E	32°40.7271	′N	4178	m
PC-07	136°52.9287	′E	32°49.7383	′N	4062	m
PC-08	136°58.1650	′E	32°39.7155	′N	4184	m
PC-09	136°51.7688	′E	32°51.5179	′N	4245	m
PC-10	136°46.5181	′E	33°00.5128	′N	4334	m
PC-11	136°53.0056	′E	32°48.0758	′N	3984	m
PC-12	136°47.2198	′E	33°00.0223	′N	4347	m

Table 2. Reflectances of volcanic glass from piston core samples. Count reflects number of grains used to measure reflectance in each sample

	Burial depth		Average	Minimum	Maximum	Count
PC3	104.60-	116.60 cm	1.501	1.500	1.502	32
PC4	87.00-	92.00 cm	1.501	1.500	1.502	32
PC5	53.70-	67.70 cm	1.501	1.500	1.502	33
PC8	202.50-	204.50 cm	1.501	1.500	1.502	38
PC11	79.00-	90.00 cm	1.500	1.499	1.501	38
PC12	147.00-	158.00 cm	1.503	1.500	1.509	52

2 Sediments in the Shikoku Basin Area

The Shikoku Basin is a flat abyssal plane (Fig. 1b, c) covered by approximately 100 cm of bioturbated hemipelagic clay that is underlain by an approximately 10 cm thick ash layer (Fig. 2). This sedimentary sequence is equivalent to the upper Shikoku Basin facies of Ike et al. (2008). Similar sedimentary sequences have also been observed below trench turbidite sequences in the Nankai Trough (Taira et al. 2005; Ike et al. 2008). Optical reflectance of about 30 volcanic glass grains extracted from this ash layer suggests they are tephra. The reflective indexes of these grains are ~1.501 on average (Table 2), which suggests they are correlative with the Aira-Tn tephra layer (25120 ± 270 yr. B.P.) (Miyairi et al. 2004) and allow the calculation of an average sedimentation rate of 3–4 cm/kyr in the Shikoku Basin.

3 Sediments in the Kashinozaki Knoll Area

Hemipelagic clay on the abyssal plane surrounding the Kashinozaki Knoll contains a distinct, light-yellow pumiceous clay. While the hemipelagic clay is part of the upper Shikoku Basin facies, the yellowish pumiceous clay is likely associated with submarine landslide deposits that will be discussed below.
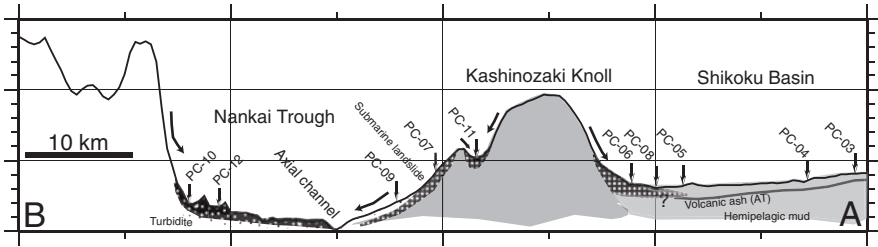
Fig. 3 Interpretation of geologic profile along the line A-B in Fig. 1C

Scars on Kashinozaki Knoll suggest that at least three submarine landslide have dissected the knoll (Ike et al. 2008; Figs. 1c and 3). Immediately below these scars, pumice grains become coarser, indicating the sediments were possibly transported as slide masses (Fig. 3).

A 4-km^2 depression atop Kashinozaki Knoll contains several layers of volcanic ash that are identical to those collected from the Shikoku Basin (Fig. 2). Two thrust planes are visible in piston core PC-11 (Fig. 4). The cause of these thrusts is unknown, but it is possible they were formed by local compression accompanying gravitational gliding.

An ash layer 200 cm below the seafloor (hereafter cm-bsf) surrounding the Knoll is illustrated in PC-08 (Fig. 2). This ash layer corresponds with the Aira-Tn tephra layer (25120 ± 270 yr. B.P.) (Miyairi et al. 2004) and allows the calculation of 4 cm/ kyr sedimentation rates around the Kashinozaki Knoll (Table 2). Note this sedimentation rate is twice that of the rate in the Shikoku Basin and is perhaps a result of additional deposition by submarine landslides.

4   Sediments in the Nankai Trough Area

A piston core collected from the bottom of the Nankai Trough contains evidence for more than six trench turbidite beds overlying a submarine landslide deposit (Fig. 2). These sandy turbidite deposits also occur in PC-07 m suggesting the extend at least as far as the mid-flank of Kashinozaki Knoll (Fig. 2). Piston cores collected from the bottom of the Nankai Trough contain volcanic ash layers 150 ~ 200 cm-bsf that appear to be the same as those observed in the Shikoku Basin (Table 2).

As discussed above, the sedimentation processes in the vicinity of the Kashinozaki Knoll, Shikoku Basin, and Nankai Trough appear to be strongly associated with submarine landslides for the following reasons:

1. At least three submarine landslides on Kashinozaki Knoll left significant headscarp scars and redistributed sediments from the flanks of the knoll onto the basin floor.
2. Hemipelagic muds in the Shikoku Basin are intercalated with reworked with debris flow deposits containing pumiceous material from the knoll that were delivered to the basin by submarine landslide processes.
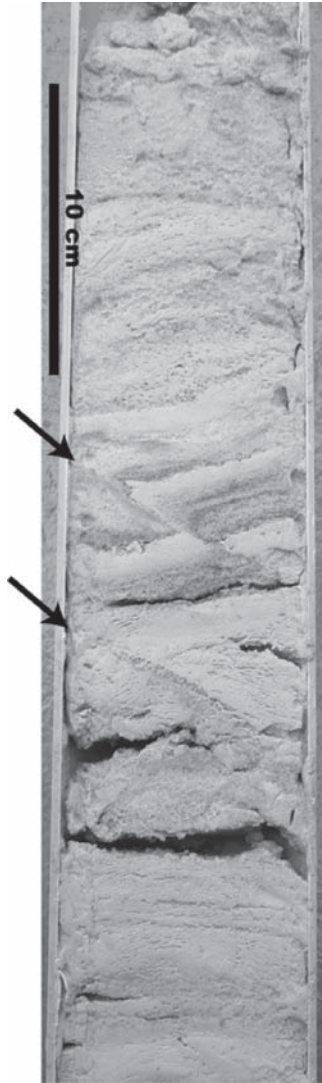
Fig. 4 Detail photo of PC-11 from 74-123 cm-bsf. Arrows indicate the positions of two thrust planes

3. Within the Nankai Trough we believe that large submarine landslides affect flow paths, which in turn alters depositional patterns along the trough. Turbidity currents through the channel distribute sediments laterally along the trough (Pickering et al. 1989). Before large-scale submarine landsliding at the toe of the Nankai prism, turbidity currents flowed along the trough without interruption. However, large submarine landslide can either block current flow or deflect the turbidity current and affect subsequent depositional patterns (Fig. 5). Following emplacement of the submarine landslide, the downstream portion of the channel is sediment starved, whereas upstream endures high sedimentation rates because
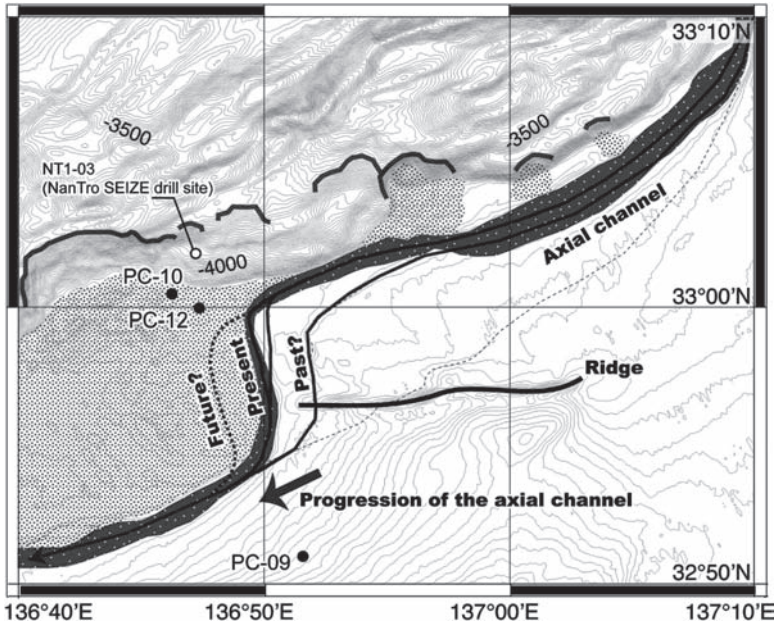
Fig. 5 Bathymetric map of the Nankai Trough showing possible flow paths along the axial channel following submarine landsliding at the toe of the prism

of damming by the landslide deposit (Underwood and Backman 1982). These dams are a short-lived, and the flow path and gradient of the axial channel are eventually restored to their original configurations (Fig. 5). The three steps on the floor of the Nankai Trough (Fig. 1c) might represent traces of past flow paths (Fig. 5). In the future, the flow path of the axial channel may reestablish itself by incising through the submarine landslide deposits (Fig. 5).

5   Concluding Remarks

This study illustrates how submarine landslides can affect both the morphology of the seafloor and sediment distribution patterns at the toe of accretionary prisms. The Nankai accretionary prism study area is subdivided according to bathymetric morphology and sedimentology of the Shikoku Basin, Kashinozaki Knoll and Nankai Trough areas. The Shikoku Basin is a flat abyssal plane that is covered by hemipelagic mud ca. 1 m thick. This mud layer is underlain by a tuffaceous sand layer ca. 10 cm thick that corresponds with the Aira-Tn tephra layer (25120 ± 270 yr. B.P.) and allows sedimentation rates of 2–4 cm/ky to be calculated for the Shikoku Basin. A characteristic light yellow pumiceous mud intercalated with hemipelagic mud is distributed on the abyssal plane surrounding the Kashinozaki

Knoll. This pumiceous mud is presumably derived from the volcanic knoll and distributed across the basin floor by mass wasting processes. At least three head-scarp scars that are likely the result of submarine landslides occur on the flanks of the knoll. Immediately below these scars, pumice layers thicken, suggesting these sediments were probably transported as landslide-related debris flows. Two fault planes noted the piston core from this location may have developed in association with this remobilization.

Along the axial channel at the bottom of the Nankai Trough, more than six trench turbidite beds have been identified in a sequence that overlies a submarine landslide deposit at the foot of the prism. The axial channel might have been initially dammed by the underlying submarine landslide deposit, which would have affected subsequent depositional patterns. In particular, damming of the axial channel would cause sediment to pond upstream and starving the downstream region of sediment.

References

Dominguez, S., Malavieille, J. and Lallemand, S.E., 2000, Deformation of accretionary wedges in response to seamount subduction: Insights from sandbox experiments. Tectonics, 19, 182–196.

Kobayashi, K., 2002, Tectonic significance of the cold seepage zones in the eastern Nankai accretionary wedge – an outcome of the 15 years' KAIKO projects: Mar Geol 187, 3–30.

Kobayashi, K., Cadet, J.P., Aubouin, J., Boulegue, J., Dubois, J., Huene, R., Jolivet, L., Kanazawa, T., Kasahara, J., Koizumi, K., Lallemand, S., Nakamura, Y., Pautot, G., Suyehiro, K., Tani, S., Tokuyama, H., and Yamazaki, T., 1987, Normal faulting of the Daiichi-Kashima Seamount in the Japan Trench revealed by the Kaiko I cruise, Leg 3, Earth Planet. Sci. Lett., 83, 257–266.

Ike, T., Moore, G.F., Kuramoto, S., Park, J-O., Kaneda, Y. and Taira, A., 2008, Tectonics and sedimentation around Kashinozaki Knoll: A subducting basement high in the eastern Nankai Trough. Isl. Arc, 17, 358–375.

Miyairi, Y., Yoshida, K., Miyazaki, Y., Matsuzaki, H. and Kaneoka, I., 2004, Improved ^{14}C dating of a tephra layer (AT tephra, Japan) using AMS on selected organic fractions: Nuclear instruments and methods in physics research Section B: beam interactions with materials and atoms 223–224.

Miyazaki, S. and Heki, K., 2001, Crustal velocity field of southwest Japan: Subduction and arc–arc collision. J. Geophys. Res., 106, 4305–4326.

Pickering, K.T., Hiscott, R.N. and Hein, F.J., 1989, Deep-marine environments–clastic sedimentation and tectonics. Unwin Hyman, London, 416 p.

Saffer, D.M. and Bekins, B.A., 2002, Hydrologic controls on the morphology and mechanics of accretionary wedges. Geology, 30, 271–274.

Seno, T., Stein, S. and Gripp, A.E., 1993, A model for the motion of the Philippine Sea Plate consistent with Nuvel I and geological data, J. Geophys. Res., 98, 17, 941–948.

Spinelli, G.A. and Underwood, M.B., 2004, Character of sediments entering the Costa Rica sub-duction zone: Implications for partitioning of water along the plate interface. Isl. Arc, 13, 432–351.

Taira, A., Curewitz, D., Hasimoto, T., Ibusuki, A, Kuramoto, S, Okano, T. and Tanaka, H. 2005, CDEX Technical Report Volume I: Nankai Trough seismogenic zone site survey: Kumano Basin seismic survey, Philippine Sea, offshore Kii Peninsula, Japan, 64p.

Tobin, H. and Kinoshita, M. 2006, NanTroSEIZE: The IODP Nankai Trough seismogenic zone experiment. Scientific Drilling, 2, 23–27.

Underwood, M.B. and Backman, S.B. 1982, Sedimentary facies associations within subduction complexes. In: Trench-forearc geology: Sedimentation and tectonics on modern and ancient active plate margins, Leggett, J.K. (Ed.), Spec. Publ. Geol. Soc. Lond., pp. 537–550.

von Huene, Ranero, C.R. and Watts, P., 2004, Tsunamigenic slope failure along the Middle America Trench in two tectonic settings. Mar. Geol., 203, 303–317.

Yamazaki, T. and Okamura, Y., 1989, Subducting seamounts and deformation of overriding forearc wedges around Japan. Tectonophys., 160, 1/4, 207–229.

Mass Wasting at the Easternmost Cyprus Arc, Off Syria, Eastern Mediterranean

E. Tahchi, R. Urgeles, C. Hübscher, and J. Benkhelil

Abstract The seafloor topography at the easternmost deformation front between the African and the Anatolian plate off Syria is dominated by the Latakia Ridge, which obliquely intersects the Syrian margin. In this study, we investigate post-Miocene depositional processes of this topographically intricate area and their relationship with mass-wasting phenomena by means of bathymetric, multi-channel seismic reflection and sediment sub-bottom profiler data. Northward of the Latakia Ridge, the Latakia Slope is characterized by steep scarps of up to 500 m height. The Pliocene-Quaternary strata are truncated by the scarps, which are located in the upward prolongation of normal fault planes. Some scarps are from erosion or non-deposition as a consequence of contour currents. Evidence for recent active tectonics is also present in the Latakia Ridge. A basement outcrop along the crest of the northern Latakia Ridge presumably reflects the transtensional faulting of this easternmost section of the African-Anatolian deformation front. The western side of the northern Latakia Ridge shows evidence of more cohesive slumping, probably owing to the overconsolidated nature of the sediment. Here a potential future slide of 11 km³ associated with a rotational fault has been identified. The sedimentary and tectonic setting has resulted in frequent mass wasting. Abundant scars and debris flow-like deposits have been observed on the flanking slopes of the Latakia canyon and the Syrian Margin. The Latakia canyon is fed by several tributary canyons which are incised into the Syrian Slope. Steep slopes, high sediment accumulation rates and active strike-slip tectonics appear to have a fundamental

E. Tahchi (✉) and R. Urgeles
Departament d'Estratigrafia, Paleontologia i Geociències Marines, Facultat de Geologia, Universitat de Barcelona, Martí i Franquès, s/n, 08028 Barcelona, Catalonia, Spain
e-mail: etahchi@univ-perp.fr

C. Hübscher
Institut für Geophysik, Universität Hamburg, Bundesstraße 55, 20146 Hamburg, Germany

J. Benkhelil
IMAGES, University of Perpignan Via Domitia, Perpignan 66860 Cedex, France

role in submarine mass-failure initiation. Mass-failure characteristics indicate that geohazards may exist from subsequent potential tsunami generation.

1   Introduction

The collision between the African and Eurasian plates produced the most striking tectonic feature in the eastern Mediterranean Sea, the Cyprus Arc. The Latakia Ridge (LR) is the eastern morphological continuity of the Cyprus Arc, it intersects obliquely the northern part of the Syrian coast and controls the complex submarine morphology of the Syrian Margin (SM) to the north (Fig. 1). Previous studies focused mainly on the plate tectonic evolution of this intricate realm (Sage and Letouzey 1990; Vidal et al. 2000; Robertson 1998). However, swath sounder data (bathymetry and backscatter imagery), high-resolution seismic-reflection, and high-frequency sediment subbottom profiler (CHIRP) data collected during the BLAC cruise (2003) revealed a clear line of evidence that the morphostructure of the LR reflects not only active tectonics, but also mass wasting and contourite deposition (Benkhelil et al. 2005).

Seismic data revealed abundant active faulting on the SM (Fig. 3 of Benkhelil et al. 2005). The western flank of the LR revealed Pliocene-Quaternary reflections truncated at the present seafloor. The question arose, whether the truncated surfaces represent slump or fault scarps, or whether the truncation results from erosion or non-deposition due to contour currents.

The aims of this study are to identify and illustrate recent depositional processes on the SM with special emphasis on mass wasting and drift deposition. Slope failures will be identified and characterized in order to understand their triggering mechanisms and pre-conditioning factors to characterize geohazard from submarine landslides.

2   Geological Setting

The present-day eastern Mediterranean Sea represents the last remnants of the Neotethys Ocean, which evolved through a complex rifting that took place in the Mesozoic (e.g. Moores et al. 1984; Robertson 1998). The northward subduction of the African plate started before the early Miocene (Eaton and Robertson 1993). In the middle to upper Miocene, the continued convergence led to the evolution of fold-thrust belts north of the Cyprus Arc, e.g. the Gelendzhic Rise and Misis Kyrenia Zone (Fig. 1) (Hall et al. 2005b). At the end of the Miocene, the compressional
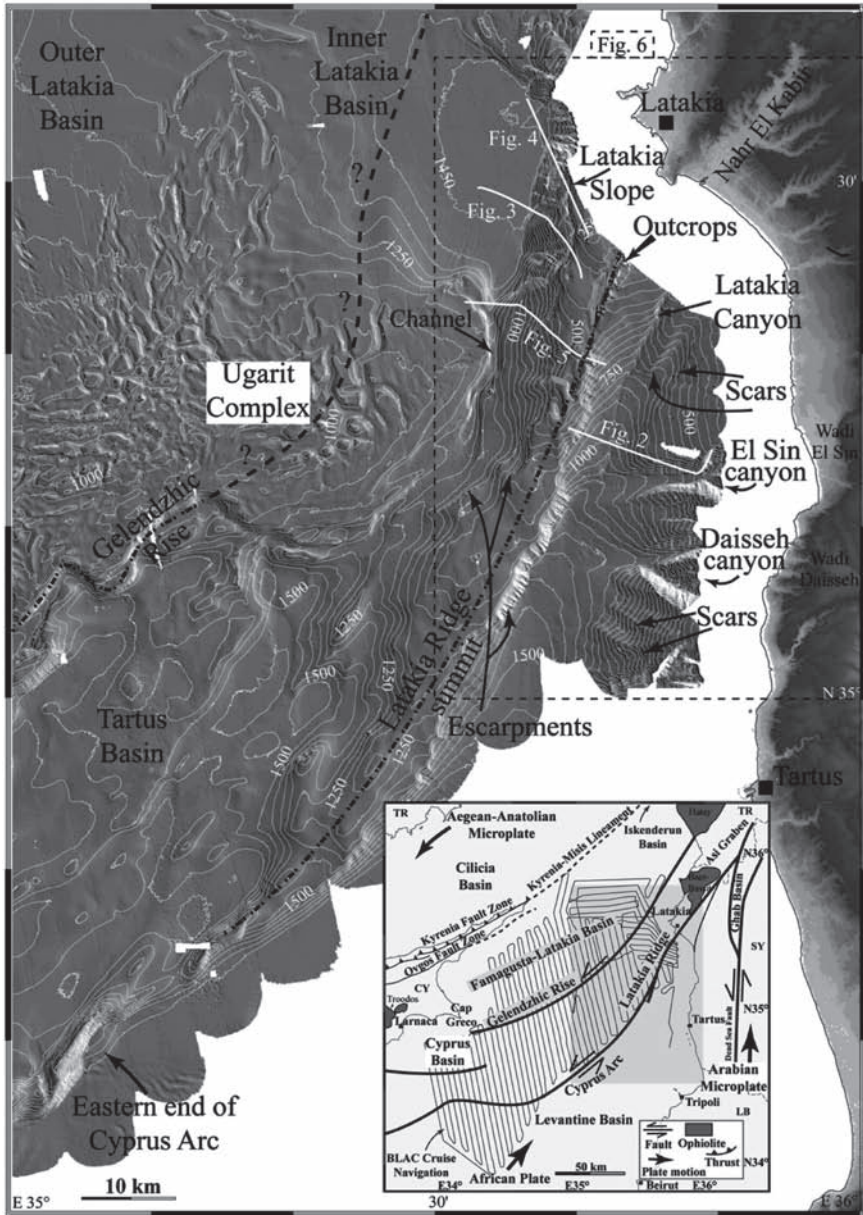
Fig. 1 Bathymetric isocontour map (contour interval = 50 m) and shaded bathymetry map of the study area showing the morphology of the seafloor and the major canyons off the Syrian margin. Boxed is the geological setting of the study area and sketch of the BLAC survey and its track lines

regime changed into a sinistral strike-slip dominated regime as a consequence of the eastward shift of the Aegean-Anatolian micro-plate (Jackson and Mc-Kenzie 1988; Hall et al. 2005a; Hall et al. 2005b). The sea-level drop of approximately 1500 m during the Messinian (Hsü et al. 1973) caused drain-age channels to incise canyons and valleys into the continental shelf (Garfunkel et al. 1979). After that major event, the sediment cover deposited on the eastern Cyprus Arc was laterally continuous and seismically well stratified (Hall et al. 2005b).

3 Data and Methods

The BLAC survey carried out aboard the R/V Le Suroît (October-November 2003) covered an area of 20,000 km^2 and collected more than 5000 km of geophysical data between Cyprus and the Syrian coast (Fig. 1). The hull-mounted EM300 multibeam swath-sounder system was used for bathymetry and backscatter imagery. The multi-channel Seismic-reflection MCS equipment consisted of two GI-guns (45 and 75 in^3) and a 300 m long six-channel streamer. Shots were fired every 12.5 s at a ship velocity of 8 km, resulting in a shot distance of 50 m. Consequently, the CDP coverage was three and the CDP-spacing was 25 m. NMO-correction was carried out with a NMO-velocity of 1500 m/s. The 3.5 kHz sub-bottom profiler (CHIRP) data post-processing included mainly frequency filtering and travel-time de-pendent amplitude amplification.

4 Results

The study area consists of four dominant features, which are termed the SM, Latakia Slope (LS), the LR, and the Inner Latakia Basin (ILB). The stratigraphic interpretation of the seismic profiles follows the nomenclature of Hall et al. (2005a; 2005b). U1 is the Pliocene-Quaternary sediment succession and is locally divided into subunits U1–1 to U1–3 (Fig. 3). U2 denotes strata deposited during the Messinian low-stand (MTDs and evaporites), and U3 labels older strata. "M" flags the Messinian unconformity separating sequences U1 and U2 in the basin, or U1 from U3 when Messinian deposits are absent on the ridge.

4.1 Syrian Margin

South of Latakia, the SM exhibits numerous canyons with east-west orientation perpendicular to the Syrian slope. The canyon flanks have an average elevation of 350 m above the canyon floor and are affected by fresh regular gullies (Fig. 2). They drain into the lower part of the Latakia Canyon at 1400 m of water depth (Fig. 1).
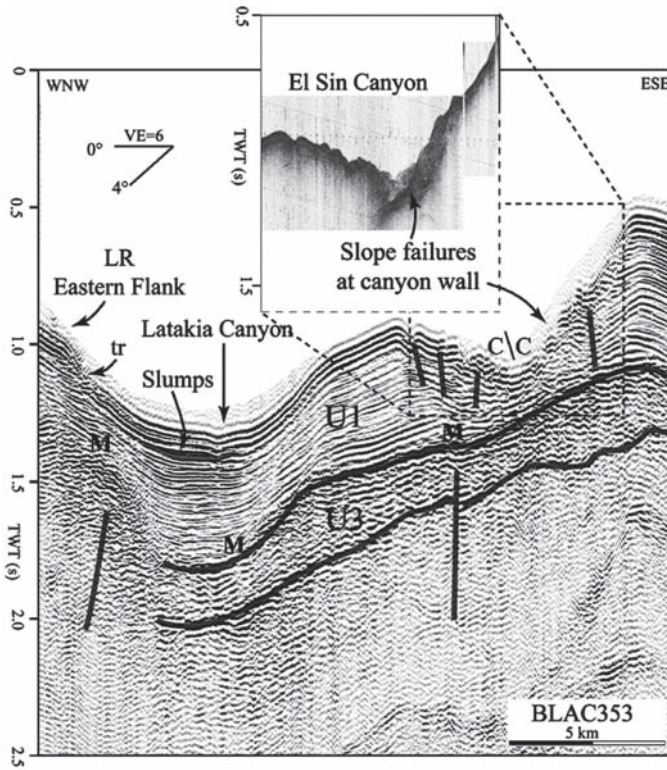
Fig. 2 Geophysical profile across the northernmost active canyon (El Sin Canyon) of the southern Syrian continental slope. C/C: Change Course. tr: Truncation

Slope failures on the canyons flanks are well observed on the shaded bathymetry map and seismic data (Figs.1 and 2).

The Latakia Canyon runs north-south and parallel to the LR and is considered the marine prolongation of the Nahr El Kabir valley in the hinterland. It receives the other canyons from the SM and broadens significantly west of the El Sin canyon, where it is covered by marine sediments deposits (Figs. 1 and 2). The Latakia Canyon is incised into U1 (Fig. 2). The lower U1 already fills the incision left by the Messinian desiccation beneath the present-day location of the Latakia canyon.

4.2 Latakia Slope

The northern segment of the SM and the LR is called the LS and extends from 35°23′ N to 35°32′ N (Fig. 1). The slope angles of the LS vary between 8° and 12°. The LS is characterized by two escarpment chains on top of each other. The upper chain comprises a concave escarpment of up to 250 m height facing the ILB to the

Fig. 3 Geophysical profile across the Latakia ridge and the Inner Latakia basin. C/C: Change Course. tr: Truncation
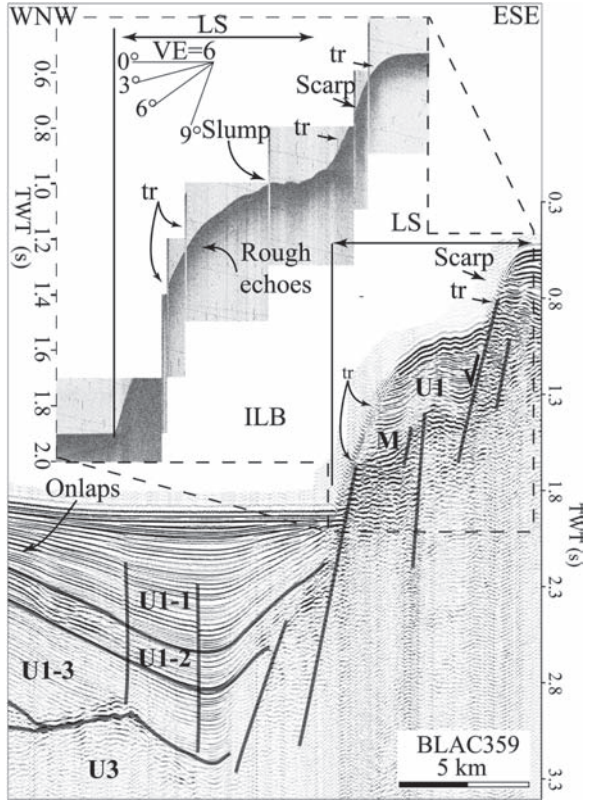
Fig. 4 Geophysical profile across the ILB and the LS. OLB: Outer Latakia Basin. tr: Truncation
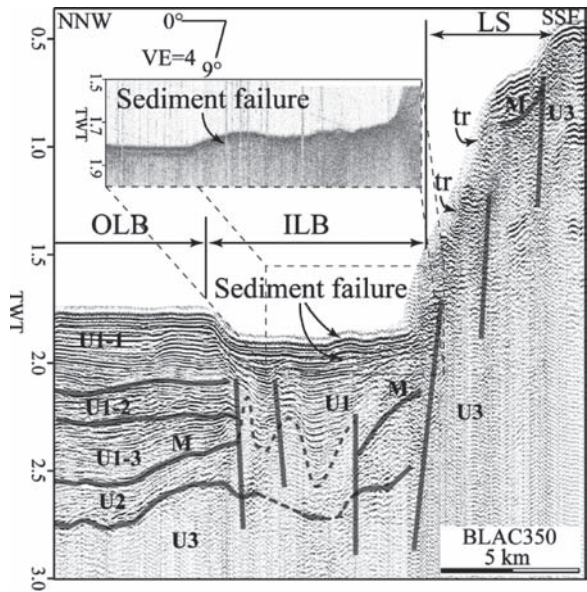
west (Fig. 3). The lower chain includes a more than 500 m high escarpment that reaches down to the basin floor of the ILB (Fig. 4). The escarpments truncate the U1 strata (Fig. 3). Most of the escarpments are correlated with fault planes which can be traced into the seismic basement. A ca. 400 m-thick pile of Pliocene-Quaternary sediments (U1) rests on the footwall block on the LS, and the sediment succession is bounded to the east by a fault plane and to the west by the truncational surface (Fig. 3).

4.3 Latakia Ridge

The LR extends from 34°45′ N to 35°25′ N (Fig. 1). It subdivides the SM into a northern and southern segment. The eastern flank of the LR is characterized by gullied escarpment with a mean height of 350 m and a slope gradient decreasing northward from 10° to 4° (Fig. 1). The western flank of the LR shows a more regular and smooth topography with slope gradients about 4°. Several escarpments about 100 m height are oblique or parallel to the LR summit (Fig. 1).

On Fig. 5, a scarp corresponds to a surficial rotational slump. On top of the LR and west of the outcrop, an erosional moat channel is present that coincides with a fault. The outcrop is clearly correlated with an active fault directly affecting the present-day sea-floor in correlation with hydrodynamic forces. East of the outcrop, the U1-strata are bent and abruptly truncated close to the seafloor (Fig. 5).

The shaded bathymetry map reveals an 18 km long channel that extends parallel the regional contours at the base of the western side of the LR (Figs. 5 and 6). The U1-strata are truncated within the channel (Fig. 5). Faults are present beneath the channel and they reach down to the seismic basement.
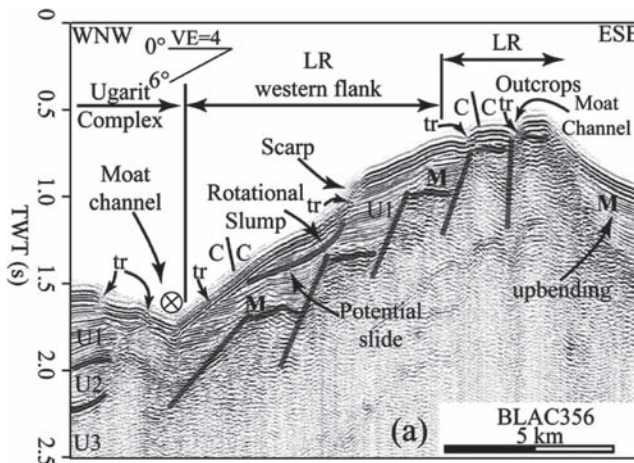
Fig. 5 Geophysical profile across the western flank of the Latakia ridge. C/C: Change Course. tr: Truncation
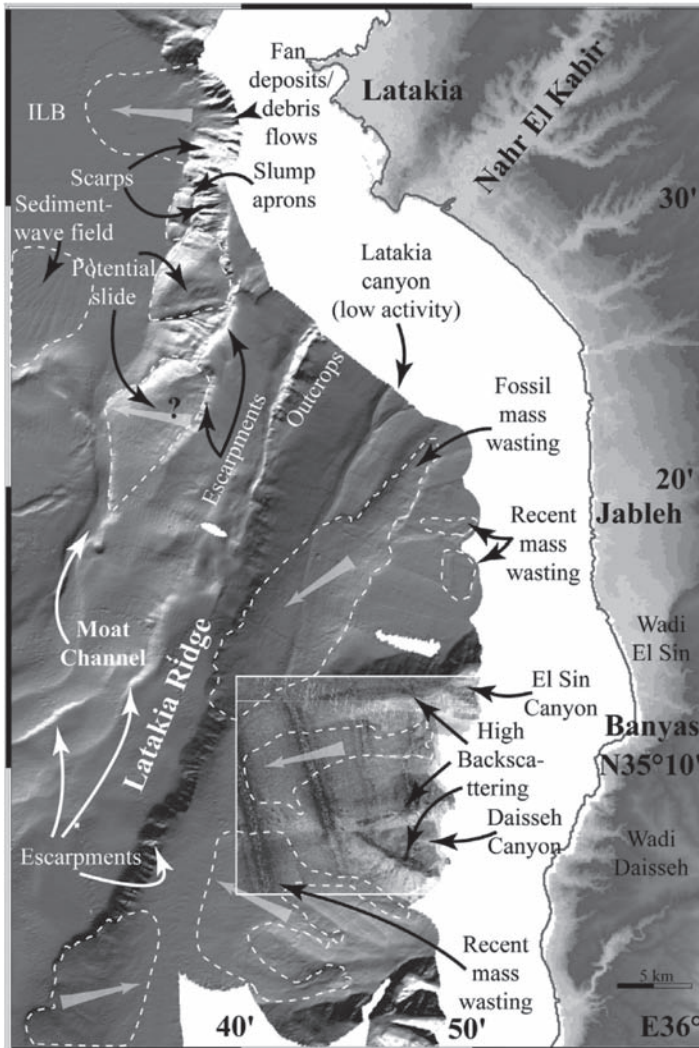
Fig. 6 Synthetic shaded map of the recent and fossil sedimentary processes over the Syrian margin deduced from bathymetry and MCS data. The mass wasting areas are bordered with a dashed white line including their general movement. Boxed is the back-scattering in the tributary canyon axis (40% transparency)

4.4 Inner Latakia Basin

The ILB west of the LS and LR is an elliptical basin located at 1500 m of water depth that throughout shows a smooth topography. On its eastern side, at the foot wall of the LS, sediment failure have accumulated and older sediment deposits are identified in the U1 sediment fill (Fig. 4). On the southern side of the ILB, the uppermost Pliocene-Quaternary sequence U1–1 shows regular interbedded layers

onlapping older strata of U1–2 (Fig. 3). Some sediment waves are located at the southern edge of the basin (Fig. 6). The sediment-wave field covers an area of about 32 km². In the central ILB, the Pliocene-Quaternary sediment succession has a maximum thickness of 0.8 s TWT (>600 m). Some faults reach from within U1–1 down to the seismic basement (Fig. 3).

5   Interpretation and Discussion

5.1   *Submarine Slope Failures*

In several areas along the LS, the upper reflections from the U1 unit are truncated close and up to the seafloor. The most prominent truncational surface is on the LS, where a gullied escarpment of more than 500 m height is present (Fig. 4). There are several processes that might explain the abrupt termination of reflections by trunca-tion, e.g. by post-depositional slumping, faulting or erosion. Mass wasting on submarine slopes may leave a slump scarp behind, which truncates strata from the gliding plane up to the seafloor. Mass failures could be therefore suggested to explain the escarpment facing the eastern side of the ILB in Fig. 4. The presence of debris-flow deposits, as imaged from seismic reflection and chirp profiles, downs-lope the LS interbedded within the Pliocene-Quaternary sequence show that it is a recurrent process that has also taken place recently.

The Latakia Canyon, which lies in the prolongation of the Nahr El Kabir River, shows interbedded slump like sediment body visible on the multichannel seimic data of Fig. 2. The failures that reach the La-takia Canyon are not recent, since the younger event is covered by younger sediments and is reincised by the canyon (Fig. 2). The east-west striking canyon walls of the SM reveal also slope failures shown for instance in Fig. 6. Materials from these canyon walls and heads form blocks of uncon-solidated sedi-ment that have moved down-slope, were deposited on the canyon floor (high back-scattering) and were subsequently reworked by turbidity currents and transported into the lower Latakia Canyon (low back-scattering).

Relatively large and recent debris flow deposits are also present on the west-east striking canyons interfluves (outlined in dashed white line on Fig. 6). An area of ca. 12 km² on the interfluves between El Sin Canyon and Daisseh Canyon and an area of ca. 25 km² south of Daisseh Canyon are covered with debris flows deposits leav-ing scours on the upper slope. On the opposite side and along the eastern flank of the LR, other scours are also abundantly present just above the gullies.

5.2   *Drift Deposits*

Alternatively, the truncational surface may be just apparent. The term "apparent truncation" describes reflection terminations at a depositional limit (non-deposition) or thin-ning below seismic resolution (Emery and Myers 1996). Those depositional

limits may characterize for instance levees of turbidite channel-levee systems (e.g. Hübscher et al. 1997) or contourite drifts (Faugères et al. 1999).

There are several observations that sediment deposition on the LR occurred under the influence of contour currents. The entire western flank of the LR is characterized by truncation (Fig. 5). The southern side of the ILB shows absence of thick mass waste deposits downslope the LR (Fig. 5). The activity of a contour current at the western flank of the LR is corroborated by the presence of the about 18 km long moat channel between the Ugarit Complex and the LR and the sediment wave field south of the ILB (Figs. 5 and 6). The U1-strata within the channel are at least apparently truncated (Fig. 5). Therefore, along the entire western LR, the U1 sediment succession can be considered as an elongated over-consolidated drift deposit. The drift deposits take place on steep slope of the western flank of the LR. Persisting supply of sediment with newer sediment load might lead to over sedimentation and destabilization of the overconsolidated sediment deposits. Erosional currents can also lead to over-steepening and weaken the sediment deposits by eroding its slip plane. A weak plane induces drift deposit material to breaks off in a slide. For in-stance in Fig. 5, the rotational slump observed of a volume of 11 km^3 is considered as a drift sediment deposition showing interbedded regular stratification and it is underlined by faults. Truncations are also identified on the upper and lower edges of the rotational slump. Therefore, the contour current may be considered as triggering mechanism and/or as preconditioning factor for mass wasting.

5.3 Mass Wasting and Tectonics

Since faults affect directly the seafloor, active tectonics has to be assumed. The most recent phase in the area is strike slip faulting. Along the crest of the LR, an elongated basement ridge has been uplifted (Figs. 5 and 6). The uplift of the outcropping ridge is clearly indicated by the upward bending and eroded strata east of the ridge. Here transtension and transpression along restraining and releasing fault bends is interpreted for the uplift. The divergent reflection pattern of the ILB deposits (Fig. 3) suggests sedi-mentation during continuous subsidence. Considering both the subsidence of the ILB and the high-angle faults at the western flanks of the LR and the LS, respectively, an extensional regime west of the LR is interpreted.

The high-angle normal fault plane within the U1-strata on the LS (Fig. 3) points towards a causative correlation between the slump and the fault. It is likely that the slump represents an incipient failure stage. The entire volume of this slide has been estimated at about 10 km^3, indicating that the scarps are mainly result of faulting (Fig. 3). Here the scarps are eroded by secondary processes (e.g. contour current).

Some smaller slump aprons are present further north on the LS. West of Latakia, a slump body of 0.2 km^3 rests on the uppermost sediments of the ILB (Fig. 6). The subbottom data prove that the slumping occurred quite recently, since no draping sediment is present.

Some of the faults bound the scars that constitute the upper part of the slip plane for different slope failures (Fig. 3), and thus they might have a role in pre-weakening

the headwall area of the observed failures prior to their initiation. In addition, some of these faults might have produced seismic ground motions of sufficient intensity (even with relatively low earthquake magnitudes) that could have triggered some of the observed slope failures (Fig. 5).

6   Conclusions

Mass wasting occurred frequently in the entire survey area. Between the SM, the LR and the LS several slump scarps, scars and deposits have been identified. The SM is clearly characterized by recent sedimentation activity that buried some of the mass wasting units into the Latakia Canyon deposits and makes it poorly detectable on the present-day seafloor (Figs. 2 and 6). The southern part of the Syrian continental slope on its lower part is also characterized by mass wasting as well as the lower Latakia Canyon which is a sort of catchments area of the neighboring instabilities originating from the SM and the LR. The walls of the east-west striking canyons, which guide the sediment transport from the shelf into the Latakia Canyon, reveal also slope failures.

Recent and continuous debris flows have also been identified on the LS, leaving slump scarps behind, which truncates strata from the gliding plane down to the seafloor (Fig. 4). Most of the observed scarps do not result from slumping or faulting. The edgewise termination of Pliocene-Quaternary strata at the escarpments of the LR results mainly from non-deposition as a consequence of contour currents and not from erosion or faulting. The contour currents caused moat channels by erosion or non-deposition (Fig. 5) and they are also considered as triggering mechanism and/or as preconditioning factor for mass wasting.

Northwest of the LR in the ILB, continuous and ongoing extension has been observed. According to the presented data, a potential rotational slump of $11\,km^3$ is present atop an angular footwall block on the western flank of the LR (Fig. 5) and another slump of $10\,km^3$, rest on a high-angle fault on the LS (Fig. 3). Other smaller slumps happened recently on the LS, and draped down the ILB basin floor (Fig. 6).

References

Benkhelil J, Bayerly M, Branchoux S, Courp T, Gonthier E, Hübscher C, Maillard A, Tahchi E (2005) La branche orientale de l'arc de Chypre. Morphostructure d'une frontière de plaques d'après les résultats de la campagne BLAC (2003). Comptes Rendus Geosci 337: 1075–1083

Eaton S, Robertson A (1993) The Miocene Pakhour Formation, southern Cyprus, and its relationship to the Neogene tectonic evolution of the eastern Mediterranean. Sed Geol 86: 273–292

Emery D, Myers K (1996) Sequence Stratigraphy. Blackwell Science, Oxford, UK

Faugères JC, Stow AVD, Imbert P, Viana A (1999) Seismic features diagnostic of contourite drifts. Mar Geol 162: 1–38

Garfunkel Z, Arad A, Almagor G (1979) The Palmahim Disturbance and its regional setting. Geol Surv Israel Bull 72: 56

Hall J, Aksu AE, Calon TJ, Yaşar D (2005a) Varying tectonic control on basin development at an active microplate margin: Latakia Basin, Eastern Mediterranean. Mar Geol 221: 15–60

Hall J, Calon TJ, Aksu AE, Meade SR (2005b) Structural evolution of the Latakia Ridge and Cyprus Basin at the front of the Cyprus Arc, Eastern Mediterranean Sea. Mar Geol 221: 261–297

Hsü KJ, Cita MB, Ryan WBF (1973) The origin of the Mediterranean Evaporites. In: Ryan W.B.F, Hsü K.J (Eds.), Init. Repts. DSDP, 13. U.S. Govt. Printing Office, Washington D.C. 1203–1232

Hübscher C, Spieß V, Breitzke M, Weber M (1997) The youngest channel-levee systems of the Bengal Fan: results from digital sediment echosounder data. Mar Geol 141: 125–145

Jackson J, McKenzie DP (1988) The relationship between plate motions and seismic moment tensors, and the rates of active deformation in the Mediterranean and Middle East. Geophys J Roy Astron Soc 93: 45–73

Moores EM, Robinson PT, Malpas J, Xenophontos C (1984) Model for the origin of the Troodos massif, Cyprus and other Mideast ophiolites. Geol 12: 223–226

Robertson A.H.F (1998) Mesozoic–Tertiary tectonic evolution of the easternmost Mediterranean area: Integration of marine and land evidence. In: Robertson AHF, Emeis KC, Richter C, Camerlenghi A (Eds.), Proc Ocean Drill Prog Sci Res 160: 723–782

Sage L, Letouzey J (1990) Convergence of the African and Eurasian Plates in the eastern Mediterranean. In: Letouzey J (Ed.), Petroleum and Tectonics in Mobile Belts. Editions Technip, Paris, 49–68

Vidal N, Klaeschen D, Kopf A, Docherty C, Von Huene R, Krasheninnikov VA (2000) Seismic images at the convergence zone from south of Cyprus to the Syrian coast, eastern Mediterranean. Tectonophys 329: 157–170

Risk Analysis for Hurricane-Wave Induced Submarine Mudslides

M.C. Nodine, R.B. Gilbert, J.Y. Cheon, S.G. Wright, and E.G. Ward

Abstract Hurricane waves in the Gulf of Mexico can trigger mudslides in the relatively weak clays in the offshore Mississippi Delta region. Mudslides can cause extensive damage to the infrastructure that supports offshore oil and gas production, including platforms and pipelines. This paper presents a method for assessing the probability and risk for future mudslides in the Delta as a function of the possible sizes of waves, bathymetry, and shear strengths of sea floor soils. The method has been calibrated to the extent possible using historical information. The method is transparent and can readily include either generic or site-specific information about soil properties and wave characteristics. The method is applied regionally to develop maps depicting the risk to locations and to pipelines. Return periods for mudslides vary significantly across the Delta, with values less than 30 years in the shallowest water and values greater than 1,000 years in the deepest water. Wave period, in addition to wave height, is an important factor in mudslide vulnerability. Mudslides are localized features, on the order of several thousand feet in lateral extent and about 50 to 150 feet deep. The areal extent and depth of mudslides are related to the lengths and widths of the storm waves that cause them.

Keywords Submarine landslides • mudslides • hurricanes • risk analysis

M.C. Nodine (✉)
GEI Consultants, Inc.,1790 38th St. #103, Boulder, CO 80302, USA
e-mail: mnodine@geiconsultants.com

R.B. Gilbert, J.Y. Cheon, and S.G. Wright
The University of Texas at Austin, Department of Civil, Architectural and Environmental Engineering, Geotechnical Engineering Program, 1 University Station, C1792, Austin, Texas 78712-0280, USA
e-mails: bob_gilbert@mail.utexas.edu; doogiezzang@mail.utexas.edu; swright@mail.utexas.edu

E.G. Ward
Offshore Technology Research Center, Texas A&M University, 1200 Mariner Drive, College Station, TX 77845, USA
e-mail: egward@tamu.edu

1 Introduction

Hurricane waves in the Gulf of Mexico can trigger mudslides in the relatively weak clays in the offshore Mississippi Delta region (Coleman et al. 1982; Hitchcock et al. 2006). Mudslides caused extensive damage to platforms and pipelines in Hurricanes Camille (1969), Ivan (2004) and Katrina (2005). The consequence of this damage in Ivan and Katrina was a significant loss of capacity for offshore oil and gas production in the Gulf of Mexico, leading to increases in the price of oil (e.g., Thomson et al. 2005; Coyne and Dollar 2005). This paper presents a method for assessing the probability and risk for future mudslides in the Delta as a function of the possible sizes of waves, bathymetry, and shear strengths of sea floor soils. The method is applied regionally to develop maps depicting the risk to lease blocks and to pipelines. It can also be applied on a project-specific basis using site-specific information about waves, bathymetry and soil shear strengths. The method is described and examples are presented to demonstrate its use.

2 Mudslide Model

The conceptual framework of the risk analysis method is to characterize the hazard caused by hurricane waves and the vulnerability caused by relatively weak soils in the Delta, and then to compare the hazard and vulnerability to assess the potential for mudslides. The hazard is shown schematically in Fig. 1; it is represented by shear stresses that are applied to the soils from wave-induced bottom pressures and from the weight of the soil when it is on a slope. These applied shear stresses can be related to the height and length of the surface waves and the slope and unit weight of the soil in the sea floor. Linear wave theory, with an adjustment to
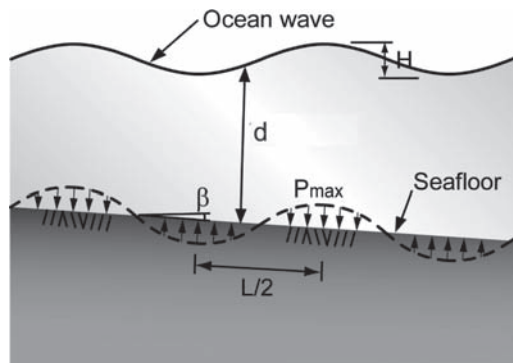
Fig. 1 Schematic of wave forces imposed on the sea floor

account for the three-dimensional shape of a wave, is adopted here to characterize the hazard (see OTRC 2008 for details).

The vulnerability is represented by the shear strength of the soil in the sea floor acting over a potential failure surface. For the predominantly normally (and under-consolidated) marine clays that comprise the Delta sea floor, the shear strength mobilized in wave loading is the undrained shear strength. A limit equilibrium model, assuming a circular failure surface and constituting an extension of a model proposed by Henkel (1970) in order to account for non-linear variations in und-rained shear strength with depth below the sea floor, is adopted here to characterize the vulnerability (see OTRC 2008 for details).

This methodology for characterizing the hazard and vulnerability has been vali-dated by comparing predictions with observed behavior in actual hurricanes. Bea et al. (1983) used the limit equilibrium model to analyze a mudslide that occurred in South Pass Lease Block 70 during Hurricane Camille in 1969. The model predicted that a mudslide would occur based on the wave hindcast and site-specific geotechnical information. Nodine et al. (2006) used the limit equilibrium model to analyze a mud-slide that occurred in Mississippi Canyon Block 20 during Hurricane Ivan in 2004. Again, the model predicted the occurrence of the mudslide. One of the interesting results of this analysis was the importance of the wave length on the hazard. Increasing the wave length increases the maximum bottom pressure for the same wave height and water depth, which may explain why Hurricane Ivan caused a com-parable amount of mudslide damage to that of Hurricane Katrina despite having smaller wave heights in the Delta (Nodine et al. 2006). A regional analysis comparing observed to predicted mudslide activity is also presented by Nodine et al. (2006). Predicted mudslides were found to compare well with mudslide damages reported.

Several important observations were made through applying this model of mud-slides to the Delta. First, the bottom slopes in the Delta are very flat (1% to 2%) and generally do not contribute much to potential for a mudslide. Hence, mudslides are mainly driven by waves. Second, it takes a relatively large wave to cause a mudslide. Nodine et al. (2007) estimated that maximum wave heights of at least 65 feet are required to cause mudslide activity. Less than 25% of all hurricanes in the Gulf of Mexico have waves this large. Third, even if a mudslide completely remolds the soil, the soil will not continue to move when the waves subside, and the mudslide will not likely propagate into a large-scale regional mudflow. Therefore, the areal extent of disturbance from a mudslide is expected to be similar in plan to the largest ocean waves, which are sustained over several thousand feet and are hundreds to thousands of feet across.

3 Risk Model

The risk associated with mudslides is defined as the expected damage from mud-slides, which is the summation of the possible damages multiplied by their corre-sponding probabilities of occurrence. The primary focus in this work is to assess

the probability of occurrence for a mudslide, both locally in terms of a specific location or facility in the Delta and regionally in terms of the collection or system of facilities throughout the Delta. We will also discuss briefly the factors that affect the potential for damage from a mudslide.

3.1 Probability for Mudslide at a Particular Location

The probability that a mudslide occurs at a particular location with a given water depth and bottom slope is assessed by dividing the problem into the hazard and the vulnerability as follows:

$$P\left(\text{Mudslide}\right)= \sum_{\text{all } p_{max},L_{H_{max}}} \left[\sum_{\text{all } s_u(z)} P\left(\text{Mudslide}\middle| s_u(z), p_{max}, L_{H_{max}}\right) P\left(s_u(z)\right)\right] P\left(p_{max}, L_{H_{max}}\right) \quad (1)$$

where P (Mudslide) is the probability a mudslide occurs, $P(\text{Mudslide}|s_u(z), p_{max}, L_{H_{max}})$ is the conditional probability that a mudslide occurs for a given profile of undrained shear strength versus depth, $s_u(z)$, together with a given combination of maximum bottom pressure, p_{max}, and wave length, $L_{H_{max}}$; $P(s_u(z))$ is the probability for a given profile of undrained shear strength versus depth at this location; and $P(p_{max}, L_{H_{max}})$ is the joint probability for a given combination of maximum bottom pressure and wave length acting on the sea floor at this location.

The conditional probability of a mudslide, $P(\text{Mudslide}|s_u(z), p_{max}, L_{H_{max}})$, is obtained by establishing the relationship between the factor of safety against a rotational failure in the sea floor and the maximum amplitude and wave length of the bottom pressure acting on the sea floor. Figure 2 shows an example of this
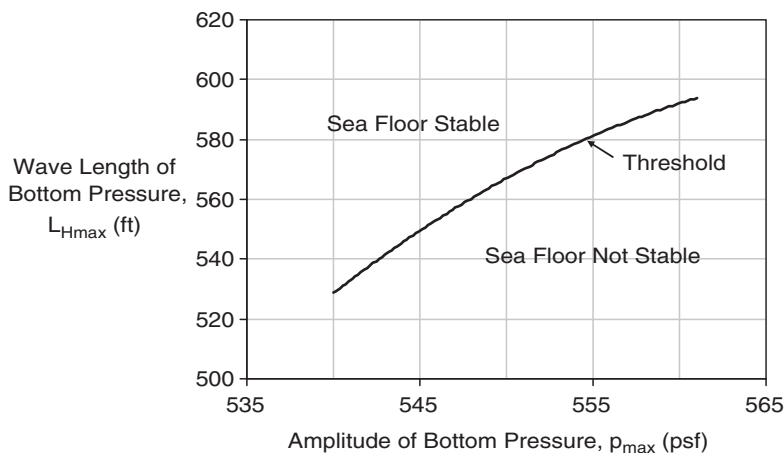
Fig. 2 Bottom pressure wave threshold to cause a mudslide for a given profile of undrained shear strength versus depth at a location in Delta (taken from OTRC 2008)

relationship for a particular location and a given profile of undrained shear strength versus depth; the threshold line separates the combinations of (p_{max}, $L_{H_{max}}$) that produce a factor of safety less than one from those combinations that produce a factor of safety greater than one. The threshold bottom pressure generally increases as the length of the bottom pressure wave increases because the critical slip surface is moving deeper into stronger soil. (An exception is when the soil profile includes weaker layers at depth.) This threshold depends on the profile of undrained shear strength versus depth as well as the bottom slope at the location of interest. The profile of undrained shear strength with depth is extremely variable across the Delta (Hooper 1980; Roberts et al. 1976). For the purposes of mudslide risk analysis at a site where shear strength data are available, one shear strength profile may be assumed to represent the site and $P(s_u(z)) = 1.0$ for that profile, or several shear strength profiles may be assumed to be equally probable or weighted appropriately with different values for $P(s_u(z))$ reflecting the available information. There may well be uncertainty in the shear strength profile even when site-specific shear strength data are available due to the small area sampled by a single boring relative to the area of interest for a pipeline or a platform.

The amplitude and length of the pressure wave are related to ocean waves as follows. The maximum pressure is approximated from the height and length of the largest ocean wave, H_{max} and $L_{H_{max}}$, and the depth of the water, d, using linear wave theory (Wiegel 1964) with a correction factor to account for the three-dimensional shape of the wave, I_{3D} (OTRC 2008):

$$P_{max} = \frac{\gamma_w}{2}\left(H_{max}\bigg/\cosh\left(\frac{2\pi}{L_{H_{max}}}d\right)\right)I_{3d} \tag{2}$$

The wave length associated with the largest wave is found by assuming that the period for the largest wave is approximated by 90% of the peak spectral period, T_p (the period associated with the most wave energy in a series of waves) (Haring et al. 1976):

$$L_{H_{max}} = \frac{g(0.9 \times T_p)^2}{2\pi}\tanh\left(\frac{2\pi d}{L_{H_{max}}}\right) \tag{3}$$

where $L_{H_{max}}$ is found implicitly, $L_{H_{max}} = f^{-1}(T_p)$. For a given sea state, which is defined as an interval of time over which the mean maximum wave height, $\mu_{H_{max}}$, and peak spectral period are reasonably constant and is typically taken to be 3 h in the Gulf of Mexico during a hurricane, the probability that the maximum wave height exceeds a particular value during that sea state is obtained from the Forristall probability distribution (Forristall 1978):

$$P\left(H_{max} > h_{max}\middle|\mu_{H_{max}}\right) = 1 - \exp\left[-e^{-\frac{\pi}{\sqrt{6}}\left(\frac{1}{0.07\mu_{H_{max}}}\right)\left(h_{max} - \mu_{H_{max}}\left(1 + \frac{0.577 \times 0.07\sqrt{6}}{\pi}\right)\right)}\right] \tag{4}$$

The probability that the maximum bottom pressure exceeds a threshold for a given sea state and three-dimensional correction factor is then obtained by combining Eqs. 2, 3, and 4:

$$P\left(P_{max} > \frac{\gamma_w}{2}\left(h_{max}\left/\cosh\left(\frac{2\pi}{L_{H_{max}} = f^{-1}\left(T_p\right)}d\right)\right)\right)I_{3d}\left|\mu_{H_{max}},T_p,I_{3d}\right.\right) = P\left(H_{max} > h_{max}\left|\mu_{H_{max}}\right.\right) \quad (5)$$

Therefore, Eq. 1 can be re-stated in terms of the variables defining a sea state:

$$P\left(\text{Mudslide}\right)=$$

$$\sum_{\text{all } m_{H_{max}},T_p,I_{3D}}\left[\sum_{\text{all } s_u(z)}P\left(\text{Mudslide}\left|s_u(z),\mu_{H_{max}},T_p,I_{3D}\right.\right)P\left(s_u(z)\right)\right]P\left(\mu_{H_{max}},T_p,I_{3D}\right) \quad (6)$$

where the threshold for p_{max} is established as in Fig. 5 for a given profile of undrained shear strength versus depth and peak spectral period at a particular location (water depth and bottom slope).

To represent the possible sea states that may occur in the future in the mudslide prone area of the Mississippi Delta, API Bulletin 2INT-MET Interim Guidance on Hurricane Conditions in the Gulf of Mexico (API 2007) is used. This guidance provides a probabilistic description of possible 3-h-long sea states in terms of the mean maximum wave height and the peak spectral period. Wave heights and peak spectral periods are given for return periods ranging from 10 to 10,000 years. In order to simplify the analysis, we discretized the probabilities of the mean maximum wave heights into eight bins as shown in Fig. 3. The values of the wave heights in Fig. 3
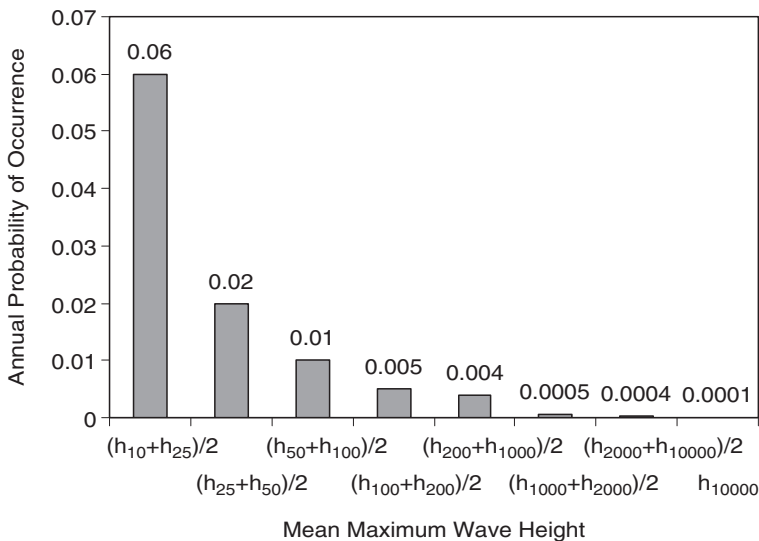
Fig. 3 Probability distribution for maximum wave height at any location (taken from API 2007, where h_x is the value for $\mu_{H_{max}}$ with an annual probability of $1/x$ of being exceeded) (taken from OTRC 2009)

are dependent on the water depth, i.e. the wave height with a 10% probability of occurrence will be larger for 500-ft-deep water than it will be for 100-ft deep water. API (2007) provides wave heights for water depths up to about 1,000 feet, as well as for "deep water," in which the effect of the sea floor on the wave height is assumed to be negligible.

The peak spectral periods of storm waves are assumed by API (2007) and in this analysis to be independent of water depth, meaning that the periods of waves in a given storm are directly related to the heights of the waves in deep water. Furthermore, the peak spectral period is assumed to be related to the largest waves in the hurricane, or the waves near the eye. To illustrate this assumption, Fig. 4 shows the peak spectral period versus mean maximum wave height from hindcast data for the Delta in Hurricanes Ivan and Katrina. The curve labeled "Average" represents the average relationship between the largest mean maximum wave height and the corresponding peak spectral period for all hurricanes in the Gulf of Mexico in the past 60 years including Ivan and Katrina (from a proprietary database.) This average relationship is used to relate wave height and wave period in API (2007). The peak spectral period for the waves in the Delta in Ivan is greater than that for the waves in Katrina and greater than the average curve (Fig. 4). The difference between Ivan and Katrina is that the eye of Katrina passed over the Delta while that for Ivan passed 90 miles east of the Delta. Therefore, the largest waves in Katrina were in the Delta and the peak spectral period for these waves falls on the average curve (Fig. 4). Conversely in Ivan, the waves in the Delta were not as high as those near the eye, but they had a relatively large peak spectral period, approximately equal to that near the eye (Fig. 4). Figure 4 shows why the peak spectral period is
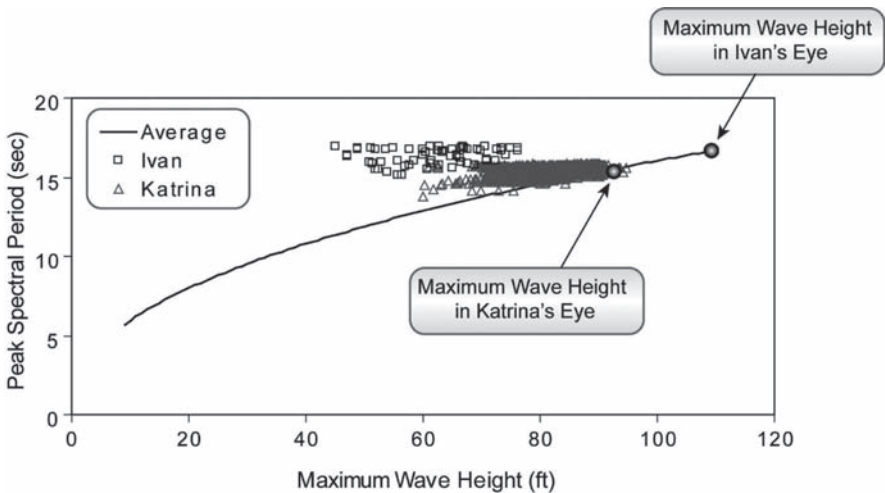
Fig. 4 Relationship of peak spectral period with maximum wave height for Hurricanes Ivan and Katrina in the Delta region, and the average relationship for historical hurricanes in the Gulf of Mexico (taken from OTRC 2008)

such an important factor in the potential mudslides. Hurricanes Ivan and Katrina caused similar mudslide damage in the Delta even though Ivan's eye was well east of the Delta and Katrina's passed over the Delta, and even though the waves were not as high in the Delta during Ivan as during Katrina.

In order to capture the complex relationship between peak spectral period and mean maximum wave height (Fig. 4), the following approach is used to find the conditional probability for a particular value of the peak spectral period, given the mean maximum wave height. If a particular mean maximum wave height occurs in the Delta, $\mu_{H_{max, delta}}$, it means that the mean maximum wave heights in the storm are at least as large as those in the Delta, or $\mu_{H_{max, anywhere}} \geq \mu_{H_{max, delta}}$. In order to account for the effects of wave height, "deep water" is used as a convenient reference point in comparing different locations. The probability that $\mu_{H_{max, anywhere}} \geq \mu_{H_{max, delta}}$ can be calculated from the distribution shown in Fig. 6. Likewise, the probability that the largest mean maximum wave heights in the storm, i.e., the waves near the eye or $\mu_{H_{max, eye}}$, can be calculated as follows:

$$
\begin{aligned}
P\left(\mu_{H_{max,eye}} \mid \mu_{H_{max,delta}}\right) &= P\left(\mu_{H_{max,eye}} \mid \mu_{H_{max,anywhere}} \geq \mu_{H_{max,delta}}\right) \\
&= \frac{P\left(\mu_{H_{max,anywhere}} > \mu_{H_{max,delta}} \mid \mu_{H_{max,eye}}\right) P\left(\mu_{H_{max,eye}}\right)}{P\left(\mu_{H_{max,anywhere}} \geq \mu_{H_{max,delta}}\right)}
\end{aligned}
\tag{7}
$$

The relationship between the peak spectral period and the mean maximum wave height near the eye (the "average" curve in Fig. 4) then provides the means to relate the peak spectral period to the mean maximum wave height in the Delta:

$$
P\left(T_p = g\left(\mu_{H_{max,eye}}\right) \mid \mu_{H_{max,delta}}\right) = P\left(\mu_{H_{max,eye}} \mid \mu_{H_{max,delta}}\right)
\tag{8}
$$

where $T_p = g(\mu_{H_{max, eye}})$ is the "average" curve in Fig. 4. An example of the conditional probability distribution for the peak spectral period given the mean maximum wave height (in deep water) is shown in Fig. 5. Note that when there are large waves in the Delta, it is most likely that the eye is near the Delta (the smallest possible value for the peak spectral period in Fig. 5); however, it is also possible that the eye was not in the Delta and the peak spectral period for the waves in the Delta will be greater.

The correction factor in Eq. 2, I_{3D}, accounts for the reduction in the maximum bottom pressure due to the three-dimensional shape of the largest wave. The variability in the pressure ratio is modeled using a simple probability distribution based on data gathered from a selection of directional spectra from hindcasts of Hurricanes Ivan and Katrina (OTRC 2008). The mean pressure ratio of 0.66 is assigned a probability of 0.5, the mean plus and minus one standard deviation (0.72 and 0.60, respectively) are each assigned probabilities of 0.25, and the probability distribution for I_{3D} is independent of the mean maximum wave height of the peak spectral period.

The approach to establish the joint probability for the bottom pressure characteristics, $P(\mu_{H_{max}}, T_p, I_{3D})$ in Eq. 6, is depicted with the event tree shown on Fig. 6.
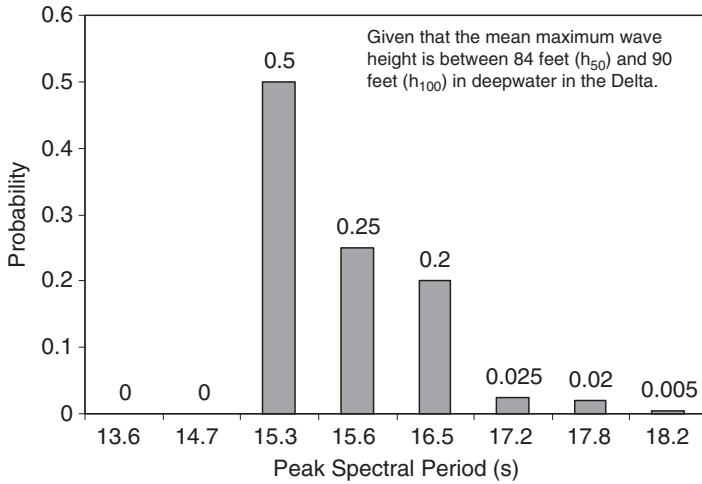
Fig. 5 Conditional probability distribution for peak spectral period given that the mean maximum wave height is between 84 and 90 feet in deep water in the Delta, or between the 50-year and 100-year return period values for any water depth in the Delta (taken from OTRC 2009)
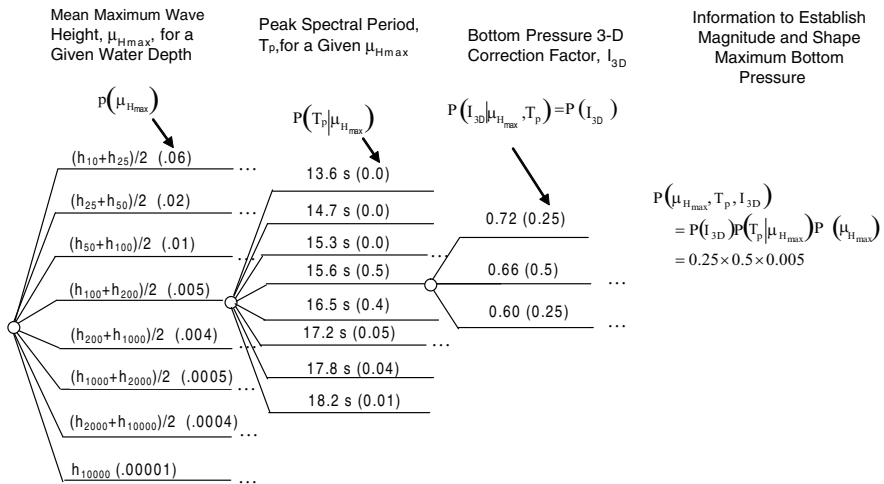
Fig. 6 Event tree representing the hazard for wave-induced mudslides (taken from OTRC 2008)

Each branch in the tree represents a possible value for a parameter describing the magnitude and shape of the wave-induced bottom pressures, and the number in parentheses is the probability of that particular value occurring. The first set of branches in Fig. 6 characterizes the magnitude of the sea state in terms of the mean maximum wave height in a 3-hour period. The probabilities for these values correspond to the probability of that mean maximum wave height occurring annually, and they

depend on the water depth. The next set of branches in Fig. 6 characterizes the wave period associated with the mean maximum wave height, which depends on the wave height at the eye of the storm and can be determined using Eq. 8. The final set of branches characterizes the correction factor to account for the three-dimensional shape of the maximum wave.

3.2   *Consequence of a Mudslide*

Assessing the risk associated with mudslides includes considering the potential consequence or damage caused by a mudslide as well as the probability that a mudslide will occur. The approach described above to predict the occurrence of mudslides also provides valuable insight into the potential consequences.

The geometry of a mudslide is expected to be closely related to the geometry of the ocean waves. The depth of disturbance is approximately 5% to 10% of the wave length, or 50 to 100 feet below the mudline. The areal extent of disturbance from a single wave is about the same as the length and width of the wave, or about a thousand feet long by hundreds of feet across. The total area of disturbance may be a bit larger due to multiple failures caused by a sustained wave passing over. Lastly, even considering the remolded shear strength of the weak clays in the Delta, the flat sea floor is stable without significant wave loading, meaning that the disturbed soil does not spread beyond the area disturbed by the wave. To illustrate the expected geometry of mudslides, waves were simulated (Zhang et al. 1999) based on the hindcast information from Hurricane Katrina at South Pass Lease Block 70. A representative profile of undrained shear strength was used and assumed to be the same throughout the entire block. The resulting pattern of mudslides in this simulation, represented by the locations for which the largest bottom pressure was sufficient to cause a factor of safety less than 1.0, is shown in Fig. 7a. The pattern of disturbance mimics the geometry of the largest waves, and it resembles post-hurricane surveys of actual mudslide features in the Delta (Fig. 7b). Figures 7a, b represent different locations but the sizes and shapes of the simulated and sonar-detected disturbances are similar. In summary, mudslides tend to be rather localized features and the total areal extent of disturbance on the sea floor is primarily related to the length of time over which waves large enough to cause mudslides are present.

While mudslides are localized features, they are large and deep enough to damage pipelines and platforms if these are located within the volume of disturbance. The main concern with a pipeline is that the movement will lead to excessive longitudinal forces (tension and/or bending) that rupture the pipeline. A mudslide can also bury a pipeline below tens of feet of soil, making it difficult to locate and maintain. A mudslide can even push a pipeline far enough off of its route that regulatory issues arise. With platforms, the lateral forces imposed by the rotation of the mudslide can cause a failure of the platform legs/piles, leading to a structural collapse. Conversely, both pipelines and platforms will not necessarily be damaged
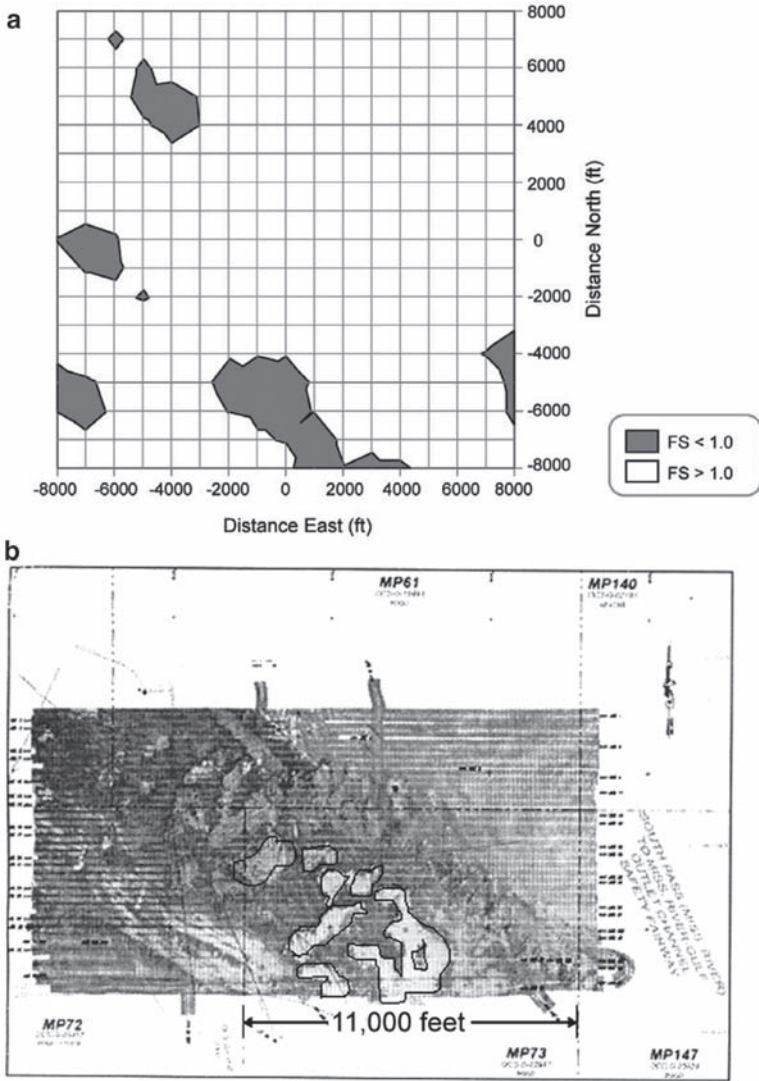
Fig. 7 (**a**) Simulated pattern of mudslide during Katrina (taken from Nodine et al. 2007) and (**b**) side-scan sonar images of mudslides in Delta after Ivan (adapted from Thomson et al. 2005).

by a mudslide. Pipelines in particular can span over disturbed areas and tolerate movements without rupturing (e.g., Thomson et al. 2005). In addition, hurricanes can damage pipelines and platforms in the Delta without mudslides occurring; bottom currents can move pipelines large distances off alignment and waves and winds can damage platforms.

4   Examples

The following examples illustrate several applications for the practical risk model described above.

4.1   Siting a New Platform

Consider the proposed location for a new platform. The annual probability that a mudslide will occur at a particular location in the Delta is shown in Fig. 8; the annual probability is depicted as a return period, where the return period is equal to inverse of the annual probability. This figure does not include site-specific geotechnical data and reflects the range of possible profiles of undrained shear strength with depth based on a sample of borings located throughout the Delta. The differences in return period across the Delta in this regional perspective (Fig. 8) indicate differences in water depth and bottom slope.

A location in Fig. 8 corresponds to an area affected by a single large storm wave, on the order of several thousand feet across and taken here as 4,000 by 4,000 feet in plan. Since a platform facility is comparable in size to the area impacted by a single wave, the probability shown in Fig. 8 is comparable to the probability that a mudslide will intersect the platform itself.
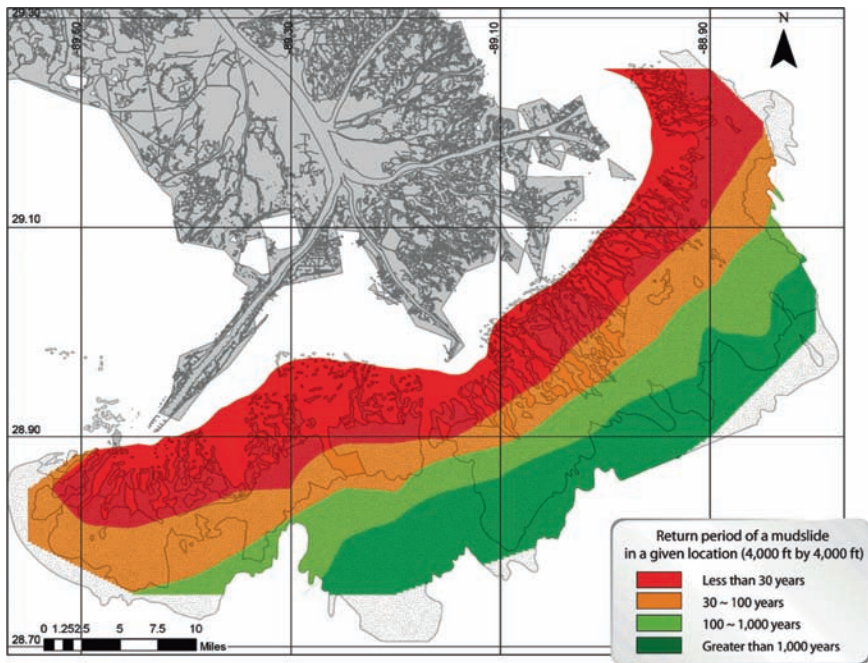
Fig. 8 Return periods of a mudslide occurring at a 4,000- by 4,000-ft location (taken from OTRC 2009; base map from Coleman et al. 1982)

For the specific location under consideration, the return period is 200 years (i.e., it is in the region with a return period between 100 and 1,000 years in Fig. 8) and the annual probability of a mudslide is 0.005. Over the 30-year design life for this facility, the probability of having at least one mudslide is $1 - e^{-30/200} = 0.14$. If we assume that the $30,000,000 facility is destroyed in a mudslide, then the expected damage is about $4,000,000 over the lifetime of the facility.

This expected cost of a mudslide can then be compared against available options for reducing the risk. For example, we could design the facility to be able to withstand the forces from a mudslide. If it is possible to accomplish this design for less than $4,000,000, then it would be worthwhile to pursue. We could also abandon the site and not build a platform. If the loss in potential revenue from not producing oil here is less than $4,000,000, then this alternative would be worthwhile.

4.2 Value of Site-Specific Soil Boring

Let's say it will cost $10,000,000 to strengthen the platform to withstand the forces of a mudslide. Since the expected cost of damage over the lifetime is less ($4,000,000), it would not be worthwhile to spend that much to reduce the risk. However, the sample of regional borings used to produce Fig. 8 includes a wide range of profiles of undrained shear strength versus depth because the soils in the Delta are highly variable. It may be valuable to first get site-specific geotechnical data before deciding whether to strengthen the platform.

Each profile of undrained shear strength versus depth considered produces a different probability that a mudslide will occur at this location over the 30-year design life. If a site-specific boring is drilled and the calculated probability that a mudslide will occur is greater than 1/3 (the $10,000,000 cost to strengthen the platform divided by the $30,000,000 cost of failure), then the option of strengthening the platform is worthwhile because it will cost less than the expected cost of damage. Based on the sample of regional borings, there is a 20% chance that a site-specific boring will lead to strengthening the platform. In addition, we can reduce the total expected cost (of either damage or strengthening the platform) from the expected damage of $4,000,000 if we do not obtain a site-specific boring and choose not to strengthen the platform to $3,000,000 if we decide whether or not to strengthen the platform based on a site-specific boring. Therefore, the value of a site-specific boring is $4,000,000–$3,000,000 = $1,000,000, and it would be worthwhile to obtain a site-specific boring if it will cost less than $1,000,000.

4.3 Existing Pipeline System Risk

One of the challenges associated with the distributed pipeline and platform systems located at present in the Delta is that a single mudslide can damage the entire system. For example, a pipeline carrying oil from production in deep water that traverses

the Delta can shut down a significant portion of the production from the Gulf of Mexico if it is ruptured. In order to assess the probability of a mudslide occurring over a larger area than the "points" considered in Fig. 8, the following assumptions are made about how variables are related spatially:

1. The size of the storm (mean maximum wave height) and the period of the maximum wave (relative to the wave height) are assumed to be perfectly correlated among locations with the same depth, as a storm that affects one location will similarly affect other nearby locations and the relationship between wave height and period tends to remain similar throughout an individual hurricane based on the hindcast data.
2. The variation in H_{max} within a given sea state and the bottom-pressure correction factor are assumed to be statistically independent between 4,000-foot by 4,000-foot locations in order to realistically model the variability in maximum wave heights and bottom pressures at nearby locations in the same storm.
3. The profile of undrained shear strength versus depth is also assumed to be statistically independent among 4,000-foot by 4,000-foot locations. This assumption is based on the observation that soil properties vary over relatively short distances (on the order of 1,000 feet or less) in the Delta.

With these assumptions, the variables that are statistically independent between points in assessing the probability of a mudslide (Eq. 6) are first separated from those that are perfectly correlated between points:

$$P\left(\text{Mudslide} \middle| \mu_{H_{max}}, T_p\right)_i = \sum_{\text{all } I_{3D}} \left[\sum_{\text{all } s_u(z)} P\left(\text{Mudslide} \middle| s_u(z), \mu_{H_{max}}, T_p, I_{3D}\right) P\left(s_u(z)\right) \right]$$

$$P\left(I_{3D}\right) \tag{9}$$

where $P(\text{Mudslide}|\mu_{H_{max}}, T_p)_i$ is the probability of a mudslide occurring at a particular point i with a given water depth and bottom slope. Then, the probability of at least one occurrence of a mudslide over an area comprising n statistically independent locations:

$$P\left(\text{At Least One Mudslide in n points} \middle| \mu_{H_{max}}, T_p\right) = 1 - \prod_{i=1}^{n}\left[1 - P\left(\text{Mudslide} \middle| \mu_{H_{max}}, T_p\right)\right] \tag{10}$$

Finally, the annual probability of at least one mudslide occurring over the total area is obtained by summing the probabilities given a sea state over all of the possible sea states:

$$P\left(\text{At Least One Mudslide in n points}\right) =$$

$$\sum_{\text{all } \mu_{H_{max}}, T_p} P\left(\text{At Least One Mudslide in n points} \middle| \mu_{H_{max}}, T_p\right) P\left(\mu_{H_{max}}, T_p\right) \tag{11}$$

The map in Fig. 9 illustrates the risk of pipeline damage throughout the Mississippi Delta region using this approach. Pipelines reported by the Minerals Management Service as of 2006 are shown in the figure. The annual probability that a mudslide will impact a pipeline is calculated in each of 70 sub-regions (each containing about 20 4,000-foot by 4,000-foot points). This probability is calculated by determining
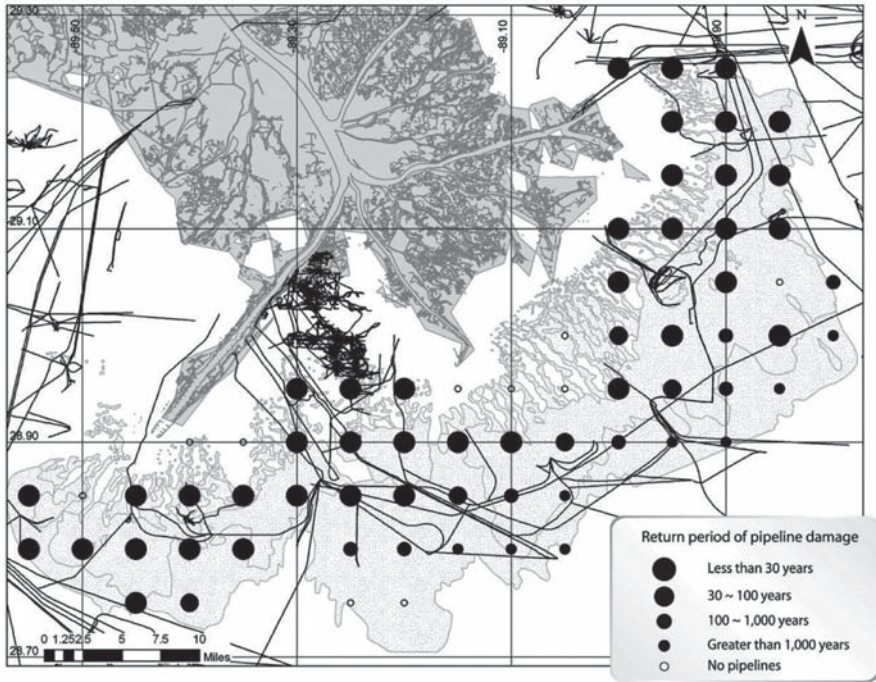
Fig. 9 Return periods for mudslides impacting existing pipelines (taken from OTRC 2009; base map from Coleman et al. 1982)

in each sub-region the number of 4,000-foot by 4,000-foot areas out of the total of 20 that contain pipelines. For example, if 50% of a sub-region is covered with pipelines, then there are 10 of 20 possible areas where a mudslide could impact a pipeline. Return periods of at least one mudslide impacting a pipeline in each sub-region are represented by symbols of various sizes, with larger return periods corresponding to larger symbols. A hollow symbol indicates that there are no pipelines in a region, and therefore a mudslide would not cause any damage to infrastructure.

The map in Fig. 9 provides useful information for planning purposes. It shows where the probability of a pipeline failure due to mudslides is the greatest, either because there are a large number of pipelines or the probability of a mudslide is high. It shows that the annual probability of mudslides impacting pipelines is high; the return period is less than 30 years throughout much of the Delta.

5   Conclusions

A practical method is proposed for assessing the probability and risk of wave-induced mudslides in the Mississippi Delta. The method has been calibrated to the extent possible using historical information. It is transparent and can readily include either generic or site-specific information about soil properties and wave characteristics.

The following conclusions were reached in developing and applying this method:

- Return periods for mudslides vary significantly across the Delta, with values less than 30 years in the shallowest water and values greater than 1,000 years in the deepest water. Three major storms, Camille, Ivan, and Katrina, have caused significant and widespread mudslide activity in the past 40 years.
- The risk for mudslide damage increases as the water depth decreases, the slope of the bottom increases, and the amount of infrastructure in a particular area increases.
- Wave period, in addition to wave height, is an important factor in mudslide vulnerability. Waves in Hurricanes Ivan and Katrina had longer-than-average periods, and Hurricane Ivan, in particular, caused significantly more mudslide activity than other storms of its magnitude due to its very long wave periods in the Delta.
- Mudslide vulnerability is highest in shallow water and in areas with low shear strengths. Areas of the Delta that have these characteristics have generally experienced mudslides in large hurricanes in the past, and it is likely that these areas will experience more mudslide activity in future storms.
- Slope angle is not a significant factor in mudslide vulnerability except in the deeper parts of the mudslide prone area (water depths greater than about 300 feet).
- Mudslides are localized features, on the order of several thousand feet in lateral extent and about 50 to 150 feet deep. The areal extent and depth of mudslides are related to the lengths and widths of the storm waves that cause them. Mudslides are not likely to lead to large-scale, regional mudflows due to the very flat slopes in the mudslide prone area and the large amount of local variation in soil shear strength.

References

American Petroleum Institute (2007) Interim Guidance on Hurricane Conditions in the Gulf of Mexico. Am Phys Inst Bull 2, INT-MET, May 2007

Bea RG, Wright SG, Sircar P, Niedoroda AW (1983) Wave-Induced Slides in South Pass Lease Block 70, Mississippi Delta, J Geotechn Eng 109(4)

Coleman JM, Prior DB, Garrison LE (1982) Subaqueous Sediment Instabilities in the Offshore Mississippi River Delta: Environmental Information on Hurricanes, Deep Water Technology, and Mississippi Delta Mudslides in the Gulf of Mexico, Bur Land Manage Open File Rep 80–02

Coyne MJ, Dollar JJ (2005) Shell Pipeline's Response and Repairs after Hurricane Ivan. Proc. Offshore Technology Conference, Houston, Texas, OTC Paper No. 17734

Forristall GZ (1978) On Statistical Distribution of Wave Heights in a Storm. J Geophys Res 83: 2353–2358

Haring RE, Osborne AR, Spencer LP (1976) Extreme Wave Parameters Based on Continental Shelf Storm Wave Records. Proc. Fifteenth Coastal Engineering Conference, Honolulu, Hawaii, Am Soc Civil Eng 1(10): 151–170

Henkel DJ (1970) The Role of Waves in Causing Submarine Landslides. Geotechnique 20(1): 75–80

Hitchcock C, Givler R, Angell M, Hooper JR (2006) A Pilot Study for Regionally-Consistent Hazard Susceptibility Mapping of Submarine Mudslides. Proc. Offshore Technology Conference, Houston, Texas, OTC Paper No. 18323

Hooper JR (1980) Crustal Layers in Mississippi Delta region of the Gulf of Mexico Mudflows. Proc. Offshore Technology Conference, Houston, Texas, OTC Paper No. 3770

Minerals Management Service (2006) Pipelines in Gulf of Mexico Region. ArcInfo EEO File 8219–148, 409:677

Nodine MC, Gilbert RB, Wright SG, Ward EG (2006) Mudflows and Mudslides during Hurricane Ivan. Proc. Offshore Technology Conference, Houston, Texas, OTC Paper No. 18983

Nodine MC, Gilbert RB, Wright SG, Cheon JY, Wrzyszczynski M, Coyne M, Ward EG (2007) Impact of Hurricane-Induced Mudslides on Pipelines. Proc. Offshore Technology Conference, Houston, Texas, OTC Paper No. 18983

OTRC (2008) Mudslides During Hurricane Ivan and an Assessment of the Potential for Future Mudslides in the Gulf of Mexico. Final Project Report, Offshore Technology Research Center, Prepared by Nodine MC, Wright SG, Gilbert RB, Ward EG, Cheon JY, Prepared for Minerals Management Service, Herndon, Virginia

OTRC (2009) Addendum to Mudslides During Hurricane Ivan and an Assessment of the Potential for Future Mudslides in the Gulf of Mexico. Final Project Report, Offshore Technology Research Center, Prepared by Nodine MC, Wright SG, Gilbert RB, Ward EG, Cheon JY, Prepared for Minerals Management Service, Herndon, Virginia

Roberts HH, Cratsley DW, Whelan T (1976) Stability of Mississippi Delta region of the Gulf of Mexico Sediments as Evaluated by Analysis of Structural Features in Sediment Borings. Proc. Offshore Technology Conference, Houston, Texas, OTC Paper No. 2425

Thomson J, Garrett M, Taylor M, and George, T (2005) Sonar surveys for pipeline inspection show extent of pipeline displacement and seafloor instability following Hurricane Ivan. Proc. Offshore Technology Conference, Houston, Texas, OTC Paper No. 17738

Wiegel RL (1964) Oceanographical Engineering. Prentice Hall, Inc., Englewood Cliffs, NJ

Zhang J, Yang J, Prislin I, Wen J, Hong K (1999) Deterministic Wave Model for Short-Crested Ocean Waves, Part I. Theory and Numerical Scheme. Appl Ocean Res 21: 167–188

GIS-Based Assessment of Submarine Mudflow Hazard Offshore of the Mississippi Delta, Gulf of Mexico

C. Hitchcock, R. Givler, M. Angell, and J. Hooper

Abstract Documented changes in bathymetry and geologic features have been incorporated into a GIS-based approach to map hurricane-induced mudflow susceptibility on the seafloor offshore of the Mississippi Delta. Available bathymetric data were interpreted to delineate areas of relative sea-floor stability over the past century, areas of active mudflow transport, and areas of active mudflow lobe deposition, incorporating mapping by Coleman et al. (1982). Our research is designed to provide regionally-consistent hazard information for the siting and design of pipelines and structures using readily available datasets. Based on interpretation of available datasets for the Mississippi Delta region, and our results for a test area using post-Hurricane Ivan (pre-Hurricane Katrina) bathymetric data, mudflow transport within the Delta generally occurs within well-defined submarine channels or gullies, spreading out onto the seafloor in deeper water to form over-lapping lobes of thick, viscous silty clay. Semi-stable areas between the mudflow channels locally provide the least hazardous locations for siting of future production facilities and pipeline routing. The zone of overlapping mudflow lobes located downslope of the gullies is an area of recent deposition vulnerable to mudflow overruns from upslope mudflows.

1 Introduction

High-rate accumulation of low shear strength, low permeability sediment within the shallow Gulf of Mexico at the mouth of the Mississippi River Delta coincides with an offshore area of significant oil and gas production (Fig. 1).

C. Hitchcock (✉), R. Givler, M. Angell, and J. Hooper
Fugro (William Lettis & Associates, Inc.), 1777 Botelho Drive, Suite 262, Walnut Creek, CA 94598, USA
e-mail: hitch@lettis.com
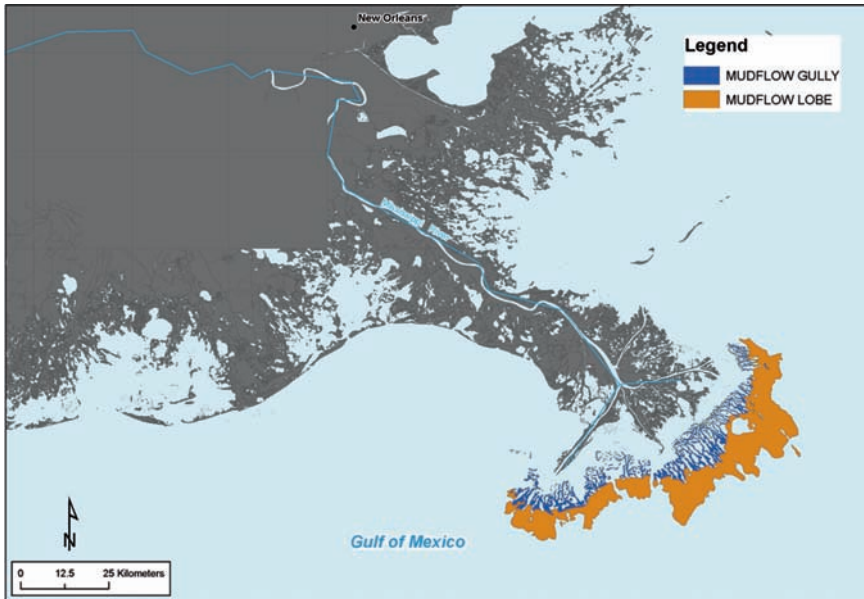
Fig. 1 Regional map showing Mississippi Delta study area

The potential for large mudflows damaging to production facilities and pipelines is greatest within, and downslope of, these unstable deposits on the delta submarine apron. Sediment transport generally occurs within well-defined submarine channels or gullies, spreading out onto the seafloor in deeper water to form overlapping mud lobes of thick, viscous silty clay (Hooper 1980; Coleman et al. 1982). Wave-induced bottom pressures accompanying large hurricanes trigger large-scale failures of these sediments, causing mudflow overruns of deep-water regions (Hooper and Suhayda 2005). Slopes exhibiting marginal static stability, and areas of past submarine failure, usually are the most susceptible to hurricane-induced failure. Oversteepened slopes in recent mudflow lobes are particularly prone to failure.

In this paper, we present a GIS-based approach for mapping mudflow suscep-tibility using existing datasets. We digitized and analyzed available bathymetric and geologic map data to de-lineate areas of relative seafloor stability over the past century, areas of active mudflow transport, and areas of mudflow deposition (Hitchcock et al. 2006). In the absence of comprehensive borehole and material properties databases, comparison of bathymetric data over time is combined with existing seafloor mapping by Coleman et al. (1982) to delineate likely areas of elevated hazard for erosion and related mudflow failures. In addition, we conducted new geomorphic mapping of the seafloor to classify the recency of mudslide move-ment and mudflow lobe deposition.

1.1 Geologic Setting

The Balize delta, or 'birdsfoot delta', is an active depositional delta that began prograding in the Gulf of Mexico over 1,000 years ago (Saucier 1963). The delta is supplied with sediment by three major distributary channels (Southwest Pass, South Pass, and Pass A Loutre). Although partial capture of the Mississippi River flow by the Atchafalaya River has diminished sediment supply to the Balize delta within the last several 100 years (Kesel 1988; Roberts 1997), the major river distributaries have grown seaward at an average rate of 100 to 200 ft/yr over the past 150 years (Morgan 1977). Deposition rates as high as 1 to 2 ft/yr at the mouths of the distributary channels result in rapid accumulation of low shear strength, low permeability sediment (Coleman et al. 1982; Hooper and Suhayda 2005).

The submerged delta apron therefore consists of thick, very weak sediments that are inherently unstable and vulnerable to hurricane wave-induced failure (Bea et al. 1975; Hooper 1980). Rapid sedimentation can change the slope of the seafloor, causing oversteepening and loading of the underlying sediments (Lindsay et al. 1984). Associated increased pore-water pressure and buildup of methane gas increases the susceptibility of accumulated sediment to failure (Wheland et al. 1978; Roberts 1997). As a result, wave-induced bottom pressures accompanying large hurricanes can cause significant failures of the accumulated sediments (Bea et al. 1975; Hooper 1980; Hooper and Suhayda 2005).

Geologic mapping by Coleman et al. (1982) has provided the context for regional and site-specific studies over the past 27 years. However, with deposition rates of 1 to 2 ft/yr, much has changed in the submarine environment including several major hurricanes. The impacts of large hurricanes (Ivan, Katrina, Rita, Ike, Gustav) to oil and gas infrastructure have been significant but the locations of change to the seafloor as a result of hurricane-induced waves and currents are poorly documented.

1.2 Mudflow Hazard

Mudflows along the submerged Mississippi delta are part of a dynamic system of sediment transport and deposition (Fig. 2). Mudflow transport generally occurs within well-defined submarine gullies (Shepard 1955; Hooper 1980; Coleman et al. 1982). Local accumulation of sediment coupled with scour during mudflow transport results in highly variable, and unstable, conditions within the gullies.

Semi-stable areas between the mudflow gullies locally are vulnerable to failure as the gullies grow in length and width over time, cannibalizing the gully margins. However, areas between mudflow gullies are believed to be generally stable with low sediment accumulation rates (Coleman et al.1982). As a result, these areas have long been targeted for siting of future production facilities and pipelines.

The mudflow gullies supply a complex zone of overlapping mudflow lobes in deeper water. The mud-flow lobe deposition area, located downslope of the gullies, is a region of recent to active deposition vulnerable to mudflow overruns from upslope

Fig. 2 Interpreted multi-beam bathymetry showing mudflow gullies (*blue*), mudflows (*orange*), and inferred transport (*white arrows*). White line is the 1982 gulfward extent of gullies from Coleman et al. (1982) and yellow line is interpreted 2005 extent
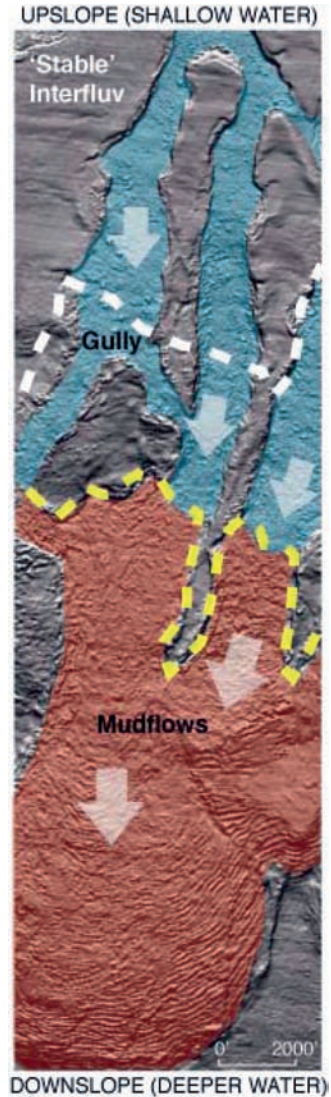
gullies and mudflows. Localized damage of pipelines and production facilities is well documented in this zone (Coleman et al. 1982; Hooper and Suhayda 2005).

2 Approach

Geographic information systems (GIS) technology enables compilation and mapping of susceptibility to failure of the land and seafloor (e.g. Hitchcock et al. 1999). Using a criteria matrix, we ranked key factors that influence submarine stability by

assigning point scores for map units (rate of change, slope, and geologic unit) in each map layer (Fig. 3). The point scores within a series of derivative GIS map layers are summed in a single interpretative map layer depicting mudflow susceptibility. This approach allows for inclusion of additional data layers and also enables the extrapolation of relatively limited site-specific, material properties data derived from boreholes and laboratory testing.

The GIS data compilation and evaluation process involved the following steps: (1) compilation of available bathymetric data and development of a composite bathymetric base map; (2) development of derivative map layers that depict rates of change of the seafloor (deposition and erosion) from historic bathymetric maps; (3) development of a submarine slope gradient map from bathymetric data; (4) digitization of available geologic mapping and tectonic structures from Coleman et al. (1982) to create a geologic map layer; (5) revision of the geologic map layer to incorporate independent interpretation of multibeam bathymetric data; (6) development of a mud-flow susceptibility criteria matrix; (7) derivation of a point score system for integration of map units for each map layer, and (8) summation of associated point scores for each layer to develop a derivative mudflow susceptibility map. Below we discuss the data and methods used to develop the susceptibility map and interpret the relative contribution of various criteria for each map layer.

The study area in the Mississippi Delta is unique in that an historic record, supported by detailed bathymetric data, exists of the seafloor over the past 140 years. Bathymetry in 1874 was compiled and drafted by Coleman et al. (1982) from maps that span the period 1872 to 1874 and incorporated copies of original soundings. Coleman et al. (1982) also provide regionally consistent bathymetry collected between 1977 and 1979.

Bathymetric data provides valuable information used to delineate submarine landforms, including individual mudflows, and derive seafloor slope. Also, these data are essential for interpretation of long-term patterns of sediment transport and deposition. In particular, comparison of bathymetric surveys provides information on changes in the seafloor bottom over time. Sediment accumulation and erosion rates derived from comparison of bathymetric surveys allow for interpretation of locations, amounts, and frequency of mass movement on the seafloor (Coleman et al. 1982). However, available bathymetric datasets vary in how seafloor measurements were collected with associated variations in resolution, accuracy, and sources of potential error that make direct comparison of the seafloor in different time periods difficult.

Geologic mapping of seafloor features provides valuable information on the processes associated with mudflow failure, transport, and deposition. Important geologic factors influencing the susceptibility of mud deposits to failure include the genesis (source), composition, and age of seafloor sediment. For this project, polygons of map units derived from Coleman et al. (1982) were digitized into a geologic map layer. Interpretation of multi-beam bathymetric data allowed revision and updating of mudflow lobe features in the mudflow deposition zone (e.g. Fig. 4).

Relative ages of underwater landforms are estimated based on the relative positions of sediments (e.g. the law of superposition with younger sediments covering older ones) and evaluation of relative geomorphic expression of landform surfaces. For example, mud-flow channels with rough surfaces typically have moved recently
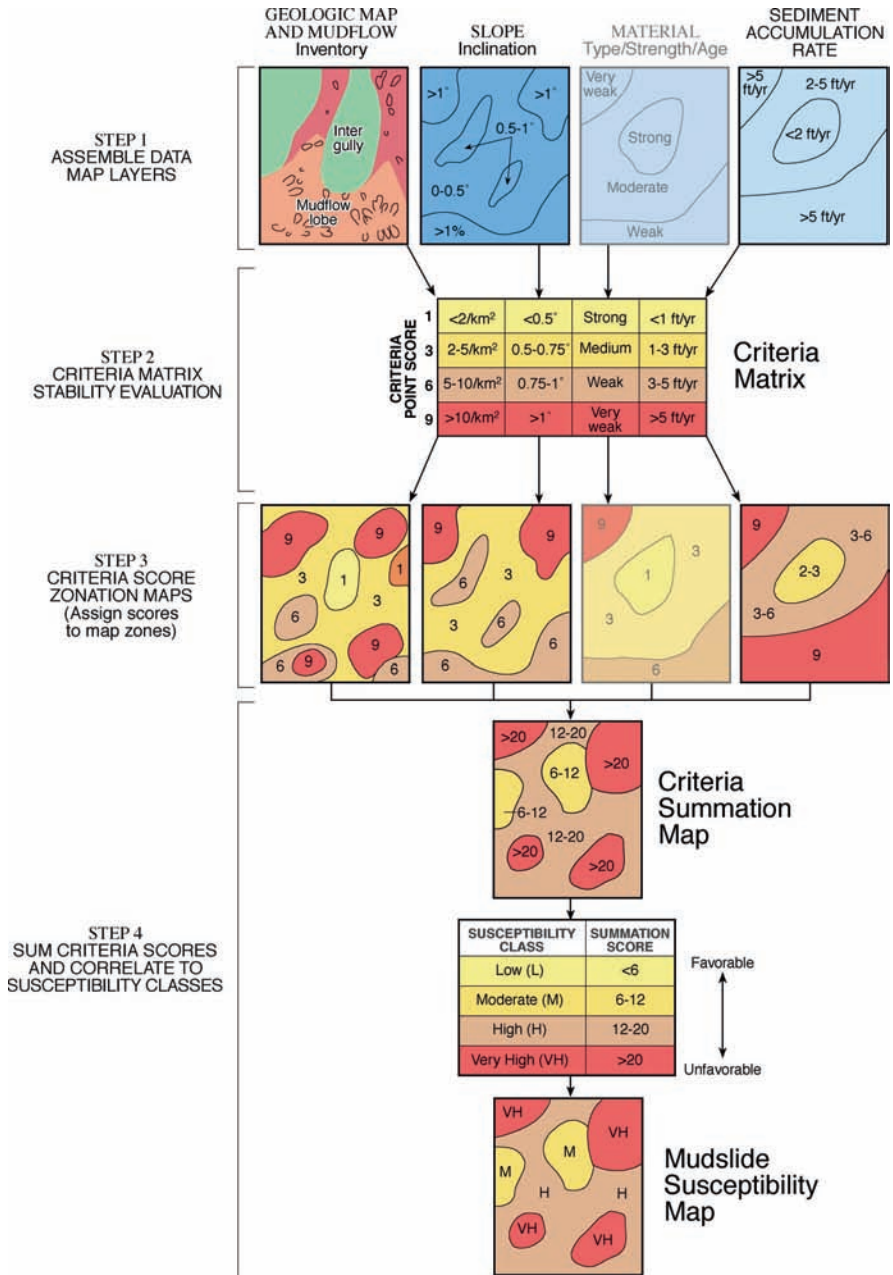
Fig. 3 Flow chart showing GIS-based mudflow susceptibility mapping procedure (adapted after Bachhuber and Hengesh 2000)
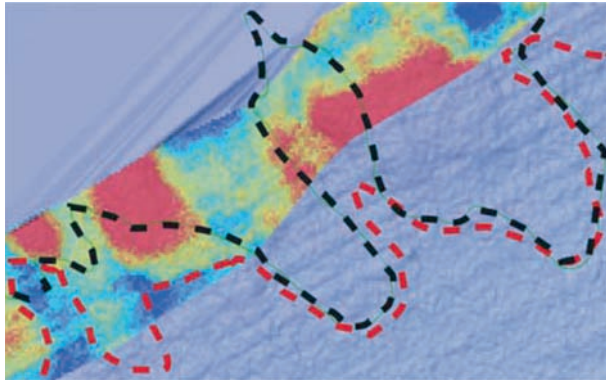
Fig. 4 Modification of mudlobe front from Coleman et al. (1982), shown as black line, to that based on 1989 NOAA multi-beam data, shown as red line. Colored band shows difference between 1989 and 1979 bathymetry with warm areas (*yellow through red*) depicting net accumulation
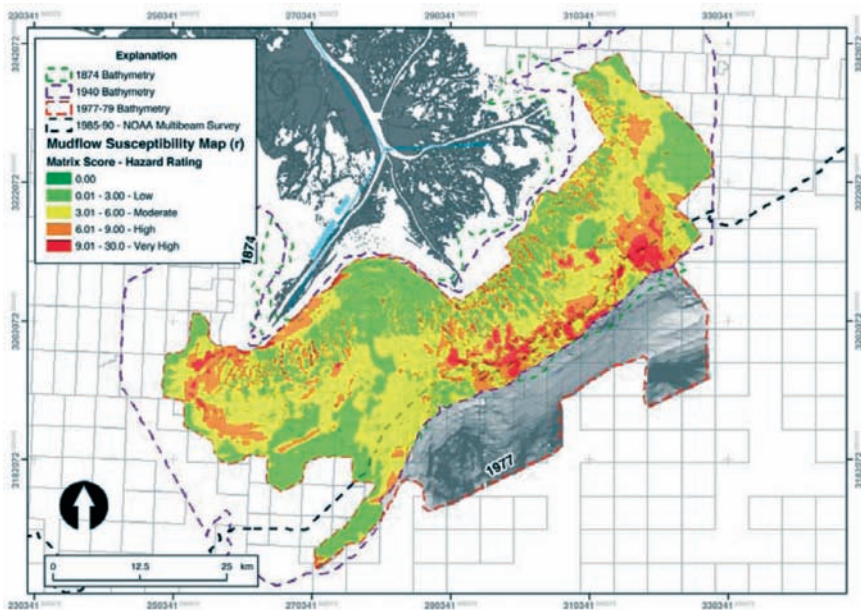
Fig. 5 Mudflow susceptibility map of study area with higher hazard areas shown in warmer colors

(i.e. within a year or two). Thus, detailed mapping provides information on the age and, indirectly, relative strength of stored sediment.

Based on relative age and activity, mudflow gullies typically are most active areas of sediment transport on the seafloor and are assigned the highest hazard point score (Fig. 5). Mudflow lobes are areas of recent deposition and vulnerable

to mudflow overruns from upslope mudflows and slope failures, and thus also assigned high hazard. Older marine landslides are assigned lower hazard ratings, as is slightly disturbed seafloor. Areas of undisturbed seafloor as mapped by Coleman et al. (1982) have the lowest associated hazard and point score.

3 Results

Our final mudflow hazard map (Fig. 5) depicts areas of relative susceptibility to mudflow failure and related change, i.e. local erosion or burial. Areas of 'very high' mudflow susceptibility may have extensive mudflows triggered during winter storms or by hurricanes along with associated submarine slope failures on steep slopes. Industry structures may be damaged by mudflow transport and deposition of new mudflows. Based on documented regional pipeline damage from Hurricane Ivan (Coyne and Dollar 2005; Mirza et al. 2006), our mapping appears to have adequately captured areas of greatest net seafloor change and associated damage, including locations of damaged platforms.

Comparison of post-Ivan bathymetric data with pre-Ivan data for a test area allows us to compare locations where mudflows likely occurred with our GIS-based mapping (Fig. 6). Our mapping adequately characterizes the largest mudflow lobes
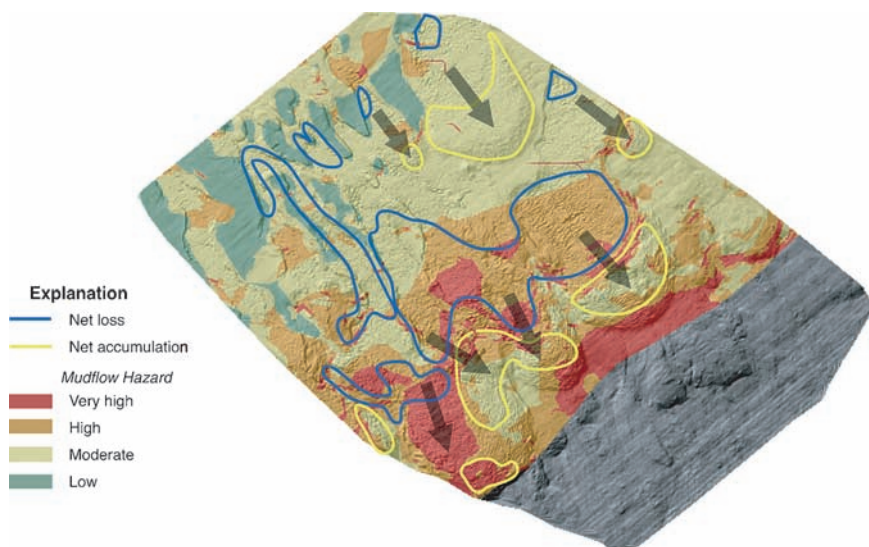
Fig. 6 Comparison of areas of net seafloor accumulation and loss derived from post-Hurricane Ivan multi-beam dataset with mudflow hazard map derived from 1977–1979 geologic mapping and bathymetric data provided in Coleman et al. (1982). Arrows show inferred directions of mass movement (from Hitchcock et al. 2006)

that have moved since 1977–1979 and which present the largest hazard. Comparison of bathymetric surveys performed in 1977–1979 and 2004 show that these large flows are migrating downslope.

4 Discussion

Our approach focused on delineating and ranking areas of greatest historic change for the Mississippi delta area as part of our map-based evaluation of portions of the seafloor with the highest likelihood of future failure. However, equally important, are areas of the seafloor that apparently have been relatively stable over time and thus likely less susceptible to future failure.

Major areas of net sediment accumulation are located off the main distributaries. These areas have progressed seaward but continue to be directly connected to deposition at the mouths of the distributaries. Major and minor mudflow gullies appear to have remained in relatively the same locations over the same time periods, with relatively minor lateral shifts. The deposition zone, located downslope of the gullies is an area of net change with recent to active deposition. A northeast-trending zone of sediment accumulation present offshore of South Pass from 1874 to 1977, coincides with a region of relatively steep slopes formed by the front of young mudflow lobes. The high slopes and high-rates of deposition suggest the mudflow lobe deposition zone should continue to be considered a very high hazard area as existing and new infrastructure may be damaged by future mudflows.

In particular, localized damage and burial of pipelines and production facilities is largely due to mudflow overruns from upslope gullies and mudflows. The distal portion of the mudflow lobe deposition zone coincides with the headward migration of salt-related growth faults near the shelf edge. This association suggests a possible relationship between the two processes and associated potential hazards in this area. Although a distinctly separate process from that of sediment transport and deposition, long-term displacement on these faults cause local steepening of submarine slopes that may serve to intensify slope failures.

Although locally associated with sediment transport and associated high mudflow hazard, major and minor mudflow gullies appear to have remained in relatively the same locations over the same time period, with minor lateral shifts. In particular, the residual map derived from the difference between the 1940 and 1874 bathymetric data sets highlighted: (1) a northeast-trending zone of mid-slope deposition and (2) poorly expressed south-southeast-trending zones of net seafloor loss (Fig. 7a). The seafloor loss areas roughly coincide with mudflow gullies (e.g. regions of active mudflow transport to the mudflow lobe front) mapped by Coleman et al. (1982). The residual map derived from the difference between the 1977–1979 and 1940 bathymetric data sets shows less deposition in the center of the zone of gully transport and much better expression of the mudflow gullies (Fig. 7b).
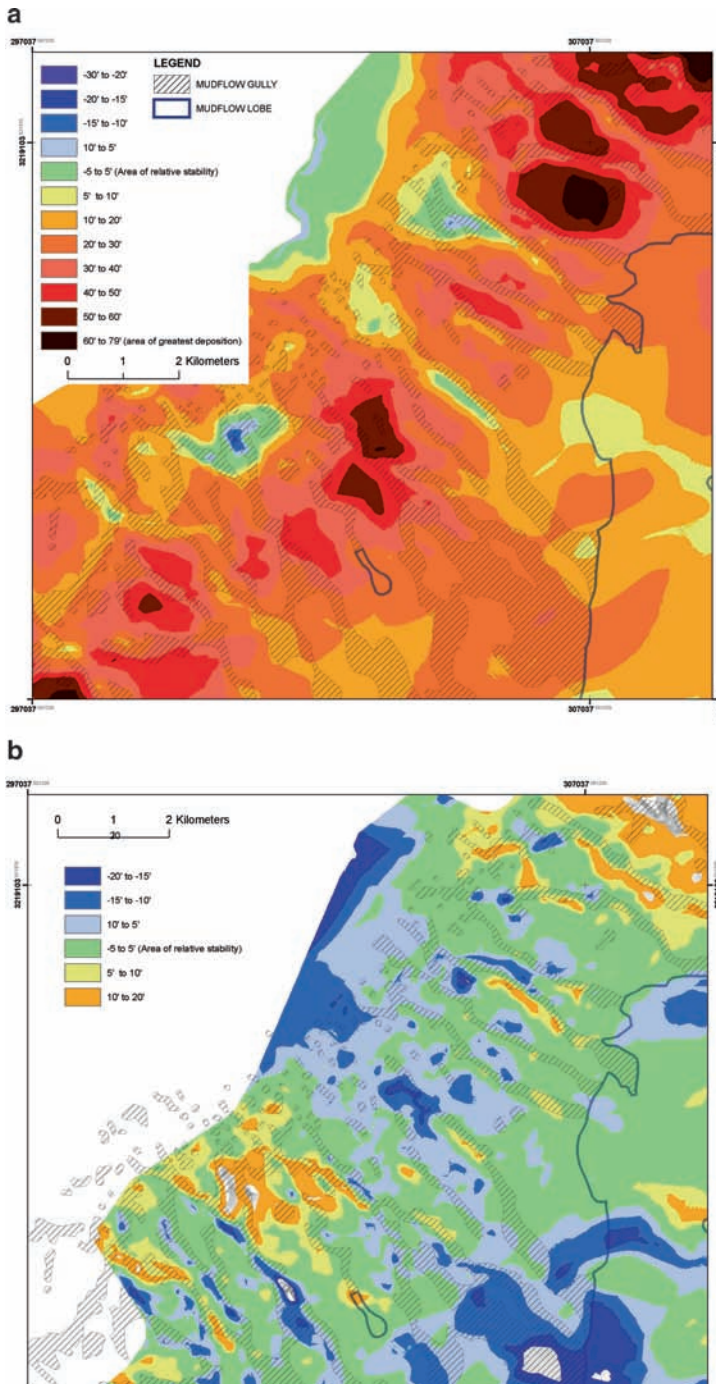
Fig. 7 Residual maps of seafloor change produced by (**a**) the difference between 1940 and 1874 bathymetry and (**b**) between 1977–1979 and 1940 bathymetry

This apparent evolution could reflect sediment bypass of the former depositional areas during progressive mudflow transport events or may capture the seafloor impact of Hurricane Camille in 1969.

Based on interpretation of the post-Ivan bathymetry, areas of net seafloor erosion are most closely associated with mudflow gullies (Fig. 2). These gullies appear to have been emptied between 1977–1979 and 2004, with the intervening gully interfluves relatively unchanged during this same period. Net seafloor loss also is closely associated with downslope failure of large mudflow lobes, in 300 to 400 feet of water, with net deposition within the mudflow lobe front. Failure of the mudflow lobes appears to consist primarily of downslope slumping with net loss in the uphill portion of the mudflow lobes and net deposition downslope. This deposition consists of mudflow lobe overflow onto older lobes, causing over-steepended mudfront slopes.

Progression of the mudflow into the gulf appears to be accompanied by gulfward development of gullies (e.g. limits of gully region shown on Fig. 4). Areas of relative stability located between active mudflow gullies likely primarily consist of older sediment. Age of the sediment following its last failure episode is a major material factor controlling future failure (Hooper 1980; Hooper and Suhayda 2005). The younger the deposit, the more likely it is to fail in the next large storm. Remnants of seafloor between mudflow lobes that don't fail as mudflows likely serve to channel the gully flows and become increasing stable as part of the gulfward evolution of the gully system into deeper water.

5 Conclusions

Using existing data, we have developed, and applied, a GIS-based approach for delineating the relative susceptibility of underwater slopes to mudflows. Our hazard mapping incorporates all available, existing datasets to produce updated hazard maps that rank the seafloor susceptibility to mudflow failure and provide a framework for inclusion and interpretation of recent and future bathymetric data, geologic mapping, and compilation of geotechnical data. Based on comparison with post Hurricane Ivan bathymetric data and published pipeline damage reports, our map of mudflow hazards accurately characterized areas of relatively high hazard. As previously identified and mapped by Coleman et al. (1982), these areas are associated with active mudflow channels and the mudflow lobe deposition front. Our mapping approach can be used on a regional basis to highlight relative mudflow hazard or, by incorporating detailed site-specific data, to evaluate hazards for pipeline corridors and siting of production facilities.

References

Bachhuber JL, Hengesh JV (2000) Seismic hazard zonation of greater San Juan area, northern Puerto Rico Coastal Plain: Proceedings Sixth International Conference on Seismic Zonation, Earthquake Engineering Research Institute, November 2000, Palm Springs, California

Bea RG, Bernard HA, Arnold P, Doyle EH (1975) Soil movements and forces developed by wave-induced slides in the Mississippi Delta: Journal of Petroleum Technology 7:500–514

Coleman JM, Prior DB, Garrison LE (1982) Subaqueous sediment instabilities in the offshore Mississippi River Delta: Environmental Information On Hurricanes Deep Water Technology, and Mississippi Delta Mudslides in the Gulf of Mexico, Bureau of Land Management Open-File Report 80:1–49

Coyne MJ, Dollar JJ (2005) Shell Pipeline's Response and Repairs after Hurricane Ivan, OTC Paper #17734

Hitchcock C, Givler R, Angell M, Hooper JR (2006) A Pilot Study for Regionally-Consistent Hazard Susceptibility Mapping of Submarine Mudslides. OTC paper #18323

Hitchcock C-S, Loyd R-C, Haydon W-D (1999) Mapping liquefaction hazards in Simi Valley, Ventura County, California: Environmental and Engineering Geoscience 5:441–458

Hooper JR (1980) Crustal layers in Mississippi Delta mudflows, OTC Paper #3370:277–287

Hooper JR (1996) Foundation soil motion in South Pass 47, Offshore Technology Conference, OTC Paper #7953

Hooper JR, Suhayda JN (2005) Hurricane Ivan as a geologic force: Mississippi Delta Front sea-floor failures: OTC Paper #17737

Kesel RH (1988) The decline in the suspended load of the lower Mississippi River and its influence on adjacent wetlands: Environmental Geology and Water Science 11:271–281

Mirza S, Skinner J, Mathew A, Ekstrom L (2006) Hurricane Ivan-Pipeline Damage, Integrity Assessment and on Bottom Stability, OTC Paper #18183

Morgan DJ (1977) Recent geologic history and geomorphology of the Mississippi River Delta: Geoscience and Man, XVI, Louisiana State University, p. 34

Roberts HH (1997) Dynamic changes of the Holocene Mississippi River Delta plain: The delta cycle: Journal of Coastal Research 13:605–627

Saucier R (1963) Recent geomorphic history of the Ponchartrain basin: Louisiana State University Coastal Studies Series 9, 114 p

Shepard RP (1955) Delta-front valleys bordering the Mississippi distributaries: Geological Society of America Bulletin 66:1489–1498

Whelan T, Ishmael JT, and Rainey GB (1978) Gas-sediment interactions in Mississippi delta sediments: Offshore Technology Conference, OTC Paper #3166

Spatial Analysis of Shallow Slope Instability Incorporating an Engineering Geological Ground Model

B. Mackenzie, J. Hooper, and D. Rushton

Abstract Within a GIS (geographical information system), spatial analysis techniques can be used to apply deterministic methods for identifying and mapping areas susceptible to shallow submarine mass movements. This paper describes such a method which allows spatially widespread, rapid, repeatable and cost-effective evaluation of shallow submarine slope risk. A deterministic approach has the advantage of providing a quantitative output; useful in subsequent project risk assessment. The use of GIS in this way is well established. Many of the method limitations described in the literature can now be overcome. This paper describes some advances through which these limitations are being addressed, and the compromises that still need to be made. The paper places emphasis on GIS modeling of the full three-dimensional variation of geotechnical input parameters. This approach allows the type of sophisticated ground model now becoming available from regional engineering geological and geohazard studies to be harnessed and exploited. The approach described in the paper has been applied on deepwater oil and gas projects having development areas of over 1,000 km^2.

1 Introduction

Submarine slope instability is a risk to many offshore oil and gas developments, particularly in deepwater areas. Authors have described risks and associated mitigating measures in various deepwater regions (Jeanjean et al. 2005;

B. Mackenzie (✉), J. Hooper, and D. Rushton
Fugro GeoConsulting Limited, Fugro House, Hithercroft Road, Wallingford, Oxfordshire, OX10 9RB, UK
e-mail: b.mackenzie@fugro.co.uk

Hooper and Prior 1989 (Gulf of Mexico); Kvalstad et al. 2002 (Norwegian Sea); Evans et al. 2007 (West Nile Delta); Orren and Hamilton 1998 (Caspian Sea)).

In order to design, install and successfully bring onstream an oil and gas development in an area of potential submarine slide activity, the slide instability risks must not only be understood, but must be quantified. This is the only way that the project can relate and balance the risks, and mitigating effort, to the overall project value.

The overall quantified slope instability risk is an aggregate of component probabilities and consequences, including: (i) the probability of slide occurrence, (ii) the probability of the slide then spatially impacting development infrastructure, and (iii) the probability that this impact will cause damage having a cost. This paper focuses on the first stage of this quantitative risk assessment process – the prediction of slide occurrence. However, it will be seen that, if a predictive method can also output key physical slide attributes such as spatial extent and thickness, then the method also helps quantify the damage consequence, another step in the risk assessment process.

2   Landslide Prediction Methods and GIS Applicability

Different techniques exist to predict slide occurrence. Some authors (Soeters and Van Westen 1996; Van Westen et al. 1997; Dai and Lee 2001) have placed these techniques into four categories: inventory, heuristic, statistical and deterministic. Each method has its relative merits and limitations, as summarized in Table 1.

All the techniques originate from methods first developed for slope stability assessment in onshore environments. However, they are also generally applicable in the submarine environment, for instance by using high resolution seabed bathymetry data in place of aerial imagery to perform submarine slide inventory mapping.

Table 1 can be viewed as showing a progression, from top to bottom, from qualitative to quantitative stability risk assessment. All of the methods also lend themselves to GIS implementation. In the simplest case, a GIS represents an ideal tool to compile, manage and present a landslide inventory, with the added advantage that that the accompanying slide parameters can be included in a GIS attribute table. Hitchcock et al. (2006) describe the implementation of a heuristic approach using GIS technology to map mudflow susceptibility in the Gulf of Mexico. Here, the relative contributions of geology, slope, and bathymetric drivers were ranked and captured in an expert-assigned scoring system. These scores were then aggregated and assigned a mudflow susceptibility class (low, moderate, high, very high) which was then mapped over the study area.

Authors have previously described the use of GIS to apply deterministic slope stability methods (Graham 1984; Wu and Sidle 1995; Dai and Lee 2001). Jeanjean et al. (2005) describe the application of a deterministic method to identify areas having a low safety factor against shallow slope failure, over an entire field of interest. The input soil strength varied over the field, but was a constant value with depth at any given location. In the case of the deterministic method, GIS spatial analysis techniques can be used directly to realize the method's key advantage - the calculation of factors of safety (FOS) against slide failure. Via probabilistic methods

Table 1 Summary of predictive methods for landslide occurrence

Technique	Description	Advantage(s)	Limitation(s)
Inventory	Shows location of existing landslides on a map, accompanied by key characterization parameters: e.g. type, subtype, size, activity	Straight-forward; yields good insight into whole slope instability record of an area	Basic; time-consuming; does not directly identify areas susceptible to new landslides
Heuristic	Use algorithms to estimate landslide potential based on terrain input variables	Incorporates expert opinion	Poor reproducibility of results due to high reliance on expert experience; high subjectivity in weightings and ratings assigned
Statistical	Statistical determination of combinations of variables that have led to past failures. Statistical methods include multi-variate or Bayesian approaches	Mathematically incorporates existing knowledge into predictive tool; data-driven; objective	Complexity of analysis, especially with large numbers of causative terrain parameters
Deterministic	Use slope stability analysis and limit equilibrium methods to calculate factor of safety	Yields quantitative results; repeatable	Landslide mechanisms need to be assumed and simplified, e.g. one-dimensional infinite slope theory; requires detailed input data and good knowledge of ground conditions

(e.g., Nadim et al. 2003), the FOS can be developed into a probability of failure thus enabling fully quantified risk assessment. Building on the assertion that a quantified risk assessment is ultimately required for an offshore oil and gas development to achieve sanction, it follows that a deterministic approach should be applied at some stage. This paper focuses on the implementation, using GIS, of the deterministic method to obtain FOS against shallow slide failure. It is nevertheless important to emphasize that a deterministic approach should still be preceded and substantiated by other methods, and that no one method should be applied alone in achieving an overall understanding of the slope instability risk to a project.

3 Deterministic Slope Stability Analysis

3.1 Limitations and Advances

The limitations of the deterministic method include its reliance on detailed input data and a good knowledge of the seabed conditions. However, advances in deep-water bathymetric and geotechnical data acquisition, twinned with advances in

engineering geology and geohazard assessment (e.g., Thomas et al. 2009) are reducing the uncertainties inherent with these limitations. These advances are leading to the availability of sophisticated and spatially resolute terrain and soil models for many of the world's slide-prone deepwater development areas. The amount of information available would form an overwhelming dataset for interpretation in anything other than a GIS-based terrain analysis.

Another previously noted limitation of GIS implementation of deterministic models is the inability to model the influence of neighboring pixels (neighborhood operations), and the inability to model the third dimension (depth). This need no longer be a limitation, as will be described, with an emphasis on modeling depth variability.

Table 1 also notes that landslide mechanisms need to be simplified for implementation in a numerical-based GIS mapping algorithm. This might be true for a solution performed completely within GIS. However, parallel advances using hybrid solutions are reducing the reliance on simplified models. Xie at al. (2003) describe a method enabling full 3D analysis through a combination of GIS spatial analysis and an external column-based 3D slope stability model.

Overall, GIS implementation of a deterministic slope analysis remains a technical compromise, but one in which *not all* of the current limitations need apply. In the analysis described herein, the modeled landslide is maintained at a relatively simple level (one-dimensional infinite slope), but incorporates a complex, spatially resolute and depth-dependent ground model. The use of numerical-based mapping methods in GIS enables this analysis to be performed rapidly over wide areas. Furthermore, despite the complexity of the ground model, it remains a model and is consequently subject to uncertainty. However, the use of GIS also allows the rapid design and execution of sensitivity studies in which the ground model can be parametrically varied.

3.2   Infinite Slope Theory Formulation

The basic formula giving FOS against shallow mass movement is as follows, where shear resistance and shear load are calculated over the same hypothesized failure surface:

$$FOS \quad = \quad \frac{available\,shear\,resistance}{applied\,shear\,load} \tag{1}$$

For an infinite slope under static submerged conditions, and where mass movement results simply from an imbalance between downslope gravity load and soil undrained shear strength, Eq. 1 can be expressed:

$$FOS \quad = \quad \frac{s_u}{\gamma' z \sin \beta \cos \beta} \tag{2}$$

where: s_u = soil undrained shear strength (kPa) at depth z
z = depth of failure plane below, and parallel to, seabed (m)
γ' = soil submerged unit weight, average to depth z (kN/m^3)
β = seabed slope (°)

Equation 2 can be further modified to model drained soil response, and also to incorporate non-static loading such as the effect of a downslope seismic acceleration, as follows:

$$FOS = \frac{(s_u/z) + (\gamma' \cos^2 \beta - \gamma\, k_{seis} \cos\beta\sin\beta)\tan\phi'}{\gamma' \cos\beta\sin\beta + \gamma\, k_{seis} \cos^2 \beta} \tag{3}$$

where: γ = soil total unit weight (kN/m^3)
ϕ' = soil effective friction angle (°)
k_{seis} = seismic acceleration coefficient (-)

The product of the seismic acceleration coefficient, k_{seis}, and the acceleration due to gravity gives the seismic acceleration. The use of the seismic acceleration coefficient in this way represents a recognized simplification where the additional downslope load is applied as a quasi-static load equal to the product of the soil mass and its resolved downslope acceleration.

Further adaptations can be made to Eq. 3 to incorporate the effects of excess pore-water pressure in the soil, and also the influence of external loads, such as might be imposed by seabed structures or pipelines on the seabed. Equation 3, and variants, allowing for external structure loading and excess pore-water pressure, have been used by the author in region-wide GIS assessments of seabed susceptibility to shallow mass movements. These assessments have used, as their input, GIS ground models derived from regional engineering geological studies. A description of the type of ground model typically now available is given below, followed by a description of its actual implementation in a GIS slope stability assessment.

4   GIS Ground Model Availability – State of the Art

4.1   Ground Model Components

The term ground model, in this context, encompasses the data required to characterize seabed topography and the geotechnical and geological conditioning factors, including the temporal element. Combined, these govern the occurrence, size and extent of shallow slide events. A typical process for the development of the ground model is described by Thomas et al. (2009). Seabed topography is now typically available to the slope stability engineer as a digital three-dimensional surface derived from ultra-ultra high resolution autonomous underwater vehicle (AUV) survey data. AUV bathymetry data typically exist at a resolution of 2.5 m, or finer, for today's deepwater development projects.

The geotechnical and geological conditioning factors are those parameters required to compute soil shear resistance and loading, the balance between which governs stability. With reference to Eqs. 2 and 3, these include undrained shear strength (s_u), total and submerged unit weight (γ, γ'), and effective friction angle (ϕ').

4.2 Representation of Full Spatial Variability

In reality the above parameters vary spatially as a function of depth as well as location. The seabed model sourced by the GIS stability analysis should ideally reflect this. A convenient means of defining the geotechnical variability across a site is to use terrain systems or soil provinces (Campbell 1984). A soil province is defined as an area within which soil conditions share a similar stratigraphic sequence; usually the soils within a given soil province have shared a similar geological and geomorphological history. There is often a visible correlation between soil province mapping and bathymetry, since the seabed bathymetry can reveal much about the process by which the soil has arrived at its present state.

Figure 1a shows a portion of seabed terrain, and highlights four individual locations which have each been subject to different geological or geomorphological processes. The simple block model in Fig. 1b depicts these processes schematically. Consequently, each location has a different shear strength profile (Fig. 2), a key parameter in assessing shallow slide potential.
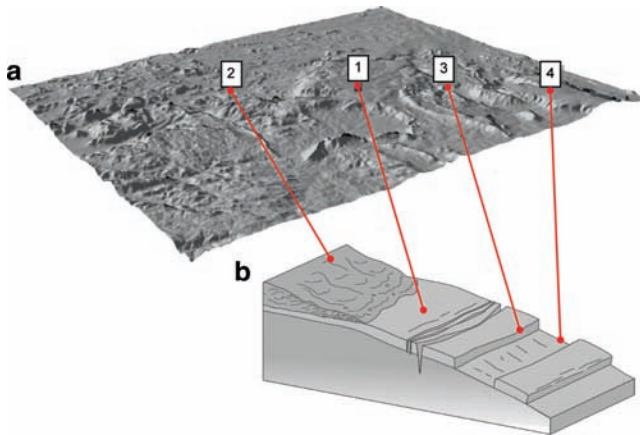
Fig. 1 (**a**) Three-dimensional seabed rendering (×2.5 vertical exaggeration) of shallow slope instabil-ity study area, showing locations affected by different geological or geomorphological processes. Marked areas: (1) normally consolidated deposit, (2) underconsolidated debris flow deposit, (3) pull-apart window, exposing overconsolidated deposit, and (4) block slide on failure plane having residual strength. (**b**) Simple block model idealizing typical locations of the four different processes marked in Fig. 1a
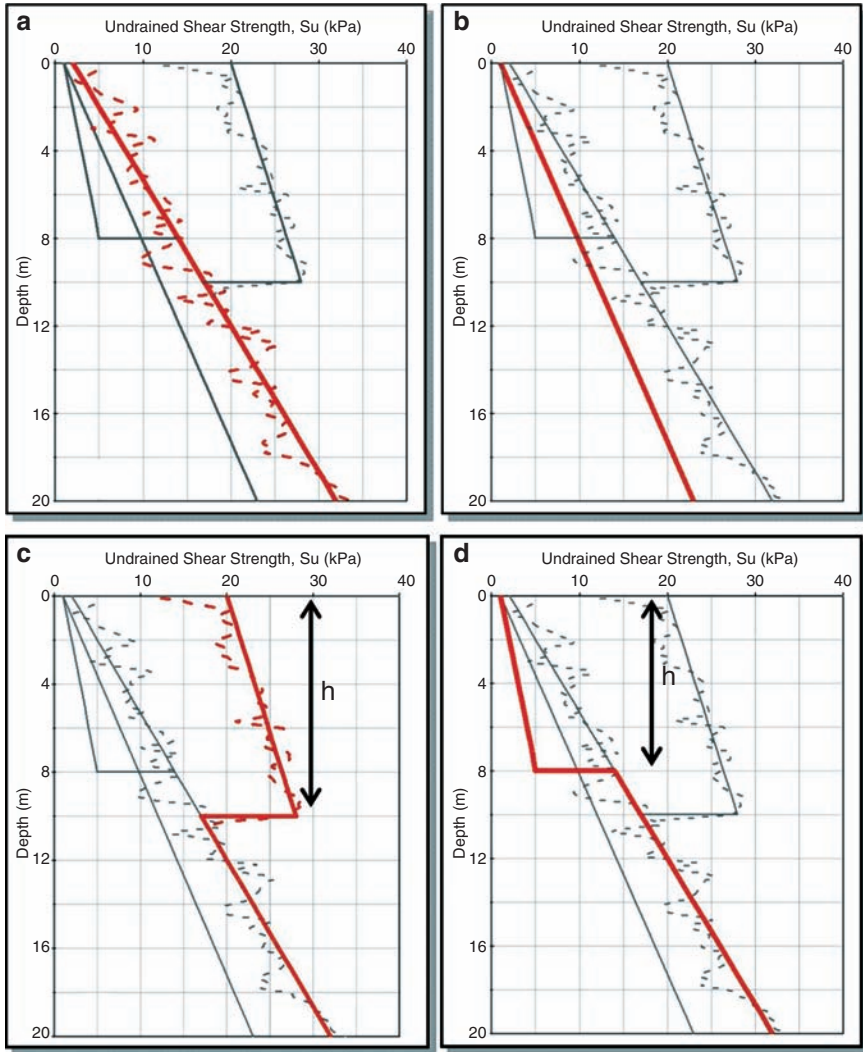
Fig. 2 Characteristic design undrained shear strength profiles for each location highlighted in Fig. 1. (**a**) Location 1 (normally consolidated); (**b**) Location 2 (underconsolidated); (**c**) Location 3 (overconsolidated); and (d) Location 4 (residual/previous slide). Each location's profile (*bold line*) is superimposed on a composite of the other profiles (*faint lines*). The dashed profiles represent the strength profiles derived directly from cone penetration test data. 'h' denotes the elevation to a strength profile discontinuity

On Fig. 1a, Location 1 sits in a normally consolidated depositional environment, for which one would expect a low shear strength at the immediate seabed, below which the strength would increase linearly with depth (constant shear strength gradient). Location 2 represents an underconsolidated deposit. Here, owing to recent higher deposition rates, or in this case loading from an earlier mass movement

event, the soil contains excess pore-water pressure and hence exhibits a lower strength than if normally consolidated. At Location 3 the soils are slightly overconsolidated; here surface soil has been removed by previous slide activity and the underlying unloaded soil is slowly weakening, just like an excavation on land – but remains stronger than a normally consolidated seabed soil. Location 4 has been subject to previous slide movement, and comprises a layer of disturbed, weaker mass flow deposit separated from the underlying soil by a shear plane.

Examination of the seabed and sub-seabed in this way, especially if assisted by shallow geophysical and geotechnical site investigation data, allows delineation into soil provinces. These provinces lend themselves to GIS mapping and subsequent spatial analysis of the seabed and sub-seabed extremely well. An important point to note is that, within any soil province, the layer change elevations (denoted at depth 'h' in Fig. 2c, d) need not be a fixed GIS attribute for that soil province. Rather, and better still, these elevations are themselves defined in a GIS isopach layer resulting from a geophysical interpretation. In other words, although the soil layering follows a set *sequence* within a soil province, the layer thicknesses and hence the soil parameters are fully spatially variable. The cross-referencing of stratigraphic elevations from isopach maps allows for computational efficiency, as opposed to storing depth-variable data on a per-location basis.

5 GIS Implementation and Results

5.1 Implementation

The required numeric seabed model parameters are captured in a suite of GIS raster surfaces. A raster surface is a grid of pixels, or raster cells, where each cell has a value assigned based on the soil province in which the cell lies (or based on an isopach layer in the case of continuously mapped stratigraphic elevation).

For the depth-variable parameters such as undrained shear strength (s_u), raster surfaces defining s_u at the top of each stratigraphic layer, and defining the gradient of s_u within each layer, are produced. These are readily generated from a GIS soil province map, likely to have initially been created as a vector map with lines or polygons delineating the soil provinces. A GIS soil province vector map is a convenient and effective data management tool, since all key parameters can be captured as data attributes.

Figure 3 reproduces the GIS attribute table for the study area introduced earlier in Fig. 1. The soil province map, and its underlying attribute table, is then used to spawn individual parameter surfaces on a stratigraphic layer-by-layer basis. At the same time, these individual parameter surfaces are converted into raster format. Through the resulting suite of raster surfaces, the GIS then has the full 'picture' of the spatial variability of the key parameters over the study area, including buried strength discontinuities on previous slide planes.

FID	Shape*	Soil_Prov	Desc	No_Layers	L1_z_top	L1_z_base	L1_Su_top	L1_Su_grad	L1_Gamma	L2_z_top	op	L5_Su_grad	L5_Gamma
0	Polygon	1	Normally Consolidated	1	0.0	999.0	2.0	1.5	4.5	0	0	0	0
1	Polygon	2	Underconsolidated	1	0.0	999.0	1.0	1.1	3.5	0	0	0	0
2	Polygon	3	Overconsolidated upper l	2	0.0	10.0	20.0	0.8	6.5	0	0	0	0
3	Polygon	4	Previous slide history	2	0.0	8.0	1.0	0.5	3.0	0	0	0	0

Record: |◄ ◄ | 1 | ► ►| | Show: All Selected | Records (0 out of 4 Selected) | Options ▾

Fig. 3 Example attribute table for a soil province polygon map. Each data row corresponds to a mapped soil province. A suite of raster surfaces is produced using this attribute table, with raster cell values corresponding to each attribute field. The stratigraphic boundary depths, such as captured in the data field 'L1_z_base' above, can alternatively be sourced from an isopach map to give a truly continuous variation over the study area

GIS spatial analysis is used to perform raster-based algebraic operations using the seabed model. The slope stability equation is evaluated in a raster algebra expression which yields an output raster surface of FOS. This is calculated on a cell-by-cell basis, using the appropriate strength, density, slope, and other geological controls, and triggering factors captured in the suite of input raster maps. In the case of an included seismic load, the seismic acceleration coefficient, k_{seis}, is also required in the raster algebra expression. This can be programmed as a region-wide constant, or alternatively taken from GIS map layer, where a seismic ground response analysis has been performed and peak ground acceleration mapped as a variable with soil province or proximity to source.

5.2 Results

The spatial analysis is repeated on a soil layer-by-layer basis. This is not a computationally intensive task, although geoprocessing techniques can further increase efficiency. The analysis outputs a suite of predicted FOS surfaces, each showing the spatial variation of predicted safety factor appropriate for each layer top or base. These can be analyzed in further raster algebra operations to seek and map, for example, the minimum safety factor in each raster cell (Fig. 4a, b), and the depth at which the minimum safety factor is predicted to occur (Fig. 4c). Figure 4c is essentially a color scale map of critical shear depth, which could alternatively be output as a contour map. This critical shear depth map enlightens us in two ways: firstly, by examination, it reveals the existence and size of potentially spatially extensive failure planes. Secondly, it indicates the probable thickness of a potential slide block, a key physical attribute used when assessing the damage level caused by a slide on a seabed structure.

Superposition of a slope aspect map (Fig. 4d) helps indicate slide direction, and where unstable zones might move in unison, diverge, or collide. From the results mapping, simple risk metrics can also be generated, such as percentage of overall study area predicted to be at risk, for differing assumed input conditions.
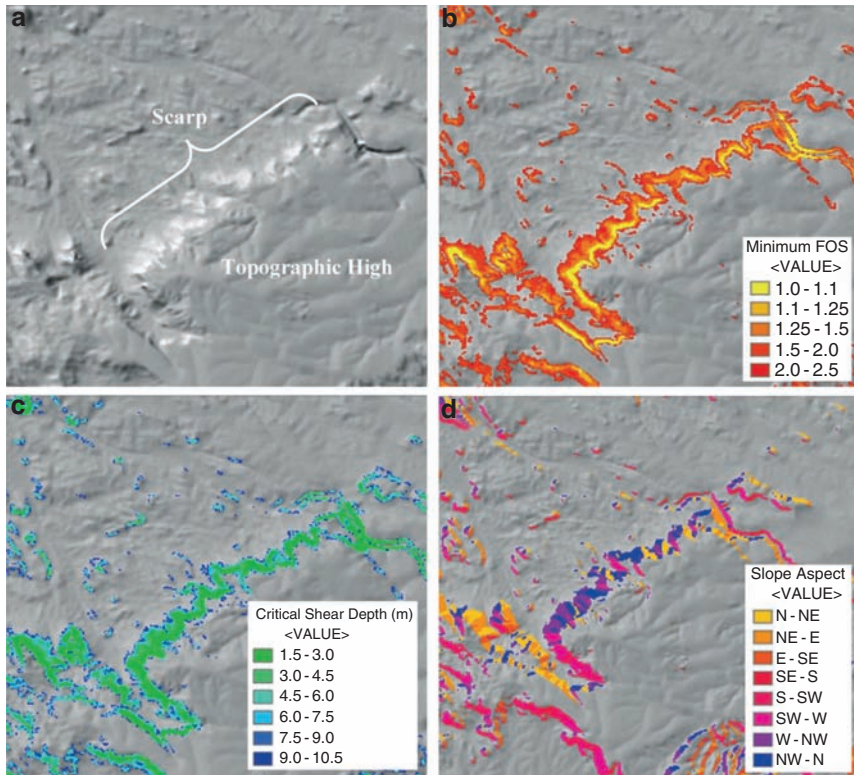
Fig. 4 (**a**) (*top left*): Seabed terrain image – selected portion of study area, focusing on topographical high and associated scarp. (**b**) (*top right*): GIS spatial analysis results for selected area showing color-shaded factor of safety against shallow slope failure. (**c**) (*bottom left*): Results showing predicted slide thickness. (**d**) (*bottom right*): Results showing slope aspect of slide-susceptible zones

Of more importance to the facilities engineer is the identification of at-risk zones which are coincident with, or close to, planned seabed infrastructure. The ability to do this in a GIS requires a simple overlay operation with the proposed infrastructure map

6 Conclusions

The paper has described a method allowing a spatially resolute and fully variable soil model to be incorporated in a deterministic analysis of seabed slide instability within a GIS. The use of a deterministic analysis needs to be accompanied by other expert-applied assessments; however, a deterministic approach is ultimately required to deliver the numerical information required to perform a quantified project risk assessment.

The ability to capture the full depth variability in the ground model, including strength profile discontinuities, represents a key advance. This approach allows the analysis to estimate the likelihood of slide re-activation as well as new movements. It also allows estimation of slide thickness. Slide thickness is a key parameter used in the soil-structure interaction analysis to assess the damage consequence for seabed structures.

Simplifications regarding slide mechanics still currently need to be made in order to implement a deterministic slide analysis in a GIS. However, this compromise is balanced by the ability of the method to analyze rapidly such large extents of seabed, while using a more representative ground model. This makes it a cost-effective option for performing parametric sensitivity studies, arguably not possible by any other means.

References

Campbell KJ (1984) Predicting offshore soil conditions. Proc Offshore Technol Conf, Houston, Texas.

Dai FC, Lee CF (2001) Terrain-Based Mapping of Landslide Susceptibility using a Geographical Information System: a Case Study. Can Geotech J 38:911–923.

Evans T, Usher N, Moore R (2007) Management of Geotechnical and Geohazard Risks in the West Nile Delta. Proceed 6th Intern Offshore Site Investigation and Geotechnics Conf: Confronting New Challenges and Sharing Knowledge, Soc Underwater Technol, Lond.

Graham J (1984) Methods of Slope Stability Analysis. In: Brunsden D, Prior DB (Eds) Slope Instability, Wiley, New York, pp. 171–215.

Hitchcock C, Givler R, Angell M, Hooper JR (2006) A Pilot Study for Regionally-Consistent Hazard Susceptibility Mapping of Submarine Mudslides. OTC 18323, Proc Offshore Technol Conf, Houston, Texas.

Hooper JR, Prior DB (1989) Regional Analysis of Slope Stability for Deepwater Engineering. Oceans 09, sponsored by the Mar Technol Soc & Oceanic Eng Soc IEEE 5:1536–1540.

Jeanjean P, Liedtke E, Clukey E, Hampson K, Evans T (2005) An Operator's Perspective on Offshore Risk Assessment and Geotechnical Design in Geohazard-Prone Areas. Frontiers in Offshore Geotech: ISFOG 2005.

Kvalstad T, Gauer P, Kayina AM, Nadim F, Bryn P (2002) Slope Stability at Ormen Lange. Conference Proc Offshore Site Investigation and Geotechnics: Diversity and Sustainability, Soc Underwater Technol, Lond.

Nadim F, Krunic D, Jeanjean P (2003) Probabilistic Slope Stability Analyses of the Sigsbee Escarpment. OTC 15203, Proc Offshore Technol Conf, Houston, Texas.

Orren R, Hamilton I (1998) Frontier Geohazard Site Investigations – Experiences from the Caspian Sea. Offshore Site Investigation and Foundation Behaviour: New Frontiers, Soc Underwater Technol, Lond.

Soeters R, Van Westen CJ (1996) Slope Instability Recognition, Analysis, and Zonation. Landslides: Investigation and Mitigation, NERC Transportation Res Board Spec Rep 247:129–177.

Thomas S, Hooper JR, Clare M (2009) Constraining Submarine Geohazards to the Past: A Conceptual Review of the Assessment of the Potential Impact of Submarine Mass Movements on the Planning of Seabed Developments. Proc 4th Intern Symp on Submari Mass Movements and their Consequences, Austin, Texas.

Van Westen CJ, Rengers N, Terlien MTJ, Soeters R (1997) Prediction of the Occurrence of Slope Instability Phenomena through GIS-Based Hazard Zonation. Geologische Rundschau 86:404–414.

Wu W, Sidle R (1995) A Distributed Slope Stability Model for Steep Forested Basins. Water Resour Res 31:2097–2110.

Xie M, Esaki T, Zhou G, Mitani Y (2003) Geographical Information Systems-Based Three-Dimensional Critical Slope Stability Analysis and Landslide Hazard Assessment. J Geotech Geoenviron Eng 129:1109–1118.

Estimating the Empirical Probability of Submarine Landslide Occurrence

E.L. Geist and T. Parsons

Abstract The empirical probability for the occurrence of submarine landslides at a given location can be estimated from age dates of past landslides. In this study, tools developed to estimate earthquake probability from paleoseismic horizons are adapted to estimate submarine landslide probability. In both types of estimates, one has to account for the uncertainty associated with age-dating individual events as well as the open time intervals before and after the observed sequence of landslides. For observed sequences of submarine landslides, we typically only have the age date of the youngest event and possibly of a seismic horizon that lies below the oldest event in a landslide sequence. We use an empirical Bayes analysis based on the Poisson-Gamma conjugate prior model specifically applied to the landslide probability problem. This model assumes that landslide events as imaged in geophysical data are independent and occur in time according to a Poisson distribution characterized by a rate parameter λ. With this method, we are able to estimate the most likely value of λ and, importantly, the range of uncertainty in this estimate. Examples considered include landslide sequences observed in the Santa Barbara Channel, California, and in Port Valdez, Alaska. We confirm that given the uncertainties of age dating that landslide complexes can be treated as single events by performing statistical test of age dates representing the main failure episode of the Holocene Storegga landslide complex.

Keywords Submarine landslides • age dating • probability

E.L. Geist (✉) and T. Parsons
U.S. Geological Survey, 345 Middlefield Road, MS 999. Menlo Park, CA 94025, USA
e-mail: egeist@usgs.gov

1 Introduction

Estimating the likelihood of submarine landslide occurrence is an important component of an overall hazard assessment. This likelihood applies not only to the direct hazard posed by this geologic phenomenon to offshore structures, pipelines, and submarine cables but also to the indirect hazard of tsunami generation. For the latter, knowledge of both the distribution of landslide sizes and the distribution of events in time is necessary to comprehensively quantify tsunami hazards at a coastline (Geist et al. 2009; Geist and Parsons 2009). The distribution of submarine landslide sizes has been suggested to follow a power-law, in the case of debris avalanches off the north coast of Puerto Rico (ten Brink et al. 2006) or a log-normal distribution in the case of debris flows off the U.S. Atlantic coast (Chaytor et al., 2009). In this paper, we instead focus on methods to determine the rate of occurrence of submarine landslides in time, where recurrent landslides are embedded in a well-developed stratigraphic sequence. We also limit our analysis to empirical techniques. Computational techniques have been developed to determine landslide probability based on the probability distribution of the triggering mechanism (i.e., strong seismic ground motion for most of the landslides considered) (ten Brink et al., 2009) and based on long-term stratigraphic simulations (Hutton and Syvitski 2004). However, there is significant uncertainty in determining the probability of slope failure conditioned upon not only the triggering mechanism but also geotechnical parameters such as the factor of safety and distribution of pore pressure. Where data exist on the past occurrence of submarine landslides, we argue that uncertainty in occurrence rates is better quantified by empirical techniques.

The objective of determining probability is obviously hampered by the lack of an instrumental record of submarine landslide occurrence (as we have for submarine earthquakes) and the sparse number of age dates from core data relative to the number of submarine mass movements that have been mapped throughout the world. However, we can avail ourselves of probabilistic techniques that have been previously developed to estimate earthquake occurrence rates from onshore paleoseismic sequences (i.e., from excavation trenches across faults or from coastal records of coseismic subsidence/uplift). The problem of predicting the occurrence rate of both earthquakes and landslides from paleo-events share some similarities: in determining the occurrence rates, one has to take into account the open time intervals (before the first and after the last event in the sequence) as well as the uncertainty in age dating the horizons. For the paleoseismic problem, both Bayesian and Monte Carlo techniques have been developed (Savage 1994; Ogata 1999; Parsons 2008). One difference between observed submarine landslide sequences and onshore paleoseismic sequences is that for landslides, we often only have age dates of the most recent event and the age date from a horizon that underlies the landslide sequence. After a brief description of the field data used to identify landslide sequences, we introduce an empirical Bayes analysis particularly suited for this case. The empirical Bayes analysis is based on a Poisson distribution that assumes landslide events are independent from one to another. Finally, we examine whether landslide complexes

such as Storegga, in the Norwegian Sea, can be treated as a single event for the empirical Bayes analysis in Section 4.

2   Data

Two types of data are needed for this analysis: (1) geophysical data to both map landslides at the sea floor and to identify previous occurrences of landslides in cross section and (2) age dates of sediment that bracket the landslide event. Multibeam bathymetry and side scan sonar technologies have successfully been used to map landslide complexes in great detail. In cross-section, older landslides are identified from seismic reflection data using a variety of controlled sources, depending on the desired resolution and depth of acoustic penetration.

To date a landslide, ideally age dates from pre- and post-landslide rocks are obtained from cores along its distal edge (e.g., Normark et al. 2004). It is also possible to tie seismic reflectors above and below the landslide to ages from nearby drill holes (e.g., Fisher et al. 2005). The method of dating is typically radiocarbon analysis of microfossils, though other techniques are also used (e.g., Lee 2009). Dating submarine landslides is complicated by uncertainty that arises from the large carbon reservoir in the oceans, which causes radiocarbon ages of marine samples to appear several hundred years older than coeval terrestrial samples to globally varying degrees (Stuiver and Braziunas 1992). It is rare to have dates for all landslides in an observed sequence – typically we may only have the date of the youngest landslide and the date of a seismic horizon that underlies the landslide sequence.

3   Empirical Bayes Analysis

Bayesian methods are particularly well suited to estimate the empirical probability and associated uncertainty from small sample sizes. To start with, we assume that landslide events occur in time according to a Poisson distribution, such that the number of events n occurring in time t is distributed according to

$$p(n|\lambda, t) = \frac{(\lambda t)^n e^{-\lambda t}}{n!} \qquad (1)$$

where λ is the rate or intensity parameter of the distribution. This distribution is commonly used for phenomena that are rare, but have very many opportunities to happen. One property of the Poisson distribution is that the time between events (inter-event times) are independently distributed. In addition, in its cumulative form, the probability that one or more events will occur in a particular time window does not vary with the time since the last event.

For many observed submarine landslide sequences, the dates of individual landslide events are unknown. However landslides occur in a stratigraphic sequence, and commonly, a datable horizon exists below the sequence. The rate parameter λ itself is uncertain and can be treated as a random variable. To estimate the distribution of values that λ can attain for this type of problem, we can use Bayes theorem, which states that for any parameter θ and set of empirical data $z = z_{1,...},...,z_{m}$, the posterior distribution $\pi(\theta|z)$ is given by

$$\pi(\theta|Z) = \frac{L(Z|\theta)\,\pi(\theta)}{\int L(Z|\theta)\,\pi(\theta)\,d\theta} \tag{2}$$

where $L(z|\theta)$ is the likelihood function, $\pi(\theta)$ is the prior distribution and the integral in the denominator is the marginal probability.

The empirical Bayes approach is greatly simplified if one chooses a prior probability distribution that is "conjugate" to the likelihood function: that is, if the resulting posterior distribution is in the same distribution family (e.g., the exponential distribution family) as the prior distribution. The distribution pairs are often called "conjugate priors". The conjugate prior to the Poisson distribution is the Gamma distribution, with a probability density function given by

$$f(x) = \frac{\beta^{\gamma} x^{\gamma-1} e^{-\beta x}}{\Gamma(\gamma)} \tag{3}$$

where the mean is γ/β and the variance is γ/β^{2}. Taking the rate parameter λ as the random variable in the prior distribution Eq. 3, it can be shown that with a Poisson likelihood function, the corresponding posterior distribution is also a Gamma distribution (Mortgat and Shah 1979; Campbell 1982) such that

$$\pi(\lambda|z) = \frac{(\beta')^{\gamma} \lambda^{\gamma'-1} e^{-\beta'\lambda}}{\Gamma(\gamma')} \tag{4}$$

This is often called the Poisson-Gamma model. The posterior distribution parameters γ' and β' are calculated from the number of landslide occurrences (N) and the time period of observation (T):

$$\gamma' = N + (\mu/\sigma)^{2} \tag{5}$$

$$\beta' = T + \mu/\sigma^{2} \tag{6}$$

where μ and σ are the best estimate of the mean and standard deviation for the rate parameter λ (Mortgat and Shah 1979; Campbell 1982). The resulting posterior probability of the rate parameter is almost identical to that determined from generalized Monte Carlo analysis, such as used in Parsons and Geist (2009), where discrete event intervals were not used. Applying this Poisson-Gamma model to submarine landslide occurrence, we can estimate the most likely mean return time ($1/\lambda$) and

uncertainty through equation Eq. 4. A similar formulation has been developed by Savage (1994) for analyzing paleoseismic horizons, but using the Beta-Binomial conjugate prior model.

3.1 Case Study 1: Santa Barbara Channel

The Bayes Poisson-Gamma model is first applied to a landslide sequence identified in the Santa Barbara Channel, southern California (Fisher et al. 2005) that includes the Goleta landslide complex as its youngest event. Submarine landslides there may present a significant tsunami hazard (Borrero et al. 2001). A seismic reflection profile across the Goleta landslide complex shows several landslide events (Fig. 1). The seismic horizon labeled "A" (yellow line) is estimated to be 170 ka old from correlating seismic horizons with an oxygen-isotope curve (red line) at a nearby Ocean Drilling Project hole (Site 893).

For this example, therefore, we take the number of landslide occurrences (*N*) as three and the time base as 170 ka. The resulting distribution of mean return times from the Poisson-Gamma model is shown by the blue curve in Fig. 2.

Fisher et al. (2005) indicate that a seismic horizon B (not shown on Fig. 1) underlies the deepest landslide and is correlated with a 200 ka biostratigraphic age
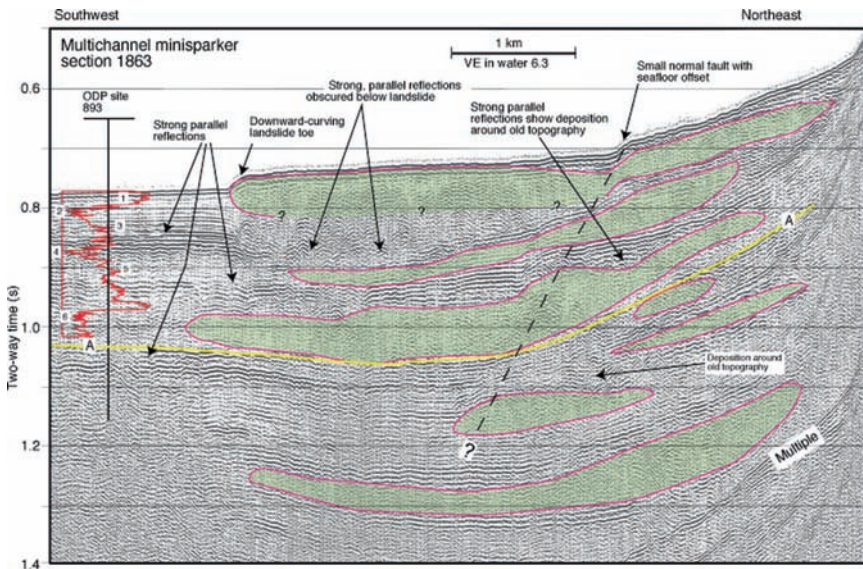
Fig. 1 High-resolution minisparker seismic reflection data oriented parallel to the axis of the Goleta landslide complex. Red outline and green shading indicates interpreted landslide deposits. Red curve is the oxygen isotope variation from ODP site 893. Numbers represent marine isotope stages. Figure from Fisher et al. (2005)
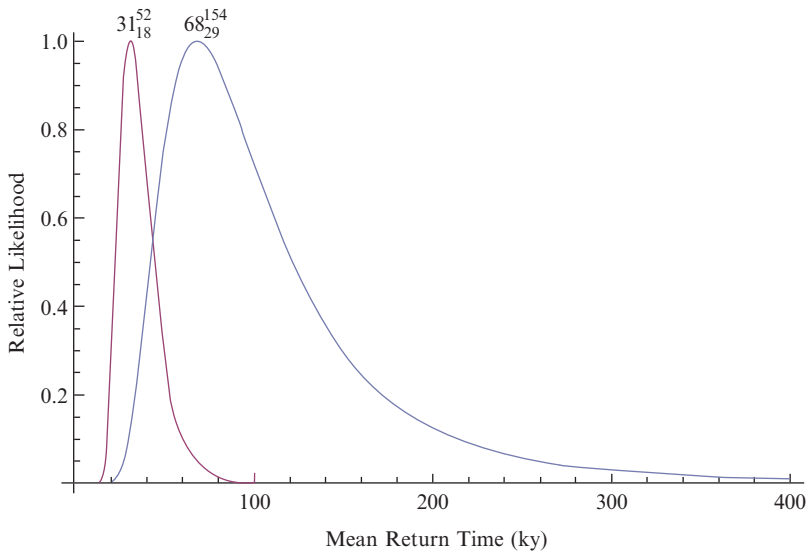
Fig. 2 Distribution of mean return times ($1/\lambda$) for two estimates of the occurrence of landslides in Santa Barbara Channel. Blue curve: three landslide occurrences younger than Horizon A (170 ka) shown in Fig. 1. Red curve: seven landslide occurrences younger than approximately 200 ka. Most likely mean return time (ka) and 95% confidence range (indicated by sub- and superscripts) in the mean return time indicated for each curve

at the nearby ODP hole. The corresponding rate estimate based on all of the imaged landslides and the age of horizon B is shown by the red curve (Fig. 2). It should be noted, however, that this curve includes much smaller landslides than the Goleta landslide complex. In addition, although the red curve appears to have less uncertainty than the blue curve, the 200 ka age used in calculating the red curve may be more uncertain than the age of Horizon A used in the blue curve.

3.2   Case Study 2: Port Valdez

The next case study we examine is landslide occurrence in Port Valdez, Alaska, an enclosed fjord. Ryan et al. (this volume) used seismic reflection data to find that as many as five debris flow events underlie the most recent one, which was triggered by the M = 9.2 1964 Great Alaska earthquake. Hence, in the statistical analysis $N = 6$. The 1964 earthquake in Port Valdez triggered several nearly simultaneous debris flows, one of which destroyed part of the town of Valdez. Other flows generated tsunamis resulting in high tsunami runups around the coastline. The ages of older debris flows are estimated by determining the sedimentation rate in Port Valdez. The first debris flow event before the 1964 debris flow is interpreted to be contemporaneous with the penultimate megathrust
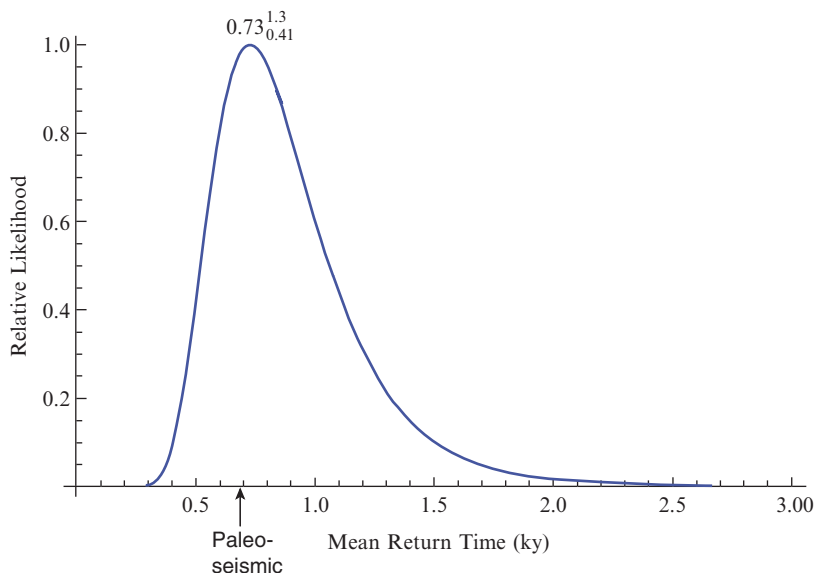
Fig. 3 Distribution of mean return times $(1/\lambda)$ for debris flows in Port Valdez ($N = 5$). Blue curve: time base is 4 ka. Most likely mean return time (ka) and 95% confidence range (sub- and super-scripts) in the mean return time indicated above curve. Mean return time for paleoseismic events (0.69 ka) indicated by arrow (Carver and Plafker 2008)

earthquake (approximately 913–808 yr BP from a nearby paleoseismic site). Ryan et al. (this volume) suggest that all of the debris flows imaged in the seismic reflection data were triggered by large megathrust earthquakes younger than 4 ka. Therefore, in the statistical analysis the time period of observation is $T = 4{,}000$ years. The resulting distribution of mean return times is shown in Fig. 3.

The most likely mean return time of 730 years is very close to the 690 year mean return time (excluding open intervals) of megathrust earthquakes from paleoseismic data (Carver and Plafker 2008), supporting the hypothesis of Ryan et al. (this volume).

4 Sub-Events Within Landslide Complexes

Within landslide complexes such as Goleta, there are often numerous sub-events identified from geophysical data. Sub-events are defined here as individual landslides in a complex that can be distinguished using geophysical and geologic data. Two questions then arise: (1) with regard to the hazards landslides pose, do sub-events occur essentially simultaneously (e.g., with respect to the phase speed of wave propagation for tsunami hazards)? (2) Can sub-events be considered as occurring simultaneously with regard to the above empirical probability analysis (i.e., as independent events), given

the uncertainty in the age dates? The Holocene Storegga landslide complex presents an ideal case for analysis of these questions, because of the detailed observations of the complex from many authors and the large dimensions of the failure.

4.1   Case Study 3: The Holocene Storegga Landslide Complex

The Holocene Storegga landslide complex in the Norwegian Sea has been mapped in detail using multibeam bathymetry, side-scan sonor, and ROV-based bathymetry (see summary by Haflidason et al. 2005). In addition, overlapping relationships between sub-events are established from high resolution seismic reflection data, and absolute age dates of many of the sub-events have been obtained from cores.

Most sub-events are dated during the time of the main failure and have a mean of approximately 7250 yr BP (Haflidason et al. 2005). There are also as many as 10 other small sub-events that have younger age dates and are not simultaneous with the main failure. It is likely that most, if not all, of these later small failures are related to (i.e., conditional upon) the main event, owing to their location along the northern slide escarpment.

If the entire Holocene Storegga complex failed more or less synchronously, then the dates associated with the main failure can be assumed to follow a normal distribution owing to uncertainties in age-dating techniques (although the actual distribution may be more complex) (Bronk Ramsey 1998; Steier and Rom 2000). Alternatively, we might expect intervals between different sub-events to follow an exponential distribution as in the earlier examples discussed in this paper. To decide between the alternatives, we used the Shapiro-Wilk test (Shapiro and Wilk 1965; Stephens 1974) which is useful for testing empirical distributions based on small sample sizes. The test on the ensemble of failure dates associated with the main failure ($N = 45$) indicates that the normal distribution hypothesis can be rejected at a 90% confidence level. If, however, we exclude just the single youngest date from that ensemble (6,460 yr BP associated with a small sub-event near the head of the Holocene Storegga complex), then the normal distribution hypothesis cannot be rejected. Because the younger sub-events are much smaller than other sub-events that make up the main episode, it is reasonable to treat this landslide complex as a single event in geologic time. However, because of the uncertainty related to age dating, we cannot determine whether sub-events occurred alone or together with other sub-events in terms of the hazards they pose. Overlapping relationships and geotechnical arguments can aid in this determination (e.g., Locat et al., 2009).

6   Conclusions

Determining the hazards posed by submarine landslides is partly dependent on an understanding of their probability of occurrence. Assuming that multiple occurrences of large landslide complexes imaged by seismic reflection data represent

independent events, the primary probability distribution parameter that is estimated is the rate parameter (λ). Ideally, in locations where we have a sequence of landslide events, we would also have age dates of sediment that bracket each of the landslides to which we could directly apply statistical techniques developed to analyze paleoseismic sequences (Savage 1994; Ogata 1999; Parsons 2008). Presently, however, we typically only have age dates of the youngest landslide and of a seismic horizon that lies below all of the landslide events. Applying the Bayes Poisson-Gamma model to this situation, we determine the most likely ages and 95% confidence bounds for two examples: from the Santa Barbara Channel and Port Valdez. Analysis of the age dates representing the main failure episode of the Holocene Storegga landslide complex suggests that landslide complexes can be treated independently for this analysis, given uncertainty in age dating techniques. This analysis treats the Poissson probability as stationary (i.e., constant λ). However, the rate of occurrence may be linked to glacial cycle and climate change (e.g., Lee 2009; Ryan et al. this volume), that would imply a non-stationary Poisson process. More age dates of both global and local landslide sequences are needed to determine the long-term variation in λ.

References

Borrero JC, Dolan JF and Synolakis CE (2001) Tsunamis within the eastern Santa Barbara Channel. Geophys Res Let 28: 643–647.

Bronk Ramsey C (1998) Probability and dating. Radiocarbon 40: 461–474.

Campbell KW (1982) Bayesian analysis of extreme earthquake occurrences. Part I. Probabilistic hazard model. Bull Seismol Soc Am 72: 1689–1705.

Carver G and Plafker G (2008) Paleoseismicity and neotectonics of the Aleutian subduction zone – an overview. In: Freymueller JT, Haeussler PJ, Wesson RL and Ekström G (eds) Active Tectonics and Seismic Potential of Alaska. Geophysl Mono Ser 179. Am Geophys Union, Washington, D.C., pp. 350.

Chaytor JD ten Brink US Solow AR and Andrews BD (2009), Size distribution of submarine landslides along the U.S. Atlantic Margin, Mar Geol 16–27.

Fisher MA, Normark WR, Greene HG, Lee HJ and Sliter RW (2005) Geology and tsunamigenic potential of submarine landslides in Santa Barbara Channel, southern California. Mar Geol 224: 1–22.

Geist, E.L., and T. Parsons (2009), Assessment of source probabilities for potential tsunamis affecting the U.S. Atlantic Coast, Mar Geol 264, 98–108.

Geist EL, Parsons T, ten Brink US and Lee HJ (2009) Tsunami Probability. In: Bernard EN and. Robinson AR (eds), The Sea 15: 93–135. Harvard Univ Press, Cambridge, Mass.

Haflidason H, Lien R, Sejrup HP, Forsberg CF and Bryn P (2005) The dating and morphometry of the Storegga Slide. Mar and Petrol Geol 22: 123–136.

Hutton EWH and Syvitski JPM (2004) Advances in the numerical modeling of sediment failure during the development of a continental margin. Mar Geol 203: 367–380.

Lee, H. J. (2009), Timing of occurrence of large submarine landslides on the Atlantic ocean margin, Mar Geol 53–64.

Locat, J., H. Lee, U. ten Brink, D. Twichell, E.L. Geist, and M. Sansoucy (2009), Geomorphology, stability and mobility of the Currituck slide, Mar Geol 28–40.

Mortgat CP and Shah HC (1979) A Bayesian model for seismic hazard mapping. Bull Seismol Soc Am 69: 1237–1251.

Normark WR, McGann M and Sliter RW (2004) Age of Palos Verdes submarine debris avalanche, southern California. Mar Geol 203: 247–259.

Ogata Y (1999) Estimating the hazard of rupture using uncertain occurrence times of paleoearthquakes. J Geophys Res 104: 17 995–18 014.

Parsons T (2008) Monte Carlo method for determining earthquake recurrence parameters from short paleoseismic catalogs: Example calculations for California. J Geophys Res 113: doi:10.1029/2007J–B004998.

Parsons T and Geist EL (2009) Tsunami probability in the Caribbean region. Pure and Applied Geophysics 165: 2089–2116.

Ryan HF, Lee HJ, Haeussler PJ, Alexander CR and Kayen RE (this volume) Historic and paleo-submarine landslide deposits imaged beneath Port Valdez, Alaska: implications for tsunami generation in a glacial fiord. In: Mosher DC, Shipp C, Moscardelli L, Baxter C, Chaytor J and Lee H (eds) Submarine Mass Movements and Their Consequences IV, Advances in Natural and Technological Hazards Research. Springer, New York.

Savage JC (1994) Empirical earthquake probabilities from observed recurrence intervals. Bull Seismol Soc Am 84: 219–221.

Shapiro SS and Wilk MB (1965) An analysis of variance test for normality (complete samples). Biometrika 52: 591–611.

Steier P and Rom W (2000) The use of Bayesian statistics for 14C dates of chronologically ordered samples: A critical analysis. Radiocarbon 42: 183–198.

Stephens MA 1974 EDF statistics for goodness of fit and some comparisons. J Am Stat Assoc 69: 730–737.

Stuiver M and Braziunas TF (1992) Modeling atmospheric ^{14}C influences and ^{14}C ages of marine samples to 10,000 BP. Radiocarbon 35: 137–189.

ten Brink US, Geist EL and Andrews BD (2006) Size distribution of submarine landslides and its implication to tsunami hazard in Puerto Rico. Geophys Res Lett 33: doi:10.1029/2006GL026125.

ten Brink, US, Lee HJ, Geist EL, and Twichell D (2009), Assessment of tsunami hazard to the U.S. Atlantic Coast using relationships between submarine landslides and earthquakes, Mar Geol 65–73.

Constraining Geohazards to the Past: Impact Assessment of Submarine Mass Movements on Seabed Developments

S. Thomas, J. Hooper, and M. Clare

Abstract This paper presents a conceptual review of submarine mass movements and associated hazards such as run-out and turbidity currents, and their implications for the planning of exploration and development activities. Submarine mass movements are placed in the context of ground models and geohazard scenarios from which conditioning factors and trigger mechanisms can be assessed and event magnitudes estimated. The approach to dating these events in order to derive a frequency is discussed with reference to radiometric, biostratigraphic and Optically Stimulated Luminescence techniques that have been successfully deployed in recent projects. The need for good stratigraphic control, both seismostratigraphic and lithological, is emphasized. Based on the ground model and geohazard scenarios, ground movement at different locations within the mass movement system can be inferred. This understanding along with predicted soil conditions derived from the ground model and evolutionary history of the site allows the potential consequences on well conductors, facilities and flowlines to be assessed and the need for geohazard design and mitigation evaluated. These findings indicate the constraints on possible exploration and development activities.

Keywords Geohazard assessment • mass movement • seabed development • ground model • integrated study • geohazard design • mitigation • geohazard core logging

1   Introduction

Varnes (1978) presented a synthesis of onshore landslide classification, recognition, avoidance, and control that made a significant step forward from previously published work and built on a wealth of new data available from site investigations

S. Thomas (✉), J. Hooper, and M. Clare
Fugro GeoConsulting Limited, Engineering Geology and Geohazards Team, Fugro House, Hithercroft Road, Wallingford, Oxfordshire, OX10 9RB, UK
e-mail: s.thomas@fugro.co.uk

and academic research. Today we find ourselves in a similar position in the offshore environment, with a relatively recently acquired arsenal of 2D and 3D seismic surveys, high-resolution seafloor images, deepwater cores, in-situ tests, and an enhanced knowledge of mass movement processes (e.g., Lee et al. 1993; Mulder and Cochonat 1996) and conditioning factors (e.g., Masson et al. 2006). With an increased interest in deeper water projects, it is necessary for the offshore industry to identify hazards that are known to, or have the potential to, exist within a given environment and to understand their potential for impact on exploration or development activities. Traditionally when planning for submarine developments, routes or locations have been sought that avoid known geohazards. When exploring deepwater prospects it may be necessary to determine not whether the hazard can be avoided, but rather which route or location will suffer the least impact.

1.1   Submarine Mass Movements – What Are the Hazards?

The classification promoted by Mulder and Cochonat (1996) defines mass movements in terms of their occurrence as either mass slides or gravity flows. Such a division differentiates those processes that are the direct effects of mass slide activity (e.g., creep, translation, rotation, and avalanche) from those that may have evolved downslope from the point of failure (e.g., mass flows and turbidites). While this classification scheme is static, the dynamic interrelationship between mass movements has been well developed in recent publications such as Masson et al. (2006). The scheme of Mulder and Cochonat (1996) has been implemented by the authors to facilitate understanding of the adverse impact that submarine mass slides and their run-out may have on developments and to guide geohazard assessment (Table 1).

Two typical types of offshore structures are considered in Table 1 – vertical foundations (which may include, but not be limited to, piles, conductors, and caissons) and seabed-laid or shallow-buried installations (such as pipelines, flowlines, and cables). Recent work undertaken by the authors has shown that the latter may suffer in particular from geohazard impact as they can span a considerable length across many geohazard-prone areas, offering little resistance to significant mass movement events. It should be borne in mind that small gravity-based or shallow-skirted structures are not included in Table 1, but may be important components in a field development. While not a comprehensive study, Table 1 details the difference in potential geohazard impact dependent upon the location of a structure relative to mass movement. For instance, a piled foundation at the crest of a rotational failure may be subjected to vertical compression (downdrag), however a similar structure at the base of the same failure would undergo vertical extension (uplift). For simple modeling purposes, structures such as pipelines may be considered as horizontal piles; therefore the direction of applied lateral force will control the nature of deformation. Pipeline compression typically results from a parallel movement at the toe of a translational slide, whilst a perpendicular force may create dragging. In addition to these impacts, the nature of run-out will determine whether a flow has potential for loading, scour, or subsequent burial of the structure.

Table 1 Potential impacts of offshore mass movements on subsea structures dependent upon location or orientation to movement direction. The listing of impacts on foundations and seabed structures is not intended to be exhaustive, although it should be noted that not all of the impacts have potential to occur concurrently

Mass Movement Classification	Mass Movement Mechanism	Impact on Foundations ⊠		Impact on Pipeline/Flowline/Cable ○		
		Profile View	Nature of Force on Foundation	Plan View	Orientation of Movement to Installation	
					Parallel	Perpendicular
Mass Slide	Creep		Rotation About Base		Dragging Rupture Spanning	Dragging Rupture Spanning
	Translational Slide		Translation Downdrag at Crest Uplift at Toe		Stretching at Crest Compression at Toe Loss of Support Rupture Spanning	Dragging Loss of Support Rupture Spanning
	Rotational Slide		Rotation About Top Downdrag at Crest Uplift at Toe		Stretching at Crest & Toe Loss of Support Rupture Spanning	Dragging Loss of Support Rupture Spanning
	Debris Avalanche		Translation/ Rotation +/- Downdrag +/- Uplift		Compression & Stretching Loss of Support Rupture Spanning, Burial	Dragging Loss of Support Rupture Spanning Burial
Gravity Flow / Mass Flow	Debris Flow		Loading Burial Scour		Compression Burial Loading Scour	Dragging Burial Loading Scour
	Liquefied Flow		Loading Burial Scour		Compression Burial Loading Scour	Dragging Burial Loading Scour
	Fluidised Flow		Loading Burial Scour		Compression Burial Loading Scour	Dragging Burial Loading Scour
Gravity Flow / Turbidity Current	High Density Turbidity Current		Loading? Burial? Scour		Burial Loading Scour	Burial Loading Scour
	Low Density Turbidity Current		Scour?		Scour	Scour

1.2 The Geohazard Assessment Process

Geohazard assessment is required not only to predict those geological processes that may pose significant threat to a development, but to place them in a spatial and temporal context through an understanding of the evolutionary history of the site. This should allow for those geohazards with negligible, or no potential for occurrence to be eliminated, thus reducing the risk profile to the development. Table 2 details some of the tools available to modern geohazard assessment including both traditional and innovative technologies, but these tools should not be considered in isolation from each other. Integration of all available data, along with a geohazard-focused data acquisition program, is essential for a fit-for-purpose review and assessment.

For a determination of actual geohazards the authors find that multiple data acquisition is essential, promoting that as well as obtaining standard geotechnical

Table 2 Some of the tools and techniques available for a modern marine geohazard assessment, detailing typical outputs from each method of data acquisition or analysis

Geohazard assessment tool	Geohazard assessment output
Swath bathymetry	Geomorphological mapping to identify areas of potential mass movement
Ultra high resolution CHIRP data acquired from Autonomous Underwater Vehicle (AUV)	Lateral and vertical extents of mass movement deposits
Geographic Information System (GIS)	Soil province/terrain unit mapping; interrogation of spatial data; provision of data for quantitative slope stability analyses
Geotechnical testing	Soil properties such as step changes in undrained shear strength; identification of soil type for engineering purposes
Detailed geohazard core logging	Facies-driven classification; understanding of sedimentology; identification of type and magnitude of events; guides geochronological sub-sampling
Geochronological analysis	Determination of event frequency; correlation with conditioning/triggering factors
Mineralogical testing	Data may guide interpretation of sediment provenance/behavior

samples there is a need for long core samples to be taken specifically for the purposes of detailed geohazard core logging. Where cores have been subsampled for geotechnical testing, often significant sections of the stratigraphic record are removed, thereby allowing for whole event deposits to be missed, adding uncertainty to derivations of event frequencies and magnitudes. Experience of the authors has proven that reliance solely upon geophysical data may often overestimate event magnitudes, as multiple stacked mass movement deposits may appear as one large seismic unit on sub-bottom profiles, where individual deposits are below the limits of separability on seismic records. Therefore use of the term *mass movement complex* is promoted herein to describe seismostratigraphically mapped features, and *mass movement deposit* is reserved for those individual units identified from lithostratigraphic core logging.

The process of data integration should be an iterative process, identifying requirements and locations for further data acquisition at every step of the assessment. Figure 1 summarizes a geohazard assessment, from a regional-scale desk study, through a site-specific survey and investigation and finally to a deliverable. It is this deliverable that will directly inform a risk assessment (which may be qualitative, semi-quantitative, or quantitative), providing information for engineering design and/or mitigation. The key outputs of this process are a *geohazard inventory* and a *ground model* that are updated throughout the assessment process and form the discussion in the next section.
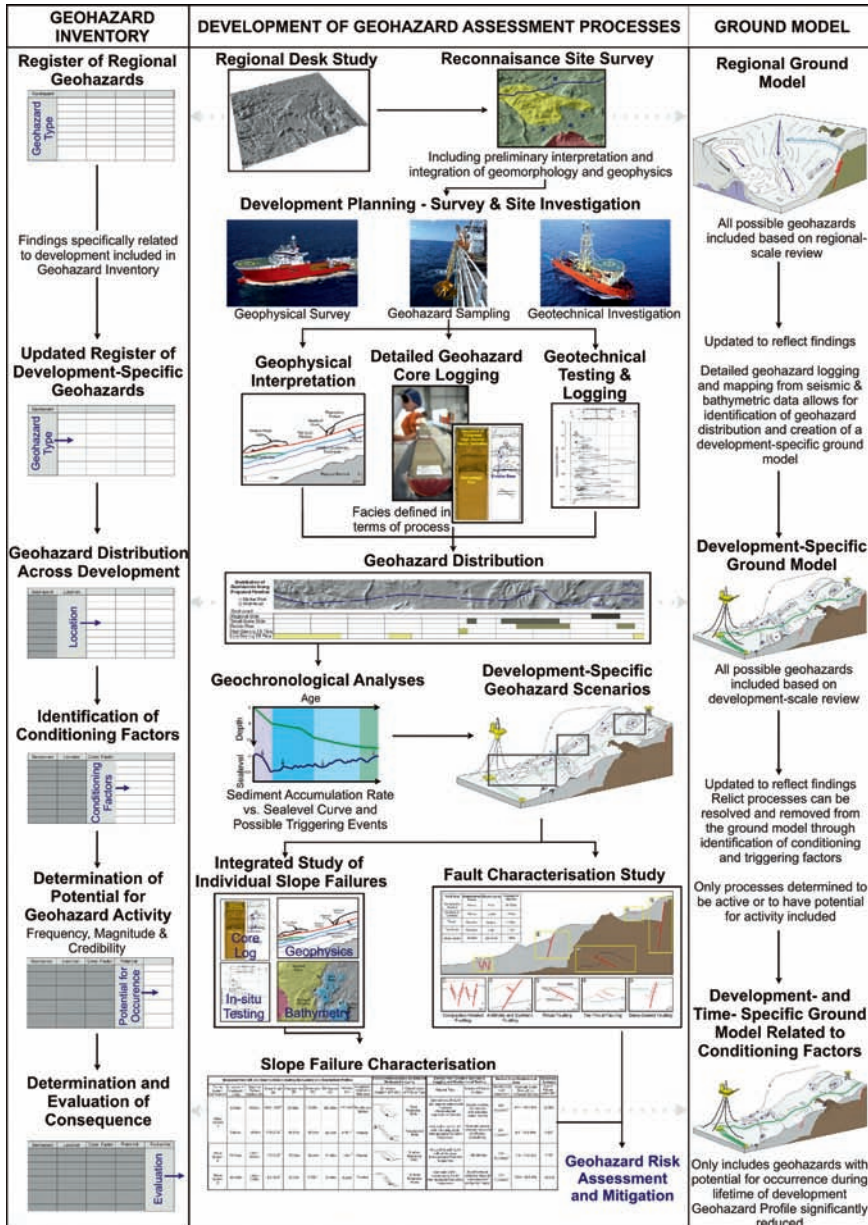
Fig. 1 A conceptual geohazard assessment process detailing how the various stages guide and update a geohazard inventory and ground model as development-specific and time-specific data become available. The final stages of assessment provide data that feed directly into front-end engineering design (FEED), modeling impact studies, and risk assessment. All images property of Fugro GeoConsulting Limited

2   Three-Dimensional Geohazard Visualization

A ground model includes a three-dimensional visualization of geohazards at a development detailing their geomorphological, bathymetrical, and geological context. By considering all geohazards in a spatial framework, a focused study can be conducted that is specific to the proposed offshore development. Figure 2 details a conceptual ground model for a typical deepwater development comprising a spar platform with spread moorings, manifolds, flowlines, and an export pipeline. The impacts of potential geohazards are varied and often significantly controlled by the seafloor topography. A geohazard inventory should be compiled concurrently with the synthesis of a ground model that aims to list all those geological processes that may have adverse consequences for the development. As the process of assessment continues, it is possible to update and populate the inventory with more specific information including spatial extents, potential for activity, frequency, magnitude, impact, evaluation, mitigation measures required, and an assessment of risk.

In order to progress the assessment to the evaluation of specific impacts, and any mitigation required, a development layout plan or route corridor is required to identify those geohazards that could potentially impact wells, facilities, or infrastructure. A *geohazard scenario* differs from the ground model in that it represents a higher-resolution study, focusing on either an individual geohazard or a specific geohazard-prone area within the development. For example, this may take the form of one scenario for direct mass slide impact, one for turbidity current activity, and another for contourite development. A *terrain systems* approach may be applied to
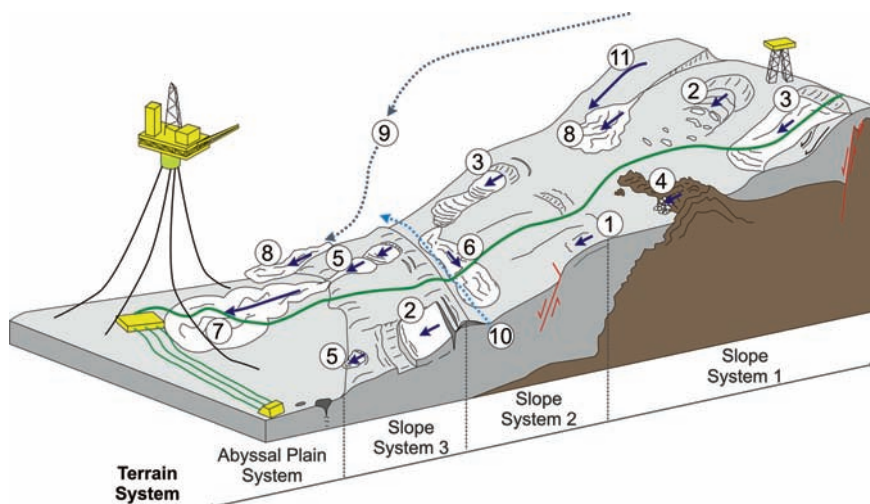
Fig. 2   A conceptual ground model illustrating a terrain system approach for geohazard assessment. Annotations are as follows: 1 – Creep; 2 – translational slide; 3 – rotational slide; 4 – debris avalanche; 5 – debris flow; 6 – liquefied/fluidized flow; 7 – high density turbidity current; 8 – low density turbidity current; 9 – hyperpycnal flow; 10 – along contour flow; 11 – laminar flow

demarcate areas particularly susceptible to different geohazards within a large development, and their predicted spatial relationship to events (Mackenzie et al. 2009). Terrain units or provinces may be identified using the approach introduced by Campbell (1984) which involves a systematic and interactive synthesis of regional geological, seismic and ground-truth data. Further to this integration, and an appreciation of a combined dataset, it is possible to make preliminary suggestions as to conditioning and/or triggering factors for mass movement.

2.1   Benefits of Visualizing Geohazards

There are many benefits provided by a ground model approach, but primarily derive from forcing the assessor to review all conceivable geohazards in a spatial context and with specific relation to the proposed development. Downslope evolution of mass movement processes is considered, particularly with respect to direction and location of impact on seabed structures. The ground model provides a means to focus attention on relevant geohazards and, while initially developed as a conceptual model, it gains sophistication with inputs provided from different geohazard assessment tools. Simply by considering them in spatial context it may be possible to eliminate certain geohazards from the inventory due to falsification with evidence or lack of credibility for their occurrence. That being said, consideration of spatial controls is often not enough to significantly refine a geohazard risk profile. Geological processes must therefore be placed in a temporal context which is determined by means of a resolute seismostratigraphy calibrated with a custom-designed geohazard core logging-derived lithostratigraphy, and geochronological analyses. It is important to bear in mind that the seafloor environment does not typically suffer from denudation in the same way as onshore sites and apparently 'fresh' features indicative of submarine mass movement may in fact represent failure that occurred several thousand or tens of thousands of years ago.

3   Determination of Event Frequency – Application of Geochronological Techniques

The principle of uniformitarianism holds that the present is the key to the past and vice versa. With this in mind, determination of those past events that occurred in similar environmental conditions to that of the present day is key to geohazard assessment. Likewise, geohazards can be considered as unlikely where their conditioning and triggering factors can be constrained to past environmental conditions or events. Acquiring accurate dates for emplacement of submarine mass movement deposits is fraught with obstacles. It is necessary for a successful geohazard assessment to deploy a suite of complimentary dating techniques so that any inaccuracies can be minimized. Spurious dates could lead to the identification of an incorrect

conditioning factor (e.g., sea level rise vs. fall) or miss a direct trigger altogether, such as an earthquake or volcanic caldera collapse. Thus the need for a focused and informed sampling and testing strategy is suggested combining biostratigraphic, radiometric and luminescence dating techniques on appropriate materials whose stratigraphic position and geological significance is clearly understood. This section details some of the most useful geochronological techniques that may be employed, but is by no means an exhaustive review of available methods.

3.1   Radiometric Dating Techniques

The most reliable method for constraining emplacement dates during the last 45 ka is by ^{14}C dating of pelagic sediment immediately above the mass movement deposit (Owen et al. 2007). In order to provide the most accurate result this technique should be coupled with a biostratigraphic analysis which identifies the contemporaneous assemblage of carbonate-shelled organisms (such as planktonic foraminifera). This is necessary as a result of mixing that may occur at seabed, due to bottom current activity for example or in the sediment column by burrowing benthic organisms (Loubere et al. 1995). The effects of bioturbation can be pronounced in certain environments, skewing the apparent age of the shells selected, and hence the inferred age of the sediment. Identification of a microfossil assemblage may also provide information about former ocean surface water temperatures and availability of oxygen at the sea floor which can be built into the environmental component of the ground model, informing discussion of potential conditioning factors. If the stratigraphic sequence is relatively complete, and sufficient samples are investigated biostratigraphically, then a climate change profile can be developed which can function as a proxy, but less resolute, dating method through the known climatostratigraphy. ^{87}Sr/^{86}Sr dating is another radiometric technique which is suited to older sediments (in excess of 500 ka – McArthur et al. 2001) and, in conjunction with ^{14}C, has been employed successfully on several recent geohazard assessments performed by the authors. Limitations of ^{87}Sr/^{86}Sr are similar to those of ^{14}C, but also may be affected by non-marine Sr ratios such as may be provided by fluvial systems (McArthur et al. 2001).

3.2   Optically Stimulated Luminescence Dating

Optically Stimulated Luminescence (OSL) dating is a relatively new dating technique applied to marine sediments which attempts to determine age of emplacement by measuring the time since quartz grains contained within a deposit were last exposed to sunlight (Aitken 1992). OSL may be used on sediments as old as 250 ka and is therefore a useful technique to provide data between the upper limits of ^{14}C and the lower practical limits of ^{87}Sr/^{86}Sr. A minimum practical limit for this technique

appears to be about 1,000 years (Aitken 1992). The limitations of the technique are similar to radiometric techniques. Success also requires delivery to the testing laboratory of intact sediment samples that have been protected from re-exposure to sunlight. Experience of the authors with this technique in the marine environment has yielded reasonable success, with correlatable dates from OSL and ^{14}C techniques typically varying less than 12% (based on currently unpublished Fugro results).

3.3 A Geohazard-Focused Geochronological Approach

Combination of the above techniques and others, such as ^{210}Pb and ^{137}Cs dating in very young sediments (about 150 to <50 years BP), will allow for a higher degree of confidence to be placed in the dates determined and in the interpretations made in the geohazard assessment. A successfully targeted geochronological testing program will be predicated on the stratigraphy, with key laterally continuous seismic horizons targeted in order to provide an age-calibrated seismostratigraphic framework for the development area. A good understanding of the lithostratigraphy, and sedimentological features should also be developed prior to any geochronological testing. This avoids the negative effects that may be caused by sampling from bioturbated horizons, reworked sediments or any other post-depositional diagenetic processes.

4   Assessment of Ground Movement

There is significant data in the public realm (e.g., Owen et al. 2007) providing evidence that submarine mass movement activity is more active during periods of relative sea level lowstand and transition, certainly at high and mid latitudes. The experience of the authors is primarily derived from passive margin settings and it has been observed that in such settings climatic changes have provided the conditioning for episodes of submarine mass movements (based on currently unpublished Fugro results). Therefore, mass movements in periods of relatively high sea levels, such as at the present day, can be inferred in many instances to have a reduced likelihood for occurrence or can be constrained to the geological past entirely.

Through a synthesis of data acquired from all available sources (Table 2) it is possible to conduct an integrated study of specific failures and characterize them according to the criteria defined in Table 3. The parameters listed provide data that can be directly input to slope stability analyses (e.g., MacKenzie et al. 2009), risk assessment and impact modelling studies (e.g., Niedoroda et al. 2000; Bruschi et al. 2006; Parker et al. 2008), and include geomorphological, geological, geotechnical, and geochronological data. Such characterization will indicate whether failure is of significant size to impact a development, whether it has potential to occur, and at what orientation the development or structure will be impacted. This will allow for

Table 3 A conceptual slope failure characterization detailing outputs from various geohazard assessment tools. It should be noted that the information above, while credible, is not based on any specific locality

		Measured from GIS and Seismic Data including Bathymetry and Sub-bottom Profiles							Interpretation assisted by Detailed Geohazard Logging		Derived from Detailed Geohazard Logging and Geotechnical Testing		Derived from Geotechnical Data		Geochron. Analysis
Terrain System	Location of Headwall Scarp	Depth to Failure Surface (h)	Slope Angle (α)	Displacement (δ)	Width (W)	Length (L)	Volume (V_f)	Orientation Relative to Structure	Schematic Diagram of Failure	Classification of Failure Type	Material Type	Nature of Failure Surface	Submerged Unit Weight (γ')	Residual Shear Strength (τ_r)	Age of Failure (years BP)
Slope System 1	2.00km Marker Post	75m	10.0 - 12.0°	35m	100m	250m	625.0km³	Parallel and Oblique		Deep Rotational Slide	Very soft to stiff CLAY with organic carbon-rich horizons (Hemipelagite/Sapropel Sequence)	Organic carbon-rich horizon with elevated water content	4.0 - 8.0 kN/m³	41.0 - 49.0 kPa	27,000
	3.00km Marker Post	15m	17.5 - 20.0°	30m	50m	25m	9.4km³	Parallel		Translational Slide	Very soft to soft CLAY with thin beds of silt (Hemipelagite/Turbidite Sequence)	Polished contact between clay units of differing consistency	3.0 - 6.5 kN/m³	9.0 - 13.0 kPa	1,300
Slope System 2	25.00km Marker Post	5m -12m	7.5- 12.0°	20m	15m	20m	1.8km³	Parallel		Shallow Rotational Slide	Very soft to soft CLAY with silt laminae (Hemipelagite/Turbidite Sequence)	Silt laminae	3.0 - 5.0 kN/m³	8.5 - 21.0 kPa	<450
Slope System 3	40.00km Marker Post	3m - 6m	5.5- 10.0°	12m	10m	20m	0.2km³	Parallel		Multiple Rotational Slides	Very soft to firm, locally sandy CLAY (Hemipelagite/Contourite Sequence)	Unconformable contact at base of oversteepened contourite mound	3.5 - 7.5 kN/m³	10.0 - 16.0 kPa	10,300

an evaluation to be made as to whether the geohazard can be eliminated from further consideration, mitigated against, requires further assessment, or presents such a high risk that it must be avoided or accepted by the development.

5   Conclusions and Way Forward

When considering submarine developments, especially in geohazard prone areas such as in deeper water, Locat and Lee (2002) asked the questions: where did and where will mass movement occur; how frequently will it occur; what are the triggering mechanisms; what is the area of influence; and can a previous failure be reactivated? The phrasing of the questions may vary, but the answers provide the framework for a geohazard assessment. For the purposes of planning, design, installation, and operation of a deepwater development a geohazard assessment should encompass the following tasks:

- Comprehensive desk study establishing a *ground model* and *geohazard inventory,* such as that proposed by Clayton and Power (2002). These documents become an auditable record of the process of geohazard assessment undertaken in the effective planning of seabed developments.
- Identification and mapping of geohazards from regional geophysical and geological information within both the public and private domains. This provides essential information to develop scopes of work for optimized and fit-for-purpose geophysical and geotechnical data acquisition.
- Ongoing revision of the *geohazard inventory* and *ground model* based on updated knowledge so they evolve from conceptual to development-specific models.
- Use of GIS for data organization, regional analyses and slope stability assessment (e.g., Mackenzie et al. 2009).
- Essential data collection and evaluation tools to be used in future geohazards site investigations should be chosen from the following.
- Region-wide multibeam bathymetry for geomorphological analysis of the seafloor.
- Ultra high-resolution surveys using AUV with CHIRP for early identification and mapping of shallow mass movement deposits.
- Long piston cores for sampling of geohazards identified in the ground model. To be used for comprehensive lithological and geotechnical analyses.
- Supplementary box cores to ensure that recovery of the youngest sediments where piston coring of recent mass movements may disperse these sediments on impact.
- Seabed Cone Penetration Tests (CPT) used to geotechnically evaluate mass movement complexes. Geotechnical information calibrates seismostratigraphic units and increases the sophistication of the ground model in terms of its usefulness for conceptual foundation engineering studies.

It may be impossible to entirely preclude the potential for mass movement to occur at a seabed development; however, by using the tools above, and following the assessment procedure detailed in this paper, it may be possible to constrain such a hazard to the geological past, and significantly reduce the level of risk posed to the development during its engineering lifetime.

References

Aitken MJ (1992) Optical dating. Quat Sci Rev 11:127–132

Bruschi R, Bughi S, Spinasse M, Torselletti E, Vitali L (2006) Impact of debris flows and turbidity currents on seafloor structures. Nor J Geol 89:317–337

Campbell KJ (1984) Predicting offshore soil conditions. Proc Ann Offshore Technol Conf, Houston, Texas, 7–9 May, OTC Paper Number 4692

Clayton CRI, Power PT (2002) Managing geotechnical risk in deepwater. Proc Int Conf Offshore Site Investig, London, Soc Underwater Technol 425–439

Lee HJ, Schwab WC, Booth JS (1993) Submarine landslides: an introduction. In: Schwab WC, Lee HJ, Twichell DC (eds) Submarine Landslides: selected Studies in the US Exclusive Economic Zone. US Geol Surv Bull:1–13

Locat J, Lee HJ (2002) Submarine landslides: advances and challenges. Can Geotech J 39:193–212

Loubere P, Meyers P, Gary A (1995) Benthic foraminiferal microhabitat selection, carbon isotope values, and association with larger animals: a test with Uvigerina peregrine. J Foraminifer Res 25:1107–1110

Mackenzie B, Hooper J, Rushton, D (2009) Spatial analysis of shallow slope instability incorporating an engineering geological ground model. Submarine mass movements and their consequences IV. Fourth International Symposium on Submarine mass movements and their consequences 365–376

Masson DG, Harbitz CB, Wynn RB, Pedersen G, Lovholt F (2006) Submarine landslides: processes, triggers and hazard prediction. Philos Trans R Soc 364:2009–2039

McArthur JM, Howarth RJ, Bailey TR (2001). Strontium isotope stratigraphy: LOWESS Version 3. Best-fit line to the marine Sr-isotope curve for 0 to 509 Ma and accompanying look-up table for deriving numerical age. J Geol 109:155–169

Mulder T, Cochonat P (1996) Classification of offshore mass movements. J Sed Res 66:43–57.

Niedoroda AW, Reed CW, Parsons BS, Breza J, Forristall GZ, Mullee JE (2000) Developing engineering design criteria for mass gravity flows in deepsea slope environments. Proc Ann Offshore Technol Conf, Houston, Texas, OTC Paper Number 12069

Owen M, Day S, Maslin M (2007) Late Pleistocene submarine mass movements: occurrences and causes. Quat Sci Rev 26:958–978

Parker EJ, Traverso C, Moore R, Evans T, Usher N (2008) Evaluation of landslide impact on deepwater submarine pipelines. Proc Ann Offshore Technol Conf, Houston, Texas, 5–8 May, OTC Paper Number 19459

Varnes DJ (1978) Slope movement types and processes. In: Schuster RL, Krizek RJ (eds) Special Report 176: Landslides: analysis and control. National Research Council, Washington DC

Evaluating Gas-Generated Pore Pressure with Seismic Reflection Data in a Landslide-Prone Area: An Example from Finneidfjord, Norway

E.C. Morgan, M. Vanneste, O. Longva, I. Lecomte, B. McAdoo, and L. Baise

Abstract On the 20th of June, 1996, a multi-phase landslide that initiated under water and retrogressed onto land ultimately killed four people, destroyed several houses, and undermined a major highway in Finneidfjord, Norway, an area with a known history of landsliding in the Holocene. Geological and environmental conditions inherent to the 1996 slide include excess fluid/gas pressure (particularly in gas-bearing sediment). In this study, we quantify pore pressures within the free gas accumulation at very shallow sub-surface depths using seismic reflection data. The gas front (a few meters below the seabed) produces a strong, polarity-reversed reflection, dramatically attenuating sub-surface reflections. On x-ray images of cores collected from the $5\,km^2$ large gas zone, gas appears as vesicular spots. We use a previously published method incorporating continuous wavelet transforms to quantify attenuation produced by gas-bearing sediment. Taking the output from this method, and knowing or assuming values for other physical parameters, we invert for in situ pressure and equivalent thickness of the free gas layer. We compare our results to pressure data collected from a single piezometer penetrating the gas front. This analysis demonstrates the utility of seismic reflection data in analyzing the dominant parameter in submarine slope stability (i.e. excess pore pressure), which could be useful in assessing geohazards in similar geological environments.

E.C. Morgan (✉) and L. Baise
Tufts University, Dept of Civil and Envir Eng, 200 College Ave, Anderson Hall,
Rm 113, Medford, MA 02155, USA
e-mail: eugene.morgan@tufts.edu

M. Vanneste
NGI/ICG, P.O. Box 3930, Ullevål Stadion, N-0806 Oslo, Norway

O. Longva
NGU/ICG, 7491 Trondheim, Leiv Eirikssons vei 39, Trondheim, Norway

I. Lecomte
NORSAR/ICG, P.O. Box 53, N-2027 Kjeller, Norway

B. McAdoo
Vassar College, Dept of Earth Sci and Geog, Poughkeepsie, NY 12604, USA

1   Introduction

Finneidfjord, Norway, was the scene of a large submarine landslide, which initiated
underwater on June 19th, 1996. The landslide did not start to cut back onshore until
about 00:15 on the 20th of June (Best et al. 2003). Ultimately, the landslide mobi-
lized approximately 1 million m³ of sediment, and claimed four lives, several
houses, and a stretch of highway. The geomorphology of the slide scar (visible in
swath bathymetry (Fig. 1c)) and eyewitness accounts indicate that the landslide
occurred in as many as five stages, with initial failure taking place on the steepest
section of the slope (Longva et al. 2003). Initial detachment occurred in Holocene
silty clay, but successive failure stages involved the underlying late-glacial, soft,
sensitive clays (including quick clays) (Ilstad et al. 2004). Factors likely contribut-
ing to failure include build-up of excess pore pressures by free gas accumulation
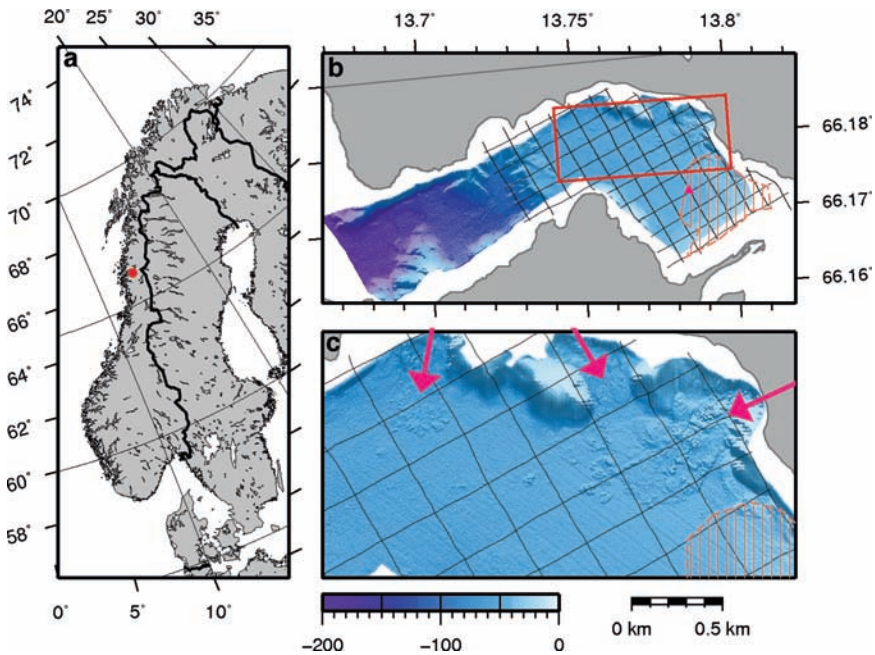
Fig. 1 Location of Finneidfjord, Norway (**a**), with progressively higher scale views of the 1996
slide bathymetry (**b** and **c**; *red outline in* (**b**) indicates extent of (**c**)). Gridded black lines over
bathymetry represent 2D seismic transects collected in 2006, while the orange hatched area covers
observed seismic blanking by free gas. Note the piezometer location (*triangle in* (**b**)), and the
evidence of previous slides WNW of the 1996 debris flow (*arrows in* (**c**), *with the 1996 event
marked by the far right arrow*). One core is right next to this piezometer, but the other cores and
the other piezometer are omitted from this map because they do not penetrate the gas zone.

(Best et al. 2003), groundwater seepage, or human activities, and a sudden increase in overburden stress by the placement of fill on the shore (Gregersen 1999). Vertical seismic profiling reveals a history of submarine slope failure (Fig. 1) that goes back since the retreat of the glaciers, suggesting that phenomena associated with the 1996 event may occur further afield. Several landslides have happened over the last decades, hinting that incipient failures could happen in the near future, with consequences for society.

To further investigate slope stability, additional data collection from Finneidfjord includes high-resolution 2D seismic surveys covering much of the fjord, four sediment cores, and two in situ piezometers. Of particular interest is an area of shallow gas accumulation in the southern end of the fjord. The top of the free gas zone (gas front) is characterized by a high-amplitude, polarity-reversed reflector. The density difference between overlying saturated sediment and underlying gas-bearing sediment causes this signature, however the density of the gas is partially a function of the overpressure. Underneath the gas front, acoustic energy becomes highly attenuated (Fig. 2; Best et al. 2003; Seifert et al. 2008). Whereas this phenomenon makes it difficult to delineate underlying stratigraphy, it allows for deriving important information of the gas zone itself. A piezometer (pink triangle in Fig. 1b) in the gas-bearing sediment recorded excess pore pressures at two sub-seabed depths for 18 months, and gas bubbles appear as vesicles in x-rays of a core taken adjacent to this piezometer. Even though no direct evidence of free gas exists at the 1996 slide scar, areas of gas exist south and west of the scar (Fig. 1), and the reflection associated with the gas-bearing sediment can be traced over the landslide area. This strong reflection coincides with textural variations in the sediment cores, which
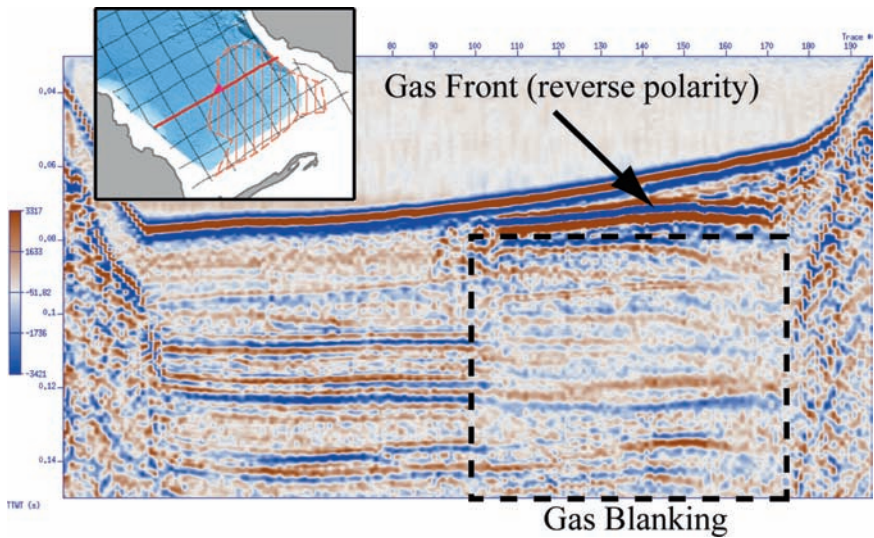
Fig. 2 A seismic profile across the gas zone. The gas front appears as a distinct, polarity-reversed reflection. Attenuation is pronounced underneath the gas front. Note the differences in frequency and amplitude above and below the gas front.

would likely trap upward migrating gas bubbles. The accumulation of gas-generated excess pore pressure at the Holocene silty clay and late glacial clay lithological boundary could initiate sliding along that boundary (Stegmann et al. 2007).

Sediments partially saturated with even small amounts of gas highly attenuate P-wave transmission (Carcione and Picotti 2006; Pride et al. 2004). In this case, wave-induced pore fluid flow constitutes the primary intrinsic loss mechanism, which operates at the mesoscopic scale (thickness of gas saturation larger than pore size, but smaller than wavelength). The inverse of quality factor (Q^{-1}) quantitatively parameterizes intrinsic attenuation. Low Q (high damping) indicates strong attenuation, whereas media with large Q (low attenuation) transmit seismic waves with less energy loss. For geologic media, Q can vary as a function of frequency (f), and this relationship is often depicted as an attenuation curve (Q^{-1} versus f). The amount of attenuation for a given frequency depends on a multitude of physical parameters for the soil matrix and pore fluid(s). The more compliant pore fluid (with lower viscosity; in this case, gas) largely controls the shape of the attenuation curve (Carcione and Picotti 2006). These curves typically have a single minimum (Q_m) with an associated frequency (f_m) for a single attenuation mechanism, or a broad minimum covering a range of f for multiple mechanisms.

In the study presented here, we used recent advances in seismic signal processing and seismic attenuation modelling to estimate gas-generated excess pore pressures. Li et al. (2006) present a way to find Q using continuous wavelet transforms (CWTs). CWTs provide excellent time-frequency localization of a signal's energy, which is lost with conventional Fourier transforms (Li et al. 2006). This implies that the CWT method does not suffer from time-windowing problems that can hinder the spectral ratio technique from estimating accurate Q values, and Pinson et al. (2008) acknowledge that the spectral ratio technique requires a large frequency range, which the CWT method does not. Quantifying the attenuation of a medium bearing free gas allows for the inversion of the rock physics equations of Carcione and Picotti (2006) to obtain gas density (ρ_g) and thickness ($d2$). The latter parameter corresponds to the thickness of a sub-layer of gas phase (separated from the liquid phase). Carcione and Picotti (2006) calculate attenuation curves for given media with water and methane as pore fluids. Knowing (or assuming) all the required physical parameters for the gas-bearing medium at Finneidfjord (except ρ_g and $d2$), and using the equations of Carcione and Picotti (2006) within a genetic algorithm, we adjust these two gas parameters to optimize the output attenuation metrics (Q_m and f_m) to our observed attenuation metrics (Q and f). ρ_g and $d2$ can be translated into total pressure and saturation, and subtracting hydrostatic pressure from total pressure gives excess pore pressure.

2   Methods

We use 2D seismic data collected from Finneidfjord in 2006 (survey lines in Fig. 1). The data are recorded in a single-channel streamer towed at zero offset. The source was an airgun with relevant frequencies between 40 and 500 Hz. The receivers

sampled at approximately 2,600 Hz. Processing of the traces included a trapezoidal band-pass filter of 20–40–500–600 Hz, as well as spherical divergence correction and multiple removal. The shallow water depths (~30 m on average) imply that the latter procedure was very important.

2.1 Quantifying Attenuation

Our application of the CWT to assess Q of the gas-bearing sediment follows the procedure outlined by Li et al. (2006), where the effective Q at a reflection (Q_{eff}) is estimated by the peak scale (a_p) of the scalogram (squared modulus of the wavelet coefficients) at the time of that reflection (t) by:

$$Q_{eff} = \frac{mt}{a_p} \tag{1}$$

where m is the modulating frequency of the Morlet wavelet (the mother wavelet used in the CWT). Knowing Q_{eff} at the interfaces bounding a layer, the Q of that layer is then:

$$Q = \frac{t_{below} - t_{above}}{\dfrac{t_{below}}{Q_{eff,below}} - \dfrac{t_{above}}{Q_{eff,above}}} \tag{2}$$

Figure 3 demonstrates this procedure on a synthetic seismogram generated by the software NORSAR-2D. We model the source pulse as a Ricker wavelet, and pass this through a layered model with prescribed Q (for P-waves), density (ρ), and P-wave velocity (v_p). We calculate Q values for the two intermediate layers that are bound by reflections (and thus Q_{eff} values), and assume $Q = Q_{eff}$ for the very top and very bottom layers that are not bound by reflections (red curve, far right panel of Fig. 3). Only the calculated Q values of the middle two layers agree with the original model Q values. f_{eff} is equal to $1/a_p$, and then the layer f is found by substituting f for Q in Eq. 2.

Applying the above method to our seismic profile, we manually pick horizons at two reflections to define our gassy layer: the horizon at the large trough of the reverse-polarity reflection associated with the gas front, and another arbitrary reflection just below the gas front. Using the Morlet wavelet in all our CWTs, we transform the seismic signals of each trace associated with the horizons into scalograms. We can then pick the peak energies at the reflections, take the associated scales, and translate the scales into Q and f. To diminish error introduced by noise in the seismic data, we smoothed the Q_{eff} values and f_{eff} along each horizon with a median filter before calculating the Q values for the layer.
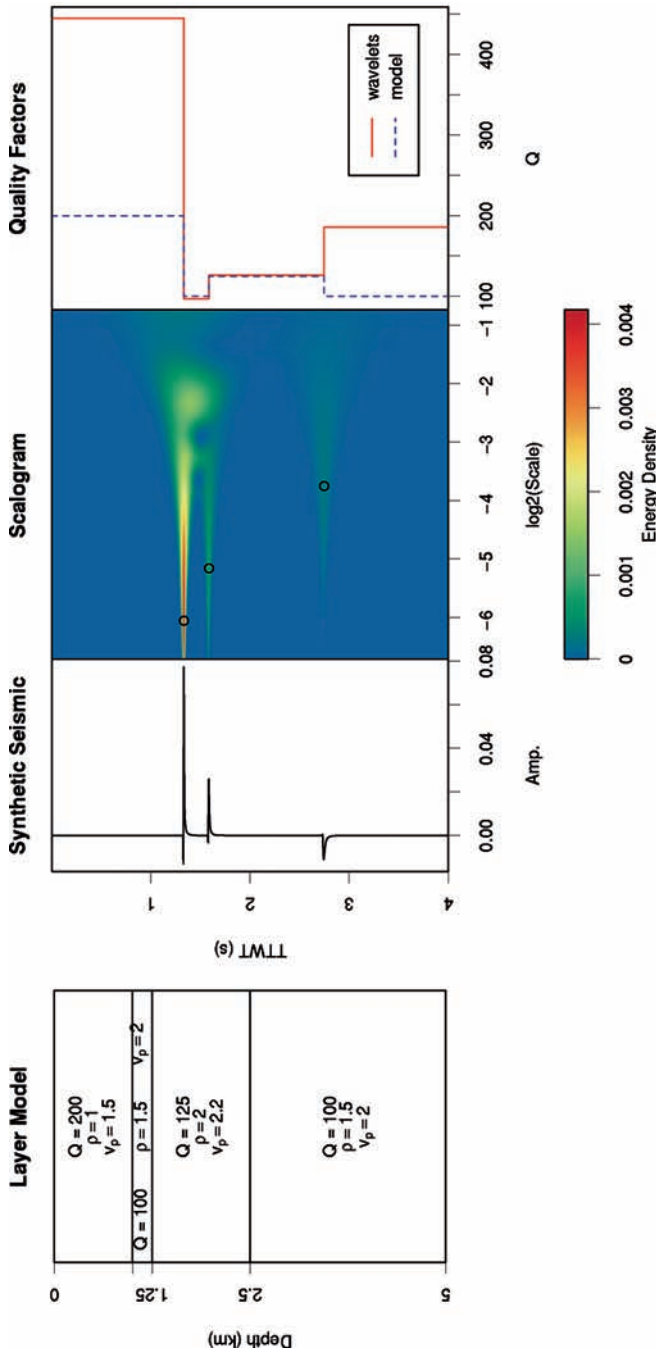
Fig. 3 An example of finding Q using a synthetic seismogram. The 2D layer model (*far left*) includes Q values for P-waves. The software NORSAR-2D was used to generate the synthetic seismogram (*center left*) recorded at a receiver co-located with the source (*Ricker wavelet*). Taking the squared modulus of the wavelet transform of the seismogram gives the scalogram (*center right*), which depicts energy density in time and wavelet scale space. The black circles on the scalogram represent the energy peaks, and the scales of these peaks give the effective quality factors associated with each reflection. It is only possible to get valid Q values for the middle two layers, since they are bound by reflections (*note that the red curve (calculated values) matches the dashed blue curve (model values) for these layers, far right panel*).

2.2 Gas Properties

Knowing Q and f for a medium, it is possible to invert the attenuation equations of Carcione and Picotti (2006) to obtain gas properties. For the forward case, these authors calculate attenuation curves (Q^{-1} versus f) for media saturated with a combination of water and methane. We use a genetic algorithm to adjust the two gas parameters (ρ_g and $d2$) until the minimum Q (Q_m) and associated frequency (f_m) of the modeled curves match the measured values of Q and f (Fig. 4). Q approximates Q_m because the most attenuation (the most loss of energy) occurs at the peak scale (Li et al. 2006).

Many other physical parameters for the media of interest must be constrained for this optimization to work properly. Because the loss mechanism depends heavily on pore fluid flow, the attenuation curves show high sensitivity to porosity (ϕ) and, to a lesser extent, permeability (κ). Lacking field measurements for these two parameters, we assumed literature values for the unconsolidated silty clay from Schön 1996 (Table 1). The gas bulk modulus (K_g) is a function of gas density and temperature (Carcione and Picotti 2006), and the piezometer in the gas zone recorded a mean temperature $T \approx 7°C$. We assumed literature values for the viscosities of gas and water, for the bulk (K_s) and shear (μ_s) moduli of clay, for the bulk moduli of water, and for the density of water and clay particles (Table 1). We calculated layer
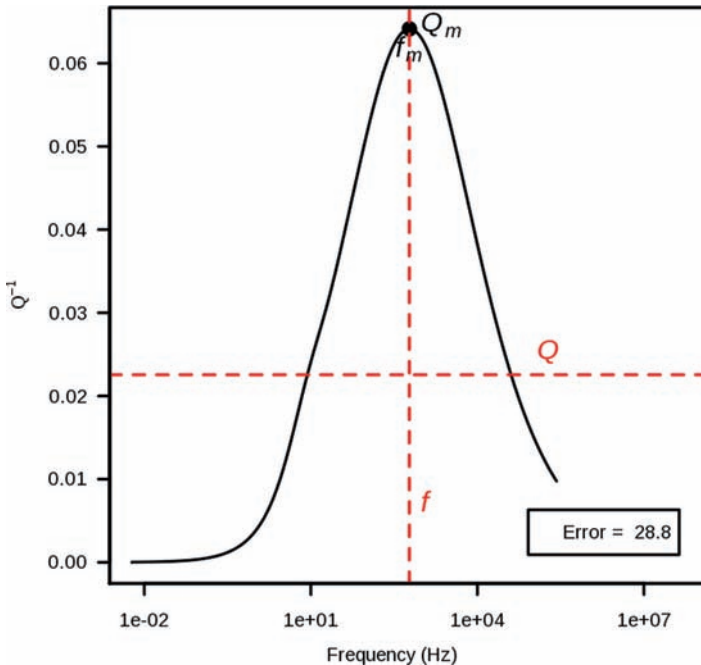
Fig. 4 An example attenuation curve. The genetic algorithm adjusts parameters so that the Q_m and f_m of the curve match the measured values Q and f. Error is the square root of the sum of squared differences between these pairs of values.

Table 1 Initial parameters

Parameter	Value
Porosity (ϕ)	0.70 [a]
Permeability (κ)	1e-17 m^2 [a]
Solid grain bulk modulus (K_s)	25 GPa [b]
Solid grain shear modulus (μ_s)	9 GPa [b]
Solid grain density (ρ_s)	2,550 Kg/m^3 [b]
Water density (ρ_w)	1,040 Kg/m^3 [b]
Temperature (T)	7°C [c]
Gas viscosity (η_g)	0.00015 Pa·s [b]
Water viscosity (η_w)	0.003 Pa·s [b]
P-wave velocity (v_p)	1,500 m/s [a]

Soil (unconsolidated silty clay), methane, and seawater parameters used to initialize the genetic algorithm. Initial gas thickness (d2), density (ρ_g), and bulk modulus (K_g) values varied from trace to trace, so are not included in this table.

[a] are values taken from Schön 1996

[b] are values taken from Carcione and Picotti 2006

[c] are field measurements

thickness from the two-way travel time (TWTT) between the horizons using an assumed P-wave velocity of 1,500 m/s.

To start the genetic algorithm, we initially estimated d2 as 5% of the entire layer thickness (5% gas saturation) and ρ_g as the density of methane gas whose pressure is in equilibrium with hydrostatic pressure. This estimate of ρ_g assumes that the gas inclusions are not expanding or shrinking (Wheeler et al. 1990), which would indicate pressure disequilibrium. The genetic algorithm then selects random samples of these two parameters from normal distributions where the initial estimates are the mean values. The random sample pair that yields the least error between its attenuation curve and the measured Q and f serves as the mean values for the distributions in the next iteration, and also competes against this next generation of pairs. Error is the square root of the sum of squared differences between measured Q and f and the Q_m and f_m from the curve. Iterations proceed until the algorithm produces sufficiently small error (< 1), or ceases to improve the error over 100 iterations. The genetic algorithm also allows us to vary other parameters in the physical equations at the same time as the gas parameters are "evolving". To compensate for uncertainty in the assumed literature values, we let ϕ, κ, μ_s, and K_s vary by small amounts. Also, K_g was recalculated in terms of ρ_g for each iteration.

3   Results

Figure 5 shows measured Q and f values for each trace along a single transect through the gas zone at Finneidfjord, as well as the optimal values of d2 and ρ_g. Some of the values did not achieve a low enough level of error (< 1) by the end of

the optimization, and are colored grey in Fig. 5. Ignoring the points with large error (≥ 1), Q values range between 5 and 37, with a median of 12, and f ranges between 84 and 499 Hz, with a median of 136 Hz. We report the median values (instead of the mean) here because this metric better estimates the central tendency of skewed samples.
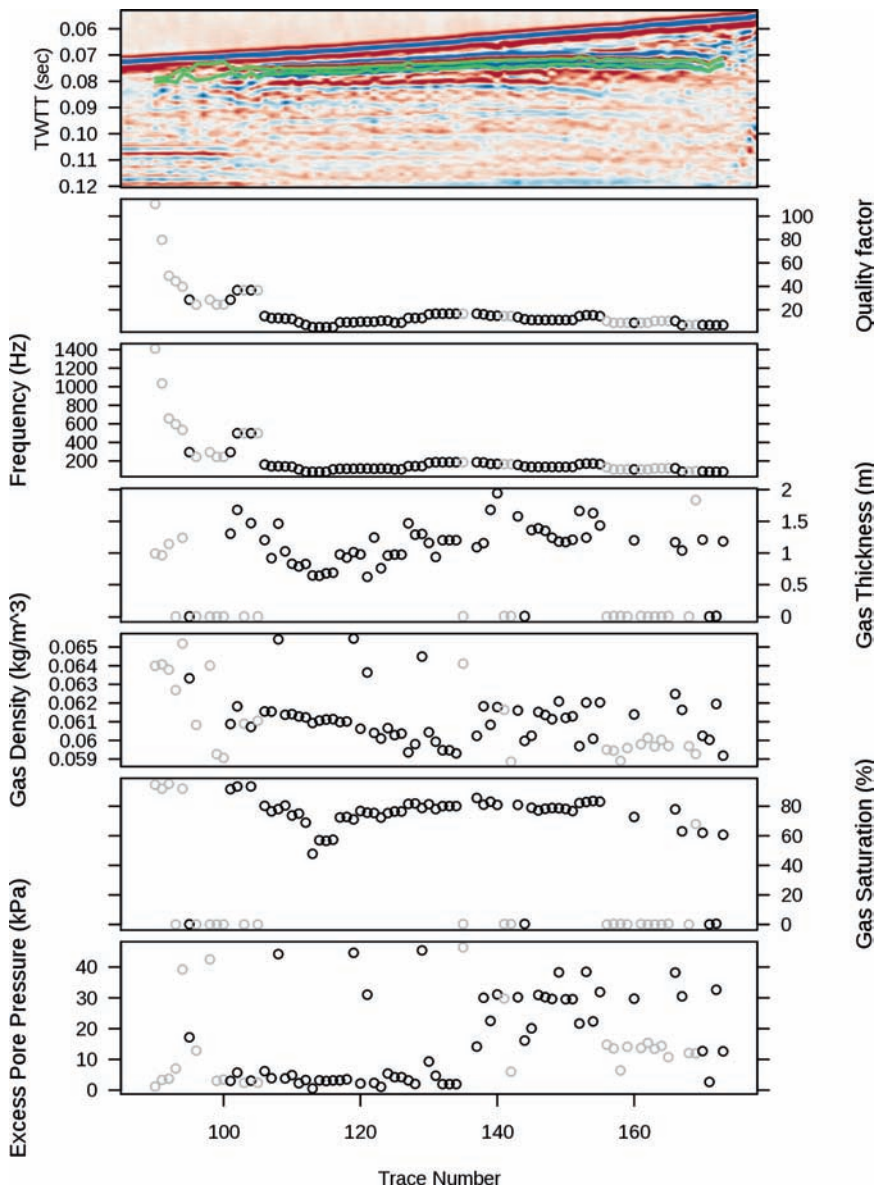
Fig. 5 Results from the CWT method and subsequent physical equation inversion for the seismic profile from Fig. 2. The green lines on the seismic profile (*top panel*) represent the picked gas front horizon (*top*) and a lower arbitrary reflection. Values associated with errors ≥ 1 are in grey.

It is reassuring that all the *f* values greater than 500 Hz (the highest frequency containing source energy) have high amounts of error. The majority of *d2* values range from 0.62 to 1.94 m, with four exceptions that share values similar to the erroneous values (~1 mm), which should be neglected.

Checking the assumption that our gas heterogeneities are of mesoscopic scale, we consider pore size to be on the order of the mean grain size (80 μm), and the minimum wavelength to correspond to the maximum attenuation frequency for non-erroneous points ($\lambda = 1{,}500$ m/s $\div$ 499 Hz = 3.0 m). All the gas thicknesses (*d2*) fall within this range. We convert *d2* to saturation by dividing it by the total thickness. Finally, we calculate excess pore pressure using $P = \rho_g \cdot R \cdot (T + 273)/M$ (methane) (where the gas constant $R = 519.4$ J/kg·K, and the molar mass of methane M(methane) = 0.016 kg/mole), and then subtract hydrostatic pressure from the total gas pressure (*P*).

The other parameters we allowed to vary (ϕ, κ, μ_s, and K_s) tended towards values appropriate for more granular sediment than silty clay. The resultant medians of the parameters ϕ, κ, μ_s, and K_s along the horizons were approximately 0.5, 8e-11 m^2, 47 GPa, and 45 GPa, respectively. The first two values are typical of fine sand, silty sand, or sandy silt, while the latter two values are relatively close to the elastic properties for quartz (Schön 1996).

4   Discussion

The results with large error (grey points in Fig. 5) generally appear towards either end of the profile. On the left side of the profile, these errors can be explained by the seismic data, where very little attenuation takes place below the horizon (a reflection below appears with normal amplitude). These errors are reassuring because it should not be possible to model the gas attenuation mechanism in spots where it does not exist. However, there is one point (trace #95) at this end that did not result in an error ≥ 1, and one can see in the subsequent results that this trace shares values in common with the neighboring erroneous traces. The results for this trace should be ignored, since this trace clearly does not display evidence of intrinsic attenuation. The cause of error in the traces towards the right side of the profile likely originates from a combination of lower hydrostatic pressures and greater layer thicknesses than other traces in the profile, indicating there may be an area of sample space that the genetic algorithm currently does not cover very well.

As mentioned in the introduction, a piezometer installed in the gas zone recorded average excess pore pressures of ~2.0 kPa and ~0.5 kPa at 3.1 and 5.3 m below the seafloor. This piezometer lies approximately 10 m northwest of trace #101 (the closest trace). The results show relatively low excess pore pressures at and around this trace, where the value at trace #101 is 3.0 kPa and the median at that end of the profile (traces 90 – 135) is 3.3 kPa (excluding results with high error). The gas front sits at a depth between the two piezometer sensors, so the difference in excess pore pressure at the profile and at the piezometer may not only be due to lateral variation,

but vertical as well. Gas saturation around trace #101 varies from 48% to 93% (neglecting the points with large error and the one point with a value similar to the erroneous values). The larger saturation values seem unreasonable considering the core collected adjacent to the piezometer showed bubbles as discrete vesicles in X-rays.

Considerable variability exists in these results even after removing the data points with large error, but trends can still be distinguished. Ignoring the few erratically low values, a distinct trend can be seen in the gas saturation results, where larger saturation values drop steeply around trace #115. Perhaps these values mark a gas migration route, such as one of the possible gas chimneys observed in Best et al. 2003. Gas saturation also decreases towards the right side of the profile. This could signify a lateral discontinuity in the sedimentary textural variation responsible for trapping the gas, which would escape through this shallower end. While the excess pore pressures in the left side of the profile show more uniformity around 3.3 kPa, values on the right side have much more variability at much larger pressures (nearly 10 fold). Also, the excess pore pressures with error < 1 are more sparsely distributed on the right side than on the left. While values on this side could be possible, 30 kPa of excess pore pressure seems highly unlikely, especially given the larger uncertainty with those values. The values on the left side can be somewhat validated by the piezometer recording in that vicinity, while there currently exists no such way to validate the results on the right side of the profile.

5   Conclusion

Excess pore pressure generated by shallow gas accumulations can be quantified from seismic reflection data using continuous wavelet transforms and subsequent inversion of theoretical attenuation models using a genetic algorithm. CWTs can reliably measure P-wave attenuation with considerably high time resolution. Applying this technique on seismic traces from Finneidfjord, and then inverting for gas density and relative thickness, gives a broader perspective of excess pore pressure (and thus landslide hazard) in that area. For the 1996 slide, an estimated 5 kPa of excess pore pressure could have induced failure (Best et al. 2003). Smaller values on the deeper section of slope (median of 3.3 kPa) indicate that the slope in this study is not likely to fail by this mechanism, however much larger (but more uncertain) pressures are calculated on the shallower portion of the slope. One piezometer certainly does not suffice in validating the method presented here, and this method should also be tested in different environments and conditions. Nevertheless, the results are promising, and this method offers a cost-effective and non-intrusive way of evaluating pore pressures in submarine, landslide-prone areas.

References

Best AI, Clayton CRI, Longva O, Szuman M (2003) The role of free gas in the activation of submarine slides in Finneidfjord. First Int Sympos Submar Mass Mov Conseq, EGS-AGU-EUG Joint Meeting, Kluwer, Nice, France

Carcione JM, Picotti S (2006) P-wave seismic attenuation by slow-wave diffusion: Effects of inhomogeneous rock properties. Geophysics 71(3): 01–08

Gregersen O (1999) Kvikkleireskredet i Finneidfjord 20 juni 1996. NGI Rep 980005–1, NGI, Oslo

Ilstad T, De Blasio FV, Elverhøi A, Harbitz CB, Engvik L, Longva O, Marr JG (2004) On the frontal dynamics and morphology of submarine debris flows. Mar Geol 213: 481–497

Li H, Zhao W, Cao H, Yao F, Shao L (2006) Measures of scale based on the wavelet scalogram with applications to seismic attenuation. Geophysics 71(5): V111–V118

Longva O, Janbu N, Blikra LH, Bøe R (2003) The 1996 Finneidfjord Slide: seafloor failure dynamics. First Intern Sympos Submar Mass Mov Conseq, EGS-AGU-EUG Joint Meeting, Kluwer, Nice, France

Pinson LJW, Henstock TJ, Dix JK, Bull JM (2008) Estimating quality factor and mean grain size of sediments from high-resolution marine seismic data. Geophysics 73(4): G19–G28

Pride SR, Berryman JG, Harris JM (2004) Seismic attenuation due to wave-induced flow. J Geophys Res 109: B01201

Schön JH (1996) Physical properties of rocks: fundamentals and principles of petrophysics 18. Elsevier, New York

Seifert A, Stegmann S, Mörz T, Lange M, Wever T, Kopf A (2008) In situ pore-pressure evolution during dynamic CPT measurements in soft sediments of the western Baltic Sea. Geo Mar Lett 28: 213–227

Stegmann S, Strasser M, Anselmetti F, Kopf A (2007) Geotechnical in situ characterization of subaquatic slopes: the role of pore pressure transients versus frictional strength in landslide. Geophys Res Lett 34: L07607

Wheeler SJ, Sham WK, Thomas SD (1990) Gas pressure in unsaturated offshore soils. Can Geotech J 27: 79–89

Historic and Paleo-Submarine Landslide Deposits Imaged Beneath Port Valdez, Alaska: Implications for Tsunami Generation in a Glacial Fiord

H.F. Ryan, H.J. Lee, P.J. Haeussler, C.R. Alexander, and R.E. Kayen

Abstract During the 1964 M9.2 great Alaskan earthquake, submarine-slope failures resulted in the generation of highly destructive tsunamis at Port Valdez, Alaska. A high-resolution, mini-sparker reflection profiler was used to image debris lobes, which we attribute to slope failures that occurred both during and prior to the 1964 megathrust event. In these reflection profiles, debris lobe deposits are indicated by acoustically opaque units that are separated by undisturbed parallel-layered reflectors. Near-surface debris lobes attributed to the 1964 earthquake include: (1) a debris lobe over 30 m thick that emanates from the fiord-head delta in eastern Port Valdez; and (2) debris flow lobes incorporating large, intact blocks up to 40 m high in western Port Valdez, off the Shoup Glacier moraine. In addition to the near-surface debris lobes, we imaged at least five additional debris lobe deposits buried beneath the 1964 deposit. The debris lobe directly beneath the 1964 deposit has a similar thickness and spatial distribution as the 1964 deposit. However, the older, deeper, debris lobes are thinner, less extensive, and separated by thinner sequences of parallel-layered reflectors. Glacier retreat and concomitant build-up of the fiord-head delta combined with longer time intervals between megathrust events may have resulted in more extensive delta failures and thus thicker debris lobes through time.

Keywords Submarine landslide • tsunami • Alaska • earthquake • fiord

H.F. Ryan (✉), H.J. Lee, and R.E. Kayen
U.S. Geological Survey, 345 Middlefield Rd., MS 999, Menlo Park, CA, USA
e-mail: hryan@usgs.gov

P.J. Haeussler
U.S. Geological Survey, Anchorage, AK, USA

C.R. Alexander
Skidaway Institute of Oceanography, Savannah, GA

1 Introduction

The Great Alaskan Earthquake of 1964 (Mw = 9.2) resulted in significant damage to coastal communities in southeastern Alaska, primarily as the result of tsunamis. In the town of Valdez, Alaska, 32 people died and the town was severely damaged and subsequently relocated (Fig. 1). Port Valdez was the site of the highest tsunami heights recorded anywhere in Alaska during this event, with tsunami waves reaching a height of 52 m. Studies conducted immediately following the earthquake indicated that there were significant changes in fiord-head delta bathymetry at the eastern end of Port Valdez (Coulter and Migliaccio 1966; Plafker et al. 1969). However, the largest tsunami wave heights were located in western Port Valdez near the Shoup Glacier (Fig. 1; Plafker et al. 1969).

Today, Port Valdez is of particular strategic interest as it is at the southern terminus of the trans-Alaska oil pipeline. New studies of submarine landslide-generated tsunamis in Port Valdez were initiated after the acquisition of multibeam bathymetry by the National Oceanographic and Atmospheric Administration (NOAA) (Fig. 1). The new bathymetry revealed large blocks at the seafloor, which were considered to be a probable source for the devastating tsunamis in Port Valdez in 1964 (Lee et al. 2006, 2007). Analyses of pre- and post-1964 bathymetric surveys from Port Valdez revealed a net removal of sediment from eastern Port Valdez, with a net deposition in western Port Valdez (Lee et al. 2007). Based on an interpretation of subbottom chirp profiles, the 1964 debris flows had an estimated volume of 1 km^3, which was over twice the volume calculated from bathymetric differences.
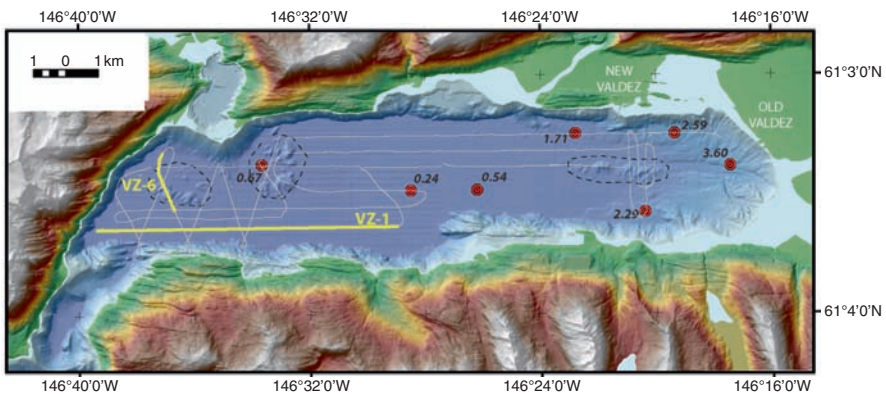
Fig. 1 Multibeam imagery of Port Valdez (*blues* 0 to −320 m water depth) combined with high resolution LIDAR topography (*green-brown to white*, 0 to 1,350 m land elevation) showing landslide-related blocks (*outlined by dashed lines*) discussed in text. Tracklines of mini-sparker subbottom profiles collected in 2007 are shown in white with locations of profiles shown in paper in yellow. The location of all of the gravity cores analyzed for 137Cs are shown (*red dots*) and labeled with the most recent sediment accumulation rate in cm/yr

This suggests that significant sediment from the fiord floor was incorporated into the debris flows (Lee et al. 2007).

In the present paper, we present new high-resolution mini-sparker reflection profiles along with gravity cores and vibracores to better document the extent, volume, and character of both the 1964 submarine landslide deposits and those from previous failures. A preliminary attempt is made to: (1) correlate the older lobes to previous earthquakes on the Alaskan megathrust; and (2) relate variations in the location, thickness, and extent of the debris lobes to variable climatic conditions in the Holocene.

2   Methods

Lee et al. (2007) presented geophysical (including multibeam bathymetry and sub-bottom chirp profiles) and sedimentological data for initial studies of tsunamigenic submarine slope failures in Port Valdez. In that study, very high-resolution chirp data acquired using an Edgetech 512i system often showed limited subsurface penetration. As a result, additional sub-bottom profiles were collected in 2007 using a single channel SIG 2Mille 50-tip mini-sparker system (Fig. 1). This system was operated at a power of 500 joules with a frequency range of 160 Hz-1.5 Khz, which penetrated to depths of up to 700 ms two-way travel time (TWTT).

Additional sediment gravity cores and vibracores were also collected in 2007 that recovered samples up to 2 m in length. The gravity cores were analyzed for the short half-life radioisotope ^{137}Cs to determine post-1964 sedimentation rates (see Alexander and Venherm 2003 for discussion of methods). P-wave velocities from cores were used for estimating velocities to convert TWTT to depth.

3   Results

One of the main objectives of the mini-sparker cruise was to image the base of the large blocks to confirm that the blocks were indeed landslide-related, and not in-situ basement. A subbottom profile collected across one of the blocks south of Shoup Bay shows a strong reflector that is continuous beneath the block (Fig. 2). We interpret this reflector to correspond to the base of the deformation induced by the movement of the blocks and related landslide, with acoustically transparent and/or chaotic units above the reflector on either side of the block (Fig. 2). Mini-sparker profiles collected across other blocks beneath both western and eastern Port Valdez showed similar continuous reflectors beneath the blocks.

The importance of the blocks in generating the 1964 tsunami in western Port Valdez is illustrated by the multibeam bathymetric data. Figure 3 shows the bathymetry of the basin floor of western Port Valdez with the color bar set to emphasize a narrow 10-m water depth interval (237–247 m). Semi-circular bathymetric highs occur
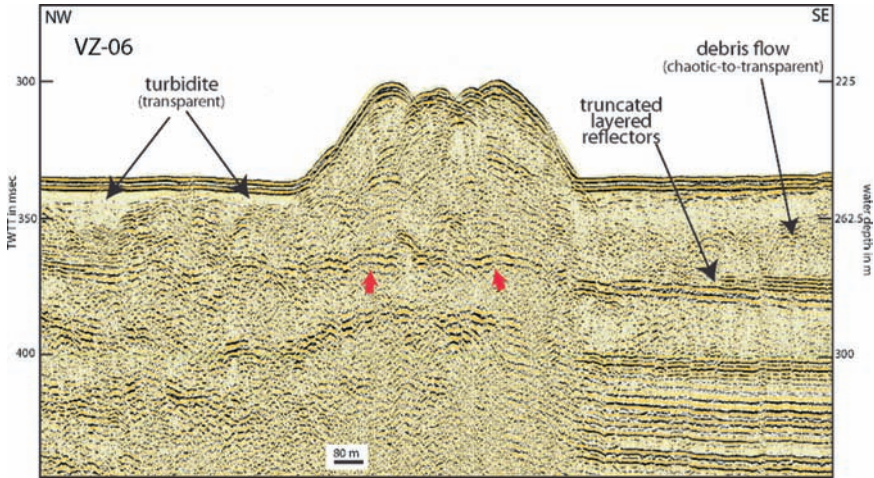
Fig. 2 Mini-sparker profile collected across one of the blocks imaged on the multibeam bathymetry (see Fig. 1 for location). A strong reflector (*delineated by red arrows*) is imaged beneath the block. The reflector has a slight velocity pull-up owing to a higher acoustic velocity with-in the block with respect to seawater. Note the hyperbola at the surface of the block as the result of irregular block topography

south of and radiating from the large blocks, suggesting that the blocks translated from the north, where the Shoup Glacier moraine is located. The blocks have pushed away existing basin sediments inducing compressive deformation and producing semi-circular relief. Further evidence of the importance of these blocks in generating tsunamis comes from observations of estimated wave heights, direction of wave propagation, and damage that occurred at Port Valdez in 1964 (Fig. 3; Plafker et al. 1969). The highest, most destructive waves occurred near Shoup Bay, with the directions of the waves emanating from the blocks. Assuming that the blocks are from the Shoup Glacier moraine, large, intact blocks up to 40-m high translated for over a km across the fiord floor.

A second main objective of this study is to determine whether pre-1964 submarine landslide deposits are present beneath Port Valdez. The stratigraphy of the main fiord sediment fill is dominated by two acoustic facies: a parallel to subparallel laminated facies and an acoustically chaotic to transparent facies with a less common transparent facies (Figs. 3 and 4). The well-laminated facies is common to many fiords and is considered to represent normal, background sedimentation. Major rivers (Lowe River and Valdez Glacial Stream) discharge sediment into the eastern end of Port Valdez where a prominent fiord-head delta is located. The layered facies is most likely composed of turbidites that originated from the failure of the fiord-head delta as well as hemipelagic sediment. Layered reflectors dominate the deeper fiord-fill in western Port Valdez (Fig. 4). Because of the relatively low mini-sparker power source combined with interference from the water bottom multiple, acoustic basement is too deep in places to be imaged on mini-sparker profiles.
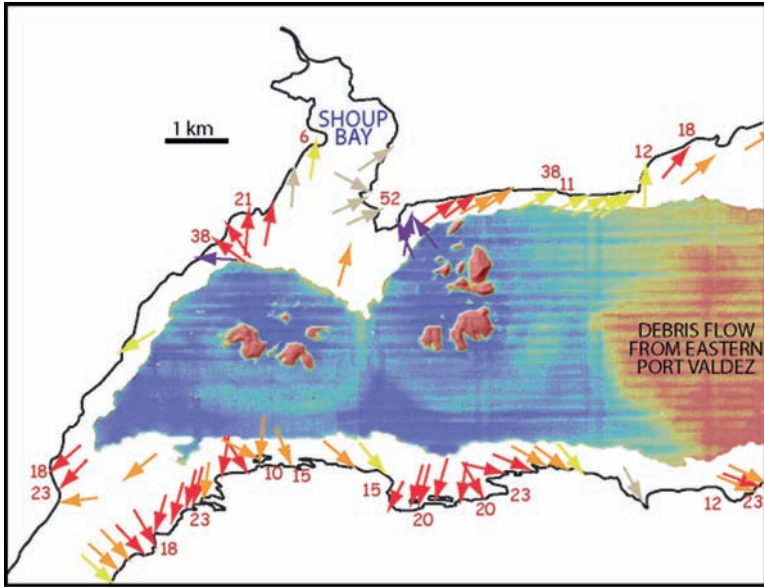
Fig. 3 Multibeam imagery of the floor of western Port Valdez over the depth range of 237 to 247 m. Note the semi-circular bathymetric highs that surround the blocks off of Shoup Bay. Numbers in red are tsunami wave heights in meters estimated after the 1964 earthquake (Plafker et al. 1969). The arrows refer to the inferred direction of wave movement and are color-coded to the magnitude of damage from beige (least amount of damage) to yellow to orange to red, to purple (extensive damage) (for additional information refer to Plafker et al. 1969)
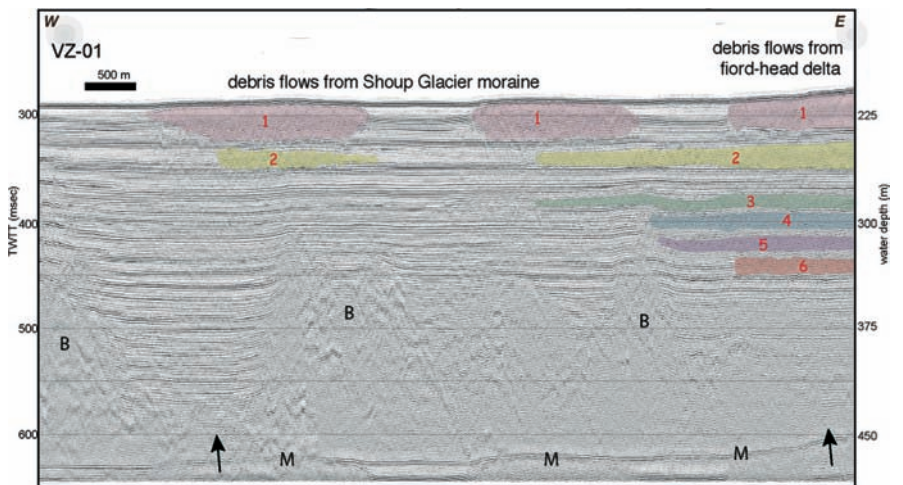
Fig. 4 E-W mini-sparker reflection profile collected in southwestern Port Valdez (see Fig. 1 for location). The acoustically opaque facies have been colored and labeled 1–6; the layer-parallel facies occurs in between the opaque facies. At least 6 debris lobes are imaged; the deeper lobes are thinner, spatially more restricted and separated by thinner intervals of layered reflectors. The M denotes the water bottom multiple; the B acoustic basement. The arrows point to layered reflectors imaged at the deepest part of the section near the water bottom multiple

However, von Huene et al. (1967) collected a single-channel airgun record profile along the axis of Port Valdez. They determined that the maximum sediment fill in the fiord is on the order of 450 m and noted that layered sediment dominates the upper two-thirds of the fill. The deepest, non-layered unit is inferred to be glacial in origin, but deposited prior to the complete withdrawal of ice from Port Valdez (von Huene et al. 1967).

Intercalated between the layered sediments are acoustically chaotic to transparent units and, notably in the near-surface interval, a transparent unit. The near-surface transparent unit is interpreted to be a turbidite facies with a ponding geometry. Beneath the transparent unit is a chaotic to transparent unit that is locally lens-shaped and in places truncates layered reflectors below (Fig. 4). We interpret the chaotic to transparent facies to consist of debris lobe deposits generated by submarine landslides triggered by earthquakes on the Alaskan megathrust. The termination of reflectors is the result of either scouring (especially for debris flows emanating from eastern Port aldez) or fold and thrust-type deformation of basin sediments forced by slide blocks (see Schnellmann et al. 2005; Cauchon-Voyer et al. 2008) off the Shoup Glacier moraine. As many as six debris lobes can be correlated between mini-sparker profiles (Fig. 4). Isopach maps of the three shallowest debris lobes are shown in Fig. 5. Although the mini-sparker profiles do not cover all of Port Valdez, differences in the thickness and the distribution of the debris lobes are evident (Fig. 5). The shallowest debris lobe 1 is also the thickest (as thick as 42 m) and the most extensive (covering most of western Port Valdez). One reason that debris lobe 1 is locally very thick is that large blocks (shown in bathymetry data in Fig. 1) are incorporated in this deposit. Debris lobe 2 has a similar distribution as lobe 1, however, it only has a maximum thickness of 34 m. None of the deeper debris lobes (3–6) are imaged in western Port Valdez off of Shoup Bay, and they are generally thinner than lobes 1 and 2. For example, debris lobe 3 has a maximum thickness of only 13 m (Fig. 5). Although compaction may be responsible for some of the de-crease in thickness of the debris lobes with depth, the coarser nature of the debris flows suggests that this would be minimal.

4   Discussion

The 1964 earthquake on the Alaskan megathrust triggered landslides emanating from two primary sources: the fiord-head delta in eastern Port Valdez and the Shoup Glacier moraine (Figs. 1 and 3). These landslide-generated debris lobes are acoustically chaotic-to-transparent and include large relatively intact blocks such as are evident off the mouth of Shoup Bay. Beneath the 1964 debris lobe are several acoustically chaotic-to-transparent units that we also attribute to landslide generated debris flows triggered by paleoseismic events. The acoustic character of these units is similar to that imaged in a more detailed study of multiple prehistoric slump deposits triggered by earthquakes in Switzerland (Schnellmann et al. 2002). Although we have not directly sampled the paleo-debris lobes, their similarity to
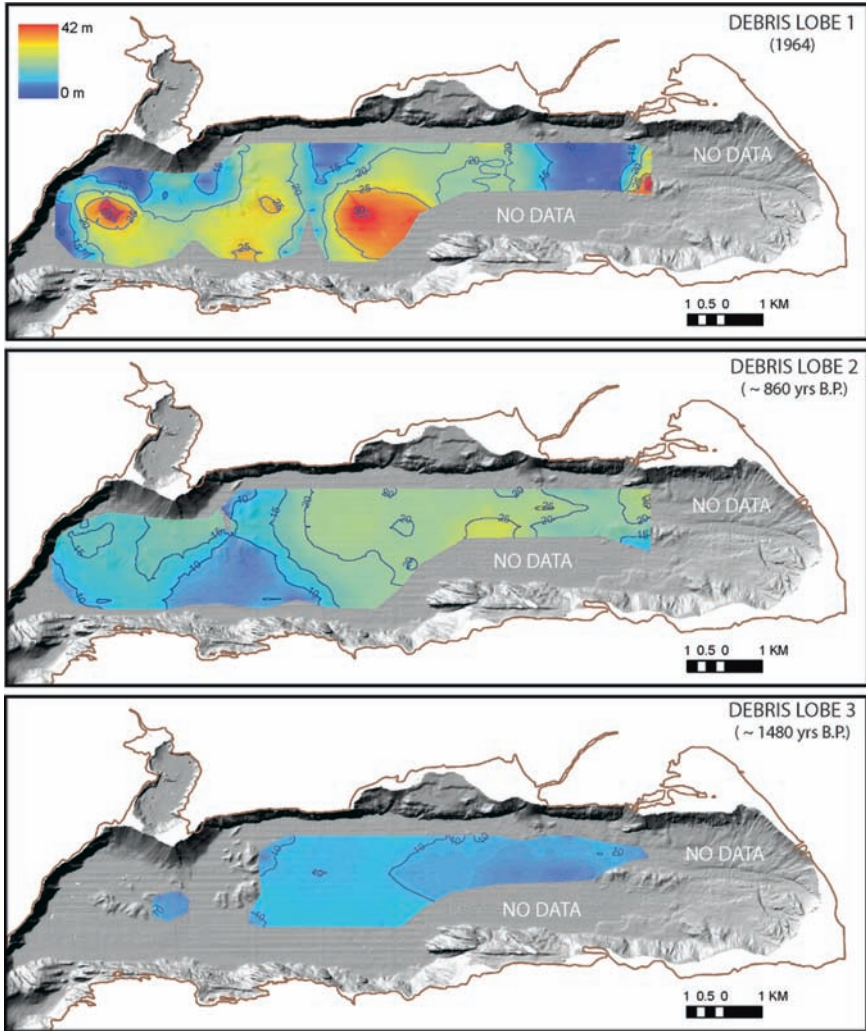
Fig. 5 Isopach maps showing the thicknesses of the 3 shallowest debris flows (including transported and deformed basin-sediment) based on an acoustic velocity of 1,600 m/s. The thickness, extent and volume of the debris lobes vary with time. The ages of the lobes are assumed to correlate with previous Aleutian megathrust earthquake that have been dated using paleo-seismology methods (Carver and Plafker 2008). Contour interval is 5 m. North is toward the top of the images

the 1964 debris lobe suggests that these were also triggered by earthquakes on the Alaskan megathrust and that we can relate the spatial and temporal changes in the distribution of the debris lobes to potential differences in the recurrence and/or size of a megathrust event.

We attempt to date the paleo-debris flow deposits by measuring the thickness of layered sediment deposited between the debris flows (in areas where erosion of the layered section is minimal) and then applying sedimentation rates derived from gravity cores to calculate the amount of time needed to deposit the layered sediment between debris flow deposits. Based on ^{137}Cs peaks in gravity cores, the modern sedimentation rate varies from 3.6 cm/yr in eastern Port Valdez to 0.2 cm/yr at a site in central Port Valdez (Fig. 1; Lee et al. 2007). As a check on whether these modern rates can be applied to the entire Holocene, a time-averaged sedimentation rate for central Port Valdez was estimated by dividing the total thickness of sediment fill by the time since the fiord became deglaciated. Based on ^{14}C ages of buried peat deposits collected near the shores of Port Valdez, the fiord is estimated to have been deglaciated by about 9 ka (Williams and Coulter 1981) or perhaps as early as 12 ka (Reger 1983). Using a minimal thickness of post-glacial retreat sediment of 300 m (based on TWTT to deepest imaged layered reflectors and an average acoustic velocity of 1,800 m/s) and an age for glacial retreat out of Port Valdez of 12 ka, the minimum time-averaged sedimentation rate is on the order of 2.5 cm/yr. This value is an order of magnitude higher than the modern rate for central Port Valdez. Jaeger et al. (1998) demonstrated that in areas that are dominated by large sedimentary events with long recurrence intervals (greater than 100 yrs), Holocene sediment accumulation rates can be 5 to 10 times greater than 100 yr rates.

Since sedimentation in Port Valdez is most likely dominated by large events, we use the time-averaged sedimentation rate of 2.5 cm/yr to date debris lobe 2. We estimate that debris lobe 2 was deposited between 670 and 1080 yrs prior to debris lobe 1. This age is consistent with the date for the penultimate megathrust earthquake (913–808 yrs B.P.) based on paleo-seismology studies (Carver and Plafker 2008). Beget (2007) found paleo-tsunami sand sheets at several sites near the head of Port Valdez, which dated at a similar time (within error bars) as the penultimate event (Carver and Plafker 2008). This substantiates a link between the deposition of debris lobe 2 and the timing of the penultimate earthquake on the Alaskan megathrust. If we accept the premise that all of the debris lobes formed as the result of landslides, induced by prolonged shaking during a great earthquake along the megathrust, we can assign tentative ages to the other debris lobes. Based on paleo-seismological studies, the timings of other well-constrained earthquake events on the megathrust are centered around 1,480, 2,125, 2,700, 3,060, 3,390, and 4,105 yrs B.P. (see Carver and Plafker 2008 for additional details). The first four of these events would presumably correspond to debris lobes 3 through 6. Note that the time interval between the 1964 and penultimate earthquakes (ca. 875 yrs) is longer than that between any of the other events. Also note that for megathrust earthquakes occurring prior to ~4 ka, there is no corresponding thick debris lobe deposit that is resolvable in our data (although very thin debris flow deposits may be intercalated within the layered sediment in the deeper fiord fill).

The Holocene climate in Alaska has been punctuated by several time periods of glacial advancement (e.g. the Little Ice Age) separated by warmer times of glacial retreat (e.g. the Medieval Warm Period) (Calkin et al. 2001; Hu et al. 2001; Reyes

et al. 2006). During the past 2,000 years, there have been 3 time periods when temperatures in Alaska were relatively warm: A.D. 0–300, A.D. 850–1200 and post-A.D. 1800 (Hu et al. 2001). Both the 1964 and penultimate event occurred following times of glacial retreat that occurred during the twentieth century and the Medieval Warm Period; these debris lobes were also the thickest and most spatially extensive of the debris lobes. Glacial advances occurred from 1550–1250 B. P. and 3500–2500 B.P. (Reyes et al. 2006), which included the time frame when the other debris lobes (with the possible exception of debris lobe 4) were deposited.

We propose that at times of glacial retreat, increased sedimentation to the fiord-head delta results in thicker deposits of underconsolidated sediment with low shear strength (e.g. Hampton et al. 1996), which may be more prone to larger failures when triggered by a megathrust earthquake. A lengthening of the recurrence interval between megathrust earthquakes would also allow for the accumulation of thicker packages of sediment that could potentially fail. This may explain why the thickness of the 1964 debris lobe was greater than that of the older lobes as it occurred after the longest recurrence interval for megathrust earthquakes and soon after a rapid retreat of Valdez Glacier (Molnia 2008). Thus glacier retreat resulted in the build-up of a fiord-head delta that was prone to failure, which combined with longer recurrence intervals between megathrust earthquakes may have resulted in the generation of thicker debris lobes through time. It is unclear why the Shoup Glacier moraine apparently only failed during the 1964 and penultimate earthquakes. Glacial retreat from the Shoup Bay terminal moraine beginning in the late 1700's A.D. (Post and Viens 2000) and also perhaps during the Medieval Warm Period (ca. 850–1200 A.D.) may have facilitated the failure of the moraine.

5   Conclusions

Coherent block failures of the Shoup Glacier moraine combined with debris flows from the fiord-head delta contributed to large tsunami-wave runups during the M9.2 Alaskan megathrust earthquake in 1964. Major earthquake-triggered land-slide events have occurred previously at Port Valdez, with at least five additional debris lobes older than the 1964 event imaged on reflection profiles. The debris lobe beneath the 1964 deposit correlates well with the timing of the penultimate event on the Alaskan megathrust (ca. 1090 A. D.; Carver and Plafker 2008). Older debris lobes (3–6) are generally thinner and separated by thinner sequences of layered sediment. Variations in the thickness and spatial extent of the debris lobes are probably tied to the amount of sediment that has accumulated at the fiord-head delta in eastern Port Valdez. Failures from the fiord head delta contributed to all six of the debris lobes; however, failure of the Shoup Bay moraine appears to have only occurred during the 1964 and the penultimate events. The thickest and most extensive debris lobes were generated during the 1964 and penultimate events that occurred during relatively warm periods (e.g. the twentieth century and the Medieval Warm Period). The failure of the Shoup Glacier moraine resulted in the

generation of much higher tsunami waves than failures attributed to the fiord-head delta; this is the focus of ongoing research.

References

Alexander CR, Venherm C (2003) Modern sedimentary processes in the Santa Monica, California continental margin: sediment accumulation, mixing and budget. Mar Environ Res 56:177–204

Beget J (2007) Earthquake, landslide and tsunami hazards in the Port Valdez area, Alaska. Consultation to the Prince William Sound Citizen's Advisory Council, Alaska Beget Consulting, Fairbanks, AK 55

Calkin PE, Wiles GC, Barclay DJ (2001) Holocene coastal glaciation of Alaska. Quat Sci Rev 20:449–461

Carver G, Plafker G (2008) Paleoseismicity and neotectonics of the Aleutian subduction zone – an overview. In: Freymueller JT, Haeussler PJ, Wesson RL, Ekström G (eds) Active Tectonics and Seismic Potential of Alaska, Geophys Monogr Ser 179. Am Geophys Union, Washington, 350 pp., ISBN 978-0-87590-444-3, AGU Code GM1794443

Cauchon-Voyer G, Locat J, St-Onge G (2008) Late-Quaternary morpho-sedimentology and submarine mass movements of the Betsiamites area, Lower St. Lawrence Estuary, Quebec, Canada. Mar Geol 251:233–252

Coulter HW, Migliaccio RR (1966) Effects of the earthquake of March 27, 1964 at Valdez, Alaska. US Geol Surv Prof Pap 542-C, 36

Jaeger JM, Nittrouer CA, Scott ND, Milliman JD (1998) Sediment accumulation along a glacially impacted mountainous coastline. Northeast Gulf of Alaska. Basin Res 10:155–173

Hampton MA, Lee HJ, Jocat J (1996) Submarine landslides. Rev Geophys 34:33–59

Hu FS, Ito E, Brown TA, Curry BB, Engstrom DR (2001) Pronounced climatic variations in Alaska during the last two millennia. Proc Natl Acad Sci 98:10552–10556

Lee HJ, Ryan HF, Kayen RE, Haeussler PJ, Dartnell P, Hampton MA (2006) Varieties of submarine failure morphologies of seismically-induced landslides in Alaskan fjords. Nor J Geol 86:221–230

Lee HJ, Ryan HF, Haeussler PJ, Kayen RE, Hampton MA, Locat J, Suleimani E, Alexander CR (2007) Reassessment of seismically induced, tsunamigenic submarine slope failures in Port Valdez, Alaska, USA. In: Lycousis V, Sakellarion D, and Locat J (eds) Submarine mass movements and their consequences, 357–365

Molnia BF (2008) Glaciers of North America – Glaciers of Alaska. In Williams RS Jr, and Ferrigno JG (eds) Satellite image atlas of glaciers of the world. US Geol Surv Prof Pap 1386-K, 525

Plafker G, Kachadoorian R, Eckel EB, Mayo LR (1969) Effects of the earthquake of March 27, 1964 on various communities. US Geol Surv Prof Pap 542-G, 50

Post A, Viens RJ (2000) Preliminary bathymetry of Shoup Basin and late Holocene changes of Shoup Glacier, Alaska. US Geol Surv Water-Resources Investig Rep 94–4093, 11

Reger RD (1990) Deglaciation of the Allison-Sawmill Creeks area, south shore of Port Valdez, Alaska. Alsk Div Geol Geop Surv, Public Data File 90–18, 10

Reyes AV, Wiles GC, Smith DJ, Allen S, Jackson S, Larocque S, Laxton S, Lewis D, Calkin PE, Clague JJ (2006) Expansion of alpine glaciers in Pacific North America in the first millennium A. D. Geology 34:57–60

Schnellmann M, Anselmetti FS, Giardini D, McKenzie JA, Ward SN (2002) Prehistoric earthquake history revealed by lacustrine slump deposits. Geology 30:1131–1134

Schnellmann M, Anselmetti FS, Giardini D, McKenzie JA (2005) Mass movement-induced fold-and-thrust belt structures in unconsolidated sediment in Lake Lucerne (Switzerland). Sedimentology 52:271–289

von Huene R, Shor GG Jr, Reimnitz E (1967) Geological interpretation of profiles in Prince William Sound, Alaska. Geol Soc Am Bull 78:259–268

Williams JR, Coulter HW (1981) Deglaciation and sea-level fluctuations in Port Valdez, Alaska. In: Albert NRD, Hudson T (eds) The United States Geological Survey in Alaska: Accomplishments during 1979, US Geol Surv Circ 823-B, B78–B80

Multibeam Bathymetry Investigations of Mass Movements in Lake Le Bourget (NW Alps, France) Using a Portable Platform

G. Ledoux, P. Lajeunesse, E. Chapron, and G. St-Onge

Abstract Here we report on a recent survey undertaken on Lake Le Bourget (NW Alps, France) using a multibeam echosounder mounted on a portable and shallow-draft platform. The 3.6×2.8 m survey platform can be transported from one lake to another and deployed within a few hours. Its shallow draft allows surveying in areas as shallow as 3 m, while the multibeam echosounder allows maximum sounding depths of 500 m. The collected data have allowed identifying two main areas of the lake affected by mass movements. In the northwest sector of the lake, a large mass wasting deposit of 1.8 km^2 is found at the base of a very steep slope. This large deposit may be correlated with a major late-glacial mass-wasting event that triggered a seiche in Lake Le Bourget. To the north of this deposit a mass-wasting deposit is interpreted to have been caused by the AD 1822 earthquake. In the southeast sector of the lake, many lobes and a large mass wasting deposit are reported for the first time. The presence of gas-rich sediments in this area has prevented acoustic penetration and thus their identification during previous seismic surveys. The occurrence of mass movements is correlated with interflow deposition zones. In addition to the mass movements, a series of collapse craters are identified in the northern sector of the lake. These collapse craters are located near the head scars of an incipient slide. Considering that earthquakes are common in the region and can cause liquefaction within the lake sediments, there is a possibility that this incipient slide may further develop and eventually generate a massive (>107 m^3) slide.

G. Ledoux (✉) and P. Lajeunesse
Université Laval, Centre d'études nordiques & Département de géographie,
Québec, QC, Canada, G1V 0A6
e-mail: gregoire.ledoux.1@ulaval.ca; Patrick.Lajeunesse@ggr.ulaval.ca

E. Chapron
Université d'Orléans, CNRS/INSU, Université François Rabelais-Tours, Institut des Sciences de la Terre d'Orléans (ISTO)-UMR 6113, 1A rue de la Férollerie, F-45071 Orléans cedex 2, France
e-mail: emmanuel.chapron@univ-orleans.fr

G. St-Onge
Université du Québec à Rimouski, Institut des sciences de la mer de Rimouski (ISMER),
Rimouski, QC, Canada, G5L 3A1
e-mail: guillaume_st-onge@uqar.qc.ca

1   Introduction

Glacial lakes are environments that are prone to the occurrence of sublacustrine mass movements due to their high sediment supply during deglaciation, steep slopes and, in many cases, location in tectonically active regions (Chapron et al. 2004). In the Western Alps, disturbed lake sediment layers have been attributed to major postglacial seismic events (Beck et al. 1996; Chapron et al. 1996, 1999; Guyard et al. 2007). Previous studies conducted in Lake Le Bourget (NW Alps) using seismic and sidescan sonar data revealed the presence of sublacustrine mass-movement features that include slumps, slides, debris flows and homogenites (i.e., seiche deposits) that were attributed to the Holocene seismic activity (Chapron et al. 1996, 1999, 2004; Chapron 1999). The location of this lake in an active seismo-tectonic region and the presence of thick layers of deglacial and postglacial sediments on its steep slopes are conditions that are favorable for the occurrence of sublacustrine mass movements. In this paper, we present new multibeam echosounder data collected in 2008 in Lake Le Bourget. The data image in great detail the mass movements that were reported in previous studies and bring new information on the occurrence of mass movements in areas of the lake that were not well documented.

1.1   Regional Setting

Lake Le Bourget (45° 45′ N, 52° 5′ E) is a narrow over-deepened basin of glacial origin oriented North–South (Fig. 1). This warm monomictic and mesotrophic lake is 18 km long, 2–3 km wide and has a maximum depth of 146 m. The water level is currently at an altitude of 231.5 m. The pluvionival watershed of Lake Le Bourget is about 629 km^2. The two main tributaries of the lake are the Leysse and the Sierroz rivers (Chapron 1999). The lake is located in a syncline underlain by Tertiary molasse deposits. This molassic basin is bordered on the South-East by the Subalpine chains and on the North-West by the inner Jura mountains. Lake Le Bourget is surrounded by the first ranges of the south end of the Jura Mountains that mainly consist of Jurassic and Cretaceous limestone. It is located in an area of strike-slip transfer faults and is bounded in the North by the Culoz Fault and in the South by the Col du Chat Fault (Fig. 1). Earthquakes generated by recent tectonic movements in the region reached maximum magnitudes of 6 on the Richter scale (Thouvenot et al. 1990).

Lake Le Bourget is a relic of a large postglacial lake that filled the glacial valley eroded by the Rhone and Isere glaciers (Bravard 1987). During deglaciation, the main tributary of this lake was the Rhone River. The progradation of the Rhone fan delta has gradually filled the northern sector of the lake, which is now occupied by
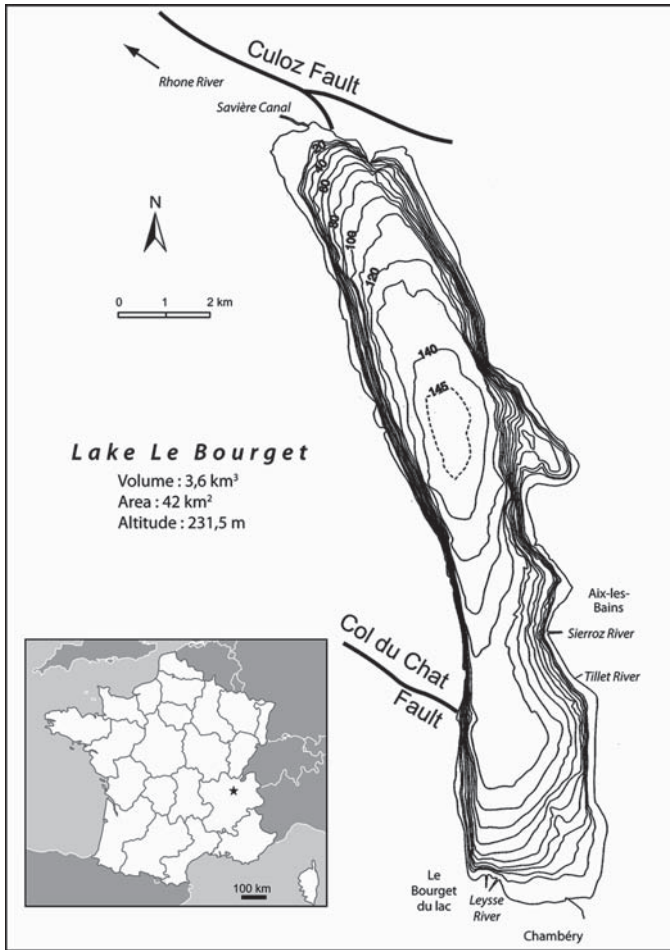
Fig. 1 Location and bathymetry (Chapron, 1999) of Lake Le Bourget (NW French Alps)

the Chautagne and Lavour swamps. This filling led to the isolation of the lake, which then induced a drastic reduction in the sedimentary inputs from the Rhone. Following this event, only major floods of the Rhone entered the lake through its natural outlet, the Saviere canal, and/or the Chautagne swamp (Chapron 1999).

1.2   Previous Work

In 1991 and 1993, two seismic surveys (sparker source and a single-channel streamer) were conducted by the Renard Center of Marine Geology (RCMG) of

Ghent University and the Laboratoire de Géodynamique des Chaînes Alpines (LGCA) of University of Savoie (van Rensbergen et al. 1999; Chapron 1999). Those campaigns used a sparker source and allowed the identification of five main seismic units within the sedimentary infill of Lake Le Bourget, which reaches a total thickness of 250 m. The sedimentary sequence is composed -from base to top- of glacial outwash deposits (unit 1), glacio-lacustrine sediments (unit 2), proglacial lacustrine fans (unit 3), alluvial fan deltas (unit 4) and a Holocene lacustrine drape of mainly authigenic sediments (unit 5) (van Rensbergen et al. 1999). In 2000, the RCMG conducted another seismic survey in the northern sector of the lake using a SEISTEC boomer at a mean frequency of 3.5 kHz (Chapron et al. 2004). In 2002, the Institut des Sciences de la Terre d'Orléans (ISTO) of Orléans University, performed a very high-resolution seismic survey in the main basin (Chapron et al. 2005) with a chirp source (modulating frequency centered at 12 kHz). The 8–15.5 m thick authigenic lacustrine drape (unit 5) is characterized by a parallel-stratified seismic facies of varying amplitude that conformably drapes the morphology of the basin (Chapron et al. 2004, 2005). Chapron et al. (2002, 2005) and Arnaud et al. (2005) have shown that the seismic reflectors within this Holocene lacustrine drape correspond to an alternation of inter- and underflow deposits identified on short gravity and long piston cores. These flood deposits highlighted a significant increase of clastic sedimentation since 2800 years BP.

In the entire northern basin, the Holocene sediment drape is underlain by the Hautecombe Disturbed Unit (HDU), a late-Glacial deposit associated with a major mass-movement event, which affected the northwestern slope of the lake basin (Chapron et al. 1996). The HDU is a 24 m thick chaotic unit with an irregular base that extends across the entire northern part of the lake, north of the Sierroz delta (Chapron et al. 1996). In the central sector of the northern basin, the HDU is partly covered with a 4 m thick reflection-free layer interpreted as a seiche deposit (van Rensbergen et al. 1999).

Numerous mass movements have been identified by the seismic surveys and sedimentological analysis (Chapron et al. 1996, 1999, 2002, 2004, 2005; van Rensbergen et al. 1999). They include slumps, slides, debris flows, seiche deposits, as well as creeping and slide-induced compression features. Most of coeval sublacustrine mass movements identified in the sedimentary infill of lake basins in the western, central and south central Alps in France, Switzerland and Italy have been attributed to earthquakes (Siegenthaler et al. 1987; Beck et al. 1996; Schnellmann et al. 2002; Fanetti et al. 2008). In Lake Bramant (French western Alps), Guyard et al. (2007) identified a slump caused by the AD 1881 Allemond earthquake and attributed a turbidite to the AD 1822 Chautagne earthquake. The epicenter of the 1822 earthquake was located near the Culoz fault. This earthquake resulted in the formation of a large subaqueous slide (ca. 840,000 m³) in Lake Le Bourget. This slide and the earthquake wave propagation triggered a violent seiche effect during the event and resulted in a 19 cm thick seiche deposit occurring today at 20 cm below the sediment surface in the deepest part of the lake (Chapron et al. 1999).

2   Data and Methods

The multibeam echosounder survey was conducted on a 3.6 m × 2.8 m UWITEC®
portable coring platform (Figs. 2a–c). This sectionalized platform is easily trans-
portable from one lake to another and can be deployed within a few hours. Its shallow
draft (<1 m) allows surveys in areas as shallow as 3 m. The high-resolution bathy-
metric data of Lake Le Bourget was obtained using a Reson Seabat 8101 (240 kHz)
multibeam echosounder installed through the coring hole of the platform (Fig. 2c).
More than 80 h and about 220 km of multibeam recordings allowed us to cover the
entire surface of the lake floor below depth of 5 m with a grid size of 5 m at a vertical
accuracy of <1 m. The movements of the platform were measured by an IXSEA
Octans III motion sensor while the multibeam processor applied compensations for
the attitudes. Sound velocity profiles were collected using a SeaBird SBE-19 CTD
profiler and the corrections were applied to the multibeam data. An SXBlue II
(Geneq Inc.) GPS receiver with a horizontal accuracy of <2.5 m was used to georef-
erence the data. The collected multibeam data was processed using the Hypack 8.0®
software on a Panasonic Toughbook® portable and waterproof computer. Visualization
of the bathymetry and the lake floor geomorphology was achieved with the
Fledermaus® software and mapping was realized with ArcGIS 9.2®.

3   Results

3.1   Bathymetry

The bathymetry of Lake Le Bourget is characterized by a North–South oriented basin
(Fig. 3). This basin reaches a maximum depth of 146 m in the north central portion of
the lake. The western basin slopes of the lake are very steep and range between 10°
and 50°; the eastern basin slopes are generally smoother and range between 10° and
20° but can reach maximum values of 30°. Well-documented molasse sequences
outcropping on land also occur along the NW slopes of the lake and locally form
plateaus allowing sediments deposition (Fig. 4). The northern and the southern part
of the lake are characterized by lower slopes of 2° to 4°.
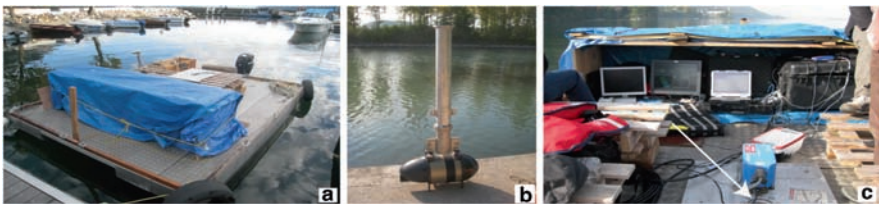
Fig. 2   (**a**) Multibeam survey platform, (**b**) Reson Seabat 8101 mount and (**c**) installation through
the coring hole (shown by *arrow*)
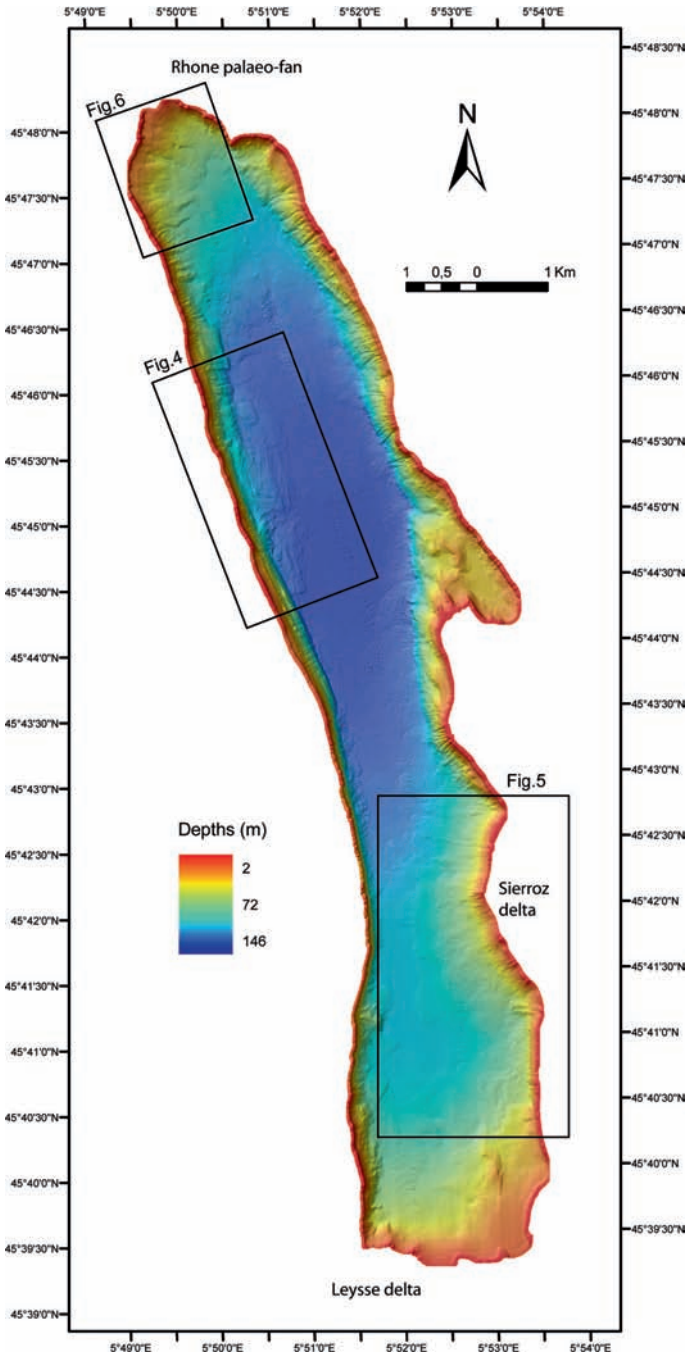
Fig. 3 Multibeam bathymetry of Lake Le Bourget showing the Sierroz, the Leysse and the Rhone palaeo-fan and the localization of the figures
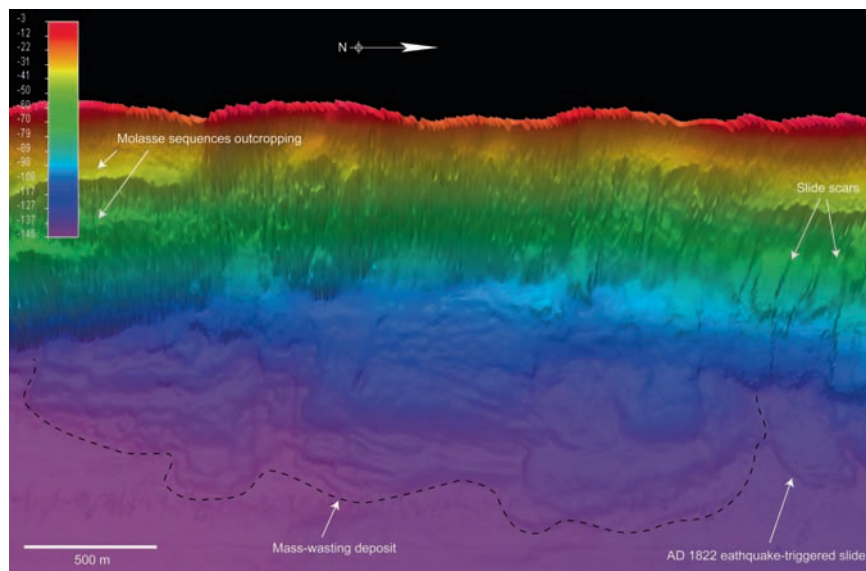
Fig. 4 Multibeam bathymetry of the northwestern slope of basin of Lake Le Bourget showing a large mass-wasting and the 1822 earthquake-triggered sublacustrine slide identified by Chapron et al. (1999)

3.2 *Lacustrine Sediment Disturbances*

3.2.1 **Mass-Wasting Deposits**

Mounds of sediment with hummocky upper surface located at the base of steep slopes are interpreted as mass-wasting deposits (MWDs). Large MWDs can be identified along the northwestern slope of the basin (Fig. 4) and at the South of the Sierroz delta (Fig. 5). Side scars are clearly noticeable on both sides of the MWD situated south of the Sierroz delta (Fig. 5). Smaller MWDs are scattered all around the lake basin and can be observed beside the Col du Chat fault, in the southwestern part of the lake, and along the eastern slope of the basin. Beside the large MWD of the northwestern slope, a well preserved lobe-shape MWD of $300 \times 325 \, \text{m}$ associated with slide scars on its upper slope suggests the occurrence of a recent slide (Fig. 4). The size of the MWDs observed in Lake Le Bourget ranges between a few thousands to several tens of thousands m². These MWDs can extend more than 600 m from the base of the slopes.

3.2.2 **Debris Flow Deposits**

Large lobe-like features are located along the Sierroz delta slope (Fig. 5). These lobes are interpreted as debris flow deposits and could represent the evolution of slides or slumps into debris flows (e.g., Mulder and Cochonat 1996). These debris
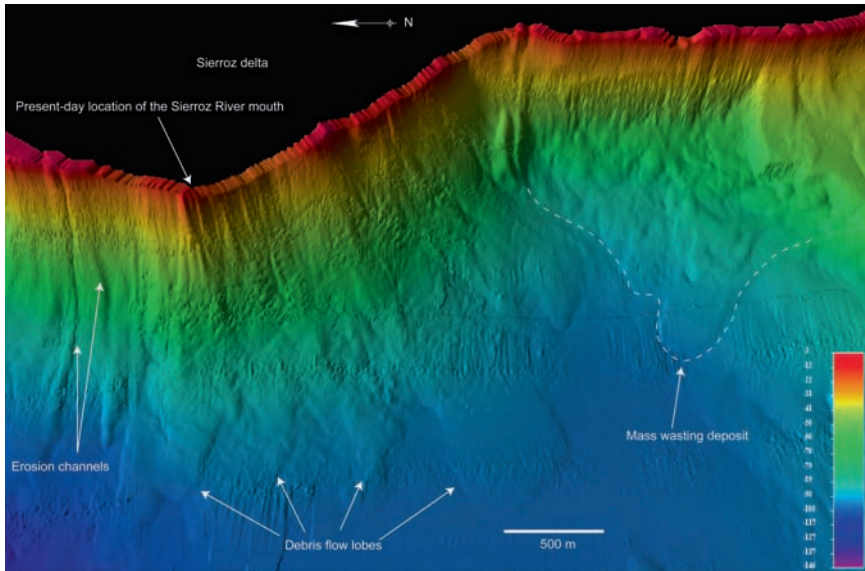
Fig. 5 Multibeam bathymetry of the Sierroz delta slope showing debris flow lobes, channels eroded by debris flows and a mass-wasting deposit

flow lobes can extend nearly 800 m on the lake floor from the base of the slopes and reach few hundred thousands of m^2. Most of the lobes observed along the Sierroz delta are coalescent while others are isolated.

3.2.3 Erosion Channels and Canyons

Erosion channels are located on the Sierroz delta slope (Fig. 5) and in the northern sector of the lake (Fig. 6). The erosion channels observed on the Sierroz delta slope occur in the north of the present-day location of the mouth of the Sierroz River (Fig. 5). It is about 500 m long by 40 m wide. These erosion channels could represent the palaeo-Sierroz channel formed by frequent underflows during flash floods events formerly entering the lake at this location (Chapron 1999). The erosion channel observed in the northern sector is about 750 m long by 65 m wide (Fig. 6) and is not related to any inlet. This feature suggests the occurrence of recent gravity reworking processes affecting the shallow water littoral platform. Numerous canyons are also observed along the steep slopes of the lake basin. These canyons are probably active, as shown by the occurrence of slope aprons downslope.

3.2.4 Collapse Craters

Small circular depressions are revealed by the multibeam data in the northern sector of the lake (Fig. 6). These depressions are interpreted as collapse craters, as identified by Chapron et al. (1996, 2004) on side scan sonar and seismic data. They are 10–20 m
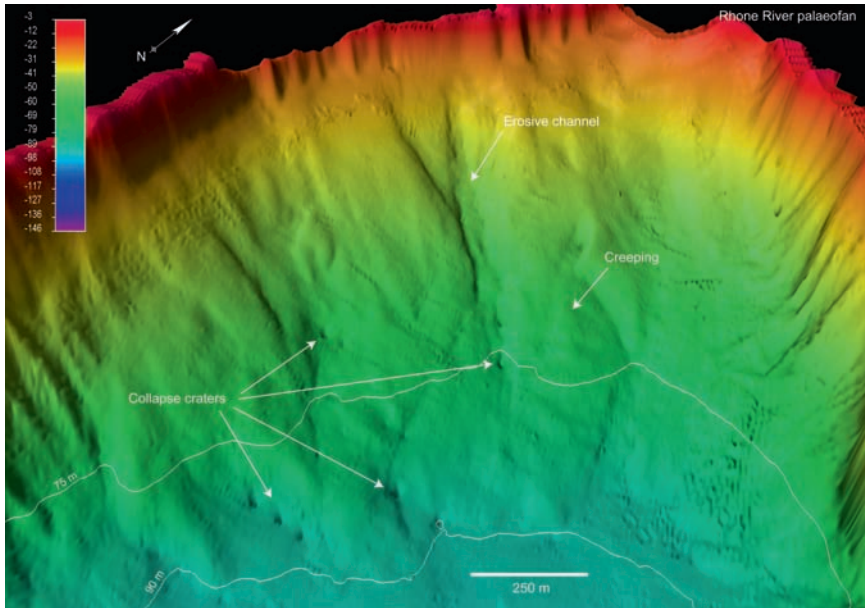
Fig. 6 Multibeam bathymetry of the northern sector of Lake Le Bourget showing collapse craters, erosion channel and the 75 and 90 m isobaths were occur the incipient scar of the ongoing sediment slide identified by Chapron et al. (2004) on sub-bottom profiles

in diameter and their central depression can be 0.5–2 m deep. The collapse craters identified on the Rhone palaeo-fan are located between 70 and 90 m deep. These collapse craters are interpreted as resulting from the expulsion of water and/or gas migration due to faults in the sediment (Chapron et al. 2004), and to sediment liquefaction induced by earthquakes or by the increasing pore-pressure due to sediment loading, a common process in this environment (Allen 1982). Chapron et al. (2004) have shown that the funnels associated with these collapse craters affect the entire Holocene sediment drape, which is about 10 m thick in this area. These authors have demonstrated lateral water and/or gas accumulation and migration between the HDU and the Holocene sediment drape. Rippled surface situated beside the erosion channel of the Rhone palaeo-fan highlight the occurrence of creeping in gas rich sediments (Fig. 6), which suggest that a large area of the Rhone palaeo-fan is affected by ongoing gravity reworking processes.

4 Discussion

The new multibeam data presented in this paper reveal that the northwestern and the southeastern sectors of Lake Le Bourget are strongly affected by mass movements. These mass movements are located where the Holocene sediment cover is the thickest, reaching 24 m locally (van Rensbergen et al. 1999). The multibeam data shows for the

first time that mass movements also affected the southeastern portion of the lake near the Sierroz delta slope (Fig. 5), where gas-rich sediments are preventing sub-bottom seismic profiling. Sedimentary inputs from the Sierroz and the Leysse rivers in this part of the lake and the subsequent sedimentation on the steep delta slope (6° to 10°) are conditions that are favorable for the occurrence of mass movements in that sector. Interflows from the Leysse River are in particular derived to the east by the Coriolis force and contribute to increase sediment thickness along the southeastern portion of the lake (Chapron 1999, 2002). These sedimentary inputs and the degradation of organic matter into gas contribute to decrease the shear strength by increasing sediment drape thickness and thus, higher downslope moving forces (Allen 1982).

There is presently no river that flows into the lake along the northwestern sector of Lake Le Bourget. Therefore, mass movements identified in this area do not occur on the slope of a delta. However, the large and rapid sediment inputs from the Rhone River interflows during deglaciation (van Rensbergen et al. 1999) and the Holocene have been deflecting to the west by the Coriolis force, which favored sediment deposition in this sector (Chapron et al. 2002, 2005). This enhanced fined-grained sediments to accumulate along the western slope of the basin and thus, the possibility of mass movement triggering. The rippled topography of the large MWD identified in this sector occurs where Chapron et al. (1996) identified a large sublacustrine slide that can be linked to the formation of the HDU. The size of the identified deposit as well as its morphology suggests that this feature could be associated with the slide-induced HDU that is now buried and draped by 10 m of Holocene sediments. Beside this large MWD, the lobe-shape MWD with slide scar in the upper slope (Fig. 4) occurs where Chapron et al. (1999) identified a slide triggered by the AD 1822 earthquake. The well pre-served slide scar and slide-induced compressions on the upper surface of the lobe-shape deposit suggest that it corresponds to the AD 1822 earthquake-triggered slide.

Some of the collapse craters reported here within the Rhone palaeo-fan occur in gas-rich sediments. Due to the absence of signal penetration in such sedimentary conditions, most of these collapse craters have not been observed in previous studies using sub-bottom profilers. Our multibeam data show that collapse craters occur in an area characterized by a network of small disruptions associated with the incipient scars of an ongoing large sublacustrine sediment slide of $\sim 10^7$ m^3 (Chapron et al. 2004). According to Chapron et al. (2004), these scars are located along the 75 m and the 90 m isobaths. These incipient scars and the small disruptions have probably contributed to the expulsion of fluid and/or gas trough the impermeable Holocene sediments that formed collapse craters at these depths. Our results are consistent with the work of Chapron et al. (2004) and demonstrate that this sector of the Rhone palaeo-fan shows signs of slope instability. In addition to the presence of gas in the sediment that increases pore pressure and thus reducing sediment strength (Nisbet and Piper 1998), the presence of these collapse craters could be related to gas desta-bilization. According to Rothwell et al. (1998), most of the large slides result from gas destabilization. A small earthquake or even a new sediment supply delivered by a flooding river could lead to a slide (Nisbet and Piper 1998). Earthquakes are common in the region and major Rhone River floods can enter into the lake by the Saviere Canal. Such conditions are favorable for a large slide triggering in the

northern sector of Lake Le Bourget. This slide is susceptible to generate a seiche that could have significant consequences along the inhabited shores of the lake.

5   Conclusion

In this paper, we report on a multibeam echosounder survey conducted in Lake Le Bourget (NW Alps) using a shallow-draft and portable platform. The new multibeam data allowed us to identify features that have not been reported in previous studies due to the limited signal penetration of acoustic sediment profilers in gas-rich sediment zones. This study allowed the identification of two major areas of the lake that are affected by mass movements. In the northwest of the basin, a large deposit of ~1.8 km² can be identified at the base of the steep slope. This large deposit could be associated with a major late-glacial mass movement that led to the formation of a thick disturbed unit (HDU) covered by a seiche deposit. The subaqueous slide caused by the AD 1822 earthquake can also be observed in detail for the first time in the northwestern sector of the lake. Many mass movement features, such as debris flow lobes and a large mass-wasting deposit are also reported here for the first time along the southeastern slope of the lake. In the northern portion of the lake, collapse craters are situated in an area of a network of small disruptions associated with the incipient scars of an ongoing large sublacustrine sediment slide. The relationship between the seismo-tectonic setting of the region and the sublacustrine mass movements has been demonstrated in previous studies on several alpine lakes. In order to improve the understanding of the causes of mass movement triggering in Lake Le Bourget, further studies involving sub-bottom profiling and coring data should date Holocene MWDs and take into account the possible link between Holocene lake level fluctuations and anthropogenic factors along this populated lake shore, especially along the Sierroz delta (Aix-les-Bains urban area).

References

Allen JRL (1982) Sedimentary Structures: Their Character and Physical Basis. Elsevier, Amsterdam.
Arnaud F, Revel M, Chapron E et al (2005) 7200 years of Rhone river flooding activity in Lake Le Bourget, France: a high-resolution sediment record of NW Alps hydrology. Holocene 15:420–428.

Beck C, Manalt F, Chapron E et al (1996) Enchanced seismicity in the early post-glacial period: evidence from the post-Würm sediments of Lake Annecy, northwestern Alps. J Geodyn 22:155–171.

Bravard JP (1987) Le Rhone: Du Léman à Lyon. La Manufacture, Lyon.

Chapron E (1999) Contrôle climatique et sismo-tectonique de la sédimentation lacustre dans l'Avant-Pays Alpin (Lac du Bourget) durant le Quaternaire récent. Géologie Alpine, Mémoire H.S. 30.

Chapron E, Van Rensbergen P, Beck C et al (1996) Lacustrine sedimentary record of brutal events in Lake Le Bourget (Northwestern Alps-Southern Jura). Quaternaire 7:155–168.

Chapron E, Beck C, Pourchet P et al (1999) 1822 earthquake-triggered homogenite in Lake Le Bourget. Terra Nova 11:86–92.

Chapron E, Desmet M, De Putter T et al (2002) Climatic variability in the northwestern Alps, France, as evidenced by 600 years of terrigenous sedimentation in Lake Le Bourget. Holocene 12:177–185.

Chapron E, Van Rensbergen P, De Batist M et al (2004) Fluid-escape features as a precursor of a large sublacustrine sediment slide in Lake Le Bourget, NW Alps, France. Terra Nova 16:305–311.

Chapron E, Arnaud F, Noël H et al (2005) Rhone river flood deposits in Lake Le Bourget: a proxy for Holocene environmental changes in the NW Alps, France. Boreas 34:404–416.

Fanetti D, Anselmetti FS, Chapron E et al (2008) Megaturbidite deposits in the Holocene basin fill of Lake Como (Southern Alps, Italy). Palaeogeogr Palaeoclimatol Palaeoecol 259: 323–340.

Guyard H, Chapron E, St-Onge G et al (2007) High-altitude varve records of abrupt environmental changes and mining activity over the last 4000 years in the Western French Alps (Lake Bramant, Grandes Rousses Massif). Quat Sci Rev 26:2644–2660.

Mulder T, Cochonat P (1996) Classification of offshore mass movements. J Sediment Geol 66:43–57.

Nisbet EG, Piper DJW (1998) Giant submarine landslides. Nat 392:329–330.

Rothwell RG, Thomson J, Kähler G (1998) Low-sea-level emplacement of a very large Late Pleistocene 'megaturbidite' in the western Mediterranean Sea. Nat 392:377–380.

Schnellman M, Anselmetti FS, Giardini D et al (2002) Prehistoric earthquake history revealed by lacustrine slump deposits. Geol 30:1131–1134.

Siegenthaler C, Finger W, Kelts K et al (1987) Earthquake and seiche deposits in Lake Lucerne, Switzerland. Eclogae Geologica Helvetiae 80:241–260.

Thouvenot F, Frechet J, Guyoton F et al (1990) SISMALP: an automatic phone-interrogated seismic network for the western Alps. Cahiers du Centre Européen de Géodynamique et de Séismologie 1:1–10.

van Rensbergen P, De Batist M, Beck C et al (1999) High-resolution seismic stratigraphy of glacial to interglacial fill of a deep glacigenic lake: Lake Le Bourget, Northwestern Alps, France. Sediment Geol 128:99–129.

Morphodynamic and Slope Instability Observations at Wabush Lake, Labrador

D. Turmel, J. Locat, G. Cauchon-Voyer, C. Lavoie, P. Simpkin, G. Parker, and P. Lauzière

Abstract Since 1964, Iron Ore Company of Canada (IOCC) has deposited iron tailings resulting from mining operations into Wabush Lake, Western Labrador. Bathymetric surveys were carried out between 2004 and 2008 as part of the overall environmental IOCC plans to maintain safe disposal strategies of tailings into the lake. In this paper, we present the evolution in distribution and morphological characteristics over the last 4 years of the tailings overlying lacustrine sediments and bedrock. In 2004, a high definition multibeam survey of Wabush Lake was carried out for the first time and revealed lake floor features, including a fine network of channels and a delta foreslope with well-developed knickpoints. Other features such as older subaqueous mass movement scars and an esker were also identified. The delta foreslope channels, in 2004, led into a deeper long channel connected with the deepest part of the lake where turbidite deposition took place. A second bathymetric survey was carried out in 2006. Many of the features seen on the 2004 map were already buried by the advancing delta front. Results indicate that the 2004 channel system was almost completely obliterated with the generation of many new others. Development of the knickpoints is also observed where some are still present and

D. Turmel (✉), J. Locat, and G. Cauchon-Voyer
Laboratoire d'études sur les risques naturels, Département de géologie et de génie géologique, Université Laval, Québec, G1K 7P4, Canada
e-mail: dominique.turmel.1@ulaval.ca

C. Lavoie
Department of Geosciences, Hamilton College, Clinton, New York, 13323, USA

P. Simpkin
IKB Technologies Limited, 1220 Hammonds Plains Road, Bedford, Nova Scotia, Canada B4B 1B4

G. Parker
Ven Te Chow Hydrosystems Lab, Department of Civil Engineering, College of Engineering, University of Illinois at Urbana-Champaign, IC 61802, USA

P. Lauzière
Iron Ore Company of Canada, Environment Department, P.O. Box 10000, Labrador City, NL, Canada A2V 2L8

new ones are discovered. A third bathymetric survey conducted in 2008 demonstrates a different spatial arrangement of features. Well developed wider channels and new knickpoints are observed on the foreslope delta. The sequential analysis of 2004, 2006 and 2008 surveys proved to be a useful tool to evaluate: (1) the rate of infilling of the lake, where accumulation took place and by which mechanisms (2) the evolution of the foreslope delta gradient and, (3) the evolution of instability areas. Our results indicate that these recently developed techniques are useful tools for monitoring underwater tailings disposal and stability.

Keywords Landslides • knickpoints • tailings • sediments transport

1   Introduction

Wabush Lake, is located near Labrador City, Western Labrador, Eastern Canada (Fig. 1). Since 1964, Iron Ore Company of Canada (IOCC) discharges annually a volume of more than 100 m^3 of iron tailings at the southern part of the lake resulting from mine operations. With such a high sedimentation rate and the closed-like basin morphology of the lake (Fig. 2), Wabush Lake is a unique large-scale natural laboratory for studying sedimentary processes in an extremely dynamic environment. This study is part of an ongoing environmental plan of IOCC to maintain and improve the disposal strategies of iron tailings in the context of sustainable development. In general, tailings are transported to the near shore area of the lake by up to five pipelines discharging more or less at the same place at a given time. As the delta progrades, the pipelines are extended and their discharging points are often moved laterally. However, we can consider that the sedimentation progress into the Wabush Lake could be characterized as an advancing point source delta.

This paper focus on results obtained from three bathymetric surveys conducted on 2-year intervals from 2004 to 2008. On this sequential analysis of the lakefloor, we observed a topset, foreset and bottomset deltaic system, including a complex network of channels and multiple mass-transport movements such as knickpoints and landslides, characterized by planar and lateral spread failures. Particular attention will be given to the formation process of the channels and knickpoints in the southern and central part of the lake.

2   Methods

The multibeam sonar system used during the first survey, during July 23–28th 2004, was a Kongsberg Simrad EM-3000. In 2006 and 2008, a Reson Seabat 8101 system has been used. The surveys were held between July 11–20th in 2006 and between August 12th and September 2nd in 2008. All three surveys were calibrated on the same datum and the GPS precision (x, y) was about 1 m horizonal (using CDGPS in 2004 and 2006 and WAAS in 2008).
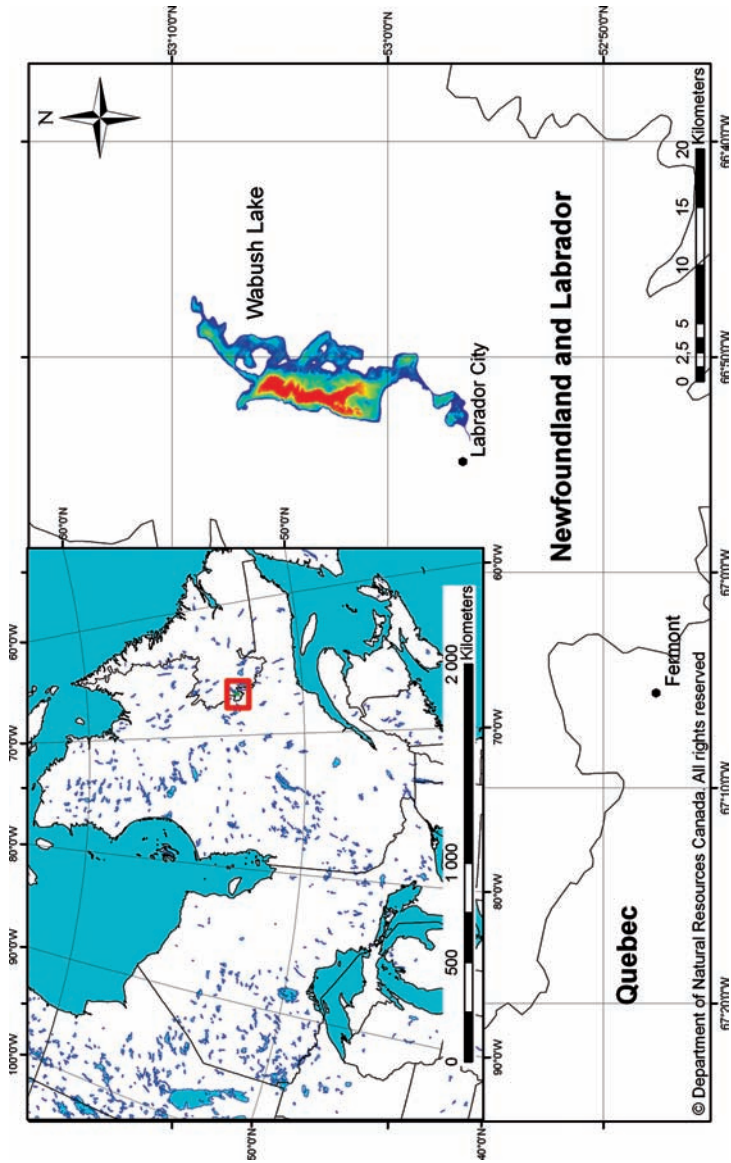
Fig. 1 Localization of Wabush Lake
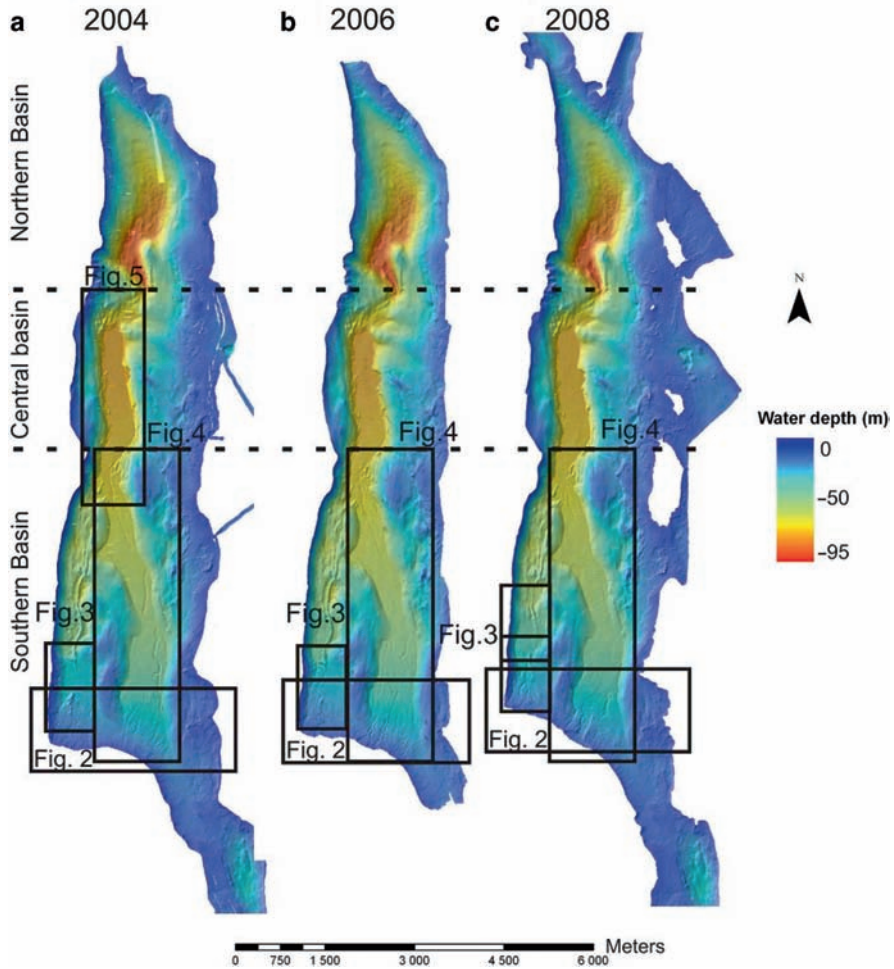
Fig. 2 Bathymetric maps of 2004 (**a**), 2006 (**b**) and 2008 (**c**) and localization of Figs. 2–6

3 Results

Wabush Lake is subdivided in three different parts: the Southern, the Central and the Northern Basin (Fig. 2). The 2004 bathymetric survey shows for the first time the subaqueous part of the tailings delta located in the southern part of the Southern Basin (Fig. 1a). At that time, most of the transport system was carried out via the eastern side of the lake.

On the eastern part of the delta frontset, channels of less than 2 m deep and about 20 m wide are observed (Figs. 3a and 5a). This system of channels connects itself to two wider channels at water depth of around 30 m. The west channel is 50 m wide
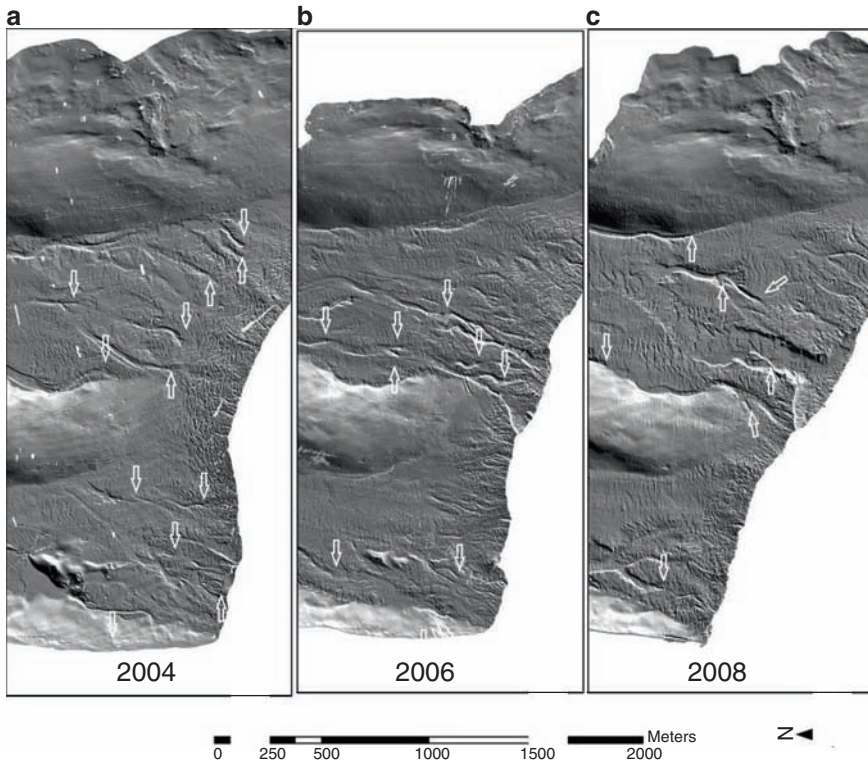
Fig. 3 Hillshade from the bathymetric map showing different channels and knickpoints (*arrows*)
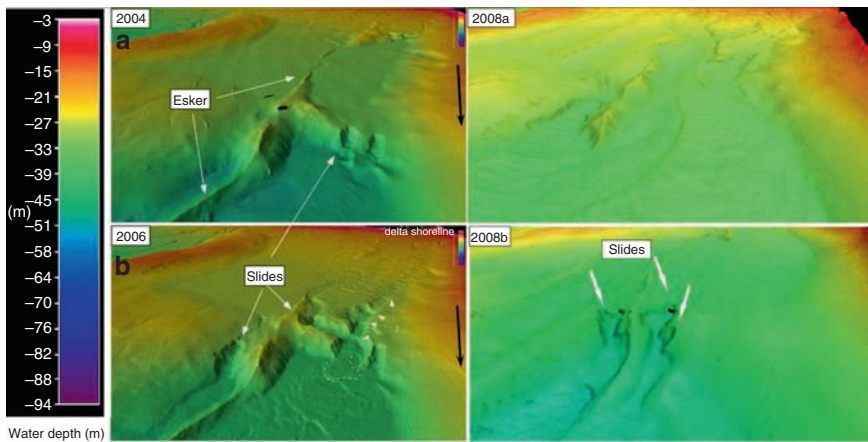
Fig. 4 Oblique view of a knickpoint migrating in the western part of the southern basin (see Fig. 1 for location). Part (d) of this figure shows new knickpoints developing in the lake, approximately 300 m from the others knickpoints. (modified from Locat and Lee 2009)
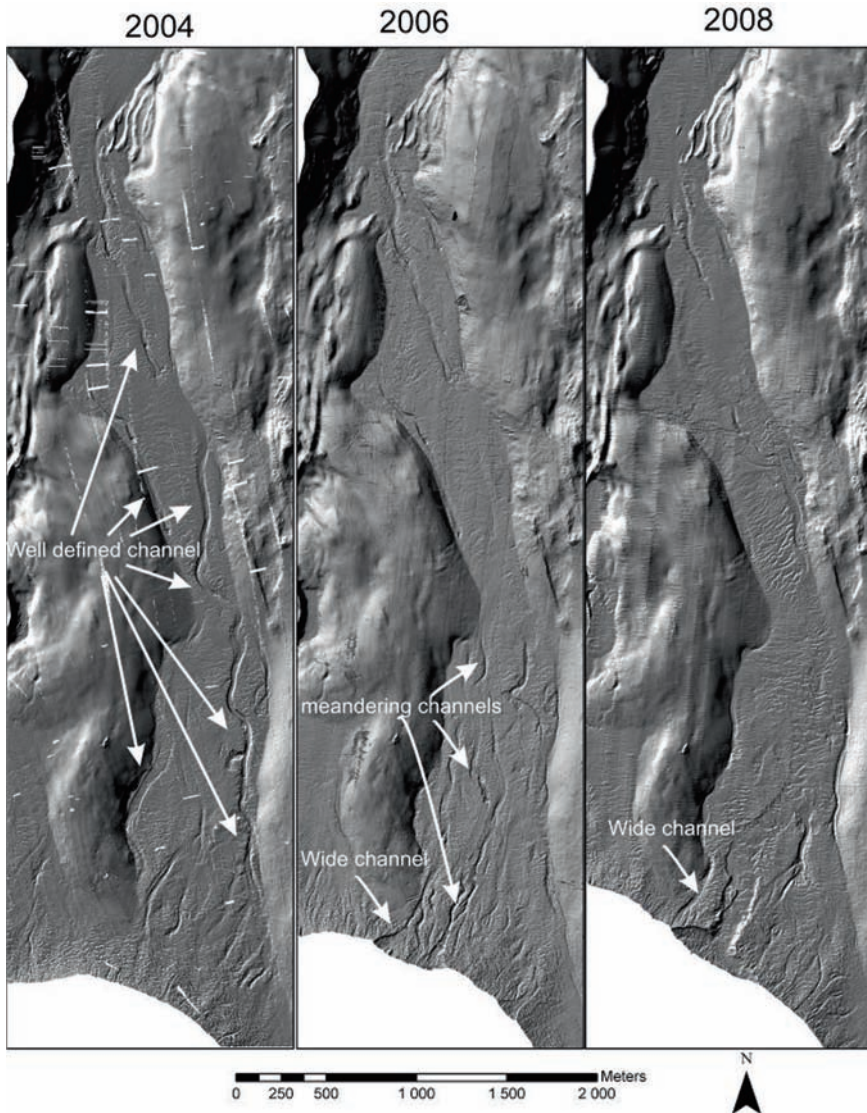
Fig. 5 Hillshade image of the western part of the central basin. This figure is located in Fig. 1

and 1.5 m deep, whereas the east channel is 25 m wide with a greater depth up to 5 m. This latter one is meandering down to the Central Basin, where it disappears (Fig. 4a). In the western part of the delta, channels are also observed, but they are not going down the central part of the lake. An esker of more than 3 km long is also discovered in this part of the lake (Fig. 4 a–d). An esker is a long and winding ridge of stratified sand and gravel deposited under a glacier.

Knickpoints are found on the frontset of the delta where turbidity currents are continuously formed due to the constant flow of tailings into the lake (Figs. 3a and 4a). Knickpoints are topographic depressions, characterized by a steep scarp slope and a flatter profile downslope. In the 2004 chart, they are formed on a mean slope of 1.8 (±0.9) degrees and can have a width up to 70 m (mean of 21 m). The mean scarp-slope of knickpoints is 13.8 (±5.8) degrees. Statistics are from all the knickpoints marked by an arrow on Fig. 3a–c. In the western part of the Southern Basin, two major knickpoints are also identified (Fig. 4a). These two parallel knickpoints have a scarp height of 6 m, an upslope of 4 degrees, a downslope of 5 degrees, and a scarp slope of 30 degrees. Their width is 22 m for the western one and 30 m for the other one.

In the central basin, two large landslides are visible (Fig. 6). The first one, located on the western flank, has a slide scarp of 1.2 km long, an average height of 2 m and an estimated volume of eroded sediments of about 0.5 Mm^3. The planar failure occurred on an average slope of 14 degrees. On the eastern flank, the other landslide is about 400 m long and 600 m wide. The estimated volume of displaced sediments is about 2.4 mm^3 and according its ridge-like morphology is interpreted as a lateral spread failure (Locat and Lee 2002).

A second bathymetric survey was conducted in 2006. The results show a significant evolution of the morphology of the lake floor since 2004 (Figs. 2b–5b). Using the spatial position of the 4 m isobath, the delta has prograded, between 2004 and 2006, 150 m in the eastern part of the delta to about 250 m in the western part. About 40 million tons of sediments have been discharged in the lake between 2004 and 2006.

The 2006 bathymetric data reveals that the single and well-defined channel reaching the central part of the lake is no longer present, as it was visible in 2004.
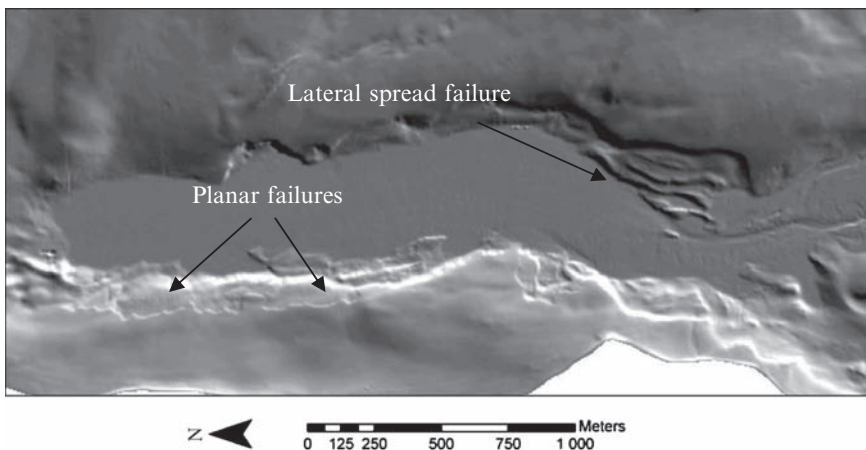
Fig. 6 Hillshade of the central basin from the 2004 bathymetric map showing planar failures and lateral spread failure. This figure is located in Fig. 1

However, the presence of many channels on the delta foreset is observed (Figs. 3b and 5b). A new wide and shallow channel is formed on the delta frontset, just where the subaerial channel formed by the tailings discharge is reaching the shoreline. The upstream section of this underwater channel has a conical shape, with a width of more than 250 m. This channel meanders for more than 1 km down into the lake.

Some of the knickpoints visible in 2004 are still present in 2006 (Fig. 3b) and new ones were discovered. In the western part of the Southern Basin, the two knick-points described earlier are still present, but their dimensions have evolved since the first multibeam survey (Fig. 4b). The western channel has migrated toward the coast line by about 20 m. The overall morphology of this knickpoint is similar to the 2004 description (i.e. same width, depth and slope angles). By 2006, the eastern channel has migrated upstream by about 175 m. A landslide is also visible in the scar of the knickpoint. The volume of displaced material, at that time, is estimated at ~76,000 m³.

Differential bathymetry maps (2006–2004, Fig. 7a) show that most of the tail-ings were deposited within the southern basin during this time interval. Tailings accumulation in the central basin is <0.5 m/year, whereas it reaches 5 m in the southern basin and >15 m near the delta shoreline. An example of the significant change in the sediment dynamics is the complete infilling of the main channel of the southern basin (shown in red in Fig. 7a).

The 2008 bathymetric data (Figs. 2c–5c) shows a very different morphology compared to the 2006 survey. This is mainly due to a major change in the disposal pattern on the delta: the mine has concentrated the routing of the pipelines to fill the western part of the lake. Approximately 50 m of sediments have been dis-charged into the lake between 2006 and 2008. Discharge rates between 2006 and 2008 were about 25 m/year, where it was of 20 m/year between 2004 and 2006.

There was significant deposition in the western part of the lake, reaching as much as 10 m in some area, which led to the progradation of the delta over a large portion of the esker. Some new channels are visible where the two knickpoints presented earlier were located (Fig. 4c). However, due to the very high sedimenta-tion rate, it is difficult to link these channels to knickpoint migration. On the other hand, in the same area, two new major knickpoints are presently forming along the esker (Fig. 4d). These knickpoints are ~5 m high, present a downslope of 5 degrees, a scarp slope of about 30 degrees and an upper slope of 4 or 5 degrees. These knickpoints look very similar to the ones described earlier.

A very different spatial arrangement in the channels can be observed when com-paring the 2008 bathymetric chart to the 2004 and 2006 charts. In 2004, there were two main channels grading down to the central basin, whereas in 2006 several small channels were present in the Southern Basin, but none of them reached the central basin. In 2008, there is one main channel (Figs. 3c and 5c) and two smaller chan-nels following the eastern and the western flank of the eastern part of the Southern Basin. The main channel has a width of >500 m for the first 150 m and narrows down to a width of 160 m for the following 500 m. Several hydraulic jumps are vis-ible in this channel and some ripples are also visible. The two smaller channels are intermittent and they are not connected to the central basin. There are also less
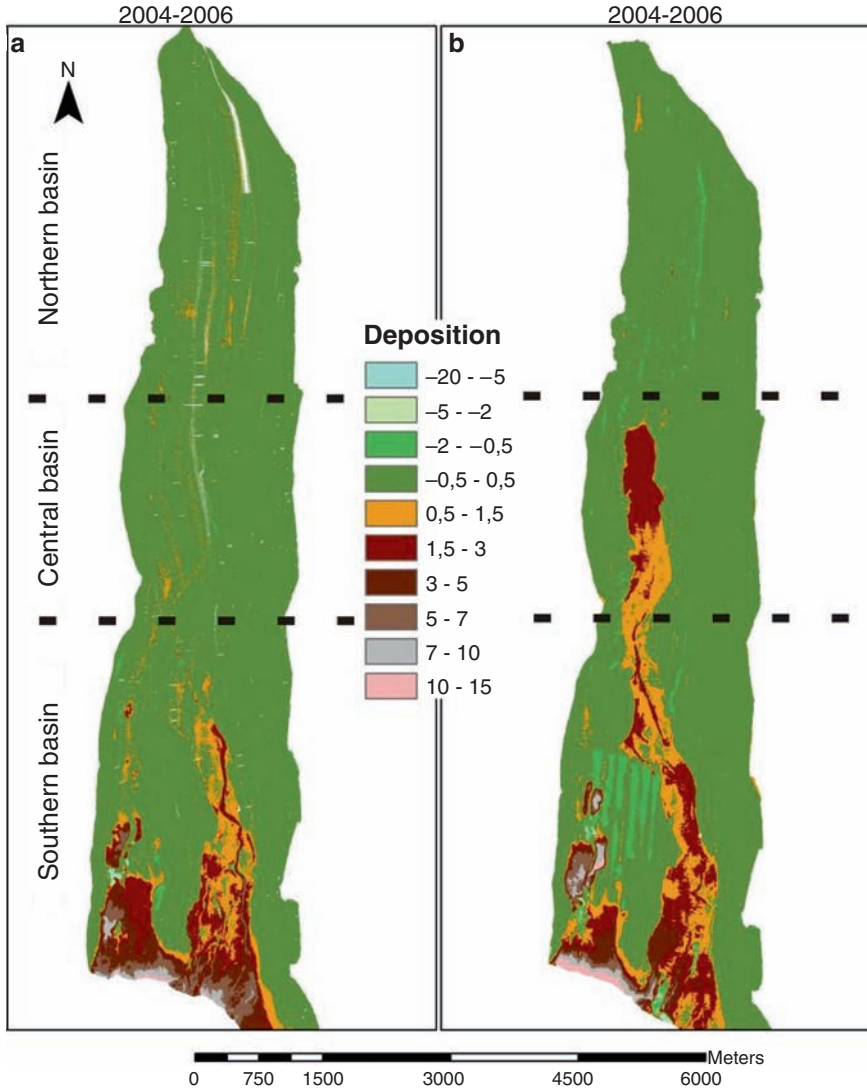
Fig. 7 Differential bathymetry maps. Deposition in meter

knickpoints visible in 2008 than in the previous two surveys. This difference may be due to the presence of a main channel draining most of the sediment supply in the deeper part of the lake.

In the central basin, debris from the western flank landslide are now mainly buried under the tailings. No landslides were identified in this sector of the lake between 2004 and 2008 and no channel has developed in the central sector of the lake.

The differential bathymetry map for 2006–2008 (Fig. 7b) shows that most of the sediment accumulation took place in the western part of the central basin, where the shoreline prograded for >400 m, while it has moved <75 m in the eastern part of the southern basin. This is mostly due to changes in the disposal strategies. The 2006–2008 differential map shows less accumulation in the western sector of the lake, while there has been >2 m of accumulation in the central basin, compare to <0.5 m of accumulation between 2004 and 2006.

4   Discussion

Wabush Lake is a very dynamic environment with significant change in the already high sedimentation rates due to the tailing disposal practices of IOCC that have been studied. The morphology of the lakefloor indicates that the sedimentation in the lake mostly occurred by avalanche process from the delta topset to the frontset and by hyperpicnal flows such as turbidity current in the deeper parts of the lake. The latter one has been also observed in other similar environments such as the ones created in laboratory (e.g. Kostic and Parker 2003). According to Normark et al. (1979) and Mitchell (2006), knickpoints are initiated by a change in turbidity current characteristics over an erodible bed. The 2004–2006 differential bathymetric chart shows that these turbidity currents did not supply sediments in the distal portion of the deltaic complex, as less than 1 m of sediments were deposited in the Central Basin. On the other hand, the 2006–2008 differential map shows sediments accumulation of more than 2 m located more than 6 km away from the delta (Fig. 7b). According to our results, it seems that large channels may serve as a bypass for turbidity currents that will carry sediments quite farther. As described above, the 2004 and 2006 charts do not show well-defined channels in comparison with a large channel described on the delta frontset of the last bathymetric map. The smaller channels as mapped in the earlier charts may restrain distal deposition.

Our results show many knickpoints mostly located in shallow areas of the lake, less than 30 m deep, but also at a depth up to 70 m. According to the hypothesis that large sedimentation in the deepest part of the lake is due to hyperpicnal flows sedimentation and these currents can travel a distance of more than 5 km to reach the deeper parts of the lake, we proposed that the knickpoints are initiated by turbidity currents. The example of knickpoint migration presented in Fig. 3 shows that this migration process may mobilize significant volume of material in a mode similar to an infinite slope (slab) failure process. It may be possible to identify them in instability areas. More geotechnical investigations on these knickpoints are in process.

In the deepest part of the lake, two landslide scars are visible (Fig. 6). The first one is located on the western flank of the trench and is characterized by planar failures. The resulting debris is now largely buried by the intensive tailing discharges. This landslide occurred on a relatively steep slope, and may have been triggered by sediment accumulation at the top of this slope or by the nearby mining activities.

Geotechnical investigations will be necessary to better understand these planar failures, and coring in the debris may be helpful to approximate the age of this landslide. The other landslide present in the Central Basin seems older. A lateral spread failure implies a weak layer of sediments where failure plane occurred. The development of such a failure plane implies toe erosion or a large earthquake. However, there have not been any major historical earthquakes reported in this area. The option to account for a triggering mechanism for this landslide is erosion of the material at the toe of the slope. As seen on Fig. 4, large channels are present near this landslide in 2004 and 2006.

These channels may have created significant toe erosion of the slope if the turbidity currents were strong enough. This would imply that this landslide occurred when the mine was operating and this could be validated using detailed coring and dating estimation of sedimentation rates. Coring of lake floor sediments at this site is required and may help to better understand this landslide, as some seismites layers may be encountered in the lake. In such a case, this may provide some relative estimates of the seismic hazard for this area.

5   Conclusion

Wabush Lake is an active sedimentary environment resulting of the dynamic disposal of mine tailings. Three bathymetric surveys have been conducted since 2004. With more than $100\,m^3$ of tailings discharged into the lake each year, the delta progrades at a rate of > 100 m/year. Turbidity currents are generated at the mouth of the so-formed river. These hyperpycnal flows may reach a distance of more than 5 km from the river mouth. According to the 2008 bathymetric chart, these flows seem to be channelized by one major channel, which allow them to develop further and transport sediments in the central basin of the lake. However, this process did not take place in 2006 and 2004, where little sedimentation occurred in the distal part of the lake and where only small channels were observed.

Geophysical surveys also reveal a complex lakebed morphology, involving multiple mass-movements as knickpoints and landslides characterized by planar and lateral spread failures. Knickpoints are mostly found in the shallower part of the lake, even if some were developed as deep as 70 m. Our results also show that some of these knickpoints have migrated upstream. Planar and lateral spread failures are found in the central basin. The location and morphology of the area where planar failures are observed needs to be investigated in more detail, particularly to investigate the potential role of nearby mine blasting on the stability of lacustrine sediments. Lateral spread failure may be due to an old earthquakes or by the erosion at the toe of the slope due to the passage of turbidity currents. Sampling and geotechnical investigations are necessary to be able to understand these failures. Sequential multibeam surveys is an efficient tool for evaluating the rate of infilling of the lake, to detect deposition centers, as well as to describe the evolution of the instability areas.

References

Kostic, S., and Parker, G. 2003. Progradational sand-mud deltas in lakes and reservoirs. Part 1. Theory and numerical modeling Formation des deltas de sable et de boue dans les lacs et les réservoirs. 1 ière Partie. Théorie et modélisation numérique. J Hydraul Res 41: 127–140.

Locat, J., and Lee, H.J. 2002. Submarine landslides: advances and challenges. Can Geotech J 39: 139–212.

Locat, J., and Lee, H.J. 2009. Submarine Mass Movements and Their Consequences: An Overview. In Landslides – Disaster Risk Reduction. Springer, Berlin Heidelberg. pp. 115–142.

Mitchell, N. 2006. Morphologies of knickpoints in submarine canyons. Bull Geol Soc Am 118: 589–605.

Normark, W., Piper, D., and Hess, G. 1979. Distributary channel, sand lobes, and mesotopography of Navy Submarine Fan, California Borderland, with applications to ancient fan sediments. Sedimentology 26: 749–774.

Climate-Induced Turbidity Current Activity in NW-African Canyon Systems

R. Henrich, T.J.J. Hanebuth, Y. Cherubini, S. Krastel, R. Pierau, and C. Zühlsdorff

Abstract A major outcome from studying the sedimentary archives of the Timiris Canyon off Mauritania and the Dakar Canyon off Senegal was a clear climatically controlled triggering of turbidite events. The records of both canyons display a high frequency of siliciclastic turbidite activity during deglacial sea level rise, obviously being induced by remobilisation of huge eolian dune fields that had expanded close to the shelf edge during glacial exposure. Further in glacial periods, frequent turbidite beds are recorded in the Timiris Canyon and sporadic turbidites occur also during intermediate sea level rises in the late phase of Heinrich events. The latter seem also to be related to a general increased dust supply and remobilisation of local dunes.

Keywords Submarine canyons • turbidite frequencies • hyperarid continental margins • climate archives in canyons

R. Henrich (✉)
University of Bremen, Faculty of Geosciences and MARUM, PO Box 330 440, 28334 Bremen, Germany
e-mail: henrich@uni-bremen.de

T.J.J. Hanebuth and S. Krastel
MARUM — Center for Marine Environmental Sciences, and Faculty of Geosciences, University of Bremen, Klagenfurter Strasse, 28359 Bremen, Germany

C. Zühlsdorff
Department of Earth Science, University of Bergen, Allégaten 41, 5007 Bergen, Norway

S. Krastel
Christian-Albrechts-Universität zu Kiel, Leibniz-Institut für Meereswissenschaften, IFM-GEOMAR, Gebäude 4, Wischhofstrasse 1-3, 24148 Kiel, Germany

Y. Cherubini
Helmholtz Centre Potsdam, GFZ German Research Centre for Geosciences, Telegrafenberg, B 452, D-14473 Potsdam, Germany

1   Introduction

The Atlantic continental margin off Saharan Africa hosts one of the largest dust sources on Earth (Goudie and Middleton 2001) and today, hemipelagic particle flux from coastal upwelling and dust supply are the dominant sediment sources along the NW-African margin; subordinate fluvial input is restricted to the northernmost sector of Morocco (Holz et al. 2004). During glacial times, the hyper-arid core region of the Sahara was considerably expanded due to increased aridity and overall higher wind speeds. As a consequence, dust export to the ocean increased immensely (Sarnthein 1978; Sarnthein et al. 1982), and huge erg systems took place on the shelves (Lancaster et al. 2002). In addition, deposition of eolian sand turbidites occured on the slope (Sarnthein and Diester-Hass 1977).

Between 18°N and 20°N along the NW-African margin, the slope seafloor is characterised by channelled sediment transport within numerous well-developed canyon systems and a series of shelf-cutting gullies (Fig. 1). The most noticeable system is the meandering Timiris Canyon running westwards from the shelf break for at least 450 km down to a water depth greater than 4,000 m (Krastel et al. 2004; Antobreh and Krastel 2006). South of this area, the margin hosts a huge young slide complex, i.e. the Mauritania Slide Complex (Henrich et al. 2008) and no larger canyons are found until the more humid Senegalese margin off Dakar; e.g., Dakar Canyon, Cayar Canyon (Kounkou and Barusseau 1988). Previous studies clearly demonstrated that these canyons strongly influence the evolution of sedimentary regimes on the continental slope (Zühlsdorff et al. 2007, 2008; Hanebuth and Henrich 2009). Since they serve as major conduits for turbidity currents transporting shelf and upper slope material, continuous sedimentary records inside such a system may be used as important climate archives. This article intends to summarize our present knowledge on how these canyon systems, the Timiris Canyon off Mauritania and the Dakar Canyon off Senegal, dominate with general sediment dynamics on these particular margins, and how their sedimentary archives document past climatic changes and sea-level oscillations.

1.1   Regional Settings

The study area off Mauritania is located close to the northernmost boundary between the modern northern hemisphere Trade wind system and the African monsoonal system in southern direction (Nicholson 2000). Both atmospheric systems interact with each other by shifting seasonally northward due to summer Trade wind weakening and southward by Trade winds strengthening in winter. Similar climatic shifts are also recognised on longer time scales, with the effect of humidification when monsoonal patterns prevail and aridification when Trade winds become stronger. In response to these changes, strong seasonal upwelling centers are located on the outer shelf (Wefer and Fischer 1993) which are traced by high concentrations of organic matter in the sediments (Fütterer 1983). In glacial times, these upwelling centres shifted towards the upper slope due to sea level lowering (Matthewson et al. 1995; Martinez et al. 1999).
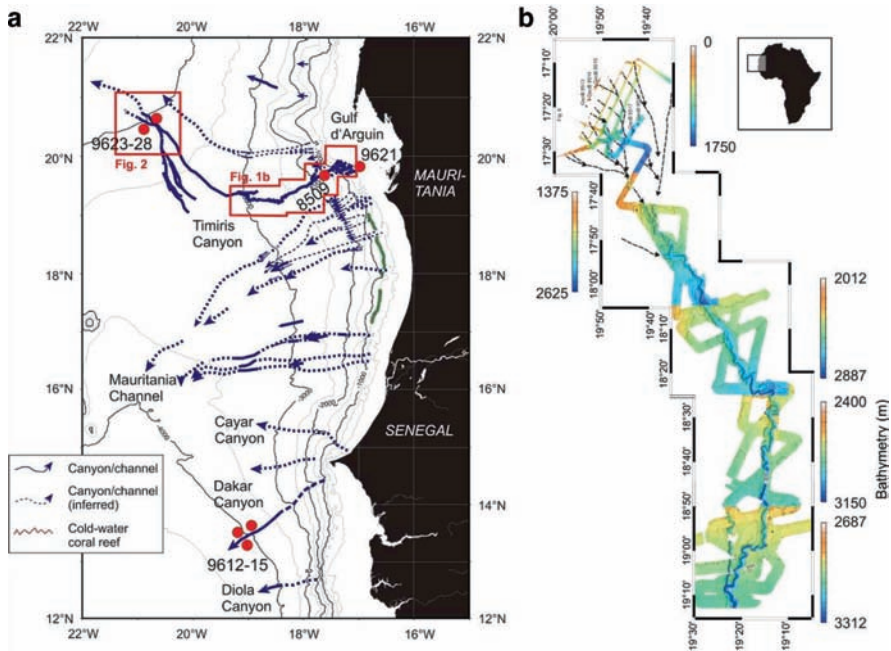
Fig. 1 (**a**) Distribution of canyons along the NW-African margin in the sector off Mauritania and Senegal. Locations of studied cores indicated by red dots. (**b**) Bathymetric map of the Timiris Canyon compiled from Hydrosweep mapping during Cruise M58/1

North of Cap Timiris, the generally narrow Mauritanian shelf expands significantly and forms the shallow marine Gulf d'Arguin. The continental slope off the Gulf d'Arguin is steep with a gradient of up to 6° in its upper part (Antobreh and Krastel 2006), and the shelf edge is incised by numerous channels, especially in the south (Fig. 1). A series of ~15 tributary gullies cuts into the shelf edge merging together further downslope to form the Timiris Canyon (Fig. 1). These tributaries have the capacity to collect current-driven material from the shelf. In its upper course, the canyon cuts deeply into the basement whilst a channel-levee system developed further downslope (Antobreh and Krastel 2006). In contrast to this, the Dakar Canyon runs straight downslope incising up to 700 m in its upper course (Fig. 1). In the distal part the incising depth decreases to less than 20 m at the continental rise and the canyon splits into a main active channel and a channel remnant filled with stratified sediments.

1.2 Methods

Shallow-acoustic and seismic profiling and sediment coring were carried out during Cruises M58/1 (Schulz et al. 2003) and M65/2 (Krastel et al. 2006) with the German research vessel Meteor. In this study, we use published data from sediment cores from the Dakar Canyon (Fig. 1, Cores 9612–9615) and from the upper Timiris Canyon (Fig. 1,
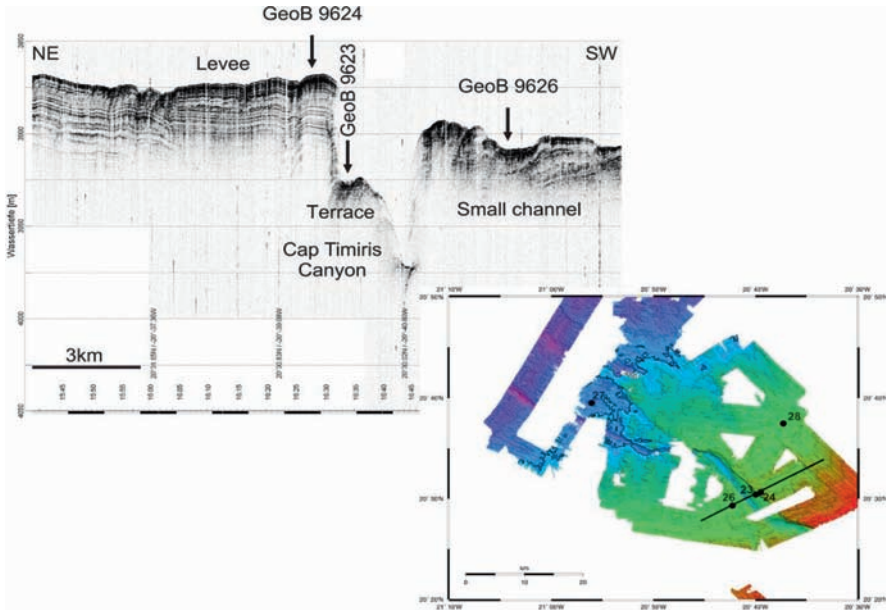
Fig. 2 Parasound profile crossing the lowermost part of the Timiris Canyon in NE-SW direction. Core locations 9624 on the north-western levee, 9,623 on a terrace inside the channel, and 9,626 in a small side-channel incising the south-eastern levee are indicated. Inlay displays Hydrosweep bathymetry with core positions

Core 8509; Zühlsdorff et al. 2007, 2008) as well as new data from the lower Timiris Canyon (Fig. 2). A bathymetric map of the distal Timiris Canyon is displayed in Fig. 2. In the upper course of this sector the canyon runs SE-NW incising 90 m deep into the seafloor, whereas in the lower course the canyon turns westward and becomes much shallower towards its end with an incision depth of less than 20 m. Locations of cores comprise (1) an NE-SW core traverse in the upper sector: Core 9624 recovered in a northeastern levee position, Core 9623 recovered from a 40–50 m high elevated terrace inside the canyon, and Core 9626 taken from a accessory, shallow channel incising the southwestern levee. Further, (2) Core 9627 was recovered a few km north of the distal-most, shallow exit of the canyon and (3) Core 9628 about 20 km northeast of the upper course. The main box in Fig. 2 presents a Parasound profile across the sediment traverse of Cores 9624–9623–9626 displaying a well-developed horizontal reflection pattern for all core locations which is typical for hemipelagic background sedimentation with intercalation of thin turbidite beds. In the thalweg, a sharp dense reflection pattern is recognised indicative of either consolidated seafloor sediments or thick and coarse sand beds. Here, a coring attempt was not successful. The overall distribution of sediment cores over different elevations offers the opportunity to estimate volumes of the suspensions clouds running through the lower Timiris Canyon by detecting the level of over-spill, e.g. over the 40-m elevated terrace in the canyon, within the small channel on the shallow elevated SW-levee as well as on the highly elevated NE-levee. In addition, Core 9627 provides as an excellent control position for over-spilling suspension clouds discharging at the end of the canyon into the abyssal plain.

Sedimentary facies were characterised by visual core description and by structural and textural analysis of x-ray radiographs. Standard sedimentological and geochemical parameters were routinely determined on all cores in 5- to 10-cm resolution. Carbonate and total organic carbon contents were measured and the distribution of major elements of terrigenous and marine origin was analysed in 1-cm resolution with a XRF core scanner. The stratigraphy of all cores relies on (1) numerous radiocarbon samples converted into calibrated ages using CALIB in the latest version 5.0.1 (Stuiver et al. 1998; all ages shown here are given in cal ka BP) and (2) by determination of established marine oxygen isotope events taken from the oxygen isotope record measured on the planktonic foraminifer *Globigerinoides ruber* (Figs. 3 and 5).
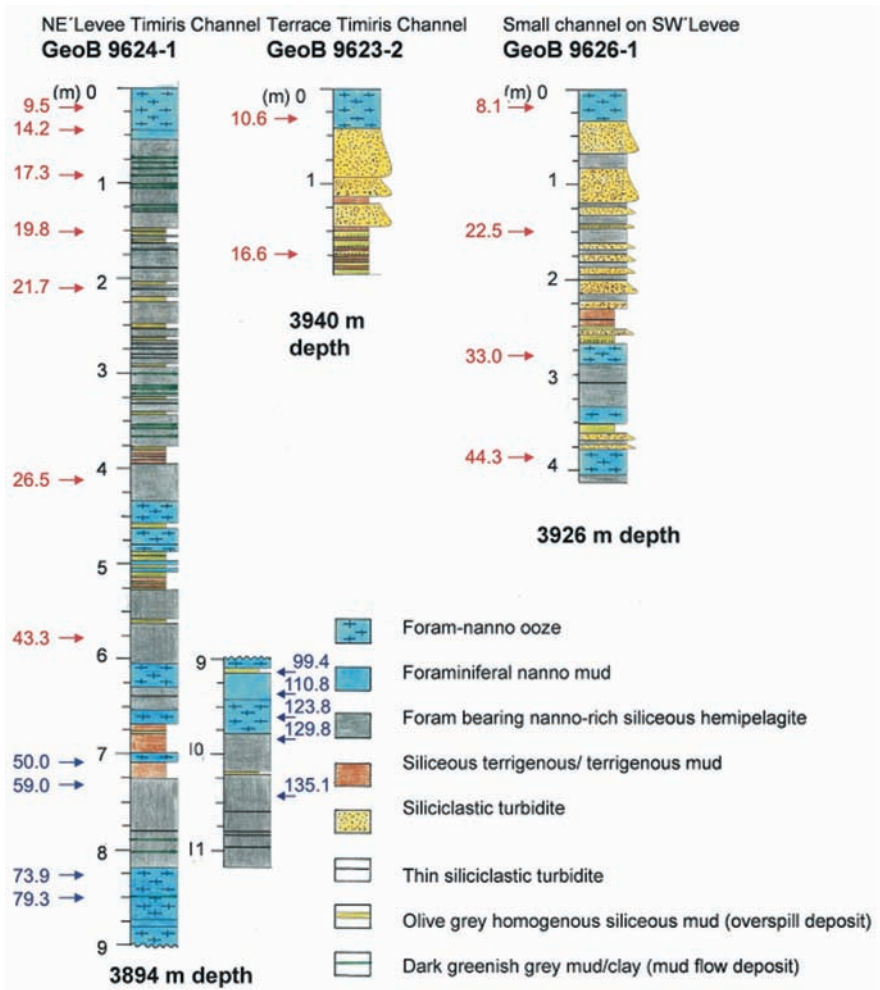
Fig. 3 Sedimentary records of Cores 9624, 9623 and 9626 displaying distribution of turbidite types and variations in composition of the hemipelagic background sediments. AMS-^{14}C dates are indicated by red arrows; blue arrows mark age determinations from Marine Isotope Stage (MIS) events in the δ^{18}O record

2 Results and Discussion

2.1 Characterization of Turbidites

Figure 3 displays the sedimentary records of cores along the NE-SW traverse across the lower Timiris Canyon. Hemipelagic background sediments comprise pale brownish to pale greenish foram-nanno and mixed siliceous-carbonaceous muddy hemipelagites. In addition, occasionally grey siliceous silty terrigenous mud layers are observed. A prominent structural feature in these sediments is moderate bioturbation (Fig. 4). Within these hemipelagic sediments numerous turbidite layers are intercalated. There are no turbidites during the last 10 ka within the interglacial sediment sections and only a few thin layers during MIS-5 stadials. In contrast, the glacial and deglacial sections bear numerous turbidite layers of different textural and structural composition and of various thicknesses. All turbidites reveal a sharp but non-erosive base and internal structural variations of Bouma C-D-E and D-E sequences. Several thick and coarse-grained turbidites show a typical fining-upward sequence with intercalated coarse to medium to fine greyish quartz sand, such as in Core 9623 from the terrace and 9626 from the small channel incised on the SW levee (Fig. 4a).

In Core 9623 an amalgamated bed occurs evidencing that two turbidity currents interacted with each other. Admixture of fine biogenic shell debris comprising fragments of molluscs, bryozoans and echinoids clearly reveals the outer shelf/uppermost continental slope as source area for these turbidites. Core 9624 on the NE levee bears numerous thin (often only few centimetres thick) turbidite layers composed of olive grey homogenous mud. Occasionally, a very thin (milliimetres to a few centimetres) layer of dark grey very fine sand occurs at their base. Based on structural and textural evidence in radiographs these mud turbidites can be classified as typical overspill deposits. These overspill turbidites also occur in the basal sections of Cores 9623 and 9626, and in particular in the lower section of Core 9627 recovered at the exit of the canyon. Fig. 4b displays a sediment section from Core 9627 which nicely illustrates variations in flow dynamics of these overspill deposits. The standard beds consist of: (1) a basal parallel-laminated and micro-cross-bedded very fine sand, (2) a middle part of alternations of parallel-laminated silt and mud layers which are occasionally modified by convolute lamination, and (3) a top layer of homogenous mud. Beside these standard beds some other beds show a repetition and a variable combination of these characteristics, likely reflecting interaction of different suspension clouds.

2.2 Terrigenous Sediment Supply to the Hemipelagic Background Sediments and Turbidite Occurrence

Carbonate and TOC records as well as records of the terrigenous portion (e.g. XRF counts of Fe and Ti) in hemipelagic sediments of the past 140 ka in Core 9624,
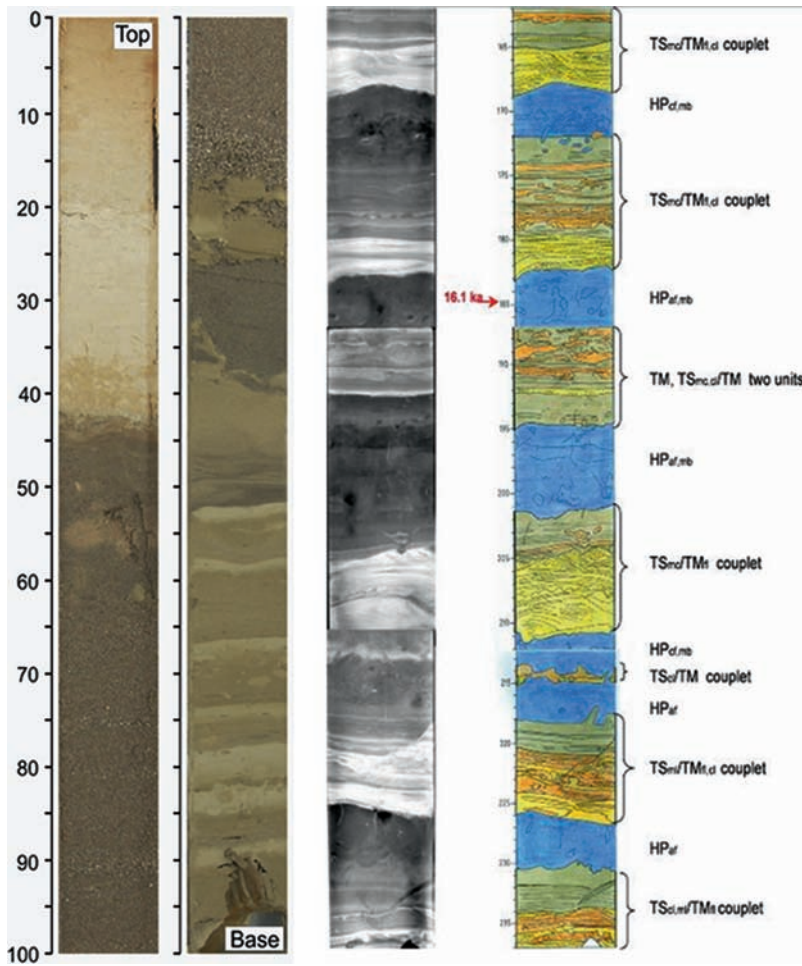
Fig. 4 (**a**: *left*) Photo of Core 9623 illustrating the high variety of turbidite types. From base to top: mud spill-over turbidites, a amalgamated siliciclastic turbidite bed, a siliciclastic turbidite with fining upward quartz sand and shell hash. (**b**: *right*): Radiographs and drawing of sedimentary structures and lithology of Core 9627 (162 to 237 cm) displaying the flow dynamics of seven spill-over turbidites and hemipelagic background sediments. Abbreviations: $HP_{af,mb}$ – hemipelagite with abundant foraminifers, moderate bioturbation; TS_{mc} – siliciclastic spill-over turbidite with micro-cross bedding; $TM_{fl,cl}$ – silty muddy spill-over turbidite with faint sub-mm-sized parallel lamination (fl), convolute lamination(cl)

from the NE levee, reveal pronounced shifts in the sedimentary regime on the lower continental slope (Fig. 5). Periods of increased terrigenous supply indicated by maximum values in Fe and Ti (Fig. 6) correlate with intervals of elevated TOC values (Fig. 5), i.e. at 70–15 ka and 140–129 ka. Sedimentation rates increase from 3–5 cm/ka during interglacial conditions to 20–40 cm/ka during glacial and early deglacial periods. This result suggests that organic matter and terrigenous material
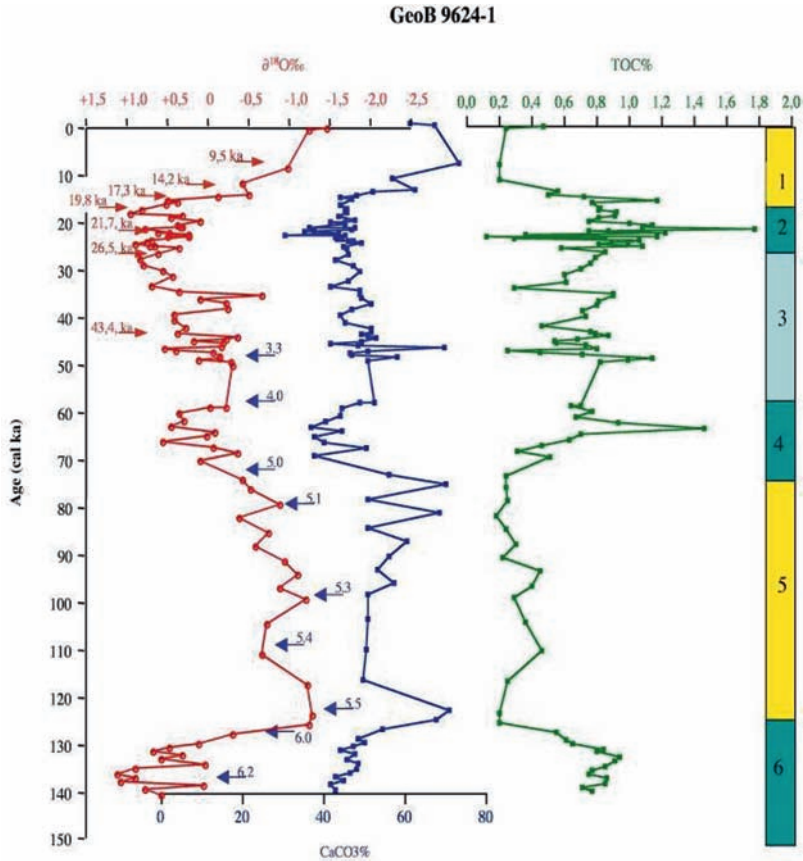
Fig. 5 Oxygen isotope, carbonate and TOC record of hemipelagic sediments in Core 9624 from the north-western levee of the distal Timiris Canyon. Stratigraphic model displaying AMS-^{14}C ages (*red arrows*) and ages points deduced from MIS events (*blue arrows*) according to the time scale of Martinson et al. (1987)

was supplied by the same mechanism, e.g. by scavenging the water column of organic matter and terrigenous particles. Previous studies have shown that Fe and Ti are good proxies for dust input to the ocean in this region (Hanebuth and Lantzsch 2009; Hanebuth and Henrich 2009). This observation is corroborated by results from grain-size analysis of contemporaneous deposits from the upper Timiris Canyon, revealing typical silt-size spectra of dust (Zühlsdorff et al. 2007). Hence, during these periods much stronger Trade winds increased offshore dust supply, strengthened upwelling intensity at the uppermost continental slope and increased sediment accumulation and subsequent downslope re-suspension over wide areas.

With regard to these aspects, the pronounced cyclic patterns of Fe and Ti during MIS 5 (Fig. 6) appear to be of particular interest since they monitor climatic
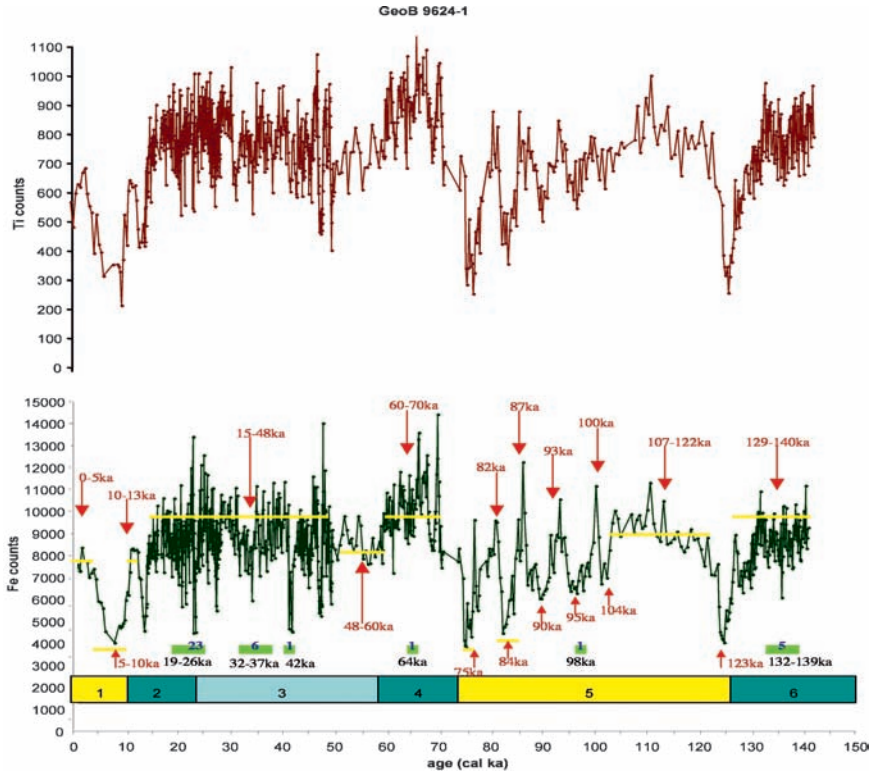
Fig. 6 Record of the portion of terrigenous material in the hemipelagic background sediments of Core 9624 as evidenced by elemental Fe and Ti intensities. Intervals of low, intermediate and high contents are marked by yellowish bars. Time intervals are indicated over the red arrows. In addition in the lower panel the number of spill-over turbidite events is indicated by olive bars and below their occurrence time is displayed

oscillations with maximum values during the cold MIS events 5.4 and 5.2 and minima during the warm intervals 5.5, 5.3 and 5.1. Turbidite over-spilling the NE-levee of the lower Timiris Canyon is observed during the following periods: 139–132 ka (5 events), 98 ka (1 event), 42 ka (1 event), 37–32 ka (6 events), and 26–19 ka (23 events). Obviously, re-suspension processes on the continental slope are coincident with these climatic peaks suggesting a trigger closely linked to climatic forcing. Release of turbidity currents always took place during these periods of high terrigenous supply (Fig. 6).

As a conclusion, these turbidites were triggered mainly by variations in overall sediment supply. During high-glacial and early deglacial time, tributary gullies on the uppermost slope were rapidly and repetitively filled with subsequent release of turbidity currents and large volumes suspension clouds passed through the lower Timiris Canyon leading to over-spilling on the NE levee. These turbidites were induced by remobilisation of huge eolian dune fields that expanded close to the

shelf edge during glacial exposure (Lancaster et al. 2002). In addition to this scenario, partial flooding of the outer shelf during successive sea-level rises in MIS 3 may have caused re-mobilization of eolian dune material.

2.3   History of Turbidite Frequency: Comparing the Timiris and Dakar Canyon Systems

Figure 7 summarizes the history of turbidite activity in the Timiris Canyon. The NE-SW sampling traverse allows monitoring of the surface level of suspensions clouds. The highest level and, thus, largest-volume suspension clouds are indicated by over-spilling turbidites detected in Core 9624 on the NE levee. A slightly lower level is reached by turbidites observed in Core 9626 but did not extend to the level of Core 9624. The smallest-volume turbidites are found on the terrace within the canyon (Core 9623). An additional monitoring position is provided by Core 8509 from a terrace within a wide area in the upper Timiris Canyon (Zühlsdorff et al. 2008). Following this depositional pattern, it is possbile to reconstruct the temporal variability of turbidite activity as follows: (1) in periods of maximum glacial lowstand (MIS 6, late MIS 3, LGM), large-volume turbidites frequently filled the entire distal Timiris Canyon spilling over the NE levee. Additionally, single events of large volume over-spilling were recorded at 98 and 64 ka; (2) during early Termination I, over-spill turbidites frequently reached the small channel incised on the SW levee, but are not recorded on the higher elevated NE levee; (3) within the canyon (Core 9623), turbidite activity continued until 11ka, but without spilling over the levees on either side. (4) The youngest turbidite activity is recorded in Core 8509 from the upper Timiris Canyon, revealing 900-year cycle during the entire Holocene (Zühlsdorff et al. 2008). These turbidites, however, attained much lower volumes, since they did not reach the distal Timiris Canyon. This correlation is, to our knowledge, the first documentation of a close coupling of short-term climatic cycles and turbidity current activity. The suggested basic trigger is that the
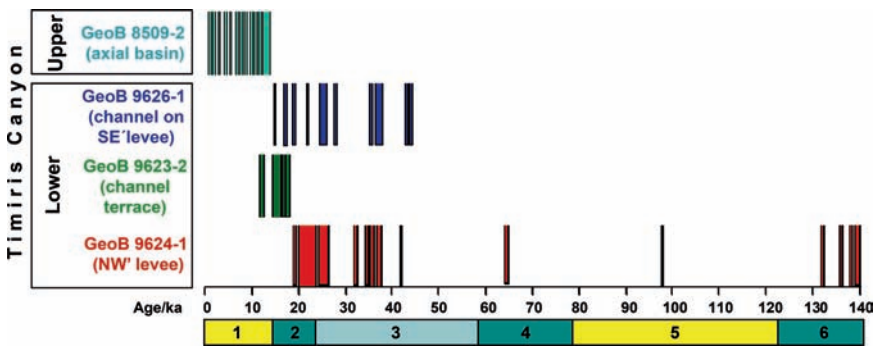
Fig. 7 Turbidite recurrence pattern in the lower and upper Timiris Canyon
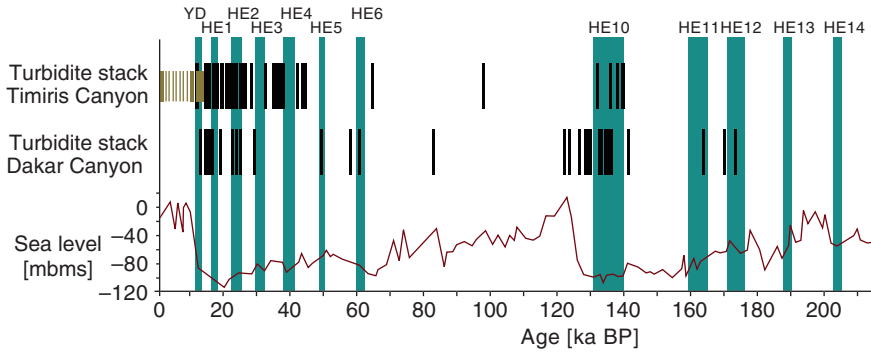
Fig. 8 Comparison of turbidite activity in the Timiris Canyon and the Dakar Canyon. Stack plot of all turbidite events recorded in these canyon systems compared to a global sea-level curve (Siddall et al. 2003). White space above and below the intervals with turbidite events represents continuous hemipelagic background sedimentation. Olive bars: special Holocene record

rhythmically appearing turbidites were linked to dust events recorded in a fine-grained shelf depocentre for the past 5 ka (Hanebuth and Henrich 2009).

Comparison of the evolution of turbidite activity in the Timiris Canyon off Mauritania with that of the Dakar Canyon off Senegal shows that both areas are today influenced by intensive dust input. Dust supply is much higher off Mauritania, however, as it is situated offshore the Saharan desert. Figure 8 displays stacked records of turbidite activity in both canyons over the last two glacial-interglacial cycles together with the sea-level reconstruction of Siddall et al. (2003).

In both canyons, high turbidity current activity is observed during glacial sea-level lowstands. High turbidite frequency also appears in both canyons at their terminations. In the Dakar Canyon, additional turbidites coincide with the timing of Heinrich events in the North Atlantic. During times of Heinrich events, the continental climate changed rapidly with evidence for concurrent higher dust supply provided by high Ti/Ca ratios (Fig. 6). Increased aridity, enhanced wind strength and reduced vegetation cover in the region of the modern Saharan-Sahelian transition may have provided a considerable source for this dust. In the Dakar Canyon, turbidity current activity ends within Termination I, whereas only in the Timiris Canyon, do recurrent small-volume turbidites extend over the entire Holocene (Zühlsdorff et al. 2008; Hanebuth and Henrich 2009).

3 Conclusions

As summary, we postulate the following evolutionary model for the activity of both NW-African canyon systems. During general and sporadic (Heinrich) sea-level lowstands, voluminous turbidity currents passed frequently through the Timiris Canyon. Subsequently, during deglacial sea-level rise, flooding of the

shelves induced erosion of dune sands and resulted in high turbidity current activity in both canyons. A major regional contrast is observed for time intervals of sea-level highstand when the hyperarid Timiris region reveals recurrent dust turbidites, whereas the Dakar Canyon is completely quiet due to a humid and vegetated hinterland.

References

Antobreh AA, Krastel S (2006) Morphology, seismic characteristics and development of Cap Timiris Canyon, offshore Mauritania: a newly discovered canyon preserved off a major arid climatic region. Mar Pet Geol 23: 37–59

Fütterer DK (1983) The modern upwelling record off Northwest Africa. In: Thiede J, Suess E (eds.), Coastal upwelling: its sediment record, Part B. Sedimentary records of ancient coastal upwelling. Plenum, London

Goudie AS, Middleton NJ (2001) Saharan dust storms: nature and consequences. Earth-Sci Rev 56: 179–204

Hanebuth TJJ, Henrich R (2009) Recurrent decadal-scale dust events over Holocene western Africa and their control on canyon turbidite activity (Mauritania). Quat Sci Rev 28: 261–270

Hanebuth TJJ, Lantzsch H (2009) A Late Quaternary sedimentary shelf system under hyperarid conditions: unravelling climatic, oceanographic and sea-level controls (Golfe d'Arguin, Mauritania, NW Africa). Mar Geol 256: 77–89

Henrich R, Hanebuth T, Krastel S et al. (2008) Architecture and sediment dynamics of the Mauritania Slide Complex. Mar Pet Geol 25: 17–33

Holz C, Stuut JB, Henrich R (2004) Terrigenous sedimentation processes along the continental margin off NW-Africa: implications from grain-size analyses of seabed sediments. Sedimentology 51: 1145–1154

Krastel S, Hanebuth TJJ, Henrich R et al. (2004) Cap Timiris Canyon: a newly discovered channel system offshore of Mauritania. EOS 85: 417–423

Krastel S, Wynn RB, Hanebuth TJJ et al. (2006) Seafloor mapping of submarine geohazards offshore Mauritania, Northwest Africa. Nor J Geol 86: 163–176

Kounkou GL, Barusseau JP (1988) Terrigenous sedimentation of the upper Quaternary in the Cayar deep-sea fan (Senegal-Gambia abyssal plain – Atlantic Ocean). Oceanol Acta 11: 359–368

Lancaster N, Kocurek G, Singhvi A et al. (2002) Late Pleistocene and Holocene dune activity and wind regimes in the western Sahara Desert of Mauritania. Geology 30: 991–994

Matthewson AP, Shimmield GB, Kroon D (1995) A 300 kyr high-resolution aridity record off the North African continent. Paleocean 10: 677–692

Martinez P, Bertrand P, Shimmield GB et al. (1999) Upwelling intensity and ocean productivity changes off Cape Blanc (northwest Africa) during the last 70,000 years: geochemical and micropaleontological evidence. Mar Geol 158: 57–74

Martinson DG, Pisias NG, Hays JD (1987) Age Dating and the orbital theory of the ice ages: development of a high-resolution 0 to 300,000-year chronostratigraphy. Quat Res 27: 1–29

Nicholson SE (2000) The nature of rainfall variability over Africa on time scales of decades to millenia: Global Planet Change 26: 137–158

Sarnthein M (1978) Sand deserts during glacial maximum and climate optimum. Nature 272: 43–46

Sarnthein M, Diester-Haass L (1977) Eolian-sand turbidites. J Sed Pet 47: 868–890

Sarnthein M, Thiede J, Pflaumann U et al. (1982) Atmospheric and oceanic circulation patterns off Northwest Africa during the past 25 millon years. In: von Rad U, Hinz K, Sarnthein et al. (eds.), Geology of the Northwest African Continental Margin. Springer

Schulz HD, Cruise participants (2003) Report and preliminary results of METEOR cruise M58/1, Dakar – Las Palmas, 15.04.2003 – 12.05.2003. Univ Bremen

Siddall M, Rohling EJ, Almogi-Labin A et al. (2003) Sea-level fluctuations during the last glacial cycle. Nature 423: 853–858

Stuiver M, Reimer PJ, Bard E et al. (1998) INTCAL98 Radiocarbon Age Calibration, 24.000 – 0 cal BP: Radiocarbon 40: 1041–1084

Wefer G, Fischer G (1993) Seasonal patterns of vertical particle flux in equatorial and coastal upwelling areas of the eastern Atlantic. Deep Sea Res 40: 1613–1645

Zühlsdorff C, Hanebuth TJJ, Henrich R (2008) Persistent periodic turbidite activity off Saharan Africa and its comparability to orbital and climate cyclicities. Geo-Mar Lett 28: 87–95

Zühlsdorff C, Wien K, Stuut JB et al. (2007) Late Quaternary sedimentation within a submarine channel-levee system offshore Cap Timiris, Mauritania. Mar Geol 240: 217–234

Section III
Submarine Mass Movements in Margin Construction and Economic Significance

Investigating the Timing, Processes and Deposits of One of the World's Largest Submarine Gravity Flows: The 'Bed 5 Event' Off Northwest Africa

R.B. Wynn, P.J. Talling, D.G. Masson, C.J. Stevenson, B.T. Cronin, and T.P. Le Bas

Abstract An extensive dataset of shallow sediment cores is used here to describe one of the World's most voluminous and extensive submarine gravity flows. The Bed 5 event, dated at ~60 ka, originated on the upper slope offshore Atlantic Morocco, in the vicinity of Agadir Canyon. The volume of initial failure was ~130 km^3 of sediment, and the failure appeared to rapidly disintegrate into a highly mobile turbidity current. Widespread substrate erosion beneath the flow occurred up to 550 km from the interpreted source, and is estimated to have added a further 30 km^3 of sediment. The flow spread upon exiting Agadir Canyon, with deposition occurring across both the Agadir Basin and Seine Abyssal Plain. Evidence for flow transformations and linked turbidite-debrite development can be found in both basins, and there are also indications for sediment bypass and fluid mud behaviour. A portion of the flow subsequently spilled out of the western Agadir Basin, and passed through the Madeira Channels prior to deposition on the enclosed Madeira Abyssal Plain at 5,400 m water depth. The total run-out distance along the flow pathway is about 2,000 km, with only about half of the pathway confined to canyon or channel environments. Our results show that large-volume submarine landslides can rapidly disintegrate into far-traveling fluid turbidity currents, and that depositional processes within such flows may be complex and spatially variable.

Keywords Landslide • turbidity current • sandwich bed • sediment cores • Morocco

R.B. Wynn (✉), P.J. Talling, D.G. Masson, C.J. Stevenson, T.P. Le Bas
National Oceanography Centre, Southampton, European Way, Southampton, SO14 3ZH, UK
e-mail: rbw1@noc.soton.ac.uk

B.T. Cronin
Deep Marine, 9 North Square, Footdee, Aberdeen, AB11 5DX, UK

1   Introduction and Data

The northwest African continental margin has hosted some of the World's largest submarine landslides during the last 200,000 years. For example, the Sahara Slide off Western Sahara, dated at ~50–60 ka, involved 600 km^3 of sediment and has a run-out distance of 700 km (Gee et al. 1999). In this example the failed sediment block partially disintegrated into a plastic debris flow, but there is no evidence for transformation into a fluid turbidity current. In contrast, the Moroccan Turbidite System has hosted several large-volume landslides that have transformed into highly mobile flows soon after failure (Wynn et al. 2002b). Deposits of these flows include some of the most voluminous turbidites in the World, with deposit volumes exceeding 100 km^3 and run-out distances of up to 2000 km. Most of the large-volume flows are siliciclastic and derived from the Moroccan margin. Flow deposits are best developed in three inter-connected depositional basins: the Agadir Basin, the Seine Abyssal Plain and the Madeira Abyssal Plain, all at water depths > 4,000 m (Fig. 1).

Here, we present an overview of one of the largest flows to have occurred in the Moroccan Turbidite System during the late Quaternary. The deposit of this flow is called Bed 5 (Wynn et al. 2002b; Frenz et al. 2009), and it is particularly interesting as it underwent multiple transformations during its passage downslope (Talling et al. 2007). Our study builds upon previous work by incorporating new sediment (piston) cores that penetrated the Bed 5 deposit in the eastern Seine Abyssal Plain. These cores were collected during research cruise JC027 in autumn 2008, and provide further evidence for flow transformations in Bed 5. In addition, the new cores allow comprehensive analysis of the source area, timing, flow pathways, deposits and processes of the Bed 5 event across the entire Moroccan Turbidite System (Fig. 1).

2   Landslide Source Area and Timing

The frequency of large-scale turbidity currents passing through the Moroccan Turbidite System is low, with roughly one event every 10,000 years (Wynn et al. 2002b). Correlation of individual flow deposits between basins is based upon (1) sand fraction mineralogy, (2) mud geochemistry and colour, (3) coccolith ratios in the mud cap, (4) microfossil-based dating of bounding hemipelagites, and (5) relative stratigraphic position compared to seafloor and volcaniclastic marker turbidites (Wynn et al. 2002b). The Bed 5 deposit has been extensively sampled throughout the Moroccan Turbidite System, and mineralogical and geochemical analyses indicate a source area on the outer shelf and/or upper slope of northwest Morocco, adjacent to upper Agadir Canyon (Fig. 1; Weaver et al. 1992; Davies et al. 1997; Wynn et al. 2002b). However, a lack of geophysical data from the source area means that the exact shape and size of the initial failure are unknown.

The Bed 5 event has been dated at ~60 ka in each of the three depositional basins of the Moroccan Turbidite System, using both coccoliths and planktonic foraminifera
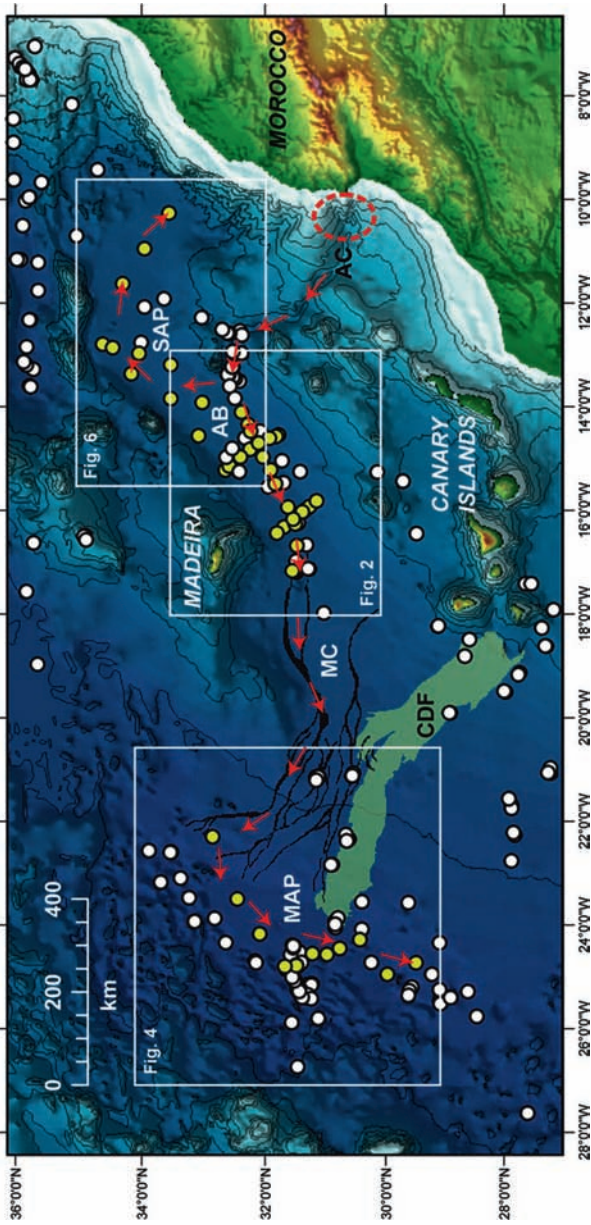
Fig. 1 Overview map of the Moroccan Turbidite System. Bathymetry is based upon GEBCO data, with contour intervals of 500 m. Core locations indicated by white circles; those illustrated in Figs. 3, 5 and 7 are highlighted in yellow. Red arrows highlight the main flow pathways for the Bed 5 event. Dashed red circle shows location of interpreted source area for the Bed 5 landslide. White rectangles indicate locations of Figs. 2, 4 and 6. Abbreviations as follows: AC = Agadir Canyon; SAP = Seine Abyssal Plain; AB = Agadir Basin; MC = Madeira Channels; MAP = Madeira Abyssal Plain; CDF = Canary Debris Flow

extracted from bounding hemipelagic sediments (Weaver and Kuijpers 1983; Davies et al. 1997; Wynn et al. 2002b). The source landslide occurred at the transition between oxygen isotope stages 4 and 3, at a time when sea-level and global temperatures were rising. It therefore seems likely that landslide initiation was linked to rapid sea-level rise of ~40 m, following a 10 kyr period of exceptionally low sea-level (Siddall et al. 2003). Just prior to the Bed 5 landslide, eustatic sea-level was actually at its lowest point for 70,000 years. However, a lack of available data from both the submarine source area and adjacent landmass, mean that the pre-conditioning factors and the specific trigger mechanism for the initial landslide cannot be determined.

3   Flow Pathways, Run-Out Distance and Deposit Volume

Analysis of grain size and bed thickness trends has allowed flow pathways for the Bed 5 event to be reconstructed in detail (Wynn et al. 2002b; Frenz et al. 2009). The coarsest basal grain sizes (gravel of 5–20 mm), and largest erosional hiatuses below the base of the bed (up to 1.0 m), are found in the eastern Agadir Basin adjacent to the mouth of Agadir Canyon (Figs. 2 and 3). This suggests a flow pathway through
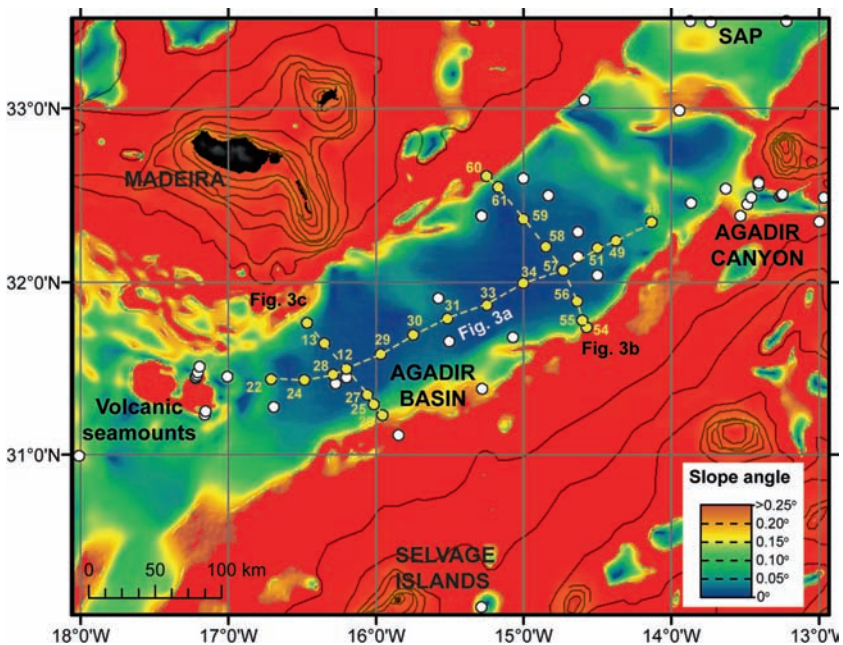
Fig. 2 Slope map of Agadir Basin, based upon GEBCO data. Slope angles across most of Agadir Basin are < 0.1°. For location see Fig. 1. Bathymetric contours spaced at 500 m intervals. Core locations shown by white circles, and those illustrated in Fig. 3 are numbered and highlighted in yellow. Yellow dashed lines indicate transect locations in Fig. 3. SAP = Seine Abyssal Plain
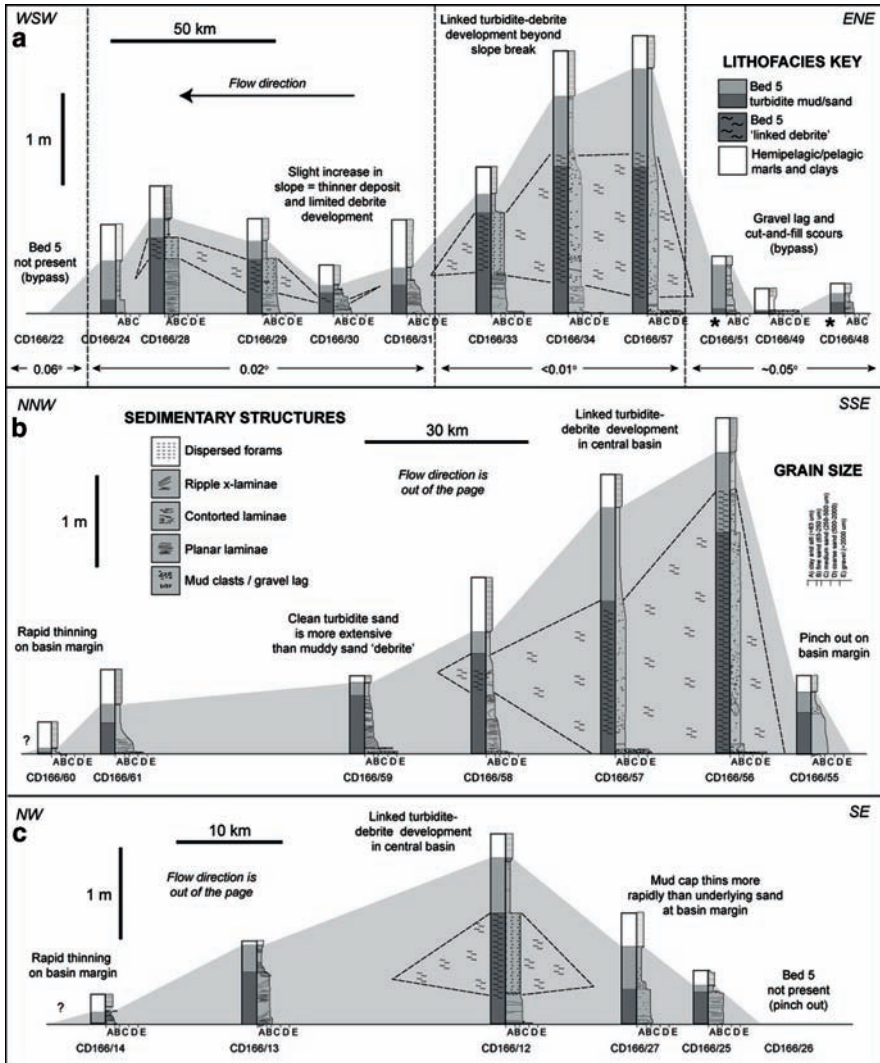
Fig. 3 Core correlation transects, showing the geometry and sediment facies of the Bed 5 deposit across Agadir Basin: (**a**) dip transect, (**b**) eastern (proximal) strike transect, (**c**) western (distal) strike transect. See Fig. 2 for locations. Transects are hung off base of Bed 5. Note the development of a thick (≥2 m) linked turbidite-debrite bed in the central basin, downstream of a marked slope break from 0.05° to < 0.01°. Cores 48 and 51, located upstream of the slope break, display highly erosive bases (marked with an asterisk) that are incised into underlying sediments for several tens of cm. Grain-size scale as follows: (A) clay and silt (<63 μm), (B) fine sand (63–250 μm), (C) medium sand (250–500 μm), (D) coarse sand (500–2,000 μm), (E) gravel (>2,000 μm)

the canyon, which is consistent with the location of the interpreted source area (Fig. 1; Frenz et al. 2009). In addition, initial analysis of several cores recovered from lower Agadir Canyon reveals the presence of significant erosional hiatuses, at a stratigraphic level consistent with Bed 5 (Talling et al. 2007).

Upon exiting Agadir Canyon, a portion of the Bed 5 flow passed westwards across Agadir Basin, before spilling into the Madeira Channels and ultimately spreading across the Madeira Abyssal Plain at a water depth of ~5400 m (Figs. 1, 4 and 5; Wynn et al. 2002b). The straight line distance from the interpreted source area and the southern Madeira Abyssal Plain is ~1600 km (Fig. 1), however, direct tracing of likely flow pathways indicates that the total flow run-out distance is probably in excess of 2,000 km. The scale of this flow, which is non-channelised for about half of its passage, is exceptional; other deep-sea flows with comparable run-out distances are largely confined within channels, e.g. Bengal Fan (Curray et al. 2003) and the Northwest Atlantic Mid-Ocean Channel (Klaucke et al. 1998).

Another portion of the Bed 5 flow moved north (and downslope) upon exiting Agadir Canyon, and entered the Seine Abyssal Plain from the southwest (Figs. 1, 6 and 7).
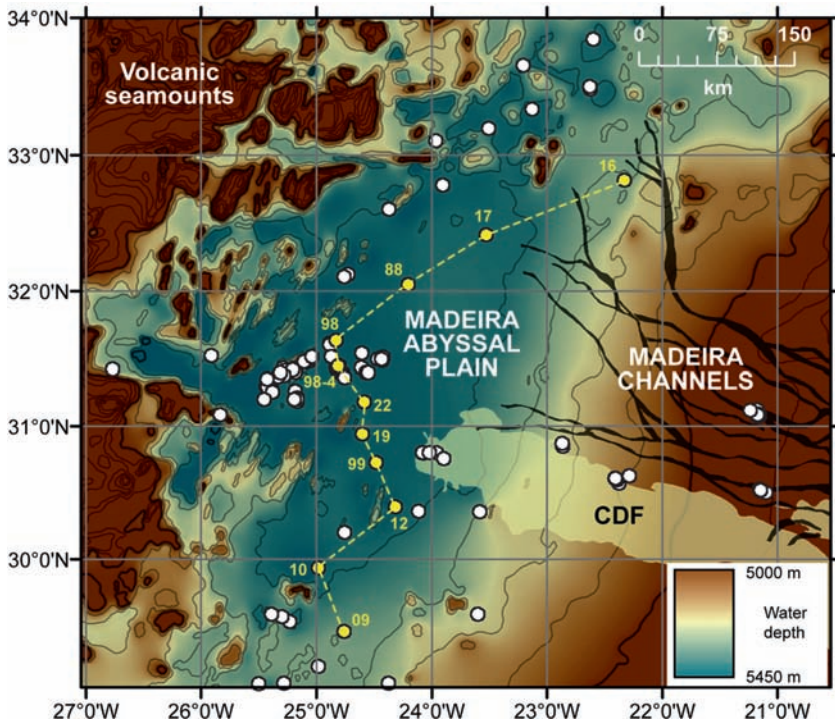
Fig. 4 Bathymetry map showing the Madeira Abyssal Plain and distal Madeira Channels, based upon GEBCO data. Note that data in this region are of insufficient quality to allow a slope map to be constructed. For location see Fig. 1. Bathymetric contours spaced at 100 m intervals; the basin floor is at ~5,400 m. Core locations shown by white circles, and those illustrated in Fig. 5 are numbered and highlighted in yellow. Yellow dashed line indicates transect location in Fig. 5. CDF = Canary Debris Flow
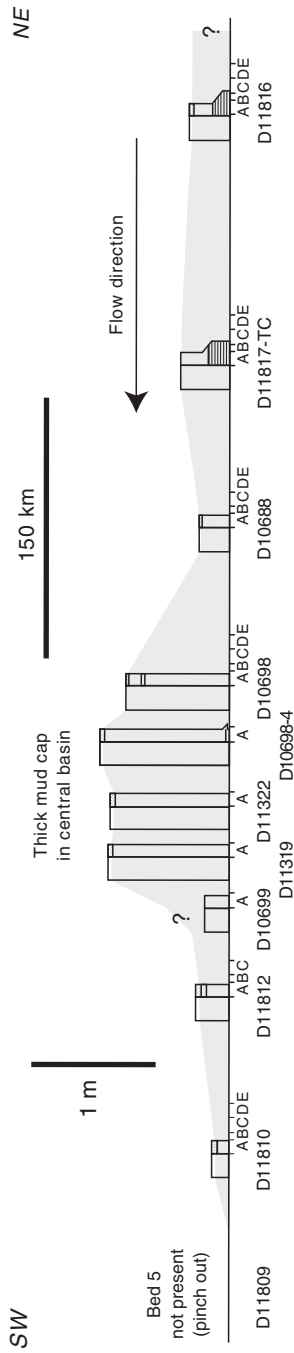
Fig. 5 Core correlation transect (~700 km long), showing the geometry and sediment facies of the Bed 5 deposit across the Madeira Abyssal Plain. See Fig. 4 for location. Transect hung off base of Bed 5. Note the development of a thick (~1 m) mud cap in the deep central basin. Lithofacies, sedimentary structures and grain size schemes same as Fig. 3
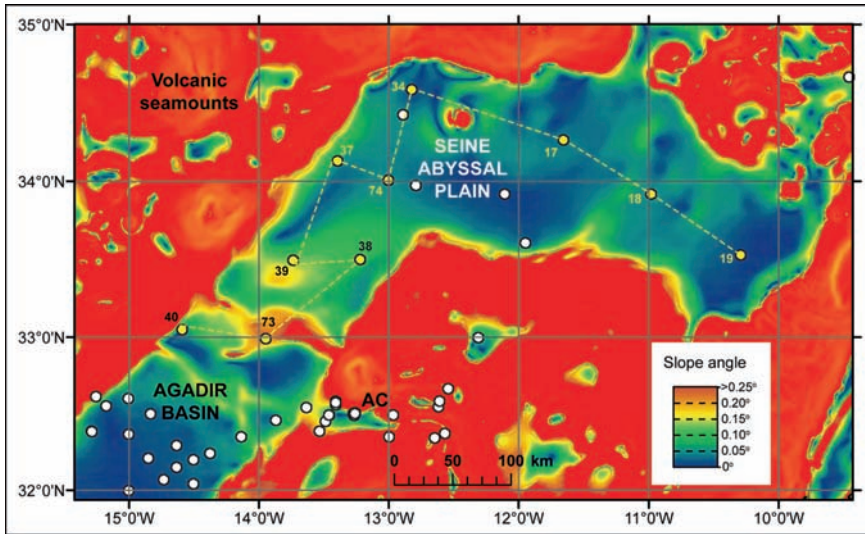
Fig. 6 Slope map of the Seine Abyssal Plain, based upon GEBCO data. Slope angles across most of the plain are < 0.1°. For location see Fig. 1. Core locations shown by white circles, and those illustrated in Fig. 7 are numbered and highlighted in yellow. Yellow dashed line indicates transect location in Fig. 7. AC = Agadir Canyon. Note that cores 40 and 73 are located on the crest and flank of a sedimentary ridge separating Seine Abyssal Plain and Agadir Basin

The flow then moved east across the plain for at least 500 km, as shown by its presence in core JC027-19 (Fig. 7). It is possible that a portion of the Bed 5 flow also passed through the series of canyons located ~150 km north of Agadir Canyon (Fig. 1). However, there is no evidence in cores from Seine Abyssal Plain for multiple graded intervals (Fig. 7), and it seems unlikely that multiple flows traveling along different pathways would result in a single fining-upwards deposit.

Investigation of bed thickness in the three depositional basins allows estimates of flow volume to be calculated for Bed 5. Volume calculations assume that bed surfaces between core locations are linear, and that no significant Bed 5 deposits occur outside of depositional basins. The bed volume is estimated at 40 km³ on the Madeira Abyssal Plain (Jones et al. 1992), 22 km³ in the Agadir Basin (Frenz et al. 2009), and 100 km³ on the Seine Abyssal Plain (in this volume). This leads to a total volume estimate of ~162 km³, although this is likely to be an under-estimate as additional Bed 5 deposits are patchily distributed outside of depositional basins, e.g. in the Madeira Channels. The Bed 5 deposits on Seine and Madeira Abyssal Plains are mud-dominated (Figs. 5 and 7), whereas in Agadir Basin there is a higher proportion of sand (both clean turbidite sand and muddy debrite sand; Fig. 3).

Analysis of benthic foraminifera assemblages from the base of the Bed 5 deposit in several cores from Agadir Basin, has revealed that ~20% of the assemblage is composed of species that live below 2,500 m water depth (Talling et al. 2007).
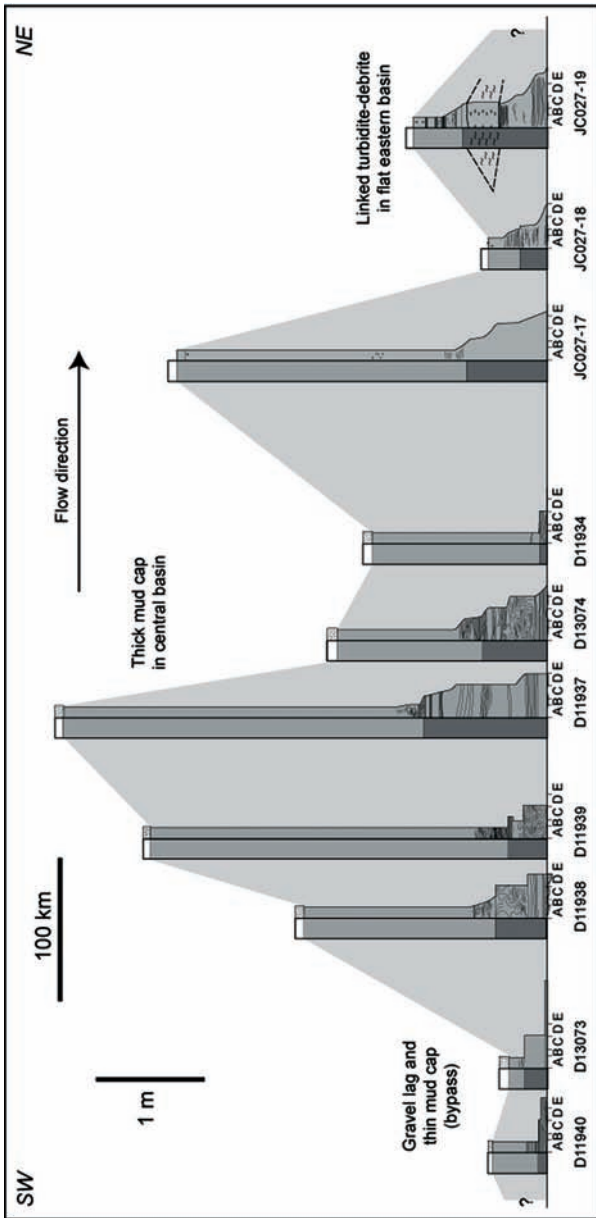
Fig. 7 Core correlation transect (~800 km long), showing the geometry and sediment facies of the Bed 5 deposit across the Seine Abyssal Plain. See Fig. 6 for location. Transect hung off base of Bed 5. Note the thick (≥2 m) mud cap in the deep central basin and development of a linked turbidite-debrite bed in the eastern basin. Lithofacies, sedimentary structures and grain size schemes same as Fig. 3

If we assume that the source landslide occurred on the upper slope/outer shelf (i.e. shallower than 2,500 m), then this material was likely incorporated into the flow through seafloor erosion in the lower Agadir Canyon and eastern Agadir Basin. This is supported by evidence for significant erosion in the lower canyon, in the form of km-scale scours and major erosional hiatuses (Wynn et al. 2002a, b, Talling et al. 2007). If we also assume that 20% deep-water benthic foraminifera equates to 20% of the deposit volume, then we estimate that ~32 km^3 of sediment was eroded from water depths > 2,500 m; this leads to a revised estimate of 130 km^3 for the initial source landslide volume.

4   Flow Processes and Deposits

Bed 5 is the most recent large-volume flow to have passed through Agadir Canyon (Wynn et al. 2002b), and widespread erosion on the canyon floor appears to be attributable to a strongly turbulent flow (Wynn et al. 2002a; Talling et al. 2007). In addition, deposits in the easternmost Agadir Basin are composed of thin gravel lags or cut-and-fill scours; these scours are up to 1.0 m deep and contain upward-fining turbidites (Figs. 3 and 7; Talling et al. 2007), again indicating well-mixed and turbulent flow conditions.

The Bed 5 flow spread rapidly upon exiting Agadir Canyon, with separate portions moving west into Agadir Basin and northeast into Seine Abyssal Plain. In the central Agadir Basin, the flow decreased in velocity upon reaching a marked decrease in slope (Fig. 3a). Although the head of the flow remained fully turbulent, and deposited upward-fining clean sands across the basin floor, the central portion of the flow collapsed and deposited ungraded muddy sand in an elongate tongue along the basin axis (Fig. 3). This flow collapse was probably a response to excessively high near-bed mud concentrations, resulting from updip erosion of fine-grained sediments in Agadir Canyon and eastern Agadir Basin. The tail of the flow formed a dilute suspension cloud that deposited a weakly graded or ungraded mud cap (see Talling et al. 2007 for a detailed discussion of depositional processes of this 'linked turbidite-debrite' deposit).

Analysis of new JC027 cores in this study has revealed that a similar linked turbidite-debrite deposit is present in the eastern Seine Abyssal Plain (Fig. 7), over 500 km from the mouth of Agadir Canyon. This deposit is similar to that seen in Agadir Basin, and comprises (1) an upward-fining basal sand turbidite with planar laminae, overlain by (2) an ungraded structureless muddy sand debrite with mud clasts, overlain by (3) a weakly-graded laminated silt turbidite with an ungraded mud cap. The presence of this apparently isolated linked turbidite-debrite, near the southeast margin of Seine Abyssal Plain, may also be related to slope gradient, with the central portion of the flow 'collapsing' and depositing *en masse* due to a velocity decrease as it crossed a particularly flat section of basin floor (slope < 0.01°) and/or approached the basin margin (Fig. 6).

Inter-basin areas are dominated by sediment bypass, for example, the channels separating Agadir Basin from Madeira Abyssal Plain (see core 22 in Fig. 3a). In these areas the Bed 5 deposit is either absent or comprises medium sands with climbing ripples and thin mud caps, indicating dilute flow conditions and/or sediment bypass in the head and centre of the flow. The lateral margins of Agadir Basin are characterised by abrupt thinning of the Bed 5 deposit, and it is noticeable that mud caps thin more abruptly onto basin margins than the basal clean sand layer (Figs. 3b and c). Conversely, mud caps thicken dramatically in the deepest parts of the enclosed Seine and Madeira Abyssal Plains (Figs. 5 and 7). If the mud was depositing from a dilute suspension it might be expected to drape evenly across the low slope angles encountered here (see Fig. 2), instead the marked lateral variations in mud cap thickness may point towards post-depositional remobilisation and fluid mud behaviour (*cf*. McCave and Jones 1988). Detailed grain size analysis of Bed 5 mud caps is currently in preparation, and will contribute to a future paper investigating depositional processes of thick 'turbidite' muds in the Moroccan Turbidite System.

5 Conclusions

This overview of the Bed 5 event has revealed some surprising phenomena, with evidence for large-scale erosion, flow transformations, fluid mud behaviour and sediment bypass occurring within a single flow. Our results reveal that some large-volume slope failures, involving $> 100\,km^3$ of sediment, can rapidly disintegrate into fluid gravity flows capable of traveling up to 2,000 km across very gentle slopes (generally $< 0.1°$). The ability to track deposits of a single gravity flow across distances > 1000 km is unique, and is made possible here by a robust chronostratigraphic framework (Weaver et al. 1992; Davies et al. 1997; Wynn et al. 2002b). Future work on the Moroccan Turbidite System will focus on the processes and deposits of other large-scale flows during the late Quaternary, while more detailed work on Bed 5 will involve investigation of erosional processes within Agadir Canyon, and depositional processes of thick mud caps in the Madeira and Seine Abyssal Plains.

References

Curray JR, Emmel FJ, Moore DG (2003) The Bengal Fan: morphology, geometry, stratigraphy, history and processes. Mar Pet Geol 19: 1191–1223

Davies TL, Van Niel B, Kidd RB et al (1997) High-resolution stratigraphy and turbidite processes in the Seine Abyssal Plain, northwest Africa. Geo-Mar Lett 17: 147–153

Frenz M, Wynn RB, Georgiopoulou A et al (2009) Provenance and pathways of late Quaternary turbidites in the deep-water Agadir Basin, northwest African margin. Int J Earth Sci. doi: 10.1007/s00531-008-0313-4

Gee MJR, Masson DG, Watts AB et al. (1999) The Saharan debris flow: an insight into the mechanics of long runout submarine debris flows. Sedimentol 46: 317–335

Jones KPN, McCave IN, Weaver PPE (1992) Textural and dispersal patterns of thick mud turbidites from the Madeira Abyssal Plain. Mar Geol 107: 149–173

Klaucke I, Hesse R, Ryan WBF (1998) Morphology and structure of a distal submarine trunk channel: The North-west Atlantic Mid-Ocean Channel between lat 53°N and 44°30′N. GSA Bull 110: 22–34

McCave IN, Jones KPN (1988) Deposition of ungraded muds from high-density non-turbulent turbidity currents. Nature 333: 250–252

Siddall M, Rohling EJ, Almogi-Labin A et al. (2003) Sea-level fluctuations during the last glacial cycle. Nat 423: 853–858

Talling PJ, Wynn RB, Masson DG et al. (2007) Onset of submarine debris flow deposition far from original giant landslide. Nature 450: 541–544

Weaver PPE, Kuijpers A (1983) Climatic control of turbidite deposition on the Madeira Abyssal Plain. Nature 306: 360–363

Weaver PPE, Rothwell RG, Ebbing J et al. (1992) Correlation, frequency of emplacement and source directions of megaturbidites on the Madeira Abyssal Plain. Mar Geol 109: 1–20

Wynn RB, Kenyon NH, Masson DG et al. (2002a) Characterization and recognition of deep-water channel-lobe transition zones. Am Assoc Pet Geol Bull 86: 1441–1462

Wynn RB, Weaver PPE, Masson DG et al (2002b) Turbidite depositional architecture across three interconnected deep-water basins on the north-west African margin. Sedimentol 49: 669–695

MTCs of the Brazos-Trinity Slope System; Thoughts on the Sequence Stratigraphy of MTCs and Their Possible Roles in Shaping Hydrocarbon Traps

R.T. Beaubouef and V. Abreu

Abstract Mass Transport Complexes (MTCs) are significant constituents of the fill of the basins of the Brazos-Trinity Slope System. These MTCs are composite stratigraphic bodies consisting of resedimented materials associated with slumps, slides, debris flows, but also subordinate turbidites, and hemipelagites. Although their composition is variable, they tend to be mud-rich. The MTCs exhibit a variety of external geometries. They commonly have erosive bases characterized by "boxy", grooved scours and mounded tops. Commonly, they are internally chaotic, but sometimes show crude stratification or fabrics related to patterns of movement and/or deformation. Because of increased awareness of the abundance of MTCs within deep marine settings and their association with other well known architectural elements, recent attempts have been made to incorporate the occurrence of MTCs into predictive sequence stratigraphic models. The models emphasize the role of relative sea level cycles in the generation of MTCs and relate this to formative processes and positions within an idealized depositional sequence. However, while some Brazos-Trinity MTCs may conform to these concepts, others do not. As such, utility of MTCs for developing sequence stratigraphic frameworks for the Brazos-Trinity system is dubious. Based on our understanding of the Brazos-Trinity Slope System it is proposed that MTCs play a role in shaping hyrdocarbon traps in analogous subsurface systems. Although some portions of these MTCs contain sufficient porous and permeable sediment to constitute hydrocarbon reservoirs, most represent seal and "waste rock" units. They can form basal, vertical and lateral seals to reservoir complexes, as well as intra-reservoir seals and baffles. Because of their erosive nature, the emplacement of MTC's has often resulted in localized or widespread termination of reservoir strata. MTC's with clay-rich lithologies form low permeability, high capillary entry pressure layers overlying these erosional surfaces. Thus, the geometry and transmissibility of contacts between MTCs and reservoir-bearing strata can

R.T. Beaubouef (✉)
Hess Corporation, Houston, TX, USA
e-mail: rbeaubouef@hess.com

V. Abreu
ExxonMobil, Houston, TX, USA
e-mail: vitor.abreu@exxonmobil.com

play an important role in defining the stratigraphic component of hyrdrocarbon traps and represent baffles or barriers to fluid flow during production.

1   Introduction

The subject of this paper is the occurrence and characteristics of Mass Transport Complexes (MTCs) in the continental slope of the Gulf of Mexico. The examples discussed are from a well known system of "mini-basins" located in the Texas continental slope; the Brazos-Trinity Slope System (Fig. 1). The system contains a variety of deposit types. Notable among these are MTCs. MTCs are here defined as composite stratigraphic bodies dominated by deposits resulting from mass wasting and remobilization of intra-slope sediments (slides, slumps, debrites), but also containing subordinate deposits of turbidity currents and hemipelagic processes.
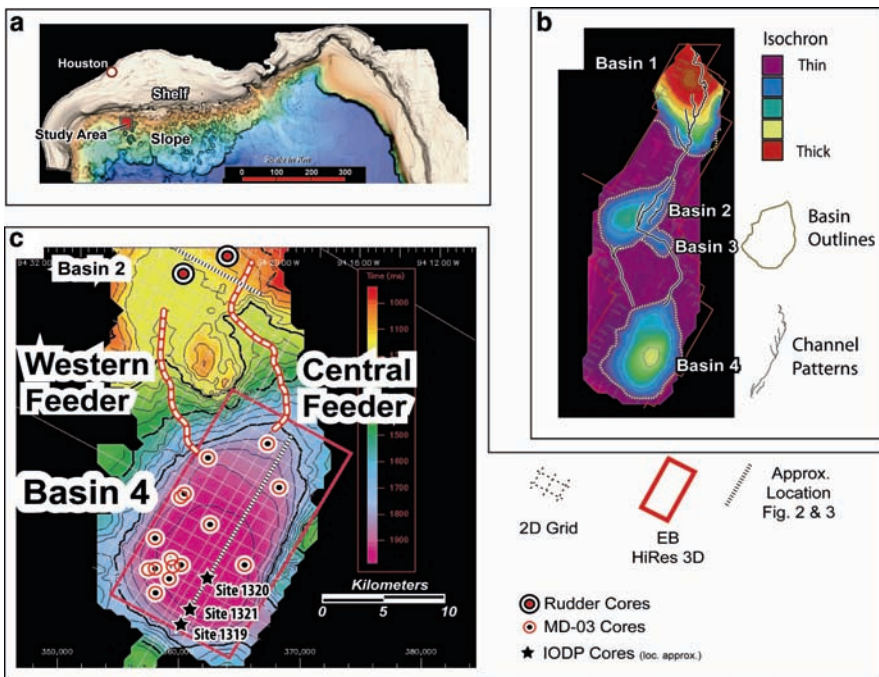
Fig. 1 Maps of study area. (**a**) Bathymetric map of Gulf of Mexico showing location, (**b**) isochron map of Basins 1–4 (Beaubouef and Friedman (2000), (**c**) TWT map of seafloor in study area showing location of seismic, log and core data (Beaubouef and Abreu 2006)

Although these MTCs comprise roughly half the fill of these basins they have received less attention than their sand-rich, turbidite-dominated counterparts. In this paper, we describe some of the MTCs within the system. The methodology employed in this study was to use existing work on the seismic stratigraphy of these basins in combination with recent core and down-hole log data to describe and characterize these deposits. The objectives of this paper are to: (a) discuss the seismic core, and log characteristics of the Brazos-Trinity MTCs, (b) briefly describe the biostratigraphic and chronostratigraphic controls used to build a preliminary age model, (c) discuss implications for sequence stratigraphic models, and (d) set forth some basic ideas for the role of MTCs in the stratigraphic component of hydrocarbon traps. It is hoped that the specific insights gained from this case study have applicability in the description and analysis of deep-water depositional systems in general.

2   Previous Work

The Brazos-Trinity Slope System has been studied by numerous workers since the early 1990s. For a review of the previous work carried out in the area the reader is referred to Winker (1996), Beaubouef and Friedman (2000), Badalini et al. (2000), Beaubouef et al. (2003), Beaubouef and Abreu (2004), Beaubouef and Abreu (2006), Mallarino et al. (2006), and Expedition Scientists (2005). The most recent work has focused on Basin 4. Beaubouef et al. (2003) used a large, short-offset, ultra-high resolution 3D seismic survey to study the basin. A second phase of investigation was designed to calibrate the seismic data through coring and logging. Mallarino et al. (2006) utilized 15 piston cores (MD-03 cores) collected by the R/V Mario Dufresne (IPEV) in 2003 (Fig. 1). From these cores, bio-stratigraphic and isotopic records were obtained. For the first time, a preliminary age model was established for the filling of Basin 4 (Mallarino et al. 2006) providing critical information regarding the chronostratigraphy of the system and the relationship between basin filling episodes and well known, late Pleistocene sea level cycles. Most recently, Basin 4 was investigated during IODP Expedition 308 (Expedition 308 Scientists 2005). During this investigation cores and downhole logs were collected at three sites (U1320, 1321, 1319; Fig. 1). These boreholes sampled the basin filling succession and some of the underlying, pre-basin deposits. These long cores and down-hole logs represent valuable data for the lithologic calibration of the available seismic data. The initial shipboard results from this investigation are available in the Preliminary Report from this leg of the cruise (Expedition Scientists 2005).

3   Geologic Setting and History of Brazos Trinity Slope System

The Brazos-Trinity Slope System (Fig. 1) is a chain of four oval-shaped intra-slope basins (Basins 1–4) of Pleistocene age in the upper to middle continental slope. These basins were directly fed from sediment delivered to the shelf edge by the

ancestral Brazos and Trinity rivers and associated deltas. Sediment delivery to the slope portion of the systems tract was associated with the stepped sea-level fall during the latest Pliestocene. Deposition within the system occurred during a period of approximately 100 Ky (Beaubouef and Friedman 2000). The basins were abandoned during the Holocene transgression and the present highstand of sea level. The four basins are connected by a southerly trending system of slope channels present at the sea floor. The channel system heads in a tributary network within Basin 1 and terminates in a distributary network in Basin 4. Basin 4 is the terminus of the depositional system. These basins are filled by stratigraphic successions ranging from less than 75 m to more than 400 m in thickness.

4 Characteristics of MTCs in Brazos Trinity Slope System

Based on seismic stratigraphy and facies, Beaubouef and Friedman (2000) interpreted the fill of these basins to exhibit vertical cyclicity reflecting alternating deposition of mass transport complexes (MTC), Distrtibutary Channel-Lobe Complexes (DLC), Leveed-Channel Complexes (LCC) and hemipelagic drape complexes (DC). The MTCs are low amplitude, chaotic seismic facies units that occur within each of the four basins. In Basin 2 there are three MTCs (Fig. 2), each of which is overlain by DLCs. In stratigraphic order, these MTCs are here referred to as B2_MTC1, _MTC2, and _MTC3. In proximal basin settings, their bases are defined by prominent erosional surfaces (surfaces of reflection termination
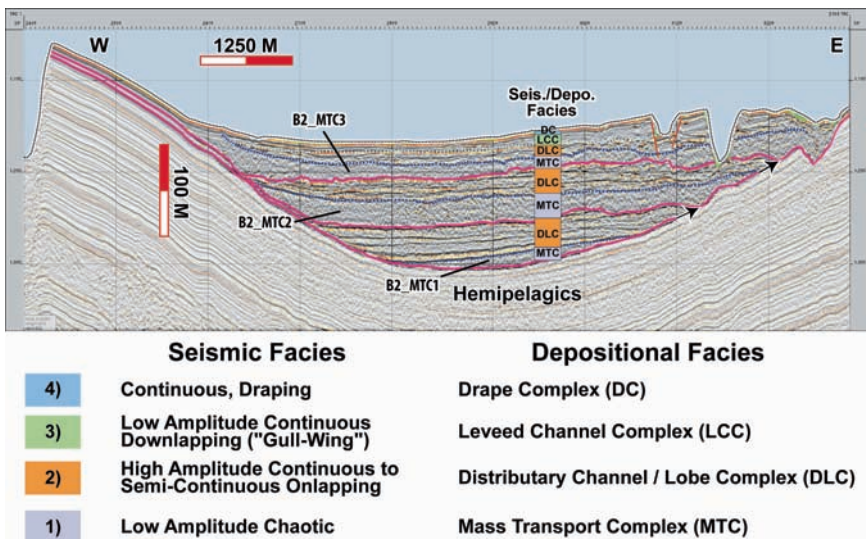
Fig. 2 2D seismic line from Basin 2 (Beaubouef and Friedmann 2000)

and truncation). In more distal settings these basal surfaces are relatively con-
formable with underlying units. The tops of the MTCs are defined by the bases
of the overlying high amplitude DLC units. The lowermost MTC (B2_MTC1) is
restricted to the deepest portion of the basin and is the most aerially limited. The
middle (B2_MTC2) and upper MTCs (B2_MTC3) are more tabular, widespread
units that exhibit irregular tops and bases. As seen in Fig. 2, both units have
highly erosive bases that truncate underlying DLCs and, in some cases, the pre-
basin hemipelagic section.

In Basin 4, there are also three separate MTCs (Fig. 3) interlayered with
DLCs (Lower, Middle and Upper Fans of Beaubouef et al. 2003). In strati-
graphic order, these are here referred to as B4_MTC1, _MTC2, and _MTC3. The
base of B4_MTC1 is defined by the prominent truncation surface above the
Lower Fan. The top of the unit is defined by the compound unconformity linking
the bases of Middle Fan and the younger MTCs. B4_MTC1 can subdivided into
an upper and lower division. Separating these divisions in the central and south-
ern part of the basin is a prominent reflection with concave geometry (Fig. 3).
The lower division is the thickest and exhibits low amplitude, chaotic seismic
facies in the areas of greatest thickness (where basal erosion is greatest), and
very low amplitude, semi-continuous seismic facies in areas where it thins. The
upper division is a thin unit with moderate to low amplitude, continuous seismic
facies which appears to be "ponded" on top of the lower division. In proximal
portions of the basin this upper division is truncated at the base of overlying units.
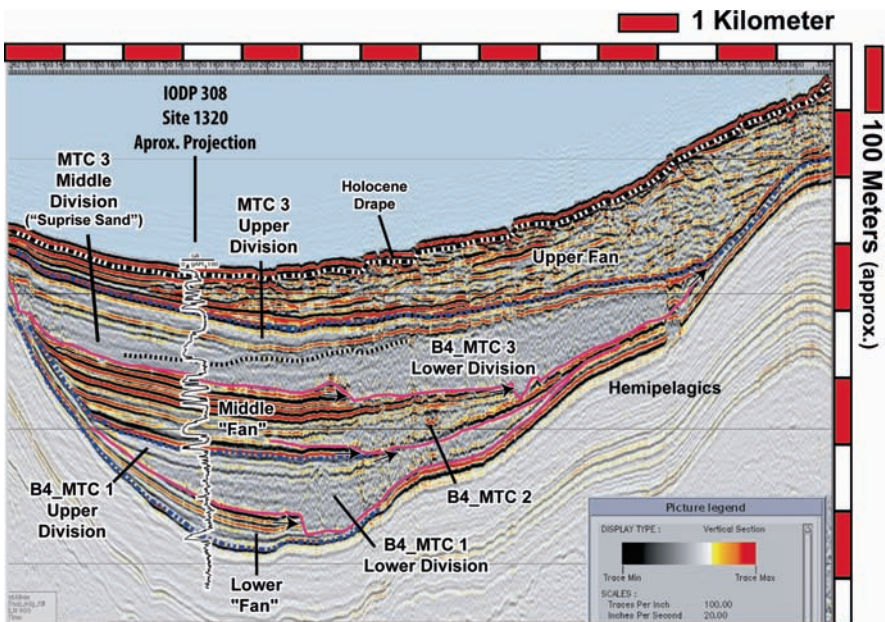
Fig. 3 In-line from EBHR3D, Basin 4 (Beaubouef et al. 2003)

B4_MTC2 is the thinnest of the Basin 4 MTCs. It is a lozenge-shaped unit with low amplitude, chaotic seismic facies that occurs within the lower part of the Middle Fan. The nature of the relationship between these units is not clear; it appears that B4_MTC2 was emplaced during deposition of the Middle Fan. In places, the base of B4_MTC2 is defined by terminations of the basal high amplitude reflections of the Middle Fan. In other places, it is in direct contact with the underlying B4_MTC1. The top is mounded and is onlapped and draped by reflections within the upper third of the Middle Fan. B4_MTC3 is the largest, most laterally extensive MTC. Its base is defined by truncation of reflections at the top of the Middle Fan. The top is defined by the base of the Upper Fan. B4_MTC3 is subdivided into three divisions (Fig. 3). The lower division a thick, wedge-shaped unit characterized by transparent to low amplitude, chaotic seismic facies. This base of the lower division is highly erosive. The middle division occurs only in the southern portion of the basin and "wedges-out" against the top of the lower division. Seismic facies within the middle division is mainly very low amplitude and continuous with reflection amplitude and continuity increasing upward. The upper division is a thin, continuous unit that thins from south to north and "pinches out" beneath the Upper Fan in the proximal portion of the basin. The base of this upper division is marked by high amplitude, continuous reflection passing over both the lower and middle divisions. The top of the upper division is the sharp base of the Upper Fan.
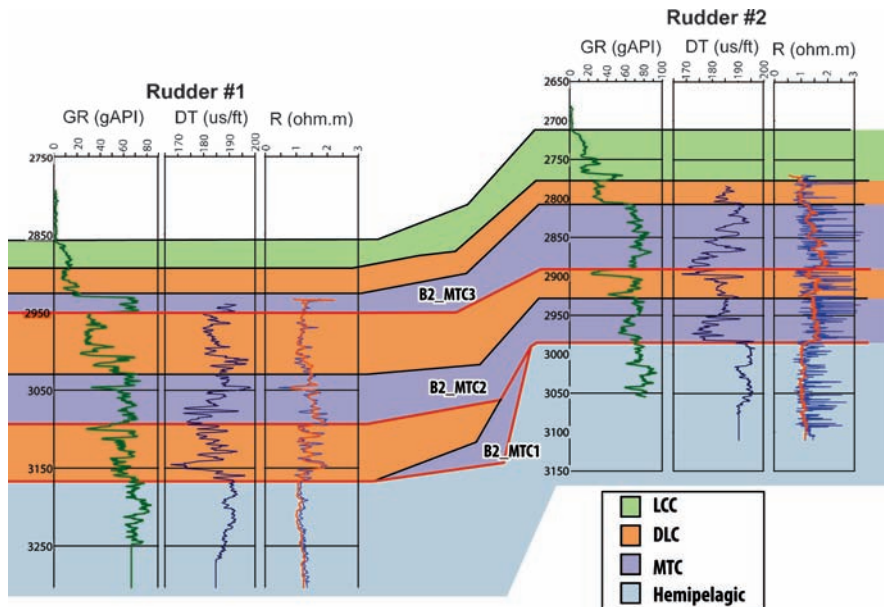
Fig. 4 Electric log cross-section from Basin 2

Electrical logs and cores are available from boreholes within Basin 2 and Basin 4 (Fig. 1). Figure 4 shows the log characteristics of the MTC-bound sequences in Basin 2. B2_MTC1 was not encountered and is shown schematically. The MTCs are characterized by high, but variable gamma ray (GR) curves consistent with clay-rich lithologies with minor amounts of silt and sand. The IODP 308 boreholes provide over 600 m of subsurface information from Basin 4 (Expedition Scientists 2005). Site 1320 is positioned to provide stratigraphic information about the basin-fill and some of the pre-basin filling strata (Fig. 5). The information confirms the previous interpretations that the seismic units characterized by high- to moderate amplitude, onlapping reflection patterns are sand-bearing (Beaubouef et al. 2003). These sandy fans are characterized by packets of very fine to lower medium sand beds inter-bedded with mud (Expedition Scientists 2005). The low amplitude, chaotic seismic facies units contain mud-rich facies containing deformed and contorted facies consistent with the previous interpretations of these units as Mass Transport Complexes (Beaubouef and Friedman 2000; Badalini et al. 2000; Beaubouef et al. 2003), but contain other facies as well.
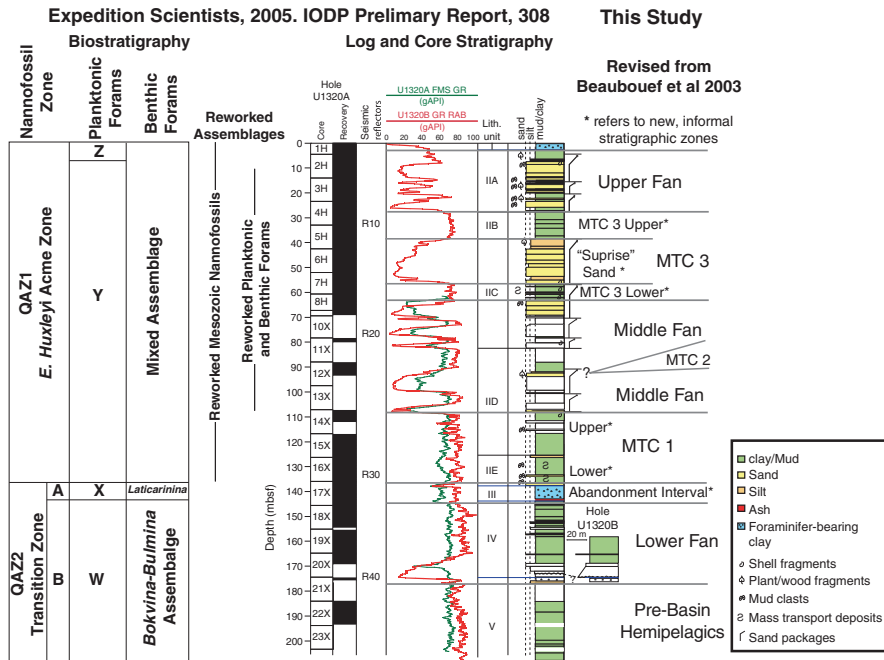
Fig. 5 Log, core characteristics of IODP308 site 1320, Basin 4. Modified from Expedition Scientists (2005)
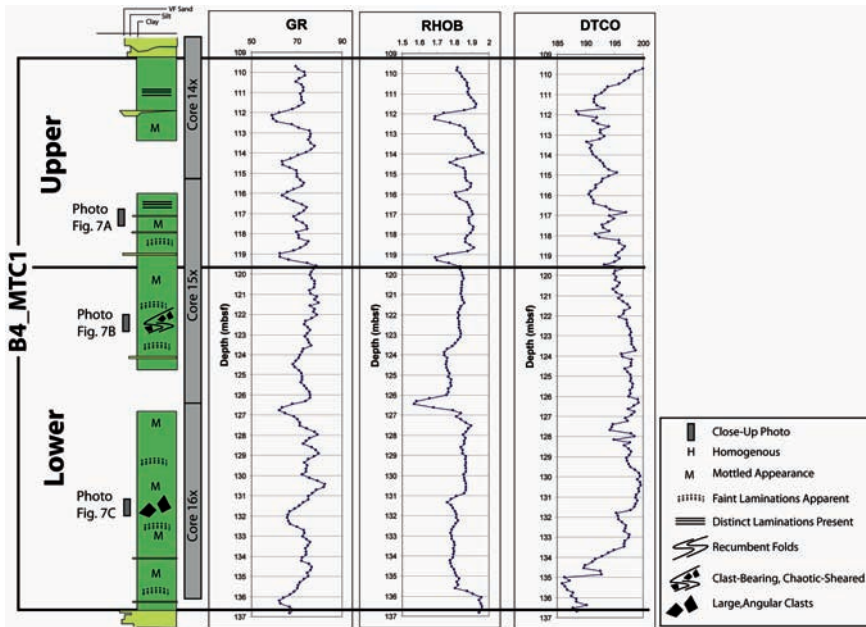
Fig. 6 Core and log characteristics of B4_MTC1, site 1320

Figure 6 shows the internal zonation of B4_MTC1. The core in the basal part of the lower division of B4_MTC1 consists of 17 m of light gray to reddish brown clay with; irregular bands of organic rich black clay, rounded clasts of dark gray clay, a contorted, mud-clast bearing interval with large angular clasts and minor, fine-grained sand. Core from the upper part of the lower division reveals greenish-gray, brownish to dark grey mottled clay with; a contorted, mud-clast bearing interval with apparent shear fabrics and rare, thin beds of silt and very fine grained sand. Core from the upper division contains 10 m of greenish-gray, brown and black mottled clay with; alternations of thin silt and fine sand beds, abundant organic matter, and occasional silt-filled burrows. Examples of core photographs for these divisions are shown in Fig. 7. Figure 8 shows the internal zonation of B4_MTC3. Given previous interpretations, the cores and logs from Sites 1320 (and 1321) provided an unexpected result within MTC3. While the lower division contains a muddy, chaotic unit, the middle division consists almost entirely of sand (hence the informal name, "Surprise Sand"). The core from the lower division contains 8 meters of contorted, mottled, dark gray-black clay with; recumbent folds, large clay clasts, abundant organic materials and minor, thin silts and sands. The middle division is an approximately 20 m thick, fining upward interval of very fine sand. The upper division of B4_MTC3 is 9 m of massive, relatively homogeneous dark green clay with occasional organic material. This unit corresponds to the "slump-derived debrite of Beaubouef et al. (2003) and the "non-hemipelagic mud" of Unit 3 of Mallarino et al. (2006).
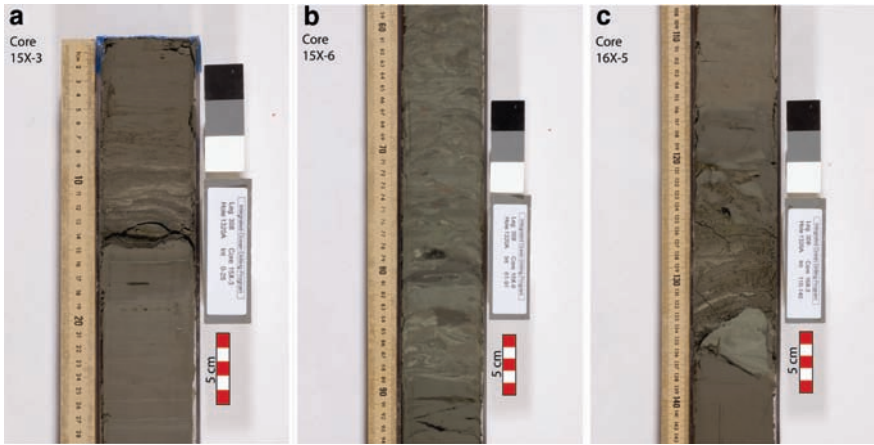
Fig. 7 Core photographs of B4_MTC_1. Locations shown in Fig. 6 (from Expedition Scientists 2005)
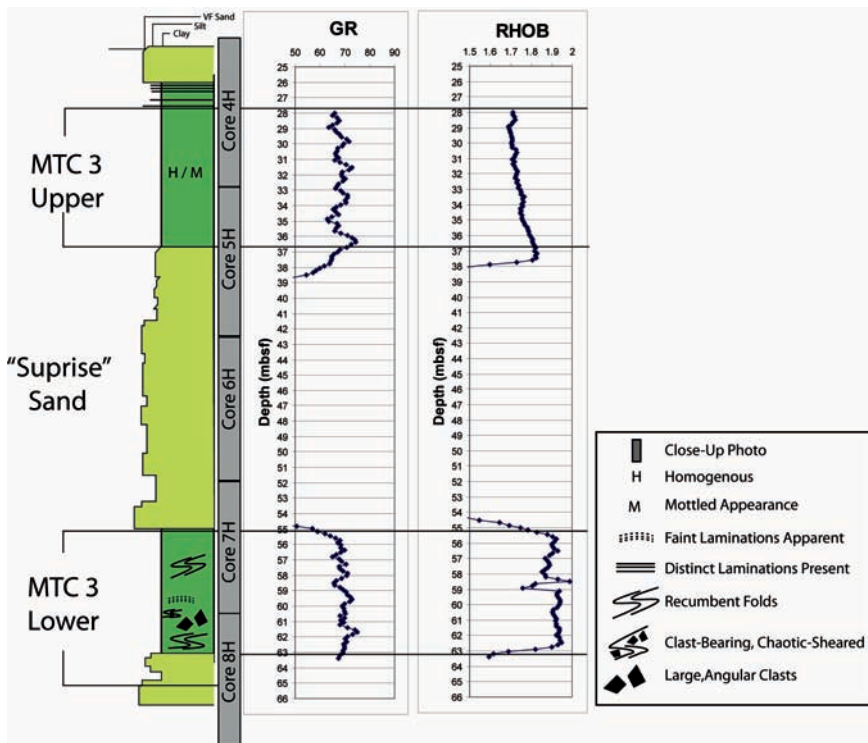
Fig. 8 Core and log characteristics of B4_MTC3, site 1320

5   Biostratigraphy and Chronostratigraphy

Biostratigraphic and chronostratigraphic control within Basin 4 is provided from analysis of the MD-03 cores (Mallarino et al. 2006) and from preliminary analysis of the IODP 308 cores (Expedition Scientists 2005). The biostratigraphic zonation for site 1320 is shown in Fig. 5. All of the MTCs in Basin 4 belong to the QAZ1 nannofossil zone, and the Y foraminifera zone of the Upper Pleistocene. No further biostratigraphic zonation of site 1320 is available at this time. The presence of reworked microfossils complicates the biostratigraphic zonation within the interval, but sheds some light on the depositional processes. The onset of high abundances of reworked Mesozoic nannofossils coincides with the base of B4_MTC1 marking a phase of high energy sediment transport following a period of sediment starvation within the basin marked by the abandonment interval (Fig. 6). Reworked benthic and planktonic forams are observed from the base of the Middle Fan to the middle portions of the Upper Fan. The abundance of these reworked forams reaches a maximum near the base of B4_MTC3 suggesting that erosion and mixing of sediment from different stratigraphic intervals was associated with the deposition of this unit. Integration of this information with results of the other IODP 308 boreholes and the work of Mallarino et al. (2006) allows a preliminary age model to be constructed, as discussed by Beaubouef and Abreu (2006), and shown in Fig. 9. The MTCs in Basin 4 were deposited in a relatively short period
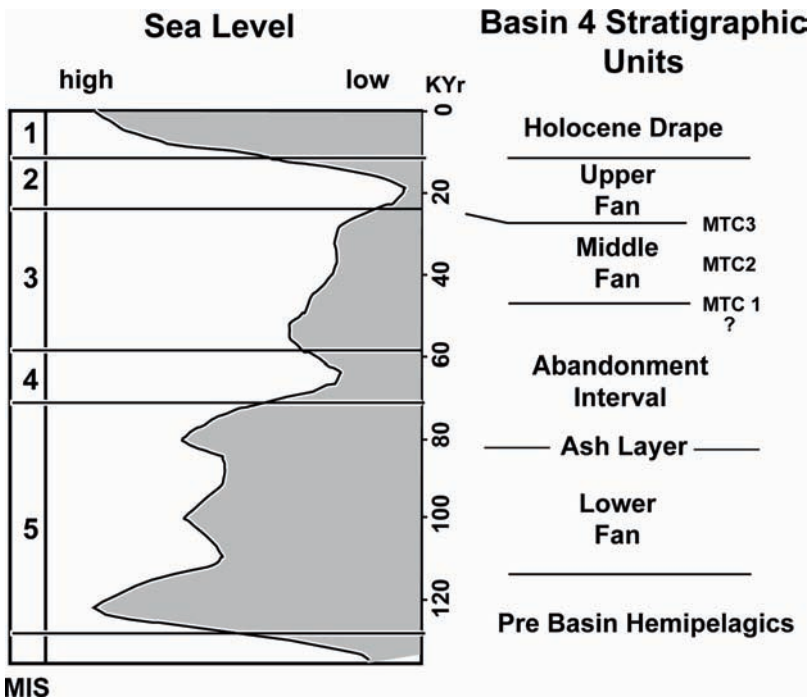
Fig. 9 Preliminary age model for Basin 4 (Beaubouef and Abreu 2006)

of time between MIS-3 and MIS-4. No additional detail about the precise ages of the MTCs and their relationship to the sea-level curve are provided by the biostratigraphic or isotopic data.

6 Stratigraphic Architectures of MTCs in Brazos Trinity Slope System

Geologic cross-sections through Basin 2 and Basin 4 are shown in Figs. 4 and 10, respectively. The bases of the MTCs correspond to prominent erosion surfaces and thickness variations of the intervening sand packages (DLCs) is largely due to this erosion. The erosion is greatest in the proximal, northern regions of the basins and diminishes in a southerly direction where the bases of the MTCs become progressively more conformable with the underlying units. Due to additional core and log information and HR 3D seismic data, we have much greater control on the architectures of MTCs within Basin 4. The lower division of B4_MTC1 is clearly derived from collapse of the eastern margin of the basin (Fig. 11). Wavy and arcuate amplitude lineations observed in datumed time slices are interpreted as indicators of flow patterns (Fig. 11b). The flow patterns indicate mass transport was directed west to southwest. Erosion and/or mass wasting at the base completely removed the northwestern portion of the Lower Fan. The upper division is interpreted as a thin-bedded, fine-grained turbidite succession that may have been deposited from dilute turbidity currents generated from the slumping and mass wasting events associated with deposition of the lower division. B4 _MTC2 is "inter-fingered" with the Middle Fan (Fig. 3). This MTC was derived from the western portion of the basin (Fig. 12) and may have been associated with the initial formation of the Western Feeder (Fig. 1). The erosional contact with the lower part of the Middle Fan is characterized by "boxy", grooved scours with abrupt terminations (Fig. 12).

Where the lower portions of the Middle Fan are removed, the two MTCs are in direct contact with one another. Of the Basin 4 MTCs, B4_MTC2 is the smallest. B4_MTC3 is the uppermost, and largest of the MTCs within Basin 4. Based on map patterns it is interpreted that his unit was mainly derived from the Western Feeder (Fig. 1). The lower division has a highly erosive base, in places cutting through the Middle Fan and down to the level of B4_MTC1. Erosion is greatest in the northern portion of the basin and decreases toward the distal reaches. Accompanying this basal erosion trend is an overall southerly thinning. As the lower division thins, it is replaced by the middle division ("Surprise Sand"). This sand-rich division is restricted to the southern regions of the basin. Based on seismic and log correlation, the middle division is continuous for over 5 km in the dip-direction. Although speculative, the middle division may have been deposited by flows generated via the emplacement of the lower division. The sand-rich nature of this division made be due to reworking of the sands from the Middle Fan. The upper division is continuous across the basin except where it is cut out by the Upper Fan in the north. Beaubouef et al. (2003) interpreted
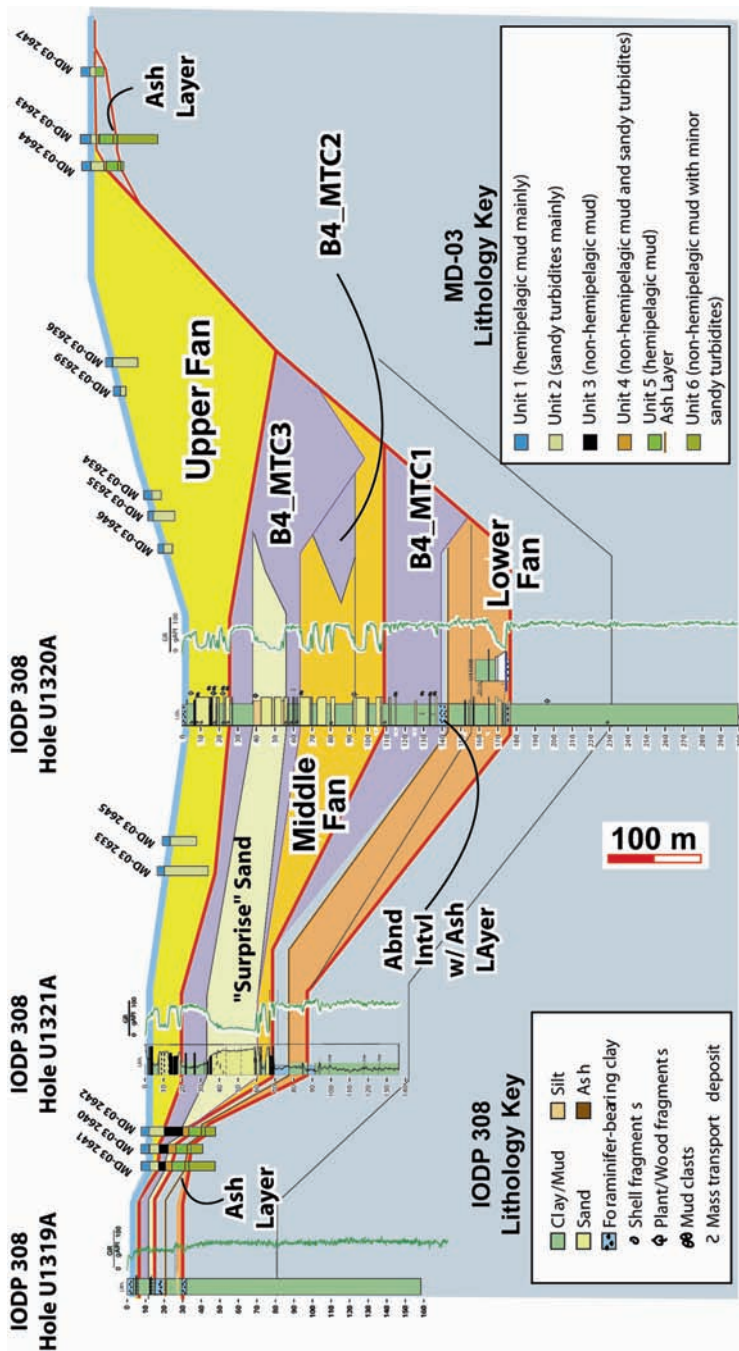
Fig. 10 Log and core-based cross-section for Basin 4. Shown are logs from IODP 308 Sites 1319, 1320, 1321 (Expedition Scientists 2005) and MD-03 cores (Mallarino et al. 2006)
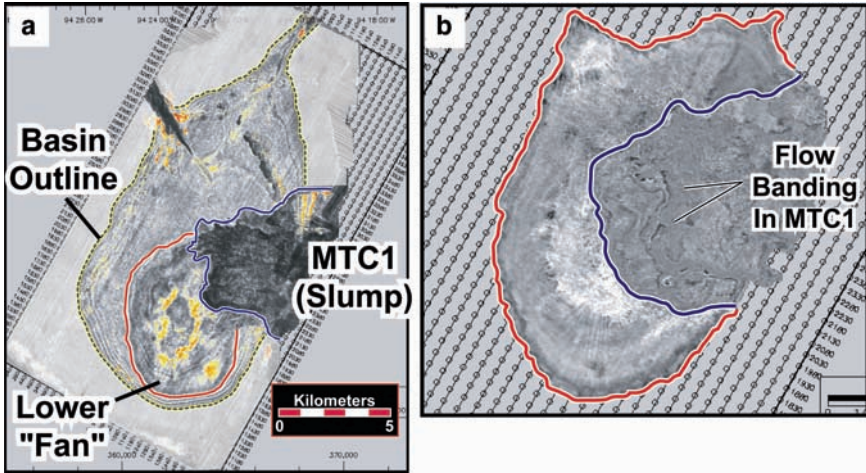
Fig. 11 Seismic amplitude maps illustrating characteristic of B4_MTC1. Images are derived from "slices" through a seismic volume "flattened" at the top of the Lower Fan interval. Variations in colors represent variations in seismic amplitude characteristics within the slices (Beaubouef and Abreu 2004)
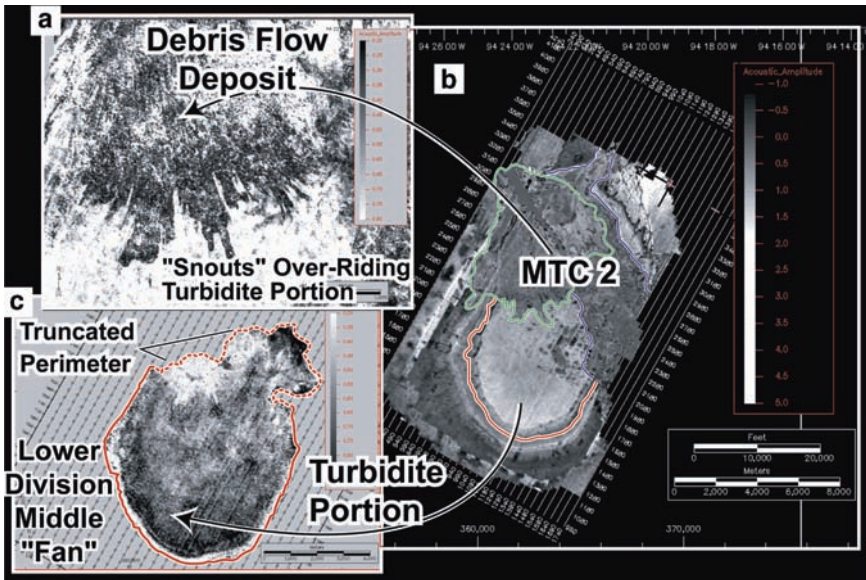
Fig. 12 Seismic amplitude maps illustrating characteristic of B4_MTC2. Images are derived from "slices" through a seismic volume "flattened" at the top of the Middle Fan interval. Variations in colors represent variations in seismic amplitude characteristics within the slices (Beaubouef and Abreu 2004)

this unit as a slump-derived debrite associated with continued mass wasting of the steep, eastern basin margin.

7 Origins of MTCs and Implications for Sequence Stratigraphic Models

Beaubouef and Friedman (2000) proposed a sequence stratigraphic model in which MTCs occur in the basal portions of lowstand systems tracts. Sequence boundaries were placed at the prominent unconformities at the bases of these distinctive units. It was inferred that: (a) mass wasting and mass transport of muddy slope materials occurred in response to the earliest portion of sea level fall and preceded the major influx of sand during the maximum sea level lowstands, and (b) these patterns repeated in response to high frequency sea level cycles during the latest Pliestocene (Fig. 9). Analysis of more recently acquired data requires aspects of the Beaubouef and Friedman model be reconsidered. Specifically, not all of the Brazos-Trinity MTCs conform to such sequence stratigraphic predictions. The MTCs are of two different types, here classified as intra-basinal and extra-basinal. Intra-basinal MTCs are derived from within the basins as slumps or slides from over-steepened, collapsed basin margin areas. B4_MTC1 is a good example of an intra-basinal MTC. Intra-basinal MTCs occur in response to local processes unique to each basin, and may occur at any time during the basin evolution regardless of sea-level stage. Extra-basinal MTCs are derived from areas outside and up-dip of the basins and entered the basins via the various feeder channels (Beaubouef and Friedman 2000). The extra-basinal MTCs tend to be the most laterally extensive and have point sourced, fan-like map patterns. Examples of extra-basinal MTCs are B2_MTC3 and the lower divisions of B4_MTC3. Extra-basinal MTCs may have occurred in response to allocyclic processes, and therefore, may have sequence stratigraphic significance. However, it can not be ruled out that extra-basinal MTCs may also have more local, autocyclic origins. Furthermore, it is questionable whether the MTCs can be reliably tied to the late Pliestocene sea level curve using biostratigraphic or isotopic data. Hence, the actual relationships between the MTCs and the high frequency sea level cycles, if any, are still not well understood. Finally, in some cases, the origins of the MTCs are not clear and the classification is indeterminate. For example, although B4_MTC2 clearly flowed into the basin from the vicinity of the Western Feeder, the unit may have formed as a local slump of the basin margin at the mouth of the channel. The observation that this MTC is "inter-fingered" with the Middle Fan is at odds with the Beaubouef and Friedman model. At this point, it would appear that the utility of MTCs for developing sequence stratigraphic frameworks for the Brazos-Trinity system is in question.

8 Discussion of Potential for Stratigraphic Traps Associated with MTCs

It has been previously shown that the sand-rich, turbidite-dominated successions within the fills of these basins constitute excellent analogs for intra-slope reservoirs. The role of the MTCs in analogous hydrocarbon traps has been less explored. In this paper, we have shown that the Brazos-Trinity MTCs contain a variety of lithofacies types and exhibit a variety of stratigraphic architectures. Some divisions of the MTCs contain sufficient porous and permeable sediment to constitute hydrocarbon reservoirs, most notably the middle division of the B4_MTC3 (the "Surprise Sand"). The other, mud-dominated divisions would represent seal and "waste rock" units within hydrocarbon traps. This concept has also been discussed by Moscardelli et al. (2006). Because of erosion at the basal surfaces of the Brazos-Trinity MTCs, localized or widespread termination of reservoir strata below these surfaces has occurred. As such, these erosion surfaces play an important role in determining the geometry and continuity of reservoirs in these settings. Furthermore, the 3D geometry of the truncated reservoir bodies often are not controlled by a single erosion surface, but rather two or more erosion surfaces that form a compound unconformity. The muddy portions of the MTCs represent basal, vertical and lateral seals to the reservoir complexes. These stratigraphic arrangements would likely represent poly-seal traps; traps involve more than one sealing surface (Milton and Bertram 1992; Corchoran; 2006). The type of lithologies directly overlying these erosion surfaces, and hence, the transmissibility of the sealing surfaces, represents a key factor in impeding fluid migration through the stratigraphic succession (Moscardelli et al. 2006). In the fill of Basin 4, reservoir-prone units are represented by the Lower, Middle and Upper Fans and the "Surprise Sand". Each of these units is partially or completely surrounded by mud-rich facies of the MTCs (Fig. 10). In the case of the Lower Fan (Fig. 11), base and lateral seal is provided by the clay-rich, pre-basin hemipelagic section. An unconformable top seal is provided by the lower division of B4_MTC3. The case of the Middle Fan is more complicated (Figs. 3 and 12). In some areas, base seal is provided by either pre-basin hemipelagics or the very fine-grained, distal equivalents of the Lower Fan. In other areas, B4_MTC1 provides base seal. An unconformable top seal is provided by the lower division of B4_MTC1. The Middle Fan may be further complicated by the intra-formational seal formed by B4_MTC2. Depending on the lithology of this uncored unit, it may partially segment or compartmentalize the trap. For the "Surprise Sand", base seal is provided by the lower division of B4_MTC3, lateral seal is provided by steeply dipping hemipelagic section in the distal portion of the basin, and top seal is provided by the homogenous clay of the upper division of B4_MTC3. The primary risks for these traps are; (a) an incomplete join between top and base seal, (b) incomplete separation of sand-rich units by the MTCs, and (c) fluid migration pathways provided by connections between reservoir units via the thinly bedded sand and silts existing in some divisions of the MTCs. In cases where

MTC's with mud-rich, high capillary entry pressure layers overly the sealing surfaces, the fluid transmissibility of the contacts will be very low and stratigraphically-assisted trapping of hydrocarbons is possible. From this brief analysis, we conclude that the distribution of mud-rich sediment is equally important as the nature of the sand-rich intervals in determining the characteristics of stratigraphic component of traps. MTCs are the main contributors of mud to these basins, but also contribute reservoir-grade material. As such, further study of the role of MTCs in shaping hydrocarbon traps is warranted.

References

Badalini G, Kneller B and Winker CD (2000) Architecture and process in the Late Pleistocene Trinity-Brazos turbidite system. Gulf of Mexico. In: Weimer, P. et al. (eds.), Deep-Water Reservoirs of the World, Gulf Coast Soc SEPM.

Beaubouef RT and Abreu V (2006) Basin 4 of the Brazos-Trinity slope system: anatomy of a Lowstand systems tract. Gulf Coast Soc Geolog Soc Trans 56: 39–49.

Beaubouef RT and Abreu V (2004) Basin 4 of the Brazos-Trinity slope system. Europ Assoc Geol Eng Paris, France, Paper A028.

Beaubouef RT, Abreu V and Van Wagoner JC (2003) Basin 4 of the Brazos-Trinity slope system: the terminal portion of a late Pleistocene lowstand systems tract. In: Roberts, H. et al. (eds.), Shelf Margin Deltas and Linked Down Slope Petroleum Systems: Global Significance and Future Exploration Potential, Gulf Coast Soc SEPM.

Beaubouef RT and Friedman SJ (2000) High resolution seismic/sequence stratigraphic framework for the evolution of Pleistocene intra slope basins, Western Gulf of Mexico: depositional models and reservoir analogs. In: Weimer, P. et al. (eds.), Deep-Water Reservoirs of the World, Gulf Coast SEPM.

Corchoran J (2006) Application of a sealing surface classification for stratigraphic related traps in the UK Central North Sea. In: Allen, MR. et al. (eds.), The Deliberate Search for the Stratigraphic Trap, Geol Soc Lond Spec Pub 254: 207–223.

Expedition Scientists (2005) Overpressure and fluid flow processes in the deepwater Gulf of Mexico: slope stability, seeps, and shallow-water flow. IODP Prelim Rep 308. doi:10:2204/iodp.pr.308.2005.

Mallarino G, Beaubouef RT, Droxler AW, Abreu V and Labeyrie L (2006) Sea level influence on the nature and timing of a minibasin sedimentary fill (northwestern slope of the Gulf of Mexico). Am Assoc Petrol Geol Bull 90: 1089–1119.

Milton NJ and Bertram GT (1992) Trap styles, a new classification based on sealing surfaces. Am Assoc Petrol Geol Bull 76: 983–999.

Moscardelli L, Wood L and Mann P (2006) Mass-transport complexes and associated processes in the offshore area of Trinidad and Venezuela. Am Assoc Petrol Geol 90 (7): 1059–1088.

Winker CD (1996) High-resolution seismic stratigraphy of a late Pleistocene submarine fan ponded by salt-withdrawal minibasins on the Gulf of Mexico continental slope. In: Proc 28th Annual Offshore Tech Conf 28 (1): 619–628.

Southeast Australia: A Cenozoic Continental Margin Dominated by Mass Transport

R. Boyd, J. Keene, T. Hubble, J. Gardner, K. Glenn, K. Ruming, N. Exon, and the crews of Southern Surveyor 10/2006 and 12/2008

Abstract The Southeast Australian continental margin extends for 1,500 km northward from Bass Strait to the Great Barrier Reef. Mass transport dominates the continental slope, which stretches from the shelf break around 150 m depth to the abyssal plain around 4,500 m depth. The continental slope has average slopes of 2.8–8.5º and extends seaward from the shelf break an average distance of 50 km. Margin structure results from Late Cretaceous rifting, producing exposed fault blocks and igneous complexes on the lower slope, and an overlying sediment wedge around 0.5 km thick, centered at the shelf break. Recent collection of multibeam echosounding and high-resolution seismic data provide a detailed view of mass-transport features over a 900 km length of the margin. The features are mostly slab slides, box canyons, and linear canyons. They are ubiquitous along the steep rifted margin, but absent in regions of gentler slopes such as submarine plateaus and failed rift arms. Submarine landslides range in scale from hundreds of small slides of <0.5 km^3 volume, up to the largest documented slide of 20 km^3. However, potential future slide masses of basement blocks up to 105 km^3 have been identified. Cores that penetrated the basal-slide surface show variable sediment accumulation, since the mass-movement event, but four penetrations show

R. Boyd (✉)
ConocoPhillips, Houston and University of Newcastle, Australia

J. Keene and T. Hubble
University of Sydney, Australia

J. Gardner
CCOM, University of New Hampshire, USA

K. Glenn
Geoscience Australia, Canberra, Australia

K. Ruming
NSW Department of Primary Industries, Maitland, Australia

N. Exon
Department of Earth and Marine Sciences, Australian National University,
ACT 0200, Australia

accumulations of <2 m, and one of <0.6 m. At current accumulation rates, these data indicate that many landslides occurred less than 25 ka, with some as recent as 6 ka. Mass movements appear to follow a pattern of box canyon development exploiting structural trends in pre-rift and syn-rift strata, until the canyon head intersects the toe of the Tertiary sediment wedge. Once this occurs, sediment creep, faulting and failure of the wedge toe migrates up slope, finally reaching the upper slope and Quaternary deltaic depocenters.

Keywords Continental margin • multibeam • mass transport • Southeast Australia • continental slope • submarine landslide

1   Background

The Southeast (SE) Australian continental margin (Boyd et al. 2004) stretches 1,500 km north from Bass Strait (37°30′ S) to the Great Barrier Reef (24° 15′ S). This passive rifted margin fronts the Tasman Sea, and by world standards is narrow, deep and sediment deficient. The SE Australian shelf is narrow and flat with a thin sediment cover, apart from a Tertiary-Quaternary depocenter up to 500 m thick beneath the shelf break. The shelf break ranges between 55 and 180 m depth, the margin varies from 48–135 km wide, and the base of the margin occurs where the continental rise joins the Tasman Abyssal Plain around the 4,500 m isobath. Cretaceous rifting began around 90 Ma, and Tasman Sea and adjacent margin formation was completed by around 65 Ma. Since then, margin subsidence has been slow and sediment accumulation minor. The margin structure consists first of bedrock outcrop along most of the coast and inner shelf, and again on the middle to lower continental slope. The middle slope is where Paleozoic fold belt rocks outcrop, adjacent to abundant igneous intrusives associated with Mesozoic-Cenozoic rifting.

Late Quaternary sea-level changes of around 120 m have resulted in the shoreline regressing to a position on the mid to outer shelf off central and southern NSW, (seaward margin of yellow color in Fig. 1), whereas in northern New South Wales (NSW) and SE Queensland, the sea-level lowstand position occurred on the upper slope. A strong south to north wave-driven longshore transport occurs at the shoreline at all sea-level positions, whereas the shelf and slope is impacted by the south-flowing East Australian Current. The coastal hinterland consists of the Paleozoic Lachlan and New England Fold Belts drained to the east by a series of small coastal rivers such as the Hunter and Clarence, with courses less than 250 km long, catchment areas of less than 22,500 km^2 and suspended sediment yields of less than 750 kilotons/year (OZcoasts 2008). Submarine slope failures on the Southeast Australian margin were first identified by Jenkins and Keene (1992) using widely spaced seismic profiles, supported by bottom photographs of one slide.
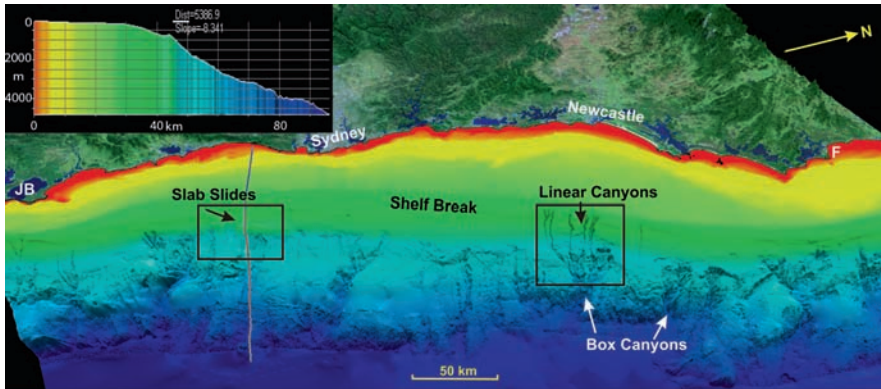
Fig. 1 The Central New South Wales (NSW) margin extends from 35°S at Jervis Bay (JB) to 32°S at Forster (F) and includes clear examples of slab slides, linear canyons and box canyons. Location of Fig. 3 is shown on left box, and Fig. 4 as right box. Profile line extends from shoreline to abyssal plain across the Bulli Slide of Fig. 3, and colors indicate depth scale

2   Methods

Investigation of mass-movement features on the SE Australian margin was conducted mainly by morphological analysis derived from bathymetric surveys, augmented by acoustic backscatter data and geological sampling of grabs, dredges and cores. Deeper subsurface data was derived from high-resolution sub-bottom profiles and lower resolution multichannel seismic data (e.g., Glenn et al. 2008). Bathymetric data used in this study were initially derived from single-beam echosounder data throughout the entire SE Australian margin provided by the Royal Australian Navy, combined with regional data sets including ETOPO2 (Smith and Sandwell 1997). More detailed data from the central NSW and SE Queensland margin were derived from four surveys on the Marine National Facility *Southern Surveyor* (SS12/2008, 10/2006, 1/2005 and 4/2003). These surveys used a *Simrad EM300* multibeam echosounder to acquire bathymetry and acoustic-backscatter data as well as both high and medium resolution seismic-reflection data. Additional deep-water data were incorporated from ship-of-opportunity tracks along the base of the margin, including R/V *Ewing* and *l'Atlante*.

Following data acquisition, raw bathymetric data from all sources was processed and merged to generate integrated data sets extending for the entire 1,500 km of the study area. These marine data sets were then displayed as depth-dependant color maps and given artificial sun illumination in *Fledermaus* software. The final bathymetric product was combined with coastal land digital elevation models that had

been draped with *Landsat* imagery (e.g. Figs. 1 and 2) to generate an integrated morphological model for the coastal and continental margin region of SE Australia. Geological sampling was used to identify sediments and rocks mapped from the geophysical surveys including more than 100 *Smith-Macintyre* grab samples, 20 cores and 25 dredges over the entire region from the 80 to the 4,000 m isobaths.

3 Mass-Movement Features

The SE Australian margin ranges in width from 48 to 135 km from the shoreline to the abyssal plain, which begins around 4,500 m depth. This variation in morphology results from tectonic rifting processes that alternated small continental crustal plateaus with steep rifted segments along the length of the margin (e.g. Fig. 2). The shelf is relatively flat, ranging between 14 and 78 km wide. The continental slope ranges from 28–90 km wide and average slopes range from a minimum of 2.8° on plateaus to a maximum of 8.5° off steeper rifted segments. This steeper continental slope is mantled with finer sediments and has a wide range of mass movement features developed along the entire 1,500 km section from Bass Strait to the Great Barrier Reef. The main mass movement and associated features include: (1) slab slides; (2) debris flows; (3) box canyons; (4) linear canyons; (5) carbonate platform slides; (6) plunge pools; and (7) pockmarks.

3.1 Slab Slides

Slab slides (Figs. 1 and 3) occur in the planar-bedded, seaward dipping, pelagic-hemipelagic carbonate and clastic-mud deposits on the upper slope. The scars are up to 250 m deep, relatively flat based, with steep (up to 15°) linear walls and a steep crown scarp. Large examples such as the Bulli and Shovel slides (Fig. 3) on slopes of around 4.5° are up to 13 km long and 5 km wide, with volumes of up to 20 km^3. They initiated right from the base of the Tertiary sediment wedge around 1,100 m depth to the upper slope in 400 m depth. In some locations, slab slides have coalesced so that entire depositional packages are missing for distances along slope of 20 km. Several slab slides have linear furrows preserved on their base. These furrows, or grooves, are up to 5 km long, 50 m deep and 300 m wide. Seismic data across slab slides show the sediment is made up of well stratified beds that failed on a bedding plane surface. Five cores that penetrated the basal slide surface had accumulated between 0.6–2.5 m of pelagic carbonate mud since the slide occurred. At average sediment rates for the margin of 0.1 m/1,000 years (Troedson and Davies 2001) these slides appear to have occurred between 6–25 ka.
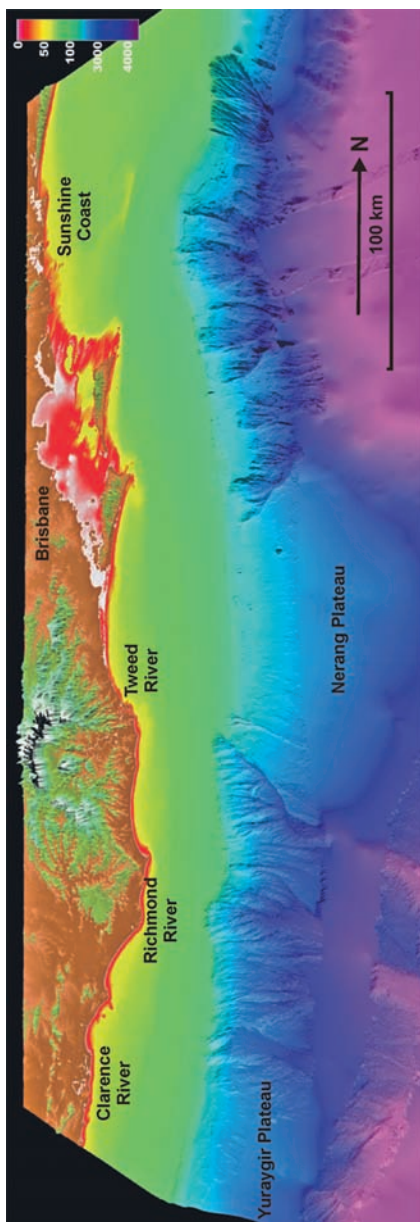
Fig. 2 The SE Queensland margin displays alternation between marginal plateaus (Nerang and Yuraygir Plateau) and steep rifted margin segments. The steep rifted margin segments are dominated by box canyons, while they are absent on the lower gradient plateaus. Box shows location of plunge pools in Fig. 5. Depth key in upper right in m
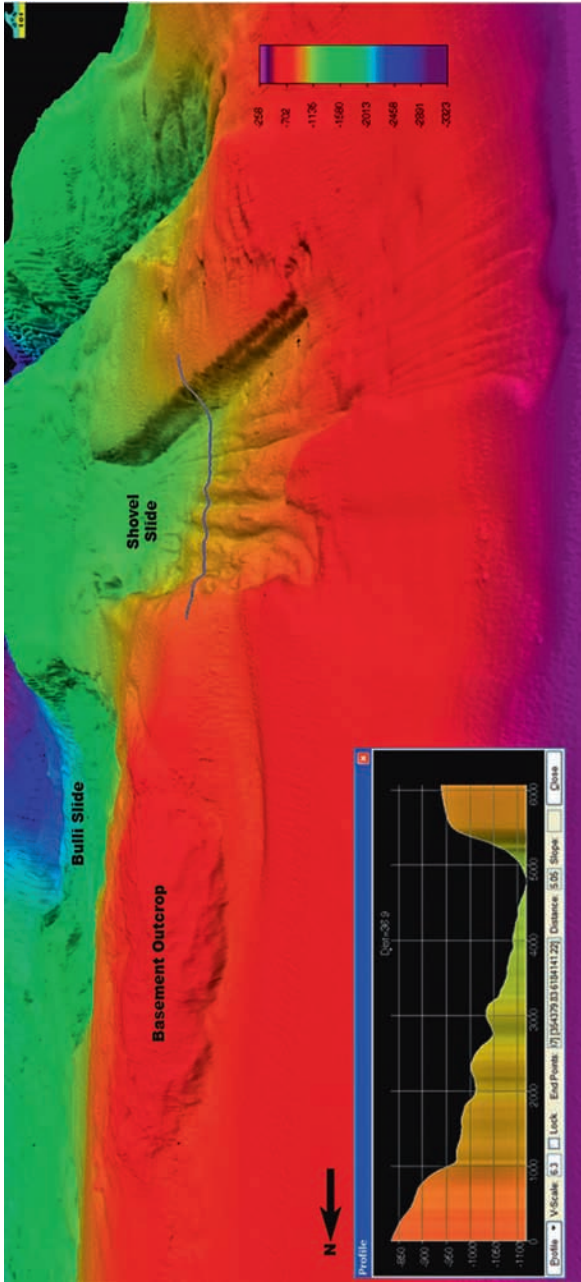
Fig. 3 View looking downslope of two slab slides (*the Shovel Slide, right; and the Bulli Slide, left*). The color bar shows water depth and the cross section shows scale. Note the grooves on the base of the Shovel Slide, the steep linear margin of the slide, and the basement outcrop above the Bulli Slide

3.2   Debris Flows

In most locations, slab slides have no sediment derived from the slide visible further down slope, and it appears as if the materials derived from the slide have been transferred to the abyssal plain. However, in a small number of locations, the slides are localized on the upper slope, and their sedimentary deposits are located immediately downslope. In these cases, the slide deposits occur as massive debris flow fields over 10 km^2 in area. The debris flow deposits spread out in a radial pattern and contain blocks up to 350 m wide and 50 m high. Slopes on which the slab slides deposited debris flows down slope were less steep and averaged 2.5°.

3.3   Box Canyons

Box Canyons (Figs. 1 and 4) are large erosional chasms on the lower to middle continental slope that extend to the base of the slope but do not connect upslope to feeder canyons or sediment supply systems. They consist of multiple erosional events, branch upslope into tributary box canyons, usually involve pre-rift basement and synrift basin rocks and may extend retrogressively upslope into the toe of the Tertiary sediment wedge. In terms of volume and extent, box canyons are the dominant erosional feature on the SE Australian margin. The box canyons are abundant along steep rifted margin segments, but poorly developed to absent on the continental plateau segments. Between Bass Strait and the Great Barrier Reef, there are around 46 box canyons, averaging 32 km apart. These erosional mass-movement features average 14 km wide and 680 m deep at the 1,500 m isobath, and frequently have slopes up to 17° on the walls. Box canyons stretch from the middle slope to the abyssal plain and average over 20 km long. Individual canyons have excavated as much as 690 km^3 of slope volume and average 220 km^3. In local examples, box canyons have coalesced along sections of steep rifted margin such as off Queensland's Sunshine Coast, leaving isolated remnants of mid to lower continental slope bedrock exposed. One example of these remnants occurs off Moreton Island, has a prominent crown crack and a volume of over 100 km^3.

3.4   Linear Canyons

In a limited number of locations along the margin, mainly low gradient segments of the upper slope and off major river systems such as the Shoalhaven, Hunter and Tweed, are located a set of narrow, linear erosional furrows incised into the Tertiary sediment wedge (e.g. Figs. 1 and 4). There are over 30 linear canyons along the margin, most located in central NSW or off Fraser Island. These linear canyons penetrate up slope to 200 m water depth, just below the shelf break off Newcastle
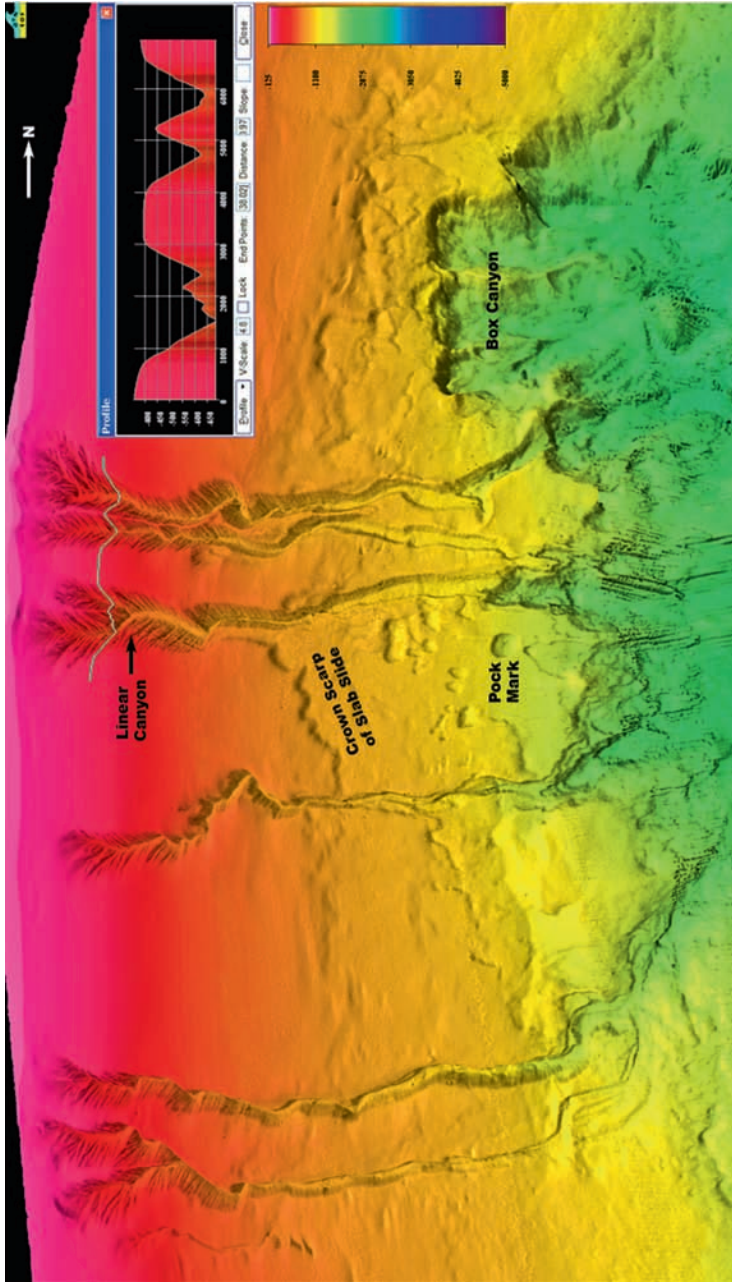
Fig. 4 Off Newcastle and the Hunter River in central NSW, upper slope deltas are incised by linear canyons (*top center*), and box canyons are retrogressing up the middle slope (*lower right*). A large pockmark is seen in the lower center (*black arrow*), below a large slab slide

(Fig. 4). Well developed examples are 800–1,900 m wide, 120–320 m deep and extend downslope for 14–22 km. Canyon wall slopes are 18–34°, the steepest developed in sediment found on this margin. Linear canyons are only found where slopes are less than 4.5°, and often display tributary rills. Off the Clarence and Richmond Rivers, the tributary rills have coalesced to form a large canyon, suggesting that isolated linear canyons are the early stage of larger, merged canyons.

3.5 Carbonate Platform Slides

The upper continental slope, north from the Clarence River in northern NSW to the Great Barrier Reef, is made up of series of backstepping Tertiary carbonate platforms with steep seaward margins. These steep lithified platform fronts have frequently failed and resulted in rock slides at the seaward margin. In some cases the slides are flanked by regions of the carbonate platform that can be observed to have crown cracks, or to have incipient slides that have partly separated from the platform front, but not yet moved down slope. The lower carbonate platform front is over 250 m high seaward of Fraser Island and has slopes of 43° over distances of 500 m.

3.6 Plunge Pools

Several of the canyon-channel systems (e.g. Sydney Canyon and off the Richmond River) have features that resemble plunge pools in their distal reaches. The plunge pools are large erosional bowl-shaped depressions and occur at abrupt drop-offs (>35°) with >200 m of relief. These depressions are 500 to 1,000 m wide in the down-channel direction and are as much as 100 m deeper than the adjacent down-channel reach. Several of the plunge pools have a depositional bar across the down-channel side of the depression. The bars are <50 m high and typically extend only partway across the channel. In a location seaward of the Richmond River in northern NSW (Fig. 5), multiple plunge pools can be seen, often in the same valley system. These plunge pools appear to be migrating upslope like a waterfall or fluvial knick points.

3.7 Pockmarks

Circular to elongate depressions occur on the upper continental slope, often isolated from other erosional and mass transport features. These depressions are mainly off central NSW and occur as groups on slide surfaces between the tributaries of the Hunter Canyon complex. The largest of the pockmarks is 1 km in diameter and 70 m deep (Fig. 4), and they appear to overlie faulting in the underlying basement above Sydney Basin coal measures.
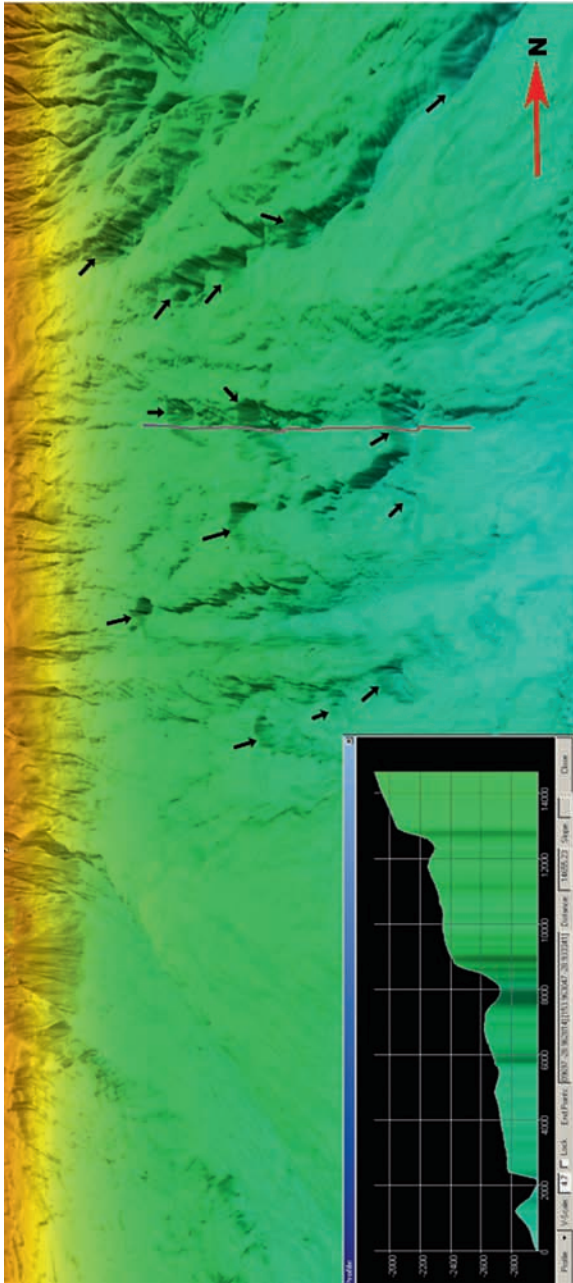
Fig. 5 Middle continental slope between 2,000 and 3,000 m depth off the Richmond River showing extensive development of plunge pools (*arrowed*). A cross section (*scales in m*) shows three plunge pools up to 200 m deep, apparently migrating up slope in the same canyon

4 Discussion

Mass movements on the SE Australian margin are in part due to the steep nature of the margin and its thin sediment cover. Rifting models interpret the SE Australian margin as an upper plate segment buttressed by igneous underplating. The dryness of the Australian continent, the relatively subdued highlands and small rivers combined to allow accumulation of only a minimal sediment cover over the slowly subsiding margin. This combination resulted in the outer shelf and upper slope being covered by a thin sediment wedge, but pre-rift and syn-rift rocks cropping out on the inner shelf and mid to lower slope. These exposed rocks are frequently located on steep slopes, cut by down-to-the-basin normal faults and often expose fault scarps on the lower slope. Over time, these unstable slopes have failed, initiating box canyons that have continued to retrogress up slope and undercut the toe of the Tertiary sediment wedge. This undercutting in turn has made the wedge unstable and initiated slab slides along bedding planes in the wedge. Another long-lasting tectonic influence on the SE Australian margin is shown by the bathymetry at the base of the continental slope conforming to the strike-slip pattern and oblique spreading of the Tasman Sea defined by Gaina et al. (1998). Offsets in the base of slope coincide with fracture zones (e.g. Hill 1992) and the location of major rectilinear canyons (e.g. Sydney and Tweed Canyons). This pattern of offset rifting also produced alternate narrow and steep rifted segments separated by wider marginal plateaus and basins (Fig. 2). Examples of wider margins are off the Queensland Gold Coast (the Nerang Plateau) and off the southern Clarence Moreton Basin (the Yuraygir Plateau). In these locations, the lower slopes of 1–2.5° inhibited the formation of box canyons. The result is a wide zone of thin slab slides generating a morphology of "creepy topography" formed from the coalescence of small slab slides for distances of up to 110 km along the margin without intervening canyons.

Gravity-driven mass transport processes are intensified in locations where slopes are over-steepened (e.g. Fig. 3). This often occurs seaward of igneous intrusives that are common along the margin, and exposed faulted basement blocks (Glenn et al. 2008). Other areas of steeper slopes combined with more recent local sedimentation are on the upper slope, seaward of major river systems. These locations are not steep enough to initiate slab slides but instead generate linear canyons that retrogress upslope through prodelta and delta front deposits. The causes of these retrogressive canyon heads in the delta deposits, currently occurring at 200–300 m water depth, are unlikely to be related to Late Quaternary sea-level lowstands, and therefore relatively little terrigenous clastic sediment has been transported to the shelf edge in recent times.

Another location of increased slopes occurs at the front of the sub-tropical carbonate platforms. Unsupported on slopes as great as 45°, the front of these platforms has failed along much of the margin where it is not buried by more recent sediment. Although relatively young, and occurring at shallow depths of 200–400 m, the carbonate platforms are lithified and fail as large blocks, sliding down onto the mid slope.

Plunge pools along continental margins have been described from multibeam data from the California and New Jersey continental margins (Lee et al. 2002), the Gulf of Alaska continental margin (Mayer et al. 2005) and the West Florida Escarpment (Gardner, J., unpublished). In all the cases, plunge pools occur where there has been an abrupt decrease in slope, suggesting excavation by a high-momentum, sediment-laden density flow. The bars suggest deposition downstream from a hydraulic jump within a sediment-laden density flow. These are presumably eroded by sediment-loaded flows as they cascade over a nick point similar to water-falls on land. This indicates the erosive power of intermittent catastrophic flows in shaping canyons on the lower slope. Pockmarks on the central NSW coast are best explained by gas or fluid escape from gas-prone source rocks in the underlying Permian coal measures.

References

Boyd R, Ruming K, Roberts JJ (2004) Geomorphology and surficial sediments of the SE Australian continental margin. Australian. J Earth Sci 51:743–764

Gaina C, Muller DR, Royer J-Y, Stock J, Hardebeck J, Symonds P (1998) The tectonic history of the Tasman Sea: a puzzle with 13 pieces. J Geophys Res 103:12413–12433

Glenn K, Post A, Keene J, Boyd R, Fountain L, Potter A, Osuchowski M, Dando N (2008) NSW continental slope survey: post-cruise report, 2008/14 RV Southern Surveyor 10/2006. Geoscience Australia Record 2008/14 160

Hill PJ (1992) Capricorn and northern Tasman Basins: structure and depositional systems. Explor Geophy 23:153–162

Jenkins CJ, Keene JB (1992) Submarine slope failures of the southeast Australian continental slope: a thinly sedimented margin. Deep-Sea Res 39:121–136

Lee SE, Talling PJ, Ernst GGJ, Hogg AJ (2002) Occurrence and origin of submarine plunge pools at the base of the US continental slope. Mar Geol 185:363–377

Mayer LA, Gardner JV, Armstrong A, Calder B, Angwenyi C, Karlipata S, Montoro-Dantes, H, Morishita T, Mustapha A. (2005) New views of the Gulf of Alaska margin mapped for UNCLOS applications. Am Geophys Union, Abstracts for Fall Meeting, San Francisco, CA

OZcoasts (2008) (accessed February 2009). http://www.ozcoasts.org.au/

Smith WHF, Sandwell DT (1997) Global seafloor topography from satellite altimetry and ship depth soundings, Science 277:1956–1962

Troedson A, Davies PJ (2001) Contrasting facies patterns in subtropical and temperate continental slope sediments: inferences from east Australian late Quaternary records. Mar Geol 172: 265–285

A Database on Submarine Landslides of the Mediterranean Sea

A. Camerlenghi, R. Urgeles, and L. Fantoni

Abstract Submarine landslides are ubiquitous along the continental margins of the Mediterranean basin and occur on tectonically-dominated margins as well as on passive margins and volcanic island flanks. Tectonically quiet zones seem to have the highest density of known events. Most landslides occur as long run-out distance debris flows, but slumps and deep-seated failures are also relatively common. In abyssal plains the distal product of massive failures is recorded as large megaturbidites, while on volcanic islands the dominant failure type is flank-collapse with development of debris avalanches. Submarine landslides, excluding megaturbidites, appear to occur in all water depths between the coastline and about 2000 m. Most landslides occupy areas ranging from a few to about 600 km^2 and volumes up to 220 km^3. Abyssal plain megaturbidites can attain 60,000 km^2 and 1,000 km^3. The landslides headwall height are clustered around two modes: 0 to 40 m for relatively small landslides and 160 to 200 m for the largest ones. Most recorded submarine landslides are relatively young in age and several events appear to group near the Pleistocene to Holocene transition.

Keywords Submarine landslide • geohazard • Mediterranean • megaturbidite • mass wasting • Pleistocene • Holocene

A. Camerlenghi (✉)
ICREA, Istitució Catalana de Recerca i Estudis Avançats, Barcelona, Spain;
Departament d'Estratigrafia, Paleontologia i Geociències Marines, Facultat de Geologia,
Universitat de Barcelona, C/Martí i Franquès, s/n, E-08028 Barcelona, Spain
e-mail: acamerlenghi@ub.edu

R. Urgeles
Departament d'Estratigrafia, Paleontologia i Geociències Marines, Facultat de Geologia,
Universitat de Barcelona, C/Martí i Franquès, s/n, E-08028 Barcelona, Spain
e-mail: urgeles@ub.edu

L. Fantoni
Dipartimento di Scienze della Terra, Università di Modena e Reggio Emilia, Via S. Eufemia,
19, 41100 Modena, Italy
e-mail: laura.fantoni@unimore.it

1   Introduction

The Mediterranean basin is a miniature ocean that has been often called a "natural geological laboratory" because of its diversity in tectonic and sedimentary environments (Fig. 1). The basin is limited by different margin types: active margins such as the incipient continental collision in the eastern Mediterranean; transcurrent tectonic margins, such as the Levant margin; young rifted margins in the three back-arc basins (Aegean, Tyrrhenian and Alboran) and in the Sicily Channel; older rifted (passive) margins bounding the Algero Provençal Sea; and passive margins re-activated by tectonic compression (the African margin from Tunisia to Morocco). Although some of the Mediterranean margins are tectonically active (Fig. 2), there are other areas considered as tectonically inactive based on the instrumental record (the Balearic promontory, the Gulf of Valencia, the Sardinia and Corsica margins, and the African Margin from Libya to Egypt).

The Mediterranean basin includes major siliciclastic sedimentary wedges fed by the Nile, Rhone, Ebro and Po rivers, as well as sediment starved margins (Balearic, West Corsica and Sardinia, Cyprus, Cyrenaica).

The Mediterranean coastline is very densely populated, totalling 160 million inhabitants sharing 46,000 km of coastline. As World's leading holiday destination, the area receives up to 30% of global tourism and an average of 135 million visitors annually (EEA 2005). When compared to other oceanic basins, the Mediterranean is more vulnerable to marine geohazards due not only to the high density of coastal population, but also to its small dimensions. The latter results in close proximity between tsunami sources (induced by either a submarine landslide or co-seismic seafloor displacement) and impact areas. During the Holocene (<10,000 years),
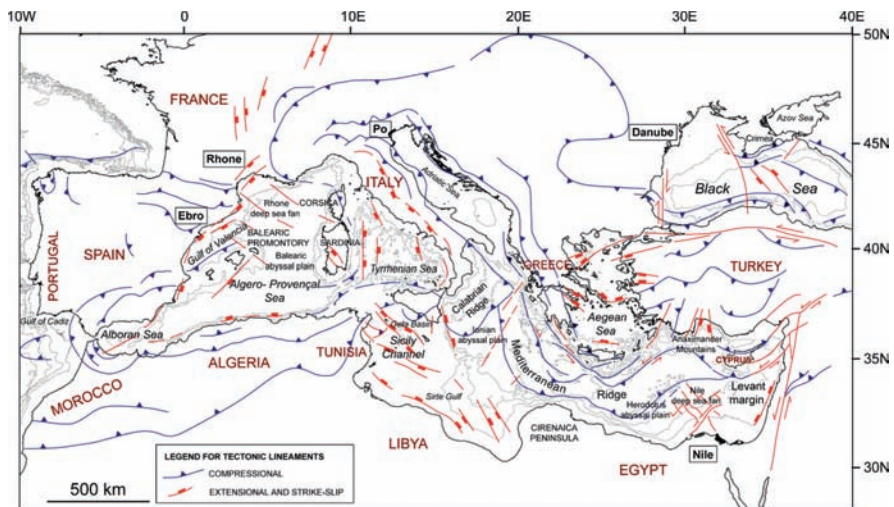
Fig. 1   Tectonic lineaments of the Mediterranean. Modified after Camerlenghi and Pini (2009)
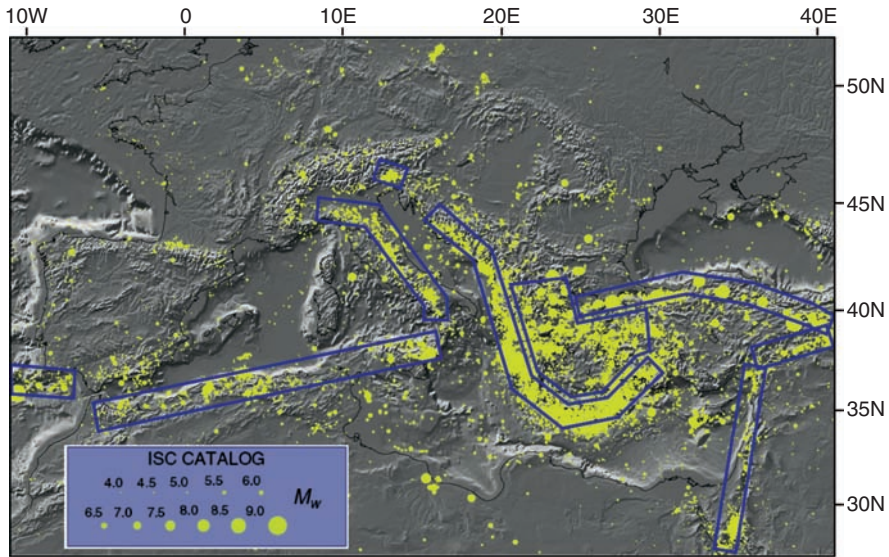
Fig. 2 Map of instrumentally recorded seismicity shallower than 50 km in the Mediterranean region. From Vannucci et al. (2004) (permission requested from the publisher). ISC: International Seismological Centre; M_w: Moment Magnitude. Blue bands: Main active deformation areas

there is evidence that tsunamis have been common in the Mediterranean basin, and that their consequences have caused severe damage to ancient coastal settlements of the Levant margin, Cyprus and the Hellenic Arc (e.g. Salamon et al. 2007; Papadopoulos and Fokaefs 2005).

With the aim to understand the causes of the sediment mass movements identified in recent years in the sedimentary record of the Mediterranean continental margins, we have undertaken a compilation of information from the scientific literature into a GIS based framework. This work provides a first step towards the analysis of geohazard from submarine landslides (e.g. Morgan et al. 2009; Camerlenghi et al. 2007) in the Mediterranean basin. Due to incomplete seafloor mapping, some information is inevitably missing and the database should be considered as in progress. However, the information gathered allows us to draw some preliminary conclusions on the occurrence of submarine landslides in relation to geological setting and sedimentary regime.

2 Methods

Information on submarine landslides reported in published research articles was entered in a geographically referenced framework using ArcGIS 9.2. For each landslide the following parameters were entered into the database: boundaries of scar

and deposit digitized from scanned or captured figures; name; geographic position; geological setting (e.g. strike slip margin, passive margin); area and volume (defined in the literature and/or calculated); thickness of the sedimentary deposit; height of the headwall; water depth of top and bottom of the headwall; typology; age; recurrence time (if any); estimated trigger mechanism; associated tsunamigenesis; availability of geotechnical information; and finally one or more reference articles.

For typology, we selected the following terms according to the terminology in the original manuscripts: Debris Avalanche; debris flow; deep-seated failure (when recognized mainly in deep penetration seismic profiles rather than bathymetric maps); glide; gravitational collapse; mass failure; mass transport; mass wasting; megaturbidite; slide; slump. Such terms often describe similar deposits. For the time being we have not modified the terminology. It is obvious that a unified terminology is needed for correct understanding and comparison of sedimentary deposits originated from submarine sediment mass transport. Slide scars (upper limit of the slide headwall) have been digitized as polylines. Deposits have been digitized as polygons. Where the volume of the deposit is not reported by authors, an approximate volume has been calculated from the minimum thickness in seismic profiles.

We are in the process of implementing the database and making it available online. For any query in the meantime, please contact the authors.

Figure 3 shows all submarine landslides of the data set superimposed on the bathymetric map of the Mediterranean sea. Summary plots of the main characteristics of the slides are displayed in Fig. 4. With an area less than $400 \, km^2$, and a volume less than $100 \, km^3$, the majority of the submarine landslides of the Mediterranean basin are relatively small in size, at least compared to the huge submarine landslides of the North Atlantic (e.g. Hühnerbach et al. 2004). Most of the slides are classified by authors as debris flow deposits or slumps, with a considerable number being classified generically as deep seated failure. However, the type of mass transport deposit that covers the largest area of seafloor is that of megaturbidites, covering an area exceeding $130,000 \, km^2$ compared to a nearly $40,000 \, km^2$ covered by all other deposits together. It must be noted that turbidites other than megaturbidites (see for comparison Cita et al. 1984a) have not been taken into account in this analysis.

3   Results

Most of the landslides originate on the mid-upper continental slope, in water depths generally shallower than 1,000 m and generate headwalls mostly less than 40 m high. However, there is also a cluster of the largest landslides with headwalls height ranging from 160 to 200 m (Fig. 4).

According to the authors whose published work has been used for this compilation, about one quarter of the landslides are believed to be recurrent events in the geological record. Only 15% of the landslides are believed to have caused a tsunami.
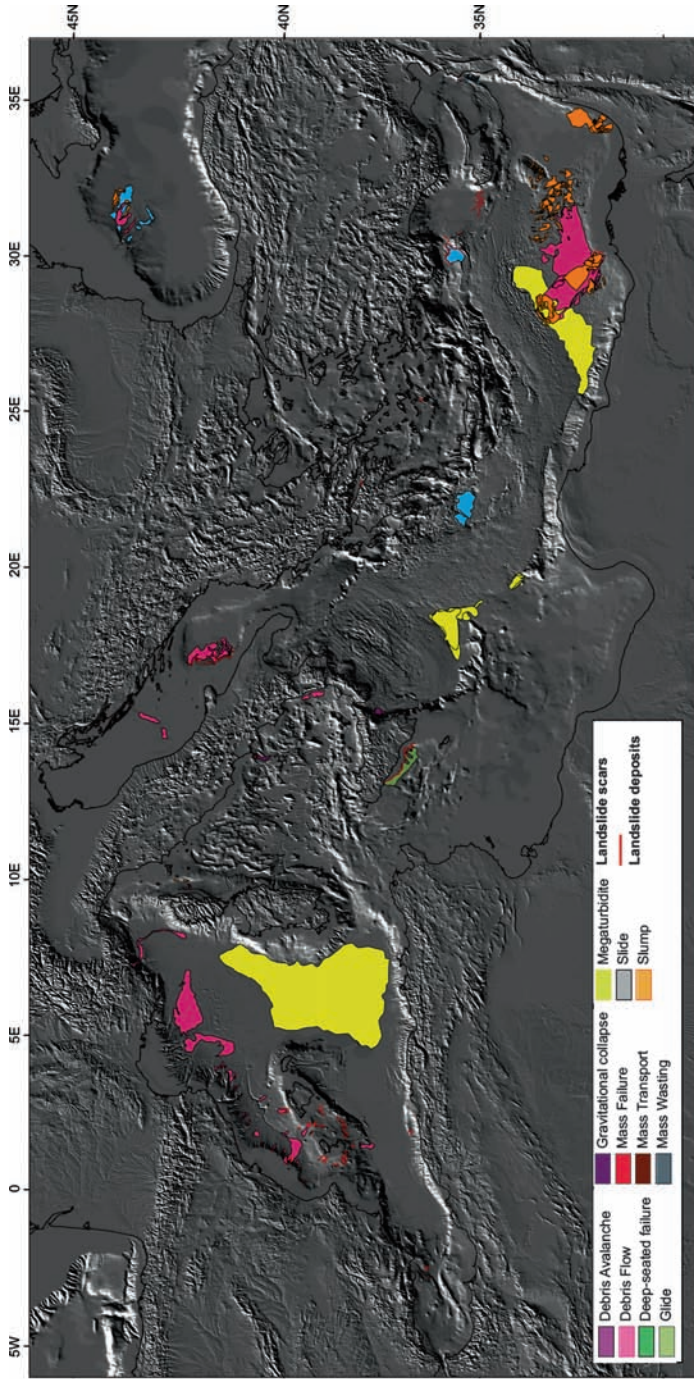
Fig. 3 Display of all the submarine landslides of the database superimposed to the shaded relief map of the bathymetry (IOC, IHO and BODC 2003; Medimap Group et al. 2008)
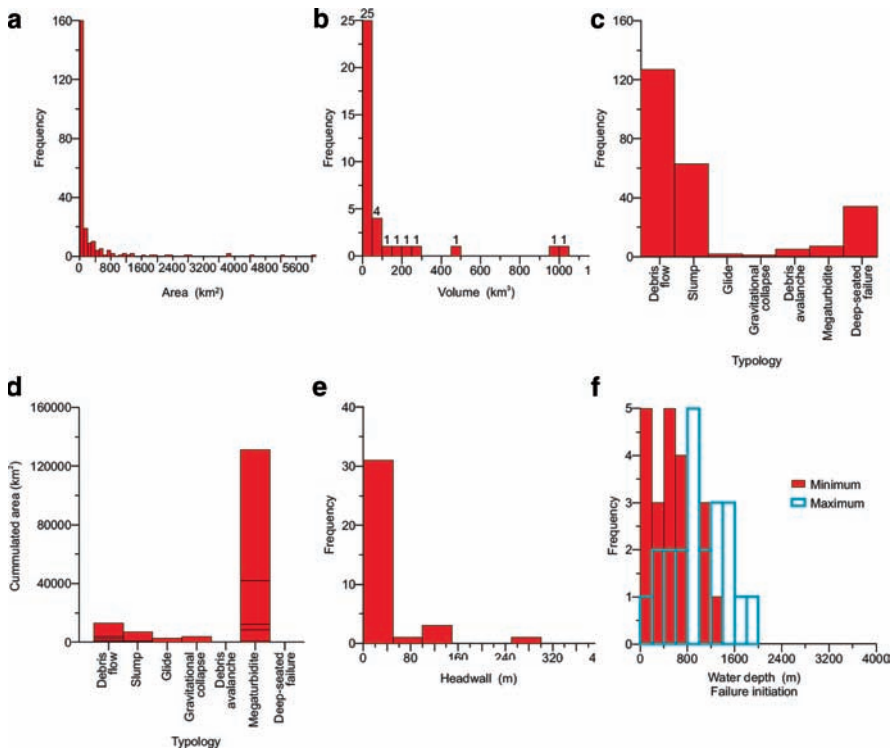
Fig. 4 Statistical distribution of significant parameters of submarine landslides in the Mediterr anean basin

3.1 Landslides Distribution with Respect to Geo-tectonic Environment

Submarine landslides occur in very different geological settings of the Mediterranean continental margins. Noticeable is the density of known events on the margins of the Balearic promontory in the Western Mediterranean (e.g. Lastras et al. 2004; 2006), which is one of the instrumentally aseismic regions (Vannucci et al. 2004) and where sedimentation is characterized by low-rate settling of carbonate pelagic particles (Canals and Ballesteros 1997). In contrast, the submarine landslides of the Nile deep sea fan (e.g. Garziglia et al. 2008), also located in a tectonically quiet region, occur in a Plio-Quaternary sedimentary succession exceeding 2,000 m in thickness (Loncke et al. 2002) whose sedimentary architecture is affected by

Miocene reactivation of the Suez-Red Sea Rift system (Mascle et al. 2000) and by thin-skinned gravity gliding and spreading above the Messinian salt layer (Gaullier et al. 2000; Loncke et al. 2006). In the case of the Ebro Margin (Casas et al. 2003; Lastras et al. 2002) and the Rhone deep sea fan (Droz et al. 2006), both considered as seismically quiet zones based on the instrumental record, recurrent mass wasting throughout the history of sediment accretion is linked to over-steepening and reduction of shear strength induced by differential compaction and associated faulting (e.g. Urgeles et al. 2006).

The tectonically active Levant margin experienced recurrent episodes of large-scale failure associated with Plio-Quaternary faults (e.g. Almagor and Wiseman 1997), either within a margin-parallel mega-shear zone (e.g. Neev et al. 1982), subduction reactivated by strike-slip faulting (Tapponnier 2004), or as a consequence of basinwards flow of Messinian salt (Frey-Martinez et al. 2005).

One intriguing aspect is the lack of evidence for modern submarine slides at the deformation front of the Calabrian and Mediterranean ridges accretionary wedges. The reason must be found in a combination of geo-tectonic factors (Camerlenghi and Pini 2009): (1) low taper angle (as low as 1°) of the accretionary prisms detaching over the ductile Messinian halite as opposed to 8–12° angle of frictional wedges, (2) low hemipelagic sedimentation rate, and (3) the barrier to deeply seated fluid migration imposed by the 3,000 m or thicker Messinian halite layer below the eastern Mediterranean foredeeps (Costa et al. 2004).

Conversely, there are large volume mass transport deposits in the Gela basin (offshore Sicily) which is under present-day salt-free deformation within the foredeep of the Maghrebian fold-and-thrust belt. One of the most extensive mass transport deposits is the 600 ka b.p. Gela submarine slide complex, up to 700 m thick, 30 km long and 90 km wide (Di Stefano et al. 1993; Trincardi and Argnani 1990). The NE portion of Gela basin is also affected by multiple slope failures originated during the late-Quaternary (Minisini et al. 2007).

Submarine landslides from volcanic flank collapse are presently not fully represented in the database, because the majority of these landslides originate above sealevel. The database will be implemented for inclusions of such landslides.

A final remark is about the several late Pleistocene megaturbidites found at shallow depth in the main abyssal plains of the Mediterranean basin: the Herodotus basin Megaturbidite (HBM, at least 20 m thick, lateral extent of 40,000 km^2 and a volume of approximately 400 km^3) (Rothwell et al. 2000; Reeder et al. 2000); The "Augias Megaturbidite", or "Homogenite" underlain by two other 10–35 m thick megaturbidites in the Ionian Abyssal Plain (e.g. Rebesco et al. 2000; Hieke 2000); and the 8–10 m thick megaturbidite of the Balearic abyssal plain (e.g. Rothwell et al. 2000; 1998; Cita et al. 1984b). These megaturbidites are thought to reflect major catastrophic collapses of the adjacent continental margins. Apart form the possible link to the Santorini Volcanic caldera collapse put forth for the "Homogenite", there is no available information on the submarine landslide from which these megaturbidites originated.
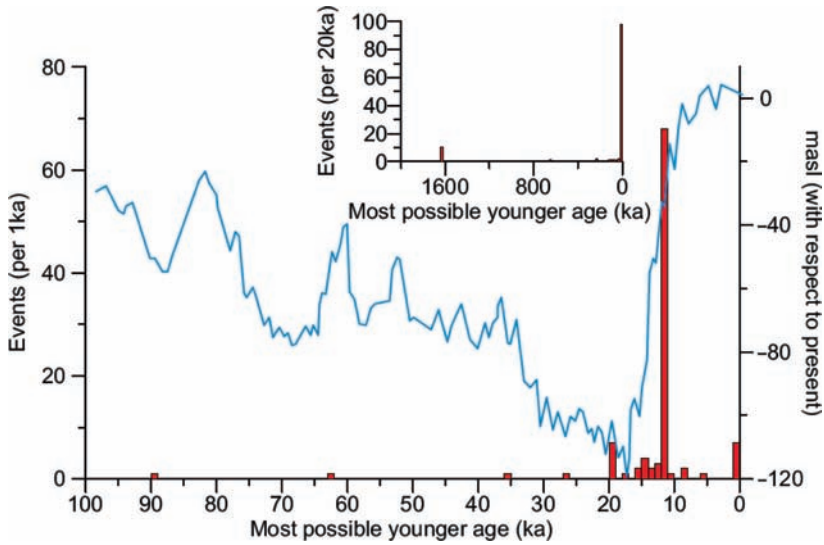
Fig. 5 Most possible youngest age spectrum of submarine landslides in the Mediterranean basin compared with the mean eustatic sea level from Pillans et al. (1998)

3.2   Age

Not all the submarine landslides in the database are supported by accurate dating information. Based on the failure age bracket provided in the literature, we have assigned a youngest possible age to each landslide. The resulting age spectrum (Fig. 5) indicates clearly that the vast majority of the landslides have occurred between 20 and 10 ka b.p., and therefore the coincidence with the last major global climatic change, corresponding to the deglaciation following the last glacial maximum, is striking.

4   Global Implications and Conclusions

The database shows unequivocally that submarine landslides are common on Mediterranean continental margins that are seismically inactive. This observation should be used to resolve the present-day paradigm often used in the scientific literature, that earthquakes are the main triggers for large submarine landslides (e.g. Masson et al. 2006; Canals et al. 2004; Locat and Lee 2002).

It is known that there are fewer large failures along present-day tectonically active margins (e.g. the Oregon margin, McAdoo and Watts 2004), than along passive continental margins (e.g. ten Brink et al. 2008). Despite larger magnitude earthquakes, the slopes of accretionary complexes and margins undergoing tectonic erosion in many places do not fail because the sediments are over-consolidated. The shear resistance

is generally higher in these sediments than in the generally under-consolidated sediments of large deep sea fans building up at passive continental margins (Camerlenghi and Pini 2009). The sediment mass movement at active margins occurs primarily in the form of cohesive failure (blocky landslides and slumps) producing high headwalls and short run-out distance on steeper slope with respect to passive margins. Despite being relatively small, these submarine landslides are indeed the ones with the higher tsunamigenic potential (McAdoo and Watts 2004).

The correlation of many of the Mediterranean submarine landslides with the last deglaciation appears to support similar observations from the North Atlantic (Lee 2008; ten Brink et al. 2008; Maslin et al. 2004; Owen et al. 2007) and may be viewed as in contrast with the classical view in basin sequence stratigraphy that build-up of deep sea fans by turbidity currents occur mostly during periods of relative sea-level fall (Falling Stage Systems Tract, e.g. Posamentier and Vail 1988).

As pointed out recently by Lee (2008) there are some key preconditioning factors that contribute to the decrease of marine sediment strength on continental margins. These are the sediment input, the interstitial fluid pressure, and gas hydrate dissociation. When these preconditioning factors produce weak sediment on a continental slope, then the cyclic loading from earthquakes, even if of low magnitude, can indeed generate slope failure. Intra-plate seismicity on passive margins induced by the isostatic response to glacial load is climatically modulated in phase with sediment input, interstitial fluid pressure, and gas hydrate dissociation.

However, because glacially induced isostatic rebound and gas hydrate dissociation likely play no role in generating slope instability of the Mediterranean continental slopes, the observed concentration of submarine landslides during the last deglaciation points to additional climate change control on initiation of slope failure in addition to seismicity. Preconditioning factors that are climatically modulated, such as the fluctuations of the ground water reservoir (Dan et al. 2007) or the deposition of sediments with typical low shear resistance, like contourites (Laberg and Camerlenghi 2008), should also be taken into consideration.

As a final remark, we want to stress that taking into account that unknown tsunami sources most probably correspond to aseismic submarine landslides (on-line Mediterranean Tsunami Catalog, 1628B.C.-to present; Institute of Computational Mathematics and Mathematical Geophysics. Novosibirsk, RUSSIA, http://tsun.sscc.ru/tsulab/On_line_Cat.htm) the second most frequent cause of tsunamis in the Mediterranean basin, after earthquakes, are submarine landslides.

Surely, not enough experience has been gained on the subject and further studies are necessary, including scientific drilling and in situ monitoring, in order to assess the geohazard potential of submarine landslides in a highly vulnerable area such as the Mediterranean basin.

References

Almagor G, Wiseman G (1997) Analysis of submarine slumping in the continental slope of the southern coast of Israel. Mar Geotech 2:349–388.

Camerlenghi A, Pini GA (2009) Mud volcanoes, olistostromes, and argille scagliose in the Mediterranean Region. Sedimentol 56:319–365.

Camerlenghi A, Urgeles R, Ercilla G, Brückman W (2007) Scientific ocean drilling behind the assessment of geo-hazards from submarine slides. Sci Drill 4:45–47.

Canals M, Ballesteros E (1997) Production of carbonate particles by phytobenthic communities on the Mallorca-Menorca Shelf, northwestern Mediterranean Sea. Deep-Sea Res II 44:611–629.

Canals M, Lastras G Urgeles R et al. (2004) Slope failure dynamics and impacts from seafloor and shallow sub-seafloor geophysical data: an overview, Mar Geol 213:9–72.

Casas D, Ercilla G et al. (2003) Recent mass-movement processes on the Ebro continental slope (NW Mediterranean). Mar Petrol Geol 20:445–457.

Cita MB, Beghi C, Camerlenghi A et al. (1984a) Turbidites and megaturbidites from Herodotus abyssal plain (eastern Mediterranean) unrelated to seismic events. Mar Geol 55:79–101.

Cita MB, Camerlenghi A, Kastens KA et al. (1984b) New findings of Bronze Age Homogenites in the Ionian Sea: geodynamic implications for the Mediterranean. Mar Geol 55:47–62.

Costa E, Camerlenghi A, Polonia A et al. (2004) Modeling deformation and salt tectonics in the Eastern Mediterranean Ridge accretionary wedge. Geol Soc Am Bull 116:880–894.

Dan G. Sultan N, Savoye B (2007) The 1979 Nice harbour catastrophe revisited: Trigger mechanism inferred from geotechnical measurements and numerical modelling. Mar Geol 245:40–64.

Di Stefano E, Infuso S, Scarantino S (1993) Plio-Pleistocene sequence stratigraphy of southwestern offshore Sicily from well logs and seismic sections in a high-resolution calcareous plankton biostratigraphic framework. In: Max MD, Colantoni P (eds) UNESCO Tech Repts Mar Sci 58:105–110.

Droz L, dos Reis AT, Rabineau M (2006) Quaternary turbidite systems on the northern margins of the Balearic Basin (Western Mediterranean): a synthesis. Geo-Mar Lett 26:347–359.

European Environmental Agency (2005) European environment outlook. EEA Report No 4/2005.

Frey Martinez J, Cartwright J, Hallw B (2005) 3D seismic interpretation of slump complexes: examples from the continental margin of Israel. Basin Res 17:83–108.

Garziglia S, Migeon S, Ducassou E et al. (2008) Mass-transport deposits on the Rosetta province (NW Nile deep-sea turbidite system, Egyptian margin): characteristics, distribution, and potential causal processes. Mar Geol 250:180–198.

Gaullier V, Mart Y, Bellaiche G et al. (2000) Salt tectonics in and around the Nile deep-sea fan: insights from the PRISMED II cruise. Geol Soc Spec Publ 174:111–129.

Hieke W (2000) Transparent layers in seismic reflection records from the central Ionian Sea (Mediterranean) – evidence for repeated catastrophic turbidite sedimentation during the Quaternary. Sediment. Geol Vol 135:89–98.

Hühnerbach V, Masson DG et al. (2004) Landslides in the North Atlantic and its adjacent seas: an analysis of their morphology, setting and behaviour. Mar Geol 213:343–362.

IOC, IHO and BODC (2003) GEBCO digital atlas (Intergovernmental Oceanographic Commission and International Hydrographic Organization) British Oceanographic Data Centre, Liverpool, U.K.

Laberg JS, Camerlenghi A (2008) The significance of contourites for submarine slope stability. In: Rebesco M, Camerlenghi A (eds) Contourites, Devel Sediment 60: 537–556.

Lastras G, Canals M, Urgeles R et al. (2004) Shallow slides and pockmark swarms in the Eivissa Channel Western Mediterranean Sea. Sedimentol 51:837–850.

Lastras G, Canals M, Amblas D et al. (2006) Eivissa slides, western Mediterranean Sea: morphology and processes. Geo-Mar Lett 26:225–233.

Lastras G, Canals M, Hughes-Clarke JE et al. (2002) Seafloor imagery from the BIG'95 debris flow, Western Mediterranean. Geol 30:871–874.

Lee HJ (2008) Timing of occurrence of large submarine landslides on the Atlantic Ocean margin. Mar Geol. doi:10.1016/j.margeo.2008.09.009.

Locat J, Lee HJ (2002) Submarine landslides: advances and challenges. Can Geotech J 39:193–212.

Loncke L, Gaullier V et al. (2002) Recent depositional pattern of the NDSF from echo-character mapping. Interactions between turbidity currents, mass-wasting processes and tectonics. Am Assoc Petrol Geol Bull 86:1165–1186.

Loncke L, Gaullier V et al. (2006) The Nile deep-sea fan: an example of interacting sedimentation, salt tectonics, and inherited subsalt paleotopographic features. Mar Petrol Geol 23:297–315.

Mascle J, Benkhelil J, Bellaiche G et al. (2000) Marine geologic evidence for a Levantine-Sinai plate, a new piece of the Mediterranean puzzle. Geol 28:779–782.

Maslin M, Owen M et al. (2004) Linking continental-slope failures and climate change: testing the clathrate gun hypothesis. Geol 32:53–59.

Masson DG, Harbitz CB, Wynn RB et al. (2006) Submarine landslides: processes, triggers and hazard prediction. Phil Trans R Soc A 364:2009–2039.

McAdoo BG, Watts P (2004) Tsunami hazard from submarine landslides on the Oregon continental slope. Mar Geol 203:235–245.

Medimap Group, Loubrieu B., Mascle J. et al. (2008) Morpho-bathymetry of the Mediterranean Sea, CIESM edition. http://www.ciesm.org/marine/morphomap.htm

Minisini D, Trincardi F, Asioli A et al. (2007) Morphologic variability of exposed mass-transport deposits on the eastern slope of Gela Basin (Sicily Channel), Basin Res 19:217–240.

Morgan JK, Silver E, Camerlenghi A et al. (2009) Addressing geohazards through ocean drilling. Sci Drill 7:15–30.

Neev D, Hall JK, Saul JM (1982) The Pelusium megashear system across Africa and associated lineament swarms. J Geophys Res 87:1015–1030.

Owen M, Day S, Maslin M (2007) Late Pleistocene submarine mass movements: occurrence and causes, Quat Sci Rev 26:958–978.

Papadopoulos GA Fokaefs A (2005) Strong tsunamis in the Mediterranean sea: a re-evaluation. ISET J Earthquake Technol Paper 463, 42:159–170.

Pillans B, Chappell J, Nash TR (1998) A review of the Milankovitch climatic beat: template for Plio-Pleistocene sea-level changes and sequence stratigraphy. Sediment Geol 122: 5–21.

Posamentier HW, Vail PR (1988) Eustatic controls on clastic deposition. II. Sequence and systems tract models. In: Wilgus CK, Hastings BS, Kendall CGSt.C, Posamentier HW, Ross CA, Van Wagoner JC (eds), Sea level changes – an integrated approach, SEPM Spec Pub 42:125–154.

Rebesco M, Della Vedova B et al. (2000) Acoustic facies of Holocene megaturbidites in the Eastern Mediterranean. Sediment Geol 135:65–74.

Reeder MS, Rothwell RG, Stow DAV (2000) Influence of sea level and basin physiography on emplacement of the late Pleistocene Herodotus Basin Megaturbidite, SE Mediterranean Sea. Mar Petrol Geol 17:199–218.

Rothwell RG, Reeder MS, Anastasakis G et al. (2000) Low sea-level stand emplacement of megaturbidites in the western and eastern Mediterranean Sea. Sediment Geol 135:75–88.

Rothwell RG, Thomson J, Kähler G (1998) Low sealevel emplacement of a very large Late Pleistocene megaturbidite in the western Mediterranean Sea. Nat 392:377–380.

Salamon A, Rockwell T, Ward SN et al. (2007) Tsunami hazard evaluation of the eastern mediterranean: historical analysis and selected modeling. Bull Seismol Soc Am 97:705–724.

Tapponnier PE, Daeron M et al. (2004) Passive-active margin inversion along the Levant plate-boundary: subduction birth and growth of Mt Lebanon. AGU Fall Meeting 2004 abs #T52B-05.

ten Brink US, Lee HJ et al. (2008) Assessment of tsunami hazard to the U.S. East Coast using relationships between submarine landslides and earthquakes. Mar Geol. doi:10.1016/j.margeo.2008.05.011.

Trincardi F, Argnani A (1990) Gela submarine slide; a major basin-wide event in the Plio-Quaternary foredeep of Sicily. Geo-Mar Lett 10:13–21.

Urgeles R, Leynaud D, Lastras G et al. (2006) Back-analysis and failure mechanisms of a large submarine slide on the Ebro slope, NW Mediterranean, Mar Geol 228:185–206.

Vannucci G, Pondrelli S, Argnani A et al. (2004) An atlas of Mediterranean seismicity. Ann Geophys Suppl 47:247–306.

Submarine Landslides Along the Algerian Margin: A Review of Their Occurrence and Potential Link with Tectonic Structures

A. Cattaneo, N. Babonneau, G. Dan, J. Déverchère, A. Domzig,
V. Gaullier, B. Lepillier, B.M. de Lépinay, A. Nouguès, P. Strzerzynski,
N. Sultan, and K. Yelles

Abstract The Algerian continental margin, a Cenozoic passive margin along the plate boundary between Eurasia and Africa presently reactivated in compression, is one of the most seismically active areas in the Western Mediterranean, having experienced several moderate to strong earthquakes in the coastal zone during the last century. The morphology of the continental slope offshore Algeria is steep and dominated by the presence of numerous canyons of variable size and seafloor escarpments that are probably the seafloor expression of active thrust-folds. Numerous submarine landslides are present along these structures, as well as asso-

---

A. Cattaneo (✉) and N. Sultan
Ifremer, GM-LES, BP 70, 29280 Plouzané, France
e-mail: antonio.cattaneo@ifremer.fr

N. Babonneau, J. Déverchère, and P. Strzerzynski
UBO-IUEM, CNRS UMR6538 Domaines Océaniques, 29280 Plouzané, France

G. Dan
Université de Brest; CNRS, UMR 6538 Domaines Océaniques; Institut Universitaire Européen de la Mer, Place Copernic, 29280 Plouzané, France; FUGRO FRANCE S.A.S, 27 Rue des Peupliers, 92752, Nanterre, France;
IFREMER, Géosciences Marines, Laboratoire Environnements Sédimentaires, Plouzané, France

A. Nouguès
Institut Polytechnique LaSalle Beauvais, Département Géosciences, Beauvais, France; FUGRO FRANCE S.A.S., Nanterre, France

A. Domzig
Midland Valley Exploration, Glasgow, UK

V. Gaullier
IMAGES, U. Perpignan, France

B. Lepillier
Ifremer, GM-LES, BP 70, 29280 Plouzané, France pres. add. TOTAL, Stavanger, Norway

B.M. de Lépinay
UMR6526 CNRS Géosciences Azur, Valbonne, France

K. Yelles
CRAAG, Algiers, Algeria

ciated with salt diapirs in the abyssal plain. Submarine landslides are expressed by seafloor scars (usually of small size) and subsurface or buried acoustically chaotic/transparent units interpreted as mass transport deposits (MTD). Compared with the most recent (superficial) small size of slide scars, buried MTDs seem to be of larger size, possibly suggesting a change in the functioning of gravity-driven processes in the margin throughout the Plio-Quaternary.

Keywords Submarine landslides • multibeam • seafloor morphology • seismic stratigraphy • Algerian margin

1 Introduction

The Algerian margin is a Cenozoic passive margin along the plate boundary between Eurasia and Africa, presently reactivated in compression. The deformation is expressed by ESE-WNW-aligned seafloor escarpements that represent the seafloor expression of thrust-folds (Déverchère et al. 2005; Domzig et al. 2006). These structures are associated with crustal shortening and moderate to large earthquakes (Nocquet and Calais 2004). The Algerian continental margin is one of the most seismically active areas in the Western Mediterranean, having experienced several moderate to strong earthquakes and tsunamis during the last century. The most violent instrumentally recorded earthquake occurred on October 10, 1980 in El Asnam (currently Chlef), and reached a magnitude (Ms) of 7.3 (El Robrini et al. 1985). More recently, on May 21, 2003 an earthquake with a magnitude (Ms) of 6.9 struck the city of Boumerdès, on the coast near Algiers, and generated significant gravity flows recognized by numerous submarine cable breaks offshore (Ayadi et al. 2003).

Numerous submarine landslides are present both at the seafloor and in the subsurface. Over three sectors marked in Fig. 1a as zones NC1, NC2 and NC3 they have been characterized as transparent or chaotic echofacies (Domzig et al. 2009; Dan et al. in press). In some cases, individual small-scale submarine landslides with a well-defined morphology were studied in detail (Dan et al. 2008; Dan et al. this volume; Nouguès et al., this volume). The aim of this paper is to provide an overview of the distribution of submarine landslides along the Algerian margin and to discuss their impact on the morphology of the Algerian margin with preliminary considerations on the relationships between the location of distinct morphologic sectors, tectonic structures, earthquake epicenters and submarine landslides.

2 Data and Methods

This paper summarizes data from four campaigns led from 2003 to 2007 in the Algerian offshore area: MARADJA 1 and 2 (2003 and 2005, R/V Le Suroît), PRISMA (2004, R/V Marion Dufresne), PRISME (2007, R/V L'Atalante). The dataset includes multibeam bathymetry, seafloor imagery (SAR side scan sonar),
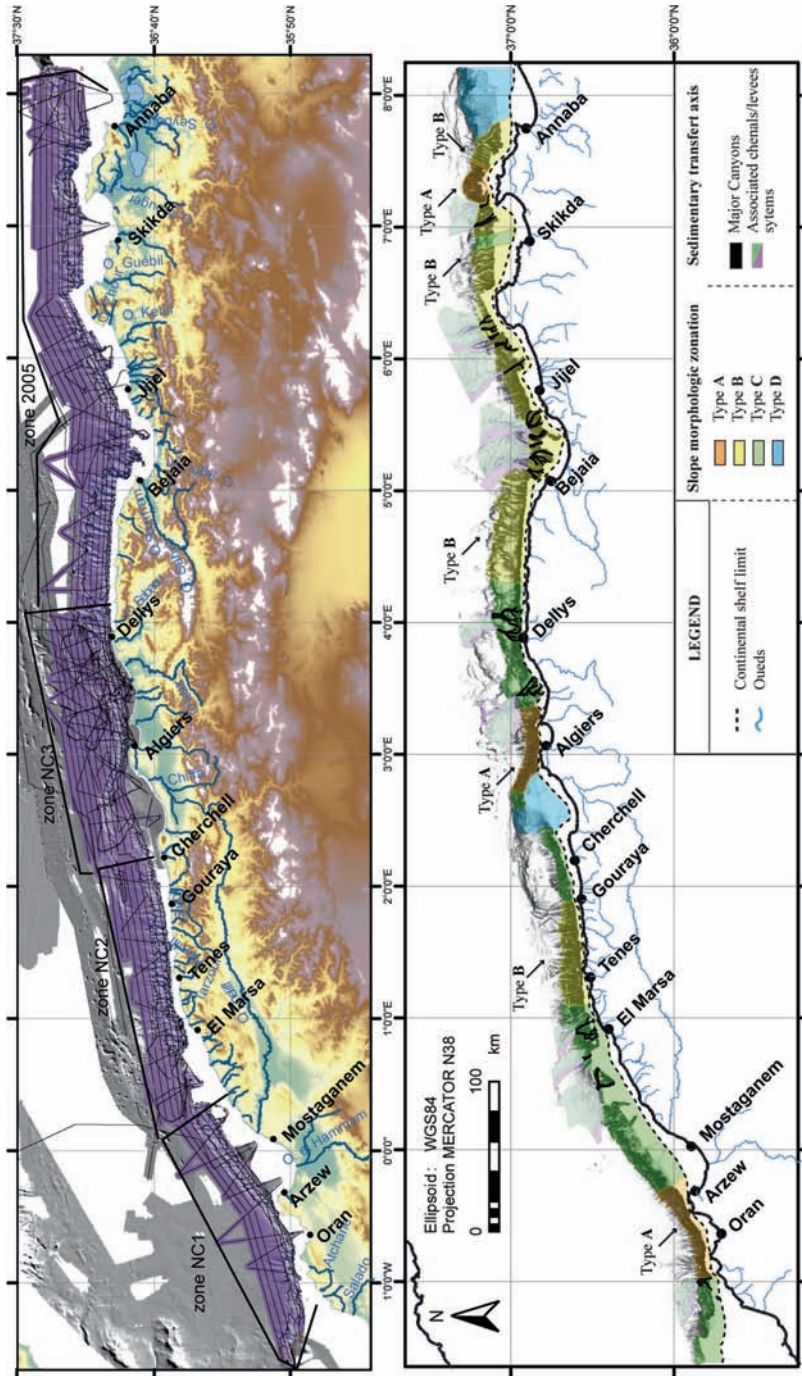
Fig. 1 Areas of multibeam bathymetry with navigation of seismic lines (*above*) and morphologic interpretation of the continental slope (*below*)

high resolution seismic reflection profiles (multichannel and CHIRP sonar; Fig. 1a). The multibeam bathymetric dataset was acquired in 2003 and 2005 with a Kongsberg Simrad EM300 multibeam system operating at 32-kHz with a horizontal resolution of 15×35 m at 1,000 m depth and a vertical accuracy of 2 to 10 m (central and lateral beams, respectively). Seafloor samples and in situ tests, cited from recent publications based on the same dataset, are not discussed extensively in this paper. Submarine landslides were identified visually as follows: (1) seafloor morphology evidence of slide scars and/or of convex-up slide deposits with distinct backscatter signature; (2) seismic reflection evidence of acoustically transparent units interpreted as MTD either buried or at the seafloor. In the maps presented in this article, slide scars are outlined in maps with lines drawn along the zone of maximum slope angle, while the acoustically-transparent deposits (MTDs) are identified by their areal extent.

3 Margin Physiography

The Algerian margin occupies the southern edge of the Western Mediterranean between 1°W and 8°E in longitude for a total coastal length of 1,280 km. It faces the Alboran and the Algero-Provençal basins. The Algerian margin is in general quite steep, with narrow plains and a few large embayments (Oran, Arzew, Algiers, Bejaia, Skikda, Annaba), where the largest Algerian cities grew (Fig. 1a, b). The Algerian continental shelf is relatively narrow (5 to 10 km wide on average). It is virtually inexistant (< 2 km) in areas offshore Dellys and Tenes, where the mountain ranges are close to the coastline, while it reaches up to 40 km in width offshore the main embayments. The continental shelf break is comprised between 100 and 200 m water depth and is indented where submarine canyon heads cut into the shelf.

The continental slope is in general steep (often >10°, locally up to 20°) cut by numerous canyons and includes some ponded slope basins (Déverchère et al. 2005). It extends from 100–200 to 2,300–2,500 m, with a very variable width commonly comprised between 8 and 20 km, with an exceptions offshore Annaba, where it attains 35 km of width. On the continental slope offshore central Algeria there are several abrupt escarpments (e.g., S2 in Fig. 2) that are probably the surface expression of active tectonic structures (Déverchère et al. 2005; Domzig et al. 2006; Kherroubi et al. 2009). The main sediment transport systems (including submarine canyons, submarine valleys with channel-levee complexes) are outlined in Fig. 1b. Several deep-sea fans are visible downslope the major canyons. Nevertheless, the link between the subaerial drainage pattern and the network of submarine canyons is still uncertain, partly because of lack of bathymetric data on the continental shelf.

A visual and semiquantitative interpretation of the seafloor morphology of the Algerian continental slope is presented in Fig. 1b. This interpretation is based on the recognition of recurrent morphological patterns in distinct sectors of the continental
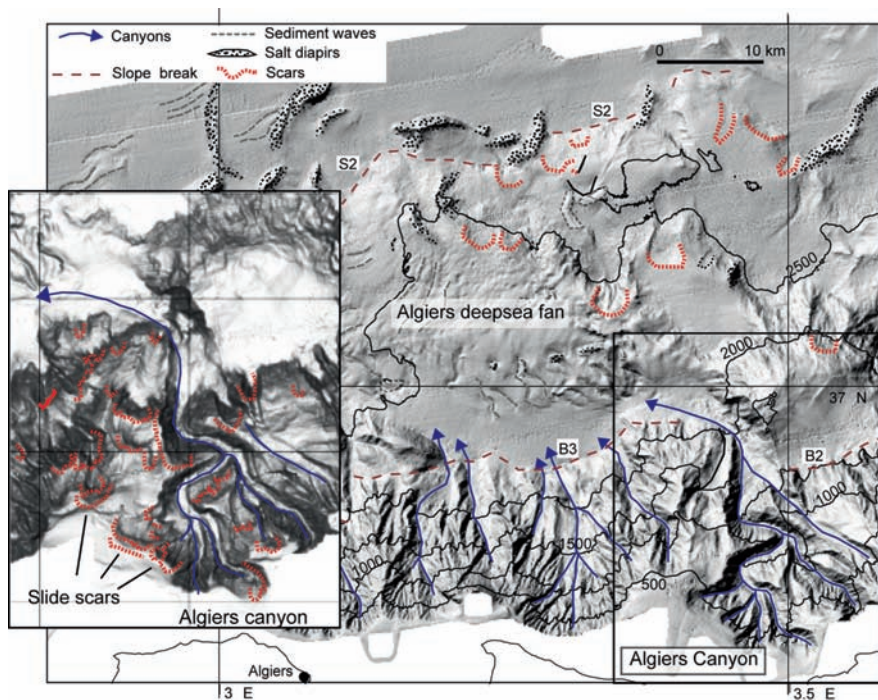
Fig. 2 Shaded relief map of the area offshore Algiers with indication of morphologic features

slope, and on the measurements of basic morphologic parameters on bathymetric sections (Nouguès 2006). The continental slope morphology (Fig. 1b) is dominated by: (A) closely spaced, small, rectilinear submarine canyons (orange pattern in Fig. 1b); (B) widely spaced, rectilinear submarine canyons (yellow pattern); (C) irregular seafloor morphology with submarine slide scars and major or composite canyons with a sinuous path (green pattern); (D) smooth morphology with homogeneous bathymetric gradient (blue pattern). The summary of the main morphologic characters is in Table 1.

The continental rise is not always identifiable along the Algerian margin. This happens in areas where submarine escarpments of probable tectonic origin terminate abruptly in the abyssal plain, like offshore the Khayr al Din bank ('Type D' area west of Algiers in Fig. 1b; Yelles et al. 2009), or where the continental slope has a step-like morphology with seafloor escarpments and slope basins, like offshore Algiers and Dellys (Déverchère et al. 2005). Where present, especially at the emplacement of major deep sea fans (Fig. 1b), the continental rise has an average bathymetric gradient of 2–3° within a bathymetric range of 2,000 to 2,700 m, and an overall width of 0 to 30 km.

In the Western Mediterranean, the maximum water depth of the abyssal plain is about 2,800 m water depth (Camerlenghi et al. 2008). The abyssal plain at the border with the Algerian margin was imaged only in a limited area, enough to show

Table 1 Main parameters of the four types of morphologies outlined in Fig. 1b

Zone type	Area (km²)	Area (%)	Slope angle ( )	Morphologic character
A	1,540	9.5	11–20°	Main feature: linear canyons with: incision 100–300 m; width 1–2 km; spacing 2–3 km
B	5,840	37	7°	Main feature: linear canyons with: incision 400–500 m; width 3–4 km; spacing 5 km
C	6,060	38.5	7–9°	Main feature: abundant submarine slide scars
				Secondary features: large, sinuous canyons with: incision > 400 m; width > 2 km
D	2,360	15	3–5°	Main feature: smooth morphology
				Secondary features: superficial landslides, scattered pockmarks

that the overall flat morphology is characterized by the presence of several seafloor irregularities, and in particular positive features due to the deformation of buried Messinian salt (Gaullier et al. 2008). Salt diapirs and salt walls in some cases produce a vertical displacement of the seafloor up to 200 m and are surrounded by thin-skin sediment instabilities.

4 Seafloor and Subsurface Instabilities Along the Algerian Margin

On the continental slope offshore Algeria, there are numerous relatively small-size submarine landslides mainly located on canyon flanks and at the foot of continental slope escarpments of tectonic origin (Déverchère et al. 2005; Dan et al. 2008; Domzig et al. 2009; Dan et al. in press). A preliminary evaluation of the presence of seafloor instabilities all along the Algerian margin consisted in an evaluation of four kinds of evidences: (1) presence of bathymetric irregularities interpreted as seafloor expression of submarine mass movements: (1a) subcircular escarpments with downslope concavity (slide scars, e.g., Fig. 2); (1b) irregular mounds with downslope convexity located downslope of slide scars (slide deposits); (2) rough bathymetry and backscatter character recognized on side scan sonar images, interpreted as the result of: (2a) abrupt changes in local slope due to sediment failure (slide headwall scarps); (2b) linear seafloor features interpreted as scours due to erosion by submarine mass movements (slide transit areas; Dan et al. this volume); and (2c) subcircular areas with a distinct backscatter compared with the surrounding seafloor and isolated blocks (areas of slide deposit and of accumulation of slide blocks); (3) presence on seismic reflection profiles (both multichannel and CHIRP profiles) of acoustically chaotic or transparent sediment accumulations with a
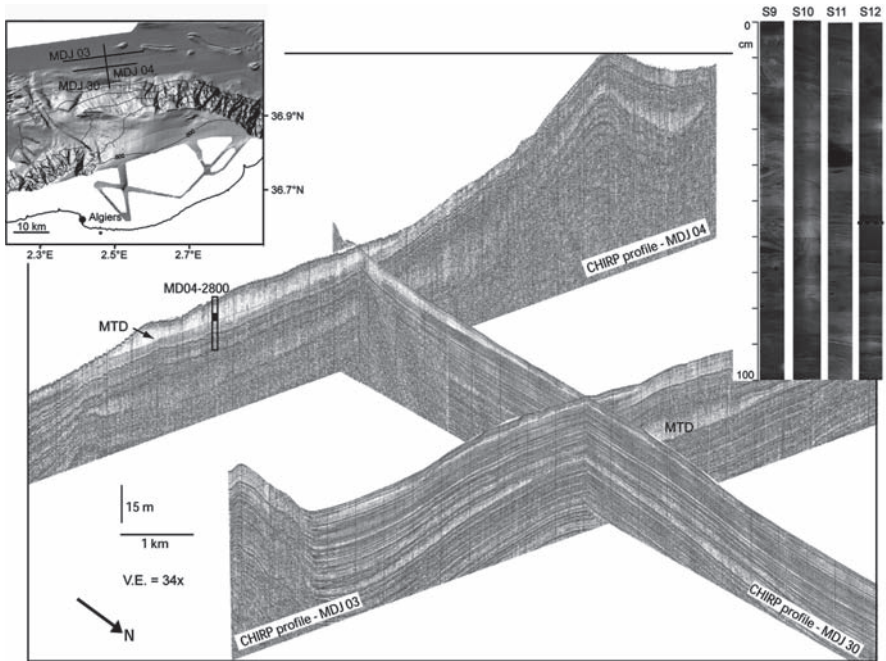
Fig. 3 CHIRP sonar profiles offshore Algiers showing evidences of MTDs. The 27.27 m long piston core MD04-2800 recovered remoulded muddy sediment as shown on X-ray images of core sections S5 to S12 (remoulded sediment is visible here from 10.92 to 16.5 mbsf, top of S9 to halfway S12)

lobate to lens-shape section, interpreted as MTD of two types: (3a) MTD visible close to the seafloor or draped by a thin veneer of post-failure sediment, often found in the vicinity of seafloor escarpments and fresh-looking slide scars with a bathymetric expression; (3b) buried MTD for which the source area was difficult to reconstruct (e.g., Fig. 3), but nevertheless interpreted as the result of mass transport accumulation by analogy with similar sedimentary bodies observed elsewhere (e.g., McAdoo et al. 2000; Huenherbach and Masson 2004); (4) for a limited number of cases, direct sampling by sediment cores of disrupted sediment accumulations containing mud clasts in a reworked matrix and/or contorted bedding. An example is presented in Fig. 3; other examples are visible in Dan et al. (this volume) and Nouguès et al. (this volume).

Figure 4 illustrates the distribution of interpreted MTDs compared with earthquake epicenters (NEIC catalog 2009) and the location of the main faults offshore (Domzig et al. 2006). The map is based on observations made offshore Oran and Tenes (Zones NC1 and NC2, Fig. 1a; Domzig et al. 2009), and offshore Algiers (Zone NC3, Fig. 1a; Dan et al. in press). Data from the easternmost area of the Maradja 2005 survey were presented in a preliminary way in Lepillier (2007). The volumes of the slides were calculated only at some places in two different ways. For slide scars (source areas, missing volume at the seafloor) the volume was calculated
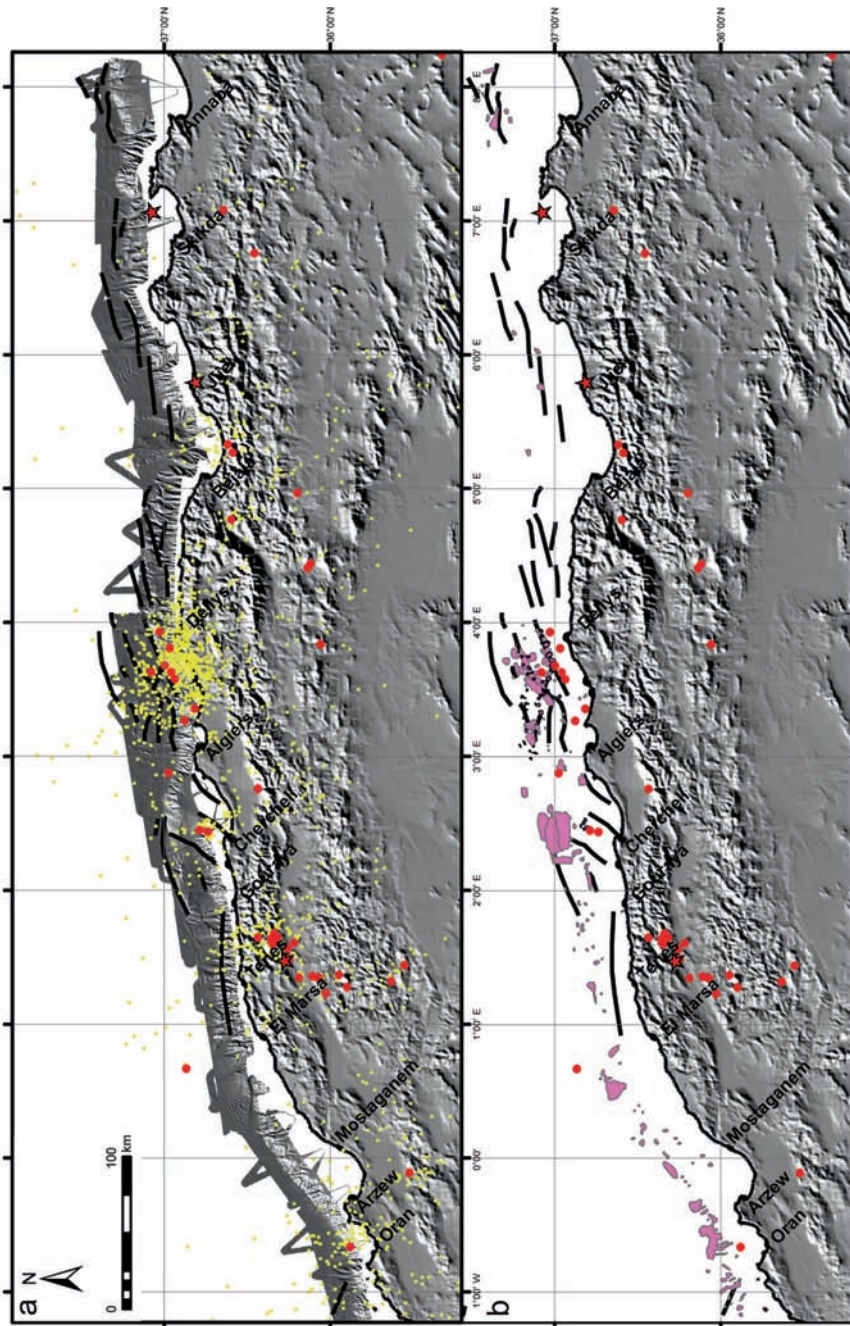
Fig. 4 (a) Earthquake epicentres (*yellow*: all NEIC events 1973–2009; *red*: the same but Ms>5; *red stars*: three strong historical earthquakes from Kherroubi et al. 2009; Yelles-Caouche et al. 2008) and main faults (*black lines*: Domzig et al. 2006). (b) Main MTD (*pink areas*: Domzig et al. 2009; Dan et al. in press)

as a rectangular prism following McAdoo et al. (2000) by Dan et al. (in press). For MTDs (deposit areas, with sediment accumulation) it was assumed that each mass transport deposit has the shape of an ellipsoid; the volume then equals "$4/3\pi abc$" (with "a", "b" and "c" being the 3 semi axes of the ellipsoid; Domzig et al. 2009).

Offshore the two sectors of Oran and Tenes (zones NC1 and NC2, Fig. 1a), more than 860 km^2 of acoustically transparent echofacies were identified. The majority of these seismic units interpreted as MTDs have an individual areal extent of 10 km^2 or less; the largest has an area of 85 km^2. The largest of these deposits are located at the foot of relatively gentle slopes, namely northwest of Kramis Deep-Sea Fan (slope gradient < 10°), and north of Cherchell (slope gradient < 20°). However, there seems not to exist a clear relationship between the slope gradient (regional or local) and the occurrence of mass-transport deposits (Domzig et al. 2009). The maximum slide deposit volume reported in the Oran-Tenes sector is 0.8 km^3 (Domzig et al. 2009), whereas in the Algiers sector it is 0.18 km^3 (Dan et al. in press). However, the calculation of the volume of the seismically transparent bodies suffered from the relatively wide spacing between seismic reflection profiles and caution is in any case necessary in the interpretation of acoustically transparent units as MTD in the absence of groundtruthing data.

5 Discussion and Conclusion

The analysis of seafloor bathymetry and seismic reflection profiles allowed to extract some preliminary conclusions about the presence and the distribution of submarine landslides along the Algerian continental margin. On the continental slope offshore Algeria, there are numerous traces of submarine landslides visible at the seafloor, most of which are relatively small-sized compared to those described along other continental margins (Domzig et al. 2009; Dan et al. in press). These superficial submarine landslides are located in preferential areas of the Algerian margins, and in particular they are associated: (1) with the major submarine canyons: at the canyon heads, along canyon flanks, and on the seafloor between major canyons; (2) with seafloor escarpment of tectonic origin up to 25 km long; (3) with salt diapirism in the abyssal plain. The majority of these superficial landslides can be classified as 'disintegrative slides' since no detectable deposit is associated with the slide scar. There seems to be a relationship between the location of the tectonic escarpments and the thin-skin landslides. It is to be investigated if this relationship is due to one or a combination of factors such as: long term growth of escarpments (that are in general the frontal side of compressional anticlines with a seaward vergence); seismic activity along these escarpments; the fact that on the flanks of the escarpments the dip of the sedimentary layers increases (Nouguès et al. this volume).

There are a number of acoustically transparent or chaotic deposits along the margin, mainly at the foot of the continental slope or of smaller morphologic escarpments (Fig. 4). The volume of these units seems larger than that measured

from the slide scars at the seafloor. Furthermore, in the Oran-Tenes zone the size of mass-transport deposits seems larger than in the central Algerian margin (Domzig et al. 2009).

Based on a limited number of studies in the area, a plausible triggering mechanism for submarine landslides are earthquakes and consequent liquefaction of potential weak layers (thin beds of silty-sandy sediment in overall muddy sections; Dan et al. 2008; Nouguès et al. this volume). This is logical along the seismically active Algerian margin. However, two main questions deserve further investigation: (1) the relationship between the distribution of possible preconditioning factors (escarpments, presence of thin sandy layers), the recurrence of likely triggering mechanisms (earthquakes), and the presence of submarine landslides; (2) the origin of the thin sandy layers.

The distribution of recent earthquake epicenters versus submarine landslides is of non immediate comprehension (Fig. 4): the earthquake epicenters are reported since 1973 onwards (NEIC catalog 2009), so they theoretically match only with the most recent landslides, by definition at the surface. Further work is necessary to establish more consistent correlations among seafloor instability and seismicity, for example by attributing an identified landslide to a defined and known earthquake event, if possible. Other studies in the Mediterranean area show that this relationship is not straightforward (e.g., Camerlenghi et al. this volume).

From the above observations it is possible to draw some more general preliminary conclusions, or rather working hypotheses to be tested: (1) there has been a major rearrangement in the way submarine gravity processes, and in particular submarine landslides shaped the Algerian margin during the Plio-Quaternary; (2) there is a relationship in the distribution of landslides with present day morphology (morphologic sectors) and with seafloor structures of tectonic origin.

References

Ayadi A et al. (2003) Strong Algerian earthquake strikes near capital city. Eos Trans Am Geophys Un 84(50):561–568.

Camerlenghi A et al. (2008) Morphogenesis of the SW Balearic continental slope and adjacent abyssal plain, Western Mediterranean Sea. Int J Earth Sci (Geol Rundsch). DOI 10.1007/s00531-008-0354-8.

Camerlenghi A et al. this volume. A database on submarine landslides of the Mediterranean Sea.

Dan G et al. (2008) Quantifying the role of sandy-silty sediments in generating slope failures during earthquakes: example from Algerian margin. Int J Earth Sci. doi 10.1007/s00531-008-0373-5.

Dan G et al. in press. Recent sedimentation patterns on the Algerian Margin (Algiers area, Southwestern Mediterranean). SEPM Spec Vol 93, accepted.

Dan G et al., this volume. Mass-transport deposits on the Algerian Margin (Algiers Area): Morphology, Lithology and Sedimentary Processes.

Déverchère J et al. (2005) Active thrust faulting offshore Boumerdes, Algeria, and its relations to the 2003 Mw 6.9 earthquake. Geophys Res Lett 32 L04311. doi:10.1029/ 2004GL021646.

Domzig A et al. (2006) Searching for the Africa-Eurasia Miocene boundary offshore western Algeria (MARADJA'03 cruise). CR Geosci 338:80–91.

Domzig et al. (2009) Deposition processes from echo-character mapping along the western Algerian margin (Oran–Tenes), Western Mediterranean. Mar Petrol Geol 26:673–694.

El Robrini M, Gennesseaux M, Mauffret A (1985) Consequences of the El-Asnam earthquakes: turbidity currents and slumps on the Algerian margin (western Mediterranean). Geo-Mar Lett 5:171–176.

Gaullier V et al. (2008) Salt tectonics in the deep Mediterranean: indirect clues for understanding the Messinian Salinity Crisis. In: Briand F (ed) CIESM Workshop Monographs 33:91–96.

Huehnerbach V, Masson DG (2004) Landslides in the North Atlantic and its adjacent seas: an analysis of their morphology, setting and behaviour. Mar Geol 213:343–362.

Kherroubi et al. (2009) Recent and active deformation pattern off the easternmost Algerian margin, Western Mediterranean Sea: New evidence for contractional tectonic reactivation. Mar Geol 261:17–32.

Lepillier B (2007) Etude qualitative et quantitative des glissements sous-marins sur la marge Algérienne. Mémoire stage III année Inst Polytéch Lasalle Beauvais (ex IGAL), 101 p.

McAdoo B et al. (2000) Submarine landslide geomorphology, U.S. continental slope. Mar Geol 169:103–136.

NEIC catalog (2009) USGS, URL: http://neic.usgs.gov/neis/epic/epic_global.html.

Nocquet J-M, Calais E (2004) Geodetic measurements of crustal deformation in the Western Mediterranean and Europe. Pure Appl Geophys 161:661–681.

Nouguès A (2006) Analyse morphologique des canyons et glissements de la pente algérienne: une vision d'ensemble sur 1200 km de marge. Mémoire de stage de III année Institut Polytéchnique Lasalle Beauvais – Géologie et Environnement (ex IGAL), 72 pp.

Nouguès A et al. this volume. Detailed analysis of a submarine landslide (SAR-27) in the deep basin offshore Algiers (Western Mediterranean).

Yelles-Chaouche AK et al. (2008) The 1856 Tsunami of Djidjelli (Eastern Algeria): seismotectonics, modeling and hazard implications for the Algerian Coast. Pure Appl Geophys XX:1–18.

Yelles AK et al. (2009) Plio-Quaternary reactivation of the Neogene margin off NW Algiers, Algeria: The Khayr al Din bank. Tectonophys. doi:10.1016/j.tecto.2008.11.030. 19pp.

Mass-Transport Deposits on the Algerian Margin (Algiers Area): Morphology, Lithology and Sedimentary Processes

G. Dan, N. Sultan, A. Cattaneo, J. Déverchère, and K. Yelles

Abstract On 21st May 2003, a damaging earthquake of Mw: 6.9 struck the region of Boumerdès 40 km east of Algiers in northern Algeria. The seismic shocks had devastating effects in the offshore area between the cities of Algiers and Dellys, where numerous cable breaks were observed. The submarine area encompassing the 2003 Boumerdès epicenter (central Algerian margin) was recently investigated using geophysical and sampling tools. It has been observed that small-size slides and mass-transport deposits occur across this area. Thus, a detailed analysis was performed on 25 submarine slides identified in water depths from 500 to 2,700 m, by measuring different morphological parameters (i.e. surface, head-scarp height, slope in the source area and in adjacent areas). Various deposits consisting of matrix supported mud-clast, distorted stratified sediments and sand-turbidite beds were observed in gravity cores near and within the most significant-size slide. Based on this work and previous studies it can be presumed that the recurrent seismic activity can be considered as the main triggering factor for failure in the central Algerian margin.

Keywords Algeria • mass-transport deposit • morphology • triggering mechanism

G. Dan (✉)
FUGRO FRANCE S.A.S, 27 Rue des Peupliers, 92752, Nanterre, France
e-mail: g.dan@fugro.com

G. Dan, N. Sultan, and A. Cattaneo
IFREMER, Géosciences Marines, Laboratoire Environnements Sédimentaires,
Plouzané, France

G. Dan and J. Déverchère
Université de Brest; CNRS, UMR 6538 Domaines Océaniques; Institut Universitaire
Européen de la Mer, Place Copernic, 29280 Plouzané, France

J. Déverchère
Université Européenne de Bretagne, Brest, France

K. Yelles
CRAAG, Centre de Recherche en Astronomie, Astrophysique et Géophysique,
Bouzaréah, Algiers, Algeria

1   Introduction

The Algerian margin is a former passive margin reactivated by compression and characterized by moderate to high seismicity (Déverchère et al. 2005). The last significant earthquake occurred in 2003 offshore the city of Boumerdès and the main shock was widely felt within a radius of approximately 400 km in Algeria. An associated tsunami was felt in southeastern Spain, including the Balearic Islands, Sardinia and also southern France (Alasset et al. 2006). In addition, a shoreline uplift marked by a continuous white band visible at rocky headlands (emerged algae) occurred between the cities of Boumerdes and Dellys (Meghraoui et al. 2004). Based on the numerous cable breaks observed on five different communication cables (France Telecom 2003) it has been presumed that a large volume of sediment was probably destabilized during the earthquake and after-shocks.

Following the Boumerdès event, numerous studies focussed on the area offshore of the epicenter in order to identify related tectonic deformation and earthquake-triggered deposits (Déverchère et al. 2005; Domzig et al. 2006; Dan 2007; Dan et al. 2008; Domzig et al. 2008; Yelles et al. 2009; Cattaneo et al. this volume). The central Algerian margin is characterized by a continental shelf of variable width and a steep continental slope (Fig. 1). The abyssal plain exhibits a complex morphology, with several curvilinear escarpments (S1 and S2, Fig. 1) probably representing the expression of active tectonic deformation in the area (Déverchère et al. 2005) and a large-scale deep-sea fan (Algiers Deep-Sea Fan, ADSF, Fig. 1). Well-developed canyons and slide scars shape the continental slope and the curvilinear escarpments (Dan 2007; Domzig et al. 2008). Salt diapirs of different shape, length and orientation are also present within the abyssal plain (Fig. 1; Gaullier et al. 2004; Domzig et al. 2006).

Numerous small-scale slides and MTDs were identified and mapped across the Algerian margin based on the seafloor analysis and seismic echo-facies (Dan 2007; Domzig et al. 2008; Cattaneo et al. this volume). Recent studies focused on a few selected cases (S1 escarpment-Dan et al. 2008; S2 escarpment-Nouguès et al. this volume) allowed the identification of triggering mechanism of different slope failures. Slope stability evaluation under gravity loading, where only the static physical properties of the sediments (unit weight, internal friction angle and undrained shear strength) are considered, showed that failure does not occur for a slope value of 5° (Dan et al. 2008). In contrast, numerical calculations carried out on the S1 escarpment under cyclic loadings showed that slope failure may occur during an earthquake characterized by a PGA in excess of 0.1 g, and also that liquefaction could be triggered in shallow silty–sandy deposits under a PGA of 0.2 g (Dan et al. 2008).

In the present paper our attention focuses on the morphological description of the eastern part of the continental slope offshore the city of Dellys, where the seafloor imprint of the Boumerdès fault has been mapped (Déverchère et al. 2005; Domzig et al. 2006) (Figs. 1 and 2). In addition, the study deals with the moprhometric analysis of 25 slides identified across the central Algerian margin in order
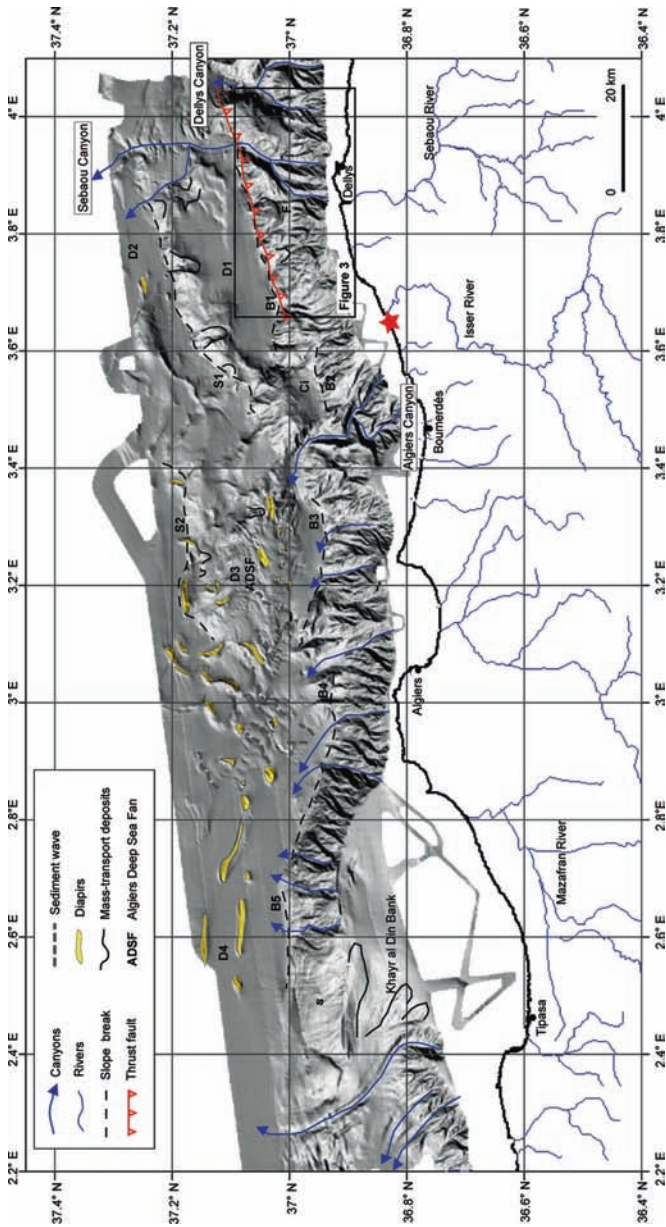
Fig. 1 Shaded relief map showing the main morphological features in the study area. Slope breaks delimiting the continental slope: B1 to B5; slope breaks delimiting the deep curvilinear escarpments: S1 and S2; Deep basins: D1 to D4 (modified from Dan et al. 2008); Thrust fault location is from Déverchère et al. (2005). Red star is the 2003 Boumerdès epicenter (Semmane et al. 2005)
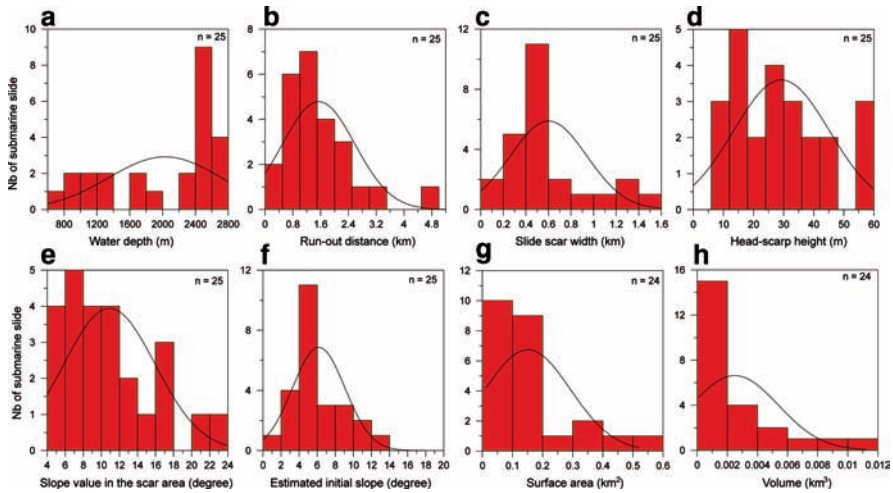
Fig. 2 Histograms showing the main morphometric parameters of the 25 slides: (**a**) water depth; (**b**) run-out distance; (**c**) slide scar width; (**d**) head-scarp height; (**e**) slope within the scar area; (**f**) initial slope; (**g**) surface area and (**h**) volume

to assess the influence of the slope angle or other morphological parameter in terms of the triggering mechanism. Furthermore, a detailed morphological presentation of the largest slide, the B1 Slide, is performed based on the bathymetry, high-resolution side-scan sonar data and gravity cores.

2 Data and Methods

The geophysical data consists of swath bathymetry (Kongsberg Simrad EM-300 and EM 1000 echosounder) from the MARADJA survey (Déverchère 2003). Deep-towed side-scan sonar images were collected during the MARADJA2 survey (Savoye 2005). Three Küllenberg cores acquired during the MARADJA2 cruise across the B1 Slide illustrate the sedimentary facies with lithologic logs, photographs and x-ray images. Sediment samples taken from two cores help constrain the age of the sediment with the performance of AMS radiocarbon dating on foraminifera tests (*Globigerinoides* and *Orbulina*). A detailed morphological analysis has been carried out on 25 slides within the Algiers area. The identification of slides was mainly based on the bathymetry analysis where the slide scars have distinct signature and convex-up slide deposits are sometimes associated. Two types of slides were distinguished based on the run-out distance: high-mobility slides with large run-out distances able to produce an evacuation zone, and low-mobility slides with short run-out that permit to have a defined downdip depositional lobe.

The different morphological parameters measured on the 25 slides are: (1) water depth at the headwall scarp, (2) total length from the headwall to the tip of the deposit (run-out), (3) slide scar width, (4) gradient in the slide scar area, (5) gradient in the adjacent unfailed area, (6) height of the headwall scarp, (7) slide surface area, and (8) slide volume. The volume was calculated as: $V = 1/2 \, (A) \, (h \cos\alpha)$; where A is the area of the scar, h is the headscarp height and α is the scar slope angle (McAdoo et al. 2000).

3 Results

3.1 *Morphology*

For the morphometric study we measured parameters on 25 selected submarine slides. The selection of these 25 slides was done with the mentality to sample many different environments: on the continental slope offshore Dellys (B1 Slide), along the S1 escarpment (6), along the S2 escarpment (8), on the Khayr al Din bank (7), and east of the Algiers submarine canyon (3). Based on the seafloor imprint, most of the slides are considered as high-mobility failures since associated deposits were rarely recognized near the slide scar. The studied slides occur in water depths ranging from 700 to 2,800 m (Fig. 2a), and are characterized by an average total length of 1.6 km and approximately 0.6 km in width (Figs 2b, c).

The head-scarp height varies from 5 to 60 m (Fig. 2d). Generally, the slope angle where slides occur ranges from 1° to 14°, and the resulting slope angle within the slide scars ranges from 4° to 24° (Figs. 2e, f). All slides, excluding the B1 Slide, have an average surface area of 0.2 km² (Fig. 2g), while the average volume is approximately 0.003 km³ (Fig. 2h).

The width of the continental shelf offshore Dellys is variable (1 to 4 km), while the continental slope ranges from 10 to 20 km in width and is characterized by the presence of a W-E directed intermediary slope break. Two major canyons incise the eastern slope while gully-like features affect the rest of the slope (Fig. 3). Submarine slides, observed as slide scars, appear located across the continental slope and within the canyons system (head, flanks and intra-canyons area). Fig. 3 illustrates the variety of slides that occur across this part of the Algerian margin.

Among these failures, the large B1 Slide was the subject of more detailed study (Fig. 4). The B1 Slide scar is located approximately 11 km seaward of the coastline offshore the city of Dellys, and occurs in a water depth of 1,750 m. The B1 Slide headwall is approximately 200 m in height and approximately 1.5 km in width (Fig. 4b). The slide scar has an amphitheatre-shape and part of the failed sediment is deposited on the continental slope between the steep lateral walls of the failure; thus the B1 Slide is considered as low-mobility (Figs. 4b, c). The slide covers a significant surface area of 4.7 km² and the estimated volume of failed sediment is approximately 0.20 km³.
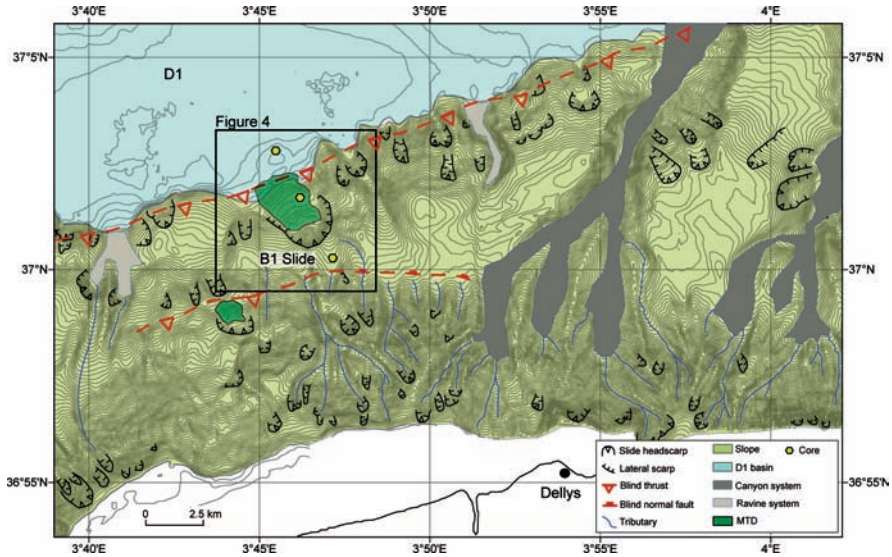
Fig. 3 Bathymetric map showing the main morphological features within the area offshore the town of Dellys. The blind thrust path is from Déverchère et al. (2005)

The side-scan sonar image located at the foot of the slope, downslope of the B1 Slide where the core KMDJ-14 was sampled is presented in Fig. 5. Areas of high backscatter (dark tones) are probably erosional tracks or linked to the presence of coarse-grained sediment (dark grey shadows). The backscatter image shows various sonar contacts identified as sub-circular features with a relief above the surrounding seafloor that are interpreted as blocks. These blocks are characterized by variable size with length between 2.5 and 50 m. Out-runner blocks are visible with backscatter images to a maximum distance of 7 km from the headwall, but they could probably reach distance beyond the coverage of the side-scan sonar survey.

Another interesting feature on the backscatter image is the presence of rectilinear glide tracks showing a slight radial direction by comparison with the longitudinal axis of the B1 Slide (Fig. 5). These glide tracks are particularly evident at the location of core KMDJ 14 and show high backscatter values (Fig. 5). The spacing of such glide tracks is in the order of 50 m and their maximum width is approximately 25 m.

3.2 Lithology and Age of Sediment

Three gravity cores were recovered along the B1 Slide on a longitudinal transect in order to recover sediment upslope the headwall scarp (KMDJ-12), the deposit within the slide scar (KMDJ-13), and the slide deposit in a more distal location (KMDJ-14).

Core KMDJ-12 is 6 m long and was recovered upslope the headwall of the B1 Slide in a water depth of 1,700 m (Fig. 6). The sediment consists of a few centimeters
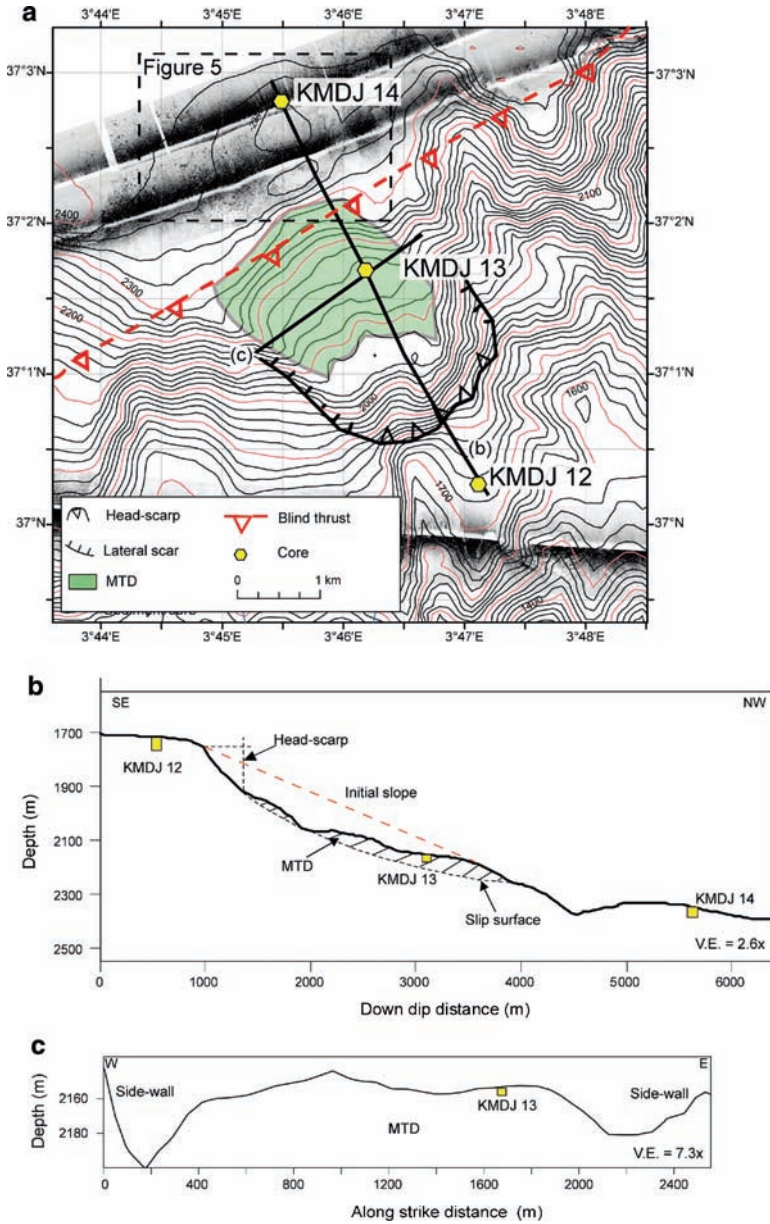
Fig. 4 (**a**) Bathymetric map showing the B1 Slide location; (**b**) down dip bathymetric profile; and (**c**) along strike bathymetric profile across the B1 Slide. The slide scar (*black line*) and the slide deposit (*green*) are clearly distinguishable. The blind thrust path is from Déverchère et al. (2005)
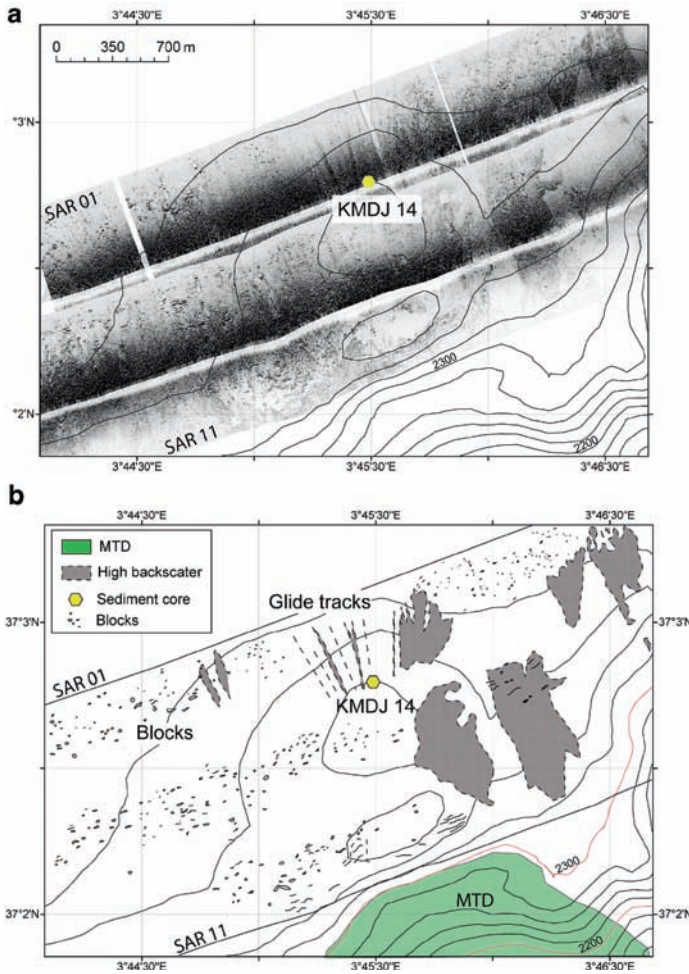
Fig. 5 (**a**) Side-scan sonar image recovered at the foot of the slope and (**b**) interpretation of the SAR image

of brown soft clay deposit overlying an approximately 2 m thick bed of soft mud clasts supported by a brown clay matrix (Fig. 6). The mud clasts are of various color (grey, beige) and size (1 to 5 cm) (Fig. 7a). Thin colored (grey, blue) clay laminae appear folded within the clayey matrix (Figs. 7b, c). A 3 cm-scale medium sand turbidite beds were recognized at 3.5, 5.6 and 5.9 m below seafloor (mbsf). A blue hard mud clast lies between the deepest two sandy beds.

Core KMDJ-13 is 3 m long and was recovered in a water depth of 2,132 m within the B1 Slide (Fig. 6). The sediment from the entire core consists of hard and soft clay clasts, characterized by various sizes and colors (Fig. 7d). A large (around 15 cm in diameter) overconsolidated clay block is observed from 1 to 1.16 mbsf. This block
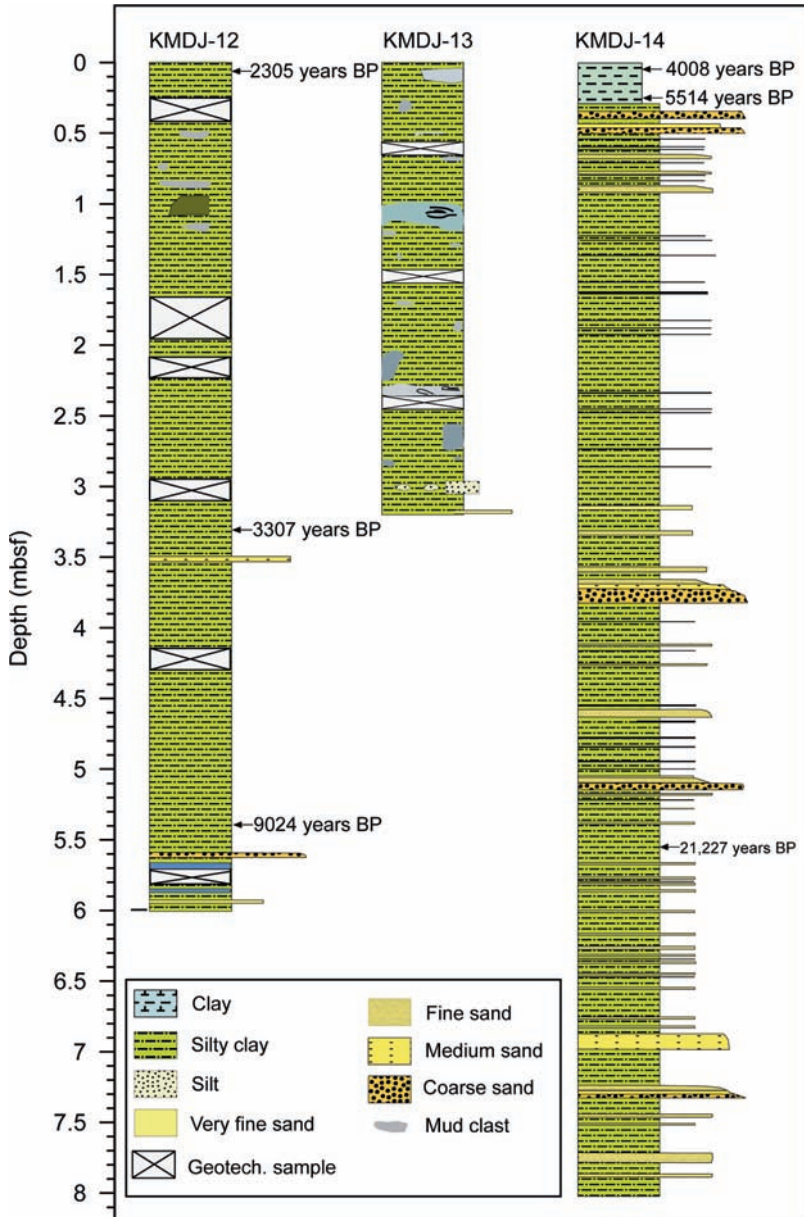
Fig. 6 Interpreted logs of core KMDJ-12, KMDJ-13 and KMDJ-14. Location of cores is in Fig. 4

presents sharp limits and an internal structure characterized by very thin silt and clay deformed laminae (Fig. 7g). It can be presumed that sediment from core KMDJ-13 is part of the failed sediment deposited 3 km downslope the headwall scarp.

Core KMDJ-14 is 8 m long and is located at the foot of the slope in a water depth of 2,312 m (Fig. 6). The sediment at the top of the core consists of 35 cm of soft brown homogenous clay that overlies two coarse-grained sand beds. The sand beds are 3 to 5 cm thick and two cm-size pebbles exist between these two beds. From these coarse-sand layers to the bottom of the core, the sediment consists of alternating fine to coarse-grained sand turbidite beds with soft clay intervals. Approximately 25 turbidite beds were counted along the core characterized by an average thickness of 8 cm (Fig. 6). The thickest turbidites exhibit a fining-up grading and erosive medium to coarse-grained sand bases.

Five AMS ^{14}C dates are done in cores KMDJ-12 and KMDJ-14 (Fig. 6). The uppermost date performed above the MTD (KMDJ-12) provided an evaluation of its age. The age of approximately 2,300 years BP suggests one of these scenarios: (a) the MTD is ancient, so it is not linked, for example, with the 2003 Boumerdès event; (b) the dating sample was contaminated by older foraminifera tests due to sediment disturbance; (c) the uppermost part of sedimentary succession at this place is missing due to technical problems while coring. An estimation of the
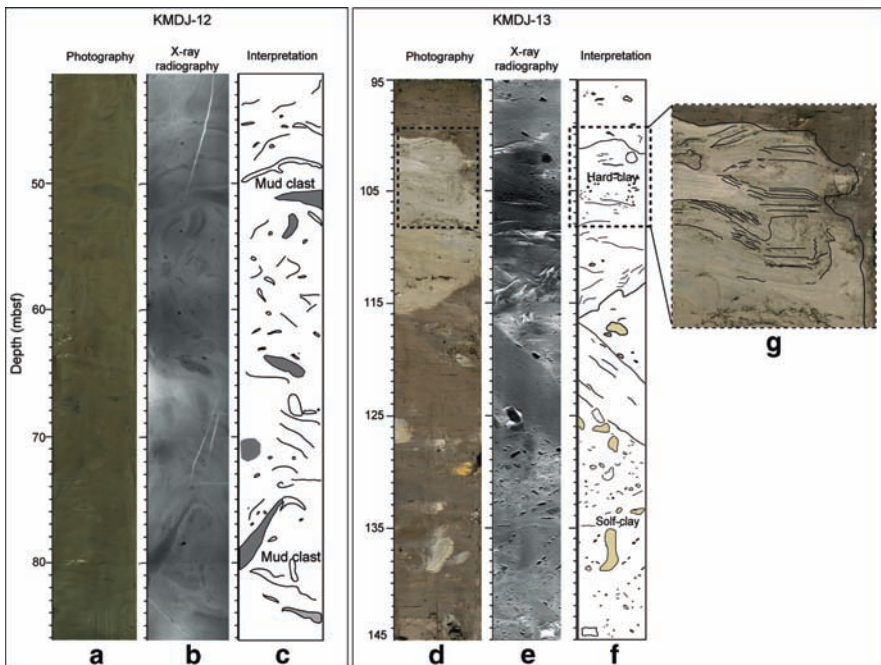
Fig. 7 Interpreted images from cores KMDJ-12: (**a**) photography, (**b**) x-ray radiography, (**c**) interpretation. Images from core KMDJ-13: (**d**) photography, (**e**) x-ray radiography, (**f**) interpretation and (**g**) zoom-in the indurated block

sediment accumulation rate (without taking into account the sediment compaction) from core KMDJ-12 at 3.3 and 5.4 m provide a value of 36 cm/1,000 years. This value is consistent with the sedimentation rate value established by Giresse et al. (2008) from sediment cores recovered across the Algerian margin. The two shallowest dates in core KMDJ-14 were performed in the uppermost hemipelagic interval in order to have an estimated age of the first coarse-grained sand turbidite. The conclusions drawn from the age results are similar to those concerning the uppermost level of core KMDJ-12.

4 Discussions and Conclusion

The interest for studying in detail the seafloor instabilities across the Algerian margin, and in particular in the offshore area affected by the 2003 Boumerdès earthquake, stemmed from four main considerations: (1) the Algiers sector is tectonically active with high to moderate seismicity (maximum earthquake magnitudes around seven, Yelles et al. 2009); (2) the margin has moderate slopes and irregular morphology; (3) there is a long historical record of earthquakes and tsunamis to which slide scars and MTDs could be linked; and (4) it is a densely populated coastal area. It has been acknowledged that the 2003 earthquake triggered landslides that probably developed downslope in submarine avalanches and caused the cables damages over around 300 km large area. Consequently, we searched for significant slide scars that may be linked to the release of significant volumes of sediment.

One of the main results of the present study is the multitude and small-scale slides observed across the central Algerian margin. The observed slides are small compared to those in other studied areas around the world (Booth et al. 1993; Hampton et al. 1996; McAdoo et al. 2000; Hühnerbach and Masson 2004; Sultan et al. 2004). In addition, recent work in the western part of the Algerian margin, between the towns of Oran and Tenes, also documented small-scale slides, similar with those found in the Algiers area (Domzig et al. 2008). Therefore, no significant size slide scars or significant recent deposits were identified in the study area that could probably be related to the 2003 event.

The only large-scale slide is the B1 Slide located on the lower part of the continental slope (Fig. 3). This feature showed the presence of a deposit within the scar and out-runner blocks that may reach 7 km from the headwall. Thus, the B1 Slide is considered as a low-mobility slide. The presence of significant-size blocks far from the foot of the slope may indicate that larger blocks have longer run-out distances probably due to their larger momentum and resistance to disintegration in their downslope movement. Smaller blocks identified near the foot of the slope are probably resulting from the disintegration of larger blocks. In addition, it has been noted that the regular spacing of the gliding tracks (about 50 m) is in agreement with the size of the out-runner blocks. Results from cores showed MTDs at two different locations: upslope the headwall (KMDJ-12) and within the slide scar (KMDJ-13). The absence of a recent drape of soft clay deposits over the MTD in

core KMDJ-13 could indicate a recent deposit. In spite of its upslope location, in a supposed undisturbed area, core KMDJ-12 is placed in a valley-like feature that could be interpreted as an evacuation zone (Fig. 3). High-backscatter patches observed at the foot of the slope probably indicating the turbidity currents high activity. In addition, coarse-grained turbidite beds observed on the core KMDJ-14 testify numerous turbiditic events. The radiocarbon dates of sediment recovered at the foot of the slope (KMDJ-14) do not provide a clear answer about the age of the shallowest reworked deposits.

It has been stated that slides occur in areas with a wide range of slope gradient, ranging from 1 to 14°. Based on the present study and conclusions from Dan et al. (2008), the slope angle (overstepping) may be considered as a minor triggering mechanism in the central Algerian margin. Recurrent seismic activity and consequently earthquakes appears to be the main triggering factor that explains the presence of numerous small-size slides in this region. It is however difficult, with the available information, to assign the occurrence of any specific slides or deposits to the 2003 Boumerdès event. Rigorous dating of recent and past MTDs or and turbidite deposits is needed in order to achieve new insights about frequency of events and their possible connection with the Algerian seismicity.

References

Alasset PJ, Hébert H, Maouche S, Calbini V, Meghraoui M (2006) The tsunami induced by the 2003 Zemmouri earthquake (Mw = 6.9, Algeria): modeling and results. Geophys J Int doi: 10.1111/j.1365–246X.2006.02912.x

Booth JS, O'Leary DW, Popenoe P, Danforth WW (1993) U.S. Atlantic continental slope landslides: their distribution, general attributes, and implication. In: Schwab WC, Lee HJ, Twichell DC (Eds.) Submarine landslides: selected studies in the U.S. exclusive economic zone, U.S. Geol Surv Bull 2002: 14–22

Dan G (2007) Processus Gravitaires et Evaluation de la Stabilité des Pentes: Approches Géologique et Géotechnique. Application à la marge algérienne et à l'effondrement de l'aéroport de Nice en 1979. PhD thesis Université de Bretagne Occidentale (UBO) spécialité Géosci Mar 463

Dan G, Sultan N, Savoye B, Deverchère J, Yelles K (2008) Quantifying the role of sandy-silty sediments in generating slope failures during earthquakes: example from Algerian margin. Intern J Earth Sci. doi 10.1007/s00531-008-0373-5

Déverchère J (2003) MARADJA cruise report, IUEM

Déverchère J, Yelles K, Domzig A, Mercier de Lépinay B, Bouillin JP, Gaullier V, Bracène R, Calais E, Savoye B, Kherroubi A, Le Roy P, Pauc H, Dan G (2005) Active thrust faulting offshore Boumerdès, Algeria, and its relations to the 2003 Mw 6.9 earthquake. Geophys Res Lett 32(L04311). doi:10.1029/2004GL021646

Domzig A, Yelles K, Le Roy C, Dévercère J, Bouillin JP, Bracène R, Mercier de Lépinay B, Le Roy P, Calais E, Kherroubi A, Gaullier V, Savoye B, Pauc H (2006) Searching for the Africa-Eurasia Moiocene boundary offshore western Algeria (MARADJA'03 cruise). C R Geosci 338:80–91. doi:10.1016/j.crte.2005.11.009

Domzig A, Gaullier V, Giresse P, Pauc H, Déverchère J, Yelles K (2008) Deposition processes from echo-character mapping along the western Algerian margin (Oran–Tenes), Western Mediterranean. Mar Petrol Geol doi:10.1016/j.marpetgeo.2008.05.006

France Telecom (2003) The greatest submarine cable disaster never observed. The story of the huge repairs process off Algeria. France Telecom Intern Rep

Gaullier V, Savoye B, Domzig A, Déverchère J, and the MARADJA Team (2004) Depositional patterns off Algeria from echo-character mapping (MARADJA 2003 cruise): possible links with the recent and historical earthquakes, EGU Nice 2004, poster, EGU04-A-06232

Giresse P, Pauc H, Déverchère J, the MARADJA shipboard scientific party (2008) Sedimentary processes and origin of sediment gravity-flow deposits on the western Algerian margin during late Pleistocene and Holocene. Mar Petrol Geol. doi:10.1016/j.marpetgeo.2008.03.011

Hampton MA., Lee HJ, Locat J (1996) Submarine landslides. Rev Geophys 34: 33–59

Hühnerbach V, Masson DG (2004) Landslides in the North Atlantic and its adjacent seas: an analysis of their morphology, setting and behaviour. Mari Geol 213: 343–362

Meghraoui M, Maouche S, Chemaa B, Cakyr Z, Aoudia A, Harbi A, Alasset PJ, Ayadi A, Bouhadad Y, Benhamouda F (2004) Coastal uplift and thrust faulting associated with the Mw = 6.8 Zemmouri (Algeria) earthquake of 21 May (2003) Geophys Res Lett 31(L19605, doi:10.1029/2004GL020466)

McAdoo BG, Pratson LF, Orange DL (2000) Submarine landslide geomorphology, US continental slope. Mar Geol 169: 103–136

Savoye B (2005) MARADJA2 cruise report, IFREMER

Semmane F, Campillo M, Cotton F (2005) Fault location and source process of the Boumerdès, Algeria, earthquake inferred from geodetic and strong motion data. Geophys Res Lett 32(L01305). doi:10.1029/2004GL021268

Sultan N, Cochonat P, Canals M, Cattaneo A, Dennielou B, Haflidason H, Laberg JS, Long D, Mienert J, Trincardi F, Urgeles R, Vorren TO, Wilson C (2004) Triggering mechanisms of slope instability processes and sediment failures on continental margins: A geotechnical approach. Mar Geol 213, 291–321

Yelles AK, Domzig A, Déverchère J, Bracène R, Mercier de Lépinay B, Strzerzynski P, Bertrand G, Boudiaf A, Winter T, Kherroubi A, Le Roy P, Djellit H (2009) Plio-Quaternary reactivation of the Neogene margin off NW Algiers, Algeria: the Khayr al Din bank. Tectonophysics doi:10.1016/j.tecto.2008.11.030. Corrected Proofs. TECTO-124432, 19

Detailed Analysis of a Submarine Landslide (SAR-27) in the Deep Basin Offshore Algiers (Western Mediterranean)

A. Nouguès, N. Sultan, A. Cattaneo, G. Dan, K. Yelles, and PRISME team

Abstract On May 21, 2003 an earthquake with a magnitude of 6.8 (Mw) struck the city of Boumerdes, located on the coast near Algiers, and generated significant gravity flows recognized by numerous submarine cable breaks. In order to investigate a possible offshore imprint of past earthquakes in terms of sediment instabilities, we analyzed one of the numerous escarpments of tectonic origin existing on the Algerian margin. This escarpment, located about 50 km NE offshore Algiers is within water depths between 2,600–2,900 m and has an average slope of 4°. A variety of geotechnical (piezocone), geophysical (swath bathymetry, Chirp echosounder and high-resolution deep-towed side scan sonar) and sedimentological (sediment cores) techniques were used to realize this work. Our study focuses on a well-defined submarine landslide scar (called SAR27) revealed by side-scan sonar images. The SAR 27 slide is small in size (0.5 × 1.7 km), but exhibits a complex morphology including a 10-m high headwall scar, tilted blocks, an area of reworked sediment and a distal deposit. Correlations between in-situ measurements, sampling and CHIRP profile provided a comprehensive understanding of the slide geometry and emphasized the role of thin silty sand beds in the slide initiation. These silty sand beds are probably acting as liquefied slip surfaces, implying a translational displacement mode which correlates the slide morphology.

A. Nouguès, N. Sultan, A Cattaneo, and G. Dan
IFREMER, Géosciences Marines, Laboratoire Environnements Sédimentaires, Plouzané, France

A. Nouguès (✉)
Institut Polytechnique LaSalle Beauvais, Département Géosciences, Beauvais, France
FUGRO FRANCE S.A.S., Nanterre, France
e-mail: a.nougues@fugro.com

K. Yelles
CRAAG, Centre de Recherche en Astronomie, Astrophysique et Géophysique, Bouzaréah, Algiers, Algeria

1   Introduction

Although evidences of submarine landslides are regularly highlighted on very gentle slopes, the triggering mechanisms of such slides remain quite imprecise. Obviously, the static driving stresses implied by the low slope angles are insignificant, and additional external mechanisms (earthquake, fluid flow, free gas …) are needed to trigger a landslide (Lee et al. 2007). Cyclic loadings generated by earthquakes contribute to this external driving stresses but may especially induce the liquefaction of granular sediment (silt or sand) and degradation and softening of soft clays properties (Pestana et al. 2000). In case of interlayered sand and clay levels, the sand layers reaching a liquefied state may become preferential slip surfaces leading to slope destabilisation (see L'Heureux et al. 2007; Dan et al. 2008 for examples of liquefaction-induced submarine slides and Bardet et al. 1999 for general considerations about liquefaction-induced ground displacements).

The Algerian margin, embodying the boundary between the European and the African plates, is a tectonically active margin (Déverchère et al. 2005). Among the several strong to moderate earthquakes which occurred in the last century on the coastal zone, the last violent seismic event ($M_w = 6.9$) struck the city of Boumerdes on May 21st 2003. The MARADJA 2 survey (2005) aimed at recognizing possible slope failures upslope from submarine cable ruptures which were recorded following the seismic shaking. A well-defined slide showing a fresh-looking submarine slide scar was revealed on a deep-towed side-scan sonar profile (the SAR27 profile). The so-called "SAR27 slide" occurs at 2,700 m of water depth on a seafloor escarpment probably of tectonic origin (S2 escarpment, Déverchère et al. 2005). This morphological feature, located approximately 50 km offshore the coastline and characterized by an average slope of 4°, displays numerous slide scars (Fig. 1). Previous studies (Dan 2007; Domzig et al. 2009; Cattaneo et al. this volume) showed the widespread presence of such small-size slides (usually about 0.2 km²) across the Algerian margin. In addition, thin sand beds interlayered in mostly clayey deposits have been described in sediment cores and determined as the main predisposing factor. The recurrent seismicity and subsequent danger of liquefaction have been pointed out as the main triggering factors explaining these numerous small-sized slides in the area (Dan et al. 2008).

The present study deals with a comprehensive analysis of the SAR27 slide. A multidisciplinary approach including geophysical, sedimentological and geotechnical data was used to constrain the geotechnical character of the slide together with its detailed architecture. In addition, we aimed to assess the presumed triggering mechanisms of the SAR27 slide and to reconstruct the sliding scenario.
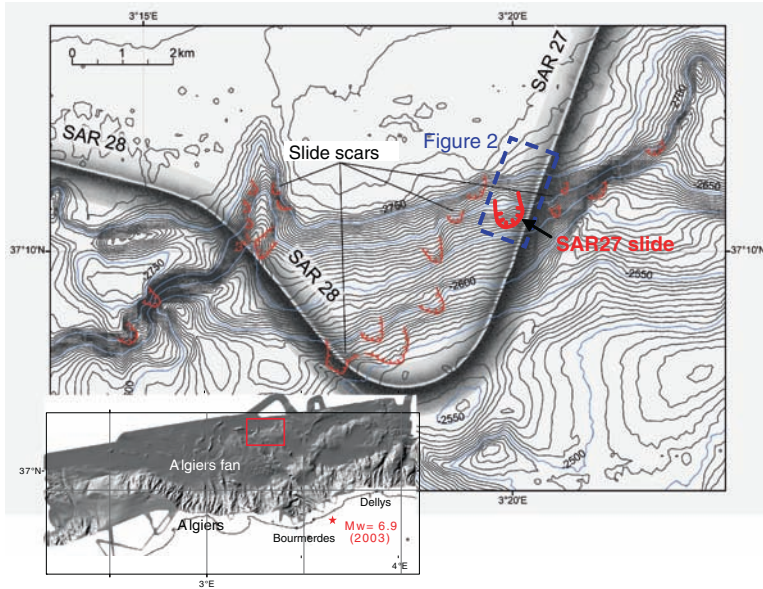
Fig. 1 Morpho-bathymetric map of the S2 escarpment, in the deep Algiers basin. Numerous slide scars (*underlined in red*) are observed in the vicinity of the SAR27 slide. The red star stands for the 2003 Boumerdes epicentre after Semmane et al. (2005)

2 Data Set and Methods

Deep-towed side-scan sonar imagery and 3.5 kHz profiles using the S.A.R. system (Système Acoustique Remorqué) as well as very high-resolution Chirp profiles were collected during the MARADJA 2 survey (Savoye 2005). Further data were acquired along the SAR27 profile during PRISME survey (Sultan 2008): five CPTu (Cone Penetration Test with pore pressure measurement, Meunier et al. 2005), three Küllenberg cores and interface-gravity cores. The cores were performed (1) upslope the headwall in an undisturbed area, (2) in the disturbed deposits and (3) at the base of the slope (Fig. 2). For general information about CPT tests and its interpretation readers are referred to Lunne et al. (1997). Evaluation of the liquefaction potential was performed according to the procedure depicted by Youd et al. (2001). Sediment core logging was performed using a Geotek Multi Sensor Core Logger (http://www.geotek.co.uk) in order to characterize the sediment density or unit weight (γ). The volume of the slide was evaluated by reconstructing the initial slope from the present bathymetric profile and by calculating the missing sediment thickness. Thus, the volume of sediment involved in the slide was extrapolated from the scar width and the deposit extent, based on sonar image and backscatter data.
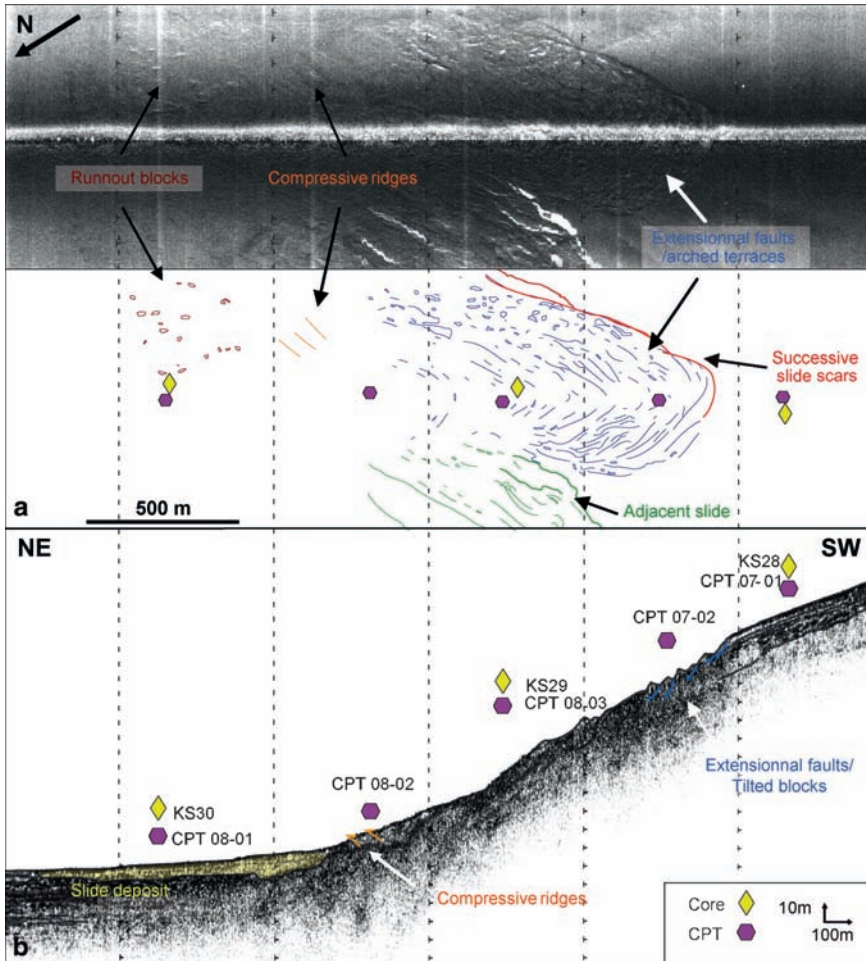
Fig. 2 SAR imagery (**a**) and associated 3.5 kHz profile (**b**) acquired along SAR27 slide

3 Results

3.1 Morphology of the Slide Area

The morphology of the SAR27 slide is clearly expressed on the side-scan sonar image (Fig. 2a). The scar consists of a 560 m wide amphitheater-shaped area including numerous arched extensional cracks. These cracks delineate terraces up to 500–700 m long, tens of meters wide and a few meters high. The arched terraces are perpendicular to the longitudinal axis of the slide (N-S) and are visible from the headscarp until 1 km downslope. The eastern flank of the slide scar reveals multiple

Table 1 Characteristics of SAR27 slide from SAR data, CHIRP profile and reconstructed slope

Slide scar	Deposit	Volumes
Width: 560 m	Extension: 1.2 × 0.8 km	Volume of the empty scar: 6.3 × 10⁶ m³
Length: 1.7 km	Thickness of the deposit: < 8 m	Volume of Base-of-Slope deposit: 3.2 × 10⁶ m³
Headwall height: ~10 m	Run-out distance of blocks: 0.65–1.85 km	Volume of evacuated sediments: 2.9 × 10⁶ m³

walls that probably correspond to successive, intersecting scars which seem to propagate upslope. The echo-sounder profile associated with the SAR image (Fig. 2b) confirms the presence of (1) a well-defined headscarp cutting undisturbed parallel reflectors corresponding to undisturbed slope deposits and (2) of tilted blocks in the upper part of the slide. Compressive ridges are observed at the base of the slope, followed by a transparent lenticular seismic facies suggesting the presence of a mass-deposit. Additionally, the SAR image shows that blocks of 3–5 m in height have been rafted, up to 1 km away of the slope break. Table 1 summarizes the main quantitative characteristics of the SAR27 slide.

3.2 Sediment Core Data

Core KS28 (Fig. 3a) is 11-m long and was collected upslope the slide headwall in order to provide the reference lithology of the undisturbed sediments. The top 1.3 m thick sediment consists of soft silty clay deposits characterized by low unit weight value (γ = 16 kN/m³). From 1.3 m down to 10 m below seafloor (mbsf) the sedimentary column is characterized by alternating silty-clay and thin cm-thick sandy layers corresponding to repeated turbidite beds (Fig. 3a, p1). From 10 mbsf to the bottom of the core, the sediment is essentially clayey. The clayey intervals from 1.3 mbsf to the bottom have a nearly constant unit weight (γ = 18.5 kN/m³).

Core KS29 (Fig. 3b) is 5-m long and was collected within the slide scar. The upper 3.5 m, consists of alternating clayey intervals and silt laminae that exhibit numerous small-scale discordances (Fig. 3b, p1) and a overall inclined bedding surfaces with 25° to 60° dip (Fig. 3b, p2). A clear discordance observed at 3.5 mbsf likely corresponds to a slip surface. The lower 1.5 m (from 3.5 to 5 mbsf) consists of horizontal, probably undisturbed clayey layers (Fig. 3b, p2). The interface gravity core recovered nearby the core confirmed that the tilting of the layers is real, and exists beneath the upper 15–20 cm corresponding to the youngest hemipelagic clays (Fig. 3b, pi).

Core KS30 (Fig. 3c) is 9-m long and was collected at the base of the slope. The upper 4.3 m of sediment is essentially clayey with fine silts laminae and show discrete internal shear surfaces (Fig 3c, p1). From 3.6 mbsf and down to 4.3 mbsf, the layers appear distorted and the layering is no more visible beneath 4 mbsf, possibly
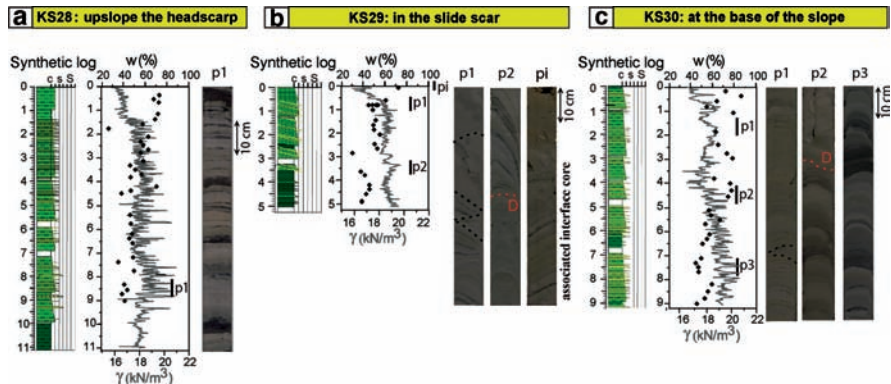
Fig. 3 Synthetic logs, unit weight (γ), water contents (w), and selected sample photos (p1–3, pi) for cores KS28 (**a**), KS 29 (**b**) and KS 30 (**c**). D: discordance, black dashed lines: internal shear surfaces. pi: photo of the associated interface core

indicating a greater degree of reworking (Fig 3c, p2). At 4.3 mbsf, the reworked unit overlies undisturbed turbidite beds (Fig 3c, p2 and p3). The upper unit (from 0 to 4.3 mbsf) is characterized by low and highly varying unit weight and high water contents compared to the underlying unit and to the reference core (KS28).

3.3 Stratigraphy Inferred from Seismic Data and CPTu

Several well-pronounced reflectors (darker lines) were identified on the Chirp profile and used to define seismic units (U1 to U5) (Fig. 4). The top unit (U1) shows several internal parallel reflectors. It overlies a unit characterized by a strong reflector at its base and only one discernable internal reflector (U2, subdivided into U2a and U2b). The underlying unit (U3) does not show any internal reflector. These top units (U1 to U3) appear to lie discordantly on the two deepest and concordant units (U4 and U5). The Unit 4 shows the most pronounced pinch-out geometry but the other units also have a tendency to thin-out seawards, and the reflectors to become less distinct or merge together (dashed lines). Additionally, two acoustically transparent units are present, presumably corresponding to: (1) some reworked sediments along the slope (gray) and (2) the SAR27 slide deposit (yellow), overlying a well-layered unit at the base of the slope.

Five CPTu were performed across the SAR27 slide. For each test, the corrected cone resistance (q_t) and excess pore pressure (Δ_u) curves are plotted along the interpreted Chirp profile (Fig. 4). The correlation between depth (in metres) and time (TWT in seconds) was done assuming a mean P-wave velocity of 1,550 m/s. All CPTs have encountered premature refusal (before 30 m of penetration), indicating that a layer with high resistance to compression was reached (black crosses at maximum CPTs depths on Fig. 4).
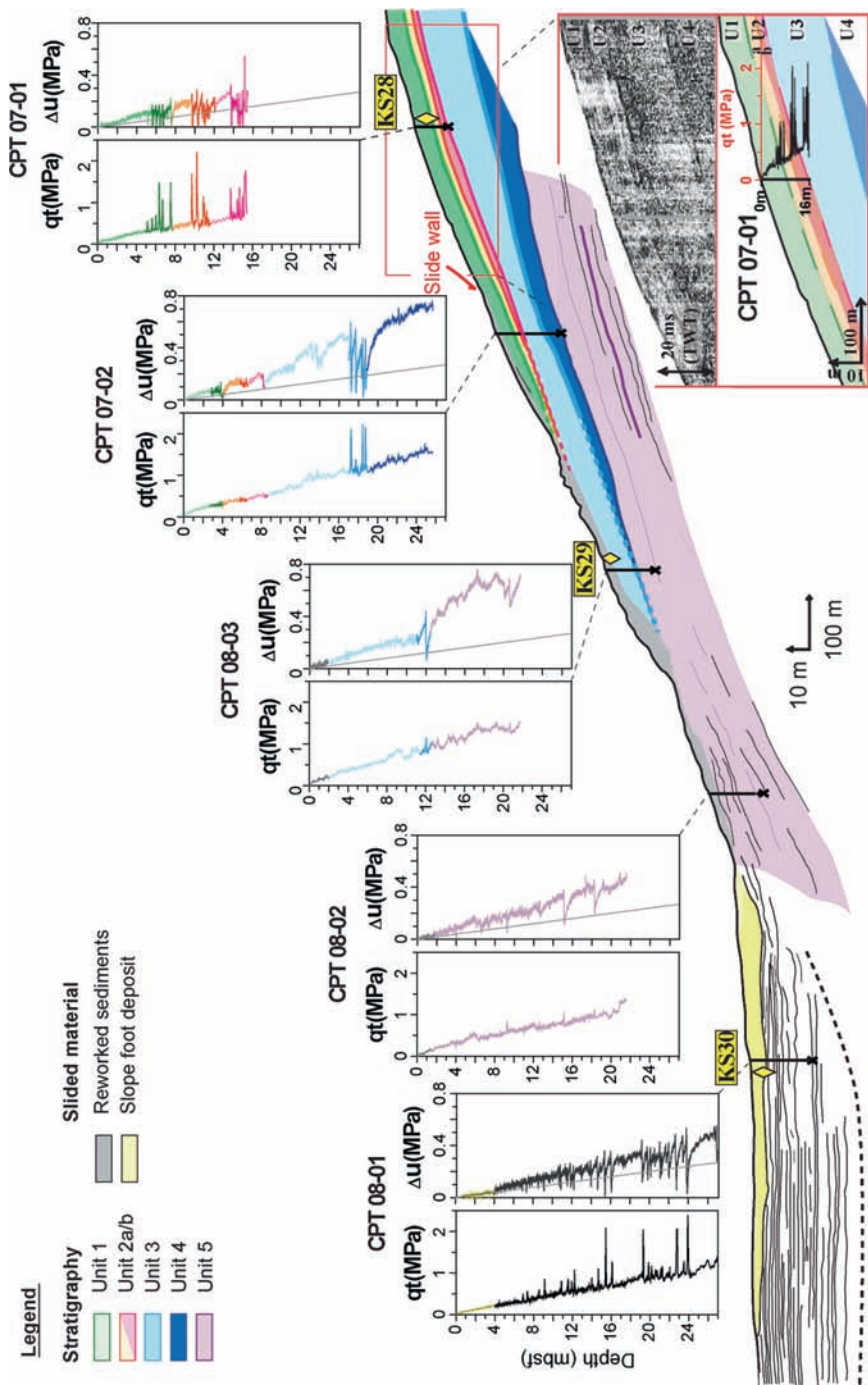
Fig. 4 Correlation between geotechnical and geophysical data. The CPT data are plotted along SAR27 interpreted CHIRP profile assuming a wave velocity of 1,550 m/s (q_t: corrected cone resistance, Δu: excess pore pressure)

Levels characterized by high q_t and low Δ_u values on the CPTu profiles are interpreted as silty sand to sand (Robertson et al. 1986) and classified as very loose to loose (Baldi et al. 1986). Intervals with lower q_t values and linear pore pressure profiles correspond to clayey materials. The coarse-grained beds appear to correlate with the high amplitude reflectors underlined on the Chirp profile (see CPT07-01 in Fig. 4). Due to the different vertical resolution of the Chirp profile (10–50 cm) and of the CPTu measurement (5–10 cm), the high amplitude seismic reflectors might correspond to several close q_t peaks on the CPTu profiles (see colored CPTu plots in Fig. 4). CPTu profiles acquired within the slide scar (CPT 07-02 and 08-03), show only very few q_t peaks. However, each reflector correlates at least one significant pressure (Δ_u) drops (high permeability) indicating the presence of some coarse-grained levels. Besides, the pink reflector (base of U2), which was strong enough to stop prematurely CPT 07-01, is barely discernable when encountered by CPT 07-02. When going seawards, the lateral decrease of the sand beds thickness in addition to the decrease of the pressure confining those loose sandy layers have probably prevent the CPTu cone to detect suitably the different reflectors.

3.4 Liquefaction Potential Assessment

It is possible to infer that liquefaction of sandy layers was a possible triggering mechanism for the SAR27 slides based on the following facts: (1) the presence of silty sand layers in a dominantly clayey lithology, (2) the recurrent regional seismicity and (3) the CPTu data showing possible 'ghost' loose sand layers (i.e. only visible through their high permeability) when going seawards. We therefore decided to assess the liquefaction potential of the SAR27 soil profile. The employed method is a simplified procedure developed from empirical correlations between soil resistance to liquefaction and CPTu tests (Youd et al. 2001). The resistance to liquefaction or CRR (Cyclic Resistance Ratio) is derived from the cone resistance corrected by the overburden effect and the fine-grained content. The CRR is then compared to the CSR (Cyclic Stress Ratio), which represents the seismic solicitation (defined by a maximal acceleration a_{max}). The Moment Magnitude (M_w) of the earthquake is also taken into account.

From CPT 07-01, four loose silty-sandy layers were identified as potentially liquefiable at 6.4, 7.5, 10.3 and 15.2 mbsf (Fig. 5). The comparison between the CRR and CSR calculated for an expectable magnitude level (Mw = 7) reveals that liquefaction could occur for an a_{max} of 0.1–0.15 g in the shallowest sand layers (corresponding to the base of U1 and U2a). In order to cause liquefaction in the deepest layer (base of U2b at 15 mbsf), accelerations of 0.2 g would be needed. For CPT 07-02, the friction was not measured, preventing an accurate calculation of the liquefaction potential for the two silty-sand levels at 17.25 and 18.75 mbsf (see CPT 07-02 on Fig. 4). However, sediment levels deeper than 15 m are rarely observed to liquefy (Krinitzsky et al. 1993). Others CPTu could not provide results in terms of liquefaction potential as no sand layers were recognized on tip cone resistance profiles.

Fig. 5 Comparison between the CSR calculated for several maximal accelerations (a_{max}) and the CRR computed from CPT 07-01
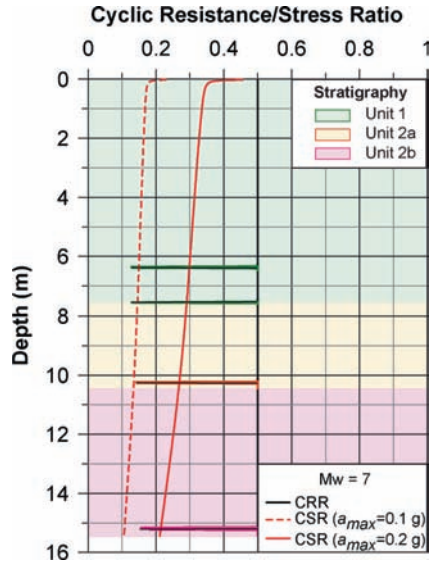
4 Discussions and Conclusion

In the upper part of the scar, numerous extensional faults and terraces indicate that the upper, mostly cohesive sediments (Unit 1 and 2) only experienced moderate displacements, whereas the smoother morphology observed downslope together with evidence of a mass-deposit attests of enhanced sediment disruption. Geometrically, the base of the Unit 3 (light blue horizon) appears to be the basal slip plane of the slide. The base of the Unit 2 (pink horizon) is interpreted as a secondary slip plane, where the tilted blocks are probably rooted in. SAR27 slide is therefore inferred to be a translational slide with multiple slip planes.

As shown by the CPT-based liquefaction analysis, the loose silty-sand layers found in cores from the SAR27 slide area are potentially liquefiable for seismic accelerations (0.1–0.2 g) that are expectable over the margin: Pelaez Montilla et al. (2003) calculated a regional expectable PGA of 0.15 g for a return period of 475 years and Laouami et al. (2006) showed from strong motion recordings of the 2003 Boumerdes earthquake that site effects could locally lead PGAs reaching 0.6 g. An earthquake and related liquefaction can therefore be considered as very probable triggering mechanisms of the SAR27 slide. However, several predisposing or aggravating factors are assumed to have played a major role in the slide initiation.

One of the main predisposing factors is the lithology, composed of successive loose sandy layers interbedded within impermeable clayey intervals. As demonstrated by Yang and Elgamal (2002), the clay layers increase sands vulnerability to liquefaction by trapping excess pore pressure and hindering its dissipation. Biscontin and Pestana (2006) also discussed the fact that the presence of these coarse-grained levels could lead to a delayed failure due to the impeded migration
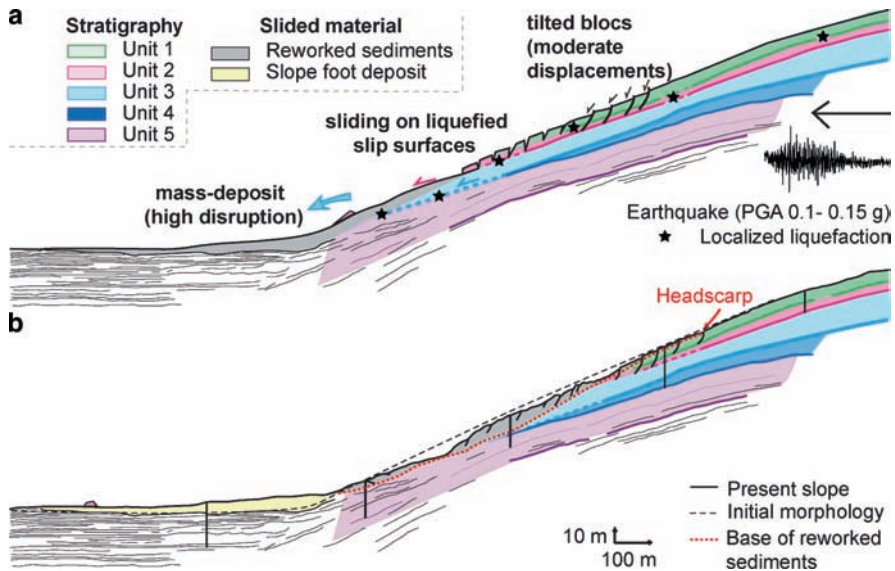
Fig. 6 Summary of the triggering and evacuation processes (**a**) expected to have generated SAR27 slide and its present morphology (**b**) reconstructed from the SAR and CHIRP data

of excess pore pressure after the end of shaking. Once liquefaction has been triggered by an earthquake, low static forces in a gentle slope can be sufficient to cause significant displacements.

In addition, the layers' thinning seawards implies a decrease of the sand levels burial depth and a correlative lateral increase of their liquefaction potential (see Sultan et al. 2008). Consequently, liquefaction was more likely to occur: (1) in the superficial, unconfined sand beds (bases of U1 and U2) but with few consequences on the general slope stability and (2) in the deepest sand beds (merged bases of U3 an U4) when they become shallower seawards, leading to sediment destabilization from the base of the slope (Fig. 6a).

The sliding scenario for the SAR27 slide involves: (a) predisposing factors, essentially due to the lithology and the layers geometry; (b) a triggering factor, very probably being an earthquake, with subsequent localized liquefaction and (c) a retrogressive failure and evacuation process inferred from the slide architecture including two modes of sediment transport: (1) a deep-based slide with moderate to high disruption as attested by the high water contents of the deposit and its smooth morphology and (2) a shallower instability in the upper layers marked by extension and moderate displacements.

Even if the SAR27 slide has a fresh morphological expression on the seafloor, the 15–20 cm thick clayey sediment present on top of the slide deposit in the interface core is likely a hemipelagic drape implying that would imply that SAR27 slide is older than the 2003 earthquake. Further detailed work on core dating is needed to ascertain this assumption, or tentatively link the SAR 27 slide to an historic event.

In addition, the search for slides showing indubitable evidences of the 2003 event as a triggering mechanism remains open (Dan et al. this volume).

References

Baldi G, Bellotti R, Ghionna V, Jamiolkowski M, Pasqualine I (1986) Interpretation of CPT's and CPTU's, part 11, drained penetration of sands. Field Instrumentation and in situ measurements, Proc 4th Internat Geotech Seminar, Singapore, pp. 143–156.

Bardet JP, Mace N, Tobita T (1999) Department of Civil Engineering, Report to PEER/PG&E, Task 4A – Phase 1, 125p. http://www.energy.ca.gov/reports/2002-01-10_600-00-031/APPENDICIES/600-00-031-A3-10.pdf, Accessed 22 February 2009.

Biscontin G, Pestana JM (2006) Factors affecting seismic response of submarine slopes. Nat Haz Earth Sys Sci 6: 97–107.

Dan G (2007) Processus Gravitaires et Evaluation de la Stabilité des Pentes: Approches Géologique et Géotechnique. Application à la marge algérienne et à l'effondrement de l'aéroport de Nice en 1979. PhD thesis Université de Bretagne Occidentale (UBO) spécialité Géosci Mar 463.

Dan G, Sultan N, Savoye B, Deverchère J, Yelles K (2008) Quantifying the role of sandy-silty sediments in generating slope failures during earthquakes: example from Algerian margin. Int J Earth Sci doi 10.1007/s00531-008-0373-5.

Déverchère J, Yelles K, Domzig A, Mercier de Lépinay B, Bouillin JP, Gaullier V, Bracène R, Calais E, Savoye B, Kherroubi A, Le Roy P, Pauc H, Dan G (2005) Active thrust faulting offshore Boumerdes, Algeria, and its relations to the 2003 Mw 6.9 earthquake, Geophys Res Lett 32 L04311. doi:10.1029/ 2004GL021646.

Domzig A, Gaullier V, Giresse P, Pauc H, Déverchère J, Yelles K (2009) Deposition processes from echo-character mapping along the western Algerian margin (Oran–Tenes), Western Mediterranean. Mar Pet Geol doi:10.1016/j.marpetgeo.2008.05.006.

Krinitzsky EL, Gould JP, Edinger PH (1993) Fundamentals of earthquake resistant construction. Wiley, New York.

Laouami N, Slimani A, Bouhadad Y, Chatelain J-L, Nour A (2006) Evidence for fault-related directionality and localized site effects from strong motion recordings of the 2003 Boumerdes (Algeria) earthquake: Consequences on damage distribution and the Algerian seismic code, Soil Dyn Earthq Eng 26(11): 991–1003.

Lee HJ, Locat J, Desgagnés P, Parsons JD, McAdoo BG, Orange DL, Puig P, Wong FL, Dartnell P, Boulanger E (2007) Submarine mass movements on continental margins. In: Nittrouer CA et al. (Eds.) Continental Margin Sedimentation: From Sediment Transport to Sequence Stratigraphy. Int Assoc Sedimentol S.P. 37: 213–274.

L'Heureux J-S, Longva O, Hansen L, Vingerhagen G (2007) The 1990 submarine slide outside The Nidelv River Mouth, Trondheim, Norway. In: Lykousis V, Sakellariou D, and Locat J (Eds.) Submarine Mass Movements and Their Consequences, 259–267.

Lunne T, Robertson PK, Powell JJM (1997) Cone Penetration Testing in Geotechnical Practice. London: Blackie Academic and Professional, 312p.

Meunier J, Sultan N, Jegou P, Harmegnies F, 2005. The Penfeld seabed penetrometer. Oceans 2005–Europe 2: 1309–1314.

Palaez JA, Hamdache M, Lopez Casado C (2003) Seismic hazard in Northern Algeria using spatially-smoothed seismicity. Results for peak ground acceleration. Tectonophys 372: 105–119.

Pestana JM, Biscontin G, Nadim F, Andersen K (2000) Modeling cyclic behavior of lightly overconsolidated clays in simple shear. Soil Dyn Earthq Eng 19: 501–519.

Robertson PK, Campagnella RG, Gillepsie D, Grieg J (1986) Use of in situ tests in geotechnical engineering, Blacksburg, ASCE, Geotech Spec Pub 6: 1263–1280.

Savoye B (2005) MARADJA2 cruise report, IFREMER.

Semmane F, Campillo M, Cotton F (2005) Fault location and source process of the Boumerdes, Algeria, earthquake inferred from geodetic and strong motion data. Geophys Res Lett 32: doi:10.1029/2004GL021268.

Sultan (2008) Prisme Cruise (R/V Atalante Toulon–Toulon; 2007): Reports and Preliminary Results. IFREMER Internal Rep Ref: IFR CB/GM/LES/08–11, pp. 180.

Sultan N, Cattaneo A, Urgeles R, Lee H, Locat J, Trincardi F, Berné S, Canals B, Lafuerza S (2008) A geomechanical approach for the genesis of sediment undulations on the Adriatic shelf. Geochem Geophys Geosyst 9: 1–25.

Yang Z, Elgamal A (2002) Influence of permeability on liquefaction-induced shear deformation. J Eng Mech Am Soc Civil Eng 128: 720–729.

Youd TL, Idriss IM, Andrus RD, Arango I, Castro G, Christian JT, Dobry R, Finn WDL, Harder LF, Hynes ME, Ishihara K, Koester JP, Liao SSC, Marcurson III WF, Marti GR, Mitchell JK, Moriwaki Y, Power MS, Robertson PK, Seed RB, Stokoe II KH (2001) Liquefaction resistance of soils: summary report from the 1996 NCEER and 1998 NCEER/NSF workshops on evaluation of liquefaction resistance of soils. J Geotech Geoenviron Eng 127: 817–833.

3D Seismic Interpretation of Mass Transport Deposits: Implications for Basin Analysis and Geohazard Evaluation

J. Frey-Martínez

Abstract Mass-transport deposits (MTDs) are widely recognized from many continental margins and are an important component of slope systems. Although MTDs have been studied since the early 1920s, much of the research has been conducted on ancient features partially preserved at outcrop. The incompleteness of outcrop examples has been a persistent obstacle to a fuller, process based analysis of their causes, mechanisms, and results. In the last few decades, increasing use has been made of geophysical techniques such as 2D reflection seismology, sonar, and multibeam bathymetry to study modern MTDs. Many valuable insights have accrued from this approach, but it is, in essence, a two-dimensional analytical framework, and suffers from many of the same limitations as the field-based approach. Recent advent of 3D seismic technology offers a novel method for investigations of both modern and subsurface MTDs that promises to add significantly to the understanding of slope failure processes. Modern, high-resolution 3D seismic surveys are now acquired on many continental margins for hydrocarbon exploration purposes, and often in areas that are or have been affected by slope failure. This means that the remarkable spatial resolving power of the 3D seismic method can be used to define the full areal extent and morphology of MTDs with a precision that cannot be achieved with any other combination of methods. This paper illustrates the potential for 3D seismic interpretation of MTDs by describing a suite of complex examples from different continental margins worldwide. The application of seismic-based analyses for seafloor and near-surface geohazard evaluation associated with submarine slope failure is also discussed.

Keywords Mass Transport Deposit • 3D seismic • geohazard • seismic geomorphology • seismic attribute

J. Frey-Martínez (✉)
Repsol-YPF, Repsol Oil Operations Libya (Akakus). Airport Road, Tripoli, Libya
e-mail: jmfreym@repsol.com

1   Introduction

Analysis of MTDs is inherently limited by the resolving power of the tools used to make the primary observation set. This is particularly the case in offshore areas where high-resolution data is often restricted in areal extend and limited to the shallow stratigraphic record. Recent development of 3D seismic techniques allows detailed visualizations of modern and buried MTDs in comparable (or superior) resolution to that achieved by multibeam bathymetry. One of the greatest strengths of the 3D seismic method is the dense, regular sampling of data over the region of interest, which provides images that accurately represent the areal extent of MTDs. In addition, the high-spatial resolution provided by 3D seismic data allows detailed seafloor analysis, interpretation of the geological environment, and calculation of parameters such as seafloor slope angles. Improved resolution also allows exceptional visualization of the internal geometry of modern and buried MTDs, hence increasing the ability to erect more sophisticated kinematic and dynamic models for mass-wasting processes. Application of 3D seismic interpretation has also proven to be a powerful tool for geohazard identification and assessment of slope failure in offshore deepwater areas (e.g., Steffens et al. 2004; Heiniö and Davies 2006; Frey-Martínez et al. 2009).

The improved spatial resolution of 3D seismic surveys is mainly due to smaller bin sizes relative to large footprints of multibeam echo sounders (Mosher et al. 2006; Bulat 2005; Carwright and Huuse 2005). Grid spacing in 3D seismic surveying is typically 25 m or less thus ensuring dense sampling in the lateral dimension comparable with the vertical resolution (Brown 2003). In addition, modern 3D seismic migration algorithms (i.e., 3D dip move out) allow accurate positioning of reflections in all directions, thus collapsing the Fresnel Zone in 3D, and allowing complex geological structures to be accurately imaged in a fully volumetric sense (Carwright and Huuse 2005). Evolving computer technology has also facilitated the proliferation of 3D seismic data with a trend of decreasing cost but increasing data quality and areal extend (Davies et al. 2004).

Application of analytical techniques derived from 3D seismic geomorphology (i.e., Posamentier 2004; Posamentier et al. 2007) has significantly facilitated the study of the three-dimensional configuration of MTDs. Seismic geomorphology integrates seismic profile analysis with various reflection attributes (i.e., amplitude, curvate, dip magnitude and azimuth) to yield accurate images of geological features. When applied to the analysis of MTDs, this approach provides detailed information of their external and internal architecture in a fully volumetric sense. The aim of this paper is to illustrate the potential for 3D seismic data as a research tool in the analysis of mass-wasting processes by describing a suite of worldwide case studies using seismic geomorphological techniques.

2   Recognition of MTDs on 3D Seismic Data

Interpretation of geomorphological features associated with mass-wasting processes on 3D seismic data is generally complex, due to their discontinuous configuration and variations in seismic response. 3D seismic technology currently allows reduced

interpretation uncertainty by using seismic geomorphological techniques (e.g., Posamentier and Kolla 2003; Posamentier et al. 2007). These techniques include (amongst others) detailed correlation between vertical and horizontal seismic profiles, seismic attribute extractions and generation of flattened horizontal slices through volumes of seismic data. The use of seismic geomorphological techniques to the study of mass-wasting processes often reveals four main geological features that are considered critical for the correct recognition of MTDs: (1) headscarp, (2) toe region, (3) basal shear surface, and (4) internal architecture. The main recognition criteria for these four features are illustrated with reference to Fig. 1 and are explained as follows.

2.1 Headscarp

The headscarp is a high-slope surface marking the shallowest portion of an MTD, where sediment excavation/evacuation initiates (Fig. 1). In plan view, it usually appears as an arcuate feature in the upslope areas of the continental margin (Fig. 2). On seismic cross-sections, it is recognized as an excisional feature, where there is an abrupt reduction of stratigraphic section in a downslope direction (Fig. 3a). Immediately downslope, there is a region of marked extensional thinning, where the MTD is frequently cut by minor listric faults (Fig. 3a). In this region, the top of the MTD tends to be depressed with respect to the undeformed strata (Fig. 3b). Upslope of the headscarp, there is generally a region affected by smaller-scale faults and fractures (i.e. crown-cracks; Fig. 2). Crown-cracks normally form in the undisplaced material adjacent to the headscarp because of extensional stresses
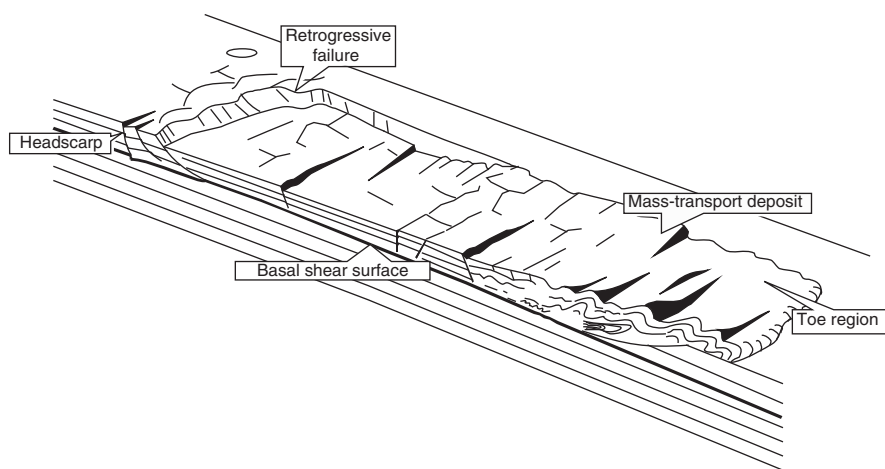
Fig. 1 Conceptual model of a Mass Transport Deposit showing the main geological features: (1) headscarp, (2) toe region, (3) basal shear surface, and (4) internal architecture
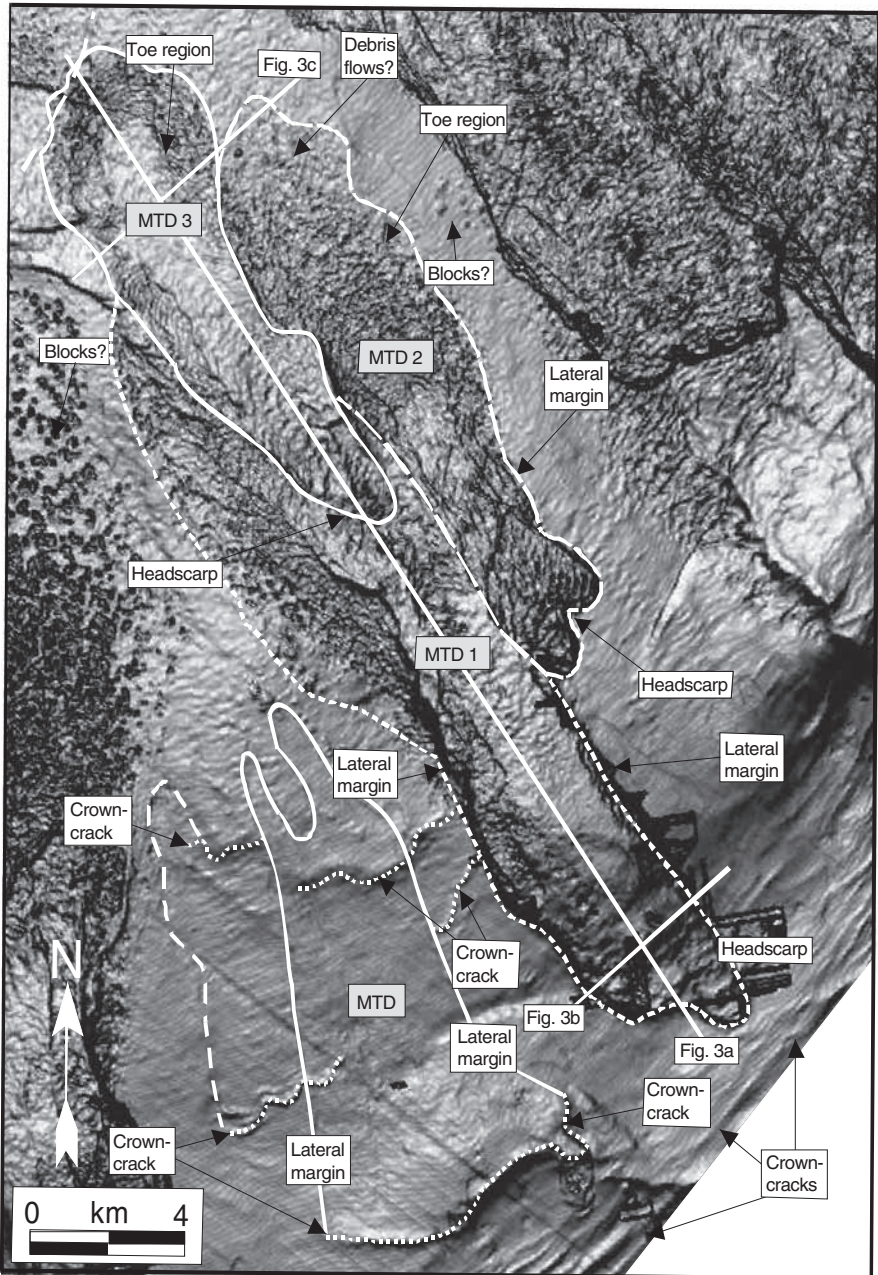
Fig. 2 Dip map extracted from the present day seabed in the Levant Basin (offshore Israel).
Various MTDs are observed as elongated bodies extending though the slope areas. Note the
presence of clear headscarps located close to the shelf-break
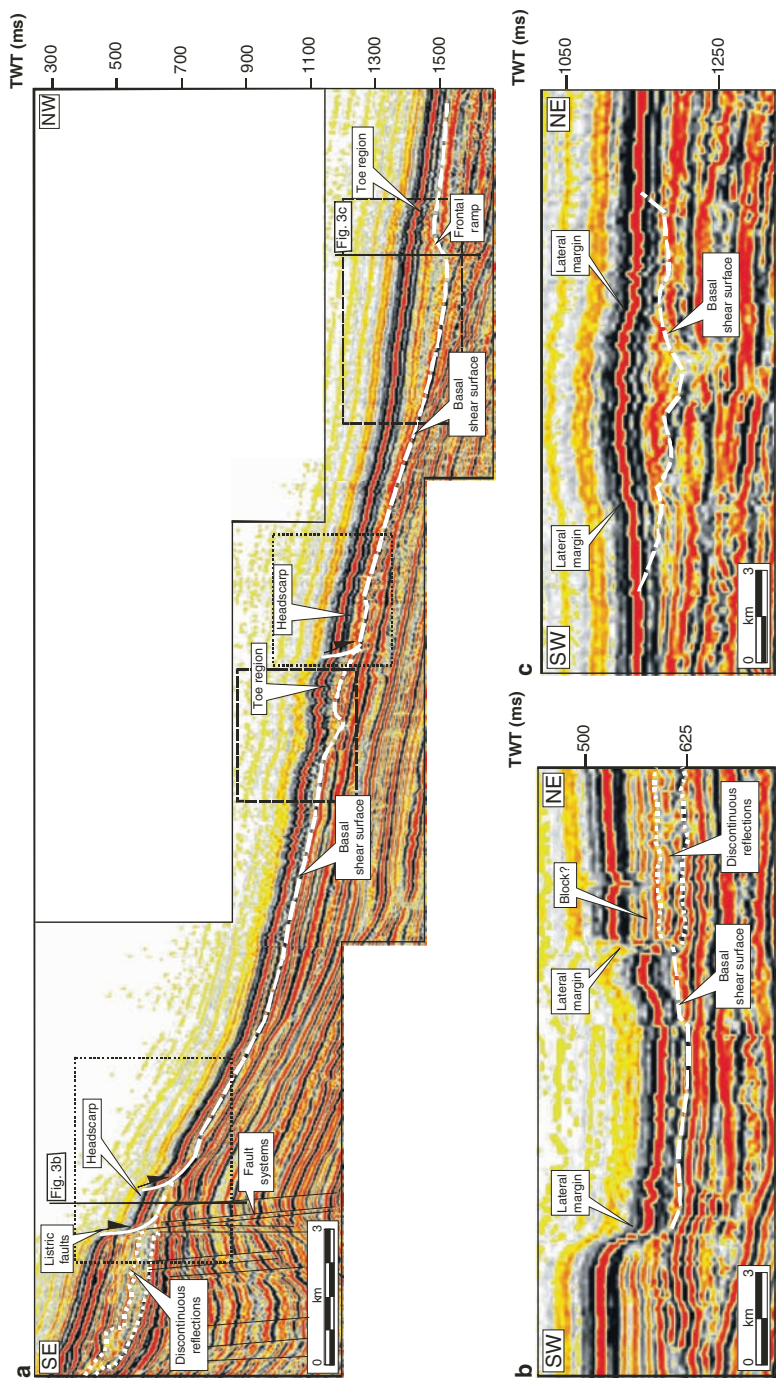
Fig. 3 Catalog of seismic sections through a recent MTD illustrating the seismic appearance of its internal parts. The white dashed line marks the basal shear surface. (**a**) Seismic section parallel to the direction of transport. Depletion (*dotted box*) and accumulation (*dashed box*) zones are clearly seen. (**b**) Seismic section perpendicular to the direction of transport through the headscarp (see Fig. 3a for location). Note the two clear lateral margins creating a negative topography and the presence of a block-like feature. (**c**) Seismic section perpendicular to the direction of transport through the toe region (see Fig. 3a for location). The lateral margins form a positive topographic relief

developed by undermining during sediment removal. Crown-cracks represent the upslope propagation of slope instability during retrogressive failure and their identification is critical to highlight potential areas for future events of mass-wasting.

2.2 Toe Region

The toe region is the downslope limit of an MTD and it corresponds to the base of the area where sediment accumulates (Fig. 2). On seismic profiles, it is usually recognized as a zone of gross thickening of stratigraphic section (Fig. 3a, c). In shallow MTDs, where seismic resolution is the greatest, toe regions appear on dipmaps as areas of intense rugosity with ridge-like features that are approximately arcuate in the downslope direction (Fig. 3a). These ridges generally appear in cross-sections as short wavelength and low relief 'crumpling' of the seabed (Fig. 2). On seismic profiles, these ridges may be recognized as discrete thrusts and folds, arranged in series into imbricated thrust and fold structures (Fig. 3a). Compressional features are invaluable as kinematic indicators since they allow direction and magnitude of translation to be constrained (Strachan 2002).

2.3 Basal Shear Surface

The basal shear surface is a critical element for the recognition of MTDs since it clearly delimits the deformed interval. This surface represents the plane above which downslope translation occurs, and corresponds to a stratigraphic layer where the sediment losses its shear strength (usually by sediment liquefaction) and it is no longer able to resist downslope gravitational shear. The basal shear surface can be identified in a similar way to unconformities i.e., by termination of stratal reflections (Fig. 3a). This is usually aided by the significant contrast between the chaotic seismic facies within the MTD and the much more continuous facies of the outer deposits (Fig. 3a). Generally, the basal shear surface forms a continuous plane that dips parallel to the underlying strata. However, it may locally ramp up and down stratigraphy to form a staircase-like geometry. Such ramps appear as conspicuous erosional features against which underlying seismic reflections truncate (Fig. 3b). Towards the headscarp, the basal shear surface exhibits a listric, concave upward appearance, cutting upslope strata (Figs. 3a and 4a). Approaching the toe region, it ramps upwards crosscutting downslope strata to form a frontal ramp (Figs. 3a and 4b).
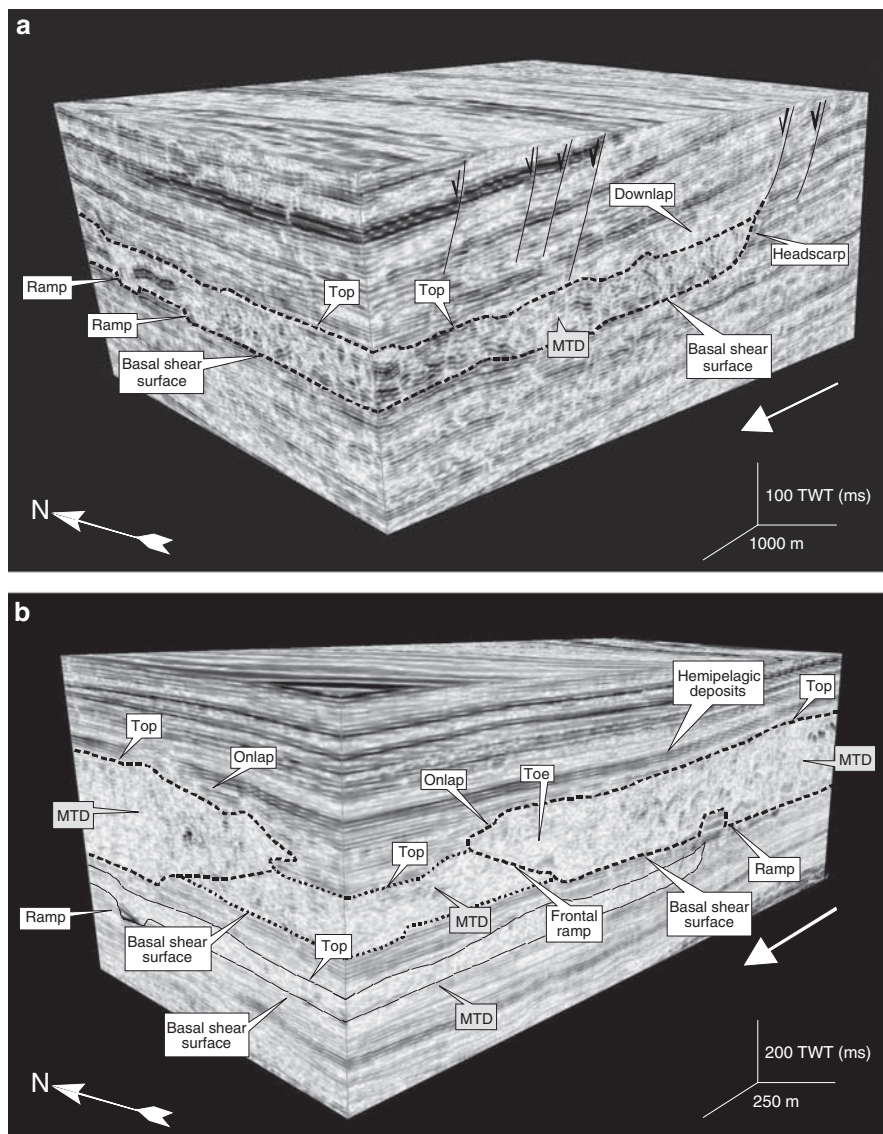
Fig. 4 3D visualization of representative MTDs. MTDs form intervals of disrupted and chaotic seismic facies enclosed by the basal shear and top surfaces. (**a**) 3D seismic volume showing the upslope parts of an MTD. Note the listric character of the basal shear surface towards the headscarp and the irregular morphology of the top surface. (**b**) 3D seismic volume showing the downslope parts of an MTD. Note the presence of a frontal ramp towards the toe of the mass-wasting deposit. MTDs delimited by thin dashed lines correspond to previous and separate mass-wasting events

2.4 Internal Architecture

Possibly the most significant advance in the analysis of MTDs resulting from application of 3D seismic interpretation is the description of their internal architecture. In this respect, additional resolving power of 3D seismic data has revealed much greater internal complexity than previously appreciated from 2D-based interpretation. As previously stated, MTDs are typically distinguished as intervals of chaotic or highly disrupted seismic facies (Fig. 4). Nevertheless, there is often sufficient coherence of individual seismic reflections to allow good visualization of internal features. MTDs undergo complex internal deformation as they move downslope. The degree and style of this deformation vary with the strength and heterogeneity of the failed mass and with the position in the deposit. In a simplistic case, upslope parts of an MTD are dominated by extensional structures (e.g., normal and listric faults), while downslope areas, where movement ceases, tend to be dominated by compressional features (e.g. folds and thrusts) (see Fig. 1).

The limited lateral correlation of the stratal reflections within MTDs means that the interpretation of such deformational structures on seismic profiles can be extremely difficult because of their highly disrupted patterns. In such cases, integration of seismic profiles and attribute maps can be an optimum method for defining their detailed internal architecture. This methodology will be further explained in the next section.

3 Seismic Attribute Characterization of MTDs

Among the various geophysical techniques available for characterizing MTDs, 3D seismic attributes have proven to be some of the most useful. Seismic attributes can generate three-dimensional volumes that facilitate the analysis of MTDs by avoiding the need to pre-interpret irregular horizons, and by enhancing sub-seismic lateral variations in reflectivity. Although there are several seismic attributes that are in common use today, geometric attribute mapping is, possibly, the most useful methodology for MTDs characterization. This technology, originally designed by the oil industry to detect subtle structures with an impact on reservoir performance (i.e., faults or fractures), is an excellent edge-detection tool, and is especially useful for defining geobodies with sharply defined margins such as MTDs. Geometric attributes include coherence, variance, dip, and azimuth, amongst others.

3.1 Coherence

Coherence is a well-established technology that measures lateral changes in waveform and is sensitive to breaks in reflectors. Bahorich and Farmer (1995)

developed coherence attributes comparing adjacent seismic waveforms using cross-correlation, semblance, and eigenstructure measures along the dip and azimuth of a seismic reflector. Coherence images often provide enhanced visualization of small-scale geologic features and allow accurate mapping of the internal architecture of MTDs. Figure 5 is a representative flattened horizontal coherence slice showing the utility of this attribute in defining complex structures within the toe region of an MTD. The interpretational approach here consisted of defining the limits between the different coherence 'facies', and correlating them with vertical profiles. Concentric linear discontinuities correspond to thrust faults as interpreted on vertical seismic profiles (e.g., C in Fig. 6). Low coherence facies in the frontal parts of the toe region coincide with intensively deformed sediments that have no original stratification preserved in the seismic character.
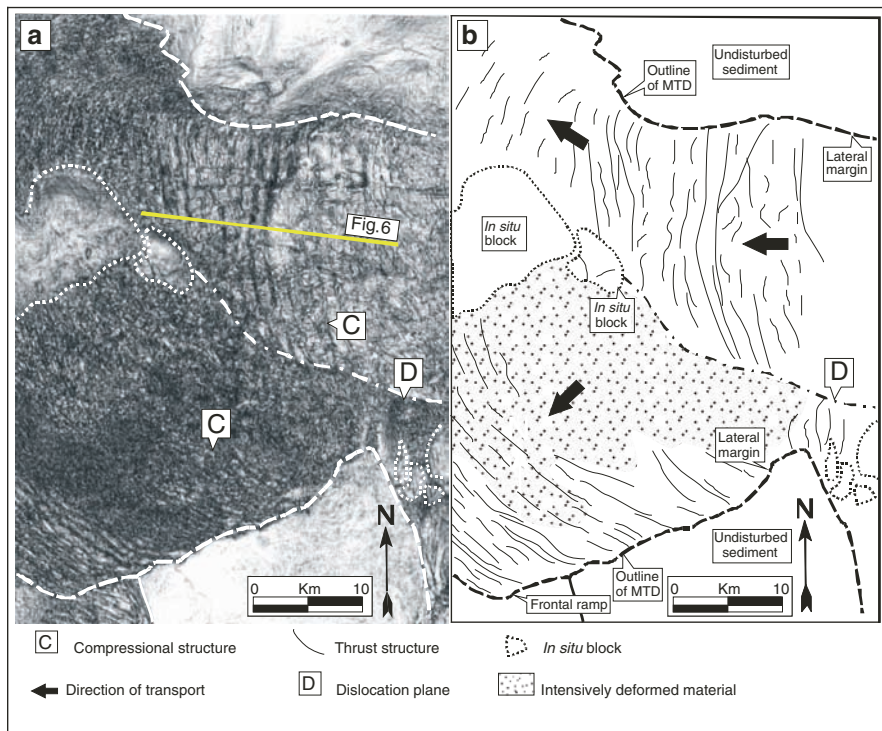
Fig. 5 (**a**) Structurally flattened horizontal coherence slice across part of the toe region of an MTD. Note the presence of arc-like concentric structures (marked C). These are interpreted as thrust fault planes. There are coherent parts within the slump deposit interpreted as "in situ" blocks. A dislocation plane (marked D) is also interpreted. (A) marks a seismic artifact. (**b**) Interpretation. The black arrows indicate the inferred directions of displacement
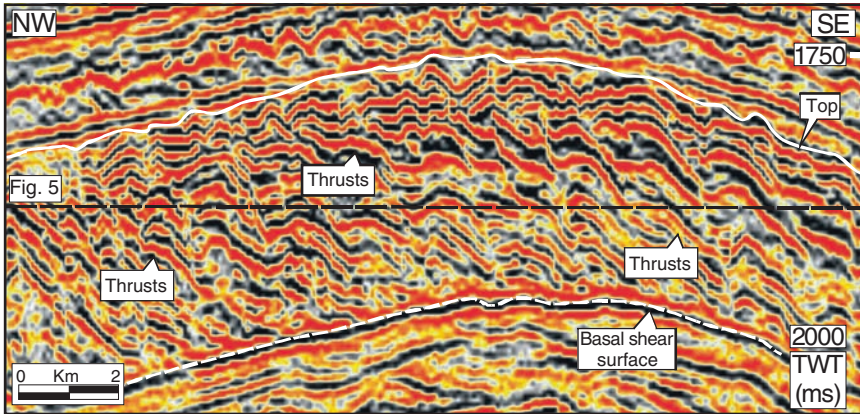
Fig. 6 Seismic profile in the dip direction along an MTD (see Fig. 5 for location). The internal parts of the MTD are composed of upslope dipping tilted seismic reflections. These reflections are offset and locally create developed listric geometries. Thrust structures ramping from the basal shear surface up to the top of the MTD and minor extensional structures (i.e. faults) are observed

3.2 Variance

Variance attribute is the result of calculating localized waveform variability over a seismic volume in both inline and crossline directions. Map views of variance data are particularly effective to identify structural and stratigraphic discontinuities, and to characterize geologic features that involve significant changes in seismic trace pattern (such as MTDs). Importantly, variance maps may not be helpful if the changes in the patterns of the neighbouring traces are gradual, in which case, all variance values are almost identical and no features are apparent. Figure 7 is a variance map of the seafloor on the Ebro Continental Margin (offshore northeastern Spain). This map clearly highlights a complex system of mass-failed features (Lubina MTD) located ca. 75 km from the present-day coastline. The Lubina MTD is inferred to be Holocene in age due to its proximity to the seafloor, covers an area of ca. 80 km^2, and has a volume of up to ca. 5 km^3 (see Frey-Martínez et al. 2009).

3.3 Dip, Azimuth, and Curvature

Dip, azimuth, and curvature are, possibly, the most comprehensive types of geometric attributes for the study of MTDs. These attributes are familiar concepts from structural geology, and are powerful tools for delineating faults, folds, and other structural elements. Rijks and Jaufred (1991) demonstrated that maps of dip-magnitude and dip-azimuth computed from interpreted horizons can highlight geologic features with significantly smaller offsets than the width of seismic wavelet, and
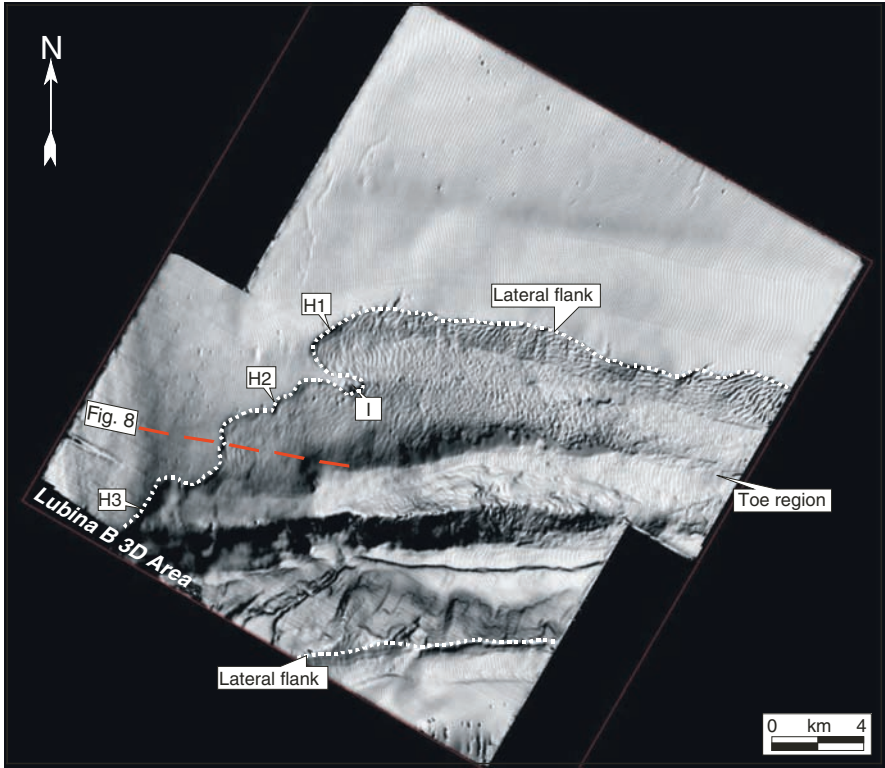
Fig. 7 Variance map extracted from the present day seabed on the Ebro Continental Margin (northeastern Spain). White dotted line marks outline of the Lubina MTD. Three headscarps (H1, H2, and H3) have been identified suggesting a complex history of instability. An area of low variance in the headscarp region is interpreted as intact deposits (I). Seismic sections (indicated with long red dashed lines) are used to illustrate the seismic character of the mass-failed deposit in Fig. 8
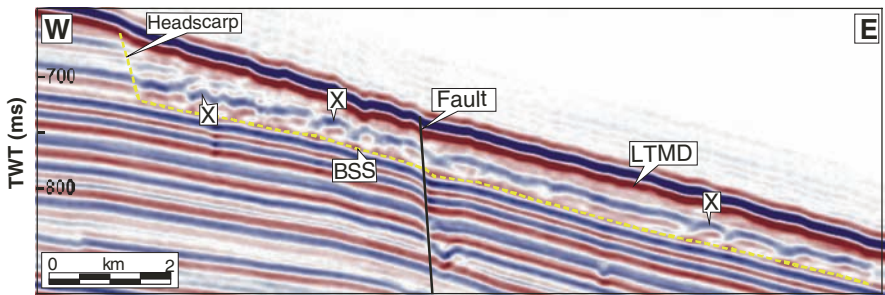
Fig. 8 Seismic profile in the dip direction along the headscarp area of the Lubina MTD (LMTD; see Fig. 7 for location). The profile is parallel to the interpreted main direction of movement. There are resolvable seismic reflectors within the mass-failed deposit (X), interpreted as extensional features. Several paleo-pockmarks are seen below the Lubina MTD. Basal shear surface (BSS) marks base of the mass-failed deposit

provide improved visualization of subtle geologic features. Reflector curvature, for instance, is well correlated to fracture intensity (Roberts 1998, 2001), which allows detailed interpretation of crown-cracks and headscarp areas. Dip, dip-azimuth, and curvature attributes can be calculated from horizon time structure maps or as volume attributes.

Figure 9 is a 3D visualization of a dip map on the continental margin of Israel. Arrows highlight a series of MTDs in a water depth ranging from 500 to 1,150 m. These MTDs involve up to an 80 m thick section of fine-grained sediments within the shallowest part of the basin succession, and are considered to be Late Pleistocene-Holocene in age. Well-developed headscarps and lateral scarps are recognised along the MTDs defining a slip domain that is chute-like, with an aspect ratio strongly elongated in a downslope direction. Toe regions appear as areas of intense rugosity with local development of ridges that are concordant with one another, and are almost arcuate in a convex downslope direction. These ridges are interpreted as compressional features.

4   Implications for Hydrocarbon Exploration and Production

Slope failure represents a major offshore geohazard, and constitutes an issue that has a bearing on safety, environment, and economy. It has been recognised that understanding the mechanisms and consequences of mass-wasting events can significantly influence offshore strategies (e.g., Piper and Normark 1982; Piper et al. 1988; Løseth et al. 2003; Shipp et al. 2004). In this section, a review of the most relevant implications to deepwater operations by the energy industry is summarized.

The importance of MTDs in the exploration and production of hydrocarbons is critical and multifold. Firstly, they are recognized worldwide as major geohazards with potential catastrophic consequences for safety and facilities in offshore operations. A variety of slope failures are known to occur in numerous offshore oil provinces such as Israel (e.g., Frey-Martínez et al. 2005), Norway (e.g., Bryn et al. 2005), the Niger Delta (e.g., Heiniö and Davies 2006), and the Gulf of Mexico (e.g., Sawyer et al. 2007). Secondly, MTDs can be critical for the hydrocarbon prospectivity of sedimentary basins as they represent a highly effective mechanism in redistributing vast amounts of sediment from shallow into deepwater settings. Thirdly, slope failures have the potential to alter the original properties and architecture of reservoir intervals, generate traps, and influence migration pathways. When mass-wasting occurs, the original stratification is modified, the lithological compositions are remixed, and the primary volumes of sediment are altered. Such modifications frequently cause a decrease in the net to gross, porosity, and permeability of the sediments, coupled with an increase in their lithological complexity. In addition, the occurrence of large-scale MTDs can trigger seal failure and vertical migration of hydrocarbons due to a rapid drop in the lithostatic pressure (e.g., Haflidason et al. 2002, 2004).
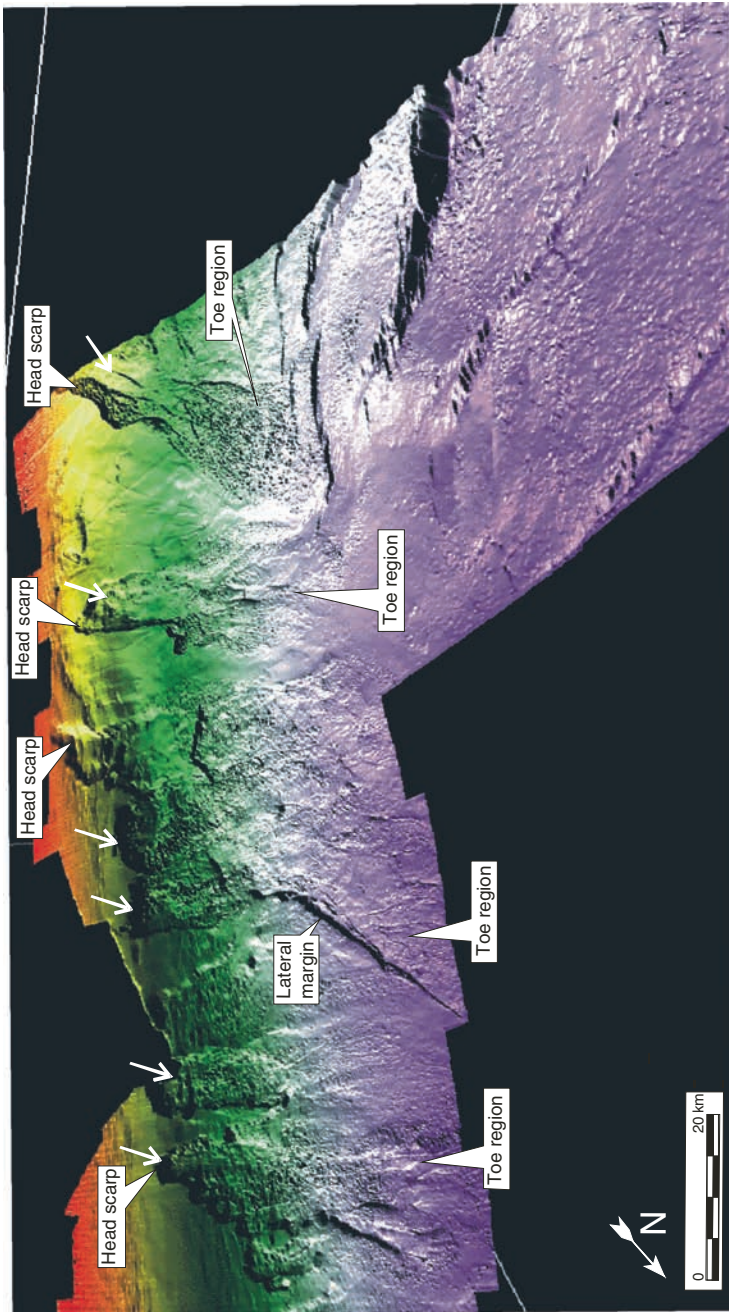
Fig. 9 3D visualization of a dipmap of the present day seabed offshore southern Israel and Gaza Strip. Several MTDs (*white arrows*) cover the slope region. These MTDs form arrays of elongated features extending from the shelf to the base of slope

Another major implication of slope failure for the exploration and production of hydrocarbons is its impact on operational performance of jetted conductors and suction anchors piles design (Newlin 2003; Shipp et al. 2004). The transportation and deformation of mass-wasting deposits causes the expulsion of water (Piper et al. 1997) and, as a consequence, the shear zones at the base of MTDs in the near-subsurface are commonly overcompacted when compared to unfailed, conformable sediments. It has been demonstrated that sediment overcompaction can reduce significantly the rate of conductor penetration during deepwater jetting operations (Shipp et al. 2004). Also, the presence of mass-wasting deposits within a development area has been confirmed to be a key design criterion for suction anchor piles (Newlin 2003). Embedment of suction anchor piles is achieved through a combination of self-weight penetration and application of an induced underpressure within the pile. Thus, presence of overcompacted surficial and near-surface mass-wasting deposits may lead to unexpected problems during pile installation, and/or adverse performance while in service (e.g., Newlin 2003).

Importantly, 3D seismic-based analyses of the type presented here are proven to be an effective approach for rig and facilities site-survey planning in offshore deepwater areas (also see Steffens et al. 2004). The high spatial resolution provided by 3D seismic data allows detailed seafloor analysis, interpretation of the geologic environment, and calculation of parameters such as seafloor slope angles.

5   Conclusions

3D seismic interpretation has proved to be a very powerful tool for analysing submarine MTDs and mass wasting processes. 3D seismic data provides excellent coverage of both recent and ancient MTDs, allowing for a better understanding of their basinal distribution and geological setting. In addition, the high spatial resolution provided by the 3D seismic data has offered a better definition of the different elements forming MTDs, which improves our ability to construct more sophisticated kinematic and dynamic models for mass-wasting processes. A further conclusion from this work is the possible value of 3D seismic data as a tool for submarine slope instability risk assessment. An interesting aspect of this approach is the possibility to map the extent of zones where diagnostic features of mass movement (i.e., crown-cracks) can be inferred, thus highlighting potential areas affected by slope instability.

References

Bahorich ME, Farmer S (1995) 3D seismic discontinuity for faults and stratigraphic features: the coherence cube. The Leading Edge 14:1053–1058.

Brown AR (2003) Interpretation of Three Dimensional Seismic Data, 6th edition, Am Assoc Pet Geol Memoir 42, 541 pp., Tulsa, OK.

Bryn P, Kjell B, Forsberg CF, Solheim A, Kvalstad TJ (2005) Explaining the Storegga Slide, In: Solheim A, Bryn P, Berg K, Mienert J (eds.) Ormen Lange – An Integrated Study for the Safe Development of a Deep-water Gas Field within the Storegga Slide Complex, NE Atlantic Continental Margin. Mar Pet Geol 22:11–19.

Bulat J (2005). Some considerations on the interpretation of seabed images based on commercial 3D seismic in the Faroe-Shetland channel. Basin Res 17:21–42.

Carwright JA, Huuse M (2005) 3D seismic technology: the geological "Hubble". Basin Res 17:1–20.

Davies RJ, Cartwright JA, Stewart SA, Lappin M, Underhill JR (2004) 3D Seismic Technology: Application to the Exploration of Sedimentary Basins. Geol Soc Lond Mem 29, 355 pp.

Frey-Martinez J, Cartwright JA, Hall B (2005) 3D seismic interpretation of slump complexes: examples from the continental margin of Israel: Basin Res 17:83–108.

Frey-Martinez J, Bertoni C, Gerard J, Matias H (2009) Submarine slope failure and fluid migration processes on the Ebro Continental: Implications for offshore exploration and development. In: Shipp RC, Weimer P, Posamentier HW (eds.), Mass-transport Deposits in Deepwater Settings. SEPM (Society for Sedimentary Geology) Special Publication, in press.

Haflidason H, Sejrup HP, Berstad IM, Nygård A, Richter T, Bryn P, Lien R, Berg K (2002) Weak layer features on the northern Storegga Slide escarpment. In: Mienert J, Weaver P (eds.) European Margin Sediment Dynamics: Springer Berlin

Haflidason H, Sejrup HP, Nygård A, Mienert J, Bryn P, Lien R, Forsberg CF, Berg K, Masson D (2004) The Storegga Slide: architecture, geometry and slide development. Mar Geol 213:201–234.

Heiniö P, Davies RJ (2006) Degradation of compressional fold belts: deep-water Niger Delta. Am Assoc Pet Geol Bull 90:753–770.

Løseth H, Wensaas L, Arntsen B, Hovland M (2003) Gas and fluid injection triggering shallow mud mobilization in the Hordaland Group, North Sea. In: Van Rensbergen P, van Hillis RR, Maltman AJ, Morley CK (eds.) Subsurface Sediment Mobilization. Geol Soc Spec Publ 216:139–157.

Mosher DC, Bigg S, LaPierre A (2006) 3D seismic versus multibeam sonar seafloor surface renderings for geohazard assessment: Case examples from the central Scotian Slope. The Leading Edge 25:1484–1494.

Newlin JA (2003) Suction anchor piles for the Na Kika FDS mooring system, part 1: site characterization and design. Deepwater Mooring Systems: Concepts, Design, Analysis, and Materials, ASCE 28–54. Houston, USA.

Piper DJW, Normark WR (1982) Effects of the 1929 Grand Banks earthquake on the continental slope off eastern Canada. Geol Surv Can Curr Res Part B, Paper 82-01B:147–151.

Piper DJW, Shor AN, Clarke JEH (1988) The 1929 "Grand Banks" Earthquake, Slump, and Turbidity Current. In: Clifton HE (ed), Sedimentologic Consequences of Convulsive Geologic Events. Geol Soc Am Spec Pap 229:77–92.

Piper DJW, Pirmez C, Manley PL, Long D, Food RD, Normark WR, Showers W (1997) Mass-transport deposits of the Amazon Fan. In: Flood RD, Piper DJW, Klaus A, Peterson LC (eds.), Proceedings of the Ocean Drilling Program, Scientific Results 155:109–146.

Posamentier HW, Kolla V (2003) Seismic geomorphology and stratigraphy of depositional elements in deep-water settings. J Sed Res 73:367–388.

Posamentier HW (2004) Seismic geomorphology: imaging elements of depositional systems from shelf to deep basin using 3D seismic data, In: Davies RJ, Cartwright JA, Stewart SA, Lappin M, Underhill JR (eds.) 3D Seismic Technology: Application to the Exploration of Sedimentary Basins. Geol Soc Spec Publ 29:11–24.

Posamentier HW, Davies RJ, Cartwright JA, Wood L (2007) Seismic geomorphology – an overview. In: Davies RJ, Posamentier HW, Wood LJ, Carwright JA (eds.) Seismic Geomorphology: Applications to Hydrocarbon Exploration and Production. Geol Soc Spec Publ 277:1–14.

Rijks EJH, Jauffred JCEM (1991) Attribute extraction: an important application in any detailed 3D interpretation study. The Leading Edge 10:11–19.

Roberts A (1998) Curvature analysis: "new" attributes for the delineation of faults, map lineaments and surface shape. 1998 AAPG Annual Convention Program with Abstracts (CD-ROM), Salt Lake City, 17–28 May.

Roberts A (2001) Curvature attributes and application to 3D interpreted horizons. First Break19:85–99.

Sawyer DE, Flemings PB, Shipp RC, Winker CD (2007) Seismic geomorphology, lithology, and evolution of the late Pleistocene Mars-Ursa turbidite region, Mississippi Canyon area, northern Gulf of Mexico. Am Assoc Pet Geol Bull 91:215–234.

Shipp RC, Nott JA, Newlin JA (2004) Physical characteristics and impact of mass transport complexes on deepwater jetted conductors and suction anchor piles. Offshore Technology Conference, OTC Paper #16751, 11 p.

Steffens GS, Shipp RC, Prather BE, Nott JA, Gibson JL, and Winker CD (2004) The use of near-seafloor 3D seismic data in deepwater exploration and production. In Davies RJ, Cartwright JA, Stewart SA, Lappin M, and Underhill JR (eds.), 3D Seismic Technology: Application to the Exploration of Sedimentary Basins. Geol Soc Spec Publ 29:35–43.

Strachan L (2002) Slump-initiated and controlled syndepositional sandstone remobilisation: an example from the Namurian of County Clare, Ireland. Sedimentology 49:25–41.

Slope Instability on the French Guiana Transform Margin from Swath-Bathymetry and 3.5 kHz Echograms

V. Gaullier, L. Loncke, L. Droz, C. Basile, A. Maillard, M. Patriat, W.R. Roest, B. Loubrieu, L. Folens, and F. Carol

Abstract Although transform margins represent ~30% of rifted margins around the world, few studies have investigated mass-movement processes in such areas and their links with this specific structural context. The French Guiana transform margin and adjacent Demerara abyssal plain have been surveyed during the GUYAPLAC cruise, collecting multibeam bathymetric data, backscatter imagery, 3.5 kHz echograms and 6-channel seismic profiles. The study area is divided into three domains: the shallow Demerara plateau, the Guiana slope and rise, and the Demerara abyssal plain. The Demerara plateau displays multi-scale slope instabilities from huge deep-seated collapses of the whole margin to surficial creeping folds and recent slumps. Giant elongated pockmarks have been also observed for the first time in this area. Fluid escape is common everywhere on the plateau and probably enhances slope instability. On the Guiana slope and rise, large stacked lobate masses have been identified testifying to repetitive failure events. Fluid escape is

V. Gaullier (✉), L. Loncke, and F. Carol
Laboratoire IMAGES – E.A. 4218, Université de Perpignan Via Domitia, 52 Avenue Paul Alduy, 66860 Perpignan Cedex, France
e-mail: gaullier@univ-perp.fr

L. Droz
UMR-CNRS 6538, IUEM, Place Nicolas Copernic, 29280 Plouzané, France

C. Basile
Laboratoire de Géodynamique des Chaînes Alpines, UMR-CNRS 5025, Observatoire des Sciences de l'Univers de Grenoble, Université Joseph Fourier, Maison des Géosciences, 1381 rue de la Piscine, 38400 St. Martin d'Hères, France

A. Maillard
LMTG, Université UPS (SVT-OMP), 14 Avenue Edouard Belin, 31400 Toulouse, France

M. Patriat, W.R. Roest, and B. Loubrieu
IFREMER, Géosciences Marines, BP70, 29280 Plouzané, France

L. Folens
Laboratoire Géosystèmes, UMR 8157, Université des Sciences et Technologies de Lille 1, Cité Scientifique, Bâtiment SN5, 59655 Villeneuve d'Ascq Cedex, France

also ubiquitous there, suggesting a dewatering of debris flows due to sediment loading. Two main types of sedimentary structures are observed on the Demerara Abyssal Plain: small meandering channels of the Amazon Fan at its eastern edge and sediment waves at its western edge, along the foot of Demerara continental slope.

1   Introduction

Slope instability on continental margins needs further study to improve our understanding of the mechanisms that trigger it and the resulting natural hazards (e.g. damages to deep-water infrastructures, tsunamis and their impact on human population). A better understanding of the triggering mechanisms of slope instabilities that are capable of mobilizing up to several hundred cubic kilometers of sediments, represents an important scientific challenge because these events have a direct influence on the morphology and evolution of margins and oceans (Amblas et al. 2004; Canals et al. 2004; Leynaud et al. 2009; and references therein). Although shear margins represent ~30% of rifted margins around the world, yet few studies have been dedicated to the characterization of mass-movement processes along these margins that display specific structurally-controlled seafloor morphology (and especially a very steep ocean-continent transition). The aim of this study is to investigate slope instability along the transform portions of the French Guiana margin and, in the future, to try to highlight the impact of the structural inheritance on these mass movements.

2   Geological Setting

The study area is located in the western Equatorial Atlantic Ocean, on the French Guiana margin, which is characterized by a broad continental shelf and a steep continental slope that is interrupted at mid-depths along the northern part of the study area by the 1,000–2,000 m deep Demerara plateau (Fig. 1). The Guiana margin is fringed by the Demerara abyssal plain off the northern part of the study area and the distal part of the Amazon Fan to the south. The study area has been structured first by the opening of the Central Atlantic during Early Jurassic times, then by the opening of the Equatorial Atlantic at the end of Early Cretaceous, along a main transform zone (Gouyet 1988; Unternehr et al. 1988; Greenroyd et al. 2008). The studied margin therefore comprises transform and divergent segments
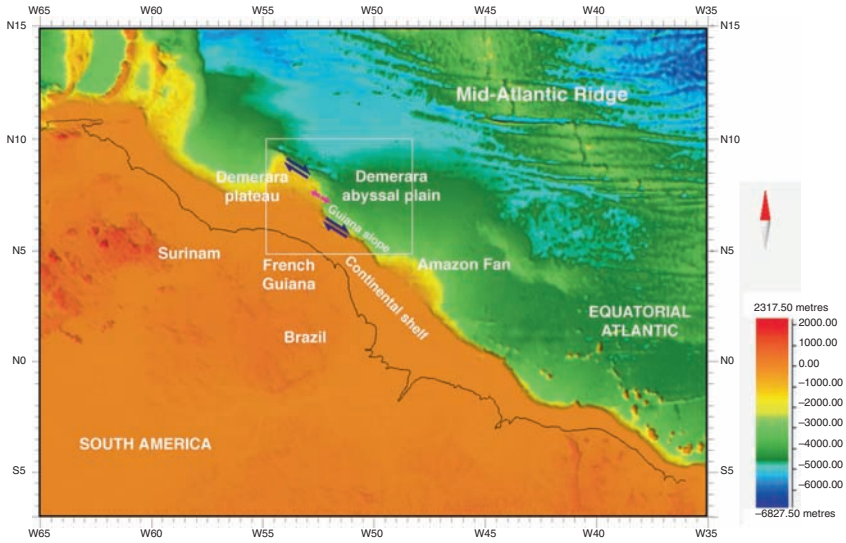
Fig. 1 Location of the study area (*white box*) situated in the western Equatorial Atlantic Ocean (Bathymetric map modified http://www.ngdc.noaa.gov, 2006). The blue and pink arrows indicate respectively the shear and divergent segments of the studied margin (Gouyet 1988; Greenroyd et al. 2008)

(Fig. 1). On the Demerara plateau, the post-rift sedimentation consists of successive wedges prograding from the continental shelf, with a maximum total thickness of 6 km at the foot of the upper continental slope. Presently, the Guiana margin is located between two major sedimentary sources, the Amazon and the Orinoco Rivers. In the abyssal plain, sedimentary thicknesses drastically increase southeastwards (i.e. towards the Amazon turbidite system (Patriat et al. 2005).

3 Dataset and Methodology

The French Guiana margin and the adjacent Demerara abyssal plain were surveyed during the GUYAPLAC cruise onboard the R/V l'Atalante (2003; Fig. 2), as a part of the EXTRAPLAC French Program (Ifremer-IFP–SHOM-IPEV). The dataset comprises: (1) EM12-Simrad multibeam bathymetry and backscatter imagery; (2) 3.5 kHz echograms with an average penetration of 50 m below seafloor; and (3) 6-channel seismic profiles. All data were acquired at a speed of 8 knots.

Bathymetric data have been processed using CARAIBES software developed by IFREMER using a 250 m resolution grid. Additional processing has been performed on data from the Demerara plateau at a 125 m resolution grid. The 3.5 kHz data have been used to produce an echo-character classification on the basis of
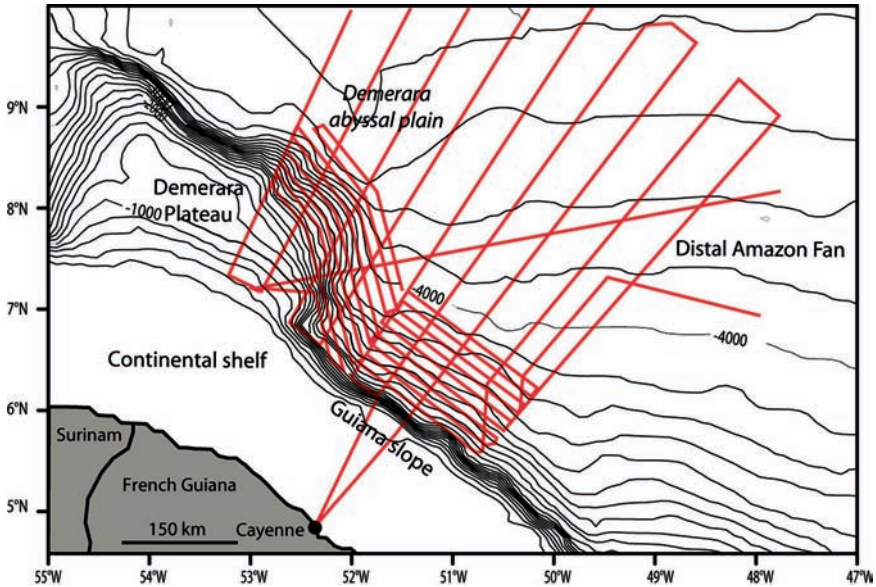
Fig. 2 Dataset of swath bathymetry, backscatter imagery, 3.5 kHz echograms and 6-channel seismic reflection profiles acquired during the GUYAPLAC cruise (2003, *red lines*)

(i) acoustic penetration and continuity of bottom and sub-bottom reflectors; (ii) micro-topography of the seafloor; and (iii) internal structures. The combination of the bathymetric and 3.5 kHz analyses allowed identification and characterization of the main sedimentary processes in the study area.

4 Results

The combined analyses of EM12-Simrad multibeam bathymetry and 3.5 kHz echograms revealed the detailed morphology of the French Guiana margin and the main sedimentary processes that have recently shaped this area (Loncke et al. 2009). Three main morphostructural domains have been identified: (1) the Demerara abyssal plain seaward; (2) the Guiana slope and rise to the South; and (3) the Demerara plateau in the western part of the study area (Fig. 3).

4.1 Demerara Abyssal Plain

This part of the study area, with water depths ranging from 4,000 to 4,800 m, is less well-imaged by our dataset than the slope domains but is characterized at its
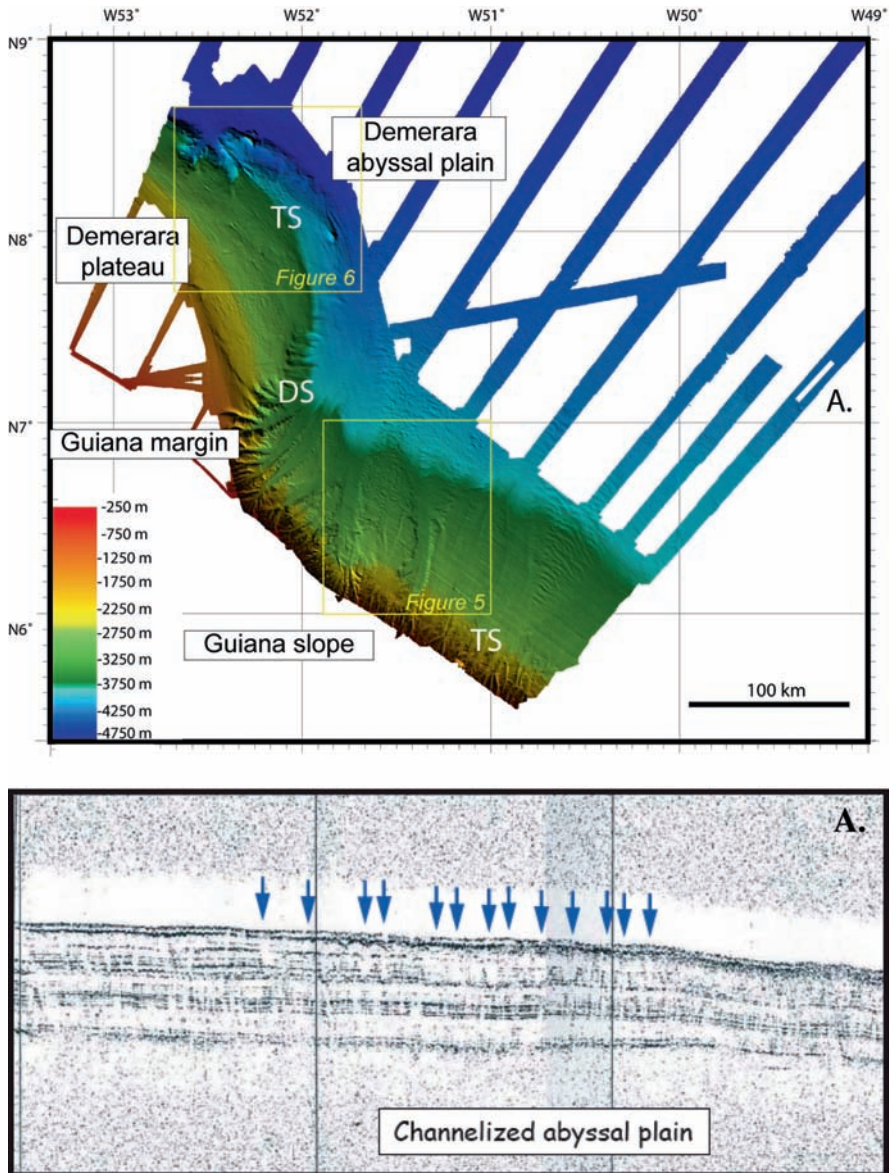
Fig. 3 EM12-Simrad color shaded bathymetric map of the French Guiana transform margin and adjacent Demerara abyssal plain (GUYAPLAC data). TS and DS correspond to transform and divergent segments of the study area. The 3.5 kHz excerpt (A) illustrates the fluid escape structures observed in the abyssal plain

eastern edge by small meandering channels belonging to the Amazon Fan and at its western edge, along the foot of Demerara continental slope, by sediment waves probably created by contour currents (Fig. 4). The abyssal plain is also affected by
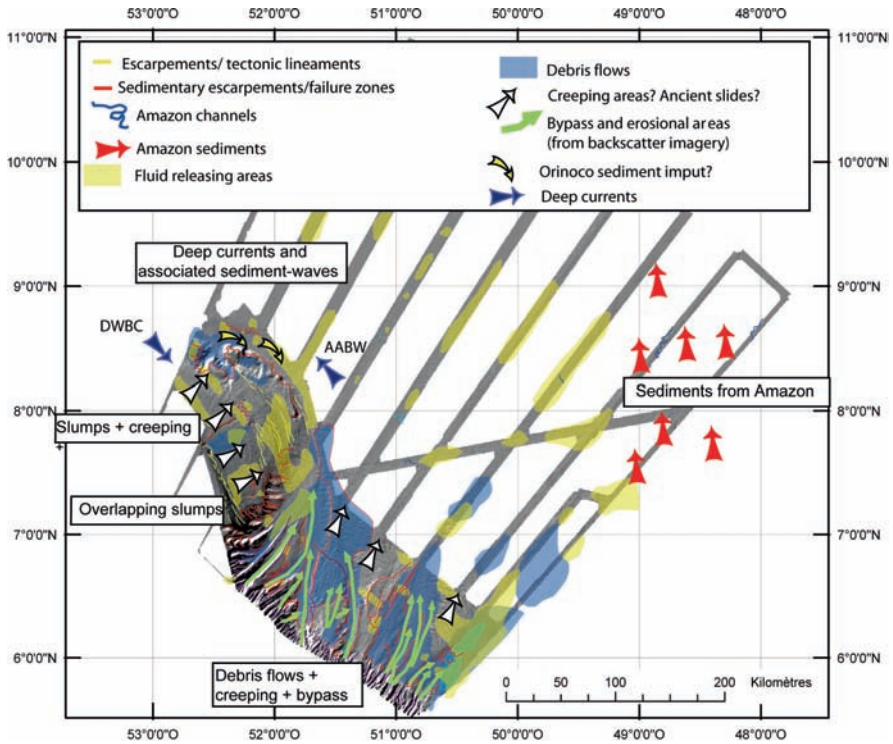
Fig. 4 Synthesis map of sedimentary processes and distribution of fluids (*in yellow*) deduced from the swath-bathymetry, backscatter imagery and 3.5 kHz echo-character mapping (Loncke et al. 2009)

numerous fluid escape structures (Fig. 3a, see also Loncke et al. 2009 for more details and examples of 3.5 kHz profiles).

4.2 Guiana Slope and Rise (Transform Segment)

The NW-SE oriented Guiana continental slope belongs to a transform margin segment (Figs. 1 and 3). The upper slope (down to 2,000 m water depth) is very steep and gullied by numerous sub-parallel canyons (Fig. 3). Downslope, the drainage network merges into a few wide (up to 5 km) U-shaped active valleys (Fig. 5). The continental rise shows several overlapping lobate masses with rough or folded surfaces that are interpreted to be mass-transport deposits (Figs. 3 through 5).

For example, the Fig. 5 shows an ancient N-S-elongated debris flow cut on both sides by two active submarine valleys and eroded on top by a network of furrows. The echo-character mapping confirms the presence of several large stacked recent mass-movement deposits (transparent, chaotic and undulating-bedded echo-types),
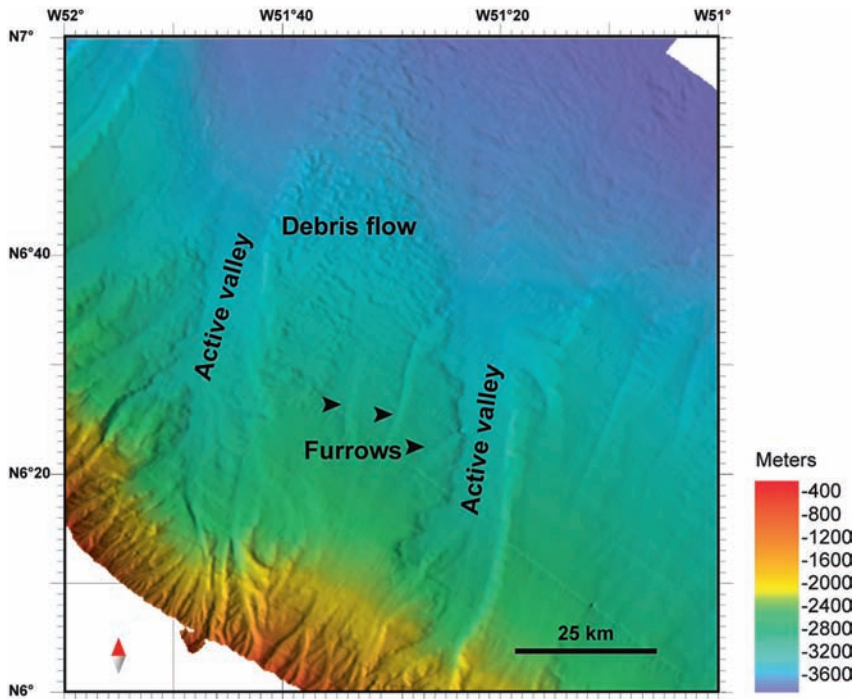
Fig. 5 Color shaded (260° azimuth, 44° elevation) bathymetric zoom focused on the Guiana slope showing large debris flow cut by active valleys (see location on Fig. 3)

testifying to repetitive destabilization events of this entire transform segment (Fig. 4). In this area, fluid or gas escape structures are frequently associated with buried transparent debris flow deposits, suggesting dewatering due to sediment loading. This dewatering process can later activate creeping of the sediments, as it has been observed on the Nile and Congo Fans (Bayon et al. 2009; Gay et al. 2004).

4.3 Demerara Plateau

The Demerara plateau is delineated by two NW-SE and N-S trending borders corresponding to the transform and divergent segments of this part of the Guiana margin (Fig. 3). The N-S divergent border is quite steep and deeply cut by canyons and failure scars, while the NW-SE transform segment is smoother and less dissected except at the northernmost end (Fig. 6). The Demerara plateau dips seaward and presents a segmented morphology with at least four "en échelon" NNW-SSE trending (i.e. parallel to the initial shear direction) slope breaks giving a "stair" aspect to the plateau (Figs. 3 and 6). These NNW-SSE structural steps seem to correspond to eastward collapses of wide blocks. On 3.5 kHz profiles (~100 km
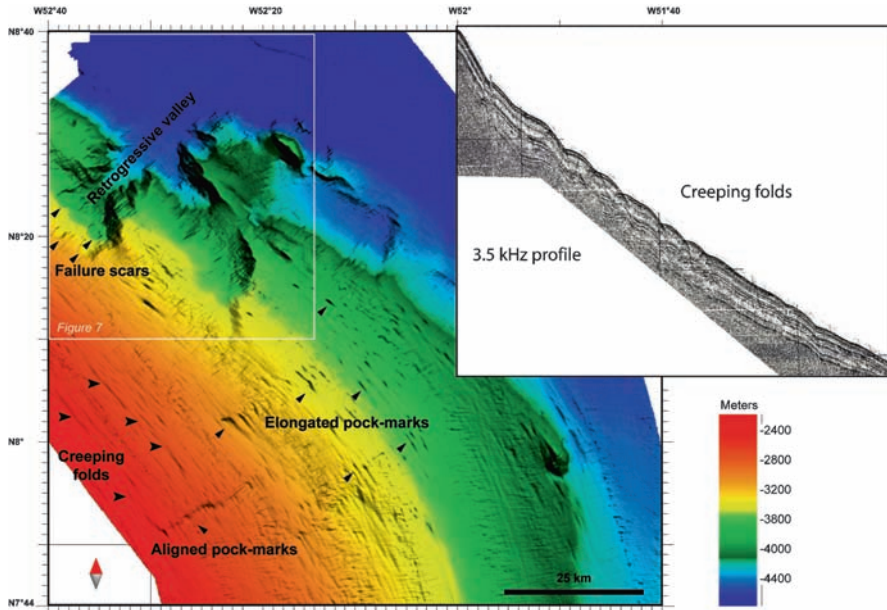
Fig. 6 Color shaded (50° azimuth, 56° elevation) bathymetric zoom focused on the Demerara plateau illustrating the rough seafloor morphology and the pock-mark field described in the text. The 3.5 kHz profile illustrates in section the creeping folds observed on the Demerara plateau

long, Loncke et al. 2009), slumps initiate upslope along the uppermost NNW-SSE slope break. Downslope, these slumps evolve to folded sediments that can correspond to compressive toe of slumps or creeping features. The sediments then thin distally into a rough to transparent mass sometimes showing seismic wipe-outs. At a deeper scale, seismic data show that this part of the margin has undergone repeated slope failure creating deep massive collapses (numerous overlapping transparent masses rooted at about 0.5 s two-way travel time below seafloor, Loncke et al. 2009). The plateau also displays a very rough surface with folds perpendicular to the slope direction probably related to creeping processes as testified by 3.5 kHz data (Fig. 6 insert).

More surprisingly, very numerous circular, elongated and/or aligned depressions have been observed on the Demerara plateau. We attribute these features, which are correlated to high reflectivity patches, to pockmarks. Some of them reach 2 km in diameter and 100 m in depth. The elongation of these features may be due to a re-shaping by the DWDC (Deep Western Boundary Current, Dengler et al. 2004). Seismic wipe-outs are also identified on the 3.5 kHz echograms all over the plateau and underline the importance of the fluid and gas discharge in this area. At the northern end of the study area, the edge of the Demerara plateau is incised by a system of canyons, that have arcuate scarps at their heads and along their flanks (Figs. 6 and 7). Downslope of these scarps the canyon floors are covered by debris flow deposits (Fig. 4).
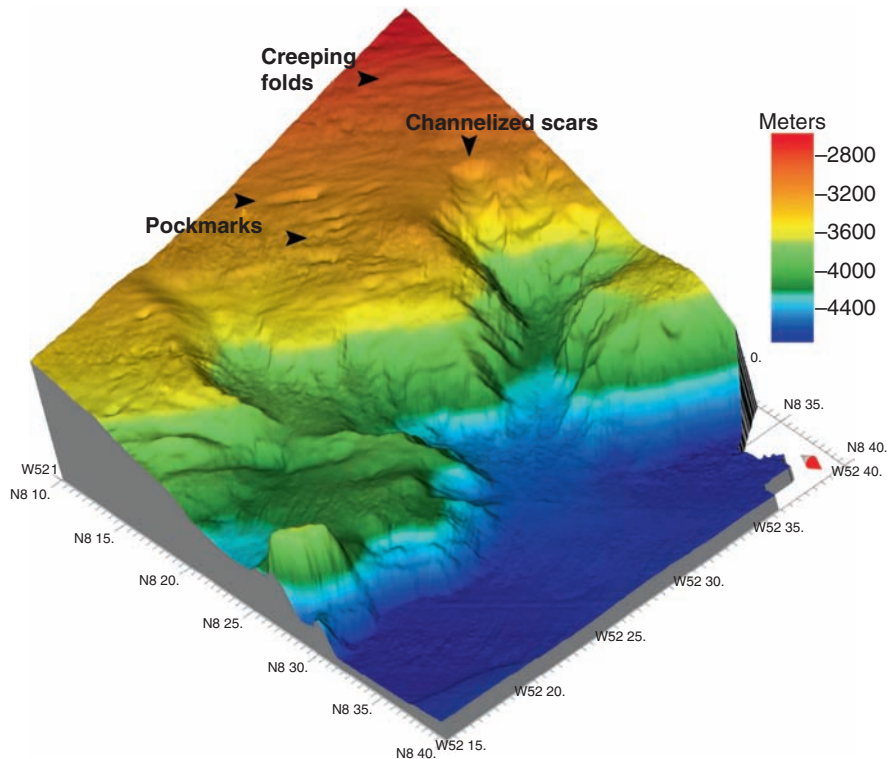
Fig. 7 3D view of the northern flank of the Demerara plateau showing the canyon network. Note the channelized scars, the creeping features and pockmarks described in the text (45° azimuth, 35° elevation, vertical exaggeration: 10)

5   Discussion and Conclusions

The dataset emphasizes the importance of slope instability in shaping the French Guiana transform margin. Sizes and styles of these mass-movements differ between the studied sectors:

- The Guiana slope and rise (transform segment), south of the Demerara Plateau, are mainly affected by huge and successive mass-movements, with slope failures generating large debris flows, sometimes buried and reworked by creeping processes.
- The whole Demerara plateau is affected by multi-scale mass-movement processes. The rough surface of the plateau is mainly deformed by creeping folds perpendicular to the slope and pockmarks. At a deeper scale, study in progress (Basile et al. 2009) shows repetitive slumping creating seaward collapse of the upper 500 m of sediments. The driving mechanism seems to be the tilting of the plateau in relation with increasing subsidence northeastward (Loncke et al. 2009). This tilting may allow the upper part of the sedimentary section to glide on décollements

sub-parallel to the bedding. The northern part of the Demerara plateau is mainly affected by small valley networks and debris flows. The lack of massive failure deposits probably indicates that the slow sliding on the plateau did not evolve, at least recently, in huge catastrophic events. Another remarkable characteristic of the study area is the abundance of circular and elongated bathymetric depressions corresponding to pockmarks, on the margin and in the abyssal plain.

Fluid escape features are also documented on 3.5 kHz echograms. Our dataset does not allow any speculation concerning the origin of the fluids, but good candidates could be the Black Shales or Cretaceous organic-rich layers on the Demerara Plateau, as suggested by Erbacher et al. (2004). In any case, these fluid escape structures seem to be closely related with slope instabilities, either along bounding faults acting as drains, or by surficial dewatering of debris flows. Whether the deformation observed at the surface is the imprint of ancient events or active features is still unclear. Given the freshness of deformations and the abundance of pockmarks, we believe that the seaward creeping processes experienced by the whole Demerara plateau are active today. Future work will be dedicated to a better understanding of the relations between structural inheritance (i.e. transform context), slope instability and fluid escape.

References

Amblàs D, Canals M, Lastras G, Berné S, Loubrieu B (2004) Imaging the seascapes of the Mediterranean. Oceanogr 17:144–155

Basile C, Maillard A, Patriat M, Roest W, Loncke L, Gaullier V (2009) Structure of Demerara plateau: Syn- and post-rift deformation at the intersection of transform and divergent margin segments. EGU General Assembly (2009), Vienna, Austria, 19–24 April 2009, Geophys Res Abst 11

Bayon G, Loncke L, Dupré S, Caprais J-C, Ducassou E, Duperron S, Etoubleau J, Foucher J-P, Fouquet Y, Gontharet S, Henderson G-M, Huguen C, Klaucke I, Mascle A, Migeon S, Olu-Le Roy K, Ondréas H, Pierre C, Sibuet M, Stadnitskaia A, Woodside J-M (2009) Multi-disciplinary investigation of fluid seepage on an unstable margin: the case of the Central Nile deep sea fan. Mar Geol 261:92–104, doi:10.1016/j.margeo.2008.10.008

Canals M, Lastras G, Urgeles R, Casamor J-L, Mienert J, Cattaneo A, De Batist M, Haflidason H, Imbo Y, Laberg J-S, Locat J, Long D, Longva O, Masson D, Sultan N, Trincardi F, Bryn P (2004) Slope failure dynamics and impacts from seafloor and shallow sub-seafloor geophysical data: case studies from the COSTA project. Mar Geol 213:9–72

Dengler M, Schott FA, Eden C, Brandt P, Fischer J, Zantopp RJ (2004) Break up of the Atlantic deep western boundary current into eddies at 8°S. Nature 432:1018–1020

Erbacher J, Mosher DC, Malone MJ et al. (2004) Proc of the Ocean Drilling Program, Init Rpts 207:94

Gay A, Lopez M, Cochonat P, Sermondadaz G (2004) Polygonal faults-furrows system related to early stages of compaction – upper Miocene to present sediments of the Lower Congo Basin. Basin Res 16:101–116

Greenroyd CJ, Peirce C, Rodger M, Watts AB, Hobbs RW (2008) Do fracture zones define continental margin segmentation? – Evidence from the French Guinan margin. Earth and Planetary Science Letters 272:553–566.

Gouyet S (1988) Evolution tectono-sédimentaire des marges guyanaise et Nord-Brésilienne au cours de l'ouverture de l'Atlantique Sud. PhD Thesis, univ Pau et des pays de l'Adour, 374 http://www.ngdc.noaa.gov, U.S. Department of Commerce, National Oceanic and Atmospheric Administration, National Geophysical Data Center, 2006. 2-minute Gridded Global Relief Data (ETOPO2v2).

Leynaud D, Mienert J, Vanneste M (2009) Submarine mass movements on glaciated and non-glaciated European continental margins: A review of triggering mechanisms and preconditions to failure. Marine and Petroleum Geology, Thematic set on: "New insights on slope instabilities from recent studies within the French Margin Program GDR Marges", 26:618–632.

Loncke L, Droz L, Gaullier V, Basile C, Roest W, Patriat M, et al (2009) Slope instabilities from echo-character mapping along the French Guiana transform margin and Demerara abyssal plain. Marine and Petroleum Geology, Thematic set on: "New insights on slope instabilities from recent studies within the French Margin Program GDR Marges", Gaullier V and Vendeville B (eds.), 26:711–723.

Patriat M, Loubrieu B, Vially R, Roest WR (2005) The Guyaplac survey, off French Guyana, American Geophysical Union, Fall Meeting 2005, Abstract #T13D-0505.

Unternehr P, Curie D, Olivet JL, Goslin J, Beuzart P (1988) South Atlantic fits and intraplate boundaries in Africa and South America. Tectonophysics 155:169–179.

Megaslides in the Foz do Amazonas Basin, Brazilian Equatorial Margin

C.G. Silva, E. Araújo, A.T. Reis, R. Perovano, C. Gorini, B.C. Vendeville, and N. Albuquerque

Abstract Recent analysis of multi-channel seismic data provides new evidence that mass-transport deposits have been recurrent elements in the Foz do Amazonas Basin during the Middle-Miocene to Recent. In regions located to the NW and SE of the Amazon Deep-sea Fan, mass movement processes remobilized thick siliciclastic series (up to 1,000 m) as huge megaslide deposits over areas up to 90,000 km^2. The Pará-Maranhão Megaslide in the SE shows a displaced block (>10^4 km^2) in association with large mass transport deposits covering an area of more than 10^5 km^2. These deposits are distally bounded by thrust faults, which propagate upwards eventually offsetting the sea floor. In addition, NW of the deep-sea fan, the Amapá Megaslide Complex presents a series of recurrent megaslides in the stratigraphic succession, bounded by listric normal faults and tear zones on the upper slope. Associated remobilized deposits extend from more than 300 km downslope, partially involving the upper channel-levee units of the Amazon Deep-sea Fan.

C.G. Silva (✉), E. Araújo, R. Perovano, and N. Albuquerque
Universidade Federal Fluminense, Departamento de Geologia, Av. Gen. Milton Tavares de Souza, s.n., Niterói, RJ, CEP: 24210–346, Brazil
e-mail: cleverson@igeo.uff.br

A.T. Reis
Universidade do Estado do Rio de Janeiro, Faculdade de Oceanografia, Rua São Francisco Xavier, 524, 4° Andar, bl E, Rio de Janeiro/RJ. CEP: 20.550–013, Brazil

C. Gorini
Université Pierre & Marie Curie, Paris VI,.Laboratoire de Tectonique et Modélisation des Bassins Sédimentaires, UMR 7072, Place Jussieu, Case 117 tour 46–00, 75252 Paris, Cedex 05, France

B.C. Vendeville
Université de Lille1, 4 UMR 8157 Géosystèmes, Bat. SN5, USTL, 59655, Villeneuve d'Ascq Cedex – France

1   Introduction

The Foz do Amazonas Basin on the Brazilian Equatorial Margin (Fig. 1) has been influenced by immense sedimentary fluxes coming from the Amazon River, resulting in the seaward progradation of the margin and the deposition of the Amazon fan. The submarine fan is a >10 km thick turbiditic complex that started to develop during the Upper Miocene (Silva et al. 1999). Such a sedimentary context resulted in a rather smooth central basin, while to the NW and SE of the fan the margin is narrower and exhibits steep slope gradients.

Submarine mass movements and associated deposits are important elements in the Foz do Amazonas Basin. In the Amazon fan, exceptionally high sedimentation rates can induce submarine failures and sediment fluxes that contribute to the sedimentary evolution and architecture of the deep-sea fan (Damuth and Embley 1981;
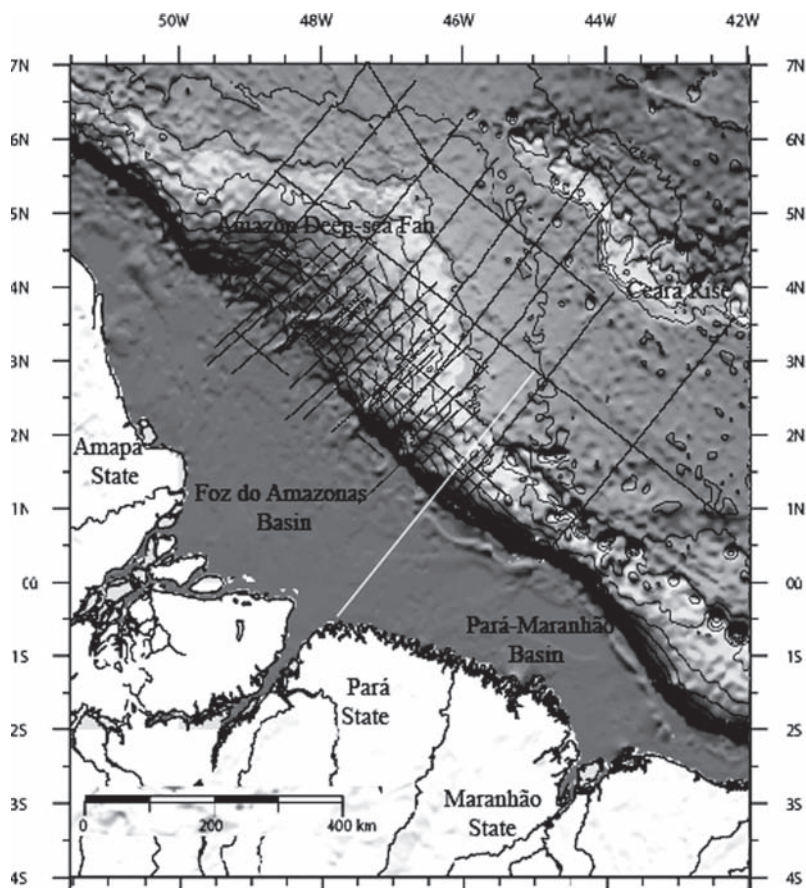
Fig. 1 Location map. Regional bathymetry (100 m and every 1,000 m) and seismic dataset used

Damuth et al. 1988; Piper et al. 1997; Maslin and Mikkelsen 1997; Pirmez and Imran 2003; Maslin et al. 2005).

The scientific literature, on the other hand, does not provide examples of studies dealing with the sedimentary series along the steep NW and SE slope segments of the Foz do Amazonas Basin margin. We used regional seismic lines to investigate features of gravitational collapse occurring along such steep margins, focusing on the recognition and description of extensive megaslides.

1.1 Database and Methods

The 2D multi-channel seismic data (Fig. 1) include approximately 15,000 km of seismic-reflection profiles. The Brazilian Navy and the Brazilian Petroleum Exploration Company (Petrobras) collected part of the data. This data set penetrates to a maximum of 13 s (TWT) and shows 5 to 10 m of vertical resolution. Geophysical survey companies operating in Brazil (FUGRO and GAIA) provided additional industrial seismic data of up to 9 s of signal penetration and the same vertical resolution. For the seismic interpretation we used SMT (8.0) Kingdom Suite®.

Regional bathymetric data are from ETOPO1 (Smith and Sandwell 1997) and higher-resolution bathymetric data on the Upper to Middle Amazon fan were compiled by the Brazilian Navy from different sources, including Petrobras, the Geophysical Data System – GEODAS (www.ngdc.noaa.gov/mgg/geodas) and from the General Bathymetric Charts of the Oceans – GEBCO (www.gebco.net).

1.2 Geological Setting

Open marine conditions in the Foz do Amazonas Basin started at the end of the Albian, with the dominance of siliciclastic sedimentation during the Upper Cretaceous (Brandão and Feijó 1994; Figueiredo et al. 2007). A carbonate platform installed during Upper Paleocene times prevailed during the Paleogene and part of the Neogene. An increased rate of the Andean uplift since the Upper Miocene (10.7 Ma – Tortonian) was responsible for increased siliciclastic input to the Amazon River that finally led to the formation of the Amazon fan (Hoorn et al. 1995; Figueiredo et al. 2007).

The Amazon fan occupies an area of approximately 160,000 km^2, from the continental shelf break down to 4,800 m water depth (Damuth et al. 1988). With a total of 10 km of sedimentary thickness deposited in 10 Ma, the average sedimentation rate is 1 mm/year (Cobbold et al. 2004). However, sedimentation rates of 0.05 to 0.1 mm/year during interglacial periods and 50 mm/year during glacial periods have been reported (Mikkelsen et al. 1997; Piper et al. 1997).

The sedimentary sequence of the Amazon fan glides along multiple detachment surfaces in a linked extensional-and-compressional system (Da Silva 2008). The extensional domain is located on the outer continental shelf and upper slope (up to

500 m deep), consisting of predominantly seaward-dipping normal listric faults. Distally, folds and thrusts running along the upper submarine fan (up to 2,000 m) characterize the compressional domain. Thrust structures can reach the sea floor, forming scarps as high as 500 m (Araújo 2008).

Previous research works on mass transport deposits in the Foz do Amazonas Basin have been focused on the Amazon fan (Damuth and Embley 1981; Piper et al. 1997). Recurrent mass-wasting events and mass-movement deposits are interbeded with channel-levee deposits (Damuth et al. 1983, 1988; Maslin and Mikkelsen 1997; Flood and Piper 1997; Piper et al. 1997; Pirmez and Imran 2003; Maslin et al. 2005). Each deposit can result in remobilized sediment masses (slumps, slides and debris flows) as large as 15,000 km^2 and reaching thicknesses of up to 200 m. Most of the surficial and subsurface mass transport deposits are recent, dated as either 41–45 or 35–37 ka, and formed during Upper Quaternary low sea-level stands (Piper et al. 1997; Maslin and Mikkelsen 1997; Maslin et al. 2005). Some even younger slides (11 to 14 ka) formed during the last sea-level rise (Maslin and Mikkelsen 1997; Maslin et al. 2005). Piper et al. (1997) and Maslin and Mikkelsen (1997) consider that during low seal-level stands, gas hydrates destabilization, higher sedimentation rates and erosion of canyon heads are the principal causes of mass movement initiation. During relative sea-level rise and high stands the rise of the hydrostatic pressure and the migration of depocenters would generate instabilities. Piper et al. (1997) cited the gravity tectonics observed in the Amazon fan as another possible cause; however, the authors did not explore this hypothesis.

2   Results

The Amazon fan sedimentation greatly affects the morphology of the Brazilian Equatorial Margin. The steep gradients (3° to 5.6°) observed on the continental slope to the NW and SE of the fan are totally subdued by the thick sedimentary sequences responsible for the fan construction (average gradients on the upper deep-sea fan are in the order of 0.8°). In the steep continental slope to the NW and SE of the Amazon fan, mass transport mobilized thick siliciclastic series (up to 1,000 m, considering a layer sound velocity of 1,800 m/s for the upper 2 s of the seismic sections) as megaslides deposits (Fig. 2) over areas up to 90,000 km^2 that are for the first time mapped in this work. These deposits are considerably thicker than the mass transport deposits mapped on the Amazon fan (Damuth and Embley 1981; Piper et al. 1997; Araújo 2008).

2.1   *The Pará-Maranhão Megaslide*

The shelf break to the SE of the deep-sea fan occurs at 100 m water depth and the upper slope gradients are in the order of 3° to 3.5°. On the upper slope, an abrupt erosional scarp (maximum vertical relief of 1,000 m), continuous along 180 km, is the headwall scarp of megaslide deposits, which extend downslope over approximately
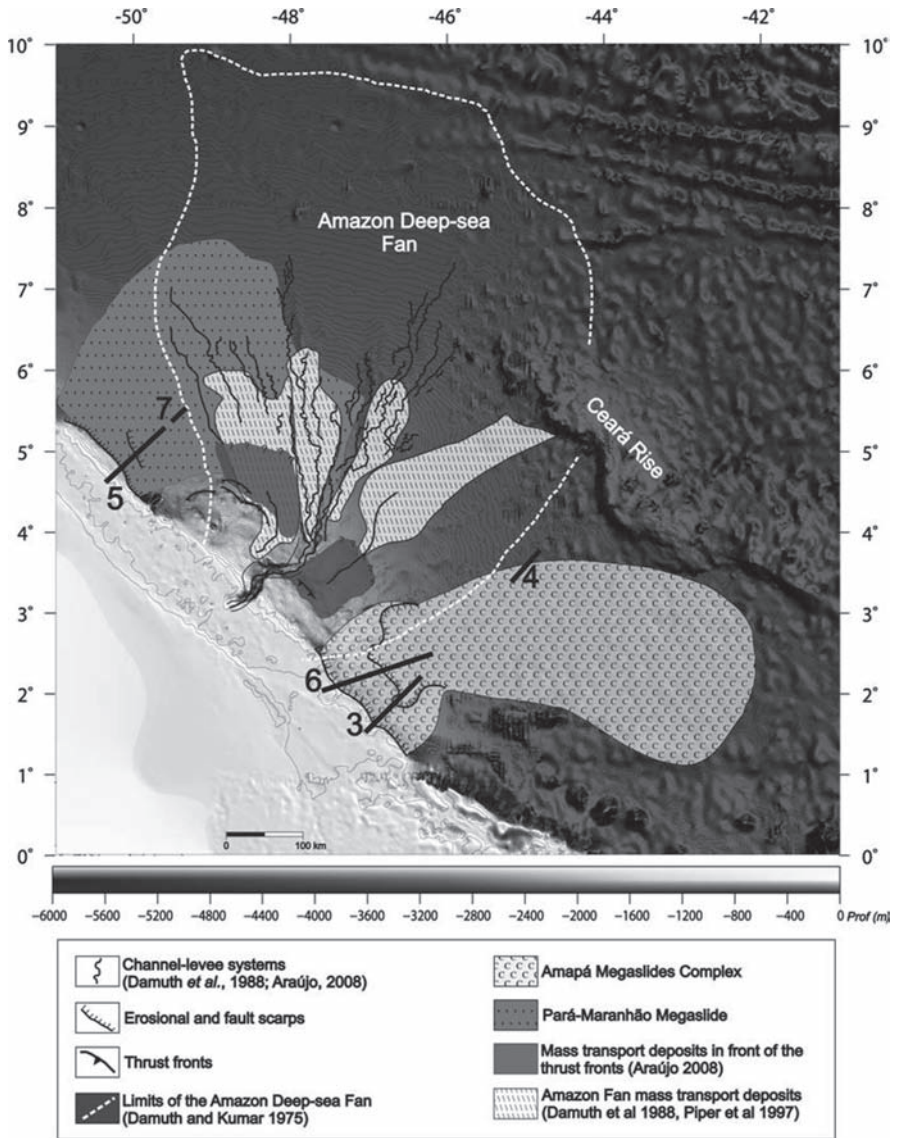
Fig. 2 Mass transport deposits and megaslides in the Foz do Amazonas Basin. Numbers indicate locations of Figs. 3–7

600 km. The megaslide has a maximum width of 200 km, covers an estimated area of 90,000 km^2 comprising about 60,000 km^3 of remobilized sediments. This megaslide was named *Pará-Maranhão Megalisde* since a great part of it extends to the neighbor Pará-Maranhão basin (Figs. 1 and 2).

Downslope from the headwall scarp, slided blocks extend over 12,500 km^2, having a thickness around 1,000 m. These blocks are faulted (normal listric faults) and rotated

(Fig. 3). The downslope limit of the displaced blocks is located at around 2,100 m deep, where there is another prominent scarp, with 700 m of vertical relief and extending laterally along 260 km (Fig. 2). Further downslope the allochtonous mass has a chaotic-to-transparent seismic facies, with a few preserved blocks showing parallel seismic reflectors. An upper unit (150 to 200 m) of parallel discontinuous reflectors still preserves the original layers; however, irregularities of the seafloor suggest a continuous activity of the mass transport processes and associated deformation (Fig. 3).

Both the headwall scarp and the displaced blocks are the source area for considerably more deformed mass transport deposits occurring downslope. These deposits are internally chaotic, suggesting debris flow, but locally present large displaced blocks that still maintain their internal layering (Fig. 3). These deposits extend to water depths of 3,800 m. The megaslide is laterally and frontally confined, favoring the development of a series of reverse faults rooted on detachment levels that progressively become shallower, thus decreasing the thickness of the mobilized deposits from 1,000 m to about 300 m basinward. Eventually they reach the seafloor forming pressure ridges (up to 50 m of relief) (Fig. 4).
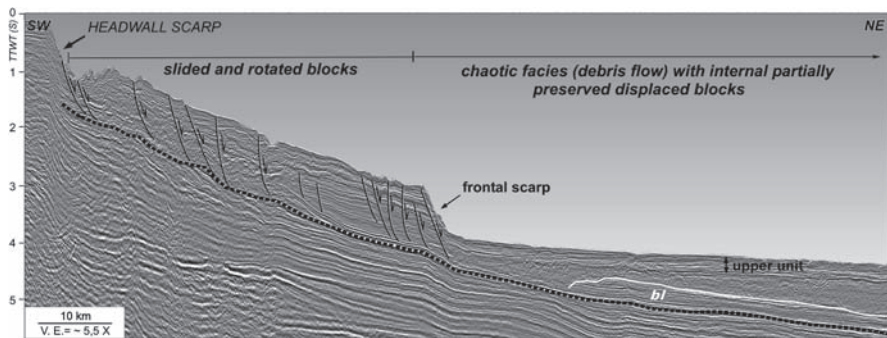
Fig. 3 Headwall scarp, displaced and rotated blocks, debris flow deposits and preserved block (*bl*) over detachment surface (*dotted line*) in the upslope portion of the Pará-Maranhão Megaslide
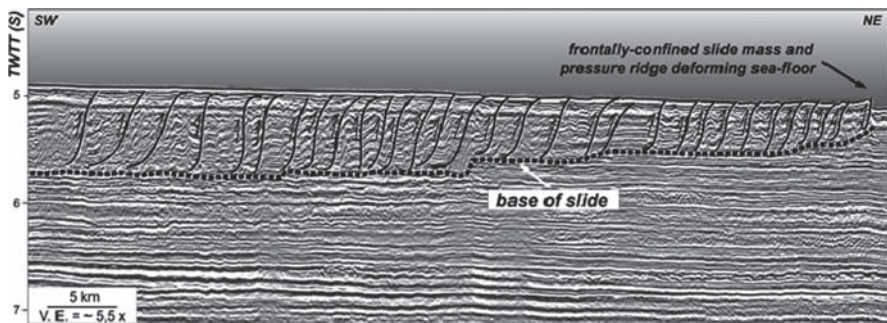
Fig. 4 Pará-Maranhão megaslide lateral confinement with reverse faults and pressure ridge

2.2   *The Amapá Megaslide Complex*

To the NW of the Amazon fan, the shelf-break is located under 200 m water deep, and the upper continental slope shows the highest local gradients in the Foz do Amazonas Basin (circa 5.5°). A continuous erosive scarp, as high as 1,800 m, extends laterally along the upper continental slope for at least 120 km (Fig. 2). Beyond 2,000 m water depths, the seafloor is again smooth, with low gradients around 0.93°, in response to the deposition in the distal portions of the Amazon fan.

The megaslide deposits mapped in this region correspond to a complex of several mass transport deposits encompassing the upper sedimentary section between 1,800 to 2,700 m thick. These successive deposits present a total estimated area of about 80,000 km², from the base of the slope (2,600 m of water depth) to a depth of about 4,000 m below sea level. Each individual deposit can vary in thickness from approximately 300 to 700 m, and present variable extensions (Fig. 5). This megaslide was named *Amapá Megaslide Complex*, after the adjacent coastal Amapá State in northern Brazil (Figs 1 and 2).

This megaslide complex starts on a headwall scarp located on the upper continental slope, where a large displaced block moved along a basal sliding surface (Fig. 5). This basal megaslide represents the first gravity collapse event in the area and is separated from the upper megaslide deposit by a thick *in situ* non-deformed unit (900 m), with layered, continuous reflectors. Above this non-deformed unit, at least five discrete megaslide deposits were recognized, each one departing from a removal scar and presenting sharp internal transitions from layered reflectors to chaotic or transparent seismic facies (Fig. 5). Further downslope the detachment
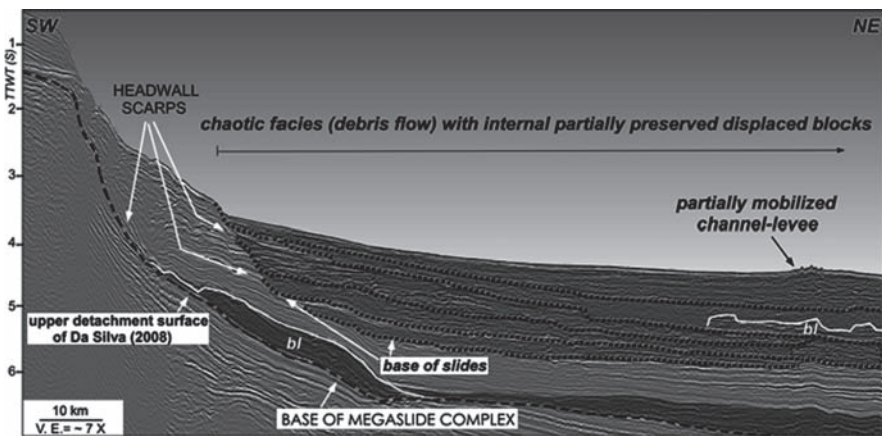
Fig. 5 Headwall scarp and upslope deposits of Amapá Megaslide Complex (*bl = preserved blocks*). Detachment surfaces (*small dashed lines*) and megaslide deposits (*darker gray*)

level shifts upward, decreasing the thicknesses of the mass transport deposits until they completely disappear in continuity with non-deformed layered reflectors. These distal domains of megaslides are still marked by prevalent, although discontinuous, layered reflectors deformed by thrusts related to frontal and lateral shortening.

3   Discussion

In contrast to mass movement deposits recognized on Amazon fan area (Damuth and Embley 1981), the Pará-Maranhão and Amapá megaslides complexes are located along portions of steep continental slopes of the Foz do Amazonas basin. The sedimentation rates in these areas are considerably lower as compared to the Amazon fan region. This may indicate that higher slope gradient is the main controlling factor to initiate mega-events of mass wasting. These megaslides are considerably larger (several 100's km long and a few 100 km's wide) and thicker (up to 1,000 m) than the mass-transport deposits recognized by Damuth and Embley (1981) and Piper et al. (1997) in the Amazon fan. Furthermore, the stratigraphic column in the Amapá and Pará-Maranhão Megaslides has recorded multiple events that, unlike the Amazon fan, are not restricted to the Upper Quaternary sedimentary section.

The Pará-Maranhão Megaslide shows 60,000 km³ of remobilized sediments, located out of the sedimentary influence of the Amazon fan. It is comparable in dimensions with other well-known megaslide such as the Storegga Slide, which has 25,000 to 35,000 km³ (Bryn et al. 2005). These scales apply to the young Pará-Maranhão Megaslide, but other older megaslides occurred deeper in the sedimentary section. On the other hand, the Amapá Megaslide Complex differs markedly from the Pará-Maranhão Megaslide, because the entire sedimentary section (1,800 to 2,700 m) was affected by a succession of megaslides. In addition the Amapá Megaslide Complex was influenced by the Amazon fan sedimentation, as observed by the presence of interlayered channel-levee systems, some of them partially remobilized by the mass-transport deposits. The thinner and more frequent episodes of mass-transport deposits that occurred in the Amapá Megaslide Complex could result from higher sedimentation rates from the Amazon fan system, leading to increased frequency of slope instabilities.

The seismic horizons along the basal detachments of each individual allochtonous mass transport deposit mapped both in the Pará-Maranhão and Amapá megaslides, present a characteristic negative polarity (Fig. 6), which may indicate fluid overpressure conditions as recognized in the Amazon fan (Silva et al. 1999; Cobbold et al. 2004; Da Silva 2008). As well as that, the regional detachment surface that serves as the basal level of both megaslide complexes laterally correlates with the regional upper detachment surface of gravity tectonics defined by Da Silva (2008) and dated as 40 Ma in the Amazon fan (Fig. 7). This stratigraphic correlation suggests that different modes of gravitational collapse that occur in the

Foz do Amazonas Basin, either in the form of gravity tectonic deformation in the Amazon fan or in the form of sediment layers disruption and mass transport in the megaslides, may reflect the regional interaction of gravitational processes of different scales and frequencies. The associated stratigraphic horizon can thus be interpreted as an impermeable regional level at basin scale, enhancing fluid overpressure, and thus potentially favoring gravitational instabilities and collapse at different domains of the Foz do Amazonas Basin.
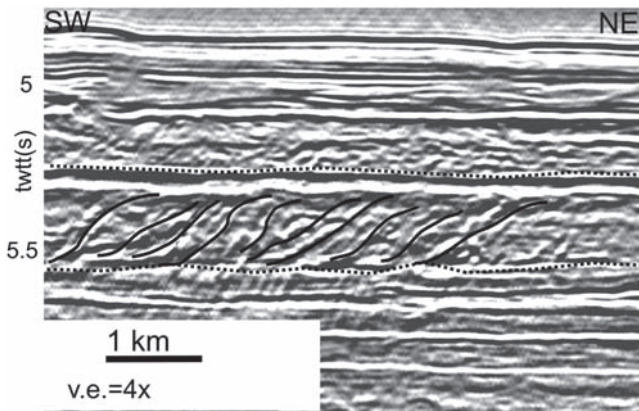
Fig. 6 Thrust sheets and reverse faults in the Amapá Megaslide Complex. Negative polarity (*white*) on the detachment surfaces (*dotted lines*) may indicate fluid overpressure
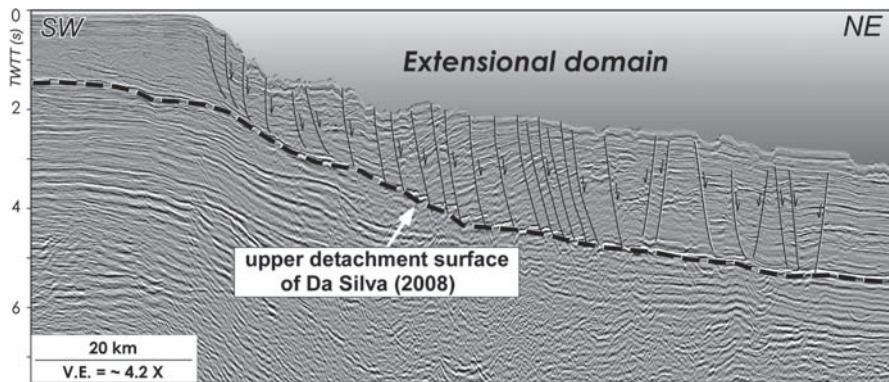
Fig. 7 Gravitational collapse over upper detachment surface in the Amazon Deep-sea Fan (Da Silva 2008). The base of Pará-Maranhão Megaslide and Amapá Megaslide Complex correlates laterally with the upper (*white dashed*) detachment surface

4   Conclusions

This study reports, for the first time, the occurrence of megaslide complexes capable of remobilizing huge allochtonous masses downslope the NW and SE slope segments of the Foz do Amazonas Basin, such as the Pará-Maranhão Megaslide and the Amapá Megaslide Complex. These megaslides have been recurrent events during the last 40 Ma, but were more frequent in the Amapá Megaslide Complex, probably because of higher sedimentation rates under the influence of the Amazon fan.

Both megaslides are located in areas of steep slopes (~3°–6°), show well-defined headwall scarps, and rotated blocks sliding along seismically well defined surfaces. Strongly deformed allochthonous masses present chaotic-to-transparent facies, interbedded laterally and vertically with non-deformed units and blocks. Thrust sheets and reverse faults, in the lateral and distal portions of the mass transport deposits, indicate laterally- and frontally-confined sediment masses, eventually developing pressure ridges that deform the seafloor.

Below both megaslides, the main base of slide correlates laterally to a regional seismic horizon that corresponds to the upper detachment surface involved in the Amazon fan gravity tectonics. This correlation suggests that the same surface acted as an impermeable layer, favoring fluid overpressure and consequently the gravitational collapse.

References

Araújo EFS (2008) Processos de instabilidade gravitacional multiescala na bacia da Foz do Amazonas: depósitos de transporte de massa e megadeslizamentos. M.Sc. Dissertation, Universidade Federal Fluminense, Brazil

Brandão JASL, Feijó FJ (1994) Bacia da Foz do Amazonas. Bol Geoc Petrobras 8: 91–99

Bryn P, Berg K, Forsberg CF, Solheim A et al. (2005) Explaining the Storegga Slide. Mar Pet Geol 22: 11–19

Cobbold PR, Mourgues K, Boyd K (2004) Mechanism of thin-skinned detachment in the Amazon Fan: assessing the importance of fluid overpressure and hydrocarbon generation. Mar Pet Geol 21: 1013–1025

Damuth JE, Embley RW (1981) Mass-transport processes on the Amazon Cone: western equatorial Atlantic. Am Assoc Pet Geol Bull 65: 629–643

Damuth J, Kowsmann RO, Flood RD, Belderson RH, Gorini MA (1983) Age relationships of distributary channels on Amazon deep-sea fan: implications for fan growth pattern. Geology 11: 470–473

Damuth JE, Flood RD, Kowsmann RO, Belderson RH, Gorini MA (1988) Anatomy and growth pattern of Amazon deep-sea fan as revealed by long-range side-scan sonar (GLORIA) and high resolution seismic studies. Am Assoc Pet Geol Bull 72: 885–911

Da Silva RJP (2008) Colapso gravitacional e estruturação da seção marinha da bacia da Foz do Amazonas no contexto de múltiplos níveis de destacamento. M.Sc. Dissertation, Universidade Federal Fluminense, Brazil

Figueiredo JJP, Zalán PV, Soares EF (2007) Bacia da Foz do Amazonas. Boletim de Geociências da. Petrobras 15 n2: 299–309

Flood RD, Piper DJW (1997) Amazon Fan sedimentation: the relationship to equatorial climate change, continental denudation, and sea-level fluctuations. Proc Ocean Drill Prog, Sci Res doi:10.2973/odp.proc.sr.155.246.1997

Hoorn C, Guerrero J, Sarmiento GA, Lorente MA (1995) Andean tectonics as a cause for changing drainage patterns in Miocene, northern South America. Geology 23: 237–240

Maslin M, Mikkelsen N (1997) Amazon Fan mass-transport deposits and underlying interglacial deposits: age estimates and fan dynamics. Proc Ocean Drill Prog, Sci Res doi:10.2973/odp. proc.sr. 155.220.1997

Maslin M, Vilela C, Mikkelsen N, Grootes P (2005) Causes of catastrophic sediment failures of the Amazon Fan. Quat Sci Rev 24: 2180–2193

Mikkelsen N, Maslin MA, Giraudeau J, Showers WJ (1997) Biostratigraphy and sedimentation rates of the Amazon Fan. Proc Ocean Drill Prog, Sci Res doi:10.2973/odp.proc.sr.155.248.1997

Piper DJW, Pirmez PL, Manley PL, Long D, Flood RD, Normark WR, Showers W (1997) Mass-transport deposits of the Amazon Fan. Proc Ocean Drill Prog, Sci Res 155. doi:10.2973/odp. proc.sr. 155.212.1997

Pirmez C, Imran J (2003) Reconstruction of turbidity currents in Amazon Channel. Mar Pet Geol 20: 823–849

Silva SRP, Maciel RR, Severino MCG (1999) Cenozoic Tectonics of Amazon Mouth Basin. Geo-Mar Lett 18: 256–262

Smith WHF, Sandwell DT (1997) Seafloor topography from satellite altimetry and ship soundings. Science 10: 1957–1962

Detached and Shelf-Attached Mass Transport Complexes on the Magdalena Deepwater Fan

G.A. Romero-Otero, R.M. Slatt, and C. Pirmez

Abstract The Magdalena submarine fan, fed mainly by the Magdalena River, is part of a Miocene-Recent accretionary prism off the Caribbean coast of Colombia, S.A. Periodic shifts of the Magdalena River controlled the evolution of the fan. The integration of multibeam bathymetry, GLORIA images, and 2D seismic profiles reveal a series of deep-water channel systems and mass transport complexes (MTCs) on the seafloor. The MTCs were subdivided into detached and shelf-attached types. Relative timing of the detached MTC processes cannot be determined due to their local character. Four major shelf attached MTCs are described from interchannel low areas. We hypothesize that these attached MTCs began to be generated during a low stand of sea level (140–120 ka) which prompted hydrostatic pressure changes and/or gas hydrate dissolution on the slope, leading to collapse. Later processes of slope deformation and slope instability continued feeding MTC's to the interchannel lows. A southerly shift of the Magdalena River depocenter (middle Pleistocene) and abandonment of the Galerazamba region channel-levee systems coincided with the lowstand.

Keywords Mass transport complexes • submarine fan • multibeam bathymetry • GLORIA sidescan sonar • thrust belts

G.A. Romero-Otero (✉) and R.M. Slatt
Conoco Phillips School of Geology and Geophysics, The University of Oklahoma, Norman, OK, USA
e-mail: gloriaromero@ou.edu

C. Pirmez
Shell International E and P., Houston, TX, USA

1   Introduction

The combination of active margin tectonics with one of the larger fluvial sediment sources to the ocean makes the Magdalena fan an important area to understand the development of MTCs. Integration of multibeam bathymetry, GLORIA image and seismic profiles were used to characterize the MTCs on the continental slope of northern offshore Colombia. This paper documents the different submarine mass movement deposits recorded on the submarine fan, by describing the morphologies of the scarps and their related deposits. The MTC classification of Moscardelli and Wood (2008) is used because it is based on seismic observation that emphasizes the relationship between mass failures and the geomorphology of their source areas. This classification is based on three main aspects: (1) sourcing regions of MTC's, (2) geomorphological expression of MTC's on their updip part and (3) dimensions and geometries of MTC's.

1.1   Regional Setting

The Magdalena submarine fan, located offshore Colombia, S.A. (Fig. 1) is a bathymetric feature that is part of the accretionary wedge complex formed by the collision of the
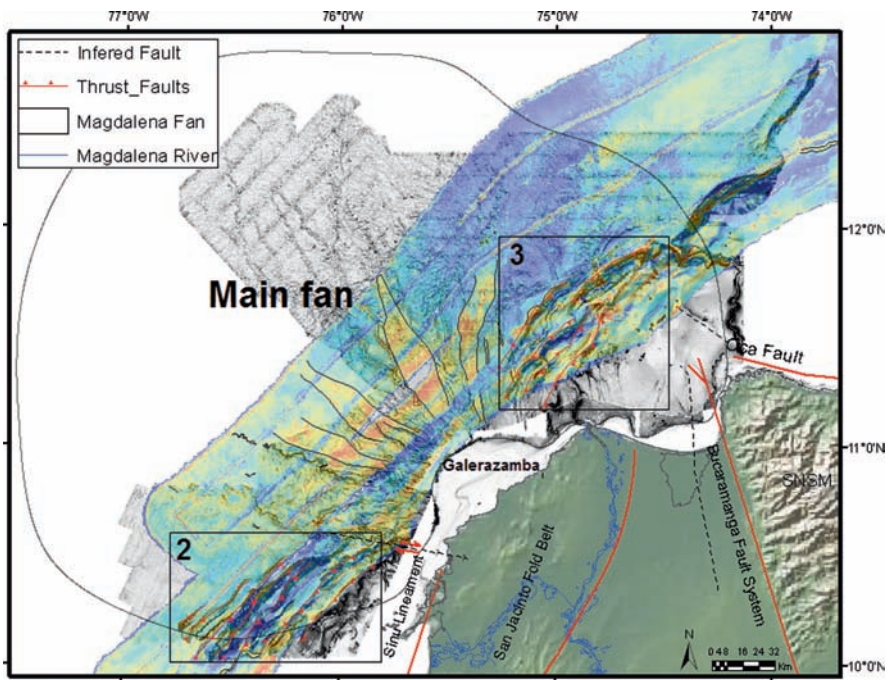
Fig. 1 Location and general structure of the area of study offshore Colombia, Northern South America. Location of Figs. 2 and 3

Caribbean and South American plates (Duque-Caro 1979; Breen 1989). Deepwater fan sedimentation started during the middle Miocene, fed by the Magdalena River, covering an area of about $68,000 km^2$, a volume of $180,000 km^3$, and extends into areas >4,000 m of water depth (Reading and Richards 1994; Kolla and Buffler 1984).

Ercilla et al. (2002) reported large MTC's with a radial distribution throughout the continental slope. Tongue-shaped mass flow deposits smooth the slope between channel systems and perpendicular to thrust ridges. They are characterized by erosive (concave) and depositional (convex) sections of the slope. The uplifting of the continental shelf, steep gradients and the high availability of uncompacted sediments in the abandoned Galerazamba area seem to have played an important role in the development of large-scale mass flows. In addition, interchannel lows formed barriers to confine the sediment flows (Estrada et al. 2005b).

The fan is subdivided into: (1) thrust deformed belts (TDB) and (2) main fan area. The deformed area includes the arcuate northeast and southwest TDB, expressed on the sea floor as ridges (Figs. 1–3). The main fan area is characterized by leveed channel systems (CLS), large-scale MTCs, and slumps scarps (Fig. 1). The eastern part of the main fan contains the oldest CLS at the sea floor (Kolla and Buffler 1984; Ercilla et al. 2002; Estrada et al. 2005a). The western part of the main fan contains younger CLS and greater influence of deformation on the slope, which clearly affected the evolution of the channels (Romero-Otero et al. submitted). The CLS are partially destroyed and cannibalized by mass-flow deposits. Although,
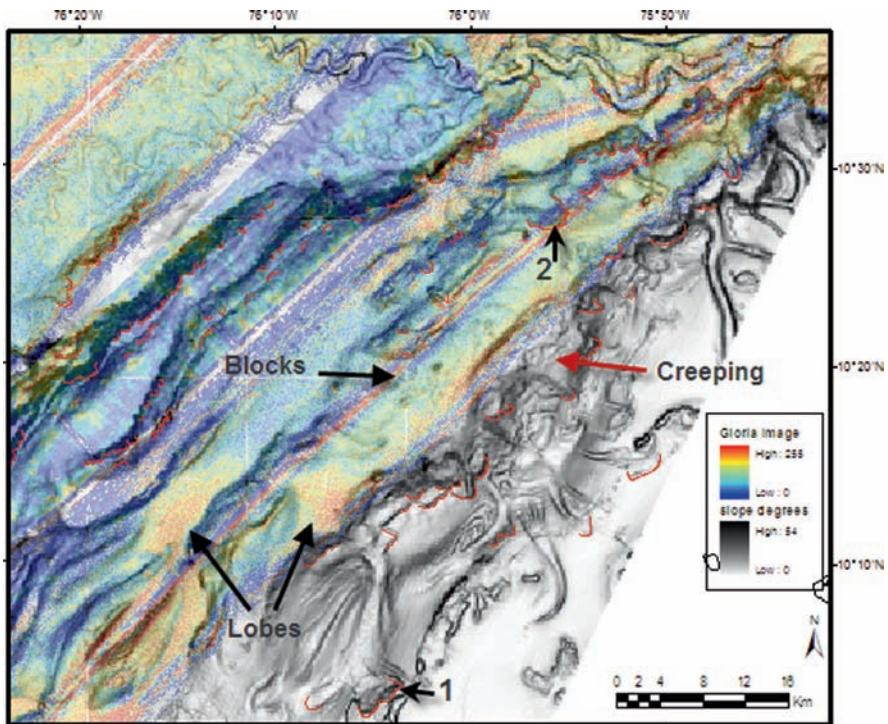
Fig. 2 Southwestern deformed belt. Arcuate scarps in red. Numbers are scarps in Table 1
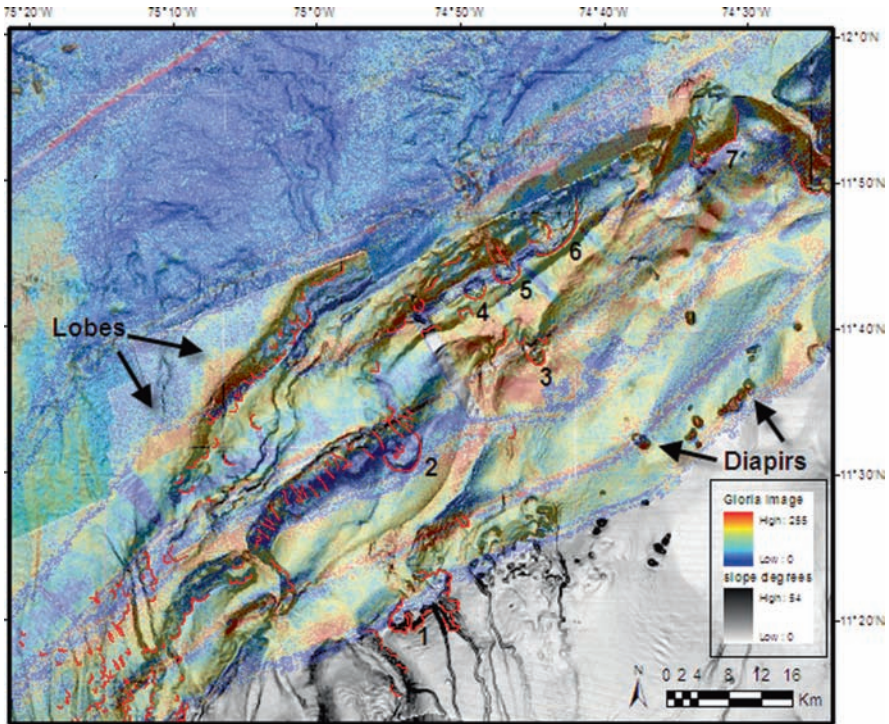
Fig. 3 Northeastern deformation belt. Major scarps are labeled with numbers characterized on Table 1. Arcuate scarps in red

deformation is not regionally extensive, it is present in the fan areas, particularly near the TDBs. The most recent active fan (multiple submarine cables breaks, Heezen 1956) is located in the northeastern TDB, where sediments are transported downslope through canyons with steep slopes (~2.5°) and gullies. These sediments are emplaced as gravity deposits filling the piggyback basins which are formed as a result of deformation. Gas hydrates, mud diapirs and slumps also have been documented in the basin (Shipley et al. 1979; Vernette et al. 1992).

1.2   Data and Methods

Data available for the study include high resolution bathymetry images of the northwest Caribbean offshore Colombia. The bathymetry covers approximately 54,000 km² of the seafloor (Fig. 1). Four different surveys cover the area of study. In 1997 the Spanish vessel Bio-Hesperides acquired approximately 15,000 km² of bathymetry data (Ercilla et al. 2002) with the multibeam echosounder SimRad EM-12 S120. Two surveys were acquired in 2002 on behalf of Ecopetrol and Total E&P, using a hull-mounted, multibeam echosounder Reson SeaBat 8169 (50 kHz

for 100 to 800 m water depths) and Simrad EM 12D (13 kHz for 800 to 3,500 m water depths). Additional bathymetry surveys that cover the shelf area and river mouth were provided by the CIOH. Bathymetry interpretations and quantification of the MTC dimensions were made using ArcMap (ESRI). These observations are complemented by a GLORIA side-scan sonar mosaic (CD40a and DIS109 expedition, Pirmez et al. 1990). Figures 1–3 are a combination bathymetry calculated of slope (degrees) and GLORIA image transparency to enhance the morphological changes. Also, a grid of 2D seismic lines was available.

2 Location and Characteristics of MTCs

The different MTCs in the area were subdivided into three groups by association with the causal mechanism based on the Moscardelli and Wood (2008) classification. Detached MTCs are associated with: TDBs and CLSs. Shelf attached MTCs are associated with inter channel lows.

2.1 *Thrust Deformed Belts MTC's*

TDB are an important bathymetric feature in the continental slope offshore Colombia. Several buried MTCs related to thrust imbricate growth were recognized at the toe of the thrusted sheets on seismic profiles, but they are not expressed on the seafloor morphology.

At the southwestern TDB seafloor morphologies are associated with slump deposits, slide blocks and collapse scours. The collapse scours are common at the front limb and back limb of the TDB (Fig. 2). Erosional features are represented by arcuate headscarps and grooves or "linear features" that commonly modify the front limbs of slope ridges (Fig. 2). Elongate scarps seem to be the sum of several small collapses at the edge of the thrust ridges (Table 1). Lobate deposits occur at the toe of the slump scarps or fill the piggyback basins as result of sediment remobilization from the front limb of the structures (Fig. 2). High reflectivity on the GLORIA images characterizes these areas of MTC deposition as well as slide blocks and evidence of sediment creep.

Evidence of MTC processes in the northwestern TDB are more pronounced. Arcuate headscarps are present on the ridges with lengths of 1 to 3.2 km. Larger collapse structures are developed on the thrust ridge flanks (Table 1) and can be traced to their associated MTCs (Fig. 3). High reflectivity on the GLORIA image is identified at the toe of some scarps and low slope areas within the piggyback basins. Lobate geometries (Fig. 3) are associated with scarps on the front limbs.

The most striking northeastern scarp feature is a narrow morphological slope collapse structure, recognizable at 1,080 mbsl and 27 km to the northeast of the river mouth (Table 1, Figs. 3, 4). The head scarp is semi-circular (cookie bite

Table 1 Morphometry of main scarps on the TDB associated with detached-MTCs. Location is shown in Figs. 3 and 4

TDB	Scarp	Water depth (mbsl)	Width (km)	Length (km)	Height (m)	Area (km²)	Volume (km³)
SW	1	202	2	4.6	80	7.7	0.61
	2	1,140	2.3	3.2	60	7.04	0.42
NE	1	1,090	3.3	10	200	32	6.4
	2	1,500	3.1	4.8	150	10.2	1.53
	3	1,780	1.6	1.8	50	3.08	0.15
	4	2,042	1.7	2.7	60	3.2	0.19
	5	2,126	2.5	3.2	95	6.4	0.6
	6	2,130	4.6	16	300	27	8.1
	7	2,460	4.7	6.5	220	28.7	6.31
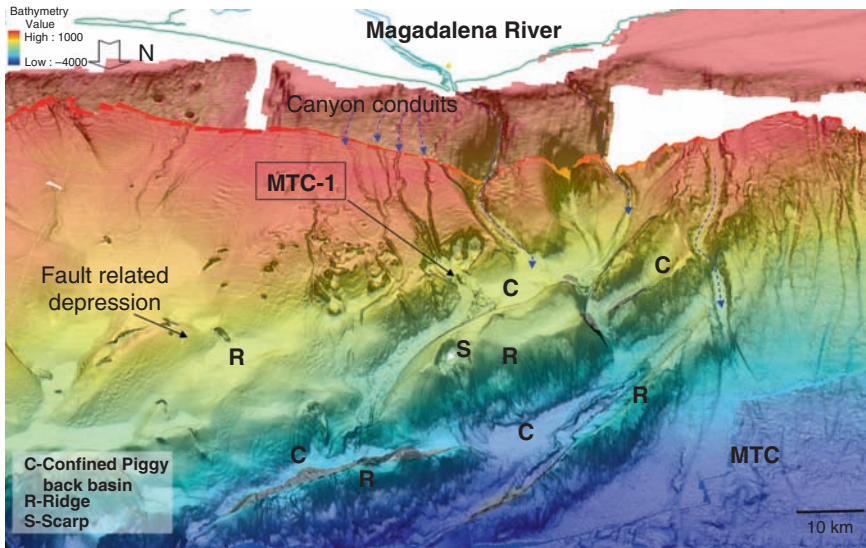
Fig. 4 Bathymetry 3D view of the northeastern section. Highlighting the location of MTC-1 and thrust ridges. Vertical exaggeration 10x

type, Moscardelli and Wood 2008) with an area of 32 km². The estimated column of sediment that has been evacuated from the escarpment reaches 300 m in height, corresponding to an evacuated volume of 6.4 km³. Minor scar features and slide blocks occur at the northeastern and southwestern walls of the scarp. Three channel conduits trend downslope from the shelf towards the MTC-1 escarpment and converge at the escarpment head. A channel-like feature occurs at the base of the escarpment that continues downslope towards confined, elongated basins between ridges, where sediment gravity flows probably were deposited (Fig. 4).

The MTC-1 deposits are represented by slump blocks (Fig. 4) covering an area of approximately 15 km². The deposits are truncated downslope by a southwest-northeast trending ridge and are deflected towards the northeast. The minimum estimated volume for the deposit is 0.27 km³ with a possible mean height of approximately 17 m. This suggests that several events were needed to generate this geometry. The runoff distance is approximately 9 km from the escarpment to the deepest part of the deposits.

2.2   Channel Walls and Levees MTC's

All of the CLSs present in the seafloor on the Magdalena Fan were abandoned after the shifts of the Magdalena River during the Pleistocene. Features such as inner levee and overbank collapses are found in some areas of the fan (Fig. 5) Levee breaks are caused by major MTCs that flowed through the abandoned conduits, modifying the morphology of the channels. It can be observed on the GLORIA image that some of the channels were cannibalized by eroding flows, leaving deposits with high reflectivity (opportunistic MTC, Fig. 6a). Arcuate scarps are found in the inner levees as a result of the deformation of some channels.
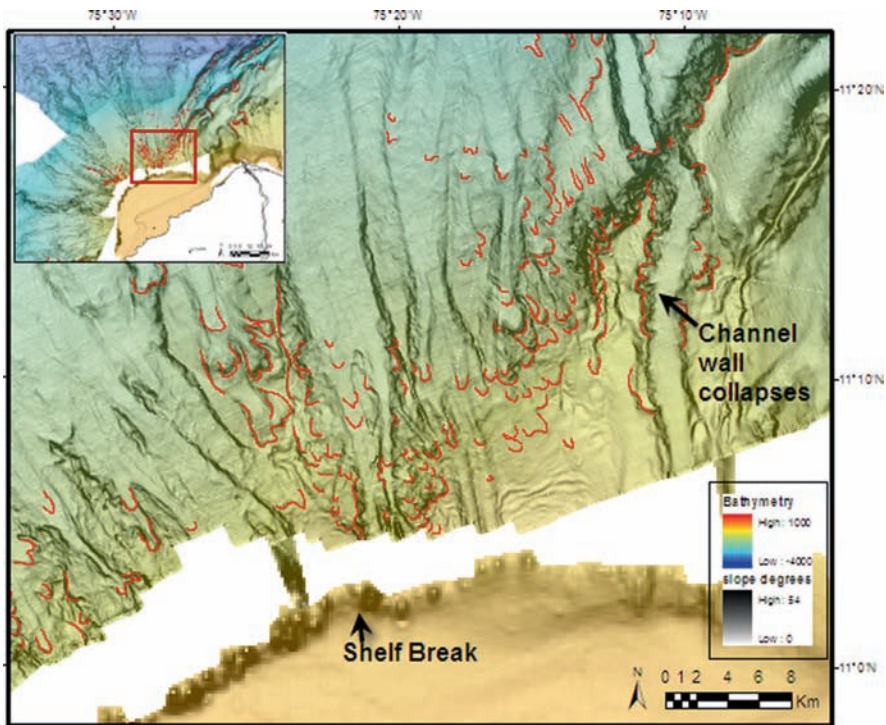
Fig. 5 Upper slope multiple arcuate scarps and canyons due to retrogradational erosion
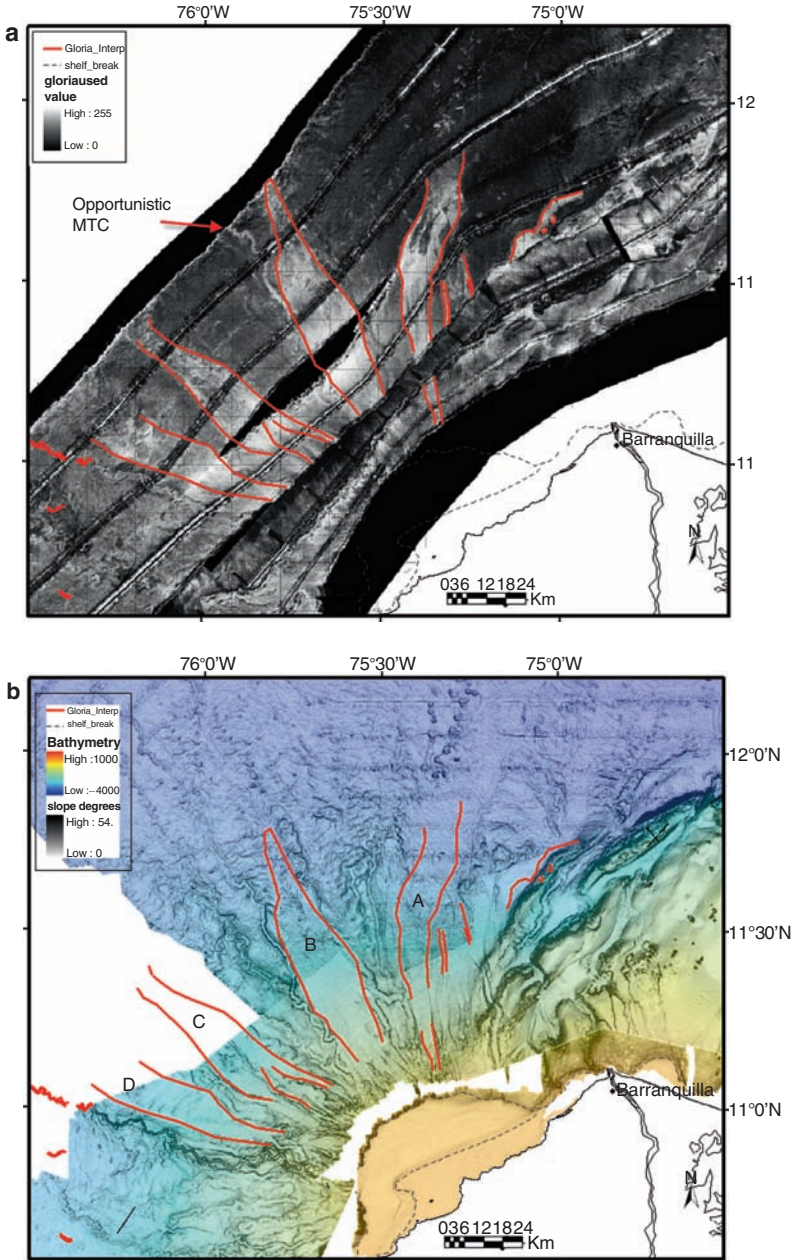
Fig. 6 GLORIA image (**a**) and bathymetry (**b**) for the main fan. Four MTCs filling the interchannel lows can be recognized. Also lobate forms (north of thrust ridges) are highlighted on both images

2.3 Interchannel Low MTC's

Shifting of CLS's through time produced interchannel low areas, with radial distribution on the slope. The interchannel lows are characterized by the presence of several large MTCs connected to the Galerazamba area, and infilling low areas adjacent to channels. The GLORIA image is characterized by four high reflectivity zones in the central fan (Fig. 6a) that correspond to interchannel lows and can be followed from near the shelf break down to the lower fan. Linear features within the MTC on GLORIA images correspond to canyons and conduits on the bathymetry image. Dimensions of the MTCs are presented in Table 2. The MTCs in the eastern area could extend farther downslope than the indicated by the high reflectivity on the GLORIA image, as indicated by the morphology of the seafloor (Fig. 6b). These MTCs may be composed of several depositional events, with the younger being characterized by higher reflectivity (Fig. 6b).

The upper slope is characterized by arcuate scarps and canyons which focus flows downslope through the interchannel lows (Fig. 5). Some of the canyons may be following the deeper abandoned channels. Downslope the floors of these lows appear to be very smooth except where cut by younger channels. Slope gradient in the interchannel lows varies from 2.5° downslope to 0.5° in the continental rise. Several arcuate scours (scarps) are located in the first 30 km downslope from the shelf break. The eastern part of the main fan exhibits higher gradients (3.5°–4°) and appears aligned with the extension of the deformation front (Fig. 5).

3 Types of MTC's

3.1 Detached MTCs

MTC-1 (Table 2) is a detached MTC confined by thrust fault-ridges barriers setting. The triggering mechanisms of detached MTCs are related to local gravitational instabilities on localized bathymetric highs. Unstable flanks collapse and generate debris flows or slumps (Moscardelli and Wood 2008) such as MTC-1. Younger deposits filled the trough and reduced the slope gradient as they stacked vertically.

Table 2 MTC classification (based on Moscardelli and Wood 2008). (WD, water depth)

MTC classification	MTC	Area (km²)	Length (km)	Width (km)	Thickness (m)	Vol. (km³)	L/W	Max WD (m)
Shelf-attached	A	705	85	12	–	–	7.1	3,300
	B	1,085	90	18	–	–	5	3,180
	C	966	80	15	–	–	5.3	~3,000
	D	716	69	12	–	–	5.7	~2,600
Detached	MTC-1	15	5.7	3.4	~20	0.27	1.7	1,590
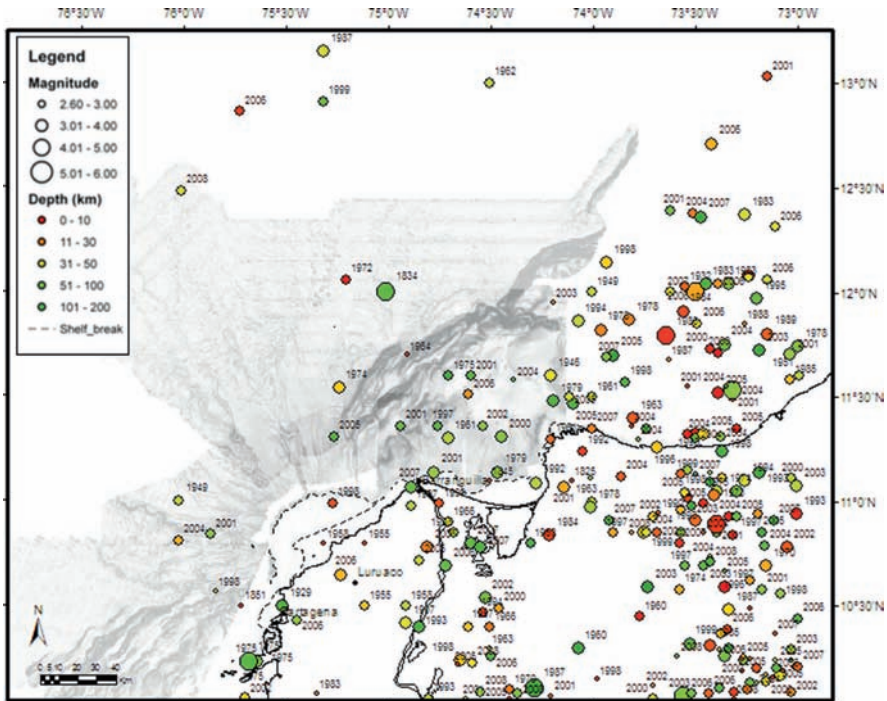
Fig. 7 Earthquake activity of the margin

The modern bathymetry shows that the deposits can reach longer run-off distances down dip, possibly reaching the basin floor for the larger events. The volumetric calculations and seismic interpretation indicate that the MTC-1 scarp is the result of several mass transport events. The scarp is associated with a trend of normal faults that have morphologic expression on the sea-bottom. It is likely that instability of the slope is due to regional deformation and local stresses, possibly amplified by local seismicity (Fig. 7). Channels at the head and toe of the escarpment indicate that slope instability is not the only trigger for the sediment flows traveling basinward through this area. Currents associated with formation of the channels may have triggered mass wasting events.

In addition to MTC-1, all TDB-related slumps can be classified as detached MTCs. Even though the major MTCs are buried in the piggyback basins or at toes of the deformation belt, continuous growth of imbricate ridges allows these mechanisms to recur in the area. Also, degradation of the thrust ridges is an important process in the TDB areas. The northeastern deformational belt is more active, with a number of detached MTCs and lobate deposits at the toe of the ridges (high reflectivity features).

Even though the deposits generated by the levee collapse are feeding the interchannel low areas, hence modifying the geometries of the large MTCs, these MTCs are classified

as detached MTCs. Increase of the slope gradient at abandoned channels generates inner levee collapses that modify the geometry of the channels margins.

3.2 Shelf-Attached MTC

The large MTC's A, B, C and D, are attached MTC's (Table 2). Whether or not the MTC's are slope-attached or shelf-attached is ambiguous with the available information. These large deposits seem to have been more likely generated after migration of the submarine fan southward, since the deposits are confined between abandoned channel levee systems, eroding and smoothing the slope with similar reflectivity on the GLORIA image. Therefore, these deposits cannot be classified as typical shelf edge delta MTCs since they are not fed directly by unstable active deltas, nor did they respond to changes in the sedimentation rates (Moscardelli and Wood 2008). However, the abandonment of the delta front may have caused instability of the shelf margin and was the source for the MTCs. Abandonment could have been initiated after the late Pleistocene shift of the fan towards the south (Dique canal) (Bordine1974; Pirmez et al. 1990; Romero-Otero et al. submitted).

Conversely, the drive mechanism for slope-attached MTCs may be associated with catastrophic and extensive collapses of the upper continental slope due to earthquakes, long-shore currents, hydrate dissociation or strong storms and/or hurricanes (Moscardelli and Wood 2008). However, in this area no large upper slope collapses have been recognized with the available data. Instead, a series of canyons and gullies that followed older channels, eroded the upper slope and channelized sediment flows through them. The abundance of these linear features on the GLORIA image and the presence of these MTCs filling all the interchannel lows indicate that this process was common for the entire fan and may not be the product of isolated catastrophic events.

3.3 Other Causal Mechanisms

Additional causal mechanisms may have been present in the Magdalena fan in order to generate the MTCs found on the slope. Besides the abandonment of the delta front as the possible main trigger, changes in the hydrostatic pressure due to sea level changes could have been involved in the generation of attached MTCs. Hydrostatic pressure changes may have induced mass collapse of the abandoned delta (Maslin et al. 2004).

Global sea level changes and climatic conditions during the Pleistocene seem to be related with many of the MTCs studied throughout the world (Maslin et al. 2004). The Colombian basin $\delta^{18}O$ records (ODP Core 999) (Martinez et al. 2007) indicate several major drops of sea level (similar to global changes) which may have influenced the stability of the shelf.

The active deformation of the area also may have constituted a major trigger for MTC's. Uplift of the shelf area may have caused remobilization of sediments contributing to the development of MTC's. There are multiple evidences for active deformation in the area. The Magdalena River shift toward the northeast (Cienaga de Santa Marta area) was a result of inland uplift (Hoover and Bebout 1985). Pleistocene units such as the La Popa Formation (coralline limestone) exhibit stress tensors (115°/24°) that respond to the tectonic models of northern South America, in addition to uplifted terraces in coastal areas (Reyes et al. 2001). Evidences of continental slope uplift are associated to high slope gradients along the eastern channel thalwegs (Romero-Otero et al. submitted), abundant scarps and retrogradational erosion.

Historic seismicity of the area (Fig. 7) shows strong activity in the northeastern sector. At least 25 earthquakes have occurred on the slope during the last 25 years (Ingeominas 2008). Their magnitude ranges from 3 to 4.5. They are distributed from a few kilometers up to 90 km of depth. However, the earthquakes cannot be directly correlated with the MTCs. Their distribution indicates that they possibly responded to stress-induced accretionary wedge deformation, with pressure release through existing faults. These events may have triggered some MTCs at unstable sectors of the slope, which were then deposited in the piggyback basins.

4 Possible Timing of Events

Relative timing of the detached MTCs cannot be determined due to their local character. Causal mechanisms are controlled by the growth of arcuate deformation fronts (east and west of the fan) and instability of active and abandoned CLS.

During the middle Pleistocene, a southerly shift of the Magdalena River depocenter resulted in abandonment of the Galerazamba CLSs. This shift coincided with a low stand of sea level (140–120 ka). We hypothesize that the MTCs in the interchannel lows could have been initiated during this sea level drop due to changes in hydrostatic pressure and/or gas hydrate dissolution on the slope, in addition to the abandonment of the Galerazamba area. Similar processes are postulated to have occurred 40–45 ka on the Amazon fan, where large MTCs are found (Maslin et al. 2005). Based on $\delta^{18}O$ records of ODP Core 999, Martinez et al. (2007) interpreted temperature changes during 120–140 ka are similar to the 40–45 ka time interval in the Amazon area. In contrast, the large MTCs in the Magdalena fan could not be related to increases in sedimentation rates due to the Andes latest deglaciation (Younger Amazon MTCs, 10–13 ka), since the delta depocenter was east of the Galerazamba shelf-edge during that time.

The multiple mass flow products of the retrogradation of the slope by continuous uplift seems to be the most recent process, retrogradation promoted erosion and modification of the upper slope, creating instability and feeding the interchannel low areas (shelf attached MTCs). The westernmost section of the fan does not exhibit the scours or the similar reflectivity response. This may indicate fundamental differences in the deformation of the slope.

5 Conclusions

The combination of bathymetry, GLORIA, and seismic profiles allowed identification of multiple MTCs on the Magdalena fan. These can be grouped into detached and shelf attached MTCs based on the causal mechanisms: (1) growth of TDB (detached), (2) instability of slope canyon and channel walls (detached), (3) major slope failures (shelf-attached).

Four major shelf-attached MTC's occur in the interchannel lows on the fan. This classification is ambiguous since there are no changes in the adjacent delta load, and there is no evidence of major slope collapse. Furthermore the regional extent of the MTCs indicates a more regional process. Causal mechanisms that could have triggered these MTCs are instability after abandonment of the delta front, sea level changes, seismic activity in the area and active deformation of the upper slope.

Possible initiation of the shelf attached MTC's may be related to the southern shift of the delta/fan and relative lowstand of sea level during the middle Pleistocene. The shelf edge may have become unstable, but further investigation is necessary to test this hypothesis. Observations of the upper slope morphologies and downslope deposits suggest that these MTCs are the result of multiple events enhanced by the retrogadational erosion of the upper slope.

References

Bordine BW (1974) Neogene biostratigraphy and paleoenvironments, lower Magdalena basin, Colombia. Ph.D. thesis, Lousiana State Univ, Baton Rouge, LA, p. 295

Breen NA (1989) Structural effect of Magdalena fan deposition on the northern Colombia convergent margin. Geology 17:34–37

Duque-Caro H (1979) Major structural elements and evolution of northwestern Colombia. In: Watkins JS, Montadert L, Dickerson PW (eds.), Geological and geophysical investigations of continental margins. Am Assoc Pet Geol Mem 29:329–351

Ercilla G, Alonso B, Estrada F, Chiocci FL, Baraza J, Farran M (2002) The Magdalena turbidite system (Caribbean Sea): Present-day morphology and architecture model. Mar Geol 185:303–318

Estrada F, Ercilla G, Alonso B (2005a) Quantitative study of a Magdalena submarine channel (Caribbean Sea): Implications for sedimentary dynamics. Mar Pet Geol 22:623–635

Estrada F, Ercilla G, Alonso B (2005b) Large-scale mass-flows in the Magdalena turbidite system. Geoph Res Abs Eur Geos Uni 7:03410

Heezen BC (1956) Corrientes de turbidez del Rio Magdalena. Bol Soc Geol Colomb 51–52:135–143

Hoover RA, Bebout DG (1985) Submarine fan diversion by tectonic processes- Magdalena fan and slope Southern Caribbean. Gulf Coast Assoc Geol Soc Trans 35:395

Ingeominas (2008) Red Sismologica Nacional de Colombia. Catalogo de sismicidad instrumental (1993–present). http://seisan.ingeominas.gov.co/RSNC/Formulario.html

Kolla V, Buffler T (1984) Seismic stratigraphy and sedimentation of Magdalena Fan Southern Colombia basin Caribbean Sea. Am Assoc Pet Geol Bull 68:316–332

Martinez JI, Mora G, Barrows TT (2007) Paleoceanographic conditions in the Western Caribbean Sea for the last 560 kyr as inferred from planktonic Foraminifera. Mar Micropaleontol 64:177–188

Maslin M, Owen M, Day S, Long D (2004) Linking continental-slope failures and climate change: Testing the Clathrate gun hypothesis. Geology 32:53–56, doi: 10.1130/G20114.1

Maslin M, Vilela C, Mikkelsen N, Grootes P (2005) Causes of catastrophic sediment failures of the Amazon Fan. Quat Sci Rev 24:2180–2193

Moscardelli L, Wood LJ (2008) New classification system for mass transport complexes in offshore Trinidad: Basin Res 20:73–98 doi: 10.1111/j1365–2117.2007.00340x [p. 26]

Pirmez C, Breen NA, Flood RD, O'Connell S, Jacobi RD, Ladd JW, Westbrook G, Franco JV, Garzon M, Arias-Isaza FA (1990) Gloria mosaic of the Magdalena deep-sea fan Northern Colombian convergent margin: Abstract. Am Assoc Pet Geol 74:741

Reading HG, Richards M (1994) Turbidite systems in deepwater basin margins classified by grain size and feeder system. Am Assoc Pet Geol Bull 78:792–822

Reyes GA, Guzmán G, Barbosa G, Zapata G (2001) Geología de las planchas 23 Cartagena y 29–30 Arjona. Memoria Explicativa. Ingeominas, Ministerio de Minas y Energía, Colombia

Romero-Otero GA, Slatt RM, Pirmez C (submitted) Evolution of the Magdalena deepwater fan in a tectonically active setting, offshore Colombia. In: Prather BE, Deptuck ME, Mohring DC, van Hoorn B, Wynn RB (eds.), Application of Seismic Geomorphology Principles to Continental Slope and Base-of-Slope Systems, Case Studies from Seafloor and Near-Seafloor Analogues, SEPM Spec Publ

Shipley TH, Houston MH, Buffler RT, Shaub FJ, McMillen KJ, Ladd JW, Worzel JL (1979) Seismic evidence for widespread possible gas hydrate horizons on continental slopes and rises. Am Assoc Pet Geol Bull 63:2204–2213

Vernette G, Maufret A, Bobier C, Briceno L, Gayet J (1992) Mud diapirism fan sedimentation and strike-slip faulting Caribbean Colombia Margin. Tectonophys 202:335–349

Character, Distribution and Timing of Latest Quaternary Mass-Transport Deposits in Texas–Louisiana Intraslope Basins Based on High-Resolution (3.5 kHz) Seismic Facies and Piston Cores

H.C. Olson and J.E. Damuth

Abstract Systematic mapping of 3.5 kHz seismic facies (echo character) reveals the geometry, scales and distribution of Late Quaternary mass-transport deposits (MTDs) within the northern Gulf of Mexico (GOM) intraslope basin province and adjacent Sigsbee Abyssal Plain. The 3.5 kHz seismic facies indicate that localized MTDs are common in the intraslope mini-basins. MTDs of larger scale occur on the upper continental slope (e.g. East Breaks Slide Complex) and seaward from the eastern base of the Sigsbee Escarpment. Approximately 120 piston cores from these deposits "ground truth" the seismic facies interpretations and reveal that the sedimentary facies of the MTDs in intraslope basins contain a spectrum of slumps, slides and debris flows. Most MTDs are muddy deposits, but sandy MTDs are also common. The presence of sandy debris flows suggests that similar, more deeply buried MTDs may constitute significant reservoir sands. Many piston cores containing MTDs were biostratigraphically and chemically zoned using *G. menardii* complex and calcium carbonate fluctuations to determine the timing and sourcing of MTDs in relation to glacio-eustatic sea-level changes associated with the Last Glacial and Holocene. This stratigraphic analysis indicates that the majority of downslope transport (including sandy turbidites, sandy and muddy debris flows, and slumps) occurred during the Last Glacial cycle. Downslope transport of MTDs during the Holocene Interglacial was rare.

Keywords Mass-transport deposits • slumps • slides • debris flows • intraslope basins • Gulf of Mexico • Late Quaternary glacio-eustatic sea-level changes • piston cores • seismic facies • planktonic foraminifera

H.C. Olson (✉)
Institute for Geophysics, Jackson School of Geosciences, The University of Texas, 10100 Burnet Rd., Bldg. 196 (ROC), Austin, TX 78758, USA
e-mail: olson@ig.utexas.edu

J.E. Damuth (✉)
Department of Earth and Environmental Sciences, University of Texas, 500 Yates St., 107 Geoscience Bldg., Arlington, TX 76019, 817-272-2976
e-mail: damuth@uta.edu

1   Introduction

The northern Gulf of Mexico is one of the best studied hydrocarbon provinces in the world. However, the majority of studies have focused on Cenozoic sedimentation and tectonic history, and relatively few studies have focused on the latest Quaternary sediments and their depositional processes in intraslope basins. Studies of Late Quaternary or "Modern" analogues can potentially provide excellent exploration models for predicting sediment facies and sand-body geometries of more deeply buried productive deposits. A better understanding of the depositional processes and lithology of the uppermost seafloor (upper 10–50 m) also promotes better risk assessment in selecting the safest locations for the placement of seabed structures related to the exploitation of hydrocarbons, including templates, piles and pipelines.

From 1998 to 2006 the industry-sponsored Gulf of Mexico Intraslope Basins (GIB) Project (Phases 1 and 2) produced a detailed, comprehensive and integrated synthesis of the late Quaternary depositional processes and facies in intraslope basins of the northern Gulf of Mexico (Olson and Damuth 2000, unpublished proprietary study; Damuth et al. 2006, unpublished proprietary study) (Fig. 1). These studies revealed that mass-transport deposits (MTDs) are very common throughout the study area (Fig. 1). Here, we present an overview of these mass-transport deposits based on interpretation of high-resolution (3.5 kHz) seismic facies, sedimentology and biostratigraphy to describe the distribution and lithologies of these MTDs, and to understand the influence of glacio-eustatic sea-level changes on control of mass-transport deposition. In this paper we use the term mass-transport deposits (MTDs) to include slides (brittle deformation), slumps (plastic deformation) and debris flows (plastic flow), as well as a combination of these deposits.

2   Data and Methods

A wide variety of very high-resolution data sets (seismic reflection, side-scan sonar, swath bathymetric maps, shallow piston cores) were utilized to effectively examine the details of latest Quaternary intraslope basin deposits (Fig. 1; contact the authors for a map showing data coverage). We described 432 piston cores and interpreted their depositional processes. The cores were collected and archived by the Institute for Geophysics, The University of Texas at Austin (UTIG) and by the U.S. Geological Survey. Core lengths range up to 12 m and average 4 to 5 m. The 71,000 km of 3.5 kHz seismic data interpreted were short ping (<5 ms) echograms acquired by UTIG during a large number of cruises conducted since the mid-1970s and by the U.S. Geological Survey during their survey of the U.S. Exclusive Economic Zone with the GLORIA long-range side-scan sonar (EEZ-SCAN 85 Scientific Staff 1987). These echograms complement our piston-core studies in the GIB study area because the 3.5 kHz records can resolve beds on the order of 12 cm, and thus reflections can sometimes be directly correlated with discrete beds, physical
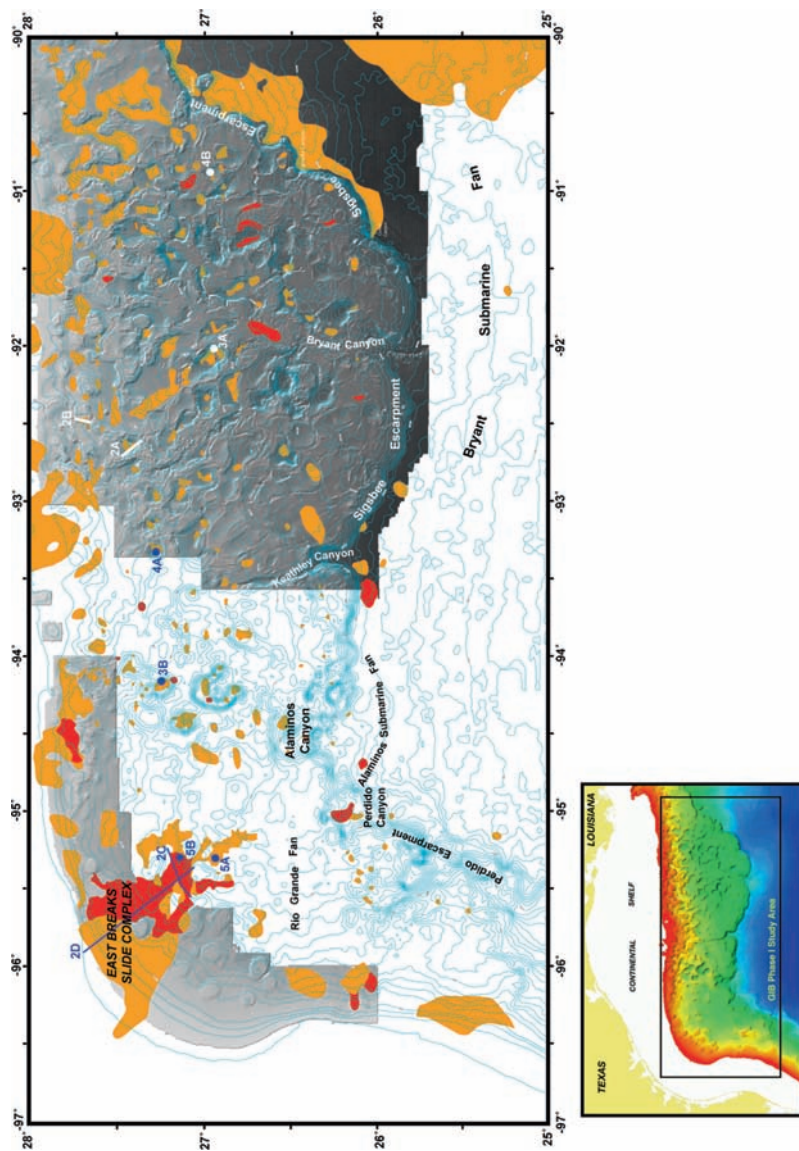
Fig. 1 Bathymetric map of the GIB Phase 1 study area in the northern Gulf of Mexico Intraslope Basin Province. The distribution of mass-transport deposits on the seafloor as mapped with 3.5 kHz seismic data is shown by the orange (Facies 1) and red (Facies 2) patterns (Olson and Damuth 2000) (see text for details). Bathymetric Data Sources: Shaded Swath Bathymetry (Sea Beam) from NOAA (NGDC). Bathymetric contours (blue) from Smith and Sandwell (1997) (Contour Interval = 100 m). Inset map shows location (Seafloor Relief Map compiled by Liu and Bryant (2000). Locations of piston cores (dots) and seismic profiles (lines) illustrated in Figs. 2–5 are shown above and identified by figure number (e.g. 2A)

properties, or other deposits (e.g. slumps, debris flows, sand beds, etc.) in the cores. To interpret the regional distribution of MTDs and other depositional processes, we constructed an echo character map of various 3.5 kHz seismic facies or 'echo types' of bottom echoes following the methodology of Damuth (1975a, 1980, and references therein).

Stratigraphic analysis of the latest Quaternary stratigraphy of a subset of 131 piston cores, including 58 with MTDs, was undertaken to determine the relationship of MTDs and other depositional processes to glacio-eustatic sea-level fluctuations. Foraminiferal biostratigraphy, especially fluctuations of *G. menardii* complex, along with fluctuations of coarse-fraction and carbonate contents were used to determine the latest Quaternary glacial/interglacial cycles in the cores (Kennett and Huddlestun 1972a, b; Ericson and Wollin 1968; Damuth 1975b; Prell and Hays 1976; Prell and Damuth 1978; Martin et al. 1990). These zonations and curves provide a stratigraphic framework that permits correlation of cores and glacial/interglacial cycles from basin to basin throughout the study area, as well as determination of the timing of mass-transport deposition.

3 Results

3.1 Seismic Character and Regional Distribution of MTDs

Seismic facies representing mass-transport deposits are very common throughout the study area. These MTDs return two distinctive 3.5 kHz seismic facies: Facies 1 returns sharp to prolonged bottom echoes with transparent internal character, commonly bounded by irregular wedge, mound, fill or lens shaped external forms (Fig. 1, orange pattern; Fig. 2a–c) and Facies 2 returns regular, overlapping to singular hyperbolic bottom echoes with varying vertex elevations (Fig. 1, red pattern; Fig. 2c and d). Numerous studies have documented that these two facies, especially Facies 1, are characteristic of MTDs imaged by 3.5 kHz profiling (e.g. see Damuth 1980 for review and references). These two facies are sometimes intragradational (e.g. Fig. 2c). Many additional areas of Facies 1 and 2 were observed and mapped in the intraslope-basin floors, but they cannot be displayed on Fig. 1 because of the small figure size.

The majority of MTDs found on intraslope-basin floors, along the upper continental slope, within portions of the East Breaks Slide Complex, east of the base of the Sigsbee Escarpment and on the southwestern portion of the Mississippi Fan (Fig 1) are Facies 1 (Fig. 2a–c). This facies is interpreted as deposits of mainly debris flows and some slumps. This facies has been cored at numerous locations and the cores confirm this interpretation (e.g. Figs. 3 and 4; see discussion below). The large area of Facies 1 in the southeast corner of the study area (Fig. 1) represents the toe of a much larger MTD on Mississippi Fan, which was first identified and mapped by Walker and Massingill (1970).
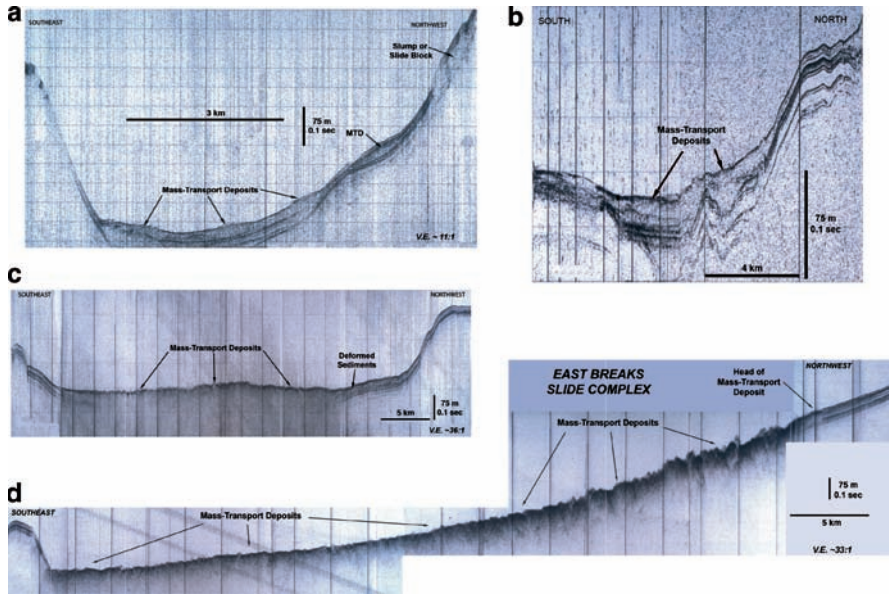
Fig. 2 Examples of 3.5 kHz seismic records from the northern Gulf of Mexico Intraslope Basin Province (Fig. 1) showing examples of seismic facies (1 and 2) interpreted as mass-transport deposits. (**a, b**) Mass-transport deposits in intraslope basin displaying characteristics of Facies 1 (orange pattern in Fig. 1). (**c**) Mass-transport deposits in an intraslope basin that return both Facies 1 and 2. (**d**) Mass-transport deposits from the East Breaks Slide Complex that return Facies 2 (red pattern in Fig. 1). Locations of profiles shown in Fig. 1

The distribution of Facies 2 is less common throughout the study area (Fig. 1). The most extensive area is returned from the East Breaks Slide Complex in the northwestern part of the study area (Figs. 1 and 2d). In this area, Facies 2 is associated with Facies 1. Facies 2 is also interpreted as gravity-controlled mass-transport deposits, which are mainly slumps and slides. Coherent or deformed blocks of various sizes that make up these deposits produce a rough sea-floor microtopography, which, in turn, is recorded as a series of small overlapping to single hyperbolae of slightly variable sizes on 3.5 kHz profiles (Fig. 2c and d). Cores recovered from areas returning Facies 2 confirm the interpretation of this facies as mass-transport deposits (see below).

3.2 Lithology of MTDs in Piston Cores

A large number of cores were taken from areas of 3.5 kHz Facies 1 and 2 (Fig. 1). Mass-transport deposits occur in the majority of these piston cores as evidenced by the presence of chaotic deposits that can clearly be interpreted as slumps, slides and debris flows (Figs. 3–5). These cores provide confirmation or "ground truth"
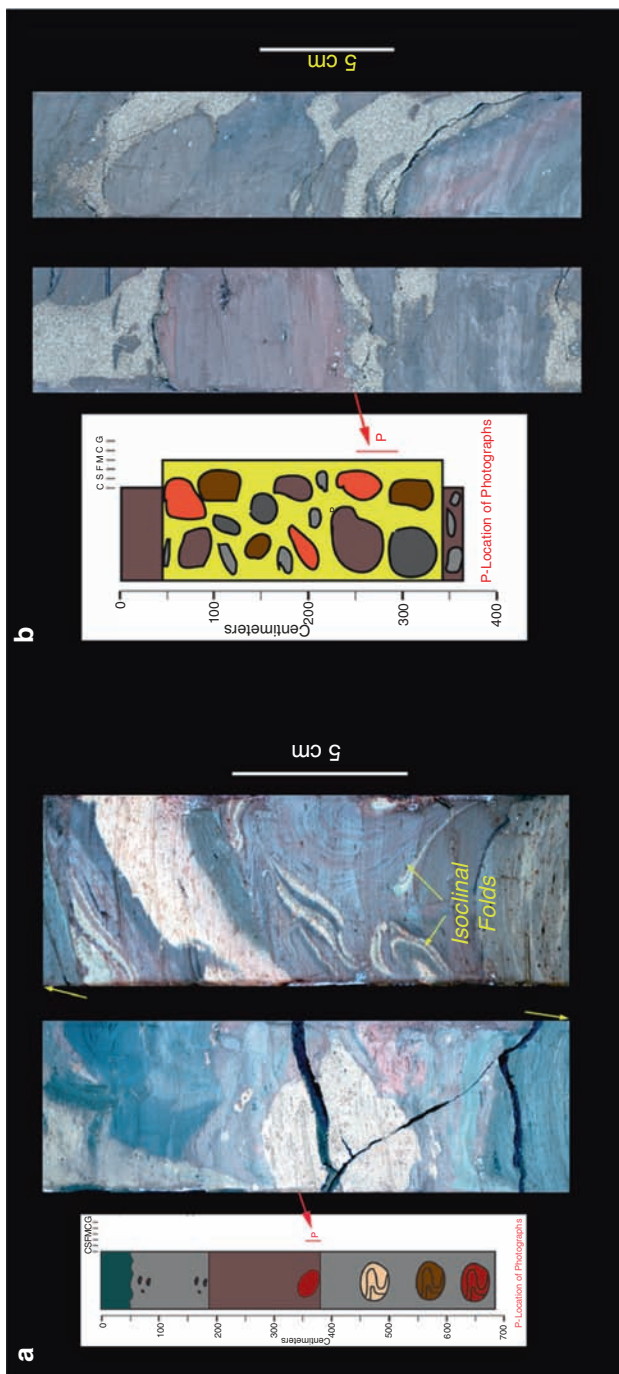
Fig. 3 Examples of piston cores from intraslope basins with mass-transport deposits. (**a**) Core IG36-3 showing close-up photographs of mud-rich debris-flow deposits composed of highly deformed and folded exotic-colored mud clasts. Graphic core log at *left*. (**b**) Core IG45-20 showing close-up photographs of sandy mass-transport deposit with large exotic mud clasts. Graphic core log at *left*. Locations of cores shown in Fig. 1
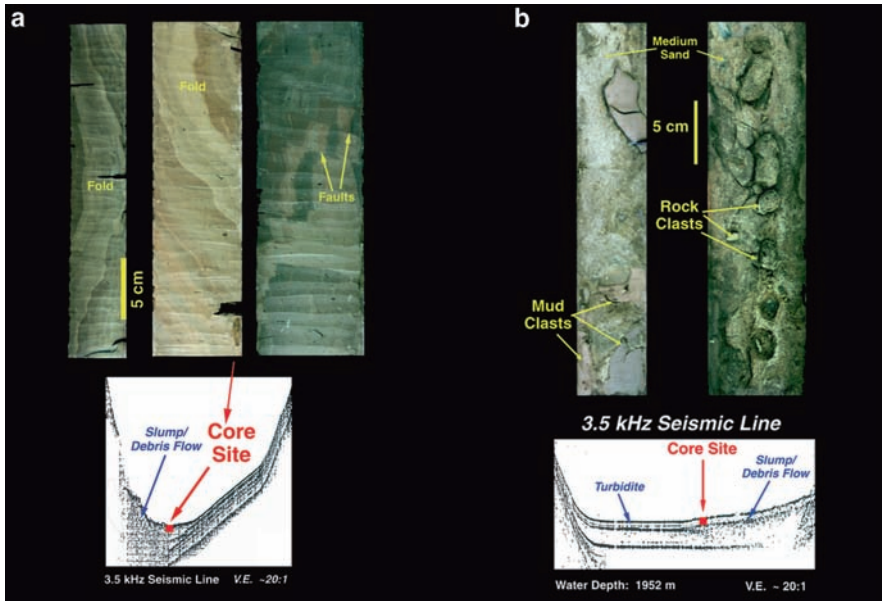
Fig. 4 (**a**) Core IG38-26 showing close-up photographs of a slump deposit in an intraslope basin. The 3.5 kHz seismic line shows that the core was taken from Facies 1 typical of slump/debris flow. (**b**) Core IG41-24 showing close-up photographs of a sandy mass-transport deposit with a matrix of fine to medium sand and large mud and rock clasts. The 3.5 kHz seismic line shows that the core was taken from Facies 1 typical of slump/debris flow. Locations of cores shown in Fig. 1

for the seismic interpretations. These MTDs contain thick intervals of disturbed, deformed bedding and layers that show variable dips, discordance, truncations, soft-sediment flowage and folds. Exotic colored (e.g. brick reddish brown) layers and variable lithologies are common and many intervals contain angular to rounded mud clasts of various sizes, shapes and colors. We generally interpret the dipping, discordant and folded intervals as slump or slide deposits (e.g. Fig. 4a) and the deposits of mud or rock clasts as debris flows (e.g. Figs. 3, 4b and 5). Of the 432 cores described, 123 contain mass-transport deposits. The depositional facies distribution is: debris flows in 96 cores, slumps in 51 cores, and slides in 8 cores (Figs. 3–5). Combinations of two or more of these processes were observed in 36 cores. The majority of slumps and debris flows are muddy deposits (Figs. 3a, 4a, and 5), but sandy debris flows are also present (Figs. 3b and 4b). Muddy mass-transport deposits are commonly cored on the East Breaks Slide Complex (Fig. 5).

Several cores taken in mass-transport deposits recovered sandy debris-flow deposits that consist of medium- to coarse-sand matrix with large exotic mud or rock clasts (Figs. 3b and 4b). The 3.5 kHz seismic facies at some of these core sites return 3.5 kHz Facies 1 consistent with mass-transport deposits (e.g. Fig. 4b); however, there currently are no criteria for predicting muddy versus sandy slump/debris-flow deposits based solely on the 3.5 kHz seismic facies character alone.
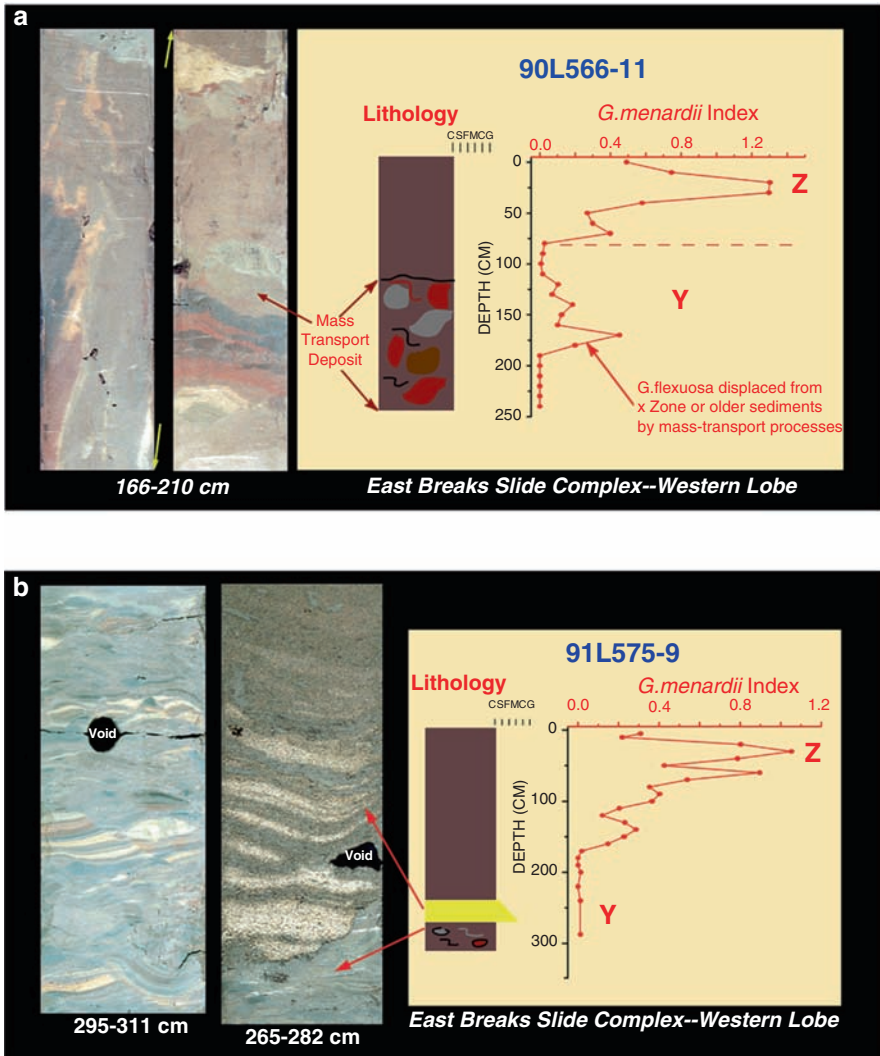
Fig. 5 Lithology, *G. menardii* index stratigraphy and close-up photos of cores from the East Breaks Slide Complex showing the timing of deposition of mass-transport deposits in relation to latest Quaternary climatic cycles. (**a**) The *G. menardii* Index curve for Core 90L566-11 shows that a muddy debris flow with large exotic mud clasts was emplaced during the latest part of the Y zone or Last Glacial. Note that *G. flexuosa*, which was deposited in sediments of the Last Interglacial (X zone) or older interglacials, were entrained in the MTD. (**b**) The *G. menardii* Index curve for Core 91L575-9 shows that a muddy debris flow followed by a sandy turbidite were deposited during the latest Y zone or Last Glacial. See text for additional discussion. Locations of cores shown in Fig. 1

The occurrence of sandy MTDs in modern intraslope basins has important implications for hydrocarbon exploration because these modern analogues imply that sand bodies consisting of mass-transport deposits may be present in deeply buried productive

zones of the GOM. MTD sand bodies will probably exhibit much different reservoir geometries than ponded turbidite reservoirs or small submarine fans in intraslope basins because plastic debris flows tend to "freeze" in place and produce thick sand bodies of irregular shape. These MTD sand bodies will have much different reservoir geometries than laterally extensive turbidites, and so, must be properly imaged and identified to accomplish efficient hydrocarbon production.

3.3 Relationship of MTDs to Glacio-eustatic Sea-Level Changes

Stratigraphic analysis of cores containing MTDs using the methods described above reveals the timing of mass-transport events within the intraslope basins in relation to glacial/interglacial cycles. Mass-transport deposition during the Holocene (Z zone) is very rare. The majority (99%) of cores stratigraphically analyzed show that mass-transport events occurred mainly during the Last Glacial cycle (Y zone) (e.g. Fig. 5). Most of the Y zone mass-transport deposits indicate that sediments were not only deposited during the glacial cycle, but were likely derived from glacial deposits (Y zone) because they do not contain *G. menardii* complex (only present during interglacials). However, in the East Breaks Slide Complex sediments originally deposited during the Last Interglacial (X zone) were remobilized during the Last Glacial (Y zone) as evidenced by the presence of *G. flexuosa* (which does not occur in sediments younger than the Last Interglacial) in some Y-zone age MTDs (e.g. Fig. 5a).

Several cores in the study area show a pattern of Y zone slumps and debris flows directly overlain by sandy turbidites (e.g. Fig. 5b). Both the mass-transport deposits and the overlying turbidites were deposited in the Y zone and do not contain any *G. menardii* components. In these cores, a single event may have triggered a slump or debris flow followed by a turbidity flow (e.g. Fig. 5b).

4 Conclusions

1. Interpretation of 3.5 kHz seismic facies in the Gulf Intraslope Basin Provence shows that localized MTDs, including slumps, slides and debris flows, are very common throughout the intraslope mini-basins of the region. In addition, large areas along the upper continental slope, portions of the East Breaks Slide Complex, seafloor east of the base of the Sigsbee Escarpment, and the southwestern portion of the Mississippi Fan have extensive MTDs.
2. Numerous piston cores taken from these MTD-interpreted seismic facies, especially in the intraslope basins, contain a variety of debris flows, slumps and slides, and provide "ground truth" of the seismic data. These chaotic deposits display thick intervals of disturbed, deformed bedding and layers that show

variable dips, discordance, truncations, flowage and folds, and are interpreted as slumps and slides. Exotic colored layers and lithologies and intervals containing angular to rounded mud clasts of various sizes, shapes and colors are interpreted as debris flows.

3. Sandy debris flows composed of fine- to medium-sand with mud and rock clasts are also present but much less common. However, the occurrence of sandy MTDs in modern intraslope basins has important implications for hydrocarbon exploration because these modern analogues imply that sandy MTDs form sand bodies in deeply buried productive zones of the GOM and will have different geometries than laterally extensive turbidite deposits.

4. Stratigraphic analysis and zonations of many cores containing MTDs show that nearly all MTDs were deposited during glacio-eustatic sea-level lowstands such as the Last Glacial (Y zone). Deposition of MTDs during glacio-eustatic high-stands such as the Holocene (Z zone) or perhaps even the Last Interglacial (X zone) has been extremely rare.

References

Damuth JE (1975a) Echo character of the western Equatorial Atlantic floor and its relationship to the dispersal and distribution of terrigeneous sediments. Mar Geol 18:17–45

Damuth JE (1975b) Quaternary climatic change as revealed by calcium-carbonate fluctuations in western Equatorial Atlantic sediments. Deep-Sea Res 22:725–743

Damuth JE (1980) Use of high-frequency (3.5–12 kHz) echograms in the study of near-bottom sedimentation processes in the deep sea: A review. Mar Geol 38:51–75

Damuth JE, Nelson CH, Olson HC (2006) Gulf of Mexico Intraslope Basins Project: GIB Phase 2 Project Atlas (hard copy atlas and digital GIS database). Oil Company Consortium, Proprietary UTIG Report

EEZ-SCAN 85 Scientific Staff (1987) Atlas of the U.S. Exclusive Economic Zone, Gulf of Mexico. U.S. Geol Surv Miscellaneous Investigation I-1864-A

Ericson DB, Wollin G (1968) Pleistocene climates and chronology in deep-sea sediments. Science 162:1227–1234

Kennett JP, Huddlestun P (1972a) Late pleistocene paleoclimatology, foraminiferal biostratigra-phy, and tephrochronology, Western Gulf of Mexico. Quat Res 2:38–69

Kennett JP, Huddlestun P (1972b) Abrupt climatic change at 90,000 Yr BP: Faunal Evidence from Gulf of Mexico Cores. Quat Res 2:384–395

Liu JY, Bryant WR (2000) Seafloor Relief of Northern Gulf of Mexico Deep Water. Texas Sea Grant College Program

Martin RE, Neff ED, Johnson GW, Krantz DE (1990) Biostratigraphy of the Pleistocene: The Ericson and Wollin zonation revisited. In: Society of Economic Paleontologists and Mineralogists (Gulf Coast Section) Eleventh Annual Research Conference, Sequence Stratigraphy as an Exploration Tool: Concepts and Practices in the Gulf Coast, Houston, TX

Olson HC, Damuth JE (2000) Gulf of Mexico Intraslope Basins Project: GIB Phase 1 Project Atlas (hard copy atlas and digital GIS database). Oil Company Consortium, Proprietary UTIG Report

Prell WL, Damuth JE (1978) The climate-related diachronous disappearance of *Pulleniatina obliquiloculata* in Late Quaternary sediments of the Atlantic and Caribbean. Mar Micropaleo 3:267–277

Prell WL, Hays JD (1976) Late Pleistocene faunal and temperature patterns of the Columbia Basin, Caribbean Sea. In: Cline RM, Hays JD (eds.), Investigation of Late Quaternary Paleoceanography and Paleoclimatology, Geol Soc Am Mem 145

Smith WHF, Sandwell DT (1997) Global seafloor topography from satellite altimetry and ship depth soundings. Science 277:1956–1962

Walker JR, Massingill JV (1970) Slump features on the Mississippi Fan, northeastern Gulf of Mexico. Geol Soc Am Bull 81:3101–3108

Upper Cretaceous Mass Transport Systems Above the Wyandot Formation Chalk, Offshore Nova Scotia

B.M. Smith, M.E. Deptuck, and K.L. Kendell

Abstract Interpretations from 18 contiguous 3-D seismic surveys, covering more than 17,000 km², show a wide variety of diagnostic geomorphic elements that indicate mass wasting was an important process in shaping the top surface of the Wyandot Formation, an Upper Cretaceous chalk unit deposited across wide areas off the coast of Nova Scotia. These geomorphic elements include a series of clearly defined ~80 m high head scarps extending more than 100 km across the margin, multiple 20 to 80 m high side scarps defining up to 40 km long failure corridors, and an irregular planform fabric above areas interpreted to correspond to bedding plane detachments, variably modified by overlying deformed strata. The latter morphology includes large >1 km wide slide blocks or erosional remnants. In addition, multiple intervals of chaotic seismic facies are recognized directly above the top Wyandot Formation seismic marker. These geomorphic features are attributed to a complex history of slope failure originating from a series of shelf-perched delta systems located 40 to 60 km landward from the paleo-continental slope break. These deltas prograded over the Wyandot Formation in the Late Cretaceous through early Paleogene. This study indicates that significant quantities of resedimented chalk may have been deposited on the outer shelf and upper slope. Such deposits could form important gas reservoirs, as demonstrated in the North Sea (e.g. Ekofisk field). However, the degree to which overlying prodelta muds were mixed with the Wyandot chalk during failure is unclear and likely has a direct bearing on the reservoir potential of resedimented chalks off Nova Scotia.

Keywords Wyandot Formation • chalk • mass wasting • head scarp • transport corridor • resedimented chalk

B.M. Smith (✉), M.E. Deptuck, and K.L. Kendell
Canada-Nova Scotia Offshore Petroleum Board, 1791 Barrington St,
Halifax, NS, Canada B2Y 4A2
e-mail: bmsmith@cnsopb.ns.ca

1   Introduction

Nova Scotia is located on the east coast of Canada with an offshore area of approximately 400,000 km² (Fig. 1). The Scotian margin developed after North America rifted and separated from the African continent during the break-up of Pangea. Red beds and evaporites were the dominant deposits during the Late Triassic rift phase, whereas typical clastic progradational sequences with periods of carbonate deposition dominated the drift phase (Wade and MacLean 1990). Near the end of the Cretaceous, a period of generally high global sea level (Haq et al. 1987) resulted in the widespread deposition of chalks, marls and marine shales of the Dawson Canyon and Wyandot formations, which blanketed shelf and slope areas off Nova Scotia (MacIver 1972; Jansa and Wade 1975).

The Upper Cretaceous Wyandot Formation was deposited on a stable shallow-water, open marine continental shelf (Jansa and Wade 1975; Ings et al. 2005), with several wells also encountering the formation in probable upper slope settings, seaward of the paleo-continental shelf edge. Limestone of the Wyandot Formation generally consists of coccolithic-foraminiferal chalks and lime mudstones that are soft, fossiliferous, and argillaceous (Wade and MacLean 1990). They are commonly interbedded with marls, calcareous shales and marine mudstones. On gamma ray logs, the Wyandot Formation commonly passes up-section from a serrated to more blocky response, interpreted to reflect a decrease in clay content towards its top
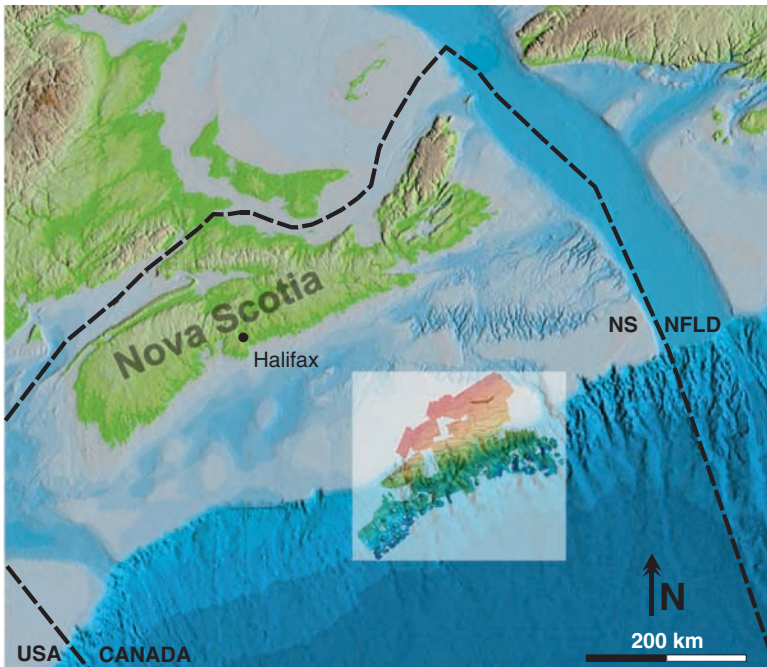
Fig. 1   Location of the study area off Nova Scotia (NS), eastern Canada. NFLD = Newfoundland

(Deptuck et al. 2003; Ings et al. 2005). Biostratigraphic age determinations indicate that across the Scotian Shelf the Wyandot Formation was deposited in the Coniacian to Maastrichtian (Wade and MacLean 1990) but in the study area, it is commonly Campanian or older (Fensome et al. 2008). The Wyandot Formation ranges in thickness from less than 50 m in the study area to greater than 250 m on the eastern Scotian shelf. The wide variation in thickness has been attributed to a combination of erosion and its proximity to prodeltaic shales associated with the influx of clastic depositional systems (i.e. in areas far removed from clastic depositional systems, like the eastern Scotian shelf, thicker intervals of chalk accumulated; MacRae et al. 2002; Fensome et al. 2008).

On seismic profiles, the top lithological boundary of the Wyandot Formation generates a high amplitude positive seismic signature that separates denser and faster velocity rocks below from less dense and lower velocity Upper Cretaceous and Paleogene clastics above. This boundary is distinctive across most of the Scotian shelf and the resulting seismic reflection is commonly used for determining the phase of seismic volumes and for calibrating well synthetic ties.

In the Sable Island area, abrupt variations in the thickness of the Wyandot Formation commonly coincide with an irregular reflection pattern on the top Wyandot seismic marker (MacRae et al. 2002). Using predominantly 2D reflection seismic profiles, previous workers interpreted the irregular top Wyandot surface as erosion resulting from ocean current scouring or submarine karst (Wielens et al. 2002; MacRae et al. 2002; Deptuck et al. 2003). The patchwork of individual 3D seismic programs used in this study, however, provides more constraints on the origin of some irregularities on the top Wyandot Formation marker across large areas of the Scotian shelf and slope. The objectives of this paper are to document the geomorphology of the top Wyandot Formation seismic marker mapped from 3D seismic data and to discuss additional processes, like mass wasting, that have strongly influenced its appearance.

2 Study Area, Data, and Methods

The study area, highlighted in the center of Fig. 1, encompasses most of the "Sable Subbasin". With 67 hydrocarbon exploration wells, this subbasin is the most densely explored area off Nova Scotia. About half of the study area lies on the present-day continental shelf in water depths less than 200 m with the other half on the continental slope in water depths up to 3,000 m.

The data set consists of 18 contiguous time-migrated 3-D seismic surveys, covering an area >17,000 km^2 above the present-day shelf and slope off Nova Scotia. The seismic surveys were acquired by several different companies between 1998 and 2002. All surveys were adjusted to zero phase and bulk shifted in time to provide a consistent data set, and the top of the Wyandot Formation was correlated to seismic at 18 well locations using synthetic seismograms.

The strong positive reflection from the top of the Wyandot Formation was mapped across the study area. The interpreted data was then gridded at spacing of
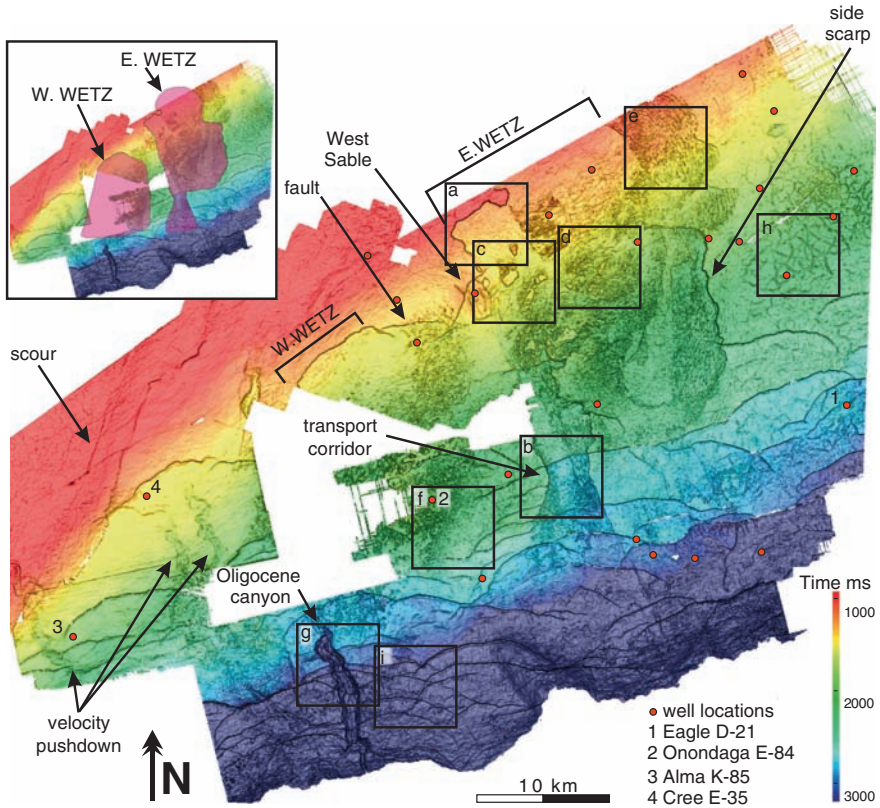
Fig. 2 Sun-illuminated 3D seismic render of the top Wyandot marker (two-way time) showing the wide variation in morphological features, including head scarps, side scarps, faults, canyons, and sediment transport corridors. The inset shows the same map with the two main Wyandot erosional zones highlighted in pink that are separated by the West Sable structural high (see text for details). The lettered boxes locate detailed dip map images shown in Fig. 3

25 by 25 m and displayed in time using Geoviz 3D visualization software, as shown in Fig. 2. In all figures, warm colors signify shorter two-way travel times (i.e. shallower areas) and cool colors represent longer two-way travel times (i.e. deeper areas). Dip magnitude maps, like the ones shown in Fig. 3, were generated using Schlumberger IESX software, and were derived from the gridded seismic data. Dark colours indicate steeper dips and lighter colours indicate shallower dips.

3 Results – Variation in Top Chalk Morphology

Meticulous mapping of the complex seismic reflection defining the top of the Wyandot Formation, combined with a fine 25 by 25 m gridding of the resulting surface, reveals a wide range of geomorphic features that range from smooth and
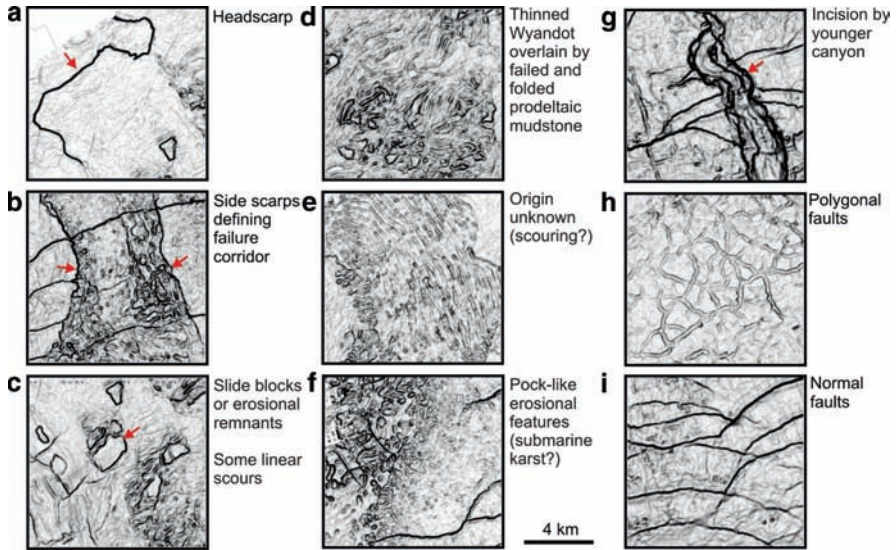
Fig. 3 Dip magnitude images showing the variation in planform geomorphology of the Wyandot marker. Darker areas correspond to steeper dips. See Fig. 2 for location and text for discussion

relatively featureless, to bumpy with a highly complex planform and cross-sectional appearance (e.g. Figs. 2–4). The top chalk morphologies in Figs. 3 and 4 are strikingly similar to features documented in the Petrel Member on the Grand Banks of Newfoundland, a Turonian chalk unit within the Dawson Canyon Formation (see Fig. 2.5 of Deptuck 2003).

Some of the most obvious geomorphic features preserved on the top Wyandot marker correspond to faults. Two varieties are apparent. The first are younger offsets associated with long-lived deep-seated down-to-the-basin listric growth faults (e.g. Fig. 3i) that form curved lineations with a dominant E-W or ENE-WSW orientation. Fault offset of the top Wyandot marker is commonly <50 to 120 m on the shelf, with >1 km of offset south of Fig. 2, where prominent salt withdrawal deformed the slope as sedimentation was focused on the hanging wall of mini-basin bounding faults. These faults are more numerous in areas interpreted to coincide with the paleo-continental shelf-edge (near the light blue shading in Fig. 2), where prominent growth took place in older stratigraphic intervals (below the top Wyandot marker). Most of these faults sole out above overpressured shale or allochthonous salt intervals. The second style of faulting corresponds to intra-formational or polygonal faults (e.g. Fig. 3h; Dewhurst et al. 1999; see also Hansen et al. 2004) that show offset is restricted to stratigraphic intervals immediately above and below the top Wyandot marker. These faults are most apparent in areas with the thickest in-situ chalk, for example near the Eagle D-21 well where the Wyandot Formation is about 190 m thick (see Ings et al. 2005). Offset along these faults is typically less than 30 m, forming a polygonal pattern of fault traces in plan view.
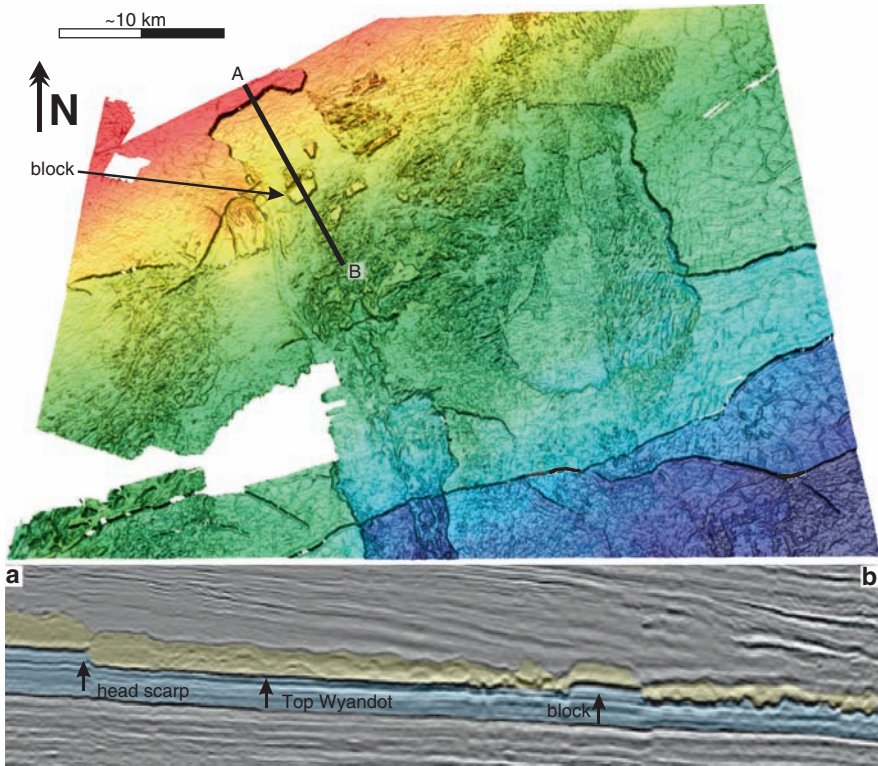
Fig. 4 Rendered time-structure perspective map showing a closer-up view of the top Wyandot marker. Seismic line AB crosses a head scarp associated with a slope failure that detached above a bedding plane located near the base of the Wyandot Formation. Although the younger chaotic mass transport deposit above the top Wyandot marker (yellow) could be associated with the same failure, it is probably associated with a younger failure composed predominantly of prodelta muds. The profile also crosses one of the isolated features interpreted as a slide block or an erosional remnant

A wide range of other geomorphic elements on the top Wyandot marker correspond to erosional features. For example, the marker is truncated along the bases of deeply incised canyons of various ages (e.g. Fig. 3g). Several sinuous to linear canyon thalwegs are apparent in the western part of Fig. 2, but these are generally much younger features (Eocene to Miocene) that only affect the top Wyandot marker in areas of maximum incision depth. In some cases the slower velocity fill of younger canyons generates 'velocity pushdown' artifacts on the top Wyandot surface (e.g. western part of Fig. 2). Other erosional features, which form the primary focus of this paper, appear to be associated with an unconformity directly above the Wyandot Formation.

They are probably associated with a top chalk unconformity identified by Doeven (1983) and Fensome et al. (2008) in Onondaga E-84. Here, all of the Campanian is absent, and lower Campanian or Santonian chalks are overlain directly by Maastrichtian clastics.
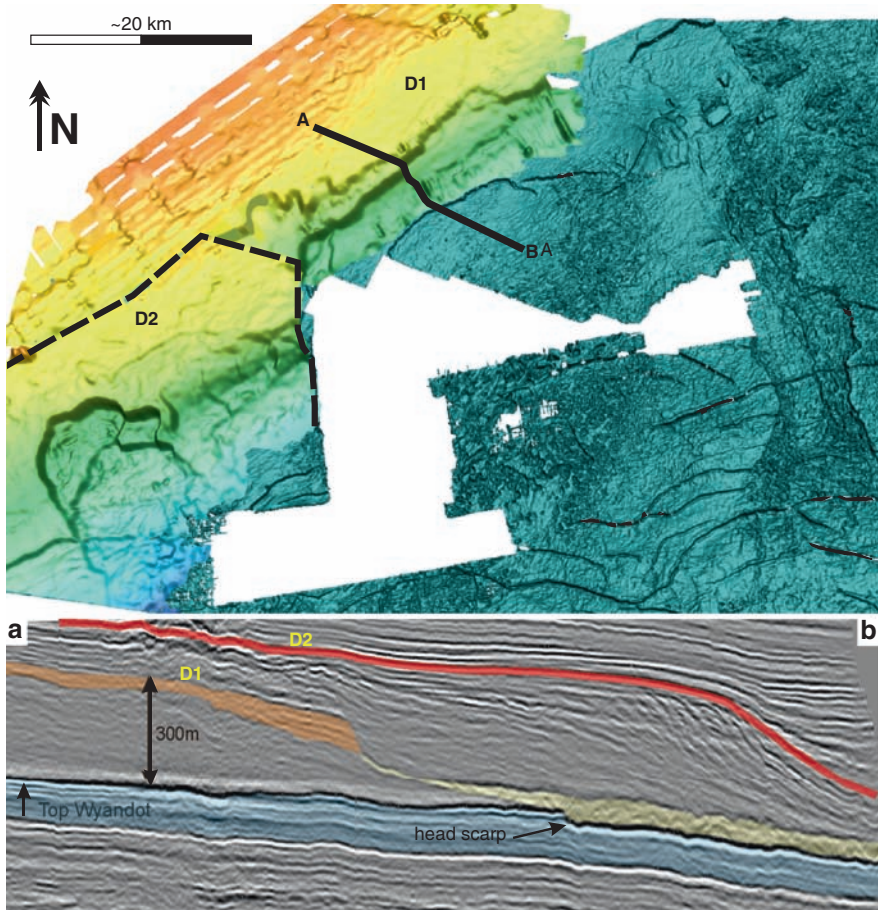
Fig. 5 Three mapped surfaces D1, D2, and the top Wyandot marker (in dark blue). Location of seismic section AB is denoted by the solid black line. The top Wyandot marker is overlain by two younger progradational surfaces. The red mapped horizon (D2) defines the western map which is cropped at the black dashed line in order to display the older clinoform surface to the east (D1) defined by the top of the orange shading on the seismic section

In the westernmost part of Fig. 2, the top Wyandot marker is smooth and continuous across elongated zones paralleling the orientation of prodelta clinoforms that overlie the marker (e.g. Fig. 5). In Fig. 5, subtle truncation of the smooth Wyandot marker is apparent below 'delta 1' (discussed later), and a much thinner Wyandot Formation was encountered in wells in these areas (e.g. 30.8 m thick at Cree E-35 and 11.5 m thick at Alma K-85). Such erosion has been attributed to scouring by shallow ocean currents that flowed parallel to the strike orientation of prodelta clinoforms (MacRae et al. 2002). Subtle 50 to 100 m wide slope-parallel linear scours above the top Wyandot marker (Fig. 2) and above younger 'prodelta

clinoform' markers (e.g. the D2 marker in Fig. 5), appear to corroborate this idea. Deptuck (2003) documented similar erosional scours above prodelta clinoforms and the Wyandot Formation on the Grand Banks of Newfoundland to the north, and attributed them to erosion associated with the ancestral Gulf Stream. Such currents promoted oversteepening of clinoform sets, preconditioning them for failure.

Some of the most striking erosional features in the study area appear to be associated with slope failures that took place above the Wyandot Formation. Several sharp vertical offsets in the top Wyandot marker elevation are seen in Fig. 4. Some of these correspond to faults described earlier but others show no offset in underlying stratigraphic layers. Despite their similar plan view appearance, they do not correspond to faults. A seismic profile across the 27 km long NE oriented lineation in Figs. 3a and 4 indicates that the downward step in the top Wyandot marker corresponds to erosion of the upper parts of the Wyandot Formation. Erosion took place roughly parallel to the base of the Wyandot Formation. The sharp downward step therefore is interpreted as a head scarp associated with a mass failure that took place after the Wyandot Formation was deposited. South of the head scarp, the failure detached above a bedding plane located somewhere near the base of the Wyandot Formation, perhaps in a mechanically weaker, more argillaceous interval. A slab of Wyandot chalk, thus, appears to have detached and broke up as it was transported to the south.

A series of lineations also trend perpendicular to the orientation of normal faults (Fig. 4). Like the interpreted head scarps, they show no offset in underlying seismic markers, and are interpreted as side scarps oriented parallel to the direction of sediment transport. Two such side scarps define a 5 km wide north–south oriented 'failure corridor' (Fig. 3b) that extends towards the paleo continental shelf edge. The distance from the head scarp to its distal end is approximately 60 km. Several north–south oriented linear scours are present on the floor of the failure corridor (see Fig. 4). A more prominent side scarp is also present east of the failure corridor. It is 37 km long, has a north–south orientation, and a somewhat irregular shape in plan view. The side scarp sharply separates the more intact polygonally faulted chalk to the east from highly complex 'deformed' top chalk surface to the west.

A wide range of morphologies are preserved within failed areas defined by head scarps and side scarps. The seismic profile in Fig. 4 crosses a 1 km wide and 2 km long angular 'block' and a more irregular fabric above the bedding plane detachment (Fig. 3c). The seismic character of the block is identical to intact intervals of chalk north of the head scarp, and this feature is interpreted as a slide block composed of chalk left behind during slab break-up. Several additional blocks are recognized to the east of the largest block (Fig. 4). It is also possible that some of these features are erosional remnants of intact chalk, though this is not our preferred interpretation. NE of the largest slide block, several positive relief features are elongated parallel to the head scarp and may be comprised of a cluster of rotated or folded slide blocks transported normal to a failure scarp located just north of the 3D seismic coverage.

In addition to the angular slide blocks interpreted in Fig. 4, some morphologies on the failed top chalk surface are of unknown origin. For example, a series of

elongated morphological features are present in Fig. 3e. They are locally v-shaped in cross section and could represent elongated scours. Alternately, they could also represent a series of rotated blocks associated with shallower failures that locally modified the top Wyandot marker. In addition, a cluster of sub-circular depressions in Fig. 3f could correspond to areas of irregular chalk dissolution (associated with submarine karst?) or could represent fluid escape structures.

3.1   Slope Failures Above the Wyandot Formation

Collectively, the head scarps, side scarps, and zones of irregular reflection character define the boundaries of a large complex area of erosion and transport across the top of the Wyandot Formation. The 'Wyandot erosion and transport zone' (WETZ for short) encompasses an area of about 1,700 km^2 and can be subdivided into two sub-areas (Eastern WETZ and Western WETZ) shown on the inset map in Fig. 2.

The Western WETZ covers an area of 700 km^2. This area is bound to the north by a 27 km long and 80 m high head scarp, which continues beyond 3D seismic coverage to the west. The western boundary of the Western WETZ is located within this data gap as shown in Fig. 2.The eastern boundary of the Western WETZ is defined by a structural high, trending south from the West Sable structure. There appears to be less Wyandot erosion above this high and the overlying MTD thins. No side scarp was identified along this eastern boundary, and instead the transition to in situ chalk is more gradual.

The Eastern WETZ covers an area of 1,000 km^2 and is more clearly defined on seismic than the Western WETZ. The 80 m high head scarp shown in Fig. 3a continues to the east beyond 3D seismic coverage, but can be traced further on 2D seismic profiles. The head scarp merges into a prominent side scarp that sharply separates the Eastern WETZ from an area of more intact, polygonally faulted chalk to the east. This prominent side scarp forms the eastern boundary of the Eastern WETZ. Its southern limit transitions gradually into a surface with less obvious erosive character, except along the prominent failure corridor that indicates failed material locally was transported to and probably beyond the paleo continental slope break. The western extent of the head scarp merges into another side scarp forming the western boundary of the Eastern WETZ. This boundary continues south along the south-trending structural high characterized by thicker in-situ chalk (south of the West Sable structure shown in Fig. 2) and eventually forms the western edge of the failure corridor.

Areas where the top Wyandot chalk surface is highly complex are commonly overlain by low amplitude chaotic mass transport deposits derived from mud-prone prodelta clinoforms in overlying Upper Cretaceous and lowermost Paleogene strata. As such, the complex fabric observed above the Wyandot Formation could be closely associated with failures derived from variably oriented clinoforms.

3.2   Relationship of Failures to Adjacent and Overlying Prograding Clastic Systems

During and after deposition of the Wyandot Formation, Campanian(?) to Maastrichtian clastics prograded from the west as a succession of delta lobes (Fensome et al. 2008). At least two delta lobes, delta 1 and delta 2 (Fig. 5) prograded from the northwest downlapping onto the chalks of the Wyandot Formation or the chaotic deposits that overlie it. These appear to be 'shelf-perched' delta systems, and within the study area the seaward most offlap break at the delta front stopped 40 to 60 km short of the paleo-continental slope break. Many of the mass transport features recorded in the top Wyandot marker are believed to be associated with failures that were triggered in slightly younger intervals corresponding to these shelf-perched deltas.

Figure 5 illustrates the aerial relationship between the younger deltas and the mass wasting features expressed on the top Wyandot marker. The top of each delta lobe has been mapped and are denoted by the orange (D1) and the red (D2) horizons on seismic section AB (Fig. 5). Delta 1 aggraded to a height of approximately 300 m prior to failure of mud rich clinoforms and to some extent sandier delta top-sets. The resulting mass transport deposit (MTD) is shaded in yellow on the seismic section. The MTD overlies the head scarp on the top Wyandot marker associated with the Western WETZ. It is unclear whether this mass transport system exploited a plane of weakness within the Wyandot Formation and eroded the upper portion of the chalks creating the scarp or whether this mass transport deposit is a later feature that simply draped a pre-existing scarp above the top Wyandot surface. The similarity in orientation of the two head scarps may imply that the southern scarp formed during an initial prodelta failure, with retrogradation producing the head scarp that truncates the seaward edge of Delta 1. If the erosion above the Wyandot Formation is a result of prodelta failure, then the resulting MTD should consist of a mixture of Wyandot carbonates and delta front to prodelta sediments. A series of younger clinoforms can also be seen downlapping onto this MTD and many additional failures appear to have been initiated as clastic systems continued to prograde. These failure deposits commonly merge with and erode into older MTDs, resulting in complicated stratigraphy in the central area of the WETZ.

A second failure scarp is evident on the younger D2 surface to the west. This younger approximately 10 km wide failure was initiated after the Wyandot surface was buried by a combination of clinoform bottom-sets and chaotic deposits associated with earlier slope failures. Therefore the Wyandot surface in this location was protected by a thicker clastic cover and was less affected by the failed delta front at the D2 surface. A secondary scarp is also evident south of the failure scarp, and may record the position of the initial failure, with retrogradational failure defining the ultimate head scarp location.

3.3 Potential Triggering Mechanisms

Numerous triggering mechanisms for these failures are possible. Norris et al. (2000) suggested that the 65 Ma Chicxulub bolide impact at the K/T boundary was responsible for slope instability and mass failure of chalks across extensive areas of the western North Atlantic. However, the presence of Maastrichtian age clastic deposits associated with prodelta clinoforms above the unconformity (Doeven 1983; Fensome et al. 2008) indicates erosion above the Wyandot Formation in the study area predates the K/T bolide impact. In addition, erosion above the Wyandot Formation is diachronous, and hence is unlikely to be associated with any single event. It is possible that oversteepening of the prodelta clinoforms, which are locally steeper than 5°, could have preconditioned them for failure. The steep gradient of these clinoforms may be associated with the passage of ocean currents that locally undercut clinoform bottom-sets, as observed in the Jeanne d'Arc Basin to the north (where time-equivalent clinoforms are as steep as 9°; see Figure 4.11 of Deptuck 2003). Ground shaking by earthquakes or short-term drops in eustatic sea level, could equally have initiated these failures.

4 Conclusions

1. Interpretations from 18 contiguous 3-D surveys, covering more than 17,000 km^2, show a wide variety of geomorphic elements that indicate mass wasting was an important process in shaping the top surface of the Wyandot Formation.
2. Head scarps, side scarps, bedding plane detachments, slide blocks or erosional remnants, scours and chaotic mass transport deposits are all recognized along or above the top Wyandot marker. They record a complex history of Late Cretaceous slope failure above the Wyandot chalk.
3. Athough most chaotic MTDs come to rest on the relatively flat-lying shelf, at least one transport corridor reached the paleo continental slope break, indicating that some resedimented chalks may have been transported into deeper water where the slope morphology is complex.
4. Erosional features associated with failures above the Wyandot Formation appear to be closely tied to prodelta slope failures shed from overlying shelf perched deltas. This close association could mean that resedimented chalks are heavily mixed with prodelta shales, making them less desirable reservoir targets.

References

Deptuck ME (2003) Post-rift geology of the Jeanne d'Arc Basin, with a focus on early paleogene submarine fans and insights from modern deep-water systems. Unpublished Ph.D. thesis, Dalhousie University, Halifax, Nova Scotia, Canada, 369 p.

Deptuck ME, MacRae RA, Shimeld JW, Williams GL, Fensome RA (2003) Revised upper cretaceous and lower paleogene lithostratigraphy and depositional history of the Jeanne d'Arc Basin, offshore Newfoundland, Canada. Am Assoc Pet Geol Bull 87:1459–1483.

Dewhurst DN, Cartwright JA, Lonergan L (1999) The development of polygonal fault systems by syneresis of colloidal sediments. Mar Pet Geol 16:793–810.

Doeven PH (1983) Cretaceous nannofossil stratigraphy and paleoecology of the Canadian Atlantic margin, Geological Survey of Canada, Bulletin 356:1–57.

Fensome RA, Crux JA, Gard IG, MacRae RA, Williams G, Thomas F, Fiorini F, Wach G (2008) The last 100 million years on the Scotian Margin, offshore eastern Canada: An event-stratigraphic scheme emphasizing biostratigraphic data. Atl Geol 44:93–126.

Hansen DM, Shimeld JW, Williamson MA, Lykke-Anderson H (2004) Development of a major polygonal fault system in Upper Cretaceous chalk and Cenozoic mudrocks of the Sable Subbasin, Canadian Atlantic Margin. Mar Pet Geol 21:1205–1219.

Haq BU, Hardenbol J, Vail PR (1987) Chronology of fluctuating sea level since the Triassic. Science 235:1156–1167.

Ings SJ, MacRae RA, Shimeld JW, Pe-Piper G (2005) Diagenesis and porosity reduction in the Late Cretaceous Wyandot Formation, Offshore Nova Scotia: A comparison with Norwegian North Sea Chalks. Bull Can Soc Pet Geol 53:237–249.

Jansa LF, Wade JA (1975) Geology of the continental margin off Nova Scotia and Newfoundland. In: van der Linden WJM and Wade JA (eds.), Offshore Geology of Eastern Canada, Geol Surv Can Pap 74–30:51–105.

MacIver NL (1972) Cenozoic and mesozoic stratigraphy of the Nova Scotia shelf. Can J Earth Sci 9:54–70.

MacRae RA, Shimeld JW, Fensome RA (2002) Cryptic erosion on the Upper Cretaceous Wyandot Formation, Sable Island area, Scotian shelf. Atlantic Geoscience Society colloquium and general meeting program and abstracts. Atl Geol 38:93.

Norris RD, Firth J, Blusztajn JS, Ravizza G (2000) Mass failure of the North Atlantic margin triggered by the Cretaceous – Paleogene bolide impact. Geology 28:1119–1122.

Wade JA, MacLean BC (1990) The geology of the southeastern margin of Canada, Chapter 5, In: Keen MJ and Williams GL (eds.), Geology of the Continental Margin of Eastern Canada, Geol Surv Can, Geol Can No 2 167–238.

Wielens HJBW, MacRae RA, Shimeld J (2002) Geochemistry and sequence stratigraphy of regional upper cretaceous limestone units, offshore eastern Canada. Org Geochem 33:1559–1569.

The Significance of Mass-Transport Deposits for the Evolution of a Proglacial Continental Slope

T.J. Huppertz, D.J.W. Piper, D.C. Mosher, and K. Jenner

Abstract The continental slope off southeast Canada has been influenced by ice sheet fluctuations in the Pleistocene. These ice sheets have supplied the bulk of the sediment, which is the driving process for the observed slope architecture. Several studies with a more local scope have explored the Late Quaternary geological history of the Scotian slope and have used the sedimentary sequence including mass-transport deposits (MTDs) to understand depositional processes on the slope over time. Using this existing understanding of the geological setting on the slope, a new slope-wide regional seismic stratigraphy was developed. This stratigraphy was used to understand variations of MTD deposition on a regional scale on the Scotian Margin. The spatial occurrence of different types of MTDs and their relationship to the regional morphology is used to establish different MTD zones. Mapping of the zones improved the understanding of slope stability and the importance of MTDs for continental-margin evolution.

Keywords Mass-transport deposits • mass failure • geohazards • seafloor geomorphology • submarine canyon • submarine valley • slope classification • Scotian Slope

1 Introduction

Mass-transport deposits (MTDs) are widely recognized along continental margins and record a component of the erosional history of continental margins. Regional studies have emphasized on the importance of mass wasting along glaciated continental margins (Canals et al. 2000; Piper 2005; Rise et al. 2005; Wilken and Mienert 2006).

T.J. Huppertz (✉)
University of Bremen, Faculty of Geosciences, FB 5 Klagenfurter Strasse
28359 Bremen, Germany
e-mail: huppertz@uni-bremen.de

D.J.W. Piper, D.C. Mosher, and K. Jenner
Geological Survey of Canada, Natural Resources Canada, Bedford Institute of Oceanography,
1 Challenger Drive, Dartmouth, Nova Scotia, B2Y 4A2, Canada

1.1 Regional Geology

The Scotian Slope (Fig. 1) is a mid-latitude margin, which has been influenced by advance and retreat of ice sheets since at least oxygen isotope stage 12, when high sedimentation rates in deeper water were first observed (Piper et al. 1994; Piper and Normark 1989). The ice sheets supplied large amounts of poorly sorted sediment to the shelf edge as till, together with suspended sand and mud in glacial outwash. Sedimentation rates on the slope are as high as 1–5 m/ka when glacial ice crossed the shelf. Major mass-transport flows were common in the late Quaternary of the Scotian Slope. Several studies with a more local approach have reported the stratigraphic and volumetric importance of such flow deposits along this margin (Berry and Piper 1993; Campbell et al. 2004; Gauley 2001; Mosher et al. 2004; Piper 2001; Piper et al. 1985; Shor and Piper 1989). Most of the flows were initiated during glacial stages, but a clear link between glaciation and MTD deposition could usually not be shown (Mosher et al. 2004). Some MTDs are related to retrogressive failure initiated on the lower rise by over-steepening by salt tectonic processes and triggered by seismic shaking (Mosher and Piper 2007). Failure was probably favored by high rates of proglacial sedimentation on the continental slope (Piper 2005). Seaward of some transverse troughs, glacigenic debris flows formed by direct flow of till into deep water. Large blocky failures resulted from failure along weak layers, as a result of erosion by canyons (Piper and Ingram 2003).

In contrast to previous studies that have focused on individual MTDs and have emphasized processes, the work reported here attempts a regional synthesis of MTDs throughout much of the Scotian margin, in order to place the formation of MTDs in a spatial and temporal context. It is based on a new Quaternary slope-wide seismic stratigraphy that was established from Huntec sparker and airgun seismic data. The stratigraphy was developed from previous studies (Campbell et al. 2004; Gauley 2001; Hundert and Piper 2008; Piper 2001) and jump-correlated (correlation based on character including presence of erosional surfaces, across canyons where no continuous sections exists) across canyons based on regional sedimentation rates and correlation using widespread MTDs. Age control for the shallow sequence is given by published radiocarbon dates in piston cores (Piper 2001); the age of markers deeper in the stratigraphy was based on correlation with till tongues on the upper slope and ties to wells (Piper 2001; Piper and Brunt 2006). The reflectors shown in Figs. 2–4 have the following approximate ages: sea bed is usually Holocene (Piper and Campbell 2002), 935 = last glacial maximum (Piper and Sparkes 1990); 880 = marine isotope stage 6 (Piper and Sparkes 1990); 800 to 845 = early Quaternary (Piper 2001; Piper and Ingram 2003). Shallow mass transport deposits along the Scotian slope have been identified using high resolution Huntec boomer and sparker systems, which can image the upper 100 m of sea bed at a vertical resolution of 1 m (Mosher and Simpkin 1999). Lower resolution airgun seismic data was used for the deeper sedimentary sequence from 100–500 m subbottom, at a resolution of tens of meters.
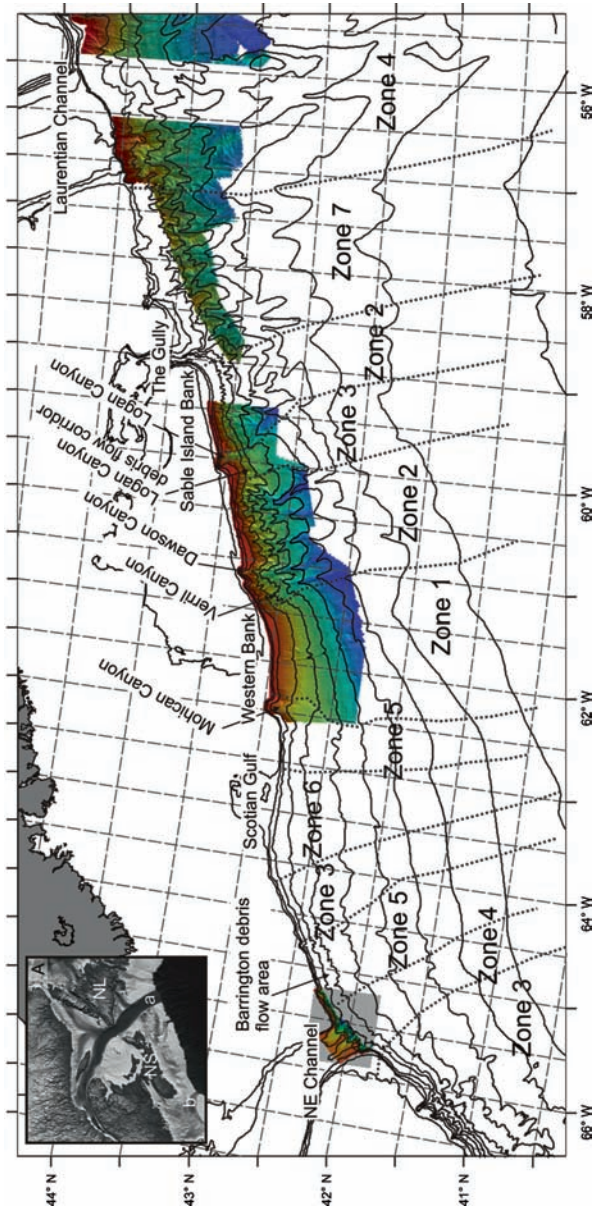
Fig. 1 Overview map of the Scotian Slope and its different MTD zones, for more details see results section; inset A shows the working area along the SE Canadian continental margin: NS: Nova Scotia, NF: Newfoundland, (**a**) Laurentian Channel, (**b**) Northeast Channel
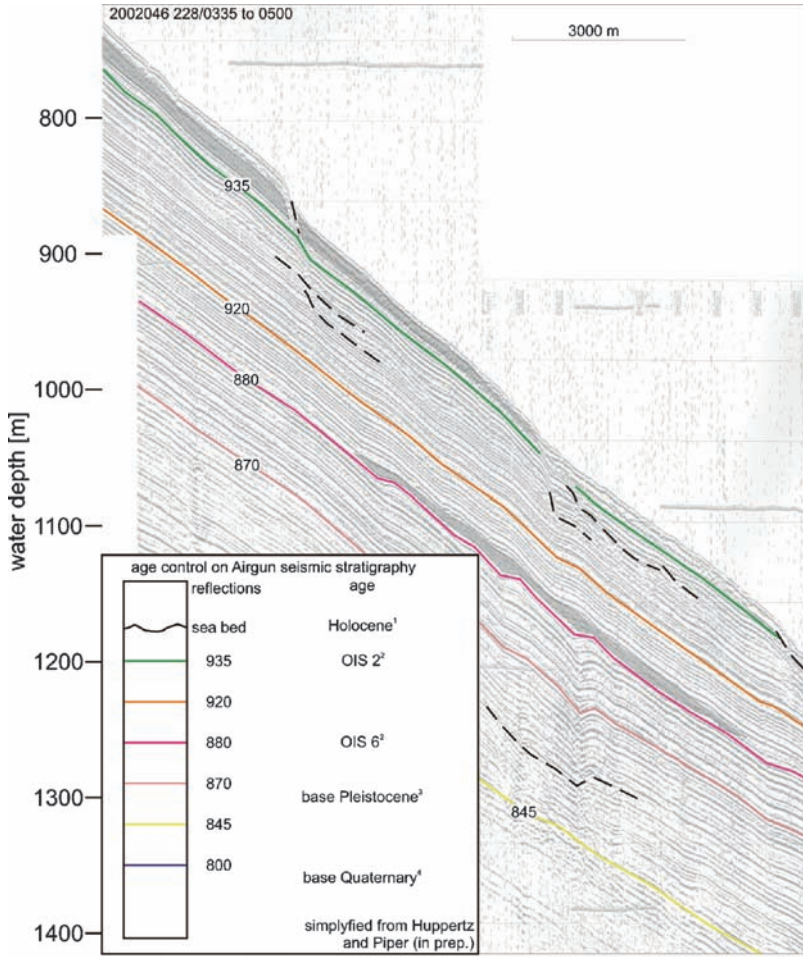
Fig. 2 Typical central Scotian slope Airgun seismic line from Zone 1 showing seismic reflectors and erosional planes (back dashed lines) and their relationship to MTDs. Deeper lying disturbances can have a pronounced impact on the upper sequence; the age control of the seismic reflections was taken from previous studies in the area: Piper and Campbell (2002), Piper and Sparkes (1990), Piper (2001) and Piper and Ingram (2003); area covered by stratigraphy box is a data gap

2   Distribution of Mass-Transport Deposits

Sediment failures occur throughout the slope area from the shelf break at ~500 m to the lower slope at 4,500 m. No clear stratigraphic variability in failures can be resolved at the resolution of the seismic correlation, but the distribution of MTDs varies spatially. Those failures that are not related to canyons, e. g. off Western
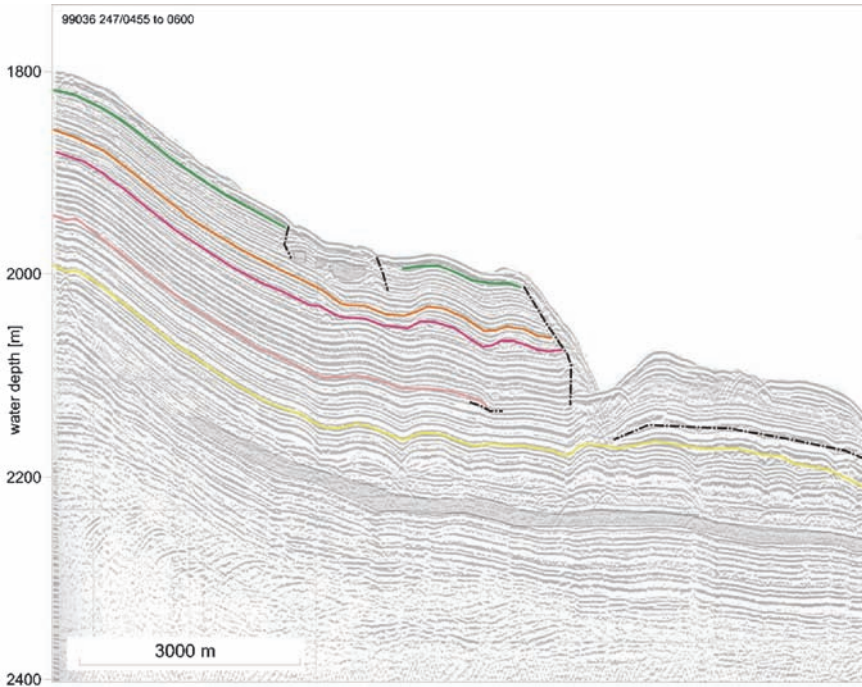
Fig. 3 Airgun seismic profile showing the age control on the major scarp at ~2,100 m water depth. The first continuous reflection under the scarp is close to the base of the Quaternary sequence. This profile is from area 1 and shows well stratified sediments with few erosional surfaces within the sequence; reflector colors as Fig. 2

Bank (Campbell 2000), can be related to scarps and failure planes upslope from the deposit (Fig. 2). Within canyons, small MTDs are interbedded with turbidite sands and appear linked to failures on canyon walls and at the heads of the canyons (Jenner et al. 2007).

Head scarps are widely found along the Scotian margin and range from a few meters to hundreds of meters high (Fig. 3), both at the seafloor and buried by younger sediment. Some scarps appear to be the result of repeated retrogressive failures (Mosher et al. 2004). The oldest scarp in the central area cuts back to at least oxygen isotope stage 6 (Fig. 3).

In some cases, more than one MTD appears geometrically linked to particular failure planes and erosional surfaces upslope and downslope (Fig. 2), implying that once established, a failure surface might evolve and release several retrogressively failed MTDs. Downslope, MTDs are commonly thinner on the mid-slope and thicker on the rise, suggesting bypassing of sediment.

Spatially, the distribution of MTDs is closely related to the shelf and slope morphology, the prevailing ice sheet regime and the occurrence of older failures in the area. Variation in these parameters has been used to classify the slope into different zones, each with different distribution of MTDs (Fig. 1, Table 1):
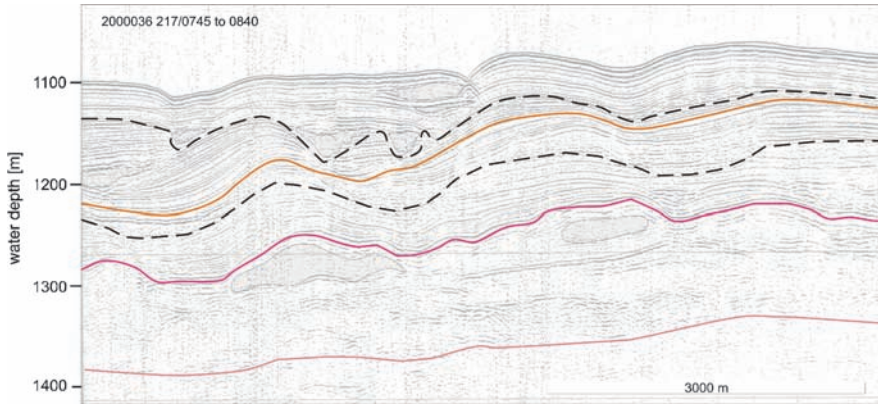
Fig. 4 Airgun seismic slope-parallel transect between the Barrington Debris flow area and the Scotian Gulf showing the sedimentary sequence in the western slope area with several small, lensoid-shaped MTDs. some of the stratified units may represent overspill deposits from turbidity activity. The black dashed lines are prominent erosional surfaces and may represent paleo-horizons

Table 1 Summary of MTD zones on the Scotian Slope; DF = debris flow, MTDs = mass-transport deposits

	Slope character	Erosion	Slope gradient	Type area
Zone 1	Smooth slope, inter-canyon areas	Few scarps	Low	Off western Bank
Zone 2	Areas highly dissected by deeply incised canyons, small lensoid MTDs on canyon floors	In canyons very high, in areas between canyons low	Variable	Verrill Canyon to Logan Canyon DF corridor
Zone 3	Abundant lenticular MTDs on low angle slopes	Locally, linked to MTDs	Low to medium	west of Scotian Gulf
Zone 4	MTDs in areas with stable canyons off shelf troughs	In canyons and areas of overspill	Low to high	NE Fan and Laurentian Fan
Zone 5	Widespread failures, no well developed canyons	High erosion, wide-spread	Medium	Albatross area, Barrington DF area
Zone 6	Widespread debris flows and cut-and-fill morphology, little stratification	Widespread	Low to medium	Off Scotian Gulf
Zone 7	Deeply incised old canyon systems with major wall failures, no canyons along shelf break	High to very high	high	easternmost Scotian Gulf

Zone 1 includes areas of smooth slope and inter-canyon areas characterized by thick, well stratified sediments with few erosional surfaces and related MTDs <20 ms thick. The overall regional slope gradient is low and lacks deeply incised canyons. The outer shelf areas are characterized by shallow banks. The type area is the slope off Western Bank between Mohican Channel and Verrill Canyon (Table 1).

Zone 2 consists of areas highly dissected by canyons, with canyon floors covered by MTDs and turbidite sands (e.g. as described by Jenner et al. 2007). Intercanyon highs between canyons are well stratified but show frequent erosional surfaces throughout, many of which terminate in arcuate headscarps. Zone 2 occurs in areas of higher regional gradient seaward of shallow banks that in many places show buried tunnel valleys (King 2001; Piper et al. 2007). The type area is the areas from Verrill Canyon to the area just west of the Logan Canyon debris flow corridor (Table 1).

Zone 3 is characterized by abundant and lenticular MTDs, which occur throughout the stratigraphic succession (Fig. 4). Individual deposits are volumetrically small. The thin interbedded stratified sediments are of minor importance and frequently show erosion and cuts; they are usually highly discontinuous. The upper slope shows discontinuous sequences with frequent erosion (Table 1).

Zone 4 is characterized by mass transport deposits in areas, where stable canyon systems off shelf troughs have been observed, e. g. off NE Fan (Robichaud 2006) and Laurentian Fan (Skene and Piper 2006). These areas are characterized by deeply incised, narrow canyons from the shelf break to almost 4,000 m water depth with MTDs along the canyon floors in the case of NE Fan and on levees in the case of Laurentian Fan (Table 1).

Zone 5 is characterized by widespread failures with no morphologically well developed canyons. The head scarps of these failures are usually difficult to identify because retrogressive failures may have eroded older head scarps. The MTDs are sometimes related to shallow canyon systems and can cover large areas downslope. They may have infilled or eroded older canyon systems completely. The individual flows are several tens of meters thick and frequently their thickness cannot be observed on the seismic data; most of the flows have a local source area and show short runout distances and blocky surfaces (Albatross area [Shor and Piper 1989] Barrington debris flow area [Mosher et al. this volume]) (Table 1).

Zone 6 is characterizes by widespread debris flows and cut-and-fill morphologies. This zone was only observed off the Scotian Gulf (Fig. 1), where almost no stratified sequences occur (Piper 2000). The lower slope is characterized by several small lobe-like structures built from few canyons on the slope (Table 1).

Zone 7 is found on the easternmost Scotian Slope and is characterized by deeply incised canyons and major wall failures (Piper and Ingram 2003) which created to major MTDs on the rise and outer slope. The complete slope is characterized by MTDs of various sizes. No stratigraphic control was possible in this area (Table 1).

3 Discussion

There are several different types of MTDs found along the Scotian slope:

(a) Massive blocky MTDs, mostly found in Zone 5 are likely derived from deeply buried, consolidated sediment on the upper to mid slope (Barrington area: Mosher et al. this volume; Albatross area: Shor and Piper 1989).

(b) Retrogressive failures like the 1929 failure. These are common in zone 1 and in intercanyon areas of Zone 2. They may be favored by high sedimentation rates from plumes; triggering may be from retrogressive failure from salt tectonics on the lower slope or from steep canyon walls.

(c) Glacigenic debris flows. As argued by Piper and Normark (submitted), these are absent on the steep slopes off Laurentian Channel and Northeast Channel, probably because they have transformed to turbidity currents. They appear to be present off the Scotian Gulf in Zone 6.

(d) Stacked small-scale lensoid-shaped MTDs. These flows are mostly found in areas with no canyons and a low slope gradient as the large parts of the western Scotian slope in Zone 3. These flows were initiated by local failures due to cutting by melt water and retrogressive failures (Hill 1984) or from mud tectonics and related oversteepening (Piper and Sparkes 1987).

(e) Major slope-wide erosion in areas of deeply incised canyons where wall failures are frequently observed. These MTDs were only observed in Zone 7 where the MTDs have eroded most of the slope sequence at least once and can be found down to the rise areas (Piper and Ingram 2003).

The observed distribution of different types of MTDs along the margin may indicate that the character of the initiated MTD is somehow related to the regional slope gradient and the processes along the slope break. The different zones have different slope gradients (Fig. 5). Overall, slope and upper rise gradients are less west of Mohican Channel than in the east. Upper slope gradients are least in Zones 1 and 6 whereas highest slope gradients are found in zone 7 and 5. Slope erosion is thus related to gradients: low MTD activity is found in Zones 1 and 2 which have low gradients, whereas steeper slopes are characterized by major slope failures (Zones 5 and 7). An exception are the shelf troughs, where major sediment transfer to the shelf break occurs, especially off the Laurentian Channel (Shaw et al. 2006) and the NE Channel (Hundert and Piper 2008), where sediment from Scotian Shelf sources creates sediment failures and characterizes the areas seaward of the troughs.

In the case of slope failures, the failed sediment consists principally of blocks of variably consolidated slope sediment (Mosher et al. 2004). The role of sediment transported directly from the shelf, such as jökulhlaups at ice maxima (Tripsanas and Piper 2008) or by storms after ice has retreated (Piper 2005) in some cases erode only surficial sediments (Canals et al. 2006), but in the case of larger event will erode deeper lithified sediment along the canyon walls (Piper et al. 2007).

The extent and frequency of sediment failure appears related to the erosional history of an area. Most of sediment failures occur over time in the same areas (mainly Zones 3, 4, 5, 6, and 7) whereas Zone 1 and the local highs of Zone 2 have been stable for most of the Quaternary (Figs. 1, 3, and 5). Therefore, sediment failure is likely related to processes, which occur again and again in the areas of observed sediment failures.

The presence of MTDs also enhances the possibility of more frequent failures in the same areas as failure can precondition for further failures (Fig. 5). Due to sediment failures, slope angle and stability are changed significantly and may promote retrogressive failure or change the pathways for turbidity currents flowing down the slope. Lobe areas, such as the area seaward of the Laurentian Channel, are only
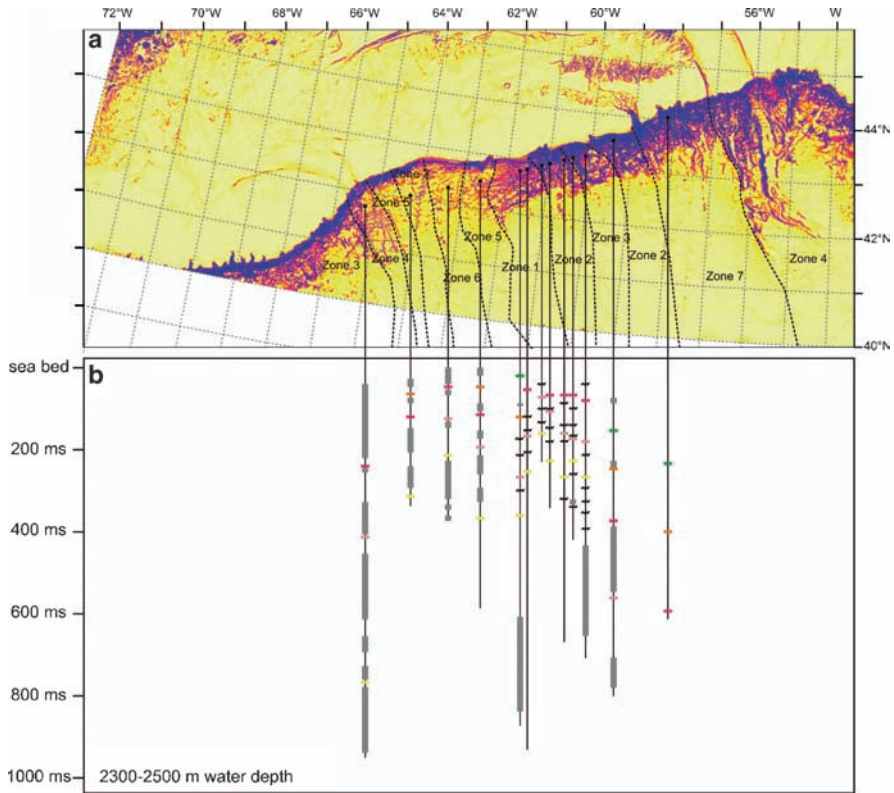
Fig. 5 (**a**) Slope gradient variations along the Scotian Slope, dark colors indicate steep slope angles; (**b**) summary figure of the spatial variation of the seismic Airgun stratigraphy (colored bars as in Fig. 2) and thicknesses of MTDs (gray bars) and erosional planes (wavy lines) on the Scotian Slope, the length of the vertical bars represents penetration depth on the seismic data; transect points between 2,300 and 2,500 m water depth

constructed in areas where frequent failures generate the lobe. Thus, over several glacial cycles, areas of failure are generally similar and can be used to predict future areas of geohazards by sediment failures (Fig. 5). Isolated sediment failures within an area are more likely related to random slope failures which are not related to cyclic events as glaciation, but are more likely related to random initiating events such as passive margin seismicity.

4 Conclusions

Construction of the Quaternary Scotian Slope has been highly impacted by several different types of mass transport deposits. The distinct character of the different types of MTDs could be used to classify the slope into seven different MTD zones.

These zones are: (1) well stratified areas with few MTDs; (2) highly canyonized areas with mostly complete sequences in intercanyon areas; (3) areas of several small-scale lensoid MTDs; (4) MTDs on local highs and canyon floors in areas with stable canyons and shelf troughs; (5) area of widespread local failures on the mid-slope with few shallow channels; (6) large blocky debris flows; and (7) areas of deeply incised canyons with slope-wide sediment failures. The spatial distribution of these different zones allows an assessment of the role of direct glacial supply, preconditioning by high sedimentation rates and older failures, and the effect of canyon erosion and regional gradient on the style of MTDs on the slope.

References

Berry JA, Piper DJW (1993) Seismic stratigraphy of the central Scotian rise: A record of continental margin glaciation. Geo-Mar Lett 13:197–206

Campbell DC (2000) Relationship of sediment properties to failure horizons for a small area of the Scotian Slope. Current research 2000-D8, Geol Surv Can

Campbell DC, Shimeld JW, Mosher DC, Piper DJW (2004) Relationships between sediment mass-failure modes and magnitudes in the evolution of the Scotian Slope, offshore Nova Scotia, Off Tech Conf Houston Texas OTC Page #16743

Canals M, Urgeles R, Calafat AM (2000) Deep sea-floor evidence of past ice streams off the Antarctic Peninsula. Geology 28:31–34

Canals M, Puig P, Durrieu de Madron X (2006) Flushing submarine canyons. Nature 444:354–357

Gauley B-JL (2001) Lithostratigraphy and sediment failure on the central Scotian slope, Dept Earth Sci Dalhousie University, Halifax, 214 p

Hill PR (1984) Sedimentary facies of the Nova Scotian upper and middle continental slope, offshore eastern Canada. Sedimentology 31:293–309

Hundert T, Piper DJW (2008) Late quaternary sedimentation on the southwestern Scotian Slope, eastern Canada: Relationship to glaciation. Can J Earth Sci 45:267–285

Jenner KA, Piper DJW, Campbell DC, Mosher DC (2007) Lithofacies and origin of late quaternary mass transport deposits in submarine canyons, central Scotian Slope, Canada. Sedimentology 54:19–38

King EL (2001) A glacial origin for Sable Island: Ice and sea-level fluctuations from seismic stratigraphy on Sable Island Bank, Scotian Shelf, offshore Nova Scotia. Curr Res 2001-D19, Geol Surv Can

Mosher DC, Piper DJW (2007) Analysis of multibeam seafloor imagery of the Laurentian Fan and the 1929 Grand Banks landslide area. In: Lykousis V, et al. (eds.), Submarine Mass Movements and Their Consequences. Springer, The Netherlands, pp. 77–88

Mosher DC, Simpkin PG (1999) Environmental marine geosciences. 1: Status and trends of marine high-resolution seismic reflection profiling: Data acquisition. Geosci Can 26:174–188

Mosher DC, Piper DJW, Campbell DC, Jenner KA (2004) Near-surface geology and sediment-failure geohazards of the central Scotian Slope. Am Assoc Petrol Geol Bull 88:703–723

Piper DJW (2000) Pleistocene ice outlets on the central Scotian Slope, offshore Nova Scotia. Curr Res 2000-D7, Geol Surv Can

Piper DJW (2001) The geological framework of sediment instability on the Scotian Slope: Studies to (1999) Open File 3920, Geol Surv Can

Piper DJW (2005) Late Cenozoic evolution of the continental margin of eastern Canada. Nor J Geol 85:305–318

Piper DJW, Brunt RA (2006) High-resolution seismic transects of the upper continental slope off southeastern Canada. Open File 5310, Geol Surv Can

Piper DJW, Campbell DC (2002) Surficial geology of the Scotian Slope, eastern Canada. Curr Res 2002-E15, Geol Surv Can

Piper DJW, Ingram S (2003) Major Quaternary sediment failures on the east Scotian Rise, eastern Canada. Curr Res 2003-D1, Geol Surv Can

Piper DJW, Normark WR (1989) Late Cenozoic sea-level changes and the onset of glaciation: Impact on continental slope progradation off eastern Canada. Mar Petrol Geol 6:336–347

Piper DJW, Sparkes R (1987) Proglacial sediment instability features on the Scotian Slope at 63°W. Mar Geol 76:15–31

Piper DJW, Sparkes R (1990) Pliocene – Quaternary geology of the central Scotian Slope. Open File 2233, Geol Surv Can

Piper DJW, Farre JA, Shor A (1985) Late quaternary slumps and debris flows on the Scotian Slope. Geol Soc Am Bull 96:1508–1517

Piper DJW, Mudie PJ, Aksu AE, Skene KI (1994) A 1 Ma record of sediment flux south of the Grand Banks used to infer the development of glaciation in southeastern Canada. Quat Sci Rev 13:23–37

Piper DJW, Shaw J, Skene KI (2007) Stratigraphic and sedimentological evidence for late Wisconsinan sub-glacial outburst floods to Laurentian Fan. Paleogeog Paleoclimat Paleoecol 246:101–119

Rise L, Ottensen D, Berg K, Lundin E (2005) Large-scale development of the mid-Norwegian margin during the last 3 million years. Mar Petrol Geol 22:33–44

Robichaud M (2006) Late quaternary evolution of the Northeast Fan, offshore Nova Scotia, Department of Earth Sciences. Dalhousie University, Halifax 98

Shaw J, Piper DJW, Fader GBJ, King EL, Todd BJ, Bell T, Batterson MJ, Liverman DGE (2006) A conceptual model of the deglaciation of Atlantic Canada. Quat Sci Rev 25:2059–2081

Shor A, Piper DJW (1989) A large late pleistocene blocky debris flow on the central Scotian slope. Geo-Mar Lett 9:153–160

Skene KI, Piper DJW (2006) Late cenozoic evolution of Laurentian Fan: Development of a glacially-fed submarine fan. Mar Geol 227:67–92

Tripsanas EK, Piper DJW (2008) Late quaternary stratigraphy and sedimentology of Orphan Basin: Implications for meltwater dispersal in the southern Labrador Sea. Paleogeog Paleoclimatol, Paleoecol 260:521–539

Wilken M, Mienert J (2006) Submarine glacigenic debris flows, deep-sea channels and past ice-stream behaviour of the East Greenland continental margin. Quat Sci Rev 25:784–810

Section IV
Submarine Mass Movements and Tsunamis

Middle to Late Miocene Slope Failure and the Generation of a Regional Unconformity Beneath the Western Scotian Slope, Eastern Canada

D.C. Campbell and D.C. Mosher

Abstract The global greenhouse to icehouse transition that occurred during the middle Cenozoic marked a major shift in the geological and oceanographic conditions in the northwest Atlantic Ocean. During this transition, strong contour currents developed and sediment input to the North American Basin increased. These events were coeval with the development of regional unconformities within the basin and along the basin margins. This study examines a widespread, Middle to Late Miocene-age unconformity preserved below the western Scotian margin and demonstrates that it is primarily the product of erosion by regional submarine mass movement, although bottom currents and channel development may have played a role in its formation. The mass-transport deposits are among the largest reported in the literature. Despite the presence of a steep upper slope in the study area, the erosion is not due to mass-wasting initiated on the upper slope, but rather erosion and seabed failure initiated on the lower slope and continental rise, followed by failure retrogression. It is suggested that salt tectonics and bottom-current activity contributed to sediment failure.

Keywords Mass-transport deposit • unconformity • bottom currents • salt tectonics

1 Introduction

Deepwater erosional unconformities are attributed to either down-slope or along-slope processes. Down-slope processes include the spectrum of gravity-driven flows associated with sediment transport into deeper parts of a basin that

D.C. Campbell and D.C. Mosher
Geological Survey of Canada, Natural Resources Canada, Bedford Institute of Oceanography, 1 Challenger Dr., Dartmouth, NS, B2Y 4A2

D.C. Campbell (✉)
Department of Earth Sciences, Dalhousie University, Halifax, Nova Scotia, Canada, B3H 4R2
e-mail: cacampbe@nrcan.gc.ca

lead to the formation of failure scars, gullies, channels and canyons (Stow and Mayall 2000). Along-slope erosion processes are associated with bottom-current activity, when current velocities exceed the threshold of deposition and form erosional terraces, abraded surfaces, contourite channels, moats and furrows (Hernández-Molina et al. 2008). Determination of the processes that formed such erosional surfaces, whether predominantly down-slope, along-slope, or mixed, has implications for understanding controls on margin evolution, paleoceanography, and sequence stratigraphy.

The global greenhouse to icehouse transition that occurred during the middle Cenozoic (Late Eocene to Middle Miocene) marked a major shift in the geological and oceanographic conditions in the northwest Atlantic Ocean. During this transition, strong contour currents developed and sediment input to the North American Basin increased. These events were coeval with the development of regional unconformities within the basin and along the basin margins (Ebinger and Tucholke 1988; Locker and Laine 1992). In many cases, the relationship between abyssal plain and continental margin unconformities is unclear. Seismic reflection data from the southwestern Scotian Slope and Rise reveal a previously undocumented, widespread erosional unconformity overlain by large-scale mass-transport deposits (MTDs). Recent studies have shown that the basal surfaces of submarine mass movements can severely erode underlying strata through processes such as basal shear and erosion by rafted, intact blocks (Frey-Martínez et al. 2006; Gee et al. 2005). The purpose of this paper is to describe the seismic geomorphology of the erosion surface and determine the relative importance of submarine mass-movement in its formation.

1.1 Study Area and Geological Setting

The study area is the continental slope and rise off southwestern Nova Scotia, Canada (Fig. 1). The passive Scotian margin is part of the Scotian basin, a 1,200 km-long basin offshore Nova Scotia that formed during Late Triassic and Early Jurassic rifting of Pangea and the opening of the Atlantic Ocean (Wade and MacLean 1990). Syn-rift evaporites (Argo Fm.) were deposited throughout the basin forming a significant salt province (Shimeld 2004). A major carbonate bank (Abenaki Fm.) developed in the Jurassic, the steep buried edge of which trends sub-parallel to the modern shelf break (Figs. 1 and 2). Cenozoic age deposits in the basin are assigned to the Banquereau (Late Cretaceous to Pliocene) and Laurentian (Pleistocene to Recent) formations (Jansa and Wade 1975). Apart from Quaternary deposits, little is known about the Cenozoic history of the outer Scotian margin (Piper 2005). Most studies have focused on the central Scotian shelf and upper slope area where data density is greatest (e.g. Wade et al. 1995; Fensome et al. 2008). These studies show that localized progradation of depositional lobes and progressively deeper canyon incision on the upper slope during periods of relative sea-level lowstands, dominated sedimentation in the area during the Cenozoic. On the lower continental slope
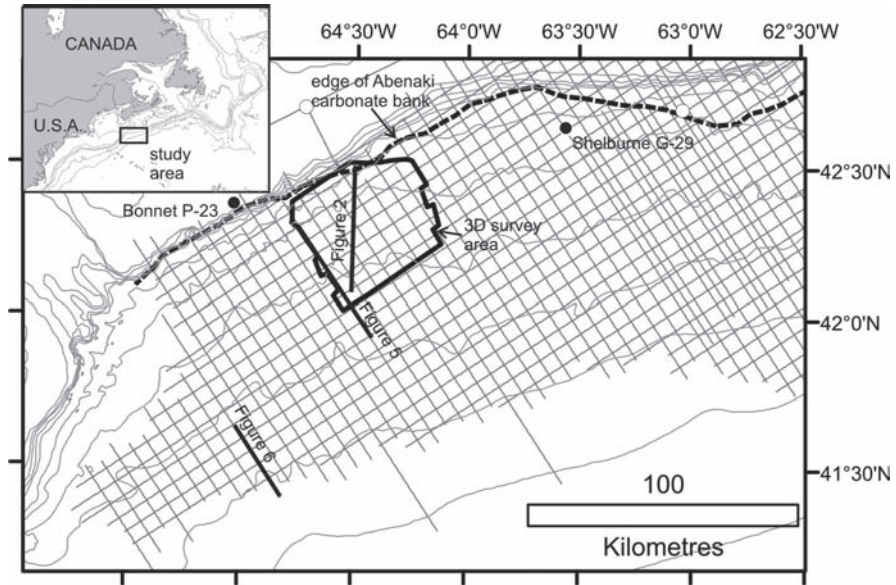
Fig. 1 Map of the study area showing locations of 3D and 2D seismic reflection data, hydrocarbon exploration wells used for age control, and figure locations. The edge of the buried Abenaki carbonate bank is shown by a dashed line
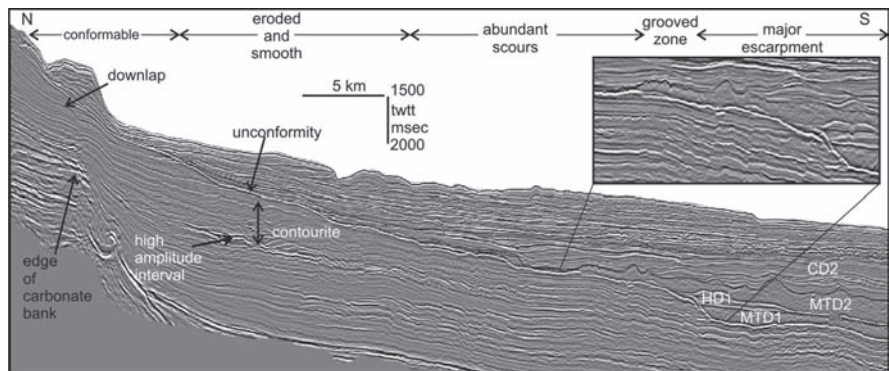
Fig. 2 Dip-oriented seismic reflection profile from the 3D seismic dataset. An extensive erosional unconformity is imaged below the modern lower slope and rise. Inset shows enlarged portion of line. Line location is shown in Figs. 1 and 4 (data courtesy of EnCana Corp.)

and rise east of the study area, Swift (1987) and Ebinger and Tulcholke (1988) reported a number of erosional unconformities in seismic reflection data and suggested a bottom-current origin with inferred ages of Oligocene, Lower Miocene, Middle Miocene, and Pliocene.

1.2   Methods

This study uses 2D and 3D marine multichannel seismic reflection data, along with biostratigraphic information from hydrocarbon exploration wells (Fig. 1). Recent biostratigraphic analysis on the Shelburne G-29 well (Fensome et al. 2008) and biostratigraphic data from the Bonnet P-23 well (Bujak Davies Group 1988) provide age control.

The 2D seismic reflection dataset used in this study is a regional grid acquired by TGS-Nopec Geophysical Company in 1998 and 1999 (Shimeld 2004). Line spacing is 8 km in the strike orientation and 4 to 8 km in the dip orientation. Hydrophone streamer length was 6 to 8 km. The acoustic source for the surveys was a 130 L tuned airgun array and the data are 80 to 106 fold. The 3D seismic reflection dataset was acquired in 2001 for EnCana Corporation (Mosher and Campbell in press). The survey covered an area of approximately 1,790 km^2, termed the Barrington exploration block. The survey consisted of 98 lines spaced 450 m apart. Each sailing line consisted of eight hydrophone streamers 6,000 m long with 240 channels per streamer. Channel separation was 25 m. The acoustic source was a 62 L tuned-airgun array generating a peak frequency of 70 Hz and a bandwidth of 5–100 Hz, implying about 5.5 m vertical resolution. Bin spacing is 12.5 by 12.5 m. Processing of both datasets was conducted by the data owner prior to this study. For the purpose of this study, the authors were given access to the upper 2 s two-way travel time (twtt) below the seafloor of the 3D seismic dataset. Seismic reflection data were interpreted in Seismic Micro Technologies Kingdom Suite and Schlumberger GeoFrame software packages. For the 3D seismic dataset, reflection horizons were mapped and interpolated to produce continuous surfaces. Seismic reflection structure, amplitude, and dip of maximum similarity attributes were used to interpret the seismic geomorphology. The dip of maximum similarity is a geometric attribute computed by first determining semblance of adjacent traces over a sliding time window and range of dips, and then extracting the dip of maximum semblance within the time window. It is useful for identifying structural discontinuities. The 2D seismic reflection data were used to map the extent of depositional elements, interpret regional structure, and to correlate events to the Shelburne G-29 and Bonnet P-23 wells. For estimates of volume and other dimensions, two-way travel time was converted to depth, using a sound velocity of 2,000 m/s based on velocity data from the Shelburne G-29 well.

2   Results

One of the most striking features in the study area is a widespread, non-conformable reflection that is recognized below the modern slope and rise (Fig. 2). The horizon truncates underlying seismic reflections in several places, while overlying reflections onlap the surface. Over much of the study area, the horizon is the product of

multiple erosion events, formed where horizons coalesce to form a single surface at the resolution of the seismic data. Laterally and basinward, the coalesced reflections separate and diverge, and it is possible to infer processes that were active during formation of the unconformity. The following sections describe the seismic reflection character and estimated age of the unconformity and the onlapping deposits.

2.1 Seismic Reflection Character of the Unconformity

On seismic reflection profiles, the unconformity appears as a strong, negative reflection (Fig. 2). Shelfward, the erosional surface becomes conformable and its erosional nature is less apparent. Laterally and basinward, the erosional nature of the unconformity is recognized as far west and south as the data extent, and at least as far east as the Shelburne G-29 well. The regional geomorphology of the unconformable surface is shown in Fig. 3. The surface dips steeply to the south seaward of the edge of the Abenaki carbonate bank. Downslope, a second regional change in gradient occurs at the southern edge of the Scotian Slope salt province (Shimeld 2004). Here, a major arcuate escarpment marks the northern edge of a buried submarine embayment. A series of broad gullies incise the surface and lead to the embayment.

Maps of 3D time-structure overlain with dip of maximum similarity show evidence of pronounced down-slope erosion (Fig. 4). In the southwestern corner of the 3D
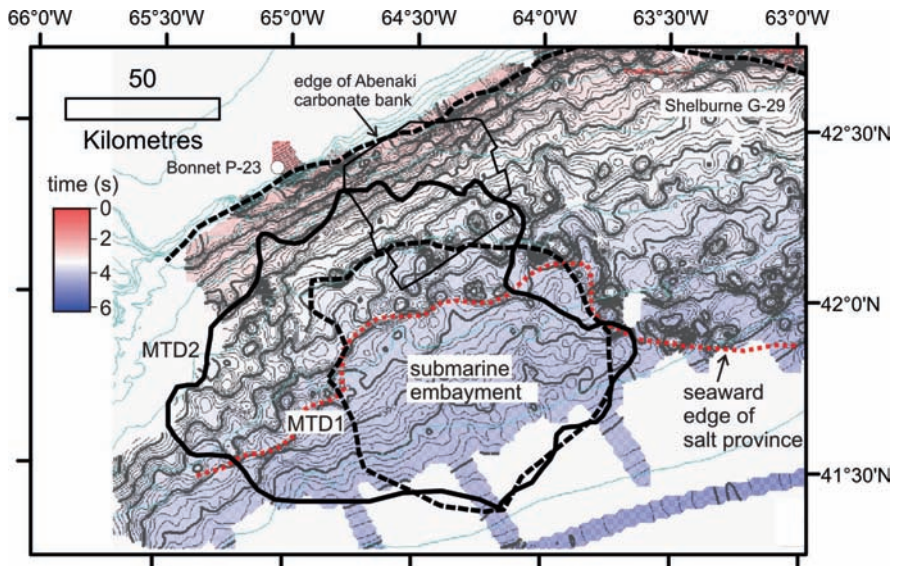
Fig. 3 Regional time-structure map of the unconformable surface. Note the submarine embayment developed seaward of the salt province. The extents of two major mass-transport deposits (MTD1 and MTD2) are shown in solid and dashed lines
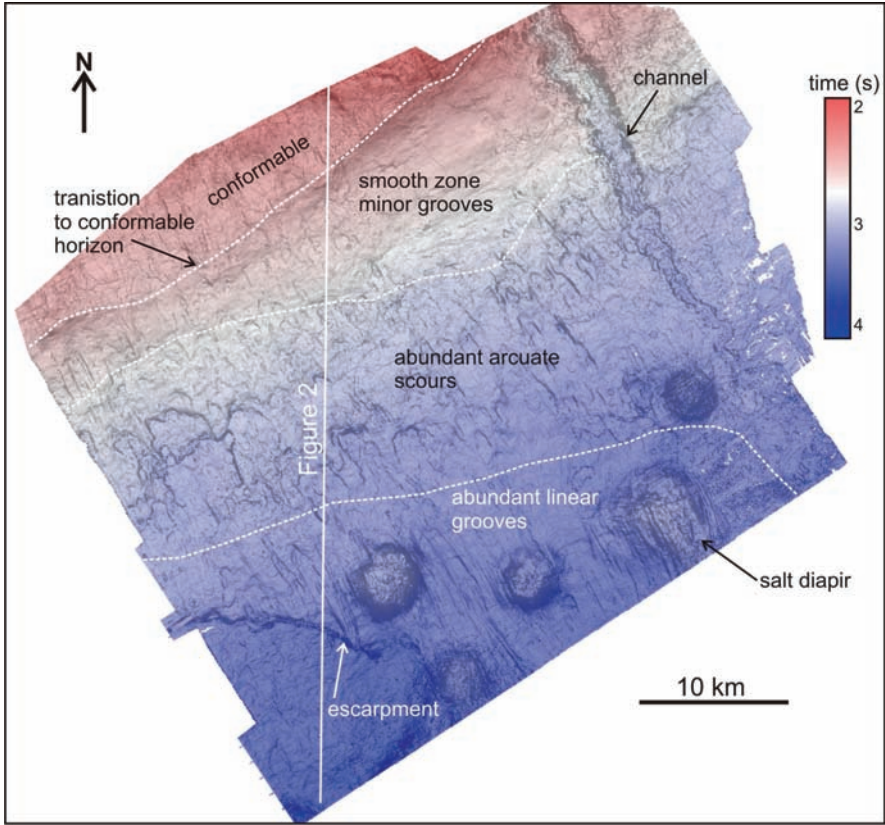
Fig. 4 Seismic geomorphology (time-structure overlain with dip of maximum similarity) of the unconformity showing evidence of extensive down-slope erosion. Map area located on Fig. 1 (data courtesy of EnCana Corp.)

dataset, a long arcuate escarpment more than 220 m high corresponds to the northern edge of the submarine embayment. Down-dip of the escarpment, the surface relief is slightly mounded and there are no lineations to indicate flow direction. Immediately north and east of the escarpment, long, linear grooves oriented down-dip characterize much of the unconformity. The grooves are up to 14 km long, 400 m wide, and 30 m deep. In the 3D data area, five dome structures are present on the unconformity and are the sub-surface expression of underlying salt diapirs. In some cases, the linear grooves pass over the diapirs and in other instances, they deviate around the features. Updip from the grooved zone, the seabed is scoured, with numerous smaller arcuate escarpments 0.5 to 4 km wide and 50 m high. This area passes up-dip to a zone that is much smoother with some subtle scars. The shelfward transition from erosional to conformable character of the surface is marked by a sharp change in gradient. In the eastern part of the 3D seismic dataset, a channel has eroded down to the level of the unconformity. The channel is up to

3 km wide and 370 m deep. The channel walls are scalloped and a sinuous channel thalweg is apparent.

The unconformity marks the top of a reflection package that thins significantly eastward towards the Shelburne G-29 well, with several prominent reflections coalescing at the well location. Biostratigraphic analysis from the well indicates a Late Miocene (Messinian) to Late Eocene (Bartonian) unconformity (Fensome et al. 2008) at the same stratigraphic level as the coalesced reflections. Correlation of the upslope, conformable portion of the erosional surface to the Bonnet P-23 well corresponds to a Middle Miocene age (Table 1), although reflection correlation across the shelf break to this well is tenuous.

2.2   Seismic Reflection Character Above the Unconformity

Five depositional elements have been mapped which onlap the unconformity (Figs. 2, 5, and 6). The first or oldest deposit has reflection characteristics typical of a separated drift (Faugères et al. 1999), and shows evidence of upslope and eastward migration. This interval is termed CD1. This deposit is recognized in the extreme southwest portion of the study area and possibly correlates with the sediment drift below the unconformity in the 3D dataset (Fig. 2). A major mass-transport deposit (MTD1) overlies

Table 1   Estimated ages of reflection horizons and units presented in this study

Horizon/Unit	Maximum age	Minimum age
Contourite deposit 2 (CD2)	Messinian	Late Pliocene
Mass-transport deposit 2 (MTD2)	Messinian	Messinian
Channel (top HD1)	Messinian	Messinian
Hemipelagic interval (HD1)	Messinian	Messinian
Mass-transport deposit 1 (MTD1)	Middle Miocene	Messinian
Contourite deposit 1 (CD1)	Middle Miocene	Messinian
Unconformity	Middle Miocene	Messinian
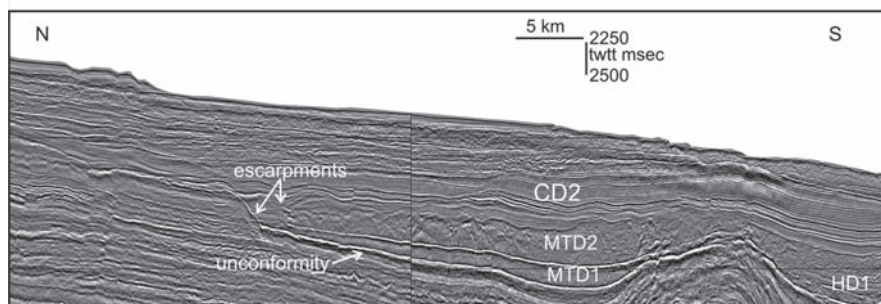
Fig. 5   Dip-oriented seismic reflection profile from the continental rise showing major escarpments associated with MTD1 and MTD2. Line location is shown in Fig. 1 (data courtesy of TGS-Nopec)
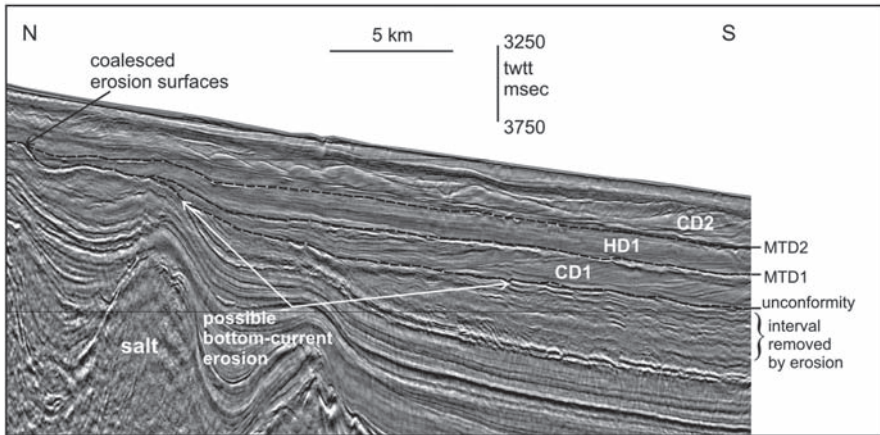
Fig. 6 Dip-oriented seismic reflection profile from the southwestern part of the study area. The earliest indication of erosion along the unconformity is associated with development of a contourite (CD1) and is enhanced at the edge of a salt diapir. Erosion surfaces merge up-dip to form a single horizon at data resolution. Line location is shown in Fig. 1 (data courtesy of TGS-Nopec)

CD1 and has typical chaotic to transparent internal reflection character, irregular surface morphology, and mounded and depression-filling geometry. This initial mass transport deposit covers an area of 6,200 km^2 and represents a volume of ~300 km^3 of failed material (Fig. 3). In 3D seismic data, the onlap of MTD1 corresponds with the large escarpment in the southwest portion of the survey and the deeply grooved zone. An interval of parallel to occasionally wavy, low amplitude reflections (HD1), likely representing hemipelagic and turbidite deposition, overlies MTD1. The deposition of HD1 was concomitant with the development of a large channel imaged in the 3D seismic data (Fig. 4). West of the large channel, much of HD1 was eroded and redeposited by the fourth element, another mass transport deposit (MTD2) which is much thicker than MTD1, covers an areal extent of 10,500 km^2 and represents a failure volume of ~680 km^3 (Fig. 3). The failure comprises large rafted blocks up to 5 km long. MTD2 onlaps the unconformity in the intensely scoured zone. A thick contourite interval (CD2) was deposited above MTD2. The onlap of CD2 with the unconformity corresponds to the smooth, up-dip portion of the unconformity in the 3D dataset.

Estimated ages of units that onlap the erosional unconformity are based on correlation with the Shelburne G-29 and Bonnet P-23 wells (Table 1). CD1 directly overlies the erosional unconformity in the southwestern part of the study area and possibly underlies the unconformity in the 3D seismic area. Because of this complicated stratigraphic relationship, CD1 is tentatively assigned a Middle to Late Miocene age. In all areas examined, MTD1 immediately overlies CD1 or the unconformity and is therefore younger. HD1, the large channel, and MTD2 are all Late Miocene age and intersect the Shelburne G-29 well at 2,200–2,320, 2,190, and 2,000 m, respectively. The second contourite interval, CD2, intersects the well from 2,000–1,660 m and is latest Miocene to Late Pliocene age.

3 Discussion

The earliest indication of erosion along the unconformity occurs at the basal surface of contourite interval CD1 (Fig. 6). In the western part of the study area, reflections underlying the base of CD1 are truncated and suggest as much as 200 m of sediment was removed from the lower slope, possibly eroded by bottom currents, enhanced where the seabed relief changes at the edge of the salt diapirs (Fig. 6). A second phase of erosion was coeval with the deposition of MTD1 (Fig. 6). It is likely that contourite deposits of CD1 failed to produce MTD1 (Fig. 2). MTD1 is confined to the submarine embayment seaward of the salt province and has a characteristic lower slope escarpment. The deeply grooved surface updip from the escarpment in the 3D dataset suggests some retrogressive failure and translation of intact blocks during formation of MTD1, however it is not possible to determine the extent of retrogression because of later erosion by MTD2. The failure of MTD2 was more extensive than MTD1 and transported a large amount of sediment deeper into the basin. The failed material comprised channel and levee sediments of HD1, as well as some contourite material from CD2. MTD2 had a significant retrogressive component and failure deposits are recognized both upslope and down slope of the edge of the salt province.

The 3D seismic reflection data provide the most definitive evidence of the processes responsible for the formation of the erosional surface. The data show that most of the erosion is attributed to mass movement and to a lesser extent, channel formation. MTD1 and MTD2 rank among the largest mass transport deposits reported in the literature (Legros 2002). Both MTDs were initiated on the continental rise, well seaward of the steep Abenaki carbonate bank edge which appears to control the position of the shelf break to this day. More recent failures of Quaternary age were sourced from the steep upper slope area (Mosher and Campbell in press). However, in the case of the two MTDs in this study, salt tectonics and perhaps contour current activity played a greater role in slope failure. There is a strong spatial relationship between the distribution of the MTDs and the limit of the salt diapir province (Fig. 3). Shimeld (2004) reported rejuvenated apparent salt uplift in the study area beginning in the late Paleogene and continuing to the Pliocene. In the study area, contour currents served to build contourite drifts and possibly erode the seabed at topographic highs. It is possible that undercutting by contour currents, supplemented by salt movement, oversteepened the lower slope in this area and contributed to failure.

4 Conclusion

This study demonstrates that a widespread, Miocene unconformity preserved below the western Scotian margin is the primarily the product of regional mass-wasting, although erosion via channel incision and contour currents may have played a lesser role. The unconformity appears to be a highly diachronous surface, formed by the

coalescing of several erosion surfaces over the course of millions of years. Submarine mass-movements, among the largest reported in the literature, produced large escarpments on the lower slope, eroded long linear grooves at their bases, and created several arcuate scours as they retrogressed. Despite the presence of a steep upper slope in the study area, the unconformity is not due to erosion and bypass of the upper slope, but rather erosion and seabed failure initiated on the continental rise, with salt tectonics and contour current activity providing possible trigger mechanisms.

References

Bujak Davies Group (1988) Palynological Analysis of the Interval 440–3950 M, Bonnet P-13, Scotian Shelf. Geological Survey of Canada Open File Report 1858:19

Ebinger CA, Tucholke BE (1988) Marine Geology of the Sohm Basin, Canadian Atlantic Margin. Bulletin of Am Assoc Petrol Geol 72:1450–1468

Faugères J-C, Stow DAV, Imbert P, Viana A (1999) Seismic features diagnostic of contourite drifts. Mar Geol 162:1–38

Fensome RA, et al. (2008) The Last 100 Million Years on the Scotian Margin, Offshore Eastern Canada: An Event-Stratigraphic Scheme Emphasizing Biostratigraphic Data. Atlantic Geol 44:93–126

Frey-Martínez J, Cartwright J, James D (2006) Frontally Confined Versus Frontally Emergent Submarine Landslides: A 3D Seismic Characterization. Mar and Petrol Geol 23:585–604

Gee MJR, Gawthorpe RL, Friedmann JS (2005) Giant Striations at the Base of a Submarine Landslide. Mar Geol 214:287–295

Hernández-Molina FJ, Llave E, Stow DAV (2008) Continental slope contourites. In: Rebesco M, Camerlenghi A (eds). Contourites. Elsevier 379–408

Jansa LF, Wade JA (1975) Geology of the Continental Margin Off Nova Scotia and Newfoundland: Geological Survey of Canada Paper 74–30, Offshore Geol Eastern Can 2:51–105

Legros F (2002) The Mobility of Long-Runout Landslides. Engin Geol 63:301–331

Locker SD, Laine EP (1992) Paleogene-Neogene Depositional History of the Middle U.S. Atlantic Continental Rise: Mixed Turbidite and Contourite Depositional Systems. Mar Geol 103:137–164

Mosher DC, Campbell DC (2010) The Barrington submarine landslide, western Scotian Slope. In: Shipp, RC, Weimer P, and Posamentier, HW (eds), Mass-transport Deposits in Deepwater Settings. Society of Economic Paleontologists and Mineralogists Special Publication 95

Piper DJW (2005) Late Cenozoic Evolution of the Continental Margin of Eastern Canada. Nor J Geol 85:231–244

Shimeld J (2004) A Comparison of Salt Tectonic Subprovinces Beneath the Scotian Slope and Laurentian Fan. In: Post PJ., Olson DL, Lyons KT, Palmes SL, Harrison PF, and Rosen N (eds). Salt–sediment interactions and hydrocarbon prospectivity: concepts, applications, and case studies for the 21st century. 24th Annual Gulf Coast Section of the Soc Econ Paleontol and Mineral Found Bob F. Perkins Research Conf, Houston, Texas, Dec. 5–8, 2004

Stow DAV, Mayall M (2000) Deep-Water Sedimentary Systems: New Models for the 21st Century. Mar and Petrol Geol 17:125–135

Swift SA (1987) Late Cretaceous-Cenozoic Development of Outer Continental Margin, Southwestern Nova Scotia. Bull Am Assoc of Petrol Geol 71:678–701

Wade JA, MacLean BC (1990) The Geology of the Southeastern Margin of Canada, Part 2: Aspects of the Geology of the Scotian Basin from Recent Seismic and Well Data. In: M.J. Keen and G.L. Williams (eds). Geology of the Continental Margin Off Eastern Canada. Edited by. Geol Surv Can, Geology of Canada no. 2:190–238

Wade JA, MacLean BC, Williams GL (1995) Mesozoic and Cenozoic Stratigraphy, Eastern Scotian Shelf: New Interpretations. Can J Earth Sci 32:1462–1473

Mass Transport Deposits on the Southwestern Newfoundland Slope

M.K. Giles, D.C. Mosher, D.J.W. Piper, and G.D. Wach

Abstract Sediment mass failure is a major process during Cenozoic development of the southwestern Grand Banks of Newfoundland margin. Recently acquired seafloor multibeam and seismic reflection data provide evidence of stacked and regionally extensive mass transport deposits (MTDs) since the middle-late Miocene. MTDs with volumes between 30 and 150 km^3 lie between the top of a Cretaceous Unconformity and mid-Pliestocene and MTDs with volumes less than 1 km^3 are recognized since the mid Pleistocene. Seaward dipping faults at the base of the mid Miocene MTD suggest zones of weakness and increase the susceptibility to failure. Sediment stability is also reduced by ongoing shallow salt deformation. These factors and sealevel lowering are key ingredients leading to sediment failure during the mid Miocene to Middle Pleiocene. During the Pleistocene, high sedimentation rates following glaciations may have generated underconsolidated sediment profiles with interbedded sandy horizons, explaining more frequent and smaller MTD sizes in the Plio-Pleistocene section. Although these factors "precondition" the sediment column to mass failure, seismicity, such as occurred in 1929, is likely the ultimate triggering mechanism.

Keywords Mass Transport Processes • mass failure • mass transport deposit (MTD) • slope sedimentation • multibeam • 3D seismic • seismicity

M.K. Giles (✉) and G.D. Wach
Department of Earth Sciences, Dalhousie University, Halifax, N.S., Canada, B3H 4J1
e-mail: mkgiles@dal.ca

D.C. Mosher and D.J.W. Piper
Geological Survey of Canada (Atlantic), Bedford Institute of Oceanography, P.O. Box 1006, Dartmouth, N.S., Canada, B2Y 4A2

1   Introduction

The southwestern Newfoundland slope outboard of the Laurentian and Halibut Channels on the Canadian east coast margin is a prospective region for hydrocarbons and an area of a historic submarine landslide. The modern seafloor geomorphology shows evidence for significant canyon and channel development and abundant evidence of mass failure deposits. The late Cenozoic section offshore southwestern Newfoundland is highly dissected by extensive mass transport deposits suggesting that this is an integral process of sediment transport for the shelf to slope region. Understanding the geological processes of slope environments through depositional patterns and structural controls is essential for knowing geohazard and engineering constraints in this complex region. Mass transport processes are also a concern to the population of the surrounding coastlines in terms of tsunami threat, as occurred in the historic 1929 Grand Banks landslide and tsunami (Mosher and Piper 2007).

In this paper, new results from bathymetric and high quality seismic data are presented. Evidence of sediment mass-failure supports the idea that mass transport processes are an important factor in the evolution of the southwestern Newfoundland margin. It is the purpose of this paper to evaluate the volume and seismic character of mass transport deposits and the stratigraphic interval within which they occur in order to assess their significance as a process in contributing sediment to the margin, as a geohazard to offshore development and surrounding coastal society infrastructure and perhaps to identify potential trigger mechanisms or at least development of pre-conditioning factors that lead to mass-failure.

1.1   Regional Geology

The Canadian east coast margin is a passive continental margin that extends from the Labrador Sea, across the Grand Banks and the Scotian margin to Georges Bank (Wade and Maclean 1990). During the Jurassic, the central North Atlantic Ocean opened and transform margin formed along the southwestern Grand Banks of Newfoundland. This tectonic feature extends to the east as the Newfoundland Fracture Zone and to the west as the Cobequid – Chedabucto southwest Grand Banks Fault system (Jansa and Wade 1975). Seaward of southwestern Newfoundland, the continental slope lies in water depths from 100 to 2500 m with mean gradients between 2° and 10°. It is incised by several large valley systems, the largest of which is Haddock Valley. Further west, the Laurentian Channel is a 700 km long, 80 km wide, glacial trough that cuts over 300 m into the continental margin (Fig. 1) (Piper et al. 1984). This feature acted as a major sediment delivery conduit and ice stream corridor for the Laurentide ice sheet. At the mouth of the Laurentian Channel lies the Laurentian Fan that is bounded to the east by the continental margin of the Grand Banks, to the west by the Scotian Shelf and Slope, and to the south by the Sohm Abyssal lain (Skene and Piper 2006).
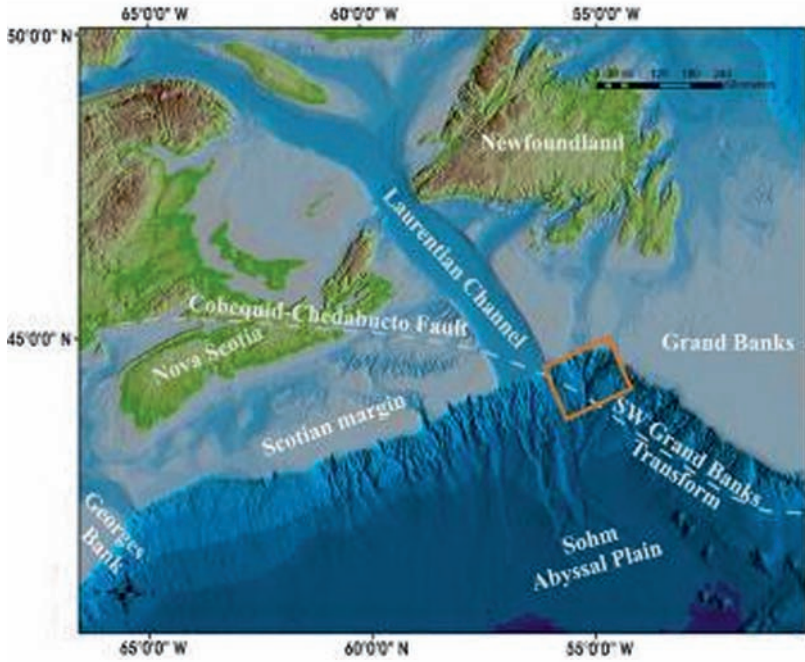
Fig. 1 Location of the study area (*orange box*) positioned on Canada's East coast. Major geographic and structural features labelled in white (Shaw and Courtney 2002)

1.2 Methods

32,150 km² multibeam sonar bathymetry data were acquired in the region in September, 2006. Details of this acquisition are reported by Mosher and Piper (2007). Seismic reflection data in the region come from a variety of vintages and resolution. 3,100 km of 2D MCS data (STP) were acquired by the Geological Survey of Canada in 1984 and 1985. Industry (TGS-Nopec) collected 34,000 line km of 2D MCS data across the Scotian and SW Newfoundland Margins in 1999. The grid spacing for the survey was 8 by 8 km. In 2002, approximately 1,500 km² of 3D seismic data with a bin spacing of 25 × 6.25 m, were collected over the southwestern Newfoundland margin in an area referred to as the Laurentian 3D prospect. Finally, a further 3,200 line-km of high resolution SCS data were acquired by the Geological Survey of Canada in 2003 and 2007. An average velocity of 2,100 m/s was used to convert from time to depth in the shallower parts of these seismic data. Key reflection horizons were mapped throughout the study area and correlated to exploration wells.

Age control for the study was established through ties to the Pliocene section on the Laurentian Fan by Piper and Normark (1989) as well as from till tongue stratigraphy

on the St. Pierre Slope by Piper et al. (2005). Based on work by Piper et al. (2005), new biostratigraphic analysis from the industry well Hermine E-94 were completed and correlated to seismic data from the STP data set. Age correlations were interpreted down the St. Pierre Slope and east into the study area using STP and TGS-NOPEC data.

2 Results

A seismic stratigraphic framework for the study area was established based on published literature and data from the surrounding shelf and slope. A marker coeval for the top Cretaceous (K99) was correlated into the study area. Three other stratigraphic markers were also correlated into the study area based on the work done by Piper et al. (2005). The middle Oligocene unconformity (O50) and a middle-late Pliocene marker (M90) are both defined by biostratigraphy from the Hermine E-94 well. A mid Pleistocene marker (Q50) has also been correlated into the study area and is based from the deepest till tongue on the St. Pierre Slope (Piper et al. 2005) (Fig. 2).

The sediment column in the Halibut channel region of the southwestern Newfoundland margin is divided into three units based on seismic facies. The lower unit, Unit 1, is the interval between the top Cretaceous unconformity (K99) and the middle-late Pliocene (M90) marker. This unit is present across the study area and has a variable thickness ranging from 900 to 1750 m, with thicker sections in the western portion of the study area. The base of this unit consists of sub-parallel to parallel, moderate amplitude reflectors which are vertically offset in some parts of the study area.
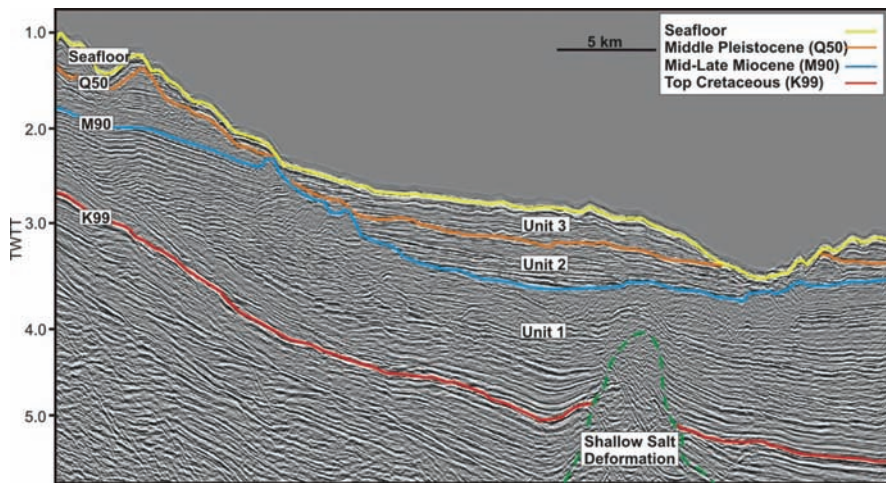
Fig. 2 Line 15 from the STP survey showing the stratigraphic framework for the Halibut Channel region of the Southwestern Newfoundland Slope
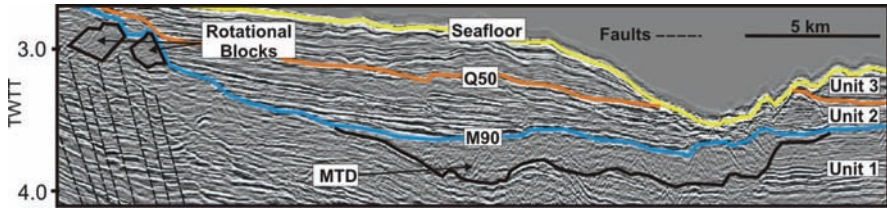
Fig. 3 STP line 15 showing the middle-late Miocene MTD and associated upslope rotational Slump blocks. Seaward dipping faults are observed in the lower left corner of the figure

Above these reflectors, there are a series of discontinuous, chaotic, moderate amplitude reflectors that continue to the M90 marker. The second unit, Unit 2, is the interval between the middle-late Pliocene (M90) marker and the mid Pleistocene (Q50) marker. Thickness varies between 150 to 500 m and consists of moderate-high amplitude, parallel reflectors at the base of the unit. On top of these reflectors, there are moderate-high amplitude packages that alternate between chaotic and fairly continuous reflectors. The upper unit, Unit 3, is not present throughout the entire data set. It is the interval between the mid Pleistocene marker (Q50) and the modern seafloor and consists of high and low amplitude, parallel to mounded reflectors with thin chaotic reflections through the section. Unit 3 varies in thicknesses ranging from 50 to 500 m and includes areas where none of the stratigraphy is preserved.

In the subsurface of the Halibut Channel region, mass transport deposits are identified by their incoherent and chaotic acoustic character. The bases of these MTDs are typically erosional with the upper surface having an undulating character. MTDs occur in Units 1, 2, and 3 at a variety of scales. In Unit 1, there is one large scale MTD that has an area of 670 km^2 and thicknesses as much as 400 m (Fig. 3). Using an average thickness of 250 m, the volume for this MTD is 167 km^3. In Unit 2, the alternating packages of chaotic and parallel reflectors are interpreted as stacks of MTDs (Fig. 4). These MTDs overlie the mid Miocene MTD in some parts of the study area. Two of the larger MTDs have been mapped in this unit. The lower MTD has a thickness between 75 and 85 m and covers an area of 400 km^2 resulting in a volume of 35 km^3. The second MTD mapped in this unit has a thickness of about 150 m, covers an area of 375 km^2 and has a volume of between 50–60 km^3. In Unit 3, the largest of the MTDs are between 20–30 m thick with volumes less than 1 km^3, reaching the limit of resolution for the Industry data.

3   Discussion

Data from the study areas show that mass transport processes occur on the southwestern Newfoundland margin in a variety of styles and magnitudes and suggest that this is an integral process of slope sedimentation in this region. In the Halibut
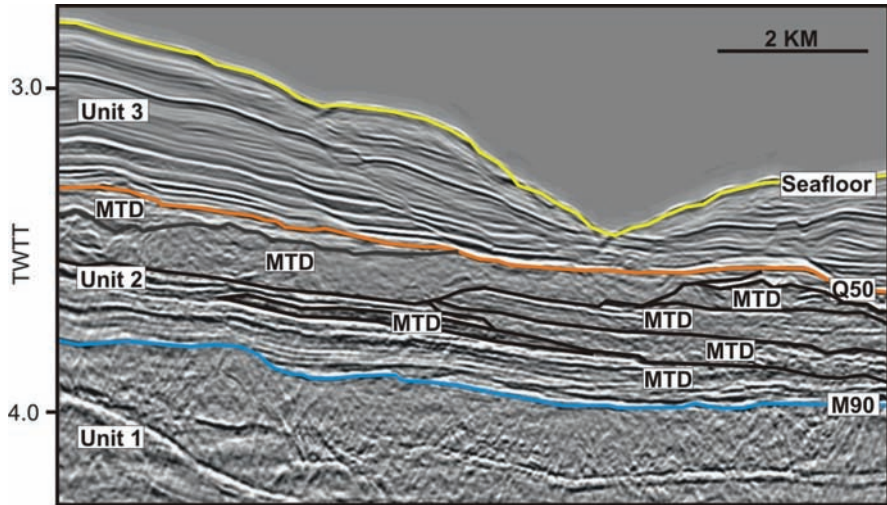
Fig. 4 Stacked MTDs observed in the TGS-NOPEC line 1306-100 from the middle-late Miocene marker to the Middle Pleistocene marker. MTDs are outlined in black

Channel area, MTDs on the scale of 30 to 150 km^3 are preserved from the top of the Cretaceous unconformity (K99) to the mid Pleistocene marker (Q50) (Unit 1 and 2) (Fig. 2), while from the mid Pleistocene marker (Q50) to the modern seafloor (Unit 3) MTDs are 20 to 30 m thick and have volumes less 1 km^3.

In Unit 1, the middle-late Miocene MTD displays 300–350 m thick rotational slump blocks in the mid-slope region, followed downslope by a blocky deposit that becomes more chaotic in the seaward direction. The blocky nature of the MTD suggests three things about this deposit: (1) the failed sediment has some structural integrity and was able to move downslope distance before it transitioned to a disturbed sediment package, likely representing a more fluidized flow, (2) an escarpment of equal size to the rotated slumps is required to provide the intact blocks, and (3) accommodation space to allow the rotated blocks to fail. The vertical offsets seen in Unit 1 have been interpreted as seaward dipping faults and are cut by middle-late Miocene MTD (Fig. 3). It could be possible that these seaward dipping reflectors have pre-conditioned the sediment and made it susceptible to failure.

The presence of shallow salt deformation in the western portion of the study area could be one mechanism that has caused the middle-late Miocene MTD to have frontally confined characteristics (Fig. 5). As the failure moved downslope, it encountered a bathymetric high, in this case a result of shallow salt deformation of the overlying sediment. East of the shallow salt deformation, the middle-late Miocene MTD follows bathymetric lows. The erosional character of this MTD indicates that it failed into a previous depression, creating a channelized flow. It is likely that the volume of the middle-late Miocene MTD is larger than 167 km^3 as the MTD likely extends outside of the region covered by the data. In Unit 2, MTDs
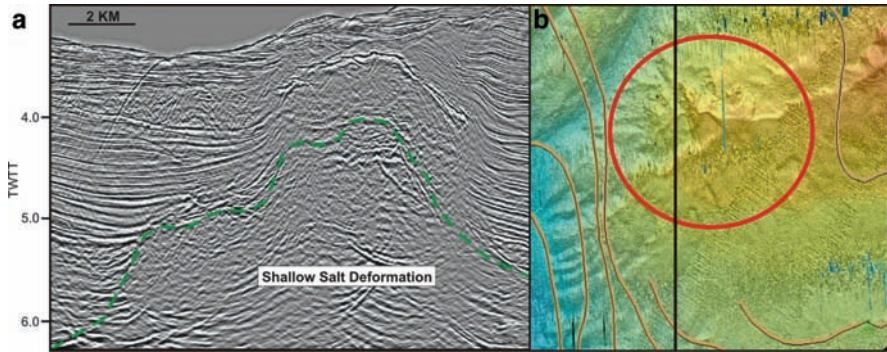
Fig. 5 Shallow salt deformation in the greater Halibut Channel region. Image A shows a seismic interpretation of shallow salt. Image B displays shallow salt deformation on the modern seafloor in multibeam sonar bathymetry data with the black line representing the seismic line

are smaller with volumes between 30 and 50 km³ compared to the large middle-late Miocene MTD but occur more frequently.

A possible explanation for having repeated failures in this area could be that the scars created by previous submarine landslides create over steepened and unstable slopes leading to retrogressive behavior. The remnant scars create accommodation space for subsequent sedimentation, leading to sediment overloading and increasing the susceptibility of failure for the area (Masson et al. 2006). Other possibilities include salt tectonics with recurring seismic activity. Seismic facies of Unit 1 suggests that the alternating high and low amplitudes represent fine and coarse grained material deposited by proglacial plumes and turbidity currents (c.f. Armitage 2009) where the smaller, chaotic packages represent local failures. In the Halibut Channel region of the study area, MTDs make up 30–40% of the sedimentary column since the top of the Cretaceous unconformity marker (K99). The influence of MTDs in this region would be higher if you account for turbidity currents and local failures that have occurred since the mid Pleistocene marker (Q50).

As shown by Mosher et al. (1994), near surface sediment (top 25 m) on the Scotian Slope is stable under static conditions. Marsters (1986), in a geotechnical study, showed that most samples from the St. Pierre Slope demonstrated apparent over-consolidation; although it was noted that there is a high percentage of silt in the samples leading to poor test quality in many instances. If sediments are statically stable on the St. Pierre Slope, having many analogues to the Scotian Slope, it is expected that an external factor is required to either increase the stress acting on seafloor sediments (Lee at el. 2007), reduce the strength of the sediment (increase the pore pressure), or some combination of the two in order to trigger a slope failure. There are several possible triggering mechanisms believed to be associated with the Newfoundland's southwestern margin: (1) Earthquakes – The Cobequid-Chedabucto fault system runs under the Laurentian Channel and Fan and along the southwestern margin of Newfoundland (Fig. 1). Seismicity is relatively low along the Canadian east coast but is slightly higher in the region of the Cobequid-Chedabucto

fault (Mazzotti and Adams 2005); (2) Sediment loading – During Late Wisconsinian glaciations, glacial outwashes rapidly deposited large amounts of sediment on the upper continental slope (King and Fader 1986), potentially generating higher pore pressures and increasing the susceptibility of sediment failure; (3) sedimentary bedforms and faults – buried sedimentary bedforms interpreted from regional seismic data suggest sandy intervals underlie St Pierre and Halibut Slope areas. Listric faults, extending from surface escarpments to these possible sand packages, provide evidence that these intervals may act as detachment surfaces, perhaps in response to generation of overpressures during seismic shaking; (4) shallow free gas is evident in cores recovered from St. Pierre Slope. Generation of gas within sediment reduces its strength properties setting up a situation for potential mass-failure; and (5) shallow salt deformation can play a role in the weakening of sediments by steepening slopes, directing fluid flow, and removing downslope support.

4 Conclusion

Mass transport processes are excellent mechanisms for transporting large volumes of sediment from the continental shelf to the abyssal plain. It is evident from seismic reflection data that the southwestern slope of Newfoundland was highly influenced by mass transport processes since at least the early Miocene. Evidence of frequent occurrence of these processes indicates that models of continental margin stratigraphy and sedimentation need to consider this process as a major contributing factor. Sediment mass failure is also a concern for the coastal communities of Atlantic Canada and for industry development in the area in terms of geohazard and tsunami risk. The size and frequency of such events is critical to understand in order to accurately assess the modern risk factor.

The conditions required for large scale submarine mass failures are not fully understood and the exact triggering mechanism responsible for a particular failure is hard to recognize with certainty. The presence of seaward dipping faults at the base of the mid Miocene MTD suggests that they create zones of weakness within the sediment column and increase the susceptibility of failure. Sediment stability is also reduced in some regions as a result of ongoing shallow salt deformation. It is probable that the seaward dipping faults, shallow salt deformation and sealevel lowering are key factors leading to sediment failure during the mid Miocene to Middle Pleistocene. During the Pleistocene, high sedimentation rates following the various glaciations may well have established conditions for failure in the region by generating underconsolidated sediment profiles. In addition, there is evidence of horizons influenced by bottom currents, generating sedimentary bedforms; likely sandy in nature. These horizons could well be susceptible to liquidfaction in event of ground accelerations. Although these factors "precondition" the sediment column to mass failure, seismicity, such as occurred in 1929, is likely the ultimate triggering mechanism.

References

Armitage DA (2009) High-resolution architectural evolution of depositional elements in deepmarine slope environments: the Quaternary Niger Delta slope, Quaternary southwest Grand Banks slope, Canada, and Cretaceous Tres Pasos formation, Chile (Ph.D. Thesis). Stanford University

Jansa LF, Wade JA (1975) Geology of the continental margin off Nova Scotia and Newfoundland. In: van der Linden WJM (ed) Offshore geology of eastern Canada Geol Surv Can Paper 74–30, 2:51–106

King LH, Fader GB (1986) Late Wisconsin glaciations of the Atlantic continental shelf of southeast Canada. Geol Surv Can Bull 363

Lee HJ, Locat J, Desgagnes P, Parsons JD, McAdoo BG, Orange DL, Puig P, Wong FL, Dartnell P, Boulanger E (2007) Submarine mass movements on continental margins. In: Nittrouer CA, Austin JA, Field ME, Kravitz JH, Syvitski JPM, Wiberg PL (eds) Continental Margin Sedimentation. Int Assoc Sediment Spec Pub 37:213–274

Marsters JC (1986) Geotechnical analysis of sediments from the eastern Canadian Continental Slope, south of St. Pierre Bank (M.Eng. Thesis). Technical University, Nova Scotia

Masson DG, Harbitz CB, Wynn RB, Pedersen G, Lovholt F (2006) Submarine land-slides: processes, triggers and hazard prediction. Philosophical Trans-actions of The Royal Society A 364:2009–2039

Mazzotti S, Adams J (2005) Rates and uncertainties on seismic moment and deformation in eastern Canada. J Geophys Res 110

Mosher DC, Moran K, Hiscott RN (1994) Late Quaternary sediment, sediment mass flow processes and slope stability on the Scotian Slope, Canada. Sediment 41:1039–1061

Mosher DC, Piper DJW (2007) Analysis of multibeam seafloor imagery of the laurentian fan and the 1929 grand banks landslide area. In: Lykousis V, Sakellariou D, Locat J (ed) Submarine Mass Movements and Their Consequences 3rd International Symposium. Advances in Natural and Techn Hazards Res 27:77–88

Piper DJW, MacDonald AWA, Ingran S, Williams GL, McCall C (2005) Late Cenozoic architecture of the St. Pierre Slope. Can J Earth Sci 42:1987–2000

Piper DJW, Normark WR (1989) Late Cenozoic sea-level changes and the onset of glaciation: impact on continental slope progradation off eastern Canada. Mar Petrol Geol 6:336–348

Piper DJW, Stow DAV, Normark WR (1984) The Laurentian Fan: Sohm Abyssal Plain. Geo-Mar Lett 3:141–146

Shaw J, Courtney RC (2002) Postglacial coastlines of Atlantic Canada: digital images. GSC OF4302

Skene KI, Piper DJW (2006) Late Cenozoic evolution of Laurentian Fan: Development of a glacially-fed submarine fan. Mar Geol 227:67–92

Wade JA, MacLean BC (1990) The Geology of the Southeastern Margin of Canada. In: Keen MJ, Williams GL (eds) Geology of the continental margin of eastern Canada. GSC no. 2:190–238

Mass Transport Events and Their Tsunami Hazard

D.R. Tappin

Abstract Mass transport events, such as those from submarine landslides, volcanic flank collapse at convergent margins and on oceanic islands, and subaerial failure are reviewed and found to be all potential tsunami sources. The intensity and frequency of the tsunamis resulting is dependent upon the source. Most historical records are of devastating tsunamis from volcanic collapse at convergent margins. Although the database is limited, tsunamis sourced from submarine landslides and collapse on oceanic volcanoes have a climate influence and may not be as hazardous as their frequency suggests. Conversely, tsunamis sourced from submarine landslides at convergent margins may be more frequent historically than previously recognized and, therefore, more hazardous.

Keywords Tsunami • submarine landslide • volcano • hazard

1 Introduction

Destructive tsunamis are mainly generated by earthquakes. However, they can also be sourced by failure of sediment and rock both on land and at the seabed. Most of these sediment/rock failures are submarine or from volcanoes, fewer are subaerial. Despite records that, in some places (e.g., Japan), go back thousands of years, there are few reliable historical accounts of tsunamis from submarine and subaerial failure but there are significantly more from volcanoes. The oldest historical records of tsunamis generated by mass failures are of volcanic lateral collapse in Japan and date back to the eighteenth century e.g., Oshima-Oshma in 1741 (e.g., Satake 2007). Historic records of devastating tsunamis resulting from subaerial landslides, are few, e.g., Scilla, Calabria in 1783 (Graziani et al. 2006) and Vaiont, Italy in 1963 (Hendron and Patten 1985).

D.R. Tappin (✉)
British Geological Survey, Nottingham, England, NG12 5GG, 44-115-936-3449
e-mail: drta@bgs.ac.uk

Although submarine landslides, including slumps, debris flows and turbidites, have been researched for decades, until recently these were rarely identified as a tsunami source. In fact they were discounted as a cause of destructive tsunamis (e.g. Jiang and LeBlond 1994; LeBlond and Jones 1995). This, despite tsunamis such as the Grand Banks in 1929 (e.g., Heezen et al. 1954; Piper and Asku 1987) and those associated with the Good Friday 1964 earthquake in Alaska, at Seward and Valdez (e.g., Lee et al. 2003). These events might have flagged the hazard from submarine landslides but they did not and it was not until 1998, when a submarine slump caused the devastating tsunami in Papua New Guinea in which 2,200 people died, that the threat from submarine landslides was fully realized (Tappin et al. 2001, 2008a). It is thus the intent of this paper to provide a broad overview of the tsunami hazard from mass transport events. The review mainly addresses tsunamis generated from submarine landslides and volcanoes, but subaerial failures are briefly considered. The objective is to review submarine mass transport processes relevant to tsunami formation and identify where mass transport events may be a real tsunami hazard.

2 Mass Transport Events

Mass transport events take place in many different environments. Hampton et al. (1996) introduced the term "landslide territory" for those areas where they are more common than elsewhere; with locations identified from unique combinations of sedimentology and physiography. The environments recognized include the open continental shelf, submarine canyon/fan systems, fjords, active river deltas and volcanic islands. In addition, Lee (2005) identified convergent margins as an important environment where submarine landslides also take place. Consideration of these landslide environments indicates several dominant controls on slope stability, that have been elucidated by Lee (2009) as: (i) sediment delivery to the continental margins; its rate, volume and type, (ii) sediment thickness, (iii) changes in seafloor conditions, which can influence hydrate stability and the possible generation of free gas, (iv) variations in seismicity and, (v) changes in groundwater flow. However in many respects these controls may be secondary to the main driving force, namely global climate change which, over the past hundreds of thousands of years, has resulted in alternating glacial and interglacial environments. The major impact of these climate changes has been on eustatic sea level. During glacial/interglacial cycles changing sea level has controlled the delivery of sediment to the oceans, as well as influencing seismicity along the continental margins, mainly through sea water loading and glacioisostacy. With regard to controls on volcanic mass failure there is an added contribution from magmatism that is driven by deep earth processes and regional structural controls on intrusion. However, climate change may affect volcanic collapse through both changes in sea level that affects slope stability (Quidelleur et al. 2008) and in rates of volcanic activity that also has an influence on flank collapse (McGuire et al. 1997).

There is a close and genetic relationship between most landslide territories and tsunami but, whereas there may be similar controls on sediment deposition and landslide triggering, in some territories, such as active river deltas, there is no evidence that mass movements have resulted in tsunamis. For example, submarine landslides are common in the Mississippi Delta. In 1969, when Hurricane Camille struck the Gulf coast, three offshore drilling platforms collapsed as a result of seabed sediment failure that resulted in a change of seabed relief of up to 12 m (e.g., Bea et al. 1983). However, there was no associated tsunami. The lack of evidence may, however, be more apparent than real. In other territories, such as open continental slopes and canyons, fjords, convergent margins and volcanoes, there is significant evidence that mass movement can result in hazardous, if not, devastating tsunamis; such as at Mt. Unzen in 1792 (Siebert et al. 1987), PNG in 1998 and Storegga at 8,200 years BP (Bondevik et al. 2005).

3 Submarine Mass Failures

3.1 Open Continental Slope and Rise

Continental margin environments are regions where sediment transfer from land to sea takes place. During changes in sea level, sediment in these regions has the potential to become unstable, in the process triggering tsunami. One of the best studied regions for submarine landslides on the open continental slope and rise is the North Atlantic (Hühnerbach et al. 2004; Lee 2009; McAdoo et al. 2000). Numerous focused initiatives, such as ENAMII (Mienert 2002) and the high scientific interest from surrounding nations have resulted in an extensive database of submarine landslides, their depositional character, age, and triggering mechanisms. In addition, the discovery off of Norway of the second largest gas field in Europe beneath the largest submarine landslide in the North Atlantic, resulted in one of the most intensive investigations into offshore slope stability ever undertaken (Solheim et al. 2005).

There are numerous submarine landslides at all scales along the Atlantic continental margins. Mechanisms of failure are numerous and include, debris flows, landslides and slumps. Submarine landslides are generally more abundant in the western North Atlantic (off Canada and the US) than in the eastern North Atlantic (off Europe). Landslides in the west are generally smaller than those in the east. On both sides of the Atlantic, most slides originate in water depths between 1,000 and 1,300 m. Three geographic regions are recognized: a glaciated margin north of 56° N (southern tip of Norway), a "glacially-influenced" margin from 26° N to 56° N, and a non-glaciated margin south of 26° N (Weaver et al. 2000).

Four giant submarine landslides border the Norwegian margin, Andøya Traenadjupet, Finneidfjord, and Storegga, with the latter the largest at 3,500 km³. Farther south, off Britain and Ireland, there are further submarine landslides including Peach and Rockall off of Scotland. The Storegga slide generated a

tsunami that hit the west coast of Norway with runups of up to 20 m (Bondevik et al. 2003). The evolution of the slide is probably representative of similar slides along the Norwegian margin. Failure took place at the end of the last glaciation or soon after deglaciation. The slide was translational with failure planes related to strain softening behavior of marine clay layers. Destabilization prior to failure is related to rapid loading from glacial deposits with generation of excess pore pressure and reduction of the effective shear strength in the underlying clays. The slide failed towards the base in a retrogressive manner. Climatic processes led to a preconditioning of the sediment mass, subsequently failing through earthquake shock that was the result of isostatic uplift driven by ice retreat. Although hydrate destabilization may contribute locally, this is not regarded as a primary driver of mass failure (Bryn et al. 2005).

Off the US margin 55 landslides have been mapped (Chaytor et al. 2007), the largest of which, the Cape Fear Slide, has a volume of 200 km^3 (Lee 2009). Landslides on the slope are generally larger than on the rise, thus having a higher potential to generate damaging tsunamis. Off of Canada, 24 submarine landslides have been identified (Piper and McCall 2003). The best known is the 1929 Grand Banks event. 41 people lost their lives in the ensuing tsunami. The tsunami was the result of a debris flow released from the Canadian shelf by earthquake shock. Recent mapping of the landslide indicates that it was relatively thin (20 m average) and probably retrogressive (Mosher and Piper 2007). Off of North Africa there are five or six large submarine landslides, including the giant Saharan debris flow. In the south Atlantic, submarine landslides lie off the Amazon Delta, with volumes of 2,500 km^3 (Maslin et al. 1998); off of southern Africa is the Agulhas Slump with a proposed volume of 20,000 km^3 (Dingle 1977) although this figure is based on pre-swath bathymetry data. Yet, of all these landslides on the margins of the Atlantic, that must number several hundred, the only direct evidence of any associated tsunami is from Storrega, where there are sedimentary deposits (Bondevik et al. 2005), and the Grand Banks, where there are survivors accounts and sediments (e.g., Tuttle et al. 2004). In the case of Storegga, the sediments have been preserved for 8,200 years.

Lee (2009) reviewed the depositional environments and known ages of submarine landslides on the margins of the Atlantic Ocean. He found that, over the past 20,000 years, there is a relatively even distribution of large landslides in the period between the last glacial maximum until about 5,000 years ago. The database is limited, however, because few slides have been dated. Notwithstanding, he found that most failures took place during glacial periods or just after. He attributed the distribution of landslide ages to the accumulation of thick sedimentary deposits on the upper continental slope during glacial periods and their failure, due to increased seismicity (caused by isostatic readjustment), during and following deglaciation.

Outside of the Atlantic, there are numerous submarine landslides. In the Mediterranean, probably the largest is the 'BIG'95 debris flow off of Spain with an area of 2,000 m^2 (Lastras et al. 2004). In the other areas, landslides have been identified off France and in the eastern Mediterranean off of Egypt and Israel. Again, there is little evidence for associated tsunami. Two major studies have been carried

on landslides off California on the US west coast. The Goleta Slide, in the Santa Barbara Channel, is a compound failure that contains both surfical slump blocks and mud flows, forming a total volume of 1.75 km^3. The slide is interpreted as Holocene in age (Fisher et al. 2005; Greene et al. 2005). There are three main lobes one of which, upon failing, has been modeled to source a tsunami wave with a runup of ~10 m. Although historical records suggest that tsunamis struck the area in the nineteenth century, these appear to be sourced from earthquakes rather than from submarine landslides. The Palos Verdes debris avalanche, located in a submarine canyon offshore of Long Beach (Bohannon and Gardner 2004), is the largest late Quaternary SMF in the inner California Borderland basins. It is dated at 7,500 years BP (Normark et al. 2004) with a volume of 0.34 km^3. Modeling indicates that it was large enough to generate a significant tsunami that would inundate the adjacent coastline (Locat et al. 2004). However, as of yet, there is no evidence of a tsunami on the adjacent coast.

3.2 Fjords

Submarine landslides are common in fjords. In glacial environments rapid sedimentation results in deposits that are susceptible to failure. Decay of organic matter deposited from rivers produces methane gas that may lead to elevated pore water pressure and further reduce sediment strength. Fjord head deltas can fail under cyclic loading (e.g., Prior et al. 1986) as at Kitimat Fjord in British Columbia in 1975. Triggered by a low tide, a landslide in the fjord created a tsunami of up to 8.2 m (Lee 1989; Prior et al. 1982). Although there was significant damage, no lives were lost. Weak sediments can also fail through earthquake shock as happened during the great Alaska earthquake of 1964. The resulting tsunamis were enormously destructive, with loss of lives and infrastructure (Hampton et al. 1993; Lee 1989; Plafker et al. 1969). At Seward a 1 km section of the waterfront failed as a result of submarine failure, creating a 10 m high tsunami (Lemke 1967). The destruction was compounded by a subsequent earthquake-generated tsunami, also 10 m high, arriving 30 min later. Most of the 13 people who died were inundated by the tsunami. At Valdez, an initial landslide volume of 0.4 km^3 increased to 1 km^3 as it incorporated sediment from the seabed (Coulter and Migliaccio 1966). The resulting tsunami attained heights locally of 52 m. Thirty-two people died in the event.

3.3 Convergent Margins

Convergent margins, like passive open continental slopes and rises, are regions of important sediment flux between the land and the sea. Their characterization into those margins where the sediment flux is significant (sediment rich)

and those where it is not (sediment starved) has implications for landslide generation, although the relationships are complex. It is not always those margins where sediment flux is large that produce the most hazardous tsunami. For example, the PNG event took place along the New Guinea trench which is sediment starved (Tappin et al. 2001). Landslides along the Sunda margin, where there is a much larger accretionary prism than in New Guinea. are small-scale and less of a hazard in sourcing destructive events (Tappin et al. 2007). Submarine landslides have been mapped on many convergent margins (McAdoo et al. 2004). Their size varies from 'super-scale' in Cascadia (Goldfinger et al. 2000) to 'small' along the Sunda margin in the Indian Ocean (Tappin et al. 2007). Along the Nankai accretionary prism, highly eroded lower slopes show little evidence of large, well-preserved submarine landslides (McAdoo et al. 2004). The Makran and Kodiak accretionary margins evidence mass wasting on the upper slopes, with the lower slopes lacking large landslides. In contrast, the sediment-starved Sanriku, Nicaragua, and Aleutian margins have large landslides.

Convergent margins are the most recent addition to landslide territory environments (Lee 2005), mainly because of the 1998 tsunami in PNG. With the gradual, but not universal, acceptance that the PNG tsunami was the result of a submarine slump there is now an expanding field of research into convergent margin events from landslides. Some of this research is based on newly acquired multibeam data, e.g., Puerto Rico, 1918 (López-Venegas et al. 2008), while new research is on re-evaluating anomalous tsunamis with runups that, to some degree, are too large in relation to their proposed earthquake source. The Alaska 1946 tsunami has always been enigmatic. An earthquake of $M_s = 7.1$ produced a disproportionately large local tsunami ($Mt = 9.3$) which claimed 167 lives (Fryer et al. 2004). A large landslide on GLORIA data indicated that this might be a more likely source but, this was not resolved on recently acquired multibeam data (Rathburn et al. 2009) so the source of the tsunami is still uncertain. The earthquake source of the Puerto Rico tsunami of 1918 has also been re-evaluated, with a landslide identified as an alternative (Hornbach et al. 2008; López-Venegas et al. 2008). The Messina tsunami and earthquake of 1908 claimed 60,000 lives, many in the tsunami. The earthquake magnitude ($M_s = 7.1$) is incompatible with both the height distribution and southward extent of local tsunami runups (Billi et al. 2008). A submarine landslide has been identified on multibeam data that may explain the inconsistency. Alternatively, the tsunami may have resulted from both the earthquake and a landslide (Tappin et al. 2008b). The Indian Ocean tsunami of 1945 was previously believed to the result of an earthquake located along the Makran margin. However, there are inconsistencies between the timing of tsunami runups and the earthquake, thus a landslide source has been proposed (Rajendran et al. 2008). Other events where there is a suspicion of a landslide contribution include the Sanriku tsunami of 1896 in which over 22,000 people perished, Flores tsunami of 1982 (Imamura et al. 1995) in which over 2,000 people died, and Java, 2006, where focused runups hint at an SMF source.

4 Volcanoes

Catastrophic volcanic flank collapse has been reported from numerous convergent margin and intra-plate locations. Mount St Helens in 1980 (Lipman et al. 1988) is the best studied recent collapse event. Although on land, it has led to an improved understanding of the processes of flank failure that has been extended into the marine domain. At coastal locations, flank collapse has the potential to create devastating tsunamis (e.g., McMurtry et al. 2003; Satake 2007). Volcanic collapse along oceanic and convergent margin volcanoes has been subject to extensive research. Study of the giant submarine landslides (GSLs) on Hawaii was seminal in identifying the potential tsunami hazard from this source. Along convergent margins collapses are smaller in scale by orders of magnitude from oceanic island failures. Historical records however, show that these pose a serious hazard because of their higher frequency and proximity to population centers. Tsunamis may be generated directly by volcanic eruption as exemplified by Santorini in 3500 BC (McCoy and Heiken 2000). Thus, to address the different tsunami sources this section provides an introduction to the processes of collapse and then considers each of the main environments where collapse may result in tsunamis.

Numerous volcanic edifices have large open amphitheater-shaped structures that have been created either by caldera or flank collapse that results in debris avalanches (e.g. Siebert 1984). These amphitheaters are at all scales. The debris avalanches of Hawaii are the largest on Earth, with the Nuuanu giant submarine landslide covering 5,000 km^2. The largest failed block, the Tuscaloosa Seamount, stands 2 km above the surrounding sea bed. The formation of volcanic avalanche amphitheaters is well known. It involves gravity sliding of large sectors of volcanoes along glide planes that steepen sharply upslope, forming near-vertical, crater-like walls at their upper ends, and that flatten down slope leaving an open breach between the low-lying tips of the amphitheatre escarpment. Slippage initially takes place as rockslides, but these disintegrate catastrophically into rock avalanches. Longer travel distances generally produce smaller blocks in the avalanche deposits. In the marine domain these features are well imaged at many volcanic locations. For example recent mapping off Ritter Island northeast of New Guinea revealed a debris avalanche that extends up to 75 km from its source (Silver et al. 2005). The deposit has three components: (i) large blocks, up to 2 km across, occur adjacent to the collapse scar, (ii) smaller (10 to 100 m) blocks, that form a series of discrete debris avalanche lobes or hummocks, are traced up to 35 km from the volcano, and (iii) landslide deposits that form a broad, thin sheet 20 km wide.

One of the major constraints in assessing the tsunami hazard from volcanic collapse is the triggering mechanism(s) because they are numerous and varied (McGuire 1996). Volcanic rift zones have been recognized on many oceanic islands such as Stromboli and the Canary Islands and have been linked to edifice failures (Siebert 1984). They concentrate magma upwelling as dyke swarms, which can

trigger instability by strength reduction through thermal or mechanical pressurization of pore fluids (Elsworth and Day 1999), or by the growth of an anomalously high topographic load (McGuire 1996). Slope angle and gravitational instability favor failure, but low-angle edifices such as oceanic shield volcanoes, the Hawaiian Islands for example, are also prone to large-scale flank destabilization. Asymmetric building onto a dipping basement can direct collapses towards a preferred direction. Such structural control of preferred landslide direction has been advocated in the Lesser Antilles (Deplus et al. 2001). Instantaneous destabilization of weakened edifices can result from strong regional earthquakes, or from seismicity along listric basement faults acting as décollement surfaces. Strength-reduction along basal volcanic layers by hydrothermal alteration and/or increased pore fluid pressure, such as during periods of high rainfall, can also favor instability. Finally, however, as McGuire (1996) points out, the main driving force of collapse is gravity.

Proposed climate controls on volcanic slope stability are intimately associated with glacial and interglacial cycles. Analysis of GRIP ice cores reveals a strong correlation over the past 110,000 years between accelerations in rates of sea level change and increased rates of explosive volcanism (Zielinski et al. 1996). These may in turn influence flank collapse (McGuire et al. 1997). Over longer time scales, large-scale flank collapse of volcanic islands may correlate with sea-level rise driven by climate change. On Hawaii, McMurtry et al. (2003) propose that large-scale flank collapse is related to increased retention of groundwater during wet and warm climates characterizing interglacial periods. Alternatively, Quidelleur et al. (2008), using a more global dataset, correlate large volume ($>10\,km^3$) collapses with glacial terminations.

4.1   Convergent Margins – Volcanic Flank Collapse

The earliest recorded historical tsunamis from flank collapse are from Japan. In 1640, on Komagatake volcano, Hokkaido, collapse resulted in a large-scale debris avalanche that upon entering the sea, caused a tsunami in which more than 700 people died (Nishimura et al. 1999). In 1741, also in Hokkaido, catastrophic volcanic collapse on Oshima-Oshima Island created a tsunami that led to approximately 2,000 fatalities (Satake 2007). The tsunami resulted in local runups of up to 13 m. In the far field, over 1,000 km to the southwest, on the coast of Korea there were runups of 3–4 m. In 1792, collapse on Mt Unzen led to a debris avalanche that swept through Shimabara City and into the Ariaka Sea. The tsunami resulted in the loss of over 10,000 lives (Miyachi 1992; Siebert et al. 1987). In Papua New Guinea, the Ritter Island sector collapse of 1888 created a local tsunami of 12–15 m (Johnson 1987). Run ups several hundred kilometers away were up to 8 m (Cooke 1981) and scores, if not hundreds of people in local villages perished. The most recent tsunami caused by a volcanic flank failure was on the 30 December 2002, on Stromboli, in the Aeolian Islands. The local tsunami was up to 10 m above sea level and caused significant damage to buildings on the eastern coast of the island but no loss of life (Tinti et al. 2005).

4.2 Convergent Margins – Eruption Tsunami

The most prominent eruption tsunamis are undoubtedly those from Krakatau in 1883 and Santorini in 3500 BC. Other examples include the 1815 eruption of Tambora in Indonesia, generated by pyroclastic flows entering the ocean (Self and Rampino 1981) and causing coastal inundation of up to 4 m (Van Padang 1971). Pyroclastic flows from the eruption of Aniakchak volcano, Alaska in 3,500 years BP resulted in a tsunami with runups as high as 15 m (Waythomas and Neal 1997). In 1883, over 36,000 people died in the Krakatau tsunami. 40 m tsunami waves were reported from Java (Simkin and Fiske 1983). The source of the tsunami is controversial, with three possible volcanic sources, (i) large-scale collapse of the northern part of Krakatau Island (Self and Rampino 1981), (ii) pyroclastic flows (e.g. Francis 1985) and, (iii) a submarine explosion (Yokoyama 1987). A submarine explosion, 1 to 5 min duration best fits the observed tsunami heights and waveforms recorded at Batavia (Normanbhoy and Satake 1995). It is possible that the smaller tsunamis were caused by pyroclastic flows (Francis 1985; Sigurdsson et al. 1991).

4.3 Oceanic Volcanoes – Flank Collapse

Volcanic flank collapses have been mapped on numerous oceanic islands. Using a combination of onshore mapping and offshore data including multibeam bathymetry and sub-seabed geophysics, we now have access to comprehensive data sets that underpin an improved understanding of flank failure at these locations. However, only a few examples have been intensely studied in the context of their potential to create tsunami.

In Hawaii, large-scale, gravitational volcanic collapses, GSLs, have long been recognized (e.g., Moore et al. 1989). Along the Hawaii-Emperor Ridge there are over 68 major landslides over 20 km in length, with some over 200 km long, with volumes exceeding 5,000 km^3. These are the largest landslides on Earth. Two main landslide morphologies are recognized, debris avalanches and slumps, with numerous variations in-between. The slumps, fail slowly by creep, thus their potential as tsunami sources is minimal; they will not be considered further. Debris avalanches form the majority of failures and these lie on slopes <3° and are formed of fragmented volcanic rock. They are ~100s m in thickness, with well defined amphitheaters at their head. They display the classic hummocky surface topography of debris avalanches. Some debris avalanches have a significant proportion of large blocks (e.g., Nuuanu and Wailau) others have smaller blocks and a greater proportion of finer material (e.g. Alika 2).

Dating of the GSLs indicates that, on average failure rate is every 100,000 years. Although occurring throughout the lifetimes of the volcanoes, the largest landslides occurred when the centers were young and unstable, were close to their maximum size, and when seismic activity was at a high level. The morphology of the GSLs, together with their large lateral extent and the fact that they travelled long distances

across the Hawaiian Deep upslope onto the Hawaiian Ridge, in places overtopping vertical elevations of hundreds of meters, indicates that they travelled at high velocities of 100 to 200 m/s. The debris avalanches are thus almost probably catastrophic, and take place as single events.

Since their discovery the tsunami potential from the Hawaii GSLs has been the subject of controversy (McMurtry et al. 2004; Moore and Moore 1988; Rubin et al. 2000; Stearns 1978). However now, a combination of seabed mapping, dating of the Alika 2 GSL, modeling its' failure as a tsunami source, and the presence of sediments at over 340 m above sea level laid down by the tsunami at the time of generation, provide strong evidence that failure of the GSL do indeed create massive tsunamis. These tsunamis locally have runups of the order of hundreds of meters above sea level. In the far field, the limited modeling available from the collapse of the Nuuanu GSL indicates a real hazard; tsunami waves tens of meters high may have struck the coasts of southern California and the Aleutian islands (Satake et al. 2002).

The GSLs of Hawaii are not unique, most oceanic volcanoes during their evolution will fail catastrophically. In the younger and more volcanically active, western Canary Islands of El Hierro, La Palma and Tenerife there are at least 14 large failures (Masson et al. 2002). These failures are smaller in volume than those in Hawaii. The debris avalanches are superficial and up to 2 km thick. They have areas of a few thousand kilometers, volumes of 50 to 200 m^3 and runouts of 50 to 100 km. Glide planes at the base of the avalanches are typically up to 10° on the upper slopes and less than 5° on the lower slopes. The majority of Canary Island failures are less than 1 million years old. The youngest, on the northwest flank of El Hierro, is 15,000 years BP. There is no regularity in the failures, but on average, as with Hawaii, they take place every 100,000 years. The most common failure mechanism is a catastrophic debris avalanche.

Despite the overall evidence from Hawaii that lateral volcanic collapse can result in hazardous tsunamis, there has been much debate about whether collapse of the Canary Islands volcanoes poses a similar risk (Wynn and Masson 2003). As with landslides in non-volcanic sediments, such as at Storegga, it has been proposed that the Canary volcanoes fail retrogressively, thus reducing their potential to create a large tsunami. Controversially, Ward and Day (2001) propose that a 500 km^3 collapse of Cumbre Vieja volcano on La Palma could create a tsunami that would be catastrophic in the near field and extremely dangerous to the east coast of America. Simulations of a smaller scale collapse on La Palma (e.g., 375 km^3; Løvholt et al. 2008) confirms that local runups would indeed be devastating, but with less significant consequences in the far field. It is clear from the modeling, that the volume of the collapse, as well the particular environment, slide mobility, as well as the model used, is important in identifying and resolving whether a hazardous tsunami would be formed. Notwithstanding the controversy over tsunami wave heights in the far field, sedimentary deposits at 188 m on Gran Canaria have been identified as sourced from a collapse tsunami (Pérez-Torrado et al. 2006) thereby indicating that a local event caused by a volcanic collapse may well be extremely dangerous to coastal communities if of sufficient volume.

5   Subaerial Failures

A number of tsunamis have been created by subaerial landslides. The most well known is at Lituya Bay in Bay in 1948 (Miller 1960). Triggered by an earthquake a 4.3 km³ landslide failed into the sea creating a tsunami up to 524 m high. Two people died in the event. The most catastrophic tsunami created by a subaerial failure, was at Vaiont in Italy in 1963 (Hendron and Patten 1985). Although perhaps not strictly a tsunami, more a seiche, the collapse was created by a combination of reservoir water drawdown and heavy rains. There were warning signs. The displaced water overtopped the dam and a 250 m high wave flooded the valley below, drowning 2,000 people. In 1783, at Scilla in Calabria, a cliff collapsed into the sea causing a devastating tsunami in which 1,500 perished (Graziani et al. 2006). The fatalities were particular heavy because survivors from the previous day's earthquake were taking shelter on the open beach at Scilla located about 1 km east of the collapse. The waves reached up to 200 m inland and up to 8.3 m run-up within the town.

6   Tsunami Hazard

Review of mass transport events in the different environments described demonstrates that they all have the potential to create hazardous if not devastating tsunamis. Assessment of the hazard and risk from tsunami however, is at an early stage and although understanding of processes has advanced significantly over the past decade the database of well studied events is still small. On the North Atlantic passive continental margins, there is a good preliminary understanding of the processes of deposition and landslide failure. Yet there is still a paucity of data to confirm or refute recent hypotheses on how these failures relate to tsunami generation. There are still too few case studies of actual events, particularly parametric modeling of tsunami generation based on the architecture of known failures. More dates of landslide failure are required to test hypotheses on climate control of mass failure processes. At first sight, the large number of landslides suggests high risk. However, the likelihood of future tsunami from slide failure may not be as great as the numerous landslides suggest. The work of Lee (2009) indicates that most landslides failed during glacial periods or just after, thus under present climatic conditions, the risk of tsunamis from submarine failures may not be as great as the number of landslides offshore suggests. But more research is required to validate this conclusion, especially the dating of more landslide events.

Apart from the major climate controls on slope stability, there are others that are effective now. On the Scotian margin, as demonstrated by the Grand Banks tsunami, there is a risk of submarine landslides triggered by earthquakes during interglacials. As noted by Piper et al. (2003) there have been three >M7 events since 1800 and these have the potential to trigger landslides. Progressive creep failure may also be a trigger (Piper et al. 2003). With regard

to tsunami magnitude, the Grand Banks landslide was in quite deep water, yet generated an event that resulted in much destruction and loss of life.

Along the US Atlantic margin the earthquake trigger risk may not be as great as off Canada (Ten Brink et al. 2009). However, salt movement may be an added threat (Hornbach et al. 2007). The lack of evidence of tsunami from onshore (or in fact offshore cored sediments) is intriguing. The preservation potential of tsunami deposits is undoubtedly low. Subsidence increases the likelihood of preservation, such as along the Cascadia margin where tsunami deposits over thousands of years have been laid down. Subsidence may not be taking place along passive margins, especially those previously subject to post glacial uplift, although there are advantages in preservation as demonstrated by the Storegga deposits preserved in elevated lakes along the Norwegian coast. Alternatively, tsunami sediments may not have been discriminated from other depositional sources such as storms. Also, given that many submarine landslides took place at lowered sea levels, the lack of deposits may be because of the width of the US continental shelf that in places is up to 200 km wide.

One aspect of landslides that is still controversial is the role of hydrate dissociation in the initiation of their failure (e.g., Maslin et al. 2004). As yet there are few definitive studies that show that this process has definitely caused a landslide. Most of the landslides dated by Lee (2009) from the last 20,000 years, were emplaced during stable or rising sea level, a period when hydrate disassociation would least be expected. In addition, the relatively poor accuracy of landslide dates makes it difficult to associate failure events with relatively short periods of sea level fall (Maslin et al. 2004). Hydrate dissociation was considered as a trigger of the Storegga slide, but this has been discounted as a major factor (Bryn et al. 2005). Although there is a lot of circumstantial evidence on the association between hydrates and submarine landslides, isotopic ice core evidence now shows that methane increase during interglacials is from non-marine sources (Sowers 2006).

With regard to other passive margins, the evidence on which to assess the hazard from submarine landslide generated tsunami is patchy. There are large mass failures off the Amazon Fan, but these are in deep water. Off southern Africa, there is the Agulhas slump. In both areas there is no evidence for associated tsunami. In other landslide territories, such as fjord regions, the well researched tsunamis associated with the Alaska, 1964 earthquake illustrate that these areas are prone, but not everywhere. Although, mass failures are known from Norway (e.g., Finneidford in 1996), there is no evidence of associated tsunami. The likelihood is perhaps that glaciers feeding the fjord head deltas in North America are of a larger scale than those in Norway. Regarding active river delta environments, the lack of tsunamis in the Gulf of Mexico, where there are numerous submarine landslides appears contradictory. Absence of tsunamis may be because the landslides are too deep, and tsunamis generated too small to notice. The storm conditions under which they are triggered may mask any associated tsunami. During a Category 5 hurricane, would a tsunami wave be identified in the storm surge?

Along convergent margins there is a tsunami hazard from both submarine landslides and volcanic flank collapse. The PNG event flagged the landslide hazard, and

recent (and continuing) re-evaluation of anomalous tsunami events suggests that some anomalous earthquake tsunamis may be the result of submarine landslides. Review of tsunami processes along convergent margins also indicates that thick and rapid sedimentation regimes are not necessarily the locations of large-scale submarine failure; in regions of frequent earthquakes more frequent and smaller landslides may result, and hence a reduced tsunami hazard. More work is required to test this hypothesis. Smooth slopes along convergent margins seem to result from frequent mass failures (McAdoo et al. 2004). However, along the Sunda margin, the slopes are heavily gullied and, mass failures frequent. More re-evaluations of anomalous tsunami events are required to assess the hazard along these margins. Small landslides, such as PNG, are a real threat at some locations, but it will be very difficult to identify potential locations where these may be located. As noted by Mosher and Piper (2007) swath bathymetry doesn't always provide definitive proof of the presence (or absence) of mass failure. Large failures have been mapped along Southern and Middle American Pacific margins, for example the massive slide off Peru (Von Huene et al. 1989). Large mass failures have also been mapped off of Costa Rica and Nicaragua (Von Huene et al. 2004). Modeling of these events indicates that their failure would result in a 50 m high tsunami wave at source. However, care has to exercised in discriminating the tsunami sources at these deep water plate boundaries. Some 'slow' earthquakes may reproduce the same effects as a submarine landslide (e.g., Pelayo and Wiens 1990). The main discrimination between a slow earthquake and landslide tsunami is that the runups from latter would be more focused, and with a significant peak runup (Tappin et al. 2008a). Additionally, there may be combined events, both earthquake and landslide as may have occurred at Messina in 1908 (Tappin et al. 2008b).

Tsunamis from volcanic flank collapse into the ocean can be catastrophic, as shown by historical events from the convergent margins of Japan and PNG (Ritter Island). Thus volcanic tsunamis at these locations are a real threat, more so because at present collapse cannot yet be predicted, as at Stromboli in 2002. They may also be very near to densely populated areas. On oceanic islands, such as Hawaii and the Canary Islands, there has been considerable debate on the mechanism of flank collapse – catastrophic or incremental – and whether the collapse creates hazardous tsunamis. Clearly at both locations any moderate if not small collapse could be very destructive locally. On Stromboli in 2002, a small failure created a local tsunami of 10 m. In the far field the resultant tsunami would depend on the scale of the collapse. Although a sedimentary slide on a passive margin, the evidence from Storegga shows that its' collapse created a tsunami that travelled at last as far as the Faeroes. The 2.5 km^3 collapse on Oshima-Oshma created a 2–3 m tsunami on Korea 1,000 km away. However, the evidence from Hawaii, and perhaps the Canary Islands, is that collapse is more likely during the early stages of volcanic evolution, thus the hazard may be small. Additionally, collapse may be more prevalent during climates not similar to those experienced at present.

References

Bea RG, Wright SG, Sicar P, Niedoroda AW (1983) Wave-induced slides in South Pass Block 70, Mississippi delta. J Geotech Eng 109:619–644.

Billi A, Funiciello R, Minelli L, Faccenna C, Neri G, Orecchio B, Presti D (2008) On the cause of the 1908 Messina tsunami, southern Italy. Geophys Res Lett 35(L06301).

Bohannon RG, Gardner JV (2004) Submarine landslides of San Pedro Sea Valley, southwest Long Beach, California. Mar Geol 203:261–268.

Bondevik S, Mangerud J, Dawson S, Dawson A, Lohne Ø (2003) Record-breaking height for 8000-year-old tsunami in the North Atlantic. EOS Trans, Am Geophys Union 84:289–293.

Bondevik S, Mangerud J, Dawson S, Dawson A, Lohne Ø (2005) Evidence for three North Sea tsunamis at the Shetland Islands between 8000 and 1500 years ago. Quat Sci Rev 24:1757–1775.

Bryn P, Berg K, Forsberg CF, Solheim A, Lien R (2005) Explaining the Storegga Slide. Marine and Petroleum Geology, 22:11–19.

Chaytor JD, Twichell DC, ten Brink US, Buczkowski BJ, Andrews BD (2007) Revisiting submarine mass movements along the U.S. Atlantic continental margin: Implications for tsunami hazard. In: Lykouosis V, Sakellariou D, Locat J (eds.), Submarine Mass Movements and Their Consequences. Springer, Dordrecht, pp. 394–403.

Cooke RJS (1981) Eruptive history of the volcano at Ritter Island. In: Johnson RW (ed.), Cooke–Ravian Volume of Volcanological Papers. Geol Surv Papua New Guinea Mem 10:115–123.

Coulter HW, Migliaccio RR (1966). Effects of the earthquake of March 27, 1964 at Valdez, Alaska 542-C. US Geol Surv Prof Pap 542-E.

Deplus C, Le Friant A, Boudon G, Komorowski JC, Villemant B, Harford C, Segoufin J, Cheminee JL (2001) Submarine evidence for large-scale debris avalanches in the Lesser Antilles Arc. Earth Planet Sci Lett 192:145–157.

Dingle RV (1977) Anatomy of a large submarine slump on sheared continental margin (southeast Africa). J Geol Soc Lond 134:293–310.

Elsworth D, Day SJ (1999) Flank collapse triggered by intrusion: The Canarian and Cape Verde Archipelagoes. J Volcanol Geotherm Res 94:323–340.

Fisher MA, Normark WR, Greene HG, Lee HJ, Sliter RW (2005) Geology and tsunamigenic potential of submarine landslides in Santa Barbara Channel, Southern California. Mar Geol 224:1–22.

Francis PW (1985) The origin of the 1883 Krakatau tsunamis. J Volcanol Geotherm Res 25:349–369.

Fryer GJ, Watts P, Pratson LF (2004) Source of the great tsunami of 1 April 1946: A landslide in the upper Aleutian forearc. Mar Geol 203:201–218.

Goldfinger C, Kulm LD, McNeill LC, Watts P (2000) Super-scale failure of the southern Oregon Cascadia margin. In: Keating B, Waythomas C, Dawson A (eds.), Special Issue on Landslides Tsunamis. Pure Appl Geophys 157:1189–1226.

Graziani L, Maramai A, Tinti A (2006) A revision of the 1783–1784 Calabrian (southern Italy) tsunamis. Nat Hazards Earth Syst Sci 6:1053–1060.

Greene HG, Murai LY, Watts P, Maher NA, Fisher MA, Paull CE, Eichhubl P (2005) Submarine landslides in the Santa Barbara Channel as potential tsunami sources. Nat Hazards Earth Syst Sci 6:63–88.

Hampton MA, Lemke RW, Coulter HW (1993) Submarine landslides that had a significant impact on man and his activities: Seward and Valdez, Alaska. In: Schwab WC, Lee HJ, Twichell DC (eds.), Submarine Landslides: Selected Studies in the US EEZ. USGS Bull 2002:123–142.

Hampton MA, Lee HJ, Locat J (1996) Submarine landslides. Rev Geophys 34:33–59.

Heezen BC, Ericsson DB, Ewing M (1954) Further evidence of a turbidity current following the 1929 Grand Banks earthquake. Deep Sea Res 1:193–202.

Hendron AJ, Patten FD (1985) The Vaiont Slide. US Army Corps Eng Tech Rep GL-85-8.

Hornbach MJ, Lavier LL Ruppel CD (2007) Triggering mechanism and tsunamogenic potential of the Cape Fear Slide complex, U.S. Atlantic margin. Geochem Geophys Geosyst 8(Q12008).

Hornbach MJ, Mondziel SA, Grindlay NR, Frohlich C, Mann P (2008) Did a submarine slide trigger the 1918 Puerto Rico tsunami? Sci Tsunami Hazards 27:1–31.

Hühnerbach V, Masson DG, Partners CP (2004) Landslides in the north Atlantic and its adjacent seas: An analysis of their morphology, setting and behaviour. Mar Geol 213:343–362.

Imamura F, Gica E, Takahashi T, Shuto N (1995) Numerical simulation of the 1992 Flores tsunami: Interpretation of tsunami phenomena in northeastern Flores Island and damage at Babi Island. Pure Appl Geophys 144:555–568.

Jiang L, LeBlond PH (1994) Three dimensional modelling of tsunami generation due to submarine mudslide. J Phys Ocean 24:559–573.

Johnson RW (1987) Large-scale volcanic cone collapse: The 1888 slope failure of Ritter Volcano, and other examples from Papua New Guinea. Bull Volcanol 49:669–679.

Lastras G, Canals M, Urgeles R, De Batist M, Calafat AM, Casamor JL (2004) Characterisation of the recent debris flow deposit on the Ebro margin, Western Mediterranean Sea, after a variety of seismic reflection data. Mar Geol 231:235–255.

LeBlond PH, Jones A (1995) Underwater landslides ineffective at tsunami generation. Sci Tsunami Hazards 13:25–26.

Lee HJ (1989) Undersea landslides: Extent and significance in the Pacific Ocean. In: Brabb EE, Harrod BL (eds.), Landslides, Extent and Economic Significance. Proceedings of the 28th International Geological Congress: Symposium on Landslides, Washington, DC, pp. 367–380.

Lee HJ (2005) Undersea landslides: Extent and significance in the Pacific Ocean, an update. Nat Hazards Earth Syst Sci 5:877–892.

Lee HJ (2009) Timing of occurrence of large submarine landslides on the Atlantic Ocean margin. Mar Geol. 264:53–64.

Lee HJ, Kayen RE, Gardner JV, Locat J (2003) Characteristics of several tsunamigenics submarine landslides. In: Locat J, Mienert J (eds.), Submarine Mass Movements and Their Consequences. Kluwer, The Netherlands, pp. 357–366.

Lemke RW (1967) Effects of the earthquake of 27 March 1964, at Seward, Alaska. US Geol Surv Prof Paper 542-E.

Lipman PW, Normark WR, Moore JG, Wilson JB, Gutmacher C (1988) The giant submarine Alika debris slide, Mauna Loa, Hawaii. J Geophys Res 93:4279–4299.

Locat J, Locat P, Lee HJ, Imran J (2004) Numerical analysis of the mobility of the Palos Verdes debris avalanche, California, and its implication for the generation of tsunamis. Mar Geol 20:269–280.

López-Venegas AM, ten Brink US, Geist EL (2008) Submarine landslide as the source for the October 11, 1918 Mona Passage tsunami: Observations and modeling. Mar Geol 254:35–46.

Løvholt F, Pedersen G, Gisler G (2008) Oceanic propagation of a potential tsunami from the La Palma Island. J Geophys Res 113(C09026).

Maslin M, Mikkelsen N, Vilela C, Haq B (1998) Sea-level- and gas-hydrate-controlled catastrophic sediment failures of the Amazon Fan. Geology 26:1107–1110.

Maslin M, Owen M, Day S, Long D (2004) Linking continental-slope failures and climate change: Testing the clathrate gun hypothesis. Geology 32:53–56.

Masson DG, Watts AB, Gee MJR, Urgeles R, Mitchell NC, Le Bas TP, Canals M (2002) Slope failures on the flanks of the western Canary Islands. Earth Sci Rev 57:1–35.

McAdoo BG, Pratson LF, Orange DL (2000) Submarine landslide geomorphology, U.S. continental slope. Mar Geol 169:103–136.

McAdoo BG, Capone MK, Minder J (2004) Seafloor geomorphology of convergent margins: Implications for Cascadia seismic hazard. Tectonics 23, TC6008.

McCoy FW, Heiken G (2000) Tsunami generated by the Late Bronze Age eruption of Thera (Santorini), Greece. Pure and Applied Geophysics, 157:1227–1256.

McGuire WJ (1996) Volcano instability: A review of contemporary themes. Geol Soc Lond Spec Pub 110:1–23.

McGuire WJ, Howarth RJ, Firth CR, Solow AR, Pullen AD, Saunders SJ, Stewart IS, Vita-Finzi C (1997) Correlation between rate of sea-level change and frequency of explosive volcanism in the Mediterranean. Nature 389:473–476.

McMurtry GM, Watts P, Fryer GJ, Smith JR, Imamura F (2003) Giant landslides, mega-tsunamis, and paleo-sea level in the Hawaiian Islands. Mar Geol 203:219–233.

McMurtry GM, Fryer GJ, Tappin DR, Wilkinson IP, Williams M, Fietzke J, Garbe-Schoenberg D, Watts P (2004) Megatsunami deposits on Kohala volcano, Hawaii, from flank collapse of Mauna Loa. Geology 32:741–744.

Mienert J (2002) Special issue: European North Atlantic Margin (ENAM II): Quantification and modelling of large-scale sedimentary processes. Mar Geol 188:1–248.

Miller D (1960) Giant waves in Lituya Bay, Alaska. Geol Surv Prof Pap 354-C.

Miyachi M (1992) Geological examination of the two old maps from the Tokugawa Era concerning the Shimabara Catastrophe. In: Yanagi T, Okada H, Ohta K (eds.), Unzen Volcano, the 1990–1992 Eruption. Nishinippon & Kyushu University Press, Fukuoka, pp. 99–102.

Moore GW, Moore JG (1988) Large-scale bedforms in boulder gravel produced by giant waves in Hawaii, sedimentologic consequences of convulsive geologic events. Geol Soc Am Spec Pap 229:101–110.

Moore JG, Clague DA, Holcomb RT, Lipman PW, Normark WR, Torresan ME (1989) Prodigious submarine landslides on the Hawaiian Ridge. J Geophys Res 94:17465–17484.

Mosher DC, Piper DJW (2007) Analysis of multibeam seafloor imagery of the Laurentian Fan and the 1929 Grand Banks landslide area. In: Lykousis V, Sakellariou D, Locat J (eds.), Submarine Mass Movements and Their Consequences. Springer, Dordrecht, pp. 77–88.

Nishimura Y, Miyaji N, Suzuki M (1999) Behavior of historic tsunamis of volcanic origin as revealed by onshore tsunami deposits. Phys Chem Earth, Part A: Solid Earth Geod 24:985–988.

Nomanbhoy N, Satake K (1995) Generation mechanism of tsunamis from the 1883 Krakatau eruption. Geophys Res Lett 22, doi: 10.1029/94GL03219.

Normark WR, McGann M, Sliter R (2004) Age of Palos Verdes submarine debris avalanche, southern California. Mar Geol 203:247–259.

Pelayo AM, Wiens DA (1990) The November 20, 1960 Peru tsunami earthquake: Source mechanism of a slow event. Geophys Res Lett 17:661–664.

Pérez-Torrado FJ, Paris R, Cabrera MC, Schneider J-L, Wassmer P, Carracedo J-C, Rodriguez-Santana Á, Santana F (2006) Tsunami deposits related to flank collapse in oceanic volcanoes: The Agaete Valley evidence, Gran Canaria, Canary Islands. Mar Geol 227:135–149.

Piper DJW, Asku AE (1987) The source and origin of the 1929 Grand Banks turbidity current inferred from sediment budgets. Geo-Mar Lett 7:177–182.

Piper DJW, Mosher DC, Gauley B-J, Jenner K, Campbell DC (2003). The chronology and recurrence of submarine mass movements on the continental slope off southeastern Canada. In: J. Locat and J. Mienert (Editors), Submarine mass movements and their consequences. Kluwer Academic Publishers, Dordrecht/Boston/London, pp. 299–306.

Piper DJW, McCall C (2003) A synthesis of the distribution of submarine mass movements on the eastern Canadian Margin. In: Locat J, Mienert J (eds.), Submarine Mass Movements and Their Consequences. Kluwer, Dordrecht/Boston/London, pp. 291–298.

Plafker G, Kachadoorian R, Eckel EB, Mayo LR (1969) Effects of the earthquake of March 27, 1964 on various communities, US Geol Surv Prof Paper 542-G.

Prior DB, Bornhold BD, Coleman JM, Bryant WR (1982) Morphology of a submarine slide, Kitimat Arm, British Columbia. Geology 10:588–592.

Prior DB, Bornhold BD, Johns MW (1986) Active sand transport along a fjord-bottom channel, Bute Inlet, British Columbia. Geology 14:581–584.

Quidelleur X, Hildenbrand A, Samper A (2008) Causal link between Quaternary paleoclimatic changes and volcanic islands evolution. Geophys Res Lett 35(L02303).

Rajendran CP, Ramanamurthy MV, Reddy NT, Rajendran K (2008) Hazard implications of the late arrival of the 1945 Makran tsunami. Curr Sci 95:1739–1743.

Rathbun AE, Levin LA, Tryon M, Gieskes JM, Martin JB, Pérez ME, Fodrie FJ, Neira C, Fryer GJ, Mendoza G, McMillan PA, Kluesner J, Adamic J, Ziebis W (2009) Geological and biological heterogeneity of the Aleutian margin (1965–4822 m). Prog Ocean 80:22–50.

Rubin KH, Fletcher CH III, Sherman C (2000) Fossiliferous Lanai deposits formed by multiple events rather than a single giant tsunami. Nature 408:675–681.

Satake K (2007) Volcanic origin of the 1741 Oshima-Oshima tsunami in the Japan Sea. Earth Planets Space 59:381–390.

Satake K, Smith JR, Shinozaki K (2002) Three-dimensional reconstruction and tsunami model of the Nuuanu and Wailau giant landslides. In: Takahashi E, Lipman P, Garcia M, Naka J, Aramaki S (eds.), Hawaiian Volcanoes: Deep Underwater Perspectives. AGU Monograph 128:333–346.

Self S, Rampino MR (1981) The 1883 eruption of Krakatau. Nature 294:699–704.

Siebert L (1984) Large volcanic debris avalanches: Characteristics of source areas, deposits, and associated eruptions. J Volcanol Geotherm Res 22:163–197.

Siebert L, Glicken H, Ui T (1987) Volcanic hazards from Bezymianny- and Bandai-type eruptions. Bull Volcanol 49:435–459.

Sigurdsson H, Carey S, Mandeville C, Bronto S (1991) Pyroclastic flows of the 1883 Krakatau eruption. Eos Trans AGU 72:377.

Silver E, et al. (2005) Island arc debris avalanches and tsunami generation. Eos Trans AGU 86:485.

Simkin T, Fiske RS (1983) Krakatau 1883: The volcanic eruption and its effects. Smithsonian Institution Press, Washington, DC.

Solheim A, Bryn P, Sejrup HP, Mienert J, Berg K (2005) Ormen Lange – an integrated study for the safe development of a deep-water gas field within the Storegga Slide Complex, NE Atlantic continental margin; executive summary. Mar Pet Geol 22:1–9.

Sowers T (2006) Late quaternary atmospheric CH4 isotope record suggests marine Clathrates are stable. Science 311:838–840.

Stearns HT (1978) Quaternary shorelines in the Hawaiian Islands. Bernice P. Bishop Museum Bull 237:57.

Tappin, DR, Watts P, McMurtry GM, Lafoy Y, Matsumoto T (2001) The Sissano Papua New Guinea tsunami of July 1998 – offshore evidence on the source mechanism. Mar Geol 175:1–23.

Tappin DR, McNeil L, Henstock T, Mosher D (2007) Mass wasting processes – offshore Sumatra. In: Lykouosis V, Sakellariou D, Locat J (eds.), Submarine Mass Movements and Their Consequences. Springer, Dordrecht, pp. 327–336.

Tappin DR, Watts P, Grilli ST (2008a) The Papua New Guinea tsunami of 17 July 1998: Anatomy of a catastrophic event. Nat Hazards Earth Sys Sci 8:1–24.

Tappin DR, Watts P, Grilli ST, Dubosq S, Billi A, Pophet N, Marani MP (2008b) The 1908 Messina tsunami. Some comments on the source: Earthquake, submarine landslide or a combination of both? Eos Trans AGU 89, Fall Meeting Suppl, Abstract S41D-07.

Ten Brink US, Lee HJ, Geist EL, Twichell D (2009) Assessment of tsunami hazard to the U.S. East Coast using relationships between submarine landslides and earthquakes. Mar Geol. 264:65–73.

Tinti S, Manucci A, Pagnoni G, Armigliato A, Zaniboni F (2005) The 30 December 2002 landslide-induced tsunamis in Stromboli: Sequence of the events reconstructed from the eyewitness accounts. Nat Hazards Earth Syst Sci 5:763–775.

Tuttle MP, Ruffman A, Anderson T, Jeter H (2004) Distinguishing tsunami from storm deposits in eastern North America: The 1929 Grand Banks tsunami versus the 1991 Halloween storm. Seismol Res Lett 75:117–131.

Van Padang M (1971) Two catastrophic eruptions in Indonesia, comparable with the Plinian Outburst of the Volcano of Thera (Santorini) in Minoan Time. Acta of the 1st Int. Sci. Cong. on the Volcano of Thera; Arch. Services of Greece, General Direction of Antiquitiest and Research, Athens: 51–63.

von Huene R, Bourgois J, Miller J, Pautot G (1989) A large tsunamogenic landslide and debris flow along the Peru Trench. J Geophys Res 94:1703–1714.

von Huene R, Ranero CR, Watts P (2004) Tsunamigenic slope failure along the Middle America Trench in two tectonic settings. Mar Geol 203:303–317.

Ward SN, Day S (2001) Cumbre Vieja volcano – potential collapse and tsunami at La Palma, Canary Islands. Geophys Res Lett 28:3397–3400.

Waythomas CF, Neal CA (1997) Tsunami generation during the 3500 yr BP Caldera-forming Eruption of Aniakchak Volcano. EOS Trans Am Geophys Union 78:F816.

Weaver PPE, Wynn RB, Kenyon NH, Evans J (2000) Continental margin sedimentation, with special reference to the north-east Atlantic margin. Sedimentology 47:239–225.

Wynn R, Masson D (2003) Canary Islands landslides and tsunami generation: Can we use turbidite deposits to interpret landslide processes. In: Locat J, Mienert J (eds.), Submarine Mass Movements and Their Consequences. Kluwer, Dordrecht, The Netherlands, pp. 325–332.

Yokoyama I (1987) A scenario of the 1883 Krakatau tsunami. J Volcanol Geotherm Res 34:123–132.

Zielinski GA, Mayewski PA, Meeker LD, Whitlow S, Twickler MS (1996) An 110,000-year record of explosive volcanism from the GISP2 (Greenland) ice core. Quat Res 43:109–118.

Hydrodynamic Modeling of Tsunamis Generated by Submarine Landslides: Generation, Propagation, and Shoreline Impact

P. Lynett

Abstract On July 17, 1998, an earthquake occurred near the Pacific coast of western Papua New Guinea (PNG), and a large tsunami followed. The death toll had been the worst from a tsunami in the previous 50 years, with over 1,000 persons killed by the 10-m waves. The exact causative mechanism of the tsunami had been the subject of considerable debate; detailed offshore investigations coupled with analysis of runup patterns eventually and convincingly indicated a slump source (e.g., Tappin et al. 2001; Synolakis et al. 2002). Since PNG, the tsunami community has expended significant energy into examining the state of knowledge regarding landslide tsunamis, with a particular hope to determine the risk associated with these events. This paper will detail some of these recent advances, as well as provide a fundamental background into the physics of wave generation by submarine mass movements. Topics to be discussed include coupling seafloor motion to the hydrodynamics, characteristics of landslide tsunami waves as compared to "traditional" subduction earthquake tsunamis, and the behavior of landslide tsunamis in shallow water.

Keywords Tsunami • landslide • hydrodynamic modeling • runup • inundation

1 Introduction

While rightly deflected after the Indian Ocean tsunami of 2004, the focus of tsunami researchers in the last decade has been largely on understanding the waves generated by submarine and subaerial landslides. Despite this effort, the wave-generating potential of a landslide and its associated risk to the coastline are difficult to assess with precision; the obvious reason for this deficiency is the complexity of the process. The deadly tsunami of Papua New Guinea (PNG) spurred much of this recent work, and has greatly assisted researchers in their understanding of the waves created

P. Lynett (✉)
Texas A&M University, College Station, TX 77843, USA
e-mail: plynett@tamu.edu

by underwater landslides. Studies into the source of PNG have been widespread (e.g., Sweet et al. 1999; Tappin et al. 1999, 2001; Geist 2000; Heinrich et al. 2000; Synolakis et al. 2002). Hydrodynamic investigations of PNG are also numerous, with some looking at the differences between landslide and seismic dislocation (e.g., Satake and Tanioka 2003), while others focus on the physical properties of the PNG waves (e.g., Lynett et al. 2003). This paper will provide a review of recent work on landslide tsunamis, broadly divided into the categories of generation, open ocean propagation, and inundation.

2   Tsunami Generation by Landslide

The properties of the disturbed free water surface above the landslide – the near-field condition – are a function of the time history of the landslide, which is then a function of typically unknown, or very difficult to quantify a-priori, properties of the seabed. The simplest description of a landslide source is solid body motion, where it is assumed that the slide or slump progresses down a constant slope as a single coherent mass. This approach has been employed by Watts (2000) both experimentally and with an empirical, curve-fitting approach applied to derive a characteristic tsunami amplitude. Numerically, solid body motion has been used within high-order accurate numerical models (e.g., Grilli and Watts 1999; Lynett and Liu 2002), in order to develop a more precise relationship between the slide and the tsunami.

From geological evidence, it is clear that large landslides degenerate into or exist primarily as debris flows and turbidity currents. One of the initial numerical modeling attempts at debris flow and tsunami generation/interaction was that of Jiang and LeBlond (1992, 1993, 1994). In this series of papers, both viscous and Bingham flow models were presented for submarine slides. Recent applications of the Jiang and LeBlond model have been widespread (e.g., Fine et al. 2001; Bornhold et al. 2003), and investigations have indicated that the choice of model, whether solid, viscous, or Bingham, has $O(1)$ effects on the generated tsunami height (Fine et al. 2003). An example of how the slide properties affect the generated wave is shown in Fig. 1. In the top row of this figure, termed case A, a dense, viscous fluid flows into a body of water, driven only by the force of gravity. The viscous fluid develops a half-arrow-head type shape upon entry as it interacts with the initially still water, and pushes a large pulse of water offshore. In the lower plot of this figure, case B, an identical initial slide volume is used, but a thin top layer of less dense fluid is placed on the dense fluid. As the slide interacts with the water, naturally these two dense fluid layers behave differently, as well as interact with each other. Interestingly, the front of the lower density fluid of case B moves as a faster rate as compared to Case A, but the generated wave is 15% less in height. This example helps to elucidate that precise modeling of the wave generation by geophysical events is very difficult.

Nearly all of the applications of these mudflow models to wave generation take a shallow water approach. Unless the slide is in extremely shallow water, essentially
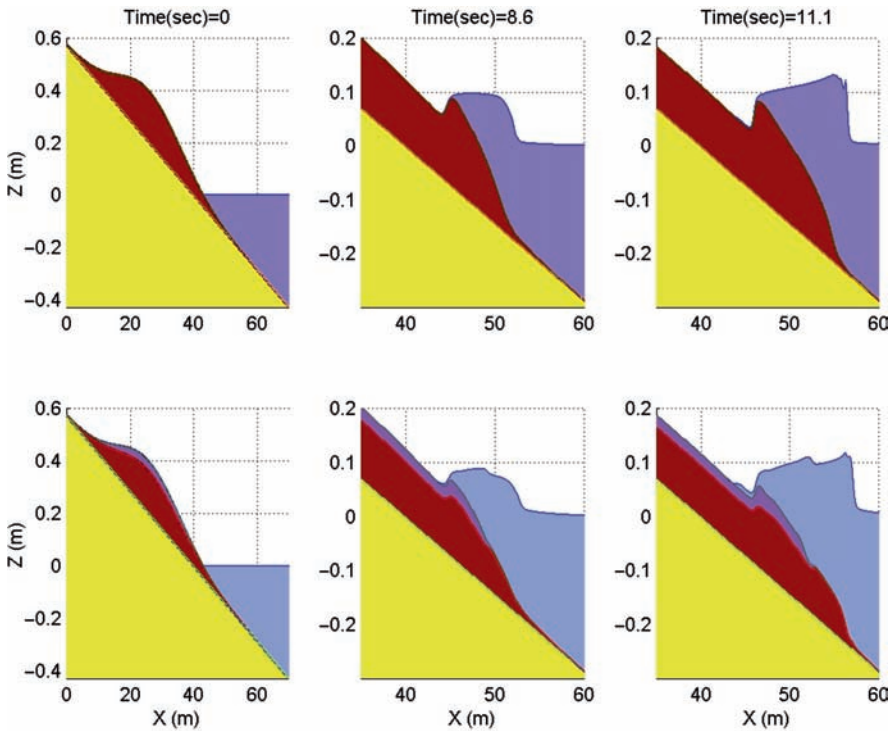
Fig. 1 In the top row are shown three spatial snapshots of a single fluid flowing into water. In the second row are snapshots, taken at the same time, of a two-fluid mass flowing into water. The two-fluid mass is meant to very roughly represent a turbidity current above a debris flow

subaerial, it is known that the nonlinear shallow water wave (NLSW) equations do not correctly capture the interaction between sliding mass and wave generation (Lynett and Liu 2002). This aspect becomes particularly troubling as one inspects the evolution of a mudflow downslope. The formation of a bore-type front face occurs (e.g., Jiang and LeBlond 1994), which has a relatively large slope. For these cases, the NLSW will greatly over-predict the wave height, due to the fact that generation of surface waves by a traveling steep-sided body is an intermediate to deep water problem (Lynett and Liu 2002).

3 Open Ocean Propagation of Landslide Tsunami

Landslide tsunamis, especially those created by large slides, can be characterized as nonlinear waves (wave height is a non-negligible fraction of the water depth) in the near field, either linear or nonlinear during open ocean propagation, and then usually nonlinear in the nearshore. Additionally, landslide waves, depending on the

horizontal length scale of the slide, can often be described as dispersive, meaning that the various important frequency components that compose the waveform travel at different speeds. This effect will cause the wave energy to spread lengthwise in the direction of propagation, and can cause the maximum energy flux reaching the shoreline to diminish. Due to this relative complexity of a landslide wave, it can be difficult to model correctly.

There are two main classes of governing equations employed to predict the evolution of water waves and the associated fluid flow: depth-integrated and fully 3D. Depth-integrated equations are those which, typically by way of an assumption of the length scale ratio, can be vertically integrated to yield an explicit equation form. The net effect of this integration is to remove the vertical dimension from the equations, leaving a 2D equation where once was a 3D equation. Elimination of the vertical dimension yields an exponential reduction in the required computational time to solve, and thus allows one to simulate phenomenon over very large spatial scales.

Focusing on tsunami research, the depth-integrated category has historically included only NLSW models. Earthquake generated tsunamis, with their very long wavelengths, are ideally matched with NLSW for transoceanic propagation. Models such as Titov and Synolakis (1995) and Liu et al. (1995) have been shown to be accurate throughout the lifeline of a seismic tsunami, and are in widespread use today. However, when examining the tsunamis generated by submarine mass failures, the NLSW can lead to errors in the wave shape and arrival time of the wave (Lynett et al. 2003). The length scale of a submarine failure tends to be much less that that of an earthquake, and thus the wavelength of the created tsunami is shorter. To correctly simulate the shorter wave phenomenon, one needs equations with excellent shallow to intermediate water properties, such as the Boussinesq equations. While the Boussinesq model too has accuracy limitations on how deep (or short) the landslide can be (Lynett and Liu 2002), it is able to simulate the majority of tsunami generating landslides.

4   Shallow Water Evolution

As the tsunami approaches the beach and turbulence effects may become important, depth-integrated models are able to provide only a coarse prediction. NLSW and Boussinesq models are by definition invicsid, and so require special treatment to capture the physical dissipation processes, such as breaking and bottom friction. Examples are the numerical dissipation in NLSW models (e.g., Liu et al. 1995) or the ad-hoc breaking models utilized in Boussinesq models (e.g., Kennedy et al. 2000). Additionally, wave interaction with complex, spatially variable structures is difficult, due to the mild slope assumptions inherent in long wave models. In order to simulate nearshore dissipation and complex wave-structure interaction with confidence, the use of a fully 3D model is required. These models tend to require substantial computer processing time, and their use for large-scale tsunami problems is currently limited.

An interesting physical phenomenon that occurs to some long waves in shallow water, and are especially relevant to landslide generated waves, is fission. Long wave fission is most commonly discussed in the literature via a solitary wave propagating over an abrupt change in depth, such as a step (e.g., Madsen and Mei 1969; Johnson 1972; Seabra-Santos et al. 1987; Losada et al. 1989; Goring and Raichlen 1992; Liu and Cheng 2001). In these cases, there is a deep water segment of the seafloor profile, where a solitary wave initially exists. In this depth, the solitary wave is of permanent form. As the solitary wave passes over the change in depth, into shallower water, the leading wave energy will try to re-discover a balance between nonlinearity and dispersion; the solitary wave. Since this new solitary wave will be a different shape and contain a lower level of mass, by conservation there must be some trailing disturbance to account for the deficient. This trailing disturbance will take the form of a rank-ordered train of solitons. Note, however, that discussion of fission in this sense is not particularly relevant to "real" tsunami modeling, where the offshore wave approaching the shelf break rarely resembles a solitary wave solution (Tadepalli and Synolakis 1996). However, the offshore wave does not need to specifically be a solitary wave for this process to occur.

In numerous eyewitness accounts and videos recorded of the 2004 Indian Ocean tsunami, there is evidence of the tsunami approaching the coastline as a series of short period (on the order of 1 min and less) breaking fronts, or bores (e.g., Ioualalen et al. 2007). These short period waves may be the result of fission processes of a steep tsunami front propagating across a wide shelf of shallow depth. Along the steep front of a very long period wave, nonlinearity will be very important. There will be a large amount of energy in high-frequency components with wavelengths similar the horizontal length of the tsunami front (on the order of 1 km). As the wave continues to shoal, the high-frequency locked waves may eventually become free waves, and will take the form of very short waves "riding" the main wave pulse. This situation is akin to an undular bore in a moving reference frame. The newly freed waves, in the nonlinear and shallow environment, will attempt to reach an equilibrium state, where frequency dispersion and nonlinearity are balanced. Thus, the fission waves will appear as solitary waves, or more generally, cnoidal waves. This fact provides some guidance as to the wavelength of these fission waves; they can be approximately calculated via solitary wave theory using the tsunami height and depth of the shelf. For example, on a shelf with depth of 30 m and an incident tsunami height of 5 m, fission waves with a wavelength of approximately 240 m and period of 13 s would be generated. In recent work looking at landslide tsunamis along the eastern U.S.A coast, where there exists a wide shallow shelf, this fission process has been investigated (Geist et al. 2009). Figure 2 gives a few numerical simulation snapshots, and shows where the fission occurs, and the eventually impact on the waveform. This simulation, run with the dispersive equations, generated fission waves with lengths in the range of 100–200 m, and required a grid size of 5 m to attain numerically convergent results. In this example, the steep fission waves break offshore, and have little impact on the maximum runup. It is noted that landslide waves may be more likely to exhibit these fission features, due to the fact that the nonlinearity of a landslide wave may be large, even as it first approaches a shelf break.
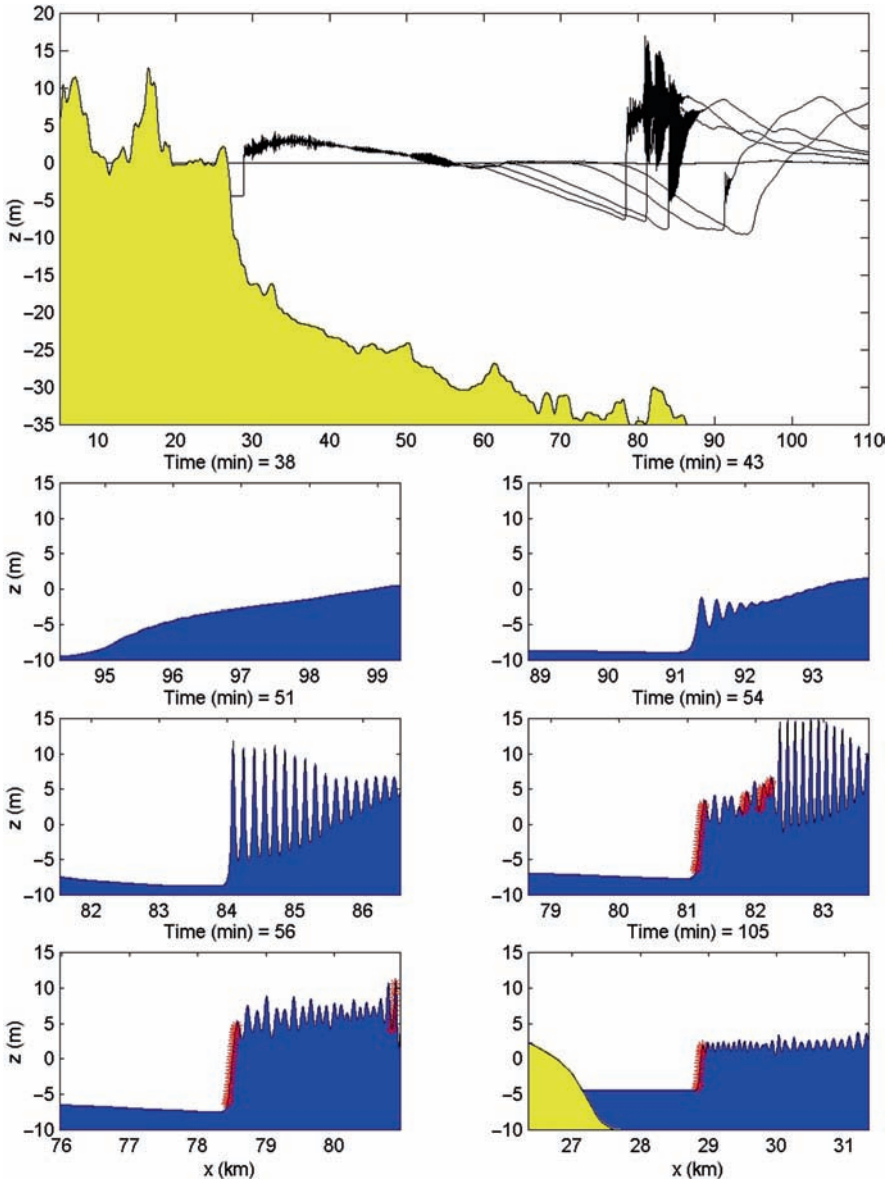
Fig. 2 Example of tsunami fission. Simulation results are from Geist et al (2009) for a landslide-generated tsunami off the east coast of the U.S.A. The top plot shows the beach profile and six free surface profiles at different times. The lower subplots are zoom-in's of those six profiles, with the times given in the individual plot titles. The red marks visible in the lowest plots indicate regions where the wave is breaking

5 Inundation

In order to simulate the flooding of dry land by a tsunami, a numerical model must be capable of allowing the shoreline to move in time. Here, the shoreline is defined as the spatial location where the solid bottom transitions from submerged to dry, and is a function of the two horizontal spatial coordinates and time. Numerical models generally require some type of special consideration and treatment to accurately include these moving boundaries; the logic and implementation behind this treatment is called a moving shoreline, or runup, algorithm.

For typical tsunami propagation models, it is possible to divide runup algorithms into two main approaches: those on a fixed grid and those on a Lagrangian or transformed domain. Note that there is no explicit difference between modeling the inundation of a seismic tsunami or a landslide tsunami, although the differences in period between the two phenomena can lead to preferences of one runup scheme over another. Both runup algorithm approaches have their advantages and disadvantages; currently fixed grid methods are found more commonly in operational-level models (e.g., Titov and Synolakis 1998), likely due in large part to their conceptual simplicity. A review of these two classes of models will be given in this section, followed by a review of the standard analytical, experimental, and field benchmarks used to validate the runup models. For additional information, the reader is directed to the comprehensive review given in Pedersen (2006).

With a fixed grid method, the spatial locations of the numerical grid points or control volumes are determined at the start of a simulation, and do not change shape or location throughout the simulation duration. These methods can be classified into extrapolation, stair-step, auxiliary shoreline point, and permeable beach techniques. The extrapolation method has its roots in Sielecki and Wurtele (1970), with extensions by Hibberd and Peregrine (1979); Kowalik and Murty (1993); and Lynett et al. (2002). The basic idea behind this method is that the shoreline location can be extrapolated using the nearest wet points, such that its position is not required to be locked onto a fixed grid point; it can move freely to any location.

Stair-step moving shoreline methods, one of the more common approaches found in tsunami models (e.g., Liu et al. 1994), reconstruct the naturally continuous beach profile into a series of constant elevation segments connected through vertical transitions. In essence, across a single cell width, the bottom elevation is taken as the average value. A cell transitions from a dry cell to a wet cell when the water elevation in a neighboring cell exceeds the bottom elevation, and transitions from wet to dry when the local total water depth falls below some small threshold value. These methods are particularly useful in finite volume and C-grid (Arakawa and Lamb 1977) type approaches (e.g., Liu et al. 1995; LeVeque and George 2004), but can be difficult to implement in centered difference models, particularly high-order models or those sensitive to fluid discontinuities, where the "shock" of opening and closing entire cells can lead to numerical noise.

Auxiliary shoreline point methods require dynamic re-gridding very near the shoreline, such that the last wet point is always located immediately at the shoreline.

Obviously, this method requires a numerical scheme that can readily accommodate non-uniform and changing node locations. There is some relation to the extrapolation methods discussed above; the moving shoreline point must be assigned some velocity, and it is extrapolated from the neighboring wet points. However, it is fundamentally different in that the shoreline point is explicitly included in the fluid domain. Thus, it would be expected that the governing conservation equations near the shoreline are more precisely satisfied here, although still dependent on the appropriateness of the extrapolation. One such method can be found in Titov and Synolakis (1995), and has been successfully applied in NSLW equation models.

Alternative to fixed grid methods is the Lagrangian approach. Here, the fluid domain is descritized into particles, or columns of fluid in depth-integrated models, that are transported following the total fluid derivative. There are no fixed spatial grid locations; the columns move freely in space and time and thus these techniques require numerical flexibility, in terms of utilizing constantly changing space and time steps. The Lagrangian approach can be described as both the more physically consistent and mathematical elegant method of describing shoreline motion. The shoreline "particle" is included in the physical formulation just as any other point in the domain (i.e., no extrapolations are necessary), and thus the shoreline position accuracy will be compromised only by the overarching physical approximation (e.g., long wave approximation) and the numerical solution scheme (e.g., second-order time integration). The cost for this accuracy is a mathematical system that can be more difficult and tedious to solve numerically, typically requiring domain transformations, mappings, and/or re-griddings. Lagrangian methods have been used successfully in finite difference and finite element nonlinear shallow water (NLSW) and Boussinesq equation models (e.g., Pedersen and Gjevik 1983; Gopalakrishnan and Tung 1983; Petera and Nasshei 1996; Zelt 1991; Ozkan-Haller and Kirby 1997; Birknes and Pedersen 2006).

6   Conclusions

As noted in a state-of-the-science paper looking at landslide tsunami hazards (Bardet et al. 2003), the physical understanding of this hazard is poor, and "there is an immediate need for research" such that we can be reasonably prepared for devastating events like PNG. This is, of course, no simple task. Extreme geophysical events are, by definition, complex and involve multi-scale processes, and landslide tsunamis are no exception. The waves are generated at a multi-phase rock-soil-water interface, where the various constituents can be moving at high speeds, with slip surfaces dictated by very local geotechnical properties. The resulting free surface waves can be both nonlinear and dispersive, implying that only a general wave model, without substantial approximation, can be used to properly model the propagation of the disturbance.

References

Arakawa A, Lamb VR (1977) Computational design of the basic dynamical processes of the UCLA general circulation model. Methods in Computational Physics, J. Chang, Ed., Academic Press, New York, 173–265.

Bardet J-P, Synolakis C, Davis H, Imamura F, Okal E (2003), Landslide tsunamis: Recent findings and research directions. Pure Appl Geophys 160:1793–1809.

Birknes J, Pedersen G (2006) A particle finite element method applied to long wave run-up, Intl J Numer Meth Fluids 52:237–261.

Bornhold B, Fine I, Rabinovich A, Thomson R, Kulikov E (2003) The Grand Banks landslide-generated tsunami of November 18, 1929: analysis and numerical modeling. Proceedings EGS-AGU-EUG Joint Assembly, Nice, France, 6–11 April, p. 1468.

Fine I, Kulikov E, Thomson R, Rabinovich A (2001) Modeling of tsunami generation by submarine and subaerial landslides. Proceedings International Tsunami Symposium, Seattle, Washington, 7–10 August, p.663.

Fine I, Rabinovich A, Thomson R, Kulikov E, Bornhold B (2003) Numerical simulation of landslide-generated tsunamis: three different models. Proceedings EGS-AGU-EUG Joint Assembly Nice, France, 6–11 April, p. 1469.

Geist EL (2000) Origin of the 17 July 1998 Papua New Guinea Tsunami: Earthquake or Landslide? Seismol Res Lett 71:344–351.

Geist EL, Lynett P, Chaytor JD (2009) Hydrodynamic Modeling of Tsunamis from the Currituck Landslide. Mar Geol 264(1–2):41–52.

Gopalakrishnan TC, Tung CC (1983) Numerical analysis of a moving boundary problem in coastal hydrodynamics. Intl J Numer Meth Fluids 3:179–200.

Goring DG, Raichlen F (1992) Propagation of long waves onto shelf. J Wtrwy Port Coast Ocean Eng 118:43–61.

Grilli ST, Watts P (1999) Modeling of waves generated by a moving submerged body. Applications to underwater landslides. Eng Anal Boundary Elem 23:645–656.

Hibberd S, Peregrine DH (1979) Surf and run-up on a beach. J Fluid Mech 95:323–345.

Heinrich P, Piatanesi A, Okal EA, Hébert H (2000) Near-field modeling of the July 17,1998 Tsunami in Papua New Guinea. Geophys Res Lett 27:3,037–3,040.

Ioualalen M, Asavanant J, Kaewbanjak N, Grilli ST, Kirby JT, Watts P (2007). Modeling the 26th December 2004 Indian Ocean tsunami: Case study of impact in Thailand. J Geophys Res doi:10.1029.

Jiang L, LeBlond PH (1992) The coupling of a submarine slide and the waves which it generates J Geophys Res 97:12,731–12,744.

Jiang L, LeBlond PH (1993) Numerical modeling of an underwater Bingham plastic mudslide and the waves which it generates. J Geophys Res 98:10,303–10,317.

Jiang L, LeBlond PH (1994) Three-dimensional modeling of tsunami generation due to a submarine landslide. J Phys Oceanog 24:559–572.

Johson R (1972) Some numerical solutions of a variable-coefficient Korteweg–de Vries equation (with application to solitary wave development on a shelf). J Fluid Mech 54:81–91.

Kennedy AB, Chen Q, Kirby JT, Dalrymple RA (2000) Boussinesq modeling of wave transformation, breaking, and runup. 1: 1D. J Wtrwy Port Coast Ocean Eng 126:39–47.

Kowalik Z, Murty TS (1993) Numerical simulation of two-dimensional tsunami runup. Mar Geod 16:87–100.

LeVeque R, George DL (2004) High-resolution finite volume methods for the shallow water equations with bathymetry and dry states. In: Liu PL, Yeh H, Synolakis C (eds) Advanced Numerical Models for Simulating Tsunami Waves and Runup, Advances in Coastal and Ocean Engineering 10, World Scientific Publishing Company, Singapore.

Losada M, Vidal V, Medina R (1989) Experimental study of the evolution of a solitary wave at an abrupt junction. J Geophys Res 94:14557–14566.

Liu PL-F, Cho Y-S, Yoon SB, Seo SN (1994) Numerical simulations of the 1960 Chilean tsunami propagation and inundation at Hilo, Hawaii, In: El-Sabh MI (ed) Recent Development in Tsunami Research, Kluwer, p. 99–115.

Liu PL-F, Cho Y-S, Briggs MJ, Kanoglu U, Synolakis CE (1995) Runup of solitary waves on a circular island. J Fluid Mech 320:259–285.

Liu PL-F, Cheng Y (2001) A numerical study of the evolution of a solitary wave over a shelf. Phys Fluids 13:1660–1667.

Lynett P, Wu T-R, Liu PL-F (2002) Modeling wave runup with depth-integrated equations. Coast Eng 46:89–107.

Lynett P, Liu PL-F (2002) A Numerical study of submarine landslide generated waves and runup. Proc R Soc Lond A 458:2,885–2,910.

Lynett P, Borrero J, Liu PL-F, Synolakis CE (2003) Field survey and numerical simulations: a review of the 1998 Papua New Guinea Tsunami. Pure Appl Geophys 160:2,119–2,146.

Madsen O, Mei CC (1969) The transformation of a solitary wave over an uneven bottom J Fluid Mech 39:781.

Özkan-Haller HT, Kirby JT (1997) A Fourier-Chebyshev collocation method for the shallow water equations including shoreline run-up. App Ocean Res 19:21–34.

Pedersen G (2006) On long wave runup models. In: Proceedings of the 3rd international workshop on long-wave runup models, June 17–18, 2004, Catalina Island, California.

Pedersen G, Gjevik B (1983) Runup of solitary waves. J Fluid Mech 142:283–299.

Petera J, Nassehi V (1996) A new two-dimensional finite element model for the shallow water equations using a Lagrangian framework constructed along fluid particle trajectories. Int J Numer Methods Eng 39:4,159–4,182.

Satake K, Tanioka Y (2003) The July 1998 Papua New Guinea earthquake: mechanism andquantification of unusual tsunami generation. Pure Appl Geophys 160:2087–2118.

Seabra-Santos F, Renouard DP, Temperville AM (1987) Numerical and experimental study of the transformation of a solitary wave over a shelf or isolated obstacles. J Fluid Mech 176:117.

Sielecki A, Wurtele MG (1970) The numerical integration of the nonlinear shallow-water equations with sloping boundaries. J Comput Phys 6:219–236.

Synolakis CE, Bardet J-P, Borrero J, Davies H, Okal E, Silver E, Sweet S, Tappin D (2002). Slump origin of the 1998 Papua New Guinea tsunami. Proc Roy Soc London, Ser. A 458:763–789.

Sweet S, Silver EA, Davies H, Matsumoto T, Watts P, Synolakis CE (1999) Seismic reflection images of the source region of the Papua New Guinea tsunami of July 17, 1998. EOS, Trans Am Geophys Union 80:F750.

Tadepalli S, Synolakis CE (1996) Model for the leading waves of tsunamis. Phys Rev Lett 77:2,141–2,144.

Tappin DR, Matsumoto T, Watts P, Satake K, McMurtry GM, Matsuyama M, Lafoy Y, Tsuji Y, Kanamatsu T, Lus W, Iwabuchi Y, Yeh H, Matsumotu Y, Nakamura M, Mahoi M, Hill P, Crook K, Anton L, Walsh JP (1999) Sediment slump likely caused Papua New Guinea tsunami. Eos Trans Am Geophys Union 80:329.

Tappin DR, Watts P, Mcmurtry GM, Lafoy Y, Matsumoto T (2001) The Sissano, Papua New Guinea tsunami of July 1998 – offshore evidence on the source mechanism. Mar Geol 175:1–23.

Titov VV, Synolakis CE (1995) Modeling of breaking and nonbreaking long wave evolution and runup using VTCS-2. J Harbors Wtrwy Port Coast Ocean Eng. 121:308–316.

Titov VV, Synolakis CE (1998) Numerical modeling of tidal wave runup. J Wtrwy Port Coast Ocean Eng 124:157–171.

Watts P (2000) Tsunami features of solid block underwater landslides. J Wtrwy Port Coast Ocean Eng 126:144–152.

Zelt JA (1991) The run-up of nonbreaking and breaking solitary waves. Coast Eng 15:205–246.

Calculations of Tsunamis from Submarine Landslides

G. Gisler, R.P. Weaver, and M. Gittings

Abstract Great underwater landslides like Storegga off the Norwegian coast leave massive deposits on the seafloor and probably produce enormous tsunamis. We have performed a numerical study of such landslides using the multi-material compressible hydrocode Sage in order to understand the relationship between the rheology of the slide material, the configuration of the resulting deposits on the seafloor, and the tsunami that is produced. Instabilities in the fluid-fluid mixing between slide material and seawater produce vortices and swirls with sizes that depend on the rheology of the slide material. These dynamical features of the flow may be preserved as ridges when the sliding material finally stops. Thus studying the configuration of the morphology of prehistoric slide relics on the abyssal plain may help us understand the circumstances under which the slide was initiated.

Keywords Tsunami • hydrodynamic simulations • submarine landslide

1 Introduction

Submarine landslides have occurred on continental slopes worldwide, and continue to do so. Triggers for such slides include earthquakes and underwater volcanoes. Increased sediment load at the top of a continental shelf or a change in thermal

G. Gisler (✉)
Physics of Geological Processes, University of Oslo, PO Box 1048 Blindern,
0316 Oslo, Norway
e-mail: galen.gisler@fys.uio.no

R.P. Weaver
Los Alamos National Laboratory, MS T086, Los Alamos, New Mexico 87545, USA
e-mail: rpw@lanl.gov

M. Gittings
Science Applications International, 3900 North Ocean Dr, #11A, Lauderdale by the Sea,
Florida 33308, USA
e-mail: mgittings0314@mac.com

conditions that moves deposited hydrates out of their regime of stability (see e.g., Kvenvolden 1993) may also initiate slides. We are interested in the relics deposited by the landslides on the seafloor, and wish to determine whether examination of such deposits could yield some understanding as to the rheology of the landslide (Wynn and Masson 2003). The characteristics of the tsunami resulting from an underwater landslide depend on the slide rheology, geometry, and other parameters. In particular, the stiffer the slide, the more energy is consumed in heating the slide material, the substrate, and the water, and the less energy is therefore available to convert into tsunami energy. In considering the potential dangers from submarine landslides, it is therefore of interest to determine the rheology of the material that would be involved in the landslide.

The energetic considerations can be derived from examining the physical configuration immediately before a landslide, and comparing to the configuration long afterwards. The only difference is the location of the slide material: resting on the continental slope (for example) before the slide, and resting on the abyssal plain afterwards. Thus the free energy which drives the dynamics of the event (landslide plus tsunami) is the difference in the gravitational potential energy of the slide material from initial shelf location to abyssal plain. As the slide begins, some of this potential energy is converted to kinetic energy as the material starts to move down the slope. Almost immediately, it begins to share this kinetic energy with the water, pushing the water ahead up and out of the way, and sucking the water behind downwards. Friction between the sliding material and the base heats up both, and entrainment of the water into eddies at the interface between slide and water leads to dissipation of the kinetic energy, further heating the slide material and water. The water sucked downwards behind the slide and pushed upwards ahead of the slide forms a dipole source for a wave that radiates in a directed pattern: radiating shoreward from the continental slope is a leading trough, while radiating seaward is a leading crest. If the wave amplitude is large, it will also interact with the atmosphere, thereby losing additional kinetic energy.

The system therefore consists of slide material, water, seafloor, and atmosphere: four different materials with different mechanical properties. The best way to study such a system numerically is by using a multi-phase multi-material dynamical code.

2   The Sage code

We use an adaptive grid Eulerian code known as Sage (Gittings et al. 2008), developed by Mike Gittings at Science Applications International and adopted for use by Los Alamos National Laboratory. The equations solved are the continuity equation,

$$\frac{\partial \rho}{\partial t} + \nabla \bullet (\rho \mathbf{v}) = 0; \tag{1}$$

the equation for the conservation of momentum,

$$\frac{\partial \rho \mathbf{v}}{\partial t} + \nabla \bullet \rho v \mathbf{v} + \nabla \bullet \sigma = 0; \tag{2}$$

and for the conservation of energy,

$$\frac{\partial \rho \varepsilon}{\partial t} + \nabla \bullet (\rho \varepsilon \mathbf{v}) + \nabla \bullet (\sigma \mathbf{v}) = 0. \tag{3}$$

In these equations ρ is density, $\mathbf{v}$ is the fluid velocity, σ the stress tensor (the trace of which is three times the thermodynamic pressure), and ε is the internal energy per unit mass. These are the Euler equations of compressible fluid flow, with the full stress tensor in Eqs. 2 and 3 replacing the usual pressure variable in order to treat materials such as solids that can support asymmetric stresses. These are supplemented with an appropriate prescription for gravity, dependent on geometry, and closed with a constitutive equation expressing the relation among the stress state, internal energy, and density. The constitutive relation for materials that do not support transverse stresses is simply a thermodynamic equation of state, but for elastic solids and plastically flowing materials more equations must be added. A wide variety of equations of state and constitutive relations, both analytical and tabular, are available within the code. The variables are discretized to an Eulerian grid with a resolution that can change at every time step according to local gradients in physical or material properties.

Each cell in the computational volume can contain, in principle, all the materials defined in the problem. At the beginning of a computational cycle, Sage computes partial stresses, internal energies, and densities for all materials in a cell. With the assumption of local thermodynamic equilibrium within a cell, a unique cell temperature is defined, and momentum conservation serves to define a unique velocity associated with the cell.

3   Problem Setup for Submarine Landslide Calculations

The problem we consider here has four materials: air, water, the sliding material, and the seafloor. For computational convenience we chose to use basalt for both the seafloor and the sliding material, distinguishing them by differences in strength (strong for the seafloor, weak for the slide) and dilation (compact for the seafloor, loose for the slide). We used tabular equations of state from the LANL Sesame library (Holian 1984; Lyon and Johnson 1992) for air and basalt, and for water we use an equation of state provided as part of the Sage package. For the seafloor and slide we use a simple analytical elastic-perfectly plastic strength model, characterized by a yield strength, a shear modulus, and a fail pressure (the bulk modulus comes out of the Sesame tabular equation of state). The compact strong basalt for

the seafloor is given a yield strength of 1 Mbar, so that it behaves elastically throughout the calculation and does not move. The loose weak basalt used for the slide has a distension parameter (ratio of compact to loose density, Herrmann 1968) of 1.5 and a nominal yield strength of only 1 bar. It begins to shift under its own weight as soon as the calculation begins. The shear modulus for the sliding material is varied, over the six runs we report here, from 1 bar to 3 kbar (see Table 1). All of these runs are two-dimensional, effectively infinite in extent in the plane perpendicular to the calculation.

All runs have identical starting configurations, as illustrated in Fig. 1. The vertical extent of the computational volume is 6 km, of which 2 km is above the ocean surface. The horizontal extent is 100 km, of which half is shown in Fig. 1. The basement consists of a continental shelf of 2° slope, starting 100 m below the ocean surface at the left boundary, and ending at a depth of 600 m and a distance of 14.3 km from the boundary. The continental slope inclines from there with a slope of 9°, ending on the abyssal plain at 4.5 km depth and 39.9 km from the boundary. The abyssal plain then continues down towards the right with a slope of 0.5°, reaching a depth of 5 km at the right boundary. The slide material is a quadrilateral region cut out from the shelf and slope, starting at a depth of 300 m and a distance 5.73 km from the left boundary, with the slide plane having an average slope of 7°. The toe of the slide material is at 3.96 km depth, 35.5 km from the boundary, and the cut point is at 1.3 km depth, 12 km from the boundary. These numerical values were chosen as

Table 1 Input and output characteristics of six submarine landslide runs

	Shear modulus of slide material (bar)	Near-field tsunami amplitude (m)	Free energy into water kinetic energy (%)	Free energy into heating of water and slide (%)
SGrYa	1	100	5.6	57
SGrZa	10	100	5.0	58
SGr0a	100	91	3.9	59
SGr1a	300	80	3.1	61
SGr2a	1,000	64	1.9	63
SGr3a	3,000	45	1.4	67
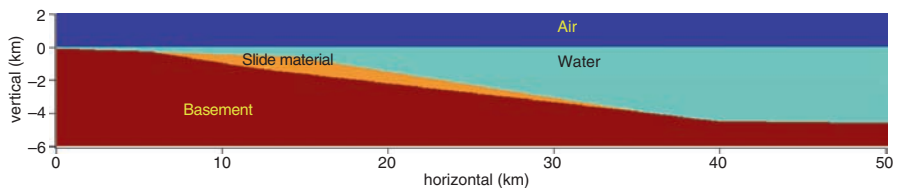
Fig. 1 Initial configuration for the runs of Table 1. The full vertical extent of the computational volume is shown, but only half the horizontal extent. There are four materials in the problem, as labeled here. Both the basement and the slide material are basalt, but while the basement basalt is made very strong, the slide material basalt is made weak enough that it begins to flow under its own weight as soon as the calculation begins. An initial hydrostatic equilibrium is calculated at the right end of the box and used to initial-ize pressures throughout the calculation

being roughly representative of a generic continental slope without a relationship to any particular location.

The acceleration due to gravity is the standard earth value of 9.80 m/s², and pressures throughout the problem are initialized by calculation of isothermal hydrostatic equilibrium on the right boundary, which is a column of 2 km air, 5 km water, and 1 km basalt, constrained by the requirement that the pressure at the water surface is 1 bar. This procedure produces initialization pressures that are too low within the basalt basement on the shelf side, but since the basalt is strong and elastic, the adjustment is made rapidly (within ~25 s) once the dynamic calculations are underway, and the calculation results are not substantially affected.

4   The Calculations

A sequence of density plots from run SGrYa, the run with the most mobile (nearly inviscid) slide material, is shown in Fig. 2. A horizontal line is drawn at the position of the original sea surface, so that it is possible to see the initial draw-down of the water as the landslide begins. The elevation of the water ahead of the slide is not visually apparent on the figure because it is of much lower amplitude. The minimum cell size in these calculations is 15 m, invisible on the figure.

The ripples on the interface between the slide material and the water are due to a two-stream, or Kelvin-Helmholtz instability (Chandrasekhar 1961). By the bottom frame in Fig. 2, at 300 s, the ripples at the head of the slide have evolved into turbidity currents, whose vertical extent is larger than or comparable to the original slide depth. Substantial mixing between water and slide material is taking place, and it would be anticipated that a slide like this would leave a relic on the seafloor having numerous ridges as remnants of the turbidity currents.

In Fig. 3 we show the energy evolution in this run. The slide's motion, beginning at the start of the calculation, is reflected in the rise of its kinetic energy curve over the first few minutes as the slide material's potential energy is converted first into kinetic energy and then into heat. At about 200 s, the slide kinetic energy peaks and is roughly equaled by the slide heat energy, which continues to rise. The water, partly pushed out of the way by the slide, and partly entrained by it, is simultaneously heated and accelerated, until about 350 s when heating begins to dominate. After this point the water loses kinetic energy very slowly as the wave propagates away from the source. After about 550 s, the leading edge of the disturbance starts to leave the computational volume, and the kinetic energy of the water retained in the volume drops accordingly. The slide decelerates strongly through friction with the bottom and resistance from the water. The calculation was terminated at 800 s, by which time heat inputs have saturated. The fraction of the slide material's initial potential energy that is transferred to the water's kinetic energy is less than 6%, as shown in Table 1, while over half the energy has gone into heating the water and the slide material. The missing energy goes mainly into heating the basement, and a small fraction into motion of the air.
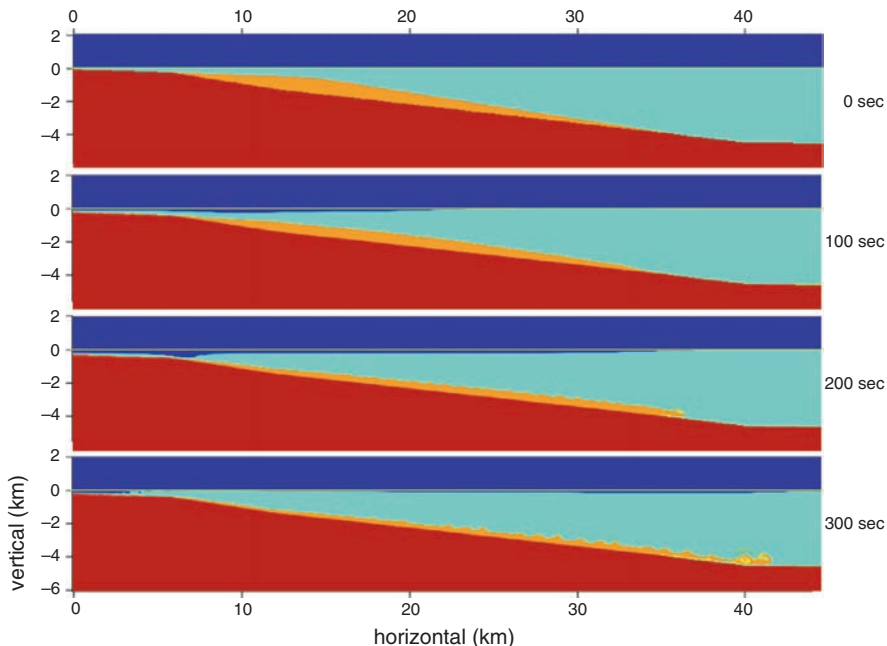
Fig. 2 Snapshots from the first 300 s of run SGrYa of Table 1. The weak material of the slide region begins to move under its own weight at the beginning of the calculation. After a minute and a half, there is already a substantial drawdown of the water surface above the head of the slide. Ripples start to form on the interface between slide and water by about 3 min, and by the time the head of the slide has reached the bottom of the slope, these ripples have become strong turbidity currents. Meanwhile water rushes in to fill the drawdown at the slide head and moves towards shore on the left, and the leading crest of the tsunami has moved off to the right
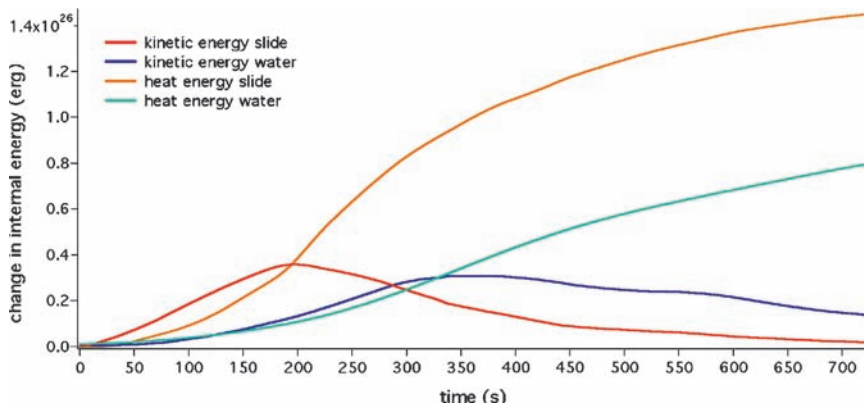
Fig. 3 Energy evolution for run SGrYa of Table 1. Plotted are kinetic energy of the slide material and water, and heat (internal) energy of the slide material and water, as a function of physical time in the calculation. The slide material acquires a great deal more heat energy than kinetic energy, even as it decelerates to a stop. The water acquires heat energy as rapidly as it does kinetic energy, and continues being heated after its kinetic energy saturates. The decline in water kinetic energy after 350 s is very slow and then becomes more rapid as the oscillatory wave motion in the water gradually moves out of the box

Snapshots from the other five runs of Table 1 are shown in Fig. 4 at a uniform time of 400 s for all runs. The dark vertical line is at the position where the continental slope meets the abyssal plain. The slide material in run SGr2a has just reached this point, while the stiffer slide material in SGr3a lags behind, and the less stiff runs above have all passed it by. The less viscous slides differ from the stiffer slides also in having a bumpier interface with the water. This difference persists to the end of the calculations in these runs, and presumably is preserved to some extent long after the slide comes to rest on the seafloor. Finally, the runnier slides produce higher amplitude tsunamis, as seen in Table 1, but also in the visually noticeable difference in the shoreward propagating wave on the left-hand side, above the continental shelf.

The tsunami amplitudes quoted in Table 1 are derived from analysis of tracer particle trajectories. At the beginning of the calculation, 200 massless Lagrangian tracer particles are distributed on the water surface and 50 m below, between 10 and 40 km from the left-hand edge of the computational volume. A trajectory plot of a sample of these tracers, from run SGr0a, is shown in Fig. 5. Each trajectory in this plot is colored by time, red at the beginning of the calculation, blue at the end.
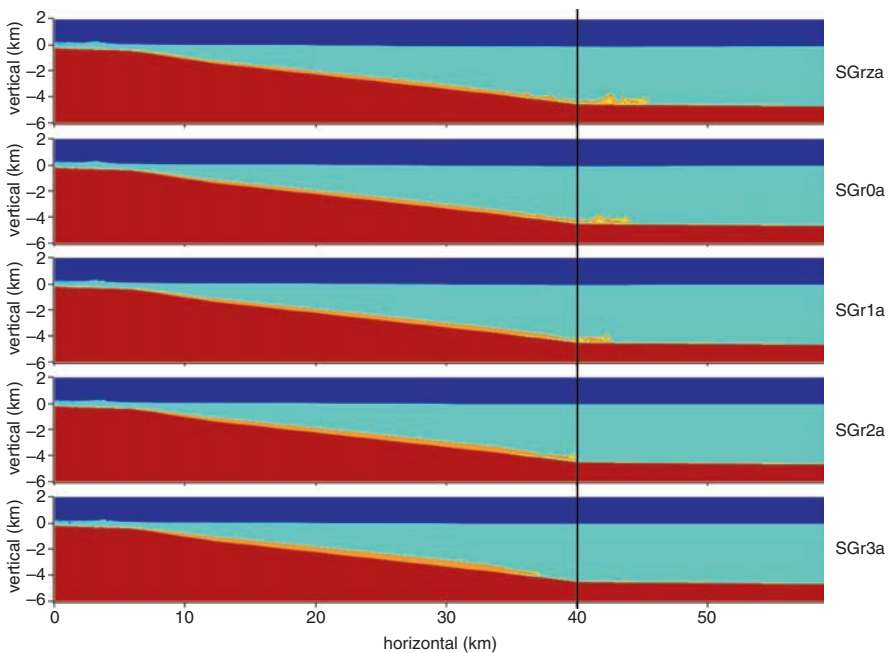
Fig. 4 Simultaneous snapshots at a time 400 s after the beginning of the calculations for five of the runs of Table 1. Run SGrYa is omitted, since its configuration at 300 s is shown in Fig. 3. The stiffest calculations are at the bottom, the runniest at the top. The dark vertical line, to guide the eye, is place where the continental slope meets the abyssal plain. The runniest slides produce more turbidity currents and will leave bumpier relics on the seafloor
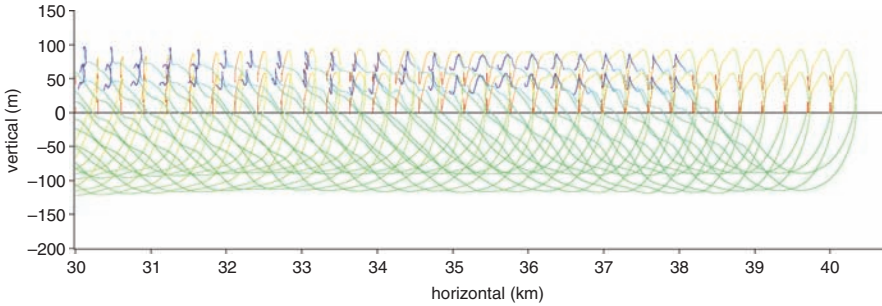
Fig. 5 Tracer particle trajectory plot for run SGr0a. Only trajectories between 30 and 40 km from the left-hand boundary are shown. Each particle's trajectory is colored to indicate physical time: red at the start of the calculation to blue at the calculation termination (800 s). For robustness, at each horizontal position we place two particles, one initially at the water surface, the other initially 50 m below. Particles start out nearly stationary, oscillating slightly with acoustic waves, until the tsunami reaches them. Then, typically, they make a slight motion outward and upward (~50 × 300 m) followed by a resurge motion downward and backward (150 × 3,000 m), and subsequently oscillate in place with the passage of subsequent waves

A typical tracer in this range (between 30 and 40 km out, close to the end of the continental slope) sits nearly stationary, drifting up and down with acoustic waves, until the tsunami passes. The particle then moves upward by about 50 m and outward by several hundred meters, then downward by about 150 m and backwards by several km as the refilling wave passes. Subsequent waves produce nearly in-place vertical motion. The arrival time of the wave at each tracer enables measurement of the outward-going tsunami velocity. We measure this between the midpoint and the bottom of the slope, at about 150 km/s. Above the abyssal plain, the tsunami speed should reach 200 m/s, from the shallow-water formula (Mader 1988) for the wave speed (= $\sqrt{gD}$, where g is the acceleration due to gravity and D the water depth).

Finally, numerical calculations being yet an imperfect art, we must examine the question of numerical resolution and how its practical limitation affects the conclusions we might draw from these calculations. In Fig. 6 we show images from a new series of runs, in identical geometry to the runs of Figs. 1–5, but with varying spatial resolution. Fortunately, it is possible to calculate a correct physical speed (and hence ultimate runout distance) at infinite resolution by taking the velocities as a function of smallest cell size and extrapolating down to zero cell size. Slide speed is found to increase as the spatial resolution is improved, suggesting that low speeds reported by previous numerical studies at lower resolution may be seriously in error. Note that the resolution used for the runs of Table 1 is the same as that for the next-to-the-best run in Fig. 6.

The roughness of the slide deposit on the abyssal plain is not treated in the extrapolation. It is likely that the scale of the irregularities produced by the two-stream
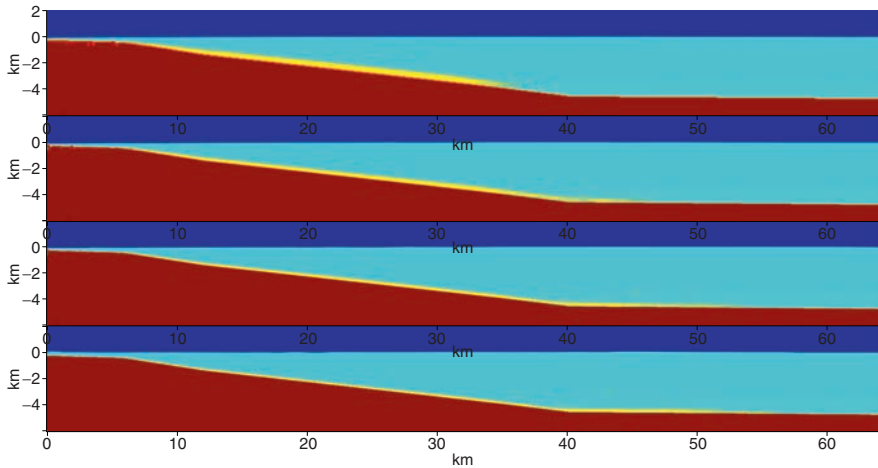
Fig. 6 Density raster plots for four two-dimensional runs of a submarine landslide with successively increasing spatial resolution at the same physical time after the slide start. The speed of the fluidized rock slide increases substantially as resolution improves, and the turbidity currents become more distinct and developed. The setup is the same as for the runs of Figs. 1–5. From the top, the finest spatial resolution in the adaptively refined grid is 62.5 m, 31.3 m, 15.6 m, and 7.8 m. The average velocities of the toe of the slide are 48 ms^{-1}, 62 ms^{-1}, 71 ms^{-1}, and 75 ms^{-1}. Extrapolating to infinitely fine spatial resolution would give an average slide velocity of 79 ms^{-1}

instability decreases with increasing resolution. In the real world, this scale will be determined by the granularity of the slide material.

5 Discussion

The amplitude of a tsunami produced by an underwater landslide is dependent on many factors, one of which is the mobility of the sliding material. Less viscous slides produce larger, more dangerous tsunamis, while stiffer slides produce more modest ones. Less viscous slides also produce longer runouts, but at the same time leave more deposits from the turbidity currents that result in the interchange and mutual entrainment between slide material and water.

If slide mobility were the only variable, we would expect long-runout slide relics to be smoother than short ones. There are, however, other variables, including slide volume, initial topography, and manner of fluidization. The failure mode could be retrogressive, progressive, or by shear band formation (Puzrin and Germanovich 2005). Viscosity may also vary within the slide itself. A slide could have a nearly friction-free bottom layer and a relatively stiff upper layer and thereby produce a runout that is both long and very smooth.

Also, the degree to which slides of solid material, being in fact granular, act as a fluid is not directly addressed here. We suspect that the granularity might make the problem of smooth, long-runout landslide deposits even more difficult.

References

Chandrasekhar S (1961) Hydrodynamic and Hydromagnetic Stability, Clarendon Press, Oxford; reprinted by Dover, 1981.

Gittings ML, Weaver RP, Clover M, Betlach T, Byrne N, Coker R, Dendy E, Hueckstaedt R, New K, Oakes WR, Ranta D, Stefan R (2008) The RAGE radiation-hydrodynamic code. Compu Sci Discov 1:015005.

Herrmann W (1968) Equation of state of crushable distended materials. Sandia National Laboratory Report SCRR 66–601, Albuquerque, New Mexico.

Holian KS (1984) T-4 Handbook of aterial properties data bases: Vol 1c, equations of state. Los Alamos National Laboratory Report LA-10610-MS, Los Alamos, New Mexico.

Kvenvolden K (1993) Gas hydrates - geological perspective and global change. Rev Geophys 31:173–187.

Lyon SP, Johnson JD (1992) Sesame: the Los Alamos National Laboratory equation of state database. Los Alamos National Laboratory Report LA-UR-92–3407, Los Alamos, New Mexico.

Mader CL (1988) Numerical Modeling of Water Waves. University of California Press, Berkeley.

Puzrin AM, Germanovich LN (2005) The growth of shear bands in the catastrophic failure of soils. Proc Math, Phys Enging Sci 461:1199–1228.

Wynn RB, Masson, DG (2003) Canary Island landslides and tsunami generation: can we use turbidite deposits to interpret landslide processes? In: Locat J, Mienert J (eds) Submarine Mass Movements and their Consequences. Kluwer Academic Publishers, Dordrecht, p 325–332.

Experiments on Tsunamis Generated by 3D Granular Landslides

F. Mohammed and H.M. Fritz

Abstract Subaerial and submarine landslides can trigger tsunamis with locally high amplitudes and runup, which can cause devastating effects in the near field region such as the 1958 Lituya bay, Alaska, 1998 Papua New Guinea and 2006 Java tsunamis. Tsunami generation by submarine and subaerial landslides were studied in the three dimensional NEES (George E. Brown, Jr. Network for Earthquake Engineering Simulation) tsunami wave basin (TWB) at Oregon State University based on the generalized Froude similarity. A novel pneumatic landslide generator was deployed to control the granular landslide geometry and kinematics. Measurement techniques such as particle image velocimetry (PIV), multiple above and underwater video cameras, multiple acoustic transducer arrays (MTA), as well as resistance wave and runup gauges were applied. The experimental data provided new insights on landslide deformation as it impacts the water surface, penetrates the water and finally deposits on the bottom of the basin. The influence of the landslide volume, shape and the impact speed on the generated tsunami waves were extensively studied. The instantaneous surface velocity fields measured using the PIV gave insight into the kinematics of the landslide and wave generation process. At high impact velocities, flow separation occurred on the slide shoulder resulting in a hydrodynamic impact crater. The measured wave profiles yielded information on the wave propagation and attenuation. The measured wave speed of the leading wave reaches the theoretical solitary wave celerity while the trailing waves are slower in nature. Attenuation functions of the leading wave crest amplitude, the wave length and the time period were obtained to study the wave behavior in the near field and far field regions. The measured wave data serves the validation and advancement of 3-dimensional numerical landslide tsunami and prediction models.

F. Mohammed (✉) and H.M. Fritz
School of Civil and Environmental Engineering, Georgia Institute of Technology,
210 Technology Circle, Savannah, GA 31407, USA
e-mail: fahd@gatech.edu; hermann.fritz@gtsav.gatech.edu

1 Introduction

Landslide generated tsunamis can occur in confined water bodies as well as at island and continental shelves and coasts where the waves can travel both in off-shore and along the shore directions. These landslide generated tsunamis with locally high amplitudes and runup can be devastative in the near field regions. In the past, major tsunamis caused by landslides were recorded at Grand Banks in 1927 (Fine et al. 2005), Lituya Bay, Alaska in 1958 (Fritz et al. 2001, 2009; Weiss et al. 2009), Vajont dam in Italy in 1963 (Müller 1964), the more recent 1998 Papua New Guinea (Synolakis et al. 2002; Bardet et al. 2003), Stromboli (Tinti et al. 2005, 2006), Java tsunamis (Fritz et al. 2007) and the ancient Storegga slide (Bondevik et al. 2005). The resulting impulse waves can cause damage due to large local runup along the coastline and overtopping of dams and reservoirs. Hence a need arises to understand the effects of the landslide characteristics on the generated tsunami waves. Physical models of landslide generated tsunami scenarios provide a detailed understanding of the wave generation and propagation mechanism as well as simultaneously assist advancement of numerical model development. These analytical and numerical models will allow hazard assessments of landslide generated tsunamis. Majority of physical experiments on landslide generated tsunamis have focused on two dimensional tsunami waves generated by landslides. These experiments were performed by either using solid blocks sliding on an incline to simulate landslide tsunamis (Heinrich 1992; Watts 2000; Walder et al. 2003; Grilli and Watts 2005) or using granular landslides (Fritz 2002; Fritz et al. 2003, 2004). Waves generated by three dimensional solid block landslides were studied by Liu et al. 2005; Panizzo et al. 2005; Enet and Grilli 2005, 2007; DiRisio et al. 2009 on flat bottoms, on sloping beaches and conical islands. The aim of the present study is to understand the generation of tsunami waves by fully three dimensional deformable granular landslides. A realistic description of the landslide is attainable by using deformable materials for the landslide as compared with solid blocks, which do not account for the landslide deformation due to slide motion, interaction with the water body and bathymetry. Herein experiments conducted in the Tsunami Wave Basin at Oregon State University are presented. The study focused on understanding the granular landslide dynamics above and under water, the generation and propagation of the resulting tsunami waves as well as the lateral onshore runup. Three dimensionality of the physical model enabled to identify the wave amplitude attenuation functions in both the radial and the angular directions away from the landslide source thus enabling us to characterize the wave evolution in the near field as well as in the far field regions.

2 Experiment Description

The landslide tsunami generator experiments were conducted at the O. H. Hinsdale Wave Research Laboratory at the Oregon State University, Corvallis. The experiments were performed in the three-dimensional NEES Tsunami Wave Basin (TWB), which is 48.8 m long, 26.5 m wide and 2.1 m deep. A unique pneumatic landslide generator was designed and built at Georgia Tech in Savannah and then shipped and deployed at the Wave Research Lab in Corvallis. The landslide tsunami generator was constructed as an open aluminum box mounted on a steel slide. The box measures 2.1 by 1.2 by 0.3 m and is filled with $0.756 m^3$ (upto 1,350 kg) of naturally rounded river gravel. The granulate material has a bulk density of 2.557 and saturated-surface density of 2.617. The slide box can be subdivided to adjust for the initial slide length and thickness. The box accelerates down the slope by means of four parallel pneumatic pistons. The landslide tsunami generator is shown in Fig. 1a.

This apparatus is capable of simulating landslides initiating both above and below the water surface. The pneumatic pistons accelerate the box to reach launch speeds up to 4 m/s at slide release. The granular landslide is accelerated in the box and released by opening the front tarp while the box is decelerated pneumatically. The entire landslide tsunami generator is positioned on a steel plate with slope 2 H:1 V. Upon deployment, the granulate slides out of the box, spreads down the slope and impacts the water surface at velocities up to 5 m/s, thereby generating the tsunami waves. After impacting the water surface, the granular landslide material deposits on a steel plate placed at the bottom of the wave basin. At the end of an experimental trial, the steel plate is lifted by means of an overhead crane and the granular material is filled back into a bucket and the box is reloaded for the next run. A typical experimental cycle is shown in Fig. 1b. During each experimental trial, a data acquisition system constantly records the entire process and measures the water surface elevation. Measurements are made relating to the shape and speed of the landslide, both above water and underwater, the wave generation process and
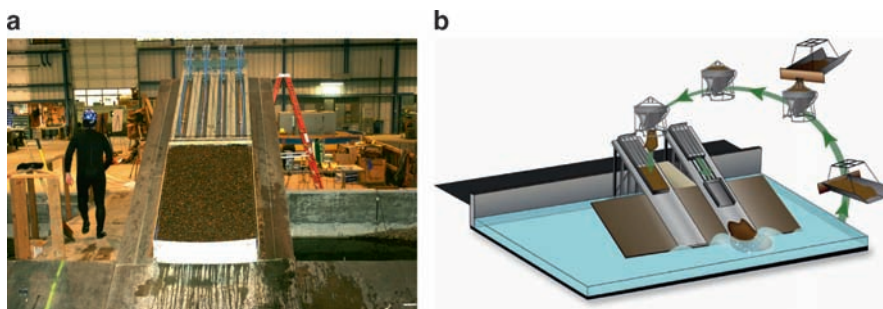
Fig. 1 Landslide Tsunami Generator, LTG. (**a**) Pneumatic acceleration mechanism with four pneumatic pistons in the upper half of the image and the filled slide box with the front tarp; (**b**) experimental cycle of the landslide granulate portrays the sled loading, pneumatic launch, landslide recovery and reloading for the sub-sequent trial

the wave propagation away from the source and the shape of the deposited slide material on the bottom of the wave basin. After all the measurements are recorded, the steel plate with the landslide deposit is lifted, the recovered slide deposit dumped into a bucket and the box refilled for the next trial.

A wide array of instrumentation is deployed in the wave basin to measure the characteristics of the granular landslide and the generated tsunami waves. Four parallel stringpots measure the box motion and provide information on the pneumatic acceleration and deceleration of the gravel filled box. Thus, before the landslide is released from the box, the slide front velocity corresponds to the box velocity. An array of above water and under water cameras is shown in Fig. 2a. These camera measurements provide an insight into the landslide kinematics and the slide shape evolution down the slope. A Multi Transducer Array (MTA) is used at the end of each trial to survey the landslide deposit and measure its shape, volume and the extent of the deposited granular material. An array of resistance wave gauges is deployed to measure the generated tsunami wave surface elevation and the tsunami runup wave elevation on the slope lateral to the landslide. The wave gauge array is shown in Fig. 2b. The wave gauges are positioned to measure the wave properties along both the radial and the angular direction in the wave basin. A high resolution ($1,600 \times 1,200$ pixels) Particle Image Velocimetry (PIV) camera is setup to record the landslide on the slope and the water surface in the impact zone. The digital, high sensitivity PIV camera with 14-bit pixel-depth is positioned at a distance of 6.8 m perpendicular to the hill slope providing an approximate 15 m² (4.5 by 3.38 m) viewing area. The PIV analysis provides an insight into the kinematics of the wave generation process and the landslide motion down the slope. All the cameras are calibrated in situ by placing calibration plates with regular dot patterns in the various measurement planes both above and underwater to account for optical refraction.

2.1 Experiment Trial Conditions

A total of 62 trials were completed with the landslide tsunami generator in the tsunami wave basin to study the tsunami generation by granular landslides. The material used for the landslide is composed of naturally rounded fine gravel spanning sieve sizes
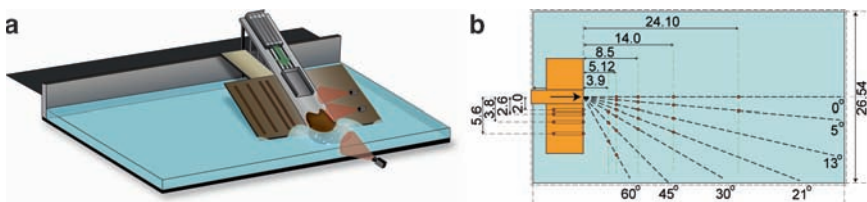
Fig. 2 Instrumentation setup. (**a**) Underwater and above water camera setup to record the landslide kinematics; (**b**) Planform of the wave gauge array installed in the TWB to measure the landslide generated tsunami wave characteristics. Distances in (m)

6.35 to 19 mm. Different trials were conducted to study the effects of varying water depths, landslide volumes and impact speeds on the generated tsunami waves. The trials were conducted at water depths of 0.3, 0.6, 0.9, 1.2 and 1.35 m. The varying water depths provide a wide range of generated waves from the shallow water depth wave regime to the intermediate water depth wave regime. Four different pneumatic launch pressures provide four different cases of landslide release velocities ranging from 2 to 4 m/s resulting in impact velocities up to 5.5 m/s. By fixing a plate midway along the length of the box, the initial mass loading of the box is restricted to half the original volume. This enables us to have two testing loads of the granular landslide material of roughly 1,350 and 675 kg. Thus the varying water depth conditions combined with the slide characteristics provide a wide range of non-dimensional parameters governing the generated tsunami wave data. This allows characterizing the effects of various slide properties and water depths on generated tsunami waves.

3 Data Analysis

3.1 Pneumatic Landslide Generator Performance

The pneumatic pistons accelerate the slide box over the first two thirds of the 2 m piston stroke, while the latter third is dedicated to pneumatic deceleration. At the maximum velocity of the box, it begins to decelerate thus releasing the landslide
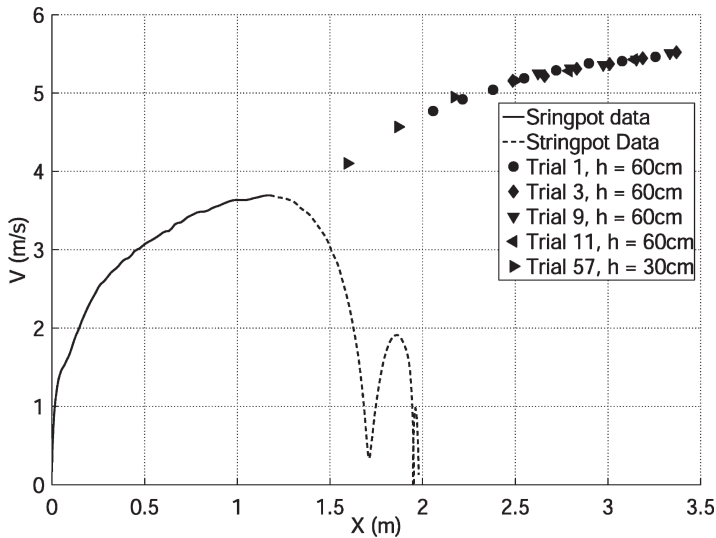
Fig. 3 Slide box displacement based on string pot recordings and landslide front veloc-ity measured from the PIV images for a case at 10 bar initial pneumatic firing pressure

material from the box. Until the release point, the landslide front velocity is the same as the box velocity. After the landslide releases from the box, the images recorded by the PIV camera are used to measure the front velocity. The landslide front velocity with the stringpot data along the slope direction is shown in Fig. 3. The coordinate system for measuring the landslide impact velocity is defined with the x-direction following the incline of the slope, the y-axis in the transverse direction along the lateral spreading of the landslide and the z-direction points perpendicularly upwards from the incline. The origin is the front of the box when at rest. By collecting all the data for similar landslide cases at all water depths and transforming to the slope fixed coordinate system, the complete evolution of the landslide front velocity above the water surface is obtained. The displacement curve of the landslide box is characterized by initial acceleration driven by the pneumatic pistons up to the release point as shown in Fig. 3. After the landslide is released from the box, further acceleration down the incline is purely influenced by gravity, friction and resistance by the surrounding fluid. Simultaneously the slide box is decelerated pneumatically to a stopping point.

3.2   Landslide Characteristics

The generated tsunami wave characteristics depend on the normalized slide impact velocity and the shape of the slide at the impact, namely the maximum width and thickness of the slide relative to the water depth. The slide widths are measured from the PIV image sequences. A combination of time stacking and image processing techniques are used to extract the information on the slide widths. From a series of images, the time stacked image of one particular row is generated by subtracting an image from its previous image and stacking one below the other. This helps in enhancing the change in the image at the next time level. The time stacked image is filtered using a circular averaging filter of radius 32 pixels to eliminate individual grains that scatter on the lateral boundary of the landslide and do not form part of the bulk slide mass that generates the tsunami waves. By applying a threshold on the grayscale of the image, it is converted into a binary image, where the white region corresponds to the slide material and the black region is the background of the slope. Then the edge of this bulk material is extracted. By subtracting the edges along each row in the image, the evolution of the width with respect to time is obtained at that particular location. By repeating this process along the length of the slope above the water surface, the complete width evolution with respect to space and time is obtained. Then the maximum width is determined across the length of the slope at each time level to obtain the maximum width evolution over time of the landslide material.

A sample time stacked image and the maximum extracted width is shown in Fig. 4a, b. The time $t = 0$ corresponds to the time of the landslide impact on the water surface. The extracted width shows the lateral spreading of the slide material to reach a maximum width followed by a gradual decrease in slide width.

A corresponding raw image sequence is shown in Fig. 4c. Side cameras are used to extract information on the evolution of the slide thickness with respect to time both above water and under water. The underwater information is limited to cases where there is sufficient visibility to identify the landslide material and extract its thickness. An edge extraction is shown for a series of underwater images at a water depth of 0.6 m, pneumatic firing pressure of 10 bar and 1,350 kg of the granular material in Fig. 5a. The landslide deposit from the MTA survey is shown in Fig. 5b. This data is extrapolated linearly to obtain the full extent of the deposit and measure the volume of the slide material that gets deposited underwater.
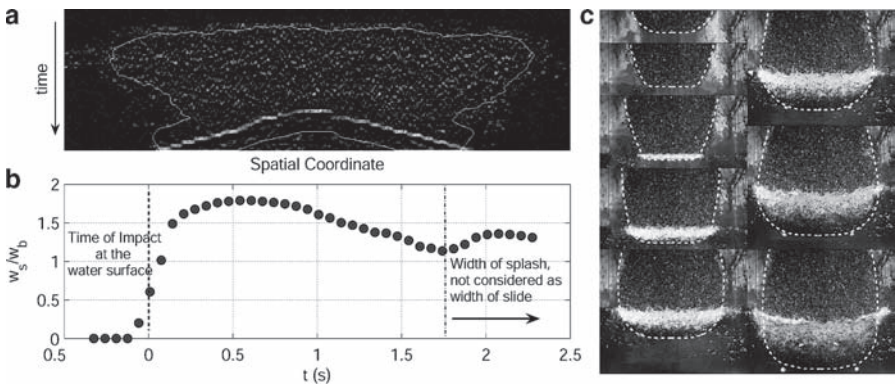
Fig. 4 Landslide width for water depth 0.6 m, 10 bar firing pressure and 1,350 kg of granular material. (**a**) Time Stacked image shown with the extracted edge of the slide material; (**b**). Landslide width evolution versus time. *t = 0* corresponds to the moment when the landslide impacts the water surface; (**c**) Lateral spreading of the landslide material above the water surface
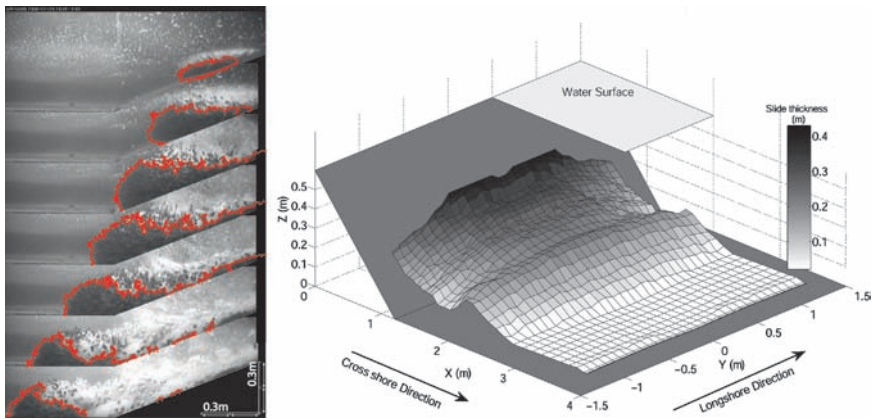
Fig. 5 Experiment case of water depth 0.6 m, pneumatic firing pressure 10 bar and 1,350 kg of granular material. (**a**) Underwater landslide thickness estimation; (**b**) granular landslide deposit surveyed by the MTA

3.3 Tsunami Wave Characteristics

The velocity on the landslide surface and the water surface is obtained from the cross-correlation analysis based processing of the PIV image sequences. The water surface is sprinkled with slightly buoyant seeding particles to enable the PIV analysis. The speckled pattern generated by the landslide granulate surface and the particles reflecting light on the water surface are used for iterative multi-pass cross correlation analysis with decreasing window sizes down to 32 by 32 pixels (Raffel et al. 1998; Fritz et al. 2003a). Since the landslide and the water surface are in two different planes, the image is rectified twice using calibration boards to obtain the PIV velocity measurements for the landslide and the water surface in m/s rather than in pixel/s. Measured velocity vectors on the landslide surface are shown in Fig. 6. The impact of the landslide on the water surface generates the first wave which travels radially away from the landslide source. The PIV analysis provides insight on the radial wave generation, the crater dynamics including the collapse and the subsequent runup with secondary wave formation after the rundown (Fritz et al. 2003b). Thus two distinct runup waves propagate in the transverse direction with high amplitudes.

The water surface elevation measured by the wave gauges along the landslide direction (0°), along a ray which is at 30° from the landslide direction and the lateral runup along shore (90°) is shown in Fig. 7. The recorded wave profiles were strongly directional, unsteady, nonlinear and mostly in the intermediate water depth wave regime. The leading wave is followed by a train of dispersive waves as seen in Fig. 7. The waves display the characteristic shape of a large trough between two crests. The first crest is generated when the landslide impacts the water surface and pushes the water column away from the landslide. The impact creates a cavity
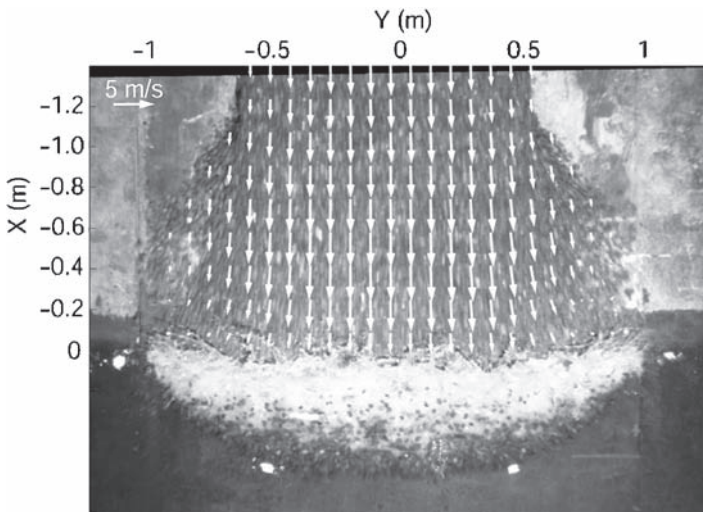
Fig. 6 Velocity vectors computed with the cross-correlation PIV-analysis on the landslide surface during the wave generation process for 10 bar pneumatic launch pressure
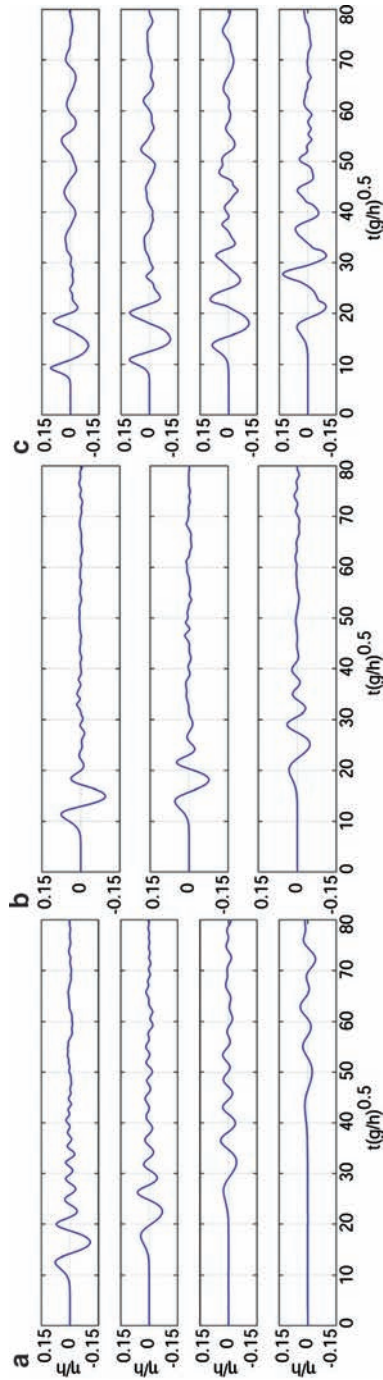
Fig. 7 Wave surface elevation measured at the resistance wave gage array: (**a**) The 0° offshore direction in prolongation of the landslide axis at X/h = 8.5, 14.2, 23.3 and 40.2; (**b**) Along a 30° ray at X/h = 6.5, 8.5 and 14.2; (**c**) Lateral along shore runup direction (90°) at Y/h = 3.3, 4.3, 6.3 and 9.3

which contributes the large trough. Then the collapse of this cavity creates a second hillslope runup and subsequently the rundown forms the second wave crest. This source oscillation is followed by decreasing repetitions of wave up rush and draw down resulting in a trailing wave train behind the first two initially dominant wave crests. By identifying the locations, where the water surface departs from the mean water level, the upcrossing points are identified. Then the water surface between two successive up crossing points is identified as a single wave and the subsequent wave crest and trough are identified.

The wave celerity is determined by measuring the time taken for the wave crests and troughs to travel the distance between subsequent wave gauges. Figure 8 shows the measured speed of the crests and troughs of the first three waves. The first wave crest speed in many cases approaches the theoretical limit celerity of the non-linear solitary wave theory, which is governed only by water depth and amplitude dispersion. The speed of a solitary wave is given by Boussinesq (1872).

$$\frac{c_1}{\sqrt{gh}} = 1 + \frac{a_1}{2h}$$

which compares with the wave celerity given by Tanaka (1986) (Glimsdal et al. 2007). However the second and the third waves are shorter in wave length and
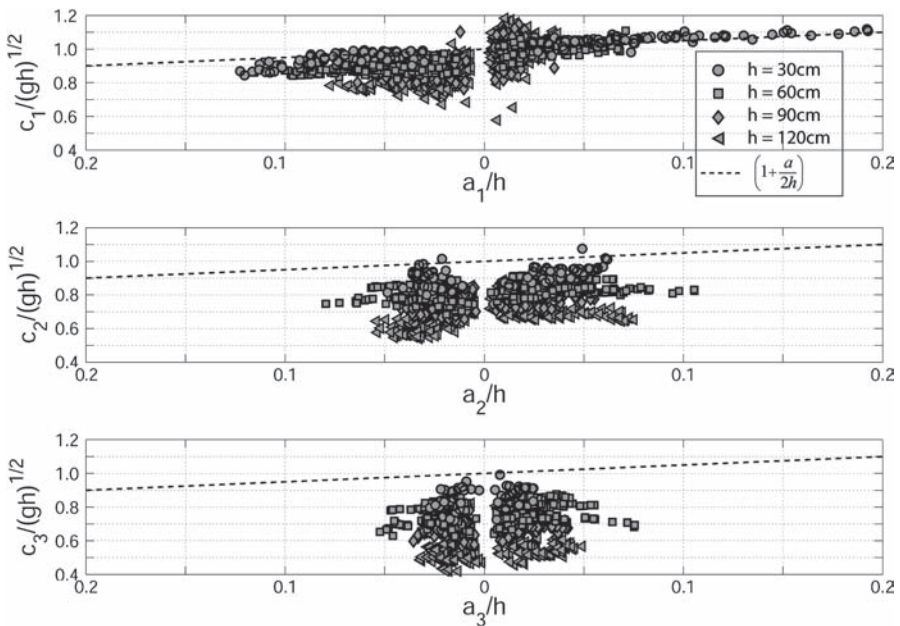
Fig. 8 Measured crest and trough speed of the first three waves between the wavegages for all the experimental trials. The amplitude is non-dimensionalized by the water depth and the speed by the shallow water speed $(gh)^{1/2}$
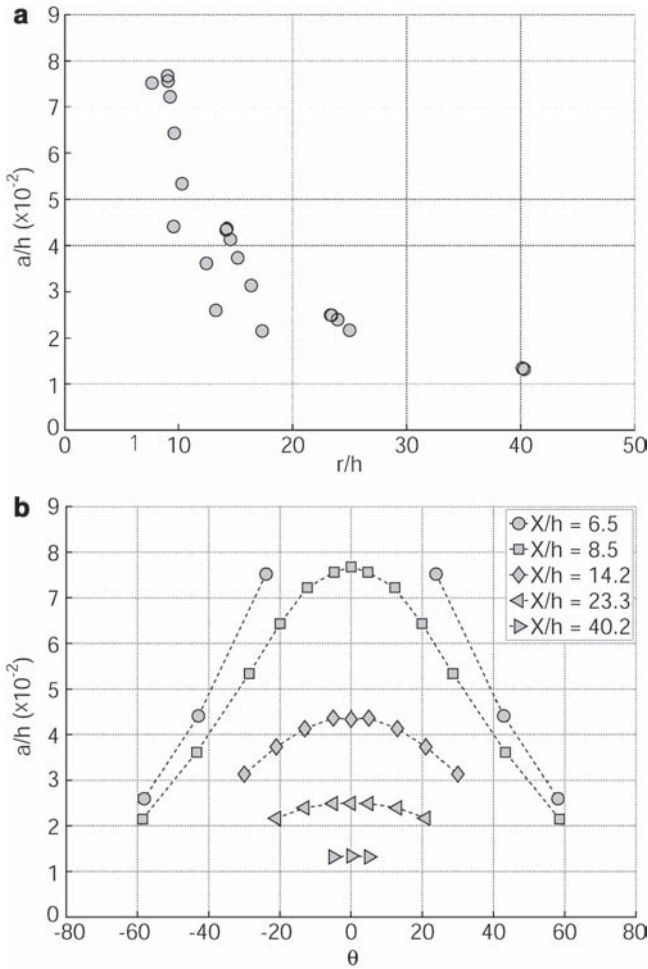
Fig. 9 Wave amplitude attenuation for water depth 0.6 m, 10 bar firing pressure and roughly 1,350 kg of slide material: (**a**) The first wave crest amplitude versus the radial distance where it is measured in the wave basin; (**b**) First wave crest amplitude versus angle for the same case

therefore travel at a reduced celerity as compared to the first wave. The source amplitudes of landslide generated tsunamis are only limited by the landslide Froude number and the relative slide thickness, and can therefore exceed source amplitudes of tectonic tsunamis. However radial spreading combined with both amplitude and frequency dispersion results in more rapid decrease in leading wave heights compared to tectonic tsunamis. Consequently landslide tsunamis can have devastating impacts on coastal communities near the source, while far field hazards are rapidly reduced. The first wave crest amplitude for an experimental case of water depth 0.6 m, firing pressure 10 bar and full load is shown in Fig. 9a. It is assumed that the wave amplitude depends on the radial coordinate as $a_1 = kr^n$, where the coefficients

k and n account for the source parameters such as the landslide impact speed, width, thickness and water depth. The wave amplitude also decays rapidly in the angular direction away from the landslide direction. The first wave crest as a function of angular direction for the same case is shown in Fig. 9b. Here u = 0° correspond to the landslide direction. The results portray *cos u* dependency on the amplitude decay in the angular direction. The initial wave characteristics are governed by the non-dimensional landslide parameters, while the wave propagation is solely dependent upon the wave parameters and water depth.

4 Discussion

The three dimensional pneumatic landslide tsunami generator was designed, constructed and successfully deployed in the NEES tsunami wave basin at OSU. The uniqueness of this apparatus lies in its large scale, ability to test with granular material and controlled acceleration of the slide. To date, 62 successful trials were completed to study the effects of landslide characteristics and water depth conditions on the generated tsunami wave. The landslide characteristics and the main tsunami parameters such as the wave speed and amplitude were determined. The generated waves are strongly directional, nonlinear and varyingly dispersive. The maximum wave amplitudes of the generated wave trains demonstrate an exponential decay with radial distance away from the landslide source and in the angular direction as well. The measured wave speed approaches the limiting theoretical approximation of the solitary wave theory, which can be used for predictions of tsunami arrival times. The landslide tsunamis exhibit more dispersive propagation than tectonic tsunamis (Glimsdal et al. 2006; Loualalen et al. 2007). Since water displacement can significantly exceed the landslide volume due to the impact cavity at high speeds, the generated wave amplitude is high at the impact location. Thus the landslide waves can be very destructive locally. However the localized tsunami source and radial spreading combined with dispersion result in rapid wave height decay with propagation distance. The PIV analysis provides an insight into the wave generation process and reveals potential for fully 3D surface and velocity reconstruction. Ultimately the analysis of landslide generated tsunami waves includes describing the entire landslide evolution as it traverses from the subaerial to the submarine regime. In particular, describing the slide width and thickness along the slope will provide an insight into rheological dependency of landslide deformation during the impact. The generated tsunami characteristics will be related to the impact velocity and shape of the slide. Further energy transfer rates between the slide and the water body will be determined. The slide and wave data is used to benchmark and advance numerical models for prediction and warning.

References

Bardet J-P, Synolakis C, Davis H, Imamura F and Okal E (2003) Landslide tsunamis: Recent findings and research directions. Pure Appl Geophys 160:1793–1809.

Bondevik S, Løvholt F, Harbitz C, Mangerud J, Dawson A and Svendson J (2005) The Storegga slide tsunami comparing field observations with numerical solutions. Mar Pet Geol 22:195–208.

Boussinesq J (1872) Théorie des ondes et des remous que se propagent le long d'un canal rectangulaire horizontal, en communiquant au liquide contenu dans ce canal des vitesses sensiblement pareilles de la surface au fond. J Math Pures Appl 17:55–108.

Di Risio M, De Girolamo P, Bellotti G, Panizzo A, Aristodemo F, Molfetta MG and Petrillo AF (2009) Landslide-generated tsunamis runup at the coast of a conical island: New physical model experiments. J Geophys Res 114: C01009, doi: 10.1029/2008JC004858.

Enet F and Grilli ST (2005) Tsunami landslide generation: Modelling and experiments. Proc., 5th Int. on Ocean Wave Measurement and Analysis, WAVES 2005, Madrid, Spain, IAHR, Paper No. 88.

Enet F and Grilli ST (2007) Experimental study of tsunami generation by three-dimensional rigid underwater landslides. J Waterway Port Coast Ocean Eng 133:442–454.

Fine I, Rabinovich A, Bornhold B, Thomson R, Kulikov E (2005) The Grand Banks landslide-generated tsunami of November 18, 1929: Preliminary analysis and numerical modelling. Mar Geol 215:45–47.

Fritz HM, Hager WH, Minor H-E (2001) Lituya Bay case: rockslide impact and wave run-up. Sci Tsunami Hazards 19:3–22.

Fritz HM (2002) Initial phase of landslide generated impulse waves. Ph.D. thesis ETH-No. 14871, Swiss Federal Institute of Technology, ETH Zürich, Switzerland.

Fritz HM, Hager WH, Minor H-E (2003a) Landslide generated impulse waves: part 1: instantaneous flow fields. Exp Fluids 35:505–519, doi: 10.1007/s00348–003–0659–0.

Fritz HM, Hager WH, Minor H-E (2003b) Landslide generated impulse waves: part 2: hydrodynamic impact craters. Exp Fluids 35:520–532, doi: 10.1007/s00348–003–0660–7.

Fritz HM, Hager WH and Minor H-E (2004) Near field characteristic of landslide generated impulse waves. J Waterway Port Coastal Ocean Eng ASCE 130:287–302, doi: 10.1061/(ASCE)0733–950X(2004)130:6(287).

Fritz HM, Kongko W, Moore A, McAdoo B, Goff J, Harbitz C, Synolakis C, et al. (2007) Extreme runup from the 17 July 2006 Java tsunami, Geophys Res Lett 34: L12602, doi:10.1029/2007GL029404.

Fritz HM, Mohammed F, Yoo J (2009) Lituya bay landslide impact generated megatsunami 50th anniversary. Pure Appl Geophys 166:153–175, doi:10.1007/s00024–008–0435–4.

Glimsdal S, Pedersen G, Langtangen H, Shuvalov V and Dypvik H (2007) Tsunami generation and propagation from the Mjølnir asteroid impact. Meteorit Planet Sci 42:1473–1493.

Glimsdal S, Pedersen G, Atakan K, Harbitz CB, Langtangen H and Løvholt F (2006) Propagation of the Dec. 26, 2004 Indian Ocean Tsunami: effects of dispersion and source characteristics. Int J Fluid Mech Res 33:15–43.

Grilli ST and Watts P (2005) Tsunami generation by submarine mass failure I: Modeling, experimental validation, and sensitivity analyses. J Waterway Port Coast Ocean Eng 131:283–297.

Heinrich P (1992) Nonlinear water waves generated by submarine and aerial landslides. J Waterway Port Coastal Ocean Eng 118:249–266.

Liu P-F, Wu T-R, Raichlen F, Synolakis CE and Borrero JC (2005) Runup and rundown generated by three-dimensional sliding masses. J Fluid Mech 536:107–144.

Loualalen M, Asavanant J, Kaewbanjak N, Grilli ST, Kirby JT and Watts P (2007) Tsunami generation by submarine mass failure: 1. Modeling of the 2004 Indian Ocean tsunami: Case study impact in Thailand. J Geophys Res 112:C07024, doi: 10.1029/2006JC003850.

Müller L (1964) The rock slide in the Vajont Valley. Rock Mech Eng Geol 2:148–212.

Panizzo A, De Girolamo P and Petaccia A (2005) Forecasting impulse waves generated by sub-aerial landslides. J Geophys Res 110:C12025, doi:10.1029/2004JC002778.

Raffel M, Willert C and Kompenhans J (1998) Particle Image Velocimetry. Springer, Berlin.

Synolakis CE, Bardet JP, Borrero J, Davies H, Okal E, Silver E, Sweet J and Tappin D (2002) Slump origin of the 1998 Papua New Guinea tsunami, Proc Roy Soc Lond Ser. A, 458: 763–789.

Tanaka M (1986) The stability of solitary waves. Phys Fluids 29:650–655.

Tinti S, Manucci A, Pagnoni G, Armigliato A and Zaniboni R (2005) The 30 December 2002 landslide-induced tsunamis in Stromboli: sequence of the events reconstructed from the eyewitness accounts. Nat Hazards Earth Sys Sci 5:763–775.

Tinti S, Maramai A, Armigiliato A, Graziani L, Manucci A, Pagnoni G and Zanoboni F (2006) Observations of physical effects from tsunamis of December 30, 2002 at Stromboli volcano, Southern Italy, Bull Volcanol 68:450–461.

Walder JS, Watts P, Sorensen OE and Janssen K (2003) Tsunamis generated by subaerial mass flows. J Geophys Res 108(B5):2236.

Watts P (2000) Tsunami features of solid block underwater landslides. J Waterway Port Coastal Ocean Eng 126:144–152.

Weiss R, Fritz HM and Wuennemann K (2009) Hybrid modeling of the mega-tsunami runup in Lituya Bay after half a century. Geophys Res Lett, 36, L09602, doi:10.1029/2009GL037814.

Distal Turbidites and Tsunamigenic Landslides of Stromboli Volcano (Aeolian Islands, Italy)

A. Di Roberto, M. Rosi, A. Bertagnini, M.P. Marani, and F. Gamberi

Abstract On 30 December 2002, a $25–30 \times 10^6$ m³ landslide on the NW flank of Stromboli volcano produced a tsunami that caused relevant damage to the Stromboli village and to the neighboring islands of the Aeolian archipelago. The NW flank of Stromboli has been the site of several, cubic kilometer-scale, landslides during the past 13 ka. In this paper we present sedimentological and compositional data of deep-sea cores recovered from a site located about 24 km north of the island. Our preliminary results indicate that: (i) turbidity currents were effectively generated by the large-scale failures and (ii) volcanogenic turbidity current deposits retain clues of the landslide source and slope failure dynamics. By analogy with Hawaii and the Canary islands we confirm that deep-sea sediments can be effectively used to assess the age and scale of past landslide events giving an important contribution to the tsunami hazard assessment of this region.

Keywords Landslide • turbidite • tsunami • Stromboli

1   Introduction

Volcanic landslides have recently been identified as one of the most hazardous geological processes on Earth (Hürlimann and Ledesma 2007). Recent studies within the geological record and at many active volcanoes have documented that

A. Di Roberto (✉) and A. Bertagnini
Istituto Nazionale di Geofisica e Vulcanologia, Sezione di Pisa,
Via della Faggiola, 32 – 56126 Pisa, Italy
e-mail: diroberto@pi.ingv.it

M. Rosi
University of Pisa, Dipartimento di Scienze della Terra, Via S. Maria, 53 – 56126 Pisa, Italy

M.P. Marani and F. Gamberi
Istituto di Scienze Marine – CNR, Sede di Geologia Marina di Bologna,
Via Gobetti 101 – 40129 Bologna, Italy

volcanic landslides are frequent, with almost one event per 25 years during the last 500 years (Siebert 1992; McGuire 1996; Voight and Elsworth 1997). Debris avalanches, lahars, explosive eruptions and lateral blasts are all phenomena that can be directly connected to catastrophic flank failures of volcanoes.

Along coastal regions or volcanic islands, the movement of landslide masses has the additional potential to produce large, sometimes devastating, tsunamis that can affect areas far from the source (e.g. Moore et al. 1989; Masson et al. 2006; McGuire 2006). Detailed offshore studies of volcanic islands show that deposits resulting from debris avalanches can comprise volumes of up to 5,000 km^3, as observed in the Hawaii Islands (Moore et al. 1989), or in the Canary archipelago (Ablay and Hürlimann 2000; Masson et al. 2002; Wynn and Masson 2003; Masson et al. 2006). It is not necessary for a volcanic landslide to be large to produce hazards, and even relatively small volume landslides have the capacity to generate high run-up tsunamis (Masson et al. 2006) depending on their vicinity to the coastline, water depth, angle of the slide, density of the slide material, the speed with which the landslide moves and other factors (Murty 2004).

As we have never observed a large volume flank collapse in real time the assessment of past volcano-induced tsunamigenic landslides has proved both difficult and controversial.

Tsunami deposits are poorly preserved on land and can be difficult to distinguish from storm events in land and marine records. The poor preservation of tsunami deposits on land has led the paleoseismology community to turn to the marine environment, where, according to authors, a complete record of seismogenic tsunamis may be preserved as turbidite sequences in submarine canyons (e.g. Adams 1990; Goldfinger et al. 2003).

Distal turbidites have also been employed to investigate volcanic landslides in Hawaii, the Canary archipelago, La Reunion Island (Garcia 1996; Ollier et al. 1998; Kanamatsu et al. 2002; Masson et al. 2002; Wynn and Masson 2003; Masson et al. 2006) and Aeolian Archipelago (Di Roberto et al. 2008).

In this paper we analyze two sea-bottom sediment sections i.e. a gravity core and a box core collected offshore the volcanic island of Stromboli respectively prior and after the Dec. 30, 2002 landslide that affected the NW slope of the island. Such event produced a 25–30 × 10^6 m^3 rock debris with associated tsunami wave that spread over most of the southern Tyrrhenian Sea. The work also aims at implementing the documentation of past potentially tsunami producing landslide events originated from Stromboli volcano during Holocene thus opening new perspectives for the assessment of the tsunami hazard in the southern Tyrrhenian sea.

2   Geological Background

Stromboli is located in the Southern Tyrrhenian Sea, a few tens of kilometers offshore from the north coast of Sicily and the Italian peninsula (Fig. 1, inset). The island, with an elevation of 924 m, represents the subaerial part of a larger volcanic edifice extending to a maximum water depth of 2,600 m.
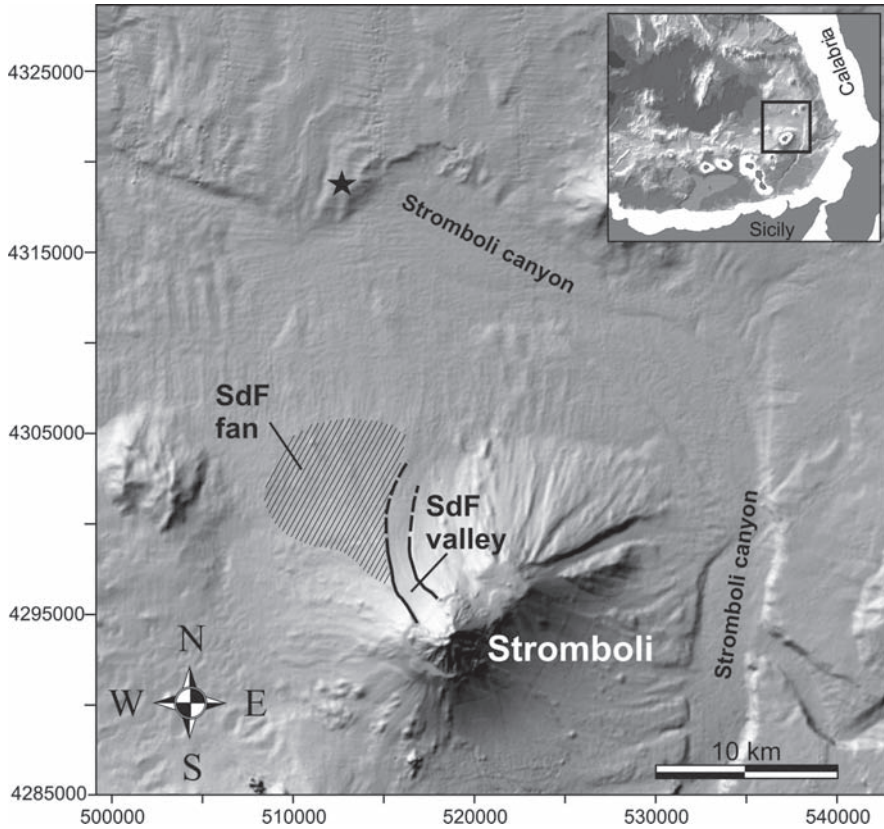
Fig. 1 Shaded relief bathymetry of the Stromboli region with highlighted the main features of Stromboli sedimentary system; the star marks the sample site; SdF: Sciara del Fuoco. Inset shows location of Stromboli Island within the south Tyrrhenian sea

Stromboli volcano was built during seven main periods of activity covering a time span of about 100 ka, i.e.: Paleostromboli I, II, and III (100-35 ka), Scari (35-25 ka), Vancori (25-13 ka), Neostromboli (13-6 ka), and Recent Stromboli (<6 ka) (Hornig-Kjarsgaard et al. 1993; Gillot and Keller 1993). Transitions between each period are marked by significant modifications of the edifice structure (caldera collapses between 100 and 25 ka and flank collapses after 25 ka; Tibaldi 2001) and changes in magma compositions (Hornig-Kjarsgaard et al. 1993; Francalanci et al. 1993). The most striking geomorphological and volcanic structure of the island is the Sciara del Fuoco (SdF) a horseshoe-shaped collapse scar that occupies the NW sector of the island. SdF structure is considered the result of at least four flank collapses that occurred in the last 13 ka involving volumes of material ranging from 0.73 ± 0.22 to 2.23 ± 0.87 km^3 (Tibaldi 2001). The younger collapse (<5,000 years ago; Kokelaar and Romagnoli 1995; Tibaldi 2001), with an estimated volume of about 0.7 km^3, resulted in the present-day SdF morphology. SdF structure continues below sea level (Fig. 1) as a depression bounded by steep walls in continuity with the flanks of the

sub-aerial SdF (Kokelaar and Romagnoli 1995). Further downslope, the SdF depression runs to the east of a large volcanoclastic fan extending from 1,000 m to 2,500 m water depth and with an estimated volume of about 4–6 km^3 (Fig. 1; Gamberi et al. 2006).

As deduced by recent physical modeling, the major flank collapses that produced the SdF had the potential to generate large and destructive tsunamis whose effects may extend throughout the Aeolian Islands and to the southern Italian coasts (Tinti et al. 2003). The most recent partial collapse of the SdF took place on 30 December 2002. Two relative small landslides, with a total volume of about 25–30 $\times$ 10^6 m^3, detached from the submarine and subaerial part of SdF respectively and generated tsunami waves up to 10 m high on the Stromboli coasts and up to 2 m high on the neighboring islands (Tinti et al. 2005). The result was severe damage to Stromboli village and limited damage on the neighboring islands. The tsunami also weakly affected Milazzo harbor, located on the northern coast of Sicily, 100 km south of Stromboli (Maramai et al. 2005).

The December 30, 2002 event and the historical record of the Stromboli volcano activity in the last century proves that besides major flank collapses, also small-scale tsunami-forming landslides may occur at Stromboli. Their higher frequency (five since 1906; Maramai et al. 2005) and the significant destructive power of the resulting tsunami waves, currently makes them among the most relevant natural hazards threatening the coastal areas of Stromboli volcano.

3   Marine Record of Stromboli Volcano Landslides

Submarine deposits of the December 30, 2002 landslide were recently identified by seafloor imagery and sampling during the TTR14 cruise aboard the R.V. Professor Logachev in August, 2004 (Marani et al. 2008a, b). The proximal part consists of chaotic, coarse-grained deposits bordered and partially covered by sand. The deposits were interpreted as deriving from cohesionless, sandy-matrix, density flows (Marani et al. 2008b). 24 km north of Stromboli a 2–3 cm-thick sand bed was interpreted as the finer grained turbidite equivalent of the proximal deposits (Marani et al. 2008b). The identification of the distal landslide deposit was facilitated by repeat sampling in September, 2002 (VST02-16) and in August, 2004 (TTR14-342), respectively prior to- and post- the December 30, 2002 collapse. The sample site (VST02-16 Lat. 39°01.100′ Lon. N 15°09.298′ E WGS 84) is an even, flat area located on a topographic high at water depth of 2458 m, on the right (east) side of the Stromboli canyon about 200 m above the canyon floor (Gamberi et al. 2006; Marani et al. 2008b) and about 24 km from the SdF shore (Fig. 1). The site, located outside the direct influence of the sedimentary dynamics of the Stromboli canyon, is thus proved to record turbidity currents generated by landslide events of the SdF with a volume comparable to the volume of December 2002 landslide (tens $\times$ 10^6 m^3). The two cores presented herein are 1 m and 38 cm long respectively (Fig. 2), and were collected from the same site, with a ±15 m accuracy in positioning.

Fig. 2 Image of collected cores: VST02-16 gravity core sampled about 4 months before the Dec. 30, 2002 Stromboli landslide; TTR14-342 box core sampled about 2 years after Dec. 30, 2002 Stromboli landslide
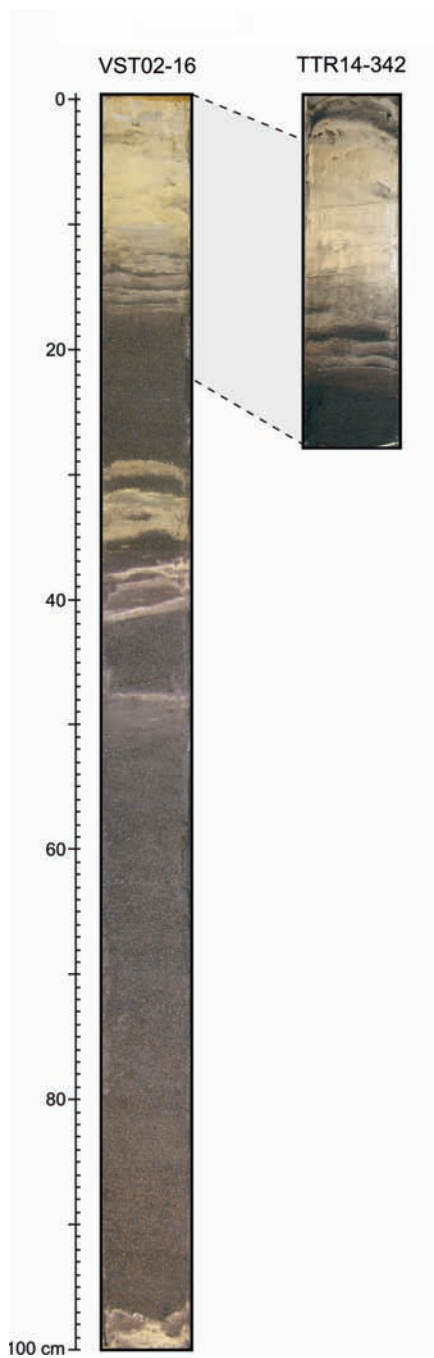
4 Methods

A detailed cores description was performed to characterize lithology, fabric, sedimentary structures, bedding thickness, and other pertinent features. 50 sub-samples were picked at intervals of about 2–3 cm. Samples were washed in an ultrasonic bath for 10 min and subsequently, sieved at one-phi intervals for grain-size characterization. The 250–125 μm and 125–63 μm fractions were then mounted on thin section with epoxy resin for component analysis.

A selection of 23 samples from VST02-16 and 11 samples from TTR14-342 were analyzed for component analysis (Fig. 3); 1,000 clasts of the most abundant grain size fractions were counted on each thin section.
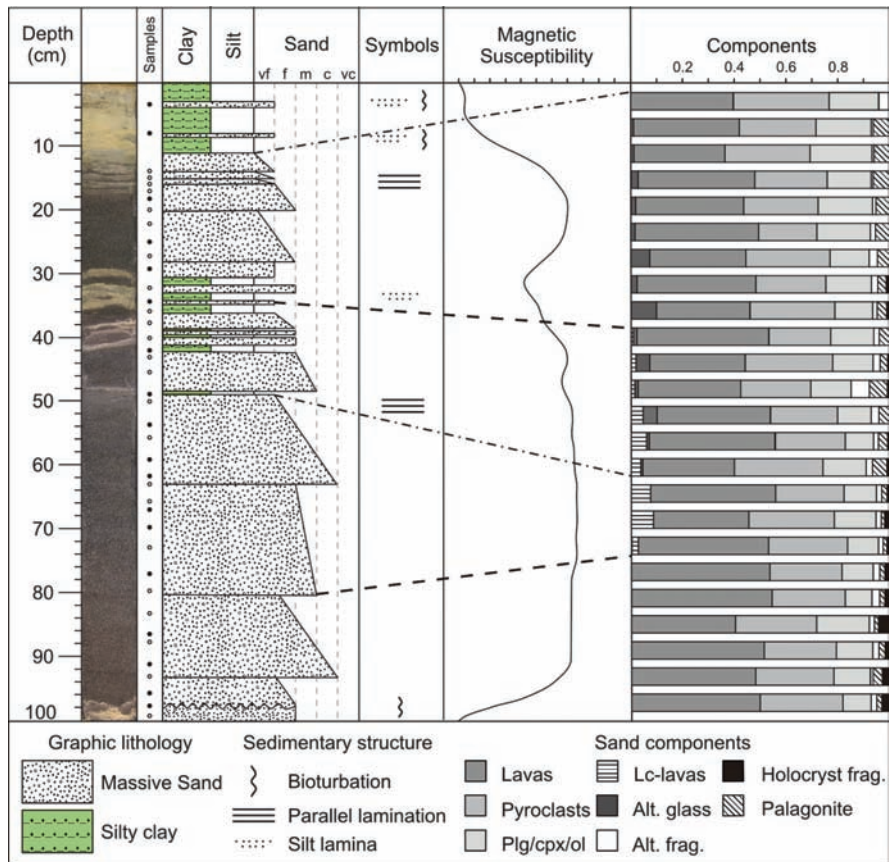
Fig. 3 Stratigraphic log, magnetic susceptibility and componentry results of VST02-16 core; Black-filled circles indicate samples that were processed for grain size analysis; white circles indicate samples that were processed for component analysis. Notice that leucitic lavas (Lc-lavas) and altered glass (Alt. glass) distribution is tightly linked to the sub-turbiditic units structures within thick sand beds between 96–48 and 30–17 cm

   Texture and composition of glass shards were also analyzed using a SEM-EDS Philips XL30 scanning electron microscope (accelerating voltage 20 kV, beam current 1 nA, working distance 10 mm), equipped with energy dispersive x-ray analysis (EDAX DX 4) at the Earth Science Department of Pisa University. For each sample a minimum amount of 30 glass particles were analyzed in raster mode, using windows ranging from $5 \times 5\,\mu m$, in highly crystalline samples, to $30 \times 30\,\mu m$ in aphiric ones. The analytical error, measured on mineral and glass standards varies from 1 wt% (concentrations higher than 15 wt%) to 10 wt% (concentrations between 1–5 wt%), increasing at low concentrations.

   Results were compared with the glass composition of subaerial Stromboli volcanics available in literature for the past 13 ka. In order to infill such existing dataset, which was partially incomplete, some additional samplings were realized. These include 8 lava and 9 scoria samples recovered on the summit part of the volcano and in a 4 m deep stratigraphic trench dug on the NE flank of the island at 335 m a.s.l. (Lat. N 38°47.499′, Long. E 15°13.459′).

5   Results

The description and analyses of the distal deposit of December 30, 2002 landslide that caps the TTR14-342 core (sampled in 2004) and that is absent in the 2002 core (Figs. 2 and 4) are reported in Marani et al. 2008b.
The 1 m long gravity core sampled in 2002 (VST02-16) consists of a sequence of dark grey to black, decimetric to millimetric-thick beds of coarse to fine sands, interlaminated and interbedded with millimeter- to centimeter- thick brownish silty-clay (Fig. 2). Beds have sharp and slightly erosive basal contacts and commonly evidence normal grading into brown clay beds. Clay beds frequently contain mm-thick layers or lenses of black, fine sand to silt that are frequently disrupted by bioturbation. Brown clay are often capped by <0.5 cm-thick layer of pale-yellow hemipelagic clays. Samples range from moderate to poorly sorted ($\sigma\Phi$ 0.705–1.371), coarse to very fine sands (MdΦ = 0.663 and 3.538). The two thicker beds, occurring at 96–48 cm and 30–17 cm are characterized by multiple, well-developed normally graded sand beds (Fig. 3). Grain size and component analysis data are shown in Fig. 3.
Sand beds consists almost entirely of volcaniclastic fragments represented by lava (35–56 vol.%), pyroclastic fragments (22.5–37 vol.%), plagioclase crystals (3.8–14.5 vol.%), pyroxene (4.4–9 vol.%), olivine crystals (≤2 vol.%) and altered volcanic fragments (3–15.5% vol.%). Few subvulcanic, holocrystalline fragments occur. Biogenic and detrital clasts (mainly metamorphic rock fragments, muscovite and microcline crystals) account for less than 2 vol.% of the deposits suggesting that the site is poorly influenced by terrigenous sediment supply. Lava fragments are generally equant, bearing crystals of plagioclase, pyroxene and olivine set in a holocrystalline to partially glassy matrix. Pyroclastic fragments consist of mainly fresh, poorly vesicular, honey-colored glass containing abundant plagioclase microlites.
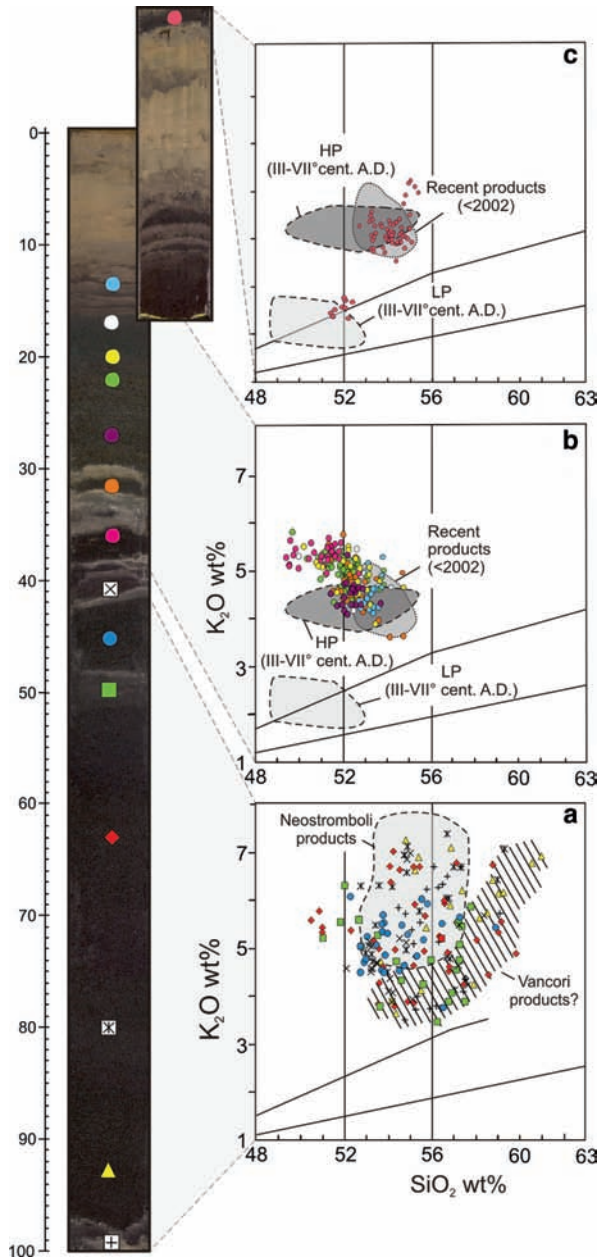
Fig. 4 Glass shards composition plotted against stratigraphic height. Notice the similarity between the glass composition of (**a**) the lowermost half of the core and Neostromboli glasses, (**b**) the uppermost half of the core and products from recent and present products emitted by Stromboli volcano. (**c**) The glass composition of the topmost layer (core TTR14), attributable to the December 30 2002 landslide (Marani et al. 2008b) is reported to complete the chemical characterization of sediment sequence.

In the uppermost layer subordinate highly vesicular, fresh and almost crystal free clear-glass clasts occur. Pyroclastic fragments have prominent angular shape with very delicate, sharp edges indicating the lack of any mechanical interaction due to reworking.

A large compositional variability is evident when the glass compositions are plotted in the K_2O-SiO_2 diagram (Fig. 4), which is traditionally employed to classify magmas erupted from Stromboli during its volcanic history (Hornig-Kjarsgaard et al. 1993; Francalanci et al. 1993). Moreover great variations in glass composition occur between the lowermost half of the core and the uppermost one.

Glass fragments of the lowermost part of the sequence (96–40 cm) have scattered composition largely covering the compositional range of Neostromboli products; minor compositions attributable to the Vancori periods also occur (Fig. 4).

Glass fragments of the uppermost part of the cores (39–13 cm) have more homogeneous compositions; from 39 to 13 cm samples describe a short evolution trend from composition slightly enriched in K_2O to composition strictly comparable with products of the Recent Stromboli (Fig.4).

It is interesting to note that from 66 to 34 cm, within the deposits likely correlating Neostromboli period a significant amount of lava fragment bearing leucite microlites occurs; leucite ($<100\,\mu m$) is usually replaced by analcime even if nuclei with original leucite composition still persist in few microlites.

The first appearance of Lc-bearing lava fragments coincides with an abrupt increase in grain size corresponding to the base of one of the stacked sand beds between 96–48 cm.

In the uppermost half of the core a consistent fraction of pyroclasts exhibit a few ten of μm-thick rim of leached glass (up to 50 wt.% loss in FeO, CaO, MgO and up to 11 wt.% gain of SiO_2) likely indicating alteration of the glass by volcanic gas or acid rainwater.

6   Discussion

The observed sedimentary structures indicate that the core is mainly composed of turbidity current deposits. The most interesting features revealed by grain size and component analysis are the multiple turbiditic-sub units contained within the two main sand units between 96–48 cm and 30–17 cm. Multiple, stacked and closely spaced sandy units with sharp base and gradational top, similar to those recovered in our sequence and interpreted as turbidites were recognized at about 320 km west of the island of Hawaii (Garcia 1996) and in Agadir basin about 300 km north of the western Canary Islands (Wynn and Masson 2003). Such deposits have been interpreted as the distal equivalent of large landslides developing with retrogressive or multi phase dynamics (Garcia 1996; Wynn and Masson 2003). Alternatively, stacked turbidites can also form as a consequence of turbidity current reflection off seafloor topography (Pickering et al. 1992) or from multiple turbidity currents reaching the sampling site along differential flow pathways (Masson 1994).

In our case no submarine structure exists beyond the flank of Stromboli canyon upon which a turbidity current could reflect; in addition the SdF submarine valley represents the only pathway through which mass flows originating on the NW flank of Stromboli volcano are funneled in the Stromboli canyon. Thus in analogy with Hawaii and Canary Islands cases we interpret the sandy sub-units recovered in Stromboli core as the result of a rapid and progressive deposition from repeated turbidity currents (gravity flows) cogenetic to landslides on the NW flank of Stromboli volcano, dominated by retrogressive collapse dynamics. The almost complete absence of hemipelagic sediment deposited between each single sub-unit suggest a very rapid, geologically-instantaneous sequence of events.

Geochemical data allow correlation of the turbidites. The sand interval occurring between 96 and 48 cm can be associated with the ~5 ka old, Neostromboli collapse. This data is confirmed by the presence of Lc-bearing lava fragments in the turbidites. On Stromboli volcano, leucitic lavas crop out almost exclusively in the summit portion of the edifice and belongs only to the final phases of Neostromboli period (Speranza et al. 2008).

Moreover, the occurrence of Lc-bearing lava limited to the uppermost stacked sand beds between 96 and 48 cm indicates that the flank collapse involved the summit portion of the volcano during its final phases thus enforcing the hypothesis that flank failure was dominated by retrogressive, multi phase dynamics.

On the basis of geochemical and textural data the uppermost thick turbidite occurring at 30–17 cm can be correlated with a flank collapse that occurred during the Recent Stromboli period. An age of ~1 ka can be roughly estimate for this event considering that the landslide deposit is overlain by only 10 cm of mostly hemipelagic mud and that the sedimentation rate in this area was calculated in 9 cm/ka^{-1} during the last 10 ka (Di Roberto et al. 2008). Even during this collapse the summit of the edifice was likely involved as inferred by the presence of volcanic gas- or acid water-leached pyroclasts in the marine deposits. Such alteration suggests a crater source where an intense volcanic gas/fluid flux is present.

Onshore studies have hypothesized that two large scale landslides occurred in the Recent Stromboli period and after the Neostromboli collapse (Tibaldi 2001). However, only one turbidite deposits in the offshore of Stromboli volcano can be correlated with a large-scale landslide event during the Recent Stromboli period. In this perspective marine archive seems to confirm the model proposed by Finizola et al. (2003) in which one of the flank collapses previously identified by Tibaldi (2001) is reinterpreted as a crater collapse (Collapses of the Pizzo pyroclastites into the Fossa craters) occurred after the transition from Neostromboli to Recent Stromboli cycles and before the collapse that gave the NW flank of Stromboli volcano the present form.

Both collapses are interpreted to have occurred with multi-phase or retrogressive dynamics as evidenced by the occurrence of stacked sand beds.

Recognized multiphase or retrogressive collapse behavior is crucial for modeling of tsunami-producing landslides at Stromboli volcano. In fact all numerical models presently proposed for Stromboli tsunamis assume landslide as a single sliding volumes detaching all at once from NW flank of Stromboli volcano and

thus producing a single tsunami wave. Such an assumption likely results in an overestimation of initial tsunami wave amplitude and thus in a overestimation of the tsunami power.

Several thinner, cm-scale turbidites occur in the recovered core thus testifying that also relative small-scale landslides occurred in the last 5 ka on the flank of Stromboli volcano. The average thickness of these turbidites is comparable to the thickness of December 30, 2002 landslide cogenetic turbidite indicating that events like December 30, 2002 have occurred also in the past. These events appear to have greater frequency with respect to that of the much larger failures since almost nine event occur in the last 5 ka.

Five tsunami were registered in the last century on Stromboli volcano (Maramai et al. 2005) but only the most recent event of December 30, 2002 is recorded in the marine environment; this can be due to the peculiar morphology of seafloor in the sampling site that allows only the larger and most energetic landslides to be recorded. Alternatively we assume that some of these tsunamis were generated by different sources (earthquake, pyroclastic flows etc).

7 Conclusions and Implications for the Tsunami Hazard Assessment

Identification of volcaniclastic turbidite offshore active volcanoes has been shown to be a powerful tool for acquiring information on the occurrence of failure events while providing baseline data for the future.

In this work we have documented that during the last 5 ka several possibly tsunamigenic landslides originated from Stromboli volcano generated sand-rich turbidity currents which travelled more than 24 km northwards and deposited up to 50 cm thick deposits above a topographic high 200 m above the canyon floor.

At least two large events are recorded in marine record of which the former can be very likely correlated to the ~5 ka old, Neostromboli flank collapse while the latter might correlate to the a younger flank collapse that occurred during the Recent Stromboli period (~1 ka). Both collapses show multi-phase or retrogressive dynamics as evidenced by the occurrence of peculiar sedimentary structures and by component and geochemical data.

Together with large landslides, almost nine small-scale landslides occurring with a greater frequency respect to that of the much larger failures were recorded by sediments, the last of whom is represented by December 30, 2002 event.

The research shows that the complete documentation of past potentially tsunami-producing landslide events of Stromboli is possible and opens new perspectives for the assessment of the tsunami hazard in the southern Tyrrhenian sea.

By analogy with Hawaii and Canary islands we confirm that deep-sea sediments can be effectively used to assess age and scale of past landslide events giving an important contribution to the tsunami hazard assessment of this region.

References

Ablay GJ, Hürlimann M (2000) Evolution of the north flank of Tenerife by recurrent giant landslides. J Volc Geoth Res 103: 135–159

Adams J (1990) Paleoseimicity of the Cascadia subduction zone: Evidence from turbidites off the Oregon-Washington margin. Tectonics 9: 569–583

Di Roberto A, Rosi M, Bertagnini A et al. (2008) Deep water gravity core from the Marsili Basin (Tyrrhenian Sea) records Pleistocenic–Holocenic explosive events and instability of the Aeolian Archipelago, (Italy). J Volc Geoth Res 177: 133–144

Francalanci L, Manetti P, Peccerillo A et al. (1993) Magmatological evolution of the Stromboli volcano (Aeolian Arc, Italy): Inferences from major and trace element and Sr isotopic composition of the lavas and pyroclastic rocks. Acta Vulcanol 3: 127–151

Gamberi F, Marani MP, Landuzzi V et al. (2006) Sedimentologic and volcanologic investigation of the deep Tyrrhenian Sea: Preliminary results of cruise VST02. Ann Geophys 49: 767–781

Garcia MO (1996) Turbidites from slope failures on Hawaiian volcanoes. In: MCGuire WJ, Jones AP, Neuberg J (eds.), Volcano instability of the Earth and Other Planets. Spec Pub Geol Soc London 110: 281–292

Gillot PY, Keller J (1993) Radiochronological dating of Stromboli. Acta Vulcanol 3: 69–77

Goldfinger C, Nelson CH, Johnson JE (2003) Holocene earthquake records from the Cascadia subjection zone and Northern San Andreas fault based on precise dating of offshore turbidites. Ann Rev Earth Planet Sci 31: 555–577

Hornig-Kjarsgaard I, Keller J, Koberski U et al. (1993) Geology, stratigraphy and volcanological evolution of the island of Stromboli, Aeolian arc, Italy. Acta Vulcanol 3: 21–68

Hürlimann M, Ledesma A (2007) Catastrophic volcanic landslides: The la Orotava events on Tenerife, Canary islands In: Evans SG, Scarascia Mugnozza G et al. (eds.), Springer

Kanamatsu T, Herrero-Bervera E, McMurtry GM (2002) Magnetostratigraphy of deep-sea sediments from areas adjacent to the Hawaiian Islands. In: Takahashi E et al. (eds.), AGU Monograph 128: 51–63

Kokelaar P, Romagnoli C (1995) Sector collapse, sedimentation and clast population evolution at an active island-arc volcano: Stromboli, Italy. Bull Volc 57: 240–262

Maramai A, Graziani L, Alessio G et al. (2005) Near- and far-field survey report of the 30 December 2002 Stromboli (Southern Italy) tsunami. Mar Geol 215: 93–106

Marani M, Gamberi F, Rosi M et al. (2008a) Deep-sea deposits of the 30 December 2002 Landslide. In: AGU (ed) The Stromboli Volcano: An Integrated Study of the 2002–2003 Eruption – Geophysical Monograph Series 182

Marani MP, Gamberi F, Rosi M, Bertagnini A, Di Roberto A (2008b) Deep-sea deposits of the Stromboli 30 December 2002 landslide. In: Calvari S, Inguaggiato S, Puglisi G, Ripepe M, Rosi M (eds.), Stromboli Volcano: an integrated study of the 2002–2003 eruption. American Geophysical Union, Geophysical Monograph 182, Washington DC, 157–169.

Marani M, Gamberi F, Rosi M et al. (2008b) Subaqueous sedimentary density flow processes and deposits of an island volcano landslide (Stromboli island, Italy), Sedimentology, doi:10.1111/j.1365-3091.2008.01043.x

Masson DG (1994) Late Quaternary turbidity current pathways to the Madeira Abyssal Plain and some constraints on turbidity current mechanisms. Basin Res 6: 17–33

Masson DG, Watts AB, Gee MJR et al. (2002) Slope failures on the flanks of the western Canary Islands. Earth Sci Rev 57: 1–35

Masson DG, Harbitz CB, Wynn RB et al. (2006) Submarine landslides: processes, triggers and hazard prediction. Phil Trans R Soc A 364: 2009–2039

McGuire WJ (1996) Volcano instability: a review of contemporary themes. In McGuire WJ, Jones AP, Neuberg J (eds.) Volcano Instability on the Earth and Other Planets. Spec Pub Geol Soc London, 1–23

McGuire WJ (2006) Global risk from extreme geophysical events: threat identification and assessment. Phil Trans R Soc A 364: 1889–1909

Moore JG, Clague DA, Holcomb RT et al. (1989) Prodigious submarine landslides on the Hawaiian Ridge. J Geophys Res 94: 17465–17484

Murty TS (2004) Tsunami wave height dependence on landslide volume. Pure Appl Geophys 160: 2147–2153

Ollier G, Cochonat P, Lenat JF et al. (1998) Deep-sea volcaniclastic sedimentary systems: an example from La Fournaise volcano, Reunion Island, Indian Ocean. Sedimentology 45: 293–330

Pickering KT, Underwood MB, Taira A (1992) Open-ocean to trench turbidity-current flow in the Nankai Trough: Flow collapse and reflection. Geology 20: 1099–1102

Siebert L (1992) Threats from debris avalanches. Nature 356: 658–659

Speranza F, Pompilio M, D'Ajello Caracciolo F et al. (2008) Holocene eruptive history of the Stromboli volcano: Constraints from paleomagnetic dating, J Geophys Res 113: B09101

Tibaldi A (2001) Multiple sector collapses at Stromboli volcano, Italy: how they work. Bull Volc 63: 112–125

Tinti S, Pagnoni G, Zaniboni F et al. (2003) Tsunami generation in Stromboli island and impact on the south-east Tyrrhenian coasts. Nat Haz Earth Sys Sci 3: 299–309

Tinti S, Manucci A, Pagnoni G et al. (2005) The 30 December 2002 landslide-induced tsunamis in Stromboli: sequence of the events reconstructed from the eyewitness accounts. Nat Haz Earth Sys Sci 5: 763–775

Voight B, Elsworth D (1997) Failure of volcano slopes. Géotechnique 47: 1–31

Wynn RB, Masson DG (2003) Canary Islands landslides and tsunami generation. In: Mienert J, Locat J (eds.) Submarine Mass Movements and their Consequences, Kluwer, Dordrecht

Tsunamigenic Risks Associated with Mass Transport Complexes in Offshore Trinidad and Venezuela

L. Moscardelli, M. Hornbach, and L. Wood

Abstract The study area is situated along the obliquely converging boundary of the Caribbean and the South American plates and proximal to the Orinoco delta. Several Plio-Pleistocene-age seafloor destabilization events have been identified in the continental margin of eastern offshore Trinidad. These mass wasting processes are thought to have been of sufficient scale to produce tsunamigenic waves. This work concentrates on the modeling of mass-failure-event-generated tsunami waves in eastern offshore Trinidad. Three different models were generated on the basis of geomorphological characteristics and causal mechanisms of mass transport complexes (MTCs): (1) slope-attached, (2) shelf-attached and (3) detached MTCs. Present-day geologic conditions suggest that detached and slope-attached mass failure events (MFEs) are more likely to occur today. In addition, modeling results indicate that detached MFEs that can occur on the collapsing flanks of mud-volcano ridges represent a higher tsunamigenic risk. These modeling results are a first approach to try to establish a tsunamigenic risk assessment in the region.

1 Introduction

The term MTC groups a variety of gravity-induced deposits that can co-occur in the same event or depositional unit (slides, slumps, and debris flows) (Dott 1963). It is well known that a sudden displacement of the seafloor through catastrophic sliding

L. Moscardelli (✉) and L. Wood
Bureau of Economic Geology, Jackson School of Geosciences,
The University of Texas at Austin, TX, USA
e-mail: lorena.moscardelli@beg.utexas.edu

M. Hornbach
Institute for Geophysics, Jackson School of Geosciences, The University of Texas at Austin, TX, USA
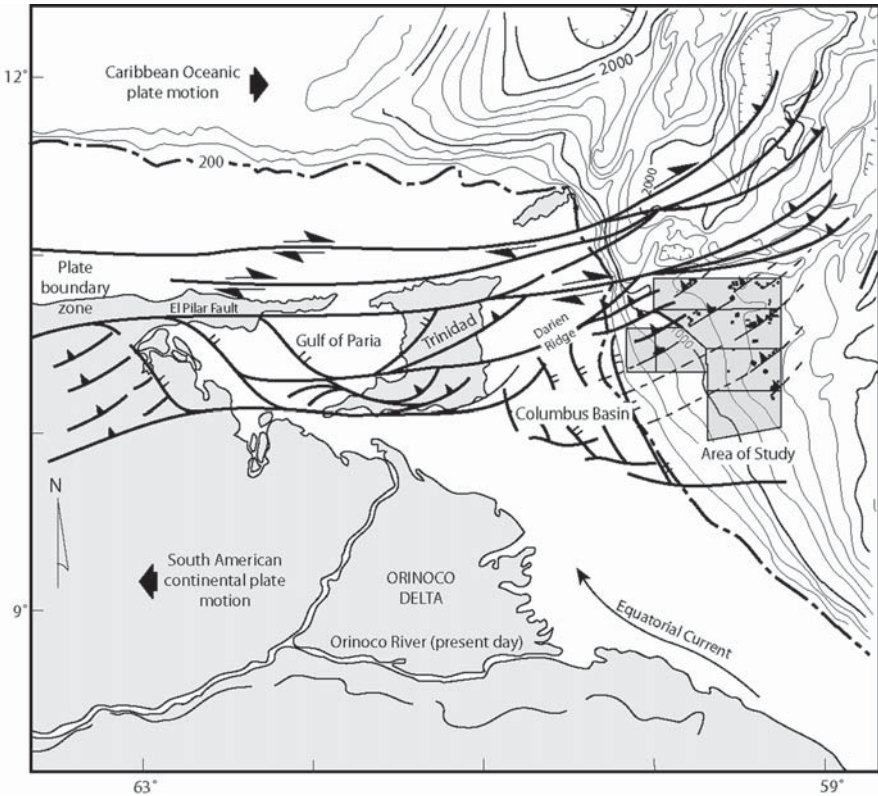
Fig. 1 Map showing the area of study located in eastern off-shore Trinidad. The area covered by the 3D seismic data and that was used in previous studies is outlined

or slumping has the potential to displace large volumes of water, generating tsunamis that can affect coastal areas and offshore infrastructure (Murty 1979; Jiang and LeBlond 1992). The 1998 Papua-New Guinea slide-triggered tsunami (Immamura and Hashi 2003) exemplifies the devastation that MFE-generated tsunamis can cause.

The focus of this study is to evaluate the tsunamigenic risks associated with the potential occurrence of MFEs in the southeastern Caribbean (Fig. 1). Our main premise is that MFEs, similar to those documented in the Plio-Pleistocene stratigraphic succession of eastern offshore Trinidad (Moscardelli and Wood 2008), could pose a tsunami risk to the coastal areas of eastern Trinidad and northeastern Venezuela if they occurred today.

Moscardelli and Wood (2008) documented that Plio-Pleistocene MTCs in the study area present remarkable differences in terms of their source regions, dimensions, geometries, and associated causal mechanisms. This variability raises questions in terms of the tsunamigenic potential that different types of MFEs might have.

In this paper, we show preliminary results associated with modeling of tsunamis that could be triggered by a variety of MFEs. The questions that we seek to address are: (1) what is the tsunamigenic hazard associated with the occurrence of MFEs in eastern offshore Trinidad? and (2) what types of MFEs present the greatest tsunamigenic risks in this region?

2 Data and Methods

The area of this study is located on the southeast margin of the tectonically active Caribbean Plate Boundary Zone in eastern offshore Trinidad (Fig. 1). The geomorphology of the Plio-Pleistocene MTCs that were used as proxies to estimate the spatial dimensions of potential future occurrences were obtained from previous work (Moscardelli and Wood 2008). Boundary conditions for each case scenario were defined on the basis of the causal mechanisms associated with each type of MFE, as well as on differences regarding their area, thickness, length, and width.

MTCs in eastern offshore Trinidad were originally described using 10,708 km^2 of high-quality 3D seismic data (Fig. 1). Moscardelli and Wood (2008) described three different types of MTCs in the study region: (1) shelf-attached MTCs, (2) slope-attached MTCs, and (3) detached MTCs (their figure 13). On the basis of this classification scheme, three case scenarios were defined in this work, each modeled to estimate the associated relative tsunamigenic risk.

The following parameters were used as input in the modeling package: location, length, width, area, and thickness of individual MTCs, as well as estimated prefailure slope angles and water depths at which failures might occur today (Table 1). Because MFEs tend to evacuate most sediment from their source area, values associated with prefailure slope angles and water depths at which failures might occur (Table 1) were obtained using present-day bathymetry data in analogous areas that have not failed (shelf-break region and flanks of mud-volcano ridges).

In this work, kilometer-scale regional bathymetric data were used in tsunami modeling to obtain first-order estimates of influences that MFEs might have in the generation of tsunami waves. More accurate tsunami wave run-up estimates require

Table 1 Input parameters to model tsunami waves generated by the occurrence of different MFEs

Case scenario	Latitude (degrees)	Longitude (degrees)	Length (km)	Width (km)	Area (km^2)	Thickness (m)	Slope angles	Water depth (m)	MFE type
1	10.4204	−60.3645	5	4	20	72	0.5	175.5	Slope attached
2	10.4669	−60.3343	1.8	2.5	4.5	50	0.5	175.5	Shelf attached
3	10.8518	−59.9571	5.6	5.5	30.8	60	6	952.5	Detached

high-resolution bathymetry data. Despite this limitation, results presented should reveal whether a significant MFE-related tsunami risk exists in this region.

To model the potential tsunami wave generated by MFEs, we first estimated slide motion, and from this, ocean-water displacement. As a first-order approach, changes in MTC shape due to dispersion during slide evolution were ignored. For bathymetry, we interpolated GEBCO 1-min, satellite-based bathymetry onto a **230**-m grid and used a Mercator projection. To approximate the shape of the initial slide motion, we assumed a smoothly shaped 3D Gaussian beam that roughly matched slide dimensions.

Displacement S of the slide's center of mass as a function of time t is given by:

$$(\gamma + C_m)\frac{d^2 S}{dt^2} = (\gamma - 1)(\sin\theta - C_n\cos\theta)g - C_d\frac{2}{\pi B}\left(\frac{dS}{dt}\right)^2 \tag{1}$$

where B = length of MTC, t = time, γ = MTC specific density, Cm is the mass density coefficient, Cd is the drag coefficient of the slide through the water, and Cn is the basal Coulomb coefficient of friction (Watts 1997; Grilli and Watts 2005)

In general, because higher slide accelerations have the potential to produce significantly larger tsunamis (Harbitz 1992), robust estimates of slide acceleration are necessary to accurately predict tsunami wave height. To determine velocity and acceleration, we adopted the method of Watts (1997) and Grilli and Watts (2005). From Watts (1997), an analytical solution for slide velocity (dS/dt) in Eq. 1 is

$$v(t) = u_t\tanh\left[\frac{a_0 t}{u_t}\right] \tag{2}$$

Where u_t is the terminal velocity of the slide and a_0 denotes initial slide acceleration which equals

$$a_0 = g(\gamma - 1)/(\gamma - C_m)\sin\theta$$

For MTCs, we estimated γ= 2, $\theta\approx3°$, and assume Cm = 1, Cd = 2 and Cn = 0.32, consistent with other slide tsunami models (e.g. Watts 1997; Grilli and Watts 2005) (Table 1).

This method may over predict slide terminal velocity (Hornbach et al. 2007), as indirect measurements of slide velocities based on timing of slide-associated submarine cable breaks suggest velocities of 6 to < 30 ms-1 for slides consisting of low-density hemipelagic mud (Heezen and Ewing 1952; Bjerrum 1971); we therefore apply an upper limit of 30 ms-1 for terminal velocities of all modeled MFEs.

The initial water wave generated by the first few seconds of motion was modeled by coupling seafloor deformation to sea level using nonlinear shallow-water wave approximations (e.g., Jiang and LeBond 1992); however, the propagating wave and

run-up estimates were modeled using the standard fully nonlinear Boussinesq wave model, FUNWAVE (Wei and Kirby 1995). The model uses a semi-implicit leapfrog approach over 308,000 km area (600 × 600 grid), with a square cell size of 925 m per side.

3 Tsunamis and Their Causal Mechanisms

Incidence of tsunamis is often related to occurrence of major earthquakes (Bryant 2001); however, the final triggering mechanism that is related to a specific tsunamigenic event can be associated with a variety of causal mechanisms, including submarine mass movements (MTC) (Tappin and Suppl 1999). The variety of processes that can trigger tsunamis suggests that not all tsunamigenic events have the same characteristics in terms of magnitude and propagation mechanisms. For example, tsunamis generated by submarine slides (e.g., PNG tsunami) have large run-up heights close to the failure area (Tappin and Suppl 1999) but have far-field effects that are more limited than earthquake tsunamis (e.g., Indian Ocean tsunami) (Okal and Synolakis 2004).

The magnitude of the run-up generated by a MFE will depend primarily on (1) volume of material that moves, (2) water depth in which the failure occurs, (3) acceleration of submarine sediment mass, (4) rheology of the material that fails, and (5) distance from shore (Pelinovsky and Poplavsky 1996). In eastern offshore Trinidad, six MTCs have been identified in the shallow subsurface. Estimated sediment volumes of these deposits and water depths at which failure occurred vary from 1 to 242 km³ and from 600 to 1,400 m, respectively. In addition, significant differences exist in terms of the rheology of sediments that fed these MTCs. The smallest MTCs were derived from collapsing flanks of mud-volcano ridges (detached MTCs). Sedimentary sources of regional MTCs were associated with shelf-edge deltas (paleo-Orinoco) and with upper-slope sediments (attached MTCs), where sandier intervals are more likely to occur (Sullivan et al. 2004; Moscardelli and Wood 2008).

According to Skvortsov and Bornhold (2007), 70% of total energy transfer from the submarine slide to surface waves occurs during initial phases of failure, and, hence, determining specific initial conditions is crucial. For this reason, when we evaluated the risks associated with MFE-generated tsunamis, we decided to define three different case scenarios that took into consideration not only dimensions of the MTCs (morphology), but also their associated geologic settings and causal mechanisms (Moscardelli and Wood 2008).

3.1 Case Scenario I: Slope-Attached MFE

Slope-attached MTCs are regionally extensive and can occupy hundreds to thousands of square kilometers. Slope-attached MTCs have scarps that can be tens of kilometers long and hundreds of meters deep. These scarps define their updip boundaries in the shelf break and upper-slope region (Fig. 2). Slope-attached
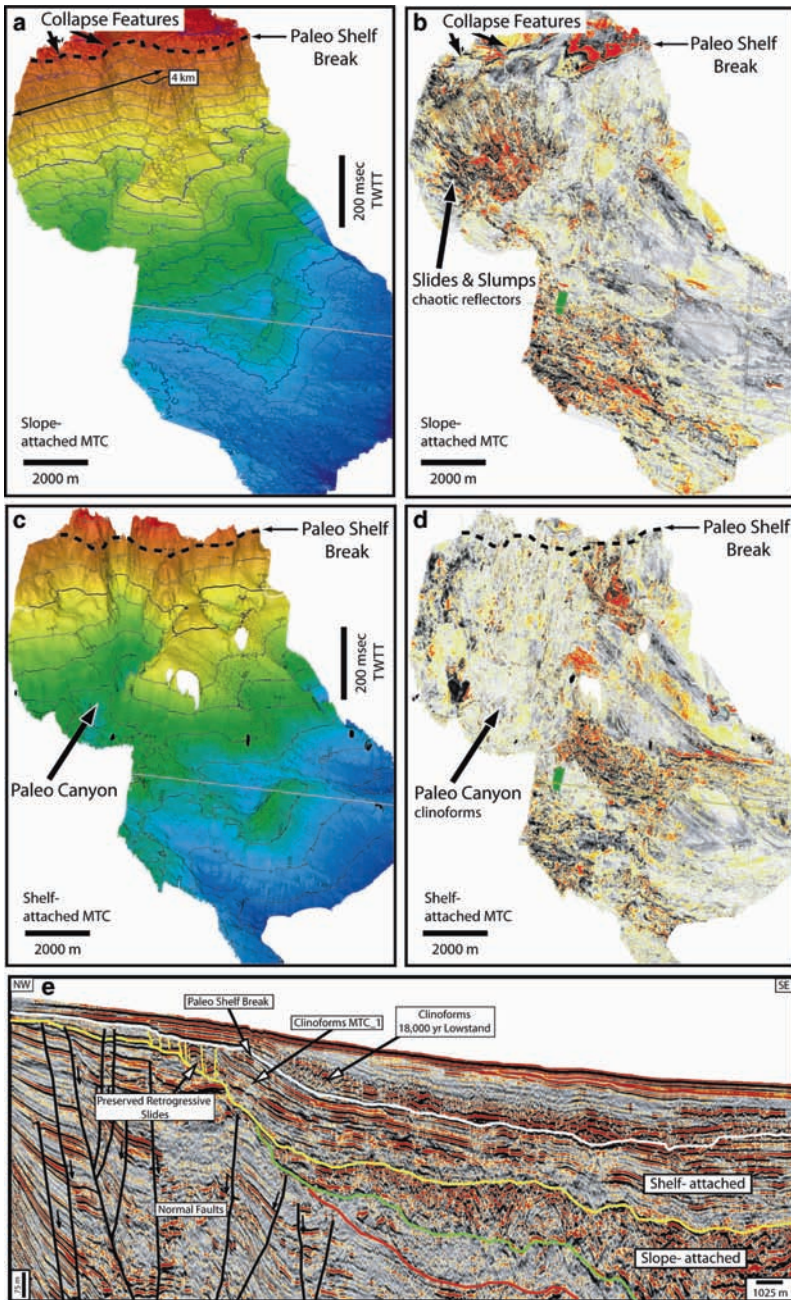
Fig. 2 (**a**) 3D visualization of horizon defining base of slope-attached MTC_2 near the shelf break. (**b**) Root-mean-square (RMS) amplitude extraction on a 20-ms window above the horizon defining base of slope-attached MTC_2. Note scar zone near shelf break and downslope mass wasting. (**c**) 3D visualization of horizon defining base of shelf-attached MTC_1. (**d**) RMS amplitude extraction on 20-ms window above the base of shelf-attached MTC_1. Note low-amplitude seismic response on axis of paleocanyon. (**e**) Dip seismic line across shelf break and upper-slope region showing seismic response and strata architecture of shelf-attached (MTC_1) and slope-attached (MTC_2) MTCs

MTCs are associated with catastrophic and almost instantaneous collapse of the upper continental slope that may be preconditioned by a variety of processes, including earthquakes, long-shore currents, hydrate dissociation, and salt deformation (Mosher et al. 2004). Slope-attached MTCs in offshore Trinidad are thought to have been preconditioned catastrophically by earthquakes or gas hydrate dissociation; these deposits cover 60 to 626 km^2 in area, 20 to 40 km in length, and 3 to 10 km in width. These morphological values include total area affected by the mass wasting event, which involves initial sediment that failed upslope and sediments that were incorporated as the flow scoured the seafloor downslope. A reexamination of 3D seismic data allowed us to measure the morphological parameters that we thought corresponded to the shape of original upslope collapses, and these measurements were used as input for the model (Table 1) (Fig. 2).

In the case of slope-attached MTCs, we used the upslope MTC_2 as described by Moscardelli and Wood (2008). According to this description, several collapse features can be seen in the upper-slope area near the paleoshelf break (Fig. 2). On the basis of an estimate of the missing vertical section and the area of the original failure, we calculated that the original material that failed was 72 m thick. Present location of the shelf break suggests that a similar failure could occur today at water depths of ~180 m, affecting the shelf-break region where slope angles are near 0.5° (Table 1). During modeling, we assumed that an upper-slope collapse generated by a slope-attached MTC occurring today would have a slightly southwest-northeast trajectory following maximum inclination of the slope-to-basin-floor transition.

3.2 Case Scenario II: Shelf-Attached MFE

Shelf-attached MTCs are also regionally extensive but are usually fed by canyon systems that cut across the outer shelf and upper-slope region, funneling considerable amounts of sediment downdip (Fig. 2). Causal mechanisms of failure can include oversteepening in the upper parts of clinoform foresets that generate gravitational instabilities (Moscardelli and Wood 2008).

Shelf-attached MTCs may be generated by relatively small retrogressive failures that occur over time and that eventually accumulate to generate the bulk of the MTC deposit downslope. For modeling purposes, we used MTC_1 as described by Moscardelli and Wood (2008); however, we recalculated length, area, and thickness of the upslope parts of MTC_1 because previous values included the total area covered by the deposit. Our estimations suggest that the area affected by initial upslope failures could reach between 4 and 5 km^2 with a thickness of ~50 m. If a similar collapse occurred today, it would affect sediments sitting at the shelf break at slope angles of 0.5° and at water depths of ~180 m (Table 1). Initial upslope failures associated with a shelf-attached MTC would move southwest-northeast toward the basin.

3.3   Case Scenario III: Detached MFE

Detached MTCs cover less than tens of square kilometers in area and a few kilometers in width and length. Detached MTCs can originate in any type of localized bathymetric high, and resulting sediments are derived locally within the minibasin of deposition. Triggering mechanisms of detached MTCs are controlled by local gravitational instabilities that can occur on the flanks of mud volcanoes and other bathymetric highs (Moscardelli and Wood 2008).

Several detached MTCs were documented in eastern offshore Trinidad (MTC_2.2, MTC_2.3, and MTC_2.4) (Moscardelli and Wood 2008); these deposits covered ~30 km^2 in area. Detached MTCs could occur today at water depths of 950 m, in which bathymetric data clearly show modern expression of active mud-volcano ridges on the seafloor (Sullivan et al. 2004) (Fig. 3). Initial failures could involve slides that can be 60 m thick. The average slope angle of mud-volcano flanks is 6° (Table 1), but maximum reported slope angles reach 18° (Sullivan et al. 2004). In this case, a northwest–southeast-moving collapse affecting the southern flank of the Darien Ridge was used to model the associated tsunamigenic event.
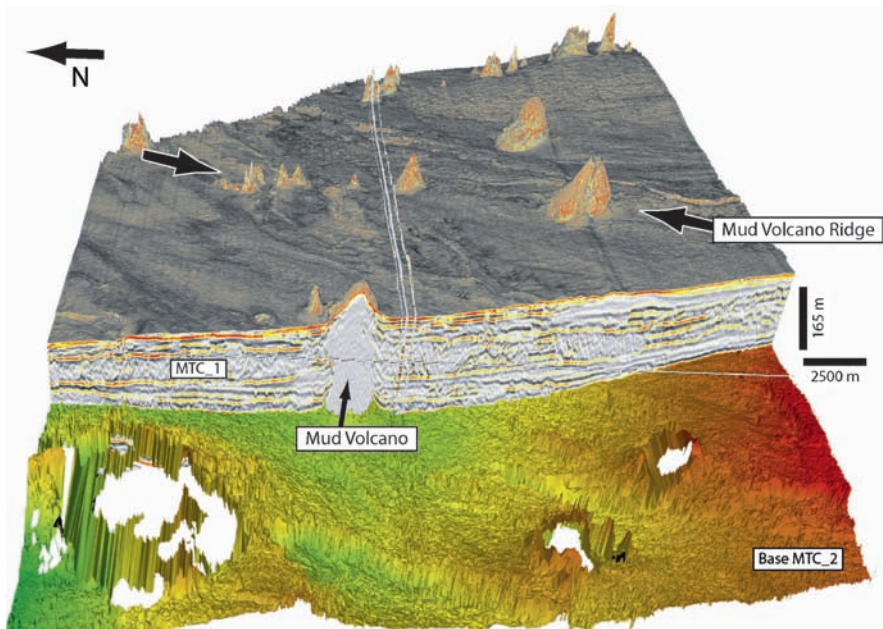
Fig. 3 Geobody between the structural surface that defines the base of slope-attached MTC_2 and the seafloor. Mud-volcano heights can be >165 m, and mud-volcano ridges have northeast-southwest orientations

4 Initial Hypothesis and Modeling Results

Our initial working hypothesis indicated that the worst-case scenario for an MFE-generated tsunami would involve an event with the following characteristics: (1) initial failure remobilizing large amounts of sediments in a relatively short period of time and (2) failures occurring at shallower depths (~175 m). The suddenness of regional tectonic instabilities that result in the occurrence of slope-attached MFEs implies an almost instantaneous remobilization of huge volumes of sediment from the upper-slope region. The sudden tectonically triggered failure and release of energy that is unique to slope-attached MFEs prompted us to think that this type of event would pose the greatest tsunamigenic risk of any studied in the area. Our purely qualitative interpretation also suggested that detached MFEs would pose the lowest tsunamigenic risk for coastal areas because these events occur farther (>120 km) from the coast and in the deeper parts of the basin (~950 m water depth).

Results of tsunami modeling are considerably different from our original qualitative expectations (Fig. 4). Modeling results revealed that detached MTCs affecting
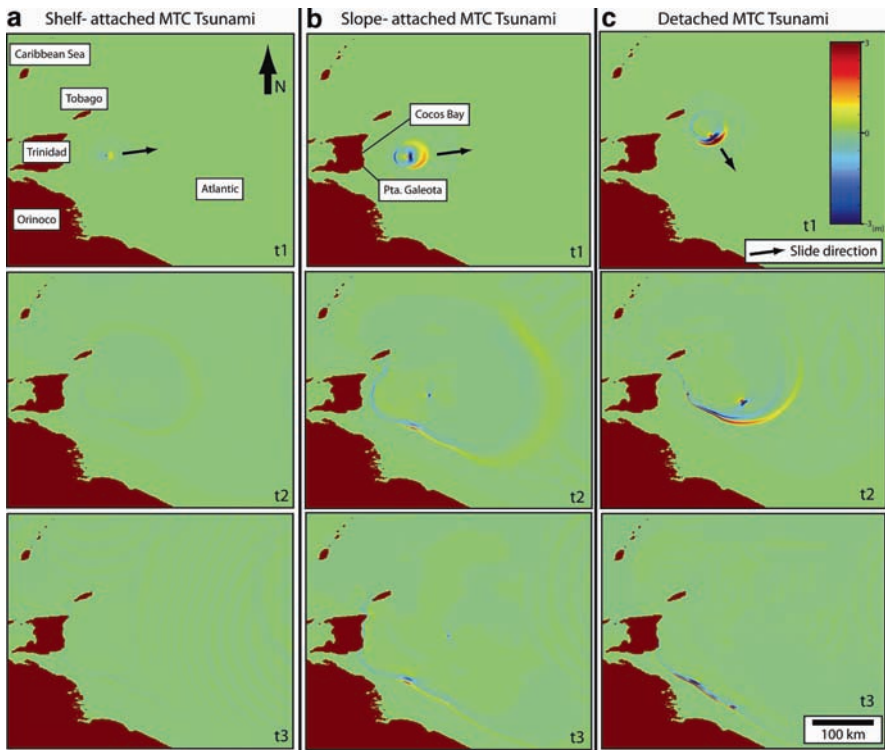
Fig. 4 Wave propagation in MTC-generated tsunamis. T1 occurs shortly after slide generation and t3 one-half hour after slide generation, when the wave reaches the east coast of Trinidad

the flanks of mud-volcano ridges in the deeper parts of the basin are the events that pose the greatest tsunamigenic risk for the east coast of Trinidad. Controlling factors seem to be steepness of mud-volcano flanks, as well as slide trajectories because flank collapses on mud-volcano ridges can occur in many different orientations. It is when sliding occurs perpendicular to shore that the model indicates a significant wave (~1 to 2 m high) could propagate towards the east eventually hitting the Trinidadian coast (Fig. 4). Prefailure slope angles on the flanks of mud-volcano ridges also play a crucial role in increasing the magnitude of water-column perturbation. Slope angles near the shelf break are usually < 1, but average prefailure slope angles at the flanks of mud-volcano ridges are ~6° and may even reach 18° (Sullivan et al. 2004). Steeper slope angles have the capacity to increase initial acceleration of the slide. Modeling also suggests that the Orinoco delta region could be affected by a tsunamigenic wave generated by a detached MFE in offshore Trinidad.

The tsunami model for slope-attached MFEs shows that an event like this could generate ~1-m-high tsunami waves that could reach the east coast of Trinidad. The propagation pattern of the wave, however, seems to suggest that effects would be more noticeable on the southern coast of Tobago (Fig. 4). The model also shows that much of the energy would propagate towards the Central Atlantic, whereas a negative-positive tsunami wave would hit the eastern coast of Trinidad first. Similar behavior, in terms of wave propagation, is observed for the tsunami wave modeled for shelf-attached MFE. However, in this case, wave heights are reduced (<0.5 m high) because the initial volume of sediments that failed was considerably lower. Our analysis also suggests that the Orinoco delta region could be affected by a tsunami if a slide occurred off Trinidad, although significant wave dispersion occurs in the delta.

5   Discussion: Present Risk of MTC Occurrences in Offshore Trinidad

The study area is within an active tectonic margin. More than 30 seismic events with varying magnitudes of Mw 1 to 5 have been reported in the study area from 2006 to 2008. Since 1983, at least three earthquakes of Mw 6 and 7 have occurred in the same geographic area (USGS online Earthquake Center). Location of some earthquake epicenters observed in this region coincides with the location of mud-volcano ridges, demonstrating that these ridges are currently active and potentially unstable. Our model of case scenario III suggests that 2-m-high tsunami waves could strike the east coast of Trinidad if a detached MFE were generated on the south flank of the Darien Ridge. Tsunami wave heights and propagation directions, however, would vary according to the volume of material that fails and the plane and orientation of failure. Historically events like this have not been reported in Trinidad.

The minimum earthquake magnitude necessary to trigger a slope-attached MFE is unknown and would probably depend on a variety of factors. Some data suggest

that slope-attached MFEs associated with the occurrence of earthquakes are usually triggered by at least M > 7 earthquakes (e.g., Papua New Guinea and Grand Banks events) (Imamura and Hashi 2003). However, Mosher et al. (1994) concluded that more frequent, lower magnitude (M > 3) earthquakes have been the likely cause of large-scale slope failures in the Scotian slope of Canada. Seismicity records from eastern offshore Trinidad indicate that relatively low intensity earthquakes are common, whereas M > 7 events are rare in this region. We do not think that the occurrence of a catastrophic slope-attached MFE is imminent in the region today; however, the geologic record shows that at least one slope-attached MFE occurred during the Plio-Pleistocene (Fig. 2) (Moscardelli and Wood 2008).

From the three scenarios that were modeled in this work, case scenario II (shelf-attached MFE) represents the least likely to occur under present-day conditions because shelf-attached MFEs have been associated with failure of shelf-edge deltas. Today the modern active Orinoco delta front is several hundred kilometers to the southwest of the modern shelf break, and current highstand sea-level conditions define a different scenario from the one prevalent at the time of MTC_1 deposition.

References

Bjerrum L (1971) Subaqueous slope failures in Norwegian fjords. Nor Geotech Inst Bull 88: 1–8.

Bryant E (2001) Tsunami; the underrated hazard. Cambridge University Press, Cambridge.

Dott RH (1963) Dynamics of subaqueous gravity depositional processes. Am Assoc Pet Geol Bull 47: 104–128.

Grilli ST and Watts P (2005) Tsunami generation by submarine mass failure. I: modeling, experimental validation, and sensitivity analysis. J Waterway Port Coast Ocean Eng 131: 283–297.

Harbitz CB (1992) Model simulations of tsunamis generated by the Storegga slides. Mar Geol 105: 1–21.

Heezen BC and Ewing WM (1952) Turbidity currents and submarine slumps, and the 1929 Grand Banks (Newfoundland) earthquake. Am J Sci 250: 849–873.

Hornbach MJ, Lavier LL and Ruppel CD (2007) Triggering mechanism and tsunamogenic potential of the Cape Fear Slide complex, U.S. Atlantic margin. Geoch Geoph Geosystems 8.

Imamura F and Hashi K (2003) Re-examination of the source mechanism of the 1998 Papua New Guinea earthquake and tsunami. Pure Appl Geoph 160: 2071–2086.

Jiang LC and LeBlond PH (1992) The coupling of a submarine slide and the surface waves which it generates. J Geophys Res 97: 12731.

Moscardelli L and Wood L (2008) New classification system for mass transport complexes in offshore Trinidad. Basin Res 20: 73–98.

Mosher DC, Moran K and Hiscott RN (1994) Late Quaternary sediment, sediment mass flow processes and slope stability on the Scotian Slope, Canada. Sedimentology 41: 1039–1061.

Mosher DC, Piper DJW, Calvin CD and Jenner KA (2004) Near-surface geology and sediment-failure geohazards of the central Scotian Slope. Am Assoc Pet Geol Bull 88: 703–723.

Murty TS (1979) Submarine slide-generated water waves in Kitimat Inlet, British Columbia. J Geophys Res 84: 7777–7779.

Okal EA and Synolakis CE (2004) Source discriminants for near-field tsunamis. Geoph J Internat 158: 899–912.

Pelinovsky E and Poplavsky A (1996) Simplified model of tsunami generation by submarine landslides. Phys Chem Earth 21: 13–17.

Skvortsov A and Bornhold B (2007) Numerical simulation of the landslide-generated tsunami in Kitimat Arm, British Columbia, Canada, 27 April 1975. J Geophys Res 112.

Sullivan S, Wood LJ and Mann P (2004) Distribution, nature and origin of mobile mud features offshore Trinidad. Program and Abstracts – GCSSEPM 24: 36.

Tappin DR and Suppl (1999) Submarine slump generation of the 1998 Papua New Guinea tsunami; the evidence so far. In Watts P, Borrero JC, Okal E, Bardet JP, Grilli S, Matsumoto T and Synolakis CE (eds) Eos, Transactions, Am Geophys Union 80: 750.

Watts P (1997) Water waves generated by underwater landslides. Pasadena, California Institute of Technology, CA.

Wei G and Kirby JT (1995) A time-dependent numerical code for extended Boussinesq equations. J Waterway Port Coast Ocean Eng 120: 251–261.

Distribution and Tsunamigenic Potential of Submarine Landslides in the Gulf of Mexico

J.D. Chaytor, D.C. Twichell, P. Lynett, and E.L. Geist

Abstract The Gulf of Mexico (GOM) is a geologically diverse ocean basin that includes three distinct geologic provinces: a carbonate province, a salt province, and canyon to deep-sea fan province, all of which contain evidence of submarine mass movements. The threat of submarine landslides in the GOM as a generator of near-field damaging tsunamis has not been widely addressed. Submarine landslides in the GOM are considered a potential tsunami hazard because: (1) some dated landslides in the GOM have post-glacial ages and (2) recent seismicity recorded within the GOM. We present a brief review of the distribution and style of submarine landslides that have occurred in the GOM during the Quaternary, followed by preliminary hydrodynamic modeling results of tsunami generation from the East Breaks landslide off Corpus Christie, TX.

1 Introduction

Submarine landslides have been studied in the Gulf of Mexico (GOM) for two reasons: first, as a hazard to offshore hydrocarbon extraction infrastructure and transportation. Second, when more deeply buried, they can serve either as hydrocarbon

J.D. Chaytor (✉)
Woods Hole Oceanographic Institution, Woods Hole, MA 02543, USA
e-mail:jchaytor@whoi.edu

D.C. Twichell
U.S. Geological Survey, Woods Hole, MA 02543, USA

P. Lynett
Texas A&M University, College Station, TX 77843, USA

E.L. Geist
U.S. Geological Survey, Menlo Park, CA 94025, USA

reservoirs or barriers in reservoirs. The threat of submarine landslides to generate tsunamis has not been widely addressed for the GOM region. We present a brief review of the literature on the distribution and style of submarine landslides that have occurred in the GOM during the Quaternary and the results of some preliminary landslide-generated tsunami modeling.

2   Setting

The GOM is dominated by three distinct geologic provinces: a carbonate province, a salt province, and canyon to deep-sea fan province (Fig. 1). Three particular aspects of the basin's evolution that should be considered in an assessment of landslide activity include: (1) Jurassic-aged Louann salt that was deposited during the early stages of basin formation (Salvador 1991), (2) the development and growth of extensive carbonate reef tracts during the late Jurassic and Cretaceous (Bryant et al. 1991), and (3) the siliciclastic sediment input during the latest Mesozoic and Cenozoic (Buffler 1991).
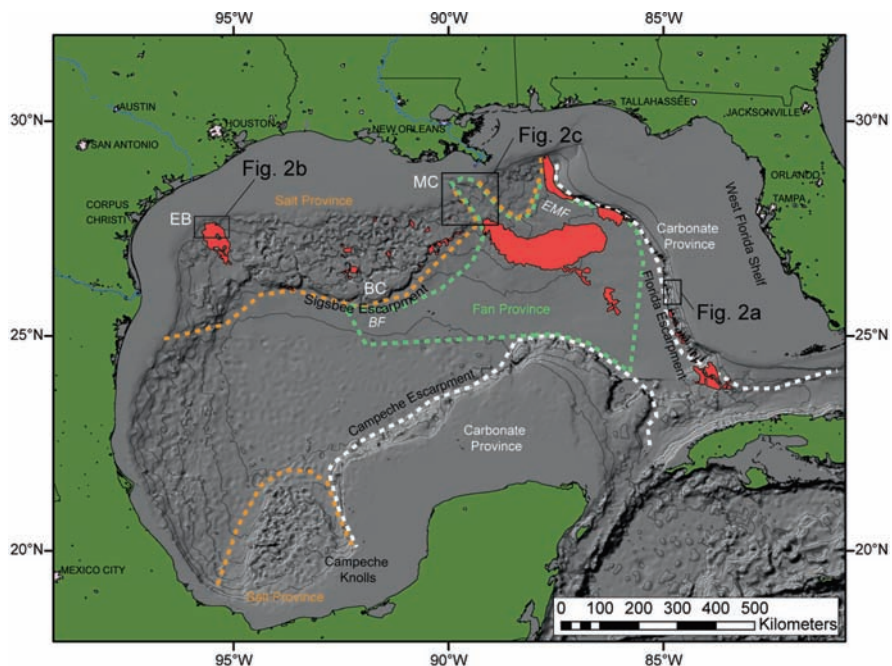
Fig. 1 Shaded bathymetry of the Gulf of Mexico. Landslide deposits are marked in red. The three primary geologic provinces of the region are highlighted by the dashed lines. EB-East Breaks Landslide, MC-Mississippi Canyon, BC-Bryant Canyon, EMF-East Mississippi Fan, BF-Bryant Fan. Bathymetry derived from Armante and Eakins (2008)

The Louann salt underlies large parts of the northern GOM continental shelf and slope. Under the upper and middle slope the salt is shaped into a network of ridges and thin salt sheets that are interrupted by sub-circular basins (mini-basins) which have thin salt or no salt underlying them. Campeche Knolls in the southwest corner of the GOM has an irregular morphology that is similar to that of the northern GOM slope, due to sediment loading of an underlying salt deposit (Fig. 1; Bryant et al. 1991).

During the Mesozoic, an extensive reef system developed around much of the margin of the GOM basin (Sohl et al. 1991). This reef system is exposed along the Florida Escarpment (FE) and the Campeche Escarpment (Fig. 1). These escarpments stand as much as 1,500 m above the abyssal plain floor, and have average gradients that commonly exceed 20° and locally are vertical. Reef growth ended during the Middle Cretaceous (Freeman-Lynde 1983; Paull et al. 1990), and subsequently the platform edges have been sculpted and steepened by a variety of erosional processes (Freeman-Lynde 1983; Paull et al. 1990; Twichell et al. 1996).

Three fan systems formed during the Pliocene and Pleistocene, the Bryant Fan (Lee et al. 1996), Mississippi Fan (Weimer 1989), and Eastern Mississippi Fan (Weimer and Dixon 1994). The Mississippi Fan is the largest of these three fans, and covers most of the eastern half of the deep GOM basin (Fig. 1). Mississippi Canyon (MC) has retained its morphologic expression on the slope, but the canyons that supplied sediment to Bryant and Eastern Mississippi Fans have been largely erased by subsequent salt tectonism and depositional processes (Weimer and Dixon 1994; Lee et al. 1996).

3 Distribution of Submarine Landslides

Submarine landslides have occurred in each of the three provinces of the GOM basin although they vary in style and size. This report will focus on landslides that are thought to have occurred during the Quaternary Period as they have the greatest implications for modern tsunami hazards.

3.1 Carbonate Province

Landslides on the West Florida Slope (WFS) above the FE are sourced in Tertiary and Quaternary carbonate deposits (Fig. 2a). Mullins et al. (1986) mapped large collapse scars along the WFS, one of which is 120 km long and 30 km wide, with 300–350 m relief. While the total volume of material removed from this feature is around 1,000 km³, there were at least 3 generations of failures, with most of the sediment removal occurring prior to the middle Miocene. Along the southern part of the WFS, Doyle and Holmes (1985) and Twichell et al. (1993) mapped another extensive area of the slope that has undergone collapse (Fig. 2a). Here the scarps
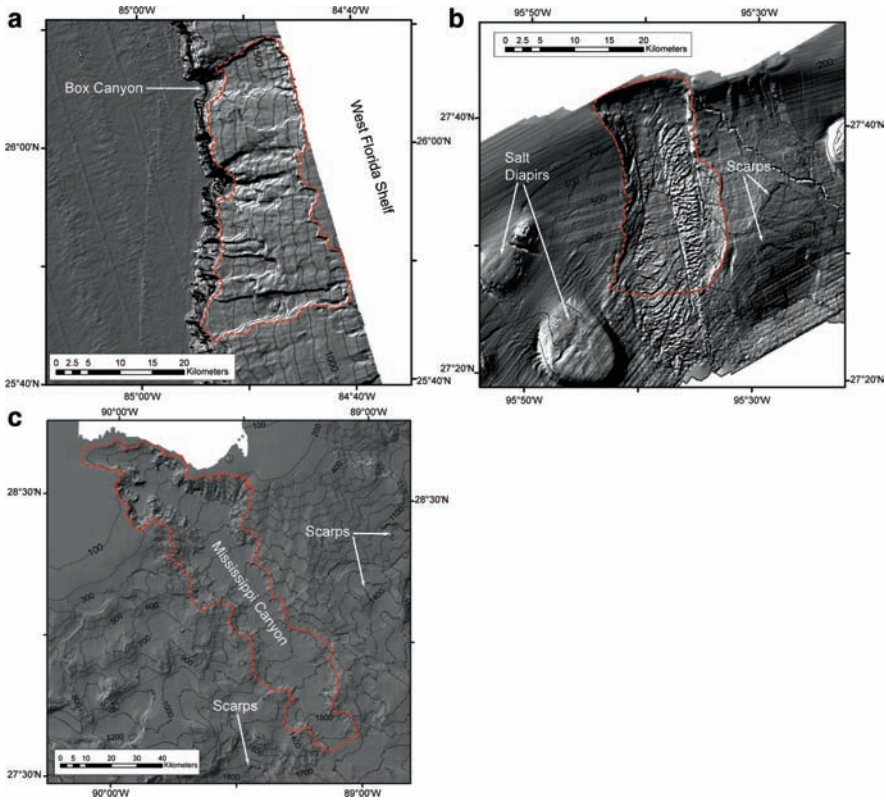
Fig. 2 (**a**) Landslide scar in carbonate platform above the central Florida Escarpment, (**b**) Upper part of the East Breaks Landslide, and (**c**) Mississippi Canyon, the source area of the landslide deposits comprising the Mississippi Fan. Red dashed polygons outline the landslide source zones (excavations) used to calculate landslide volume and area given in Table 1. Bathymetry data available at the NOAA National Geophysical Data Center

are still exposed on the seafloor and have 50–150 m relief and are 10–70 km in length. Some of the mass-movement deposits are on the slope above the FE while the remainder were likely transported farther and deposited at the base of the FE. The cross-cutting of the headwall scarps indicates that these landslides are composed of several smaller failure events (Twichell et al. 1993).

3.2 Salt Province

Landslide deposits, most of which are relatively small, have been mapped throughout the salt province using GLORIA imagery (Rothwell et al. 1991) as well as with high-resolution sidescan sonar, bathymetry, seismic profiles, and cores (Lee and

George 2004; Orange et al. 2004; Sager et al. 2004; Silva et al. 2004; Tripsanas et al. 2004). The largest of these failures, the East Breaks landslide (Fig. 2b), occurs in the northwestern GOM, is 114 km long, 53 km wide, covers about 2,250 km^2, and has been interpreted to consist of at least two debris flows (Rothwell et al. 1991). This landslide, which incises a shelf-edge delta, lies off-shore of the Colorado River system and formed during the last lowstand of sea level (Piper and Behrens 2003).

The remaining landslides within the salt province are considerably smaller and cover areas ranging from 4–273 km^2 (Fig. 1) and are sourced from the walls of the mini-basins or the Sigsbee Escarpment. While information is limited on the age of landslides in the salt province and failure of mini-basin walls throughout the province may still be active, Tripsanas et al. (2004) indicates that most of the landslides sampled in the salt province occurred during oxygen isotope stages 2 through 4 (18,170–71,000 yr BP) during the last lowstand of sea level, when salt movement due to sediment loading may have been more active in certain locations.

3.3   Canyon/Fan Province

Recent studies of the MC and Mississippi Fan (Twichell et al. 1996; Twichell et al. in press) reveal evidence of landslides at several scales. Turbidity current deposits and thin debris flow deposits associated with channel-levee development have been mapped and sampled on the distal fan (Twichell et al. 1992; Schwab et al. 1996). Some of these deposits are relatively small: covering areas less than 331 km^2, and have volumes less than 1 km^3 (Twichell et al. in press). At the other extreme is a large landslide complex that covers approximately 23,000 km^2 of the middle and upper fan (Fig. 1) and reaches 100 m in thickness (Walker and Massingill 1970; Twichell et al. 1992). The total volume of this deposit cannot be accurately estimated because of inadequate seismic coverage, but, assuming an average thickness of 75 m, the volume would be 1,725 km^3. Seismic profiles and GLORIA imagery suggest that this feature consists of at least two separate events (Twichell et al. in press). MC (Fig. 2c) appears to have been the source area for these landslide deposits (Walker and Massingill 1970; Coleman et al. 1983; Goodwin and Prior 1989). Borings and seismic data from the head of MC (Goodwin and Prior 1989) indicate that there were alternating episodes of canyon filling and excavation between 19,000 and 7,500 ybp, and Coleman et al. (1983) estimate total volume of sediment removed was approximately 8,600 km^3.

The Eastern Mississippi Fan system also has a relatively large landslide that partially buries the channel that supplied this fan. This landslide deposit is approximately 154 km long, as much as 22 km wide, and covers an area of 2,410 km^2. The volume of the deposit and its age are unknown.

4 Preliminary Analysis of Potential Landslide-Generated Tsunamigenic Sources

In the GOM, potential tsunami sources are primarily earthquakes along the Caribbean plate boundary and submarine landslides, although the importance of earthquakes within the region is being evaluated (e.g., Knight 2006). Submarine landslides in the GOM are considered a potential tsunami hazard for two reasons: (1) some dated landslides in the GOM have post-glacial ages (Coleman et al. 1983) and (2) recent seismicity recorded within the GOM (Dewey and Dellinger 2008).

The MC and East Breaks landslides, among the largest landslides in the GOM, occurred after the end of the last glacial maximum during post-glacial transgression (Piper and Behrens 2003). In addition, the Mississippi River still deposits large quantities of water-saturated sediments on the shelf and slope, making them vulnerable to over-pressurization and slope failure (Dugan and Flemings 2000).

On February 10, 2006, seismograms recorded an earthquake offshore southern Louisiana (Dewey and Dellinger 2008). While source analyses of this event cannot distinguish between a fault source and landslide, the occurrence of a magnitude 4.2 earthquake reveals the potential for ground shaking and slope failure.

4.1 Submarine Landslide Characteristics

We define three submarine landslides within the geologic provinces of the northern GOM that may have had tsunamigenic potential: (1) East Breaks; (2) Mississippi Canyon; and (3) Florida Escarpment. The U.S. gulf coast would be affected primarily by the shoreward-directed phase of the tsunami emanating from the East Breaks and MC landslides, and would be affected primarily by the outgoing tsunami from a landslide sourced from above the FE. A tsunami from a landslide on the FE would have a significant directivity effect that scales with the speed of downslope motion of the landslide (up to the phase speed of the tsunami). The characteristics and the parameters of landslides considered in preliminary tsunami source analysis are given in Table 1.

Landslide volume calculations were based on measuring the volume of material removed from the landslide source area using a technique similar to that applied by Chaytor et al. (2009). In the case of the East Breaks landslide, the source area may be somewhat larger, but bathymetry is not available for the entire landslide.

4.2 East Breaks Landslide Tsunami Modeling

Preliminary simplified hydrodynamic modeling of the East Breaks landslide has been performed to investigate the upper limits of tsunami wave height generated by this source. For modeling purposes, a 200 m resolution elevation grid was used,

Table 1 Characteristics of the landslides source regions considered in this study. Numbers in parentheses are values from other investigators

Landslide	Geologic setting	Post failure sediment	Age (years)	Single event volume (km³) Max	Single event volume (km³) Min	Single event area (km²) Max	Single event area (km²) Min	Excavation Depth (m)	Run-Out Distance (km)
East breaks	River delta/salt province	Partial canyon fill	10,000–25,000[1]	22 (60)[2]	21	520	421	~160	91 (130)[3]
Mississippi canyon	River delta/fan system	Partial canyon fill	7,500–11,000[4]	426	–	3687	–	~300 (upper canyon)	297 (442)
Florida Escarpment	Carbonate platform	None visible	Early Holocene or older[5]	16	–	648	–	~150	?

[1] Piper and Behrens (2003)
[2] Trabant et al. (2001)
[3] Rothwell et al. (1991)
[4] Coleman et al. (1983)
[5] Doyle and Holmes (1985)
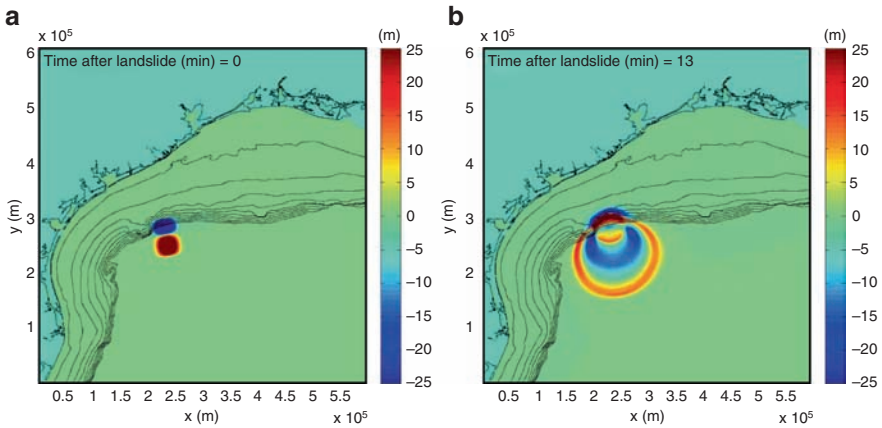
Fig. 3 Results of two-dimensional simulation of the East Break landslide (headwall depth is 160 m) at (**a**) 0 min (initiation) and (**b**) 13 min. Note the radial spreading pattern

made up of a combination of data from the U.S. Army Corp of Engineers ADCIRC (shallow water) and the NOAA 2-min ETOPO2 (deep water) databases. Two conservative assumptions were made: (1) the time scale of seafloor motion is very small when compared to that of the generated tsunami, and (2) bottom roughness and associated energy dissipation in deep water are negligible.

In initial runs, model conditions of a landslide source width of ~12 km and length of 50 km are used. As the excavation depth of the landslide is ~160 m, a trough elevation of 160 m is used as the hot-start initial free water surface condition (i.e., the free water surface response matches the change in the seafloor profile exactly), based on the knowledge of the characteristics of landslide generated waves (e.g., Lynett and Liu 2002). From this, model results (Fig. 3) indicate that wave components (backgoing and outgoing) with amplitudes greater than 20 m is initially generated. Attenuation from radial spreading is important, with wave energy predicted to propagate in all directions away from the source. Further modeling and analysis is required to determine if the entire coastline of the GOM would be impacted by a tsunami generated by this source. The magnitude of the tsunami at the coast would be determined by shallow water amplification and energy dissipation of the waves. Furthermore, using landslide durations predicted from the mobility analysis rather than hot-start conditions we expect to see a change in tsunami generation efficiency.

5   Concluding Statements and Future Work

Timing of landslides in the GOM needs to be refined to determine the likelihood of modern landslides and potential for future landslide-generated tsunamis. For example, it is not known if the Mississippi Fan landslides are associated with glacial

meltwater floods that discharged into the GOM (e.g., Aharon 2003), or whether they occurred more recently. Available age dates indicate that this large landslide complex is younger than 11,100 ybp, but the minimum age is still unknown (Twichell et al. in press). Additional modeling of potential sources is required to determine the magnitude of the initial waves, the amount of shallow water amplification, and the level of run-up expected at points around the GOM.

References

Aharon P (2003) Meltwater flooding events in the Gulf of Mexico revisited: Implications for rapid climate changes during the last deglaciation. Paleocean doi: 10.1029/2002PA000840.

Amante C, Eakins BW (2008) ETOPO1 1 Arc-Minute Global Relief Model: Procedures, Data Sources and Analysis. National Geophysical Data Center, NESDIS, NOAA, U.S. Department of Commerce, Boulder, CO.

Bryant WR, Lugo J, Cordova C, Slavador A (1991) Physiography and bathymetry. In: Salvador, A (ed) The Geology of North America, Vol. J, Gulf of Mexico Basin. Geol Soc Am, Boulder, CO, p. 13–30.

Buffler RT (1991) Seismic stratigraphy of the deep Gulf of Mexico basin and adjacent margins. In: Salvador, A (ed) The Geology of North America, Vol. J, Gulf of Mexico Basin. Geol Soc Am, Boulder, CO, p. 353–387.

Chaytor JD, ten Brink US, Solow AR, Andrews BD (2009) Size distribution of submarine landslides along the U.S. Atlantic margin. Mar Geo doi:10.1016/j.margeo.2008.08.007.

Coleman JM, Prior DB, Lindsay JF (1983) Deltaic influences on shelf edge instability processes. In: Stanley DJ, Moore GT (eds) The shelfbreak: Critical interface on continental margins, Soc Econ Paleontol Mineral Spec Pub 33: 121–137.

Dewey JW, Dellinger JA (2008) Location of the Green Canyon (offshore southern Louisiana) seismic event of February 10, 2006. U.S. Geol Surv, Open-File Rep 2008–1184, 30 pp.

Doyle LJ, Holmes CW (1985) Shallow structure, stratigraphy, and carbonate sedimentary processes of West Florida Continental Slope. Am Assoc Pet Geo Bull 69:1133–1144.

Dugan B, Flemings PB (2000) Overpressure and fluid flow in the New Jersey continental slope: Implications for slope failure and cold seeps. Science 289:288–291.

Freeman-Lynde RP (1983) Cretaceous and Tertiary samples dredged from the Florida Escarpment, eastern Gulf of Mexico. Trans Gulf Coast Assoc Geo Soc 33:91–99.

Goodwin RH, Prior DB (1989) Geometry and depositional sequences of the Mississippi Canyon, Gulf of Mexico. J Sed Pet 59:318–329.

Knight W (2006) Model predictions of Gulf and southern Atlantic coast tsunami impacts from a distribution of sources. Sci Tsunami Haz 24: 304–312.

Lee GW, Watkins JS, Bryant WR (1996) Bryant Canyon fan system: An unconfined large river-sourced system in the northwestern Gulf of Mexico. Am. Assoc. Pet. Geo. Bull. 80: 340–358.

Lee EYD, George RA (2004) High-resolution geological AUV survey results across a portion of the eastern Sigsbee Escarpment. Am Assoc Pet Geo Bull 88:747–764.

Lynett P, Liu PLF (2002) A numerical study of submarine-landslide-generated waves and run-up. Proc R Soc Lond A 458:2885–2910.

Mullins HT, Gardulski AF, Hine AC (1986) Catastrophic collapse of the West Florida carbonate platform margin. Geology 14:167–170.

Orange DL, Angell MM, Brand JR, Thomson J, Buddin T, Williams M, Hart W, Berger WJ (2004) Geologic and shallow salt tectonic setting of the Mad Dog and Atlantis fields: Relationship between salt, faults, and seafloor geomorphology. The Lead Edge 23:354–365.

Paull CK, Freeman-Lynde RP, Bralower TJ, Gardemal JM, Neumann AC, D'Argenio B, Marsella E (1990) Geology of the strata exposed on the Florida Escarpment. Mar Geol 91:177–194.

Piper JN and Behrens WE (2003) Downslope sediment transport processes and sediment distributions at the East Breaks, northwest Gulf of Mexico. In: Roberts HH et al (eds) Proc 23rd Ann Gulf Coast Sect SEPM Res Conf, Houston, TX, 359–385.

Rothwell RG, Kenyon NH, McGregor BA (1991) Sedimentary features of the south Texas continental slope as revealed by side-scan sonar and high-resolution seismic data. Am Assoc Pet Geo Bull 75:298–312.

Sager WW, MacDonald IR, Hou R (2004) Side-scan sonar imaging of hydrocarbon seeps on the Louisiana continental slope: Am Assoc Pet Geo Bull 88:725–746.

Salvador A (1991) Triassic-Jurassic. In: Salvador A (ed) The Geology of North America, Vol. J, Gulf of Mexico Basin. Geological Society of America, Boulder, CO, p. 131–180.

Schwab WC, Lee HJ, Twichell DC, Locat J, Nelson CH, McArthur WG, Kenyon NH (1996) Sediment mass-flow processes on a depositional lobe, outer Mississippi Fan. J Sed Res 66:916–927.

Silva AJ, Baxter CDP, LaRosa PT, Bryant WR (2004) Investigation of mass wasting on the continental slope and rise. Mar Geol 203:355–366.

Sohl N, Martinez E, Salmeron-Urena P, Soto-Jaramillo F (1991) Upper Cretaceous. In: Salvador A (ed) The Geology of North America, Vol. J, Gulf of Mexico Basin. Geol Soc Am, Boulder, CO, p. 205–244.

Trabant P, Watts P, Lettieri FL, Jamieson A (2001) East Breaks slump, northwest Gulf of Mexico. Offshore Tech Conf, Houston, TX, OTC12960: 231–238.

Tripsanas EK, Bryant WR, Phaneuf BA (2004) Slope-instability processes caused by salt movements in a complex deep-water environment, Bryant Canyon area, northwest Gulf of Mexico. Am Assoc Pet Geo Bull 88: 801–824.

Twichell DC, Schwab WC, Nelson CH, Lee HJ, Kenyon NH (1992) Characteristics of a sandy depositional lobe on the outer Mississippi Fan from SeaMARC IA sidescan sonar images. Geology 20:689–692.

Twichell DC, Valentine PC, Parson LM (1993) Slope failure of carbonate sediment on the West Florida Slope. In: Schwab WC et al. (eds) Submarine landslides: Selected studies in the U.S. Exclusive Economic Zone, U. S. Geol Surv Bull 2002: 69–78.

Twichell DC, Dillon WP, Paull CK, Kenyon NH (1996) Morphology of carbonate escarpments as an indicator of erosional processes. In: Gardner JV et al. (eds) Geology of the United States' Seafloor: The view from GLORIA, New York, 97–107.

Twichell DC, Nelson CH, Kenyon N, Schwab W (in press) The influence of external processes on the latest Pleistocene and Holocene evolution of the Mississippi Fan. In: Kneller B et al. (eds) External Controls on Deep Water Depositional Systems: Climate, sea-level, and Sediment Flux, SEPM Spec Pub.

Walker JR, Massingill JV (1970) Slump features on the Mississippi Fan, northeastern Gulf of Mexico. Geo Soc Am Bull 81:3101–3108.

Weimer P (1989) Sequence stratigraphy of the Mississippi Fan (Plio-Pleistocene), Gulf of Mexico. Geo-Mar Lett 9:185–272.

Weimer P, Dixon BT (1994) Regional sequence stratigraphic setting of the Mississippi Fan complex, northern deep Gulf of Mexico: Implications for evolution of the northern Gulf basin margin. In: Weimer P et al. (eds) Submarine fans and turbidite systems: Sequence stratigraphy, reservoir architecture and production characteristics, GCSEPM Found 15th Ann Res Conf 373–381.

A Study of the Tsunami Effects of Two Landslides in the St. Lawrence Estuary

R. Poncet, C. Campbell, F. Dias, J. Locat, and D. Mosher

Abstract The Lower St. Lawrence Estuary (LSLE) is a 230 km long by 50 km wide trough with a broad, flat floor with maximum water depths of 400 m and "shelves" that sit in water depths of < 60 m. It is partly filled with thick glaciomarine and post-glacial sediments and lies within close proximity to the Charlevoix Seismic Zone, the most seismically active region of eastern Canada. The purpose of this paper is to present the modelled tsunami effects of two submarine landslides from the LSLE. A regional seafloor mapping project revealed several submarine landslides on the slopes and channel floor of the LSLE. The tsunamigenic effects of two instability features in the area were investigated. The features chosen were: (1) a blocky submarine landslide that covers an area of ~3 km², a run-out distance of 1.2 km and maximum slab thickness of 20 m; and (2) a lateral spread feature with a 4 km long headwall escarpment and a maximum slab thickness of 10.5 m, which may be a candidate for a future landslide. Using a numerical wave tank, the nonlinear shallow water equations were solved for motions induced by the submarine instability features. The equations are solved numerically by the finite volume method, and the code is able to model accurately tsunami runup and drawdown.

Keywords Submarine landslide • tsunami • numerical simulation • St. Lawrence estuary

R. Poncet and F. Dias (✉)
Centre de Mathématiques et de Leurs Applications, Ecole Normale Supérieure de Cachan and CNRS, France
e-mail: Frederic.Dias@cmla.ens-cachan.fr; Raphael.Poncet@cmla.ens-cachan.fr

C. Campbell and D. Mosher
Natural Resources Canada – Atlantic, Dartmouth, Nova Scotia, Canada
e-mail: cacampbe@nrcan.gc.ca; dmosher@nrcan.gc.ca

J. Locat
Département de géologie et de génie géologique, Université Laval, Québec, Canada
e-mail: Jacques.Locat@ggl.ulaval.ca

1   Introduction

In the past, submarine landslides have not been particularly well researched because of their inaccessibility and wrongly inferred lack of direct societal consequence. However, with increasing awareness of the potential of tsunami generation and increasing development of offshore regions, there is a need for better understanding of offshore landslide processes, landslide potential and tsunami-generation capability (Locat and Lee 2002; Bardet et al. 2003). This need is coupled with great advances in underwater mapping technologies and tsunami modeling capabilities over the past decade and a half (Bardet et al. 2003). Increased resolution of seafloor bathymetry combined with improved computer processing have led to increased sophistication of tsunami wave modeling, permitting better prediction of tsunami impact potential.

Although massive landslides on the continental margin can prove devastating, such as the 1929 landslide and tsunami off the Grand Banks of Newfoundland (Mosher and Piper 2007), it is coastal landslides that can affect local communities and represent a greater hazard because of their proximity to societal infrastructure (Mosher et al. 2004; Mosher 2008). These locally generated landslides can directly impact marine infrastructure, but also can cause tsunamis that impact subaerial infrastructure with great consequence.

The Laurentian Valley coastal zone of Quebec, along the St. Lawrence River and estuary, is an area of thick Quaternary sediment accumulation, elevated seismicity and human habitation. In some areas, the sediments have been leached by meteoric processes making them geotechnically "sensitive". Mazzotti (2007) explains higher than expected seismicity potential in this region because of elevated strain rates related to ongoing postglacial rebound along the paleotectonic suture that forms the valley (Fig. 1). Lamontagne (2009) reviews potential seismic triggers to submarine landslides in this region. Along the banks and submarine slope of the St. Lawrence estuary and the Saguenay Fjord are numerous examples of mass failure (e.g. Cauchon-Voyer et al. 2007; Levesque et al. 2006; Urgeles et al. 2001). Most are prehistoric but a few are recent, e.g. 1663 and circa 1860 (Cauchon-Voyer et al. 2007). Depending upon conditions of failure and location, a modern instability event in these areas could readily cause damage to underwater structures and generate waves that impact coastal infrastructure and potentially propagate up river.

2   Regional Geological Setting

The St. Lawrence Estuary trends parallel to a faulted contact between Appalachian and St. Lawrence Platform bedrock to the south and Grenvilian basement to the north (Fig. 2) (Campbell et al. 2008). The contact forms the Laurentian Channel trough which varies from a half graben to graben structure, bounded by normal faults to the north and south (Tremblay et al. 2003; Pinet et al. 2008). Thick deposits of Quaternary sediments partially fill the Laurentian Channel trough and there is evidence that most of the Quaternary sediments in the Estuary were
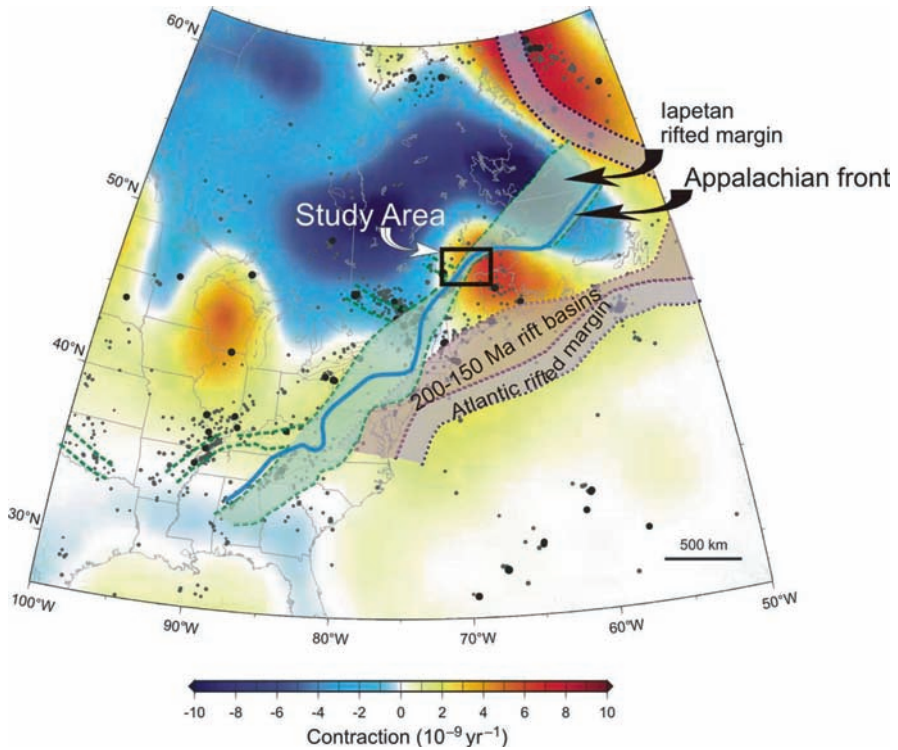
Fig. 1 Calculated postglacial rebound strain rates and seismicity (*black dots*) of eastern North America overlain with major tectonic elements (from Mazzotti 2007). The Appalachian front passes up the St. Lawrence valley and through the study area
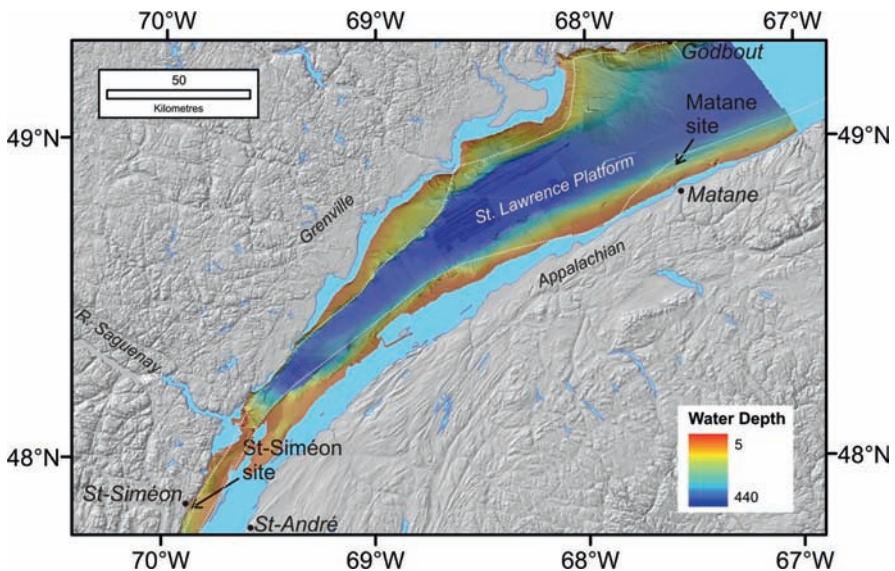
Fig. 2 Map of the St. Lawrence Estuary showing the Matane and St-Siméon study areas. *White dashed lines* delineate contact between major bedrock units (boundaries modified from Pinet et al. 2008)

deposited during the last deglaciation (Syvitski and Praeg 1989; St-Onge et al. 2008). The modern seafloor morphology can, therefore, be attributed to recent glacial excavation and erosive processes, as well as much older regional tectonic elements.

The trough-like morphology of the St. Lawrence Estuary provides an excellent natural laboratory for studying submarine instability features. The deepest part of the trough is only 440 m deep and is, therefore, very accessible. Shelf areas flank the north and south sides of the trough in water depths of 60 m or less. The slopes that mark the transition from shelf to estuary floor range from > 4° along the northern slope and 1°–3° along the southern slope. A number of large rivers enter the estuary from the north and have built deltas and submarine fans.

2.1   Study Sites

Two submarine landslide locations were selected in the Lower St. Lawrence Estuary in order to model the tsunamigenic effects of the landslides. The study sites are described below.

2.1.1   Location 1 – Matane

The Matane location is interpreted as a lateral spread feature. The location has been described previously by Campbell et al. (2008). Regionally, the slope off Matane has the lowest gradient in the study area. Multibeam bathymetry data reveal a fissure on the seabed in the area in ~ 200 m water depth approximately 7 km offshore from the town of Matane, Québec (Figs. 2 and 3). The main fissure is 4 km long, 180 m wide and 15 m deep with *en echelon* fractures present at the western portion of the fissure (Fig. 3). Approximately 800 m downslope, compressional ridges are present (Figs. 3 and 4). Gas venting features (pockmarks) are common on the seafloor in this area. High resolution seismic reflection data show an area of acoustic wipeout below the fissure (Fig. 4). Downslope from the fissure, seismic reflections are continuous with the exception of the upper 10 m which is incoherent and undulates. The disturbed interval is conformably overlain by ~2 m of acoustically stratified sediment, giving the feature an age of ~500 years through correlation with dated piston cores in the area (Campbell et al. 2008).

The Matane location was selected because it provides a unique opportunity to model the potential tsunamigenic effects of an area that may fail in the future. Because the area has not failed completely, it is possible to accurately determine the parameters δ and μ for the models (see below). If the seabed fails at this location and a slide develops, the slab thickness would likely be 10–11 m and the seabed would fail along the transition between homogeneous glaciomarine clay and postglacial silty clay. Campbell et al. (2008) have shown that seabed failure in the area is common at this stratigraphic level.
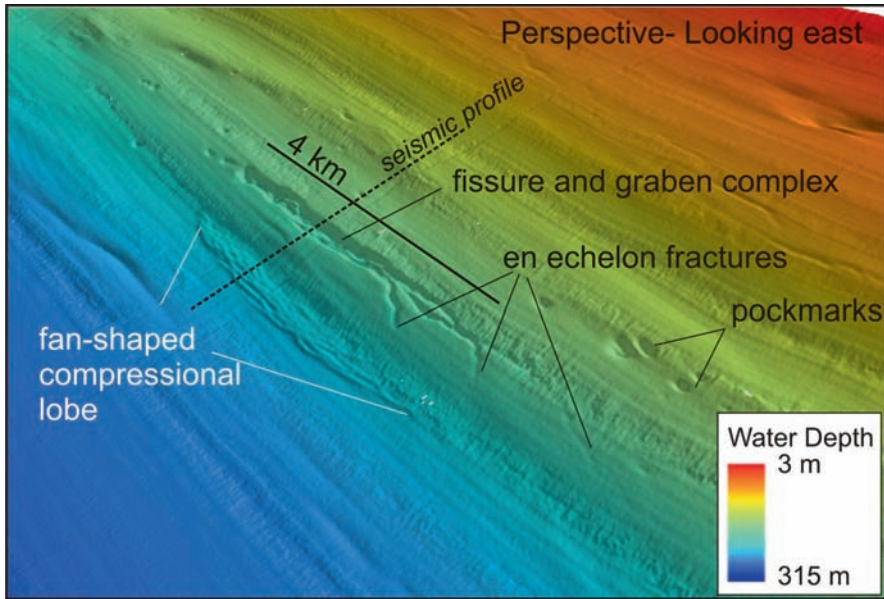
Fig. 3 Perspective view of high resolution bathymetry of the lateral spread feature at the Matane site. Note the graben developed at the headwall of the slide and the compressional folds at the toe (modified from Campbell et al. 2008)
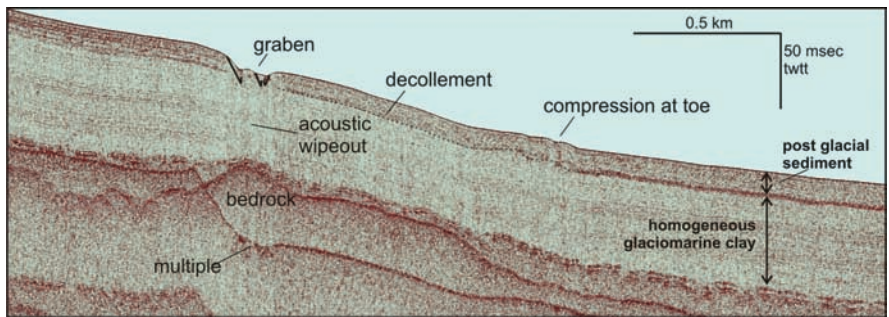
Fig. 4 High resolution seismic reflection profile across the Matane site. The slide decollement is approximately 11 m below the seabed at the transition between homogeneous glaciomarine clay and post glacial sediments (modified from Campbell et al. 2008)

2.1.2 Location 2 – St-Siméon

The St-Siméon location is interpreted as a blocky coastal landslide along the northern flanks of the St. Lawrence Estuary (Figs. 2 and 5). Along this section of the St. Lawrence Estuary, the northern slope exceeds 15° and the seafloor drops dramatically to a flat channel floor at a depth of ~90 m (Fig. 5). Multibeam bathymetry mapping reveals that much of the seafloor at the base of the steep northern slope is
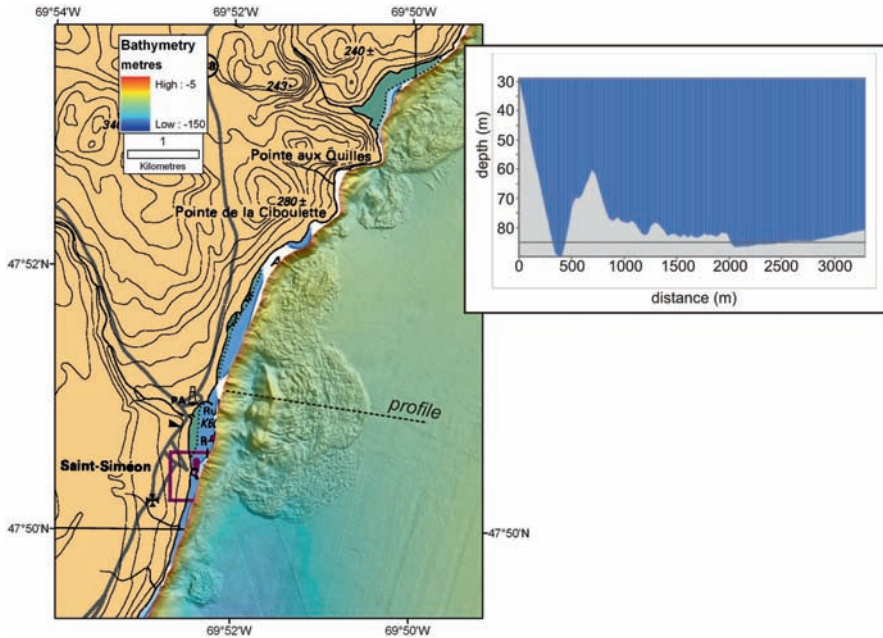
Fig. 5 High resolution bathymetry map of the St-Siméon site. The inset shows a depth profile across the landslide. The slope of the headwall exceeds 15°. Individual slide blocks are up to 20 m thick

covered with landslide deposits. The St-Siméon slide comprises large, intact blocks up to 20 m thick and up to 1 km² in area. The deposit is likely composed of glacial till which is the dominant surficial material in the area. The failure may have had a sub-aerial component as well, given its close proximity to the shore.

The St-Siméon location was selected because it appears to be representative of the style of failure that has occurred along much of this part of the Estuary. The deposit is located just a few hundred meters offshore from the village of St-Siméon (Fig. 5).

3   The VOLNA Code

The VOLNA code is an efficient numerical wave tank, which solves the nonlinear shallow water equations on unstructured triangular meshes, with an emphasis on tsunami and storm surge numerical modeling. It uses a finite volume method, blending a second order approximate HLLC spatial Riemann solver together with a third order Runge-Kutta time integration algorithm. The code was described and validated following the standards described in Synolakis et al. (2008). By using unstructured grids, flow computations can be carried out in almost any area. Moreover, the resolution of the computational domain can be adjusted to the simulation features. Here, the meshes are thoroughly refined near the landslide areas
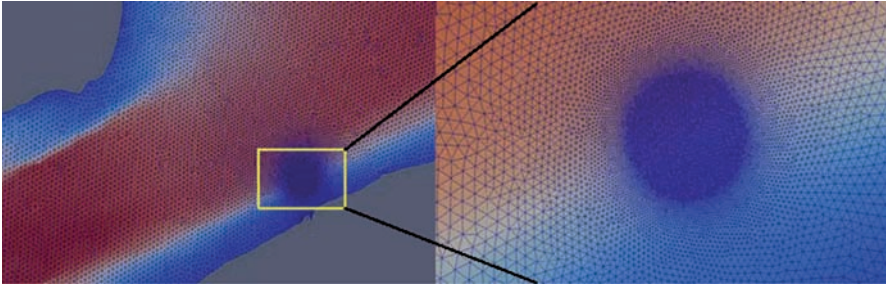
Fig. 6 Computational mesh used for the Matane landslide scenario. The respective typical characteristic lengths of coarse and fine triangles are 1 km and 30 m

(Fig. 6), achieving orders of magnitude savings in terms of grid size, compared to Cartesian grids with similar fine resolution.

VOLNA has been validated against several analytical solutions and wave tank experiments. In particular, it is able to accurately reproduce wave runup and drawdown, as well as the generation of a tsunamigenic wave from seafloor motion.

Numerical simulations of landslide generated tsunamis have been carried out with VOLNA, for the Matane and St-Siméon scenarios. The bathymetry was interpolated on the computational mesh using natural neighbors' interpolation (Sibson 1981). The landslide induced seafloor motion is included in the code by using an analytical Gaussian-shaped mass moving with constant acceleration (Liu et al. 2003). In both cases, the mesh size was approximately 150,000 triangles.

4 Results

In the Matane case, the tsunamigenic wave stays mostly confined near its generation zone, and only small disturbances (between 4 or 5 cm) propagate downstream or upstream. The tsunami takes approximately 15 min to reach Godbout on the opposite side, where the maximal surface elevation can vary between 10 and 40 cm, depending on local bathymetry features. Figure 7 represents the evolution of the water height at two different locations. In Matane, one would expect a leading depression wave. The fact that the landslide occurs so close to the shore probably explains why the leading depression wave is not seen. Figure 9 represents a snapshot of the free surface at two different moments: one just after the beginning of the landslide, and one just before the tsunami hits the opposite side.

In the St-Siméon case, the landslide mass is higher, and the estuary shallower. Hence, the wave hitting the shore on the opposite side of the St. Lawrence River is more important, i.e. up to 5 m high. The first wave takes 5 min to reach the opposite side. In Fig. 8, the free surface elevation at St-André is plotted, which is across the St. Lawrence with respect to St-Siméon. One can see two snapshots of the water elevation in Fig. 10.
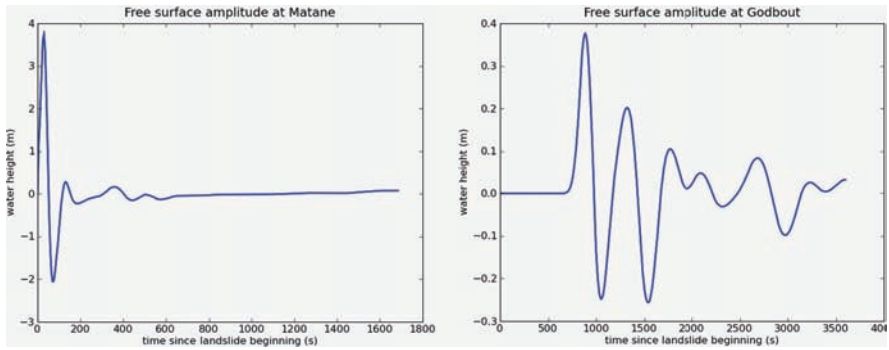
Fig. 7 Evolution of the water height near Matane (*left*), and near Godbout (*right*), on the opposite side of the St. Lawrence river with respect to Matane. Note the difference in vertical scales between the left and right plots
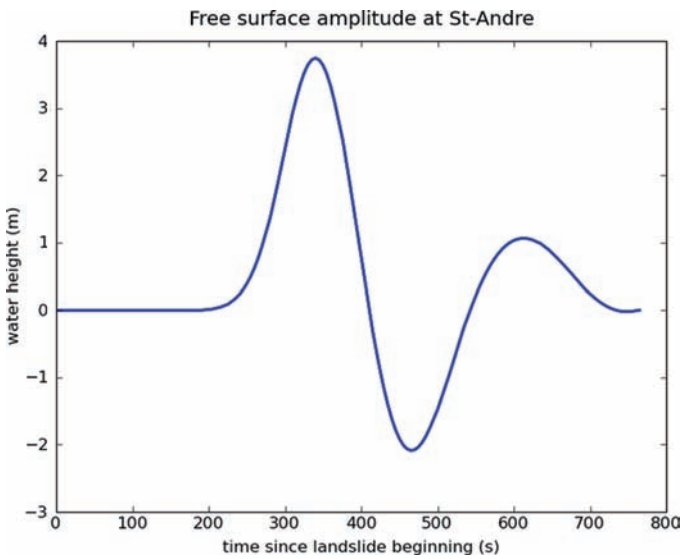
Fig. 8 Free surface elevation at St-André (on the opposite side of the St. Lawrence with respect to St-Siméon)
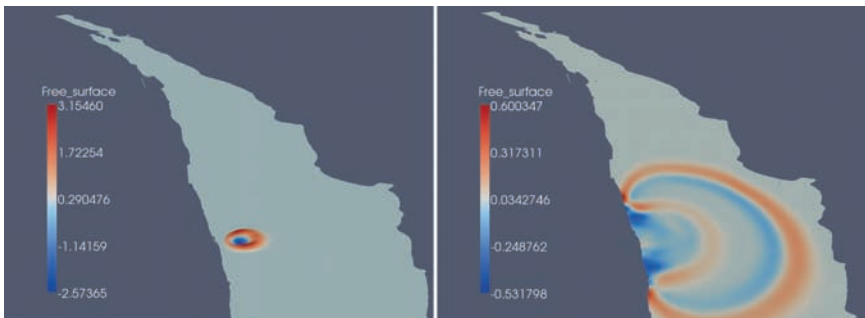
Fig. 9 Free surface elevation (in meters) at times 1 min (*left*) and 10 min (*right*) for the Matane case
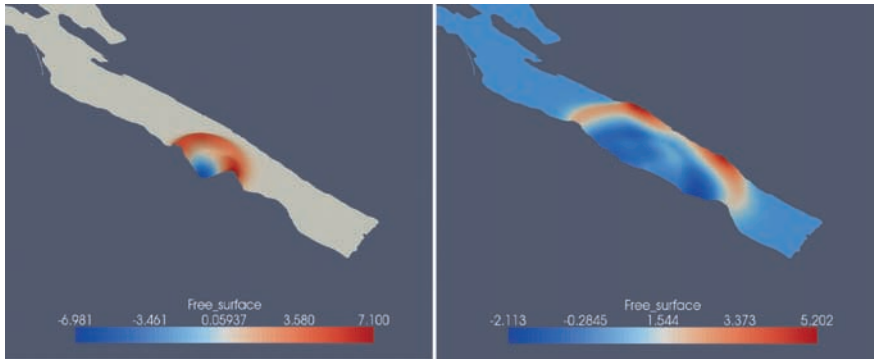
Fig. 10 Free surface elevation (in meters) at times 100 s (*left*) and 300 s (*right*) for the St-Siméon case

High precision inundation simulations, using both refined bathymetric and topographic data, might be useful in assessing risks for coastal communities, and might be carried out in the future with VOLNA. Moreover, it would also be interesting to simulate, in the St-Siméon case, the propagation of the tsunami all the way to Québec City, and obviously to model the actual seafloor motion, instead of using empirical formulas to infer the initial wave profile (Synolakis 2003).

At this stage, we emphasize that no conclusions can be drawn, in particular to support or invalidate the past occurrence of tsunamis in the St. Lawrence Estuary. It is also too early to draw any conclusions on the emergency preparedness of communities on both shores. With additional research, we may find that some of the assumptions we have used are too crude. Moreover, no sensitivity analysis has been performed. We do not know how the various parameters of the landslide (size, aspect ratio, slow creep versus sudden movement, etc.) affect the resulting wave. There is a strong need for additional research.

5   References

Bardet J-P, Synolakis CE, Davies HL, Imamura F and Okal EA (2003) Landslide tsunamis: recent findings and research directions. Pure Appl Geophys 160: 1793–1809.

Campbell DC, Duchesne M and Bolduc A (2008) Geomorphological and geophysical evidence of Holocene seafloor instability on the southern slope of the Lower St. Lawrence Estuary, Québec. In: Locat J, Perret, D, Turmel D, Demers D and Leroueil S (eds), 4th Canadian Conference on Geohazards: from Causes to Management, Les Presses de l' Université Laval, Québec, pp. 367–374.

Cauchon-Voyer G, Locat J and St-Onge G (2007) Submarine mass movements in the Betsiamites area, Lower St. Lawrence Estuary, Québec, Canada. In: Lykousis V, Sakellariou D and Locat J (eds), Submarine Mass Movements and Their Consequences, III. Springer, The Netherlands, pp. 233–241.

Lamontagne M (2009) Possible Earthquake Triggers of Submarine Landslides in the Estuary of the St. Lawrence River: Insights from the Earthquake Catalogue. Geol Surv Can Open File Rep 6007, 1 CD-ROM.

Levesque CL, Locat J and Leroueil S (2006) Dating submarine mass movements triggered by earthquakes in the Upper Saguenay Fjord, Québec, Canada. Nor J Geol 86: 231–242.

Liu PL, Lynett P and Synolakis PE (2003) Analytical solutions for forced long waves on a plane sloping beach, J Fluid Mech 478: 101–109.

Locat J, Lee HJ (2002) Submarine landslides: advances and challenges. Can Geotech J 39: 193–212.

Mazzotti S (2007) Geodynamic models for earthquake studies in intraplate North America. Geol Soc Am Spec Pap 425: 17–33.

Mosher DC (2008) Submarine mass-movements in Canada: geohazards with far reaching implications. In: Locat J, Perret, D, Turmel D, Demers D and Leroueil S (eds), 4th Canadian Conference on Geohazards: from Causes to Management, Les Presses de l' Université Laval, Québec, pp. 55–62.

Mosher DC, Piper DJW (2007) Analysis of multibeam seafloor imagery of the Laurentian Fan and the 1929 Grand Banks landslide area. In: Lykousis V, Sakellariou D and Locat J (eds), Submarine Mass Movements and Their Consequences, III. Springer, The Netherlands, pp. 77–88.

Mosher DC, Monahan PA, Barrie JV and Courtney RC (2004) Coastal submarine failures in the Strait of Georgia, British Columbia: landslides of the 1946 Vancouver Island earthquake. J Coast Res 20: 277–291.

Pinet N, Duchesne M, Lavoie D, Bolduc A and Long B (2008) Surface and subsurface signatures of gas seepage in the St. Lawrence Estuary (Canada): significance to hydrocarbon exploration. Mar Petrol Geol 25: 271–288.

Sibson R (1981) A brief description of natural neighbor interpolation (Chapter 2). In: Barnett V (ed), Interpreting Multivariate Data. Wiley, Chichester, pp. 21–36.

St-Onge G, Lajeunesse P, Duchesne MJ and Gagne H (2008) Identification and dating of a key Late Pleistocene stratigraphic unit in the St. Lawrence Estuary and Gulf (Eastern Canada). Quat Sci Rev 27: 2390–2400.

Synolakis CE (2003) Tsunami and Seiche. In: Chen F-W and Scawthorn C (eds) Earthquake Engineering Handbook, p 9–1–9–90, CRC, Boca Raton.

Synolakis CE, Bernard EN, Titov VV, Kânoglu U and Gonzalez FI (2008) Validation and verification of tsunami numerical models. Pure Appl Geophys 165: 2197–2228.

Syvitski JPM, Praeg DB (1989) Quaternary sedimentation in the St. Lawrence Estuary and adjoining areas, eastern Canada: an overview based on high resolution seismo-stratigraphy. Géographie Phys Quat 43: 291–310.

Tremblay A, Long B and Massé M (2003) Supracrustal faults of the St. Lawrence rift system, Quebec: kinematics and geometry as revealed by field mapping and marine seismic reflection data. Tectonophys 369: 231–252.

Urgeles R, Locat J, Lee H, Martin F and Konrad J-M (2001) The Saguenay Fjord: integrating marine geotechnical and geophysical data for spatial slope stability hazard analysis. An Earth Odyssey, 54th Can Geotech Soc Conf Proc. Bitech Publishers Ltd., Richmond, B.C., pp. 768–775.

The Pliocene Shelburne Mass-Movement and Consequent Tsunami, Western Scotian Slope

D.C. Mosher, Z. Xu, and J. Shimeld

Abstract Submarine mass-movement is a significant process along continental margins, even along passive margin slopes. Interpretation of seismic reflection profiles along the Scotian margin, for example, indicates the Cenozoic section is dominated by mass transport deposits (MTD) at a spectrum of scales. Occasional exceptionally large MTDs are observed which seem particularly foreign in a passive continental margin setting. The Shelburne MTD was recognized from exploration industry seismic reflection data along the western Scotian Slope. It is a buried Plio/Pleistocene feature that extends in excess of 100 km from the upper slope to the abyssal plain and maps to an area in excess of 5,990 km^2 and a volume >862 km^3. Its features demonstrate that it is a frontally-emergent MTD with a slump portion and a debris flow/run-out portion. Tsunami simulations were generated for this event, one assuming the slump portion generated the tsunami, the other, both the slump and debris flow contributed. For a mass movement comparable in scale to the Shelburne MTD, these simulations demonstrate that the city of Halifax, Nova Scotia, would be impacted within 70 to 80 minutes by a 13–25 m high wave, depending on the MTD source volume (slump or slump and debris field).

Keywords Submarine landslide • mass-failure • mass-transport deposit • tsunami • geohazard • seismic reflection

D.C. Mosher (✉) and J. Shimeld
Geological Survey of Canada, Natural Resources Canada Bedford, Institute of Oceanography,
1 Challenger Dr., Dartmouth, NS, Canada B2Y 4A2
e-mail: dmosher@nrcan.gc.ca; jshimeld@nrcan.gc.ca

Z. Xu
Canadian Hydrographic Service, Fisheries and Oceans Canada, Maurice-LaMontagne Laboratory,
PO Box 1000, Mont-Joli, Quebec, G5H 3Z4 Canada
e-mail: Zhigang.Xu@dfo-mpo.gc.ca

1 Introduction

On November 18, 1929, a submarine landslide off the Grand Banks of Newfoundland caused a devastating tsunami (Mosher and Piper 2007), demonstrating that even passive continental margins are prone to submarine geologic hazards. The landslide and ensuing turbidity current severed 12 undersea trans-Atlantic communication cables (Doxsee 1948) and the tsunami claimed 28 lives on the south coast of Newfoundland. Mosher and Piper (2007) showed from seafloor multibeam bathymetric data that there is little telltale geomorphologic evidence that a catastrophic event as recent as 80 years ago occurred; the slope morphology looks much the same as the remainder of the continental margin. In contrast, seismic imaging of the eastern Atlantic margin has led to the understanding that submarine mass failure is a significant process along the continental slope; mass transport deposits (MTD) probably comprising in excess of 50% of the stratigraphic section. These deposits occur at a spectrum of scales, but occasional exceptionally large (>100's of km^3) MTDs are observed. The initiating mechanisms of such deposits along passive margins remain enigmatic. Additionally, given that a seemingly geologically unrecognizable mass-failure generated a tsunami in 1929, there is a question as to the tsunami-generating capability of these exceptionally large MTDs. The Shelburne mega-slump is one such mass failure identified on seismic data from the western Scotian Slope (Fig. 1). Study of its stratigraphic position, morphology and seismic attributes are used to determine its origin and depositional style, and its metrics are used to numerically synthesize a resulting tsunami and its potential impact.

1.1 Regional Geology

Rifting of the Nova Scotia margin began in the Middle Triassic to Early Jurassic (230–175 Ma), followed by Jurassic seafloor spreading (Wade and MacLean 1990). Thick Jurassic and Cretaceous strata overlie Triassic salt (Wade and MacLean 1990), the latter of which has mobilized into significant salt diapirs and salt canopies that affect even the modern seafloor morphology. Prodeltaic shales accumulated along the Scotian margin during the Tertiary and continued fine-grained sediment progradation dominated through to the present. Deep canyon incision during major sea level lowstands occurred through the Tertiary and again in the Quaternary. In the later Miocene, the Western Boundary Under-current influenced sediment distribution on the margin (Campbell and Mosher, this volume) creating unconformities in some locations and sedimentary deposits in others. Rapid sedimentation of largely fine-grained sediments ensued with the onset of terrestrial glaciation during the Pliocene and ice sheets extended close to the shelf edge in the Pleistocene, drastically affecting sea level and shelf and slope sedimentation processes (Mosher et al. 2004). Low-grade seismicity along the margin occurs even into the present, in part related to remnant glacial rebound strain and in part inherited from old tectonic terrains (Mazzotti 2007).
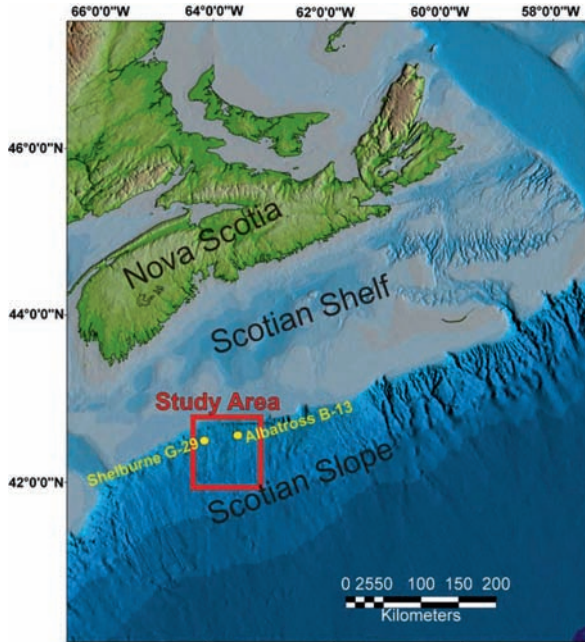
Fig. 1 Study area location on the Scotian margin, also showing the location of two adjacent exploration wells

1.2 Methods

The principal data set used in this research is part of a 2D multichannel seismic grid (8 × 8 km-spacing) covering the Scotian margin with 35,000 line-km of data. These data were acquired for with the vessel Geco-Prakla using a 7,918 in^3 airgun array towed at 7.5 m depth and an 8,000 m long hydrophone array consisting of 320 channels with 25 m group interval. The shot point interval was 37.5 m resulting in 106-fold data. Signals were sampled for 14 s at a 2 ms sample interval. Data were processed with re-sampling to 4 ms, radon multiple attenuation, spherical divergence and exponential gain recovery, deconvolution, brute stack, NMO, DMO stack, FK filter and Kirchoff migration, time variant filter, FX deconvolution and relative amplitude scaling. Seismic data were imported into Seismic Micro-Technology Inc. Kingdom Suite version 8.2 interpretation software for imaging and horizon tracing. Horizons were digitally picked and isochron maps rendered within this software suite.

The tsunami model used for this study is based on a set of depth-averaged, linearized shallow water equations with the Coriolis force and frictional force included. The numerical algorithm for the simulation is similar to that proposed by Heaps (1969), but the dynamics is assembled in a highly sparse matrix. With such

a dynamics matrix, we can use it in one of two ways: (1) matrix-vector multiplication, and (2) vector-matrix multiplication. The latter is suitable to generating all-source Green's function (Xu 2007) for tsunami preparedness when the source of a tsunami cannot be known beforehand. In this study, we know the location and metrics of a tsunami source and we wish to know how the consequent tsunami propagates and affects the near and far fields. This scenario calls for the first way of using the dynamics matrix; thus the tsunami simulations presented in this paper are obtained recursively by such matrix-vector multiplications, with the initial vector related to the area and height of the slump and debris flow. The model is on a spherical coordinate and grid resolution is 5 minutes in both longitudinal and latitudinal directions.

2 Results

2.1 Seismic Mapping

Investigation of the TGS seismic grid along the Scotian margin led to identification of many MTDs in the Cenozoic succession. Some of these MTDs are exceptionally large, involving >100 km^3 of sediment. One of the largest and youngest identified is referred to as the Shelburne megaslump (Shimeld et al. 2003), located adjacent to the Shelburne G-29 exploration well on the western Scotian Slope (Fig. 1). This well was drilled in 1985 in 1,154 m water depth to a target depth of 4,005 m. The Albatross B-13 exploration well, drilled in 1,341 m water depth to a total depth of 4,046 m, is about 10 km to the east of the MTD.

The Shelburne MTD appears to consist of two fundamental parts, based on the seismic reflection profiles: at the upslope portion, in present water depths of 750–1,350 m, is a <700 ms thick deposit of folded and faulted stratigraphy (Figs. 2 and 3). The base of this deposit rests on top of conformable reflections. The top of the deposit is irregular because of faults and contorted folds, but it has been infilled with chaotic reflections, leveling out the terrain. Above this contorted and incoherent unit, there is largely coherent stratigraphy that is ~600 ms thick at its upslope extent and 100–200 ms thick above the folds at the outboard end. The contorted unit truncates abruptly against a ramp of undeformed stratigraphy (Figs. 2 and 3), marked in Fig. 2 at the downslope position of the labeled slump. Laterally, the unit defines a sharp contact with undisturbed stratigraphy in a similar ramp-like contact. This upslope deformed part of the Shelburne MTD maps to an area of 260 km^2.

The second part of the Shelburne MTD commences at the aforementioned undeformed ramp. The contorted unit abuts against the ramp in the downslope direction and then continues on top of undeformed section, creating a deposit of incoherent and deformed reflections that is initially about a maximum of 400 ms thick. The base of this deposit defines a high amplitude reflector which appears to occasionally skip to different stratigraphic levels. The top of the unit is highly irregular with
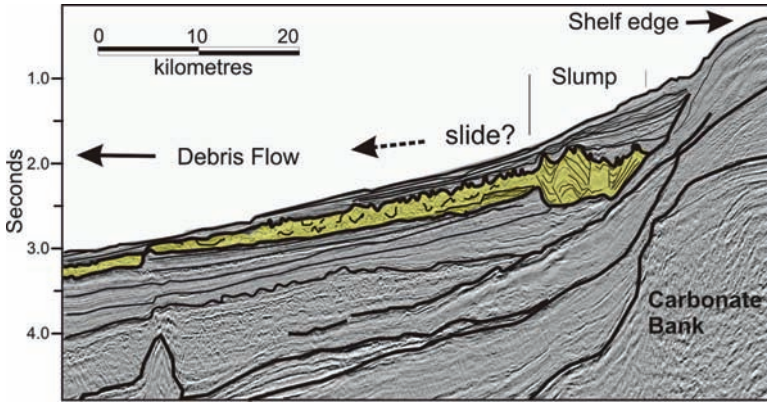
Fig. 2 Seismic profile showing the upslope portion of the Shelburne MTD (*highlighted in yellow*). The slump transitions to a debris flow in a frontally-confined manner, with a possible slide portion involved in the transition
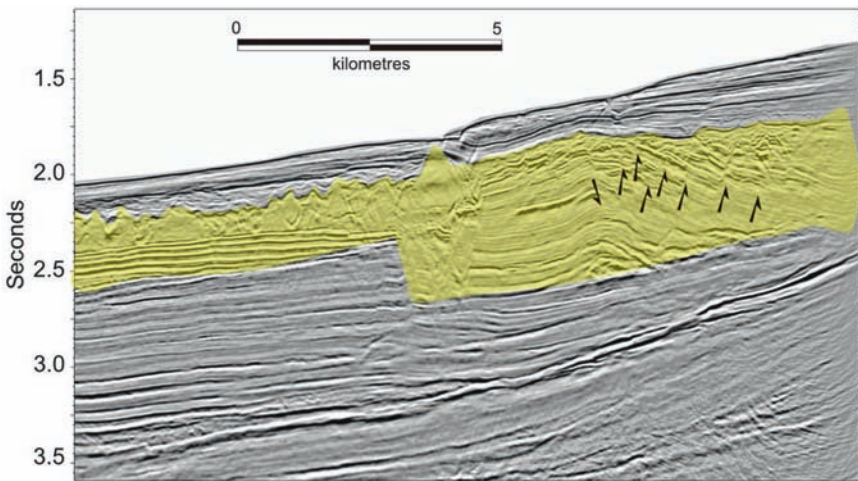
Fig. 3 Dip seismic profile showing an enlargement of the slump region of the Shelburne MTD. It demonstrates a rotational component in the upslope region, frontal confinement downslope, and over-topping the frontal ramp as a slide/debris flow

relief of 10's to >100 ms. Internally, the deposit consists of a mélange of coherent but contorted and incoherent reflections. Beyond about 14 km downslope of the ramp, internal reflections of the deposit become nearly incoherent and it's top is smooth relative to the initial portion. Occasional high amplitude reflection events appear within the deposits that are coherent over kilometers of distance. The unit thins distally from the contorted unit, extending 80 km in the downslope direction

and fanning out laterally (along strike) to the east and west, covering a total area of about 5,730 km². Along its lateral and downslope edges, the incoherent unit develops into conformable, high amplitude and coherent reflections.

There are no direct velocity data within the Shelburne MTD, but ties to the Shelburne G-29 well log data show the equivalent interval has velocities averaging about 2,000 m/s. This value is in agreement with refraction velocity analyses conducted further to the east in the Torbrook block (LeBlanc et al. 2007). This value of 2,000 m/s was used to convert time–thickness to thickness in meters. As line spacing is insufficient over the feature to directly derive its spatial dimensions, the total volume was calculated by first determining sediment thickness along line, then generating an isopach map using a grid interval of 800 × 800 m (Fig. 4) with an inverse-weighted distance technique. The volume of each grid element was calculated using the thickness value for that element and then all grid elements were summed to provide total volume for the feature. Using this technique, the average thickness of the upslope portion of the feature is ~450 m and its volume is 117 km³, covering an area of 260 km² (Table 1).
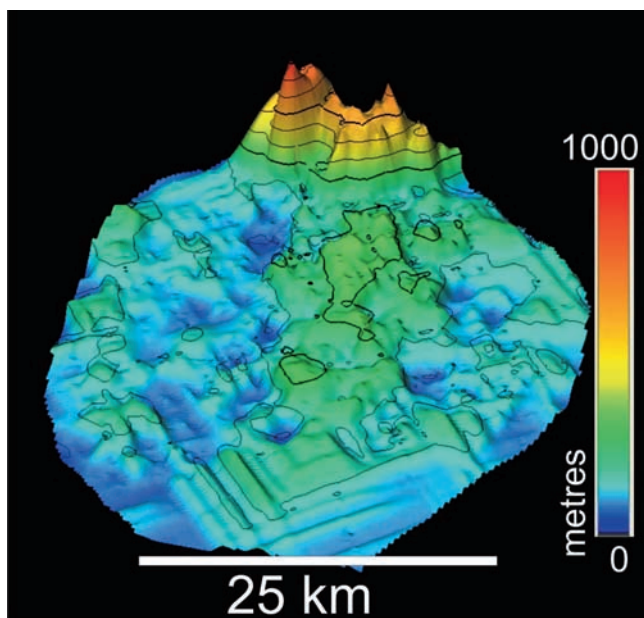
Fig. 4 Isopach of the Shelburne MTD, upslope perspective view

Table 1 Metrics of the Shelburne MTD

	Area (km²)	Thickness (km)	Volume (km³)	Dip length (km)
Slump	260	0.450	117	10
Debris	5,730	0.129	745	80
Total	5,990		862	90

The second portion of the MTD, with strongly incoherent reflections, covers an area of 5,730 km². Its average thickness is 129 m and total volume is 745 km³. The total volume of mobilized sediment for the Shelburne MTD, therefore, is about 862 km³ affecting a total area of about 5,990 km² (Fig. 4). The entire unit rests on a major regional unconformity that spans nearly the entire Scotian margin (Campbell and Mosher, this volume). With ties to the Shelburne G-29 well, this unconformity is recognized to be probable mid-Miocene in age. The top of the MTD appears to be capped by sediment judged to be Late Pliocene to very Early Pleistocene in age. The mass failure, therefore, likely occurred about the time of the Plio-Pleistocene boundary.

2.2   Tsunami Simulation

The characteristics of a tsunami generated by a submarine landslide are mainly determined by the volume, the initial acceleration, the maximum velocity, the water depth and the possible retrogressive behaviour of the landslide (Harbitz et al. 2006). Two tsunami models were calculated and simulations were produced (Fig. 5); (1) the input function used only the metrics of the slump portion of the MTD, and (2) the input function used the slump and debris flow components. There is little knowledge of volumes of material that may have been displaced as a translational slide versus slump, yet a slide may be more efficient at generating a tsunami than a slump (Grilli and Watts 2005). For the purposes of these tsunami solutions, the seafloor is assumed to have displaced by an instantaneous vertical displacement of the MTD thickness and area. It is also assumed that the water depth at the time of failure was equivalent to todays. Wave dissipation and friction are considered in the numerical solution.

Figure 5a shows the synthesized tsunami wave field, generated by the slump portion of the MTD, as it strikes Halifax. The initial wave is negative because of the style of seafloor displacement reflected at the sea surface. This surface deformation results in initial drawdown impacting most of the central and southwestern coast of Nova Scotia at about 50 minutes post failure, followed by a 13 m-high wave striking Halifax at about 70 minutes (Fig. 5b). Figure 5c shows the tsunami wave field generated by the slump and debris flow combined. In this case, because the centre of deformation is slightly outboard, the leading negative wave arrival time at Halifax is 60 minutes post-failure and the first inundation wave reaches Halifax, the capital and principal population centre at about 75 minutes (Fig. 5d). Due to local topographic wave amplification, it is over 25 m in height. The wavefront of the tsunami impacts the eastern seaboard of the U.S. coastline after about 180 minutes, again with a leading negative wave. In the first scenario (slump only), the inundation wave is only 0.13 m high at New York. In the second scenario, with the slump and debris field, the inundation wave is 3 m at New York. The tsunami wave hits Bermuda
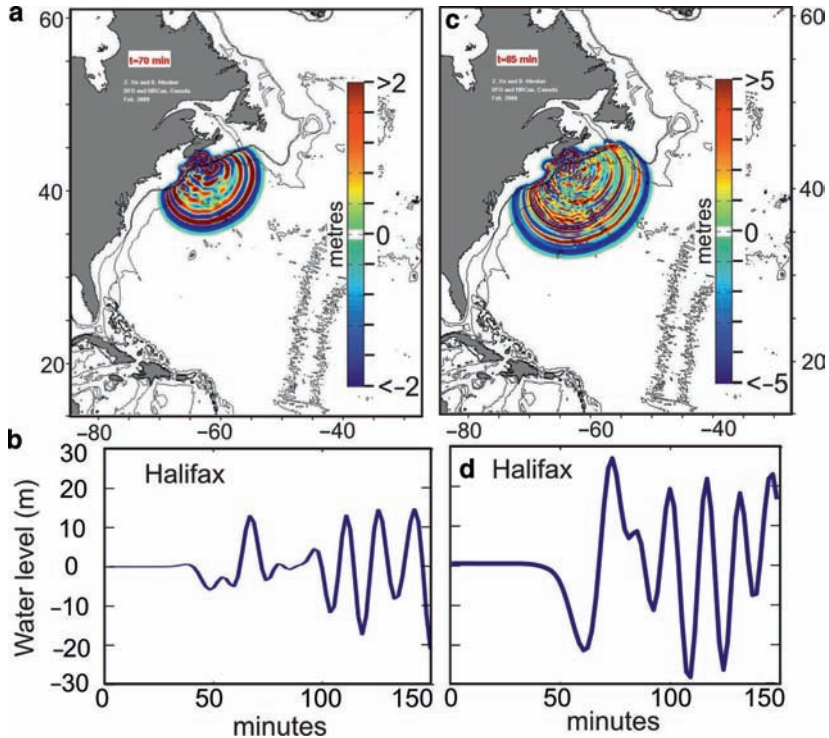
Fig. 5 Results of tsunami simulations based on initiation by the Shelburne MTD. (**a**) and (**b**) show results from a tsunami generated solely by the slump, whereas (**c**) and (**d**) show results from a tsunami generated by the slump and debris flow. In both cases, the leading wave is negative as a result of the initial landslide displacement, followed by a positive inundation wave. In scenario (**a**), a 13 m high tsunami wave strikes Halifax at about 70 minutes post-failure. In scenario (**b**), a 28 m high wave strikes Halifax at about 80 minutes post-failure

at about the same time as Halifax; over five times the distance, but the wave velocity is greater in deep water.

3   Discussion and Conclusion

The two principal units of the Shelburne MTD describe a "frontally-emergent" submarine landslide as defined by Frey-Martinez et al. (2006), with a blocky initial portion terminating abruptly against a ramp and then a thinner deposit of chaotic reflections overtopping the ramp and spreading downslope. This initial portion, showing folding, contortion and faulting, is interpreted to represent the initial

slump of the Shelburne landslide, enlarged in the seismic profile on Fig. 3 and shown as the thickest portion in the isopach map on Fig. 4. This upslope portion shows clear evidence of seaward dipping faults and landward-verging folds, probably in response to initial extension and rotation during failure (Fig. 3). Outboard, the faults are landward dipping and folds seaward-verging in response to compression of the mass abutting the ramp (Figs. 2 and 3), thus the slump appears to have been partially contained by this ramp. Material of incoherent reflections infill low areas on top of the deposit (i.e. in the synclines of folds and grabens of faults), likely material that slumped onto the deposit after initial rotation and translation of the main mass.

The MTD overtops the frontal ramp at its downdip and outboard position and spills onto what is probably the paleo-seafloor. It spreads downslope and laterally as a ~200 to 400 m thick debris flow, although initial coherent stratigraphy within the deposit probably reflects a slide component. Coherent but contorted reflections within the flow and its hummocky surface at this upslope portion suggest that the flow was blocky, perhaps transporting relatively intact blocks of sediment as it transitioned from a slump to slide to a debris flow. Beyond about 14 km downslope from the ramp, the surface of the deposit is smoother and internal reflections are chaotic, suggesting a well-mixed debris flow. Occasional coherent and relatively continuous reflectors within the deposit may represent internal flow shear or confluence of different branches of the flow. The deposit occasionally skips to lower or higher stratigraphic levels, likely reflecting the complexities in the paleo-seafloor. At its lateral extents, contorted reflections merge into laterally coherent reflections, likely representing transition of the failure from debris flow to turbidity current.

The Shelburne MTD maps from available seismic data to a total area of nearly 5,990 km², and a volume of 862 km³. This volume is five times that of the 1929 Grand Banks landslide (Piper and Aksu 1987; McCall et al. 2005), and equivalent to the initial failure of the Storegga slide (Storegga is an accumulation of at least three distinct events) (Haflidison et al. 2005; Mason et al. 2006). Although the trigger mechanism for the Shelburne MTD is beyond the subject of this study, it is presumably earthquake initiated, as suggested by Mosher et al. (1994) for most mass-failures on the Scotian margin and as was the case for the 1929 landslide. The Grand Banks and Storegga landslides are known to have generated tsunamis that impacted surrounding coastlines. In the case of the 1929 event, wave heights of 3–8 m are estimated with run up elevations of 13 m (Ruffman 1997; Clague et al. 2003). For the Storegga submarine landslide, maximum run up heights of 20 m above the contemporaneous high tide level are suggested (Bondevik et al. (2005). Bondevik et al. (2005) and Lovholt et al (2005) modeled tsunamis from this slide, assuming retrogressive slide behaviour and calculated open water wave heights between 5.7 and 7.2 m and wave heights in excess of 20 m at a coastal site proximal to the source (Sula, Norway). Our two tsunami simulations for the Shelburne MTD; one generated by just the slump portion of the MTD and another by the slump and debris flow, demonstrate open water wave heights of 2 and 5 m, respectively. Inundation waves striking Halifax, 200 km from the failure site, arrive 70–80 minutes

post-failure with wave heights of 13–25 m. If such waves inundated Halifax at the time of the failure, all evidence onshore would either be now submerged or eliminated by subsequent Pleistocene glaciations. In both scenarios, such events today would clearly pose significant risk to life and societal infrastructure along the Nova Scotia coastline.

References

Bondevik S, Lovholt F, Harbitz C, Mangerud J, Dawson A, Scendsen JI (2005) The Storegga slide tsunami – comparing field observations with numerical simulations. Mar Pet Geol 22: 195–208.

Campbell DC and Mosher DC (this volume) Middle Cenozoic unconformities and slope failure on the western Scotian margin. In: Mosher DC et al (eds) Submarine Mass Movements and Their Consequences IV. Springer, The Netherlands.

Clague JJ, Munro A, Murty TS (2003) Tsunami hazard and risk in Canada. Nat Hazards 28: 433–461.

Doxsee WW (1948) The grand banks earthquake of November 18, 1929. Publ Dom Obs 7.

Frey-Martinez J, Cartwright J, James D (2006) Frontally confined versus frontally emergent submarine landslides: a 3D seismic characterization. Mar Petrol Geol 23: 585–604.

Grilli ST, Watts P (2005) Tsunami generation by submarine mass failure: modeling, experimental validation, and sensitivity analyses. J Waterw Port C 131: 283–297.

Haflidason H, Lien R, Sejrup HP, Forsberg CF, Bryn P (2005) The dating and morphemetry of the Storegga Slide. Mar Petrol Geol 22: 123–136.

Harbitz CB, Løvholt F, Pedersen G, Masson DG (2006) Mechanisms of tsunami generation by submarine landslides: a short review. Nor J Geol 86: 255–264.

Heaps NS (1969) A two-dimensional numerical sea model. Philos Trans R Soc Lon A, Math Phys Sci, 265: 93–137.

LeBlanc C, Louden K, Mosher DC (2007) Gas hydrates on the Nova Scotia Slope: velocity models from wide-angle seismic profiles. Mar Petrol Geol 24: 321–334.

Lovholt F, Harbitz CB, Haugen KB (2005) A parametric study of tsunamis generated by submarine slides in the Ormen Lange/Storegga area off western Norway. Mar Petrol Geol 22: 219–231.

Mason D, Harbitz C, Wynn R, Pederson G, Lovholt F (2006) Submarine landslides: processes, triggers and hazard protection. Philos Trans R Soc 364: 2009–2039.

Mazzotti S (2007) Geodynamic models for earthquake studies in intraplate North America. In: Stein S, Mazzotti S (eds) Continental Intraplate Earthquakes Science, Hazard, and Policy Issues. Geol Soc Am Spec Pap 425: 17–33.

McCall C, Morrison ML, Piper DJW, (2005) Geological data from the St. Pierre Slope around the epicentre of the 1929 Grand Banks earthquake. Geol Surv Can Open File: 4879.

Mosher DC, Moran KM and Hiscott RN (1994) Late Quaternary sediment, sediment mass-flow processes and slope instability on the Scotian Slope. Sedimentol 41: 1039–1061.

Mosher DC, Piper DJW (2007) Analysis of multibeam seafloor imagery of the Laurentian Fan and the 1929 Grand Banks landslide area. In: Lykousis V, Dimitris S, Locat J (eds) Submarine Mass Movements and Their Consequences, III. Springer, The Netherlands, 77–88.

Mosher DC, Piper DJW, Campbell DC, Jenner KA (2004) Near surface geology and sediment failure geohazards of the central Scotian Slope. Am Assoc Petrol Geol Bull 88: 703–723.

Piper DJW, Aksu AE (1987) The Source and origin of the 1929 Grand Banks turbidity current inferred from sediment budgets. Geo-Mar Lett 7: 177–182.

Ruffman A (1997) Tsunami runup mapping as an emergency preparedness planning tool: the 1929 tsunami in St. Lawrence, Newfoundland. Geomarine Associates, Contract Report for Emergency Preparedness Canada (EPC), Ottawa, Ontario 1: 107 pp.

Shimeld JW, Warren SN, Mosher DC, MacRae RA (2003) Tertiary-aged megaslumps under the Scotian Slope, south of the LaHave Platform, offshore Nova Scotia. In: Joint Meet, Program with Abstr, Geol Soc Am (NE Sect) and the Atl Geosci Soc, Halifax, Nova Scotia.

Wade JA, MacLean BC (1990) Aspects of the geology of the Scotian Basin from recent seismic and well data. In: Keen MJ, Williams GL (eds) Geology of the continental margin off eastern Canada. Geol Surv Can, Geology of Canada, No. 2 (also Geol Soc Am, The Geology of North America, I-1: 190–2380).

Xu Z (2007) The all-source Green's function and its applications to tsunami problems. Sci Tsunami Hazards 26: 59–69.

Author Index

Subject Index